

Detecting few-body quantum chaos: out-of-time ordered correlators at saturation

Dragan Marković^{a,b} and Mihailo Čubrović^b

^a*Department of Physics, University of Belgrade, Studentski Trg 12-16, 11000 Belgrade, Serbia*

^b*Center for the Study of Complex Systems, Institute of Physics Belgrade, University of Belgrade, Pregrevica 118, 11080 Belgrade, Serbia*

E-mail: vokramnagard@gmail.com, cubrovic@ipb.ac.rs

ABSTRACT: We study numerically and analytically the time dependence and saturation of out-of-time ordered correlators (OTOC) in chaotic few-body quantum-mechanical systems: quantum Henon-Heiles system (weakly chaotic), BMN matrix quantum mechanics (strongly chaotic) and Gaussian random matrix ensembles. The growth pattern of quantum-mechanical OTOC is complex and nonuniversal, with no clear exponential regime at relevant timescales in any of the examples studied (which is not in contradiction to the exponential growth found in the literature for many-body systems, i.e. fields). On the other hand, the plateau (saturated) value of OTOC reached at long times decreases with temperature in a simple and universal way: $\exp(\text{const.}/T^2)$ for strong chaos (including random matrices) and $\exp(\text{const.}/T)$ for weak chaos. For small matrices and sufficiently complex operators, there is also another, high-temperature regime where the saturated OTOC grows with temperature. Therefore, the plateau OTOC value is a meaningful indicator of few-body quantum chaos. We also discuss some general consequences of our findings for the AdS/CFT duality.

KEYWORDS: AdS-CFT Correspondence, Field Theories in Lower Dimensions, Random Systems, Matrix Models

ARXIV EPRINT: [2202.09443](https://arxiv.org/abs/2202.09443)

Contents

1	Introduction	1
2	OTOC in quantum-mechanical systems	3
2.1	An upper bound on OTOC saturation	4
3	OTOC for random matrix ensembles	5
3.1	Estimate of the OTOC and its plateau	6
3.1.1	Kinematic OTOC	7
3.1.2	OTOC for dense and/or random operators	9
3.2	Numerical checks	9
4	OTOC for weakly and strongly chaotic Hamiltonians	11
4.1	Weak chaos: perturbation theory	12
4.2	Weak chaos: examples and numerics	15
4.3	Strong chaos: numerics and the return to random matrices	18
5	Discussion and conclusions	19
A	Detailed structure and calculation of OTOC for Gaussian orthogonal ensembles	21
A.1	The large matrix limit	24

1 Introduction

Recent years have seen a renewed interest in classical and quantum chaos in the context of high-energy physics, black holes and AdS/CFT, thanks to the relation of chaos to quantum information theory and the information problems of black holes. Sharp and reasonably rigorous results such as the celebrated MSS chaos bound [1] and its subsequent refinements [2, 3] establish a connection between chaos and the fundamental properties of gravity and black holes [4, 5]. Maximal chaos, with the Lyapunov exponent $\lambda = 2\pi T$ at temperature T , is reached for strongly coupled field theories in the large N limit, which have a classical gravity dual with a black hole. In [2] and other works it is explicitly shown how the Lyapunov exponent changes with finite N effects.

However, it has been pointed out many times, also in the pioneering MSS paper [1], that the multiple notions of quantum chaos in the literature mean different things. The out-of-time ordered correlation function (OTOC), given by the expectation value of the commutator of some operators A and B at times 0 and t :

$$C(t) \equiv \langle |[A(t), B(0)]|^2 \rangle, \quad (1.1)$$

is a natural quantity in quantum field theories, i.e. many-body systems, and defines the quantum Lyapunov exponent λ as the exponent of the time growth of OTOC. However, the classical limit of this exponent does not necessarily have much to do with the classical Lyapunov exponent λ_{class} , obtained by solving the variational equations [6–8]. The reason is the noncommutation of the three limits to be taken: the classical limit $\hbar \rightarrow 0$, the long-time limit $t \rightarrow \infty$, and the small initial variation limit $\delta x(0) \rightarrow 0$. The crucial insight of [7, 8] is that the mechanism of scrambling may be the chaotic dynamics, in which case λ_{class} is related though still not identical to the OTOC exponent (quantum Lyapunov exponent) λ , or it may originate in local instability (hyperbolicity), in which case even regular systems may have a nonzero λ exponent and likewise chaotic systems may have λ which is completely unrelated to the classical counterpart.

This mismatch between the classical and quantum Lyapunov exponent is just the tip of the iceberg. The problem is twofold: not only what is the relation between the quantum (OTOC) exponent and classical chaos, but also what is the relation between the quantum Lyapunov exponent λ and other indicators of quantum chaos such as, first and foremost, level statistics. The bread and butter of quantum chaos is the famous Dyson threefold way leading to the Wigner surmise, the level repulsion statistics determined solely by the time reversal properties of the Hamiltonian [10], which follows from the random matrix approximation of chaotic Hamiltonian operators [11]. It is no secret for several years already that the black hole quasinormal mode spectra follow the random matrix statistics [12], and the OTOC of a Gaussian unitary ensemble (GUE) has been computed analytically in terms of Bessel functions in [13, 14]; the outcome is close to the expected behavior of large- N field theories only at long timescales, longer than the scrambling time; at shorter timescales there are important differences. The authors of [13] have reached a deep conclusion in this respect: random matrices have no notion of locality as the correlation of any pair of eigenvalues is described by the same universal function. This is why the OTOC of a GUE system deviates from that of a local field theory at early times, when the perturbation in field theory has not had time to spread yet (i.e. when it is still localized). Therefore, the level repulsion does not imply the usual picture of the chaotic (exponential) OTOC behavior. However, we do not know yet how this correlates to the behavior of *few-body* or more precisely few-degrees-of-freedom quantum systems as opposed to the large- N field theories with a gravity dual. In few-body systems the notion of locality (and a classical gravity dual) does not exist anyway and the main problem found by [13] is irrelevant; at the same time, such systems are often very well described by random matrix statistics, i.e. Wigner-Dyson statistics [10]. In this paper we aim to understand the behavior of OTOC in such systems. Running a bit forward, we can say that the *growth* of OTOC is rather unremarkable: we find no universal trend, and little connection to level statistics. This confirms the results found for specific examples in [8, 15].

The relation of OTOC, level statistics and the classical Lyapunov exponent was studied for few-body systems (quantum mechanics) in [8, 15–18] and the picture is inconclusive. One can have a nonzero growth exponent in integrable systems,¹ whereas fast scrambling with

¹This actually correlates with the classical variational equations in hyperbolic systems, which show exponential growth even in absence of chaos.

the exponent close to $2\pi T$ or at least growing linearly in T has not been found even in some clearly chaotic systems [8, 9]. Arguments for many-body systems such as spin chains even suggest that quantum-chaotic systems with Gaussian spectral statistics generically never show fast scrambling [19], but no claims of such generality have been tested or formulated for few-body quantum chaos.

Various indicators of chaos relevant also for small systems, and their relation to OTOC and scrambling were studied by [20–27] among others. In particular, in [26] some important insights can be found: even in small systems devoid of the locality notion, OTOC can be interpreted as a measure of delocalization of a state in phase space, and the oscillatory component of the OTOC dynamics has to do with the power spectrum of the system. This last insight provokes a more general question: can we learn something from the quasi-stationary regime of OTOC, where no systematic growth is present but only oscillations? In this paper we provide a partial answer from a detailed study of this saturated (asymptotic, plateau) OTOC regime: the magnitude of the OTOC average at the plateau has a simple temperature dependence, and apparently can differentiate between weak chaos (dominantly Poissonian level distribution with some admixture of the Wigner-Dyson statistics) and strong chaos (clear Wigner-Dyson level repulsion). We will demonstrate this on three representative systems: the quantum Henon-Heiles Hamiltonian, whose classical limit has mixed (regular/chaotic) phase space and thus we expect on average weak chaos, a simplified BMN matrix model (at small N) exhibiting strong chaos for most initial conditions, and Gaussian random matrices, the prototype of strong quantum chaos. The long-time limit of OTOC behaves in subtly different ways in each case.

Before we start, one caveat is in order (we will consider this issue in more detail later on): one might think that the saturated OTOC value is always trivially determined by the system size. We typically assume that the OTOC function C as defined in (1.1) behaves roughly as $C(t) \sim c/N^2 \times \exp(\lambda t)$ with c of order unity, so when $t \sim t_* \equiv \log N^2/\lambda$ the growth of $C(t)$ stops and OTOC approximately reaches unity (when appropriately normalized). But the twist is precisely that c is system-specific and in general poorly known. The leading N^2 behavior indeed determines the OTOC values for N large, but when N and c are comparable within an order of magnitude the effects of fluctuations and finite N corrections are significant. This is at the root of our observations in this work.

The plan of the paper is as follows. In section 2 we recapitulate and generalize some results on computing OTOC in quantum mechanics, and show how OTOC sensitively depends on both the Hamiltonian and the operators A, B from the definition (1.1). In section 3 we apply the general formalism to random matrix ensembles and show that the OTOC growth is a complicated and nonuniversal function but that its asymptotic value behaves in a rather simple way. Section 4 discusses the behavior of OTOC for deterministic quantum-chaotic Hamiltonians. Section 5 sums up the conclusions.

2 OTOC in quantum-mechanical systems

Consider a four-point time-disordered correlation function for a quantum-mechanical system in $0 + 1$ dimensions at temperature $T = 1/\beta$. Starting from the usual definition (1.1) as the

squared module of the commutator of the two operators A and B , we can write it out as

$$C(t) = \frac{1}{Z} \langle |[A(t), B(0)]|^2 \rangle = \frac{1}{Z} \sum_n e^{-\beta E_n} \langle n | [A(t), B(0)]|^2 | n \rangle, \quad (2.1)$$

where the averaging is both thermal and quantum mechanical: $\langle \dots \rangle = \text{tr} e^{-\beta H} \langle \text{vac} | \dots | \text{vac} \rangle$. We can pick a basis of states and express the above defining expression in terms of matrix elements of the operators (this closely follows the derivation in [8, 16]):

$$C(t) = \frac{1}{Z} \sum_{nm} e^{-\beta E_n} \langle n | [A(t), B(0)] | m \rangle \langle m | [A(t), B(0)] | n \rangle = \frac{1}{Z} \sum_{nm} e^{-\beta E_n} |c_{mn}(t)|^2, \quad (2.2)$$

where we have inserted the completeness relation $1 = \sum_m |m\rangle \langle m|$. For a single element $c_{mn}(t)$ one gets:

$$\begin{aligned} c_{mn}(t) &= \langle n | [e^{iHt} A e^{-iHt}, B] | m \rangle = \\ &= \sum_k \left(\langle n | e^{iHt} A e^{-iHt} | k \rangle \langle k | B | m \rangle - \langle n | B | k \rangle \langle k | e^{iHt} A e^{-iHt} | m \rangle \right) = \\ &= \sum_k \left(\langle n | e^{iE_n t} A e^{-iE_k t} | k \rangle \langle k | B | m \rangle - \langle n | B | k \rangle \langle k | e^{iE_k t} A e^{-iE_m t} | m \rangle \right) = \\ &= \sum_k \left(a_{nk} b_{km} e^{-iE_{kn} t} - b_{nk} a_{km} e^{-iE_{mk} t} \right), \end{aligned} \quad (2.3)$$

where in the second line we have again inserted a completeness relation and in the third line we have used the fact that we work in the energy eigenbasis. The outcome is expressed in terms of the matrix elements a_{mn}, b_{mn} of the operators in the energy basis. In practice, it may or may not be possible to compute these analytically. Specifically, for $A = x, B = p$, we get the analogue of the classical Lyapunov exponent. From now on we call this the kinematic OTOC as it is directly related to the classical trajectory. Let us now see what general bounds can be put on (2.3) from the properties of quantum-mechanical Hamiltonians.

2.1 An upper bound on OTOC saturation

We begin with a very general and very formal result, which immediately makes it clear that in a generic quantum-mechanical system (integrable or nonintegrable) OTOC can be bounded from above by a quantity which solely depends on the energy spectrum of the Hamiltonian and the choice of the operators A and B . This upper bound remains valid no matter what is the time dependence of OTOC, even if it does not have a nonzero growth exponent at all (which is quite generic in quantum mechanics). Starting from the basic equations (2.2)–(2.3), let us denote $C_{nmk} = a_{nk} b_{km}$ and $D_{nmk} = -b_{nk} a_{km}$, and estimate a single coefficient $c_{mn}(t)$ in the sum. We clearly have

$$\begin{aligned} |c_{mn}(t)| &= \left| \sum_k C_{nmk} e^{-iE_{kn} t} + D_{nmk} e^{-iE_{mk} t} \right| \leq \sum_k |C_{nmk} e^{-iE_{kn} t} + D_{nmk} e^{-iE_{mk} t}| \Rightarrow \\ |c_{mn}(t)|^2 &\leq \left(\sum_k |C_{nmk} e^{-iE_{kn} t} + D_{nmk} e^{-iE_{mk} t}| \right)^2 \leq \sum_k |C_{nmk} e^{-iE_{kn} t} + D_{nmk} e^{-iE_{mk} t}|^2 \leq \\ &\leq \sum_k \left(|C_{nmk}|^2 + |D_{nmk}|^2 + 2|C_{nmk}| |D_{nmk}| \cos(E_{mk} - E_{kn}) t \right), \end{aligned} \quad (2.4)$$

where N is the matrix size. In the second and third line we have used the inequality between the arithmetic and harmonic mean. Now we can bound the value of $C(t)$:

$$0 \leq C(t) \leq \frac{1}{Z} \sum_{nmk} e^{-\beta E_n} \left(|C_{nmk}|^2 + |D_{nmk}|^2 + 2|C_{nmk}||D_{nmk}| \cos(E_{mk} - E_{kn}) t \right) \quad (2.5)$$

This means that $C(t)$ is bounded at all times by an oscillatory function of time, whose frequencies are linear combinations of three eigenenergies ($E_{mk} - E_{kn} = E_m + E_n - 2E_k$). Such a combination is generically always nonzero for a chaotic system except when the energies coincide, e.g. $E_m = E_n = E_k$ (according to the non-resonance condition). Therefore, since OTOC is typically a non-decreasing function of time, the behavior of $C(t)$ for t large is roughly its maximum value and is likely close to the right-hand side in (2.5). This suggests that the OTOC dynamics after saturation likely consists of a very complex oscillatory pattern (with $\sim N^3$ frequencies if the Hilbert space has dimension N) superimposed on a plateau. The numerics will indeed confirm such behavior.

Another estimate, which is time-independent and relevant for our main result — the magnitude of the saturation (plateau) OTOC value, is obtained from the triangle and mean inequalities:

$$\begin{aligned} |c_{mn}(t)|^2 &\leq \left| \sum_k C_{nmk} e^{-iE_{kn}t} \right|^2 + \left| \sum_k D_{nmk} e^{-iE_{mk}t} \right|^2 \leq \sum_k |C_{nmk}|^2 + \sum_k |D_{nmk}|^2 \Rightarrow \\ C(t) &\leq \frac{1}{Z} \sum_{nm} e^{-\beta E_n} \left(|(A \cdot B)_{nm}|^2 + |(B \cdot A)_{nm}|^2 \right) \leq \frac{2}{Z} \sum_{nm} e^{-\beta E_n} |(A \cdot B)_{nm}|^2, \end{aligned} \quad (2.6)$$

where we have used the obvious relations $\sum_k C_{nmk} = (A \cdot B)_{nm}$ and $\sum_k D_{nmk} = (B \cdot A)_{nm} = (A \cdot B)_{mn}^* = (A \cdot B)_{nm}$, assuming also the hermiticity of the operators. For some models (e.g. random matrices, Henon-Heiles), this sum can be estimated in a controlled way and provides an approximation for the plateau of OTOC. These estimates are obviously very simple and very weak (in the mathematical sense) but provide us with a framework into which we can insert specific A , B and H (the Hamiltonian with energies E_n) and perform back-of-the-envelope calculations which explain the numerical findings.

3 OTOC for random matrix ensembles

Random matrix theory [10, 11] provides a highly detailed and rigorous (within its starting assumptions) stochastic effective description of the few-body quantum chaos, and allows an analytic calculation of OTOC along the lines of (2.3). Let us focus on Gaussian orthogonal ensembles of size $N \times N$, appropriate when there is full time reversal invariance. It is known [10] that the joint distribution all the elements of all eigenvectors is obtained simply from the statistical independence of the eigenvectors from each other and of the elements in each eigenvector (and the orthogonality of the eigenvectors):

$$P(\{c\}) = \left(\prod_{n=1}^N \delta \left(\sum_i (c_i^n)^2 - 1 \right) \right) \left(\prod_{n < m} \delta \left(\sum_i c_i^n c_i^m \right) \right), \quad (3.1)$$

where $i = 1 \dots N$ is the component of the eigenvector and $1 \leq n, m \leq N$ count the eigenvectors themselves, i.e. the energy levels; so the n -th eigenvector $|n\rangle$ is represented by the column vector $\psi^{(n)}$ with the elements (c_1^n, \dots, c_N^n) . Special cases like the probability distribution for the p -tuple of elements of a single eigenvector are obtained from (3.1) by integrating out all the other elements [10]. We will also need the probability distribution of the energy levels $\{E\} = E_1, E_2, \dots, E_N$, the celebrated Wigner-Dyson distribution function [10]:

$$\mathcal{P}(\{E\}) = \text{const.} \times \prod_{n < m} |E_n - E_m|^b \exp\left(-\sum_k \frac{E_k^2}{\sigma^2}\right), \quad (3.2)$$

where σ is the standard deviation, fixing the unit of energy, and $b = 1, 2$ or 4 for orthogonal, unitary and symplectic ensembles respectively. Most of our work is independent of the symmetry class, however our default class will be the Gaussian orthogonal ensemble (GOE) with $b = 1$ when not specified otherwise.

3.1 Estimate of the OTOC and its plateau

The idea is to use the results recapitulated in the previous section to find the ensemble expectation value of OTOC from the “master formulas” (2.2)–(2.3). Representing the eigenvectors and the operators as matrices in some (arbitrary) basis we can obviously write out

$$a_{nk} = \sum_{ij} \psi_i^{(n)} \psi_j^{(k)} A_{ij} \Rightarrow \langle a_{nk} \rangle = \int d^N \psi^{(n)} \int d^N \psi^{(k)} P(\psi^{(n)}, \psi^{(k)}) \psi_i^{(n)} \psi_j^{(k)} A_{ij}, \quad (3.3)$$

and similarly for b_{nk} . Inserting the above expression for the matrix elements into (2.3), multiplying $c_{mn}(t)$ by its complex conjugate taking into account the reality of the eigenvectors and relabelling the indices in the sums where convenient we find (denoting the average over the random matrix ensemble by $\langle C(t) \rangle$):

$$\begin{aligned} \langle C(t) \rangle = & \int d^{N^2} \{c\} \int d^N \{E\} \mathcal{P}(\{E\}) P(\{c\}) \sum_{n,m} \sum_{k,k'} \sum_{i_1,2} \sum_{j_1,2} \sum_{i'_1,2} \sum_{j'_1,2} \sum c_{j_1}^k c_{i_2}^k c_{j_1}^{k'} c_{i_2}^{k'} c_{i_1}^n c_{i_1}^n c_{j_2}^m c_{j_2}^m e^{-\beta E_n} \times \\ & \times \left(A_{i_1 i_2} A_{i'_1 i'_2} B_{j_1 j_2} B_{j'_1 j'_2} e^{i(E_{k'} - E_k)t} + A_{i_2 j_2} A_{i'_2 j'_2} B_{i_1 j_1} B_{i'_1 j'_1} e^{i(E_k - E_{k'})t} - \right. \\ & \left. - A_{i_2 j_2} A_{i'_1 i'_2} B_{i_1 j_1} B_{j'_1 j'_2} e^{i(E_k + E_{k'} - E_m - E_n)t} - A_{i_1 i_2} A_{i'_2 j'_2} B_{j_1 j_2} B_{i'_1 j'_1} e^{i(E_m + E_n - E_k - E_{k'})t} \right), \end{aligned} \quad (3.4)$$

where $\{c\}$ determines the whole set of N^2 random elements $c_j^{(n)}$ with $j, n = 1 \dots N$ and likewise $\{E_n\}$ is the whole set of eigenenergies. All the sums run from 1 to N . The integral over the eigenvector elements $\{c\}$ in (3.4) produces only an overall constant as these coefficients do not couple to the other quantities (in fact the integral $d^{N^2} \{c\}$ is a textbook Jeans integral, but we do not need its value as it only produces an N -dependent, T -independent constant). The remaining integral, over the eigenenergies, is again a sum of products of Jeans-type integrals but with an additional linear term $-\beta E$ in the exponent. Notice that the imaginary (sine) terms in (3.4) cancel out when the sum is performed; this

is a consequence of the module squared in $|c_{mn}|^2$, i.e. of the reality of OTOC. Now we see that (3.4) becomes a sum where each term is a product of factors of the form

$$p_i(E_i)e^{-E_i^2/4\sigma^2-\beta E_i} \cos(sE_it), \quad s \in \{0, 1\},$$

where p_i is some polynomial and s may be zero or unity, i.e. some terms have this factor and some do not. Every such term is a Jeans-type integral. The number of terms in $\mathcal{P}(\{E\})$ equals the number of partitions of $N(N-1)b/2$, and the sums over the coefficients $\{c\}$ bring altogether N^{12} terms. When everything is said and done (for details see appendix A), the final outcome, ignoring the multiplicative constant factors, reads:

$$\begin{aligned} \langle C(t) \rangle = & \prod_{a=1}^4 \sum_{\substack{\alpha_j^a = N(N-1)b/2 \\ \alpha_1^a, \dots, \alpha_N^a}} \left[{}_1F_1 \left(\frac{1+\alpha^a}{2}, \frac{1}{2}, \frac{\sigma^2}{4} (\beta-it)^2 \right) \right. \\ & + (\beta-it) {}_1F_1 \left(\frac{2+\alpha^a}{2}, \frac{3}{2}, \frac{\sigma^2}{4} (\beta-it)^2 \right) + {}_1F_1 \left(\frac{1+\alpha^a}{2}, \frac{1}{2}, \frac{\sigma^2}{4} (\beta+it)^2 \right) \\ & \left. + (\beta+it) {}_1F_1 \left(\frac{2+\alpha^a}{2}, \frac{3}{2}, \frac{\sigma^2}{4} (\beta+it)^2 \right) \right], \end{aligned} \quad (3.5)$$

where ${}_1F_1$ is the confluent hypergeometric function. The sum runs over all partitions of $N(N-1)b/2$, and the product has four terms as each factor $|c_{mn}|^2$ has four matrix elements of A and B .

3.1.1 Kinematic OTOC

In order to move further we need to specify at least to some extent the operators A and B . We will consider (1) the kinematic OTOC, with $A = x$, $B = p$ (2) generic sparse operators, with $O(N)$ nonzero elements in the matrices a_{mn} and b_{mn} , and (3) dense operators A and B , with $O(N^2)$ nonzero elements, in particular the case when the operators A , B are themselves represented by Gaussian random matrices. Let us estimate OTOC for each case.

For the kinematic OTOC, $A_{ij} = x_i \delta_{ij}$ is diagonal and in the large- N limit B can be approximated as $B_{ij} \sim \delta_{ij}/x_i$. The Kronecker deltas reduce the number of terms in the sums over $\{c\}$ to N^4 , the number of partitions $\sum_j \alpha_j = n$ can be approximated as $p(n) \sim \exp(\pi\sqrt{2n/3})/\sqrt{n}$, and the general expression (3.4) becomes²

$$\langle C(t) \rangle \sim e^{\pi\sqrt{\frac{1}{3}}N} N^3 e^{\frac{\sigma^2\beta^2}{4}} \left(W_0(\sigma\beta) + Q_1 \left(\cos \frac{\sigma^2\beta t}{2} \right) W_1(\sigma\beta) + Q_2 \left(\sin \frac{\sigma^2\beta t}{2} \right) W_2(\sigma\beta) \right), \quad (3.6)$$

where $W_{0,1,2}$ are polynomials in $\sigma\beta$ of degree $N(N-1)b/2 \sim N^2b/2$, Q_1 is an even polynomial (with only even powers) of the same degree, and Q_2 is an odd polynomial of the same degree. Each coefficient in the polynomials $W_{0,1,2}$ comes from $\sim N^2$ terms (appendix A), therefore the size of the coefficients scales approximately with N^2 . Eq. (3.6)

²One might be surprised by the unusual dependence on N . This happens because we have not normalized $C(t)$ by the product $\langle AA \rangle \langle AA \rangle$ as it is usually done. With appropriate normalization, $C(t)$ would of course be of order unity.

is a very complicated oscillating function as many terms are involved. But if we are only interested in the average value of $C(t)$ at long times, we may simply ignore the oscillations (which in the first approximation average out to some value of order unity) and write the estimate for the long-term, saturated or plateau OTOC value that we denote by C_∞ :

$$C_\infty \sim \langle C(t \rightarrow \infty) \rangle \sim e^{\pi\sqrt{\frac{b}{3}}N} N^3 e^{\frac{\sigma^2\beta^2}{4}} W_0(\sigma\beta) \quad (3.7)$$

We deliberately do not write $\lim_{t \rightarrow \infty}$ in the above definition as the limit in the strict sense does not exist because of the oscillatory functions, and in addition our derivation is obviously nothing but a crude estimate. A similarly rough estimate of the temperature dependence of C_∞ can be obtained in the following way. For sufficiently large $\sigma\beta$, roughly $\sigma\beta/N^2 > 1$, the polynomial W_0 is dominated by the highest-degree term and we have, from (3.7):

$$C_\infty \sim (\sigma\beta)^{\frac{N^2b}{2}} e^{\frac{\sigma^2\beta^2}{4}} + \dots \sim e^{\frac{\sigma^2}{4T^2}} + \dots, \quad (3.8)$$

where in the second step we have assumed $\beta \gg 1$ so that the power-law prefactor $\beta^{N^2b/2}$ becomes negligible compared to the exponential. We deliberately emphasize that there are other terms in the expansion (...), including also a constant term (from the zeroth-order term in W_0). This is important as it tells us that the scaling is in general of the form $C_\infty \approx \text{const.} + \exp(\sigma^2/4T^2)$, i.e. the temperature dependence is superimposed to a constant. This is also expected as the (appropriately normalized) saturated value C_∞ should always be of order unity, and the temperature dependence will only account for the relatively small differences between the plateau values of $C(t)$, as we will see later in figures 1 and 2.

On the other hand, for sufficiently small $\sigma\beta$, the polynomial W_0 can be estimated as a geometric sum of monomials in $-\sigma\beta N^2$ (remember the terms in W_0 have alternating signs):

$$C_\infty \sim \frac{e^{\frac{\sigma^2\beta^2}{4}}}{1 + \sigma\beta N^2} \sim 1 - \sigma\beta N^2 + O(\beta^2). \quad (3.9)$$

We have now reached an important point: the plateau OTOC falls off exponentially with $1/T^2$ at low temperatures³ and grows as a function of $1/T$ at high temperatures (we are not sure which function, as there are higher order terms in addition to the one written in (3.9), and there is no clearly dominant term like the exponential at large β), with the crossover temperature:⁴

$$T_c \sim \sigma N^2. \quad (3.10)$$

If we consider a pair of arbitrary sparse operators A and B , the whole above reasoning remains in place, except that the products of matrix elements such as $A_{i_1 i_2} A_{i'_1 i'_2} B_{j_1 j_2} B_{j'_1 j'_2}$ remain as arbitrary constants. Therefore we get the same qualitative behavior with two regimes and a crossover between them. The crossover temperature is very high for typical $N \gg 1$ (otherwise the random matrix formalism makes little sense) and finite σ (again, $\sigma \rightarrow 0$ makes little sense). In particular, in the $N \rightarrow \infty$ limit the crossover temperature becomes infinite and the only regime is the exponential decay.

³Actually, the falloff rate equals $\text{const.}/T^2$ with some system-specific constant, but for brevity we will denote it schematically as the $1/T^2$ regime throughout the paper.

⁴The crossover temperature is determined simply as $\beta_c \sigma N^2 = 1$, i.e. whether the terms in W_0 grow or decay at higher and higher order.

3.1.2 OTOC for dense and/or random operators

Now consider the case when the matrix elements in (3.5) are generically all nonzero (and for now nonrandom, i.e. we fix the operators and do not average over them). The large- t limit yields the expression

$$\langle C(t) \rangle \sim e^{\pi\sqrt{\frac{b}{3}}N} N^{11} e^{\sigma^2(\beta^2-t^2)} [q_0(\sigma t) w_0(\sigma\beta) + q_1(\sigma t) w_1(\sigma\beta + it, \sigma\beta - it)], \quad (3.11)$$

where $q_{0,1}$ and w_0 are polynomials of degree $N(N-1)b/2 \sim N^2b/2$, and w_1 is the polynomial of the same total degree of two variables, $\sigma\beta + it$ and $\sigma\beta - it$. The coefficients of $w_{0,1}$ are proportional to products of matrix elements $A_{i_1j_1} B_{k_1l_1} \dots A_{i_8j_8} B_{k_8l_8}$, which are roughly proportional to $|A|^8|B|^8$. The long-time limit yields

$$C_\infty \sim \frac{e^{\pi\sqrt{\frac{b}{3}}N}}{N^5} (|A||B|)^8 e^{\frac{\sigma^2\beta^2}{4}} w_0(\sigma\beta)w_1(\sigma\beta, \sigma\beta), \quad (3.12)$$

but now a typical coefficient of the polynomials $w_{0,1}$ behaves as $N^2(|A||B|)^8$. Therefore, the scaling in the low-temperature regime remains the same as (3.8): $C_\infty \sim \exp(\sigma^2/T^2)$. But the high-temperature regime yields

$$C_\infty \sim 1 - \sigma\beta N^2 (|A||B|)^8 + O(\beta^2), \quad (3.13)$$

therefore the crossover now happens at

$$T_c \sim \sigma N^2 (|A||B|)^8 \quad (3.14)$$

and therefore may be lower than the very high value (3.10), depending on the norm of the operators A and B .

Finally, if the operators A and B are both random Hermitian matrices (for concreteness, from the Gaussian unitary ensemble with the distribution function Π and the standard deviation ξ), we need to average also over the distribution functions for A and B and work with the double average $\langle\langle C(t) \rangle\rangle$:

$$\langle\langle C(t) \rangle\rangle \equiv \int d^N\{a\} \int d^N\{b\} \Pi(\{a\}) \Pi(\{b\}) \langle C(t) \rangle \sim \xi^{N^2} \langle C(t) \rangle. \quad (3.15)$$

This estimate is very crude, based simply on the fact that the distribution functions Π have $\sim N^2/2$ pairs of the form $(a_i - a_j)^2$. The important point is that the scaling from (3.13) that behaves essentially as $\sim \xi^{16}$ now becomes $\sim \xi^{N^2}$, therefore the crossover temperature is significantly reduced compared to (3.14) and behaves as $T_c \sim \sigma N^2 \lambda^{N^2}$. So for random operators the crossover may happen at temperatures that are not very high and thus can be clearly visible in the numerics and experiment.

3.2 Numerical checks

Now we demonstrate numerically that the crude estimates from the previous subsection indeed make sense and describe the characteristic behavior of OTOC. Our chief goal is to understand the behavior of C_∞ , however it is instructive to start from the time dependence

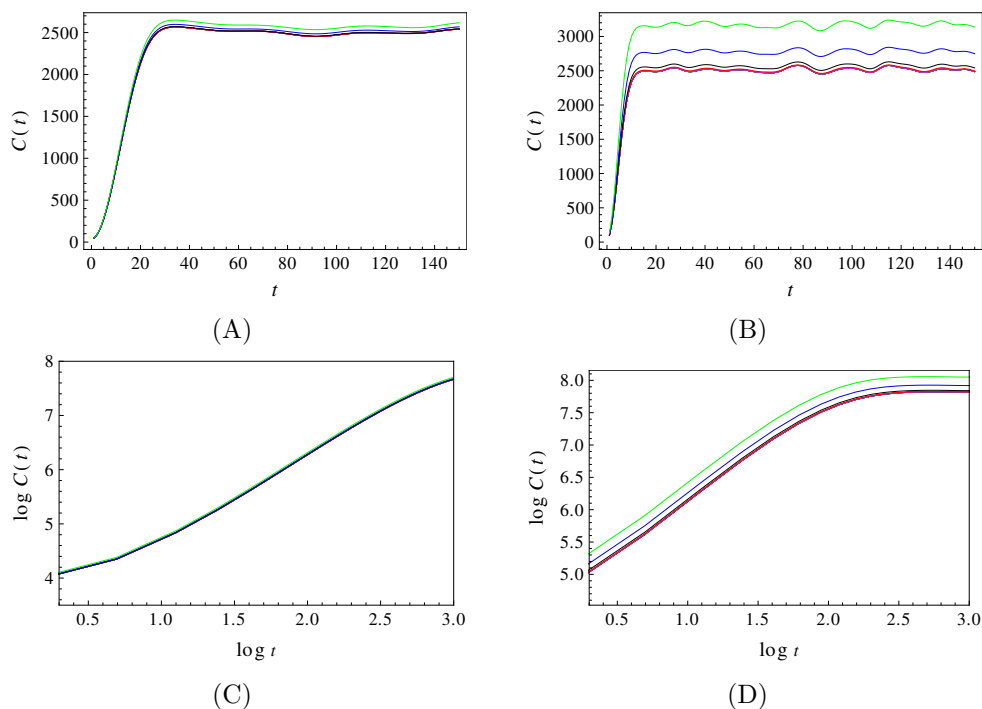


Figure 1. Numerically computed and averaged kinematic OTOC $C(t)$ for an ensemble of $l = 1000$ Gaussian orthogonal matrices of size $N = 20$ for the deviation $\sigma = 0.02$ (A, C) and $\sigma = 0.05$ (B, D), at temperatures 0.67 (black), 1.00 (blue), 1.25 (green), 2.50 (magenta), 5 (red). The plots (A, B) show the linear scale and the plots (C, D) the log-log scale. Crucially, the growth regime is not exponential and is actually closer to a power law. The growth ends on a plateau with superimposed oscillations. The plateaus differ slightly for different temperatures — the main effect we look at in this paper. Times is in units $1/\sigma$ in all plots.

of the kinematic OTOC (figure 1). We find the expected pattern of early growth followed by a plateau, however the growth is closer to a power law than to an exponential; this follows from the polynomial terms in (3.6), although the power law is not perfect either, as we see in the panels (A, C). This is in line with the prediction of [13], where the authors find

$$\langle C(t) \rangle \approx J_1^4(2t)/t^4 + t(t/2 - 1), \quad (3.16)$$

for a slightly different ensemble of random matrices (J_1 is the Bessel function of the first kind). This function is also neither an exponential nor a power law but at early times it is best approximated by a power law at leading order (at long times it falls off exponentially but the saturation is reached already prior to that epoch). In figure 2 we focus on the plateau behavior. It has the form of a constant function with superimposed aperiodic oscillations, and the differences of the plateau values are the subject of our theoretical predictions. These are relatively small and become important only when N is finite and not very large. In figure 2 we plot again the time dependence of the kinematic OTOC but now we focus on long timescales, to confirm that the plateau is indeed stable, and to show the very complex oscillation pattern superimposed on the plateau.

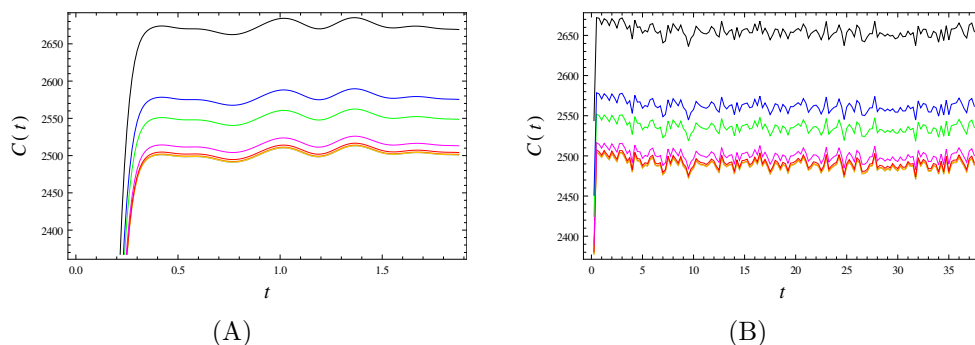


Figure 2. Numerically computed and averaged kinematic OTOC $C(t)$ for an ensemble of $l = 1000$ Gaussian orthogonal matrices of size $N = 60$ for the deviation $\sigma = 0.1$, at temperatures 0.67 (black), 1.00 (blue), 1.25 (green), 2.50 (magenta), 5 (red), 10 (orange), 20 (yellow) and 100 gray. In (B) we plot the same as in (A) but over a longer timescale, showing that the plateau remains stable for long times, i.e. represents true asymptotic behavior.

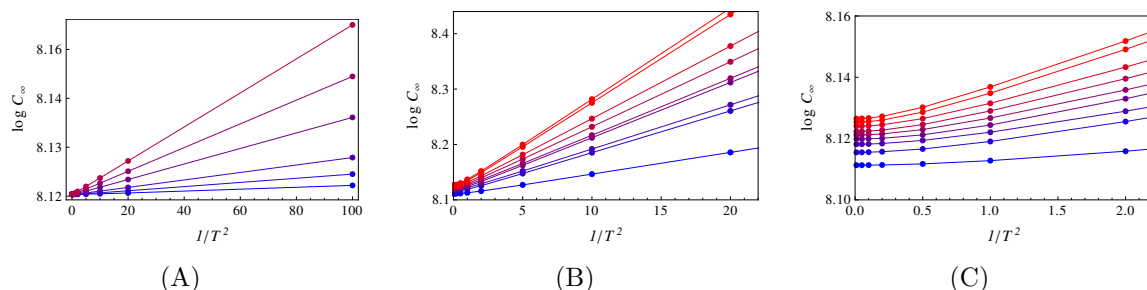


Figure 3. (A) The logarithm of the amplitude of the plateau C_∞ of the kinematic OTOC for the deviations $\sigma = 0.05, 0.1, 0.2, 0.4, 0.6, 0.8$ (blue to red) as a function of temperature for β values. The linear dependence is nearly perfect, in accordance with the predicted scaling $\log C_\infty \propto 1/T^2$. The matrix size is $N = 20$. (B) Same as (A) but for the deviation $\sigma = 0.4$ and varying matrix size $N = 10, 20, 40, 60, 80, 100$ and 120 (blue to red). In (C) we bring the zoom-in of the plot (B) for high temperatures. Apart from a slight deviation near $\beta = 0$, the behavior for larger matrices is still fully consistent with the analytical prediction. The solid lines are just to guide the eye.

Figure 3 confirms our main prediction for the low-temperature regime (again for the kinematic OTOC) — clear linear scaling of $\log C_\infty$ with $1/T^2$ in a broad range of temperatures. At small inverse temperatures there is some deviation from the linear scaling law but this we also expect. Looking now at the OTOC for a pair of random Hermitian operators in figure 4, we detect also the other regime at small enough temperatures — $\log C_\infty$ decays with the inverse temperature. This regime is likely present also in figure 3, but only at extremely high temperatures (which we have not computed in that figure).

4 OTOC for weakly and strongly chaotic Hamiltonians

For quasi-integrable few-degrees-of-freedom Hamiltonians one would naively expect that OTOC closely resembles the Lyapunov exponent, at least for high quantum numbers, approaching the classical regime. As we have already commented in the Introduction, it

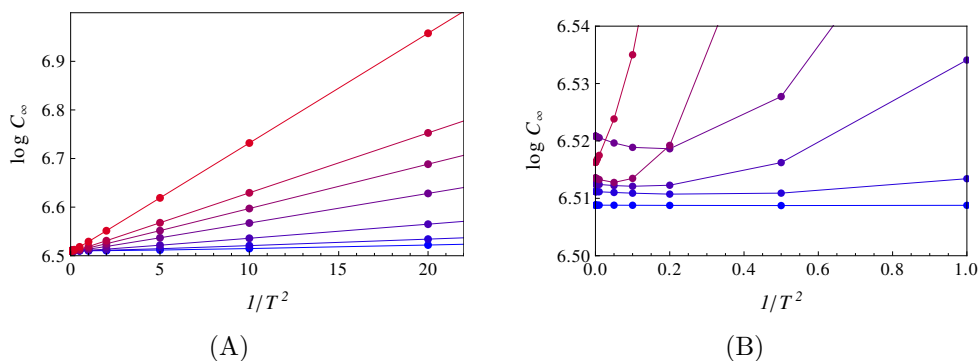


Figure 4. The saturated OTOC $C_\infty(T)$ of a pair of dense random operators A and B for the Gaussian orthogonal random Hamiltonian with $\sigma = 0.01, 0.05, 0.1, 0.2, 0.4, 0.6, 0.8$ (blue to red). In (A), looking at the full range of C_∞ values, it is obvious that the dominant regime is still the $\exp(c/T^2)$ scaling. However, focusing on the low- σ ensembles (B), we notice the high-temperature growing behavior of the OTOC plateau which is absent for sparse operators.

is known that this is not true in general [6, 8, 9, 16, 17] and that both chaotic systems with zero quantum Lyapunov exponent and regular systems with a nonzero exponent exist. We will now try to find some common denominator of OTOC dynamics in (deterministic) quantum-mechanical systems. It will quickly become clear from our general analysis of the master formula (2.3) that the function $C(t)$ is as complicated as for random matrices (indeed, even more so). But we will again construct an upper bound for the saturated OTOC value and arrive at a rough scaling estimate.

4.1 Weak chaos: perturbation theory

As an example of a quasi-integrable system (of the form $H = H_0 + \epsilon V$ where H_0 is integrable and the perturbation V makes it nonintegrable for $\epsilon \neq 0$) consider the Henon-Heiles Hamiltonian

$$H = \frac{1}{2} (p_x^2 + p_y^2) + \frac{1}{2} (\omega_x^2 x^2 + \omega_y^2 y^2) + \epsilon \left(x^2 y - \frac{1}{3} y^3 \right), \tag{4.1}$$

a well-known paradigm for classical chaos with applications in galactic dynamics and condensed matter. For $\epsilon = 0$ it obviously reduces to a 2D linear harmonic oscillator and becomes integrable. As we know, nonintegrability does not always imply chaos; indeed, this is a typical system with mixed phase space, with both chaotic and regular orbits. Chaotic orbits proliferate only when the perturbation is larger than some finite ϵ_c ; they are almost absent at low energies, numerous at intermediate energies and again absent at very high energies when the potential energy is negligible compared to the kinetic energy [28, 29]. For such a quasi-integrable system our idea is to apply elementary perturbation theory in the occupation number basis to estimate OTOC starting from (3.4). We will present the perturbation theory in a fully general way, for an arbitrary Hamiltonian $H_0 + \epsilon V$, and some of the conclusions will also turn out to be quite general. Only at the end we will show the quantitative results for the Henon-Heiles system (4.1).

Let us write the perturbative expression for OTOC. Replacing the initial basis states $|n\rangle$ with the first-order⁵ perturbatively corrected states $|n + \delta n\rangle$ and introducing likewise the perturbative corrections $\delta a_{mn}, \delta b_{mn}$ for the matrix elements of A and B , the equation (2.3) becomes

$$\begin{aligned}
c_{mn}^{(1)} &= c_{mn} + \sum_k (\delta a_{mk} b_{kn} + a_{mk} \delta b_{kn}) e^{-iE_{km}t} - \sum_k (\delta b_{mk} a_{kn} + b_{mk} \delta a_{kn}) e^{-iE_{nk}t} = \\
&= c_{mn} + \sum_{kl} (\delta_{ml} a_{lk} b_{kn} + \delta_{kl}^* a_{lm}^* b_{kn} + \delta_{kl} b_{ln} a_{mk} + \delta_{nl}^* b_{lk}^* a_{mk}) e^{-iE_{km}t} + (a \leftrightarrow b) e^{-iE_{nk}t} = \\
&= c_{mn} + \left(\delta \cdot A \cdot B + A^\dagger \cdot \delta^\dagger \cdot B + A \cdot \delta \cdot B + A \cdot B^\dagger \cdot \delta^\dagger \right)_{mn} e^{-iE_{km}t} + (A \leftrightarrow B)_{mn} e^{-iE_{nk}t}.
\end{aligned} \tag{4.2}$$

Now we insert this result into (2.2) and apply the Cauchy-Schwarz-Bunyakovski inequality:

$$\begin{aligned}
C^{(1)}(t) &= \frac{1}{Z} \sum_{mn} e^{-\beta E_n} |c_{mn}^{(1)}|^2 \leq \\
&\leq \frac{1}{Z} \sum_{mn} e^{-\beta E_n} \left(|c_{mn}|^2 + |\delta \cdot A \cdot B + A^\dagger \cdot \delta^\dagger \cdot B + A \cdot \delta \cdot B + A \cdot B^\dagger \cdot \delta^\dagger|_{mn}^2 + (A \leftrightarrow B) \right) = \\
&= C(t) + \frac{1}{Z} \left(4\text{Tr} \left(B^\dagger \cdot A^\dagger \cdot \delta^\dagger \cdot \tilde{\rho}^2 \cdot \delta \cdot A \cdot B \right) + 4\text{Tr} \left(B^\dagger \cdot \delta \cdot A \cdot \tilde{\rho}^2 \cdot A^\dagger \cdot \delta^\dagger \cdot B \right) \right) \leq \\
&\leq C_\infty + \frac{8}{Z} |\tilde{\rho}|^2 |A|^2 |B|^2 |\delta|^2 \equiv C_\infty + \delta C_\infty,
\end{aligned} \tag{4.3}$$

where $\tilde{\rho} \equiv \text{diag}(\exp(-\beta E_n))$ is the non-normalized density matrix. In the above derivation, we have also used the definition of trace and the definition of thermal expectation values $\langle A \rangle \equiv \text{Tr}(\rho \cdot A)$. The norm of a matrix is defined as usual by $|A|^2 \equiv \text{Tr} A^\dagger A$. This estimate manifestly replaces $C(t)$ by its asymptotic (maximum) value, as we have replaced the terms containing the time-dependent phase factors by their time-independent norms.

In order to move further, notice first that $|\tilde{\rho}|^2 = \sum_n \exp(-2\beta E_n) = Z(2\beta)$ for a canonical ensemble with the diagonal density matrix that we consider here. This means, from (4.3), that the temperature dependence is encapsulated in the ratio $Z(2\beta)/Z(\beta)$. The prefactor will again differ between dense and sparse A, B and V . For sparse matrices, we can write $|A|^2 \sim N a^2$ whereas for dense matrices we have $|A|^2 \sim N^2 a^2$, assuming that all matrix elements have some characteristic magnitude a . Obviously, if this is not true the outcome will be more complicated, but it seems this does not influence the temperature dependence. For concreteness we assume sparse A and B . For sparse V with nonzero elements of order v concentrated near the diagonal (this is true for the Henon-Heiles Hamiltonian and in general for perturbations expressed as low-degree polynomials in coordinates and momenta), we can estimate $|\delta|^2 \sim N v^2 / \omega^2$. Here we assume an approximately equidistant spectrum of H_0 with frequency (neighboring level spacing) ω . This yields:

$$C_\infty^{(1)} \sim C_\infty + \frac{Z(2\beta)}{Z(\beta)} N^3 a^2 b^2 \frac{v^2}{\omega^2}. \tag{4.4}$$

⁵The whole argument works the same way also for higher-order perturbation theory; we assume first order just for simplicity.

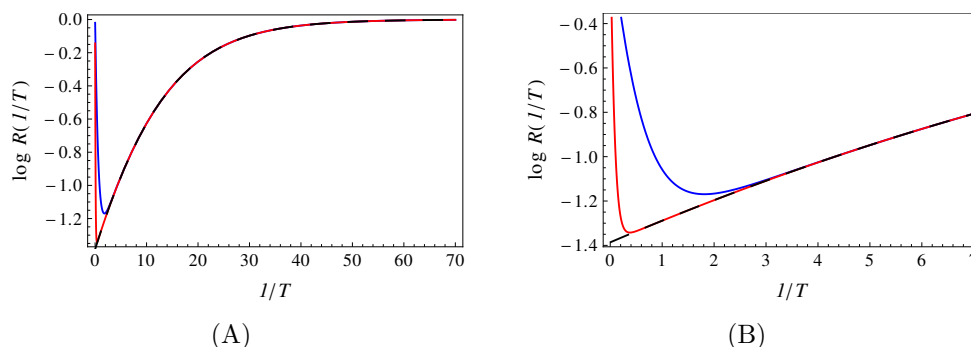


Figure 5. The thermal dependence factor of $\log C_\infty$ for weak perturbative chaotic systems, given by $Z(2\beta)/Z(\beta)$ with $\beta = 1/T$ the inverse temperature, here given for a 2D linear harmonic oscillator with the frequencies $\omega_x = \omega_y = 0.1$, with $N = 20$ levels (blue) and with $N = 150$ levels (red). We also plot the sum over $N = \infty$ levels (black). In (A) we zoom in at high β /low temperatures, and in (B) we focus on smaller β /larger T . The $N = 150$ plot is already quite close to the monotonic $N = \infty$ dependence but at high temperatures there is always a region decaying with β , before the approximately linear $\log R(1/T)$ dependence sets in, just like in the numerical results. At very low temperatures the ratio saturates, as we see in the panel (A). This ensures that our estimate for the saturated OTOC has a finite limit at zero temperature. The overall scale is arbitrary as the R factor is always multiplied by various other factors.

For a dense perturbation V , the only factor that changes is $|\delta|$. Assuming again the utterly simple situation where all matrix elements of V are roughly equal v , we have $\delta_{mn} \sim v/E_{mn} \sim v/(\omega(m-n))$, which yields a series that can be summed analytically. However, we will not pursue this further as the temperature dependence is universal in all cases, given by the simple ratio of the partition functions:

$$C_\infty \propto R(\beta) \equiv \frac{Z(2\beta)}{Z(\beta)} \rightarrow \frac{\sum_{j=1}^N e^{-2\beta\omega}}{\sum_{j=1}^N e^{-\beta\omega}} \rightarrow \frac{e^{\beta\omega}}{1 + e^{\beta\omega}}. \quad (4.5)$$

The first simplification holds when H_0 is a 1D harmonic oscillator, and the second one when $N \rightarrow \infty$. But the basic result (the ratio of partition functions) always holds. We are in fact more interested in the 2D harmonic oscillator, which is the integrable part of the Henon-Heiles Hamiltonian. For that case, we plot the sum (for finite N) in figure 5. Of course, the analysis of the function $R(\beta)$ is trivial — we plot it in the figure merely to emphasize the qualitative agreement with the numerics.

As a final remark, what we have found is the correction of the OTOC plateau δC_∞ . There is still the unperturbed value of C_∞ for the integrable Hamiltonian H_0 . We know that this can be nonzero and even quite large because of local instability [6, 7, 9]. We are mainly interested in the opposite situation, when the scrambling chiefly comes from chaos so that OTOC does not grow when $H = H_0$. In this case $C^{(1)} \approx \delta C_\infty$ and the temperature dependence is primarily determined by (4.4). In the next subsection we will look both at the Henon-Heiles system where this holds, and a perturbed inverse chaotic oscillator where H_0 is unstable.

4.2 Weak chaos: examples and numerics

As our main example we can now study the Henon-Heiles system of eq. (4.1). Starting from the nonperturbed Hamiltonian (2D harmonic oscillator), we will express the nonzero elements of $c_{mn}(t)$ exactly, i.e. we will not use the estimates (4.3) as the perturbation is quite simple and amenable to analytic treatment. Denoting a basis state by the quantum number $n = (n_x, n_y)$, we can write the amplitudes $c_{n_x n_y n'_x n'_y}$ as products of amplitudes of the two decoupled subsystems $c_{n_x n_y n'_x n'_y} = C_{n_x n'_x} C_{n_y n'_y}$, with

$$\begin{aligned} C_{n_x n_x} &= -n_x \omega_x \cos t \\ C_{n_x, n_x-2} &= \frac{i}{2} \sqrt{n_x-1} \left(\sqrt{n_x+1} e^{-i\omega_x t} - \sqrt{n_x+2} e^{i\omega_x t} \right) \\ C_{n_x, n_x+2} &= \frac{i}{2} \sqrt{n_x+1} \left(\sqrt{n_x-1} e^{i\omega_x t} - \sqrt{n_x-2} e^{-i\omega_x t} \right), \end{aligned} \tag{4.6}$$

and all other elements are zero; for the y quantum numbers the coefficients are the same with $(n_x, \omega_x) \mapsto (n_y, \omega_y)$. For nonzero ϵ , the off-diagonal matrix elements can be represented exactly as

$$c_{n_x n'_x n_y n'_y}(t) = \epsilon \delta_{|n_x-n'_x|-2} \delta_{|n_y-n'_y|-1} \sqrt{m_x(m_x-1)} \sqrt{m_y+1}, \quad m_{x,y} \equiv \min(n_{x,y}, n'_{x,y}). \tag{4.7}$$

The state vectors are now easily calculated in textbook perturbation theory. We have compared the analytic calculation to the numerics and find that they agree within a relative error ≤ 0.04 ; therefore, one may safely use (4.6)–(4.7) in order to speed up the computations and avoid numerical diagonalization of large matrices.

The magnitude of the plateau value of $C(t)$, computed by long-time averaging similarly to the random matrix calculations in section 3, are given in figure 6. At large T values, C_∞ decays with $1/T$, at intermediate values it shows an exponential growth with $1/T$ just like $R(1/T)$ in figure 5, and as the temperature goes to zero it reaches a finite value. In figure 7 we consider a system with much reduced state space, with $N = 25$. We expect that for small N the existence of two regimes is more clearly visible, and that the crossover temperature is higher. This is indeed what happens, although the exact form of the function $C_\infty(1/T)$ is not very well described by the analytical result. As we have made many crude approximations, this is not surprising: our analytical result still explains the existence of two regimes and the crossover between them.⁶ One unexpected finding is that the high-temperature regime is apparently universal for all perturbation strengths and scales as $C_\infty \propto \exp(-4\pi/T)$. This is probably specific for the Henon-Heiles system; we do not understand it at present.

It is instructive to look at the energy level statistics of the Henon-Heiles system for the same parameters that we have used for the OTOC calculation, in order to understand the relation of OTOC to chaos. In figure 8 we plot the histograms of the neighboring level

⁶One might regard such truncation of the state space as artificial and unphysical. It is clearly just a technical step in order to show the effect we seek for more clearly, however in principle it can be realized by introducing an additional external potential. In other contexts, e.g. finite spin systems, a finite Hilbert space is perfectly natural.

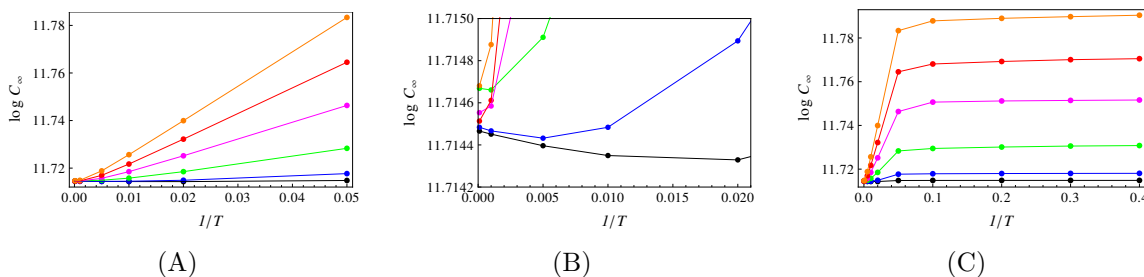


Figure 6. (A) The saturated kinematic OTOC value C_∞ for a range of inverse temperatures $\beta = 10^{-4}, 10^{-3}, 5 \times 10^{-3}, 0.01, 0.02, 0.05$ and a range of perturbation strengths $\epsilon = 1, 2, 5, 10, 15, 20$ (black, blue, green, magenta, red, orange). Here we see the scaling $C_\infty \propto \exp(c/T)$, with c growing with ϵ . In the (B) panel we zoom in the high-temperature region, to show that for $\epsilon \leq 5$ there is also the other regime where C_∞ grows with T . Since the number of points in this interval is small it is not easy to judge the form of T -dependence. In (C) we focus on the opposite regime, at very low temperature, showing that C_∞ saturates as $T \rightarrow 0$. This is again in accordance with the $\beta \rightarrow \infty$ limit of $Z(2\beta)/Z(\beta)$. The system is truncated to $N = 144$ levels.

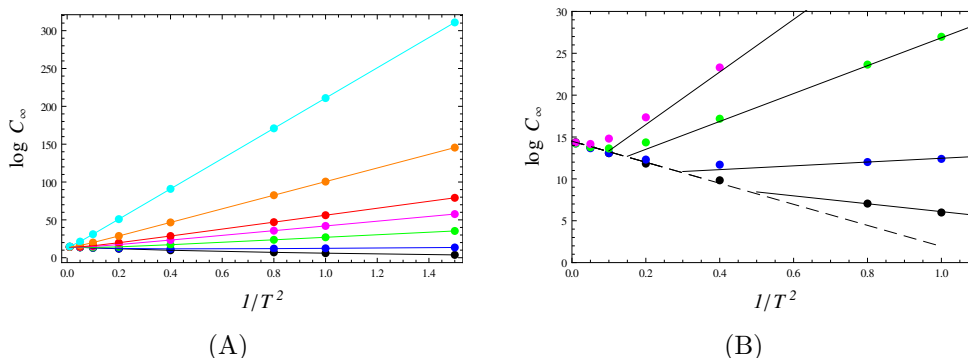


Figure 7. The saturated kinematic OTOC value $C_\infty(T)$ for the truncated Henon-Heiles model with $N = 25$ levels. The perturbation strength is $\epsilon = 0.1, 0.3, 0.5, 0.7, 0.9, 1.5, 3.0$ (black, blue, green, magenta, red, orange, cyan). Already in (A) we see that for $\epsilon \leq 0.5$ there is a finite crossover temperature T_c so that C_∞ grows with temperature for $T > T_c$. Since T_c goes down when the Hilbert space is reduced, we can observe the high-temperature regime very clearly and see that it collapses to a universal law $C_\infty \sim \exp(-4\pi/T)$. This is seen in the panel (B) where we zoom in at the interesting region.

spacing. Even for large ϵ , the regular (Poisson) component is dominant over the chaotic (Wigner-Dyson) component. In other words, the classically mixed phase space, with the increasing chaotic component, is almost completely regular in the quantum regime; quantum chaos is “weaker”, as is often found in the literature [33]. For us, the fact that the system is outside the Wigner-Dyson regime means that indeed the behavior of C_∞ is a good litmus test of quantum dynamics, behaving (at low temperatures) as $\exp(1/T^2)$ or $\exp(1/T)$ for strong or weak chaos respectively.⁷ Indeed, we would not expect that a system which is well described by perturbation theory shows strong level repulsion.

⁷In fact, this is only true provided that the scrambling is chaos-related, i.e. that the integrable limit with $\epsilon = 0$ and $H = H_0$ does not scramble significantly. We will come to this issue in the next paragraph.

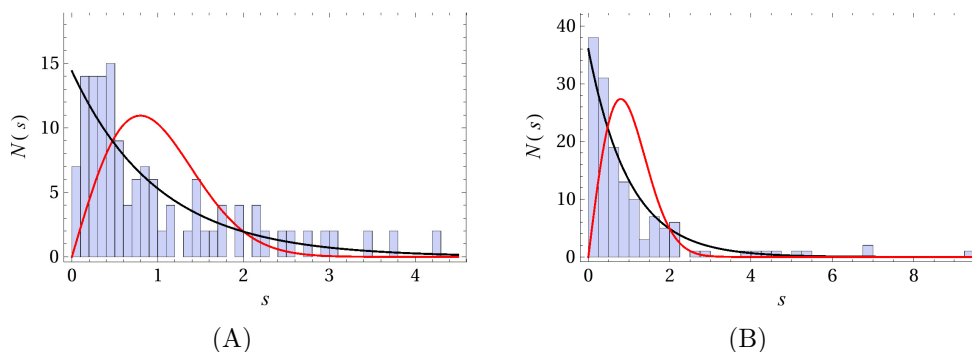


Figure 8. Distribution of neighboring energy level spacings $N(s)$ for the Henon-Heiles Hamiltonian with $\epsilon = 0.1$ (A) and $\epsilon = 1.5$ (B). In each plot we compare the level distribution to the Poisson law ($\exp(-s)$) and the Wigner-Dyson law for orthogonal matrices ($s \exp(-\pi s^2/4)$). The distribution is dominantly Poissonian even for large perturbations, although there is a small admixture of Wignerian statistics. The perturbative dynamics of the Henon-Heiles system is always weakly chaotic in quantum mechanics (despite being classically strongly chaotic for large enough ϵ).

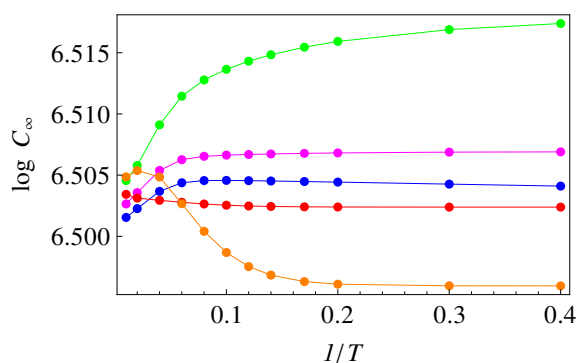


Figure 9. Temperature dependence of the asymptotic OTOC C_∞ for the inverse Henon-Heiles Hamiltonian, with $\omega_x^2 = 4\omega_y^2 = -1$, and perturbation strength $\epsilon = 0, 0.1, 0.5, 0.9, 1.5$ (blue, green, magenta, red, orange). The curves are more or less flat and without a clear trend, as the scrambling is rooted in local instability, not chaos.

Finally, it is instructive to look at the inverse Henon-Heiles system, with $(\omega_x^2, \omega_y^2) \mapsto (-\omega_x^2, -\omega_y^2)$, so that H_0 is the inverse harmonic oscillator. As already found in the literature, scrambling is significant already at $\epsilon = 0$, and this contribution dominates even at high ϵ , at all temperatures. In other words, neither the perturbation nor the temperature have a significant influence over C_∞ . This is fully in accordance with the result (4.3) and the morale is that OTOC directly describes scrambling, and chaos only indirectly, through the scrambling, *if the scrambling originates mainly from chaos*; if not, OTOC is largely insensitive to chaos. Therefore, the temperature dependence of the OTOC value, derived from the assumptions about the dynamics (perturbative chaos or strong, random-matrix chaos) cannot be seen when there is a strong non-chaotic component to scrambling (figure 9).

4.3 Strong chaos: numerics and the return to random matrices

As a final stroke, we will now examine a strongly chaotic system which is also relevant for black hole scrambling and related problems in high energy physics. This is the bosonic sector of the D0 brane matrix model known as the BMN (Berenstein-Maldacena-Nastase) model [30], obtained as a deformation of the BFSS (Banks-Fischler-Shenker-Susskind) model [31] by a mass term and a Chern-Simons term. This model has been studied in detail in the context of non-perturbative string and M theory. It is known to describe the dynamics of M theory on pp-waves and is also related to the type IIA string theory at high energies; for details one can look at the original papers or the review [32]. Following [33–36], we focus solely on the bosonic sector which is enough to have strongly chaotic dynamics with equations of motion that are not too complicated. The quantum-mechanical Hamiltonian of the BMN bosonic sector reads:⁸

$$H = \text{Tr} \left(\frac{1}{2} \Pi^i \Pi^i - \frac{1}{4} [X^i, X^j] [X^i, X^j] + \frac{1}{2} \nu^2 X^a X^a + \frac{1}{8} \nu^2 X^\alpha X^\alpha + w \varepsilon_{abc} X^a X^b X^c \right) \\ i \in \{1 \dots 9\}, \quad a, b, c \in \{1, 2, 3\}, \quad \alpha \in \{4 \dots 9\}, \quad (4.8)$$

where Π^i are the canonical momenta, X^i the canonical variables, ε_{abc} is the Levi-Civita tensor, and $\nu^2 > 0$ is the mass deformation which also determines the size of the Chern-Simons deformation (the last term in (4.8)). Following [35], we will study the “mini-BMN” model with $X^\alpha = 0$, so we effectively only have three degrees of freedom. The matrices $X_{1,2,3}$ and $P_{1,2,3}$ are $N \times N$ matrices. For this example we have to abandon the master formulas for OTOC (2.2)–(2.3) as it is very difficult to find the quantities c_{mn} — for this we would have to perform exact diagonalization of the Hamiltonian (4.8). Instead, we follow [36] and write a truncated system of equations directly for the expectation values $\langle X^a \rangle$ and $\langle P^a \rangle$ and the two-point correlators $\langle X^a X^b \rangle$, $\langle \Pi^a X^b \rangle$ and $\langle \Pi^a \Pi^b \rangle$, where the expectation value is obtained through the trace over the density matrix: $\langle X^a \rangle \equiv \text{Tr}(\rho X^a)$. The equations read (for their derivation see [36]):

$$\partial_t \langle X^a \rangle = \frac{1}{N} \langle \Pi^a \rangle \\ \frac{1}{N} \partial_t \langle \Pi^a \rangle = \langle X^b \rangle \langle X^b \rangle \langle X^a \rangle - 2 \langle X^b \rangle \langle X^a \rangle \langle X^b \rangle + \langle X^a \rangle \langle X^b \rangle \langle X^b \rangle + \nu^2 \langle X^a \rangle + w \varepsilon_{abc} \langle X^b \rangle \langle X^c \rangle + \\ + \left(X^a \langle X^b X^b \rangle - \langle X^b X^b \rangle X^a + X^b \langle X^a X^b \rangle - \langle X^a X^b \rangle X^b + w \varepsilon_{abc} \langle X^b X^c \rangle \right), \quad (4.9)$$

where the last line contains the leading quantum corrections: all possible terms with a single contraction of the classical equation of motion, and the summation over repeated indices is understood. The equations of motion for the two-point correlators are obtained again by writing the classical equations of motion for the bilinears $\Pi^a \Pi^b$, $\Pi^a X^b$ and $X^a X^b$

⁸Do not confuse with the classical action considered in [33, 35].

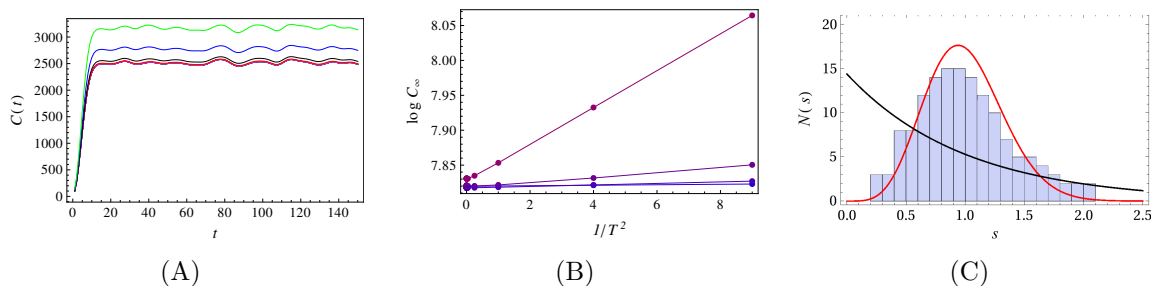


Figure 10. (A) Time dynamics $C(t)$ for the truncated quantum-mechanical mini-BMN model, with $\nu = 0.1, 0.3, 0.5, 1.0$ (red, black, blue, red), shows the expected pattern of growth followed by an oscillating plateau. (B) Temperature dependence of the saturated value $C_{\infty}(T)$ for the same values of ν (blue to red) has the same $\exp(1/T^2)$ scaling as the random matrix ensembles. The level spacing statistics, shown in (C) for $\nu = 0.5$, is indeed quite close to the Gaussian unitary ensemble (full red curve) and clearly at odds with the Poisson statistics (full black curve), confirming that this system is within the scope of our random matrix calculation.

and taking all possible single contractions in each term. This yields:

$$\partial_t \langle X^a X^b \rangle = \frac{1}{N} \left(\langle \Pi^a X^b \rangle + \langle X^a \Pi^b \rangle \right) \quad (4.10)$$

$$\begin{aligned} \partial_t \langle \Pi^a X^b \rangle = & \frac{1}{N} \langle \Pi^a \Pi^b \rangle + N \langle X^a X^b \rangle \langle X^c X^c \rangle - N \langle X^c X^c \rangle \langle X^a X^b \rangle + N \langle X^b X^c \rangle \langle X^a X^c \rangle - \\ & - N \langle X^a X^c \rangle \langle X^b X^c \rangle + \nu^2 \langle X^a X^b \rangle \end{aligned} \quad (4.11)$$

$$\begin{aligned} \partial_t \langle \Pi^a \Pi^b \rangle = & N \langle X^a X^b \rangle \langle X^c X^c \rangle - N \langle X^c X^c \rangle \langle X^a X^b \rangle + N \langle X^b X^c \rangle \langle X^a X^c \rangle - \\ & - N \langle X^a X^c \rangle \langle X^b X^c \rangle + \nu^2 \langle X^a X^b \rangle + (a \leftrightarrow b). \end{aligned} \quad (4.12)$$

As explained in [36], this truncated system is obtained by assuming a Gaussian approximation for the wavefunctions. Therefore, we solve the truncated quantum dynamics of the mini-BMN model — essentially a toy model, but it will serve our purpose. Now that we have set the stage, we can express the kinematic OTOC as $C(t) = \langle X^a \Pi^b \rangle - \langle \Pi^a X^b \rangle$ and study its dynamics. The outcome is given in figure 10. We are essentially back to the random matrix regime of section 3 — there is a clear scaling $C_{\infty} \sim \exp(1/T^2)$ (we do not see the other regime, but again it may well be there for sufficiently high temperatures), and the level distribution is a near-perfect fit to the Wigner-Dyson curve. Therefore, if a Hamiltonian is strongly chaotic, then both the level distribution and the OTOC plateau are well described by the random matrix theory.

5 Discussion and conclusions

In this paper we have formulated a somewhat unexpected indicator of quantum chaos, useful mainly in few-body (few-degrees-of-freedom) systems. While OTOC has become the quintessential object in the studies of quantum chaos and information transport, characterized mainly by its growth rate — the (quantum) Lyapunov exponent, in our examples its growth pattern tends to be quite nonuniversal and “noisy” (in the sense that it depends sensitively on the system at hand and the operators we look at). Our analytic

treatment of OTOC dynamics is quite sketchy, however both analytical and numerical results strongly suggest there is no clear exponential growth. At first glance, one might think that this finding is completely at odds with the established wisdom, however this is not true. In the literature, exponential growth is mainly characteristic for systems with a classical gravity dual (and reaches its maximum when the dual contains a thermal black hole horizon). There are abundant examples of quantum chaotic systems which do not have an exponentially growing OTOC (we especially like [19] but there are many other published examples). The exponential growth follows, in the AdS/CFT picture, from the shock wave dynamics in a classical gravity background, and need not exist when the background is not classical or when the gravity dual does not exist at all. This is precisely what happens here: the Henon-Heiles Hamiltonian is certainly nothing like a strongly coupled large N field theory, while the truncated mini-BMN model comes closer (it is actually related to discretized Yang-Mills) but we tackle it at finite N and thus away from the fast scrambling dual. For random matrices, our findings for $C(t)$ are in line with the rigorous results of [13]. As pointed out in that work, the crucial difference between random matrices and strongly coupled field theories is that the former have no notion of locality neither in time nor in space. In our small systems, the spatial locality is irrelevant anyway but if the system is not sufficiently chaotic there will still be long-term temporal correlations in dynamics (this indeed gives rise to different scaling regimes for strong and weak chaos).

On the other hand, what we have found is that the long-time OTOC behavior, when it becomes essentially stationary, with a complex oscillation pattern, is surprisingly regular — behaving as $\exp(1/T^2)$ and $\exp(1/T)$ respectively in strong and weak chaos. This indicator seems to have a stronger connection to quantum chaos in the sense of level statistics than the Lyapunov exponent; in all examples we have studied the $\exp(1/T^2)$ regime and the Wigner-Dyson level distribution go hand in hand. At very high temperatures we detect also a different regime, when the OTOC plateau grows with temperature. This regime seems less universal, and we do not understand it very well. One might think that the plateau value should not carry any useful information; it is often laconically stated that OTOC reaches saturation when the initial perturbation has spread all over the system and that this saturation value is unity when OTOC is appropriately normalized. This is roughly true, however “spreading all over the system” is not a rigorous notion — depending on the system and the operators A, B in OTOC, the perturbation may never spread completely due to symmetry constraints, specific initial conditions, quasi-integrals of motion etc. Such factors are particularly important in finite systems (quantum mechanics as opposed to quantum field theory) that we study. Looking at the figures, one sees that differences in the asymptotic OTOC value C_∞ tend to be small, and C_∞ tends to be about the same to an order of magnitude in all cases. We conjecture that such differences would dwindle to zero in the field limit.

A simple intuitive explanation for the falloff of asymptotic OTOC with temperature is the following: we expect that higher temperatures lead to faster information spreading and quicker equilibration. Therefore, it is logical that the plateau value will be lower, so that the system needs less time to reach it, i.e. it needs less time to equilibrate.

We note in passing that we have confirmed that scrambling can originate from at least two distinct mechanisms: local instability and chaos, so in the former case the relation of OTOC to chaos is largely lost. This is a known fact in many examples already [6, 7, 9, 16, 26] and we emphasize it here merely as a reminder to the reader that the OTOC-chaos connection is really a relation of three elements: OTOC-scrambling-chaos, and if the second link is missing no attempt should be made to understand chaotic dynamics from OTOC.

We conclude with some speculations. The OTOC plateau value, as we found, is a rather universal function of temperature, and it is essentially a finite-size fluctuation of the correlation function, when the system is small enough that the relative size of fluctuations does not go to zero. We may then look for universality and the connections to chaotic dynamics in other similar quantities, e.g. the average fluctuation of the expectation value of some operator during thermalization. Such a quantity remains nonzero also in AdS/CFT at large N , and may relate our results to the more familiar fast scrambling, strongly correlated holographic systems.

Acknowledgments

This work has made use of the excellent Sci-Hub service. Work at the Institute of Physics is funded by the Ministry of Education, Science and Technological Development and by the Science Fund of the Republic of Serbia, under the Key2SM project (PROMIS program, Grant No. 6066160).

A Detailed structure and calculation of OTOC for Gaussian orthogonal ensembles

In this appendix we consider the calculation of OTOC for random matrix systems in some more detail, and describe the detailed structure of the correlation function $C(t)$. Let us first denote, for the sake of brevity:

$$\sum_{\text{tot}} \equiv \sum_{n,m} \sum_{k,k'} \sum_{i_1,i_2} \sum_{j_1,j_2} \sum_{i'_1,i'_2} \sum_{j'_1,j'_2}, \quad \mathbf{C} \equiv c_{j_1}^k \dots c_{j'_2}^m.$$

Denote also the products of matrix elements of the operators A, B entering the expression (3.4) by $\chi_1, \chi_2, \chi_3, \chi_4$. Now the expression for $\langle C(t) \rangle$ can be written as:

$$\begin{aligned} \langle C(t) \rangle = & \sum_{\text{tot}} \int P(\{c\}) d^{N^2} \{c\} \int \mathcal{P}(\{E\}) d^N E e^{-\beta E_n} \mathbf{C} \\ & \times \left(\chi_1 e^{i(E_{k'} - E_k)t} + \dots + \chi_4 e^{i(E_m + E_n - E_{k'} - E_k)t} \right) \end{aligned} \quad (\text{A.1})$$

As we have noticed in the main text, the integral over \mathbf{C} yields just a numerical constant. Let us therefore evaluate the energy integral $I_1 = \int d^N \{E\} \mathcal{P}(\{E\}) e^{-\beta E_n} \chi_1 e^{i(E_{k'} - E_k)t}$. We have:

$$I_1 = \int \int \dots \int dE_n \int dE_k \int dE_{k'} \mathcal{P}(\{E\}) e^{-\beta E_n} \times \chi_1 e^{i(E_{k'} - E_k)t}. \quad (\text{A.2})$$

The absolute values of the differences can be written out in the obvious way:

$$\prod_{n < m} |E_n - E_m| = \sum_i (-1)^{\pi(i)} E_1^{\alpha_{1,i}} E_2^{\alpha_{2,i}} \dots E_N^{\alpha_{N,i}}, \quad (\text{A.3})$$

where all $\alpha_{i,j}$ are some (positive) integer exponents and $\pi(i)$ is the appropriate sign factor 0 or 1. Therefore, I_1 can be reorganized as:

$$I_1 = \sum_j \chi_1 \prod_{i \neq n, k, k'} \int E_i^{\alpha_{i,j}} e^{-E_i^2} dE_i \int dE_n e^{-\beta E_n} e^{-E_n^2} \int dE_k e^{iE_{k'} t} e^{-E_{k'}^2} \int dE_k e^{-iE_k t} e^{-E_k^2}. \quad (\text{A.4})$$

Note that the part $\prod_{n < m} |E_n - E_m|$, is not essential for the general behavior, since the singular integral $\int E_i^{\alpha_{i,j}} e^{-E_i^2} dE_i$ is either some constant (if α is even), or zero if α is odd. Otherwise for $i \neq j$

$$\int \prod_{l < i < l'} E_i e^{-E_j^2} dE_j = \text{const.} \times \prod_{l < i < l'} E_i. \quad (\text{A.5})$$

Therefore, we only focus on calculating integrals of the form

$$\int dE_n \int dE_k \int dE_{k'} e^{-\beta E_n} \times e^{-E_n^2 - E_k^2 - E_{k'}^2} \chi_1 e^{i(E_{k'} - E_k)t}, \quad (\text{A.6})$$

which yields the closed-form expression for the temperature dependence of I_1 :

$$I_1 \sim \delta_{k,k'} e^{\beta^2/4} + (1 - \delta_{k,k'}) e^{\beta^2/4} e^{-t^2/2}, \quad (\text{A.7})$$

where $\delta_{k,k'}$ is the Kronecker delta, reminding us that the main contribution comes from the terms with $E_k = E_{k'}$ which generically means $k = k'$. It is clear that a similar calculation holds for the other parts of $\langle C(t) \rangle$. This produces the temperature scaling found in the main text for random matrices, of the form $\langle C(t) \rangle \sim e^{1/4T^2}$. But the time dependence is more complicated. In order to see this, we look at the structure of the polynomial factors in I_1 in some more detail. We see immediately that $\langle C(t) \rangle$ will also have dependence on t^{2n}, β^n . Start from

$$\int E_i^{\alpha_i} e^{-iE_i t} e^{-E_i^2} dE_i = e^{-t^2/4} \int (u - it/2)^{\alpha_i} e^{-u^2} du, \quad (\text{A.8})$$

where $E_i = u - it/2$. Let us look at two cases: α_i even and α_i odd. For any α_i the polynomial will have the form:

$$(u - it/2)^{\alpha_i} = \sum_{j=0}^{\alpha_i} \gamma_j u^j (it/2)^{\alpha_i - j}. \quad (\text{A.9})$$

Assume first that α_i is even. This means that j and $\alpha_i - j$ are of same parity. For even j the Gaussian integral evaluates to some constant, but we will also have the prefactor of $(it/2)^{\alpha_i - j}$, for all even $j \leq \alpha_i$. The odd powers (j odd) will disappear because of the symmetric domain of integration. For α_i odd, j and $\alpha_i - j$ will be of different parity so again, only even j give a nonzero integral. In conclusion, the integral (A.6) with polynomial prefactors included will have the form:

$$\int E_i^{\alpha_i} e^{-iE_i t} e^{-E_i^2} dE_i = e^{-t^2/4} Q(t^{2n}), \quad (\text{A.10})$$

where $Q(t^{2n})$ is a real polynomial depending on even powers of t , and $2n \leq \alpha_i$. Alternatively, for α_i odd, we get:

$$\int E_i^{\alpha_i} e^{-iE_i t} e^{-E_i^2} dE_i = i e^{-t^2/4} R(t^{2n+1}), \quad (\text{A.11})$$

where $R(t^{2n+1})$ is a real polynomial depending on odd powers of t , and $2n + 1 \leq \alpha_i$. Analogous logic holds for the β dependence. Now we look back at I_1 :

$$I_1 = \text{const.} \int E_n^{\alpha_n} dE_n \int E_k^{\alpha_k} dE_k \int E_{k'}^{\alpha_{k'}} dE_{k'} e^{-\beta E_n} \times e^{-E_n^2 - E_k^2 - E_{k'}^2} \chi_1 e^{i(E_{k'} - E_k)t}. \quad (\text{A.12})$$

When we write out the products of energies, we have the following types of monomials in the resulting polynomial:

1. QQU
2. QRU
3. QQV
4. QRV ,

with the prefactor $\delta_{k,k'} e^{-t^2/2} e^{\beta^2/4}$. Here, Q, R are polynomials of t and are U/V are polynomials of even/odd powers of β respectively. Note however that QR and RQ give the same structure after integration.

The other integral appearing when writing out the master formula for OTOC is

$$K_n = \int E_n^{\alpha_n} e^{-\beta E_n} e^{-iE_n t} e^{-E_n^2} dE_n. \quad (\text{A.13})$$

According to the same logic as for I_1 , it is not hard to get the equivalent form of K_n (leaving out the exponentially decaying terms):

$$K_n = e^{\beta^2/4} e^{i\beta t/2} \int \sum_j \gamma_j u^j (\beta/2 + it/2)^{\alpha_n - j} e^{-u^2} du. \quad (\text{A.14})$$

Now we will use the fact that OTOC is a real function, as we can see also from the definition (2.2). Therefore, all imaginary parts must vanish. From this fact we reach a few important conclusions:

1. In the structure of I_1 , the combination QR is impossible, thus we will only have polynomials of t with an even exponent, and no restriction for polynomials of β as it is a real integral, and no term has to vanish.
2. In the structure of K_n , when we have the factor $\cos(\beta t/2)$, only even powers of t and arbitrary powers of β can survive.
3. In the structure of K_n when we have the factor $\sin(\beta t/2)$, only odd powers of t and arbitrary powers of β can survive.

The conclusion of the above analysis gives us a rough idea of what the $\langle C(t) \rangle$ looks like:

$$\langle C(t) \rangle = e^{\frac{\beta^2}{4}} W_0(\sigma\beta) + e^{\frac{\beta^2}{4}} \left(\cos\left(\frac{\beta t}{2}\right) Q(t^{2n}) W_1(\sigma\beta) + \sin\left(\frac{\beta t}{2}\right) R(t^{2n+1}) W_2(\beta^n) \right), \tag{A.15}$$

where W_0, W_1, W_2 are arbitrary polynomials of β . This is the form found also in the main text, with the exception that in the main text we have rescaled the combination βt as $\beta t/\sigma^2$ in order to have a dimensionless expression.

A.1 The large matrix limit

In the limit $N \rightarrow \infty$ we can say more on the structure of OTOC. We can first schematically rewrite (A.15) together with any exponentially suppressed corrections as

$$\langle C(t) \rangle = e^{\frac{\beta^2}{4}} Q(t^{2n}) W(\sigma\beta) \left(L_1 + L_2 e^{-t^2/2} \right). \tag{A.16}$$

Here we have first absorbed all time and β dependence of (A.15) into the functions Q and W respectively, and then we have included the exponentially suppressed correction coming from the $k \neq k'$ terms in the integrals I_1 and K_n . By L_1, L_2 we denote the constant (time- and temperature-independent) factors. In general one can write L_1 as

$$L_1 = \sum_{j=1}^N \sum_{i=0}^j c_i \binom{j}{i} \tag{A.17}$$

We can easily estimate the second sum. Namely,

$$\left(\sum_{i=0}^j c_i \binom{j}{i} \right)^2 \leq \left(\sum_{i=0}^j c_i^2 \right) \left(\sum_{i=0}^j \binom{j}{i}^2 \right), \tag{A.18}$$

by the Cauchy-Schwarz-Bunyakovski inequality. Next, the well known formula $\sum_{i=0}^j \binom{j}{i}^2 = \binom{2j}{j}$ yields

$$\sum_{i=0}^j c_i \binom{j}{i} \leq \text{const.} \times \sqrt{\binom{2j}{j}}. \tag{A.19}$$

To get rid of the binomial coefficient we will use the Stirling's formula and get

$$\sqrt{\binom{2j}{j}} = \sqrt{\frac{(2j)!}{j!j!}} \approx \sqrt{\frac{\sqrt{4\pi j} \frac{(2j)^{2j}}{e^{2j}}}{2\pi j \frac{(j^j)^2}{(e^j)^2}}} \approx \text{const.} \times \frac{2^j}{j^{1/4}}. \tag{A.20}$$

Finally we reach the result:

$$L_1 \approx \text{const.} \times \sum_{j=1}^N \frac{2^j}{j^{1/4}} \approx \text{const.} \times \frac{2^{N+1}}{N^{1/4}}, \tag{A.21}$$

for $N \rightarrow \infty$. Exactly the same logic goes for L_2 .

In the large matrix limit it is possible to show explicitly what we know has to happen: OTOC reaches a plateau. Looking at (A.16), the condition to reach the plateau for times longer than some scale t_0 is

$$e^{-\frac{t^2}{2}} Q(t^{2n}) (L_1 + L_2 e^{-t^2/2}) = \text{const.} \quad t > t_0. \quad (\text{A.22})$$

It is more convenient to look at the forms given in (A.15). First let us look at the condition $Q(t^{2n}) = \text{const.} \times e^{t^2/2}$. The exponential term can be represented as a series; equating it with $Q(t^{2n})$ we get

$$\sum_j \alpha_j t^{2j} = \text{const.} \times \sum_j \frac{t^{2j}}{2^j j!}, \quad (\text{A.23})$$

thus, we need $\alpha_j \sim \frac{1}{2^j j!}$, which we know is the case from (A.9). For the second term the situation is similar:

$$\sum_j \beta_j t^{2j} = \text{const.} \times \sum_j \frac{t^{2j}}{j!}, \quad (\text{A.24})$$

so we need to have $\beta_j \sim \frac{1}{j!}$; this is true by $\cos(\beta t/2) = Q(t^{2n})W(\beta^{2n})$ and $\sin(\beta t/2) = Q(t^{2n+1})W(\beta^{2n+1})$, since the terms in the Taylor expansions of the left-hand sides behave as $\sim \frac{1}{j!}$.

We can also look at the opposite limit in which $t \rightarrow 0$. Let us rearrange (A.16):

$$\langle C(t) \rangle = L'_1 Q(t^{2n}) e^{-t^2/2} + L'_2 Q(t^{2n}) e^{-t^2}. \quad (\text{A.25})$$

Now, simply using the definition of Q and expanding into a series we get:

$$\langle C(t) \rangle = L'_1 \left(1 - \frac{t^2}{2} + o(t^4) \right) (q_0 + q_1 t^2) + L'_2 \left(1 - t^2 + o(t^4) \right) (q_0 + q_1 t^2). \quad (\text{A.26})$$

After some algebra we get:

$$\langle C(t) \rangle = Q_0 + Q_1 t^2 + Q_2 t^4 + o(t^4) = P(t). \quad (\text{A.27})$$

We see now that OTOC behaves in a very simple way for early times; this expansion is also consistent with the result (3.16) of [13].

Open Access. This article is distributed under the terms of the Creative Commons Attribution License ([CC-BY 4.0](https://creativecommons.org/licenses/by/4.0/)), which permits any use, distribution and reproduction in any medium, provided the original author(s) and source are credited.

References

- [1] J. Maldacena, S.H. Shenker and D. Stanford, *A bound on chaos*, *JHEP* **08** (2016) 106 [[arXiv:1503.01409](https://arxiv.org/abs/1503.01409)] [[INSPIRE](https://inspirehep.net/literature/1503014)].
- [2] S.H. Shenker and D. Stanford, *Stringy effects in scrambling*, *JHEP* **05** (2015) 132 [[arXiv:1412.6087](https://arxiv.org/abs/1412.6087)] [[INSPIRE](https://inspirehep.net/literature/1412608)].
- [3] S. Kundu, *Extremal chaos*, *JHEP* **01** (2022) 163 [[arXiv:2109.08693](https://arxiv.org/abs/2109.08693)] [[INSPIRE](https://inspirehep.net/literature/2109086)].

- [4] Y. Sekino and L. Susskind, *Fast Scramblers*, *JHEP* **10** (2008) 065 [[arXiv:0808.2096](#)] [[INSPIRE](#)].
- [5] N. Lashkari, D. Stanford, M. Hastings, T. Osborne and P. Hayden, *Towards the Fast Scrambling Conjecture*, *JHEP* **04** (2013) 022 [[arXiv:1111.6580](#)] [[INSPIRE](#)].
- [6] E.B. Rozenbaum, L.A. Bunimovich and V. Galitski, *Early-Time Exponential Instabilities in Nonchaotic Quantum Systems*, *Phys. Rev. Lett.* **125** (2020) 014101 [[arXiv:1902.05466](#)] [[INSPIRE](#)].
- [7] T. Xu, T. Scaffidi and X. Cao, *Does scrambling equal chaos?*, *Phys. Rev. Lett.* **124** (2020) 140602 [[arXiv:1912.11063](#)] [[INSPIRE](#)].
- [8] K. Hashimoto, K. Murata and R. Yoshii, *Out-of-time-order correlators in quantum mechanics*, *JHEP* **10** (2017) 138 [[arXiv:1703.09435](#)] [[INSPIRE](#)].
- [9] K. Hashimoto, K.-B. Huh, K.-Y. Kim and R. Watanabe, *Exponential growth of out-of-time-order correlator without chaos: inverted harmonic oscillator*, *JHEP* **11** (2020) 068 [[arXiv:2007.04746](#)] [[INSPIRE](#)].
- [10] F. Haake, S. Gnutzman and M. Kuś, *Quantum signatures of chaos*, Springer-Verlag, Berlin, Germany (2019).
- [11] M.L. Mehta, *Random matrices*, Academic, New York, U.S.A. (2004).
- [12] J.S. Cotler et al., *Black Holes and Random Matrices*, *JHEP* **05** (2017) 118 [*Erratum ibid.* **09** (2018) 002] [[arXiv:1611.04650](#)] [[INSPIRE](#)].
- [13] J. Cotler, N. Hunter-Jones, J. Liu and B. Yoshida, *Chaos, Complexity, and Random Matrices*, *JHEP* **11** (2017) 048 [[arXiv:1706.05400](#)] [[INSPIRE](#)].
- [14] J. Cotler and N. Hunter-Jones, *Spectral decoupling in many-body quantum chaos*, *JHEP* **12** (2020) 205 [[arXiv:1911.02026](#)] [[INSPIRE](#)].
- [15] W. Kirkby, D.H.J. O’Dell and J. Mumford, *False signals of chaos from quantum probes*, [arXiv:2108.09391](#) [[INSPIRE](#)].
- [16] T. Akutagawa, K. Hashimoto, T. Sasaki and R. Watanabe, *Out-of-time-order correlator in coupled harmonic oscillators*, *JHEP* **08** (2020) 013 [[arXiv:2004.04381](#)] [[INSPIRE](#)].
- [17] A. Bhattacharyya, W. Chemissany, S.S. Haque, J. Murugan and B. Yan, *The Multi-faceted Inverted Harmonic Oscillator: Chaos and Complexity*, *SciPost Phys. Core* **4** (2021) 002 [[arXiv:2007.01232](#)] [[INSPIRE](#)].
- [18] W. Kłobus, P. Kurzyński, M. Kuś, W. Laskowski, R. Przybycień and K. Życzkowski, *Transition from order to chaos in reduced quantum dynamics*, *Phys. Rev. E* **105** (2022) 034201 [[arXiv:2111.13477](#)] [[INSPIRE](#)].
- [19] B. Bertini, P. Kos and T. Prosen, *Exact Spectral Form Factor in a Minimal Model of Many-Body Quantum Chaos*, *Phys. Rev. Lett.* **121** (2018) 264101 [[arXiv:1805.00931](#)] [[INSPIRE](#)].
- [20] S. Pappalardi, A. Russomanno, B. Žunkovič, F. Iemini, A. Silva and R. Fazio, *Scrambling and entanglement spreading in long-range spin chains*, *Phys. Rev. B* **98** (2018) 134303 [[arXiv:1806.00022](#)] [[INSPIRE](#)].
- [21] K. Okuyama, *Spectral form factor and semi-circle law in the time direction*, *JHEP* **02** (2019) 161 [[arXiv:1811.09988](#)] [[INSPIRE](#)].

- [22] Q. Hummel, B. Geiger, J.D. Urbina and K. Richter, *Reversible quantum information spreading in many-body systems near criticality*, *Phys. Rev. Lett.* **123** (2019) 160401 [[arXiv:1812.09237](#)] [[INSPIRE](#)].
- [23] H. Goto and T. Kanao, *Chaos in coupled Kerr-nonlinear parametric oscillators*, *Phys. Rev. Res.* **3** (2021) 043196 [[arXiv:2110.04019](#)] [[INSPIRE](#)].
- [24] N.D. Varikuti and V. Madhok, *Out-of-time ordered correlators in kicked coupled tops and the role of conserved quantities in information scrambling*, [arXiv:2201.05789](#) [[INSPIRE](#)].
- [25] A.V. Kirkova, D. Porras and P.A. Ivanov, *Out-of-time-order correlator in the quantum Rabi model*, *Phys. Rev. A* **105** (2022) 032444 [[arXiv:2201.06340](#)] [[INSPIRE](#)].
- [26] J.R.G. Alonso, N. Shammah, S. Ahmed, F. Nori and J. Dressel, *Diagnosing quantum chaos with out-of-time-ordered-correlator quasiprobability in the kicked-top model*, [arXiv:2201.08175](#) [[INSPIRE](#)].
- [27] K. Hashimoto, K. Murata, N. Tanahashi and R. Watanabe, *A bound on energy dependence of chaos*, [arXiv:2112.11163](#) [[INSPIRE](#)].
- [28] J. Aguirre, J.C. Vallejo and M.A.F. Sanjuán, *Wada basins and chaotic invariant sets in the Hénon-Heiles system*, *Phys. Rev. E* **64** (2001) 066208.
- [29] H.E. Kandrup, C. Siopis, G. Contopoulos and R. Dvorak, *Diffusion and scaling in escapes from two-degree-of-freedom Hamiltonian systems*, *Chaos* **9** (1999) 381 [[astro-ph/9904046](#)] [[INSPIRE](#)].
- [30] D.E. Berenstein, J.M. Maldacena and H.S. Nastase, *Strings in flat space and pp waves from $N = 4$ super Yang-Mills*, *JHEP* **04** (2002) 013 [[hep-th/0202021](#)] [[INSPIRE](#)].
- [31] T. Banks, W. Fischler, S.H. Shenker and L. Susskind, *M theory as a matrix model: A Conjecture*, *Phys. Rev. D* **55** (1997) 5112 [[hep-th/9610043](#)] [[INSPIRE](#)].
- [32] K.L. Zarembo and Y.M. Makeenko, *An introduction to matrix superstring models*, *Phys. Usp.* **41** (1998) 1 [[INSPIRE](#)].
- [33] Y. Asano, D. Kawai and K. Yoshida, *Chaos in the BMN matrix model*, *JHEP* **06** (2015) 191 [[arXiv:1503.04594](#)] [[INSPIRE](#)].
- [34] G. Gur-Ari, M. Hanada and S.H. Shenker, *Chaos in Classical D0-Brane Mechanics*, *JHEP* **02** (2016) 091 [[arXiv:1512.00019](#)] [[INSPIRE](#)].
- [35] X. Han and S.A. Hartnoll, *Deep Quantum Geometry of Matrices*, *Phys. Rev. X* **10** (2020) 011069 [[arXiv:1906.08781](#)] [[INSPIRE](#)].
- [36] P.V. Buividovich, M. Hanada and A. Schäfer, *Quantum chaos, thermalization, and entanglement generation in real-time simulations of the Banks-Fischler-Shenker-Susskind matrix model*, *Phys. Rev. D* **99** (2019) 046011 [[arXiv:1810.03378](#)] [[INSPIRE](#)].

The bound on chaos for closed strings in Anti-de Sitter black hole backgrounds

Mihailo Čubrović

*Scientific Computing Lab, Center for the Study of Complex Systems,
Institute of Physics Belgrade, University of Belgrade,
Pregrevica 118, 11080 Belgrade, Serbia*

E-mail: mcubrovic@gmail.com

ABSTRACT: We perform a systematic study of the maximum Lyapunov exponent values λ for the motion of classical closed strings in Anti-de Sitter black hole geometries with spherical, planar and hyperbolic horizons. Analytical estimates from the linearized variational equations together with numerical integrations predict the bulk Lyapunov exponent value as $\lambda \approx 2\pi T n$, where n is the winding number of the string. The celebrated bound on chaos stating that $\lambda \leq 2\pi T$ is thus systematically modified for winding strings in the bulk. Within gauge/string duality, such strings apparently correspond to complicated operators which either do not move on Regge trajectories, or move on subleading trajectories with an unusual slope. Depending on the energy scale, the out-of-time-ordered correlation functions of these operators may still obey the bound $2\pi T$, or they may violate it like the bulk exponent. We do not know exactly why the bound on chaos can be modified but the indication from the gauge/string dual viewpoint is that the correlation functions of the dual gauge operators never factorize and thus the original derivation of the bound on chaos does not apply.

KEYWORDS: Gauge-gravity correspondence, AdS-CFT Correspondence, Integrable Field Theories, Black Holes

ARXIV EPRINT: [1904.06295](https://arxiv.org/abs/1904.06295)

Contents

1	Introduction	1
2	String dynamics in static black hole backgrounds	5
2.1	Fixed points and near-horizon dynamics	7
3	Lyapunov exponents and the bound on chaos	10
3.1	Variational equations and analytical estimates of Lyapunov exponents	11
3.1.1	Thermal horizon	11
3.1.2	Away from the horizon	12
3.1.3	Extremal horizon	13
3.1.4	Lyapunov time versus event time	14
3.1.5	Dimensionful constants	14
3.2	Numerical checks	15
4	Toward a physical interpretation of the modified bound	15
4.1	Dual gauge theory interpretation	15
4.1.1	Operators dual to a ring string?	16
4.1.2	Planetoid string	18
4.2	The limits of quasiclassicality	20
4.3	Ring string scattering amplitude and the relation to OTOC	20
4.3.1	Eikonal approximation	21
4.3.2	Beyond the eikonal approximation: waves on the string	23
5	Discussion and conclusions	25
A	Summary of the numerics	28

1 Introduction

Sharp results like inequalities and no-go theorems are often the cornerstones of our understanding of physical phenomena. Besides being appealing and captivating, they are easy to test as they provide a sharp prediction on a certain quantity, and we can often learn a lot by understanding the cases when such bounds need to be generalized or abandoned. The upper bound on the Lyapunov exponent (the rate of the growth of chaos), derived in [1] inspired by hints found in several earlier works [2–7], is an example of such a result, which is related to the dynamics of nonstationary correlation functions and provides insight into the deep and important problem of thermalization and mixing in strongly coupled systems.

It is clear, as discussed also in the original paper [1], that there are cases when the bound does not apply: mainly systems in which the correlation functions do not factorize even at arbitrarily long times, and also systems without a clear separation of short timescales (or collision times) and long timescales (or scrambling times). A concrete example of bound violation was found in [8] for a semiclassical system with a conserved angular momentum (inspired by the Sachdev-Ye-Kitaev (SYK) model [9–12]) and in [13], again for a SYK-inspired system. In the former case, the reason is clear: the orbits that violate the bound are precisely those that cannot be treated semiclassically, so the violation just signals that the model used becomes inaccurate; in the latter case things are more complicated and the exact reason is not known. Finally, in [14] systematic higher-order quantum corrections to the bound are considered. The bound is in any case a very useful benchmark, which can tell us something on long-term dynamics of the system at hand, i.e. if some bound-violating mechanisms are at work or not.

Although the bound on chaos is mainly formulated for field theories in flat spacetime, it has an intimate connection to gravity: the prediction is that fields with gravity duals saturate the bound. This makes dynamics in asymptotically anti-de Sitter (AdS) spacetimes with a black hole particularly interesting: they have a field theory dual,¹ and black holes are conjectured to be the fastest scramblers in nature [2, 3], i.e., they minimize the time for the overlap between the initial and current state to drop by an order of magnitude. Some tests of the bound for the motion of particles in the backgrounds of AdS black holes and an additional external potential were already made [15]; the authors find that the bound is systematically modified for particles hovering at the horizon and interacting with *higher spin* external fields. When the external field becomes scalar, the exact bound by Maldacena, Shenker and Stanford is recovered (as shown also in [16]).

The idea of this paper is to study the bound on chaos in the context of *motion of strings in AdS black hole geometries*. Asymptotically AdS geometry is helpful not only because of the gauge/gravity duality, but also for another reason: AdS asymptotics provide a regulator, i.e., put the system in a box, making its dynamics more interesting (in asymptotically flat space, most orbits immediately escape to infinity with no opportunity to develop chaos). Now why consider strings instead of geodesics? Because geodesics are not the best way to probe the chaos generated by black holes: we know that geodesics in AdS-Schwarzschild, AdS-Reissner-Nordstrom and AdS-Kerr backgrounds (and also in all axially symmetric and static black hole geometries) are integrable, and yet, since the horizon in all these cases has a finite Hawking temperature, there should be some thermalization and chaos going on. The logical decision is therefore to go for string dynamics, which is practically always nonintegrable in the presence of a black hole. We look mainly at the Lyapunov exponents and how they depend on the Hawking temperature. We will see that the bound of [1] is surprisingly relevant here, even though the bound was formulated for *field theories* with a *classical gravity dual*, whereas we look at the *bulk* dynamics of *strings*, which go beyond the realm of Einstein gravity. At first glance, their Lyapunov exponents should not saturate (let alone violate) the bound; in fact, at first glance, it is not

¹Of course, one should be careful when it comes to details; it is known that for some field contents in the bulk the boundary theory does not exist.

obvious at all how to relate the Lyapunov exponent of classical bulk orbits to the result [1], which defines the Lyapunov exponent in terms of the out-of-time ordered correlation functions (OTOC).² An important discovery in relation to this issue was made in [17], where the authors consider a holographically more realistic string (open string dual to a quark in Brownian motion in a heat bath), compute the Lyapunov exponent in dual field theory, and find that it exactly saturates the bound. However, their *world-sheet* theory, i.e., their induced metric itself looks somewhat like gravity on AdS_2 ; therefore, close connection to the Einstein gravity result is understandable. Our situation is different not only because the ring string configurations have worldsheet actions very different from Einstein gravity but also because we look mainly at the Lyapunov exponents of the bulk orbits.³ We will eventually look also at the OTOC in dual field theory and find that the “quantum” Lyapunov exponents do not in general coincide with the classical bulk values. However, the subject of OTOC functions is more complicated as it requires one to consider the backreaction on the background, and studying the behavior of the ring string in such backreacted geometry is in general more difficult than for the open string of [17]. Therefore, we mostly leave the OTOC and quantum Lyapunov exponent for future work.

At this point we come to another question, distinct but certainly related to the chaos bound: the story of (non)integrability in various curved spacetimes. For point particles (i.e., motion on geodesics) it is usually not so difficult to check for integrability, and symmetries of the problem usually make the answer relatively easy. However, integrability in string theory remains a difficult topic. Most systematic work was done for top-down backgrounds, usually based on the differential Galois theory whose application for string integrability was pioneered in [19]. Systematic study for various top-down configurations was continued in [20–22]; [21] in particular provides the results for strings in a broad class of brane backgrounds, including Dp-brane, NS1 and NS5 brane configurations. The bottom line is that integrable systems are few and far apart, as could be expected. Certainly, $\text{AdS}_5 \times S^5$ is an integrable geometry, as could be expected from its duality to the (integrable) supersymmetric Yang-Mills field theory. In fact, direct product of AdS space and a sphere is integrable in any dimension, which is obvious from the separability of the coordinates. But already a marginal deformation destroys integrability; a specific example was found analytically and numerically in [23], for the β -deformation of super-Yang-Mills and its top-down dual. More information can be found, e.g., in the review [24].

The first study of integrability in a black hole background was [25], where the nonintegrability of string motion in asymptotically flat Schwarzschild black hole background was shown. In [26] the first study for an AdS black hole background (AdS-Schwarzschild) was performed, putting the problem also in the context of AdS/CFT correspondence. In [27] the work on top-down backgrounds was started, considering the strings

²In addition, the scrambling concept of [2, 4–7] is more complex; it is about the equilibration of the black hole and its environment after something falls in. In other words, it necessarily includes the perturbation of the black hole itself. We do not take into account any backreaction so we cannot compute the scrambling time, only the Lyapunov exponent.

³Another example where the bound is modified (by a factor of 2) in a theory that goes beyond Einstein gravity is [18].

on the $\text{AdS} \times T^{1,1}$ geometry generated in a self-consistent top-down way. For the top-down AdS-Sasaki-Einstein background the nonintegrability was proven analytically [19]. Finally, AdS-soliton and AdS-Reissner-Nordstrom were also found to be nonintegrable in [28, 29]. So most well-known in AdS/CFT have nonintegrable string dynamics: AdS-Schwarzschild, AdS-Reissner-Nordstrom, AdS soliton and AdS-Sasaki-Einstein.⁴ Other results on (non)integrability can be found in [30–33]; the list is not exhaustive.

Apart from the usual spherical static black holes (neutral and charged), we consider also non-spherical horizons with constant curvature. Among them are also the zero-curvature black branes, with infinite planar horizons, which are most popular in applied holography. But it is known that more general horizons can be embedded in AdS space (in general not in Minkowski space). Such black holes are usually called topological black holes, first constructed in [34–37] and generalized in [38]. The term topological is in fact partly misleading, as the backgrounds considered in some of the original papers [35] and also in our paper are not necessarily of higher topological genus: besides spherical and planar horizons, we mainly consider an infinite, topologically trivial hyperbolic horizon with constant negative curvature (pseudosphere).⁵

The reader might wonder how important the non-spherical black holes are from the physical viewpoint. In fact, as shown in the aforementioned references, they arise naturally in spaces with negative cosmological constant, i.e., in AdS spaces, for example in the collapse of dust [39], and the topological versions are easily obtained through suitable gluings (identifications of points on the orbit of some discrete subgroup of the total symmetry group) of the planar or pseudospherical horizon. Another mechanism is considered in [34], where topological black holes are pair-created from instanton solutions of the cosmological C-metric (describing a pair of black holes moving with uniform acceleration). More modern work on constant-curvature black holes and some generalizations can be found in [40–42], and AdS/CFT correspondence was applied to topological black holes in [43]. But our main motivation for considering non-spherical black holes is methodological, to maximally stretch the testing ground for the chaos bound and to gain insight into various chaos-generating mechanisms. In hindsight, we find that hyperbolic are roughly speaking most chaotic, because moving on a manifold of negative curvature provides an additional chaos-generating mechanism, in addition to the black hole.

The plan of the paper is the following. In the next section we write down the equations of motion for a closed string in static black hole background, inspect the system analytically and numerically and show that dynamics is generically non-integrable. In the third section we compute the Lyapunov exponents numerically and estimate them analytically, formulating a generalized bound in terms of the local temperature and the string winding number. The fourth section is a rather speculative attempt to put our results in the context of the dual field theory and the derivation of the original bound from [1]; we will also try to clarify the relation of the bulk classical Lyapunov exponent to the decay rates of OTOC functions in dual field theory. The last section sums up the conclusions.

⁴In [26, 29] it was shown that Reissner-Nordstrom black holes in asymptotically flat space are also nonintegrable.

⁵In fact, constant-curvature black holes would be a more suitable term than topological black holes.

2 String dynamics in static black hole backgrounds

A constant curvature black hole in $N + 1$ spacetime dimensions is a geometry of constant curvature with the metric [34–36]

$$\begin{aligned}
 ds^2 &= -f(r)dt^2 + \frac{dr^2}{f(r)} + r^2 d\sigma_{N-1}^2 \\
 f(r) &= r^2 + k - \frac{2m}{r^{N-2}} + \frac{q^2}{r^{2N-4}},
 \end{aligned}
 \tag{2.1}$$

where $d\sigma_{N-1}^2$ is the horizon manifold, which has curvature k , and m and q define the mass and charge of the black hole. It is a vacuum solution of the Einstein equations with constant negative cosmological constant and thus interpolates to AdS space with radius 1. From now on let us stick to $N = 3$ unless specified otherwise. For $k = 1$ we have the familiar spherical black hole. For $k = 0$ we get the planar horizon (black brane) popular in AdS/CFT applications.⁶ Finally, for $k = -1$ the horizon is an infinite hyperbolic sheet (pseudosphere), with the symmetry group $SO(2, 1)$.⁷ Notice that k can always be rescaled together with the coordinates on σ_2 thus we only consider $k = -1, 0, 1$. The metric of the horizon surface takes the form

$$d\sigma_2^2 = d\phi_1^2 + \text{sink}^2 \phi_1 d\phi_2^2, \tag{2.2}$$

with $\text{sink}(x) = \sin x$ for $k = 1$, $\text{sink}(x) = x$ for $k = 0$ and $\text{sink}(x) = \sinh(x)$ for $k = -1$.

A closed string with tension $1/\alpha'$ on the worldsheet (τ, σ) with target space X^μ and the metric $G_{\mu\nu}$ is described by the Polyakov action:

$$S = -\frac{1}{2\pi\alpha'} \int d\tau d\sigma \sqrt{-h} h^{ab} G_{\mu\nu}(X) \partial_a X^\mu \partial_b X^\nu + \epsilon^{ab} B_{\mu\nu}(X) \partial_a X^\mu \partial_b X^\nu. \tag{2.3}$$

In our black hole backgrounds we always have $B_{\mu\nu} = 0$ so we can pick the gauge $h^{ab} = \eta^{ab} = \text{diag}(-1, 1)$. This gives the Virasoro constraints

$$G_{\mu\nu} \left(\dot{X}^\mu \dot{X}^\nu + X'^\mu X'^\nu \right) = 0, \quad G_{\mu\nu} \dot{X}^\mu X'^\nu = 0, \tag{2.4}$$

where we introduce the notation $\dot{X} \equiv \partial_\tau X$, $X' \equiv \partial_\sigma X$. The first constraint is the Hamiltonian constraint $H = 0$. We consider closed strings, so $0 \leq \sigma \leq 2\pi$. From the second constraint the following ansatz is consistent (of course, it is not the only one possible):

$$\mathcal{T} = \mathcal{T}(\tau), \quad R = R(\tau), \quad \Phi_1 = \Phi_1(\tau), \quad \Phi_2 = n\sigma. \tag{2.5}$$

We denote the (dynamical) target-space coordinates $X_\mu(\tau, \sigma)$ by capital letters $\mathcal{T}, R, \Phi_1, \Phi_2$, to differentiate them from the notation for spacetime coordinates t, r, ϕ_1, ϕ_2 in the metric (2.1). The form (2.5) was tried in most papers exploring the integrability and chaos

⁶With periodic identifications on σ_2 one gets instead a toroidal horizon.

⁷If we identify the points along the orbits of the little group of $SO(2, 1)$, we get a genus g surface with $g \leq 2$, and the horizon becomes compact and topologically nontrivial, hence the term topological black holes for this case.

of strings [19, 25–29]. It is not an arbitrary ansatz: the winding of Φ_2 follows from the equations of motion, i.e., from the fact that Φ_2 is a cyclic coordinate, leading to the solution $\ddot{\Phi}_2 = 0$. Since Φ_2 has trivial dynamics, from now on we will denote $\Phi \equiv \Phi_1$. The equations of motion follow from (2.3):

$$\partial_\tau (f\dot{\mathcal{T}}) = 0 \Rightarrow E \equiv f\dot{\mathcal{T}} = \text{const.} \tag{2.6}$$

$$\ddot{R} + \frac{f'}{2f}(E^2 - \dot{R}^2) + fR (\dot{\Phi}^2 - n^2 \text{sink}^2 \Phi) = 0 \tag{2.7}$$

$$\ddot{\Phi} + \frac{2\dot{R}}{R}\dot{\Phi} + \frac{n^2}{2}\text{sink}(2\Phi) = 0. \tag{2.8}$$

Clearly, the stationarity of the metric yields the first integral E with the informal meaning of mechanical energy for the motion along the R and Φ coordinates (it is not the total energy in the strict sense). The system is more transparent in Hamiltonian form, with the canonical momenta $P_{\mathcal{T}} = -E = -f\dot{\mathcal{T}}$, $P_R = \dot{R}/f$, $P_\Phi = R^2\dot{\Phi}$:⁸

$$H = \frac{f}{2}P_R^2 + \frac{1}{2R^2}P_\Phi^2 + \frac{n^2}{2}R^2\text{sink}^2\Phi - \frac{E^2}{2f} = 0, \tag{2.9}$$

the second equality being the Virasoro constraint. We thus have a 2-degrees-of-freedom system (due to the integral of motion E , i.e., the cyclic coordinate \mathcal{T}), with a constraint, effectively giving a 1.5-degrees-of-freedom system, moving on a three-dimensional manifold in the phase space (R, P_R, Φ, P_Φ) . Notice that the motion along a geodesic is obtained for $n = 0$; in this case, the system is trivially separable and becomes just motion in a central potential. For nonzero n , the Hamiltonian (2.9) is not separable and the system is nonintegrable.⁹ On the other hand, for a point particle all constant-curvature black holes have a full set of integrals of motion leading to the integrability of geodesics: for the sphere, the additional integrals (besides E) are L^2 and L_z from $\text{SO}(3)$, and for the pseudosphere these are K^2 and K_z from $\text{SO}(2,1)$. For the planar black hole we obviously have $P_{x,y}$, the momenta, as the integrals of motion. Of course, if we consider compactified surfaces, the symmetries become discrete and do not yield integrals of motion anymore. Therefore, truly topological black holes are in general nonintegrable even for geodesics.¹⁰

⁸In this and the next section we put $\alpha' = 1/\pi$, as we only consider classical equations of motion, which are independent of α' . In section 4, when calculating the quantities of the dual gauge theory, we restore α' as it is related to the 't Hooft coupling, a physical quantity.

⁹One can prove within Picard-Vessiot theory that no canonical transformation exists that would yield a separable Hamiltonian, so the system is nonintegrable. We will not derive the proof here, as it is not very instructive; the nonintegrability of the spherical case was already proven in [26, 29], and the existence of nonzero Lyapunov exponents will *de facto* prove the nonintegrability for the other cases. One extra caveat is in order for the planar case. For $k = 0$ and $\text{sink}\Phi = \Phi$, the Hamiltonian is still not separable, and dynamics is nonintegrable. One could change variables in the metric (2.1) as $(\phi_1, \phi_2) \mapsto (\phi'_1 = \phi_1 \cos \phi_2, \phi'_2 = \phi_1 \sin \phi_2)$, and the string with the wrapping $\Phi'_2 = n\sigma$ would provide an integrable system, with the separable Hamiltonian $H' = \frac{f}{2}P_R^2 + \frac{1}{2R^2}P_{\Phi'}^2 + \frac{n^2}{2}R^2 - \frac{E^2}{2f}$. But that is a *different* system from (2.9): even though a change of variables is clearly of no physical significance, the wrapping $\Phi'_2 = n\sigma$ is physically different from $\Phi_2 = n\sigma$. Integrability clearly depends on the specific string configuration.

¹⁰For special, fine-tuned topologies and parameters, one finds integrable cases (even for string motion!) but these are special and fine-tuned; we will consider these cases elsewhere as they seem peripheral for our main story on the chaos bound.

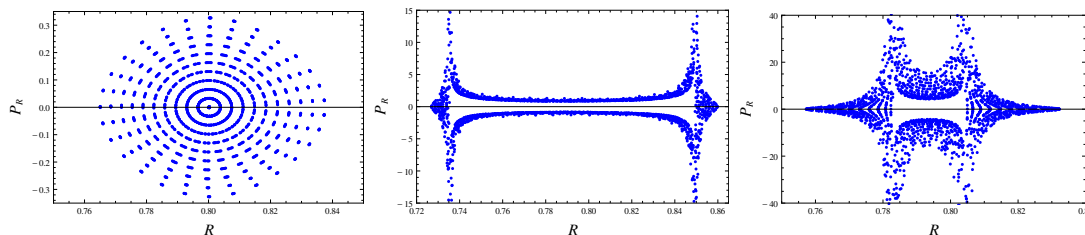


Figure 1. Poincaré section (R, P_R) for orbits starting at the apparent horizon (removed for a distance of 10^{-4} from the event horizon), at increasing temperatures $T = 0.00, 0.05, 0.10$, for a planar black hole with $m = 1$ and charge parameter q determined by the temperature. The coordinate and momentum are in units of AdS radius.

2.1 Fixed points and near-horizon dynamics

For a better overall understanding of chaos in string motion, let us sketch the general trends in dynamics first. For spherical black holes, this job was largely done in [26, 29, 44] and for similar geometries also in [27, 28]. We will emphasize mainly the properties of near-horizon dynamics that we find important for the main story.

Typical situation can be grasped from figure 1, where the Poincaré sections of orbits starting near the horizon are shown for increasing temperatures of the horizon, as well as figures 2 and 3 where we show typical orbits in the $x - y$ plane for different temperatures and initial conditions.

1. Higher temperatures generally increase chaos, with lower and lower numbers of periodic orbits (continuous lines in the Poincaré section in figure 1) and increasing areas covered with chaotic (area-filling) orbits. This is also obvious from the figure 2.
2. Orbits closer to the horizon are more chaotic than those further away; this will be quantified by the analysis of the Lyapunov exponents. This is logical, since the equations of motion for strings in pure AdS space are integrable, and far away from the horizon the spacetime probed by the string becomes closer and closer to pure AdS. An example of this behavior is seen in figure 3(A).
3. The previous two trends justify the picture of the thermal horizon as the generator of chaos. However, for an extremal or near-extremal *hyperbolic* horizon there is a slight discrepancy — in this case, moving away from the horizon increases the chaos. In other words, there is yet another mechanism of chaos generation, independent of the temperature and not located precisely at the horizon, which is subleading and not very prominent, except when it is (almost) the only one, i.e., when the horizon is (near-)extremal. This is demonstrated in figure 3(B).

When we come to the consideration of the Lyapunov exponents, we will identify the horizon-induced scrambling and the chaotic scattering as the chaos-inducing mechanisms at work for $r \rightarrow r_h$ and for intermediate r , respectively.

Consider now the radial motion from the Hamiltonian (2.9). Radial motion exhibits an effective attractive potential $E^2/2f$ which diverges at the horizon. The Φ -dependent terms

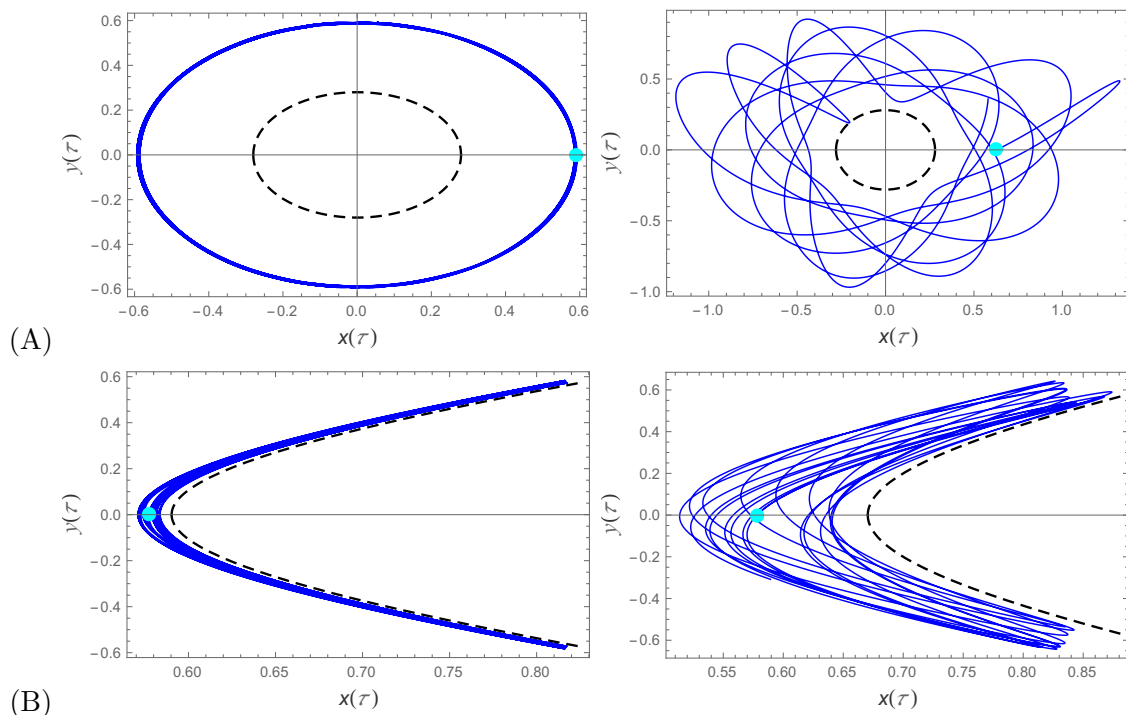


Figure 2. Thermal horizon as the generator of chaos. We show the orbits in the vicinity of the spherical (A) and hyperbolic (B) horizon, at $T = 0.01$ (left) and $T = 0.10$ (right); obviously, hot horizons generate more chaos than cold ones. The light blue dot is the initial condition of the orbit (the position of the point on the string with $\Phi = 0$ at $\tau = 0$).

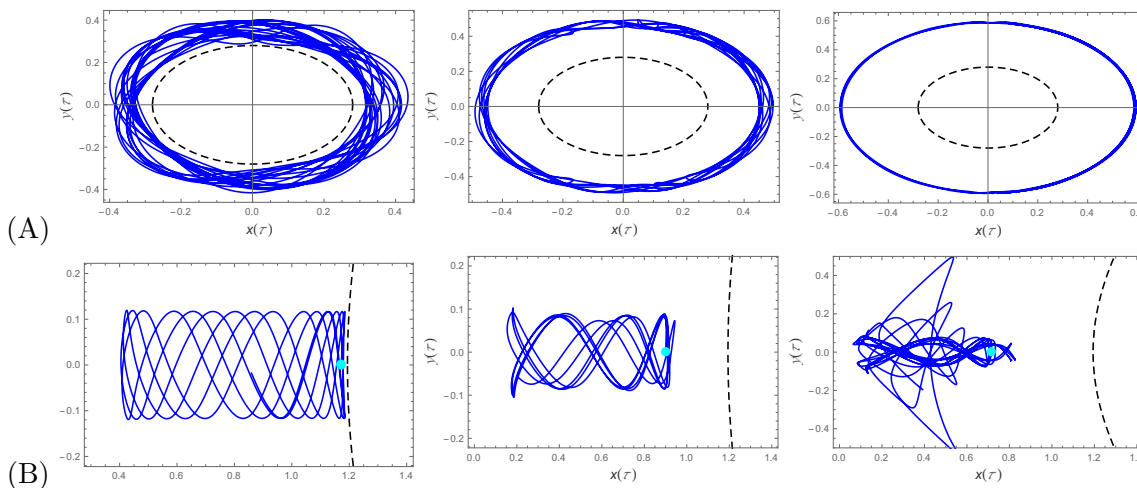


Figure 3. Thermal horizon and hyperbolic scattering as generators of chaos. In (A) and (B), we show the orbits in the vicinity of the spherical and hyperbolic horizon, respectively, at the small temperature $T = 0.01$ and starting at increasing distances from the horizon. In (A), the further from the horizon, the more regular the orbit becomes. But in the hyperbolic geometry (B), the thermally-generated chaos is negligible; instead, the orbit becomes chaotic as it explores larger and larger area of the hyperbolic manifold. Hence for hyperbolic horizons, an additional, non-thermal generator of chaos exists: it is the hyperbolic scattering. Light blue dots are again the initial positions of the string origin ($\Phi = 0$).

proportional to R^2 and $1/R^2$ are repulsive and balance out the gravitational attraction to some extent but they remain finite for all distances. For R large, the repulsion proportional to n^2 dominates so for large enough distances the string will escape to infinity. For intermediate distances more complex behavior is possible: the string might escape after some number of bounces from the black hole, or it might escape after completing some (non-periodic, in general) orbits around the black hole. The phase space has invariant planes given by $(R, P_R, \Phi, P_\Phi) = (R_0 + E\tau, E/f_0, N\pi, 0)$, with $R_0 = \text{const.}$ and $f_0 \equiv f(R_0)$ and N an integer. It is easy to verify this solution by first plugging in $\dot{\Phi} = 0$ into (2.8) to find Φ ; eq. (2.7) and the constraint (2.9) then reduce to one and the same condition $\dot{R}^2 = E^2$. We discard the solution with the minus sign (with $R = R_0 - E\tau$) as R is bounded from below. Pictorially, this solution means that a string with a certain orientation just moves uniformly toward the black hole and falls in, or escapes to infinity at uniform speed, all the while keeping the same orientation. Besides, there is a trivial fixed point at infinity, $(R, P_R, \Phi, P_\Phi) = (\infty, 0, N\pi, 0)$, found also in [26, 29].

We are particularly interested if a string can hover at a fixed radial slice $R = r_0 = \text{const.}$. Let us start from the spherical case. Inserting $R = r_0, \dot{R} = 0$ into eq. (2.8) leads to the solution in terms of the incomplete Jacobi sine integral sn (Jacobi elliptic function of the first kind, Jacobi E -function), and two integration constants to be determined. The other equation, (2.7), is a first-order relation for $\dot{\Phi}$ acting as a constraint. Solving it gives a Jacobi elliptic function again, with one undetermined constant, and we can match the constants to obtain a consistent solution:

$$\sin \Phi(\tau) = \text{sn} \left(\frac{E\sqrt{|f'_0|}}{\sqrt{2r_0 f_0}} \tau, \frac{2n^2 r_0 f_0^2}{E^2 |f'_0|} \right). \tag{2.10}$$

The value of r_0 is found from the need to satisfy also the Hamiltonian constraint. The constraint produces a Jacobi elliptic function with a different argument, and the matching to (2.10) reads

$$2f(r_0) + r_0 f'(r_0) = 0. \tag{2.11}$$

This turns out to be a cubic equation independent of the black hole charge, as the terms proportional to q cancel out. It has one real solution, *which is never above the horizon*. The solution approaches the horizon as $f'(r_0)$, approaches zero, and $r = r_h$ is obviously a solution of (2.11) for $f'(r_h) = 0$. However, the $r \rightarrow r_h$ limit is subtle in the coordinates we use because some terms in equations of motion diverge, so we need to plug in $f(r) = 0$ from the beginning. Eqs. (2.6), (2.8) then imply $\dot{R} = E$, i.e., there is no solution at constant R except for $E = 0$. This is simply because the energy is infinitely red-shifted at the horizon, i.e., E scales with f (eq. (2.6)), thus indeed unless $\dot{\mathcal{T}} \rightarrow \infty$, which is unphysical, we need $E = 0$. Now solving eq. (2.7) gives the same solution as before, of the form $\text{sn}(C_1\tau, C_2)$, with undetermined constants $C_{1,2}$, which are chosen so as to establish continuity with the solution (2.10). For an extremal horizon of the form $f \sim a(r - r_h^2) \equiv a\epsilon^2$, a smooth and finite limit is obtained by rescaling $E \mapsto E\epsilon^2$. Now expanding the sn function in ϵ produces simply a linear function at first order in ϵ :

$$\Phi(\tau) = E\tau/\sqrt{ar_0} + O(\epsilon^3). \tag{2.12}$$

Therefore, a string can hover at the extremal horizon, at strict zero temperature, when its motion (angular rotation) becomes a simple linear winding with a single frequency. Such an orbit is expected to be linearly stable, and in the next section we show it is also stable according to Lyapunov and thus has zero Lyapunov exponent. Finally, from (2.7) and (2.11) the radial velocity \dot{R} in the vicinity of a non-extremal horizon behaves as:

$$\dot{R}^2 \approx E^2 + 4\pi T r_h (r - r_h)^2, \tag{2.13}$$

meaning that \dot{R} grows quadratically as the distance from the horizon increases. This will allow us to consider near-horizon dynamics at not very high temperatures as happening at nearly constant radius: the string only slowly runs away.

For a hyperbolic horizon the calculation is similar, changing $\sin \mapsto \sinh$ in the solution (2.10). The constraint (2.11) is also unchanged (save for the sign of k in the redshift function), and the final conclusion is the same: the string can only balance at the zero temperature horizon (but now such a horizon need not be charged, as we mentioned previously). The zero temperature limit is the same linear function (2.12). For a planar horizon things are different. For $\dot{R} = 0$, we get simply harmonic motion $\Phi = C_1 \cos n\tau + C_2 \sin n\tau$, which is consistent with the constraint $H = 0$. But eq. (2.7) implies exponential motion instead, $D_1 \sinh n\tau + D_2 \cosh n\tau$. Obviously, there is no way to make these two forms consistent. Accordingly, no hovering on the horizon (nor at any other fixed radial slice) is possible for a planar black hole. But the same logic that lead to (2.13) now predicts oscillating behavior:

$$R(\tau) \approx E^2 + 4\pi T r_h (r - r_h)^2 (n^2 \cos^2 n\tau - \sin^2 n\tau). \tag{2.14}$$

Therefore, even though there are no orbits at all which stay at exactly constant R , we now have orbits which oscillate in the vicinity of the horizon forever. Averaging over long times now again allows us to talk of a string that probes some definite local temperature, determined by the average distance from the horizon.

The point of this (perhaps tedious and boring) qualitative analysis of possible orbits is the following. No orbits at fixed distance from the horizon are possible, *but* at low temperatures a string that starts near the horizon will spend a long time in the near-horizon area. Therefore, we can study the influence of the low-temperature horizon as the main chaos-generating mechanism by expanding the variational equations for the Lyapunov exponents in the vicinity of the horizon, This we shall do in the next section.

3 Lyapunov exponents and the bound on chaos

In general, Lyapunov exponents are defined as the coefficients λ of the asymptotic exponential divergence of initially close orbits; in other words, of the variation δX of a coordinate X :

$$\lambda \equiv \lim_{t \rightarrow \infty} \lim_{\delta X(0) \rightarrow 0} \frac{1}{t} \log \frac{|\delta X(t)|}{|\delta X(0)|}, \tag{3.1}$$

and the variation is expected to behave as $\delta X \sim \delta X(0) \exp(\lambda t)$ for t large and $\delta X(0)$ small enough in practice. This definition makes sense for classical systems; in quantum

mechanics, the linearity of the state vector evolution guarantees zero exponent but the intuition that initially small perturbations eventually grow large in a strongly coupled system remains when we look at appropriately defined correlation functions, like the OTOC used in [1]. We should first make the following point clear. In a classical nonlinear system, the presence of deterministic chaos leads to positive Lyapunov exponents even in absence of temperature or noise. Quantum mechanically, as we explained, the linearity of evolution means that exponential divergence is only possible in a thermal state, and this situation leads to the temperature bound on the Lyapunov exponents. This is easy to see upon restoring dimensionful constants, when the bound from [1] takes the form $\lambda \leq 2\pi k_B T/\hbar$, and indeed in a classical system where $\hbar \rightarrow 0$ no bound exists. In the context of our work, which effectively reduces to the classical Hamiltonian (2.9) which has no gravitational degrees of freedom, it is not *a priori* clear if one should expect any connection to the bound on chaos: instead of a QFT correlation function or its gravity dual, we have classical dynamics, and the Hawking temperature of the black hole is not the local temperature probed by the string. But we will soon see that analytical and numerical estimates of λ nevertheless have a form similar to the chaos bound of [1].

Before we proceed one final clarification is in order. One might worry that the Lyapunov exponents are gauge-dependent, as we consider equations of motion in terms of the worldsheet coordinate τ , and for different worldsheet coordinates the variational equations would be manifestly different; in other words, the definition (3.1) depends on the choice of the time coordinate (denoted schematically by t in (3.1)). Indeed, the value of λ clearly changes with coordinate transformations, however it has been proven that the *positivity* of the largest exponent (the indicator of chaos) is gauge-invariant; the proof was derived for classical general relativity [45] and carries over directly to the worldsheet coordinate transformations. This is all we need, because we will eventually express the τ -exponent in terms of proper time for an inertial observer, making use of the relation $\tilde{T} = -E/f$. This could fail if a coordinate change could translate an exponential solution into an oscillating one (because then λ drops to zero and it does not make sense to re-express it units of proper time); but since we know that cannot happen we are safe.

3.1 Variational equations and analytical estimates of Lyapunov exponents

3.1.1 Thermal horizon

Consider first a thermal black hole horizon at temperature T , with the redshift function behaving as $f = 4\pi T(r - r_h) + O((r - r_h)^2)$. Variational equations easily follow from (2.6)–(2.7):

$$\delta\ddot{R} - \frac{E^2}{(R - r_h)^2}\delta R - 4\pi T \left(\dot{\Phi}^2 - n^2 \text{sink}^2\Phi \right) \delta R - 8\pi T(R - 2r_h)R\dot{\Phi}\delta\dot{\Phi} + 4\pi n^2 TR \text{sink}(2\Phi)\delta\Phi = 0 \quad (3.2)$$

$$\delta\ddot{\Phi} + n^2 \text{sink}(2\Phi) + \frac{2}{r_h}\dot{\Phi}\delta\dot{R} = 0, \quad (3.3)$$

with on-shell solutions $R(\tau), \Phi(\tau)$. This system looks hopeless, but it is not hard to extract the leading terms near the horizon which, as we explained, makes sense at low temperatures.

Therefore, we start from the solutions (2.10), (2.12), (2.14), adding a small correction $(r_0, \Phi(\tau)) \rightarrow (r_0 + \Delta R(\tau), \Phi(\tau) + \Delta\Phi(\tau))$. Then we expand in inverse powers of $r_0 - r_h$, and express the angular combinations $\dot{\Phi}^2 \pm \text{sink}^2\Phi$ making use of the constraint (2.9). When the dust settles, the leading-order equations simplify to:

$$\delta\ddot{R} - \left(16(\pi T)^3 \frac{n^2}{E^2}(r_0 - r_h) - 32(\pi T)^3 \frac{Cn}{E^2\phi_0}(r_0 - r_h)^2 \right) \delta R = 0 \quad (3.4)$$

$$\delta\ddot{\Phi} + n^2 \langle \text{cosk}^2(2\Phi) \rangle \delta\Phi = 0, \quad (3.5)$$

where $C = C(k, E)$ is a subleading (at low temperature) correction whose form differs for spherical, planar and hyperbolic horizons. From the above we read off that angular motion has zero Lyapunov exponent (the variational equation is oscillatory, because $\langle \text{cosk}^2(2\Phi) \rangle \geq 0$) but the radial component has an exponent scaling as

$$\tilde{\lambda}(T) \sim 4\sqrt{(\pi T)^3(r_0 - r_h)} \frac{n}{E} \left(1 - (r - r_h) \frac{C}{\phi_0 n} \right). \quad (3.6)$$

Now we have calculated the Lyapunov exponent in worldsheet time τ . The gauge-invariant quantity, natural also within the black hole scrambling paradigm, is the proper Lyapunov exponent λ , so that $1/\lambda$ is the proper Lyapunov time for an asymptotic observer. To relate $\tilde{\lambda}$ to λ , we remember first that the Poincare time t is related to the worldsheet time τ through (2.6) as $|dt| \sim E/f \times d\tau$. Then we obtain the proper time as $t_p = t\sqrt{-g_{00}} = t\sqrt{f}$, where near the thermal horizon we can write $f \approx 4\pi T(r - r_h)$. This gives¹¹

$$\lambda(T) \sim 2\pi T n \left(1 - \epsilon \frac{C}{\phi_0 n} \right). \quad (3.7)$$

At leading order, we get the estimate $2\pi T n$, with the winding number n acting as correction to the original bound.

3.1.2 Away from the horizon

At intermediate radii we can do a similar linear stability analysis starting from $f \sim r^2 + k + A/r$ where A is computed by series expansion (with just the AdS term $r^2 + k$ in f , without the leading black hole contribution A/r , we would trivially have integral motion and zero λ ; but this approximation applies at large, not at intermediate distances). In this case the equations of motion yield $R \sim \tau\sqrt{E^2 - 1}$, and the variational equations, after some algebra, take the form

$$\delta\ddot{R} - \frac{2}{R}(k + R^2)\delta\dot{\Phi} + E \left(\frac{3kR^2}{R^2 + k} + 1 \right) \delta R = 0. \quad (3.8)$$

One can show again that $\delta\dot{\Phi}$ is always bounded in absolute value, thus the third term determines the Lyapunov exponent. The exponent vanishes for $k > -1/3$ (because the equations becomes oscillatory) and for $k \leq -1/3$ we get

$$\lambda \sim \sqrt{-(3k + 1)E}. \quad (3.9)$$

¹¹We introduce the notation $\epsilon \equiv r - r_h$.

Since the curvature only takes the values $-1, 0, 1$, the prediction (3.9) always holds for hyperbolic horizons. Notice that this same term (the third term in (3.8)) appears as subleading in the near-horizon expansion, so we can identify it with $C(k, E)$ and write (3.7) as $\lambda(T) \sim 2\pi T n (1 - \epsilon|(3k + 1)E|/(\phi_0 n))$. This holds for any k , and we see that $C \leq 0$; thus the bound is only approached from below as it should be.

In absence of negative curvature, i.e., for $k > 0$, we have vanishing C at leading order in $1/R$ but subleading contributions still exist, so both the slight non-saturation of the limit $2\pi T n$ near-horizon (for small ϵ) and a parametrically small non-zero Lyapunov exponent at intermediate distances will likely appear, which we see also in the numerics. That the motion is chaotic on a pseudosphere (negative curvature) is of course no surprise; it is long known that both particles and waves have chaotic scattering dynamics on pseudospheres [46]. We dub this contribution the scattering contribution to the Lyapunov exponent, as opposed to the scrambling contribution. It is largely independent of temperature and largely determined by the geometry of the spacetime away from the horizon.

3.1.3 Extremal horizon

For an extremal horizon we replace f by $f \sim a(r - r_h)^2 = a\epsilon^2$, and plug in this form into the variational equations. Now the result is (for concreteness, for the spherical horizon)

$$\delta\ddot{R} - \left(\frac{a^2\epsilon^4 r_h^2 n^2}{2a\epsilon r_h - 2a\epsilon^2} \right) \delta R = 0 \tag{3.10}$$

$$\delta\ddot{\Phi} + n^2 \langle \text{cosk}(2\Phi) \rangle \delta\Phi = 0, \tag{3.11}$$

leading to a vanishing exponent value:

$$\tilde{\lambda}(T) \sim \sqrt{a r_h / 2n} \epsilon^{3/2} \rightarrow 0. \tag{3.12}$$

Obviously, this also means $\lambda = 0$ — there is no chaos at the extremal horizon. This is despite the fact that the string motion in this case is still nonintegrable, which is seen from the fact that no new symmetries or integrals of motion arise in the Hamiltonian in this case. The horizon scrambling is proportional to temperature and does not happen at $T = 0$, but the system is still nonintegrable and the chaos from other (scattering) origins is still present. In particular, the estimate (3.8)–(3.9) remains unchanged.

The estimates (3.7), (3.9), (3.12) are the central sharp results of the paper. We can understand the following physics from them:

1. At leading order, we reproduce (and saturate) the factor $2\pi T$ of the Maldacena-Shenker-Stanford bound, despite considering classical dynamics only.
2. The bound is however multiplied by the winding number n of the ring string. The spirit of the bound is thus preserved but an extra factor — the winding number — enters the story.
3. Taking into account also the scattering chaos described by (3.9), the results are in striking accordance with the idea of [2]: there are two contributions to chaos, one

proportional to the black hole temperature and solely determined by the scrambling on the horizon, with the universal factor $2\pi T$ expected from the concept of black holes as the fastest scramblers in nature, and another determined by the (slower) propagation of signals from the horizon toward the AdS boundary, which we call the scattering term, as it is determined also by dynamics at large distances.

4. For a particle ($n = 0$), we correctly get $\lambda = 0$, as the geodesics are integrable.
5. The temperature appearing in (3.7) is always the Hawking temperature of the black hole T .

In the next section, when we consider the AdS/CFT interpretation, we will try to shed some more light on where the modification of the bound $2\pi T \mapsto 2\pi T n$ comes from.

3.1.4 Lyapunov time versus event time

In the above derivations we have left one point unfinished. We have essentially assumed that $R(\tau) \approx \text{const.} = r$ and treated the difference $\epsilon = r - r_h$ as a fixed small parameter. This is only justified if the local Lyapunov time $1/\tilde{\lambda}$ is much shorter than the time to escape far away from r_h and the horizon, or to fall into the black hole. In other words, it is assumed that the Lyapunov time is much shorter than the “lifetime” of the string (let us call it event time t_E). Now we will show that this is indeed so. For the spherical black hole, upon averaging over the angle Φ , we are left with a one-dimensional system

$$\dot{R}^2 + R^2 f(R) \frac{E^2 f'(R)}{R f^2(R)} = E^2, \tag{3.13}$$

which predicts the event time as

$$t_E \sim \int_{r_0}^{r_h, \infty} \frac{dR}{\sqrt{|E - E f'(R) R f^2(R)|}} \approx \frac{\pi r_h}{\sqrt{2}} \frac{1}{\sqrt{4\pi T \epsilon n}} \approx \frac{\pi r_h}{\sqrt{2}} \times \frac{\tilde{\lambda}^{-1}}{\epsilon}. \tag{3.14}$$

In other words, the event times are roughly by a factor $1/\epsilon$ longer than Lyapunov times, therefore our estimate for λ should be valid. In (3.14), we have considered both the infalling orbits ending at r_h , and the escaping orbits going to infinity (for the latter, we really integrate to some $r_\infty > r_0$ and then expand over $1/r_\infty$). An orbit will be infalling or escaping depending on the sign of the combination under the square root, and to leading order both cases yield a time independent of r_0 (and the cutoff r_∞ for the escaping case). The hyperbolic case works exactly the same way, and in the planar case since $R(\tau)$ oscillates the event time is even longer (as there is no uniform inward or outward motion). For extremal horizons, there is no issue either as $r = r_h$ is now the fixed point.

3.1.5 Dimensionful constants

One might wonder what happens when dimensionful constants are restored in our results for the Lyapunov exponents like (3.7) or (3.9): the original chaos bound really states $\lambda \leq 2\pi k_B T / \hbar$, and we have no \hbar in our system so far. The resolution is simple: the role of \hbar is played by the inverse string tension $2\pi\alpha'$, which is obvious from the standard form

of the string action (2.3); the classical string dynamics is obtained for $\alpha' \rightarrow 0$. Therefore, the dimensionful bound on chaos for our system reads $\lambda = 2\pi k_B T n / 2\pi\alpha' = k_B T n / \alpha'$. Another way to see that α' takes over the role of \hbar in the field-theory derivation [1] is that the weight in computing the correlation functions for a quantum field is given by the factor $\exp(-1/\hbar \int \mathcal{L})$, whereas for a string the amplitudes are computed with the weight $\exp(-1/2\pi\alpha' \int \mathcal{L})$. In the next section, we will also look for the interpretation in the framework of dual field theory. In this context, α' is related to the number of degrees of freedom in the gauge dual of the string, just like the Newton's constant G_N is related to the square of the number of colors N^2 in the gauge dual of a pure gravity theory. But the issues of gauge/string correspondence deserve more attention and we treat them in detail in section 4.

3.2 Numerical checks

We will now inspect the results (3.7), (3.9), (3.12) numerically. Figure 4 tests the basic prediction for the horizon scrambling, $\lambda \approx 2\pi T n$ at low temperatures: both the n -dependence at fixed temperature (A), and the T -dependence at fixed n (B) are consistent with the analytical prediction. All calculations were done for the initial condition $\dot{R}(0) = 0$, and with energy E chosen to ensure a long period of hovering near the horizon. The temperatures are low enough that the scattering contribution is almost negligible. In figure 5 we look at the scattering term in more detail. First we demonstrate that at zero temperature, the orbits in non-hyperbolic geometries are regular (A): the scattering term vanishes at leading order, and the scrambling vanishes at $T = 0$. In the (B) panel, scattering in hyperbolic space at intermediate radial distances gives rise to chaos which is independent of the winding number, in accordance to (3.7). To further confirm the logic of (3.7), one can look also at the radial dependence of the Lyapunov exponent: at zero temperature, there is no chaos near-horizon (scrambling is proportional to T and thus equals zero; scattering only occurs at finite $r - r_h$), scattering yields a nonzero λ at intermediate distances and the approach to pure AdS at still larger distances brings it to zero again; at finite temperature, we start from $\lambda = 2\pi T n$ near-horizon, observe a growth due to scattering and fall to zero approaching pure AdS.

4 Toward a physical interpretation of the modified bound

4.1 Dual gauge theory interpretation

The ring string wrapped along the σ coordinate is a very intuitive geometry from the viewpoint of bulk dynamics. However it has no obvious interpretation in terms of the gauge/gravity duality, and the Hamiltonian (2.9) itself, while simple-looking, is rather featureless at first glance: essentially a forced nonlinear oscillator, it does not ring a bell on why to expect the systematic modification of the Maldacena-Shenker-Stanford bound and what the factor n means. Thus it makes sense to do two simple exercises: first, to estimate the energy and spin of the operators corresponding to (2.5) to understand if it has to do with some Regge trajectory; second, to consider some other string configurations, with a more straightforward connection to the operators in gauge theory. Of course, finite

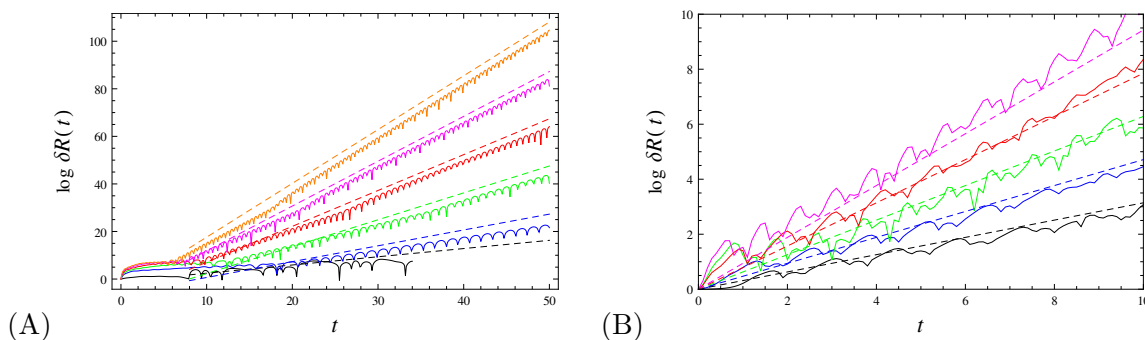


Figure 4. (A) Logarithm of the relative variation of the coordinate R , for a spherical AdS-Reissner-Nordstrom black hole, for a fixed temperature $T = 0.04$ and increasing winding numbers $n = 1, 2, 3, 4, 5, 6$ (black, blue, green, red, magenta, orange). Full lines are the numerical computational of the function $\log(\delta X(\tau)/\delta X(0)) = \lambda\tau$, so their slopes equal the Lyapunov exponents λ . Dashed lines show the analytically predicted bound $\log \delta X = 2\pi T n \tau + \log X_0$. Numerically computed variations almost saturate the bounds denoted by the dashed lines. The calculation for $n = 1$ is stopped earlier because in this case the orbit falls in into the black hole earlier than for higher n . (B) Same as (A) but for a hyperbolic AdS-Schwarzschild black hole, at fixed $n = 1$ and increasing temperature $T = 0.050, 0.075, 0.100, 0.125, 0.150$ (black, blue, green, red, magenta), again with analytically predicted bounds shown by the dashed lines. For the two highest temperatures (red, magenta) the computed slopes are slightly above the bound probably because the near-horizon approximation does not work perfectly well. The short-timescale oscillations superimposed on the linear growth, as well as the nonlinear regime before the linear growth starts in the panel (A) are both expected and typical features of the variation δR (Lyapunov exponents are defined asymptotically, for infinite times).

temperature horizons are crucial for our work on chaos, and saying *anything* precise about the gauge theory dual of a string in the black hole background is extremely difficult; we will only build some qualitative intuition on what our chaotic strings do in field theory, with no rigorous results at all.

Let us note in passing that the ring string configurations considered so far are almost insensitive to spacetime dimension. Even if we uplift from the four-dimensional spacetime described by (t, r, ϕ_1, ϕ_2) to a higher-dimensional spacetime $(t, r, \phi_1, \phi_2, \dots, \phi_{N-2})$, with the horizon being an $N - 2$ -dimensional sphere/plane/pseudosphere, the form of the equations of motion does not change if we keep the same ring configuration, with $\Phi_1 = \Phi_1(\tau, \sigma)$, $\Phi_2 = n\sigma$, $\Phi_3 = \text{const.}, \dots, \Phi_{N-2} = \text{const.}$ — this is a solution of the same eqs. (2.6)–(2.8) with the same constraint (2.9). The difference lies in the redshift function $f(r)$ which depends on dimensionality. This, however, does not change the main story. We can redo the calculation of the radial fixed point from the second section, to find a similar result — a string can oscillate or run away/fall slowly in the vicinity of a horizon, and the variational equations yield the same result for the Lyapunov exponent as before. It is really different embeddings, i.e., different Polyakov actions, that might yield different results.

4.1.1 Operators dual to a ring string?

We largely follow the strategy of [47] in calculating the energy and the spin of the string and relating them to the dual Yang-Mills theory. In fact, the ring string is quite close to

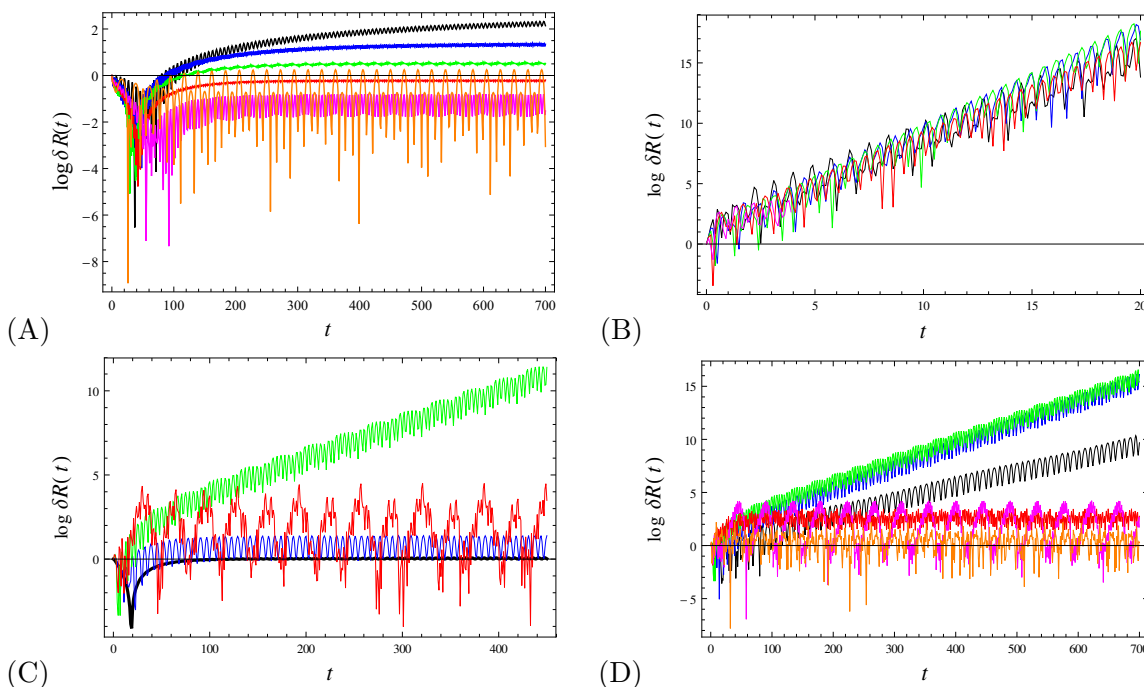


Figure 5. (A) Logarithm of the radial variation δR for near-horizon orbits with $n = 1, 2, 3, 4, 5, 6$ (black, blue, green, red, magenta, orange) in a planar extremal Reissner-Nordstrom geometry. All curved asymptote to a constant, i.e., (almost) zero slope, resulting in $\lambda \approx 0$. (B) Same as previous for an extremal hyperbolic black hole. Now the Lyapunov exponent is nonzero, and equal for all winding numbers: in absence of thermal scrambling, the chaos originates solely from scattering, which is independent of n . (C) The Lyapunov exponent in zero-temperature hyperbolic black hole background for $n = 1$ and $r = r_h, 1.1r_h, 1.2r_h, 1.3r_h$ (black, blue, green, red) starts at zero (no scrambling, no scattering), grows to a clear nonzero value for larger radii due to scattering, and again falls to zero for still larger distances, as the geometry approaches pure AdS (D) Lyapunov exponent in $T = 0.02$ hyperbolic black hole background for $n = 1$ and $r = r_h, 1.1r_h, 1.2r_h, 1.3r_h, 1.4r_h, 1.5r_h$ (black, blue, green, red, magenta, orange) starts at the scrambling value (black), reaches its maximum when both scrambling and scattering are present (blue, green) and then falls to zero when AdS is approached (red, magenta, orange).

what the authors of [47] call the oscillating string, *except* that we allow one more angle to fluctuate independently (thus making the system nonintegrable) and, less crucially, that in [47] only the winding number $n = 1$ is considered.

Starting from the action for the ring string (2.3), we write down the expressions for energy and momentum:

$$\mathcal{E} = \frac{1}{2\pi\alpha'} \int d\tau \int d\sigma P_{\mathcal{T}} = \frac{E}{\alpha'} \int_{\phi_1}^{\phi_2} \frac{d\Phi}{\dot{\Phi}} \tag{4.1}$$

$$\mathcal{S} = \frac{1}{2\pi\alpha'} \int d\tau \int d\sigma P_{\Phi} = \frac{1}{\alpha'} \int_{\phi_1}^{\phi_2} \frac{d\Phi}{\dot{\Phi}} R^2(\Phi) \dot{\Phi}, \tag{4.2}$$

where the second worldsheet integral gives simply $\int d\sigma = 2\pi$ as R, Φ do not depend on σ , and we have expressed $d\tau = d\Phi/\dot{\Phi}$; finally, the canonical momentum is conserved, $P_{\mathcal{T}} = E$,

and in the expression for the spin we need to invert the solution $\Phi(\tau)$ into $\tau(\Phi)$ in order to obtain the function $R(\Phi)$. We are forced to approximate the integrals. Expressing $\dot{\Phi}$ from the Hamiltonian constraint (2.4), we can study the energy in two regimes: small amplitude $\phi_0 \ll \pi$ which translates to $E/T \ll 1$, and large amplitude $\phi_0 \sim \pi$, i.e., $E/T \sim 1$. For these two extreme cases, we get:

$$\mathcal{E} \approx \frac{4r_0 \sqrt{f(r_0)}}{\alpha'} \phi_0 = \frac{4E}{\alpha'n}, \quad \phi_0 \ll \pi \quad (4.3)$$

$$\mathcal{E} \approx \frac{\pi E}{\alpha'n}, \quad \phi_0 \sim \pi \quad (4.4)$$

For the spin similar logic gives

$$\mathcal{S} \approx \frac{8r_0 E}{\alpha' \sqrt{f(r_0)}} \phi_0 = \frac{8E^2}{\alpha'n} \frac{1}{f(r_0)} \approx \frac{8E^2}{\alpha'n} \frac{1}{4\pi T \epsilon}, \quad \phi_0 \ll \pi \quad (4.5)$$

$$\mathcal{S} \approx \frac{4E^2}{\alpha'n} \sqrt{\frac{2f'(r_0)r_0}{f^3(r_0)}} \approx \frac{8E^2}{\alpha'n} \frac{\sqrt{2\pi}}{4\pi T \epsilon}, \quad \phi_0 \sim \pi. \quad (4.6)$$

The bottom line is that in both extreme regimes (and then presumably also in the intermediate parameter range) we have $\mathcal{E} \propto E/\alpha'n$ and $\mathcal{S} \propto E^2/\alpha'nT\epsilon$; as before $\epsilon = r - r_h$ and it should be understood as a physical IR cutoff (formally, for $r \rightarrow r_h$ the spin at finite temperature diverges; but we know from section 2 that in fact no exact fixed point at constant r exists, and the average radial distance is always at some small but finite distance ϵ). Therefore, we have $\mathcal{E}^2 \propto \mathcal{S}/\alpha'nT\epsilon$.

The presence of temperature in the above calculation makes it hard to compare the slope to the familiar Regge trajectories. But in absence of the black hole, when $f(r) = 1$, we get

$$\mathcal{E} = 4E/\alpha'n, \quad \mathcal{S} = 8E^2/\alpha'n \Rightarrow \mathcal{E}^2 = 2\mathcal{S}/\alpha'n. \quad (4.7)$$

For $n = 1$, this is precisely the leading Regge trajectory. For higher n the slope changes, and we get a different trajectory. Therefore, the canonical Lyapunov exponent value $\lambda = 2\pi T$ precisely corresponds to the leading Regge trajectory. We can tentatively conclude that the winding string at finite temperature describes complicated thermal mixing of large-dimension operators of different dimensions and spins, and these might well be sufficiently nonlocal that the OTOC never factorizes and the bound from [1] does not apply.

4.1.2 Planetoid string

In this subsection we consider so-called planetoid string configurations, also studied in [47] in the zero-temperature global AdS spacetime and shown to reproduce the leading Regge trajectory in gauge theory. This is again a closed string in the same black hole background (2.1) but now the solution is of the form¹²

$$\mathcal{T} = e\tau, \quad R = R(\sigma), \quad \Phi_1 = \Phi_1(\tau), \quad \Phi_2 = \Phi_2(\sigma), \quad (4.8)$$

¹²The authors of [47] work mostly with the Nambu-Goto action but consider also the Polyakov formulation in the conformal gauge; we will stick to the Polyakov action from the beginning for notational uniformity with the previous section. For the same reason we keep the same coordinate system as in (2.1).

where the auxiliary field e is picked so as to satisfy the conformal gauge, and any additional coordinates Φ_3, Φ_4, \dots and $\Theta_1, \Theta_2, \dots$ are fixed. The Lagrangian

$$L = -\frac{1}{2f} (R')^2 - \frac{e^2}{2} f + \frac{R^2}{2} \left(-\dot{\Phi}_1^2 + \sin^2 \Phi_1 \Phi_2'^2 \right) \quad (4.9)$$

has the invariant submanifold $\Phi_1 = \omega\tau, \Phi_2 = \text{const.}$ when the dynamics becomes effectively one-dimensional, the system is trivially integrable and, in absence of the black hole, it is possible to calculate exactly the energy and spin of the dual field theory operator. This is the integrable case studied in [47, 48], and allowing Φ_2 to depend on σ seems to be the only meaningful generalization, because it leads to another submanifold of integrable dynamics with $R = r_0 = \text{const.}, \Phi_2 = n\sigma$ and the pendulum solution for Φ_1 :

$$\sin \Phi_1(\tau) = \text{sn} \left(\ell\tau, -\frac{n^2}{\ell^2} \right), \quad (4.10)$$

where $\ell^2 = \dot{\Phi}_1^2 - n^2 \sin^2 \Phi_1$ is the adiabatic invariant on this submanifold. With two integrable submanifolds, a generic orbit will wander between them and exhibit chaos. The variational equations can be analyzed in a similar fashion as in the previous section. Here, the chaotic degree of freedom is $\Phi_1(\tau)$, with the variational equation

$$\delta\ddot{\Phi}_1 - \Phi_2'^2 \cos(2\Phi_1) = 0, \quad (4.11)$$

which in the near-horizon regime yields the Lyapunov exponent

$$\lambda = 2\pi T n, \quad (4.12)$$

in the vicinity of the submanifold (4.10). In the vicinity of the other solution ($\Phi_1 = \omega\tau, \Phi_2 = \text{const.}$), we get $\lambda = 0$. Chaos only occurs in the vicinity of the winding string solution, and the winding number again jumps in front of the universal $2\pi T$ factor.

Now let us see if this kind of string reproduces a Regge trajectory. In the presence of the black hole the calculation results in very complicated special functions, but we are only interested in the leading scaling behavior of the function $\mathcal{E}^2(\mathcal{S})$. Repeating the calculations from (4.1)–(4.2), we first reproduce the results of [47] in the vicinity of the solution $\Phi_1 = \omega\tau$: for short strings, we get $\mathcal{E} \sim 2/\omega T, \mathcal{S} \sim 2/\omega^2 T^2$ and thus $\mathcal{E}^2 \propto 2\mathcal{S}$, precisely the result for the leading Regge trajectory. Now the Regge slope does not depend on the temperature (in the short string approximation!). This case, as we found, trivially satisfies the original chaos bound ($\lambda = 0$, hence for sure $\lambda < 2\pi T$). In the vicinity of the other solution, with $R = r_0$, things are different. Energy has the following behavior:

$$\mathcal{E} \sim \frac{8\pi T}{\alpha' n}, \quad \ell \ll 1 \quad (4.13)$$

$$\mathcal{E} \sim \frac{8\pi^2 T}{\alpha' \ell}, \quad \ell \gg 1. \quad (4.14)$$

For the spin, the outcome is

$$\mathcal{S} \sim \frac{2r_0^2 \ell}{\alpha' n}, \quad \ell \ll 1 \quad (4.15)$$

$$\mathcal{S} \sim \frac{2r_0^2}{\alpha'}, \quad \ell \gg 1, \quad (4.16)$$

so in this case there is no Regge trajectory at all, i.e., no simple relation for $\mathcal{E}^2(\mathcal{S})$ because the scale r_0 and the quantity ℓ show up in the $\mathcal{E}^2(\mathcal{S})$ dependence even at zero temperature.

In conclusion, the strings that can violate the chaos bound have a strange Regge behavior in the gauge/string duality, in this case in a more extreme way than for the ring strings (even for $n = 1$ no Regge trajectory is observed). The strings which have $\lambda = 0$ and thus trivially satisfy the bound on the other hand obey the leading Regge trajectory.

4.2 The limits of quasiclassicality

One more thing needs to be taken into account when considering the modification of the chaos bound. Following [8], one can suspect that the violating cases are not self-consistent in the sense that they belong to the deep quantum regime when semiclassical equations (in our case for the string) cease to be valid and quantum effects kill the chaos. For a ring string this seems not to be the case. To check the consistency of the semiclassical limit, consider the energy-time uncertainty relation $\Delta\mathcal{E}\Delta t \geq 1$. The energy uncertainty is of the order of $E/\alpha'n$ as we found in (4.3)–(4.4), and the time uncertainty is precisely of the order of the Lyapunov time $1/2\pi Tn$; the uncertainty relation then gives $E \geq 2\pi Tn^2\alpha'$. On the other hand, we require that the spin \mathcal{S} should be large in the classical regime: $\mathcal{S} \gg 1$. This implies $E^2 \gg 4\pi T\epsilon n\alpha'$ or, combining with the uncertainty relation, $Tn^3\alpha' \gg \epsilon$. Roughly speaking, we need to satisfy simultaneously $Tn^2 \leq 1/\alpha'$ and $Tn^3 \gg \epsilon/\alpha'$, which is perfectly possible: first, we need to have small enough α' (compared to Tn^2), as could be expected for the validity of the semiclassical regime; second, we need to have sufficiently large $n/\epsilon \gg 1$, which can be true even for $n = 1$ for small ϵ , and for sure is satisfied for sufficiently large n even for $\epsilon \sim 1$. In conclusion, there is a large window when the dynamics is well-described by the classical equations (and this window even grows when $n \gg 1$ and the violation of the chaos bound grows).

4.3 Ring string scattering amplitude and the relation to OTOC

So far our efforts to establish a field theory interpretation of a ring string in black hole background have not been very conclusive, which is not a surprise knowing how hard it is in general to establish a gauge/string correspondence in finite-temperature backgrounds and for complicated string geometries. Now we will try a more roundabout route and follow the logic of [4–6], constructing a gravity dual of the OTOC correlation function, which has a direct interpretation in field theory; it defines the correlation decay rate and the scrambling time of some boundary operator. In [17] this formalism was already applied to study the OTOC of field theory operators (heavy quarks) dual to an open string in BTZ black hole background, hanging from infinity to infinity through the horizon in eikonal approximation. That case has a clear interpretation: the endpoints of the string describe the Brownian motion of a heavy quark in a heat bath. As we already admitted, we do not have such a clear view of what our case means in field theory, but we can still construct the out-of-time ordered correlator corresponding to whatever complicated boundary operator our string describes.

We will be deliberately sketchy in describing the basic framework of the calculation as it is already given in great detail in [4–6]. The idea is to look at the correlation func-

tion $\langle\langle \hat{V}_{x_1}(t_1)\hat{W}_{x_2}(t_2)\hat{V}_{x_3}(t_3)\hat{W}_{x_4}(t_4) \rangle\rangle$ of some operators V, W at finite temperature (hence the expectation value $\langle\langle(\dots)\rangle\rangle$ includes both quantum-mechanical and thermal ensemble averaging). The time moments need not be ordered; we are often interested in the case $\Re t_1 = \Re t_3 \equiv 0, \Re t_2 = \Re t_4 = t$.¹³ This correlation function corresponds to the scattering amplitude between the in and out states of a perturbation sourced from the boundary. The propagation of the perturbation is described by the bulk-to-boundary propagators K . The perturbation has the highest energy at the horizon since the propagation in Schwarzschild time becomes a boost in Kruskal coordinates, and the perturbation, however small at the boundary, is boosted to high energy in the vicinity of the horizon. In the Kruskal coordinates defined the usual way:

$$U = -e^{\frac{t-r_*}{2r_h}}, \quad V = e^{\frac{t+r_*}{2r_h}}, \quad r_* = \int_r^\infty \frac{dr}{f(r)}, \quad (4.17)$$

the scattering amplitude becomes

$$D = \prod_{i=1}^4 \int d^2 p_i \int d^2 x_i K^*(p_3; x_3) K^*(p_4; x_4) K(p_1; x_1) K(p_2; x_2)_{\text{out}}(p_3^U, p_4^V; x_3, x_4 | p_1^U, p_2^V; x_1, x_2)_{\text{in}}. \quad (4.18)$$

The propagators are expressed in terms of the Kruskal momenta $p_i = (p_i^U, p_i^V)$ and the coordinates $x_i = (x_i^1, x_i^2)$ in the transverse directions. The in-state is defined by (p_3^U, x^3) at $U = 0$, and by (p_4^V, x^4) at $V = 0$, and analogously for the out-state. The form of the propagators is only known in the closed form for a BTZ black hole (in 2+1 dimensions), but we are happy enough with the asymptotic form near the horizon. For simplicity, consider a scalar probe of zero bulk mass, i.e., the conformal dimension $\Delta = D$, and at zero black hole charge, i.e., for a Schwarzschild black hole. The propagator then behaves as ($\tilde{\omega} \equiv \omega/4\pi T$):

$$K(p^U, p^V) \sim \frac{\pi}{\sinh(\frac{\pi}{T})} \frac{1 - e^{-\pi\tilde{\omega}}}{\Gamma(-i\tilde{\omega}) \Gamma(i\tilde{\omega})} \frac{e^{-i\tilde{\omega}t}}{(p^U)^{1+i\tilde{\omega}} + (p^V)^{1-i\tilde{\omega}}} e^{i(p^U V + p^V U)}. \quad (4.19)$$

The task is thus to calculate the amplitude (4.18) with the propagators (4.19). In the eikonal approximation used in most of the literature so far, the problem boils down to evaluating the classical action at the solution. However, it is not trivial to justify the eikonal approximation for a ring string. Let us first suppose that the eikonal approximation works and then we will see how things change if it doesn't.

4.3.1 Eikonal approximation

If the energy in the local frame near the horizon is high enough, then we have approximately $p_1^U \approx p_3^U \equiv p, p_2^V \approx p_4^V \equiv q$ so that $p_1^V \approx p_2^U \approx p_3^V \approx p_4^U \approx 0$, and for a short enough scattering event (again satisfied if the energy and thus the velocity is high enough) the coordinates are also roughly conserved, therefore the amplitude $\langle\text{out}|\text{in}\rangle$ is diagonal and can be written as a phase shift $\exp(i\delta)$. The point of the eikonal approximation is that the

¹³In the Schwinger-Keldysh finite-temperature formalism the time is complex, with the imaginary time axis compactified to the radius of the inverse temperature.

shift δ equals the classical action. The action of the ring configuration is

$$S = \frac{1}{2\pi\alpha'} \int d\tau \int d\sigma \left(\frac{\dot{R}^2}{2} (\dot{\Phi}_1^2 - n^2 \sin^2 \Phi_1) + \frac{\dot{R}^2}{2f} + \frac{f}{2} \dot{\mathcal{T}}^2 \right). \quad (4.20)$$

We will consider again the string falling slowly in the vicinity of the horizon (see eqs. (2.10)–(2.14)) and put $\dot{R} \rightarrow 0, R(\tau) \approx r_0, r_0 - r_h \ll r_h$. Now we need to pass to the Kruskal coordinates and then introduce the new variables $\mathbb{T} = (V + U)/2, X = (V - U)/2$. In these coordinates the near-horizon geometry in the first approximation is Minkowskian and we can easily expand around it as required for the eikonal approximation. The action and the energy (to quartic order in the fluctuations) are now

$$S = \frac{1}{2\pi\alpha'} \int d\tau \int d\sigma \left[\frac{1}{2} (-\dot{\mathbb{T}}^2 + \dot{X}^2 + r_0^2 \dot{\Phi}^2 + r_0^2 n^2 \sin^2 \Phi^2) \left(1 + \frac{\mathbb{T}^2 - X^2}{2} \right) \right] \quad (4.21)$$

$$\mathcal{E} = \frac{1}{2\pi\alpha'} \int d\tau \int d\sigma \frac{\dot{\mathbb{T}}}{(1 - \mathbb{T}^2 + X^2)^2}. \quad (4.22)$$

As a sanity check, for $n = 0$ the fluctuations of the (\mathbb{T}, X) variables in the action (4.21) are the same as in [17], although we use a different worldsheet parametrization. The dynamics of the angle Φ crucially depends on the winding number. One consequence is that the on-shell action is nontrivial already at quadratic order. For the solution (2.10) — the slowly-moving near-horizon string — we can assume $\dot{\mathbb{T}}, \dot{X} \ll \dot{\Phi}$, so the equations of motion yield as approximate on-shell solutions

$$\mathbb{T} = \mathbb{T}_0 e^{nr_0\tau/\sqrt{2}}, \quad X = X_0 e^{-nr_0\tau/\sqrt{2}}, \quad (4.23)$$

so that, as the perturbation dies out, the string approaches the locus $\mathbb{T}_0 = 0 \Rightarrow U = -V \Rightarrow t \rightarrow \infty$. Inserting (4.23) into (4.21), we obtain, after regularizing the action:

$$S^{(0)} = \frac{nr_0}{2\alpha'} \mathbb{T}_0^2 + \dots \quad (4.24)$$

$$\mathcal{E}^{(0)} = \frac{\sqrt{2}}{\alpha'} \mathbb{T}_0 + \dots \quad (4.25)$$

Therefore, $S^{(0)} = (\mathcal{E}^{(0)})^2 \times nr_h \alpha' / 4$ (where we have plugged in $r_0 \approx r_h$): the action is proportional to the square of energy, which equals $\mathcal{E}^2 = pq$ in the center-of-mass frame. This is perfectly in line with the fast scrambling hypothesis. Plugging in $\delta = S^{(0)}$ into the amplitude in (4.18) and rescaling

$$T_{13} \equiv e^{2\pi T t_1} - e^{2\pi T t_3^*}, \quad T_{24} \equiv e^{-2\pi T t_4^*} - e^{-2\pi T t_2} \quad (4.26)$$

$$p^U = \frac{p}{i} \frac{1}{T_{13}}, \quad p^V = \frac{q}{i} \frac{1}{T_{24}} \quad (4.27)$$

we obtain:

$$D = N_\omega^4 \left(e^{2\pi T t_1} - e^{2\pi T t_3^*} \right)^2 \left(e^{-2\pi T t_4^*} - e^{-2\pi T t_2} \right)^2 \int \frac{dp}{p^2} \int \frac{dq}{q^2} e^{-p-q-i\frac{pq}{T_{13}T_{24}} \frac{\alpha' nr_h}{4}}, \quad (4.28)$$

with N_ω containing the first two factors in (4.19) which only depend on ω and T . Introducing the change of variables $p = Q \sin \gamma, q = Q \cos \gamma$, we can reduce (4.28) to an exponential integral. With the usual contour choice for OTOC $\Im t_i = -\epsilon_i, \Re t_1 = \Re t_3 = 0, \Re t_2 = \Re t_4 = t$, we end up at leading order with

$$D \sim 1 + 2i\alpha' n r_h e^{2\pi T t} \Rightarrow \lambda_{\text{OTOC}} \sim 2\pi T, t_* \sim \frac{1}{2\pi T} \log \frac{1/\alpha'}{n r_h}. \quad (4.29)$$

Therefore, the Lyapunov time as defined by the OTOC in field theory precisely saturates the predicted bound $2\pi T$, and in the eikonal approximation is not influenced by the winding number n . On the other hand, the scrambling time t_* is multiplied by a factor of $\log(1/\alpha' n)$ (the horizon radius can be rescaled to an arbitrary value by rescaling the AdS radius, thus we can ignore the factor of r_h). The factor $1/\alpha'$ appears also in [17] and plays the role of a large parameter, analogous to the large N^2 factor in large- N field theories: the entropy of the string (the number of degrees of freedom to be scrambled) certainly grows with $1/\alpha'$. For a ring string, this factor is however divided by n , as the number of excitations is reduced by the implementation of the periodic winding boundary condition. Therefore, the winding of the ring string indeed speeds up the chaotic diffusion, by speeding up the scrambling. However, the faster scrambling is not seen in the timescale of local divergence which, unlike the classical Lyapunov exponent, remains equal to $2\pi T$; it is only seen in the timescale on which the perturbation permeates the whole system.

In conclusion, *the violation of the Maldacena-Shenker-Stanford limit for the bulk Lyapunov exponent in AdS space in the eikonal approximation likely corresponds to a decrease of scrambling time in dual field theory, originating from reduction in the number of degrees of freedom.*

4.3.2 Beyond the eikonal approximation: waves on the string

What is the reason to worry? Even if the scattering is still elastic and happens at high energies and momenta (therefore the overlap of the initial and final state is diagonal in the momenta), it might not be diagonal in the coordinates if the string oscillations are excited during the scattering. These excitations might be relevant for the outcome.¹⁴ However, the quantum mechanics of the string in a non-stationary background is no easy matter and we plan to address it in a separate work. In short, one should write the amplitude (4.18) in the worldsheet theory and then evaluate it in a controlled diagrammatic expansion. For the black hole scrambling scenario, the leading-order stringy corrections are considered in [6]; the Regge (flat-space) limit is the pure gravity black hole scrambling with the Lyapunov exponent $2\pi T$ and scrambling time determined by the large N . We need to do the same for the string action (4.21) but, as we said, we can only give a rough sketch now.

¹⁴With an open string hanging from the boundary to the horizon as in [17] this is not the case, since it stretches along the radial direction and the scattering event — which is mostly limited to near-horizon dynamics because this is where the energy is boosted to the highest values — remains confined to a small segment of the string, whereas any oscillations propagate from end to end. However, a ring string near the horizon is *wholly in the near-horizon region all the time*, and the string excitations may happily propagate along it when the perturbation reaches the area $UV \approx 0$.

The amplitude (4.18) is given by the worldsheet expectation value

$$\mathcal{A} = \prod_i \int d^2 z_i \langle \hat{V}(z_1, \bar{z}_1) \hat{W}(z_2, \bar{z}_2) \hat{V}(z_3, \bar{z}_3) \hat{W}(z_4, \bar{z}_4) \rangle \quad (4.30)$$

with the action (4.20), or (4.21) in the target-space coordinates (\mathbb{T}, X) accommodated to the shock-wave perturbation. Here, we have introduced the usual complex worldsheet coordinates $z = \tau + i\sigma, \bar{z} = \tau - i\sigma$. We thus need to compute a closed string scattering amplitude for the tachyon of the Virasoro-Shapiro type, but with nontrivial target-space metric and consequently with the vertex operators more complicated than the usual plane-wave form. This requires some drastic approximations. We must first expand the non-Gaussian functional integral over the fields $\mathbb{T}(z, \bar{z}), X(z, \bar{z}), \Phi(z, \bar{z})$ perturbatively, and then we can follow [6] and [49] and use the operator-product expansion (OPE) to simplify the vertex operators and decouple the functional integral over the target-space coordinates from the worldsheet integration. First we can use the worldsheet reparametrization to fix as usual $z_1 = \infty, z_2 = z, z_3 = 1, z_4 = 0$. The most relevant regime is that of the highly boosted perturbation near the horizon, with $|z| \sim 1/s$. At leading order in the expansion over \mathbb{T}, X , the action (4.21) decouples the Gaussian functional integral over the (\mathbb{T}, X) coordinates from the pendulum dynamics of the Φ coordinate. We can just as easily use the (U, V) dynamics, with $1/2(\dot{\mathbb{T}}^2 - \dot{X}^2) \mapsto -2\dot{U}\dot{V}$; this is just a linear transformation and the functional integral remains Gaussian. The states in U and V coordinates are just the plane waves with $p_1 = p_3 = p, p_2 = p_4 = q$, but the Φ states are given by some nontrivial wavefunctions $\psi(\Phi)$. Altogether we get

$$\begin{aligned} \mathcal{A} &= \int d^2 z \int DUDVD\Phi \exp \left[-\frac{1}{2\pi\alpha'} \int d^2 z' \left(-2\dot{U}\dot{V} + r_h^2 \left(\dot{\Phi}^2 + n^2 \sin^2 \Phi \right) \right) \right] \hat{V}_1 \hat{W}_2 \hat{V}_3 \hat{W}_4 \\ \hat{V}_{1,3} &= g(U_{1,3}) e^{\mp i p U_1} \psi^\mp(\Phi_{1,3}), \quad \hat{W}_{2,4} = g(V_{2,4}) e^{\mp i q V_{2,4}} \psi^\mp(\Phi_{2,4}), \end{aligned} \quad (4.31)$$

where we denote by the index $i = 1, 2, 3, 4$ the coordinates depending on z_i and the coordinates in the worldsheet action in the first line depend on z' which is not explicitly written out to save space. The higher-order metric corrections in U and V give rise to the weak non-plane-wave dependence of the vertices on U and V , encapsulated in the functions g above. We will disregard them completely, in line with considering the decoupled approximation of the metric as written explicitly in the action in (4.31). The functional integral over U, V is easily performed but the Φ -integral is formidable. However, for small $|z|$, we can expand the ground state solution (2.10) in z, \bar{z} , which corresponds to the linearized oscillatory behavior and the functional integral becomes Gaussian: $\dot{\Phi}^2 + n^2 \sin^2 \Phi \mapsto \dot{\Phi}^2 + n^2 \Phi^2$. With the effective potential for the tachyon $V_{\text{eff}}(\Phi) = n^2 \Phi^2$, the worldsheet propagator takes the form

$$G^\Phi(z, \bar{z}, z', \bar{z}') = K_0(n|z - z'|) \sim \log \frac{n|z - z'|^2}{2}. \quad (4.32)$$

For the plane wave states we take the ansatz $\psi(\Phi) = e^{i\ell\Phi}$, where $\ell = l - i\nu$, with $l \in \mathbb{Z}$ being the angular momentum and $0 < \nu \ll 1$ the correction from the interactions (fortunately we will not need the value of ν). The worldsheet propagator for the flat (U, V) coordinates

has the standard logarithmic form. Now we use the fact that $1/|z| \sim s = pq$ to expand the vertices for \hat{W}_2 and \hat{W}_4 in OPE. The OPE reads

$$: \hat{W}_2 \hat{W}_4 : \sim \exp(iqz\partial V_2 + iq\bar{z}\bar{\partial}V_2) \exp(i\ell z\partial\Phi_2 + i\ell\bar{z}\bar{\partial}\Phi_2) |z|^{-2 - \frac{2\pi\alpha'}{r_h^2}(\ell^2 - n^2/2)}, \quad (4.33)$$

which follow from the action of the Laplace operator on the state $e^{i\ell\Phi}$. This finally gives

$$\mathcal{A} = \text{const.} \times \int d^2z : \hat{W}_2 \hat{W}_4 : \exp\left(-\frac{\pi\alpha'}{2}pq \log|1-z|^2\right) \exp\left[\frac{\pi\alpha'}{r_h^2}\ell^2(G^\Phi(z) + G^\Phi(1-z))\right]. \quad (4.34)$$

The above integral results in a complicated ratio of the ${}_1F_1$ hypergeometric functions and gamma functions. We still have three possible poles, as in the Virasoro-Shapiro amplitude. In the stringy regime at large pq , the dominant contribution must come from $\ell \sim l = 0$, for the other pole brings us back to the purely gravitational scattering, with $S \propto pq$, whereby the local scrambling rate remains insensitive to n , as we have shown in the eikonal approximation. The stringy pole yields the momentum-integrated amplitude

$$D \sim \int \frac{dp}{p^2} \int \frac{dq}{q^2} \exp\left[-p - q - (pqe^{-2\pi T t})^{1 + \frac{\pi\alpha'}{r_h^2}n^2}\right] \sim 1 + \text{const.} \times e^{2\pi T(1 + \pi\alpha'n^2)}$$

$$\lambda_{\text{OTOC}} \sim 2\pi T(1 + \pi\alpha'n^2), \quad (4.35)$$

showing that the Lyapunov scale $2\pi T$ is modified (we again take $r_h = 1$ for simplicity). We conclude that *in the strong stringy regime the Lyapunov exponent in dual field theory behaves as $2\pi(1 + \pi\alpha'n^2)T$, differing from the expected chaos bound for nonzero winding numbers n .* Thus, if the classical gravity eikonal approximation does not hold, the modification of the bulk Lyapunov exponent also has an effect on the OTOC decay rate in field theory.

Once again, the above reasoning has several potential loopholes: (1) we completely disregard the higher-order terms in the metric, which couple that radial and transverse dynamics (2) we assume only small oscillations in Φ (3) we disregard the corrections to vertex operators (4) we disregard the corrections to the OPE coefficients. These issues remain for future work.

5 Discussion and conclusions

Our study has brought us to a sharp formal result with somewhat mystifying physical meaning. We have studied classical chaos in the motion of closed strings in black hole backgrounds, and we have arrived, analytically and numerically, at the estimate $\lambda = 2\pi T n$ for the Lyapunov exponent, with n being the winding number of the string. This is a correction by the factor of n of the celebrated chaos bound $\lambda \leq 2\pi T$. However, one should think twice before connecting these things. From the bulk perspective, what we have is different from classical gravity — it includes string degrees of freedom, and no gravity degrees of freedom. Therefore, the fast scrambler hypothesis that the black holes in Einstein gravity exactly saturate the bound is not expected to be relevant for our system

anyway, but the question remains why the bound is modified *upwards* instead of simply being unsaturated (in other words, we would simply expect to get $\lambda < 2\pi T$). The twist is that the Lyapunov exponent in the bulk is related to but in general *distinct* from the Lyapunov exponent in field theory, usually defined in terms of OTOC. Apparently, one just should not uncritically apply the chaos bound proven for the correlation function decay rates in flat-space quantum fields to worldsheet classical string dynamics.

Therefore, it might be that the field theory Lyapunov time does not violate the bound at all. The timescale of OTOC decay for a field theory dual to the fluctuating string is calculated in [17]: OTOC equals the expectation value of the scattering operator for bulk strings with appropriate boundary conditions. The field-theory Lyapunov time is then determined by the phase shift of the collision. In particular, [17] finds the saturated bound $\lambda = 2\pi T$ as following from the fact that the phase shift is proportional to the square of the center-of-mass energy. On the other hand, [6] predicts that the Lyapunov exponent is lower than the bound when stringy effects are considered. We have done first a completely classical calculation of OTOC and have found, expectedly perhaps, that the $2\pi T$ bound is exactly obeyed. Then we have followed the approximate scheme of [49] to include the one-loop closed string tachyon amplitude as the simplest (and hopefully representative enough?!) stringy process. For a ring string background, this gives an *increased* value for the field-theory Lyapunov rate, yielding some credit to the interpretation that complicated string configurations encode for strongly nonlocal operators, which might indeed violate the bound. But as we have explained, the approximations we took are rather drastic. We regard a more systematic study of loop effects in string chaos as one of the primary tasks for future work.

To gain some more feeling on the dual field theory, we have looked also at the Regge trajectories. In one configuration, the strings that violate the bound n times are precisely those whose Regge trajectory has the slope n times smaller than the leading one (and thus for $n = 1$ the original bound is obeyed and at the same time we are back to the leading Regge trajectory). In another configuration, the strings that violate the bound describe no Regge trajectory at all. However, it is *very* hard to say anything precise about the gauge theory operators at finite temperature. Deciphering which operators correspond to our strings is an important but very ambitious task; we can only dream of moving toward this goal in very small steps. What we found so far makes it probable that complicated, strongly non-local operators correspond to the bound-violating strings, so that (as explained in the original paper [1]) their OTOC cannot be factorized and the bound is not expected to hold.¹⁵

¹⁵In relation to the gauge/string duality it is useful to look also at the gauge theories with N_f flavors added, which corresponds to the geometry deformed by N_f additional D-branes in the bulk. In [50] it was found that the system becomes nonintegrable in the presence of the flavor branes (expectedly, as it becomes non-separable), but the Lyapunov exponent does not grow infinitely with the number of flavors, saturating instead when the number of colors N_c and the number of flavors become comparable. This is expected, as the D3-D7 brane background of [50] formally becomes separable again when $N_f/N_c \rightarrow \infty$ (although in fact this regime cannot be captured, the calculation of the background ceases to be valid in this case). In our case the winding number n is a property of the string solution, not geometry, and the Hamiltonian (2.9) seems to have no useful limit for $n \rightarrow \infty$, thus we do not expect the estimate $2\pi T n$ will saturate.

Preparing the final version of the paper, we have learned also of the work [52] where the n -point OTOCs are studied following closely the logic of [1] and the outcome is a factor of n enlargement, formally the same as our result. This is very interesting but, in the light of the previous paragraph, we have no proof that this result is directly related to ours. It certainly makes sense to investigate if the winding strings are obtained as some limit of the gravity dual for the n -point correlations functions. We know that n -point functions in AdS/CFT are a complicated business. The Witten diagrams include bulk propagators carrying higher spin fields that might in turn be obtained as string excitations. Just how far can one go in making all this precise we do not know for now.

In relation to [15, 16] one more clarifying remark should be given. In these works, particles in the vicinity of the horizon are found to exhibit chaos (either saturating the bound or violating it, depending on the spin of the background field). At first glance, this might look inconsistent with our finding that for $n = 0$, when the string degenerates to a particle, no chaos occurs; after all, we know that geodesic motion in the background of spherically symmetric black holes is integrable, having a full set of the integrals of motion. But in fact there is no problem, because in [15, 16] an additional external potential (scalar, vector, or higher-spin) is introduced that keeps the particle at the horizon, balancing out the gravitational attraction. Such a system is of course not integrable anymore, so the appearance of chaos is expected. The modification of the bound in the presence of higher-spin fields might have to do with the findings [51] that theories with higher-spin fields can only have gravity duals in very restricted situations (in particular, higher spin CFTs with a sparse spectrum and large central charge or, roughly speaking, massive higher spin fields, are problematic).

Another task on the to-do list, entirely doable although probably demanding in terms of calculations, is the (necessarily approximate) calculation of the black hole scattering matrix, i.e., the backreaction of the black hole upon scattering or absorbing a string, along the lines of [7]. In this paper we have worked in the probe limit (no backreaction), whereas the true scrambling is really the relaxation time of the black hole (the time it needs to become hairless again), which cannot be read off solely from the Lyapunov time; this is the issue we also mentioned in the Introduction, that local measures of chaos like the Lyapunov exponent do not tell the whole story of scrambling. Maybe even a leading-order (tree-level) backreaction calculation can shed some light on this question.

Acknowledgments

I am grateful to K. Schalm and M. V. Medvedyeva for helpful discussions. I also thank to D. Giataganas, L. A. Pando Zayas and J. Kasi for insightful remarks. Special thanks goes to the anonymous referee for his stimulating question which has improved the quality of the final manuscript. This work has made use of the excellent Sci-Hub service. Work at the Institute of Physics is funded by Ministry of Education, Science and Technological Development, under grant no. OI171017.

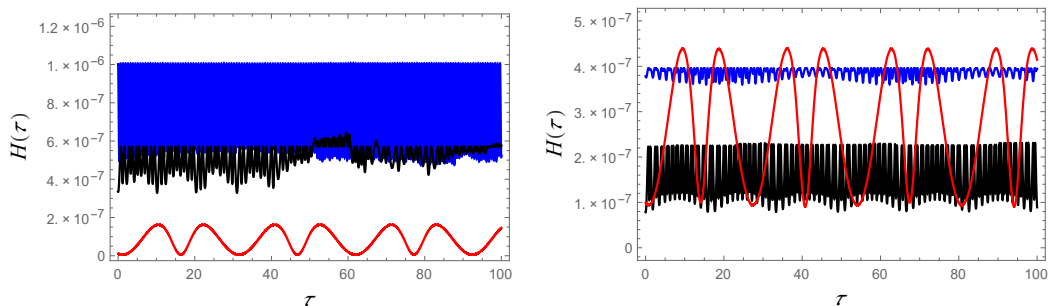


Figure 6. Check of the Hamiltonian constraint $H = 0$ during an integration for the spherical, planar and hyperbolic black hole (black, blue, red respectively), at temperature $T = 0.01$ (left) and $T = 0.10$ (right). The accuracy of the constraint is a good indicator of the overall integration accuracy, it is never above 10^{-6} and has no trend of growth but oscillates.

A Summary of the numerics

We feel it necessary to give a short account of the numerical methods used. The string equations of motion (2.6)–(2.8) present us with a system of two ordinary second-order differential equations with a constraint. This numerical calculation is not very difficult, and it would be trivial if it were not for two complicating factors. First, the constraint itself is the main complication; it is non-holonomic and cannot be easily eliminated. Second, the system is rather stiff, with \dot{R} in particular varying for several orders of magnitude. We did the integration in the `Mathematica` package, using mostly the `NDSolve` routine, and controlling both the relative and the absolute error during the calculations. The constraint problem is solved serendipitously by ensuring that the initial conditions satisfy the constraint and then adjusting the required absolute and relative error tolerance so that the constraint remains satisfied. A priori, this is a rather unlikely way to succeed but we find it works in most cases. Only in a few integrations we needed to write a routine which shoots for the condition $H = 0$ at every timestep, using the `NDSolve` routine in the solver; the shooting itself we wrote using the tangent method which is handier for this problem than the built-in routines. The usual analytic way, making use of the Lagrange multipliers, seems completely unsuitable for numerical implementation in this problem. In figure 6 we show the evolution of the constraint for a few examples, demonstrating the stability of the integration. We have also checked that the functions $R(\tau), \Phi(\tau)$ converge toward definite values as the precision and accuracy (relative and absolute error per step) are varied.

Open Access. This article is distributed under the terms of the Creative Commons Attribution License ([CC-BY 4.0](https://creativecommons.org/licenses/by/4.0/)), which permits any use, distribution and reproduction in any medium, provided the original author(s) and source are credited.

References

- [1] J. Maldacena, S.H. Shenker and D. Stanford, *A bound on chaos*, *JHEP* **08** (2016) 106 [[arXiv:1503.01409](https://arxiv.org/abs/1503.01409)] [[INSPIRE](https://inspirehep.net/literature/1503014)].
- [2] Y. Sekino and L. Susskind, *Fast scramblers*, *JHEP* **10** (2008) 065 [[arXiv:0808.2096](https://arxiv.org/abs/0808.2096)] [[INSPIRE](https://inspirehep.net/literature/786613)].

- [3] N. Lashkari, D. Stanford, M. Hastings, T. Osborne and P. Hayden, *Towards the fast scrambling conjecture*, *JHEP* **04** (2013) 022 [[arXiv:1111.6580](#)] [[INSPIRE](#)].
- [4] S.H. Shenker and D. Stanford, *Black holes and the butterfly effect*, *JHEP* **03** (2014) 067 [[arXiv:1306.0622](#)] [[INSPIRE](#)].
- [5] D.A. Roberts, D. Stanford and L. Susskind, *Localized shocks*, *JHEP* **03** (2015) 051 [[arXiv:1409.8180](#)] [[INSPIRE](#)].
- [6] S.H. Shenker and D. Stanford, *Stringy effects in scrambling*, *JHEP* **05** (2015) 132 [[arXiv:1412.6087](#)] [[INSPIRE](#)].
- [7] J. Polchinski, *Black hole S matrix*, [arXiv:1505.08108](#) [[INSPIRE](#)].
- [8] T. Scaffidi and E. Altman, *Chaos in a classical limit of the Sachdev-Ye-Kitaev model*, *Phys. Rev. B* **100** (2019) 155128 [[arXiv:1711.04768](#)] [[INSPIRE](#)].
- [9] S. Sachdev and J. Ye, *Gapless spin fluid ground state in a random, quantum Heisenberg magnet*, *Phys. Rev. Lett.* **70** (1993) 3339 [[cond-mat/9212030](#)] [[INSPIRE](#)].
- [10] O. Parcolet and A. Georges, *Non-Fermi liquid regime of a doped Mott insulator*, *Phys. Rev. B* **59** (1998) 5341 [[cond-mat/9806119](#)].
- [11] A. Kitaev, *A simple model of quantum holography (part 1)*, talk at KITP, April 7, 2015, <http://online.kitp.ucsb.edu/online/entangled15/kitaev/>.
- [12] A. Kitaev, *A simple model of quantum holography (part 2)*, talk at KITP, May 27, 2015, <http://online.kitp.ucsb.edu/online/entangled15/kitaev2/>.
- [13] E. Marcus and S. Vandoren, *A new class of SYK-like models with maximal chaos*, *JHEP* **01** (2019) 166 [[arXiv:1808.01190](#)] [[INSPIRE](#)].
- [14] A.L. Fitzpatrick and J. Kaplan, *A quantum correction to chaos*, *JHEP* **05** (2016) 070 [[arXiv:1601.06164](#)] [[INSPIRE](#)].
- [15] K. Hashimoto and N. Tanahashi, *Universality in chaos of particle motion near black hole horizon*, *Phys. Rev. D* **95** (2017) 024007 [[arXiv:1610.06070](#)] [[INSPIRE](#)].
- [16] S. Dalui, B.R. Majhi and P. Mishra, *Presence of horizon makes particle motion chaotic*, *Phys. Lett. B* **788** (2019) 486 [[arXiv:1803.06527](#)] [[INSPIRE](#)].
- [17] J. de Boer, E. Lladrés, J.F. Pedraza and D. Vegh, *Chaotic strings in AdS/CFT*, *Phys. Rev. Lett.* **120** (2018) 201604 [[arXiv:1709.01052](#)] [[INSPIRE](#)].
- [18] J.R. David, S. Khetrpal and S.P. Kumar, *Local quenches and quantum chaos from perturbations*, *JHEP* **10** (2017) 156 [[arXiv:1707.07166](#)] [[INSPIRE](#)].
- [19] P. Basu and L.A. Pando Zayas, *Analytic nonintegrability in string theory*, *Phys. Rev. D* **84** (2011) 046006 [[arXiv:1105.2540](#)] [[INSPIRE](#)].
- [20] A. Stepanchuk and A.A. Tseytlin, *On (non)integrability of classical strings in p-brane backgrounds*, *J. Phys. A* **46** (2013) 125401 [[arXiv:1211.3727](#)] [[INSPIRE](#)].
- [21] Y. Chervonyi and O. Lunin, *(Non)-integrability of geodesics in D-brane backgrounds*, *JHEP* **02** (2014) 061 [[arXiv:1311.1521](#)] [[INSPIRE](#)].
- [22] C. Núñez, J.M. Penín, D. Roychowdhury and J. Van Gersel, *The non-integrability of strings in massive type IIA and their holographic duals*, *JHEP* **06** (2018) 078 [[arXiv:1802.04269](#)] [[INSPIRE](#)].
- [23] D. Giataganas, L.A. Pando Zayas and K. Zoubos, *On marginal deformations and non-integrability*, *JHEP* **01** (2014) 129 [[arXiv:1311.3241](#)] [[INSPIRE](#)].

- [24] N. Beisert et al., *Review of AdS/CFT Integrability: An Overview*, *Lett. Math. Phys.* **99** (2012) 3 [[arXiv:1012.3982](#)] [[INSPIRE](#)].
- [25] A.V. Frolov and A.L. Larsen, *Chaotic scattering and capture of strings by a black hole*, *Class. Quant. Grav.* **16** (1999) 3717 [[gr-qc/9908039](#)] [[INSPIRE](#)].
- [26] L.A. Pando Zayas and C.A. Terrero-Escalante, *Chaos in the gauge/gravity correspondence*, *JHEP* **09** (2010) 094 [[arXiv:1007.0277](#)] [[INSPIRE](#)].
- [27] P. Basu and L.A. Pando Zayas, *Chaos rules out integrability of strings on $AdS_5 \times T^{1,1}$* , *Phys. Lett.* **B 700** (2011) 243 [[arXiv:1103.4107](#)] [[INSPIRE](#)].
- [28] P. Basu, D. Das and A. Ghosh, *Integrability lost: Chaotic dynamics of classical strings on a confining holographic background*, *Phys. Lett.* **B 699** (2011) 388 [[arXiv:1103.4101](#)] [[INSPIRE](#)].
- [29] P. Basu, P. Chaturvedi and P. Samantray, *Chaotic dynamics of strings in charged black hole backgrounds*, *Phys. Rev.* **D 95** (2017) 066014 [[arXiv:1607.04466](#)] [[INSPIRE](#)].
- [30] Y. Asano, D. Kawai, H. Kyono and K. Yoshida, *Chaotic strings in a near Penrose limit of $AdS_5 \times T^{1,1}$* , *JHEP* **08** (2015) 060 [[arXiv:1505.07583](#)] [[INSPIRE](#)].
- [31] Y. Asano, H. Kyono and K. Yoshida, *Melnikov's method in string theory*, *JHEP* **09** (2016) 103 [[arXiv:1607.07302](#)] [[INSPIRE](#)].
- [32] D. Giataganas and K. Sfetsos, *Non-integrability in non-relativistic theories*, *JHEP* **06** (2014) 018 [[arXiv:1403.2703](#)] [[INSPIRE](#)].
- [33] T. Ishii, K. Murata and K. Yoshida, *Fate of chaotic strings in a confining geometry*, *Phys. Rev.* **D 95** (2017) 066019 [[arXiv:1610.05833](#)] [[INSPIRE](#)].
- [34] R.B. Mann, *Pair production of topological anti-de Sitter black holes*, *Class. Quant. Grav.* **14** (1997) L109 [[gr-qc/9607071](#)] [[INSPIRE](#)].
- [35] D.R. Brill, J. Louko and P. Peldan, *Thermodynamics of (3+1)-dimensional black holes with toroidal or higher genus horizons*, *Phys. Rev.* **D 56** (1997) 3600 [[gr-qc/9705012](#)] [[INSPIRE](#)].
- [36] L. Vanzo, *Black holes with unusual topology*, *Phys. Rev.* **D 56** (1997) 6475 [[gr-qc/9705004](#)] [[INSPIRE](#)].
- [37] D. Birmingham, *Topological black holes in anti-de Sitter space*, *Class. Quant. Grav.* **16** (1999) 1197 [[hep-th/9808032](#)] [[INSPIRE](#)].
- [38] R.B. Mann, *Topological black holes — outside looking in*, *Annals Israel Phys. Soc.* **13** (1997) 311 [[gr-qc/9709039](#)] [[INSPIRE](#)].
- [39] W.L. Smith and R.B. Mann, *Formation of topological black holes from gravitational collapse*, *Phys. Rev.* **D 56** (1997) 4942 [[gr-qc/9703007](#)] [[INSPIRE](#)].
- [40] Y.C. Ong, *Hawking evaporation time scale of topological black Holes in anti-de Sitter spacetime*, *Nucl. Phys.* **B 903** (2016) 387 [[arXiv:1507.07845](#)] [[INSPIRE](#)].
- [41] Y. Chen and E. Teo, *Black holes with bottle-shaped horizons*, *Phys. Rev.* **D 93** (2016) 124028 [[arXiv:1604.07527](#)] [[INSPIRE](#)].
- [42] C.V. Johnson and F. Rosso, *Holographic heat engines, entanglement entropy and renormalization group flow*, *Class. Quant. Grav.* **36** (2019) 015019 [[arXiv:1806.05170](#)] [[INSPIRE](#)].
- [43] R. Emparan, *AdS/CFT duals of topological black holes and the entropy of zero-energy states*, *JHEP* **06** (1999) 036 [[hep-th/9906040](#)] [[INSPIRE](#)].

- [44] A.L. Larsen, *Chaotic string-capture by black hole*, *Class. Quant. Grav.* **11** (1994) 1201 [[hep-th/9309086](#)] [[INSPIRE](#)].
- [45] A.E. Motter, *Relativistic chaos is coordinate invariant*, *Phys. Rev. Lett.* **91** (2003) 231101 [[gr-qc/0305020](#)] [[INSPIRE](#)].
- [46] N.L. Balazs and A. Voros, *Chaos on the pseudosphere*, *Phys. Rept.* **143** (1986) 109 [[INSPIRE](#)].
- [47] S.S. Gubser, I.R. Klebanov and A.M. Polyakov, *A semi-classical limit of the gauge/string correspondence*, *Nucl. Phys. B* **636** (2002) 99 [[hep-th/0204051](#)] [[INSPIRE](#)].
- [48] H.J. de Vega and I.L. Egusquiza, *Planetoid string solutions in 3 + 1 axissymmetric spaces*, *Phys. Rev. D* **54** (1996) 7513 [[hep-th/9607056](#)] [[INSPIRE](#)].
- [49] R.C. Brower, J. Polchinski, M.J. Strassler and C.-I. Tan, *The pomeron and gauge/string duality*, *JHEP* **12** (2007) 005 [[hep-th/0603115](#)] [[INSPIRE](#)].
- [50] D. Giataganas and K. Zoubos, *Non-integrability and chaos with unquenched flavor*, *JHEP* **10** (2017) 042 [[arXiv:1707.04033](#)] [[INSPIRE](#)].
- [51] E. Perlmutter, *Bounding the space of holographic CFTs with chaos*, *JHEP* **10** (2016) 069 [[arXiv:1602.08272](#)] [[INSPIRE](#)].
- [52] P. Basu and K. Jaswin, *Higher point OTOCs and the bound on chaos*, [arXiv:1809.05331](#) [[INSPIRE](#)].

Quantum criticality in photorefractive optics: Vortices in laser beams and antiferromagnets

Mihailo Čubrović*

Scientific Computing Laboratory, Institute of Physics, University of Belgrade, Pregrevica 118, 11080 Belgrade, Serbia

Milan S. Petrović

*Institute of Physics, P.O. Box 57, 11001 Belgrade, Serbia
and Texas A&M University at Qatar, P.O. Box 23874, Doha, Qatar
(Received 5 December 2016; published 9 November 2017)*

We study vortex patterns in a prototype nonlinear optical system: counterpropagating laser beams in a photorefractive crystal, with or without the background photonic lattice. The vortices are effectively planar and have two “flavors” because there are two opposite directions of beam propagation. In a certain parameter range, the vortices form stable equilibrium configurations which we study using the methods of statistical field theory and generalize the Berezinsky-Kosterlitz-Thouless transition of the XY model to the “two-flavor” case. In addition to the familiar conductor and insulator phases, we also have the perfect conductor (vortex proliferation in both beams or “flavors”) and the frustrated insulator (energy costs of vortex proliferation and vortex annihilation balance each other). In the presence of disorder in the background lattice, a phase appears which shows long-range correlations and absence of long-range order, thus being analogous to glasses. An important benefit of this approach is that qualitative behavior of patterns can be known without intensive numerical work over large areas of the parameter space. The observed phases are analogous to those in magnetic systems, and make (classical) photorefractive optics a fruitful testing ground for (quantum) condensed matter systems. As an example, we map our system to a doped $O(3)$ antiferromagnet with \mathbb{Z}_2 defects, which has the same structure of the phase diagram.

DOI: [10.1103/PhysRevA.96.053824](https://doi.org/10.1103/PhysRevA.96.053824)**I. INTRODUCTION**

Nonlinear and pattern-forming systems [1–3] have numerous analogies with strongly correlated systems encountered in condensed matter physics [4,5], and on the methodological level they are both united through the language of field theory, which has become the standard language to describe strongly correlated electrons [6,7] as well as nonlinear dynamical systems [8]. In the field of pattern formation, some connections to condensed matter systems have been observed; see, e.g., Ref. [4]. More recently, extensive field-theoretical studies of laser systems were performed, e.g., Refs. [9–12], and also compared to experiment [13]. However, this topic is far from exhausted and we feel many analogies between quantum many-body systems and pattern-formation dynamics remain unexplored and unexploited. In particular, nonlinear optical systems and photonic lattices are flexible and relatively cheap to build [3] and they can be used to “simulate” a broad spectrum of phenomena concerning band structure, spin ordering, and conduction in strongly correlated electron systems; some of the work in this direction can be found in Refs. [14,15].

Our goal is to broaden the connections between the strongly correlated systems and nonlinear optics and to put to work the mighty apparatus of field theory to study the patterns in a nonlinear optical system from the viewpoint of phase transition theory: Pattern dynamics in certain cases shows critical behavior which is analogous to phenomena seen in magnetic systems. To that end, we use the formalism of perturbative field theory and renormalization group analysis but we also perform numerical simulations from the first principles, i.e., directly integrating the equations of motion to provide an *independent*

check of our main conclusions. We also establish a connection to an $O(3)$ antiferromagnetic model which is encountered in the study of strongly correlated electron systems. The analogy is not just qualitative: We construct the phase diagrams of both systems and find they have the same structure. Introducing disorder into the system further enriches the physics, and it is physically motivated: In optics, disorder is rooted in the imperfections of the photonic lattice, and in magnetic systems it comes from the quenched spin impurities which are regularly found in realistic samples. It turns out that in both cases a glassy phase arises. This is another important research topic and it is again appealing to realize glasses in photonic lattice systems, where the parameters are easy to tune.

A. On topology and vortices

The key phenomenon which governs the phenomenology of the systems studied is the existence of topologically nontrivial solutions or *topological solitons* [16]: These are the solutions which map the physical boundary of the system to the whole configuration space of the field, so one explores all field configurations by “going around the system.” For example, in a two-dimensional system (in the x - y plane) with $U(1)$ phase symmetry, the configuration space is a circle (the phase lies between 0 and 2π) and the boundary of the physical space (i.e., the two-dimensional plane) is again a circle, the “boundary” of the plane at infinity. The topological soliton is a pattern of the $U(1)$ field which spans the whole phase circle (its phase goes from 0 to 2π), as one moves around the far-away circle in the x - y plane. Of course, this is the vortex—the most famous and best studied topological configuration. Similar logic leads to the classification of topological defects of other, more complicated symmetry groups. A potential source of confusion is that in nonlinear dynamics and theory of partial

*mclubrovic@gmail.com

differential equations, the “integrable” solutions, i.e., linearly (often also nonlinearly) stable solutions which can be obtained by inverse scattering or similar methods and which propagate through each other without interacting, are also called solitons, or more precisely *dynamical solitons*. In optics, they are often called spatial solitons. Dynamical solitons in nonlinear optics are a celebrated and well-studied topic [17–22]; they show an amazing variety of patterns and phenomena like localization, Floquet states [14], etc. But in general they do not have a topological charge. In contrast, topological solitons carry a topological charge (winding number for vortices) and their stability is rooted in topological protection (conservation of topological charge).

The phenomenon of vortices is perhaps best known in three spatial dimensions. The phase of the wave function can wind, forming a vortex line. These vortices are stable when the phase symmetry is broken by magnetic field. Famously, vortices may coexist with the superconducting order ($U(1)$ symmetry breaking) in type-II superconductors or exist only in the normal phase, upon destroying the superconductivity (type I). The primary example in two spatial dimensions is the vortex unbinding phase transition of infinite order found by Berezinsky *et al.* for the planar XY model [23]. The formal difference between the two- and three-dimensional vortices is that the latter gives rise to an emergent gauge field; this does not happen in the XY -like system in two dimensions [24]. While the nonlinear optical system we study is three-dimensional, its geometry and relaxational dynamics make it natural to treat it as a $(2 + 1)$ -dimensional system (the x and y coordinates are spatial dimensions, the z direction has the formal role of time, and physical time t has the role of a parameter). We therefore have a similar situation to the XY model: pointlike vortices in the plane (and no gauge field).

Vortex matter is known to emerge in liquid helium [25], Bose-Einstein condensates [26], and magnetic systems [27]. The basic mechanisms of vortex dynamics are thus well known. However, unusual physics can arise if the system has multiple components and each of them can form vortices which mutually interact. This is precisely our situation: We have a system of two laser beams propagating in opposite directions, and we will compare it to a two-component antiferromagnet. So far, such situations have been explored in multicomponent superconductors [28] which have attracted some attention, as they can be realized in magnesium diboride [29]. But these are again bulk systems, not planar. Vortices in planar multicomponent systems have not been very popular, an important exception being the two-component Bose-Einstein condensates of Ref. [30], which were found to exhibit complex vortex dynamics; in these systems, contrary to our case, the two components have an explicit attractive interaction, unlike our case where they interact indirectly, by coupling to the total light intensity (of both components).

B. The object of our study

In this paper, we study phases and critical behavior of topological configurations (vortices and vortex lattices) in a specific and experimentally realizable nonlinear optical system: laser beams counterpropagating (CP) through a photorefractive (PR) crystal. This means we have an elongated PR crystal

(with one longitudinal and two transverse dimensions) and two laser beams shone onto each end. We thus effectively have two fields, one forward propagating and one backward propagating. The optical response of the crystal depends nonlinearly on the *total* intensity of both beams, which means the beams effectively interact with each other. This system has been thoroughly investigated for phenomena such as dynamical solitons [17,31,32], vortex stability on the photonic lattice [18–20,33–36], and global rotation [37]. We will see that the CP beams are an analog of the two-component planar antiferromagnet, which can further be related to some realistic strongly correlated materials [38–40]. The two beams are now equivalent to two sublattices which interact through a lattice deformation or external field. The PR crystal is elongated and the axial propagation direction has the formal role of time, which has a finite span, the length of the crystal. For the antiferromagnet, the third axis is the usual imaginary time compactified to the radius $1/T$, i.e., inverse temperature. Both systems contain vortices as topological defects, i.e., solutions with integer topological charge. In the PR optical system, vortices arise as a consequence of the $U(1)$ symmetry of the electromagnetic field. In the antiferromagnets we consider, the $O(3)$ symmetry of the antiferromagnet gives rise to \mathbb{Z}_2 -charged defects, which exhibit the same interactions as the vortices. The optical system is not subject to noise (i.e., it lives at zero temperature), and thus the criticality we talk about is obviously not the same as thermodynamic phase transitions. Phase transitions happen upon varying the parameters, not temperature, so they may be described as quantum critical phenomena in the broad sense taken in Ref. [38]—any critical behavior controlled not by thermal fluctuations but by parameter dependence.

In the PR counterpropagating beam system, our focus are the vortices but in order to study them we need to do some preparational work. We first recast the system in Lagrangian and then in Hamiltonian form so it can be studied as a field theory, which depends parametrically on the time t . Then we consider the time dynamics of the system and show that in a broad parameter range the patterns relax to a static configuration which can be studied within *equilibrium* field theory. Along the way, we also study the stability of topologically trivial (vortex-free) configurations and then consider the phases of the static vortex configurations. The analytical insight we obtain also allows us to avoid overextensive numerics—analytical construction of the phase diagram tells us which patterns can in principle be expected in different corners of the parameter space. By “blind” numerical approach, this result could only be found through many runs of the numerics.

In the antiferromagnetic spin system, the nontopological excitations are simple: They are spin waves, perturbed away from the noninteracting solution by the quartic terms in the potential. There are no dynamical solitons. But we will see that topological excitations lead to a phase diagram which, after reasonable approximations, can be *exactly* mapped to the phase diagram of the photorefractive crystal. The reason is that both can be reduced to an effective Hamiltonian for a *two-component* vortex system; i.e., every vortex has two charges or two “flavors.” In the photorefractive crystal it happens naturally, as there are two beams, forward and

backward propagating. In the Heisenberg antiferromagnet it is less obvious and is a crucial consequence of the collinearity of the spin pattern. We will focus on common properties of the two systems and map the phase diagrams onto each other. In the antiferromagnetic system, different phases are separated by quantum phase transitions—phase transitions driven by the quantum fluctuations instead of temperature.

On disorder

It is known that impurities pin the vortices and stabilize them. This leads to frozen dynamics even though no symmetry is broken, the phenomenon usually associated with glasses. In simple systems such as the Ising model with disorder, one generically has two phases: The disordered (paramagnetic) phase remains and the ordered (magnetic) phase is replaced by a regime with algebraic correlations and no true order. In many cases, such phases are called glasses. The exact definition of a glass is lacking; normally, they show (i) long-range correlations, (ii) absence of long-range order, i.e., of a nonzero macroscopic order parameter, and (iii) “frozen dynamics,” i.e., free energy landscape with numerous local minima in which the system can spend a long time [41,42]. While the most popular example are probably spin glasses in Ising-like models such as Sherrington-Kirkpatrick and Edwards-Anderson models, glasses are also known to appear in the XY model with disorder in two dimensions, the Cardy-Ostlund model, which postulates both random couplings and a random magnetic field [43–45]. Our model is essentially a two-flavor generalization of the XY model, although in order to solve it we need to simplify it. According to Refs. [43–45], the details differ depending on how the disorder is implemented, but the two-phase system (paramagnetic, i.e., disordered, and glass) is ubiquitous. In the two-component version, the phase diagram becomes richer, and on top of the glassy phase and the insulator (disordered) phase we find a few other phases. In nonlinear optics, the topic of random lasers has attracted considerable attention [9–12,46]. Here one has a complex version of the XY model, with the additional complication that not only phase but also amplitude is free to vary, but only with random couplings (no random field). On top of the glassy and the disordered phase, one or two additional phases appear.

In the presence of disorder, the relation to magnetic systems in condensed matter physics is very inspiring, since a number of complex materials show different ordering mechanisms (spin and charge density waves, superconductivity, etc.) in parallel with significant influence of disorder. Just as in the disorder-free case, we are particularly interested in possible spin-glass phenomena in doped insulating $O(3)$ antiferromagnets [39,40,47–49] and in the last section we will discuss also the spin-glass phase in such systems.

C. The plan of the paper

The structure of the paper is as follows. In the next section, we describe the dynamical system which lies at the core of this paper: counterpropagating laser beams in a photorefractive crystal. We give the equations of motion and repackage them in the Lagrangian form. In Sec. III, we study the vortex dynamics: We construct the vortex Hamiltonian and classify the order parameters. Then we study the renormalization group (RG)

flow and obtain the phase diagram. Finally, we discuss the important question of how to recognize the various phases in experiment: What do the light intensity patterns look like and how do they depend on the tunable parameters? Section IV brings the same study for the system with disorder. After describing the disordered system, we perform the replica trick for the disordered vortex Hamiltonian and solve the saddle-point equations to identify the phases and order parameters, again refining the results with RG calculations. The fifth section takes a look at a doped collinear antiferromagnet, a model encountered in the description of many strongly coupled materials, and shows how the dynamics of topological solitons is again described by a two-flavor vortex Hamiltonian. We discuss the relation between the phase diagrams of the two systems and the possibilities of modeling the condensed matter systems experimentally by the means of photorefractive optics. The last section sums up the conclusions. In Appendix A, we describe the numerical algorithm we use to check the analytical results for the phase diagram. In Appendix B, we show in detail that the CP beams are capable of reaching equilibrium (i.e., stop changing in time)—if they would not, the application of equilibrium field theory would not be justified. Appendix C discusses the stability of nonvortex configurations—although somewhat peripheral to the main topic of the paper, it is useful to better understand the geometry of patterns. In Appendix D, we give the (routine) algebra that yields the vortex interaction Hamiltonian from the microscopic equations. Appendix E contains an improved mean-field theory for the clean system, which we do not use much throughout the paper but we include it for completeness (we prefer either the simplest single-vortex mean-field reasoning or the full RG analysis, which are described in the main text). Appendix F discusses an important technicality concerning the CP geometry, i.e., the specific boundary conditions of the CP beam system where the boundary conditions for one beam are given at the front face and for the other at the back face of the crystal. Appendix G contains some details on mean-field and RG calculations of the phase diagram for the dirty system: The dirty case includes some tedious algebra we feel appropriate to leave out from the main text.

II. THE MODEL OF COUNTERPROPAGATING BEAMS IN THE PHOTOREFRACTIVE CRYSTAL

We consider a photorefractive crystal of length L irradiated by two laser beams. The beams are paraxial and propagate head on from the opposite faces of the crystal in the z direction. Photorefractive crystals induce self-focusing of the beams—the vacuum (linear) wave equation is modified by the addition of a frictionlike term, so the diffusion of the light intensity (the broadening of the beam) is balanced out by the convergence of the beam onto an “attractor region.” The net result is the balance between the dissipative and scattering effects, allowing for stable patterns to form. The physical ground for this is the redistribution of the charges in the crystal due to the Kerr effect. The nonlinearity, i.e., the response of the crystal to the laser light, is contained in the change of the refraction index which is determined by the local charge density. A sketch of the system is given in Fig. 1. Before entering the crystal, the laser beams can be given any desirable pattern of both intensity

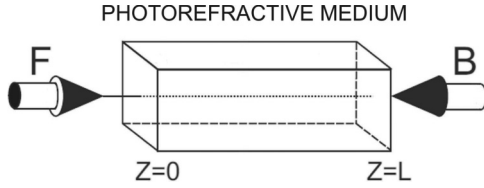


FIG. 1. Sketch of the experimental setup for the study of the CP beams in the PR crystal. The crystal has the shape of a parallelepiped, and the beams propagate along the longitudinal, z axis: the forward (F) beam from $z = 0$ to $z = L$, and the backward (B) beam the other way round. The intensity patterns are observed at the transverse faces of the crystal, at $z = 0$ and $z = L$.

and phase. In particular, one can create vortices (winding of the phase) making use of the phase masks [3] or other, more modern ways.

Assuming the electromagnetic field of the form $\mathbf{E} = e^{i\omega t + i\mathbf{q}\cdot\mathbf{r}}(F e^{ikz} + B e^{-ikz})$, we can write equations for the so-called envelopes F and B of the forward- and backward-propagating beams along the z axis (the frequency, transverse, and longitudinal momentum are denoted respectively by ω, \mathbf{q}, k). The wave equations for F and B are now

$$\begin{aligned} \pm i \partial_z \Psi_{\pm}(z; x, y; t) + \Delta \Psi_{\pm}(z; x, y; t) \\ = \Gamma E(z; x, y; t) \Psi_{\pm}(z; x, y; t), \end{aligned} \quad (1)$$

where the plus and minus signs on the left-hand side stand for the forward- and backward-propagating component of the beam amplitude doublet $\Psi \equiv (\Psi_+, \Psi_-) \equiv (F, B)$, and Γ is the dimensionless PR coupling constant. The two beams (flavors of the field Ψ) will from now on be denoted either by F/B or more often by Ψ_{\pm} . We will use α as the general flavor index for summation, e.g., $\Psi_{1\alpha} \Psi_{2\alpha} = \Psi_{1+} \Psi_{2+} + \Psi_{1-} \Psi_{2-}$. The charge field E on the right-hand side of the equation is the electric field sourced by the charges in the crystal (i.e., it does not include the external electric field of the beams). Its evolution is well represented by a relaxation-type equation [17]:

$$\begin{aligned} \frac{\tau}{1 + I(z; x, y; t)} \partial_t E(z; x, y; t) + E(z; x, y; t) \\ = - \frac{I(z; x, y; t)}{1 + I(z; x, y; t)}. \end{aligned} \quad (2)$$

Here, $I \equiv I_{\Psi} + I_x$ is the total light intensity at a given point, $I_{\Psi} \equiv |F|^2 + |B|^2$ is the beam intensity, and I_x the intensity of the fixed background. The meaning of I_x is that the crystal is all the time irradiated by some constant light source, independent of the counterpropagating beams with envelopes F, B . We will usually take a periodic lattice as the background, allowing also for the defects (missing cells) in the lattice when studying the effects of disorder. The relaxation time is τ . The time derivative $\partial_t E$ is divided by $1 + I$, meaning that the polarizability of the crystal depends on the total light intensity: Strongly irradiated regions react faster. In the numerical calculations, we solve Eqs. (1) and (2) with no further assumptions, as explained in Appendix A. For analytical results, we will need to transform them further, assuming a vortex pattern.

The equation for the charge field has no microscopic basis; it is completely phenomenological, but it excellently represents

the experimental results [3]. Notice that the derivative $\partial_t E$ in (2) is strictly negative (since intensity is non-negative): It thus has the form of a relaxation equation, and one expects that a class of solutions exists where $\partial_t E(t \rightarrow \infty) \rightarrow 0$, i.e., the system relaxes to a time-independent configuration. We show this in Appendix B; in the main text we will not discuss this issue but will simply take the findings of Appendix B for granted. Notice that there are also parameter values for which no equilibrium is reached [37,50,51].

For slow time evolution (in the absence of pulses), we can Laplace transform the equation (2) in time [$E(t) \mapsto E(u) = \int_0^{\infty} dt e^{-ut} E(t)$] to get the algebraic relation

$$\begin{aligned} E(z; x, y; u) &= - \frac{\Psi^{\dagger} \Psi + I_x - \tau E_0}{1 + \tau u + I_x + \Psi^{\dagger} \Psi} \\ &= -1 + \frac{1 + \tau u + \tau E_0}{1 + \tau u + I_x + \Psi^{\dagger} \Psi}. \end{aligned} \quad (3)$$

The original system (1) can now be described by the Lagrangian:

$$\begin{aligned} \mathcal{L} &= i \Psi^{\dagger} \sigma_3 \partial_z \Psi - |\nabla \Psi|^2 + \Gamma \Psi^{\dagger} \Psi \\ &\quad - \Gamma(1 + \tau E_0 + \tau u) \ln(1 + \tau u + I_x + \Psi^{\dagger} \Psi), \end{aligned} \quad (4)$$

where σ_3 is the Pauli matrix $\sigma_3 = \text{diag}(1, -1)$. One can introduce the effective potential

$$V_{\text{eff}}(\Psi^{\dagger}, \Psi) = -\Gamma \ln \frac{e^{\Psi^{\dagger} \Psi}}{(1 + \tau u + I_x + \Psi^{\dagger} \Psi)^{1 + \tau(E_0 + u)}}, \quad (5)$$

so we can write the Lagrangian as $\mathcal{L} = i \Psi^{\dagger} \sigma_3 \partial_z \Psi - |\nabla \Psi|^2 - V_{\text{eff}}(\Psi^{\dagger}, \Psi)$. This is the Lagrangian of a nonrelativistic field theory (a nonlinear Schrödinger field equation) in $2 + 1$ dimensions (x, y, z), where the role of time is played by the longitudinal distance z and the physical time t (or u upon the Laplace transform) is a parameter. The span of the z coordinate $0 < z < L$ will influence the behavior of the system, while the dimensions of the transverse plane are not important for the effects we consider.

Our main story is now the nature and interactions of the topologically nontrivial excitations in the system (4). A task which is in a sense more basic, the analysis of the topologically trivial vacua of (4) and perturbative calculation of their stability, is not of our primary interest now, in part because this was largely accomplished by other methods in Refs. [31,32]. We nevertheless give a quick account in Appendix C; first, because some conclusions about the geometry of the patterns can be carried over to vortices, and second, to give another example of applying the field-theoretical formalism whose power we wish to demonstrate and popularize in this paper.

III. VORTICES AND MEAN FIELD THEORY OF VORTEX INTERACTIONS

A. The classification of topological solutions and the vortex Hamiltonian

Now we discuss the possible topological solitons in our system. Remember once again that they differ from dynamical

solitons such as those studied in Ref. [17] and references therein. In order to classify the topologically nontrivial solutions, consider first the symmetries of the Lagrangian (4). It describes a doublet of two-dimensional (2D) complex fields which interact solely through the phase-invariant total intensity $I = \Psi^\dagger \Psi$ (and the spatial derivative term $|\nabla \Psi|^2$), while in the kinetic term $\Psi^\dagger \sigma_3 \partial_z \Psi$ the two components have opposite signs of the “time” derivative, so this term cannot be reduced to a functional of I . The intensity I has the symmetry group $SU(2)$ (the isometry group of the three-dimensional sphere in Euclidean space) and the kinetic term has the group $SU(1,1)$ (the transformations which leave the combination $|F|^2 - |B|^2$ invariant, i.e., the isometry of the hyperboloid). The intersection of these two is the product $U(1)_F \otimes U(1)_B$: The forward- and backward-propagating doublet (F, B) has phases $\theta_{F,B}$ which can be transformed independently, as $\theta_{F,B} \mapsto \theta_{F,B} + \delta\theta_{F,B}$.

The classification of possible topological solitons is straightforward from the above discussion [52]. They can be characterized in terms of homotopy groups. We remind readers that the homotopy group π_n of the group G is the group of transformations which map the group manifold of G onto the n -dimensional sphere S_n . In D -dimensional space, the group π_{D-1} therefore classifies what a field configuration looks like from far away (from infinity): It classifies the mappings from the manifold of the internal symmetry group of the system to the spherical “boundary shell” in physical space at infinity. Since the beams in our PR crystal effectively see a two-dimensional space (we regard z as time), we need the first homotopy group π_1 to classify the topological solitons. Since $\pi_1(U(1)) = \pi_1(S_1) = \mathbb{Z}$ and $\pi_1(\mathbb{G} \otimes \mathbb{G}) = \pi_1(\mathbb{G}) \otimes \pi_1(\mathbb{G})$ for any group \mathbb{G} , the topological solutions are flavored vortices, and the topological charge is the pair of integers $\{Q_F, Q_B\}$.

Let us now derive the effective interaction Hamiltonian for the vortices and study the phase diagram. In principle, this story is well known: For a vortex at \mathbf{r}_0 , in the polar coordinates (r, ϕ) , we write $\Psi(\mathbf{r}) = \psi \exp(i\theta(\mathbf{r}))$ for $|\mathbf{r} - \mathbf{r}_0|/|\mathbf{r}_0| \ll 1$, and a vortex of charge Q has $\theta(\phi) = Q\phi/2\pi$. In general the phase has a regular and a singular part, $\nabla \Psi = \psi(\nabla \delta\theta + \nabla \times \zeta \mathbf{e}_z)$, where finally $\zeta = Q \ln |\mathbf{r} - \mathbf{r}_0|$. The difference in the CP beam system lies in the existence of two beam fields (flavors) and the nonconstant amplitude field $\psi_{\pm}(r)$, so the vortex looks like

$$\Psi_{0\pm}(\mathbf{r}) = \psi_{0\pm}(r) e^{i\delta\theta_{\pm}(\phi) + i\theta_{0\pm}(\phi)}. \quad (6)$$

When we insert this solution into the equations of motion (or, equivalently, the Lagrangian), it is just a matter of algebra to obtain the vortex Hamiltonian, analogous to the well-known one but with two components (flavors) and their interaction. We refer the reader to the Appendix D for the full derivation. The outcome is perhaps expected: We get the straightforward generalization of the familiar Coulomb gas picture for the XY model where all interactions of different flavors, F - F , B - B , and F - B , are allowed. In order to write the Hamiltonian (and further manipulations with it) in a concise way, it is handy to introduce shorthand notation $\vec{Q} \equiv (Q_+, Q_-)$, $\vec{Q}_1 \cdot \vec{Q}_2 \equiv Q_{1+}Q_{2+} + Q_{1-}Q_{2-}$, and $\vec{Q}_1 \times \vec{Q}_2 \equiv Q_{1+}Q_{2-} - Q_{1-}Q_{2+}$. For the self-interaction within a vortex \vec{Q}_1 , we have $\vec{Q}_1 \cdot \vec{Q}_1 =$

$Q_{1+}^2 + Q_{1-}^2$ but $\vec{Q}_1 \times \vec{Q}_1 \equiv Q_{1+}Q_{1-}$ (i.e., there is a factor of 2 mismatch with the case of two different vortices). Now for vortices at locations $\mathbf{r}_i, i = 1, \dots, N$ with charges $\{Q_{i+}, Q_{i-}\}$ we get

$$\begin{aligned} \mathcal{H}_{\text{vort}} = & \sum_{i < j} (g \vec{Q}_i \cdot \vec{Q}_j + g' \vec{Q}_i \times \vec{Q}_j) \ln r_{ij} \\ & + \sum_i (g_0 \vec{Q}_i \cdot \vec{Q}_i + g_1 \vec{Q}_i \times \vec{Q}_i). \end{aligned} \quad (7)$$

The meaning of the Hamiltonian (7) is obvious. The first term is the Coulomb interaction of vortices; notice that only like-flavored charges interact through this term (because the kinetic term $|\nabla \Psi|^2$ is homogenous quadratic). The second term is the forward-backward interaction, also with Coulomb-like (logarithmic) radial dependence. This interaction comes from the mixing of the F and B modes in the fourth term in Eq. (D2), and it is generated, as we commented in Appendix D, when the amplitude fluctuations $\delta\psi_{\alpha}(r)$, which couple linearly to the phase fluctuations, are integrated out. In a system without amplitude fluctuations, i.e., classical spin system, this term would not be generated. The third and fourth terms constitute the energy of the vortex core. The self-interaction constants g_0, g_1 are of course dependent on the vortex core size and behave roughly as $g \ln a/\epsilon, g' \ln a/\epsilon$, where ϵ is the UV cutoff. The final results will not depend on ϵ , as expected, since g_0, g_1 can be absorbed in the fugacity y (see the next subsection). Expressions for the coupling constants in terms of original parameters are given in (D11).

In three space dimensions, vortices necessitate the introduction of a gauge field [24] which, in multicomponent systems, also acquires the additional flavor index [28,53]. In our case, there is no emergent gauge field and the whole calculation is a rather basic exercise at the textbook level but the results are still interesting in the context of nonlinear optics and analogies to magnetic systems: They imply that the *phase* structure (vortex dynamics) can be spotted by looking at the *intensity* patterns (light intensity I or local magnetization \mathcal{M} ; see the penultimate section).

B. The phase diagram

1. The mean-field theory for vortices

The phases of the system can be classified at the mean field level, following, e.g., Refs. [24,41]. In order to do that, one should construct the partition function, assuming that well-defined time-independent configuration space exists. We have already mentioned the question of equilibration and address it in detail in Appendix B. Knowing that the system reaches equilibrium (in some part of the parameter space), we can count the ways in which a system of vortices can be placed in the crystal—this is by definition the partition function \mathcal{Z} . First, the number of vortices N can be anything from 0 to infinity; second, the vortex charges can be arbitrary; and finally, the number of ways to place each vortex in the crystal is simply the total surface section of the crystal divided by the size of the vortex. Then, each vortex carries a Gibbs weight proportional to the energy, i.e., the vortex Hamiltonian (7) for a single

vortex.¹ Let us focus first on a single vortex. If the vortex core has linear dimension a and the crystal cross section linear dimension Λ , the vortex can be placed in any of the $(\Lambda/a)^2$ cells (and in the mean-field approach we suppose the vortex survives all the way along the crystal, from $z = 0$ to $z = L$, so there is no additional freedom of placing it along some subinterval of z). This gives

$$\mathcal{Z} = \sum_{Q_+, Q_-} \left(\frac{\Lambda}{a}\right)^2 e^{-L\mathcal{H}_1} = \sum_{Q_+, Q_-} e^{2\ln\frac{\Lambda}{a} - L(g\vec{Q} \cdot \vec{Q}_+ + g'\vec{Q} \times \vec{Q}_-) \ln\frac{\Lambda}{a}}. \quad (8)$$

Remember that \mathcal{H} is energy density along the z axis, so it appears multiplied by L . The factor $\ln(\Lambda/a)$ in the second term of the exponent comes from the Coulomb potential of a single vortex (in a plane of size Λ). The exponent can be written as $-L\mathcal{F}^{(1)}$, with $\mathcal{F}^{(1)} = \mathcal{H}_1 - (1/L)S_1$, recovering the relation between the free energy $\mathcal{F}^{(1)}$ and entropy $S^{(1)}$ of a single vortex. The entropy comes from the number of ways to place a vortex of core size a in the plane of size $\Lambda \gg a$: $S \sim \ln(\Lambda/a)^2$. Suppose for now that elementary excitations have $|Q_{\pm}| \leq 1$, as higher values increase the energy but not the entropy, so they are unlikely (when only a single vortex is present). Now we can consider the case of single-charge vortices with possible charges $(1, 0), (-1, 0), (0, 1), (0, -1)$, and the case of two-charge vortices where F and B charge may be of the same sign or opposite signs, $(1, 1), (-1, -1), (1, -1), (-1, 1)$:

$$\mathcal{F}_0^{(1)} = \left(g - \frac{2}{L}\right) \ln\frac{\Lambda}{a}, \quad \vec{Q} = (\pm 1, 0) \text{ or } \vec{Q} = (0, \pm 1), \quad (9)$$

$$\mathcal{F}_1^{(1)} = \left(2g - g' - \frac{2}{L}\right) \ln\frac{\Lambda}{a}, \quad (Q_+, Q_-) = (\pm 1, \mp 1), \quad (10)$$

$$\mathcal{F}_2^{(1)} = \left(2g + g' - \frac{2}{L}\right) \ln\frac{\Lambda}{a}, \quad (Q_+, Q_-) = (\pm 1, \pm 1). \quad (11)$$

Now we identify four regimes, assuming that $g, g' > 0$:²

(1) For $L > 2/g$, a vortex always has positive free energy so vortices are unstable like in the low-temperature phase of the textbook Berezinsky-Kosterlitz-Thouless (BKT) system. This is the vortex-free phase where the phase $U(1)_F \otimes U(1)_B$ does not wind. This phase we logically call *vortex insulator* in analogy with the single-flavor case.

(2) For $2/g > L > 1/(g - g'/2)$, a double-flavor vortex always has positive free energy but single-flavor vortices are stable; in other words, there is proliferation of vortices of the form $\vec{Q} = (Q_+, 0)$ or $\vec{Q} = (0, Q_-)$. This phase is like the conductor phase in a single-component XY model, and the

topological excitations exist for the reduced symmetry group, i.e., for a single $U(1)$. We thus call it *vortex conductor*; it is populated mainly by single-flavor vortices $(Q, 0), (0, Q)$.

(3) For $1/(g - g'/2) > L > 1/(g + g'/2)$, double-vortex formation is only optimal if the vortex has $Q_+ + Q_- = 0$, which corresponds to the topological excitations of the diagonal $U(1)_d$ symmetry subgroup, the reduction of the total phase symmetry to the special case $(\theta_F, \theta_B) \mapsto (\theta_F + \delta\theta, \theta_B - \delta\theta)$. In other words, vortices of the form $(Q_+, -Q_-)$ proliferate. Here, higher charge vortices may be more energetically favorable than unit-charge ones, contrary to the initial simplistic assumption, the reason being that the vortex core energy proportional to gQ_+^2 may be more than balanced out by the intravortex interaction proportional to $-g'Q_+^2$ (depending on the ratio of g and g'). This further means that there may be multiple ground states of equal energy (frustration). We thus call this case *frustrated vortex insulator* (FI); it is populated primarily with vortices of charge $(Q, -Q)$.

(4) For $1/(g + g'/2) > L$ vortex formation always reduces the free energy, no matter what the relation between Q_+ and Q_- is, and each phase can wind separately: $(\theta_F, \theta_B) \mapsto (\theta_F + \delta\theta_F, \theta_B + \delta\theta_B)$. Vortices of both flavors proliferate freely at no energy cost and for that reason we call this phase *vortex perfect conductor* (PC). We deliberately avoid the term superconductor to avoid the (wrong) association of this phase with the vortex lines and type I or type II superconductors familiar from the three-dimensional (3D) vortex systems: Remember there is no emergent gauge field for the vortices in two spatial dimensions, and we only have perfect conductivity in the sense of zero resistance for transporting the (topological) charge, but no superconductivity in the sense of breaking a gauge symmetry.

A more systematic mean-field calculation will give the phase diagram also for an arbitrary number of vortices. This is not so interesting as it already does not require much less work than the RG analysis, which is more rigorous and more accurate for this problem. For completeness, we give the multivortex mean-field calculation in Appendix E.

One might worry that the our whole approach misses the CP geometry of the problem, i.e., the fact that the Ψ_+ field has a source at $z = 0$ and the Ψ_- field at $z = L$. In Appendix F, we show that nothing is missed at the level of approximations taken in this paper, i.e., mean-field theory in this subsection and the lowest-order perturbative RG in the next one. Roughly speaking, it is because the sources are irrelevant in the RG sense—the bulk configuration dominates over the boundary terms. The appendix states this in much more precise language.

2. RG analysis

We have classified the symmetries and thus the phases of our system at the mean-field level. To describe quantitatively the borders between the phases and the phase diagram, we will perform the renormalization group (RG) analysis. Here we follow closely the calculation for conventional vortex systems [24]. We consider the fluctuation of the partition function $\delta\mathcal{Z}$ upon the formation of a virtual vortex pair at positions $\mathbf{r}_1, \mathbf{r}_2$ with charges $\vec{q}, -\vec{q}$ (with $\mathbf{r}_1 + \mathbf{r}_2 = 2\mathbf{r}$ and $\mathbf{r}_1 - \mathbf{r}_2 = \mathbf{r}_{12}$), in the background of a vortex pair at positions

¹Again, this is not generally true for out-of-equilibrium configurations but if the system reaches equilibrium, i.e., stable fixed point, this follows by usual statistical mechanics reasoning.

²One specificity of multicomponent vortices is that the coupling constants may be negative, as can be seen from (D11). In that case, the ordering of the four regimes (how they follow each other upon dialing L) changes but the overall structure remains.

$\mathbf{R}_1, \mathbf{R}_2$ (with $\mathbf{R}_1 + \mathbf{R}_2 = 2\mathbf{R}$ and $\mathbf{R}_1 - \mathbf{R}_2 = \mathbf{R}_{12}$) with charges \bar{Q}_1, \bar{Q}_2 . This is a straightforward but lengthy calculation and we state just the main steps. First, it is easy to show that the creation of single-charge vortices is irrelevant for the RG flow so we disregard it. Also, we can replace the core self-interaction constants $g_{0,1}$ with the fugacity parameter defined as $y \equiv \exp[-\beta(g_0 + g_1) \ln \epsilon]$. Here we introduce the notation $\beta \equiv L$ in analogy with the inverse temperature β in standard statistical mechanics, in order to facilitate the comparison with the literature on vortices in spin systems, and also with antiferromagnetic systems in Sec. V.³

Now from the vortex Hamiltonian $\mathcal{H}_{\text{vort}}$ the fluctuation equals (at the quadratic order in y and r)

$$\begin{aligned} \frac{\delta \mathcal{Z}}{\mathcal{Z}} &= 1 + \frac{y^4}{4} \sum_{q_{\pm}} \int dr_{12} r_{12}^3 e^{g\bar{q} \cdot \bar{q} + g'\bar{q} \times \bar{q}} \\ &\times \left[\int dr r^2 (g\bar{Q}_1 \cdot \bar{q} + g'\bar{Q}_1 \times \bar{q}) \right. \\ &\times \nabla \ln |\mathbf{R}_1 - \mathbf{r}| + (g\bar{Q}_2 \cdot \bar{q} + g'\bar{Q}_2 \times \bar{q}) \\ &\left. \times \nabla \ln |\mathbf{R}_2 - \mathbf{r}| \right]^2. \end{aligned} \quad (12)$$

Notice that ∇ is taken with respect to \mathbf{r} . The above result is obtained by expanding the Coulomb potential in r_{12} (the separation between the virtual vortices being small because of their mutual interaction) and then expanding the whole partition function (i.e., the exponent in it) in y around the equilibrium value \mathcal{Z} . The term depending on the separation r_{12} is the mutual interaction energy of the virtual charges, and the subsequent term proportional to r^2 is the interaction of the virtual vortices with the external ones (the term linear in r cancels out due to isotropy). Then by partial integration and summation over $q_{\pm} \in \{1, -1\}$ we find

$$\begin{aligned} \frac{\delta \mathcal{Z}}{\mathcal{Z}} &= 1 + y^4 [8\pi g^2 \bar{Q}_1 \cdot \bar{Q}_2 + 8\pi (g')^2 \bar{Q}_1 \cdot \bar{Q}_2 \\ &+ 16\pi g g' \bar{Q}_1 \times \bar{Q}_2] I_3 \ln R_{12} \\ &+ y^4 [4\pi g(g + g') (\bar{Q}_1 \times \bar{Q}_1 + \bar{Q}_2 \times \bar{Q}_2) \\ &\times I_1 + 8(g')^2 I_1] \ln \epsilon, \end{aligned} \quad (13)$$

with $I_n = \int_{\epsilon a}^{\Lambda a} dr r^{n+g+g'}$. Now, by taking into account the definition of the fugacity y , rescaling $\Lambda \mapsto \Lambda(1 + \ell)$, performing the spatial integrals, and expanding over ℓ , we can equate the bare quantities g, g', y in (7) with their corrected values in $\mathcal{Z} + \delta \mathcal{Z}$ to obtain the RG flow equations:

$$\begin{aligned} \frac{\partial g}{\partial \ell} &= -16\pi(g^2 + g'^2)y^4, & \frac{\partial g'}{\partial \ell} &= -2\pi g g' y^4, \\ \frac{\partial y}{\partial \ell} &= 2\pi(1 - g - g')y. \end{aligned} \quad (14)$$

³Of course, the physical meaning of β in our system is very different: We have no thermodynamic temperature or thermal noise, and the third law of thermodynamics is not satisfied for the ‘‘temperature’’ $1/\beta = 1/L$. We merely use the β notation to emphasize the similarity between free energies of different systems, not as a complete physical analogy.

Now let us consider the fixed points of the flow equations. If one puts $g' = 0$, they look very much like the textbook XY model RG flow, except that the fugacity enters as y^4 instead of y^2 (simply because every vortex contributes two charges). They yield the same phases as the mean-field approach as it has to be, but now we can numerically integrate the flow equations to find exact phase borders. The fugacity y can flow to zero (meaning that the vortex creation is suppressed and the vortices tend to bind) or to infinity, meaning that vortices can exist at finite density. At $y = 0$, there is a fixed line $g + g' = 1$. This line is attracting for the half-plane $g + g' > 1$; otherwise, it is repelling. There are three more attraction regions when $g + g' < 1$. First, there is the point $y \rightarrow \infty, g = g' = 0$ which has no analog in single-component vortex systems. Then, there are two regions when $g \rightarrow \infty$ and $g' \rightarrow \pm\infty$ (and again $y \rightarrow \infty$). Of course, the large g, g' regime is strongly interacting and the perturbation theory eventually breaks down, so in reality the coupling constants grow to some finite values g_*, g'_* and g_{**}, g'_{**} rather than to infinities. The situation is now the following:

(1) The attraction region of the fixed line is the vortex insulator phase: The creation rate of the vortices is suppressed to zero.

(2) The zero-coupling fixed point attracts the trajectories in the vortex perfect conductor phase: Only the fugacity controls the vortices and arbitrary charge configurations can form. Numerical integration shows that this point also has a finite extent in the parameter space.

(3) In the attraction region of the fixed point with $g_* < 0$ and $g'_* > 0$ (formally they flow to $-\infty$ and $+\infty$, respectively), same-sign F and B charges attract each other and those with the opposite sign which repel each other. This is the frustrated insulator.

(4) The fixed point with $g_{**}, g'_{**} < 0$ (formally both flow to $-\infty$) corresponds to the conductor phase.

The RG flows in the g - g' plane are given in Fig. 2. Full RG calculation is given in Fig. 2(b); for comparison, we include also the mean-field phase diagram (following from the previous subsection and Appendix E) in Fig. 2(a). In the half-plane $g + g' > 1$ every point evolves toward a different, finite point (g, g') in the same half-plane. In the other half-plane we see the regions of points moving toward the origin or toward one of the two directions at infinity. The PC phase (the attraction region of the point $(0, 0)$) could not be obtained from the mean field calculation (i.e., it corresponds to the single point at the origin at the mean field level).

It may be surprising that the coupling constants can be negative, with like charges repelling and opposite charges attracting each other. However, this is perfectly allowed in our system. In the usual XY model, the stiffness is proportional to the kinetic energy coefficient and thus has to be positive. Here, the coupling between the fluctuations of F and B beams introduces other contributions to g, g' and the resulting expressions (D11) give bare values of g, g' that can be negative, and the stability analysis of the RG flow clearly shows that for nonzero g' , the flow can go toward negative values even if starting from a positive value in some parameter range. If we fix $g' = 0$, the flow equations reproduce the ones from the single-component XY model, and the phase diagram is reduced to just the $g' = 0$ line. If we additionally suppose that

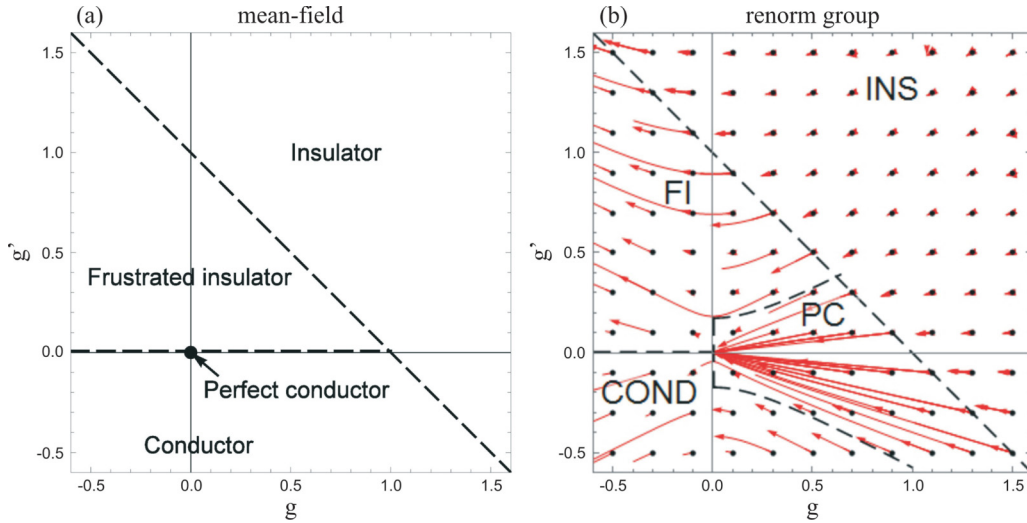


FIG. 2. Phase diagram for the clean system in the g - g' plane, at the mean-field level (a) and with RG flows (b). We show the flows for a grid of initial points, denoted by black dots; red lines are the flows. Four phases exist, whose boundaries are delineated by black dashed lines. In the mean-field calculation (a) all phase boundaries are analytical. In the RG calculation, the straight line $g + g' = 1$ is obtained analytically whereas the other phase boundaries can only be found by numerical integration of the flow equations (14). The flows going to infinity are the artifacts of the perturbative RG; they probably correspond to finite values which are beyond the scope of our analytical approach. Notice how the flows in the $g + g' > 1$ phase all terminate at different values.

the bare value of g is non-negative, than we are on the positive $g' = 0$ semiaxis in the phase diagram—here we see only two phases, insulator (no vortices, $g \rightarrow \text{const.}$) and perfect conductor ($g \rightarrow 0$). However, for g' fixed to zero (that is, with a single flavor only), the perfect conductor reduces to the usual conductor phase of the single-component XY model—in other words, we reproduce the expected behavior.

Physically, it is preferable to give the phase diagram in terms of the quantities Γ, τ, I, I_x, L that appear in the initial equations of motion (1) and (2): The light intensities can be directly measured and controlled, whereas the relaxation time and the coupling cannot, but at least they have a clear physical interpretation. The relations between these and the effective Hamiltonian quantities y, g, g' are found upon integrating out the intensity fluctuations to obtain (7) and the explicit relations are stated in (D11). Making use of these we can easily plot the phase diagram in terms of the physical quantities for comparison with experiment. However, for the qualitative understanding we want to develop here, it is much more convenient to use g, g' as the phase structure is much simpler.

As an example, we plot the Γ - g' diagram in Fig. 3 (we have kept g' to keep the picture more informative; the Γ - L and Γ - I diagrams contain multiple disconnected regions for each phase). The noninteracting fixed point $g = g' = 0$ is now mapped to $\Gamma = 0$. The tricritical point where the PC, the FI, and the conductor phases meet is at $R = 1$. Therefore, the rule of thumb is that low couplings Γ produce stable vortices with conserved charges—the perfect vortex conductor. Increasing the coupling pumps the instability up, and the kind of instability (and the resulting phase) is determined by the relative strength of the photonic lattice compared to the propagating beams. Obviously, such considerations are only a rule of thumb and detailed structure of the diagram is more complex. This is one of the main motives of this study—blind numerical search for patterns without the theoretical approach

adopted here would require many runs of the numerics for a good understanding of different phases.

C. Geometry of patterns

Now we discuss what the intensity pattern $I(\mathbf{r})$ looks like in various phases, for various boundary conditions. This is very important as this is the only thing which can be easily measured in experiment—phases θ_α are not directly observable, while the intensity distribution is the direct outcome of the imaging of the crystal [31]. We shall consider three situations. The first is a single Gaussian beam on zero

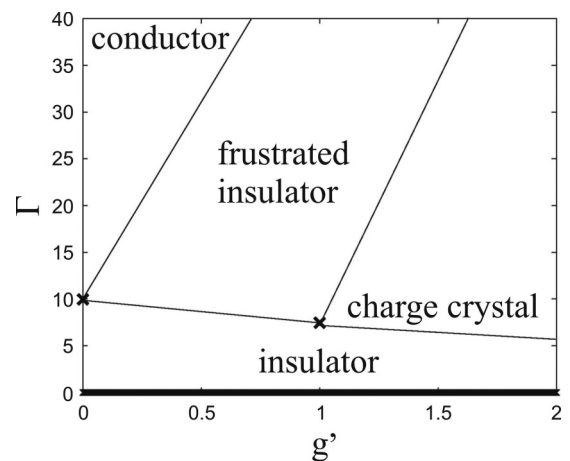


FIG. 3. Typical phase diagram for the system without disorder, in the Γ - g' plane. There are two discrete fixed points and the critical line at $\Gamma = 0$, which corresponds to the critical line $g + g' = 1$ in the previous figure. We also see two discrete fixed points, corresponding to $g_{*,**}, g'_{*,**}$. The advantage of physical parameters is that the location of these fixed points in the Γ - I plane can be calculated directly from the numerics (or measured from the experiment).

background ($I_x = 0$), with Gaussian initial intensity profile $|F(z = 0, \mathbf{r})|^2 = |B(z = L, \mathbf{r})|^2 = \mathcal{N} \exp(-r^2/2s^2)$ and possibly nonzero vortex charges: $\arg \Psi_{\pm}(\mathbf{r}) \sim \exp(Q_{F,B}\phi)$, with $\mathbf{r} = (r \cos \phi, r \sin \phi)$. The second case is a quadratic vortex lattice of F and B beams, so the initial beam intensity is $I_0 = \sum_{i,j} \exp[-(x - x_i)^2/2s_0^2 - (y - y_j)^2/2s_0^2]$, with $x_{i+1} - x_i = y_{i+1} - y_i \equiv b = \text{const.}$, the situation particularly relevant for analogies with condensed matter systems. In the third case, we have again a quadratic vortex lattice but now on top of the background photonic square lattice, which is either coincident or off phase (shifted for half a lattice spacing) with the beam lattice. The background intensity is thus of the form $I_x = \sum_{i,j} \exp[-(x - x_i)^2/2s^2 - (y - y_j)^2/2s^2]$.

First of all, it is important to notice that there are two kinds of instabilities that can arise in a vortex beam:⁴

(1) There is an instability which originates in the imbalance between the diffusion and self-focusing (crystal response) in favor of diffusion in *high-gradient regions*: If a pattern $I(x, y)$ has a large gradient ∇I , the kinetic term in the Lagrangian (4), i.e., the diffusion term in (1) is large and the crystal charge response is not fast enough to balance it as we travel along the z axis, so the intensity rapidly dissipates and the pattern changes. Obviously, the vortex core is a high-gradient region so we expect it to be vulnerable to this kind of instability. This is indeed the case: In the center of the vortex the intensity diminishes, a dark region forms, and the intensity moves toward the edges. We dub this the core or central instability (CI), and in the effective theory it can be understood as the decay of states with low fugacity y , i.e., high self-interaction constants g_0, g_1 . This instability prevents the formation of vortices in the insulator phase, or limits it in the frustrated insulator and conductor phases.

(2) There is an instability stemming from the dominance of diffusion over self-focusing in *low-intensity regions of sufficient size and/or convenient geometry*. At low intensity, the charge response is nearly proportional to I [from Eq. (2)], so if I is small diffusion wins and the intensity dissipates. If there is sufficient inflow of intensity from more strongly illuminated regions, it may eventually balance the diffusion, but if the pattern has a long “boundary”, i.e., outer region of low intensity, it will not happen and the pattern will dissipate out or reshape itself to reduce the low-intensity region. We call this case the edge instability (EI). For a vortex, it happens when the positive and negative vortex charges tend to redistribute due to Coulomb attraction and repulsion. In our field theory Hamiltonian (7), this instability dominates in the conductor and perfect conductor phases.

Let us first show how the CI and EI work for a single beam with nonzero vortex charge. In Fig. 4, we show the intensity patterns for a single vortex with charges (1,0) and (3,0) as the x - y cross sections (transverse profiles) in the middle of the

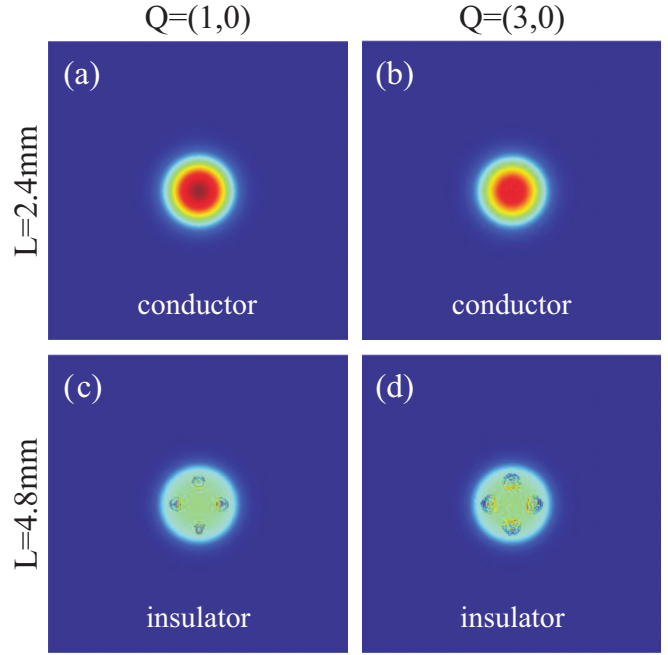


FIG. 4. Transverse profiles for a single Gaussian beam for two different propagation distances, $L = 2.4$ mm (top) and $L = 4.8$ mm (bottom), with vortex charges (1,0) [(a), (c)] and (3,0) [(b), (d)], at the back face of the crystal ($z = L$). The regime on top [(a), (b)] corresponds to the conductor phase, which has a single conserved vortex charge Q_F . This vortex charge conservation prevents significant instabilities; nevertheless, the multi-quantum vortex (3,0) shows the onset of CI; notice the reduced intensity and incoherent distribution of the beam in the central region in the top right panel (the CI is expected to grow roughly as $Q_+^2 + Q_-^2$). The insulator phase only preserves the $F - B$ invariance but not the vortex charge, and in the absence of topological protection the vortices can annihilate into the vacuum. Here we see the EI taking over for both charges; four unstable regions appear near the boundary, violating the circular symmetry and dissipating away the intensity of the vortex. Parameter values: FWHM $40 \mu\text{m}$, $\Gamma I_0 = 41$, $t = 10\tau$.

crystal, i.e., for $z = L/2$. The parameters chosen (Γ, I_0, R, L) correspond to the conductor phase (top) and the insulator phase (bottom). In top panels, for $Q_+^2 + Q_-^2 = 1$, the core energy is not so large and CI is almost invisible. For $Q_+^2 + Q_-^2 = 9$, we see the incoherence and the dissipation in the core region, signifying the CI. The conductor phase allows the proliferation of vortices but only those with $|Q_{\pm}| \leq 1$ are stable. In the bottom panels, both vortices have almost dissipated away due to EI, which starts from discrete poles near the boundary.⁵ Indeed, the insulator phase has no free vortices, no matter what the charge. In Fig. 5, we see no instability even for a high-charge vortex in the perfect conductor phase (top), whereas the frustrated insulator phase (bottom) shows strong EI for the like-charged vortex (3,3) since this fixed point has $g'_* > 0$, but the (3, -3) vortex is stable. Notice that we could not expect

⁴They are distinct from the bifurcations which happen also in topologically trivial beam patterns and lead to the instability which eventually destroys optical (nontopological) solitons. These instabilities have been analyzed in Appendix C and in more detail in Ref. [32], where the authors have found them to start from the edge of the beam and result in the classical “walk through the dictionary of patterns.”

⁵As a rule, it follows the sequence (C9) found in Appendix C from the pole structure of the propagator, though some of the steps can be absent, e.g., for a single Gaussian vortex there is no C_2 stage.

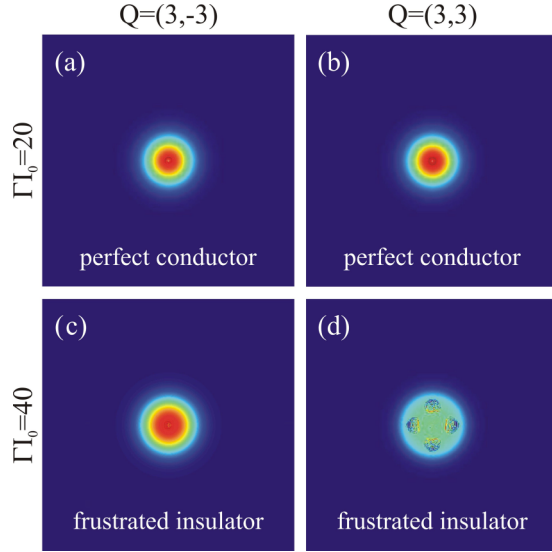


FIG. 5. Transverse profiles for a single Gaussian beam for two different coupling strengths, $\Gamma I_0 = 20$ (top) and $\Gamma I_0 = 40$ (bottom), with vortex charges $(3, -3)$ [(a), (c)] and $(3, 3)$ [(b), (d)] at the back face of the crystal ($z = L$). The regime on top corresponds to the perfect conductor phase, where the vortices of all charges freely proliferate—both vortices are reasonably stable. The bottom case is in the frustrated insulator phase—the forward-backward coupling makes the $(3, 3)$ vortex unstable from EI while the $(3, -3)$ vortex survives. Parameter values: FWHM $40 \mu\text{m}$, $L = 2 \text{ mm}$, $t = 10\tau$.

CI for this case since the sum $Q_+^2 + Q_-^2 = 9$ is the same in both cases—if for $Q_- = -Q_+$ the vortex has no CI, then for $Q_- = Q_+$ it cannot have it either (since the value $Q_+^2 + Q_-^2$ is the same).

We have thus seen what patterns to expect from CI and EI and also what kind of stable vortices to expect in different phases: The perfect conductor phase allows free proliferation of vortices of any charge, the conductor phase allows only single-quantum vortices (or vortices with sufficiently low $Q_+^2 + Q_-^2$) while others dissipate from CI, the frustrated insulator supports the vortices with favorable charges (or favorable charge distribution in multiple-vortex systems) while others disintegrate from EI, and the insulator phase supports no vortices—they all dissipate from CI or EI, whichever settles first (depending on the vortex charges).

The case rich with analogies with condensed matter systems is the square vortex lattice on the background photonic square lattice, Fig. 6. Here we can also appreciate the transport processes. The photonic lattice is coincident with the beam lattice and equal in intensity, so $\Gamma(I_0 + I_x) = 2\Gamma I_0$. In the perfect conductor phase [Fig. 6(a)], the vortices are stable and coherent and keep the uniform lattice structure. In the conductor phase [Fig. 6(b)], the CI is visible but the lattice structure survives. The bottom panels show the nonconducting phases: frustrated insulator [Fig. 6(c)] and insulator [Fig. 6(d)]. The insulator loses both lattice periodicity and the Gaussian profile of the vortices but the frustrated insulator keeps the regular structure: From EI the intensity is *inverted* and the resulting lattice is *dual* to the original one [compare Fig. 6(c) to Fig. 6(a)]. The phase patterns $\theta_F(x, y; z = L/2)$

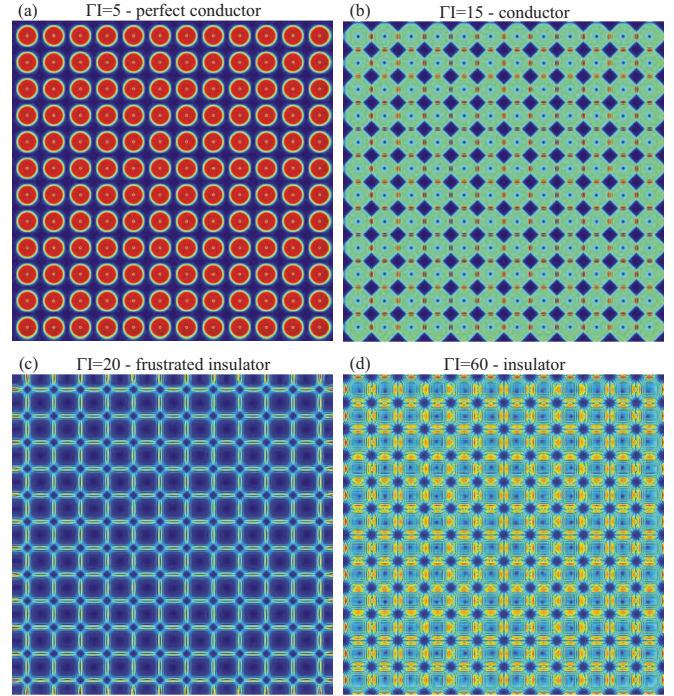


FIG. 6. Vortex lattice with Gaussian profile for $\Gamma I = 5$ [PC, panel (a)], $\Gamma I = 15$ [conductor, panel (b)], $\Gamma I = 20$ [FI, panel (c)], and $\Gamma I = 60$ [insulator, panel (d)]. The perfect conductor phase has a coherent vortex lattice and no instabilities. Conductor exhibits a deformation of the vortex lattice and the reduction of the full $O(2)$ symmetry, starting from the *center*, whereas the FI exhibits the reduction of symmetry and the inversion of the lattice due to *edge* effects. Notice how both phases have reduced symmetry compared to PC but retain coherence. Only the insulator phase loses not only symmetry but also coherence; i.e., the intensity diffuses and the pattern is smeared out. Transverse size of the lattice is 512×512 in computational space; same lattice size, FWHM, and lattice spacing are used for all subsequent figures unless specified otherwise. Parameter values: $L = 4.8 \text{ mm}$, $t = 10\tau$, FWHM $10 \mu\text{m}$, and lattice spacing equal to FWHM.

and $\theta_F(x, z; y = 320 \mu\text{m})$ for the perfect conductor (top) and the frustrated insulator phase (bottom) are shown in Fig. 7. Here we see the vortex charge transport mechanism in a PC: The vortices are connected in the sense that the phase θ_F is coherently traveling from one vortex to the next. In the FI phase, the phase is initially frozen along the z axis, until the transport starts at some $z \approx L/2$.

It may be instructive to take a closer look at the lattice dynamics of the most interesting phase: the frustrated insulator. In Fig. 8, we inspect square lattices on the photonic lattice background for several charges of the form $(Q_+ = 3, Q_-)$. The first row shows how the vortices lose stability and develop CI as the total square of the charge grows [from Fig. 8(a) to Fig. 8(c)]. Figures 8(d)–8(i) show how the g' coupling favors the opposite sign of Q_+ and Q_- and how the optimal configuration is found for $Q_- = -3$. This is easily seen by minimizing the free energy over Q_- : It leads to the conclusion that the forward-backward coupling favors the “antiferromagnetic” ordering in the sense that $Q_+ + Q_- = 0$.

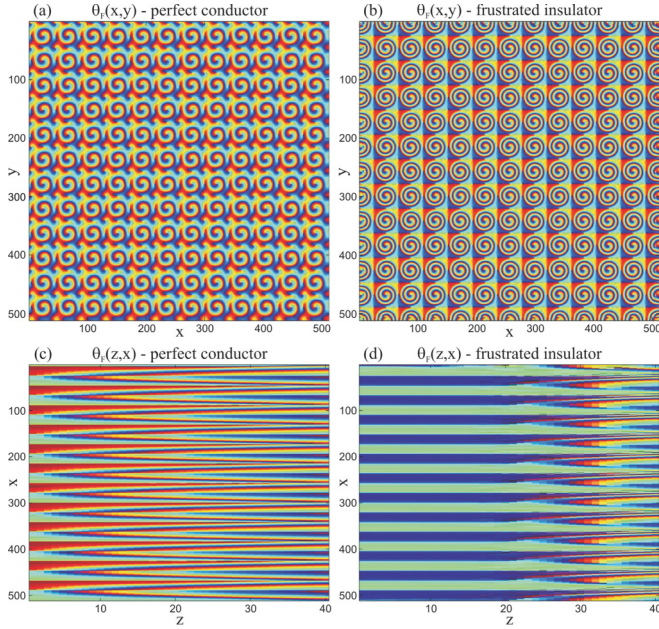


FIG. 7. Same system as in panels (a) and (c) from the previous figure (PC and FI phases) but now we plot the phase θ_F , as the transverse cross section $\theta_F(x,y; z = L/2)$ [(a), (b)] and as the longitudinal section along the PR crystal $\theta(x,z; y = 320 \mu\text{m})$ [(c), (d)]. The perfect conductor phase has well-defined vortices in contact which allows the transport of the vortex charge through the lattice and shows as the periodical modulation of the phase along the z axis (vortex lines). The frustrated insulator keeps well-defined vorticity even though the intensity map undergoes inversion [Fig. 6(c)] with frozen phase along the z axis, so there is no vorticity transport until some $z \approx L/2 = 2.4 \text{ mm}$, when the phase stripes develop into vortex lines. The unit on the x and y axis is $1 \mu\text{m}$ (1 in computational space) and on the z axis 0.12 mm (120 in computational space).

Finally, it is interesting to see how the FI phase at high intensities and coupling strengths contains a seed of translation symmetry breaking which will become important in the presence of disorder. In Figs. 9 and 10, we give intensity and phase transverse profiles across the PC-FI transition and deep into the FI phase at large couplings. The intensity maps show the familiar inverse square lattice but the phase maps show stripelike ordering, i.e., translation symmetry breaking along one direction in Figs. 10(c) and 10(d)—horizontal and vertical lines with a repeating constant value of the phase θ_F on all lattice cells along the line. This is a new instability, distinct from CI and EI. We cannot easily derive this instability from the perturbation theory in Appendix C as it is a collective phenomenon and cannot be understood from a single beam.

IV. THE SYSTEM WITH DISORDER

Consider now the same system in the presence of quenched disorder. This is a physically realistic situation: The disorder corresponds to the holes in the photonic lattice which are caused by the defects in the material. The defects are in fixed positions, i.e., they are quenched, whereas the beam is dynamical and can fluctuate. Now $I_x(\mathbf{r}) \rightarrow I_x(\mathbf{r}) + I_h(\mathbf{r})$; i.e.,

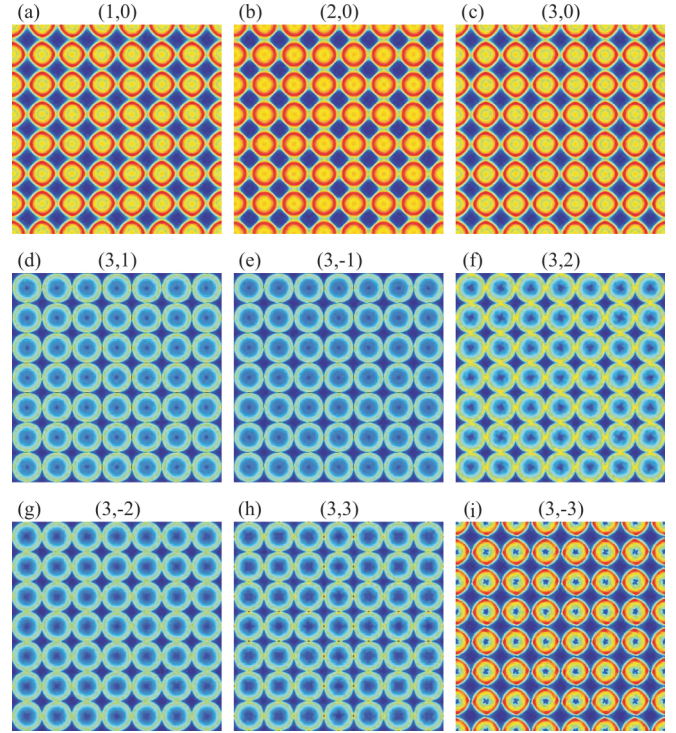


FIG. 8. Transverse profiles for vortex lattices with different charges in the FI phase. In the first row [(a)–(c)], we see how the CI gets stronger and stronger as the total vortex core energy grow (with the square of the total charge). The second and third rows show the growth of CI from $(3,0)$ to $(3, \pm 3)$ (notice the increasingly reduced intensity in the center and the strong ringlike structure of the beams) but also the forward-backward interaction which favors the configurations $(3, -3), (3, -2), (3, -1)$ over $(3, 3), (3, 2), (3, 1)$. In particular, the $(3, -3)$ lattice is the optimal configuration of all $(3, Q_-)$ configurations even though it has greater CI than say $(3, 0)$ (notice the small dark regions in the center), because the $\sum_{ij} gg' Q_{i+} Q_{i-} \ln r_{ij}$ term minimizes the EI—notice there is no “spilling” of intensity from one vortex to the next. The parameters are $\Gamma I = 20, L = 2.5 \text{ mm}$.

the quenched random part $I_h(\mathbf{r})$ is superimposed to the regular background (whose intensity is I_x). The disorder is given by some probability distribution, assuming no correlations between defects at different places. As in the disorder-free case, the lattice is static and “hard”, i.e., does not backreact due to the presence of the beams. One should, however, bear in mind that the backreaction on the background lattice can sometimes be important as disregarding it violates the conservation of the angular momentum [37]. Disregarding the backreaction becomes exact when $I_x + I_h \gg |\Psi|^2$, i.e., when the background irradiation is much stronger than the propagating beams.

To treat the disorder, we use the well-known replica formalism [54]. For vortex-free configurations, typical experimental values of the parameters suggest that the influence of disorder is small [31, 33, 35]. However, the influence of disorder becomes dramatic when vortices are present. This is expected, since holes in the lattice can change the topology of the phase field θ_{\pm} (the phase now must wind around the holes). Our equations of motion are still given by the Lagrangian (4), but with $I_x \mapsto I_x + I_h$. In our analytical calculations, we assume

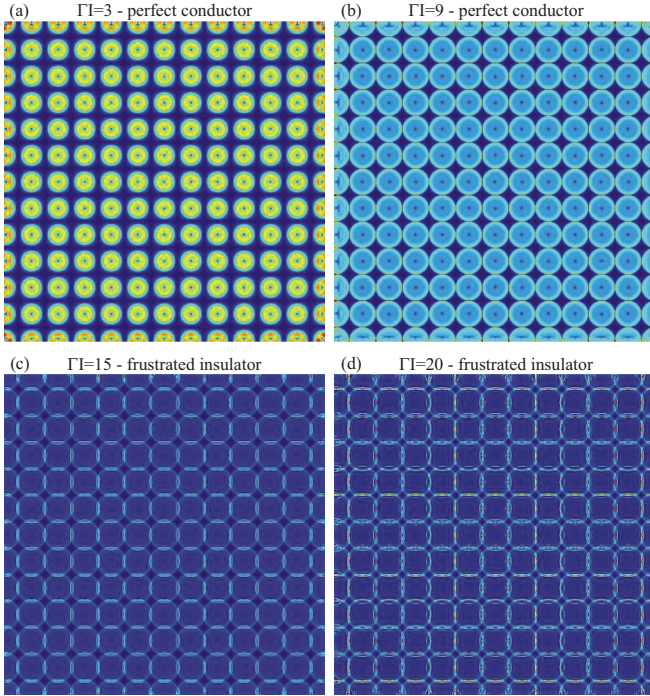


FIG. 9. Intensity maps for the quadratic vortex lattice with charges (1,1), for increasing values of $\Gamma I = \Gamma(I_0 + I_x)$. The transition from the PC phase [(a), (b)] into the FI phase [(c), (d)] happens at about $\Gamma I \approx 12$. The edge instability sets in progressively, in accordance with what we saw in the previous figure, leading eventually to an inverse square lattice. Propagation length $L = 5$ mm.

that a defect in the photonic lattice changes the lattice intensity from I_x to $I_x + I_h$, with Gaussian distribution of “holes” in I_h , which translates to the approximately Gaussian distribution of the couplings g, g', g_0, g_1 . In the numerics, however, we do a further simplification and model the defects in a discrete way; i.e., at a given spot either there is a lattice cell of intensity I_1 (with probability h), or there is not (the intensity is zero, with probability $1 - h$). This corresponds to $I_x = I_1/2, I_h = \pm I_1/2$ so the disorder is discrete. Due to the central limit theorem, we expect that the Gaussian analytics should be applicable to our numerics.

A. The replica formalism at the mean-field level

To study the system with quenched disorder in the photonic lattice, we need to perform the replica calculation of the free energy of the vortex Hamiltonian (7). We refer the reader to the literature [41,42] for an in-depth explanation of the replica trick. In short, one needs to average over the various realizations of the disorder *prior* to calculating the partition function, i.e., prior to averaging over the dynamical degrees of freedom (vortices in our case). This means that we need to perform the disorder average of the free energy, i.e., the logarithm of the original partition function $-\ln \mathcal{Z}$, and not the partition function \mathcal{Z} itself. The final twist is the identity $\ln \mathcal{Z} = \lim_{n \rightarrow 0} (\mathcal{Z}^n - 1)/n$: We study the Hamiltonian consisting of n copies (replicas) of the original system and then *carefully*

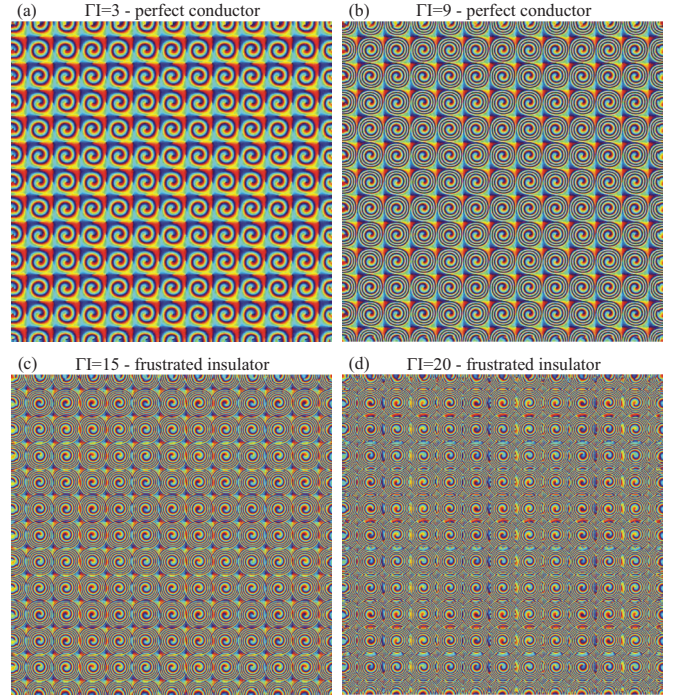


FIG. 10. Transverse phase maps for the F beam for the same cases as in Fig. 9. As the coupling strength ΓI grows toward very large values (d), the violation of translation symmetry becomes obvious: Notice the vertical and horizontal phase stripes. This instability gives rise to the charge density wave ordering in the presence of disorder.

take the $n \rightarrow 0$ limit.⁶ The partition function of the replicated Hamiltonian reads

$$\mathcal{Z} = \lim_{n \rightarrow 0} \text{Tr} \exp \left[- \sum_{\mu=1}^n \mathcal{H}_{\text{vort}}(Q^{(\mu)}) \right], \quad (15)$$

where $Q^{(\mu)}$ are the vortex charges in the μ th replica of the system. In the original Hamiltonian (7), the disorder turns the interaction constants into quenched random quantities $g_{ij}, g'_{ij}, g_{0;ij}, g_{1;ij}$, so we can compactly write our interaction term as

$$\mathcal{H}_{\text{vort}} = \sum_{ij} \sum_{\alpha\beta} Q_{i\alpha} J_{ij}^{\alpha\beta} Q_{j\beta} \quad (16)$$

with $J_{ij}^{++} = J_{ij}^{--} = g_{ij}(1 - \delta_{ij}) \ln r_{ij} + g_0 \delta_{ij}$, $J_{ij}^{+-} = J_{ij}^{-+} = g'_{ij}(1 - \delta_{ij}) \ln r_{ij} + g_1 \delta_{ij}$. Now we again make the mean-field approximation for the long-ranged logarithmic interaction. Similar to the clean case, for $i \neq j$ we approximate $g \ln r_{ij} \sim g' \ln r_{ij} \sim \ln \Lambda$, knowing that $g, g' \sim 1$ and assuming that average intervortex distance is of the same order of magnitude as the system size Λ , and for the core energy we likewise get $g_0, g_1 \sim \ln a/\epsilon \sim -\ln \epsilon \sim \ln \Lambda$. The result is that all terms in $J_{ij}^{\alpha\beta}$, both for $i \neq j$ and $i = j$, are on average of the order $\ln \Lambda \gg 1$, and the mean-field approach is justified. We will sometimes denote the 2×2 matrices in the flavor space by hats (e.g., $\hat{J} = J^{\alpha\beta}$).

⁶Care is needed as the $n \rightarrow 0$ limit does not in general commute with the thermodynamic limit.

The final Hamiltonian (16) has the form of the random-coupling and random-field Ising-like model: Random couplings stem from the stochasticity of J_{ij} values and random field from the fact that $\langle J_{ij} \rangle \neq 0$ introduces terms linear in $Q_{i\alpha}$, i.e., an effective external field coupling to the “spins.” We have arrived at this model through three steps of simplification: our microscopic model is a type of the XY -glass model (Cardy-Ostlund model [55]), a well-known toy model for disorder. At this stage, our model is similar to the work of Refs. [9,10], only with two components instead of one. Then we have written the effective vortex Hamiltonian with Coulomb-like interaction, disregarding the topologically trivial configurations. This is a rather extreme approximation but a necessary one as it is very complicated to consider the full model with vortices. Finally, we have approximated the logarithmic potential with a constant all-to-all vortex coupling. Such an approximation

(essentially the infinite dimension limit) is frequently taken and lies at the heart of the solvable Sherington-Kirkpatrick Ising random coupling model [41]. Our case differs from the Sherington-Kirkpatrick model as it (i) has also a random field, (ii) has two flavors, and (iii) has the Ising spins taking arbitrary integer values. From the random XY model it differs by (i) and (ii) above, and also by considering only vortices and no nontopological spin configurations. The additional phases we get in comparison to Refs. [9,10] and its generalization in Refs. [11,12,46] come from the interactions between the forward and backward flavors. But bearing in mind the drastic approximations we take, we stress that we cannot aspire to solve either the XY model or the resulting Ising-like model in any rigorous way (certainly not at the level of rigor of mathematical physics). We merely try to obtain a crude understanding.

The Gaussian distribution of defects reads $p(J_{ij}^{\alpha\beta}) = \exp[-(J_{ij}^{\alpha\beta} - J_0^{\alpha\beta})(\hat{\sigma}^{-2})_{\alpha\beta}(J_{ij}^{\alpha\beta} - J_0^{\alpha\beta})]$, where the second moments are contained in the matrix $\sigma_{\alpha\beta}$, with $\sigma_{+-} = \sigma_{-+}$. In this case, we get the replicated partition function

$$\bar{Z}^n = \int \mathcal{D}[Q_{i\alpha}^{(\mu)}] \int \mathcal{D}[J_{ij}^{\alpha\beta}] \exp \left[-\frac{1}{2} \sum_{i,j=1}^N \sum_{\alpha,\beta} (J_{ij}^{\alpha\beta} - J_0^{\alpha\beta}) \sigma_{\alpha\beta}^{-2} (J_{ij}^{\alpha\beta} - J_0^{\alpha\beta}) - \sum_{\mu=1}^n \sum_{i,j=1}^N \sum_{\alpha,\beta} \beta J_{ij}^{\alpha\beta} Q_{i\alpha}^{(\mu)} Q_{j\beta}^{(\mu)} \right]. \quad (17)$$

We can now integrate out the couplings $J_{ij}^{\alpha\beta}$ in (17) and get

$$\bar{Z}^n = \text{const.} \int \mathcal{D}[Q_{i\alpha}^{(\mu)}] \exp \left[\frac{1}{2} \beta^2 \sum_{\mu,\nu=1}^n \sum_{i,j=1}^N \sum_{\alpha,\beta} Q_{i\alpha}^{(\mu)} Q_{j\beta}^{(\nu)} (\hat{\sigma}^2)_{\alpha\beta} Q_{j\alpha}^{(\mu)} Q_{i\beta}^{(\nu)} - \beta \sum_{\mu=1}^n \sum_{i,j=1}^N \sum_{\alpha,\beta} J_0^{\alpha\beta} Q_{i\alpha}^{(\mu)} Q_{j\beta}^{(\mu)} \right]. \quad (18)$$

Integrating out the disorder has generated the nonlocal quartic term proportional to the elements of $\sigma_{\alpha\beta}^2$. The additional scale given by the average disorder concentration means we cannot scale out $\beta = L$ anymore, and it becomes an additional independent parameter. The partition function can be rewritten in the following way, usual in the spin-glass literature [42,54]. We can introduce the nonlocal order parameter fields

$$p_\alpha^{(\mu)} = \frac{1}{N} \sum_{i=1}^N Q_{i\alpha}^{(\mu)}, \quad q_{\alpha\beta}^{(\mu\nu)} = \frac{1}{N} \sum_{i,j=1}^N Q_{i\alpha}^{(\mu)} Q_{j\beta}^{(\nu)}, \quad (19)$$

which have the meaning of overlap between different metastable states. The rest is just algebra, although rather tedious: One rewrites the Hamiltonian in terms of new order parameters, and then one can solve the saddle-point equations for p_α and $q_{\alpha\beta}$, or do an RG analysis. The calculation is found in Appendix G.

The mean-field analysis yields six phases:

(1) One phase violates both the replica symmetry and the flavor symmetry, breaking it down to identity. We dub this phase *vortex charge density wave* (CDW), as it implies spatial modulation of the vortex charge, leading to nonzero net charge density $\sum_i Q_{i\alpha}^{(\mu)}$ in some parts of the system even if the boundary conditions are electrically neutral (the *total* net charge density must still be zero due to charge conservation). Vortices take their charges from $\mathbb{Z} \otimes \mathbb{Z}$.

(2) The second phase violates the replica symmetry in both flavors and reduces the flavor symmetry but does not break it down to identity. Instead, it reduces it to the diagonal subgroup

$U(1)_F \otimes U(1)_B \rightarrow U(1)_d$, so it has nonzero density of the vortex charge in a given replica $\sum_i Q_{i+}^{(\mu)} = -\sum_i Q_{i-}^{(\mu)}$. Again, the charge density is locally nonzero but now with an additional constraint resulting in frustration (multiple equivalent free energy minima). This is thus the dirty equivalent of the frustrated insulator phase and we dub it *vortex glass*, as it has long-range correlations (because of the logarithmic interactions between charged areas), does not break spatial symmetry, and exhibits frustration; its charges are from $\pi_1[U(1)_d] = \mathbb{Z}$.

(3) The remaining phases have no nonzero vortex charge density fluctuation and are similar to the phases in the clean system. Vortex perfect conductor violates the replica symmetry of all three fields q^{++}, q^{--}, q^{+-} and allows free proliferation of vortices with charges $(Q_+, Q_-) \in \mathbb{Z} \otimes \mathbb{Z}$.

(4) Frustrated vortex insulator preserves the replica symmetry of $q^{\pm\pm}$ but has nonzero value, with broken replica symmetry, of the mixed q^{+-} field, which gives $U(1)_d$ vortices, with charges $Q_+ = -Q_- \in \mathbb{Z}$.

(5) Vortex conductor preserves the replica symmetry of the mixed q^{+-} order parameter but violates it in $q^{\pm\pm}$, resulting in the proliferation of single-flavor vortices with \mathbb{Z} charge.

(6) Vortex insulator fully preserves the replica symmetry, all order parameters are zero, and vortices cannot proliferate. RG analysis will show that insulator survives only at zero disorder; otherwise it generically becomes CDW.

The phase diagram (given in Fig. 11 in the next subsection) now contains six phases (only five are visible for the parameters chosen in the figure): CDW, insulator, FI,

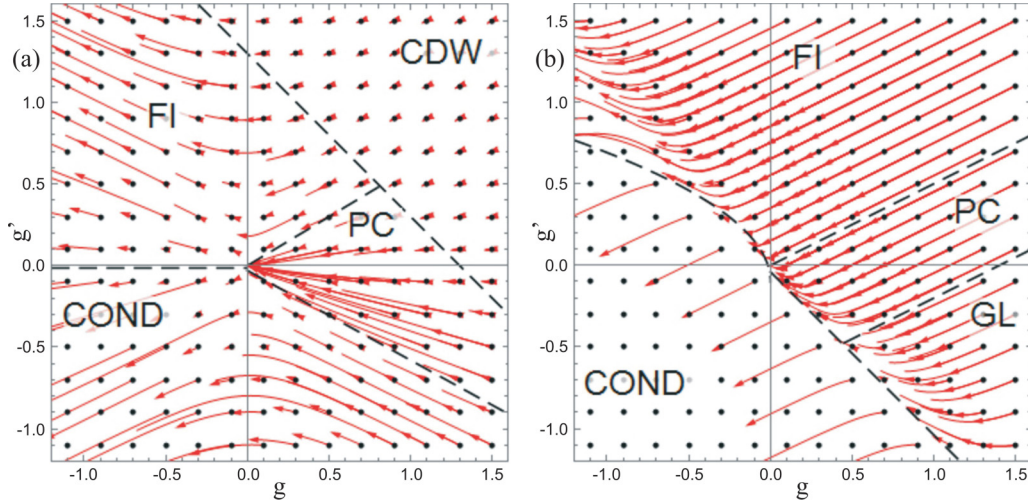


FIG. 11. Phase diagram for the system with lattice disorder in the g - g' plane together with RG flows, with red lines denoting the flows starting at the initial conditions denoted by black points. The dashed black lines are approximate phase boundaries from mean-field theory, for $\sigma^2 = 0.4$ (a) and $\sigma^2 = 1.2$ (b). In panel (a), the area where $g + g' + \beta^2\sigma^2 > 1$ is inhabited by the flows toward nonuniversal values of (g, g') which belong to the CDW phase and the opposite region is divided between the attraction regions of $(0, 0)$, $(g_* \rightarrow \infty, g'_* \rightarrow \infty)$, and $(g_{**} \rightarrow \infty, g'_{**} \rightarrow -\infty)$ —the familiar PC, FI, and conductor phases. In panel (b), for $\sigma^2 = 1.2$, the disorder becomes relevant in the glass phase (denoted by “GL”), whose RG flows end on the half-line of fixed points $g + g' + \beta^2\sigma^2 = 1, g' < 0$. For our parameter values, this line happens to pass almost through the origin; in general, this is not necessarily the case. The nondisordered phases (flowing to $\sigma^2 = 0$) FI, conductor, and PC have survived. Propagating length is $L = 3.0$ nm.

conductor, PC, and the glassy phase. The insulator phase is now of measure zero in the (g, g', σ^2) plane, existing only for the points at $\sigma^2 = 0$; for generic nonzero values we have a CDW. For simplicity, we have plotted the phase diagram for $\sigma_{++}^2 = \sigma_{--}^2 = \sigma_{+-}^2 \equiv \sigma^2$.

B. RG analysis and the phase diagram

To study the RG flow, we can start from the replicated partition function (18), inserting the definition of the couplings $J_{ij}^{\alpha\beta}$ and keeping the vortex charges $Q_{i\alpha}^{(\mu)}$ as the degrees of freedom (without introducing the quantities $p_\alpha^\mu, q_{\alpha\beta}^{(\mu\nu)}$). The basic idea is the same: We consider the fluctuation $\delta(\bar{\mathcal{Z}}^n)$ upon the creation of a vortex pair at $\mathbf{r}_{1,2}$ with charges $\vec{q}_1^{(\mu)}, -\vec{q}_2^{(\mu)}$, in the background of the vortices $\vec{Q}_{1,2}^{(\nu)}$ at positions $\mathbf{R}_{1,2}$. Likewise, we introduce the fugacity parameter $y^{(\mu)}$ to account for the vortex core energy. However, this problem is much harder than the clean problem and one has to resort to many approximations to perform the calculation. In its most general form, the problem is still open, in the sense that all known solutions suppose a certain form of replica symmetry breaking or truncate the RG equations [42]. The RG analysis is thus less useful in the disordered case but at least the numerical integration of the flow equations is supposed to give a more precise rendering of the phase diagram compared to the mean field theory. We again describe the calculation in Appendix G and jump to the results.

The fixed point of the flow equations lies either at infinite y or at $y = 0$ like in the clean case. This is again controlled by the equation for $\partial y / \partial \ell$ but now depending on the combination $g + g' + \beta^2\sigma^2$ instead of $g + g'$ in the clean case (for simplicity, we consider the case where $\sigma_{\alpha\beta}^2$ are all equal). The following cases appear:

(1) When the fugacity flows toward infinity, we reproduce the phases and the fixed point values (g, g', σ^2) from the clean case: The PC flows toward $(0, 0, 0)$, the FI toward $(g_*, g'_*, 0)$, and the conductor toward $(g_*, g'_{**}, 0)$ with $g_* \rightarrow -\infty, g'_* \rightarrow -\infty, g'_{**} \rightarrow \infty$. Notice that all these phases flow to $\sigma^2 = 0$; i.e., disorder is irrelevant.

(2) When the fixed point lies at $y = 0$, one possibility is that all parameters (g, g', σ^2) flow toward some nonuniversal nonzero values. The attraction region of this point is the CDW phase: The disorder term stays finite as well as the couplings. In particular, the points on the half-plane $g + g' > 0, \sigma^2 = 0$ stay at $\sigma^2 = 0$ (with constant coupling values) and this is the insulator phase from the clean case. Notice that $\sigma^2 > 0$ now; i.e., disorder is relevant. For $\sigma^2 < 1$, this are the only fixed points when $y = 0$.

(3) However, for sufficiently strong disorder ($\sigma^2 > 1$), there is a new line of fixed points at $y = 0$ with a finite attraction region, corresponding to a new phase. For $\beta > 1$, the right-hand side of the second RG equation in (G19) has a zero at nonzero g' and there are trajectories flowing toward $(y, g, g', \sigma^2) = [0, g, g'(g), \sigma^2(g)]$ and not toward an arbitrary nonuniversal value of σ^2 . This is precisely the glass phase, where disorder is again relevant. At the lowest order, the relation between g, g', σ^2 at the fixed point line is given by the relation $g + g' + \beta^2\sigma^2 = 1$.

Now we have made contact between the mean-field classification of phases and the fixed points and regions of the RG flow. The flows in the (g, g') plane are given in Fig. 11. The parameter space is four-dimensional so the phase structure is different at different disorder concentrations σ^2 . In Fig. 11(a) for $\sigma^2 = 0.4$, the phase structure is similar to the clean case; we see the same four phases except that insulator (no stable vortices) is replaced by the CDW phase with localized vortices. In Fig. 11(b) for $\sigma^2 = 1.2$, the CDW phase is replaced by

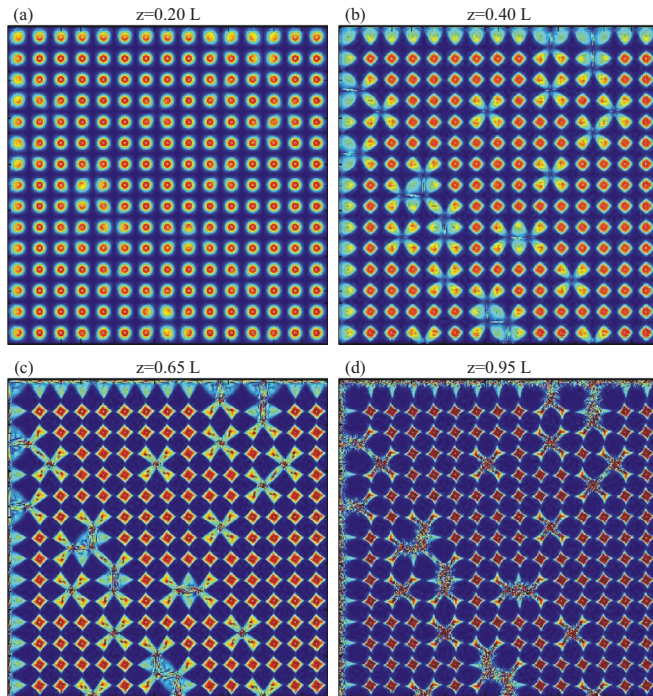


FIG. 12. Transverse profile for the PC phase in a Gaussian beam lattice on a background lattice, for four different propagation distances. The vortex charge is $(1, 1)$, which is sufficiently low that the CI does not destroy the vortices. We see some CI-induced symmetry reduction from $O(2)$ to C_4 but the overall lattice structure is preserved. Parameter values are $\sigma^2 = 0.1, \Gamma I = 20, L = 2$ mm, FWHM for the CP beams is $9 \mu\text{m}$ and for the photonic lattice $6 \mu\text{m}$.

another disordered phase, the glasslike regime. Importantly, the glass phase does not cross the $g' = 0$ axis, meaning that a single-flavor system even with disorder could not support a glass. We thus conjecture that the transition at $\sigma^2 = 1$ is of first order, as the change is the structure of the (g, g') phase diagram is discontinuous, and we do not see how this could happen if the first derivative $\partial\mathcal{F}/\partial\rho_{\pm}$ (the derivative of the free energy with respect to vortex charge density) is continuous. However, we have not checked the order of this transition by explicit calculation. The phase structure is further seen in the $\sigma^2 - g'$ diagram, where we see the glass phase emerge at some value of the disorder. This is discussed further in the next section, where we study the equivalent antiferromagnetic system (with the same structure of the phase diagram, Fig. 16).

C. Geometry of patterns

The two previously considered mechanisms of instability—central instability and edge instability—remain active also in the presence of disorder. However, in the presence of disorder there is a third, inherently collective effect that we dub *domain instability* (DI). It follows from the fact that the self-focusing term ΓE grows with intensity I : More illuminated regions react faster [Eqs. (1) and (2)]. In the presence of background lattice, there will be regions of initially zero beam intensity I_0 where the regular lattice cells have some nonzero intensity I_x . Approximating $I = I_0 + I_x \approx I_x = \text{const.}$, our equations in the vicinity of the defect (hole) in the background lattice

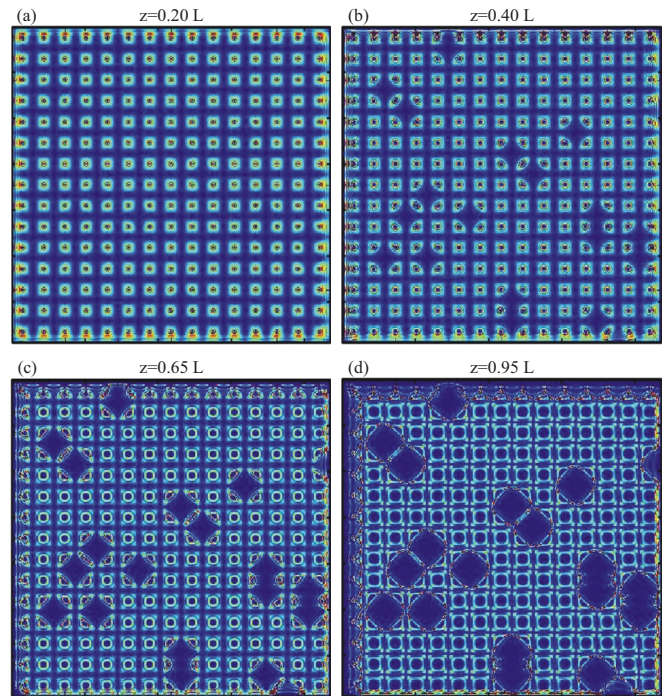


FIG. 13. Transverse profile for the FI phase, present in the same system as in Fig. 12 but for $\Gamma I = 40$. Now both the CI [low-intensity regions in the beam center in panels (a) and (b)] and the EI [lattice inversion in panels (c) and (d)] are present. The net result is the lattice inversion, and the vortex charge dissipates along the inverse lattice.

becomes the Schrödinger equation in a step potential (equal to I_x in the regular parts of the photonic lattice, and equal to zero where a hole is found), so the z -dependent part of the solution is of the form $\sum_k e^{i\lambda_k z}$ and the eigenenergies along z are gapped by the inverse length: $\lambda_k > 1/L$. For small eigenenergies, the transmission coefficient is very low, whereas for large energies it approaches unity. Thus for $1/L$ large (i.e., there are few λ_k 's which are larger than $1/L$), most of the intensity remains confined by the borders of the defect and the intensity does not spill but for small $1/L$ the beam profile is deformed by the “spilling” into the hole regions. For vortices, there is an additional Coulomb interaction in the x - y plane, meaning the effective potential is not piecewise constant anymore (even in the simplest approximation) but the qualitative conclusion remains: Large L brings global reshaping of the intensity profile.

The other phases are analogous to the ones in the clean case, though with a general trend that the presence of disorder decreases the stability of vortex patterns. The PC and FI phases are shown in Figs. 12 and 13. In this section, we only look at the lattices, as the notion of disorder is inapplicable for a single beam. Consider first the patterns in the PC phase (Fig. 12). Compared to the clean case [Fig. 6(a)], the symmetry is much reduced, from $O(2)$ to C_4 , but the vortices are conserved and the original lattice structure (outside the holes) is clearly visible. The FI (Fig. 13) shows mainly EI (and to a smaller extent CI), which together lead to the lattice inversion. The rule of thumb for differentiating the conductor and PC on one side from the CDW and FI on the other side is precisely the presence of the lattice inversion. The absence of the charge transport is

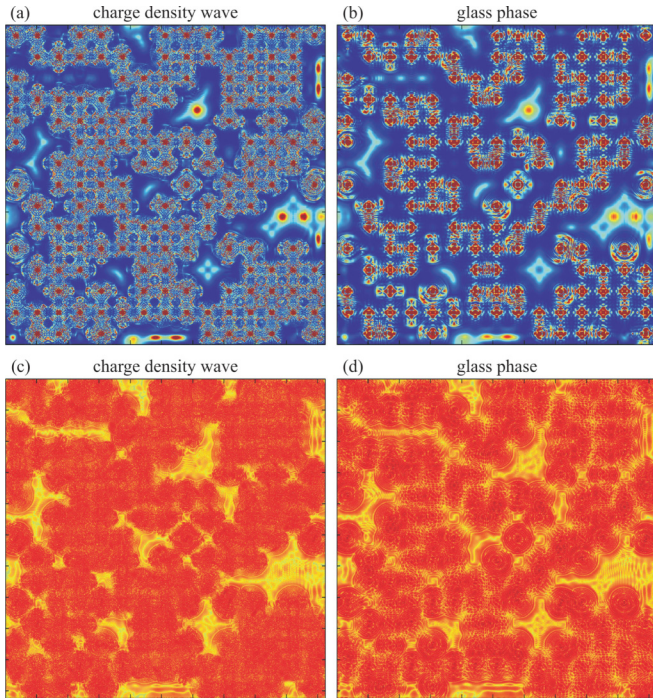


FIG. 14. Transverse profiles for the charge density wave [panels (a) and (c)] and the glass phase [panels (b) and (d)]: intensity maps (top) and vortex charge density maps (down). The telltale difference is that the CDW loses the regular lattice as the intensity “flows” between the regular and the defect regions and we see the DI at work. Glass, on the other hand, consists of domains with coherent (well-defined) vortices though with reduced symmetry (C_4) mostly due to EI. The charge density forms a connected network in the glass phase and transport is possible, whereas in a frustrated insulator the charge is stuck in isolated points.

best appreciated in the phase images: The charge pins to the defects and localizes toward the end of the crystal (i.e., for z near L). Only near the edges we see high vorticity, somewhat analogous to topological insulators, which only have nonzero conductivity along the edges of the system.

The CDW versus the glass phase is given in Fig. 14. The charge density wave [Figs. 14(a) and 14(c), $L = 240 \mu\text{m}$] exhibits the diffusion of intensity due to DI, and the vortex beams are in general asymmetric and not clearly delineated. In Figs. 14(b) and 14(d), where $L = 120 \mu\text{m}$ with all other parameters the same, there is a clear border between defects and the regular parts of the lattice and the intensity is concentrated in the vortex cores. We give also the vortex charge density map in Figs. 14(c) and 14(d) in addition to the intensity maps in Figs. 14(a) and 14(b) as the charge density shows why the CDW is insulating: Even though individual beams diffuse and smear out in *intensity*, the regions of nonzero vortex charge are disjoint and no global conduction can occur. Glass is divided into ordered domains in intensity but the vortex charges form a connected network which supports transport. This is analogous to the percolation transition in a disordered Ising model [56,57] and we may expect that the CDW-glass transition follows the same scaling laws near the critical point. However, we have not checked this explicitly and we leave it for further work.

V. THE CONDENSED MATTER ANALOGY: COLLINEAR DOPED HEISENBERG ANTIFERROMAGNET

The two-beam photorefractive system can serve as a good model for quantum magnetic systems. The most obvious connection is to multicomponent XY antiferromagnets (i.e., two-dimensional Heisenberg model): Planar spins are nothing but complex scalars, and the vortex Hamiltonian remains identical ($\pi_1[\text{SO}(2)] = \pi_1[\text{U}(1)] = \mathbb{Z}$). The nonlinearity in the spin system is different and usually much simpler, but that typically does not influence the phase diagram (the symmetry structure remains the same). Such connection is so obvious it does not require further explanations. Our point is that the CP beams in a PR crystal can also describe more general magnetic systems in the presence of topological solutions described by homotopy groups different from \mathbb{Z} . In particular, we want to point out a connection with a two-sublattice antiferromagnetic system which has some time ago enjoyed considerable popularity as a possible description of magnetic ordering in numerous planar strongly coupled electron systems, including cuprate high- T_c superconductors [5,38,58]. This is the collinear doped antiferromagnet defined on two sublattices. When coupled to a charge density wave (speaking about the usual $\text{U}(1)$ electromagnetic charge) and a superconducting order parameter, it becomes a toy model of cuprate materials (one variant is given in Ref. [58]). In the light of what we know today, the ability of this model to realistically describe the cuprate physics is quite questionable; but even so it is an interesting magnetic system on its own, and it was already found in Refs. [39,47] to exhibit a spin-glass phase, though in a slightly different variant (in particular, with spiral instead of collinear ordering).

Let us formulate the model. While the material is a lattice on the microscopic level, here we are talking about an effective field theory model. The order parameter is the staggered magnetization

$$M(\mathbf{r}) = \sum_{\alpha=1,2} \mathbf{M}_\alpha(\mathbf{r}) \cos(\mathbf{n} \cdot \mathbf{r}), \quad (20)$$

where $\alpha \in \{1,2\}$ is the sublattice “flavor” index (analogous to the α index for the F and B beam in the previous sections)⁷ and each component \mathbf{M}_α is a three-component spin, describing the internal, i.e., spin degree of freedom (we label the spin axes as X, Y, Z). The total spin is thus the sum of the spins of the two components, and \mathbf{n} is the modulation vector. The modulation gives rows of alternating staggered magnetization in opposite directions as in Fig. 15(a). This stands in contrast with the spiral order, where the modulation vectors become \mathbf{n}_α , i.e., differ for the two sublattices, and are themselves space dependent [39]. The ordered phase of the collinear system has the nonzero expectation value of the staggered magnetization along one direction, which can be chosen as the Z axis (“easy axis”), where the spin fluctuations about the easy axis remain massless, and the symmetry is broken from $\text{O}(3)$ to $\text{O}(3)/\text{O}(2)$. The spiral order, on the other hand, breaks the symmetry down to identity, as the order parameter is a dreibein [39].

⁷Sometimes we will denote the sublattices by \pm instead of 1,2 for compactness of notation.

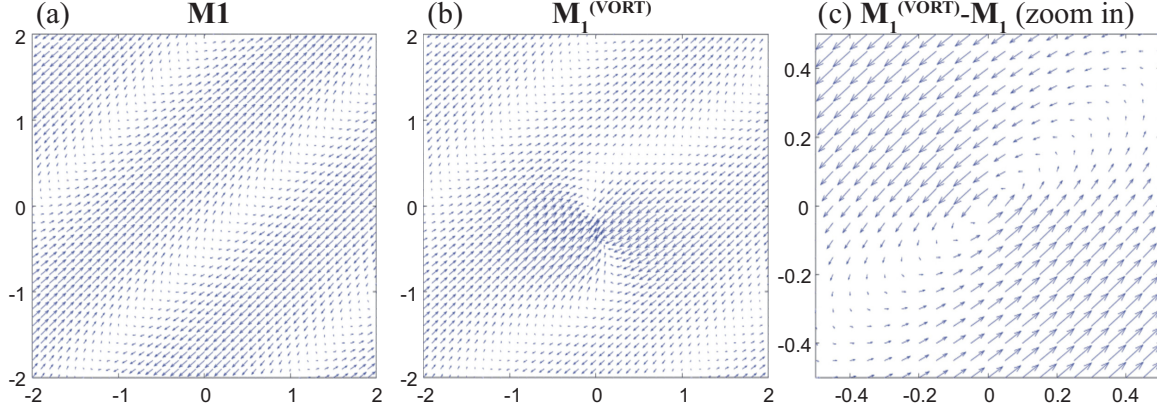


FIG. 15. Numerical realization of the spin pattern (staggered magnetization \mathbf{M}_1) in the collinear $O(3)$ antiferromagnet. Magnetization is three dimensional and we give the projection in the XY plane, $\mathbf{M}_1 \cdot \mathbf{n}_{XY} \equiv M_\perp$. In panel (a), we show the characteristic collinear spin pattern in absence of vortices. In panel (b), we plot $\mathbf{M}_1^{(\text{VORT})}$, a \mathbb{Z}_2 -charged point vortex defect with $Q = 1$. In panel (c), we give an enlargement of the vortex from panel (b) shown as the difference $\mathbf{M}_1^{(\text{VORT})} - \mathbf{M}_1$ to show more clearly the structure of the vortex—now the regular periodic pattern is absent and we appreciate the pointlike structure of the vortex. The parameters are $u = r = 1$ and $v = 0.5$.

The symmetry conditions (isotropy in absence of external magnetic field) determine the Hamiltonian up to fourth order, as discussed in Ref. [58]:

$$\mathcal{H}_{\text{af}} = \frac{1}{2g_M} \left[\left(\frac{1}{c_M} \partial_\tau \mathbf{M}_\alpha \right)^2 + |\nabla \mathbf{M}_\alpha|^2 + \frac{r}{2} |\mathbf{M}_\alpha|^2 \right] + \frac{u_0}{2} |\mathbf{M}_\alpha|^4 - v_0 (|\mathbf{M}_1|^2 + |\mathbf{M}_2|^2)^2. \quad (21)$$

The antiferromagnetic coupling is g_M , the spin stiffness is c_M , and the effective mass of spin wave excitations is r . The fourth-order coupling u_0 comes from the “soft” implementation of the constraint $|\mathbf{M}_\alpha| = 1$ ⁸ and v_0 is the anisotropy between the two sublattices, justified by the microscopic physics [5,58]. The Hamiltonian can be transformed by rescaling τ and x, y , together with the couplings $u_0 \mapsto u$ and $v \mapsto v_0$ to set $g_M = c_M = 1$ so that the kinetic term becomes isotropic, giving

$$\mathcal{H}_{\text{af}} = \frac{1}{2} (\partial_\tau M)^2 + \frac{1}{2} |\nabla M|^2 + \frac{r}{2} |M|^2 + \frac{u}{2} (|M|^2)^2 - v |\mathbf{M}_1|^2 |\mathbf{M}_2|^2, \quad (22)$$

where we have also rewritten the quartic terms for convenience. Without anisotropy, the energy of the system is a function of $|\mathbf{M}_1|^2 + |\mathbf{M}_2|^2$ only and the symmetry group is the full $O(6)$. With $v \neq 0$, the symmetry is reduced to $O(3)_1 \otimes O(3)_2$: The internal spin symmetry in each sublattice remains unbroken but the spatial rotation symmetry between the layers is broken down to just the discrete flip. Compare this to the $U(1) \otimes U(1)$ symmetry in the PR system: There, it is the internal phase symmetry that remains unbroken.

⁸One could also enforce the constraint exactly, through the nonlinear σ model, as was done in Ref. [39]. While the leading term of the “vortex” Hamiltonian would remain the same in that case, the amplitude fluctuations have different dynamics which influences some terms of the Hamiltonian and thus its RG flow (though probably not the very existence of the glass phase).

A. \mathbb{Z}_2 vortices

Remember that topological solitons are classified by homotopy groups and that we work in a two-dimensional plane. The relevant group is again the first homotopy group, $\pi_1[O(3)] = \mathbb{Z}_2$. For simplicity, we will call these excitations “vortices,” bearing in mind that the only possible charges are $Q_\alpha = \pm 1$ and not all integers. A realization of the vortex with $Q = 1$ is shown in Fig. 15(b). Since the spins are three-dimensional (the figure shows the projection in the XY plane), it becomes clear that vortex charge is only defined modulo 2; i.e., it makes no sense to talk about charges $|Q| > 1$. For example, winding around twice in the XY plane can be done along a closed line in the XYZ space which can be contracted to a point. That could not happen for the two-dimensional phase $U(1)$ precisely because there is no extra dimension. In Fig. 15(b), the vortex is superimposed onto the regular configuration: It is recognizable as a contact point between two lines of alternating staggered magnetization. In Fig. 15(c) we have subtracted the regular part and only the vortexing spin pattern is shown: Here we see the vortex interpolates between two opposite spin orientations in two opposite directions in the plane.

Now let us derive the effective Hamiltonian of the vortices. For the \mathbb{Z}_2 vortex, a loop in real space is mapped onto a π arc in the internal space, so the vortex can be represented as

$$\mathbf{M}_\alpha(r, \phi) = \int d\phi' e^{\frac{i}{2}(\phi' - \phi)\hat{\ell}_3} \mathbf{m}_\alpha, \quad (23)$$

giving (the matrices $\ell_{1,2,3}$ represent the $so(3)$ algebra)

$$\mathbf{M}_\alpha = \begin{pmatrix} \cos \phi & \mp \sin \phi & 0 \\ \pm \sin \phi & \cos \phi & 0 \\ 0 & 0 & 1 \end{pmatrix} \begin{pmatrix} m_{1\alpha} \\ m_{2\alpha} \\ m_{3\alpha} \end{pmatrix}, \quad (24)$$

where \mathbf{m}_α is the magnetization amplitude, analogous to the beam amplitude ψ_α in the optical system. The leading-order, noninteracting term in (22) gives the following for the energy of a single vortex of charge \tilde{Q} :

$$E_1 = 2\pi (|\mathbf{m}_X \times \mathbf{e}_Z|^2 + |\mathbf{m}_Y \times \mathbf{e}_Z|^2) \ln \Lambda = 2\pi |\mathbf{m}_{\perp\alpha}|^2 \ln \Lambda, \quad (25)$$

which is in fact independent of the sign of \vec{Q} (as could be expected, as it is in general proportional to $\vec{Q} \cdot \vec{Q}$ which is a constant for parity vortices). The vortex singles out an easy axis (Z axis) around which the staggered magnetization winds (ϕ being the winding angle). This allows one to introduce $\mathbf{m}_{\alpha\perp} \equiv (m_{X\alpha}, m_{Y\alpha}, 0)$. A vortex pair with charges \vec{Q}_i and \vec{Q}_j has the binding energy

$$\begin{aligned} E_2 &= 2\pi \vec{Q}_i \cdot \vec{Q}_j (|\mathbf{m}_1 \times \mathbf{e}_Z|^2 + |\mathbf{m}_2 \times \mathbf{e}_Z|^2) \ln r_{ij} \\ &= 2\pi |\mathbf{m}_{\perp\alpha}|^2 \vec{Q}_i \cdot \vec{Q}_j \ln r_{ij}. \end{aligned} \quad (26)$$

Now we should integrate out the amplitude fluctuations as we did in Appendix D for the CP beams. This again leads to the coupling between different flavors, giving a vortex Hamiltonian analogous to (7):

$$\mathcal{H}_{\text{vort}} = \sum_{i<j} (g \vec{Q}_i \cdot \vec{Q}_j + g' \vec{Q}_i \times \vec{Q}_j) \ln r_{ij} + \sum_i \vec{\mu} \cdot \vec{Q}_i. \quad (27)$$

Two obvious differences with respect to the optical system are (i) the charges are now limited to the values ± 1 , and (ii) there is a term linear in charge density, which acts as a chemical potential. The latter arises from the coupling of the *three-dimensional* spin waves (i.e., the topologically trivial excitations of the amplitude \mathbf{m}_α) to the vortices. Remember that in the CP system, the amplitude fluctuations also couple to the vortices, but there is no third, Z axis of the order parameter so no linear term appears. The microscopic expressions for the effective parameters g, g', μ_α read

$$g = m_\perp^2 + \frac{4r + 6um_\perp^2}{(2v + \frac{3}{2}um_\perp^2 + \frac{v}{2}m_\perp^2)(2r + \frac{3}{2}um_\perp^2 - \frac{v}{2}m_\perp^2)}, \quad (28)$$

$$g' = -\frac{4vm_\perp^2}{(2v + \frac{3}{2}um_\perp^2 + \frac{v}{2}m_\perp^2)(2r + \frac{3}{2}um_\perp^2 - \frac{v}{2}m_\perp^2)}, \quad (29)$$

$$\mu_\alpha = \frac{1}{2} m_\perp m_z, \quad (30)$$

assuming $m_{1\perp} = m_{2\perp} \equiv m_\perp$. Now the RG calculation is similar to the optical case but the nonzero chemical potential introduces two differences. First, there is obviously the additional term proportional to the total charge of the virtual pair of vortices, $\mu_\alpha(q_{1\alpha} + q_{2\alpha})$. Second, there is no charge conservation as the expectation value of the total vortex charge is now $\langle \vec{Q} \rangle = \partial \mathcal{F} / \partial \vec{\mu} \neq 0$. Thus we need to take into account not only the fluctuations with zero net charge (virtual vortex pairs with charges $\vec{q}_1 \equiv \vec{q}$ and $\vec{q}_2 \equiv -\vec{q}$) but also the situations with arbitrary pairs \vec{q}_1, \vec{q}_2 .⁹ This modifies the variation of the

partition function from (12) and (13) to

$$\begin{aligned} \frac{\delta \mathcal{Z}}{\mathcal{Z}} &= 1 + \frac{y^4}{4} \sum_{\vec{q}_{1,2}} \int dr r^2 r_{12}^3 e^{-g\vec{q}_1 \cdot \vec{q}_2 - g'\vec{q}_1 \times \vec{q}_2 - \vec{\mu} \cdot \vec{q}'} \\ &\times \left[\int dr r^2 (g \vec{Q}_1 \cdot \vec{q} + g' \vec{Q}_1 \times \vec{q}) \nabla \ln |\delta \mathbf{R}_1| \right. \\ &\left. + (g \vec{Q}_2 \cdot \vec{q} + g' \vec{Q}_2 \times \vec{q}) \nabla \ln |\delta \mathbf{R}_2| \right]^2 \\ &+ \frac{y^4}{4} \sum_{\vec{q}_{1,2}} \int dr r^2 r_{12}^3 e^{-g\vec{q}_1 \cdot \vec{q}_2 - g'\vec{q}_1 \times \vec{q}_2 - \vec{\mu} \cdot \vec{q}_1} \\ &\times \left[\int dr r^2 (g \vec{Q}_1 \cdot \vec{q}_0 + g' \vec{Q}_1 \times \vec{q}_0) \nabla \ln |\delta \mathbf{R}_1| \right. \\ &\left. + (g \vec{Q}_2 \cdot \vec{q}_0 + g' \vec{Q}_2 \times \vec{q}_0) \nabla \ln |\delta \mathbf{R}_2| \right]^2, \end{aligned}$$

where we have introduced $2\vec{q} \equiv \vec{q}_1 - \vec{q}_2, \vec{q}_0 \equiv \vec{q}_1 + \vec{q}_2$ and $\delta \mathbf{R}_{1,2} \equiv \mathbf{R}_{1,2} - \mathbf{r}$. The mixed term which includes both \vec{q} and \vec{q}_0 vanishes due to isotropy. By matching the terms in the resulting expression with the original Hamiltonian, we find the recursion relations:

$$\begin{aligned} \frac{\partial g}{\partial \ell} &= -16\pi y^4 (g^2 + g'^2), & \frac{\partial g'}{\partial \ell} &= -16\pi y^4 g g', \\ \frac{\partial \vec{\mu}}{\partial \ell} &= 0, & \frac{\partial y}{\partial \ell} &= (1 - g - g' - \mu_+ - \mu_-) y. \end{aligned} \quad (31)$$

Crucially, the chemical potential does not run which could be guessed from dimensional analysis (it couples to dimensionless charge). This is the same system as (14) up to the trivial rescaling of the coupling constants and the shift of the critical line $g + g' = 1$ in the PR system to the line $g + g' + \mu_+ + \mu_- = 1$. It becomes obvious that the phase diagrams are equivalent and can be mapped onto each other.

B. Influence of disorder

The disorder in a doped antiferromagnet comes from electrically neutral metallic grains quenched in the bipartite lattice. Being metallic and neutral, they are naturally modeled as magnetic dipoles \mathbf{X} quenched in the bipartite lattice. This picture stems from the microscopic considerations in Ref. [48]. We again assume the Gaussian distribution of the disorder as $p(X) \propto \exp(-|\mathbf{X}|^2/2\sigma_X^2)$. The disorder dipoles are one and the same for both sublattices, so \mathbf{X} has no flavor (sublattice) index. The minimal coupling of the dipoles to the lattice spins $\partial_i \mapsto \partial_i - i \hat{\ell}_i X_i$ gives

$$\mathcal{H}_{\text{af}} \mapsto \mathcal{H}_{\text{dis}} = \mathcal{H}_{\text{af}} + \nabla \mathbf{M}_\alpha \cdot (\mathbf{X} \times \mathbf{M}_\alpha) + M^2 X^2. \quad (32)$$

Now the replica calculation requires the multiplication of the M field into n copies and performing the Gaussian integral over the disorder. The initial distribution of the disorder $p(X)$ gives rise to two independent Gaussian distributions: for the couplings $J_{ij}^{\alpha\beta}$ with dispersion matrix $\sigma_{\alpha\beta}^2$ and for the chemical potential μ_i^α with the dispersion vector ξ_α^2 . The resulting

⁹In the CP beam system, the total vortex charge can be nonzero if the boundary conditions at $z = 0, L$ have nonzero total vorticity. But there we had no *bulk* chemical potential so the total vorticity in the crystal could not change during the propagation along z . Here, we have a *bulk* term in the Hamiltonian which violates charge conservation.

Hamiltonian is

$$\begin{aligned} \mathcal{H}_{\text{dis}} = & \sum_{\mu=0}^n \left(\frac{1}{2} |\partial_{\tau} \mathbf{M}_{\alpha}^{(\mu)}|^2 + \frac{1}{2} |\nabla \mathbf{M}_{\alpha}^{(\mu)}|^2 \right. \\ & \left. + \frac{u}{2} |\mathbf{M}_{\alpha}^{(\mu)}|^2 - v |\mathbf{M}_1^{(\mu)}|^2 |\mathbf{M}_2^{(\mu)}|^2 \right) \\ & + \frac{\sigma^2}{4} \sum_{\mu, \nu=0}^n (\nabla \mathbf{M}_{\alpha}^{(\mu)} \times \mathbf{M}_{\alpha}^{(\mu)}) \cdot (\nabla \mathbf{M}_{\alpha}^{(\nu)} \times \mathbf{M}_{\alpha}^{(\nu)}), \quad (33) \end{aligned}$$

where we have disregarded the subleading logarithmic term ($\sim \ln |\mathbf{M}_{\alpha}^{(\mu)}|$). Now making use of the representation (23) and plugging it into (33) gives the disordered vortex Hamiltonian

$$\begin{aligned} \beta \mathcal{H}_{\text{vort}} = & \sum_{\mu, \nu=1}^n \sum_{i, j=1}^N \left[\frac{\beta^2}{2} \mathcal{Q}_{i\alpha}^{(\mu)} \mathcal{Q}_{i\beta}^{(\nu)} \mathcal{Q}_{j\alpha}^{(\mu)} \mathcal{Q}_{j\beta}^{(\nu)} \right. \\ & \left. - \beta \mathcal{Q}_{i\alpha}^{(\mu)} J_0^{\alpha\beta} \mathcal{Q}_{j\beta}^{(\mu)} + \beta^2 \mathcal{Q}_{i\alpha}^{(\mu)} \xi^2 \mathcal{Q}_{i\alpha}^{(\nu)} \right] \\ & - \sum_{\mu=1}^n \sum_{i=1}^N \beta \xi^2 \mu_0^{\alpha} \mathcal{Q}_{i\alpha}^{(\mu)}. \quad (34) \end{aligned}$$

Of course, we could have arrived at the same effective action starting from the vortex Hamiltonian (27), taking the infinite-range approximation and identifying $J_{ij}^{\alpha\beta} = g_{ij} \ln r_{ij}$ and similarly for other components of $J_{ij}^{\alpha\beta}$ as we demonstrated for the PR system. The final result has to be same at leading order.

The next step is to rewrite the Hamiltonian in terms of the order parameters $p_{\alpha}^{(\mu)}, q_{\alpha\beta}^{(\mu)}$ defined in (19). Compared to the effective action for the photonic lattice with disorder in Eq. (G4), there are two extra terms in the resulting action S_{eff} : One is proportional to the dispersion ξ^2 and the other to the mean chemical potential $\bar{\mu}_0$. The former term just introduces the shift $J_0^{\alpha\beta} \mapsto J_0^{\alpha\beta} - \sigma^2/2\beta$ and the latter term, linear in the vortex charges and proportional to the chemical potential, introduces solutions with nonzero net vortex charge density. Looking back at the results of the saddle-point calculation in Eqs. (19) and (G14), this tells us that the relation between the phase diagrams is the following. The phases with no net vortex charge density—insulator, conductor, frustrated insulator, and perfect conductor—remain the same as in the PR system, since both the average coupling value $J_0^{\alpha\beta}$ (which gets shifted) and the term proportional to the chemical potential μ_{α} couple only to $\vec{p}^{(\mu)}$. For brevity, denote $J_0^{\pm\pm} \equiv J_0^{\pm}$ and notice that $J_0^{-+} = J_0^{+-}$. The structure of phases with nonzero $\vec{p}^{(\mu)}$ depends on the zeros of the saddle-point equation

$$\begin{aligned} J_0^{\pm} p^{\pm} + \left(\frac{J_0^{+-}}{\beta} - \frac{\beta}{2} \xi^{\pm} \right) p^{\mp} + (p^{\pm})^{-1} \\ - \frac{\mu_0^{\pm} (\sigma^{\pm\pm})^2 + \mu_0^{\mp} \sigma_{\pm}^2}{\beta} = 0, \quad (35) \end{aligned}$$

analogous to (G13), where the one-step replica symmetry breaking implies $p_{\mu}^{\pm} = (p^{\pm}, \dots, p^{\pm})$. Now the equation is cubic and the structure of solutions is different from (G14). We could not find the solution in the closed form but it is clear that a pair of cubic equations will have either a

single solution (p^+, p^-) or nine combinations (p^+, p^-), not necessarily all different. Numerical analysis of (35) reveals only two inequivalent solutions, analogous to (G14), i.e., one of them has a single free energy minimum and the other one a pair of degenerate minima. Therefore, we again have two disordered solutions, one of which is glassy (frustrated).

Now we can write down also the RG equations for the effective action (34). In this calculation, we put $\xi_{\alpha}^2 = \sigma_{\alpha\beta}^2 \equiv \sigma^2$ for simplicity. Following the same logic as earlier, the equations are found to be¹⁰

$$\begin{aligned} \frac{\partial g}{\partial \ell} &= -8\pi(g + g')^2 y^4 \cosh(2\beta^2 \sigma^2) \\ &\quad \times \cosh(2\beta^2 \sigma^2) - 8\pi(g - g')^2 y^4, \\ \frac{\partial g'}{\partial \ell} &= -\pi(g + g')^2 y^4 \cosh(2\beta^2 \sigma^2) \\ &\quad \times \cosh(2\beta^2 \sigma^2) - \pi(g - g')^2 y^4, \\ \frac{\partial y}{\partial \ell} &= 2\pi(1 - g - g' - \mu_+ - \mu_- - \beta^2 \sigma^2) y, \\ \frac{\partial \mu}{\partial \ell} &= -8\pi \mu, \\ \frac{\partial \sigma^2}{\partial \ell} &= -2\pi \beta^4 \sigma^4 y^4. \quad (36) \end{aligned}$$

Like in the clean case, the chemical potential is irrelevant and the solutions for fixed point are the same as for the PR beams, including the spin-glass fixed point. We conclude that the phase structure of the optical system is repeated in strongly correlated doped antiferromagnets, which also exhibit the spin-glass phase and have the phase diagram sketched in Fig. 16. In this context, it is more interesting to plot the phase diagram in the $\sigma^2 - 1/g'$ plane, mimicking the $x - T$ phase diagram of quantum critical systems [38] (remember that the coupling constants g, g' behave roughly as inverse temperature in XY -like models). Bear in mind that all phases shown are about vortex dynamics; i.e., one should not compare Fig. 16 to the textbook phase diagram of high-temperature superconductors, which accounts also for the charge or stripe order and the superconducting order. All vortex phases would be located inside the pseudogap regime of the superconductor, where various exotic orders can coexist (assuming, of course, that our model is an adequate approximation of the magnetic order in a cuprate or similar material, which is a complex question). Crucially, the spin-glass phase (blue curves) flows toward *finite disorder* σ^2 , whereas the remaining two phases end up at zero disorder, either at infinite $1/g'$ (PC, red flows) or at zero $1/g'$ (conductor, green flows). The RG flows in the conductor phase are almost invisible in the figure, as the flows are much slower than in the remaining two phases.

Discussion

Early papers which found and explored the spin-glass phase in a very similar model are Refs. [39,40,47,49]. The

¹⁰For the most general case of different and nonscalar $\sigma_{\alpha\beta}^2$ and ξ_{α}^2 , the flow equations for them complicate significantly and we will not consider them.

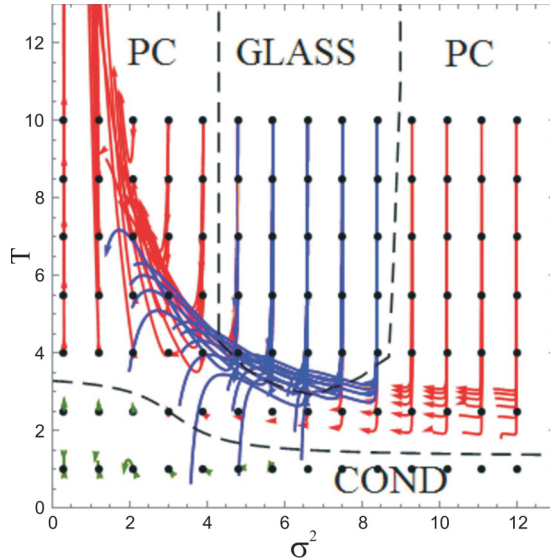


FIG. 16. The phase diagram of the two-sublattice-doped Heisenberg antiferromagnet model in the σ^2 - T plane (we have rescaled $\sigma^2 \mapsto 12\sigma^2$). Since $T \sim 1/g'$, we can alternatively understand the vertical axis as $1/g'$. Black dashed curves are approximate phase boundaries. RG flows (starting from black dots) are colored differently according to the phase they belong to: spin glass (blue), PC (red), and conductor (green). At high temperatures, the vortex conductor becomes either a perfect vortex conductor or a spin glass. Spin glass (blue) is recognized by the fact that the RG equations flow to nonzero disorder at finite and large g' (low temperatures). The PC phase (red) flows toward zero disorder and zero coupling (infinite T), collapsing practically to a single trajectory. The flows for the conductor (green) end up at $T = \sigma^2 = 0$ but are not shown to scale in the figure. Parameter values are $u = r = 1$ with varying v so as to have $g = -0.5$ for all trajectories.

main difference is that the papers cited consider the spiral (noncollinear) spin order. These works are all inspired by the cuprate materials, the most celebrated brand of high-temperature superconductors. While Refs. [40,47] explore in detail the transport properties, we have no pretension either to provide a realistic model of cuprates or to explore in detail all the properties of the spin-glass phase. We are content to see that the PR system of \mathbb{Z} vortices reproduces the phase structure of a certain kind of dirty Heisenberg antiferromagnets (with $O(3)$ spins and \mathbb{Z}_2 vortices), besides the more obvious connection to systems which directly reproduce the \mathbb{Z} vortices in multicomponent $U(1)$ systems like multicomponent Bose-Einstein condensates and type-1.5 superconductors.

VI. CONCLUSIONS

We have investigated the light intensity patterns in a nonlinear optical system consisting of a pair of counterpropagating laser beams in a photorefractive crystal. We have studied this system as a strongly interacting field theory and have focused mostly on the formation and dynamics of vortices. The vortices show a remarkable collective behavior and their patterns are naturally classified in the framework of statistical field theory: The effective action shows several different

phases with appropriate order parameters, and the system is essentially an XY model with two flavors, i.e., two kinds of vortex charge, for the two beams. The interaction between the flavors is the central reason that the total energy of the Coulombic interactions between the vortices in general cannot be locally minimized at every point. In the presence of disorder, a phase with multiple free energy minima arises, where the absence of long-range order is complemented by the local islands of ordered vortex structure, and which resembles spin glasses.

The phase diagram is simple in terms of the effective parameters—vortex coupling constants—and quite complex when expressed in terms of the experimentally controllable quantities—the intensity of the laser beams, the intensity of the background photonic lattice, and the properties of the photorefractive crystal (the last is not controllable but can be estimated reasonably well [3]). The lesson is that the approach we adopt can save us from demanding numerical work if the space of original parameters is blindly explored. Our phase diagrams can serve as a starting point for guided numerical simulations, suggesting what phenomena one should specifically look for. So far the field-theoretical and statistical approach was not much used in nonlinear optics (important exceptions are Refs. [9–12, 14, 15, 50, 51, 59, 60]). We hope to stimulate work in this direction, which is promising also because of the potential of the photorefractive systems to serve as models of strongly correlated condensed matter systems. They make an excellent testing ground for various models because of the availability and relatively low cost of experiments.

In this work, we have focused on the relation of the photorefractive counterpropagating system to the model of an $O(3)$ doped antiferromagnet with two sublattices. The authors of previous works on this model [40,47,48,58] were motivated mainly by the ubiquitous problem of understanding the pseudogap phase in cuprate superconductors. The applicability of the model to this particular problem is still an open question; it may well be that cuprate physics goes far beyond. Nevertheless, it is an important quantum magnetic system in its own right and serves as an illustration of how one can simulate condensed matter systems in photorefractive optics.

Another field where vortices are found as solutions of a nonlinear Schrödinger equation are cold atom systems and Bose-Einstein condensates [26]. Notice, however, that Bose-Einstein condensates in optical traps are usually (but not always; see Ref. [30]) three-dimensional systems with vortex lines (rather than XY -type systems with point vortices) and our formalism would be more complicated there: In three spatial dimensions, vortices give rise to emergent gauge fields. The multicomponent systems of this kind give rise to so-called type-1.5 superconductors [53], which are a natural goal of further study.

A more complete characterization of the glasslike phase is also left for further work. The reader will notice we have devoted very little attention to the correlation functions in various parameter regimes or the scaling properties of susceptibility, which should further corroborate the glassy character of the system. This is quite difficult in general but very exciting as it offers an opportunity to tune the parameters (e.g., disorder strength) freely in the optical system and study the glasslike phase and its dynamics.

ACKNOWLEDGMENTS

We are grateful to Mariya Medvedyeva and Vladimir Juričić for careful reading of the manuscript. Work at the Institute of Physics is funded by Ministry of Education, Science and Technological Development, under Grants No. OI171033 and No. OI171017. M.P. is also supported by the NPRP 7-665-1-125 project of the Qatar National Research Fund (a member of the Qatar Foundation).

APPENDIX A: NUMERICAL ALGORITHM

In order to solve numerically the system [(1) and (2)], we employ a variation on the method of Refs. [61,62]. The method does not make use of any analytical ansatz: It is an *ab initio* numerical procedure which integrates the equations of motion. The system has four independent variables: the transverse coordinates (x, y) , the longitudinal coordinate (formal time) z , and the (physical) time t . That means we have essentially three nested loops: (i) At every z slice we integrate the transverse Laplacian and the interaction terms for the whole z axis, (ii) we advance the time t , and (iii) we repeat the whole procedure until reaching some time t_f , which certainly should be much longer than the relaxation time τ .

The important point is the very different natures of the initial and boundary conditions for various coordinates. The boundary conditions in the (x, y) plane, i.e., at the crystal edge are not crucial: We have either just one or a few Gaussian beams whose intensity drops exponentially away from the center and is practically zero at the crystal edge, or we have a large lattice consisting of many (of the order of 50–100) Gaussian beams so the edge effects only affect a small portion of the whole lattice. Therefore, imposing periodic boundary conditions (stemming naturally from the integration in Fourier space, see the next paragraph) are perfectly satisfying. Crucially, however, the CP geometry means that $F(t; z = 0; x, y) = F_0(x, y)$ and $B(t; z = L; x, y) = B_0(x, y)$ are given functions, fixed for all times. We thus have a two-point boundary value problem along z and have to iterate the z integration several times until we reach the right solution. Finally, the initial condition for the relaxation equation (2) is that the crystal is initially at equilibrium, meaning that $E(t = 0) = -I_x/(1 + I_x)$; specifically, for zero background lattice, $E(t = 0) = 0$.

The algorithm now has the following structure:

(1) The innermost loop integrates in the x - y plane. This is a Poisson-type (elliptic) equation, thus we employ the operator-split method, integrating the Laplacian operator in the Fourier space and the interaction term (the EF and EB terms) in real space, in the second-order leapfrog scheme. Thus, at every time instant $t_i = i \Delta t$, we start from $z = 0$ where we set the condition $F(i \Delta t; z = 0; x, y) = F_0(x, y)$, divide the z axis into N steps of size $\Delta z = L/N$, and at every slice $z = j \Delta z$ perform the frog’s leap: We do the fast Fourier transform (FFT) to turn the (x, y) dependence into (q_x, q_y) dependence,¹¹ then we advance the Laplacian for $\Delta z/2$ as $F(i \Delta t; j \Delta z; \mathbf{q}) \equiv \tilde{F}_{i,j}^{(0)} \mapsto \tilde{F}_{i,j}^{(1)} = \exp(-iq^2 \Delta z/2) \tilde{F}_{i,j}^{(0)}$, and then we do the inverse FFT and advance the interaction in real space as

$F_{i,j}^{(2)} = \exp[i\Gamma E(i \Delta t; j \Delta z; x, y)] F_{i,j}^{(1)}$. Finally we do the FFT again and advance the Laplacian for the remaining half-step, $\tilde{F}_{i,j+1} = \exp(-iq^2 \Delta z/2) \tilde{F}_{i,j}^{(2)}$. Once we reach $j = N$, the integration goes backward, along the same lines, updating now the B field [starting from $B_0(x, y)$], where all signs in the exponents of the above formulas are to be reversed. When we reach $z = 0$ again, we are done. In this loop, we use the field $E_{1,j}$ as already known for all j .

(2) The above loop will, in general, produce results inconsistent with the charge field $E_{i,j}$ because the equation for E couples F and B and we have ignored that by integrating the two fields one after the other instead of simultaneously. This is, of course, commonplace in two-point boundary value problems: Either only one boundary condition can be imposed exactly and the other is shot for or, as in our case, both are imposed exactly but at the cost of the solution being inconsistent with the equations, so we have to iterate the system to arrive at the correct solution everywhere. The second loop thus iterates the first loop A times, at each step updating the charge field as $E_{i,j}^{(a-1)} \mapsto E_{i,j}^{(a)} = E_{i-1,j} - \tau [E_{i,j}^{(a-1)} + I_{i,j}^{(a-1)} / (1 + I_{i,j}^{(a-1)})] / (1 + I_{i,j}^{(a-1)})$. The number of iterations A is not fixed: We stop iterations when the intensity pattern stabilizes, $\sum_j \sum_{x,y} (I_{i,j}^{(a)} - I_{i,j}^{(a-1)}) < \epsilon$, for some tolerance ϵ . Here, $I_{i,j}$ refers to total intensity, i.e., $|F|^2 + |B|^2 + I_x$.

(3) Finally, the outermost loop integrates in time t , from $t = 0$, with the initial condition $E(t = 0) = -I_x / (1 + I_x)$ given above. The integration time t_f is divided into $M = t_f / \Delta t$ intervals, and at the end of each step we update $(F_{i,j}, B_{i,j}, E_{i,j}) \mapsto (F_{i+1,j}, B_{i+1,j}, E_{i+1,j})$. Only the charge field is directly integrated (as written above), in the first-order, Euler scheme. The beam envelopes depend on time only parametrically, through $E(t)$, and they evolve by using an updated $E_{i,j}$ in the first two loops at every time step.

This procedure is very close to that in Ref. [61]; the main difference is that we use a second-order (leapfrog) scheme, while on the other hand our time integration is of the lowest, linear order instead of second order as in Ref. [61].

APPENDIX B: TIME-DEPENDENT PERTURBATION THEORY AND THE EXISTENCE OF EQUILIBRIUM CONFIGURATIONS

1. Stability analysis: fixed points and limit cycles

In this appendix, we consider the time evolution of the CP beams and show the existence of a stable equilibrium point with nonzero intensity. This means that the system reaches a stationary state for long times, justifying the basic assumption of the paper that one can study the vortex configurations within equilibrium statistical mechanics. Not all patterns are stable: Depending on the boundary conditions and parameter values, the system may or may not have a stable equilibrium, and nonequilibrium solutions in photorefractive optics are well known [37,50]. For our purposes, however, it is enough to identify the region of parameter space where the equilibrium exists; other cases are not the topic of this paper.

The time evolution of the beams Ψ_α and the charge field E in (k, q) space is obtained by differentiating Eqs. (1) with respect to time and plugging in $\partial E / \partial t$ from the relaxation

¹¹We denote the fields in Fourier space with a tilde, e.g., \tilde{F} .

equation (2):

$$\begin{aligned}\frac{\partial \Psi_{\alpha}^{\pm}}{\partial t} &= -\frac{\Gamma}{\tau} \frac{[(1+I)E + I]}{\alpha k - q^2 - \Gamma E} \Psi_{\alpha}^{\pm}, \\ \frac{\partial E}{\partial t} &= -\frac{1}{\tau} [(1+I)E + I].\end{aligned}\quad (\text{B1})$$

This system has three equilibrium points. One is the 0 point,

$$(\Psi_{+}^{\pm}, \Psi_{-}^{\pm}, E) = \left(0, 0, -\frac{I_x}{1+I_x}\right),$$

and the remaining two are related by a discrete symmetry $\Psi_{\pm} \mapsto \Psi_{\mp}$, so we denote them as “ \pm ” points, with the “+” point being

$$(\Psi_{+}^{\pm}, \Psi_{-}^{\pm}, E) = \left(\sqrt{\frac{E(1+I_x) + I_x}{1+E}} e^{i\phi_{\pm}}, 0, E\right),$$

and the “−” point has instead $\Psi_{+} = 0$ and $\Psi_{-} = \sqrt{(E(1+I_x) + I_x)/(1+E)} \exp(i\phi_{-})$. Notice that the phase ϕ_{\pm} remains free to vary, so this solution supports vortices. The 0 point is the trivial vacuum, i.e., the zero-intensity configuration with only background lattice. The fluctuation equations about this point to quadratic order read

$$\begin{aligned}\partial_t X &= -\left[-f_{+} X_1 X_5, -f_{+} X_2 X_5, -f_{-} X_3 X_5, -f_{-} X_4 X_5, \right. \\ &\quad \left. -\frac{1}{1+I_x} (X_1^2 + X_2^2 + X_3^2 + X_4^2) - (1+I_x) X_5 \right],\end{aligned}\quad (\text{B2})$$

where we have introduced the real variables $X_{1,3} = \text{Re} \delta \Psi_{\pm}$, $X_{2,4} = \text{Im} \delta \Psi_{\pm}$, $X_5 = \delta E$ and

$$f_{\pm} = \frac{\Gamma(1+I_x)^2}{\Gamma I_x \mp (1+I_x)(k \pm q^2)}.\quad (\text{B3})$$

The system (B2) is degenerate at linear order; thus, we need a quadratic order expansion to analyze stability. The simplest approach is to construct a Lyapunov function for Eq. (B2). The function $V(X) = X^2$ is positive for and only for $X \neq 0$, and its derivative is

$$\begin{aligned}\frac{dV}{dt} &= -2f_{+}(X_1^2 + X_2^2)X_5 - 2f_{-}(X_3^2 + X_4^2)X_5 \\ &\quad -\frac{1}{1+I_x} (X_1^2 + X_2^2 + X_3^2 + X_4^2)X_5 - (1+I_x)X_5^2,\end{aligned}\quad (\text{B4})$$

which is strictly negative for X nonzero if $f_{\pm} > 0$ and $X_5 > 0$. However, we always have $X_5 > 0$ because dX_5/dt in the full relaxation equations (B1) has a strictly negative right-hand side and E grows monotonically from zero to $-I_x/(1+I_x)$, and at any finite t we have $E(t) - E(t \rightarrow \infty) = X_5 > 0$. Thus the trivial equilibrium point is *locally* stable for $f_{+} > 0, f_{-} > 0$, i.e., $k > q^2$. It is much harder to construct the Lyapunov function for the global equations (B1): In this case, there are no additional symmetries and the stability of higher dimensional systems is in general an extremely difficult topic. Thus there may well be regions far away from the 0 point which do not flow toward it.

The “ \pm ” pair is quite hard to study. All hope of expanding the system to second order and understanding the resulting complicated five-variable system is lost. This time, however, we can do a nontrivial first-order analysis as the system is nondegenerate and nicely reduces to the (X_1, X_5) subsystem. Rescaling $X_1 \mapsto (1+E_0)^{-3/4} [I_x + E_0(1+I_x)]^{1/2}$ and $t \mapsto t\{(1+E_0)/[I_x + E_0(1+I_x)]\}^{1/4}$, the equation of motion for the \pm point reads

$$\begin{aligned}\partial_t \begin{pmatrix} X_1 \\ X_5 \end{pmatrix} &= \begin{pmatrix} -\frac{a_{\pm}}{\Gamma E_0 + k + q^2} & -1 \\ 1 & -\frac{a_{\pm}}{\Gamma E_0 + k + q^2} \end{pmatrix} \begin{pmatrix} X_1 \\ X_5 \end{pmatrix} \\ &\quad + O(X_1^2 + X_5^2; X_2, X_3, X_4),\end{aligned}\quad (\text{B5})$$

with a_{\pm} being some (known) *positive* functions of Γ, E_0, I_x (independent of k, q). This is precisely the normal form for the Andronov-Hopf bifurcation [63], and the bifurcation point lies at $k = -\Gamma E_0 - q^2$. As a reminder, the bifurcation happens when the off-diagonal element in the linear term changes sign: The fixed point is stable when $a_{\pm}/(\Gamma E_0 + k + q^2)$ is positive. The sign of the nonlinear term determines the supercritical or subcritical nature of the bifurcation. A negative sign means the fixed point is stable everywhere before the bifurcation and is replaced by a stable limit cycle after the bifurcation (supercritical). A positive sign means the fixed point coexists with the stable limit cycle before the bifurcation and the (X_1, X_5) plane is divided among their attraction regions; after the bifurcation there is no stable solution at all (subcritical).¹²

In conclusion, stable + equilibrium exists for $k > -\Gamma E_0 - q^2$ where E_0 is best found numerically. Exactly the same condition holds for the − point. For $k < -\Gamma E_0 + q^2$, dynamics depends on the sign of the nonlinear term in (B5): For the positive sign, we expect periodically changing patterns. If the term is negative and the bifurcation is subcritical, various possibilities arise: The system may wander chaotically between the + and the − point, or it may end up in the attraction region of the 0 point and fall onto the trivial solution with zero intensity. Naively, the attraction regions of the two fixed points (\pm and 0) are separated by the condition $-\Gamma E_0 - q^2 = q^2$, i.e., $q_c = \sqrt{-\Gamma E_0(\Gamma, \tau)/2}$, where we have emphasized that E_0 is in general nonuniversal. The actual boundary may be more complex, however, as our analysis is based on finite-order expansion around the fixed points, which is not valid far away from them.

The outcome is that the system generically has stable trivial and nontrivial (nonzero intensity) equilibria, in addition to time-dependent, periodic, or aperiodic solutions. Numerical integration gives a similar picture of the stability diagram in Fig. 17. Numerically we find that the stability limit is $k > \Gamma - q^2$, i.e., $E_0 \approx -1$. The region of applicability of our formalism lies in the top right corner of the diagram (nontrivial equilibrium), above $k \approx 1/L$. Formally, both k and q can be any real numbers. In practice, however, k is discrete and its minimal value is of the order $1/L$. The spatial momentum q

¹²One should not take the stability in the whole (X_1, X_5) plane in the supercritical case too seriously. We have expand the equations of motion in the vicinity of the fixed points and the expansion ceases to be valid far away from the origin.

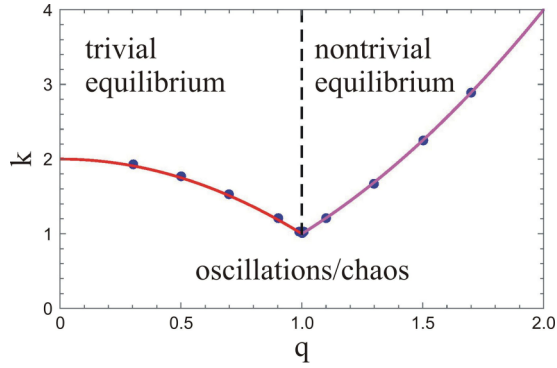


FIG. 17. Stability diagram in the q - k plane. The onset of instability for $k < k_c(q)$ is found numerically for a range of q values. The solid lines are the analytical prediction for the stability of the 0 point ($k_c = q^2$, magenta) and of the + point ($k_c = \Gamma E_0 - q^2 \approx \Gamma - q^2$, red). The black dashed line at $q = q_c \approx 1$ separates the stability regions of the two points. The domain of applicability of our main results is the top left corner (nontrivial equilibrium), above $k > k_{\min} \sim 1/L$ and for not very large q values. Parameter values: $\Gamma = 2, I_x = 0$.

lies between the inverse of the transverse length of the crystal (which is typically an order of magnitude smaller than L , i.e., minimal q can be assumed equal to zero) and some typical small-scale cutoff which in our case is the vortex core size. We made no attempt to study the nonequilibrium behavior in detail or to delineate the boundary between the oscillatory and the chaotic regime since it is irrelevant for the main story of the paper.

From a practical viewpoint, the Γ - I_x plane can be divided into two regions. One of them has a single stable “+” or “-” equilibrium or a $+ \mapsto -$ limit cycle whose amplitude vanishes in the thermodynamic limit at all scales, i.e., for all (k, \mathbf{q}) . This region can be legitimately described within the formalism of partition functions and equilibrium field theory. The second region flows toward the trivial fixed point and does not support vortices—this can also (trivially) be described by our formalism, as it always corresponds to the insulator regime, with no stable vortices. Thus the consistency check is that our method predicts no other phases in this region but insulator. In the third regime, long-term dynamics is either a limit cycle with amplitude of order unity or chaos. This regime was studied in detail in some earlier publications (e.g., Ref. [3] and references therein), and it cannot be reached within our present formalism.

2. Numerical checks

Now we complement the analytical considerations with numerical evidence that the phases described in the main text exist as long-term stable configurations. In Fig. 18, we show the time evolution of a vortex lattice in three different phases, where a visual inspection clearly suggests the system approaches equilibrium. In contrast, in Fig. 19 we see first a pattern that oscillates forever, i.e., follows a limit cycle [Fig. 19(a)], becomes incoherent [wandering chaotically over the unstable manifold, Fig. 19(b)], or dissipates away (reaching the 0-fixed point), in Fig. 19(c). The loss of stability corresponds to an Andronov-Hopf bifurcation, as found earlier for nonvortex patterns in Ref. [32].

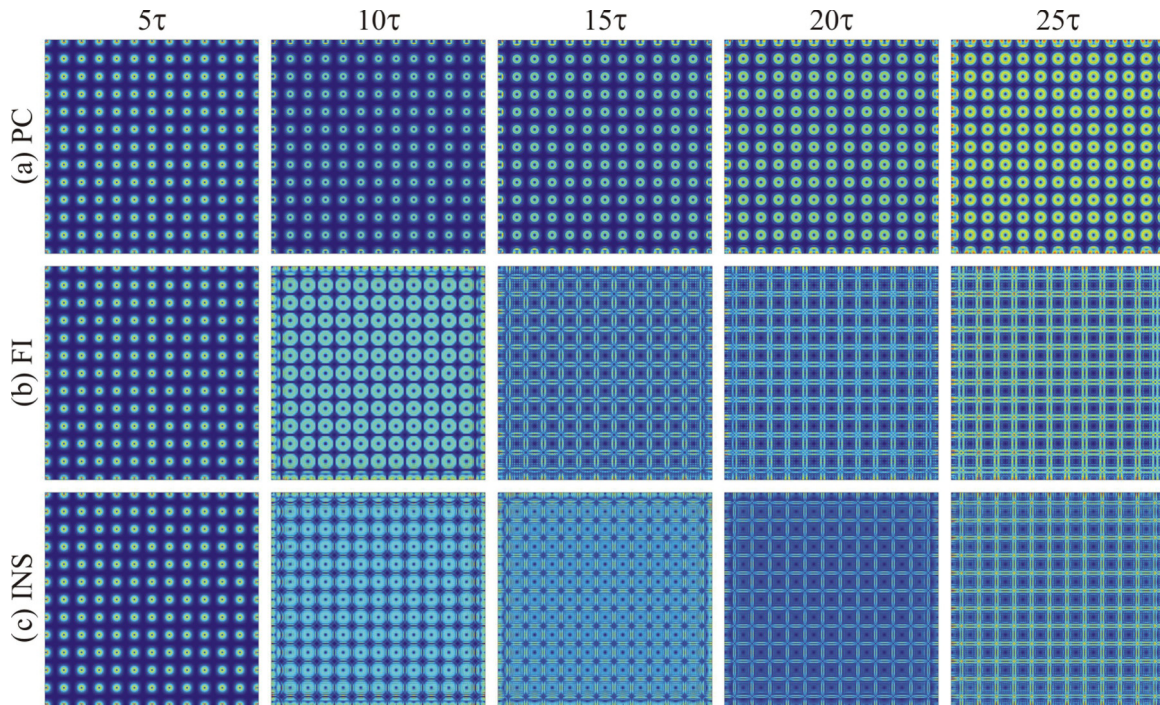


FIG. 18. Time evolution of patterns at five different times: (a) perfect conductor phase, (b) frustrated insulator phase, and (c) insulator phase. In all cases, the approach to equilibrium is obvious, and we expect that for long times a thermodynamic description is justified. The parameters are the same as in Fig. 6, for the corresponding phases.

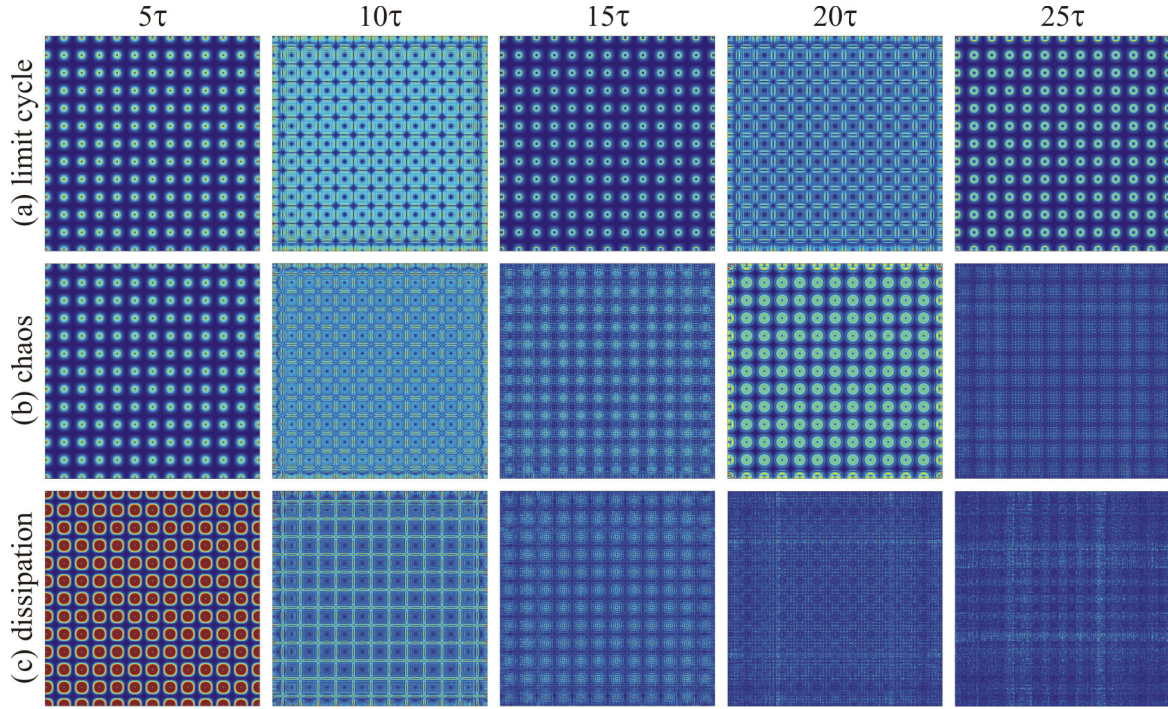


FIG. 19. Time evolution of nonequilibrium patterns. In panel (a), the limit cycle leads to permanent oscillatory behavior, in panel (b) wandering along the unstable manifold between the equilibrium points gives rise to chaos, and in panel (c) dissipation wins and dynamics dies out. The parameters are the same as in the previous figure, except that the length L is increased three times.

Dynamics can be most easily traced by looking at the numerically computed relaxation rate

$$\frac{1}{X} \frac{dX}{dt} = \frac{\sum_{x,y} |X(t_{j+1}x,y) - X(t_j;x,y)|^2}{\sum_{x,y} |X(t_j;x,y)|^2}, \quad (\text{B6})$$

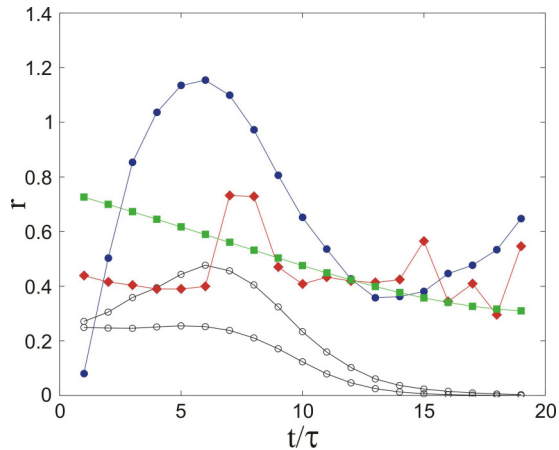


FIG. 20. Time evolution of the relaxation rate r for the various situations from Figs. 18 and 19, illustrating the relaxation to nontrivial (non-zero-intensity) equilibrium, i.e., “ \pm ”-fixed points [Figs. 18(a), 18(c), hollow black circles], limit cycle [Fig. 19(a), full blue circles], chaos [Fig. 19(b), full red romboids], and the relaxation to trivial (zero-intensity) equilibrium, i.e., 0 fixed point [Fig. 19(c), full green squares]. In the main text, we study the cases like the black curves, where time-independent stable configurations are seen. The symbols are data points from numerics and the lines are just to guide the eye.

which is expected to reach zero for a general relaxation process, where in the vicinity of an asymptotically stable fixed point $X \sim X_{\text{eq}} + xe^{-rt}$ will be generically nonzero for a limit cycle or chaos and will asymptote to a constant value for the 0 point, where $X_{\text{eq}} = 0$, so we get $(1/X)dX/dt \sim r$. Figure 20 summarizes these possibilities. The black curves, corresponding to Figs. 18(a) and 18(c), show the situation which is in the focus of this work—the approach toward static equilibrium. The blue curve shows the limit cycle leading to periodic oscillations. The green curve corresponds to the chaotic regime with aperiodic dynamics and no relaxation, as in Fig. 19(b). Finally, the red curve corresponding to the pattern which radiates away in Fig. 19(b) reaches a constant value of r . In conclusion, the system shows roughly four classes of dynamics: fixed point, limit cycle, chaos, and incoherence. Our work only covers the first of the four, but the bifurcation diagrams in the previous subsection give a good hint of the part of the parameter space which contains them, facilitating experimental or numerical verification.

APPENDIX C: PERTURBATION THEORY AND STABILITY ANALYSIS

In this appendix, we develop the perturbation theory of the photorefractive beam system starting from the Lagrangian (4). The perturbation theory yields the criterion for the stability of the intensity patterns as they propagate along the z axis. Formally, it is just the perturbative diagrammatic calculation of the propagator. This calculation explicitly excludes topologically nontrivial patterns and thus is somewhat peripheral for our main goal, understanding the vortex dynamics. But the general ways by which an envelope Ψ_{\pm} can evolve along the z axis and

become unstable remain valid also for vortices. In particular, we will end up with a classification of geometrical symmetries of the intensity pattern $\Psi^\dagger\Psi$; the same symmetries are seen in vortex patterns and are an important guide for numerical and experimental work—how to recognize instabilities and also phases of the system.

Our system is strongly nonlinear, thus a naive perturbation theory about the trivial vacuum, i.e., constant beam intensity is out of question. The right way is to perturb about a nontrivial solution, which approximates a stable pattern. This means we treat the light intensity as constant in time z but nonconstant in space (x, y) . This is the hallmark of spatial dynamical solitons: They propagate with a constant profile along the z axis and to a good approximation do not interact with each other and do not radiate [3]. We thus write $\Psi = \Psi_0 + \delta\Psi$, giving $\Psi^\dagger\Psi = I_0 + F_0(\delta\Psi_+^\dagger + \delta\Psi_+) + B_0(\delta\Psi_-^\dagger + \delta\Psi_-) + \delta\Psi^\dagger\delta\Psi + O(|\delta\Psi|^2)$ with $F_0^2 + B_0^2 = I_0$. The lowest-order Lagrangian for Ψ_0 now reads

$$\begin{aligned} \mathcal{L}_0 = & \Psi_0^\dagger \Delta \Psi_0 + \Gamma I_0 - \Gamma(1 + \tau u + \tau E_0) \\ & \times \ln(1 + \tau u + I_x + I_0), \end{aligned} \quad (\text{C1})$$

which determines the shape of the solution $\Psi_0(x, y)$ in the first approximation. The dynamical term with $\partial_z\Psi$ drops out (it is proportional to the equation of motion for Ψ). Nontrivial propagation in time z is obtained from second-order expansion of the potential which is given in the next appendix in Eq. (D1) and we will not copy it here. Varying the quadratic expansion with respect to the fluctuation $\delta\Psi$ gives the linearized equation of motion for $\delta\Psi$:

$$\begin{aligned} [\pm i\sigma_3\partial_z - q^2 + \Gamma - (1 + \tau u + \tau E_0)]\delta\Psi^\mp \\ \mp \Gamma \frac{1 + \tau u + \tau E_0}{(1 + \tau u + I_x + I_0)^2} \delta\Psi^\pm = 0, \end{aligned} \quad (\text{C2})$$

where $\delta\Psi^+ \equiv \delta\Psi^\dagger, \delta\Psi^- \equiv \delta\Psi$. In homogenous spacetime (z, x, y) , we can transform to momentum space in both transverse and longitudinal directions. In the transverse plane, we get $(x, y) \mapsto (q_x, q_y)$ and $\Delta \mapsto -q^2$. The longitudinal coordinate or time z transforms as $z \mapsto k_n$ where $k_n = \pi n/L$, so the time maps to discrete frequencies. The reason is, of course, that its domain is finite, corresponding to the crystal length L .

Now we can derive the bare propagator (Green's function) of the fluctuating dynamical field $\delta\Psi$ by inserting the appropriate source $S(z)$ on the right-hand side of Eq. (C2). Normally, the source in the equation for the Green's function is just the Dirac δ function but the counterpropagating nature of our beams imposes a two-sided source:

$$S(z) = \begin{pmatrix} \delta(z) & 0 \\ 0 & \delta(z - L) \end{pmatrix}. \quad (\text{C3})$$

With this source (also Fourier-transformed in z), Eq. (C2) gives the bare propagator $G_{\alpha\beta}^{(0)}$ for the fields $\delta\Psi_{\alpha\beta}^\pm$:

$$\begin{aligned} G_{\alpha\beta}^{(0)}(k_n, q) = & [-ik_n S_{\alpha\gamma}(k_n) + A_{\alpha\delta}^* S_{\delta\gamma}(k_n) - B_{\alpha\delta} S_{\delta\gamma}(k_n)] \\ & \times [-k_n^2 + A_{\gamma\delta}^* A_{\delta\beta} - B_{\gamma\delta} B_{\delta\beta}^* + [A^*, B]_{\gamma\beta}]^{-1}. \end{aligned} \quad (\text{C4})$$

The auxiliary matrices A, B are defined as follows:

$$\begin{aligned} A_{\alpha\beta} = & i \begin{pmatrix} P_0 + P_1 - q^2 & P_0 \\ -P_0 & -P_0 - P_1 + q^2 \end{pmatrix}, \\ B_{\alpha\beta} = & i \begin{pmatrix} P_0 & P_0 \\ -P_0 & -P_0 \end{pmatrix}, \end{aligned} \quad (\text{C5})$$

where $P_1 = (1/4)I_0\Gamma(1 + \tau u + \tau E_0)/(1 + \tau u + I_x + I_0)^2$, $P_0 = \Gamma - \Gamma(1 + \tau u + \tau E_0)/(1 + \tau u + I_x + I_0)$, and $S(k_n) = \text{diag}(1, e^{ik_n L})$.

Now we have the basic ingredient of the perturbation theory: the bare propagator. The self-energy correction Σ of the propagator from the potential V_{eff} can be expanded in a power series over $\delta\Psi$, which gives an infinite tower of vertices. Simple combinatorial considerations give the expansion

$$\begin{aligned} \Sigma = & \sum_{j_1, j_2, j_3 \in \mathbb{N}} \frac{(-1)^{j_1+j_2+j_3} (j_1 + j_2 + j_3 - 1)!}{j_1! j_2! j_3!} \\ & \times \frac{\Gamma(1 + \tau u + \tau E_0)}{(1 + \tau u + I_0 + I_x)^{j_1+j_2+j_3+1}} (\Psi_0^\dagger \delta\Psi)^{j_1} \\ & \times (\Psi_0 \delta\Psi^\dagger)^{j_2} (\delta\Psi^\dagger \delta\Psi)^{j_3}, \end{aligned} \quad (\text{C6})$$

and the contraction over the internal indices of $\Psi^\pm, \delta\Psi^\pm$ is understood. Now we can formulate the diagrammatic rules. We have two kinds of propagators, $G^{(0)}$ and its Hermitian conjugate. The mean-field values Ψ_0^\pm are external sources. The term of order (j_1, j_2, j_3) contains $j_1 + j_3$ propagator lines $G^{(0)}$ (j_1 of them ending with the source Ψ_0) and $j_2 + j_3$ lines $(G^{(0)})^\dagger$ (j_2 of them ending with a source Ψ_0^\dagger); altogether, there are $j \equiv j_1 + j_2 + 2j_3$ lines. The expansion has to be truncated at some j . Since the mass dimension of Ψ is 1, the (j_1, j_2, j_3) diagram has the scaling dimension $2 - 2(j_1 + j_2 + 2j_3) < 0$, so *all* diagrams are irrelevant in the IR. This means we can make a truncation at small j .¹³ The leading terms are those where the order of the perturbation in $\delta\Psi^\pm$, which equals $j_1 + j_2 + 2j_3$, is the smallest. This gives two classes of diagrams, one with $j_1 = 1, j_2 = j_3 = 0$ and another with $j_2 = 0, j_1 = j_3 = 0$. They contain a single external source and introduce the wave-function renormalization, $G^{(0)} \mapsto ZG^{(0)}$, which does not influence the stability analysis. The four quadratic terms [with $(j_1, j_2, j_3) = (2, 0, 0), (0, 2, 0), (1, 1, 0), (0, 0, 1)$] introduce a mass operator. Only the terms $(1, 1, 0)$ and $(0, 0, 2)$ are trivial (noninteracting); the other two are interacting as they contain $(\delta\Psi^\pm)^2$ and require the calculation of an internal loop, giving the dressed propagator

$$G_{\alpha\beta}^{-1}(k_n, q) = [G^{(0)}(k_n, q)]_{\alpha\beta}^{-1} + (m^2)_{\alpha\beta}, \quad (\text{C7})$$

where the mass squared is a *positive* matrix, because the corresponding coefficients in (C6) have positive signs [from the term $(-1)^{j_1+j_2+j_3}$ with $j_1 + j_2 + j_3 = 2$] and the integral of the bare propagator is also positive. Explicitly, it reads

$$(m^2)_{\alpha\beta} = \frac{\Gamma(1 + \tau u + \tau E_0)}{(1 + \tau u + I_0 + I_x)^2} \sum_{k_n} \int_0^\infty dq q G_{\alpha\beta}^{(0)}(k_n, q), \quad (\text{C8})$$

¹³We do not worry about the UV divergences: We have an effective field theory and the UV cutoff is physical and finite.

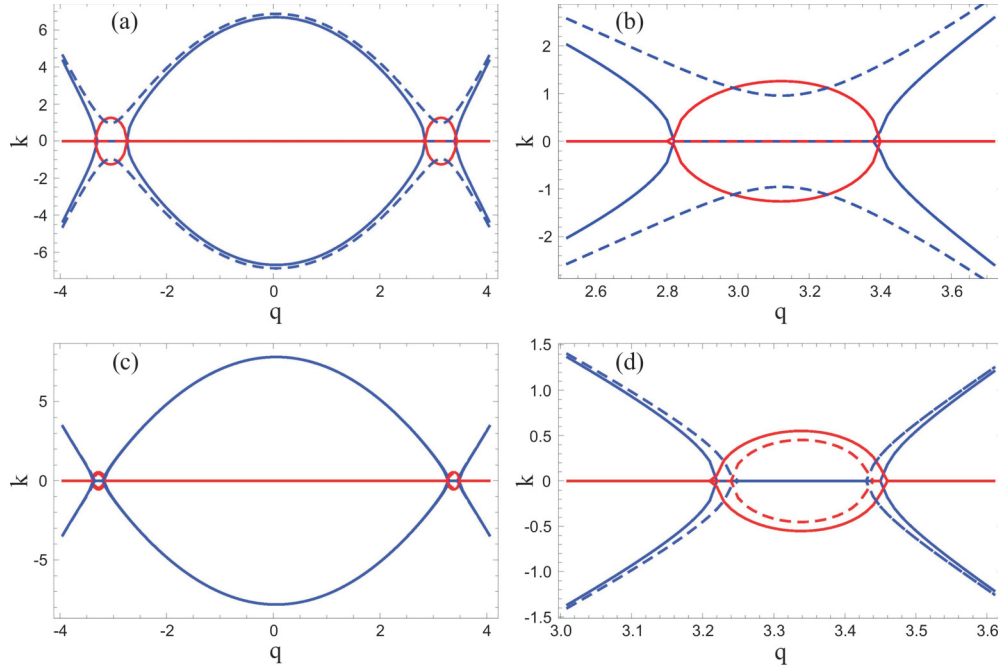


FIG. 21. Dispersion relation (position of the poles of the propagator) $k(q)$, where k is the continuous approximation of the discrete effective momentum $k_n = \pi nL$, for $I_x = 0$ [(a), (b)] and $I_x = 1$ [(c), (d)]. The plots (b) and (d) are enlargements of the plots (a) and (c). Blue lines denote $\text{Re}k$ and red lines show $\text{Im}k$. Notice that the propagator contains only k_n^2 and q^2 , so the pole has two copies with opposite signs and is either real or pure imaginary. Dashed lines are the corrected relations, with dressed propagator instead of the bare one. In the top panels, the region of instability, with $\text{Im}k_n \neq 0$, is cured by the nonlinear corrections, whereas in the bottom panels the instability remains. This generically happens at finite q and corresponds to the edge instability. Parameter values: $I_0 = 1$, $\Gamma = 15$, $L = 10$ mm.

where the discrete “frequency” k_n is summed in steps of π/L . Other than the mass renormalization, the dressed propagator has the same structure as the bare one. Now we will consider what this means for the stability of the patterns.

1. The pole structure, stability, and dispersion relations

Consider the poles of the propagator defined by the zeros of the eigenvalues of the matrix $G_{\alpha\beta}^{-1}(k_n, q)$. The stable solution corresponds to the situation where the perturbation $\delta\Psi_{\pm}$ dies out along z , so the stability of the solution is determined by the condition that the pole in q should have a nonpositive imaginary part, i.e., that a small perturbation decays. The denominator depends on k_n, q solely through k_n^2, q^2 ; it is linear in k_n^2 and quadratic in q^2 . Therefore, each of the two eigenvalues λ_{\pm} defines two pairs of opposite poles, $\pm q_{*+}, \pm q_{*-}, \pm q_{**+}, \pm q_{**-}$. Out of these, two pairs are positive for all parameter values, so no imaginary part can arise, and we have either two pairs of centrally symmetric imaginary poles, or one such pair, or none at all. We thus expect the sequence of symmetry-breaking transitions:

$$O(2) \longrightarrow \mathbb{C}_4 \longrightarrow \mathbb{C}_2. \quad (\text{C9})$$

Full circular symmetry is expected when there is no instability. With a single pair of unstable eigenvalues, we expect a square-like pattern with \mathbb{C}_4 symmetry, and with two pairs only a single reflection symmetry axis remains, yielding the group \mathbb{C}_2 . Only in the presence of disorder in the background lattice intensity pattern I_x can we expect the full breaking of the symmetry

group down to unity, but this is an *explicit* breaking and is not captured by this analysis.

The dispersion relation for a typical choice of parameter values is represented in Fig. 21, where we plot the location of the pole $k(q)$ in the continuous approximation (interpolating between the k_n values), with real parts of the pole in blue and imaginary in red. Since we have two pairs of opposite eigenvalues, the dispersion is P symmetric in x, y , and z (remember that time is really another spatial dimension), and any dispersion relation with a nonzero imaginary part will have a branch in the upper half-plane, i.e., an unstable branch. The only way out of instability is that the pole is purely real, i.e., infinitely sharp—this quasiparticle-like excitation signifies a solitonic solution. In Fig. 21, the dashed lines are drawn with the bare propagator $G^{(0)}$ and the full lines with the dressed propagator G , for the sets of parameter values. The perturbation always reduces the instability, i.e., the magnitude of the imaginary part of the poles—in Figs. 21(a) and 21(b) completely, resulting in zero imaginary part, and in Figs. 21(c) and 21(d) only partially. This reduction of instability likely explains the fact that linear stability analysis works extremely well for hyper-Gaussian beams (which have most power at small values of q), as found in Ref. [32].

The fact that the imaginary region always lies at finite q implies that the instability always starts at a finite scale, which corresponds to the behavior seen in the edge instability, which is shown, e.g., in Fig. 4. In order to understand the central instability, which starts from a single point, corresponding to $q \rightarrow \infty$, one needs to take into account also the higher order corrections from the potential (C6) which, as we discussed,

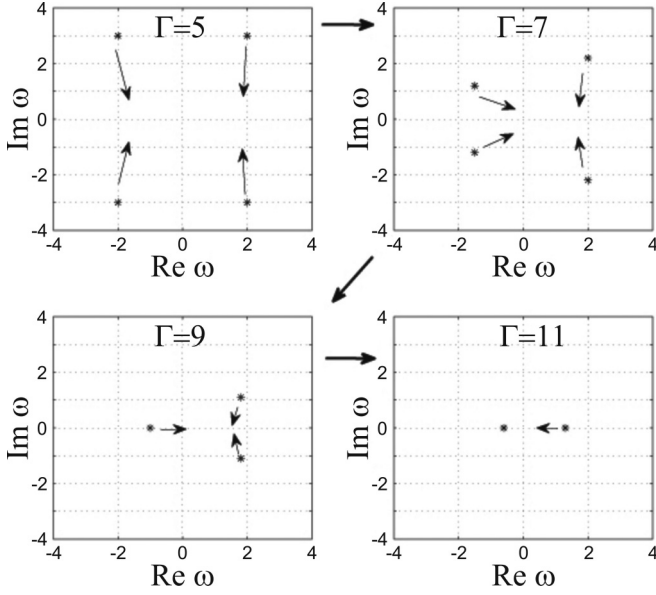


FIG. 22. The movement of the poles in the complex momentum plane in the case of central instability, for four different values of the PR coupling constant $\Gamma = 5, 7, 9, 11$. The complex momentum k is denoted by ω . Starting from the \mathbb{C}_4 -symmetric situation with two pairs of complex-conjugate poles, we first break the symmetry down to \mathbb{C}_2 and eventually lose all geometric symmetry as the two pairs merge into two real poles. Parameter values $I_0 = I_x = 1, L = 10$ mm.

diverge at $q \rightarrow \infty$. While we always have a natural UV cutoff, it may happen that the corrections become large (though finite) before that UV scale is reached. We postpone a detailed account for the subsequent publication, and content ourselves to give only the diagram of the movement of the poles in the complex plane. Higher order terms bring q -dependent corrections and break the inversion symmetry, resulting in the evolution of poles, as in Fig. 22. The instability corresponds to the situations where at least one pole has a positive imaginary part, i.e., the first three situations in the figure. The last pattern, with no symmetry at all and two real poles, is stable (but not asymptotically stable, as there is no pole with nonzero negative imaginary part).

The analysis performed here is obviously incomplete, and we have contented ourselves merely to give a sketch of how the instabilities considered in the main text arise, as well as to formulate a perturbation scheme which allows one to study such phenomena. Further work along the lines of Refs. [20,32,36] is possible by making use of our formalism, and we plan to address this topic in the future.

APPENDIX D: DERIVATION OF THE VORTEX HAMILTONIAN FROM THE MICROSCOPIC LAGRANGIAN

Starting from the vortex solution (6), we want to obtain an effective Hamiltonian for the vortex-vortex interaction. The task is to separate the kinetic term of the winding phase (with $\nabla\theta_{0\pm} = \sum_i Q_{\pm} \ln |\mathbf{r} - \mathbf{r}_i|$) from (i) the intensity fluctuations $\delta\psi_{\pm}$ about some background value $\psi_{0\pm}$ and (ii) the nonvortex phase fluctuations ($\delta\theta_{\pm}$) in (6). The first task requires us

to integrate out the amplitude fluctuations in the quadratic approximation. We first write $\Psi = \Psi_0 + \delta\Psi$ and expand the Lagrangian to quadratic order:

$$\begin{aligned} \mathcal{L} &= \mathcal{L}_0 + \mathcal{L}_2, \\ \mathcal{L}_0 &= \frac{1}{2} \partial_r \psi_0^\dagger \partial_r \psi_0 + \frac{I_0}{2r^2} |\nabla\theta_{0\alpha}|^2, \\ \mathcal{L}_2 &= \frac{1}{2} \partial_r \delta\Psi_\alpha^\dagger \partial_r \delta\Psi_\alpha \\ &\quad + \frac{1}{2r^2} \delta\Psi_\alpha^\dagger |\nabla\theta_{0\alpha}|^2 \delta\Psi_\alpha + V_{\text{eff}}(\delta\Psi_{\pm}), \\ V_{\text{eff}}(\delta\Psi^{\pm}) &= -\Gamma \delta\Psi^\dagger \delta\Psi - \Gamma \frac{1 + \tau u + \tau E_0}{2(1 + \tau u + I_x + I_0)^2} \\ &\quad \times [(\Psi_0 \delta\Psi^\dagger)^2 + (\Psi_0^\dagger \delta\Psi)^2 - 2(1 + \tau u + I_x + I_0) \\ &\quad \times \delta\Psi^\dagger \delta\Psi - (\Psi_0 \sigma_2 \delta\Psi^\dagger)(\Psi_0^\dagger \sigma_2 \delta\Psi)]. \end{aligned} \quad (\text{D1})$$

The zeroth-order (nonfluctuating) term \mathcal{L}_0 determines the intensity $I_0 = \psi_0^\dagger \psi_0$ and produces the kinetic term for the vortex phase θ_α , which gives just two decoupled copies of the conventional XY vortex gas. The quadratic part \mathcal{L}_2 becomes quite involved when we separate the amplitude $\delta\psi$ and the phase $\delta\theta$. Inserting (6) into (D1), one gets a quadratic action for $\delta\psi_\alpha$ and $\delta\theta_\alpha$. The rest gives a coupled quadratic action for the amplitude and phase fluctuations. Altogether, the Lagrangian is

$$\begin{aligned} \mathcal{L} &= \frac{1}{2} (\delta\psi_+^2 + \delta\psi_-^2) + \frac{1}{2r^2} (\delta\psi_+^2 + \delta\psi_-^2) |\nabla\theta_\alpha|^2 \\ &\quad + \delta\psi_\alpha \hat{K}_{\alpha\beta} \delta\psi_\beta + (\delta\psi_\alpha^\dagger \psi_\alpha \nabla\theta_\alpha \nabla\delta\theta_\alpha + \text{H.c.}) + \dots, \end{aligned} \quad (\text{D2})$$

where (\dots) denote all terms of cubic or higher order in amplitude or phase fluctuations $\delta\psi_\alpha, \delta\theta_\alpha$, and we have left out the constant terms independent of all field values. Primes denote the derivatives with respect to r . The first term defines the intensity fluctuations through $\psi_\alpha(r)$, and the second term (transformed through partial integration) yields the aforementioned conventional Coulomb gas of vortices after inserting the vortex solution from (6) for θ_α . The third term has the meaning of stiffness or mass matrix for intensity fluctuations and the last term gives rise to the coupling between the flavors, upon integrating out $\delta\psi$. The matrix \hat{K} is

$$\begin{aligned} \hat{K} &= \frac{1}{(b + \frac{3}{2}I_0)(b - \frac{1}{2}I_0)} \begin{pmatrix} b + \frac{I_0}{2} & I_0 \\ I_0 & b + \frac{I_0}{2} \end{pmatrix}, \\ b &= \Gamma \frac{1 + \tau E_0}{2(1 + \tau E_0)^2} (2 + 2I_x + 3I_0). \end{aligned} \quad (\text{D3})$$

The action is quadratic in $\delta\psi$; therefore, we know how to integrate it out and obtain an effective action depending only on phase fluctuations. To do that, we need to solve the eigenvalue equation for $\delta\psi$ obtained from (D2), which reads

$$\partial_{rr} \delta\psi_\alpha - K_{\alpha\beta} \delta\psi_\beta = \left(\frac{|\nabla\theta|^2}{2r^2} + \lambda_{\pm} \right) \delta\psi_\alpha, \quad (\text{D4})$$

and is solved by diagonalizing the system $\delta\psi_\alpha \mapsto \delta\chi_\alpha = U_{\alpha\beta}\delta\psi_\beta$ and reducing it to the Bessel equation:

$$\delta\chi_\pm(r) = \sqrt{r}\{C_\pm J_\nu[\sqrt{2(K_{11} \mp K_{12} - \lambda_\pm)}r] + D_\pm Y_\nu[\sqrt{2(K_{11} \mp K_{12} - \lambda_\pm)}r]\}, \quad (\text{D5})$$

with $\nu = \sqrt{1/4 + |\nabla\theta|^2}$, where J_ν, Y_ν are Bessel functions of the first and second kinds, respectively. For well-defined behavior close to the vortex core (for $r \sim a$), we have $D_\pm = 0$, and C_\pm are arbitrary as the equation is linear. The eigenvalues $\lambda_{n\pm}, n = 0, 1, \dots$ are obtained by requiring that the fluctuation decays to zero at the crystal edge $r = \Lambda$:

$$\sqrt{2K_{11} \mp K_{12} - \lambda_{n\pm}}\Lambda = j_n(\nu), \quad (\text{D6})$$

where j_n is the n th zero of the Bessel function J_ν . The values $\lambda_{n\pm}$ are impossible to express analytically in closed form; however, it is not necessary for our purposes as $\Lambda \gg a$. The functional determinant obtained after integrating out χ_\pm is now expressed in terms of the eigenvalues:

$$\begin{aligned} \mathcal{K}_{\alpha\beta} &= \ln \left(\prod_n \lambda_{n\alpha} \lambda_{n\beta} \right)^{-1/2} \\ &= -\frac{1}{2} \sum_n \ln \left(K'_\alpha + K'_\beta + \frac{2j_n(\nu)^2}{\Lambda^2} \right) \sim \\ &\quad -\frac{\Lambda}{2} (K'_\alpha + K'_\beta) + O\left(\frac{1}{\Lambda}\right), \end{aligned} \quad (\text{D7})$$

where $K'_\pm = 2K_{11} \mp K_{12}$. Now we are left with a solely phase-dependent quadratic Lagrangian:

$$\mathcal{L} = \psi_{0\alpha} \nabla\theta_\alpha \nabla\delta\theta_\alpha \hat{\mathcal{K}}_{\alpha\beta} \psi_{0\beta} \nabla\theta_\beta \nabla\delta\theta_\beta + \frac{I_0}{2r^2} |\nabla\theta_\alpha|^2. \quad (\text{D8})$$

The final task is to integrate out the phase fluctuations, which is a trivial Gaussian integration, yielding

$$\mathcal{L} = \frac{I_0}{2r^2} |\nabla\theta_\alpha|^2 + I_0 \nabla\theta_\alpha \mathcal{K}_{\alpha\beta}^{-1} \nabla\theta_\beta. \quad (\text{D9})$$

The resulting Lagrangian now depends only on the vortexing phases θ_α . The first term is carried from the original Lagrangian, and it does not mix the flavors. But the second term, stemming from the fluctuations, has nonzero mixed \pm cross terms. The quadratic derivative terms can be transformed by partial integration to the familiar Coulomb gas form of the XY model, with the same-flavor coupling which is already present in absence of fluctuations, *and* the coupling between the vortices of different flavors. Thus the existence of two beams together with the fact that amplitude and phase fluctuations do not decouple give us a richer system, with interaction between two vortex flavors. For future use, it is more convenient to look at the vortex Hamiltonian $\mathcal{H}_{\text{vort}}$ —the difference from the Lagrangian lies just in the sign of the term V_{eff} . This finally yields the Hamiltonian [for Eq. (7), repeated here for convenience]:

$$\begin{aligned} \mathcal{H}_{\text{vort}} &= \sum_{i < j} (g \vec{Q}_i \cdot \vec{Q}_j + g' \vec{Q}_i \times \vec{Q}_j) \ln r_{ij} \\ &\quad + \sum_i (g_0 \vec{Q}_i \cdot \vec{Q}_i + g_1 \vec{Q}_i \times \vec{Q}_i), \end{aligned} \quad (\text{D10})$$

with $r_{ij} \equiv |\mathbf{r}_i - \mathbf{r}_j|$, and the indices $1 \leq i, j \leq N$ sum over all the vortices. The coupling constants g, g', g_0, g_1 are the result of integrating out the intensity fluctuations and in general are given by rather cumbersome (and not very illustrative) functions of Γ, I_0, τ . We give the expressions at leading order just for comparison with numerics:

$$\begin{aligned} g &= I_0 + \frac{4b + 2I_0}{(2b + 3I_0)(2b - I_0)}, \\ g' &= \frac{4I_0}{(2b + 3I_0)(2b - I_0)}, \\ b &= \Gamma \frac{1 + \frac{\tau}{L} - \tau \frac{I_0 + I_x}{1 + I_0 + I_x}}{2(1 + \frac{\tau}{L} - \tau \frac{I_0 + I_x}{1 + I_0 + I_x})^2} \left(2 + 2\frac{\tau}{L} + 2I_x + 3I_0 \right). \end{aligned} \quad (\text{D11})$$

These expressions are used later to redraw the phase diagram in the space of physical parameters Γ, I_0, I_x, L .

APPENDIX E: MULTIVORTEX MEAN-FIELD THEORY

For a mean-field treatment of a system with multiple vortices, we start from the Hamiltonian (7) and introduce the order parameter fields in the following way. Denote the number of vortices with charge (1, 1) by ρ_{2+} and the number of vortices (1, -1) by ρ_{2-} ; due to charge conservation, this means we also have ρ_{2+} vortices of type (-1, -1) and ρ_{2-} vortices with charge (-1, 1). The number of single-charge vortices of type (1, 0) and (0, 1) is denoted by ρ_{1+} and ρ_{1-} , respectively. Denote also $\rho_2 \equiv \rho_{2+} + \rho_{2-}$ and $\delta\rho_2 \equiv \rho_{2+} - \rho_{2-}$ (notice that $-\rho_2 \leq \delta\rho_2 \leq \rho_2$), and finally $\rho_1 \equiv \rho_{1+} + \rho_{1-}$. We insert this into the vortex Hamiltonian $\mathcal{H}_{\text{vort}}$ and assume that the long-ranged logarithmic interaction $\ln r_{ij}$ justifies the mean-field approximation: For $i \neq j$, we can approximate $\ln r_{ij} \sim \ln \Lambda$, assuming that average intervortex distance is of the same order of magnitude as the system size. For the core energy, we know that $g_0, g_1 \sim \ln(a/\epsilon) \sim -\ln\epsilon \sim \ln\Lambda$, where in the last equality we have assumed that the UV cutoff ϵ is of similar order of magnitude as the inverse of the IR cutoff $1/\Lambda$, which is natural.¹⁴ Thus all terms are proportional to $L \ln \Lambda$ and we can write

$$\begin{aligned} \mathcal{F}_{\text{mf}} &= \beta \ln \frac{\Lambda}{a} [2(g-1)\rho_2 + 2g'\delta\rho_2 + (g-1)\rho_1] \\ &\equiv A\rho_2 + B\delta\rho_2 + \frac{B}{2}\rho_1. \end{aligned} \quad (\text{E1})$$

We use the notation $\beta \equiv L$ to emphasize the analogy with the free energy of spin vortices, where β is the inverse temperature. The analogy is purely formal as our system is not subject to thermal noise. Now the ground state is determined by minimizing the free energy, i.e., the effective action of the system. Notice that \mathcal{F}_{mf} is linear in the fields $\rho_2, \delta\rho_2, \rho_1$ so the optimal configurations have either $\mathcal{F}_{\text{mf}} = 0$ or $\mathcal{F}_{\text{mf}} \rightarrow -\infty$, and the mean-field densities $\rho_{1,2}$ are either zero or arbitrary

¹⁴Nevertheless, this is clearly not a rigorous argument. Our mean-field calculation is somewhat sketchy and merely assumes that the long-range interactions can safely be modeled as a uniform vortex charge field.

(formally infinite). This is a well-known property of the 2D Coulomb gas and has to do with the fact that (assuming the cutoff dependence has been eliminated) this system is conformal invariant in the insulator phase, so all finite densities ρ are equivalent: There is no other scale to compare ρ to. Likewise, the prefactor β can be absorbed into the definition of the coupling constants g, g' and thus is not an independent parameter (this is well known also from the single-flavor case). Minimizing (E1) is an elementary exercise and we find again four regimes, corresponding to the four phases we guessed based on the single-vortex free energy $\mathcal{F}^{(1)}$:

(1) For $A > 0, A > |B|$, the minimum is reached for $\rho_2 = \delta\rho_2 = \rho_1 = 0$. In the ground state, there are no vortices at all—the system is a vortex insulator.

(2) For $B > 0, A + B < 0$, giving $g + g' < 1, g' > 0$, the free energy has its minimum for $\rho_2 > 0$ and $\delta\rho_2 = -\rho_2$ (notice that $-\rho_2 \leq \delta\rho_2 \leq \rho_2$). This means $\rho_{2+} = 0, \rho_{2-} > 0$, so opposite-charged vortices $(Q, -Q)$ proliferate, and the system is dominated by the interactions between the charges. This is the frustrated vortex insulator regime. Since $g' < 0$, the single-charge vortices (density ρ_1) are suppressed.

(3) For $B < 0, A + B < 0$, i.e., $g + g' < 1, g' < 0$, the minimum is reached for $\rho_2 = \delta\rho_2 > 0$, i.e., $\rho_{2-} = 0$, so the vortices (Q, Q) can proliferate. However, since $g' < 0$, there is also nonzero single-flavor density ρ_1 and the proliferation of vortices $(Q, 0)$ and $(0, Q)$ which generically dominate over two-flavor vortices. This is the conductor phase, with mostly single-flavor vortices (as in the standard XY model).

(4) The point $A = B = 0$ is special: Naively, from (E1), arbitrary nonzero $\rho_1, \rho_2, \delta\rho_2$ are allowed. Of course, higher order corrections will change, this but the energy cost of vortex formation will generically be smaller than in previous phases. This is the vortex perfect conductor phase. In the mean-field approach, it looks like a single point, but that will turn out to be an artifact of the mean-field approach: For small nonzero A, B the system still remains in this phase.

In terms of the original parameters g, g' , one sees the insulator phase is given by $g + g' > 1$, and the conductor and the FI are separated by the line $g' = 0$. We can now sketch the phase diagram, which is given in Fig. 2(a), side by side with the more rigorous diagram obtained by the RG flow, in Sec. III B 2.

APPENDIX F: COUNTERPROPAGATING BOUNDARY CONDITIONS

In the derivation of the vortex Hamiltonian and its RG analysis, we have pulled under the rug the treatment of the CP boundary conditions: The effective Hamiltonian (and consequently the partition function and the phase diagram) depends solely on the bulk configuration, and nowhere can one see the fact that $\Psi_+(z = 0; \mathbf{r}, t)$ and $\Psi_-(z = L; \mathbf{r}, t)$ are fixed. Now we will explicitly show that these boundary conditions are irrelevant in the RG sense; i.e., they contribute additional, boundary terms to the effective Hamiltonian, but these terms do not change the fixed points to which the solution flows.

The full Hamiltonian with correct CP boundary conditions is obtained by adding the F source at $z = 0$ and the B source at $z = L$ to the Lagrangian \mathcal{L} from (4) or, equivalently, to the equations of motion. The sources impose the conditions $F(z =$

$0; x, y, t) = F_0(x, y)$ and $B(z = L; x, y, t) = B_0(x, y)$ so they equal

$$J_+ = F_0(x, y)\delta(z), \quad J_- = B_0(x, y)\delta(z - L), \quad (\text{F1})$$

and the full Lagrangian is

$$\begin{aligned} \mathcal{L}_{\text{CP}} = \mathcal{L} + J_+\Psi_+ + J_-\Psi_- \mapsto \mathcal{L} + F_0(x, y)\Psi_+(z; x, y, t) \\ + e^{ikz}B_0(x, y)\Psi_-(z; x, y, t). \end{aligned} \quad (\text{F2})$$

Unlike the Dirac δ source (C3) for the Green's function, now the source has nontrivial dependence on transverse coordinates. Now we can insert the vortex solution (6) in both Ψ_{\pm} and F_0, B_0 and repeat the steps from the subsequent derivation. The vortex charges in F_0 can be denoted by $\vec{P}_{i'}^{(+)} \equiv (P_{i'+}, 0)$ and $\vec{P}_{i'}^{(-)} \equiv (0, P_{i'-})$; by definition, the $+$ component of B_0 as well as the $-$ component of F_0 are zero and thus carry no vorticity. The primed indices refer to the vortices in the input beams, and the nonprimed, like before, to the bulk vortices. Notice the source term changes sign upon performing the Legendre transform, appearing as $-J_+\Psi_+ - J_-\Psi_-$ in the Hamiltonian.

Now we will check if the RG flow of the Hamiltonian with boundary terms is affected by the sources. In the notation introduced above, the total vortex Hamiltonian is

$$\begin{aligned} \mathcal{H}_{\text{CP}} = \sum_{i,j} (g\vec{Q}_i \cdot \vec{Q}_j + g'\vec{Q}_i \times \vec{Q}_j) \ln r_{ij} \\ + \sum_{i',j} \delta(z) P_{i'+} (gQ_{j+} + g'Q_{j-}) \ln r_{i'j} \\ + \sum_{i,j'} \delta(z - L) P_{j'-} (gQ_{i-} + g'Q_{i+}) \ln r_{ij'}. \end{aligned} \quad (\text{F3})$$

Notice there is no source-source interaction: Same-flavor interaction cannot exist as $P_{i'-} = P_{j'+} = 0$, and cross-flavor interaction does not exist as J_+ and J_- exist at different z values, i.e., the cross term would be proportional to $\delta(z)\delta(z - L)$ and thus vanishes. The presence of sources breaks the spatial homogeneity, complicating the traces (integrals over the positions of virtual vortex-antivortex pairs), but does not change the main line of the calculation. The fluctuation of the partition function due to vortex pair creation is now

$$\begin{aligned} \frac{\delta\mathcal{Z}}{\mathcal{Z}} = 1 + \frac{y^4}{4} \sum_{\vec{q}} \int d^2r \\ \times \int d^2r_{12} e^{-C(\vec{q}, \mathbf{r}_1; -\vec{q}, \mathbf{r}_2) - \sum_j [D_j^+(\vec{q}, \mathbf{r}_1) - D_j^-(\vec{q}, \mathbf{r}_2)]} \\ \times [e^{C(\vec{Q}_1, \mathbf{R}_1; \vec{q}, \mathbf{r}_1) + C(\vec{Q}_1, \mathbf{R}_1; -\vec{q}, \mathbf{r}_2) + C(\vec{Q}_2, \mathbf{R}_2; \vec{q}, \mathbf{r}_1) + C(\vec{Q}_2, \mathbf{R}_2; -\vec{q}, \mathbf{r}_2)} \\ - 1]. \end{aligned} \quad (\text{F4})$$

We have denoted $C(\vec{Q}_1, \mathbf{R}_1; \vec{Q}_2, \mathbf{R}) \equiv (g\vec{Q}_1 \cdot \vec{Q}_2 + g'\vec{Q}_1 \times \vec{Q}_2) \ln R_{12}$, and the coupling to the sources is encapsulated in the function

$$D_j^{\pm}(\vec{q}, \mathbf{r}) \equiv \delta(z - z_{\pm})(g_{\pm}\vec{q} \cdot \vec{P}_{j'} \mp g'_{\pm}\vec{q} \times \vec{P}_{j'}) \ln |\mathbf{r} - \mathbf{r}_{j\pm}|, \quad (\text{F5})$$

with $z_+ = 0, z_- = L$. The coupling constants g_{\pm}, g'_{\pm} are obtained from g, g' in (F4) by replacing

$$I_0 \mapsto \sqrt{I_0 I_{\pm}}, \quad (\text{F6})$$

with $I_+ = |F_0|, I_- = |B_0|$. Now the exponential of the extra term with sources also needs to be expanded in r_{12} , as the combinations $2\mathbf{r} = \mathbf{r}_1 + \mathbf{r}_2, \mathbf{r}_{12} = \mathbf{r}_1 - \mathbf{r}_2$ do not decouple anymore and exact integration is impossible. After writing $D_{j'}^{\pm}(\vec{q}, \mathbf{r}_{1,2}) = D_{j'}^{\pm}(\vec{q}, \mathbf{r}) \pm \mathbf{r}_{12} \cdot \nabla D_{j'}^{\pm}(\vec{q}, \mathbf{r}) + \dots$ and similarly for C , we notice first that the zeroth-order terms from $D_{j'\pm}$ cancel out: $D_{j'}^{\pm}(\vec{q}, \mathbf{r}) + D_{j'}^{\pm}(-\vec{q}, \mathbf{r}) = 0$. Then we get (at quadratic order in r_{12} in the integrand):

$$\begin{aligned} \frac{\delta \mathcal{Z}}{\mathcal{Z}} &= 1 + \frac{y^4}{4} \sum_{j'} \int d^2 r \int d^2 r_{12} e^{-C(\vec{q}, \mathbf{r}_{12}; -\vec{q}, \mathbf{0})} \\ &\times \left\{ \mathbf{r}_{12} \cdot [\nabla C(\vec{Q}_1, \mathbf{R}; \vec{q}, \mathbf{r}) + \nabla C(\vec{Q}_2, \mathbf{R}; -\vec{q}, \mathbf{r})] \right. \\ &+ \frac{r_{12}^2}{2} \left| \nabla C(\vec{Q}_1, \mathbf{R}; \vec{q}, \mathbf{r}) + \nabla C(\vec{Q}_2, \mathbf{R}; -\vec{q}, \mathbf{r}) \right|^2 \left. \right\} \\ &\times [\mathbf{r}_{12} \cdot [1 - \nabla D_{j'}^+(\vec{q}, \mathbf{r}) + \nabla D_{j'}^-(\vec{q}, \mathbf{r})] \\ &+ \{\mathbf{r}_{12} \cdot [\nabla D_{j'}^+(\vec{q}, \mathbf{r}) + \nabla D_{j'}^-(\vec{q}, \mathbf{r})]\}^2] + \dots \\ &\equiv 1 + \frac{y^4}{4} [I_{10} + I_{20} - I_{11} + O(r_{12}^3)]. \quad (\text{F7}) \end{aligned}$$

The integral I_{mn} is the term with the contribution of order r_{12}^m from the second line in the integrand and with the contribution of order r_{12}^n from the third line. The integrands in I_{mn} are thus of order $m+n$ in r_{12} , m coming from the expansion of $D_{j'}^{\pm}$ and n from the expansion of C . By homogeneity, $I_{01} = 0$ and I_{02} is the same integral that appears in absence of sources, whose calculation was used in obtaining (13) and which gives the right-hand side of the RG flow (14). The remaining integral I_{11} is the new ingredient, and the only one which depends on the sources. Representing it as

$$\begin{aligned} I_{11} &= \frac{\pi^2}{4} \sum_{j'} \sum_{\alpha=\pm} \sum_{\sigma=1,2} \delta(z - z_{\alpha}) \\ &\times (g_{\alpha} \vec{Q}_{\sigma} \cdot \vec{P}_{j'\alpha} + g'_{\alpha} \vec{Q}_{\sigma} \times \vec{P}_{j'\alpha}) \\ &\times \nabla \frac{1}{|\mathbf{R}_{12}|} \cdot \nabla \frac{1}{|\mathbf{r}_{j'\alpha}|} \tilde{I}_{j'\alpha}, \quad (\text{F8}) \end{aligned}$$

we compute the integral $\tilde{I}_{j'\alpha}$ in polar coordinates:

$$\tilde{I}_{j'\alpha} = \frac{1}{2} \int_0^{2\pi} d\theta_j \ln(r_{12}^2 - 2r_{12}r_{j'\alpha} \cos \theta_j + r_{j'\alpha}^2) \Big|_{\Lambda_1}^{\Lambda_2}, \quad (\text{F9})$$

where $\theta_{j'\alpha}$ is the angle between $\mathbf{r}_{j'\alpha}$ and \mathbf{r}_{12} . Assuming the RG scale changes as $\Lambda_1 = \Lambda, \Lambda_2 = \Lambda(1 + \ell)$, for small ℓ we can expand the integrand, getting

$$\begin{aligned} \tilde{I}_{j'\alpha} &= \int_0^{2\pi} d\theta_j \frac{\Lambda^2 - \Lambda r_{j'\alpha} \cos \theta_j}{\Lambda^2 - 2\Lambda r_{j'\alpha} \cos \theta_j + r_{j'\alpha}^2} \ell + O(\ell^2) \\ &= 2\pi \ell + O(\ell^2). \quad (\text{F10}) \end{aligned}$$

The complicated dependence on the positions of the sources disappears completely in the first order in ℓ .¹⁵ Altogether, by comparing the outcome of (F7) to the original Hamiltonian (F3), we see that the renormalization of the bulk interaction between \vec{Q}_1 and \vec{Q}_2 is unaffected by the sources, given as before by the I_{02} term, and the source-bulk coupling renormalizes with a strictly negative shift (as $\tilde{I}_{j'\alpha} = 2\pi > 0$). The flow equations for g, g' couplings are unchanged, being the same as in (14). The bulk-to-boundary couplings g_{\pm}, g'_{\pm} have the flow equations

$$\frac{\partial g_{\pm}}{\partial \ell} = -\pi^3 N \ell, \quad \frac{\partial g'_{\pm}}{\partial \ell} = -\frac{\pi^3}{2} N \ell, \quad (\text{F11})$$

where $N = \sum_{j'} \sum_{\alpha} 1$ is the total vorticity of the sources. This obviously flows to $g_{\pm}, g'_{\pm} = 0$.

Intuitively, one may wonder how come such an important thing as the CP geometry has no bearing on the vortex dynamics; surely the behavior of a copropagating system would be expected to differ from a counterpropagating system. The answer is that the CP geometry does enter our calculations—the B beam has an extra minus sign in the equations of motion (1) (alternatively, in the Lagrangian in Eq. (4)); equivalently, the symmetry group of the effective potential in the Lagrangian is $SU(1,1)$, not $SU(2)$ as it would be for two copropagating beams. Finally, let us emphasize again that in the numerical simulations we directly solve the propagation equations (1) together with (2); i.e., we directly take into account the CP boundary conditions—no analytical approximations whatsoever are used in the numerics, and no use is made of the effective vortex Hamiltonian.

APPENDIX G: ORDER PARAMETERS AND RG ANALYSIS OF THE CP VORTICES IN THE PRESENCE OF DISORDER

1. Saddle-point solutions

We start by rewriting the replicated partition function $\tilde{\mathcal{Z}}^n$ in terms of $p_{\alpha}, q_{\alpha\beta}$ and inserting the constraints which encapsulate their definition in Eq. (19):

$$\begin{aligned} 1 &\mapsto \int \mathcal{D}[\lambda_{(\mu)}^{\alpha}] \exp \left[\lambda_{(\mu)}^{\alpha} \left(p_{\alpha}^{(\mu)} - \frac{1}{N} \sum_{i=1}^N \mathcal{Q}_{i\alpha}^{(\mu)} \right) \right], \quad (\text{G1}) \\ 1 &\mapsto \int \mathcal{D}[\lambda_{(\mu\nu)}^{\alpha\beta}] \exp \left[\lambda_{(\mu\nu)}^{\alpha\beta} \left(q_{\alpha\beta}^{(\mu\nu)} - \frac{1}{N} \sum_{i,j=1}^N \mathcal{Q}_{i\alpha}^{(\mu)} \mathcal{Q}_{j\beta}^{(\nu)} \right) \right]. \quad (\text{G2}) \end{aligned}$$

We have five constraints, $\lambda_{(\mu\nu)}^{++}, \lambda_{(\mu\nu)}^{--}, \lambda_{(\mu\nu)}^{+-} = \lambda_{(\mu\nu)}^{-+}, \lambda_{(\mu)}^{+}, \lambda_{(\mu)}^{-}$, for the corresponding five order parameters in (19). We can denote

$$\hat{K} \equiv \begin{pmatrix} \lambda_{(\mu\nu)}^{++} & \lambda_{(\mu\nu)}^{+-} \\ \lambda_{(\mu\nu)}^{+-} & \lambda_{(\mu\nu)}^{--} \end{pmatrix}, \quad \vec{\lambda} \equiv \begin{pmatrix} \lambda_{(\mu)}^{+} \\ \lambda_{(\mu)}^{-} \end{pmatrix}. \quad (\text{G3})$$

We will also sometimes leave out the replica indices μ, ν to avoid cramming the notation too much. Now we can first integrate out the vortex degrees of freedom $\mathcal{Q}_{i\alpha}^{(\mu)}$ from (18)

¹⁵The additional assumption is that $\Lambda > r_{j'\alpha}$ so the integrand contains no poles; this is clearly justified as Λ is the length cutoff.

to get the effective action

$$S_{\text{eff}} = -\frac{\beta^2}{4} \sum_{\mu, \nu=1}^n [\sigma_{++}^2 (q_{++}^{(\mu\nu)})^2 + 2\sigma_{+-}^2 (q_{+-}^{(\mu\nu)})^2 + \sigma_{--}^2 (q_{--}^{(\mu\nu)})^2] - \beta \sum_{\mu=1}^n [J_0^+ (p_+^{(\mu)})^2 + 2J_0^{+-} p_+^{(\mu)} p_-^{(\mu)} + J_0^- (p_-^{(\mu)})^2] + \frac{1}{2} \ln \det \hat{K} - \frac{1}{4} \vec{\lambda} \hat{K}^{-1} \vec{\lambda} - \sum_{\mu, \nu=1}^n (\lambda_{(\mu\nu)}^{++} q_{++}^{(\mu\nu)} + \lambda_{(\mu\nu)}^{+-} q_{+-}^{(\mu\nu)} + \lambda_{(\mu\nu)}^{--} q_{--}^{(\mu\nu)}) - \sum_{\mu=1}^n \vec{\lambda}_{(\mu)} \cdot \vec{p}^{(\mu)}. \quad (\text{G4})$$

The saddle-point equations for the constraints give the constraints in terms of the expectation values $q^{(\mu\nu)}, p^{(\mu)}$. Luckily, the equation for $\vec{\lambda}$ is easy:

$$\frac{\partial S_{\text{eff}}}{\partial \vec{\lambda}} = \hat{K}^{-1} \vec{\lambda} - \vec{p} = 0, \quad (\text{G5})$$

so we immediately solve $\vec{\lambda} = \hat{K} \vec{p}$. Now plugging this into the equations for the three remaining constraints yields

$$\frac{\partial S_{\text{eff}}}{\partial \lambda_{\pm\pm}} = \frac{1}{2} \frac{X \lambda_{\pm\pm}^{-1}}{X^2 - Y^2} - q_{\pm\pm} + \frac{1}{4} (p_{\pm})^2 = 0, \quad (\text{G6})$$

$$\frac{\partial S_{\text{eff}}}{\partial \lambda_{+-}} = \frac{Y \lambda_{+-}^{-1}}{X^2 - Y^2} - q_{+-} + \frac{1}{2} p_+ p_- = 0. \quad (\text{G7})$$

We have denoted $X = \det \lambda_{++} = \det \lambda_{--}, Y = \det \lambda_{+-}$ (these have a well-defined limit for $n \rightarrow 0$). It is trivial to write $\lambda_{\pm\pm}, \lambda_{+-}$ from the above expressions, and we can feed the solutions for all the constraints into the effective action and then solve the saddle-point equations for the order parameters $p_{\pm}, q_{++}, q_{--}, q_{+-}$. Full equations are too complex to be solved, even approximately. We will simplify the problem with the following reasoning. The sums over single-replica order parameters generically scale as $\sum_{\mu} p_{\pm}^{(\mu)} \sim \sum_{\mu} (p_{\pm}^{(\mu)})^2 \sim n$, whereas the double-replica parameters have $\sum_{\mu, \nu} q_{\alpha\beta}^{(\mu\nu)} \sim n^2$. This means that in the limit $n \rightarrow 0$, the p_{\pm} terms dominate over $q_{\alpha\beta}$ terms. Therefore, if $p_{\pm} \neq 0$ we can disregard the quantities $q_{\alpha\beta}$ or expand in a series over them, simplifying the equations significantly. Only if the replica symmetry breaking imposes $p_{\pm} = 0$ (not every replica-symmetry-breaking configuration does so) are the $q_{\alpha\beta}$ order parameters significant, and the saddle-point equations with $p_{\pm} = 0$ are again approachable.

Consider first the case $p_{\pm} = 0$. After some algebra, the effective action is now

$$S_{\text{eff}} = -\frac{\beta^2}{4} \sum_{\mu, \nu=1}^n [\sigma_{++}^2 (q_{++}^{(\mu\nu)})^2 + 2\sigma_{+-}^2 (q_{+-}^{(\mu\nu)})^2 + \sigma_{--}^2 (q_{--}^{(\mu\nu)})^2] + \frac{1}{2} \ln(X^2 |q^{++}|^{-1} \cdot |q^{--}|^{-1} - 4Y^2 |q^{+-}|^{-2}). \quad (\text{G8})$$

Consider first the ansatz when the $q^{\pm\pm}$ fields are nonzero, whereas the mixed-flavor field q^{+-} is zero. In this case, the second term in (G8), coming from the determinant \hat{K} , simplifies further and we get the saddle-point equation

$$-\frac{\beta^2}{2} \sigma_{\pm\pm}^2 q^{\pm\pm} - \frac{1}{2} (q^{\pm\pm})^{-1} = 0, \quad (\text{G9})$$

which is the same as for the infinite-range spin-glass Ising model [42,54]. One obvious solution is $q^{\pm\pm} = q^{+-} = 0$, the completely disordered system with no vortex proliferation—the familiar insulator phase. It is easy to check that this is indeed a minimum of the effective action S_{eff} . There is also a replica-symmetric but nontrivial solution

$$q_{(\mu\nu)}^{\pm\pm} = Q_0^{\pm\pm} + (1 - Q_0^{\pm\pm}) \delta_{\mu\nu}, \quad (\text{G10})$$

which yields the solution $Q_0^{\pm\pm} = 1 - 1/(\beta\sigma^{\pm\pm})$. However, this solution is unstable and is not observable. A stable nontrivial solution is obtained if the replica symmetry is broken. The ansatz is well known from the spin-glass literature (e.g., Ref. [42]) and has a $\rho \times \rho$ matrix $Q^{\pm\pm}$ on the block-diagonal and the constant zero elsewhere, with

$$\hat{Q}^{\pm\pm} = Q_1^{\pm\pm} + (1 - Q_1^{\pm\pm}) \delta_{\mu\nu}, \quad \mu, \nu = 1, \dots, \rho. \quad (\text{G11})$$

Equation (G9) suggests that $Q_1^{\pm\pm} > 0$ for sufficiently large β , i.e., small L . However, no analytical solution for the elements $Q_1^{\pm\pm}$ exists and they have to be solved for numerically, by plugging in the solution into the effective action and minimizing it. This is an easy task (for chosen values of the parameters and disorder statistics) but we will not do it here as we do not aim at quantitative accuracy anyway; we merely want to sketch the phase diagram. Now if the third field q^{+-} is nonzero, it satisfies the same equation as (G9) just with $\sigma_{++}^2 \mapsto 2\sigma_{+-}^2$. The three combinations of nonzero order parameters correspond to the three familiar phases: $q^{\pm\pm} \neq 0$ is the conductor, $q^{+-} \neq 0$ is the frustrated insulator, and $q^{\pm\pm}, q^{+-} \neq 0$ is the perfect conductor.

The solutions with $\vec{p} \neq 0$ yield new physics. In this case, we have at leading order $\lambda_{\pm\pm} = -2X/(X^2 - Y^2)(p_{\pm})^{-2}, \lambda_{+-} = -2Y/(X^2 - Y^2)(p_+ p_-)^{-1}$, so the effective action is

$$S_{\text{eff}} = -\beta \sum_{\mu=1}^n [J_0^+ (p_{(\mu)}^+)^2 + 2J_0^{+-} p_{(\mu)}^+ p_{(\mu)}^- + J_0^- (p_{(\mu)}^-)^2] - \ln p^+ p^- + O(|q^{\alpha\beta}|^2) + O\left(\frac{|q^{\alpha\beta}|}{|\vec{p}|^2}\right), \quad (\text{G12})$$

giving the saddle-point equation

$$J_0^{\pm} p_{(\mu)}^{\pm} + \frac{J_0^{+-}}{\beta} p_{(\mu)}^{\mp} + (p_{(\mu)}^{\pm})^{-1} = 0, \quad (\text{G13})$$

which easily gives

$$p^{\pm} = s_1 \sqrt{\frac{1}{J_0^{\pm} + s_2 \frac{J_0^{+-}}{\beta} \sqrt{\frac{J_0^{\pm}}{J_0^{\mp}}}}}, \quad (\text{G14})$$

with $s_{1,2} \in \{\pm 1\}$. The solution is the same for every μ and $p_{(\mu)}^{\pm} = (p^{\pm}, p^{\pm}, \dots, p^{\pm})$. Now, depending on the sign of the

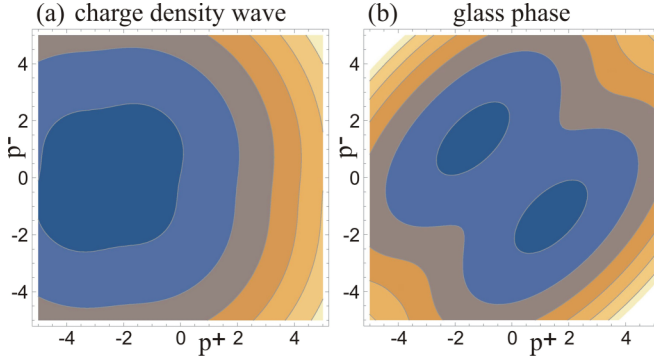


FIG. 23. Free energy (effective action $S_{\text{eff}}^{(\mu)}$) in a given replica subsystem in a photonic lattice with quenched disorder, for the case when the order parameter $p^\pm = \sum_i Q_{i\pm}$ has a nonzero saddle-point solution for the action in a given subsystem (replica). Darker (blue) tones are lower values. The ground states of the system are the local minima. In panel (a) for $J^+ = -J^- = 1$, there is a single local minimum. In case (b), for $J^+ = -J^- = 1$, we see two distinct minima of equal height, for two different nonzero values of p^\pm . Such potential energy landscape fits the description of glassy systems.

determinant $J_0^+ J_0^- - (J_0^{+-})^2$, the solutions for different $s_{1,2}$

2. RG flow equations

The starting Hamiltonian is the same as in (18). Now we will write it out more explicitly, keeping the distance-dependent parts:

$$\beta \mathcal{H}_{\text{eff}} = \beta \sum_{\mu=1}^n \sum_{i,j} (\bar{g}_c \vec{Q}_i^{(\mu)} \cdot \vec{Q}_j^{(\mu)} + \bar{g}'_c \vec{Q}_i^{(\mu)} \times \vec{Q}_j^{(\mu)}) \ln r_{ij} - \frac{\beta^2}{2} \sum_{\mu,v=1}^n \sum_{i,j} Q_{i\alpha}^{(\mu)} Q_{i\beta}^{(v)} \sigma_{\alpha\beta}^2 Q_{j\alpha}^{(\mu)} Q_{j\beta}^{(v)}. \quad (\text{G15})$$

We have denoted the elements of J_0 by $J_0^{++} = J_0^{--} = \bar{g}_c, J_0^{+-} = J_0^{-+} = \bar{g}'_c$ (the bars over the letter remind us that these are disorder-averaged values). The fluctuation of the partition function is completely analogous to the clean case, only it has the additional nonlocal quartic term. It can again be expanded over r_{12} as in (12) but the quartic term contains no small parameter for the power series expansion and has to be kept in the exponential form. Starting from the expression for the fluctuation analogous to the clean case (12), we get

$$\frac{\delta \mathcal{Z}}{\mathcal{Z}} = 1 + \frac{y^4}{4} \sum_{\vec{q}^{(\rho)}, \vec{q}^{(\sigma)}} e^{-\frac{\beta^2}{2} (\vec{q}^{(\rho)}, -\vec{q}^{(\sigma)}, \vec{q}^{(\rho)}, -\vec{q}^{(\sigma)}) + \frac{\beta^2}{2} (\vec{Q}^{(\mu)}, \vec{q}^{(\rho)}, \vec{Q}^{(v)}, \vec{q}^{(\sigma)})} \int dr_{12} r_{12}^3 e^{g \vec{q}^{(\rho)} \cdot \vec{q}^{(\sigma)} + g' \vec{q}^{(\rho)} \times \vec{q}^{(\sigma)}} \times \left[\int drr^2 (g \vec{Q}_1^{(\mu)} \cdot \vec{q}^{(\rho)} + g' \vec{Q}_1^{(\mu)} \times \vec{q}^{(\rho)}) \nabla \ln |\mathbf{R}_1 - \mathbf{r}| + (g \vec{Q}_2^{(\mu)} \cdot \vec{q}^{(\rho)} + g' \vec{Q}_2^{(\mu)} \times \vec{q}^{(\rho)}) \nabla \ln |\mathbf{R}_2 - \mathbf{r}| \right]^2. \quad (\text{G16})$$

We have used the notation

$$(\vec{q}_1, \vec{q}_2, \vec{q}_3, \vec{q}_4) \equiv \sigma_{++}^2 (q_1 + q_3 + q_2 + q_4) + \sigma_{+-}^2 (q_1 + q_3 - q_2 + q_4) + \sigma_{-+}^2 (q_1 - q_3 + q_2 - q_4) + \sigma_{--}^2 (q_1 - q_3 - q_2 - q_4). \quad (\text{G17})$$

Now we trace out the fluctuations first by integrating over r and doing some simple algebra:

$$\frac{\delta \mathcal{Z}}{\mathcal{Z}} = \left[1 + 16y^4 (g + g')^2 \cosh(\beta^2 \sigma_{++}^2 + \beta^2 \sigma_{+-}^2) \cosh(\beta^2 \sigma_{--}^2 + \beta^2 \sigma_{-+}^2) (\vec{Q}_1^{(\mu)} \cdot \vec{Q}_2^{(v)} + \vec{Q}_1^{(\mu)} \times \vec{Q}_2^{(v)}) \ln R_{12} \right] \times \left[1 + 16y^4 (g - g')^2 \cosh(\beta^2 \sigma_{++}^2 - \beta^2 \sigma_{+-}^2) \cosh(\beta^2 \sigma_{--}^2 - \beta^2 \sigma_{-+}^2) (\vec{Q}_1^{(\mu)} \cdot \vec{Q}_2^{(v)} - \vec{Q}_1^{(\mu)} \times \vec{Q}_2^{(v)}) \ln R_{12} \right] \times \left[1 - 2\pi y^4 e^{-\frac{\beta^2}{2} (\sigma_{++}^2 (q_+^{(\mu)} q_+^{(v)})^2 + \sigma_{+-}^2 (q_+^{(\mu)} q_-^{(v)})^2 + \sigma_{-+}^2 (q_-^{(\mu)} q_+^{(v)})^2 + \sigma_{--}^2 (q_-^{(\mu)} q_-^{(v)})^2)} \int drr^{1-\beta} e^{g \vec{q}^{(\mu)} \cdot \vec{q}^{(v)} + g' \vec{q}^{(\mu)} \times \vec{q}^{(v)}} \right]. \quad (\text{G18})$$

The next step is the summation over all possible ± 1 charges of virtual vortices $\vec{q}^{(\mu)}, \vec{q}^{(v)}$ (the two replica indices mean two summations from 1 to n), which requires quite some algebra. The renormalized partition function $\tilde{\mathcal{Z}}^n$ finally gives the RG flow

may be minima or saddle points. In either case, we have a phase with nonzero local charge density, which is the meaning of \vec{p} . If there are multiple minima, we call this phase vortex glass. The reader may argue that true glass should satisfy more stringent conditions and that our phase is not a true glass. Depending on the viewpoint this may well be accepted, and we use the term “glass phase” merely as shorter and more convenient than “phase with power-law correlation decay, no long-range order, and frustrated free energy landscape.” The phase with a single minimum will be called charge density wave, as it has a unique ground-state configuration yielding macroscopically nonzero charge density; i.e., it has a true long-range order. On the other hand, with multiple minima the replica-averaged charge density sums to zero. The landscape, i.e., the effective action of the system for given replica (μ) as a function of p^\pm , is given in Fig. 23 as the density map of the function $S_{\text{eff}}(p^+, p^-)$ dependence for $J_0^+ = -J_0^- = 1$ (glass phase, A) and $J_0^+ = J_0^- = 1$ (charge density wave, B). We see that the glassy phase shows two inequivalent minima in each replica, with $s_1 = -s_2 = \pm 1$ in Eq. (G14), so the total action, the sum of actions of all replica subsystems, can have one and the same value for many configurations, the definition of a highly frustrated system, one of the reasons we dub this phase glass. The charge density wave only has a single minimum for $s_1 = s_2 = 1$.


equations:

$$\begin{aligned}
 \frac{\partial g}{\partial \ell} &= -8\pi(g + g')^2 y^4 \cosh(\beta^2 \sigma_{++}^2 + \beta^2 \sigma_{+-}^2) \cosh(\beta^2 \sigma_{--}^2 + \beta^2 \sigma_{+-}^2) \\
 &\quad - 8\pi(g - g')^2 y^4 \cosh(\beta^2 \sigma_{++}^2 - \beta^2 \sigma_{+-}^2) \cosh(\beta^2 \sigma_{--}^2 - \beta^2 \sigma_{+-}^2), \\
 \frac{\partial g'}{\partial \ell} &= -\pi(g + g')^2 y^4 \cosh(\beta^2 \sigma_{++}^2 + \beta^2 \sigma_{+-}^2) \cosh(\beta^2 \sigma_{--}^2 + \beta^2 \sigma_{+-}^2) \\
 &\quad - \pi(g - g')^2 y^4 \cosh(\beta^2 \sigma_{++}^2 - \beta^2 \sigma_{+-}^2) \cosh(\beta^2 \sigma_{--}^2 - \beta^2 \sigma_{+-}^2), \\
 \frac{\partial y}{\partial \ell} &= 2\pi \left[1 - g - g' - \frac{\beta^2}{4} (\sigma_{++}^2 + 2\sigma_{+-}^2 + \sigma_{--}^2) \right] y, \quad \frac{\partial \sigma_{\alpha\beta}^2}{\partial \ell} = -2\pi \beta^4 \sigma_{\alpha\beta}^4 y^4.
 \end{aligned} \tag{G19}$$

As discussed in the main text, the fixed point must lie either at $y = 0$ or $y \rightarrow \infty$, depending on the magnitude of $g + g' + \beta^2 \sigma^2$. For $y \rightarrow 0$, three clean fixed points remain, which flow to zero disorder: These correspond to PC, FI, and conductor. The disordered fixed point also has $y \rightarrow 0$ but the disorder is nonzero: This is the CDW phase from the mean-field analysis, the dirty analog of the insulator. Finally, when $y \rightarrow \infty$ and nonzero σ^2 at the fixed point, we expect glassy behavior.

-
- [1] M. Cross and P. Hohenberg, Pattern formation outside of equilibrium, *Rev. Mod. Phys.* **65**, 851 (1993).
 - [2] M. I. Rabinovich, A. B. Ezersky, and P. D. Weidman, *The Dynamics of Patterns* (World Scientific, Singapore, 2000).
 - [3] C. Denz, M. Schwab, and C. Weillnau, *Transverse Pattern Formation in Photorefractive Optics* (Springer, Berlin, 2003).
 - [4] L. I. Pismen, *Vortices in Nonlinear Fields* (Oxford University Press, London, 1999).
 - [5] A. Auerbach, *Interacting Electrons and Quantum Magnetism* (Springer, Berlin, 1994).
 - [6] E. Fradkin, *Field Theories of Condensed Matter Systems* (Addison-Wesley, Redwood City, CA, 1991).
 - [7] A. M. Tsvelik, *Quantum Field Theory in Condensed Matter Physics* (Cambridge University Press, Cambridge, UK, 2003).
 - [8] P. Cvitanović, R. Artuso, R. Mainieri, G. Tanner, and G. Vattay, ChaosBook.org version 15 [chaosbook.org].
 - [9] L. Leuzzi, C. Conti, V. Folli, L. Angelani, and G. Ruocco, Phase Diagram and Complexity of Mode-Locked Laser: From Order to Disorder, *Phys. Rev. Lett.* **102**, 083901 (2009).
 - [10] C. Conti and L. Leuzzi, Complexity of waves in nonlinear disordered media, *Phys. Rev. B* **83**, 134204 (2011).
 - [11] F. Antenucci, C. Conti, A. Crisanti, and L. Leuzzi, General Phase Diagram of Aultimodal Ordered and Disordered Lasers in Closed and Open Cavities, *Phys. Rev. Lett.* **114**, 043901 (2015).
 - [12] F. Antenucci, A. Crisanti, and L. Leuzzi, Complex spherical 2 + 4 spin glass: A model for nonlinear optics in random media, *Phys. Rev. A* **91**, 053816 (2015).
 - [13] N. Ghofraniha, I. Viola, F. Di Maria, G. Barbarella, G. Gigli, L. Leuzzi, and C. Conti, Experimental evidence of replica symmetry breaking in random lasers, *Nat. Commun.* **6**, 6058 (2015).
 - [14] M. C. Rechtsman, J. M. Zeuner, Y. Plotnik, Y. Lumer, D. Podolsky, F. Dreisow, S. Nolte, M. Segev, and A. Szameit, Photonic Floquet topological insulators, *Nature (London)* **496**, 196 (2013).
 - [15] Y. Plotnik, M. Rechtsman, D. Song, M. Heinrich, J. Zeuner, S. Nolte, Y. Lumer, N. Malkova, J. Xu, A. Szameit, Z. Chen, and M. Segev, Observation of unconventional edge states in “photonic graphene,” *Nat. Mater.* **13**, 57 (2014).
 - [16] R. Rajaraman, *Solitons and Instantons* (North Holland, Amsterdam, 1989).
 - [17] M. S. Petrović, M. R. Belić, C. Denz, and Yu. S. Kivshar, Counterpropagating optical beams and solitons, *Lasers Photon. Rev.* **5**, 214 (2011).
 - [18] M. I. Rodas-Verde, H. Michinel, and Yu. S. Kivshar, Dynamics of vector solitons and vortices in two-dimensional photonic lattices, *Opt. Lett.* **31**, 607 (2006).
 - [19] T. J. Alexander, A. S. Desyatnikov, and Yu. S. Kivshar, Multivortex solitons in triangular photonic lattices, *Opt. Lett.* **32**, 1293 (2007).
 - [20] B. Terhalle, T. Richter, A. S. Desyatnikov, D. N. Neshev, W. Krolikowski, F. Kaiser, C. Denz, and Yu. S. Kivshar, Observation of Multivortex Solitons in Photonic Lattices, *Phys. Rev. Lett.* **101**, 013903 (2008).
 - [21] D. Y. Tang, H. Zhang, L. M. Zhao, and X. Wu, Observation of High-Order Polarization-Locked Vector Solitons in a Fiber Laser, *Phys. Rev. Lett.* **101**, 153904 (2008).
 - [22] H. Zhang, D. Y. Tang, L. M. Zhao, and X. Wu, Dark pulse emission of a fiber laser, *Phys. Rev. A* **80**, 045803 (2009).
 - [23] V. L. Berezinsky, Destruction of long-range order in one-dimensional and two-dimensional systems having a continuous symmetry group. I Classical systems, *Sov. Phys. JETP* **32**, 493 (1971); J. Kosterlitz and D. Thouless, Ordering, metastability and phase transitions in two-dimensional systems, *J. Phys. C* **6**, 1181 (1973).
 - [24] H. Kleinert, *Superflow and Vortex Lines*, Vol. 1 of Gauge Fields in Condensed Matter (World Scientific, Singapore, 1989).
 - [25] P. W. Anderson, Two new vortex liquids, *Nat. Phys.* **3**, 160 (2007).
 - [26] A. L. Fetter, Rotating trapped Bose-Einstein condensates, *Rev. Mod. Phys.* **81**, 647 (2009).
 - [27] J. D. Sau and S. Sachdev, Mean-field theory of competing orders in metals with antiferromagnetic exchange interactions, *Phys. Rev. B* **89**, 075129 (2014).
 - [28] E. Babaev, J. Carlström, M. Silaev, and J. M. Speight, Type 1.5-superconductivity in multicomponent systems, *Phys. C* **533**, 20 (2017).
 - [29] M. Silaev and E. Babaev, Microscopic derivation of two-component Ginzburg-Landau model and conditions of its applicability in two-band systems, *Phys. Rev. B* **85**, 134514 (2012).
 - [30] X. Ma, R. Driben, B. Malomed, T. Meoer, and S. Schumacher, Two-dimensional symbiotic solitons and vortices in binary

- condensates with attractive cross-species interaction, *Nat. Sci. Rep.* **6**, 34847 (2016).
- [31] M. Petrović, D. Jović, M. Belić, J. Schröder, P. Jander and C. Denz, Two Dimensional Counterpropagating Spatial Solitons in Photorefractive Crystals, *Phys. Rev. Lett* **95**, 053901 (2005).
- [32] D. M. Jović, M. S. Petrović, and M. R. Belić, Counterpropagating pattern dynamics: From narrow to broad beams, *Opt. Commun.* **281**, 2291 (2008).
- [33] M. S. Petrović, D. M. Jović, M. S. Belić, and S. Prvanović, Angular momentum transfer in optically induced photonic lattices, *Phys. Rev. A* **76**, 023820 (2007).
- [34] M. Petrović, D. Träger, A. Strinić, M. Belić, J. Schröder, and C. Denz, Solitonic lattices in photorefractive crystals, *Phys. Rev. E* **68**, 055601(R) (2003).
- [35] M. S. Petrović, Counterpropagating mutually incoherent vortex-induced rotating structures in optical photonic lattices, *Opt. Exp.* **14**, 9415 (2006).
- [36] B. Terhalle, T. Richter, K. Law, D. Görries, P. Rose, T. Alexander, P. Kevrekidis, A. Desyatnikov, W. Krolikowski, F. Kaiser, C. Denz, and Yu. S. Kivshar, Observation of double-charge discrete vortex solitons in hexagonal photonic lattices, *Phys. Rev. A* **79**, 043821 (2009).
- [37] D. M. Jović, S. Prvanović, R. D. Jovanović, and M. S. Petrović, Gaussian induced rotation in periodic photonic lattices, *Opt. Lett.* **32**, 1857 (2007).
- [38] S. Sachdev, *Quantum Phase Transitions* (Cambridge University Press, Cambridge, UK, 1999).
- [39] N. Hasselmann, A. H. C. Neto, and C. M. Smith, Spin-glass phase of cuprates, *Phys. Rev. B* **69**, 014424 (2003).
- [40] V. Juričić, L. Benfatto, A. O. Caldeira, and C. Morais Smith, Dynamics of Topological Defects in a Spiral: A Scenario for the Spin-Glass Phase of Cuprates, *Phys. Rev. Lett* **92**, 137202 (2004).
- [41] M. Mezard, G. Parisi, and M. A. Virasoro, *Spin Glass Theory and Beyond* (World Scientific, Singapore, 1987).
- [42] T. Castellani and A. Cavagna, Spin-glass theory for pedestrians, *J. Stat. Mech.* (2005) P05012.
- [43] A. Perret, Z. Ristivojevic, P. Le Doussal, G. Schehr, and K. Wiese, Super-Rough Glassy Phase of the Random Field XY Model in Two Dimensions, *Phys. Rev. Lett.* **109**, 157205 (2012).
- [44] C. A. Bolle, V. Aksyuk, F. Pardo, P. L. Gammel, E. Zeldov, E. Bucher, R. Boie, D. J. Bishop, and D. R. Nelson, Observation of mesoscopic vortex physics using micromechanical oscillators, *Nature (London)* **399**, 43 (1999).
- [45] S. Bogner, T. Emig, A. Taha, and C. Zeng, Test of replica theory: Thermodynamics of two-dimensional model systems with quenched disorder, *Phys. Rev. B* **69**, 104420 (2004).
- [46] A. Crisanti and L. Leuzzi, Spherical $2 + p$ glass model: An analytically solvable model with a glass-to-glass transition, *Phys. Rev. B* **73**, 014412 (2006).
- [47] V. Juričić, L. Benfatto, A. O. Caldeira, and C. Morais Smith, Dissipative dynamics of topological defects in frustrated Heisenberg spin systems, *Phys. Rev. B* **71**, 064421 (2005).
- [48] L. Benfatto, M. Silva-Neto, V. Juričić, and C. Morais Smith, Derivation of the generalized nonlinear sigma model in the presence of the Dzyaloshinskii Moriya interaction, *Phys. B (Amsterdam, Neth.)* **378**, 449 (2006).
- [49] V. Juričić, M. B. Silva-Neto, and C. Morais Smith, Lightly Doped as a Lifshitz Helimagnet, *Phys. Rev. Lett.* **96**, 077004 (2006).
- [50] A. Gordon and B. Fisher, Phase transition theory of pulse formation in passively mode-locked lasers with dissipation and Kerr nonlinearity, *Opt. Commun.* **223**, 151 (2003).
- [51] A. Gordon and B. Fischer, Phase Transition Theory of Many-Mode Ordering and Pulse Formation in Lasers, *Phys. Rev. Lett* **89**, 103901 (2002).
- [52] N. D. Mermin, The topological theory of defects in ordered media, *Rev. Mod. Phys.* **51**, 591 (1979).
- [53] M. Silaev and E. G. Babaev, Microscopic theory of type-1.5 superconductivity in multiband systems, *Phys. Rev. B* **84**, 094515 (2011).
- [54] J. Cardy, *Scaling and Renormalization in Statistical Physics* (Cambridge University Press, Cambridge, UK, 1996).
- [55] J. L. Cardy and S. Ostlund, Random symmetry-breaking fields and the XY model, *Phys. Rev. B* **25**, 6899 (1982).
- [56] M. Castellana and G. Parisi, Non-perturbative effects in spin glasses, *Nat. Sci. Rep.* **5**, 8697 (2015).
- [57] D. S. Fisher and D. A. Huse, Equilibrium behavior of the spin-glass ordered phase, *Phys. Rev. B* **38**, 386 (1988).
- [58] J. Zaanen, Quantum phase transitions in cuprates: Stripes and antiferromagnetic supersolids, *Phys. C (Amsterdam, Neth.)* **317**, 217 (1999).
- [59] O. Gat, A. Gordon, and B. Fischer, Solution of a statistical mechanics model for pulse formation in lasers, *Phys. Rev. E* **70**, 046108 (2004).
- [60] R. Weill, A. Rosen, A. Gordon, O. Gat, and B. Fischer, Critical Behavior of Light in Mode-Locked Lasers, *Phys. Rev. Lett* **95**, 013903 (2005).
- [61] O. Sandfuchs, F. Kaiser, and M. R. Belić, Dynamics of transverse waves and zigzag instabilities in photorefractive two-wave mixing with a feedback mirror, *J. Opt. Soc. Am. B* **18**, 505 (2001).
- [62] O. Sandfuchs, F. Kaiser, and M. R. Belić, Self-organization and Fourier selection of optical patterns in a nonlinear photorefractive feedback system, *Phys. Rev. A* **64**, 063809 (2001).
- [63] V. I. Arnol'd, V. S. Afraimovich, Yu. S. Il'yashenko, and L. P. Shil'nikov, *Bifurcation Theory and Catastrophe Theory* (Springer-Verlag, Berlin, 1994).

Spontaneous isotropy breaking for vortices in nonlinear left-handed metamaterialsTrivko Kukolj ^{*}*Scientific Computing Laboratory, Center for the Study of Complex Systems, Institute of Physics Belgrade, University of Belgrade, Serbia and Department of Physics, Faculty of Sciences, University of Novi Sad, Trg Dositeja Obradovića 4, Novi Sad, Serbia*Mihailo Čubrović [†]*Scientific Computing Laboratory, Center for the Study of Complex Systems, Institute of Physics Belgrade, University of Belgrade, Serbia*

(Received 15 July 2019; revised manuscript received 11 October 2019; published 25 November 2019)

We explore numerically and analytically the pattern formation and symmetry breaking of beams propagating through left-handed (negative) nonlinear metamaterials. When the input beam is a vortex with topological charge (winding number) Q , the initially circular (isotropic) beam acquires the symmetry of a polygon with Q , $2Q$, or $3Q$ sides, depending on the details of the response functions of the material. Within an effective field-theory model, this phenomenon turns out to be a case of spontaneous dynamical symmetry breaking described by a Landau-Ginzburg functional. Complex nonlinear dependence of the magnetic permittivity on the magnetic field of the beam plays a central role, as it introduces branch cuts in the mean-field solution, and permutations among different branches give rise to discrete symmetries of the patterns. By considering loop corrections in the effective Landau-Ginzburg field theory we obtain reasonably accurate predictions of the numerical results.

DOI: [10.1103/PhysRevA.100.053853](https://doi.org/10.1103/PhysRevA.100.053853)**I. INTRODUCTION**

The idea of a material with negative refraction index was first considered long before it could be realized in experiment, in the now famous paper by Veselago [1], in 1968. He considered a material with negative electric permeability ϵ and magnetic permittivity μ , and predicted a number of interesting properties in such systems, among them negative refraction. Only much later did it become possible to combine elements with negative ϵ and negative μ at a microscopic level, as a composite metamaterial. First experimental realizations were reported in [2,3]. Negativity, or left-handedness, is typically only achieved in a narrow frequency range, close to the resonant frequency of the conductive elements of the metamaterial. This was the original motivation for studying nonlinear effects in these systems. Nonlinearities can be strengthened by appropriate design at the microscopic level. The study of nonlinear phenomena in metamaterials started with [4]. This has become a broad and important field in metamaterials research [5]. Nonlinear phenomena like solitons [6,7], nonlinear surface waves [8], modulational instability [9,10], and ultrashort pulses [11] were observed. Other work in left-handed metamaterials relevant for our paper includes, among others, [12–20]. We have no intention of being exhaustive in this short review of the literature; we merely mention the results we have directly used or found particularly inspiring.

The focus of our paper is the dynamics of symmetry breaking in intensity patterns of electromagnetic waves propagating through a left-handed nonlinear metamaterial. Numerical solutions of the equations of motion reveal that circular

(usually Gaussian) input beams turn into polygonal patterns, with some discrete symmetry. This fits the textbook notion of symmetry breaking, more specifically dynamical symmetry breaking. The general theory of dynamical criticality is by now well developed [21] and has been applied to numerous systems [22]. In [22], a systematic theory of isotropy-breaking transition is presented, though mainly for periodic and quasiperiodic structures (convection in fluids, fluctuations in quasicrystals). The basic mechanism is that the system develops momentum eigenmodes of a fixed module but with multiple discrete directions on the sphere $|\mathbf{k}| = \text{const}$ in momentum space. In nonlinear negative materials, the situation is complicated by the strong frequency dependence of the magnetic permittivity but the same basic logic remains. At a fundamental level, this situation can be understood from the viewpoint of a spatially nonuniform Landau-Ginzburg theory. Quantitative accuracy is, however, hard to achieve; this requires cumbersome perturbative calculations. Ultimately, numerical work is the best way to describe the patterns in detail; they look like polygons or, occasionally, necklaces, with C_{3Q} , C_{2Q} , or C_Q symmetry, depending on the parameter regime; here, Q is the topological charge of the beam, a property we will discuss in detail in the next paragraph. The paper [10] is very important in this context: it starts from the model derived in [9] and studies mainly necklace configurations, which consist of discrete beads (spots of high intensity) distributed more or less uniformly along a circle. The authors find the same C_{3Q} symmetry that we see. Our goal is to gain a detailed understanding of the phenomenon, and move beyond single beams toward collective behavior and interactions.

We have chosen to study this phenomenon on vortices, topologically nontrivial solutions where the phase of the

^{*}trivko98@gmail.com[†]mcubrovic@gmail.com

complex electric and magnetic field winds one or more times along a closed line encircling the vortex core. Vortices appear in many systems described by a complex field, i.e., a field with $U(1)$ phase invariance [23,24]. In optics, this is just the complex beam envelope of the electric and magnetic field. The phase of any complex wave function or field can wind along some closed line around a defect, forming a vortex. Famously, vortices may coexist with the superconducting order [$U(1)$ symmetry breaking] in type-II superconductors or they may exist only in the normal phase, upon destroying the superconductivity (type I). Pattern-forming systems like fluids and soft matter often have rich vortex dynamics [22]. Other examples of vortex matter in nature arise in liquid helium [25], Bose-Einstein condensates [26], and magnetic systems [27]. In two spatial dimensions, interactions among the vortices lead to a vortex unbinding phase transition of infinite order found by Berezinsky, Kosterlitz, and Thouless for the planar XY model [28]. We study a three-dimensional metamaterial but with an elongated geometry, so we treat it as a $2 + 1$ -dimensional system (the x and y coordinates are spatial dimensions and the z direction has the formal role of time). We therefore have a similar situation to the XY model but with different equations of motion and different phenomena.

In addition to direct numerical and analytical study of the equations of motion, we also propose an effective field-theory Lagrangian which gives slightly different equations but captures the key properties of the system. The Lagrangian form makes it easier to understand some of the phenomenology we find in numerical simulations; the foundations of the symmetry breaking are obtained from this model in a natural way. Numerical work is done with original equations of motion, as they are directly grounded in the microscopic physics. The Lagrangian is just a phenomenological tool to facilitate the theoretical understanding. It is difficult (and perhaps impossible) to package the exact original equations in a Lagrangian form because the system is strongly nonlinear *and* dissipative. Dissipative systems can be encapsulated in a Lagrangian (our Lagrangian is also dissipative) but with some limitations, and there is certainly no general method to write down a Lagrangian for a broad class of dissipative systems.

The structure of the paper is the following. In the next section we describe the model of a nonlinear left-handed metamaterial, following closely the wave propagation equations used in previous research, e.g., in [4,6,7] and others, which correspond to a specific experimentally realizable metamaterial. We also formulate and motivate the field-theory model of the system. In the third section, we describe our numerical findings, above all the anisotropy of the intensity patterns. The fourth section offers the theoretical explanation for the patterns: first by a direct approximate solution of the propagation equations, and then also from field theory, which makes the physics of the symmetry breaking particularly clear. In the fifth section we briefly discuss how to check our predictions in experiment and how prominent the effects of symmetry breaking are compared to other possible instabilities in realistic metamaterials. The last section sums up the conclusions. We have included some long calculations in the Appendices.

II. WAVE EQUATIONS IN A NONLINEAR LEFT-HANDED METAMATERIAL

We adopt the model of [4,7] to describe a left-handed metamaterial with a nonlinear response. Microscopically, the material is realized as a lattice of split-ring resonators and wires. In the terahertz range, this is an experimentally well-studied system [3]. In [6], a detailed microscopic derivation is given, starting from the current transport equations in the resonator-wire system. The outcome is a nonlinearity similar to that postulated phenomenologically in [4]. We adopt essentially the same model, described by the electric permeability ϵ and the magnetic permittivity μ :

$$\epsilon(E, E^\dagger) \equiv \epsilon(|E|^2) = (\epsilon_{D0} + \alpha|E|^2) \left(1 - \frac{\omega_0^2}{\omega(\omega + i\gamma)} \right), \quad (1)$$

$$\mu(H, H^\dagger) \equiv \mu(|H|^2) = 1 + \frac{F\omega^2}{\omega_{0NL}^2(|H|^2) - \omega^2 + i\Gamma\omega}, \quad (2)$$

with $\alpha = 1$ or -1 for self-focusing or self-defocusing nonlinearity, respectively. Frequency is denoted by ω and ϵ_{D0} is the linear part of the permittivity. By F , γ , and Γ we denote the filling factor of the material and the electric and magnetic damping coefficients. Equations (1) and (2) allow us to model also the real (lossless) dielectric response by putting $\gamma = 0$. For the magnetic field, the permittivity will in general stay complex even for $\Gamma = 0$, as the nonlinear frequency of the resonator rings ω_{0NL} can always have a nonzero imaginary part. This frequency is related to the magnetic field through the relation ($X \equiv \omega_{0NL}/\omega_0$):

$$|H|^2 = \alpha A^2 \frac{(1 - X^2)[(X^2 - \Omega^2)^2 + \Omega^2\gamma^2]}{X^6}, \quad (3)$$

where $\Omega \equiv \omega/\omega_0$, ω_0 is the eigenfrequency of the rings, and A is a parameter which can be derived microscopically [4,6,7]; for our purposes, it can be treated just as a phenomenological parameter. This cubic equation yields three branches for ω_{0NL}^2 . All these branches are physical and correspond to different possible nonlinear oscillations [7]. Now the equations of motion are just the Maxwell equations in a medium described by (1) and (2), in the approximation of slowly changing beam envelopes. We assume an elongated (cylindrical or parallelepipedal) slab of metamaterial, so we can employ the paraxial beam approximation (e.g., [29]). The beam is initially collimated along the longitudinal axis z and focuses or defocuses slowly in the transverse x - y plane due to the nonlinearity of the material. The electric and magnetic field $\hat{E}(t; x, y, z)$ and $\hat{H}(t; x, y, z)$ are directed along the z axis. From now on, the speed of light is put to unity, $c = 1$. All the steps in deriving the nonlinear Schrödinger-like equation are well known so we merely state the final result here, which is quite close to the equations used in [13] in $1 + 1$ dimension, or the equations found in [9–11]. Full derivation can be found in Appendix A. The equations of motion turn out to be

$$-\frac{i}{b}\partial_z E = \nabla_\perp^2 E + [\omega^2\epsilon(|E|^2)\mu(|H|^2) - k^2]E - \frac{\nabla_\perp\mu(|H|^2)}{\mu(|H|^2)}\nabla_\perp E - i\frac{\partial_z\mu(|H|^2)}{2\mu(|H|^2)}E, \quad (4)$$

$$-\frac{i}{b}\partial_z H = \nabla_\perp^2 H + [\omega^2\epsilon(|E|^2)\mu(|H|^2) - k^2]H. \quad (5)$$

Here, $\nabla_{\perp} \equiv (\partial_x, \partial_y)$ is the nabla operator in the transverse plane, k is the wave vector along the z direction, and b is the characteristic propagation length along the z axis. Equations of motion (4) and (5) together with the equations (1) and (3) for the permittivities contain the following five parameters: ϵ_{D0} , F , Γ , γ , and ω_0 . Realistic values for all the parameters are discussed in [7]. The natural length scale of the model is dominated by the $1/\omega_0$ scale. Dimensional analysis of the terms on the right-hand side of (4) determines the length scale b in (4) and (5) as $b \sim 1/\omega_0$. Both in analytical and in numerical calculations, we express the transverse coordinates (x, y) in millimeters but the longitudinal coordinate z is often stated in units of b . This is because the length scales of all patterns in the transverse plane are similar whereas the propagation lengths along z can vary by an order of magnitude as γ and Ω are varied, so it is more natural to express them in terms of the characteristic distance b .

A. field-theoretical model

For some theoretical considerations it is useful to formulate a Lagrangian (gradient) model which captures the essential features of the equations of motion (4) and (5). As it often happens in studies of complex nonlinear pattern-forming systems, we cannot easily write the original equations in such a form. Instead, we construct a field theory which yields equations of motion somewhat different from the original ones but which still give the same phenomenology, and are able to explain the results of numerical calculations with the equations (4) and (5).

Let us think what such a field theory would look like. The terms with the gradient of magnetic permittivity obviously introduce dissipation, which physically originates from the losses in the inductive rings of the metamaterial. In general, dissipative systems do not have a Lagrangian, although a number of generalized Lagrangian approaches exist for dissipative systems: either with more general functional forms of the Lagrangian, or with a dissipative function in addition to the Lagrangian, or with extra degrees of freedom [30,31]. We will take the first, most conventional of the three approaches: we will consider a conventional Lagrangian (no dissipative function, no extra degrees of freedom) which gives slightly generalized equations of motion compared to (4) and (5), with dissipative terms for both electric and magnetic fields coming from the complex terms in the effective potential. The effective action reads

$$\begin{aligned} \mathcal{L} &= \mathcal{L}_E + \mathcal{L}_H, \\ \mathcal{L}_E &= \frac{i}{2\mu(|H|^2)} (E \partial_z E^\dagger - E^\dagger \partial_z E) \\ &\quad + \frac{|\nabla_{\perp} E|^2}{\mu(|H|^2)} + \frac{k^2 |E|^2}{\mu(|H|^2)} - \omega^2 \epsilon(|E|^2) |E|^2, \\ \mathcal{L}_H &= \frac{i}{2\epsilon(|E|^2)} (H \partial_z H^\dagger - H^\dagger \partial_z H) \\ &\quad + \frac{|\nabla_{\perp} H|^2}{\epsilon(|E|^2)} + \frac{k^2 |H|^2}{\epsilon(|E|^2)} - \omega^2 \int_0^{HH^\dagger} dx \mu(x). \end{aligned} \quad (6)$$

The last term in \mathcal{L}_E equals $-\omega^2 \int_0^{EE^\dagger} dx \epsilon(x)$, analogously to the corresponding term in \mathcal{L}_H , but since ϵ is polynomial in

$E^\dagger E$ the integral can be solved explicitly. Now (6) gives the equations of motion:

$$-\frac{i}{b} \partial_z E = \nabla_{\perp}^2 E + [\epsilon(|E|^2) \mu(|H|^2) - k^2] E - \frac{i \partial_z \mu(|H|^2)}{\mu(|H|^2)} E - \frac{\nabla_{\perp} \mu(|H|^2)}{\mu(|H|^2)} \nabla_{\perp} E - \Phi_H, \quad (7)$$

$$-\frac{i}{b} \partial_z H = \nabla_{\perp}^2 H + [\epsilon(|E|^2) \mu(|H|^2) - k^2] H - \frac{i \partial_z \epsilon(|E|^2)}{\epsilon(|E|^2)} H - \frac{\nabla_{\perp} \epsilon(|E|^2)}{\epsilon(|E|^2)} \nabla_{\perp} H - \Phi_E, \quad (8)$$

where $\Phi_{E,H}$ are related to the fluxes of the electric and magnetic field (prime denotes the derivative of ϵ and μ with respect to their arguments $E^\dagger E$ and $H^\dagger H$):

$$\begin{aligned} \Phi_H &= \frac{\epsilon'(|E|^2)}{\epsilon^2(|E|^2)} \left(\frac{i}{2} (H \partial_z H^\dagger - H^\dagger \partial_z H) \right. \\ &\quad \left. + |\nabla_{\perp} H|^2 + k^2 |H|^2 \right), \end{aligned} \quad (9)$$

$$\begin{aligned} \Phi_E &= \frac{\mu'(|H|^2)}{\mu^2(|H|^2)} \left(\frac{i}{2} (E \partial_z E^\dagger - E^\dagger \partial_z E) \right. \\ &\quad \left. + |\nabla_{\perp} E|^2 + k^2 |E|^2 \right). \end{aligned} \quad (10)$$

These are the extra terms compared to the physical equations (4) and (5).¹ Inserting $\partial_z E^\pm$ from the equations of motion (7) and (8) into the above we derive

$$\Phi_E = \frac{\mu'}{\mu} \nabla_{\perp} \left(\frac{E \nabla_{\perp} E^\dagger - E^\dagger \nabla_{\perp} E}{\mu} \right), \quad (11)$$

and analogously for Φ_H , with $\epsilon \leftrightarrow \mu$, $E \leftrightarrow H$. This term is proportional to a total derivative, and is therefore related to the flux $(E \nabla_{\perp} E^\dagger - E^\dagger \nabla_{\perp} E)/\mu$. For slowly changing ϵ and μ , which is often the case in our system (i.e., for ϵ' , $\mu' \ll \epsilon$, μ), this term is small, which partly justifies the choice (6) for the Lagrangian. But the ultimate justification, as it frequently happens, is that *a posteriori* we will find that this model is able to explain the features observed in the numerics. Therefore we will not try to interpret the term (11) in detail.

III. GEOMETRY AND STABILITY OF VORTICES

We will now sum up our numerical results which demonstrate the breaking of the circular symmetry of the vortex beams and their decay during the propagation. We always start from a Gaussian input beam with a topological charge Q , of the form $E(r, \phi; z=0) = E_0 \times e^{-r^2/2\sigma^2} e^{iQ\phi}$ and analogously for the magnetic field, with amplitude H_0 but with the same vortex charge Q . Therefore, we always give an exact vortex as an input. The parameters of the model were chosen so that the permittivities ϵ and μ , given by (1) and (2), respectively, are of order unity. This serves to limit the dissipative effects, so that the propagation along the longitudinal direction can be clearly observed. Same phenomena are found for arbitrary values of

¹The dissipative term proportional to $\nabla_{\perp} H$ in (8) is also absent in the original equations, but that one is easy to interpret: we make both \mathcal{L}_E and \mathcal{L}_H complex, so both fields have dissipative dynamics.

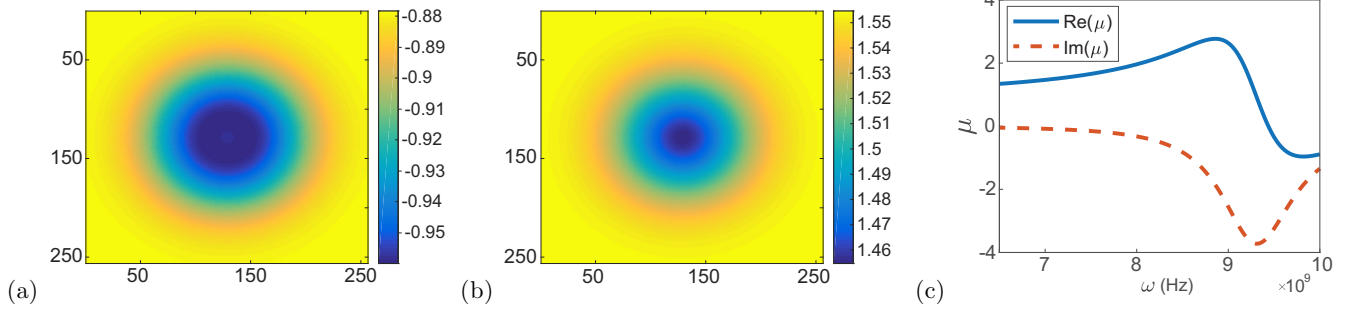


FIG. 1. The radial profile of μ for a left-handed medium (a) and a right-handed medium (b), for a vortex of charge $Q = 1$. The profiles are radially symmetric in accordance with the fact that μ depends strictly on the magnitude of the magnetic-field vector $|H|^2$. The real (blue) and imaginary (red) values of the complex permeability μ vs the frequency of the beam ω are displayed in (c). For frequencies higher than the eigenfrequency of the resonator rings ω_0 , the real part of the permeability is negative, essentially yielding a left-handed medium. The figure is made for dissipative ϵ ; for lossless ϵ the behavior is similar.

ϵ and μ but on a different length scale. We do not aim at a stamp-collecting exhaustive description of patterns for all possible parameter values, so we will focus on just a few relevant cases. We are mainly interested in left-handed materials ($\epsilon, \mu < 0$) and how they compare to right-handed ones, so for the dielectric constant we always choose the self-defocusing Kerr nonlinearity ($\alpha = -1$) with a linear part $\epsilon_{D0} = 12.8$, which has both a left-handed and a right-handed regime. To check the effects of dissipation, we either adopt $\gamma = 0$ in (1), i.e., the lossless case, or we tune γ so that $\omega_0^2/(\omega^2 + i\gamma\omega) = 1/2$. In other words, we impose either $\text{Im}\epsilon = 0$ or $\text{Im}\epsilon = \text{Re}\epsilon$. This is for simplicity and to avoid probing a huge parameter space for all possible γ values; from now on we will call these cases simply lossless ϵ and dissipative ϵ . The filling factor is $F = 0.4$ and the magnetic dampening coefficient is $\Gamma = 10^9$ Hz; these values are kept fixed in all calculations. Numerical calculations are performed with an operator split algorithm described in detail in the Appendices of [32].

The nonlinear frequency of the oscillator rings is obtained as a solution to (3). Of the three branches of the solution, we take the one that yields a negative real value of μ for $\omega > \omega_0$ (Fig. 1). We have freely taken $\omega = 9.8 \times 10^9$ Hz to represent a left-handed medium, and $\omega = 7.0 \times 10^9$ Hz to represent a right-handed medium. The transverse profiles are displayed in Fig. 1. We see there is a well-defined left-handed regime.

Now we discuss the transverse intensity profile for different initial beam configurations, with vortex input beams as explained in the beginning. We observe the following features.

(1) Circular symmetry of the vortex input always breaks down to a discrete group.

(a) In a dissipative left-handed medium, the discrete symmetry group for a vortex of charge Q is C_{3Q} , before breaking down to simple C_2 axial symmetry at longer distances [Fig. 2(a)].

(b) In a dissipative right-handed medium, the discrete symmetry group for a vortex of charge Q is C_{2Q} , before breaking to C_Q and then to C_2 axial symmetry at longer distances [Fig. 2(b)].

(c) In a lossless left-handed medium, the discrete symmetry group for a vortex of charge Q is C_{3Q} for very short distances, before quickly breaking down to C_Q and finally C_2 [Fig. 2(c)].

(d) In a lossless right-handed medium, the discrete symmetry group for a vortex of charge Q is C_{2Q} , before breaking to simple C_2 axial symmetry at longer distances [Fig. 2(d)].

(2) Vortices decay approximately exponentially as they propagate along the longitudinal axis. Figure 4 shows the intensity of the beam across the z axis, for various regimes. At early z values, total intensity may behave nonmonotonically and nonuniversally but on longer scales it decays exponentially. For different charges, the intensity curves collapse to a unique exponential function at large z . As could be expected, lossless and dissipative cases differ somewhat and collapse to different curves.

The bottom line is that there is a vocabulary of patterns with C_Q , C_{2Q} , and C_{3Q} symmetries. One of them dominates in each case (left and right handed, dissipative and lossless) but at longer propagation distances the symmetry can change, before the intensity drops to near zero from dissipation. The final stadium of C_2 symmetry is only seen at very low intensities, so it might be practically unobservable in experiment; that is why we say the vocabulary only has three possible patterns, excluding C_2 .

The findings above are further corroborated by Fig. 3, which shows the vortices with different charges $Q = 1, 2$, and 3 in the same regime [dissipative left handed (a) and lossless left handed (b)]. As claimed above, the symmetry is C_{3Q} in panel (a), and (except at small z values) C_Q in panel (b). Finally, it is obvious that there is some mixing of patterns: the polygons are never exactly regular, so the groups C_n are certainly not exact symmetries; we use the C_n nomenclature merely for convenience.

One interesting phenomenon in Fig. 2(c) is that the pattern rotates along the z axis. This can be understood as excitation of multiple angular modes (of the form e^{ilz} with various l numbers) as the beam travels along the sample. This is a well-known consequence of nonlinear terms [5,29] and typically depends on the relative strength of nonlinear mode interactions compared to energy density $|E|^2 + |H|^2$ and dissipation γ . We will not explore it in quantitative detail in this paper as it is only tangential to our main topic of radial symmetry breaking; as one can see, the structure remains the same; just the orientation changes.

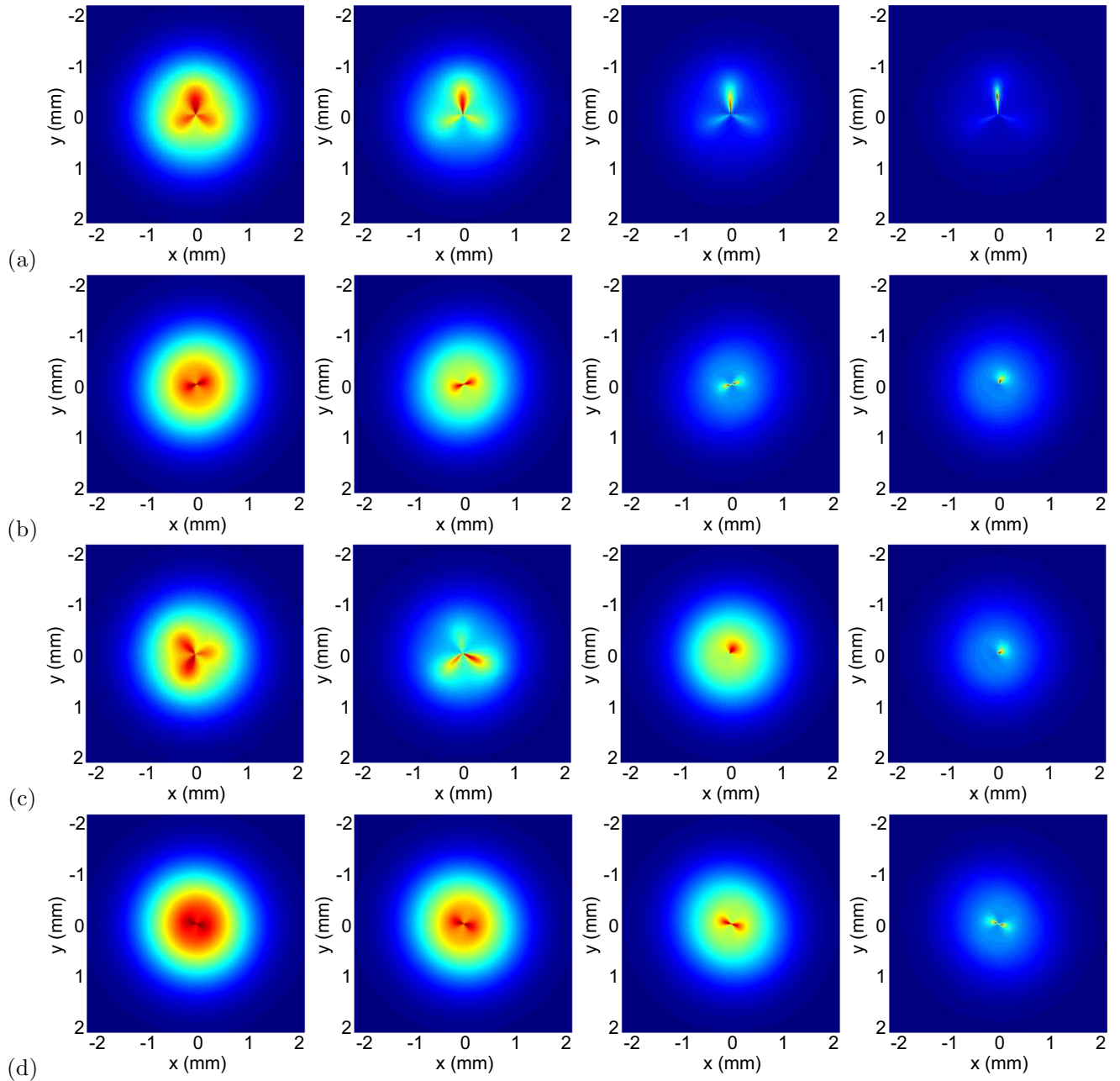


FIG. 2. The patterns for a $Q = 1$ vortex, in a left- and right-handed dissipative medium [(a) and (b), respectively], and in a left- and right-handed lossless medium [(c) and (d), respectively], at longitudinal slices $z = 2b, 4b, 6b,$ and $8b$, showing the $C_{3Q}, C_{2Q}, C_{3Q}/C_Q,$ and C_{2Q} regimes. The remaining parameters are defined in the text at the beginning of this section.

One might rightly worry that the initial conditions which contain a vortex in both electric and magnetic field are not very realistic, as in most materials the electric field dominates the optical response. Therefore, in experimental practice, one typically prepares a vortex in the electric field making use of phase masks or some other method, and the initial magnetic-field distribution is completely analytic. In Appendix B we repeat the calculations from Fig. 3 and show that the outcome is the same, including the vocabulary of patterns and their C_n shapes. Therefore, the E - H symmetric ansatz is merely a matter of convenience, and the realistic regime where $|H| \ll |E|$ is in fact covered by our paper.

Figure 4 shows that at long times the decay of intensity is universal for given dielectric dampening coefficient γ , which suggests the main mechanism of dissipation is in fact the radiative loss. This is because we deliberately chose ϵ and μ with small imaginary parts (for ϵ it can also be zero), so the losses in the medium are not so important when it comes to total energy (they are still important for being nonlinear and influencing the patterns). One important difference between the lossless medium (black and blue symbols in Fig. 4) and the dissipative medium (red, magenta) is that the former has a short interval of growing intensity, before reaching the universal regime of radiative decay. The physical reason is

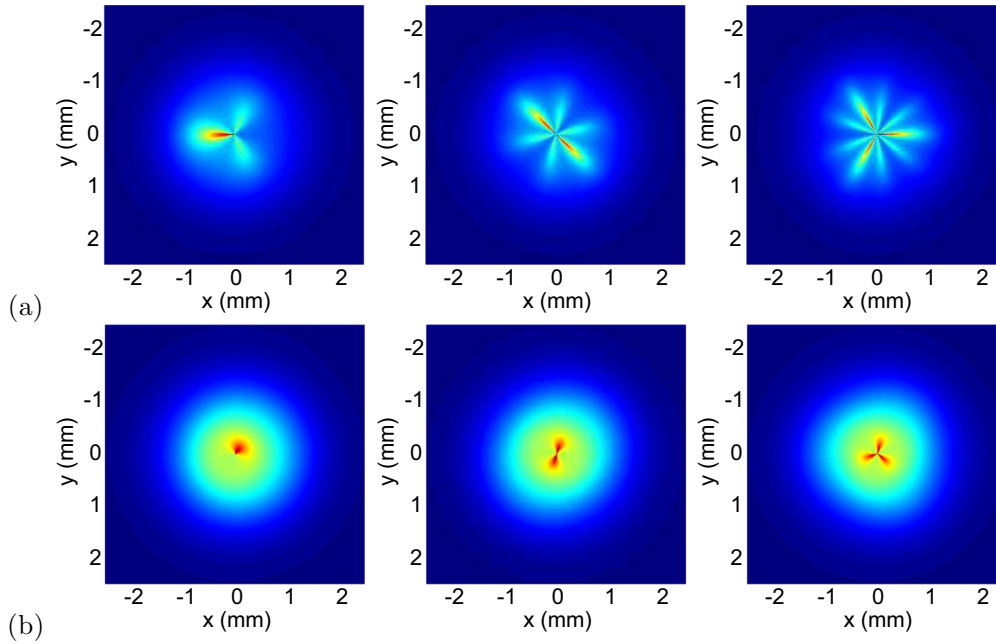


FIG. 3. The patterns for $Q = 1, 2,$ and 3 vortices (left to right), in a dissipative (a) and lossless (b) left-handed metamaterial. The behavior for three different charges confirms the previous conclusions for the type of symmetry encountered. All parameters except for the vortex charge are the same as for Fig. 2. The propagation distance is $z = 5b$ in (a) and $z = 8b$ in (b).

that the polarization, i.e., the rearrangement of charges in the self-defocusing metamaterial, reduces the overall electrostatic potential energy of the medium, and this energy becomes available to the beam, increasing its intensity. Clearly, once the radiative losses overcome the total potential energy available, the intensity decays. The growth is clearly a transient effect which cannot persist for long z intervals. A formal way to understand this is that the nonconservation of energy is encoded by the last term in (4), which can have a positive or

negative imaginary part depending on the sign of $\partial_z \mu / \mu$. At large values of z , we expect to enter a universal regime where this sign is constant, because the radiation loss dominates over nonlinearities and the exchange of energy between the beam and the medium; this is the universal decay regime in the figure.

IV. THE THEORY OF VORTEX EVOLUTION

The phenomenology described in the previous section can be understood on several levels. At the crudest level, we can introduce a variable-separation ansatz in the equations of motion and then linearize them in the amplitude (but not in the phase). This picture explains the C_{2Q} patterns, but not the C_{3Q} and C_Q regimes. It also does not explain the instabilities, that is, the changes and disappearance of patterns during the z propagation. For the full picture it is necessary to take into account the nonlinear effects through the loop corrections, i.e., to move perturbatively beyond the amplitude-linearized solution. A qualitative insight of the symmetry breaking can, however, be obtained also in a simpler and more elegant way, directly from the symmetry analysis of the model Lagrangian (6). Therefore, after finishing the amplitude-linearized analysis and the loop corrections from nonlinearity, we will obtain the same results from a unified mean-field treatment of the (nonlinear) model Lagrangian.

A note on terminology is in order. The solutions we find are not the textbook type of vortex with phase dependence solely of the type $e^{iQ\phi}$; rather, the dependence on the phase is more complicated, i.e., the phase is doing more than just the winding, but it is still true that the circulation of the phase around some point (the location of the vortex core) is an integer—the topological charge of the vortex. Such solutions are sometimes called spirals [22] whereas the term

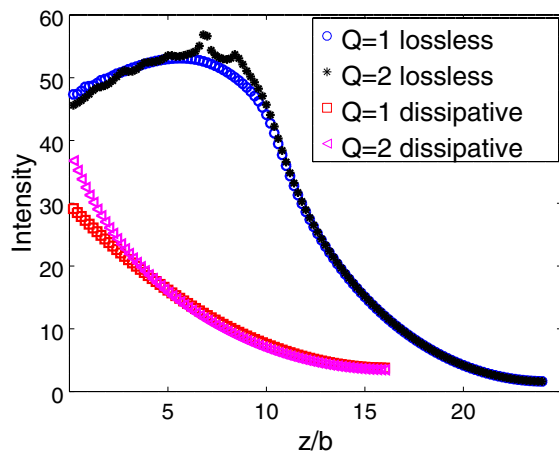


FIG. 4. Decay of the total intensity $I = \int dx \int dy (E^2 + H^2)$ in computational units for $Q = 1$ and 2 , for a lossless (blue circles, black stars) and dissipative (red squares, magenta triangles) left-handed material. At early times the behavior is complicated and nonuniversal but at late times it collapses to an exponential curve. This is expected when loss through radiation dominates. The oscillatory features of the $Q = 2$ lossless case (black) are likely due to finite numerical resolution.

“vortex” is reserved for the simple winding-phase solutions. We nevertheless stick to the widespread term “vortex” for any topologically charged solution under the fundamental group of the $U(1)$ phase symmetry.

A. Amplitude-linearized solution

We will separate variables in the equations of motion (4) and (5) [or the Lagrangian equations (7) and (8), which do not differ from the original equations at the amplitude-linearized level] and then plug in the vortex ansatz. The vortex ansatz is a solution which has a winding phase Φ with some winding number Q , for a constant (averaged) value of the permittivity $\mu_c = \text{const}$, because we ignore the nonlinear dependence of μ on $|H|$. The vortex solution of winding number (topological charge) Q in cylindrical coordinates (r, ϕ, z) can be separated into regular and vortex parts:

$$E = E_{\text{reg}} + E_{\text{vort}}. \quad (12)$$

We represent the vortex part as

$$E_{\text{vort}}(r, \phi, z) = Z_E(z)R_E(r)e^{iQ\phi - i\Phi(\phi)}, \quad (13)$$

and analogously for the magnetic field. Along the z axis we get $Z_E(z) = e^{i\lambda z}$ as expected, and the eigenvalue λ is arbitrary for now, i.e., it is determined by the boundary conditions along the z axis. Upon inserting (13) into (4), the equation separates into the angular part and the radial part. The former reads

$$\Phi'' - i(\Phi')^2 + 2iQ\Phi' + i\lambda^2 = 0, \quad (14)$$

where l is the eigenvalue of the angular part. This is the crucial equation—the phase dynamics is nonlinear because μ is in general complex and the terms with $\nabla_{\perp}\mu$ contain nonlinear dependence on the phase. The equation is easily solved by first introducing $w \equiv \Phi'$ and then reducing it to quadratures. The outcome is

$$\Phi(\phi) = \cos(\sqrt{Q^2 + l^2}\phi + C_l). \quad (15)$$

In other words, we still stay with a winding solution but various winding numbers (equal to $\sqrt{Q^2 + l^2}$) are possible when multiple modes are excited. Clearly, only the solutions with integer windings are physical, otherwise they would not be single valued. The most general solution is thus a superposition of solutions $Z_E(\lambda, l; z)\Phi_E(\lambda, l; \phi)R_E(\lambda, l; r)$ with different l modes so as to result in a single-valued function. Now the radial part acquires the form

$$R_E'' + \frac{1}{r}R_E' + \left(\frac{\lambda}{r^2} - k^2 + \epsilon_{D0}\tilde{\omega}^2\right)R_E + \frac{\alpha\mu_c\tilde{\omega}^2}{E_c^2}R_E^3 = 0, \quad (16)$$

with $\tilde{\omega} \equiv \omega[1 - \omega_0^2/(\omega^2 + i\omega\gamma)]$. If we disregard the cubic term (amplitude-linearized approximation),² the well-known solution in terms of Bessel functions is obtained:

$$R_E(r) \approx c_E^{(1)}(\lambda, l)J_{Q_l}(ar) + c_E^{(2)}(\lambda, l)Y_{Q_l}(ar), \\ Q_l \equiv \sqrt{Q^2 + l^2}, \quad a \equiv \sqrt{\lambda - \epsilon_{D0}\mu_c\tilde{\omega}/\omega E_0^2 - k^2}. \quad (17)$$

²This is justified at least in some interval of z values, as the system is dissipative and loses power $\int(E^2 + H^2)$, so the amplitude progressively decreases along z .

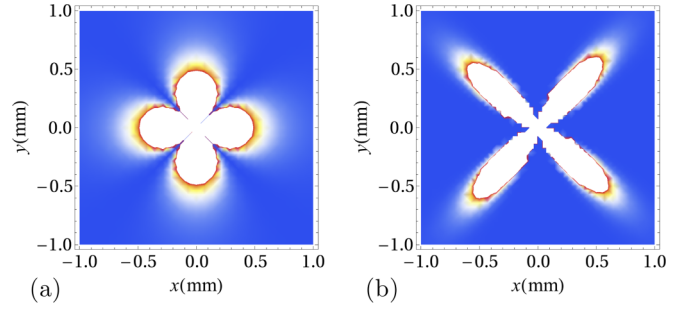


FIG. 5. Polygonal pattern $|E|^2$ for a vortex of charge $Q = 2$, for $k = 2$, $\epsilon_{D0} = 12.8$, and $\mu_c = 1.004$ (values of all parameters and constants in the main text), at radial slice $z = 1$, for a single vortex mode $l = 0$ (a), and for a linear combination of modes with $l = 0, 1$, and 2 decaying at infinity (b). The symmetry is $C_{2Q} = C_4$, which does not explain the C_Q and C_{3Q} regimes. Obviously, the crude picture of breaking the radial symmetry works but full explanation is lacking. It will come from the loop corrections.

Here, J and Y are the Bessel functions of first and second kind, respectively. Similar solutions $Z_H(z)$, $\Phi(\phi)$, and $R_H(r)$ are obtained for the magnetic field. The angular equation is identical for both fields: for this reason we have one solution Φ for both E and H . The eigenvalues λ and l and the values of the constants $c_{E,H}^{(1,2)}$ are determined by the boundary conditions. Obviously, (15) imposes the C_{2Q} symmetry, if $l = 0$. This simplest case is not necessarily the stable solution. We might have a sum over many l values. In principle, such sums may yield more complicated patterns, however we will see that when the physically reasonable boundary conditions are implemented (decay at infinity, single valuedness everywhere) one typically always has the robust C_{2Q} pattern. One important consequence of the fact that multiple l modes are possible is that due to nonlinear effects a new l mode can be created during the propagation along the z axis. We have already seen an example in Fig. 2(c). A quantitative analysis of this phenomenon requires a full nonlinear model and so can only be studied within the formalism of the next section.

This solution is not very satisfying but reproduces some of the features from the numerics, summarized at the start of the previous section: (1) the reduction of the full $O(2)$ symmetry down to a discrete symmetry C_n for some $n \in \mathbb{N}$, i.e., the polygonal form of the vortex, and (2) the value $n = 2Q$ is true in some but not in all situations. We show the solutions for a single angular mode from (15) and (17) in Fig. 5(a). In Fig. 5(b), we show a linear combination of angular modes with $l = 0, 1$, and 2 , with the coefficients $c_{E,H}^{(1,2)}$ in (17) chosen so that the total intensity still decays sufficiently fast at infinity. The symmetry is still C_{2Q} . Apparently, the regimes with the C_Q and C_{3Q} symmetries require loop corrections from nonlinear μ to be taken into account.

B. Loop corrections

The origin of the breaking of radial symmetry is the fact that a discrete set of modes in Fourier space is selected. This is best seen from the Fourier transform of the solutions (15) and (17). We will calculate the propagator $G(\mathbf{u})$ at

constant z , i.e., the Fourier transform $\mathbf{r} \mapsto \mathbf{u}$ of the solution with a Dirac delta source. This source imposes the boundary condition $R_E(0) \rightarrow \infty$, $\int dr r \cos \phi R_E(r) = 1$, giving $c_E^{(1)} =$

0 , $c_E^{(2)} = 2\pi/\Gamma(Q/2)$ in (17). Fourier transforming $(x, y) \mapsto (u_x, u_y)$ we get for a single mode (17), making use of the Bessel and Lommel integrals:

$$G_{E,H}(\mathbf{u}) = \frac{2\pi}{\Gamma(Q/2)} \frac{e^{iQ(\pi/2+\phi)}}{au} \left(\frac{\sin[(u-a)\Lambda]}{u-a} - \frac{\cos[(u+a)\Lambda - \pi Q]}{u+a} \right) + \frac{2\pi}{\Gamma(Q/2)} \frac{e^{-iQ(\pi/2+\phi)}}{au} \left(\frac{\cos[(u-a)\Lambda + \pi Q]}{u-a} - \frac{\cos[(u+a)\Lambda]}{u+a} \right). \quad (18)$$

Here, Λ is the ultraviolet (UV) small-length and high-momentum cutoff, i.e., the Fourier transform is performed by integrating $\int_{1/\Lambda}^{\infty} dr \int_0^{2\pi} d\phi$. The cutoff has a clear physical meaning: $1/\Lambda$ is the size of the vortex core (where the vortex ansatz stops working because the gradient of the field becomes too high). We clearly do not get anything new by just Fourier transforming. The goal is to move beyond the amplitude-linearized approximation of the previous section by considering the effects of nonconstant permittivity μ instead of constant (averaged) μ_c . This calculation is essentially elementary but might be tedious and boring for readers who are not fond of perturbative field theory. Most of the integrations are in Appendix C. Even the rest of this subsection can be skipped until the the equation (22), where we discuss the final result.

Putting μ from (3) in place of μ_c requires the solutions for ω_{NL} in terms of the magnetic field. The solutions are readily found from the Cardan formulas (we do not give them explicitly as they are cumbersome and not very illustrative). But the form of the H dependence of ω_{NL} is seen already from the Viète formula:

$$(\omega_{\text{NL}}^{(1)})^2 + (\omega_{\text{NL}}^{(2)})^2 + (\omega_{\text{NL}}^{(3)})^2 = \frac{1 + 2\Omega^2}{1 + |H|^2/\alpha E_c^2}, \quad (19)$$

so the solutions depend on $|H|^2$ only, with no higher powers of the magnetic field. Inserting this into \mathcal{L} , we get the nonlinear correction of the form

$$\delta\mathcal{L} = g_{2,0,0}|\nabla_{\perp}E|^2 + g_{0,2,0}|E|^2 + g_{0,2,2}|E|^2|H|^2 + g_{2,0,2}|\nabla_{\perp}E|^2|H|^2. \quad (20)$$

We thus have two quartic interaction terms and two quadratic terms. We do not intend to calculate the loop corrections in full detail; it is not worth the effort as we only want to capture the symmetry, i.e., the form of the angular dependence. First of all, the quadratic corrections $g_{2,0,0}$ and $g_{0,2,0}$ trivially renormalize the parameters in the bare propagator and do not change its functional form. Lowest-order non-trivial loop corrections to the self-energy come from $g_{0,2,2}$ and $g_{2,0,2}$. The electric field receives the correction $G_E^{-1} \mapsto (G_E + \Sigma_E^{(1)} + \Sigma_E^{(2)})^{-1}$ with

$$\Sigma_E^{(1)} = g_{0,2,2} \int d\mathbf{u}' G_H(\mathbf{u}') \approx g_{0,2,2} e^{3iQ/2} \sin(\pi Q) \ln \Lambda, \\ \Sigma_E^{(2)} = \frac{3}{2} g_{0,2,2} \int d\mathbf{u}' \int d\mathbf{u}'' G_H(\mathbf{u}') G_H(\mathbf{u}'') G_E(\mathbf{u} - \mathbf{u}' - \mathbf{u}'') \\ \approx \text{const} \times [a^{3/2} \cos(3Q\phi/2) - 2iQ^2 \ln a]. \quad (21)$$

We will write all equations for E , because this field receives interesting corrections from the gradient of μ [Eqs. (4) and (7)]. The magnetic field does not couple to the permeability ϵ in the same way in the original equation (5), and in the Lagrangian form (8) it does but ϵ does not contain such strong (nonpolynomial) nonlinearities as μ . One- and two-loop corrections appear not only in the self-energy but also in the vertex operators. However, the vertex corrections only have a weak momentum dependence and consequently the coordinate dependence (geometric patterns) of the solution is not significantly affected by them. For that reason we will not discuss them in detail.

The correction $\Sigma_E^{(1)}$ is the Hartree correction with a single vacuum bubble which is not very interesting: it merely introduces an additional mass term and does not influence the momentum dependence and thus the geometry of the patterns. As could be expected from power counting, it is logarithmically divergent in the UV cutoff Λ . Of course, this is not a problem in an effective theory; we have already explained the physical meaning of Λ . The watermelon diagram $\Sigma_{E,H}^{(2)}$ is crucial: it is momentum dependent. Its calculation is found in Appendix C. An informal way to estimate its effect is the following: the leading contribution comes from the region where $\mathbf{u} \approx \mathbf{u}' - \mathbf{u}''$ because this is a pole of the self-energy correction. Then we are left with angular integrals only, and they reduce to integrals of products of three rational functions [for the three propagators in (21)] of the half angle—this gives rise to $3\phi/2$ in the argument of the cosine. Now the dressed propagator $(G_{E,H}^{-1} + \Sigma)^{-1}$ needs to be Fourier transformed back to real space. We will only do this approximately (it is likely impossible to do exactly in closed form). The outcome is

$$E_{\text{vort}}(r, \phi, z) = \frac{e^{(i\lambda - 2Q^2 \ln a)z} \cos(Q\phi)}{\sqrt{kr}} \\ \times \left[c_E^{(1)}(\lambda, l) \left(1 + \frac{(2\pi)^{3/2} g_{0,2,2}}{\Gamma(Q/2)^3} \cos(3Q\phi/2) \right) + c_E^{(2)}(\lambda, l) \left(1 + \frac{(2\pi)^{3/2} g_{0,2,2}}{\Gamma(Q/2)^3} \sin(3Q\phi/2) \right) \right]. \quad (22)$$

No doubt the reader sees that the terms $\cos(3Q\phi/2)$ and $\sin(3Q\phi/2)$ give a pattern $|E_{\text{vort}}|^2$ with $3Q$ branches, in addition to the $2Q$ polygons obtained from the term $\cos(Q\phi)$. The interference between the two patterns might (1) break the symmetry completely and (2) lead to C_Q

symmetry if the relative phase between the leading term and the corrections is approximately $2\pi/Q$. Both cases are seen in numerical work: C_{3Q} appears in all left-handed materials [Figs. 2(a) and 2(c)], and elements of C_Q symmetry are present in almost all cases at long propagation distances z [Figs. 2(a)–2(c) and 3].

The self-energy has an imaginary part [equivalently, the solution (22) exhibits exponential decay in z], meaning that these configurations are not stable—they are only seen up to some propagation distance z . The exact order (along z) and stability of each of the patterns depend on the details of the permeability ϵ . One important and universal lesson is, however, that the decay rate [the real part of the exponent in (22)] is proportional to Q^2 , therefore the higher the value of $|Q|$ the faster it decays. This supports the general intuition that vortices with high winding numbers are not stable. But unlike the simplest case of the XY model or a superfluid where the stability only allows $Q = \pm 1$ we can in principle have arbitrarily high Q as we have seen also in the numerics; their lifetimes are smaller and smaller as Q grows, but still finite. The exponential decay itself is also confirmed by the numerics, as seen from Fig. 4.

C. Isotropy breaking: The look from the action

The basic mechanism leading to the symmetry breaking $O(2) \mapsto C_{3Q} \mapsto C_{2Q} \mapsto C_Q$ is seen already from the model Lagrangian (6). The symmetry breaking is essentially the consequence of the interplay of the nonlinear-sigma-model form of the kinetic term and the complex nonlinearity of the magnetic permeability μ . Therefore, we can take a static approximation of the z dynamics, ignoring the z dependence; clearly, in that framework we can only obtain the vocabulary of patterns, not the relative stability of C_Q , C_{2Q} , and C_{3Q} .³ The separation of variables remains a natural ansatz, and the vortex nature of the solution implies $E_{\text{vort}} = E_0(r)e^{i\Theta(\phi)}$ with $\oint d\phi \Theta(\phi) = 2\pi Q$ and analogously for the magnetic field. The Lagrangian (6) then becomes

$$\mathcal{L} = \frac{(E'_0)^2 + \frac{(\Theta')^2}{r^2} + k^2 E_0^2}{\mu} + \frac{(H'_0)^2 + \frac{(\Theta')^2}{r^2} + k^2 H_0^2}{\epsilon}. \quad (23)$$

The fact that μ contains $\omega_{\text{NL}}^2(|H|^2)$, which is in turn the solution of the cubic equation, introduces a branch cut in H because of the cubic roots. This is the simplest explanation of the origin of the C_{3Q} symmetry. More quantitatively, the story follows exactly the Landau-Ginzburg paradigm: while the initial Lagrangian only depends on $|E|^2$ and $|H|^2$ and thus preserves isotropy, the saddle-point solution is given by the equation

$$\frac{\epsilon(\nabla_{\perp}^2 - H)E - \epsilon' \nabla_{\perp} E \cdot \nabla_{\perp} H}{\epsilon^2} + \frac{\mu'}{\mu^2} |H|^{-1/3} = 0, \quad (24)$$

where we have used that $\mu = \mu(\omega_{\text{NL}}^2)$ and $\omega_{\text{NL}}^2 = \omega_{\text{NL}}^2(|H|^{2/3}, |H|^{4/3})$ (from the Cardan formulas). With the ansatz adopted above, the amplitude equation for $E_0(r)$ is the

nonlinear amplitude equation (16). The equation for the phase part Θ is more interesting. It reads

$$\frac{(\Theta')^2 \left(1 - \frac{\epsilon' E_0}{\epsilon H_0}\right) - k}{\epsilon} + \frac{2\mu'}{3\mu^2} |H|^{-1/3} = 0. \quad (25)$$

The cubic root carries a branch cut, and the last term really evaluates to $2\mu'/3\mu^2 \times H_0^{-1/3} e^{-i\Theta/3 + 2n\pi i/3}$ with $n = -1, 0$, and 1 . The solution Θ_0 which satisfies the phase winding condition is obtained in implicit form as

$$i(\Theta_0 + 2\pi n/3) = K_n \ln \left[\frac{k \left(1 - \frac{\epsilon' E_0}{\epsilon H_0}\right)}{E_0^2 + H_0^2} \sec^2 \left(\frac{Q}{2} \phi \right) \right], \quad (26)$$

where K_n is a constant determined by the amplitude solution and depending also on $n = -1, 0$, and 1 ; its exact value is hard to find analytically as we do not know the solution to the amplitude equation in the nonlinear regime. But that is not crucial for our general argument. The point is that the system can choose a solution with any of the values $n = -1, 0$, and 1 ; i.e., even though the equations of motion (and the Lagrangian) are isotropic, the solution is not. Each n branch behaves as $\approx 1/\cos^2(Q\phi/2)$, only they are rotated by $\pm 2\pi/3$ with respect to each other, and each of them has a C_Q symmetry. Put together, the three branches give C_{3Q} patterns. But all that holds if two of the cubic roots are complex. If all cubic roots are real, the phase remains single valued, and we only have C_Q symmetry, coming directly from (26) if we fix $n = 0$, i.e., if we only keep a single branch.⁴

What is the regime in which cubic roots are real and the symmetry is C_Q , as opposed to the complex roots and C_{3Q} patterns? The easiest way is to look at the cubic equation (3) for the magnetic permeability (and the nonlinear frequency ω_{NL}). For $\mu > 0$ (right-handed regime), the roots are all real and C_{3Q} patterns cannot occur. Indeed, the C_{3Q} phase is only present in Figs. 2(a) and 2(c), in left-handed media.

This approach is much more physical and elegant than the tour-de-force calculations of the previous two sections but it does not give explicit solutions for E and H ; it only classifies the symmetries of the solution. This is why we still needed the perturbative linear and two-loop analysis, to arrive at more quantitative results.

The saddle-point solution (26) is nonlinear, unlike the linearized solution found in the first subsection (15). It is not a vacuum in the usual field-theory sense, however, as it is not constant. We are dealing with dynamical criticality of the kind discussed in [21]. In the vicinity of this solution, the Lagrangian describes the fluctuations of amplitude δE and δH , and the fluctuations of phase $\delta \Phi$. Similar to the $O(3)$ -type spin models [23] and multibeam optical systems [32], and unlike simple XY-type models, the phase and amplitude fluctuations mix. By analyzing the fluctuation equations, it should be possible to understand analytically also the transition from the left-handed to the right-handed regime as the parameters are varied, i.e., what are the instabilities that drive it. We will not

³We could take the ansatz $e^{i\lambda z}$ instead; it would merely modify $k^2 \mapsto k^2 - \lambda$.

⁴We use the fact that a cubic equation has either one or all three solutions real.

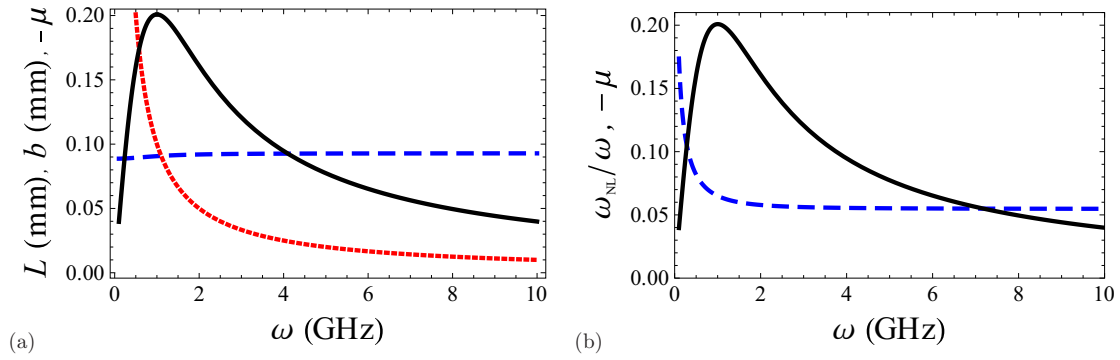


FIG. 6. (a) Frequency dependence of the typical propagation length scale for the dissipation of the vortex a^{2Q^2} (blue dashed line) and for the evolution of the symmetry-breaking C_n patterns (red dotted line). The symmetry breaking is detectable as long as the pattern evolution is faster than the dissipation, i.e., as long as the red curve is below the blue one. This is obviously the case for most of the frequency range. We also plot the frequency dependence of the negative permittivity $-\mu$ (black full line; because of the minus sign large positive values in the plot are really large negative values of μ). The left-handed regime is most prominent at intermediate frequencies, which are also inside the regime of the symmetry breaking. (b) Frequency dependence of the relative strength of nonlinear interactions $\omega_{\text{NL}}/\omega$ (blue dashed line) together with negative permittivity $-\mu$ as in (a) (black full line). Our calculations, based on a pair of nonlinear Schrödinger-like equations, are reliable as long as the nonlinearity is not too strong. This is again the case for all but very small frequencies, and again includes the left-handed regime.

attempt that here; it is a long subject that deserves separate work.

V. TOWARD EXPERIMENTAL VERIFICATION AND APPLICATIONS

We will now briefly discuss what an experimentalist can learn from our results and what to look for in practical work. Wave propagation through the metamaterial can be observed by measuring the transmission coefficients S_{ij} . From these coefficients, one can also reconstruct the electric-field intensity $|E|^2$, which can be directly compared to our intensity maps like Figs. 2 and 3 [33]. Another quantity which can be measured is the voltage waveform, which can be used to construct amplitude envelopes [34].

Therefore, the predicted symmetry breaking is in principle directly observable. But the question remains how widespread it will be for realistic values of the parameters. From a more applied viewpoint, this question is reversed: how to make a vortex transmission through a left-handed waveguide stable. In other words, how *not* to observe the symmetry breaking. It is true that the phenomenon disappears as soon as the vortex charge is zero, i.e., when the beam is not a vortex. However, the vortex patterns are likely important in applications. First, as a topologically protected object with conserved charge, a vortex is among the natural candidates for computational devices and information transmission (for the same reasons that solitons are also interesting in that regard: they are robust to noise, carry a discrete “quantum” number, i.e., charge, and are stable to small local perturbations). Second, in the presence of impurities in the sample, vortices can form in a nonlinear metamaterial from the initially nonvortexing beam [23].

Let us focus on the left-handed regime, which is the most interesting and the most relevant for applications. The first condition is therefore to be in the frequency regime with $\mu(\omega) < 0$. This can be checked directly from Eq. (2) as we did in Fig. 1(c). The second issue is that the symmetry breaking takes some finite time, i.e., some finite propagation length, which is of order b ; as can be seen from Fig. 3 and

directly from Eqs. (4) and (5), this is the length scale over which the patterns change. On the other hand, the one-loop calculation (22) shows that the intensity decays with the rate $\sim a^{-2Q^2}$. As long as this is less than the characteristic length b , one will likely not see the symmetry breaking but just eventual dissipation of the beam. Therefore, these two scales should be compared for some reasonable parameter values. We show this in Fig. 6(a) for $F = 0.4$, $\epsilon_{D0} = 12.8$, $\gamma = 1$ GHz, and $\omega_0 = 10$ GHz. Apparently, the length scale of the C_n pattern development (red dotted line) is nearly always shorter than the dissipation scale (blue dashed line), so we expect that the effect predicted in the paper is readily seen in experiment, at least for $Q = \pm 1$. For larger vortex charges, the dissipation grows quickly and high Q values are probably not easily observed. Conversely, if the goal is to keep a stable radially symmetric vortex pattern, one should remain at small frequencies, although for $\omega \ll \omega_0$ the material is not strongly left handed, as can be seen from the $-\mu(\omega)$ dependence, also given in the figure.

There is still one remaining issue. Our theoretical approach, based on a pair of nonlinear Schrödinger-like equations, inherently disregards some effects. It describes a quasi-monochromatic wave without wave mixing or dissipation due to higher harmonic generation [5]. Such phenomena become significant for strong nonlinearities, so we should compare the nonlinearities in ϵ and μ to the typical energy (frequency) scale of the vortex. In Eqs. (1) and (2) the approximate ratios of the nonlinear to linear terms are given by $|E|^2/\epsilon_{D0}$ and $\omega_{\text{NL}}/\omega_0 \sim (A/H)^{1/3}$. The first scale is frequency independent and solely depends on the beam intensity. The second scale depends on frequency and needs to be inspected more closely. In Fig. 6(b) we plot the nonlinearity ratio for the magnetic field for a range of frequencies ω , again together with the permittivity to make sure we are at the same time in the left-handed regime. The relative nonlinearity strength quickly saturates around a value $0.06 \ll 1$, so we are rather confident that our equations of motion still make sense.

Altogether, the conclusion is that the breaking of radial symmetry is observable by standard means (measuring the

transport coefficients and reconstructing the intensity map at the exit face of the metamaterial), as long as the frequency of the wave is not too low. This kind of instability kicks in at shorter propagation lengths [of order 0.1 mm in Fig. 6(a)] than the nonlinear diffraction effects studied for breathers in [35], suggesting that vortex signals are more fragile and less convenient for information transmission.

VI. DISCUSSION AND CONCLUSIONS

Our main result is contained already in the title—left-handedness and nonlinearity together create the breaking of the $O(2)$ symmetry down to a discrete group, with the pattern vocabulary consisting of the C_{3Q} , C_{2Q} , and C_Q patterns. In the right-handed system with the same nonlinearity the isotropy is broken again, but the pattern vocabulary only has C_{2Q} and C_Q stages. How exactly the patterns evolve into each other and through which instabilities is not universal, and it depends on the exact form of ϵ and μ . In our model, the ϵ dependence is mainly encapsulated in the dissipation γ : the left-handed nondissipative case is usually dominated by C_Q after a much shorter C_{3Q} phase, whereas the dissipative left-handed metamaterials most prominently show C_{3Q} patterns. For the right-handed materials, nondissipative and dissipative dynamics show mainly C_{2Q} and C_Q patterns, respectively.

A detailed account of the pattern dynamics was only possible through numerical work. But the vocabulary itself—the existence of symmetries C_{3Q} , C_{2Q} , and C_Q —we were able to understand analytically. The dynamic Landau-Ginzburg picture reveals this as a consequence of the cubic root nonlinearity in the magnetic permittivity, and the fact that the cubic equation has either two complex roots in the left-handed regime or all three real roots in the right-handed regime, and the presence or absence of dissipation in the electric permeability. In the framework of our field theory model, the second derivative of the free energy (on-shell Lagrangian, Landau-Ginzburg functional) likely has a jump when the symmetry changes. This is a strong encouragement that the phenomena we observe here, and in general the walk through the pattern vocabulary, can be understood from the viewpoint of order and disorder transitions.

Similar phenomena were studied also in [15,18] and above all [10], where C_{3Q} necklaces were found, within a model of left-handed metamaterials given in [15] and similar to ours. Clearly, we have not exhausted this subject; more research is still needed to fully understand the transition between different symmetries and their instabilities. Vortices in metamaterials seem to be a promising arena, as in a metamaterial the nonlinearity and the frequency band where the material is left-handed can to some extent be tuned at will. Therefore, the phase diagram of collective vortex interactions can also be studied, and is an obvious topic for future work.

ACKNOWLEDGMENTS

This work has made use of the Sci-Hub service. We are grateful to Milan Petrović and Mariya Medvedyeva for helpful remarks. We also thank the referees for some important and stimulating questions. Work at the Institute of Physics is funded by Ministry of Education, Science, and Technological Development, under Grant No. OI171017.

APPENDIX A: DERIVATION OF THE EQUATIONS OF MOTION FROM THE MAXWELL EQUATIONS

Start from the definitions $\hat{D} = \epsilon \hat{E}$ and $\hat{B} = \mu \hat{H}$ and the Maxwell equations in the absence of external charges and currents ($\rho = \hat{j} = 0$):

$$\begin{aligned} \nabla \cdot \hat{D} = \rho = 0, \quad \nabla \cdot \hat{B} = 0, \quad \nabla \times \hat{E} = -\partial_t \hat{B}, \\ \nabla \times \hat{H} = 4\pi \hat{j} + \partial_t \hat{D} = \partial_t \hat{D}. \end{aligned} \quad (\text{A1})$$

We make the following assumptions.

(1) We assume small gradients of the permittivities ϵ and μ , so their second and higher derivatives are disregarded. Since $\omega \propto k$, it means that mixed derivatives of the form $\partial_t \nabla \epsilon$ are also disregarded. In other words, the characteristic length scale l along the z axis on which ϵ and μ change is assumed to be large compared to the characteristic scale b of the changes in E and H .

(2) We assume that the time dependence is harmonic so $\partial_t = -i\omega$.

Acting on the last equation by $\nabla \times$ and making use of the identity $\nabla \times \nabla \times \hat{H} = -\nabla^2 \hat{H} + \nabla(\nabla \cdot \hat{H})$, one gets for the left-hand side

$$\begin{aligned} \nabla \times \nabla \times \hat{H} &= -\nabla^2 \hat{H} + \nabla \left(\nabla \cdot \frac{\hat{B}}{\mu} \right) \\ &= -\nabla^2 \hat{H} + \nabla \left(\frac{1}{\mu} \nabla \cdot \hat{B} \right) - \nabla \left(\frac{\nabla \mu}{\mu^2} \cdot \hat{B} \right) \\ &= -\nabla^2 \hat{H} + \nabla \left(\frac{1}{\mu} \nabla \cdot \hat{B} \right) - \nabla \cdot \left(\frac{\nabla \mu}{\mu^2} \right) \hat{B} \\ &\quad - \frac{\nabla \mu}{\mu^2} \nabla \cdot \hat{B} = -\nabla^2 \hat{H} + 0 + O(1/l^2) + 0 \\ &= -\nabla^2 \hat{H}, \end{aligned} \quad (\text{A2})$$

where we used $\nabla \cdot \hat{B} = 0$ and disregarded the second derivative of μ . The right-hand side yields

$$\begin{aligned} \nabla \times \nabla \times \hat{H} &= \nabla \times (\partial_t \hat{D}) = -i\omega \nabla \times \hat{D} = -i\omega \nabla \times (\epsilon \hat{E}) \\ &= -i\omega (\nabla \epsilon) \hat{E} - i\omega \epsilon \nabla \times \hat{E} \\ &= -i\omega (\nabla \epsilon) \hat{E} - \omega^2 \epsilon \mu \hat{H} = O(1/l^2) + \omega^2 \epsilon \mu \hat{H}, \end{aligned} \quad (\text{A3})$$

so we obtain

$$\nabla^2 \hat{H} + \omega^2 \epsilon \mu \hat{H} = 0. \quad (\text{A4})$$

For the \hat{E} field we start from the third Maxwell equation, act by $\nabla \times$, and find for the left-hand side

$$\begin{aligned} \nabla \times \nabla \times \hat{E} &= -\nabla^2 \hat{E} + \nabla(\nabla \cdot \hat{E}) = -\nabla^2 \hat{E} - \nabla \left(\nabla \cdot \frac{\hat{D}}{\epsilon} \right) \\ &= \nabla^2 \hat{E} - \nabla \left(\frac{1}{\epsilon} \nabla \cdot \hat{D} \right) + \nabla \left(\frac{\nabla \epsilon}{\epsilon^2} \right) \epsilon \hat{E} \\ &\quad + \frac{\nabla \epsilon}{\epsilon^2} \nabla \cdot \hat{D} = -\nabla^2 \hat{E} + 0 + O(1/l^2) + 0 \\ &= -\nabla^2 \hat{E}, \end{aligned} \quad (\text{A5})$$

and for the right-hand side we get

$$\begin{aligned}\nabla \times \nabla \times \hat{E} &= -\partial_t(\nabla \times \hat{B}) = -\partial_t(\nabla \times \hat{B}) \\ &= -\partial_t[\nabla \times (\mu \hat{H})] = -\partial_t[(\nabla \mu) \hat{H} + \mu \nabla \times \hat{H}] \\ &= -(\partial_t \nabla \mu) \hat{H} - \nabla \mu \cdot \partial_t \hat{H} - \partial_t(\mu \partial_t \hat{D}) \\ &= O(1/l^2) - \frac{\nabla \mu}{\mu} \nabla \hat{E} + \omega^2 \epsilon \mu \hat{E},\end{aligned}\quad (\text{A6})$$

so

$$\nabla^2 \hat{E} + \omega^2 \epsilon \mu \hat{E} - \frac{\nabla \mu}{\mu} \nabla \hat{E} = 0. \quad (\text{A7})$$

For our geometry we take the paraxial beam approximation, with the ansatz $\hat{E} = E(x, y)e^{i(kz - \omega t)}$, $\hat{H} = H(x, y)e^{i(kz - \omega t)}$, so the nabla acts as

$$\nabla \hat{E} = (\nabla_{\perp} E, \partial_z E + ikE)e^{i(kz - \omega t)}, \quad (\text{A8})$$

and the Laplacian operator acts as

$$\nabla^2 \hat{E} = (\nabla_{\perp}^2 E + 2ik\partial_z E - k^2 E)e^{i(kz - \omega t)}, \quad (\text{A9})$$

and analogously for the magnetic field. Now to write the equations motion in the final form we rescale $E \rightarrow E \times 2kb$, $H \rightarrow H \times 2kb$, and $z \mapsto z \times 2kb$, where b is some characteristic length scale along the z axis, and divide the equations by bk^2 to obtain the equations (4) and (5), reprinted here for convenience:

$$\begin{aligned}-\frac{i}{b}\partial_z E &= \nabla_{\perp}^2 E + [\omega^2 \epsilon (|E|^2) \mu (|H|^2) - k^2] E \\ &\quad - \frac{\nabla_{\perp} \mu (|H|^2)}{\mu (|H|^2)} \nabla_{\perp} E - i \frac{\partial_z \mu (|H|^2)}{2\mu (|H|^2)} E,\end{aligned}\quad (\text{A10})$$

$$-\frac{i}{b}\partial_z H = \nabla_{\perp}^2 H + [\omega^2 \epsilon (|E|^2) \mu (|H|^2) - k^2] H. \quad (\text{A11})$$

For comparison to the equations given in [4,7,12], one needs (1) to rescale $H \mapsto \omega^2/c^2 H$ to get the term $-\gamma^2 H = -k^2/\omega^2$ in (A11) and (2) to absorb the factor $-k^2$ in (A10) in the definition of ϵ_{D0} . This is possible as ϵ and μ have a constant term (equal ϵ_{D0} and 1, respectively) so the product $\epsilon\mu$ also has a constant term proportional to ϵ_{D0} , and the contribution $k^2 E$ can be absorbed as $\epsilon_{D0} \mapsto \epsilon_{D0} - k^2$. We thus arrive at a system identical to that from [4], except for the extra terms for the propagation along the z axis.

APPENDIX B: CONFIGURATIONS WITH NO VORTICITY IN THE MAGNETIC FIELD

Here we show that our results stay valid also when only the electric field has vortex patterns whereas the magnetic field starts analytic everywhere. As we discuss in the main text, this situation is experimentally more relevant than the one assumed in most calculations in the paper (that both the

electric and the magnetic field have a vortex as they enter the material). The electric field is typically a few orders of magnitude more intense than the magnetic field, as seen in [4]. Therefore, one typically controls the electric field directly, imposing a given boundary condition at the front end of the material. Despite this fact, the magnetic field remains very important: the coupled equations of motion (4) and (5) require both E and H to be nonzero. Indeed, as explained in [4], the left handedness comes as a consequence of the hysteresis-type dependence of the magnetic permittivity on H . So while it is crucial that E and H are both nonzero, it is also true that the results should remain valid for $|H| \ll |E|$, and for the boundary condition that only has a vortex in E at the front of the metamaterial, not for H . With such boundary conditions and the same parameter values as before, Fig. 7 repeats the calculations of Fig. 3. Obviously, the symmetries remain the same and the similarity of the results for the two cases is striking. Obviously, the $|E|^2$ map is insensitive to the details of the initial magnetic-field pattern, as one expects from experiments and common wisdom in nonlinear optics. We are thus content that the numerically simplifying assumption of identical $z = 0$ boundary conditions for E and H does not put into question the findings of our paper.

APPENDIX C: THE CALCULATION OF THE SELF-ENERGY DIAGRAMS

We discuss here in some more detail the equations (21) from the main text. First we give the expressions for the couplings $g_{2,0,0}$, $g_{0,2,0}$, $g_{2,0,2}$, and $g_{0,2,2}$, which come from the expansion over the magnetic field H of the nonlinear dependence $\mu(H)$ in (20):

$$g_{2,0,0} = \frac{\alpha E_c^4 \omega_0^2 - (\omega - i\Gamma)\omega\alpha E_c^8}{H_0 + \alpha E_c^4 [\omega_0^2 - (\omega - i\Gamma)\omega\alpha E_c^2]}, \quad (\text{C1})$$

$$g_{0,2,0} = (k^2 - \lambda^2)g_{2,0,0}, \quad (\text{C2})$$

$$g_{2,0,2} = 2\alpha E_c^2 H_0 \frac{\omega_0^2 - (\omega - i\Gamma)\omega\alpha E_c^4}{\{H_0 + \alpha E_c^4 [\omega_0^2 - (\omega - i\Gamma)\omega\alpha E_c^2]\}^2}, \quad (\text{C3})$$

$$g_{0,2,2} = (k^2 - \lambda^2)g_{2,0,2}. \quad (\text{C4})$$

For simplicity, we will treat the case when $\lambda = k$ and thus $g_{0,2,0} = g_{0,2,2} = 0$. This simplifies the calculations substantially while it does not change the symmetry of the solution. It is possible to evaluate the diagram $\Sigma^{(1)}$ exactly in terms of sine and cosine integrals Si and Ci. The angular integration is straightforward; the integration over u results in four combinations of the trigonometric integrals, for the four terms in (18). Three of the four integrals are finite and therefore they just shift the mass term. The third term of the propagator is logarithmically divergent:

$$\Sigma_3^{(1)} = \frac{4\pi \sin \pi Q}{Q\Gamma(Q/2)} e^{-3i\pi Q/2} \frac{1}{a^2} \{\gamma_E + \ln \Lambda + (-1)^Q a [\cos(a\Lambda) \text{Ci}(a\Lambda) + \sin(a\Lambda) \text{Si}(a\Lambda)]\}. \quad (\text{C5})$$

To judge the effect of this term, we should extract the mass squared r_m of the bare propagator, writing it out for small u :

$$G(\mathbf{u} \rightarrow 0) = \frac{2\pi}{\Gamma(Q/2)} \frac{1}{u(u^2 - a^2)} \{e^{iQ(\pi/2+\phi)} [\cos(a\Lambda - \pi Q) - \sin(a\Lambda)] + e^{-iQ(\pi/2+\phi)} [\cos(a\Lambda + \pi Q) - \cos(a\Lambda)]\}. \quad (\text{C6})$$

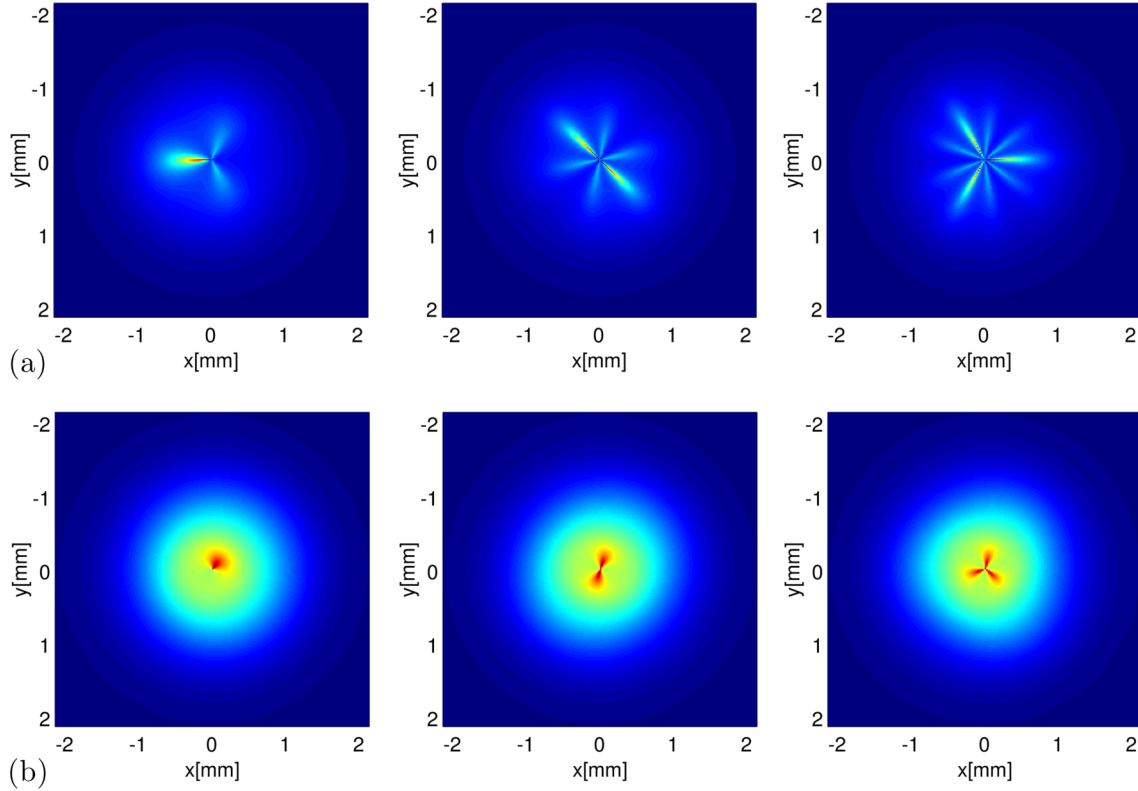


FIG. 7. The patterns for $Q = 1, 2,$ and 3 vortices (left to right), in a dissipative (a) and lossless (b) left-handed metamaterial. All parameters are the same as in Fig. 3 but the boundary condition at $z = 0$ is now a vortex for the electric field E and a homogenous background for H . The symmetries and the whole qualitative picture are the same as before, confirming that the predictions of the paper do not require preparing a vortex in magnetic field at the entry.

Since $G^{-1}(\mathbf{u} \rightarrow 0) \propto u = 0$, the bare propagator is massless. The one-loop correction $\Sigma^{(1)}$ therefore gives a cutoff-dependent mass $r_M \sim \ln \Lambda$, which could be absorbed in the overall normalization of the propagator. As we declared in the main text, the one-loop self-energy does not do much.

The crucial diagram $\Sigma^{(2)}$, the popular watermelon diagram, cannot be calculated exactly. It can be evaluated in the regime of small external momentum \mathbf{u} , i.e., when $u < u', u''$; more precisely, we can look at the regime when $u < u_0 < u', u''$ for some (arbitrary) scale u_0 and expand in a series in u/u_0 . Let us denote such an entity by $\Sigma^{(2)}(\mathbf{u}; u_0)$: it contains enough information for our purposes: we are interested mainly in angular integrations which determine the symmetry, and these can be done exactly as they separate from the integrations over the module u in the small- u limit. For $\mathbf{u} = 0$ the watermelon diagram reads (with $\int \equiv \int_0^{2\pi} d\phi' \int_0^{2\pi} d\phi'' \int du' \int du''$)

$$\Sigma^{(2)} \approx \int \frac{G(\mathbf{u}')G(\mathbf{u}'')}{v} \{e^{iQ[\pi/2+(\phi-\phi'-\phi'')]} [\cos(a\Lambda - \pi Q) - \sin(a\Lambda)] + e^{-iQ[\pi/2+(\phi-\phi'-\phi'')]} [\cos(a\Lambda + \pi Q) - \cos(a\Lambda)]\},$$

$$v \equiv \sqrt{(u')^2 + (u'')^2 - 2u'u'' \cos(\phi - \phi' - \phi'')}. \quad (\text{C7})$$

One angular integration is performed by taking $\phi' \mapsto \phi' + \phi''$, which makes the ϕ'' integral completely trivial, and the ϕ' integral is evaluated in terms of the elliptic integrals E and K . The outcome is finite, hence it is observable (not only at the cutoff scale) and reads

$$\Sigma^{(2)}(0; u_0) = \left(\frac{2\pi}{a\Gamma(Q/2)}\right)^3 e^{3iQ/2} \cos(3Q\phi/2)^2 \int du' \int du'' \frac{[(u')^2 - (u'')^2](u' + u'')E\left(-\frac{4u'u''}{(u'+u'')^2}\right)}{(u')^2(u'')^2[(u')^2 - a^2][(u'')^2 - a^2][(u')^2 - (u'')^2]}$$

$$= \frac{1}{4\pi} \left(\frac{2\pi}{a\Gamma(Q/2)}\right)^3 e^{3iQ/2} \cos(3Q\phi/2)^2 (a^{3/2} - 1/\Lambda^{3/2}) + O(1/\Lambda^2). \quad (\text{C8})$$

In particular, this means that a nontrivial mass term is acquired, of the order $a^{3/2}$. This mass is anisotropic, and the factor $\cos(3Q\pi/2)^2$ is all we need for the $3Q$ polygon. The leading correction in u/u_0 is in fact inessential for the symmetry, but it is

important as it contains a nonzero imaginary part, introducing a finite lifetime for such patterns. It reads

$$\begin{aligned}\Sigma^{(2)}(u; u_0) &= \int \frac{G(\mathbf{u}')G(\mathbf{u}'')}{w} \{e^{iQ[\pi/2+(\phi'-\phi'')]}[\cos(a\Lambda - \pi Q) - \sin(a\Lambda)] + e^{-iQ[\pi/2+(\phi'-\phi'')]}[\cos(a\Lambda + \pi Q) - \cos(a\Lambda)]\} \\ &= \frac{1}{4\pi} \left(\frac{2\pi}{a\Gamma(Q/2)} \right)^3 e^{3iQ/2} \left(\frac{2ia^{3/2}}{\pi} \sin(3Q\phi/2) + \frac{2\Lambda^{3/2}}{\pi} \cos(3Q\phi/2) \right), \\ w &\equiv \sqrt{(u')^2 + (u'')^2 - 2u'u'' \cos(\phi' - \phi'') - 2u[u' \cos(\phi - \phi') + u'' \cos(\phi - \phi'')]}.\end{aligned}\quad (\text{C9})$$

At leading order, this tedious expression behaves like $1/r^3$, falling off much quicker than the bare propagator (18), which goes as $1/\sqrt{r}$ (most obvious from the Bessel-function form of the real-space solution), suggesting that the shape of the vortex, which is mainly determined by long-distance behavior, is not much influenced by the finite- u correction to $\Sigma^{(2)}$.

-
- [1] V. G. Veselago, The electrodynamics of substances with simultaneously negative values of epsilon and mu, *Usp. Fiz. Nauk* **92**, 517 (1967) (in Russian).
- [2] R. A. Shelby, D. R. Smith, and S. Schultz, Experimental verification of a negative index of refraction, *Science* **292**, 77 (2001).
- [3] T. J. Yen, W. J. Padilla, N. Fang, D. C. Vier, D. R. Smith, J. B. Pendry, D. N. Basov and D. Zhang Terahertz magnetic response from artificial materials, *Science* **303**, 1494 (2004).
- [4] A. A. Zharov, I. V. Shadrivov and Y. S. Kivshar, Nonlinear Properties of Left-Handed Metamaterials, *Phys. Rev. Lett.* **91**, 037401 (2003).
- [5] M. Lapine, I. V. Shadrivov and Y. S. Kivshar, Colloquium: Nonlinear metamaterials, *Rev. Mod. Phys.* **86**, 1093 (2014); A. Baev, P. N. Prasad, H. Agren, M. Samoć and M. Wegener, Metaphotonics: An emerging field with opportunities and challenges, *Phys. Rep.* **594**, 1 (2015).
- [6] I. V. Shadrivov, N. A. Zharova, A. A. Zharov and Y. S. Kivshar, Nonlinear transmission and spatiotemporal solitons in metamaterials with negative refraction, *Optics Express* **13**, 1291 (2005).
- [7] I. V. Shadrivov and Y. S. Kivshar, Spatial solitons in nonlinear left-handed metamaterials, *J. Opt. A: Pure Appl. Opt.* **7**, S68 (2005).
- [8] I. V. Shadrivov, A. A. Sukhorukov, Y. S. Kivshar, A. A. Zharov, A. D. Boardman and P. Egan, Nonlinear surface waves in left-handed materials, *Phys. Rev. E* **69**, 016617 (2004).
- [9] S. Wen, Y. Wang, W. Su, Y. Xiang, X. Fu and D. Fan, Modulation instability in nonlinear negative-index material, *Phys. Rev. E* **73**, 036617 (2006).
- [10] S. Z. Silahli, W. Walasik and N. M. Litchinitser, Modulation instability of structured-light beams in negative-index metamaterials, *J. Opt.* **18**, 054010 (2016).
- [11] N. L. Tsitsas, N. Rompotis, I. Kourakis, P. G. Kevrekidis and D. J. Frantzeskakis, Higher-order effects and ultrashort solitons in left-handed metamaterials, *Phys. Rev. E* **79**, 037601 (2009).
- [12] I. V. Shadrivov, A. A. Sukhorukov and Y. S. Kivshar, Guided modes in negative-refractive-index metamaterials, *Phys. Rev. E* **67**, 057602 (2003).
- [13] A. Namdar, I. V. Shadrivov and Y. S. Kivshar, Backward Tamm states in left-handed metamaterials, *App. Phys. Lett.* **89**, 114104 (2006).
- [14] H. Liu, J. Lei, G. Jiang, X. Guan L. Ji, and Z. Ma, Observation of tunable nonlinear effects in an analogue of superconducting composite right/left hand filter, *Sci. Rep.* **5**, 14846 (2015).
- [15] L. Fan, Z. Chen, Y.-C. Deng, J. Ding, H. Ge, S.-Y. Zhang, Y.-T. Yang and H. Zhang, Nonlinear effects in a metamaterial with double negativity, *App. Phys. Lett.* **105**, 041904 (2014).
- [16] A. O. Korotkevich, K. E. Rasmussen, G. Kovačič, V. Roytburd, A. I. Maimistov and I. R. Gabitov, Optical pulse dynamics in active metamaterials with positive and negative refractive index, *J. Opt. Soc. Am. B* **30**, 1077 (2013).
- [17] M. Saha, A. K. Sarma, Modulation instability in nonlinear metamaterials induced by cubic-quintic nonlinearities and higher order dispersive effects, *Opt. Commun.* **291**, 321 (2005).
- [18] Y. Shen, P. G. Kevrekidis, G. P. Veldes, D. J. Frantzeskakis, D. DiMarzio, X. Lan, and V. Radisic, From solitons to rogue waves in nonlinear left-handed metamaterials, *Phys. Rev. E* **95**, 032223 (2017).
- [19] M. Liu, D. A. Powell, I. V. Shadrivov, M. Lapine and Y. S. Kivshar, Spontaneous chiral symmetry breaking in metamaterials, *Nat. Comm.* **5**, 4441 (2014).
- [20] M. A. Gorchach, D. A. Dobrykh, A. P. Slobozhanyuk, P. A. Belov and M. Lapine, Nonlinear symmetry breaking in photometamaterials, *Phys. Rev. B* **97**, 115119 (2018).
- [21] M. C. Cross and P. C. Hohenberg, Pattern formation outside of equilibrium, *Rev. Mod. Phys.* **65**, 851 (1993).
- [22] M. I. Rabinovich, A. B. Ezersky, and P. D. Weidman, *The Dynamics of Patterns* (World Scientific, Singapore, 2000).
- [23] L. I. Pismen, *Vortices in Nonlinear Fields* (Oxford University, London, 1999).
- [24] H. Kleinert, *Gauge Fields in Condensed Matter Physics* (World Scientific, Singapore, 1989).
- [25] P. W. Anderson, Two new vortex liquids, *Nature Physics* **3**, 160 (2007).
- [26] A. L. Fetter, Rotating trapped Bose-Einstein condensates, *Rev. Mod. Phys.* **81**, 647 (2009).
- [27] J. D. Sau and S. Sachdev, Mean-field theory of competing orders in metals with antiferromagnetic exchange interactions, *Phys. Rev. B* **89**, 075129 (2014).
- [28] V. L. Berezinsky, Razrushenie dalnego poryadka v odnomernykh i dvumernykh sistemakh s neprerivnoy gruppyo simmetrii I. Klassicheskije sistemy, *JETF* **59**, 907 (1970) (in Russian); J. Kosterlitz and D. Thouless, Ordering, metastability and phase transitions in two-dimensional systems, *J. Phys. C* **6**, 1181 (1973).
- [29] R. W. Boyd, *Nonlinear Optics* (Academic, New York, 2008).
- [30] J. L. Cieslinski and T. Nikiciuk, A direct approach to the construction of standard and non-standard Lagrangians for dissipative-like dynamical systems with variable coefficients, *J. Phys. A* **43**, 175205 (2010).

- [31] T. Shah, R. Chattopadhyay, K. Vaidya and S. Chakraborty, Conservative perturbation theory for nonconservative systems, *Phys. Rev. E* **92**, 062927 (2015).
- [32] M. Čubrović and M. S. Petrović, Quantum criticality in photorefractive optics: Vortices in laser beams and antiferromagnets, *Phys. Rev. A* **96**, 053824 (2017).
- [33] P. Alitalo, S. Maslovski and S. Tretyakov, Experimental verification of the key properties of a three-dimensional isotropic transmission-line superlens, *J. Appl. Phys.* **99**, 124910 (2006).
- [34] A. B. Kozyrev and D. W. van der Weide, Trains of envelope solitons in nonlinear left-handed transmission line media, *Appl. Phys. Lett.* **91**, 254111 (2007).
- [35] A. D. Boardman, N. King, R.-C. Mitchell-Thomas, V. N. Malnev, and Y. G. Rappoport, Gain control and diffraction-managed solitons in metamaterials, *Metamaterials* **2**, 145 (2008).



String Theory, Quantum Phase Transitions, and the Emergent Fermi Liquid

Mihailo Cubrovic *et al.*
Science **325**, 439 (2009);
DOI: 10.1126/science.1174962

This copy is for your personal, non-commercial use only.

If you wish to distribute this article to others, you can order high-quality copies for your colleagues, clients, or customers by [clicking here](#).

Permission to republish or repurpose articles or portions of articles can be obtained by following the guidelines [here](#).

The following resources related to this article are available online at www.sciencemag.org (this information is current as of April 4, 2014):

Updated information and services, including high-resolution figures, can be found in the online version of this article at:

<http://www.sciencemag.org/content/325/5939/439.full.html>

Supporting Online Material can be found at:

<http://www.sciencemag.org/content/suppl/2009/06/25/1174962.DC1.html>

This article **cites 22 articles**, 1 of which can be accessed free:

<http://www.sciencemag.org/content/325/5939/439.full.html#ref-list-1>

This article has been **cited by** 38 article(s) on the ISI Web of Science

This article has been **cited by** 3 articles hosted by HighWire Press; see:

<http://www.sciencemag.org/content/325/5939/439.full.html#related-urls>

This article appears in the following **subject collections**:

Physics

<http://www.sciencemag.org/cgi/collection/physics>

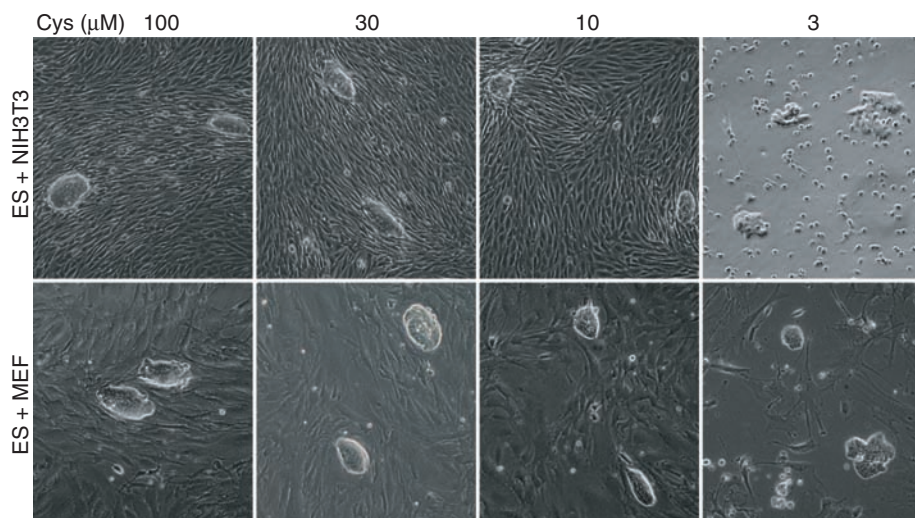


Fig. 6. Effects of cysteine deprivation on the growth of ES, MEF, and 3T3 cells. Cocultures of ES/MEF or ES/3T3 cells were subjected for 2 days to media containing varying amounts of supplemented cysteine. Cysteine deprivation severely impeded MEF cell growth at 10 and 3 μM and 3T3 growth at 3 μM (see also fig. S5). Although colony morphology was altered under the most severe conditions of cysteine deprivation, ES cell colonies were observed under all culture conditions tested.

of three inactivating mutations (13). Although highly conserved in gene organization, as well as primary amino acid sequence of the predicted TDH open reading frame, the human TDH gene carries AG-to-GG splice acceptor mutations in exons 4 and 6, as well as a nonsense mutation within exon 6 wherein arginine codon 214 is replaced by a translational stop codon. Whereas polymorphic variation within the human population has been observed for the exon 4 splice acceptor mutation, with some individuals carrying the normal AG splice acceptor dinucleotide and others carrying the GG variant, all individuals genotyped to date carry both the splice acceptor and nonsense mutations in exon 6. Reverse transcriptase-PCR analysis of TDH transcripts expressed in human fetal liver tissue showed complete skipping of exon 4 and either complete skipping or aberrant splicing of exon 6 (fig. S8). Given that exons 4 and 6 encode segments of the enzyme critical to its function and that truncation via the nonsense codon at amino acid 214 would also be predicted to yield an inactive variant, it appears that the human gene is incapable of producing an active TDH enzyme. Remarkably, all metazoans whose genomes have been sequenced to date, including chimpanzees, appear to contain an intact TDH gene (14). Unless humans evolved adaptive capabilities sufficient to overcome three mutational lesions, it would appear they are TDH deficient.

Human ES cells grow at a far slower rate than mouse ES cells, with a doubling time of 35 hours (15). Whether the slower growth rate of human ES cells reflects the absence of a functional TDH enzyme can perhaps be tested by introducing, into human ES cells, either a repaired human TDH gene or the intact TDH gene of a closely related mammal. That this strategy might work is supported by the expression in human cells of a functional form of the 2-amino-3-ketobutyrate-

CoA ligase enzyme that converts the short-lived product of TDH-mediated catabolism of threonine into acetyl-CoA and glycine (Fig. 1B). It is possible that the culture conditions used to grow human ES cells do not match the ICM environment of the human embryo, in which the cell division cycle is more rapid than the 35-hour doubling time of cultured human ES cells (16). If human ES cells do not use the TDH enzyme to acquire an advantageous metabolic state for rapid growth, and if conditions can be adapted to facilitate the rapid proliferation of human ES cells in culture, the tools and approaches that we describe here may prove useful. As often happens in science, findings made in one experimental system

can open avenues of investigation useful for other matters of inquiry. Finally, it is important to consider whether humans benefit from some form of selective advantage as a consequence of mutational inactivation of the TDH gene.

References and Notes

1. B. Alberts *et al.*, in *Molecular Biology of the Cell* (Garland, New York, ed. 5, 2007), p. 1.
2. M. H. L. Snow, *J. Embryol. Exp. Morphol.* **42**, 293 (1977).
3. A. G. Smith, *Annu. Rev. Cell Dev. Biol.* **17**, 435 (2001).
4. B. P. Tu *et al.*, *Proc. Natl. Acad. Sci. U.S.A.* **104**, 16886 (2007).
5. L. Warren, J. M. Buchanan, *J. Biol. Chem.* **229**, 613 (1957).
6. H. Weissbach, A. Peterkofsky, B. G. Redfield, H. Dickerman, *J. Biol. Chem.* **238**, 3318 (1963).
7. E. A. Phear, D. M. Greenberg, *J. Am. Chem. Soc.* **79**, 3737 (1957).
8. R. A. Dale, *Biochim. Biophys. Acta* **544**, 496 (1978).
9. E. Almaas, B. Kovacs, T. Vicsek, Z. N. Oltvai, A. L. Barabasi, *Nature* **427**, 839 (2004).
10. J. L. Hartman, *Proc. Natl. Acad. Sci. U.S.A.* **104**, 11,700 (2007).
11. T. Kazuo *et al.*, *J. Bacteriol.* **185**, 4483 (2003).
12. F. A. Brook, R. L. Gardner, *Proc. Natl. Acad. Sci. U.S.A.* **94**, 5709 (1997).
13. A. J. Edgar, *BMC Genet.* **3**, 18 (2002).
14. K. D. Pruitt, T. Tatusova, D. R. Maglott, *Nucleic Acids Res.* **35**, D61 (2007).
15. M. Amit *et al.*, *Dev. Biol.* **227**, 271 (2000).
16. K. Hardy, A. H. Handyside, R. M. T. Winston, *Development* **107**, 597 (1989).
17. We thank B. Tu for the help with LC-MS/MS analysis; J. De Brabander and J. Ready for guidance on the chemical properties of threonine analogs; E. Olson for providing the AOK-5P line of iPSC cells; D. Chong for technical assistance with in situ hybridization assays; and J. Goldstein, M. Rosen, and W. Neaves for helpful scientific input. This work was funded by an NIH Directors Pioneer Award, and unrestricted funds provided to S.L.M. by an anonymous donor.

Supporting Online Material

www.sciencemag.org/cgi/content/full/1173288/DC1
Materials and Methods
Figs. S1 to S8

9 March 2009; accepted 17 June 2009
Published online 9 July 2009;
10.1126/science.1173288

Include this information when citing this paper.

String Theory, Quantum Phase Transitions, and the Emergent Fermi Liquid

Mihailo Čubrović, Jan Zaanen, Koenraad Schalm*

A central problem in quantum condensed matter physics is the critical theory governing the zero-temperature quantum phase transition between strongly renormalized Fermi liquids as found in heavy fermion intermetallics and possibly in high-critical temperature superconductors. We found that the mathematics of string theory is capable of describing such fermionic quantum critical states. Using the anti-de Sitter/conformal field theory correspondence to relate fermionic quantum critical fields to a gravitational problem, we computed the spectral functions of fermions in the field theory. By increasing the fermion density away from the relativistic quantum critical point, a state emerges with all the features of the Fermi liquid.

Quantum many-particle physics lacks a general mathematical theory to deal with fermions at finite density. This is known as the “fermion sign problem”:

There is no recourse to brute-force lattice models because the statistical path-integral methods that work for any bosonic quantum field theory do not work for finite-density Fermi systems.

The nonprobabilistic fermion problem is known to be of exponential complexity (1), and in the absence of a general mathematical framework, all that remains is phenomenological guesswork in the form of the Fermi-liquid theory describing the state of electrons in normal metals and the mean-field theories describing superconductivity and other manifestations of spontaneous symmetry breaking. This problem has become particularly manifest in quantum condensed matter physics with the discovery of electron systems undergoing quantum phase transitions that are reminiscent of the bosonic quantum critical systems (2) but are governed by fermion statistics. Empirically well-documented examples are found in the “heavy fermion” intermetallics, where the zero-temperature transition occurs between different Fermi liquids with quasi-particle masses that diverge at the quantum critical point [(3) and references therein]. Such fermionic quantum critical states are believed to have a direct bearing on the problem of high-critical temperature (high- T_c) superconductivity because of the observation of quantum critical features in the normal state of optimally doped cuprate high- T_c superconductors [(4); (5) and references therein].

A large part of the fermion sign problem is to understand this strongly coupled fermionic quantum critical state. The emergent scale invariance and conformal symmetry at critical points is a benefit in isolating deep questions of principle. The fundamental problem is: How does the system get rid of the scales of Fermi energy and Fermi momentum that are intrinsically rooted in the workings of Fermi-Dirac statistics (6, 7)? From another perspective, how can one construct a renormalization group with a relevant “operator” that describes the emergence of a statistics-controlled (heavy) Fermi liquid from the critical state (3), or perhaps the emergence of a high- T_c superconductor? Here, we show that a mathematical method developed in string theory has the capacity to answer at least some of these questions.

String theory for condensed matter. Our analysis makes use of the AdS/CFT correspondence: a duality relation between classical gravitational physics in a $d + 1$ -dimensional “bulk” space-time with an anti-de Sitter (AdS) geometry and a strongly coupled conformal (quantum critical) field theory (CFT), with a large number of degrees of freedom, that occupies a flat or spherical d -dimensional “boundary” space-time. Applications of AdS/CFT to quantum critical systems have already been studied in the context of the quark-gluon plasma (8, 9), superconductor-insulator transitions (10–14), and cold atom systems at the Feshbach resonance (15–17), but so far the focus has been on bosonic currents [see (18, 19) and references therein]. Although

AdS/CFT is convenient, in principle the ground state or any response of a bosonic statistical field theory can also be computed directly by averaging on a lattice. For fermions, statistical averaging is not possible because of the sign problem. There are, however, indications that AdS/CFT should be able to capture finite-density Fermi systems as well. Ensembles described through AdS/CFT can exhibit a specific heat that scales linearly with the temperature characteristic of Fermi systems (20), zero sound (20–22), and a minimum energy for fermionic excitations (23, 24).

To address the question of whether AdS/CFT can describe finite-density Fermi systems and the Fermi liquid in particular, we compute the single charged fermion propagators and the associated spectral functions that are measured experimentally by angle-resolved photoemission spectroscopy (“AdS-to-ARPES”) and indirectly by scanning tunneling microscopy. The spectral functions contain the crucial information regarding the nature of the fermion states. These are computed on the AdS side by solving for the on-shell (classical) Dirac equation in the curved AdS space-time background with sources at the boundary. A temperature T and finite $U(1)$ chemical potential μ_0 for electric charge is imposed in the field theory by studying the Dirac equation in the background of an AdS Reissner-Nordstrom black hole. We do so with the expectation that the $U(1)$ chemical potential induces a finite density of the charged fermions. The procedure to compute the retarded CFT propagator from the dual AdS description is then well established (8, 19). Relative to the algorithm for computing bosonic responses, the treatment of Dirac waves in AdS is more delicate but straightforward; details are provided in (25). The equations obtained this way are solved numerically and the output is the retarded single fermion propagator $G_R(\omega, k)$ at finite T . Its imaginary part is the single fermion spectral function $A(\omega, k) = -(1/\pi) \text{Im} \text{Tr}[i\gamma^0 G_R(\omega, k)]$ that can be directly compared with ARPES experiments (26).

The reference point for this comparison is the quantum critical point described by a zero chemical potential ($\mu_0 = 0$), zero temperature ($T = 0$), and conformal and Lorentz invariant field theory. (Below, we use relativistic notation where $c = 1$.) Here the fermion propagators $\langle \bar{\Psi}\Psi \rangle \equiv G(\omega, k)$ are completely fixed by symmetry to be of the form

$$G_{\Delta_\Psi}^{\text{CFT}}(\omega, k) \sim \frac{1}{(\sqrt{-\omega^2 + k^2})^{d-2\Delta_\Psi}} \quad (1)$$

where Δ_Ψ is the scaling dimension of the fermion field. Through the $\text{AdS}_{d+1}/\text{CFT}_d$ dictionary, Δ_Ψ is related to the mass parameter in the $d + 1$ -dimensional AdS Dirac equation. Unitarity bounds this mass from below in units of the AdS radius $mL = \Delta_\Psi - d/2 > -1/2$ (we set $L = 1$ in the remainder). The choice of which value to use for m will prove essential to show the emergence of the Fermi liquid. The lower end of the unitarity-bound $m = -1/2 + \delta$, $\delta \ll 1$, corresponds to introducing a fermionic conformal operator with weight $\Delta_\Psi = [(d - 1)/2] + \delta$. This equals the scaling dimension of a nearly free fermion. Even though the underlying CFT is strongly coupled, the absence of a large anomalous dimension for a fermion with mass $m = -1/2 + \delta$ argues that such an operator fulfills a spectator role and is only weakly coupled to this CFT. We therefore use such values in our calculations. Our expectation is that the Fermi liquid, as a system with well-defined quasi-particle excitations, can be described in terms of weakly interacting long-range fields. As we increase m from $m = -1/2 + \delta$, the interactions increase and we can expect the quasi-particle description to cease to be valid beyond $m = 0$. For that value $m = 0$, and beyond $m > 0$, the naïve scaling dimension Δ_O of the fermion-bilinear $O_{\Delta_O} = \bar{\Psi}\Psi$ is marginal or irrelevant, and it is hard to see how the ultraviolet conformal theory can flow to a Fermi-liquid state, assuming that all vacuum state changes are caused by the condensation of bosonic oper-

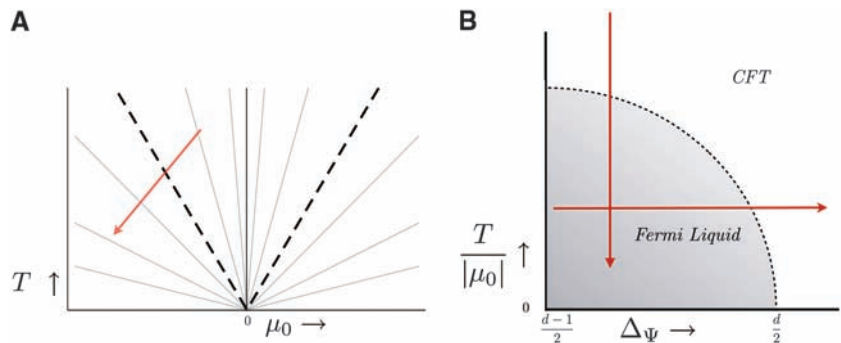


Fig. 1. (A) The phase diagram near a quantum critical point. Gray lines depict lines of constant μ_0/T ; the spectral function of fermions is unchanged along each line if the momenta are appropriately rescaled. As we increase μ_0/T we cross over from the quantum critical regime to the Fermi liquid. (B) The trajectories in parameter space (μ_0/T , Δ_Ψ) studied here. We show the crossover from the quantum critical regime to the Fermi liquid by varying μ_0/T while keeping Δ_Ψ fixed; we cross back to the critical regime varying $\Delta_\Psi \rightarrow d/2$ for μ_0/T fixed. The boundary region is not an exact curve but only a qualitative indication.

Institute-Lorentz for Theoretical Physics, Leiden University, P.O. Box 9506, Leiden, Netherlands.

*To whom correspondence should be addressed. E-mail: kschalm@lorentz.leidenuniv.nl

ators. This intuition is borne out by our results: When $m \geq 0$, the standard Fermi liquid disappears. A similar approach to describing fermionic quantum criticality (27) discusses the special case $m = 0$ or $\Delta_\Psi = d/2$ in detail; an early attempt to describe the $m = 0$ system is (28).

The emergent Fermi liquid. With an eye toward experiment, we consider the AdS₄ dual to a relativistic CFT₃ in $d = 2 + 1$ dimensions (25). We do not know the detailed microscopic CFT, nor do we know whether a dual AdS with fermions as the sole $U(1)$ charged field exists as a fully quantum-consistent theory for all values of $m = \Delta_\Psi - d/2$, but the behavior of fermion spectral functions at a strongly coupled quantum critical point can be deduced nonetheless. Aside

from Δ_Ψ , the spectral function will depend on the dimensionless ratio μ_0/T as well as the $U(1)$ charge g of the fermion; we set $g = 1$ from here on, as we expect that only large changes away from $g = 1$ will change our results qualitatively. We therefore study the system as a function of μ_0/T and Δ_Ψ . Our approach is sketched in Fig. 1B. We first study the spectral behavior as a function of μ_0/T for fixed $\Delta_\Psi < 3/2$; then we study the spectral behavior as we vary the scaling dimension Δ_Ψ from 1 to $3/2$ for fixed μ_0/T coding for an increasingly interacting fermion. Note that our setup and numerical calculations necessitate a finite value of μ_0/T ; all our results are at nonzero T .

Our analysis starts near the reference point $\mu_0/T \rightarrow 0$, where the long-range behavior of

the system is controlled by the quantum critical point (Fig. 1A). Here we expect to recover conformal invariance, as the system forgets about any well-defined scales, and the spectral function should be controlled by the branchcut at $\omega = k$ in the Green's function (Eq. 1): (i) For $\omega < k$ it should vanish. (ii) At $\omega = k$ we expect a sharp peak, which for $\omega \gg k$ scales as $\omega^{2\Delta_\Psi-d}$. Figure 2A shows this expected behavior of spectral function for three different values of the momentum for a fermionic operator with weight $\Delta_\Psi = 5/4$ computed from AdS₄ following the setup in (25).

Turning on μ_0/T while holding $\Delta_\Psi = 5/4$ fixed shifts the center location of the two branchcuts to an effective chemical potential $\omega = \mu_{\text{eff}}$; this bears out our expectation that the $U(1)$ chemical potential induces a finite fermion density. Although the peak at the location of the negative branchcut $\omega \sim \mu_{\text{eff}} - k$ stays broad, the peak at the other branchcut $\omega \sim \mu_{\text{eff}} + k$ sharpens distinctly as the size of μ_0/T is increased (Fig. 2B). We identify this peak with the quasi-particle of the Fermi liquid and its appearance as the crossover between the quantum critical regime and the Fermi-liquid regime. The spectral properties of the Fermi liquid are very well known and display a number of uniquely identifying characteristics (29, 30). If this identification is correct, all these characteristics must be present in our spectra as well.

1) The quasi-particle peak should approach a delta function at the Fermi momentum $k = k_F$. In Fig. 2B we see the peak narrow as we increase k , then peak and broaden back out as we pass $k \sim k_F$ (recall that $T = 0$ is outside our numerical control and the peak always has some broadening). In addition, the spectrum should vanish identically at the Fermi energy $A(\omega = E_F, k) = 0$, independent of k (Fig. 2C).

2) The quasi-particle should have linear dispersion relation near the Fermi energy with a renormalized Fermi velocity v_F different from the underlying relativistic speed $c = 1$. In Fig. 3 we plot the maximum of the peak ω_{max} as a function of k . At high k we recover the linear dispersion relation $\omega = |k|$ underlying the Lorentz invariant branchcut in Eq. 1. Near the Fermi energy and Fermi momentum, however, this dispersion relation changes to a slope $v_F \equiv \lim_{\omega \rightarrow E_F, k \rightarrow k_F} (\omega - E_F)/(k - k_F)$ clearly less than unity.

Note that the Fermi energy E_F is not located at zero frequency. Recall, however, that the AdS chemical potential μ_0 is the bare $U(1)$ chemical potential in the CFT. This is confirmed in Fig. 3 from the high- k behavior: Its Dirac point is μ_0 . On the other hand, the chemical potential felt by the IR fermionic degrees of freedom is renormalized to the value $\mu_F = \mu_0 - E_F$. As is standard, the effective energy $\tilde{\omega} = \omega - E_F$ of the quasi-particle is measured with respect to E_F .

3) At low temperatures, Fermi-liquid theory predicts the width of the quasi-particle peak to

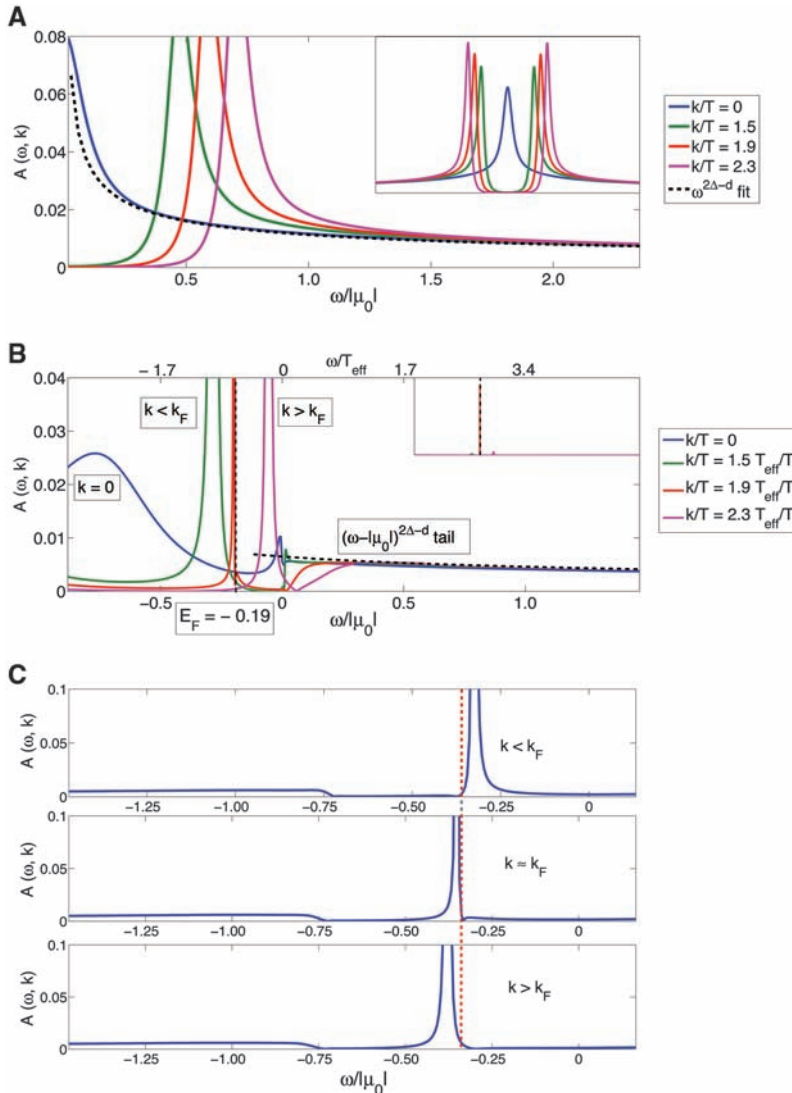


Fig. 2. (A) The spectral function $A(\omega, k)$ for $\mu_0/T = 0.01$ and $m = -1/4$. The spectral function has the asymptotic branchcut behavior of a conformal field of dimension $\Delta_\Psi = d/2 + m = 5/4$: It vanishes for $\omega < k$, save for a finite T tail, and for large ω it scales as $\omega^{2\Delta_\Psi-d}$. (B) The emergence of the quasi-particle peak as we change the chemical potential to $\mu_0/T = -30.9$ for the same value $\Delta_\Psi = 5/4$. The three displayed momenta k/T are rescaled by a factor T_{eff}/T for the most meaningful comparison with those in (A) (25). The insets show the full scales of the peak heights and the dominance of the quasi-particle peak for $k \sim k_F$. (C) Vanishing of the spectral function at E_F for $\Delta_\Psi = 1.05$ and $\mu_0/T = -30.9$. The deviation of the dip location from E_F is a finite temperature effect; it decreases with increasing μ_0/T .

grow quadratically with temperature. Figure 4, A and B, shows this distinctive behavior up to a critical temperature, $T_c/\mu_0 \sim 0.16$. This temper-

ature behavior directly follows from the fact that the imaginary part of the self-energy $\Sigma(\omega, k) = \omega - k - [\text{Tr } i\gamma^0 G(\omega, k)]^{-1}$ should have no linear

term when expanded around E_F : $\text{Im } \Sigma(\omega, k) \sim (\omega - E_F)^2 + \dots$. This is shown in Fig. 4, C and D.

These results give us confidence that we have identified the characteristic quasi-particles at the Fermi surface of the Fermi liquid emerging from the quantum critical point.

We now discuss how this Fermi liquid evolves when we increase the bare μ_0 (Fig. 5). Similar to the fermion chemical potential μ_F , the fundamental control parameter of the Fermi liquid, the fermion density ρ_F , is not directly related to the AdS μ_0 . We can, however, infer it from the Fermi momentum k_F that is set by the quasi-particle pole via Luttinger's theorem $\rho_F \sim k_F^d$. The more illustrative figure is therefore Fig. 5B, which shows the quasi-particle characteristics as a function of k_F/T . We find that the quasi-particle velocities decrease slightly with increasing k_F , rapidly leveling off to a finite constant less than the relativistic speed. Thus, the quasi-particles become increasingly heavy as their mass $m_F \equiv k_F/v_F$ approaches linear growth with k_F . The Fermi energy E_F also shows linear growth. Suppose the heavy Fermi-quasi-particle system has the underlying canonical nonrelativistic dispersion relation $E = k^2/(2m_F) = k_F^2/(2m_F) + v_F(k - k_F) + \dots$; in that case, the observed Fermi energy E_F should equal the renormalized Fermi energy $E_F^{(\text{ren})} \equiv k_F^2/(2m_F)$. Figure 5B shows that these energies E_F and $E_F^{(\text{ren})}$

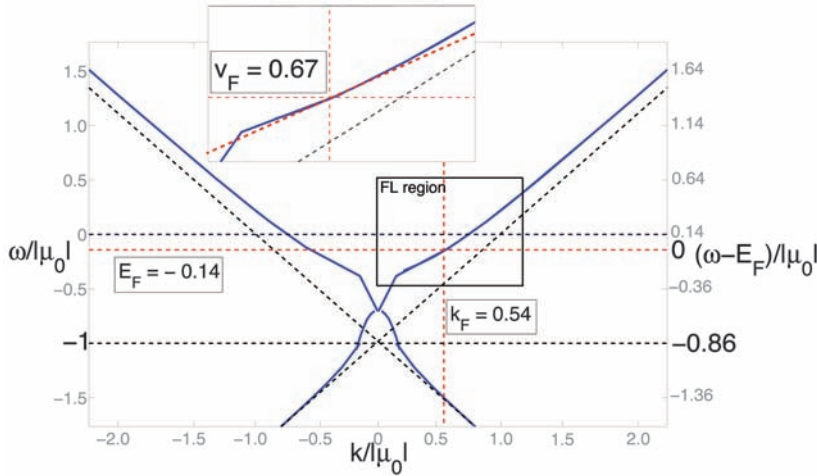
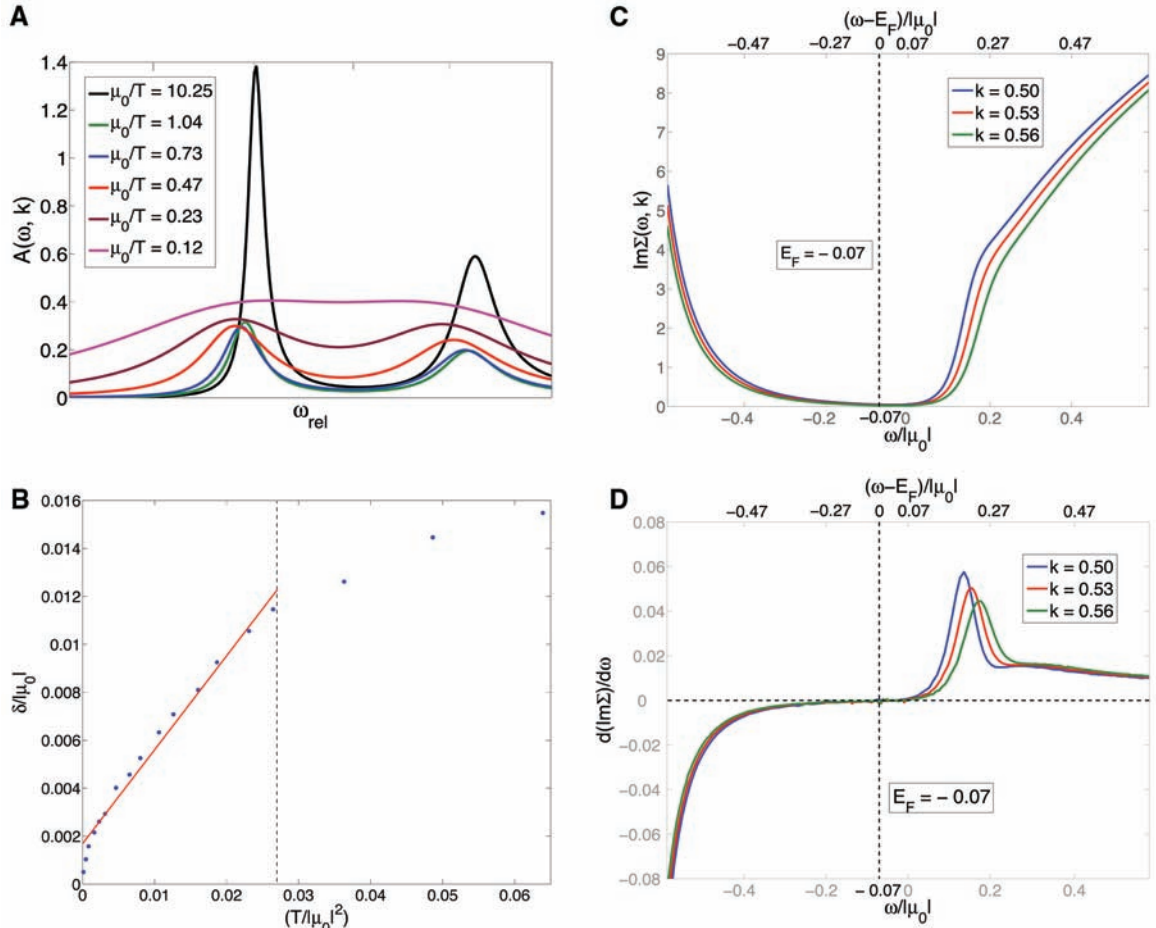


Fig. 3. Maxima in the spectral function as a function of k/μ_0 for $\Delta_\psi = 1.35$ and $\mu_0/T = -30.9$. Asymptotically for large k the negative- k branchcut recovers the Lorentz-invariant linear dispersion with unit velocity, but with the zero shifted to $-\mu_0$. The peak location of the positive- k branchcut that changes into the quasi-particle peak changes noticeably. It gives the dispersion relation of the quasi-particle near (E_F, k_F) . The change of the slope from unity shows renormalization of the Fermi velocity. This is highlighted in the inset. Note that the Fermi energy E_F is not located at $\omega_{\text{AdS}} = 0$. The AdS calculation visualizes the renormalization of the bare chemical potential $\mu_0 = \mu_{\text{AdS}}$ to the effective chemical potential $\mu_F = \mu_0 - E_F$ felt by the low-frequency fermions.

Fig. 4. (A) Temperature dependence of the quasi-particle peak for $\Delta_\psi = 5/4$ and $k/k_F \approx 0.5$; all curves have been shifted to a common peak center. (B) The quasi-particle peak width $\delta \sim \text{Re } \Sigma(\omega, k = k_F)$ for $\Delta_\psi = 5/4$ as a function of T^2 ; it reflects the expected behavior $\delta \sim T^2$ up to a critical temperature T_c/μ_0 , beyond which the notion of a quasi-particle becomes untenable. (C and D) The imaginary part of the self-energy $\Sigma(\omega, k)$ near E_F, k_F for $\Delta_\psi = 1.4$, $\mu_0/T = -30.9$. The defining $\text{Im } \Sigma(\omega, k) \sim (\omega - E_F)^2 + \dots$ dependence for Fermi-liquid quasi-particles is faint in (C) but obvious in (D). It shows that the intercept of $\partial_\omega \text{Im } \Sigma(\omega, k)$ vanishes at E_F, k_F .



track each other remarkably well. We therefore infer that the true zero of energy of the Fermi quasi-particle is set by the renormalized Fermi energy as deduced from the Fermi velocity and Fermi momentum.

Although the true quasi-particle behavior disappears at $T > T_c$, Fig. 5A indicates that in the limit $k_F/T \rightarrow 0$ the quasi-particle pole strength vanishes, $Z_k \rightarrow 0$, while the Fermi velocity v_F remains finite; v_F approaches the bare

velocity $v_F = 1$. This is seemingly at odds with the heavy Fermi liquid relation $Z_k \sim m_{\text{micro}}/m_F = m_{\text{micro}}v_F/k_F$. The resolution is the restoration of Lorentz invariance at zero density. From general Fermi liquid considerations it follows that $v_F = Z_k(1 + \partial_k \text{Re} \Sigma|_{E_F, k_F})$ and $Z_k = 1/(1 - \partial_\omega \text{Re} \Sigma|_{E_F, k_F})$, where $\partial_{k,\omega}$ Re Σ refers to the momentum and energy derivatives of the real part of the fermion self-energy $\Sigma(\omega, k)$ at k_F, E_F . Lorentz invariance imposes $\partial_\omega \Sigma' = -\partial_k \Sigma'$, which allows

Fig. 5. The quasi-particle characteristics as a function of μ_0/T for $\Delta_\Psi = 5/4$. (A) The change of k_F, v_F, m_F, E_F , and the pole strength Z (the total weight between half-maxima) as we change μ_0/T . Beyond a critical value $(\mu_0/T)_c$ we lose the characteristic T^2 broadening of the peak and there is no longer a real quasi-particle, although the peak is still present. For the Fermi liquid, k_F/T rather than μ_0/T is the defining parameter. (B) We can invert this relation, and (B) shows the quasi-particle characteristics as a function of k_F/T . Note the linear relationships of m_F and E_F to k_F and that the renormalized Fermi energy $E^{(\text{ren})} \equiv k_F^2/(2m_F)$ matches the empirical value E_F remarkably well.

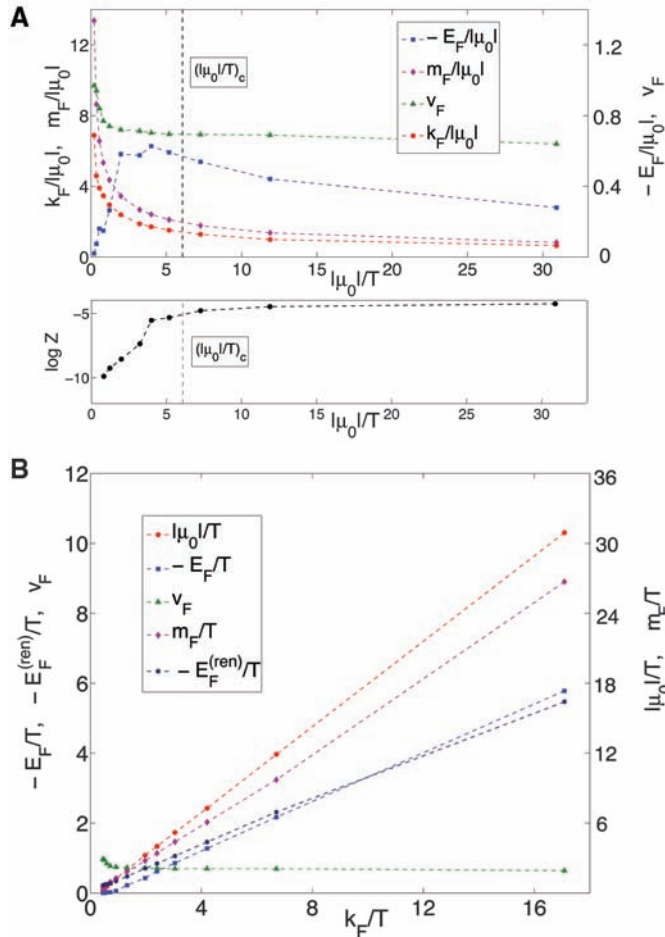
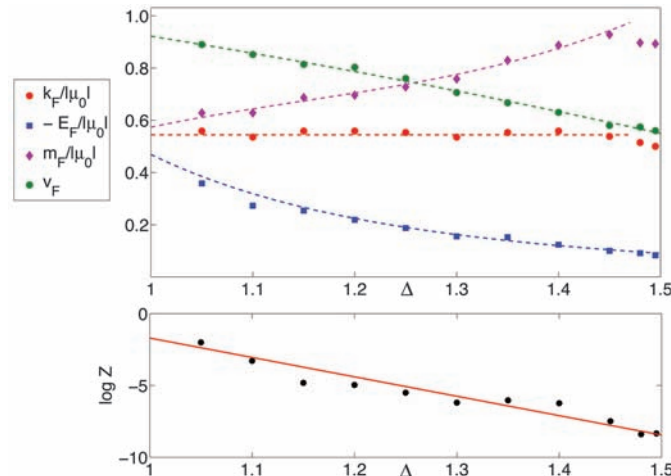


Fig. 6. The quasi-particle characteristics as a function of the Dirac fermion mass $-1/2 < m < 0$ corresponding to $1 < \Delta_\Psi < 3/2$ for $\mu_0/T = -30.9$. The upper panel shows the independence of k_F of the mass. This indicates Luttinger's theorem if the anomalous dimension Δ_Ψ is taken as an indicator of the interaction strength. Note that v_F and E_F both approach finite values as $\Delta_\Psi \rightarrow 3/2$. The lower panel shows the exponential vanishing pole strength Z (the integral between the half-maxima) as $m \rightarrow 0$.



for vanishing Z_k with $v_F \rightarrow 1$. Interestingly, the case has been made that such a relativistic fermionic behavior might be underlying the physics of cuprate high- T_c superconductors (31).

Finally, we address the important question of what happens when we vary the conformal dimension Δ_Ψ of the fermionic operator. Figure 6 shows that the Fermi momentum k_F stays constant as we increase Δ_Ψ . This completes our identification of the new phase as the Fermi liquid: It indicates that the AdS dual obeys Luttinger's theorem, if we can interpret the conformal dimension of the fermionic operator as a proxy for the interaction strength. We find furthermore that the quasi-particle pole strength vanishes as we approach $\Delta_\Psi = 3/2$. This confirms our earlier assumption that it is essential to study the system for $\Delta_\Psi < d/2$ and that the point $\Delta_\Psi = d/2$, where the naive fermion bilinear becomes marginal, signals the onset of a new regime. Because the fermion bilinear is marginal at that point, this ought to be an interesting regime in its own right, and we refer to (27) for a discussion thereof (32). Highly remarkable is that the pole strength vanishes in an exponential fashion rather than the anticipated algebraic behavior (6, 7). This could indicate that an essential singularity governs the critical point at $\Delta_\Psi = d/2$, and we note that such a type of behavior was identified by Lawler *et al.* in their analysis of the Pomeranchuk instability in $d = 2 + 1$ dimensions using the Haldane patching bosonization procedure (33). Note that this finite μ_0/T transition as we vary Δ_Ψ has no clear symmetry change, similar to (7). However, this may be an artifact of the fact that our theory is not quantum mechanically complete (25). Note also that the quasi-particle velocity and the renormalized Fermi energy $E_F = v_F(k - k_F) - E$ stay finite at the $\Delta_\Psi = 3/2$ transition with $Z \rightarrow 0$, which could indicate an emergent Lorentz invariance for the reasons discussed above.

Concluding remarks. We have presented evidence that the AdS dual description of strongly coupled field theories can describe the emergence of the Fermi liquid from a quantum critical state, as a function of both density and interaction strength, as encoded in the conformal dimension of the fermionic operators. From the AdS gravity perspective, it was unclear whether this would happen. Sharp peaks in the CFT spectral function correspond to so-called quasi-normal modes of black holes (34), but Dirac quasi-normal modes have received little study [see, e.g., (35)]. It is remarkable that the AdS calculation processes the Fermi-Dirac statistics essential to the Fermi liquid correctly. This is manifested by the emergent renormalized Fermi energy and the validity of Luttinger's theorem. The AdS gravity computation, however, is completely classical without explicit quantum statistics, although we do probe the system with a fermion. It would therefore be interesting to fully understand the AdS description of what is happening, in particular how the emergent scales

E_F and k_F feature in the geometry. An early indication of such scales was seen in (24, 36) in a variant of the story that geometry is not universal in string theory: The geometry depends on the probe used, and different probes experience different geometric backgrounds. The absence of these scales in the general relativistic description of the AdS black hole could thus be an artifact of the Riemannian metric description of space-time.

Regardless of these questions, AdS/CFT has shown itself to be a powerful tool to describe finite-density Fermi systems. The description of the emergent Fermi liquid presented here argues that AdS/CFT is uniquely suited as a computational device for field theory problems suffering from fermion sign problems. AdS/CFT represents a rich mathematical environment and a new approach to qualitatively and quantitatively investigate important questions in quantum many-body theory at finite fermion density.

References and Notes

1. M. Troyer, U. J. Wiese, *Phys. Rev. Lett.* **94**, 170201 (2005).
2. S. Sachdev, *Quantum Phase Transitions* (Cambridge Univ. Press, Cambridge, 1999).
3. J. Zaanen, *Science* **319**, 1295 (2008).
4. D. van der Marel *et al.*, *Nature* **425**, 271 (2003).
5. J. Zaanen, *Nature* **430**, 512 (2004).
6. T. Senthil, *Phys. Rev. B* **78**, 035103 (2008).
7. F. Krüger, J. Zaanen, *Phys. Rev. B* **78**, 035104 (2008).

8. D. T. Son, A. O. Starinets, *Annu. Rev. Nucl. Part. Sci.* **57**, 95 (2007).
9. S. S. Gubser, A. Karch, <http://arxiv.org/abs/0901.0935> (2009).
10. C. P. Herzog, P. Kovtun, S. Sachdev, D. T. Son, *Phys. Rev. D* **75**, 085020 (2007).
11. S. A. Hartnoll, P. K. Kovtun, M. Muller, S. Sachdev, *Phys. Rev. B* **76**, 144502 (2007).
12. S. S. Gubser, *Phys. Rev. D* **78**, 065034 (2008).
13. S. A. Hartnoll, C. P. Herzog, G. T. Horowitz, *Phys. Rev. Lett.* **101**, 031601 (2008).
14. S. A. Hartnoll, C. P. Herzog, G. T. Horowitz, *J. High Energy Phys.* **0812**, 015 (2008).
15. D. T. Son, *Phys. Rev. D* **78**, 046003 (2008).
16. K. Balasubramanian, J. McGreevy, *Phys. Rev. Lett.* **101**, 061601 (2008).
17. A. Adams, K. Balasubramanian, J. McGreevy, *J. High Energy Phys.* **0811**, 059 (2008).
18. S. A. Hartnoll, *Science* **322**, 1639 (2008).
19. S. A. Hartnoll, <http://arxiv.org/abs/0903.3246> (2009).
20. M. Kulaxizi, A. Parnachev, *Nucl. Phys. B* **815**, 125 (2009).
21. A. Karch, D. T. Son, A. O. Starinets, *Phys. Rev. Lett.* **102**, 051602 (2009).
22. M. Kulaxizi, A. Parnachev, *Phys. Rev. D* **78**, 086004 (2008).
23. L. Brits, M. Rozali, <http://arxiv.org/abs/0810.5321> (2008).
24. H. H. Shieh, G. van Anders, *J. High Energy Phys.* **0903**, 019 (2009).
25. See supporting material on Science Online.
26. ARPES Fermi-surface measurements assume that electrons are the only relevant charged objects. If this is so, then it measures the electron (i.e., fermion) spectral function. This spectral function is what we compute here, even though in our AdS setup the fermions are almost certainly not the only charged objects.
27. H. Liu, J. McGreevy, D. Vegh, <http://arxiv.org/abs/0903.2477> (2009).

28. S. S. Lee, *Phys. Rev. D* **79**, 086006 (2009).
29. E. M. Lifshitz, L. P. Pitaevskii, *Statistical Physics, Part 2* (Pergamon, Oxford, 1980).
30. H. J. Schulz, G. Cuniberti, P. Pieri, in *Field Theories for Low-Dimensional Condensed Matter Systems*, G. Morandi, P. Sodano, A. Tagliacozzo, V. Tognetti, Eds. (Springer, Berlin, 2000), chap. 2.
31. M. Randeria, A. Paramakanti, N. Trivedi, *Phys. Rev. B* **69**, 144509 (2004).
32. Note that the $m = 0$ spectral peak discussed in (27) is therefore not the peak we identified with the quasi-particle state. See (25).
33. M. J. Lawler, V. Fernandez, D. G. Barci, E. Fradkin, L. Oxman, *Phys. Rev. B* **73**, 085101 (2006).
34. P. K. Kovtun, A. O. Starinets, *Phys. Rev. D* **72**, 086009 (2005).
35. H. T. Cho, A. S. Cornell, J. Doukas, W. Naylor, *Phys. Rev. D* **77**, 016004 (2008).
36. M. Rozali, H. H. Shieh, M. Van Raamsdonk, J. Wu, *J. High Energy Phys.* **0801**, 053 (2008).
37. We thank F. Denef, S. Hartnoll, H. Liu, J. McGreevy, S. Sachdev, D. Sadri, and D. Vegh for discussions. Supported by a VIDI Innovative Research Incentive Grant (K.S.) from the Netherlands Organization for Scientific Research (NWO) and by a Spinoza Award (J.Z.) from NWO and the Dutch Foundation for Fundamental Research on Matter (FOM).

Supporting Online Material

www.sciencemag.org/cgi/content/full/1174962/DC1

SOM Text

Fig. S1

References

14 April 2009; accepted 16 June 2009

Published online 25 June 2009;

10.1126/science.1174962

Include this information when citing this paper.

REPORTS

Radio Imaging of the Very-High-Energy γ -Ray Emission Region in the Central Engine of a Radio Galaxy

The VERITAS Collaboration, the VLBA 43 GHz M87 Monitoring Team, the H.E.S.S. Collaboration, the MAGIC Collaboration*

The accretion of matter onto a massive black hole is believed to feed the relativistic plasma jets found in many active galactic nuclei (AGN). Although some AGN accelerate particles to energies exceeding 10^{12} electron volts and are bright sources of very-high-energy (VHE) γ -ray emission, it is not yet known where the VHE emission originates. Here we report on radio and VHE observations of the radio galaxy Messier 87, revealing a period of extremely strong VHE γ -ray flares accompanied by a strong increase of the radio flux from its nucleus. These results imply that charged particles are accelerated to very high energies in the immediate vicinity of the black hole.

Active galactic nuclei (AGN) are extragalactic objects thought to be powered by massive black holes in their centers. They can show strong emission from the core, which is often dominated by broadband continuum radiation ranging from radio to x-rays and by substantial flux variability on different time scales. More than 20 AGN have been es-

tablished as very-high-energy (VHE) γ -ray emitters with measured energies above 0.1 TeV; the jets of most of these sources are believed to be aligned with the line of sight to within a few degrees. The size of the VHE γ -ray emission region can generally be constrained by the time scale of the observed flux variability (1, 2), but its location remains unknown.

We studied the inner structure of the jet of the giant radio galaxy Messier 87 (M87), a known VHE γ -ray-emitting AGN (2–5) with a $(6.0 \pm$

$0.5) \times 10^9$ solar mass black hole (6) (scaled by distance), located 16.7 Mpc (54 million light years) away in the Virgo cluster of galaxies. The angle between its plasma jet and the line of sight is estimated to lie between 15° and 25° [see supporting online material (SOM) text]. The substructures of the jet, which are expected to scale with the Schwarzschild radius R_s of the black hole (7), are resolved in the x-ray, optical, and radio wave bands (8) (Fig. 1). High-frequency radio very-long-baseline interferometry (VLBI) observations with resolution under a milli-arc second (milli-arc sec) are starting to probe the collimation region of the jet (9). With its proximity, bright and well-resolved jet, and very massive black hole, M87 provides a unique laboratory in which to study relativistic jet physics in connection with the mechanisms of VHE γ -ray emission in AGN.

VLBI observations of the M87 inner jet show a well-resolved, edge-brightened structure extending to within 0.5 milli-arc sec (0.04 pc or $70 R_s$) of the core. Closer to the core, the jet has a wide opening angle, suggesting that this is the collimation region (9). Generally, the core can be offset from the actual location of the black hole by an unknown amount (10), in which case it could mark the location of a shock structure or the region where the jet becomes optically thin. However, in the case of M87, a weak structure

*The full list of authors and affiliations is presented at the end of this paper.

Confinement/deconfinement transition from symmetry breaking in gauge/gravity duality

Mihailo Čubrović

*Institute for Theoretical Physics, University of Cologne,
Zùlpicher Strasse 77, D-50937, Cologne, Germany*

E-mail: mcubrovic@gmail.com

ABSTRACT: We study the confinement/deconfinement transition in a strongly coupled system triggered by an independent symmetry-breaking quantum phase transition in gauge/gravity duality. The gravity dual is an Einstein-scalar-dilaton system with AdS near-boundary behavior and soft wall interior at zero scalar condensate. We study the cases of neutral and charged condensate separately. In the former case the condensation breaks the discrete \mathbb{Z}_2 symmetry while a charged condensate breaks the continuous $U(1)$ symmetry. After the condensation of the order parameter, the non-zero vacuum expectation value of the scalar couples to the dilaton, changing the soft wall geometry into a non-confining and anisotropically scale-invariant infrared metric. In other words, the formation of long-range order is immediately followed by the deconfinement transition and the two critical points coincide. The confined phase has a scale — the confinement scale (energy gap) which vanishes in the deconfined case. Therefore, the breaking of the symmetry of the scalar (\mathbb{Z}_2 or $U(1)$) in turn restores the scaling symmetry in the system and neither phase has a higher overall symmetry than the other. When the scalar is charged the phase transition is continuous which goes against the Ginzburg-Landau theory where such transitions generically only occur discontinuously. This phenomenon has some commonalities with the scenario of deconfined criticality. The mechanism we have found has applications mainly in effective field theories such as quantum magnetic systems. We briefly discuss these applications and the relation to real-world systems.

KEYWORDS: AdS-CFT Correspondence, Gauge-gravity correspondence, Holography and condensed matter physics (AdS/CMT), Holography and quark-gluon plasmas

ARXIV EPRINT: [1605.07849](https://arxiv.org/abs/1605.07849)

Contents

1	Introduction	1
2	Gravity setup	4
3	Solutions in the infrared: soft-wall and AdS-like	8
3.1	Neutral solutions	8
3.1.1	No symmetry breaking	8
3.1.2	Symmetry-breaking order parameter	9
3.2	Charged solutions	11
3.2.1	No symmetry breaking	11
3.2.2	Symmetry-breaking order parameter	12
3.3	Resume of the geometries	13
4	Phase diagram and thermodynamics	13
4.1	The condensation of the boson at $T = 0$	14
4.1.1	The neutral case	15
4.1.2	The charged case	17
4.2	Free energies and phases at zero temperature	18
4.3	Finite temperature thermodynamics	20
4.4	Structure of the phase diagram	23
5	Response functions and bound states	24
5.1	Definition and equations of motion	24
5.2	Effective Schrödinger equation for the response functions	26
5.3	Numerics	27
5.3.1	AC conductivity	27
5.3.2	Retarded propagator	29
5.3.3	Charge susceptibility	30
6	Conclusions and discussion	30
A	A short summary of numerical calculations	34

1 Introduction

The gauge/gravity duality, AdS/CFT correspondence or holography [1, 2] is by now a well-established area, providing insights into fundamental issues of string theory and quantum gravity but also into strongly-coupled physics in various areas such as quantum chromodynamics (QCD) and condensed matter systems [4]. In such studies, the spacetime has

anti de Sitter (AdS) geometry at large distances, near the boundary of the space, while the interior is deformed away from AdS by various matter and gauge fields. This means that the high-energy behavior (ultraviolet, UV) of the field theory, determined by the near-boundary geometry, is conformally invariant but the interesting low-energy (infrared, IR) physics is determined by the geometry of the interior which can look differently for various configurations of fields and matter. The basic idea is that the radial coordinate on the gravity side corresponds to the energy scale in field theory: as we travel from the boundary toward the interior, we probe lower and lower energy scales.

One outstanding problem where AdS/CFT has provided some insights is the confinement/deconfinement transition in strongly coupled gauge theories. In the confined phase, only gauge-neutral bound states (mesons or baryons) can be observed. In the deconfined phase, individual gauge-charged particles are also observable. The fact that the gauge-charged excitations confine to form gauge-neutral bound states means that a gap opens, as we only see the gauge-neutral bound states at finite energies; the number of the degrees of freedom is effectively reduced at low energies. In AdS/CFT, this in turn means that the scale of the spacetime in the dual gravity model shrinks to zero in the interior. Such geometries are called soft-wall geometries, if the scale shrinks continuously, or hard-wall geometries if the spacetime is sharply cut off at some finite radius. Soft-wall geometries (which are more realistic than the hard-wall idealization) are obtained by coupling a neutral scalar — dilaton — to the metric in a non-minimal way. They were first used in so-called AdS/QCD studies in [3, 21, 32–34].

Typically, as the temperature rises, the system undergoes a confinement/deconfinement phase transition: when the system deconfines, the free energy of individual gauge-charged particles becomes finite, and they can be observed. This is the dominant mechanism in quark-gluon plasmas in QCD. But confinement/deconfinement is also present in condensed matter systems. Here the gauge field is not microscopic but emergent in the low-energy description. In the confined phase the degrees of freedom are bound into gauge-neutral excitations which are seen as normal electrons, i.e. quasiparticles. In the deconfined regime, the excitations are gauge-charged and not observable by ordinary probes in experiment. This might explain some non-Fermi liquid materials [10–15]. This topic was addressed e.g in [29] as well as in a series of very general and systematic studies by Kiritsis and coworkers [24–26]. In such systems, it is realistic to assume that deconfinement can also happen as a quantum phase transition, at zero temperature, when some parameter is varied. Deconfined gauge theories in AdS/CFT often have full conformal symmetry (dual to AdS geometry) or at least some form of anisotropic scale covariance (with different scaling exponents along different coordinates) which arguably can be expected to hold at high energies for many realistic gauge theories [3] while a confined theory has an explicit scale because the energy of gauge-neutral bound states or, equivalently, the position of the wall z_w along the radial direction sets a scale. The confinement/deconfinement transition can thus be treated also as a symmetry-breaking transition, where scale covariance is lost. The scaling properties of dilaton spacetimes have recently become known as hyperscaling geometries [27, 30, 31] and have attracted attention also independently of the confinement/deconfinement problems.

Another class of problems where strongly-coupled models are provided by AdS/CFT are the order/disorder quantum phase transitions where some field O acquires a vacuum expectation value (VEV). A textbook example is the famous holographic superconductor [5–7] where a charged field condenses, breaking the $U(1)$ symmetry, similarly to the superconducting transition in metals. While many such systems are described by the Landau-Ginzburg paradigm, this paradigm fails in some strongly-coupled systems. Many variations of such models have been proposed [36–40] where a dilaton is also present, or it is precisely the dilaton that condenses. The work [36] in particular addresses the setup similar as in our study: a scalar which condenses in the presence of a separate dilaton (however, explicit calculation with backreaction on dilaton and geometry was not done to check if the confinement/deconfinement transition exists). This opens an alley to study the interplay of the two transitions, the confinement/deconfinement transition and the order/disorder transition.

Our idea is to explore the interplay of the two above phenomena: the confinement/deconfinement transition and the condensation of an order parameter. They might in principle be independent, or one might foster or hinder the other. Well-studied examples of holographic superconductors [5] or superconductor-dilaton systems [37, 38] suggest that order parameter condensation often makes the length scale in the interior decrease faster: a charged black AdS-Reissner-Nordström black hole, which in deep interior has the AdS_2 geometry of finite radius, upon condensation turns into a Lifshitz spacetime whose length scale vanishes in the interior [4, 7]; in [29] this was interpreted as turning a fractionalized non-Fermi liquid into a system closer to a Fermi liquid. On general grounds one also expects that an ordered system can be expressed in terms of fewer degrees of freedom (in terms of the fluctuations of the order parameter rather than all microscopic degrees of freedom).

We will however present an example where the opposite occurs, i.e. the formation of a condensate destroys the soft-wall geometry and deconfinement takes place. Thus the phase transition is not a straightforward symmetry-breaking transition: on one hand, the condensate breaks a symmetry, on the other hand, another symmetry is restored as the deconfinement happens. This happens because the confinement scale (the energy gap) vanishes so scale invariance is restored. Our main interest is how this transition looks and what is its nature. We find that the phase transition can be continuous, contrary to the prediction of the Ginzburg-Landau theory where such transitions (where the two phases have different symmetries neither of which is a subgroup of the other) can only occur through phase coexistence or a first-order transition.

This has some common logic with the deconfined criticality concept of [10, 11]. Denote the full symmetry group of the non-soft-wall geometry by \mathbb{G}_1 and its subgroup which remains after confinement by \mathbb{G}_2 . We do not know what exactly $\mathbb{G}_{1,2}$ are but generically \mathbb{G}_1 will contain some scale invariance which stems from the scaling behavior of the IR geometry, while the confined system has a scale (the confinement gap) and thus \mathbb{G}_2 does not contain any scaling symmetry. Denote further the symmetry group broken by the condensate formation by \mathbb{H}_1 and its residual subgroup by \mathbb{H}_2 (in our case, we have $(\mathbb{H}_1, \mathbb{H}_2) = (\mathbb{Z}_2, \mathbb{I})$ for the neutral scalar and $(\mathbb{H}_1, \mathbb{H}_2) = (U(1), \mathbb{I})$ for the charged scalar. Now in our paper we have a transition from the confined-disordered phase (symmetry group $\mathbb{G}_2 \otimes \mathbb{H}_1$) to the

deconfined-ordered phase with the symmetry $\mathbb{G}_1 \otimes \mathbb{H}_2$. We have $\mathbb{G}_2 < \mathbb{G}_1$ and $\mathbb{H}_2 < \mathbb{H}_1$ so the critical point partly breaks, and partly restores symmetry. The same situation occurs in deconfined criticality scenario but the detailed physics is different: at a deconfined critical point (*only* at the critical point) there is an additional topological conserved quantity which governs the transition. We will comment on this in the paper in more detail, however no direct relation or equivalence can be established at this level. We cite the deconfined criticality as an inspiration and possible direction of future work, not something that our present results are directly relevant for.

Although the specific problem of how condensation of a scalar may influence the confinement/deconfinement transition was not studied so far to the best of our knowledge, a lot of work was done on Einstein-Maxwell-dilaton systems in other contexts. After the pioneering work in [3] which first drew attention to the AdS/QCD alley of research, confinement was studied in [32–34] and more systematically in [22, 23] with finite temperature behavior further explored in [21]. These authors have studied a neutral Einstein-dilaton system and have classified geometries which lead to confinement as well as the nature of the phase transition (first-order or continuous). Charged systems have been studied in [24–27]. The non-condensed phases of our system (without the order parameter) are just a small subset of the systems studied in [25] and we will frequently compare our case to their general results throughout the paper. Charged EMD systems are particularly well studied as top-down constructions regularly include charged fields. The charged case we consider is also closely related to the dilatonic charged black holes considered in [18–20] as possible candidates for gravity duals of Fermi liquids. The issue of a scalar condensation in the presence of dilaton is also rather extensively studied, e.g. in [39, 40] but in these cases the dilaton does not lead to a soft wall geometry so there is no confinement which can be destroyed upon condensation. In [35, 37, 38] the dilaton itself is charged (i.e., a charged scalar is coupled to the curvature) and the phenomenology was found to be similar to the basic holographic superconductor [5].

In section 2 we give the gravity setup and explain our model. Section 3 sums up different solutions for the geometry, depending on the bulk mass (conformal dimensions) of the scalar field and classifies the solutions into confined and deconfined ones. In section 4 we explain how the condensation of the order parameter proceeds and how it leads to deconfinement, and finally construct the phase diagram of the system. In the fifth section we study the response functions (conductivity, charge susceptibility and the retarded propagator of the scalar field) and show how various phases and their symmetries can be inspected from the response functions which are in principle measurable quantities. The last section sums up the conclusions and discusses possible directions of further work. The appendix contains a detailed description of the numerical calculations.

2 Gravity setup

We have the Einstein-(Maxwell)-scalar-dilaton system in asymptotically AdS $_{D+1}$ space-time, with or without the Maxwell sector: the metric $g_{\mu\nu}$, the dilaton scalar Φ and the (neutral or charged) scalar χ . If the system is charged, there is also the electric field A_μ

where only the electric component A_0 is nonzero (we do not consider magnetic systems). The dilaton Φ couples to the curvature R in the string frame and is always neutral; thus unlike the models where the dilaton (actually, a non-minimally coupled scalar) is itself the charged field that condenses, we want the dilaton to perform its usual work, i.e. to control the scale (and confinement). This will be crucial to study the influence of the order parameter on the confining properties. We find it more convenient to work in the Einstein frame where the dilaton does not couple non-minimally to the metric but to the matter fields only. The scalar χ is minimally coupled to gravity and to the Maxwell field with charge q (including the possibility $q = 0$). We now have the action:

$$S = \int dt \int d^D x \sqrt{-g} (R - \Lambda + L_\Phi + L_\psi + L_{EM}) \quad (2.1)$$

$$L_\Phi = -\xi (\partial\Phi)^2 - V(\Phi) \quad (2.2)$$

$$L_\chi = -\frac{1}{2} Z(\Phi) (D\chi)^2 - \frac{m_\chi^2}{2} \chi^2 = -\frac{1}{2} Z(\Phi) (\partial\chi)^2 - \frac{q^2}{2f(z)^2} Z(\Phi) A_0^2 \chi^2 - \frac{e^{-2A}}{2\xi f} m_\chi^2 \chi^2 \quad (2.3)$$

$$L_{EM} = -\frac{1}{4} \mathcal{T}(\Phi) F^2 = -\frac{1}{2} \mathcal{T}(\Phi) (\partial A_0)^2. \quad (2.4)$$

This is just the minimal symmetry-allowed action for these fields apart from the exponential couplings of the dilaton. In string theory we would have $\xi = 4/(D-1)$ but since our model is purely phenomenological we can leave it as an arbitrary positive constant. We have subtracted the constant piece, i.e. the cosmological constant $\Lambda = -D(D-1)/2$ from the dilaton potential, so the AdS solution corresponds to $\Phi = 0$ (and $\chi = 0$). The geometry is AdS_{D+1} in the far field (UV, near-boundary) region while, with a suitable choice of $V(\Phi), Z(\Phi), \mathcal{T}(\Phi)$ it narrows into a soft wall in the interior (IR). The AdS radius is rescaled to $L = 1$. The potential of the scalar is fixed to just the mass term, like in [5, 6], as it suffices to achieve condensation (and is a consistent truncation of more elaborate, top-down potentials). As explained in [5], the field χ , even when charged, can be made real, i.e. its phase can be put to zero.

Now we come to the question of choosing the model, i.e. the dilaton potentials $V(\Phi), Z(\Phi), \mathcal{T}(\Phi)$. The basic picture of confinement in AdS/CFT means the dilaton potential should produce a soft-wall geometry but we also want to study its interplay with the establishment of (bosonic) long-range order and condensation. We want to engineer the dilaton potentials so that the scalar is unstable to condensation into a hairy black hole with $\chi(z) \neq 0$ for some m_χ^2 in the soft wall background *and* that the soft wall dilaton is in turn unstable to transition into a non-confining (non-soft-wall) solution upon the formation of scalar hair. This means that, upon dialing m_χ^2 , we should have two possible solutions for the scalar, $\chi(z) = 0$ and $\chi(z) \neq 0$, each with a different nonzero solution for the dilaton $\Phi(z)$. The following potentials will serve us well:

$$V(\Phi) = V_0 \Phi^{\frac{2\nu-2}{\nu}} e^{2\Phi} \quad (2.5)$$

$$Z(\Phi) = Z_0 e^{\gamma\Phi}, \quad D-1 < \gamma < 2D \quad (2.6)$$

$$\mathcal{T}(\Phi) = T_0 e^{\tau\Phi}, \quad \tau > 2D-4, \quad \tau^2 > \left(\gamma + \frac{D-2}{8}\right)^2 + \frac{1}{D}. \quad (2.7)$$

The limitations for γ and τ follow from the requirement that the stress-energy tensor of the EM field and also of the charged scalar field χ should stay finite and not dominate over the components of the Einstein tensor. In top-down constructions from supergravity the functions $Z(\Phi), V(\Phi), \mathcal{T}(\Phi)$ are typically all purely exponential in Φ (or linear combinations of such exponentials), with fixed exponent values. In our bottom-up approach these exponents are free parameters and by tuning these we can study the behavior we are looking for. We have added a power-law prefactor to (2.5) for reasons of better analytical tractability: the soft wall solution for the scale factor $A(z)$ is simplified with this choice for $V(\Phi)$ and at the leading order reads just $A(z) = z^\nu$ with subleading corrections for $z \rightarrow \infty$ whereas with a purely exponential $V(\Phi)$ it would have been more complicated also at leading order. We conjecture that the phase diagram and overall behavior of the system would be similar for $V \propto e^{\kappa\Phi}$. In a companion publication we derive our model from a superpotential which demonstrates the stability of the system, giving legitimacy to (2.5). The prefactors Z_0, \mathcal{T}_0 merely rescale the amplitudes of χ, A_0 and can be put to unity (they have no physical meaning). Notice the case $\nu = 1$ is special: then we get the linear dilaton theory, the potentials V, Z, \mathcal{T} become purely exponential and can be embedded in a supergravity action. Finally, the potentials (2.5)–(2.7) are the expressions in IR: near the AdS boundary they are corrected to ensure the AdS asymptotics.

For analytical considerations it is convenient to parametrize the metric as:¹

$$ds^2 = e^{-2A(z)} \left(-f(z)dt^2 + \frac{dz^2}{f(z)} + d\mathbf{x}^2 \right), \quad (2.8)$$

with the coordinates $(t, z, x_1, \dots, x_{D-1})$, where x_i are the transverse spatial coordinates, i.e. the spatial coordinates in field theory and z is the radial distance in AdS space: the AdS boundary (UV of the field theory) sits at $z = 0$ and the interior (IR in field theory) is at $z \rightarrow \infty$. At equilibrium, the fields are static, homogenous and isotropic, so they depend only on z . The equations of motion read:

$$A'' + (A')^2 = \frac{1}{D-1} \frac{1}{f^2} T_{00} + T_{zz} = \frac{1}{2(D-1)} Z(\chi')^2 + \frac{1}{D-1} \xi(\Phi')^2 \quad (2.9)$$

$$f'' - (D-1)f'A' = 2 \left(\frac{1}{f} T_{00} + T_{ii} \right) = 2e^{2A} \mathcal{T}(A'_0)^2 \quad (2.10)$$

$$\Phi'' + \left(\frac{f'}{f} - (D-1)A' \right) \Phi' - \frac{e^{-2A} \partial_\Phi V}{\xi f} - \frac{e^{2A} f}{2\xi} (\chi')^2 \partial_\Phi Z - \frac{e^{-3A}}{f} (A'_0)^2 \partial_\Phi \mathcal{T} = 0 \quad (2.11)$$

$$\chi'' + \left(\frac{f'}{f} - (D-1)A' + \Phi' \frac{\partial_\Phi Z}{Z} \right) \chi' - \frac{2e^{-2A}}{2f} m_\chi^2 \chi + \frac{q^2}{f^2} Z A_0^2 \chi = 0 \quad (2.12)$$

$$A_0'' - \left((D-3)A' - \frac{\partial_\Phi \mathcal{T}}{\mathcal{T}} \right) A_0' - \frac{2Z}{f\mathcal{T}} e^{-3A} \chi^2 A_0 = 0. \quad (2.13)$$

The prime denotes the radial derivative. As we have only two independent functions in the metric, it suffices to take two combinations of the Einstein equations. Due to homogeneity

¹In numerical calculations we find it convenient to use a different parametrization of the metric. Equations of motion and the description of the numerical algorithm can be found in appendix A.

we have $T_{x_1x_1} = T_{x_2x_2} = \dots = T_{x_{D-1}x_{D-1}} \equiv T_{ii}$ and the off-diagonal components are zero. The energy-momentum tensor $T^{\mu\nu} = T_{\Phi}^{\mu\nu} + T_{\chi}^{\mu\nu} + T_{EM}^{\mu\nu}$ reads

$$T_{\Phi}^{00} = \xi g^{zz} (\Phi')^2 - V, \quad T_{\Phi}^{zz} = T_{\Phi}^{ii} = -\xi g^{zz} (\Phi')^2 - V \quad (2.14)$$

$$T_{\chi}^{00} = \frac{Zg^{zz}(\chi')^2}{2} + \frac{Zg^{zz}A_0^2\chi^2}{2} - m_{\chi}^2\chi^2, \quad T_{\chi}^{zz} = T_{\chi}^{ii} = -\frac{Zg^{zz}(\chi')^2}{2} - \frac{Zg^{zz}A_0^2\chi^2}{2} - m_{\chi}^2\chi^2 \quad (2.15)$$

$$T_{EM}^{00} = T_{EM}^{zz} = -\mathcal{T}g^{00}g^{zz}(A_0')^2, \quad T_{EM}^{ii} = -2\mathcal{T}g^{00}g^{zz}(A_0')^2 \quad (2.16)$$

In order to have AdS asymptotics, the metric functions must satisfy $A(z \rightarrow 0) = \log z$ and $f(z \rightarrow 0) = 1$. The near-boundary expansion of the gauge field is of the form

$$A_0(z \rightarrow 0) = \mu - \rho z^{D-2} + \dots \quad (2.17)$$

which determines the chemical potential μ and the charge density ρ . One can work either in the canonical ensemble (fixing ρ) or in the grand canonical ensemble (fixing μ). For our purposes it doesn't matter much which variant we choose; in the concrete numerical examples we always fix the chemical potential. The scalar has the near-boundary behavior:

$$\chi = \chi_- z^{\Delta_-} (1 + c_{-1}z + c_{-2}z^2 + \dots) + \chi_+ z^{\Delta_+} (1 + c_{+1}z + c_{+2}z^2 + \dots) \quad (2.18)$$

where the leading and subleading branches χ_{\mp} have the conformal dimension $\Delta_{\pm} = D/2 \pm \sqrt{D^2/4 + m_{\chi}^2}$. In field theory, one of these is the source of the order parameter O_{χ} dual to χ and the other is its the vacuum expectation value (VEV). We pick χ_+ as the VEV, so the formation of the condensate means $\chi_+ \neq 0$ for $\chi_- = 0$ — nonzero subleading component (VEV) for zero leading (source) term. It usually turns out that the scalar can condense for negative enough mass squared, i.e. for $m_{\chi}^2 < m_{BF}^2$ for some bound m_{BF} (Breitenlohner-Friedmann bound [17]) that depends on the spacetime, i.e. on geometry; in AdS_{D+1} of unit radius it is $m_{BF}^2 = -D^2/4$. Similar asymptotics as in (2.18) hold for the dilaton Φ when the near-boundary form of the potential starts from a quadratic term: $V(\Phi(z \rightarrow 0)) \sim m_{\Phi}^2 \Phi^2 + \dots$. We tune m_{Φ}^2 above the bound for condensation because we never consider the condensed state of the dilaton. This leaves Φ_- as the sole free parameter. Obviously, Φ_- sources some field theory operator O_{Φ} of dimension $D/2 - \sqrt{D^2/4 + m_{\Phi}^2}$ which does not condense and thus does not break a symmetry. Still, the value of Φ_- influences the bulk solution and consequently may influence the condensation of χ or the confinement/deconfinement transition. In accordance with the main idea of the paper, we mainly focus on the condensation of O_{χ} at fixed Φ and only briefly discuss the meaning of O_{Φ} .

In absence of the scalar χ and apart from the subleading correction in the dilaton potential V , our system is one of the many cases of Einstein-dilaton and Einstein-Maxwell-dilaton systems considered systematically in [25]. Our parameter values are similar to a solution that the authors of [25] call “near-extremal case”. For each solution, we check that the value of the parameters we use for γ, δ, ν are consistent with the Gubser criterion for “good” curvature singularities in IR [16]. A good singularity means that, even though

the curvature becomes infinite at $z \rightarrow \infty$, it can be trapped by a horizon. A systematic discussion of allowed parameter values (for purely exponential potentials) can be found in the cited reference [25]. The exponent ν is also a free parameter with the limitation $\nu \geq 1$. In numerical calculations, unless specified differently, we take $\nu = 2$ and $D = 4$ for calculations, though any $D > 2$ again leads to similar results. An account of numerical calculations can be found in the appendix; the procedure is essentially iterative, repeatedly computing the profile of the scalar $\chi(z)$ and then updating the metric and the dilaton in the presence of $\chi(z)$.

3 Solutions in the infrared: soft-wall and AdS-like

3.1 Neutral solutions

3.1.1 No symmetry breaking

At zero temperature (which is central for studying the ground state) the space extends to $z \rightarrow \infty$. The authors of [23] have performed a classification of asymptotically AdS Einstein-dilaton systems (without other fields), motivated by AdS/QCD studies. Their results can be summed up as follows. The scale factor $A(z)$ either has a singularity at finite z , or at $z = \infty$. In the former case, the metric can be conformally equivalent to AdS with $A(z) \sim \alpha \log z$ (type Ib geometry), which is never confining whereas the soft-wall solutions with $A(z) \sim z^\nu$ (type Ia geometry) are confining for $\nu \geq 1$. If the singularity is to be found at finite $z = z_W$, then the logarithmic approach $A(z) \sim \log(z_W - z)$ (type IIb geometry) does not give confinement whereas a power-law $A(z) \sim 1/(z_W - z)^\nu$ (type IIa solution) does, for any ν .² We have nothing to add here: our system is a special case of the systems considered in [23], with slightly different $V(\Phi)$.

To solve our equations of motion (2.9)–(2.12), notice first that the equation (2.10) is decoupled from all matter fields and yields the solution

$$f(z) = C_0 + C_1 \int dz e^{(D-1)A(z)}. \tag{3.1}$$

A growing scale $A(z)$ in the interior would lead to a bad singularity according to the criterion of Gubser [16].³ Therefore, we need to suppose that $A(z)$ is a monotonically growing function of z , as also discussed in [23]. This in turn means that the non-constant term in (3.1) is likewise growing, so $C_1 < 0$ (in order to have a solution for the position of the horizon, defined by $f(z_{hor}) = 0$) and for correct AdS asymptotics $C_0 = 1$. Now C_1 is determined by the boundary condition in the interior: at zero temperature, the space is

²Let us quickly remind the reader where this comes from. The defining criterion for confinement is that the Wilson loop operator follows the area law. The Wilson loop, defined as the potential energy of a quark-antiquark pair separated by distance L , is holographically expressed as the action of a classical string embedded in spacetime, with a rectangular loop at the AdS boundary with sides equal to L and the time T . If the metric is of the form (2.8), one can plug it in into the expression for the string action and find the action scales as $e^{-2A(z_s)}$, where z_s is a stationary point: $A'(z_s) = 0$. From this the above conclusions follow, bearing in mind that one may have $z_s \rightarrow \infty$.

³To remind the reader, the paper [16] shows that a curvature singularity is physically meaningful if it can be obtained as the limit of a geometry with horizon, so that the horizon hides the singularity.

infinite so $C_1 = 0, f(z) = 1$ as expected for a neutral system. At nonzero temperature T , the position of the horizon is determined by the condition $f(z_h) = 0$.

We are left with one Einstein equation for $A(z)$ and two Klein-Gordon-like equations for the two scalars. It is easiest to start from an ansatz $A(z) \sim z^\nu$ to get a soft wall (type Ia) solution

$$\begin{aligned}
 A(z) &= z^\nu \left(1 + \frac{a_1}{z} + \frac{a_2}{z^2} + \dots \right) \\
 f(z) &= 1 - \frac{(D-1)^{1/\nu} \mathcal{M}}{\nu z^{\nu-1}} e^{(D-1)z^\nu}, \quad \chi(z) = 0 \\
 \Phi(z) &= \sqrt{\frac{D-1}{\nu\xi}} \sqrt{\nu z^{2\nu} + (\nu-1)z^\nu} \left(1 + \frac{\phi_{11}}{z} + \frac{\phi_{12}}{z^2} + \dots \right) + \\
 &\quad + \frac{\nu-1}{\nu\sqrt{\xi}} \log \left(\nu z^{\frac{\nu}{2}} + \sqrt{\nu^2 z^\nu + \nu^2 - \nu} \right) \left(1 + \frac{\phi_{21}}{z} + \frac{\phi_{22}}{z^2} + \dots \right). \quad (3.2)
 \end{aligned}$$

These forms are exact as $z \rightarrow \infty$ and the coefficients a_i, ϕ_{ij} can be found analytically at arbitrary order in principle. We are not interested in the details of the small z (UV) geometry, as long as enough free parameters remain that the solution can be continued to the AdS_{D+1} boundary conditions. The red shift function includes the rescaled black hole mass \mathcal{M} , which is related to the position of the horizon as $\mathcal{M} = z_h^{\nu-1}$, the horizon being determined through the transcendental equation $f(4\pi D/T) = 0$ which we will not explore here in detail. Importantly, the thermal solution smoothly crosses into the zero temperature solution and all temperatures down to $T = 0$ are defined, which is not always the case with Einstein-(Maxwell)-dilaton systems, see e.g. [25]. There is another solution, however: starting from the ansatz $A(z) \sim \alpha \log z$ we get a type Ib solution

$$\begin{aligned}
 A(z) &= \alpha \log z \left(1 + \frac{a_1}{z} + \frac{a_2}{z^2} + \dots \right), & \alpha &= \frac{\xi}{D-1+\xi} \\
 f(z) &= 1 - \frac{\mathcal{M}}{\alpha(D-1)} z^{(D-1)\alpha}, & \chi(z) &= 0 \\
 \Phi(z) &= \phi_0 \log z \left(1 + \frac{\phi_1}{z} + \frac{\phi_2}{z \log z} + \frac{\phi_3}{z^2} + \frac{\phi_4}{z^2 \log z} + \dots \right), & \phi_0 &= \frac{D-1}{D-1+\xi}. \quad (3.3)
 \end{aligned}$$

Which of these is the ground state is to be determined by comparing the free energies, our task in the next section (it turns out the confining solution Ia is the correct choice). These solutions have a curvature singularity at $z \rightarrow \infty$: the Ricci scalar for (3.2) is

$$R = -D(D-1)\nu^2 e^{2z^\nu} z^{2\nu-2} + \dots \quad (3.4)$$

which diverges for z large but can be trapped by a thermal horizon for any finite z_h so that R is finite as $z_h \rightarrow 0$. This follows from the form of $f(z)$ in (3.2) and makes the solution physically meaningful.

3.1.2 Symmetry-breaking order parameter

Now consider the symmetry-broken solution with $\chi(z) \neq 0$. If we require the physically logical (and simplest) choice of purely exponential $Z(\Phi)$ as in (2.6), then the only way

to satisfy (2.9) while keeping the scaling function $A(z) \sim z^\nu$ is to “reduce” the dilaton, i.e. make its growth slower than z^ν : otherwise, an additional source on the r.h.s. of equation (2.9) can only make $A(z)$ grow even faster, never slower (remember the r.h.s. is the kinetic energy of the scalar field which cannot be negative; adding a new nonzero field cannot reduce the sum). Thus we seek for a scalar $\chi(z)$ which, when coupled to $\Phi(z)$, gives it a logarithmic behavior $\Phi(z) \sim \phi_0 \log z$. Such a solution indeed exists. We deliberately postpone the discussion of the mechanism of the scalar instability to condensation, i.e. of the scalar fluctuations in background (3.2) which lead to the new solution discussed in this subsection. This mechanism (and the value of m_χ^2 at which it happens) will be discussed in the next section, before constructing the phase diagram. For now we are content to show that the solution exists. To the best of our knowledge, this kind of solution was not analytically constructed in earlier work.

The solution is now of type IbC (Ib with condensate):

$$\begin{aligned}
 A(z) &= \alpha \log z \left(1 + \frac{a_1}{z} + \frac{a_2}{z^2} + \dots \right), \quad \alpha = \frac{\gamma + 2}{2\gamma - 2(D - 1)} \\
 f(z) &= 1 - \frac{\mathcal{M}}{\alpha(D - 1)} z^{(D-1)\alpha} \\
 \Phi(z) &= \phi_0 \log z \left(1 + \frac{b_1}{z} + \frac{b_2}{z \log z} + \frac{b_3}{z^2} + \frac{b_4}{z^2 \log z} + \dots \right), \quad \phi_0 = \frac{D + 1}{\gamma + 1 - D} \\
 \chi(z) &= \chi_0 z^{-\frac{\gamma \phi_0}{2}}, \quad \phi_0 = \frac{D + 1}{2(\gamma + 2)} \alpha = \frac{D + 1}{\gamma - (D - 1)} \\
 \chi_0 &= \frac{\sqrt{2(\gamma^2 + 2\gamma + 2D^2(\gamma + 2 - 2\xi) - 4\xi - D((\gamma + 2)^2 + 8\xi))}}{(D + 1)\gamma}.
 \end{aligned} \tag{3.5}$$

Interestingly, the value of ν does not appear in the solution at leading order (of course, it does appear in the subleading corrections a_i, b_i). The solutions for ϕ_0, χ_0 show that we need the condition $\gamma > D - 1$ to avoid the growing metric scale in the interior. The crucial observation in the above discussion was that adding bosonic fields (for which $T_{00}/f^2 + T_{zz}$ is always positive) cannot destroy the soft wall solution. We find there is no solution with two scalars, Φ and χ , and with the couplings (2.5)–(2.6), which has a soft-wall metric scale behavior $A(z) \sim z^\nu$. This can be seen more rigorously from the superpotential approach. There is thus an interesting bifurcation-like behavior as the amplitude of the order parameter field is varied: there are two competing solutions for $\langle O_\chi \rangle = \chi(z = 0)$ but only one of them survives as $\langle O \rangle$ grows away from zero. Is this solution acceptable? The curvature behaves as

$$R = -4\alpha(3\alpha + 2)z^{2\alpha-2} + \dots \propto z^{\frac{\gamma-2D}{\gamma-D+1}}, \tag{3.6}$$

the exponent being positive precisely in the allowed interval of γ values, $D - 1 < \gamma < 2D$. Thus we again have a singularity, and it is again a “good” singularity according to [16]. This is in line with the results of [25] for “near-extremal” solutions: acceptable solutions are only those with a singularity; those without a curvature singularity are cosmological solutions with an unacceptable singularity at small z .

3.2 Charged solutions

3.2.1 No symmetry breaking

Instead of a neutral scalar we now take a charged scalar, i.e. the typical holographic superconductor setting, coupled to a dilaton. The results should not depend crucially on the spin of the charged field as long as it is integer; half-integers fields, i.e. fermions may well behave differently as they have different pressure (spatial components of the stress tensor). We will not analyze the fermionic case here.

For further convenience we adopt the terminology of [28, 29], used also in [27], to roughly classify the charged solutions in terms of the charge distribution in the bulk and how it influences the geometry. On one hand, we have (1) IR-neutral solutions where the *Maxwell contribution* to $T_{\mu\nu}$ is subleading so that the IR geometry is not influenced by $A_0(z)$ in the first approximation, as opposed to (2) IR-charged solutions where $A_0(z)$ contributes at leading order. The second criterion is whether the solution is fractionalized or coherent: (a) fractionalized solutions are those where *the charged fields* do not contribute to $T_{\mu\nu}$ and thus to geometry in the IR at leading order whereas in (b) cohesive solutions they contribute. In the fractionalized case the electric flux in the IR $\int \star [\mathcal{T}(\Phi)F]$ is non-zero while it is zero for cohesive solutions. The physical interpretation of the fractionalized/coherent dichotomy is still unclear. The logical explanation would be that in the fractionalized case the charge-carrying degrees of freedom are not those which are seen in the spectrum as they are charged under the gauge group and are not seen by the gauge-neutral probe ("gauginos"), as opposed to the gauge-neutral composite excitations of the coherent case ("mesinos"). This interpretation suggests a close relation between the confinement/deconfinement and coherence/fractionalization. The trouble is that many examples exist both of fractionalized but confined systems (the dilatonic black holes of [18–20]) and coherent but deconfined systems (the electron star and the dilatonic electron star of [29]). While confinement is about the behavior of the Wilson operator and the gauge field excitations, coherence is about the emergence of stable composite gauge-neutral excitations. Examples where the quarks emerge only after the gauge field compactifies are known in AdS/CFT [41] but the understanding of the phenomenon is lacking. We plan to address this issue in more detail in future work; here we will just state the fractionalization/coherence nature of our geometries and comment briefly on the interpretation in the conclusions. For more information on the general problems of fractionalization in this context see [19, 20, 27].

Let us now study the charged solutions. Notice first that a charged solution without condensate can only exist in the presence of a charged horizon. Such a solution must be fractionalized as none of the charge carriers have a dual VEV at the boundary. It reads

$$\begin{aligned}
 A(z) &= z^\nu \left(1 + \frac{a_1}{z} + \frac{a_2}{z^2} + \dots \right) \\
 f(z) &= 1 - \mathcal{M}(T)e^{(D-1)z^\nu} + \frac{2Q^2}{2\nu-3}e^{(\tau+4-2D)z^\nu}z^{3-2\nu} \left(1 + \frac{f_1}{z} + \frac{f_2}{z^2} + \dots \right) \\
 \Phi(z) &= z^\nu \left(1 + \frac{\phi_1 \log z}{z} + \frac{\phi_2}{z} + \dots \right), \quad \chi(z) = 0 \\
 A_0(z) &= a_0 - Qe^{-(\tau-(D-3))z^\nu}z^{1-\nu} \left(1 + \frac{a_1}{z} + \frac{a_2}{z^2} + \dots \right). \tag{3.7}
 \end{aligned}$$

Now the horizon carries the charge Q and at zero temperature $\mathcal{M}(T = 0) = 0$, so

the extremal horizon is degenerate and located at $z = \infty$. Again, we are not interested in the (complicated) analytical form of $\mathcal{M}(T)$. The electric flux at the horizon is $\sqrt{-g}g_0g_zz\mathcal{T}(\Phi)A'_0 = \mathcal{T}(\Phi)A'_0 \sim e^{-(D-3)z^\nu} \times e^{\tau z^\nu} a_1 e^{(D-3-\tau)z^\nu} \sim a_1$ which is a generically nonzero constant for $z \rightarrow \infty$, meaning that the solution is fractionalized. On the other hand, it is confining, as it is of type Ia (we call it IaQ, as it has charge) and the metric scale diminishes exponentially in the IR (we call it IaQ to emphasize it is charged). In fact, this solution is quite similar to the top-down dilatonic black hole with two-exponent potential discussed in [18–20]. Although fractionalized, it still confining so it fits into our main story: deconfinement from independent symmetry breaking.

3.2.2 Symmetry-breaking order parameter

Postulating a nonzero profile for the scalar field and requiring that the scalar contributes at leading order in the equation (2.9), we find the solution IbQC, the non-confining charged solution:

$$\begin{aligned}
 A(z) &= \alpha \log z \left(1 + \frac{a_1}{z} + \frac{a_2}{z^2} + \dots \right) \\
 f(z) &= 1 - \mathcal{M}(T) \frac{z^{(D-1)\alpha+1}}{(D-1)\alpha+1} + \frac{2Q^2}{z^\beta} \left(1 + \frac{f_1}{z} + \frac{f_2}{z^2} + \dots \right) \\
 \Phi(z) &= \phi_0 \log z \left(1 + \frac{\phi_1 \log z}{z} + \frac{\phi_2}{z} + \dots \right) \\
 \chi(z) &= \chi_0 z^{-\frac{\gamma\phi_0}{2}} \left(1 + \frac{\chi_1}{z} + \frac{\chi_2}{z^2} + \dots \right) \\
 A_0(z) &= a_0 - Qz^{-\frac{10+11\gamma+9\tau}{10+10\gamma+8\tau}} \left(1 + \frac{a_1 \log z}{z} + \frac{a_2}{z} + \dots \right), \tag{3.8}
 \end{aligned}$$

and the exponents read

$$\alpha = \frac{4 + 4\gamma + 3\tau}{5 + 5\gamma + 4\tau}, \quad \beta = \frac{2\tau + 3\gamma + 2}{4\tau + 5\gamma + 5}, \quad \phi_0 = \frac{1}{4\tau + 5\gamma + 5}. \tag{3.9}$$

The charged horizon is still degenerate at zero temperature. Comparing the stress tensors by plugging in the solution (3.8) into (2.14)–(2.16), we easily find that $T_{EM} \ll T_\Phi, T_\chi$ for $z \rightarrow \infty$, so according to the criterion of [25] the solution is IR neutral. Being of type Ib (we denote it IbQC, as it is charged and has the condensate), it is not confining, and the IR flux is $z^{-2-\frac{9\gamma+5\tau+8}{10+10\gamma+8\tau}}$ which goes to zero for $z \rightarrow \infty$ since γ and τ are positive and all the coefficients in both numerator and denominator of the exponent are positive. The solution IbQC is thus coherent and deconfined. On one hand, the fact that the non-condensed solution IaQ is fractionalized while the condensed solution IbQC is coherent is perfectly logical, since in the non-condensed case all the charge is on the horizon, whereas in the presence of the condensate it carries all the charge. The fact that the fractionalized solution is confined and the coherent one is deconfined may sound strange; e.g. in [27] the intuition is expressed that confined solutions should be coherent. But as we have already commented the zoo of field theories in gauge/gravity duality offers many counterexamples. At least, one expects that the coherent nature of the systems shows up as poles, i.e. bound states in the bottom half-plane of complex-frequency response functions of matter fields

(the scalar χ), independently of the presence or absence of confinement. We will check this in section 5.

Can we get a soft wall with charged condensate? We were unable to find such a solution either analytically or numerically. The conclusion is again that the competition of two scalars (dilaton and order parameter) destroys the confining solution. Of course, by adjusting the potentials V, Z, \mathcal{T} we could get many different phase diagrams but in the present model there is a strict competition between the soft wall and the condensate. Finally, the singularity properties of both charged solutions are analogous to the charge-neutral case: the singularities exist but are physically allowed.

3.3 Resume of the geometries

We have found five solutions: Ia, Ib, IaQ, IbC, IbQC. Only two of them compete in the same regime, Ia and Ib, and the preferred solution has to be found by computing the energy. Geometries Ia, IaQ are confined whereas Ib, IbC, IbQC are deconfined. Among the charged geometries, IaQ is fractionalized whereas IbQC is coherent, and both are IR neutral. In figure 1 we plot the metric functions $A(z), f(z)$ and the bulk profile of the dilaton and the scalar field $\Phi(z), \chi(z)$ at zero temperature, at zero chemical potential in the panel (A) and at finite chemical potential in the panel (B). The most obvious feature of the solutions is the sharp exponential fall-off of the scale factor e^{-2A} for soft-wall geometries versus much slower fall-off for deconfined solutions where the blue curve $e^{-2A}z^2$ is almost flat, i.e. the solution behaves almost as AdS in the IR. This is logical, as the volume in the IR counts the degrees of freedom of the low-energy excitations; at low enough energies, such excitations are completely absent in the confined phase. In fact, as can be seen from the analytical form of the solutions (3.5), (3.8), the factor e^{-2A} in the deconfined phase behaves as a power law just like in AdS, only with a different power. In [25, 27, 30, 31] such geometries are classified in terms of hyperscaling exponents, where the time, space and energy (i.e., radial distance in AdS) are each scale-covariant but with different exponents. It turns out these three exponents can be described by combinations of two parameters, the Lifshitz exponent ζ and the hyperscaling violation exponent θ ; if $\theta = 0$ the geometry obeys the hyperscaling whereas for $\theta \neq 0$ it is hyperscaling-violating. For a Lorentz-invariant system we have $\zeta = 1$; values different from unity mean that the dispersion relation is nonlinear and the Lorentz invariance broken. The neutral deconfined geometries (3.3) and (3.5) have $\zeta = 1$ but the hyperscaling exponent is nontrivial and reads $\theta = D(1 + \alpha)$. The charged version (3.8) has both exponents nontrivial ($\zeta > 0 \neq 1$ and $\theta \neq 0$). Note that the $\zeta < 0$ case is hard to interpret physically and thus we have checked that all of our geometries have $\zeta > 0$.

4 Phase diagram and thermodynamics

We will consider the ground state of our system as a function of the parameters and external sources of the theory. Parameters of the theory are the exponents ν, τ, γ and the conformal dimension (bulk mass) Δ_χ . The ranges of the allowed values of ν, τ, γ are chosen in such a way that the dependence on their values is smooth and unlikely to lead to

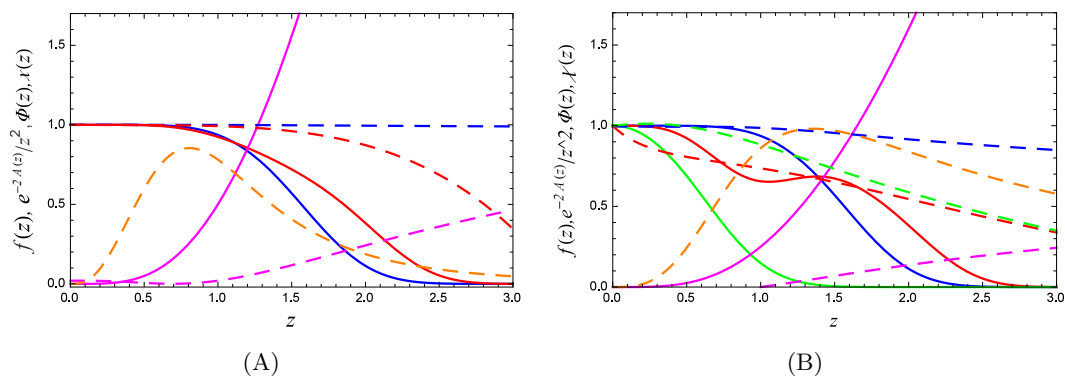


Figure 1. (A) The metric functions $e^{-2A(z)}z^2, f(z)$ (blue, red) and the bulk fields $\Phi(z), \chi(z)$ (magenta, orange) in the confined regime (geometry Ia, full lines) and in the deconfined regime (geometry IbC, dashed lines). The blue line corresponds to the ratio of the scale factor in our system and the AdS scale factor $1/z^2$. The confining regime has a soft wall in the IR and its IR scale falls practically to zero already at $z \sim 3$. (B) Same as the previous figure but for the charged field at the chemical potential $\mu = 1$; now we plot also the gauge field $A_0(z)$ (green). The basic phenomenology is the same as in (A): the soft wall broadens and the scale factor e^{-2A} has no characteristic scale z_W at which it falls off rapidly. The plots are in $D = 4$ and the parameter values are $\nu = 2, \gamma = 4$ (both A and B), and $\tau = 5$ for the charged case (B). For the neutral case we pick $m_\chi^2 = 1/4$ and $m_\chi^2 = -1/4$ whereas for the charged case we have $m_\chi^2 = 8$ and $m_\chi^2 = 4$.

phase transitions; furthermore, these exponents characterize the running couplings in field theory, which include also the information at different energy scales and probably cannot be realistically tuned. Therefore, the dependence of the thermodynamic quantities on ν, τ, γ will not be explored. The typical procedure in holographic superconductor literature would be to tune $\Delta_\chi = D/2 + \sqrt{D^2/4 + m_\chi^2}$ as a proxy for coupling strength in field theory, and this is what we shall do. The requirement for condensation fully fixes the solution $\chi(z)$, as we remind below, and we have no sources for O_χ . However, there is one free parameter in the theory at fixed parameter values: the operator O_Φ dual to the dilaton in the UV. Therefore, the phase transitions are driven by dialing the scaling dimension Δ_χ and the expectation value of the operator O_Φ dual to the dilaton. When not explicitly stated, we will assume a fixed O_Φ and study the phase transitions as a function of Δ_χ .

4.1 The condensation of the boson at $T = 0$

We expect that at some $\Delta_\chi = \Delta_c$ the neutral bosonic operator O_χ acquires a nonzero expectation value. As we know [5], the expectation value in field theory is given by the subleading term in the UV expansion (2.18) at zero source term

$$\langle O_\chi \rangle = \chi_+ |_{\chi_- = 0}. \quad (4.1)$$

One can also consider an alternative quantization where the VEV is given by χ_- , provided both terms are normalizable, but we will stick with the standard quantization. At this place one should differentiate between the neutral and the charged case. In the neutral case, no continuous symmetry is broken and the phase transition is more akin to nucleation, where

the oscillating modes of the scalar add up to a significant perturbation which eventually changes the metric. Whether the oscillations are strong enough or not to lead to a new ground state in principle depends on the parameters of the system. The charged case is expected to be simpler: here, the instability is supposed to be rooted in the Higgs mechanism which breaks the U(1) symmetry, and one expects this to happen for any charged scalar (independently of the m_χ^2 value). The charged scalar is thus expected to always condense at $T = 0$, at least in absence of the dilaton. In the presence of the dilaton, things can become more complicated, as we shall see.

4.1.1 The neutral case

The critical value of the conformal dimension⁴ Δ_c can be related to the violation of the Breitenlohner-Freedman (BF) stability bound in the interior. To remind, the idea is to rewrite the Klein-Gordon equation for the scalar with energy ω as an effective Schrödinger equation for the rescaled scalar $\tilde{\chi}(z) = \chi(z)/B(z)$ with energy ω^2 :

$$\tilde{\chi}'' - V_{\text{eff}}(z)\tilde{\chi} = -\frac{\omega^2}{f^2}\tilde{\chi}(z) \tag{4.2}$$

and the effective potential

$$V_{\text{eff}} = \frac{e^{-2A}}{f} m_\chi^2 - \frac{B'}{B} \left(\frac{f'}{f} + \frac{\partial_\Phi Z}{Z} \Phi' - (D-1)A' \right) - \frac{B''}{B}, \tag{4.3}$$

where the rescaling factor is

$$B(z) = \frac{e^{-\frac{D-1}{2}A} - \frac{\partial_\Phi Z}{2Z} \Phi}{\sqrt{f}}. \tag{4.4}$$

If the energy of χ becomes imaginary, i.e. the Schrödinger energy ω^2 becomes negative, it means there is an exponentially growing mode which likely signifies an instability, and the scaling dimension becomes complex [17]. In the Schrödinger formalism, it means that $\tilde{\chi}$ forms a bound state. We are not allowed to violate the bound in the UV, to prevent violating the AdS asymptotics assumed in the gauge/gravity duality, but an instability in the interior is perfectly allowed and signifies the change of IR physics, i.e. of the field theory ground state. In AdS-RN background, the instability of the neutral scalar is given simply by the BF bound of the near-horizon AdS₂, which equals $-1/4$ [5, 8]. We do not have a near-horizon AdS region and there is no simple formula for the critical mass (dimension) m_c^2 (Δ_c) but the logic is the same: we are looking for complex energies, i.e. bound states in the Schrödinger formalism.

In geometry Ia the effective potential reads

$$V_{\text{eff}} = m_\chi^2 e^{-2z\nu} - \frac{(D-\gamma-1)\nu(\nu-1)}{2} z^{\nu-2} + \frac{(D-\gamma-1)^2 \nu^2}{4} z^{2\nu-2} \tag{4.5}$$

which is positive and growing to infinity at large z . For any bound states to exist, we need to have a sufficiently deep and broad potential well below zero energy, i.e. the potential

⁴We will use the conformal dimension Δ_χ and the bulk mass squared m_χ^2 interchangeably as they are uniquely related to each other through $\Delta_\chi = D/2 + \sqrt{D^2/4 + m_\chi^2}$.

needs to grow to infinity also on the “left-hand side”, for small z , and fall sufficiently low in-between. Now we remember that for $z \rightarrow 0$ the potential certainly goes to positive infinity because $m_\chi^2 > -D^2/4$ (i.e., we do not want bound states in the far UV region, sitting at $z \rightarrow 0$). Now the question is what the potential looks like for some intermediate z_1 which is still large enough that the IR solution (geometry Ia) is valid. Assuming that $z_1 \sim 1$, this depends on the combination $m_\chi^2 - (D - \gamma - 1)\nu(\nu - 1)/2 + (D - \gamma - 1)^2\nu^2/4$ — the second and third term are both positive, and the question is whether there is a value of $m_\chi^2 > -D^2/4$ which is nevertheless sufficiently negative to make V_{eff} negative. This is obviously a question of numerical calculation but we can see that for $\gamma = D - 1 + \epsilon$ for ϵ small the second and the third term in (4.5) have practically zero coefficients and not too large $|m_\chi^2|$ suffices to push V_{eff} below zero in some interval. We conclude that we can expect a BF-type instability at some critical m_c^2 . We have seen this means the geometry Ia is modified, presumably into IbC, and at finite m_c^2 , analogously to the neutral holographic superconductor in AdS-RN [5, 8].

Having shown that there is indeed a mechanism for the condensation of the order parameter in the soft-wall regime, we should also check if the geometry IbC is stable in the presence of the condensate. In geometry IbC the effective potential is:

$$V_{\text{eff}} = V_\infty + \frac{m_\chi^2}{z^{2\alpha}} + \frac{\kappa(\kappa + 1)}{z^2} \tag{4.6}$$

where $\kappa = \frac{(D-1)\alpha + \gamma\phi_0}{2}$ and V_∞ is a z -independent constant. The inverse square term is always positive and the power of the mass term varies between $-\infty$ for $\gamma \rightarrow D - 1$ and -2 for $\gamma = 2D$ (we see this from the expressions for α, ϕ_0 in (3.5)). Thus the $1/z^2$ term dominates at large z for the allowed values of γ (from (2.6)) and approaches zero from above as $z \rightarrow \infty$; this means the potential approaches the constant V_∞ from above. This in turn means there is no room for bound states — the potential in the UV is positive and decaying and never falls below zero.⁵ Therefore, the geometry IbC is stable in the presence of the scalar. Numerical plot of the potential in figure 2 confirms the above discussion. In the panel (A) there is a potential well with bound states for all masses below some $m_c^2 \sim 6$ which is thus the critical value for the condensation. In panel (B) the well turns out too shallow to allow the formation of bound states: the geometry is stable. All curves are for $m_\chi^2 \geq -D^2/4$ as for this value there is a potential well near $z = 0$ and the outer AdS region becomes unstable.

In the numerical calculation, we shoot for the solution of a two-point boundary value problem which satisfies the boundary condition (2.18) for χ at the AdS boundary and the expected asymptotics for $\chi(z)$ from (3.5) in the interior. We do this as a part of the complete calculation (with backreaction on geometry, see the appendix). In this way we can find the dependence of the VEV $\langle O_\chi \rangle$ on the conformal dimension Δ_χ . In figure 3(A), the blue curve jumps at the transition, signifying that the transition is of first order. This is different from the infinite-order BKT-type (stretched-exponential) scaling laws found in [5, 8] for

⁵This picture changes for $\gamma > 2D$ — then the mass term dominates for $z \rightarrow \infty$ and for negative mass squared it forms a potential well. But in our model one always has $\gamma < 2D$ so we do not explore this case in detail.

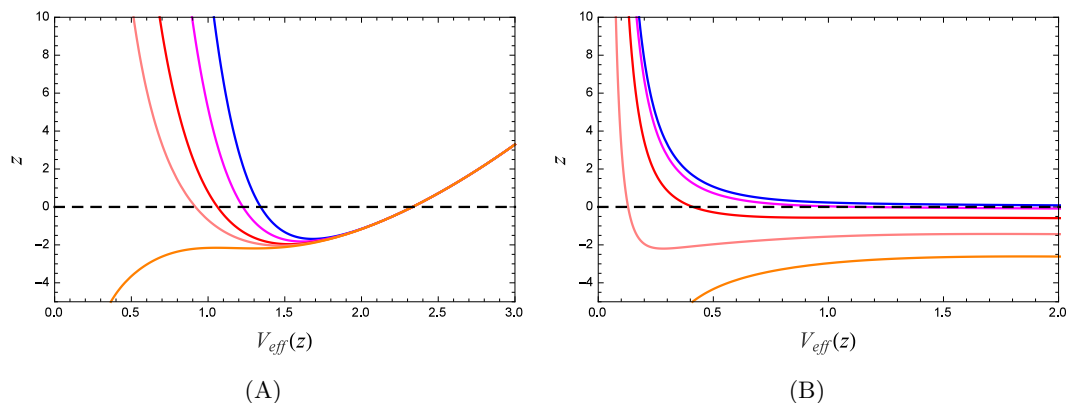


Figure 2. The effective Schrödinger potential $V_{\text{eff}}(z)$ defined by (4.3) for a range bulk masses (conformal dimensions) $m_\chi^2 = 6, 2, 0, -2, -4$ (blue, magenta, red, pink, orange) and $D = 4, \nu = 2, \gamma = 4$. The instability corresponds to bound states, i.e. existence of a sufficiently deep and broad potential well. In (A), we can fit a bound state for all masses shown, for the last one just a single bound state, thus $m_c^2 \sim 6$ corresponds to the BF bound. For such masses, the geometry will remorph and we will enter the condensed phase. This phase is stable, as in (B) the potential well is too shallow to accommodate a bound state. Notice that for $m_\chi^2 = -4$ the potential develops a well in the outer region, i.e. this is the BF bound for AdS_5 .

a neutral scalar in AdS-RN background because the BKT scaling originates in so-called Efimov states in the IR which depend on the details of the potential for the scalar [8] and would require a fine tuning of the dilaton potentials too. First-order transition is not unknown even for a charged scalar if it is non-minimally coupled to the metric [37, 38]. We also expect the condensate to vanish at higher temperatures, a case which we find too difficult for analytical work so we limit ourselves to numerics. The result is shown in figure 3: there is again a jump at the critical temperature.

4.1.2 The charged case

The charged problem can usually be understood as the textbook Abelian-Higgs instability where the gauge field develops an effective mass term $|\chi|^2 A_0$ and the mass of the scalar is effectively negative as it acquires a correction $-g^{00} A_0^2$, leading to instability and condensation. Without dilaton, in AdS-Reissner-Nordstrom background, this correction to the scalar mass grows fast enough near the horizon to produce an instability even at positive m_χ^2 [9]. For our system the equation for the charged scalar in IR geometry IaQ (eq. (3.7)) reads

$$\chi'' - \nu(\tau + 3 - \gamma - D)z^{\nu-1}\chi' - \frac{e^{(\tau-2D+2)z^\nu}}{\xi} \left(m_\chi^2 - \xi a_1^2 q^2 z^{2\nu-2} e^{(\gamma-\tau)z^\nu} \right) \chi = 0 \quad (4.7)$$

Now the negative correction to the effective mass of the scalar may grow or diminish as $z \rightarrow \infty$, depending essentially on the sign of $\gamma - \tau$. If $\gamma > \tau$ the correction dominates the bare mass term and we always have a mode growing at $z \rightarrow \infty$ but if $\gamma < \tau$ it is subleading and does not influence the behavior of $\chi(z \rightarrow \infty)$ at leading order. Looking

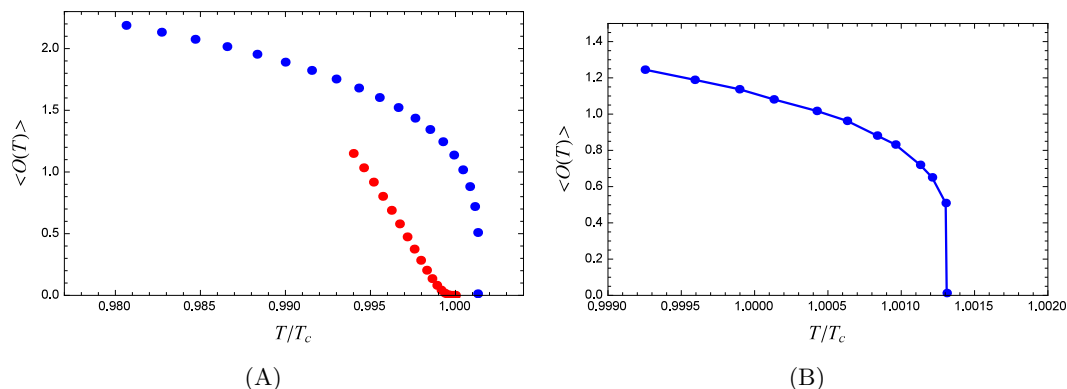


Figure 3. (A) Expectation value of the scalar $\langle O_\chi \rangle$ as a function of temperature for $m_\chi^2 = -2$, for the neutral scalar (blue) and the charged scalar with $q = 1$ (red), in $D = 4$ and for $\nu = 2, \gamma = 4$; for the charged scalar $\tau = 5$. The neutral scalar has a first-order quantum phase transition and its value jumps from zero, whereas in the charged case the quantum phase transition shows a continuous BKT-like exponential form $\exp\left(- (T_c - T)^{-1/2}\right)$. The unit of temperature is T_c — the critical temperature for the *charged* case. In (B) we zoom-in near the critical temperature for the neutral case to make it obvious that there is a jump.

at our conditions (2.5)–(2.6), we see this is always the case. Naively, one may guess that the critical value is $m_c^2 = 0$ but since our analysis ignores all subleading terms one should check numerically (numerics confirms that this is indeed the critical value, see the phase diagram in figure 7). Amusingly, the scaling with temperature and conformal dimension is now consistent with the BKT-like form:

$$\langle O_\chi \rangle = \text{const.} \times e^{-\frac{1}{\sqrt{-m_\chi^2}}}. \quad (4.8)$$

Although the numerical fit to the $e^{-1/(-m_\chi^2)^n}$ law with $n = 1/2$ is good, we cannot exclude the possibility that the exponent n weakly depends on ν and that it is not exactly $1/2$; we have no analytical estimate for n . The condensate formation is now, strictly speaking, not a consequence of the coupling with the gauge field at all (remember the term $q^2 g^{00} A_0^2$ is now exponentially suppressed) but merely the consequence of growing modes for negative scalar mass. Thus the mechanism is essentially the same as for the neutral scalar and the fact that the neutral scalar undergoes a discontinuous transition reminds us that the details of this process depend sensitively on the IR geometry. The temperature scaling is of the same form as the scaling with m_χ^2 (4.8) and is shown as red points in figure 3.

4.2 Free energies and phases at zero temperature

Now that we have explained the instability that seeds the condensation, we will compute the free energy (on-shell action) of the system as a function of Δ_χ and T , to study the order of the transition and the full phase diagram. We thus need to evaluate (2.1) on-shell for solutions Ia and IbC: $\mathcal{F} = \int d^D x L|_{Ia, IbC} + \mathcal{F}_{bnd}$. The boundary terms are given by

$$\mathcal{F}_{bnd} = \oint_{bnd} \sqrt{g_{\text{ind}}} \left(-2K - \lambda - \frac{1}{2} A_0 A_0' - \chi^2 - 2\Phi\Phi' \right), \quad (4.9)$$

Here, g_{ind} is the induced metric at the boundary, K is the trace of the extrinsic curvature, λ is the boundary cosmological constant, and the remaining terms come from the gauge field, the scalar and the dilaton. The counterterm for the scalar is in accordance with our choice that χ_+ is the VEV; had we chosen χ_- for the VEV the counterterm would be $-2\chi'\chi$, analogous to the situation for the dilaton. The comparison of free energies is best done numerically but even analytically we can draw some conclusions. Let us first consider the quantum phase transitions as a function of Δ_χ at fixed Φ_- and discuss the free energies at zero temperature.⁶ Our analytical solutions are only valid in the large z region, whereas for smaller z they cross over into the AdS_{D+1} forms, so the radial integral in (4.9) goes from some $z_1 \sim 1$. The difference between the energy of the solution Ia (we will show numerically it is indeed preferred to Ib) and IbC is

$$\mathcal{F}_{Ia} - \mathcal{F}_{IbC} \sim \chi_+^2 z^{2\Delta_\chi} + \int_{z_1}^{\infty} dz \left[(D^2 - D)z^{-(D-1)\alpha} + \chi_0^2 m_\chi^2 z^{-\gamma\phi_0} + \dots \right]. \quad (4.10)$$

The difference in free energies at leading order has terms proportional to the squared amplitude of the order parameter (in the UV — χ_- , i.e. $\langle O_\chi \rangle$ and in the IR — χ_0) but also a χ -independent term (coming from the Ricci scalar and cosmological constant terms in geometry IbC) so we expect that the transition, determined by $\mathcal{F}_{Ia} - \mathcal{F}_{IbC} = 0$ generically happens at nonzero amplitudes $\langle O_\chi \rangle, \chi_0$ and we can exclude a continuous transition. This is again in line with the discreteness of the symmetry broken and the discontinuous nature of the transition. On the other hand, for the charged geometries IaQ and IbQC there is also the boundary contribution $A_0(z \rightarrow 0)A'_0(z \rightarrow 0)$ so

$$\mathcal{F}_{IaQ} - \mathcal{F}_{IbQC} = \frac{\mu(\rho_{IaQ} - \rho_{IbQC})}{2} + \chi_+^2 z^{2\Delta_\chi} - \int_{z_1}^{\infty} dz z^{-(D-1)\alpha} \chi_0^2 (4 + 7\gamma)^2 + \dots \quad (4.11)$$

Now there is no χ -independent term and the dominant terms in the energy difference are proportional to the squared amplitude of the condensate, or to the difference in charge densities $\rho_{IaQ} - \rho_{IbQC}$ which, according to the Gauss-Ostrogradsky theorem, also has to be proportional to the bulk density of the charged field, $q^2 \chi(z)^2$. Therefore, one can expect that the energy difference grows from zero at $\langle O_\chi \rangle = 0$, as in a continuous phase transition. We have assumed that the chemical potential is kept constant across the transition (grand canonical ensemble). Now we will check our conclusions numerically.

First of all let us show that the confined solution is indeed the ground state in absence of the condensate. In figure 4(A) we plot the on-shell action of the solutions Ia (3.2) and Ib (3.3) and we see that Ia indeed always has lower energy — the system is confining. Now consider the free energies as functions of m_χ^2 and the temperature. In figure 4(B) we compare the free energies as functions of the conformal dimension for the neutral system and confirm the discontinuous nature of the transition: the curves have different derivatives at the transition point. Here we also scan for different values of the source Φ_- , which change the value of the transition point Δ_χ but, importantly, do not introduce new phases. This is easily understood from the discussion in section IV.A.1 and also from eq. (4.10). Dialing Φ_- influences the matching between the solutions in the UV and the solutions in IR without introducing new IR solutions, so we are still left with the choice between Ia

⁶At $T = 0$ the free energy is just the total energy \mathcal{E} of the system, since $\mathcal{F} = \mathcal{E} - TS$. For simplicity of notation, we will still call it \mathcal{F} just like the finite temperature case.

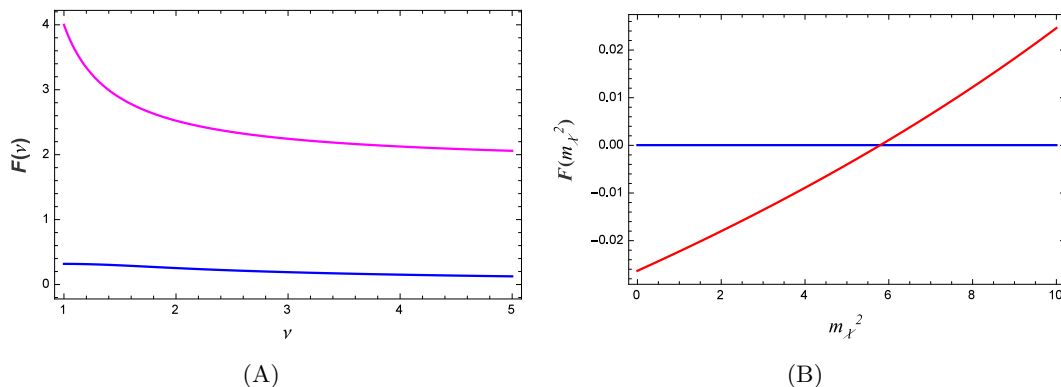


Figure 4. (A) Free energy at zero temperature as a function of the scaling exponent ν in the absence of condensate, for geometry Ia (confining, blue) and Ib (nonconfining, magenta). Obviously the soft-wall geometry always has lower free energy, thus it is always preferred: in absence of condensate we have a confining soft wall. The units on the vertical axis are arbitrary. (B) Free energy at zero temperature as a function of the bulk mass m_χ^2 for geometry Ia (confining, no condensate, blue) and for geometry IbC (nonconfining, with condensate, red). Both solutions exist before and after the critical point, where their energies $F(m_\chi^2)$ intersect at finite angle, thus the phase transition is of first order. The solid, dashed and dotted lines are from three different values of the source $\Phi_- = 0.1, 0.2, 0.5$ — the source shifts the location of the transition but does not change the behavior qualitatively. The free energy is in computational units and the parameters are $\nu = 3/2, \gamma = D = 4$.

and IbC. Concerning the scalar condensation, different values of Φ_- reshape the effective potential, influencing the point z_1 where the geometry crosses over to the IR asymptotics and thus the width of the potential well, so it starts supporting bound states for different values of m_χ^2 . Finally, the free energy difference depends on the IR quantities ϕ_0, χ_0 which are determined by the matching to the UV solution. Their values influence the location of the transition point but not the nature of the transition.

For the charged case the free energy is given in figure 5. The transition is now continuous and the zoom-in near the origin clarifies that the critical point lies at $m_\chi^2 = 0$. Interestingly, the three values of the O_Φ source now all give the same critical point, at zero mass squared. The curves for different values of O_Φ only differ in the deconfined phase, with nonzero $\langle O_\chi \rangle$, and coincide as long as no condensate forms. At first, this may sound strange. However, a look at the effective potential (4.7) shows that the negative term is now exponentially growing at large z and thus the potential well is always in the deep IR region, rather than in the middle as in the neutral case (figure 2). It is thus understandable that it is not affected by the matching to the UV solution with given Φ_- .

We have already established that our confinement/deconfinement transition may be of continuous or discontinuous nature. Both cases are in principle known even in field theory, and all the more so among the many condensed matter systems where some kind of fractionalization picture is appropriate.

4.3 Finite temperature thermodynamics

At finite temperature, the free energy is still the value of the on-shell action but the radial integration now terminates at finite z_h . In the leading term of the action in geometry Ia,

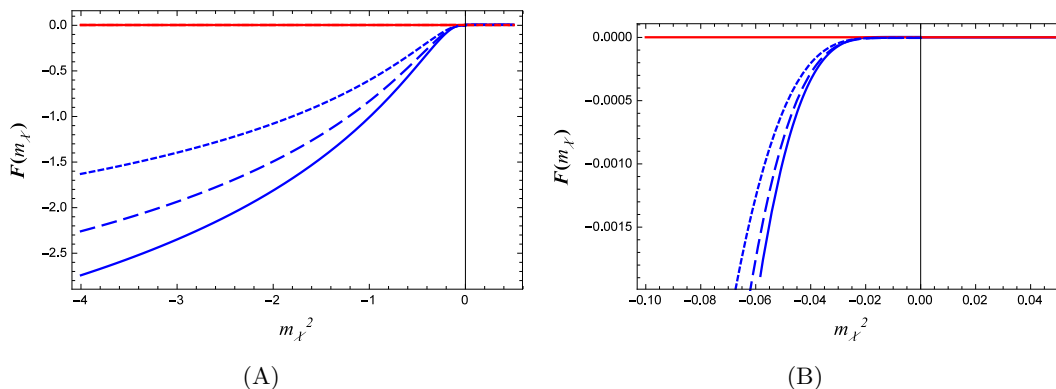


Figure 5. Same as in figure 4(B) but for the charged order parameter with $q = 1$ (A), with a zoom-in near $m_c^2 = 0$ (B). The new solution with condensate branches off smoothly and with continuous first derivative, thus the phase transition is continuous. It is consistent with BKT-like scaling $e^{-1/\sqrt{\Delta_c^2 - \Delta^2}}$. The three values of source (solid, dashed, dotted lines, same as in the previous figure) leave the critical point $m_c^2 = 0$ invariant and only influence the deconfined, condensed phase. The free energy is in arbitrary units and $\tau = 6$.

which stems from the dilaton potential:

$$\mathcal{F}_{Ia} \sim -V_0 \int_{z_1}^{z_h} dz \frac{e^{-(D-3)z^\nu}}{z^2} + \dots \tag{4.12}$$

we need to perform the radial integration from the crossover-to-AdS-scale z_1 to the horizon z_h and expand the result about z_h . Therefore, we integrate from “deep IR” at z_h to “the UV of the IR”, i.e. the location where the geometry crosses over to the asymptotic AdS_{D+1} . Clearly, the integral is dominated by the exponential term and our free energy scales as

$$\mathcal{F}(T \rightarrow 0) \propto \frac{1}{z_h^2} \Gamma_{2-1/\nu}((D-3)z_h^\nu) \sim \text{const.} \times e^{-\frac{D-2}{T^\nu} T^{3-\nu}} \tag{4.13}$$

where the power-law correction $T^{3-\nu}$ is in fact unimportant (we don’t consider $D < 3$ so the exponent $-(D-2)/T^\nu$ is always negative) and the free energy has an extremely slow growth at low T . Clearly, the entropy $S = \partial\mathcal{F}/\partial T$ is zero at zero temperature, and is extremely low at low T (much smaller than for any system with the scaling $\mathcal{F} \sim T^x$ for any power x). Thus the effective number of the degrees of freedom is much reduced because of the confinement. The same scaling is obtained for the charged case.⁷ At high temperatures (compared to the confinement gap) we can expand the action in $1/T$ and get

$$\mathcal{F}(1/T \rightarrow 0) \propto \frac{\Gamma(1-1/\nu)}{z_h^2} \sim \text{const.} \times T^2, \tag{4.14}$$

the quadratic behavior of the free energy and the linear behavior of entropy characteristic of Fermi liquids.⁸ This result was found for a dilatonic black hole in [18] and our system

⁷One may wonder whether this slow growth of entropy can actually be observed. It is possible that any amount of disorder in the system would make the entropy significantly larger. At least theoretically, however, an exponentially slow growth is not unusual in dilatonic setups, see e.g. [21].

⁸For high temperature we get $T \sim 4\pi D/z_h$ but this is not an exact relation and is not even close at low T (unlike the textbook Schwarzschild or RN black hole without the dilaton).

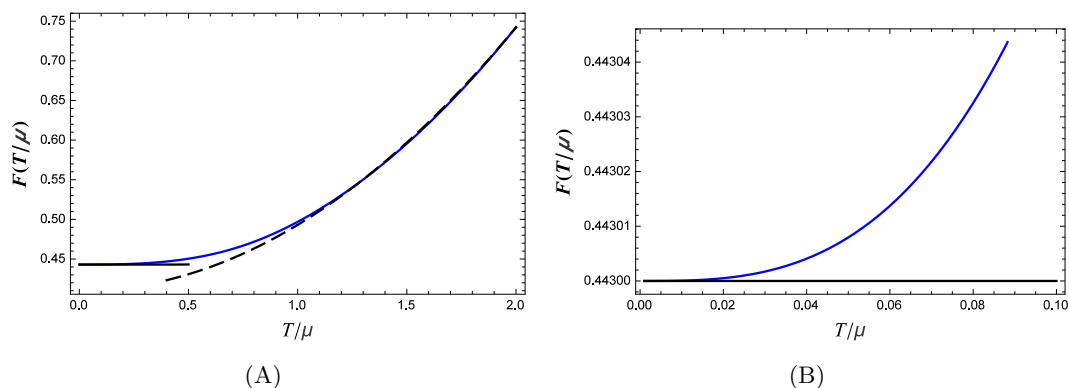


Figure 6. Temperature dependence of the free energy $\mathcal{F}(T)$ for the charged system in the confined phase ($m_\chi^2 = 4$), for $\mu = 1, \nu = 2, \gamma = 4, \tau = 6$. The dashed and the dotted black lines are the analytical estimates (4.13), (4.14) for the confined phase. In (A) we cover a broad range of temperatures, showing both the low-temperature regime with the scaling (4.13) and the high-temperature regime (4.14). In (B), we zoom in at low temperatures, showing the very slow growth of free energy and entropy. The analytical estimates for the low-temperature scalings are determined only up to the UV contribution, which was assumed approximately constant and was fit to the numerics.

behaves similarly at high temperatures (in fact, our confined charged system only differs from it by the choice of the dilaton potential, which likely influences the low-temperature behavior but not the high- T asymptotics). Even though we have no fermions in the system, the quadratic scaling is perhaps not so surprising: one may expect it in any confined system, where only the gauge-neutral bound states are observable. Notice, however, that at high temperatures we expect a dimensional scaling to take place

In the deconfined phase, the exponential scaling is gone and we have a simple scaling law for both low and high temperatures:

$$\mathcal{F}(T) \propto z_h^{-(D-1)\alpha} \sim \text{const.} \times T^x. \quad (4.15)$$

For high temperatures the exponent is $x = (D - 1)\alpha$; for low T the relation $T(z_h)$ is complicated but behaves as a power-law, so \mathcal{F} still scales as a power law of the temperature. This anomalous power law for all temperatures is precisely in line with the hyperscaling-violating nature of the system: the metric has power-law scaling and has no sharp scale where low- T regime cross over to high- T regime. These findings are illustrated in figure 6, where we plot the numerical calculation of $\mathcal{F}(T)$ together with analytical scaling laws for the confined system. We have chosen a large and positive scalar mass $m_\chi^2 = 4$ to avoid the phase transition to the condensed deconfined system, since the purpose of the figure is to study the different scaling regimes in the same phase, not the phase transition (which is discontinuous in T for the neutral system and of infinite order in T in the charged system, same as the scaling with m_χ^2). Notice that the analytical estimates (4.13)–(4.15) are only the IR contribution, and the true free energy is obtained by adding the UV contribution, which is fit as a constant in figure 6 (assuming that the T -dependence in the UV is weak, though in reality it is certainly not strictly constant).

4.4 Structure of the phase diagram

We are now in position to construct the whole phase diagram. The phases are the same both for the neutral and for the charged case, except that the critical line is of different nature (first-order and smooth, respectively). The phase diagram is sketched in figure 7. For small enough conformal dimension Δ_χ and temperature T , the scalar condenses and the system deconfines, restoring the scale invariance at low energies. As the temperature rises, the long-range order of the scalar is lost and we are back to the confined regime. This shows our main point — the confinement/deconfinement transition is triggered by the long-range order of O . What does this mean symmetry-wise? On one hand, the condensation of O certainly breaks a symmetry — \mathbb{Z}_2 (neutral) or $U(1)$ (charged). But on the other hand the deconfinement restores a symmetry: as we have explained, the deconfined geometries are anisotropically scale-covariant (hyperscaling), of the form $ds^2 = z^{-2\kappa}(-f_0 z^{-\eta} dt^2 + d\mathbf{x}^2 + f_0^{-1} z^\eta dz^2)$. In absence of charge ($f_0 = 1, \eta = 0$), all coordinates in field theory can be rescaled as $x^\mu \mapsto \lambda x^\mu$ though the energy (dual to z) scales differently (this is sometimes called generalized conformal symmetry, [25]). With nontrivial f the scaling exponent is different along different axes but there is still some invariance to dilatations (rescaling of coordinates). At the same time, in the soft-wall case with $ds^2 \propto e^{-2z^\nu}$ there is no scale invariance at all. Overall, neither phase is more symmetric than the other: denoting the symmetry group of the scaling system in field theory by \mathbb{G}_1 , we expect it to be broken in the confined phase down to some subgroup $\mathbb{G}_2 < \mathbb{G}_1$, while the symmetry of the scalar (\mathbb{Z}_2 or $U(1)$) is fully broken in the deconfined phase. Since we have a bottom-up model we don't have the explicit form of the field theory Lagrangian and so we cannot fully determine $\mathbb{G}_{1,2}$. Both certainly include the spacetime translations and rotations and \mathbb{G}_1 , as discussed, contains also dilatations. In special cases, e.g. when the field theory is $\mathcal{N} = 4$ super-Yang-Mills, it will be the full conformal group and the deconfinement will be the restoration of the full conformal symmetry. In any case, the symmetry at the critical point changes like

$$\mathbb{G}_2 \otimes \mathbb{Z}_2 \mapsto \mathbb{G}_1 \otimes \mathbb{I}, \quad \mathbb{G}_2 \otimes U(1) \mapsto \mathbb{G}_1 \otimes \mathbb{I}. \tag{4.16}$$

The neutral case where the phase transition is discontinuous could be related to the Landau-Ginzburg theory which generically predicts that in such situations, when no overall symmetry reduction occurs, the two phases can be separated by a first-order transition or by a finite area of phase coexistence. But the charged case where the transition is continuous is of non-Landau-Ginzburg type. This case in particular resembles the concept of deconfined criticality proposed as an explanation for the physics of some strongly coupled quantum critical points in $D = 3$ [10, 11]. We would like to understand how one could probe such phase diagrams in nature, having in mind the handicap that in a bottom-up gauge/gravity model we do not know the explicit form of the action to directly inspect the symmetries of different phases. We would also like to gain a better knowledge of the confinement/deconfinement transition itself: we cannot directly identify the gauge-charged and gauge-neutral degrees of freedom but we can detect the existence of bound states in the confined phase and explore their dispersion relation, a technique particularly used in AdS/QCD, where the quark confinement is recognized from the linear scaling of bound

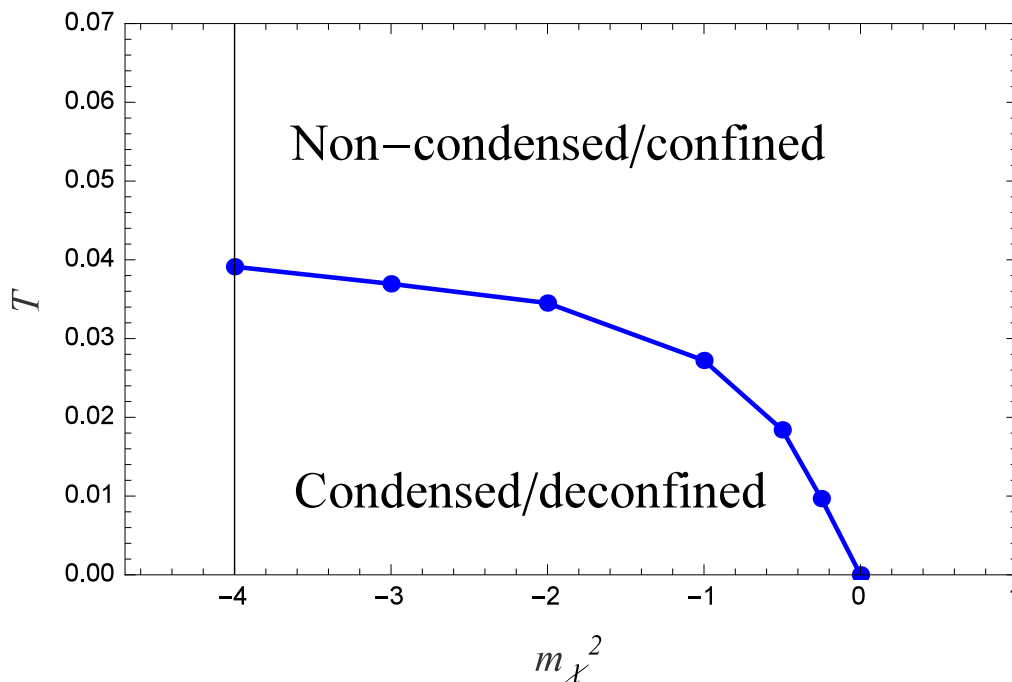


Figure 7. Phase diagram in the Δ_χ - T plane for the charged scalar. Blue dots denote the numerical results for the onset of the condensation of the scalar; the line is just to guide the eye. The condensed/deconfined phase (geometry IaQ) is located to the left and below the boundary line; the rest is the non-condensed/deconfined phase (geometry IbQC). For the neutral case the phase diagram is similar. The key finding is that the deconfinement transition coincides with the onset of the long-range order. The vertical black line denotes the BF bound for AdS_5 .

state masses, $m_n \propto n$ [22, 32–34]. We can also look for the signs of symmetry breaking in the response functions. Bound states can be detected in this way too, since they manifest as poles of correlation functions in the imaginary half-plane, separated from the possible quasiparticle peak by a gap (the binding energy).

Finally, one should have in mind that at very high temperatures it is possible that both confined and deconfined solutions (i.e., all the solutions we have considered) give way to the solution with zero dilaton profile, i.e. the system becomes just a (neutral, Schwarzschild or charged, Reissner-Nordstrom) black hole, as pointed out in [39, 40]. This depends on the parameters of the dilaton potentials; for some values such solutions exist and for some not. We have not checked the existence of this regime explicitly and will not consider it; it is not relevant for the low-temperature and zero-temperature phase transitions we consider here.

5 Response functions and bound states

5.1 Definition and equations of motion

In this section we will try to understand better the nature of different phases by computing the electric AC conductivity $\sigma(\omega, k = 0)$ and charge susceptibility $\xi(\omega, k)$ of our system as well as the retarded propagator $G_R(\omega, k)$ of the order parameter O_χ , in particular by

looking at the bottom half of the complex frequency plane where one can find the poles corresponding to the bound states typical of confined systems. In this section we consider the $T = 0$ case as we are interesting in the properties of the ground state (and its excitations encoded in the pole structure), not the finite-temperature fluctuations. According to the basic dictionary (e.g. [4]) the conductivity, as the response of the current to the imposed (transverse) electric field, is proportional to the ratio of the source and VEV terms of the fluctuation of the spatial component of the bulk electromagnetic field:

$$\delta A_x(z; \omega, k) = \delta A_x^{(0)} + \delta A_x^{(1)} z + \dots, \quad \sigma(\omega, k) = \frac{1}{i\omega} \frac{\delta A_x^{(1)}}{\delta A_x^{(0)}} + \frac{1}{i\omega} R(\omega, k), \quad (5.1)$$

where $R(\omega, k)$ is the regulator connected to the boundary counterterms in the action. Without entering into detailed discussion, we can quote that in $D = 3$ no regulator is needed ($R = 1$) whereas in $D = 4$ we have $R = k^2 - \omega^2$ [9]. Charge susceptibility is the response of the charge density to the applied electric field, and therefore can be computed analogously from the fluctuation of A_0 :

$$\delta A_0(z; \omega, k) = \delta A_0^{(0)} + \delta A_0^{(1)} z + \dots, \quad \xi(\omega, k) = \frac{\delta A_0^{(1)}}{\delta A_0^{(0)}} = \frac{\delta \rho}{\delta \mu}, \quad (5.2)$$

so the susceptibility can be interpreted as the ratio of the charge density fluctuation and the fluctuation in chemical potential. The conductivity mainly makes sense at zero momentum (in the absence of a lattice) whereas susceptibility can also be considered as a function of momentum, to study the spatial modulation of the charge density, as in [42]. The equations of motion are really the variational equations from the action (2.1)–(2.4) about the equilibrium solutions $A_0(z; \omega, k)$ and $A_x(z; \omega, k) = 0$:

$$\delta A_x'' - \left((D-3)A' - \frac{\partial_\Phi \mathcal{T}}{\mathcal{T}} \Phi' \right) \delta A_x' - \left(\frac{\omega^2}{f^2} - \frac{k^2}{f} - \frac{2q^2 e^{-3A}}{f\mathcal{T}} \chi^2 \right) \delta A_x = 0 \quad (5.3)$$

$$\delta A_0'' - \left((D-3)A' - \frac{\partial_\Phi \mathcal{T}}{\mathcal{T}} \Phi' \right) \delta A_0' - \left(\frac{\omega^2}{f^2} - \frac{k^2}{f} - \frac{4q^2 e^{-3A}}{f\mathcal{T}} A_0 \chi^2 \right) \delta A_0 = 0. \quad (5.4)$$

Even though the fluctuations $\delta A_0, \delta A_x$ are coupled to the fluctuations of the metric, we do not consider the full system of fluctuation equations here. For a charged system, this amounts to working in the limit of large charge, where the probe barely has any influence on the system.

Finally, to study the symmetry breaking we explore also the fluctuation of the scalar field $\delta\chi$ which determines the retarded propagator $G_R(\omega, k)$ of the field O in field theory. According to the dictionary, the retarded propagator is again the ratio of the leading boundary components, χ_-/χ_+ , of the fluctuation $\Delta\chi(z; \omega, k)$ which satisfies exactly the same Klein-Gordon equation (2.12) as the equilibrium solution, only at finite energy and momentum:

$$\delta\chi'' + \left(\frac{f'}{f} - (D-1)A' - \frac{\partial_\Phi Z}{Z} \Phi' \right) \delta\chi' - \left(\frac{\omega^2}{f^2} - \frac{k^2}{f} + \frac{e^{-2A}}{f} m_\chi^2 - \frac{q^2}{f^2} e^{\tau\Phi} A_0^2 \right) \delta\chi = 0. \quad (5.5)$$

Unlike the BF bound calculation, we are not exclusively interested in the case when the energy ω is pure imaginary but will consider general values of energy (with non-positive imaginary part, since the poles in the upper half-plane are forbidden).

5.2 Effective Schrödinger equation for the response functions

It is well-known (e.g. [43, 44]) that the IR behavior of the effective Schrödinger problem for various quantities like (5.3), (5.4)(5.5) is related to the energy scaling of the corresponding response functions in field theory, defined as the ratio of the leading and subleading component of the bulk field in the boundary. The aforementioned references study the case when the equation can be written in the form $A_x'' - V(z)A_x = -\omega^2 A_x$ (and similarly for any other field instead of A_x) with $V(z) \sim 1/z^2$ in the IR. The inverse-square potential is famous for allowing a conformal-invariant solution, and simple scaling arguments together with flux conservation lead to the conclusion that the z -scaling of the solutions to the Schrödinger equation in IR determines the ω -scaling of the response function (essentially, the solution is a function of ωz only, and since the flux must be conserved (z -independent) it is also ω -independent, which relates the scaling with z to the scaling with ω). In our problem, even in the deconfined case with no soft wall, the behavior of the potential is in general different from $1/z^2$, and no quantitative results on the frequency scaling can be drawn. We can, however, decide if the spectrum is gapped or continuous, and if the gaps are “hard” (zero spectral weight of the response function) or “soft” (exponentially suppressed nonzero weight).

As the charge susceptibility in dilaton systems was never studied so far, we give a more detailed analysis of the effective potential. The equation (5.4) can be recast as a Schrödinger problem with an effective potential

$$V_{\text{eff}}(z; \omega, k) = -\frac{\omega^2}{f^2} + \frac{k^2}{f} + \frac{e^{-2A}}{f} m_\chi^2 + \frac{X''}{X} + B \frac{X'}{X} \quad (5.6)$$

with $B = (D - 3)A' - \tau\Phi'$ and $X = e^{-\int B/2} = e^{(D-1)/2A - \gamma\Phi/\sqrt{f}}$. Starting from the confined phase (in the charge-neutral case), we see that the potential for the confining geometry behaves in the IR as

$$V_{\text{eff}}(z \rightarrow \infty; \omega, k) = -\omega^2 + k^2 - \frac{\nu(\nu - 1)(\tau - D + 3)}{2} z^{\nu-2} + \frac{3}{4} \nu^2 (\tau - D + 3)^2 z^{2\nu-2} + \dots, \quad (5.7)$$

thus it grows to infinity in the IR (the subleading terms were left out). For finite z (still far enough from the AdS boundary), it is positive if $\omega^2 < \omega_0^2 + k^2$ for some constant ω_0 , i.e. the spectrum is discrete and gapped for small energies. In the bulk, a gap in the spectrum simply means that there is no tunneling of the infalling solution toward the far IR at $z \rightarrow \infty$ (in the terminology of [43], the reflection coefficient is zero). This means that the integral $\int dz \sqrt{2V_{\text{eff}}(z)}/z^2$ has to diverge at large z . For (5.7) the integral behaves as $\int dz z^{\nu-3}$ and thus diverges for $\nu \geq 2$. Therefore, the gaps might be hard or soft depending on the parameters.

For $\omega > \sqrt{\omega_0^2 + k^2}$ we expect a continuum, as the effective potential does not have a well anymore. In the deconfined neutral background, the potential looks like

$$V_{\text{eff}}(z \rightarrow \infty; \omega, k) = -\frac{(D - 3)\alpha - \phi_0\tau}{2z} - \omega^2 + k^2 + \frac{3}{4z} ((D - 3)\alpha - \phi_0\tau)^2 (\log z)^2 + \dots, \quad (5.8)$$

which grows to infinity in the IR but logarithmically slowly, whereas on the other side it again depends on $\omega - \sqrt{\omega_0^2 + k^2}$. The spectrum is thus still gapped and discrete but (since

the well is now shallow, because of the logarithmic growth) the bound states are expected to come closer to each other. Also, the tunneling probability behaves as $\int dz \log z/z^2$ which is finite for $z \rightarrow \infty$, and the gaps is always soft. In the charged case, the effective potential is augmented by a positive term proportional to $q^2 A_0 \chi^2$ which is independent of ω, k . Therefore, the threshold ω_0 is increased but the qualitative behavior remains the same. Similar conclusions hold for the other response functions: the gaps are always soft for the deconfined phase, and may be hard or soft for the confined phase.

5.3 Numerics

5.3.1 AC conductivity

The AC conductivity best encapsulates the breaking of a continuous symmetry (4.16) through the existence of the zero mode. The AC conductivity on the real frequency axis, as well as in the bottom half-plane of complex ω , is given in figure 8. In this plot we show the conductivity $\Re\sigma(\omega, k = 0)$ as a function of the real frequency $\Re\omega$ for a range of $\Im\omega$ values (at zero momentum). We first show the set of curves $\Re\sigma(\Re\omega)$ computed at different $\Im\omega$ values, where the curves at different $\Im\omega$ values are vertically shifted in the figure to be visible together (panels A, B); the x -axis is the real frequency axis and the y -axis is the magnitude of the conductivity minus the vertical shift. In parallel we show the same data as two-dimensional color maps $\Re\sigma(\Re\omega, \Im\omega)$ (panels C, D); now the y -axis is the imaginary part of the frequency, and the lighter areas denote higher values. We use the same recipe to show the curves $\Im G_R(\omega, k)$ and $\xi(\omega, k)$ in later figures.

In the charged confined non-condensed system (panels A, C), there is no gap at small frequencies as the continuous U(1) symmetry is preserved. On the other hand, confinement means the existence of stable bound states ("glueballs"), i.e. poles on the real axis. These are seen as sharp peaks in $\Re\sigma(\omega)$ for real ω . For nonzero $\Im\omega$ the poles apparently turn into branch cuts (the vertical lines); the resolution of our numerics is limited so we are not sure if these are branch cuts or strings of poles along the vertical ($\Im\omega$) axis. Such poles on the real axis have been seen also in [9] in the simple holographic superconductor (without dilaton) when the scalar mass is exactly at the BF bound for AdS_{D+1} ; the relation to our result is not clear but this fact is certainly interesting and we plan to look more carefully into it. Naively, it looks like a bad metal: the AC conductivity is continuous and gapless but small except on a discrete set of real frequencies where the bound states lie.

After deconfinement and the onset of superconductivity (figure 8B, D), the Dirac delta peak at $\omega = 0$ is followed by a gap, which shows the breaking of the U(1) symmetry (this is particularly obvious in the panel B). The bound states do not sit at the real axis anymore. It is again not clear from the numerics if they turn into branch cuts or strings of poles in the complex plane but in any case they do not reach the real axis anymore. In this and further spectral plots, we use the critical temperature as a suitable unit of energy to express the frequencies and momenta; a more usual choice would be the chemical potential, but it is absent in the neutral case, so we have opted for T_c as a natural and physical scale.

Therefore, we witness both the breaking of the U(1) symmetry (Dirac delta peak followed by the gap) and the deconfinement (absence of stable bound states), but not the restoration of scale invariance since our probe is charged and sees the nonzero chemical

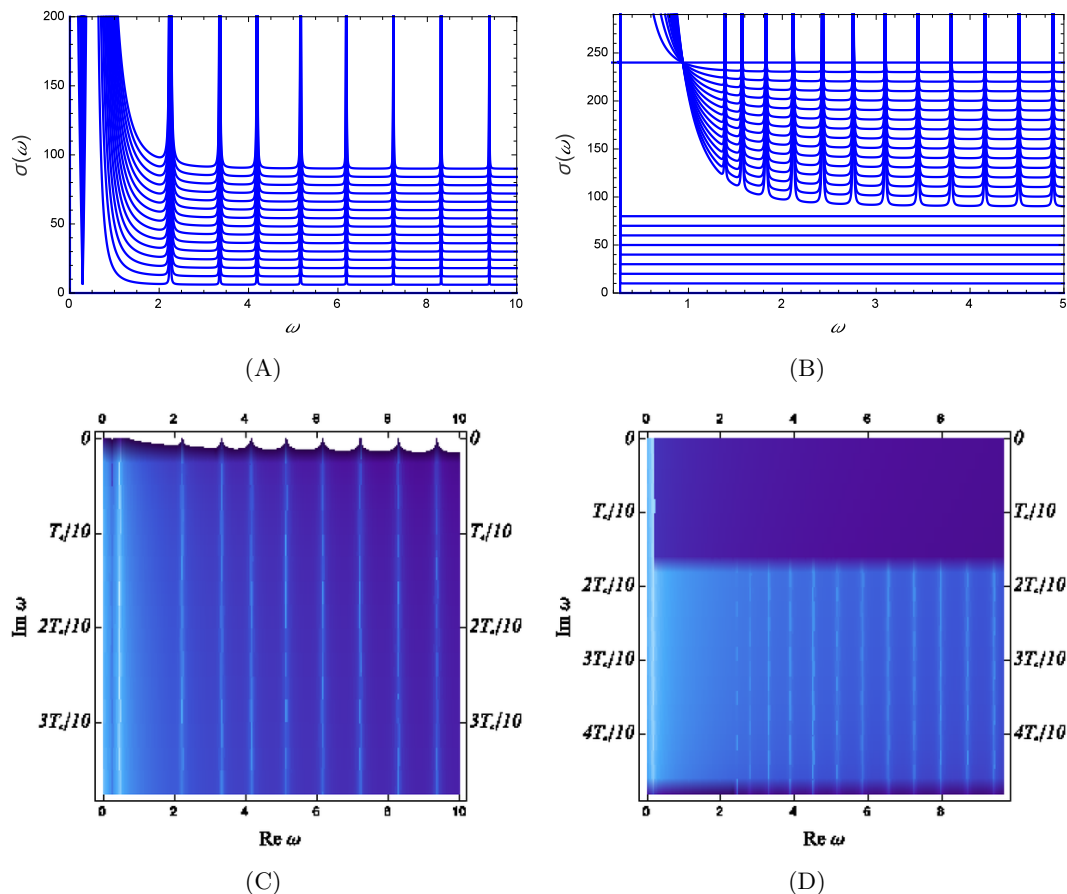


Figure 8. Conductivity $\Re\sigma(\omega)$ in the confined/non-condensed phase ($m_\chi^2 = 2$, A,C) and in the deconfined/condensed phase ($m_\chi^2 = -2$, B,D) in a U(1)-charged system at $\mu = 1$, for a range of $\Im\omega$ values starting from zero (the real axis). In the deconfined/superconducting phase there is only the $\omega = 0$ pole at the real axis (visible for the first curve in the panel B; in the color map panel D it is hard to recognize since it is very narrow), followed by a gap. The gap is expectedly absent in the confined/non-superconducting phase, as the continuous U(1) symmetry is preserved. On the other hand, the confinement/deconfinement transition is visible through the stability of bound states: in the confined regime these states have an infinite lifetime at $T = 0$ and thus manifest as sharp peaks (poles) on the real axis (the bright white spots on the real axis in the density plot). In the deconfined regime these states are pushed to a finite distance below the real axis and look more like branch cuts. For all calculations in a charged system in this section we use $D = 4, \nu = 3/2, \gamma = 4, \tau = 6, \mu = 1$ and $m_\chi^2 = 1/4$ for the confined case and $m_\chi^2 = -1/4$ for the deconfined case.

potential which sets a scale. It is instructive to compare this situation to the charge-neutral case in figure 9. The superconducting gap now has to vanish from the spectrum. Only the presence or absence of confinement is now seen — bound states as poles on the real axis (again apparently continuing as branch cuts below the real axis) in the confined regime and their absence in the deconfined regime. Notice that our confined phase is fractionalized and the deconfined phase is coherent — therefore, our poles are *not* “mesinos”, they are closer to “glueballs”, i.e. complex bound states which contain charged gauge bosons.

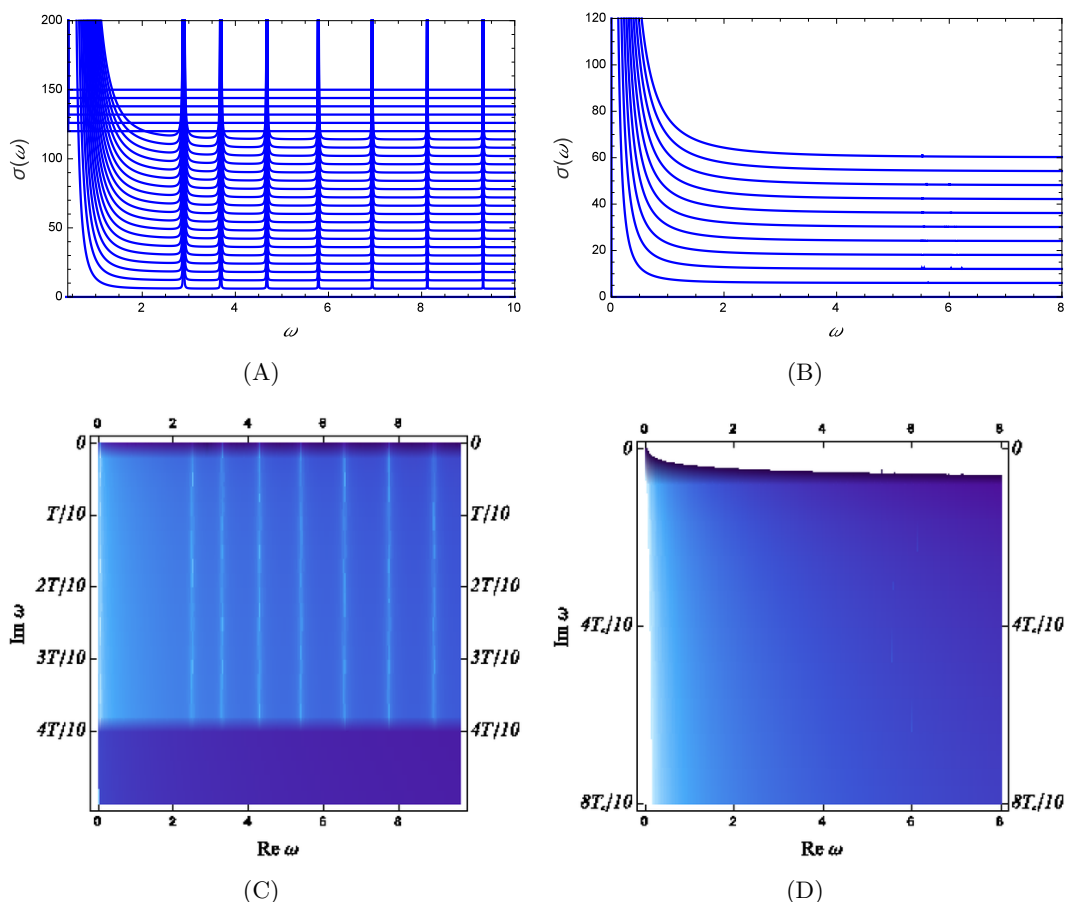


Figure 9. Conductivity $\Re\sigma(\omega)$ in the confined/non-condensed phase ($m_\chi^2 = 8$, A,C) and in the deconfined/condensed phase ($m_\chi^2 = 4$, B,D) in a neutral system, for a range of $\Im\omega$ values starting from zero (the real axis). Neither phase is superconducting thus neither phase has a gap but rather a continuous background behaving as $1/\omega^n$. But the confined case again has long-living bound states corresponding to poles on the real axis, while upon deconfinement these poles vanish completely. The parameters are $D = 4, \nu = 3/2, \gamma = 4$ and $m_\chi^2 = 4$ for the deconfined case and $m_\chi^2 = 8$ for the confined case (also in the remaining plots for the neutral system in this section).

5.3.2 Retarded propagator

A probe which specifically shows the restoration of scale invariance is the retarded propagator $G_R(\omega, k)$, given in figure 10. In the confined regime we see well-defined quasiparticles, due to nonzero chemical potential. But since quasiparticles exist at finite binding energies, the spectrum is gapped and starts from nonzero energy (A, C). Once the system is deconfined, scale invariance is restored and $G_R(\omega) \sim 1/\omega^n$ (B, D). Unlike conductivity, which is not sensitive confinement/deconfinement, the scalar probe differentiates between them: in their absence, it shows no quasiparticles. Another way to understand it is that at low energies (in deep interior) the local chemical potential behaves as $e^{-A}A_0/\sqrt{f} \sim z^{-2\alpha+\phi_0\tau/2}$ while the scale of the metric (the confinement scale) drops faster as $z^{-2\alpha}$, so the confinement scale is above the chemical potential and the probe sees no chemical potential at all.

When the system is neutral and the symmetry to be broken is discrete, we expect to see the presence/absence of scale invariance in much the same way as before but we expect no quasiparticle in either phase, since the chemical potential is zero. The plot for the neutral case is shown in figure 11: now there is indeed no quasiparticle in either phase as the chemical potential and density are zero. But we still detect a scaleful, though continuous spectrum in the confined case, whereas the deconfined case looks pretty much the same as with a charged boson — just a power-law decay. Again, this is *not* about fractionalization — the confined phase, with quasiparticles in figure 10(A,C), has “gauginos” which the gauge-neutral probe cannot see, and the deconfined phase, with no quasiparticles in figure 10(B,D), has “mesinos” which the gauge probe can see. The bottom line is that the probe apparently couples mainly to the gauge field bound states, and in general that the presence/absence of quasiparticles may not be directly related to fractionalization.

5.3.3 Charge susceptibility

Charge susceptibility is interesting as it shows the absence of metallic behavior in both the confined and deconfined phase. Both phases show a gap followed by a series of dispersing poles. This is in line with our analytical finding that both backgrounds give a potential well for δA_0 , inhabited with bound states. But since the well is rising towards infinity very slowly in the deconfined phase, the spacing between the bound states is small in this case. In [42] the authors have explored mainly the momentum dependence of the susceptibility at zero frequency, finding the Friedel oscillations and the singularity at $k = 2k_F$, as expected for a system with zero modes at *finite* momentum, resembling a Fermi surface. In figure 12, in particular in the $\omega - k$ maps (panels B,D) we see that no oscillatory behavior exists for $\chi(\omega = 0, k)$ (the bottom edge of figure 12 C,D) and in particular no pole at $\omega = 0$ exists for any finite k . This tells that our system is different from a normal metal even in the confined phase, and this is not because it is fractionalized (since the RN black hole studied in [42] is also fractionalized).

6 Conclusions and discussion

We have considered an Einstein-(Maxwell)-dilaton-scalar system where the scalar can condense (acquire a VEV) and thus break a symmetry, discrete if neutral or continuous if charged. This in turn remorphs the geometry from a soft-wall, confining form to a deconfined, power-law-scaling form. This goes against the common intuition that a condensate always “narrows” the geometry, which indeed happens in absence of a dilaton with a suitably chosen coupling, e.g. in the textbook holographic superconductor where an AdS-RN background with a near-horizon AdS₂ throat with finite AdS radius typically turns into a Lifshitz-type geometry whose scale shrinks to zero in the interior. From a general viewpoint, it is not so surprising that the huge “zoo” of dilatonic theories contains counterexamples to this behavior, as we have great freedom in choosing the dilaton potentials. But from the viewpoint of field theory and applied gauge/gravity duality, this is interesting as it tells us that we can consider situations in which breaking a symmetry with an order parameter

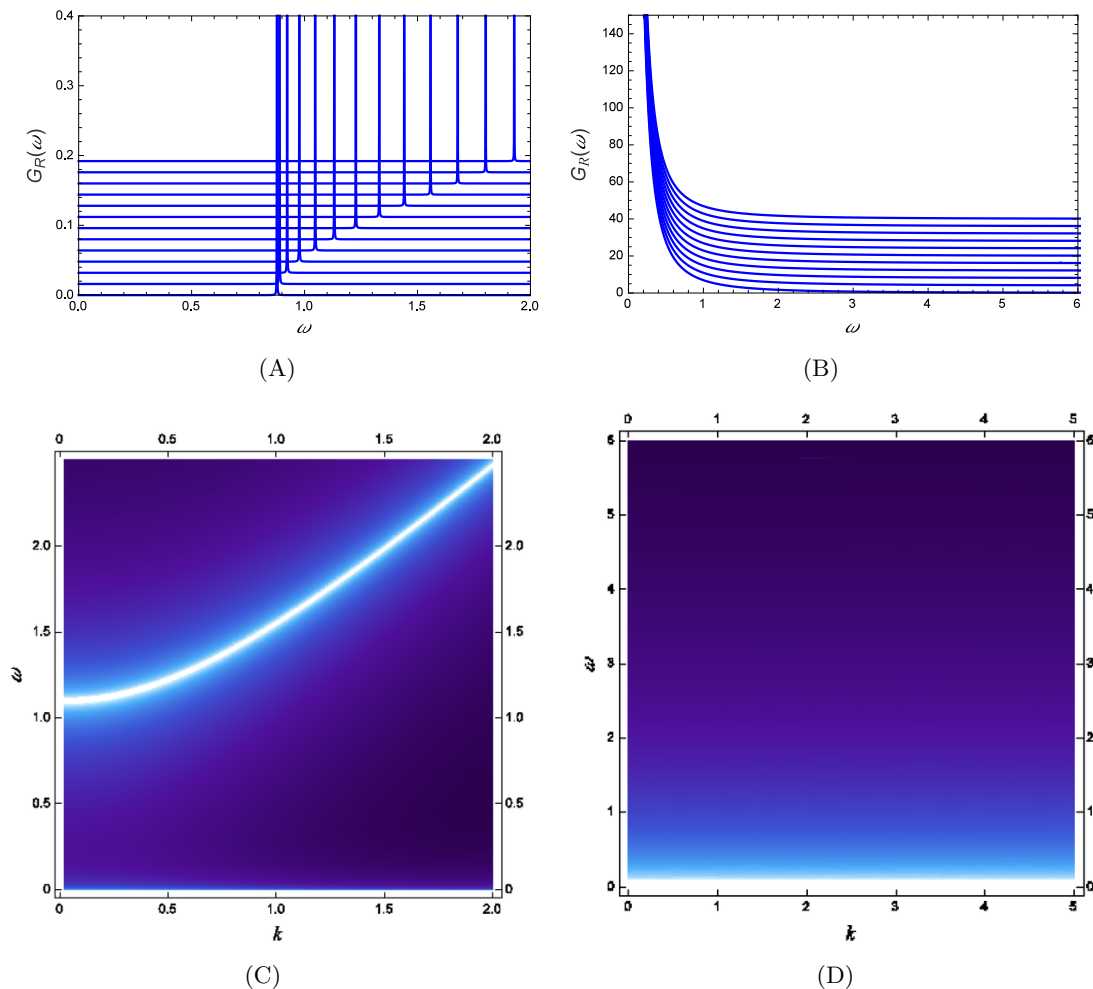


Figure 10. The retarded propagator $\Im G_R(\omega)$ for a range of momentum values ($0 < k < 1.5$) in a charged system ($\mu = 1$), in the confined regime ($m_\chi^2 = -2$, A,C) and in the deconfined regime ($m_\chi^2 = 2$, B,D). In the confined case we see gapped quasiparticle excitations, starting at $\omega \approx 1 > 0$ since we see the bound states in the soft wall which have a discrete and gapped spectrum. In field theory, it means we see gauge-neutral particles. In the deconfined regime, no quasiparticle is present and we have a featureless power-law spectrum $\Im G_R(\omega) \propto 1/\omega^n$. From the gravity viewpoint, it is because the potential has no bound states. From the field theory viewpoint, it means we have gauge-colored excitations which are not visible through a gauge-neutral probe. We thus see the deconfinement transition.

can actually restore another symmetry, since confined systems have a scale (the confinement gap) which vanishes upon condensation. In the simplest case, we can thus expect that conformal symmetry is restored. In practice, it is not the full conformal symmetry but some subset of it, i.e. some scale invariance. We therefore see a non-Ginzburg-Landau phase transition, where neither phase has a higher overall symmetry than the other and the transition can be continuous (in the charged case). This may be related to the picture of deconfined criticality proposed in [10, 11]. But one should be careful, since the transition mechanism in [10, 11] is related to the existence of a new, topological conserved quantity

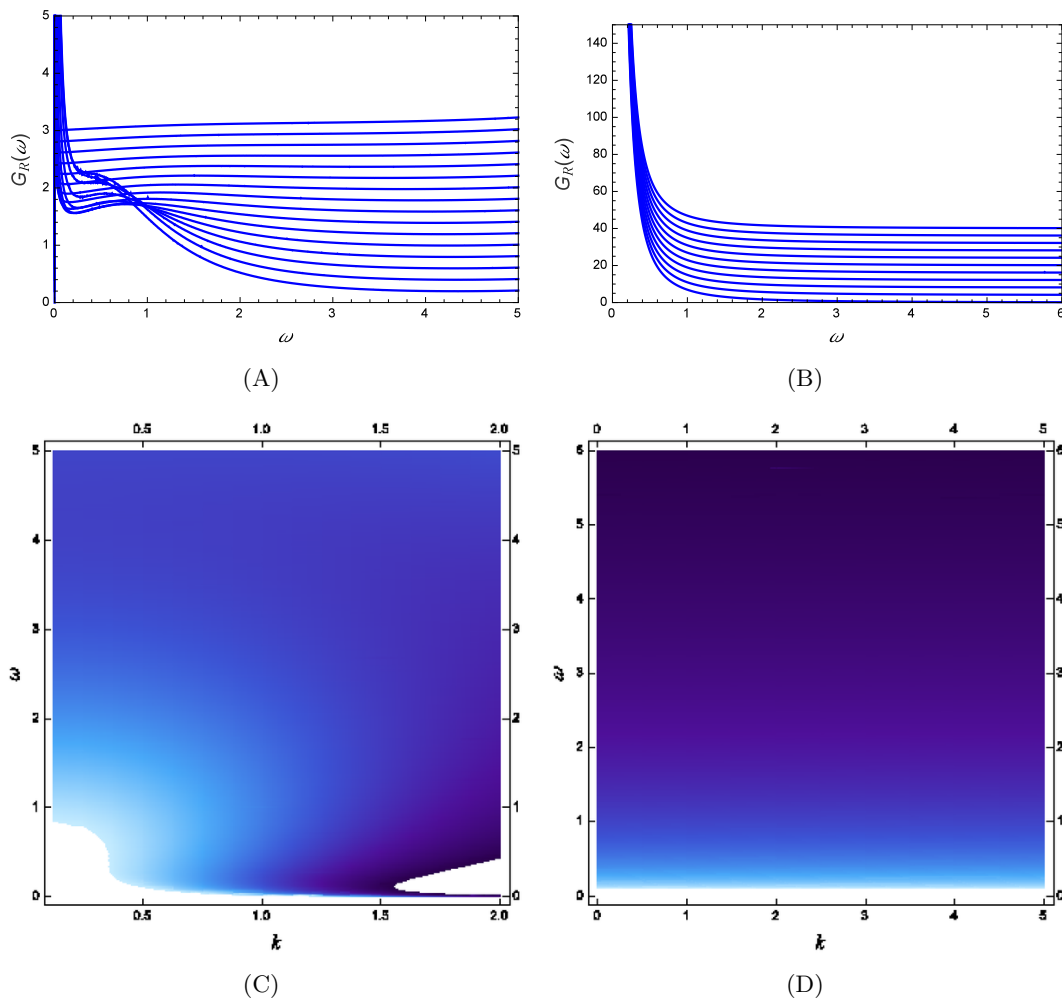


Figure 11. The retarded propagator $\Im G_R(\omega)$ in the confined/non-condensed phase (A,C) and in the deconfined/condensed phase (B,D) in a neutral system. While the deconfined case is again an almost exact power law, the confined case has a scale but no quasiparticle. The discrete Z_2 symmetry has no zero modes upon breaking. The retarded propagator is thus not so useful when the system is neutral.

which only exists at the critical point. In our setup we cannot study geometry or lattice effects and definitely cannot argue anything about topology. The connection is thus very loose and we only see it as inspiration for further work. It would be interesting to consider a setup where the topologically protected gauge flux analogous to that at a deconfined critical point can be detected.

It would also be nice to understand our system better from the gravity side, by deriving our solutions from a superpotential and inspecting how generic this behavior is, which we address in a subsequent publication. It is also interesting to apply our findings to real-world systems. While in QCD there is no obvious additional order parameter that may condense, such situations are abundant in condensed matter systems, mainly in the context of the fractionalization paradigm, where certain non-Fermi-liquid phases are argued to consist

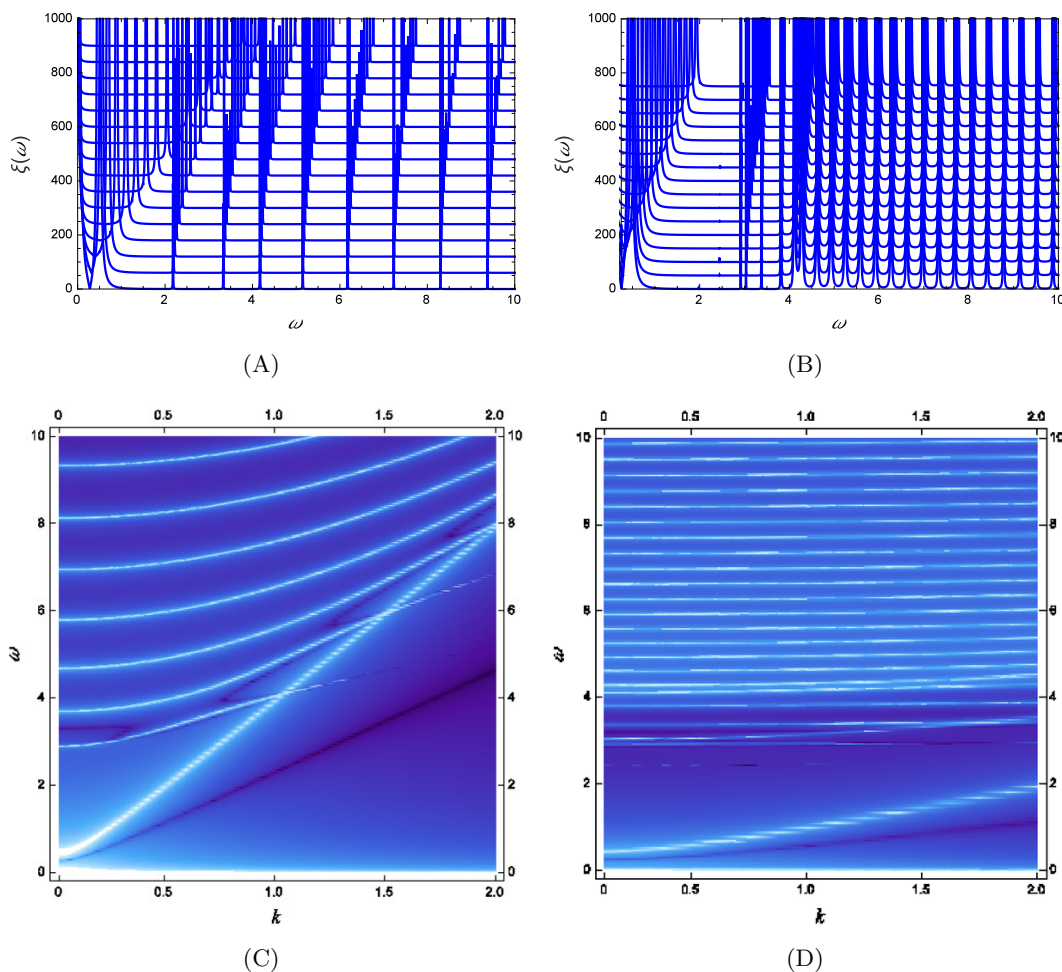


Figure 12. Charge susceptibility $\xi(\omega)$ in the confined/non-condensed phase (A,C) and in the deconfined/condensed phase (B,D) in a charged system. Both cases show bound states; this might look surprising for the deconfined case but is in accordance with the effective potentials in eqs. (5.7)–(5.8). This probe is thus not very useful for detecting the transition but shows the absence of peaks at $\omega = 0$ and $k = 2k_F > 0$, indicating that even the confined phase is different from a normal Fermi liquid.

of gauge-charged excitations which are therefore not observable as quasiparticles. This is also relevant for the heavy fermion systems, where a long-range order is present (the antiferromagnetic ordering, the SO(3) equivalent of our scalar neutral order parameter) and is connected to the disappearance of a normal Fermi liquid, which can be related to the deconfinement of the gauge-charged spinons and holons (in this case, of course, the gauge field is emergent and not microscopic) [12–15]. However, great care must be taken to interpret the fractionalization concept properly, as it is distinct from confinement — in our case, the confined phase is fractionalized and the deconfined phase is coherent. This will also be addressed in our future work.

Acknowledgments

We are grateful to A. Rosch for helpful discussions and careful reading of the manuscript as well as to M. V. Medvedyeva, K. E. Schalm and J. Zaanen for helpful discussions and support.

A A short summary of numerical calculations

For numerical work we find it more convenient to introduce a different coordinate choice where the metric reads

$$ds^2 = -\frac{f(z)h(z)dt^2}{z^2} + \frac{dx^2}{z^2} + \frac{dz^2}{f(z)z^2}. \quad (\text{A.1})$$

The boundary is again at $z = 0$ and the space extends to $z \rightarrow \infty$. It is easy to derive the relations between this parametrization and the one used in the main text. Now the boundary conditions for small z are $f(z \rightarrow 0), h(z \rightarrow 0) \rightarrow 1$. The Einstein equations read

$$zf' - Df + D + \frac{2}{D-1}T^{00} = 0 \quad (\text{A.2})$$

$$\frac{h'}{h}zf = \frac{2}{D-2}(T^{00} - T^{zz}). \quad (\text{A.3})$$

Therefore, both metric functions have first-order equations and we can only impose two boundary conditions for the metric. However, we have more than two physical requirements. The physical requirement for h (which is proportional to the scale factor e^{-2A} in the metric (2.8)) is $h(z \rightarrow \infty) \rightarrow 0$ and for f the first derivative should vanish: $f'(z \rightarrow \infty) \rightarrow 0$. In addition, in order to have an asymptotically AdS geometry we need $f(z \rightarrow 0) = 1$ and $h(z \rightarrow 0) = 1$. We implement this by introducing some cutoff z_Λ and imposing the analytical solutions we have found for the metric in section III for all $z < z_\Lambda$ (the analytical solutions of course automatically satisfy the necessary requirements in the interior). Then we start the integrator at z_Λ , using the condition $f(z = 0) = h(z = 0) = 1$ as the sole boundary condition for the numerics. At finite temperature, the space terminates at the horizon z_h whose value is determined by the temperature, and in this case f itself vanishes at the horizon: $f(z_h) = 0$. In practice, it means we use the analytical ansatz for f, h in the interval $z_h > z > z_h - \epsilon$ and start the integration at $z = z_h - \epsilon$, again with the boundary condition $h(z) = 1$.

The equations of motion for the gauge and matter fields are

$$\Phi'' - \left(\frac{h'}{2h} - (D-1)z\right)\Phi' + \frac{g_{zz}}{\xi}\partial_\Phi V - \frac{4}{\xi(D-1)}g^{00}\mathcal{T}A_0^2 = 0 \quad (\text{A.4})$$

$$A_0'' - \left(\frac{h'}{2h} - (D-3)z - \frac{\partial_\Phi \mathcal{T}}{\mathcal{T}}\Phi'\right)A_0' - 2q^2\frac{Z}{\mathcal{T}}\sqrt{g_{00}g_{zz}}|\chi|^2 = 0 \quad (\text{A.5})$$

$$\chi'' - \left(\frac{h'}{2h} - (D-1)z\right)\chi' - \frac{m_\chi^2}{\xi z^2 f} + \frac{q^2 Z}{f^2}A_0^2\chi = 0. \quad (\text{A.6})$$

Here we have three second-order equations and two boundary conditions per field. For A_0 , one condition is that the electric field should vanish in the interior: $-A_0'(z \rightarrow \infty) \rightarrow 0$

and the other is to impose the chemical potential or the charge density at the boundary ($A_0(z \rightarrow 0) = \mu$ or $A_0(z)/z^{D-2}|_{z \rightarrow 0} = -\rho$). For Φ and χ the only physically obvious boundary condition is to set the leading branch in the small- z expansion (2.18) to zero (remember we pick the dilaton potential V in the UV in such a way that the subleading branch of the dilaton also falls off quickly enough that no condensation occurs). The other boundary condition for Φ, χ is again set by the analytical expansion for z large, similar as for the metric.

It is well known that the integration is unstable if started from the boundary. We therefore start from the interior and impose all boundary conditions in the interior. Physical requirements for $z \rightarrow 0$ are then obtained by shooting. We start from $z_1 \equiv z_\Lambda$ at $T = 0$ or from $z_1 \equiv z_h - \epsilon$ at finite T and iterate the procedure in two stages. The first iteration assumes some essentially arbitrary metric in the whole space (AdS $_{D+1}$ works well) and solves first the coupled system for f, h, A_0, Φ . For f , the boundary condition is the analytical estimate $f_{\text{anal}}(z_1)$. We similarly impose the analytical estimate for Φ while for Φ' we try an arbitrary value C_1 . For h we also start from an arbitrary value C_2 . For the gauge field we impose the physical boundary condition for the derivative ($A'_0(z_1) = 0$) whereas the other condition is arbitrary ($A_0(z_1) = C_3$). We thus have three free parameters C_1, C_2, C_3 so we can shoot for the correct UV behavior of A_0, Φ, h . This procedure does *not* guarantee the correct behavior for $f(0)$ and $h(z_1)$ as we do not shoot for them but when one lands at the correct solution, these turn out to be automatically satisfied (if not, one should play around a bit with the starting values of the shooting parameter $h(z_1)$). In the next stage, we solve the equation for χ with the conditions $\chi(z_1) = C_4 \chi_{\text{anal}}(z_1)$ and $\chi'(z_1) = C_4 \chi'_{\text{anal}}(z_1)$, leaving the overall normalization C_4 as a free parameter. Then we shoot for the required behavior in the UV (this will yield the solution with nonzero VEV, if it exists; if not, it will give the solution $\chi(z) = 0$). After that, we update the metric and the stress tensor and repeat the whole procedure, again in two steps, first for f, h, Φ, A_0 and then for χ . After 5 – 10 steps (a few minutes of computation time) the procedure converges. One should check that the solution is independent of the cutoff z_1 . At zero temperature, for confining backgrounds the overall scale falls off very sharply and typically $z_1 \approx 3 - 4$ is enough while for nonconfining geometries one needs $z_\Lambda \approx 6 - 10$. At finite temperature, the size of the “analytical” region in the interior ϵ can be made quite small, of the order 10^{-3} . A cutoff in the UV is also necessary and is roughly of the size 10^{-6} .

Open Access. This article is distributed under the terms of the Creative Commons Attribution License ([CC-BY 4.0](https://creativecommons.org/licenses/by/4.0/)), which permits any use, distribution and reproduction in any medium, provided the original author(s) and source are credited.

References

- [1] E. Witten, *Anti-de Sitter space and holography*, *Adv. Theor. Math. Phys.* **2** (1998) 253 [[hep-th/9802150](https://arxiv.org/abs/hep-th/9802150)] [[INSPIRE](https://inspirehep.net/literature/481752)].
- [2] S.S. Gubser, I.R. Klebanov and A.M. Polyakov, *Gauge theory correlators from noncritical string theory*, *Phys. Lett. B* **428** (1998) 105 [[hep-th/9802109](https://arxiv.org/abs/hep-th/9802109)] [[INSPIRE](https://inspirehep.net/literature/481752)].

- [3] E. Witten, *Anti-de Sitter space, thermal phase transition and confinement in gauge theories*, *Adv. Theor. Math. Phys.* **2** (1998) 505 [[hep-th/9803131](#)] [[INSPIRE](#)].
- [4] J. Zaanen, Y. Liu, Y.-W. Sun and K. Schalm, *Holographic duality in condensed matter systems*, Cambridge University Press, (2015).
- [5] S.A. Hartnoll, C.P. Herzog and G.T. Horowitz, *Holographic superconductors*, *JHEP* **12** (2008) 015 [[arXiv:0810.1563](#)] [[INSPIRE](#)].
- [6] S.A. Hartnoll, C.P. Herzog and G.T. Horowitz, *Building a holographic superconductor*, *Phys. Rev. Lett.* **101** (2008) 031601 [[arXiv:0803.3295](#)] [[INSPIRE](#)].
- [7] G.T. Horowitz, *Introduction to holographic superconductors*, *Lect. Notes Phys.* **828** (2011) 313 [[arXiv:1002.1722](#)] [[INSPIRE](#)].
- [8] N. Iqbal, H. Liu, M. Mezei and Q. Si, *Quantum phase transitions in holographic models of magnetism and superconductors*, *Phys. Rev. D* **82** (2010) 045002 [[arXiv:1003.0010](#)] [[INSPIRE](#)].
- [9] G.T. Horowitz and M.M. Roberts, *Holographic superconductors with various condensates*, *Phys. Rev. D* **78** (2008) 126008 [[arXiv:0810.1077](#)] [[INSPIRE](#)].
- [10] T. Senthil, A. Vishwanath, L. Balents, S. Sachdev and M.P.A. Fisher, *‘Deconfined’ quantum critical points*, *Science* **303** (2004) 1490 [[cond-mat/0311326](#)].
- [11] T. Senthil, L. Balents, S. Sachdev, A. Vishwanath and M.P.A. Fisher, *Quantum criticality beyond the Ginzburg-Landau-Wilson paradigm*, *Phys. Rev. B* **70** (2004) 144407 [[cond-mat/0312617](#)].
- [12] H.v. Löhneysen, A. Rosch, M. Vojta and P. Wölfle, *Fermi-liquid instabilities at magnetic quantum phase transitions*, *Rev. Mod. Phys.* **79** (2007) 1015 [[INSPIRE](#)].
- [13] T. Senthil, S. Sachdev and M. Vojta, *Fractionalized Fermi liquids*, *Phys. Rev. Lett.* **90** (2003) 216403 [[cond-mat/0209144](#)] [[INSPIRE](#)].
- [14] T. Senthil, S. Sachdev and M. Vojta, *Quantum phase transitions out of a heavy Fermi liquid*, *Physica B* **359** (2005) 9 [[cond-mat/0409033](#)].
- [15] T. Senthil, M. Vojta and S. Sachdev, *Weak magnetism and non-Fermi liquids near heavy-fermion critical points*, *Phys. Rev. B* **69** (2004) 035111 [[cond-mat/0305193](#)] [[INSPIRE](#)].
- [16] S.S. Gubser, *Curvature singularities: the good, the bad and the naked*, *Adv. Theor. Math. Phys.* **4** (2000) 679 [[hep-th/0002160](#)] [[INSPIRE](#)].
- [17] I.R. Klebanov and E. Witten, *AdS/CFT correspondence and symmetry breaking*, *Nucl. Phys. B* **556** (1999) 89 [[hep-th/9905104](#)] [[INSPIRE](#)].
- [18] S.S. Gubser and F.D. Rocha, *Peculiar properties of a charged dilatonic black hole in AdS₅*, *Phys. Rev. D* **81** (2010) 046001 [[arXiv:0911.2898](#)] [[INSPIRE](#)].
- [19] O. DeWolfe, S.S. Gubser and C. Rosen, *Fermi surfaces in N = 4 super-Yang-Mills theory*, *Phys. Rev. D* **86** (2012) 106002 [[arXiv:1207.3352](#)] [[INSPIRE](#)].
- [20] O. DeWolfe, S.S. Gubser and C. Rosen, *Fermionic response in a zero entropy state of N = 4 super-Yang-Mills*, *Phys. Rev. D* **91** (2015) 046011 [[arXiv:1312.7347](#)] [[INSPIRE](#)].
- [21] U. Gürsoy, *Continuous Hawking-Page transitions in Einstein-scalar gravity*, *JHEP* **01** (2011) 086 [[arXiv:1007.0500](#)] [[INSPIRE](#)].

- [22] U. Gürsoy and E. Kiritsis, *Exploring improved holographic theories for QCD: Part I*, *JHEP* **02** (2008) 032 [[arXiv:0707.1324](#)] [[INSPIRE](#)].
- [23] U. Gürsoy, E. Kiritsis and F. Nitti, *Exploring improved holographic theories for QCD: Part II*, *JHEP* **02** (2008) 019 [[arXiv:0707.1349](#)] [[INSPIRE](#)].
- [24] C. Charmousis, *Dilaton space-times with a Liouville potential*, *Class. Quant. Grav.* **19** (2002) 83 [[hep-th/0107126](#)] [[INSPIRE](#)].
- [25] C. Charmousis, B. Gouteraux, B.S. Kim, E. Kiritsis and R. Meyer, *Effective holographic theories for low-temperature condensed matter systems*, *JHEP* **11** (2010) 151 [[arXiv:1005.4690](#)] [[INSPIRE](#)].
- [26] B. Gouteraux and E. Kiritsis, *Generalized holographic quantum criticality at finite density*, *JHEP* **12** (2011) 036 [[arXiv:1107.2116](#)] [[INSPIRE](#)].
- [27] B. Gouteraux and E. Kiritsis, *Quantum critical lines in holographic phases with (un)broken symmetry*, *JHEP* **04** (2013) 053 [[arXiv:1212.2625](#)] [[INSPIRE](#)].
- [28] S.A. Hartnoll, *Horizons, holography and condensed matter*, [arXiv:1106.4324](#) [[INSPIRE](#)].
- [29] S.A. Hartnoll and L. Huijse, *Fractionalization of holographic Fermi surfaces*, *Class. Quant. Grav.* **29** (2012) 194001 [[arXiv:1111.2606](#)] [[INSPIRE](#)].
- [30] K. Goldstein, S. Kachru, S. Prakash and S.P. Trivedi, *Holography of charged dilaton black holes*, *JHEP* **08** (2010) 078 [[arXiv:0911.3586](#)] [[INSPIRE](#)].
- [31] K. Goldstein, N. Iizuka, S. Kachru, S. Prakash, S.P. Trivedi and A. Westphal, *Holography of dyonic dilaton black branes*, *JHEP* **10** (2010) 027 [[arXiv:1007.2490](#)] [[INSPIRE](#)].
- [32] A. Karch, E. Katz, D.T. Son and M.A. Stephanov, *Linear confinement and AdS/QCD*, *Phys. Rev. D* **74** (2006) 015005 [[hep-ph/0602229](#)] [[INSPIRE](#)].
- [33] B. Batell and T. Gherghetta, *Dynamical Soft-Wall AdS/QCD*, *Phys. Rev. D* **78** (2008) 026002 [[arXiv:0801.4383](#)] [[INSPIRE](#)].
- [34] J.I. Kapusta and T. Springer, *Potentials for soft wall AdS/QCD*, *Phys. Rev. D* **81** (2010) 086009 [[arXiv:1001.4799](#)] [[INSPIRE](#)].
- [35] M. Cadoni, G. D'Appollonio and P. Pani, *Phase transitions between Reissner-Nordstrom and dilatonic black holes in 4D AdS spacetime*, *JHEP* **03** (2010) 100 [[arXiv:0912.3520](#)] [[INSPIRE](#)].
- [36] A. Salvio, *Transitions in dilaton holography with global or local symmetries*, *JHEP* **03** (2013) 136 [[arXiv:1302.4898](#)] [[INSPIRE](#)].
- [37] Y. Liu and Y.-W. Sun, *Holographic superconductors from Einstein-Maxwell-dilaton gravity*, *JHEP* **07** (2010) 099 [[arXiv:1006.2726](#)] [[INSPIRE](#)].
- [38] M. Cadoni, P. Pani and M. Serra, *Infrared behavior of scalar condensates in effective holographic theories*, *JHEP* **06** (2013) 029 [[arXiv:1304.3279](#)] [[INSPIRE](#)].
- [39] A. Salvio, *Holographic superfluids and superconductors in dilaton-gravity*, *JHEP* **09** (2012) 134 [[arXiv:1207.3800](#)] [[INSPIRE](#)].
- [40] Z. Fan, *Holographic superconductors with hidden Fermi surfaces*, [arXiv:1311.4110](#) [[INSPIRE](#)].
- [41] D. Mateos, R.C. Myers and R.M. Thomson, *Holographic phase transitions with fundamental matter*, *Phys. Rev. Lett.* **97** (2006) 091601 [[hep-th/0605046](#)] [[INSPIRE](#)].

- [42] M. Blake, A. Donos and D. Tong, *Holographic charge oscillations*, *JHEP* **04** (2015) 019 [[arXiv:1412.2003](#)] [[INSPIRE](#)].
- [43] G.T. Horowitz and M.M. Roberts, *Zero temperature limit of holographic superconductors*, *JHEP* **11** (2009) 015 [[arXiv:0908.3677](#)] [[INSPIRE](#)].
- [44] T. Faulkner, H. Liu, J. McGreevy and D. Vegh, *Emergent quantum criticality, Fermi surfaces and AdS₂*, *Phys. Rev. D* **83** (2011) 125002 [[arXiv:0907.2694](#)] [[INSPIRE](#)].

Chapter 21

Holographic Description of Strongly Correlated Electrons in External Magnetic Fields

E. Gubankova, J. Brill, M. Čubrović, K. Schalm, P. Schijven, and J. Zaanen

21.1 Introduction

The study of strongly interacting fermionic systems at finite density and temperature is a challenging task in condensed matter and high energy physics. Analytical methods are limited or not available for strongly coupled systems, and numerical simulation of fermions at finite density breaks down because of the sign problem [1, 2]. There has been an increased activity in describing finite density fermionic matter by a gravity dual using the holographic AdS/CFT correspondence [3]. The gravitational solution dual to the finite chemical potential system is the electrically charged AdS-Reissner-Nordström (RN) black hole, which provides a background where only the metric and Maxwell fields are nontrivial and all matter fields vanish.

E. Gubankova (✉)
ITP, J. W. Goethe-University, D-60438 Frankfurt am Main, Germany
e-mail: gubankova@th.physik.uni-frankfurt.de

E. Gubankova
ITEP, Moscow, Russia

J. Brill · M. Čubrović · K. Schalm · P. Schijven · J. Zaanen
Instituut Lorentz, Leiden University, Niels Bohrweg 2, 2300 RA Leiden, The Netherlands

J. Brill
e-mail: jellebrill@gmail.com

M. Čubrović
e-mail: cubrovic@lorentz.leidenuniv.nl

K. Schalm
e-mail: kschalm@lorentz.leidenuniv.nl

P. Schijven
e-mail: aphexedpiet@gmail.com

J. Zaanen
e-mail: jan@lorentz.leidenuniv.nl

In the classical gravity limit, the decoupling of the Einstein-Maxwell sector holds and leads to universal results, which is an appealing feature of applied holography. Indeed, the celebrated result for the ratio of the shear viscosity over the entropy density [4] is identical for many strongly interacting theories and has been considered a robust prediction of the AdS/CFT correspondence.

However, an extremal black hole alone is not enough to describe finite density systems as it does not source the matter fields. In holography, at leading order, the Fermi surfaces are not evident in the gravitational geometry, but can only be detected by external probes; either probe D-branes [3] or probe bulk fermions [5–8]. Here we shall consider the latter option, where the free Dirac field in the bulk carries a finite charge density [9]. We ignore electromagnetic and gravitational backreaction of the charged fermions on the bulk spacetime geometry (probe approximation). At large temperatures, $T \gg \mu$, this approach provides a reliable hydrodynamic description of transport at a quantum criticality (in the vicinity of superfluid-insulator transition) [10]. At small temperatures, $T \ll \mu$, in some cases sharp Fermi surfaces emerge with either conventional Fermi-liquid scaling [6] or of a non-Fermi liquid type [7] with scaling properties that differ significantly from those predicted by the Landau Fermi liquid theory. The non-trivial scaling behavior of these non-Fermi liquids has been studied semi-analytically in [8] and is of great interest as high- T_c superconductors and metals near the critical point are believed to represent non-Fermi liquids.

What we shall study is the effects of magnetic field on the holographic fermions. A magnetic field is a probe of finite density matter at low temperatures, where the Landau level physics reveals the Fermi level structure. The gravity dual system is described by a AdS dyonic black hole with electric and magnetic charges Q and H , respectively, corresponding to a $2 + 1$ -dimensional field theory at finite chemical potential in an external magnetic field [11]. Probe fermions in the background of the dyonic black hole have been considered in [12–14]; and probe bosons in the same background have been studied in [15]. Quantum magnetism is considered in [16].

The Landau quantization of momenta due to the magnetic field found there, shows again that the AdS/CFT correspondence has a powerful capacity to unveil that certain quantum properties known from quantum gases have a much more ubiquitous status than could be anticipated theoretically. A first highlight is the demonstration [17] that the Fermi surface of the Fermi gas extends way beyond the realms of its perturbative extension in the form of the Fermi-liquid. In AdS/CFT it appears to be gravitationally encoded in the matching along the scaling direction between the ‘bare’ Dirac waves falling in from the ‘UV’ boundary, and the true IR excitations living near the black hole horizon. This IR physics can insist on the disappearance of the quasiparticle but, if so, this ‘critical Fermi-liquid’ is still organized ‘around’ a Fermi surface. The Landau quantization, the organization of quantum gaseous matter in quantized energy bands (Landau levels) in a system of two space dimensions pierced by a magnetic field oriented in the orthogonal spatial direction, is a second such quantum gas property. We shall describe here following [12], that despite the strong interactions in the system, the holographic computation reveals the same strict Landau-level quantization. Arguably, it is the mean-field nature imposed by

large N limit inherent in AdS/CFT that explains this. The system is effectively non-interacting to first order in $1/N$. The Landau quantization is not manifest from the geometry, but as we show this statement is straightforwardly encoded in the symmetry correspondences associated with the conformal compactification of AdS on its flat boundary (i.e., in the UV CFT).

An interesting novel feature in strongly coupled systems arises from the fact that the background geometry is only sensitive to the total energy density $Q^2 + H^2$ contained in the electric and magnetic fields sourced by the dyonic black hole. Dialing up the magnetic field is effectively similar to a process where the dyonic black hole loses its electric charge. At the same time, the fermionic probe with charge q is essentially only sensitive to the Coulomb interaction gqQ . As shown in [12], one can therefore map a magnetic to a non-magnetic system with rescaled parameters (chemical potential, fermion charge) and same symmetries and equations of motion, as long as the Reissner-Nordström geometry is kept.

Translated to more experiment-compatible language, the above magnetic-electric mapping means that the spectral functions at nonzero magnetic field h are identical to the spectral function at $h = 0$ for a reduced value of the coupling constant (fermion charge) q , provided the probe fermion is in a Landau level eigenstate. A striking consequence is that the spectrum shows conformal invariance for arbitrarily high magnetic fields, as long as the system is at negligible to zero density. Specifically, a detailed analysis of the fermion spectral functions reveals that at strong magnetic fields the Fermi level structure changes qualitatively. There exists a critical magnetic field at which the Fermi velocity vanishes. Ignoring the Landau level quantization, we show that this corresponds to an effective tuning of the system from a regular Fermi liquid phase with linear dispersion and stable quasiparticles to a non-Fermi liquid with fractional power law dispersion and unstable excitations. This phenomenon can be interpreted as a transition from metallic phase to a “strange metal” at the critical magnetic field and corresponds to the change of the infrared conformal dimension from $\nu > 1/2$ to $\nu < 1/2$ while the Fermi momentum stays nonzero and the Fermi surface survives. Increasing the magnetic field further, this transition is followed by a “strange-metal”-conformal crossover and eventually, for very strong fields, the system always has near-conformal behavior where $k_F = 0$ and the Fermi surface disappears.

For some Fermi surfaces, this surprising metal-“strange metal” transition is not physically relevant as the system prefers to directly enter the conformal phase. Whether a fine tuned system exists that does show a quantum critical phase transition from a FL to a non-FL is determined by a Diophantine equation for the Landau quantized Fermi momentum as a function of the magnetic field. Perhaps these are connected to the magnetically driven phase transition found in AdS₅/CFT₄ [18]. We leave this subject for further work.

Overall, the findings of Landau quantization and “discharge” of the Fermi surface are in line with the expectations: both phenomena have been found in a vast array of systems [19] and are almost tautologically tied to the notion of a Fermi surface in a magnetic field. Thus we regard them also as a sanity check of the whole bottom-up approach of fermionic AdS/CFT [5–7, 17], giving further credit to the holographic Fermi surfaces as having to do with the real world.

Next we use the information of magnetic effects the Fermi surfaces extracted from holography to calculate the quantum Hall and longitudinal conductivities. Generally speaking, it is difficult to calculate conductivity holographically beyond the Einstein-Maxwell sector, and extract the contribution of holographic fermions. In the semiclassical approximation, one-loop corrections in the bulk setup involving charged fermions have been calculated [17]. In another approach, the backreaction of charged fermions on the gravity-Maxwell sector has been taken into account and incorporated in calculations of the electric conductivity [9]. We calculate the one-loop contribution on the CFT side, which is equivalent to the holographic one-loop calculations as long as vertex corrections do not modify physical dependencies of interest [17, 20]. As we dial the magnetic field, the Hall plateau transition happens when the Fermi surface moves through a Landau level. One can think of a difference between the Fermi energy and the energy of the Landau level as a gap, which vanishes at the transition point and the $2 + 1$ -dimensional theory becomes scale invariant. In the holographic D3–D7 brane model of the quantum Hall effect, plateau transition occurs as D-branes move through one another [21, 22]. In the same model, a dissipation process has been observed as D-branes fall through the horizon of the black hole geometry, that is associated with the quantum Hall insulator transition. In the holographic fermion liquid setting, dissipation is present through interaction of fermions with the horizon of the black hole. We have also used the analysis of the conductivities to learn more about the metal-strange metal phase transition as well as the crossover back to the conformal regime at high magnetic fields.

We conclude with the remark that the findings summarized above are in fact somewhat puzzling when contrasted to the conventional picture of quantum Hall physics. It is usually stated that the quantum Hall effect requires three key ingredients: Landau quantization, quenched disorder¹ and (spatial) boundaries, i.e., a finite-sized sample [23]. The first brings about the quantization of conductivity, the second prevents the states from spilling between the Landau levels ensuring the existence of a gap and the last one in fact allows the charge transport to happen (as it is the boundary states that actually conduct). In our model, only the first condition is satisfied. The second is put by hand by assuming that the gap is automatically preserved, i.e. that there is no mixing between the Landau levels. There is, however, no physical explanation as to how the boundary states are implicitly taken into account by AdS/CFT.

We outline the holographic setting of the dyonic black hole geometry and bulk fermions in Sect. 21.2. In Sect. 21.3 we prove the conservation of conformal symmetry in the presence of the magnetic fields. Section 21.4 is devoted to the holographic fermion liquid, where we obtain the Landau level quantization, followed by a detailed study of the Fermi surface properties at zero temperature in Sect. 21.5. We calculate the DC conductivities in Sect. 21.6, and compare the results with available data in graphene.

¹Quenched disorder means that the dynamics of the impurities is “frozen”, i.e. they can be regarded as having infinite mass. When coupled to the Fermi liquid, they ensure that below some scale the system behaves as if consisting of non-interacting quasiparticles only.

21.2 Holographic Fermions in a Dyonic Black Hole

We first describe the holographic setup with the dyonic black hole, and the dynamics of Dirac fermions in this background. In this paper, we exclusively work in the probe limit, i.e., in the limit of large fermion charge q .

21.2.1 Dyonic Black Hole

We consider the gravity dual of 3-dimensional conformal field theory (CFT) with global $U(1)$ symmetry. At finite charge density and in the presence of magnetic field, the system can be described by a dyonic black hole in 4-dimensional anti-de Sitter space-time, AdS_4 , with the current J_μ in the CFT mapped to a $U(1)$ gauge field A_M in AdS . We use μ, ν, ρ, \dots for the spacetime indices in the CFT and M, N, \dots for the global spacetime indices in AdS .

The action for a vector field A_M coupled to AdS_4 gravity can be written as

$$S_g = \frac{1}{2\kappa^2} \int d^4x \sqrt{-g} \left(\mathcal{R} + \frac{6}{R^2} - \frac{R^2}{g_F^2} F_{MN} F^{MN} \right), \quad (21.1)$$

where g_F^2 is an effective dimensionless gauge coupling and R is the curvature radius of AdS_4 . The equations of motion following from (21.1) are solved by the geometry corresponding to a dyonic black hole, having both electric and magnetic charge:

$$ds^2 = g_{MN} dx^M dx^N = \frac{r^2}{R^2} (-f dt^2 + dx^2 + dy^2) + \frac{R^2}{r^2} \frac{dr^2}{f}. \quad (21.2)$$

The redshift factor f and the vector field A_M reflect the fact that the system is at a finite charge density and in an external magnetic field:

$$f = 1 + \frac{Q^2 + H^2}{r^4} - \frac{M}{r^3}, \quad (21.3)$$

$$A_t = \mu \left(1 - \frac{r_0}{r} \right), \quad A_y = hx, \quad A_x = A_r = 0,$$

where Q and H are the electric and magnetic charge of the black hole, respectively. Here we chose the Landau gauge; the black hole chemical potential μ and the magnetic field h are given by

$$\mu = \frac{g_F Q}{R^2 r_0}, \quad h = \frac{g_F H}{R^4}, \quad (21.4)$$

with r_0 is the horizon radius determined by the largest positive root of the redshift factor $f(r_0) = 0$:

$$M = r_0^3 + \frac{Q^2 + H^2}{r_0}. \quad (21.5)$$

The boundary of the *AdS* is reached for $r \rightarrow \infty$. The geometry described by (21.2)–(21.3) describes the boundary theory at finite density, i.e., a system in a charged medium at the chemical potential $\mu = \mu_{\text{bh}}$ and in transverse magnetic field $h = h_{\text{bh}}$, with charge, energy, and entropy densities given, respectively, by

$$\rho = 2 \frac{Q}{\kappa^2 R^2 g_F}, \quad \varepsilon = \frac{M}{\kappa^2 R^4}, \quad s = \frac{2\pi}{\kappa^2} \frac{r_0^2}{R^2}. \tag{21.6}$$

The temperature of the system is identified with the Hawking temperature of the black hole, $T_H \sim |f'(r_0)|/4\pi$,

$$T = \frac{3r_0}{4\pi R^2} \left(1 - \frac{Q^2 + H^2}{3r_0^4} \right). \tag{21.7}$$

Since Q and H have dimensions of $[L]^2$, it is convenient to parametrize them as

$$Q^2 = 3r_*^4, \quad Q^2 + H^2 = 3r_{**}^4. \tag{21.8}$$

In terms of r_0 , r_* and r_{**} the above expressions become

$$f = 1 + \frac{3r_{**}^4}{r^4} - \frac{r_0^3 + 3r_{**}^4/r_0}{r^3}, \tag{21.9}$$

with

$$\mu = \sqrt{3} g_F \frac{r_*^2}{R^2 r_0}, \quad h = \sqrt{3} g_F \frac{\sqrt{r_{**}^4 - r_*^4}}{R^4}. \tag{21.10}$$

The expressions for the charge, energy and entropy densities, as well as for the temperature are simplified as

$$\begin{aligned} \rho &= \frac{2\sqrt{3}}{\kappa^2 g_F} \frac{r_*^2}{R^2}, \quad \varepsilon = \frac{1}{\kappa^2} \frac{r_0^3 + 3r_{**}^4/r_0}{R^4}, \quad s = \frac{2\pi}{\kappa^2} \frac{r_0^2}{R^2}, \\ T &= \frac{3}{4\pi} \frac{r_0}{R^2} \left(1 - \frac{r_{**}^4}{r_0^4} \right). \end{aligned} \tag{21.11}$$

In the zero temperature limit, i.e., for an extremal black hole, we have

$$T = 0 \quad \rightarrow \quad r_0 = r_{**}, \tag{21.12}$$

which in the original variables reads $Q^2 + H^2 = 3r_0^4$. In the zero temperature limit (21.12), the redshift factor f as given by (21.9) develops a double zero at the horizon:

$$f = 6 \frac{(r - r_{**})^2}{r_{**}^2} + \mathcal{O}((r - r_{**})^3). \tag{21.13}$$

As a result, near the horizon the AdS_4 metric reduces to $AdS_2 \times \mathbb{R}^2$ with the curvature radius of AdS_2 given by

$$R_2 = \frac{1}{\sqrt{6}}R. \quad (21.14)$$

This is a very important property of the metric, which considerably simplifies the calculations, in particular in the magnetic field.

In order to scale away the AdS_4 radius R and the horizon radius r_0 , we introduce dimensionless variables

$$\begin{aligned} r &\rightarrow r_0 r, & r_* &\rightarrow r_0 r_*, & r_{**} &\rightarrow r_0 r_{**}, \\ M &\rightarrow r_0^3 M, & Q &\rightarrow r_0^2 Q, & H &\rightarrow r_0^2 H, \end{aligned} \quad (21.15)$$

and

$$\begin{aligned} (t, \mathbf{x}) &\rightarrow \frac{R^2}{r_0}(t, \mathbf{x}), & A_M &\rightarrow \frac{r_0}{R^2}A_M, & \omega &\rightarrow \frac{r_0}{R^2}\omega, \\ \mu &\rightarrow \frac{r_0}{R^2}\mu, & h &\rightarrow \frac{r_0^2}{R^4}h, & T &\rightarrow \frac{r_0}{R^2}T, \\ ds^2 &\rightarrow R^2 ds^2. \end{aligned} \quad (21.16)$$

Note that the scaling factors in the above equation that describes the quantities of the boundary field theory involve the curvature radius of AdS_4 , not AdS_2 .

In the new variables we have

$$\begin{aligned} T &= \frac{3}{4\pi}(1 - r_{**}^4) = \frac{3}{4\pi}\left(1 - \frac{Q^2 + H^2}{3}\right), & f &= 1 + \frac{3r_{**}^4}{r^4} - \frac{1 + 3r_{**}^4}{r^3}, \\ A_t &= \mu\left(1 - \frac{1}{r}\right), & \mu &= \sqrt{3}g_F r_*^2 = g_F Q, & h &= g_F H, \end{aligned} \quad (21.17)$$

and the metric is given by

$$ds^2 = r^2(-f dt^2 + dx^2 + dy^2) + \frac{1}{r^2} \frac{dr^2}{f}, \quad (21.18)$$

with the horizon at $r = 1$, and the conformal boundary at $r \rightarrow \infty$.

At $T = 0$, r_{**} becomes unity, and the redshift factor develops the double zero near the horizon,

$$f = \frac{(r-1)^2(r^2 + 2r + 3)}{r^4}. \quad (21.19)$$

As mentioned before, due to this fact the metric near the horizon reduces to $AdS_2 \times \mathbb{R}^2$ where the analytical calculations are possible for small frequencies [8]. However, in the chiral limit $m = 0$, analytical calculations are also possible in the bulk AdS_4 [24], which we utilize in this paper.

21.2.2 Holographic Fermions

To include the bulk fermions, we consider a spinor field ψ in the AdS_4 of charge q and mass m , which is dual to an operator \mathcal{O} in the boundary CFT_3 of charge q and dimension

$$\Delta = \frac{3}{2} + mR, \tag{21.20}$$

with $mR \geq -\frac{1}{2}$ and in dimensionless units corresponds to $\Delta = \frac{3}{2} + m$. In the black hole geometry, (21.2), the quadratic action for ψ reads as

$$S_\psi = i \int d^4x \sqrt{-g} (\bar{\psi} \Gamma^M \mathcal{D}_M \psi - m \bar{\psi} \psi), \tag{21.21}$$

where $\bar{\psi} = \psi^\dagger \Gamma^t$, and

$$\mathcal{D}_M = \partial_M + \frac{1}{4} \omega_{abM} \Gamma^{ab} - iq A_M, \tag{21.22}$$

where ω_{abM} is the spin connection, and $\Gamma^{ab} = \frac{1}{2} [\Gamma^a, \Gamma^b]$. Here, M and a, b denote the bulk space-time and tangent space indices respectively, while μ, ν are indices along the boundary directions, i.e. $M = (r, \mu)$. Gamma matrix basis (Minkowski signature) is given in [8].

We will be interested in spectra and response functions of the boundary fermions in the presence of magnetic field. This requires solving the Dirac equation in the bulk [6, 7]:

$$(\Gamma^M \mathcal{D}_M - m)\psi = 0. \tag{21.23}$$

From the solution of the Dirac equation at small ω , an analytic expression for the retarded fermion Green’s function of the boundary CFT at zero magnetic field has been obtained in [8]. Near the Fermi surface it reads as [8]:

$$G_R(\Omega, k) = \frac{(-h_1 v_F)}{\omega - v_F k_\perp - \Sigma(\omega, T)}, \tag{21.24}$$

where $k_\perp = k - k_F$ is the perpendicular distance from the Fermi surface in momentum space, h_1 and v_F are real constants calculated below, and the self-energy $\Sigma = \Sigma_1 + i \Sigma_2$ is given by [8]

$$\Sigma(\omega, T)/v_F = T^{2\nu} g \left(\frac{\omega}{T} \right) = (2\pi T)^{2\nu} h_2 e^{i\theta - i\pi\nu} \frac{\Gamma(\frac{1}{2} + \nu - \frac{i\omega}{2\pi T} + \frac{i\mu_q}{6})}{\Gamma(\frac{1}{2} - \nu - \frac{i\omega}{2\pi T} + \frac{i\mu_q}{6})}, \tag{21.25}$$

where ν is the zero temperature conformal dimension at the Fermi momentum, $\nu \equiv \nu_{k_F}$, given by (21.58), $\mu_q \equiv \mu q$, h_2 is a positive constant and the phase θ is such that the poles of the Green’s function are located in the lower half of the complex frequency plane. These poles correspond to quasinormal modes of the Dirac

equation (21.23) and they can be found numerically solving $F(\omega_*) = 0$ [25, 26], with

$$F(\omega) = \frac{k_{\perp}}{\Gamma(\frac{1}{2} + \nu - \frac{i\omega}{2\pi T} + \frac{i\mu_q}{6})} - \frac{h_2 e^{i\theta - i\pi\nu} (2\pi T)^{2\nu}}{\Gamma(\frac{1}{2} - \nu - \frac{i\omega}{2\pi T} + \frac{i\mu_q}{6})}, \quad (21.26)$$

The solution gives the full motion of the quasinormal poles $\omega_*^{(n)}(k_{\perp})$ in the complex ω plane as a function of k_{\perp} . It has been found in [8, 25, 26], that, if the charge of the fermion is large enough compared to its mass, the pole closest to the real ω axis bounces off the axis at $k_{\perp} = 0$ (and $\omega = 0$). Such behavior is identified with the existence of the Fermi momentum k_F indicative of an underlying strongly coupled Fermi surface.

At $T = 0$, the self-energy becomes $T^{2\nu} g(\omega/T) \rightarrow c_k \omega^{2\nu}$, and the Green's function obtained from the solution to the Dirac equation reads [8]

$$G_R(\Omega, k) = \frac{(-\hbar_1 v_F)}{\omega - v_F k_{\perp} - h_2 v_F e^{i\theta - i\pi\nu} \omega^{2\nu}}, \quad (21.27)$$

where $k_{\perp} = \sqrt{k^2} - k_F$. The last term is determined by the IR AdS_2 physics near the horizon. Other terms are determined by the UV physics of the AdS_4 bulk.

The solutions to (21.23) have been studied in detail in [6–8]. Here we simply summarize the novel aspects due to the background magnetic field [27]

- The background magnetic field h introduces a discretization of the momentum:

$$k \rightarrow k_{\text{eff}} = \sqrt{2|qh|l}, \quad \text{with } l \in N, \quad (21.28)$$

with Landau level index l [13, 14, 25, 26]. These discrete values of k are the analogue of the well-known Landau levels that occur in magnetic systems.

- There exists a (non-invertible) mapping on the level of Green's functions, from the magnetic system to the non-magnetic one by sending

$$(H, Q, q) \mapsto \left(0, \sqrt{Q^2 + H^2}, q \sqrt{1 - \frac{H^2}{Q^2 + H^2}}\right). \quad (21.29)$$

The Green's functions in a magnetic system are thus equivalent to those in the absence of magnetic fields. To better appreciate that, we reformulate (21.29) in terms of the boundary quantities:

$$(h, \mu_q, T) \mapsto \left(0, \mu_q, T \left(1 - \frac{h^2}{12\mu^2}\right)\right), \quad (21.30)$$

where we used dimensionless variables defined in (21.15), (21.17). The magnetic field thus effectively decreases the coupling constant q and increases the chemical potential $\mu = g_F Q$ such that the combination $\mu_q \equiv \mu q$ is preserved [12]. This is an important point as the equations of motion actually only depend on this combination and not on μ and q separately [12]. In other words, (21.30) implies that the additional scale brought about by the magnetic field can be understood as

changing μ and T independently in the effective non-magnetic system instead of only tuning the ratio μ/T . This point is important when considering the thermodynamics.

- The discrete momentum $k_{\text{eff}} = \sqrt{2|qh|l}$ must be held fixed in the transformation (21.29). The bulk-boundary relation is particularly simple in this case, as the Landau levels can readily be seen in the bulk solution, only to remain identical in the boundary theory.
- Similar to the non-magnetic system [12], the IR physics is controlled by the near horizon $AdS_2 \times \mathbb{R}^2$ geometry, which indicates the existence of an IR CFT, characterized by operators \mathcal{O}_l , $l \in N$ with operator dimensions $\delta = 1/2 + \nu_l$:

$$\nu_l = \frac{1}{6} \sqrt{6 \left(m^2 + \frac{2|qh|l}{r_{**}^2} \right) - \frac{\mu_q^2}{r_{**}^4}}, \quad (21.31)$$

in dimensionless notation, and $\mu_q \equiv \mu q$. At $T = 0$, when $r_{**} = 1$, it becomes

$$\nu_l = \frac{1}{6} \sqrt{6(m^2 + 2|qh|l) - \mu_q^2}. \quad (21.32)$$

The Green's function for these operators \mathcal{O}_l is found to be $\mathcal{G}_l^R(\omega) \sim \omega^{2\nu_l}$ and the exponents ν_l determines the dispersion properties of the quasiparticle excitations. For $\nu > 1/2$ the system has a stable quasiparticle and a linear dispersion, whereas for $\nu \leq 1/2$ one has a non-Fermi liquid with power-law dispersion and an unstable quasiparticle.

21.3 Magnetic Fields and Conformal Invariance

Despite the fact that a magnetic field introduces a scale, in the absence of a chemical potential, all spectral functions are essentially still determined by conformal symmetry. To show this, we need to establish certain properties of the near-horizon geometry of a Reissner-Nordström black hole. This leads to the AdS_2 perspective that was developed in [8]. The result relies on the conformal algebra and its relation to the magnetic group, from the viewpoint of the infrared CFT that was studied in [8]. Later on we will see that the insensitivity to the magnetic field also carries over to AdS_4 and the UV CFT in some respects. To simplify the derivations, we consider the case $T = 0$.

21.3.1 The Near-Horizon Limit and Dirac Equation in AdS_2

It was established in [8] that an electrically charged extremal AdS -Reissner-Nordström black hole has an AdS_2 throat in the inner bulk region. This conclusion carries over to the magnetic case with some minor differences. We will now give a quick derivation of the AdS_2 formalism for a dyonic black hole, referring the reader to [8] for more details (that remain largely unchanged in the magnetic field).

Near the horizon $r = r_{**}$ of the black hole described by the metric (21.2), the redshift factor $f(r)$ develops a double zero:

$$f(r) = 6 \frac{(r - r_{**})^2}{r_{**}^2} + \mathcal{O}((r - r_{**})^3). \quad (21.33)$$

Now consider the scaling limit

$$r - r_{**} = \lambda \frac{R_2^2}{\zeta}, \quad t = \lambda^{-1} \tau, \quad \lambda \rightarrow 0 \text{ with } \tau, \zeta \text{ finite.} \quad (21.34)$$

In this limit, the metric (21.2) and the gauge field reduce to

$$ds^2 = \frac{R_2^2}{\zeta^2} (-d\tau^2 + d\zeta^2) + \frac{r_{**}^2}{R^2} (dx^2 + dy^2), \quad (21.35)$$

$$A_\tau = \frac{\mu R_2^2 r_0}{r_{**}^2} \frac{1}{\zeta}, \quad A_x = Hx$$

where $R_2 = \frac{R}{\sqrt{6}}$. The geometry described by this metric is indeed $AdS_2 \times R^2$. Physically, the scaling limit given in (21.34) with finite τ corresponds to the long time limit of the original time coordinate t , which translates to the low frequency limit of the boundary theory:

$$\frac{\omega}{\mu} \rightarrow 0, \quad (21.36)$$

where ω is the frequency conjugate to t . (One can think of λ as being the frequency ω .) Near the AdS_4 horizon, we expect the AdS_2 region of an extremal dyonic black hole to have a CFT_1 dual. We refer to [8] for an account of this AdS_2/CFT_1 duality. The horizon of AdS_2 region is at $\zeta \rightarrow \infty$ (coefficient in front of $d\tau$ vanishes at the horizon in (21.35)) and the infrared CFT (IR CFT) lives at the AdS_2 boundary at $\zeta = 0$. The scaling picture given by (21.34)–(21.35) suggests that in the low frequency limit, the 2-dimensional boundary theory is described by this IR CFT (which is a CFT_1). The Green's function for the operator \mathcal{O} in the boundary theory is obtained through a small frequency expansion and a matching procedure between the two different regions (inner and outer) along the radial direction, and can be expressed through the Green's function of the IR CFT [8].

The explicit form for the Dirac equation in the magnetic field is of little interest for the analytical results that follow. It can be found in [27]. Of primary interest is its limit in the IR region with metric given by (21.35):

$$\left(-\frac{1}{\sqrt{g_{\zeta\zeta}}} \sigma^3 \partial_\zeta - m + \frac{1}{\sqrt{-g_{\tau\tau}}} \sigma^1 \left(\omega + \frac{\mu_q R_2^2 r_0}{r_{**}^2 \zeta} \right) - \frac{1}{\sqrt{g_{ii} l \sigma^2 \lambda_l}} \right) F^{(l)} = 0, \quad (21.37)$$

where the effective momentum of the l th Landau level is $\lambda_l = \sqrt{2|q\hbar|l}$, $\mu_q \equiv \mu q$ and we omit the index of the spinor field. To obtain (21.37), it is convenient to

pick the gamma matrix basis as $\Gamma^{\hat{\zeta}} = -\sigma_3$, $\Gamma^{\hat{\tau}} = i\sigma_1$ and $\Gamma^{\hat{t}} = -\sigma_2$. We can write explicitly:

$$\begin{pmatrix} \frac{\zeta}{R_2} \partial_{\zeta} + m & -\frac{\zeta}{R_2} \left(\omega + \frac{\mu_q R_2^2 r_0}{r_{**}^2 \zeta} \right) + \frac{R}{r_{**}} \lambda_l \\ \frac{\zeta}{R_2} \left(\omega + \frac{\mu_q R_2^2 r_0}{r_{**}^2 \zeta} \right) + \frac{R}{r_{**}} \lambda_l & \frac{\zeta}{R_2} \partial_{\zeta} - m \end{pmatrix} \begin{pmatrix} y \\ z \end{pmatrix} = 0. \quad (21.38)$$

Note that the AdS_2 radius R_2 enters for the (τ, ζ) directions. At the AdS_2 boundary, $\zeta \rightarrow 0$, the Dirac equation to the leading order is given by

$$\zeta \partial_{\zeta} F^{(l)} = -U F^{(l)}, \quad U = R_2 \begin{pmatrix} m & -\frac{\mu_q R_2 r_0}{r_{**}^2} + \frac{R}{r_{**}} \lambda_l \\ \frac{\mu_q R_2 r_0}{r_{**}^2} + \frac{R}{r_{**}} \lambda_l & -m \end{pmatrix}. \quad (21.39)$$

The solution to this equation is given by the scaling function $F^{(l)} = Ae_+ \zeta^{-\nu_l} + Be_- \zeta^{\nu_l}$ where e_{\pm} are the real eigenvectors of U and the exponent is

$$\nu_l = \frac{1}{6} \sqrt{6 \left(m^2 + \frac{R^2}{r_{**}^2} 2|qh|l \right) R^2 - \frac{\mu_q^2 R^4 r_0^2}{r_{**}^4}}. \quad (21.40)$$

The conformal dimension of the operator \mathcal{O} in the IR CFT is $\delta_l = \frac{1}{2} + \nu_l$. Comparing (21.40) to the expression for the scaling exponent in [8], we conclude that the scaling properties and the AdS_2 construction are unmodified by the magnetic field, except that the scaling exponents are now fixed by the Landau quantization. This ‘‘quantization rule’’ was already exploited in [25, 26] to study de Haas-van Alphen oscillations.

21.4 Spectral Functions

In this section we will explore some of the properties of the spectral function, in both plane wave and Landau level basis. We first consider some characteristic cases in the plane wave basis and make connection with the ARPES measurements.

21.4.1 Relating to the ARPES Measurements

In reality, ARPES measurements cannot be performed in magnetic fields so the holographic approach, allowing a direct insight into the propagator structure and the spectral function, is especially helpful. This follows from the observation that the spectral functions as measured in ARPES are always expressed in the plane wave basis of the photon, thus in a magnetic field, when the momentum is not a good quantum number anymore, it becomes impossible to perform the photoemission spectroscopy.

In order to compute the spectral function, we have to choose a particular fermionic plane wave as a probe. Since the separation of variables is valid through-

out the bulk, the basis transformation can be performed at every constant r -slice. This means that only the x and y coordinates have to be taken into account (the plane wave probe lives only at the CFT side of the duality). We take a plane wave propagating in the $+x$ direction with spin up along the r -axis. In its rest frame such a particle can be described by

$$\Psi_{\text{probe}} = e^{i\omega t - ip_x x} \begin{pmatrix} \xi \\ \xi \end{pmatrix}, \quad \xi = \begin{pmatrix} 1 \\ 0 \end{pmatrix}. \quad (21.41)$$

Near the boundary (at $r_b \rightarrow \infty$) we can rescale our solutions of the Dirac equation, details can be found in [27]:

$$F_l = \begin{pmatrix} \zeta_l^{(1)}(\tilde{x}) \\ \xi_+^{(l)}(r_b) \zeta_l^{(1)}(\tilde{x}) \\ \zeta_l^{(2)}(\tilde{x}) \\ -\xi_+^{(l)}(r_b) \zeta_l^{(2)}(\tilde{x}) \end{pmatrix}, \quad \tilde{F}_l = \begin{pmatrix} \zeta_l^{(1)}(\tilde{x}) \\ \xi_-^{(l)}(r_b) \zeta_l^{(1)}(\tilde{x}) \\ -\zeta_l^{(2)}(\tilde{x}) \\ \xi_-^{(l)}(r_b) \zeta_l^{(2)}(\tilde{x}) \end{pmatrix}, \quad (21.42)$$

with rescaled \tilde{x} defined in [27]. This representation is useful since we calculate the components $\xi_{\pm}(r_b)$ related to the retarded Green's function in our numerics (we keep the notation of [8]).

Let \mathcal{O}_l and $\tilde{\mathcal{O}}_l$ be the CFT operators dual to respectively F_l and \tilde{F}_l , and c_k^\dagger, c_k be the creation and annihilation operators for the plane wave state Ψ_{probe} . Since the states F and \tilde{F} form a complete set in the bulk, we can write

$$c_p^\dagger(\omega) = \sum_l (U_l^*, \tilde{U}_l^*) \begin{pmatrix} \mathcal{O}_l^\dagger(\omega) \\ \tilde{\mathcal{O}}_l^\dagger(\omega) \end{pmatrix} = \sum_l (U_l^* \mathcal{O}_l^\dagger(\omega) + \tilde{U}_l^* \tilde{\mathcal{O}}_l^\dagger(\omega)) \quad (21.43)$$

where the overlap coefficients $U_l(\omega)$ are given by the inner product between Ψ_{probe} and F :

$$U_l(p_x) = \int dx F_l^\dagger i \Gamma^0 \Psi_{\text{probe}} = - \int dx e^{-ip_x x} \xi_+(r_b) (\zeta_l^{(1)\dagger}(\tilde{x}) - \zeta_l^{(2)\dagger}(\tilde{x})), \quad (21.44)$$

with $\tilde{F} = F^\dagger i \Gamma^0$, and similar expression for \tilde{U}_l involving $\xi_-(r_b)$. The constants U_l can be calculated analytically using the numerical value of $\xi_{\pm}(r_b)$, and by noting that the Hermite functions are eigenfunctions of the Fourier transform. We are interested in the retarded Green's function, defined as

$$\begin{aligned} G_{\mathcal{O}_l}^R(\omega, p) &= -i \int d^x dt e^{i\omega t - ip \cdot x} \theta(t) G_{\mathcal{O}_l}^R(t, x) \\ G_{\mathcal{O}_l}^R(t, x) &= \langle 0 | [\mathcal{O}_l(t, x), \tilde{\mathcal{O}}_l(0, 0)] | 0 \rangle \\ G^R &= \begin{pmatrix} G_\theta & 0 \\ 0 & \tilde{G}_\theta \end{pmatrix}, \end{aligned} \quad (21.45)$$

where \tilde{G}_θ is the retarded Green's function for the operator $\tilde{\mathcal{O}}$.

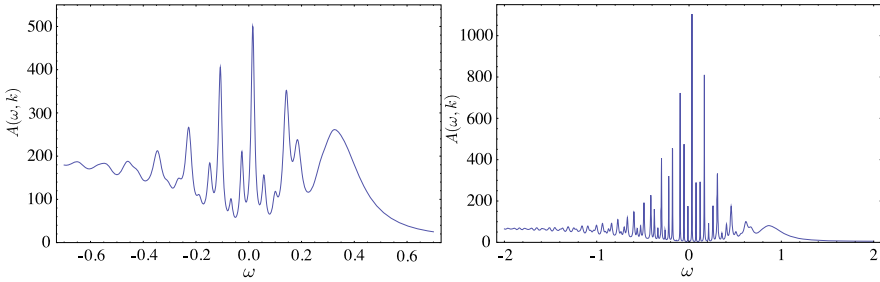


Fig. 21.1 Two examples of spectral functions in the plane wave basis for $\mu/T = 50$ and $h/T = 1$. The conformal dimension is $\Delta = 5/4$ (left) and $\Delta = 3/2$ (right). Frequency is in the units of effective temperature T_{eff} . The plane wave momentum is chosen to be $k = 1$. Despite the convolution of many Landau levels, the presence of the discrete levels is obvious

Exploiting the orthogonality of the spinors created by \mathcal{O} and \mathcal{O}^\dagger and using (21.43), the Green’s function in the plane wave basis can be written as

$$\begin{aligned}
 G_{c_p}^R(\omega, p_x) &= \sum_l \text{tr} \left(\begin{matrix} U \\ \tilde{U} \end{matrix} \right) (U^*, \tilde{U}^*) G^R \\
 &= (|U_l(p_x)|^2 G_{\mathcal{O}_l}^R(\omega, l) + |\tilde{U}_l(p_x)|^2 \tilde{G}_{\mathcal{O}_l}^R(\omega, l)). \tag{21.46}
 \end{aligned}$$

In practice, we cannot perform the sum in (21.46) all the way to infinity, so we have to introduce a cutoff Landau level l_{cut} . In most cases we are able to make l_{cut} large enough that the behavior of the spectral function is clear.

Using the above formalism, we have produced spectral functions for two different conformal dimensions and fixed chemical potential and magnetic field (Fig. 21.1). Using the plane wave basis allows us to directly detect the Landau levels. The unit used for plotting the spectra (here and later on in the paper) is the effective temperature T_{eff} [6]:

$$T_{\text{eff}} = \frac{T}{2} \left(1 + \sqrt{1 + \frac{3\mu^2}{(4\pi T)^2}} \right). \tag{21.47}$$

This unit interpolates between μ at $T/\mu = 0$ and T and is of order $T/\mu \rightarrow \infty$, and is convenient for the reason that the relevant quantities (e.g., Fermi momentum) are of order unity for any value of μ and h .

21.4.2 Magnetic Crossover and Disappearance of the Quasiparticles

Theoretically, it is more convenient to consider the spectral functions in the Landau level basis. For definiteness let us pick a fixed conformal dimension $\Delta = \frac{5}{4}$ which corresponds to $m = -\frac{1}{4}$. In the limit of weak magnetic fields, $h/T \rightarrow 0$, we should reproduce the results that were found in [6].

In Fig. 21.2(A) we indeed see that the spectral function, corresponding to a low value of μ/T , behaves as expected for a nearly conformal system. The spectral function is approximately symmetric about $\omega = 0$, it vanishes for $|\omega| < k$, up to a small residual tail due to finite temperature, and for $|\omega| \gg k$ it scales as ω^{2m} .

In Fig. 21.2(B), which corresponds to a high value of μ/T , we see the emergence of a sharp quasiparticle peak. This peak becomes the sharpest when the Landau level l corresponding to an effective momentum $k_{\text{eff}} = \sqrt{2|qh|l}$ coincides with the Fermi momentum k_F . The peaks also broaden out when k_{eff} moves away from k_F . A more complete view of the Landau quantization in the quasiparticle regime is given in Fig. 21.3, where we plot the dispersion relation (ω - k map). Both the sharp peaks and the Landau levels can be visually identified.

Collectively, the spectra in Fig. 21.2 show that conformality is only broken by the chemical potential μ and not by the magnetic field. Naively, the magnetic field introduces a new scale in the system. However, this scale is absent from the spectral functions, visually validating the discussion in the previous section that the scale h can be removed by a rescaling of the temperature and chemical potential.

One thus concludes that there is some value h'_c of the magnetic field, depending on μ/T , such that the spectral function loses its quasiparticle peaks and displays near-conformal behavior for $h > h'_c$. The nature of the transition and the underlying mechanism depends on the parameters (μ_q, T, Δ) . One mechanism, obvious from the rescaling in (21.29), is the reduction of the effective coupling q as h increases. This will make the influence of the scalar potential A_0 negligible and push the system back toward conformality. Generically, the spectral function shows no sharp change but is more indicative of a crossover.

A more interesting phenomenon is the disappearance of coherent quasiparticles at high effective chemical potentials. For the special case $m = 0$, we can go beyond numerics and study this transition analytically, combining the exact $T = 0$ solution found in [24] and the mapping (21.30). In the next section, we will show that the transition is controlled by the change in the dispersion of the quasiparticle and corresponds to a sharp phase transition. Increasing the magnetic field leads to a decrease in phenomenological control parameter ν_{k_F} . This can give rise to a transition to a non-Fermi liquid when $\nu_{k_F} \leq 1/2$, and finally to the conformal regime at $h = h'_c$ when $\nu_{k_F} = 0$ and the Fermi surface vanishes.

21.4.3 Density of States

As argued at the beginning of this section, the spectral function can look quite different depending on the particular basis chosen. Though the spectral function is an attractive quantity to consider due to connection with ARPES experiments, we will also direct our attention to basis-independent and manifestly gauge invariant quantities. One of them is the density of states (DOS), defined by

$$D(\omega) = \sum_l A(\omega, l), \quad (21.48)$$

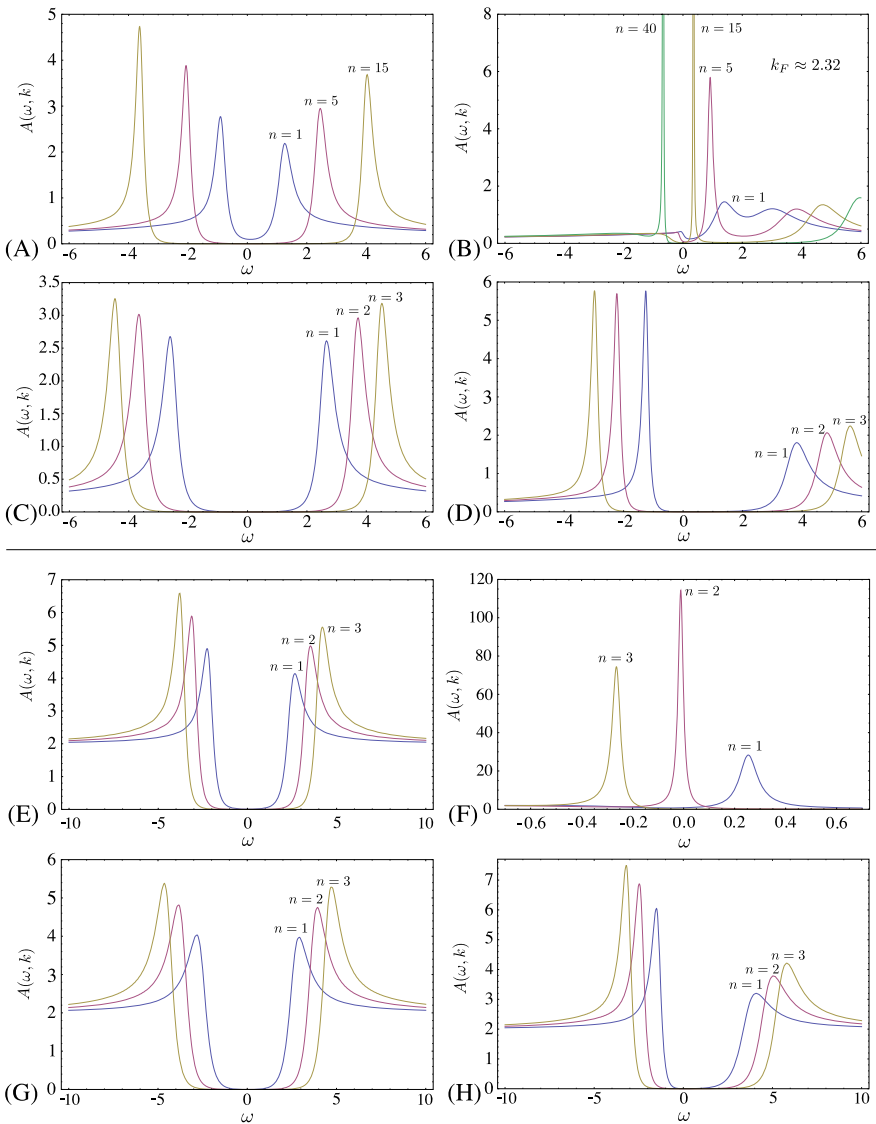


Fig. 21.2 Some typical examples of spectral functions $A(\omega, k_{\text{eff}})$ vs. ω in the Landau basis, $k_{\text{eff}} = \sqrt{2|q\hbar|n}$. The *top four* correspond to a conformal dimension $\Delta = \frac{5}{4}$ ($m = -\frac{1}{4}$) and the *bottom four* to $\Delta = \frac{3}{2}$ ($m = 0$). In each plot we show different Landau levels, labelled by index n , as a function of μ/T and h/T . The ratios take values $(\mu/T, h/T) = (1, 1), (50, 1), (1, 50), (50, 50)$ from left to right. Conformal case can be identified when μ/T is small regardless of h/T (plots in the *left panel*). Nearly conformal behavior is seen when both μ/T and h/T are large. This confirms our analytic result that the behavior of the system is primarily governed by μ . Departure from the conformality and sharp quasiparticle peaks are seen when μ/T is large and h/T is small in 21.2(B) and 21.2(F). Multiple quasiparticle peaks arise whenever $k_{\text{eff}} = k_F$. This suggests the existence of a critical magnetic field, beyond which the quasiparticle description becomes invalid and the system exhibits a conformal-like behavior. As before, the frequency ω is in units of T_{eff}

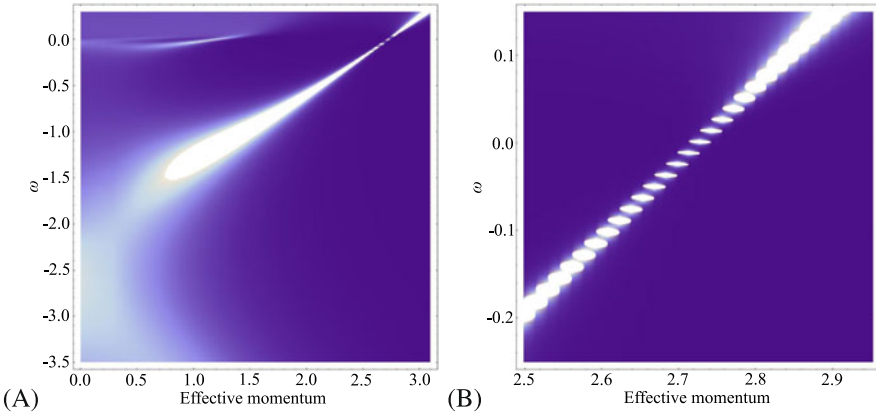


Fig. 21.3 Dispersion relation ω vs. k_{eff} for $\mu/T = 50$, $h/T = 1$ and $\Delta = \frac{5}{4}$ ($m = -\frac{1}{4}$). The spectral function $A(\omega, k_{\text{eff}})$ is displayed as a density plot. **(A)** On a large energy and momentum scale, we clearly see that the peaks disperse almost linearly ($\omega \approx v_F k$), indicating that we are in the stable quasiparticle regime. **(B)** A zoom-in near the location of the Fermi surface shows clear Landau quantization

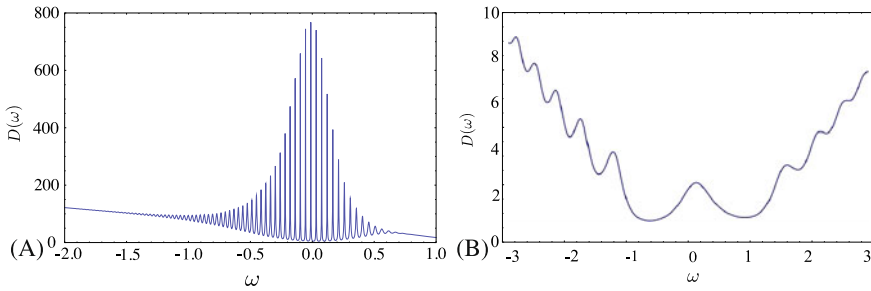


Fig. 21.4 Density of states $D(\omega)$ for $m = -\frac{1}{4}$ and **(A)** $\mu/T = 50$, $h/T = 1$, and **(B)** $\mu/T = 1$, $h/T = 1$. Sharp quasiparticle peaks from the splitting of the Fermi surface are clearly visible in **(A)**. The case **(B)** shows square-root level spacing characteristic of a (nearly) Lorentz invariant spectrum such as that of graphene

where the usual integral over the momentum is replaced by a sum since only discrete values of the momentum are allowed.

In Fig. 21.4, we plot the density of states for two systems. We clearly see the Landau splitting of the Fermi surface. A peculiar feature of these plots is that the DOS seems to grow for negative values of ω . This, however, is an artefact of our calculation. Each individual spectrum in the sum (21.48) has a finite tail that scales as ω^{2m} for large ω , so each term has a finite contribution for large values of ω . When the full sum is performed, this fact implies that $\lim_{\omega \rightarrow \infty} D(\omega) \rightarrow \infty$. The relevant information on the density of states can be obtained by regularizing the sum, which in practice is done by summing over a finite number of terms only, and then considering the peaks that lie on top of the resulting finite-sized envelope. The

physical point in Fig. 21.4(A) is the linear spacing of Landau levels, corresponding to a non-relativistic system at finite density. This is to be contrasted with Fig. 21.4B where the level spacing behaves as $\propto \sqrt{\hbar}$, appropriate for a Lorentz invariant system and realized in graphene [28].

21.5 Fermi Level Structure at Zero Temperature

In this section, we solve the Dirac equation in the magnetic field for the special case $m = 0$ ($\Delta = \frac{3}{2}$). Although there are no additional symmetries in this case, it is possible to get an analytic solution. Using this solution, we obtain Fermi level parameters such as k_F and v_F and consider the process of filling the Landau levels as the magnetic field is varied.

21.5.1 Dirac Equation with $m = 0$

In the case $m = 0$, it is convenient to solve the Dirac equation including the spin connection (see details in [27]) rather than scaling it out:

$$\left(-\frac{\sqrt{g_{ii}}}{\sqrt{g_{rr}}}\sigma^1\partial_r - \frac{\sqrt{g_{ii}}}{\sqrt{-g_{tt}}}\sigma^3(\omega + qA_t) + \frac{\sqrt{g_{ii}}}{\sqrt{-g_{tt}}}\sigma^1\frac{1}{2}\omega_{\hat{r}t} - \sigma^1\frac{1}{2}\omega_{\hat{x}x} - \sigma^1\frac{1}{2}\omega_{\hat{y}y} - \lambda_l \right) \otimes 1 \begin{pmatrix} \psi_1 \\ \psi_2 \end{pmatrix} = 0, \quad (21.49)$$

where $\lambda_l = \sqrt{2|qh|l}$ are the energies of the Landau levels $l = 0, 1, \dots$, $g_{ii} \equiv g_{xx} = g_{yy}$, $A_t(r)$ is given by (21.3), and the gamma matrices are defined in [27]. In this basis the two components ψ_1 and ψ_2 decouple. Therefore, in what follows we solve for the first component only (we omit index 1). Substituting the spin connection, we have [20]:

$$\left(-\frac{r^2\sqrt{f}}{R^2}\sigma^1\partial_r - \frac{1}{\sqrt{f}}\sigma^3(\omega + qA_t) - \sigma^1\frac{r\sqrt{f}}{2R^2}\left(3 + \frac{rf'}{f}\right) - \lambda_l \right) \psi = 0, \quad (21.50)$$

with $\psi = (y_1, y_2)$. It is convenient to change to the basis

$$\begin{pmatrix} \tilde{y}_1 \\ \tilde{y}_2 \end{pmatrix} = \begin{pmatrix} 1 & -i \\ -i & 1 \end{pmatrix} \begin{pmatrix} y_1 \\ y_2 \end{pmatrix}, \quad (21.51)$$

which diagonalizes the system into a second order differential equation for each component. We introduce the dimensionless variables as in (21.15)–(21.17), and make a change of the dimensionless radial variable:

$$r = \frac{1}{1-z}, \quad (21.52)$$

with the horizon now being at $z = 0$, and the conformal boundary at $z = 1$. Performing these transformations in (21.50), the second order differential equations for \tilde{y}_1 reads

$$\left(f \partial_z^2 + \left(\frac{3f}{1-z} + f' \right) \partial_z + \frac{15f}{4(1-z)^2} + \frac{3f'}{2(1-z)} + \frac{f''}{4} + \frac{1}{f} \left((\omega + q\mu z) \pm \frac{if'}{4} \right)^2 - iq\mu - \lambda_l^2 \right) \tilde{y}_1 = 0. \quad (21.53)$$

The second component \tilde{y}_2 obeys the same equation with $\mu \mapsto -\mu$.

At $T = 0$,

$$f = 3z^2(z - z_0)(z - \bar{z}_0), \quad z_0 = \frac{1}{3}(4 + i\sqrt{2}). \quad (21.54)$$

The solution of this fermion system at zero magnetic field and zero temperature $T = 0$ has been found in [24]. To solve (21.53), we use the mapping to a zero magnetic field system (21.29). The combination $\mu_q \equiv \mu q$ at non-zero h maps to $\mu_{q,\text{eff}} \equiv \mu_{\text{eff}} q_{\text{eff}}$ at zero h as follows:

$$\mu_q \mapsto q \sqrt{1 - \frac{H^2}{Q^2 + H^2}} \cdot g_F \sqrt{Q^2 + H^2} = \sqrt{3} q g_F \sqrt{1 - \frac{H^2}{3}} = \mu_{q,\text{eff}} \quad (21.55)$$

where at $T = 0$ we used $Q^2 + H^2 = 3$. We solve (21.53) for zero modes, i.e. $\omega = 0$, and at the Fermi surface $\lambda = k$, and implement (21.55).

Near the horizon ($z = 0$, $f = 6z^2$), we have

$$6z^2 \tilde{y}_{1;2}'' + 12z \tilde{y}_{1;2}' + \left(\frac{3}{2} + \frac{(\mu_{q,\text{eff}})^2}{6} - k_F^2 \right) \tilde{y}_{1;2} = 0, \quad (21.56)$$

which gives the following behavior:

$$\tilde{y}_{1;2} \sim z^{-\frac{1}{2} \pm \nu k}, \quad (21.57)$$

with the scaling exponent ν following from (21.32):

$$\nu = \frac{1}{6} \sqrt{6k^2 - (\mu_{q,\text{eff}})^2}, \quad (21.58)$$

at the momentum k . Using Maple, we find the zero mode solution of (21.53) with a regular behavior $z^{-\frac{1}{2} + \nu}$ at the horizon [20, 24]:

$$\begin{aligned} \tilde{y}_1^{(0)} &= N_1 (z - 1)^{\frac{3}{2}} z^{-\frac{1}{2} + \nu} (z - \bar{z}_0)^{-\frac{1}{2} - \nu} \left(\frac{z - z_0}{z - \bar{z}_0} \right)^{\frac{1}{4}(-1 - \sqrt{2}\mu_{q,\text{eff}}/z_0)} \\ &\times {}_2F_1 \left(\frac{1}{2} + \nu - \frac{\sqrt{2}}{3} \mu_{q,\text{eff}}, \nu + i \frac{\mu_{q,\text{eff}}}{6}, 1 + 2\nu, \frac{2i\sqrt{2}z}{3z_0(z - \bar{z}_0)} \right), \end{aligned} \quad (21.59)$$

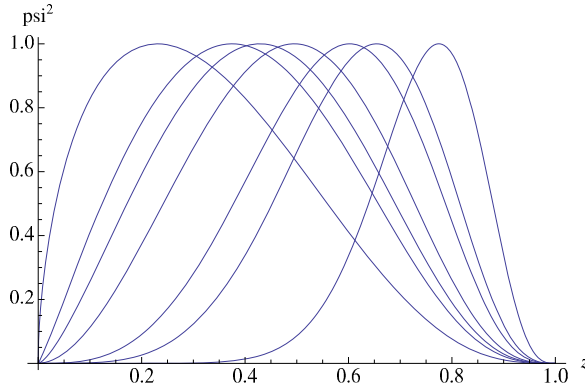


Fig. 21.5 Density of the zero mode $\psi^{0\dagger}\psi^0$ vs. the radial coordinate z (the horizon is at $z = 0$ and the boundary is at $z = 1$) for different values of the magnetic field h for the first (with the largest root for k_F) Fermi surface. We set $g_F = 1$ ($h \rightarrow H$) and $q = \frac{15}{\sqrt{3}}$ ($\mu_{q,\text{eff}} \rightarrow 15\sqrt{1 - \frac{H^2}{3}}$). From right to left the values of the magnetic field are $H = \{0, 1.40, 1.50, 1.60, 1.63, 1.65, 1.68\}$. The amplitudes of the curves are normalized to unity. At weak magnetic fields, the wave function is supported away from the horizon while at strong fields it is supported near the horizon

and

$$\tilde{y}_2^{(0)} = N_2(z - 1)^{\frac{3}{2}}z^{-\frac{1}{2}+\nu}(z - \bar{z}_0)^{-\frac{1}{2}-\nu}\left(\frac{z - z_0}{z - \bar{z}_0}\right)^{\frac{1}{4}(-1+\sqrt{2}\mu_{q,\text{eff}}/z_0)} \times {}_2F_1\left(\frac{1}{2} + \nu + \frac{\sqrt{2}}{3}\mu_{q,\text{eff}}, \nu - i\frac{\mu_{q,\text{eff}}}{6}, 1 + 2\nu, \frac{2i\sqrt{2}z}{3z_0(z - \bar{z}_0)}\right), \quad (21.60)$$

where ${}_2F_1$ is the hypergeometric function and N_1, N_2 are normalization factors. Since normalization factors are constants, we find their relative weight by substituting solutions given in (21.59) back into the first order differential equations at $z \sim 0$,

$$\frac{N_1}{N_2} = -\frac{6i\nu + \mu_{q,\text{eff}}}{\sqrt{6}k}\left(\frac{z_0}{\bar{z}_0}\right)^{\mu_{q,\text{eff}}/\sqrt{2}z_0}. \quad (21.61)$$

The same relations are obtained when calculations are done for any z . The second solution $\tilde{\eta}_{1;2}^{(0)}$, with behavior $z^{-\frac{1}{2}-\nu}$ at the horizon, is obtained by replacing $\nu \rightarrow -\nu$ in (21.59).

To get insight into the zero-mode solution (21.59), we plot the radial profile for the density function $\psi^{(0)\dagger}\psi^{(0)}$ for different magnetic fields in Fig. 21.5. The momentum chosen is the Fermi momentum of the first Fermi surface (see the next section). The curves are normalized to have the same maxima. Magnetic field is increased from right to left. At small magnetic field, the zero modes are supported away from the horizon, while at large magnetic field, the zero modes are supported near the horizon. This means that at large magnetic field the influence of the black hole to the Fermi level structure becomes more important.

21.5.2 Magnetic Effects on the Fermi Momentum and Fermi Velocity

In the presence of a magnetic field there is only a true pole in the Green's function whenever the Landau level crosses the Fermi energy [25, 26]

$$2l|qh| = k_F^2. \quad (21.62)$$

As shown in Fig. 21.2, whenever the equation (21.62) is satisfied the spectral function $A(\omega)$ has a (sharp) peak. This is not surprising since quasiparticles can be easily excited from the Fermi surface. From (21.62), the spectral function $A(\omega)$ and the density of states on the Fermi surface $D(\omega)$ are periodic in $\frac{1}{h}$ with the period

$$\Delta\left(\frac{1}{h}\right) = \frac{2\pi q}{A_F}, \quad (21.63)$$

where $A_F = \pi k_F^2$ is the area of the Fermi surface [25, 26]. This is a manifestation of the de Haas-van Alphen quantum oscillations. At $T = 0$, the electronic properties of metals depend on the density of states on the Fermi surface. Therefore, an oscillatory behavior as a function of magnetic field should appear in any quantity that depends on the density of states on the Fermi energy. Magnetic susceptibility [25, 26] and magnetization together with the superconducting gap [29] have been shown to exhibit quantum oscillations. Every Landau level contributes an oscillating term and the period of the l th level oscillation is determined by the value of the magnetic field h that satisfies (21.62) for the given value of k_F . Quantum oscillations (and the quantum Hall effect which we consider later in the paper) are examples of phenomena in which Landau level physics reveals the presence of the Fermi surface. The superconducting gap found in the quark matter in magnetic fields [29] is another evidence for the existence of the (highly degenerate) Fermi surface and the corresponding Fermi momentum.

Generally, a Fermi surface controls the occupation of energy levels in the system: the energy levels below the Fermi surface are filled and those above are empty (or non-existent). Here, however, the association to the Fermi momentum can be obscured by the fact that the fermions form highly degenerate Landau levels. Thus, in two dimensions, in the presence of the magnetic field the corresponding effective Fermi surface is given by a single point in the phase space, that is determined by n_F , the Landau index of the highest occupied level, i.e., the highest Landau level below the chemical potential.² Increasing the magnetic field, Landau levels 'move up' in the phase space leaving only the lower levels occupied, so that the effective Fermi momentum scales roughly (excluding interactions) as a square root of the magnetic field, $k_F \sim \sqrt{n_F} \sim k_F^{\max} \sqrt{1 - h/h_{\max}}$. High magnetic fields drive the effective density of the charge carriers down, approaching the limit when the Fermi momentum coincides with the lowest Landau level.

²We would like to thank Igor Shovkovy for clarifying the issue with the Fermi momentum in the presence of the magnetic field.

Many phenomena observed in the paper can thus be qualitatively explained by Landau quantization. As discussed before, the notion of the Fermi momentum is lost at very high magnetic fields. In what follows, the quantitative Fermi level structure at zero temperature, described by k_F and v_F values, is obtained as a function of the magnetic field using the solution of the Dirac equation given by (21.59), (21.60). As in [12], we neglect first the discrete nature of the Fermi momentum and velocity in order to obtain general understanding. Upon taking the quantization into account, the smooth curves become combinations of step functions following the same trend as the smooth curves (without quantization). While usually the grand canonical ensemble is used, where the fixed chemical potential controls the occupation of the Landau levels [30], in our setup, the Fermi momentum is allowed to change as the magnetic field is varied, while we keep track of the IR conformal dimension ν .

The Fermi momentum is defined by the matching between IR and UV physics [8], therefore it is enough to know the solution at $\omega = 0$, where the matching is performed. To obtain the Fermi momentum, we require that the zero mode solution is regular at the horizon ($\psi^{(0)} \sim z^{-\frac{1}{2}+\nu}$) and normalizable at the boundary. At the boundary $z \sim 1$, the wave function behaves as

$$a(1-z)^{\frac{3}{2}-m} \begin{pmatrix} 1 \\ 0 \end{pmatrix} + b(1-z)^{\frac{3}{2}+m} \begin{pmatrix} 0 \\ 1 \end{pmatrix}. \tag{21.64}$$

To require it to be normalizable is to set the first term $a = 0$; the wave function at $z \sim 1$ is then

$$\psi^{(0)} \sim (1-z)^{\frac{3}{2}+m} \begin{pmatrix} 0 \\ 1 \end{pmatrix}. \tag{21.65}$$

Equation (21.65) leads to the condition $\lim_{z \rightarrow 1} (z-1)^{-3/2} (\tilde{y}_2^{(0)} + i\tilde{y}_1^{(0)}) = 0$, which, together with (21.59), gives the following equation for the Fermi momentum as function of the magnetic field [20, 24]

$$\frac{{}_2F_1(1+\nu + \frac{i\mu_{q,\text{eff}}}{6}, \frac{1}{2} + \nu - \frac{\sqrt{2}\mu_{q,\text{eff}}}{3}, 1+2\nu, \frac{2}{3}(1-i\sqrt{2}))}{{}_2F_1(\nu + \frac{i\mu_{q,\text{eff}}}{6}, \frac{1}{2} + \nu - \frac{\sqrt{2}\mu_{q,\text{eff}}}{3}, 1+2\nu, \frac{2}{3}(1-i\sqrt{2}))} = \frac{6\nu - i\mu_{q,\text{eff}}}{k_F(-2i + \sqrt{2})}, \tag{21.66}$$

with $\nu \equiv \nu_{k_F}$ given by (21.58). Using Mathematica to evaluate the hypergeometric functions, we numerically solve the equation for the Fermi surface, which gives effective momentum as if it were continuous, i.e. when quantization is neglected. The solutions of (21.66) are given in Fig. 21.6. There are multiple Fermi surfaces for a given magnetic field h . Here and in all other plots we choose $g_F = 1$, therefore $h \rightarrow H$, and $q = \frac{15}{\sqrt{3}}$. In Fig. 21.6, positive and negative k_F correspond to the Fermi surfaces in the Green's functions G_1 and G_2 . The relation between two components is $G_2(\omega, k) = G_1(\omega, -k)$ [7], therefore Fig. 21.6 is not symmetric with respect to the x-axis. Effective momenta terminate at the dashed line $\nu_{k_F} = 0$. Taking into account Landau quantization of $k_F \rightarrow \sqrt{2|qh|l}$ with $l = 1, 2, \dots$, the plot consists of stepwise functions tracing the existing curves (we depict only positive k_F). Indeed

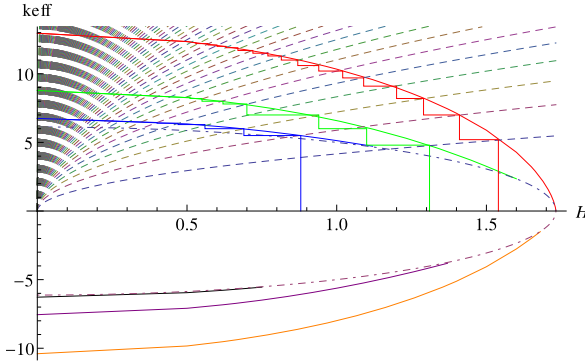
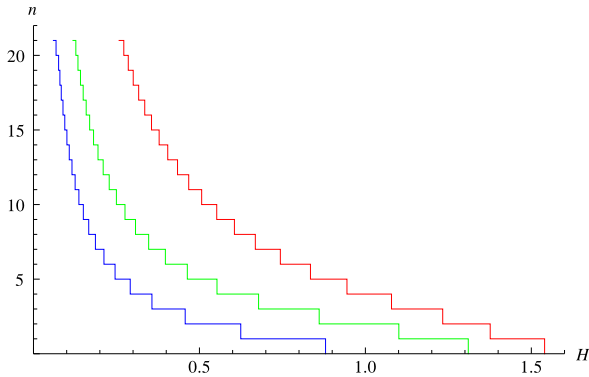


Fig. 21.6 Effective momentum k_{eff} vs. the magnetic field $h \rightarrow H$ (we set $g_F = 1$, $q = \frac{15}{\sqrt{3}}$). As we increase magnetic field the Fermi surface shrinks. *Smooth solid curves* represent situation as if momentum is a continuous parameter (for convenience), *stepwise solid functions* are the real Fermi momenta which are discretized due to the Landau level quantization: $k_F \rightarrow \sqrt{2|qh|l}$ with $l = 1, 2, \dots$ where $\sqrt{2|qh|l}$ are Landau levels given by *dotted lines* (only positive discrete k_F are shown). At a given h there are multiple Fermi surfaces. From right to left are the first, second etc. Fermi surfaces. The *dashed-dotted line* is $v_{k_F} = 0$ where k_F is terminated. Positive and negative k_{eff} correspond to Fermi surfaces in two components of the Green's function

Fig. 21.7 Landau level numbers n corresponding to the quantized Fermi momenta vs. the magnetic field $h \rightarrow H$ for the three Fermi surfaces with positive k_F . We set $g_F = 1$, $q = \frac{15}{\sqrt{3}}$. From right to left are the first, second and third Fermi surfaces



Landau quantization can be also seen from the dispersion relation at Fig. 21.3, where only discrete values of effective momentum are allowed and the Fermi surface has been chopped up as a result of it Fig. 21.3(B).

Our findings agree with the results for the (largest) Fermi momentum in a three-dimensional magnetic system considered in [31], compare the stepwise dependence $k_F(h)$ with Fig. 21.5 in [31].

In Fig. 21.7, the Landau level index l is obtained from $k_F(h) = \sqrt{2|qh|l}$ where $k_F(h)$ is a numerical solution of (21.66). Only those Landau levels which are below the Fermi surface are filled. In Fig. 21.6, as we decrease magnetic field first nothing happens until the next Landau level crosses the Fermi surface which corresponds to a jump up to the next step. Therefore, at strong magnetic fields, fewer states contribute

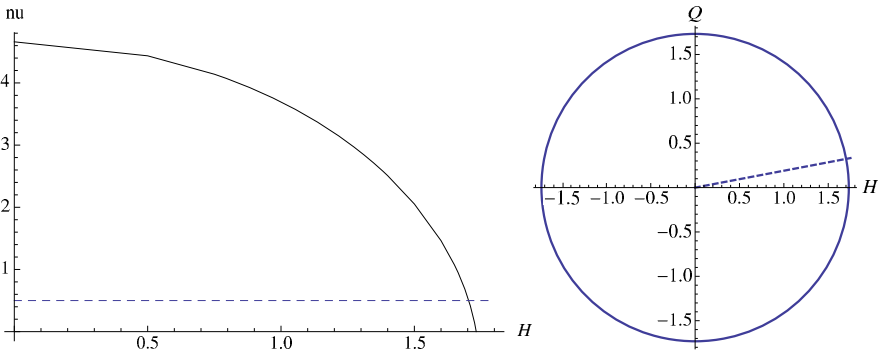


Fig. 21.8 *Left panel.* The IR conformal dimension $\nu \equiv \nu_{k_F}$ calculated at the Fermi momentum vs. the magnetic field $h \rightarrow H$ (we set $g_F=1, q = \frac{15}{\sqrt{3}}$). Calculations are done for the first Fermi surface. *Dashed line* is for $\nu = \frac{1}{2}$ (at $H_c = 1.70$), which is the border between the Fermi liquids $\nu > \frac{1}{2}$ and non-Fermi liquids $\nu < \frac{1}{2}$. *Right panel.* Phase diagram in terms of the chemical potential and the magnetic field $\mu^2 + h^2 = 3$ (in dimensionless variables $h = g_F H, \mu = g_F Q$; we set $g_F = 1$). Fermi liquids are above the *dashed line* ($H < H_c$) and non-Fermi liquids are below the *dashed line* ($H > H_c$)

to transport properties and the lowest Landau level becomes more important (see the next section). At weak magnetic fields, the sum over many Landau levels has to be taken, ending with the continuous limit as $h \rightarrow 0$, when quantization can be ignored.

In Fig. 21.8, we show the IR conformal dimension as a function of the magnetic field. We have used the numerical solution for k_F . Fermi liquid regime takes place at magnetic fields $h < h_c$, while non-Fermi liquids exist in a narrow band at $h_c < h < h'_c$, and at h'_c the system becomes near-conformal.

In this figure we observe the pathway of the possible phase transition exhibited by the Fermi surface (ignoring Landau quantization): it can vanish at the line $\nu_{k_F} = 0$, undergoing a crossover to the conformal regime, or cross the line $\nu_{k_F} = 1/2$ and go through a non-Fermi liquid regime, and subsequently cross to the conformal phase. Note that the primary Fermi surface with the highest k_F and ν_{k_F} seems to directly cross over to conformality, while the other Fermi surfaces first exhibit a “strange metal” phase transition. Therefore, all the Fermi momenta with $\nu_{k_F} > 0$ contribute to the transport coefficients of the theory. In particular, at high magnetic fields when for the first (largest) Fermi surface $k_F^{(1)}$ is nonzero but small, the lowest Landau level $n = 0$ becomes increasingly important contributing to the transport with half degeneracy factor as compared to the higher Landau levels.

In Fig. 21.9, we plot the Fermi momentum k_F as a function of the magnetic field for the first Fermi surface (the largest root of (21.66)). Quantization is neglected here. At the left panel, the relatively small region between the dashed lines corresponds to non-Fermi liquids $0 < \nu < \frac{1}{2}$. At large magnetic field, the physics of the Fermi surface is captured by the near horizon region (see also Fig. 21.5) which is $AdS_2 \times R^2$. At the maximum magnetic field, $H_{\max} = \sqrt{3} \approx 1.73$, when the black hole becomes pure magnetically charged, the Fermi momentum vanishes when it

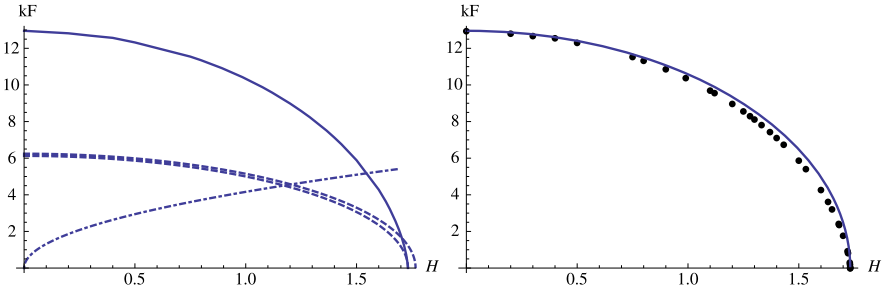


Fig. 21.9 Fermi momentum k_F vs. the magnetic field $h \rightarrow H$ (we set $g_F = 1, q = \frac{15}{\sqrt{3}}$) for the first Fermi surface. *Left panel.* The *inner* (closer to x-axis) *dashed line* is $v_{k_F} = 0$ and the *outer dashed line* is $v_{k_F} = \frac{1}{2}$, the region between these lines corresponds to non-Fermi liquids $0 < v_{k_F} < \frac{1}{2}$. The *dashed-dotted line* is for the first Landau level $k_1 = \sqrt{2qH}$. The first Fermi surface hits the *border-line* between a Fermi and non-Fermi liquids $v = \frac{1}{2}$ at $H_c \approx 1.70$, and it vanishes at $H_{\max} = \sqrt{3} = 1.73$. *Right panel.* *Circles* are the data points for the Fermi momentum calculated analytically, *solid line* is a fit function $k_F^{\max} \sqrt{1 - \frac{H^2}{3}}$ with $k_F^{\max} = 12.96$

crosses the line $v_{k_F} = 0$. This only happens for the first Fermi surface. For the higher Fermi surfaces the Fermi momenta terminate at the line $v_{k_F} = 0$, Fig. 21.6. Note the Fermi momentum for the first Fermi surface can be almost fully described by a function $k_F = k_F^{\max} \sqrt{1 - \frac{H^2}{3}}$. It is tempting to view the behavior $k_F \sim \sqrt{H_{\max} - H}$ as a phase transition in the system although it strictly follows from the linear scaling for $H = 0$ by using the mapping (21.29). (Note that also $\mu = g_F Q = g_F \sqrt{3 - H^2}$.) Taking into account the discretization of k_F , the plot will consist of an array of step functions tracing the existing curve. Our findings agree with the results for the Fermi momentum in a three dimensional magnetic system considered in [31], compare with Fig. 21.5 there.

The Fermi velocity given in (21.27) is defined by the UV physics; therefore solutions at non-zero ω are required. The Fermi velocity is extracted from matching two solutions in the inner and outer regions at the horizon. The Fermi velocity as function of the magnetic field for $v > \frac{1}{2}$ is [20, 24]

$$v_F = \frac{1}{h_1} \left(\int_0^1 dz \sqrt{g/g_{tt}} \psi^{(0)\dagger} \psi^{(0)} \right)^{-1} \lim_{z \rightarrow 1} \frac{|\tilde{y}_1^{(0)} + i\tilde{y}_2^{(0)}|^2}{(1-z)^3}, \quad (21.67)$$

$$h_1 = \lim_{z \rightarrow 1} \frac{\tilde{y}_1^{(0)} + i\tilde{y}_2^{(0)}}{\partial_k (y_2^{(0)} + i\tilde{y}_1^{(0)})},$$

where the zero mode wavefunction is taken at k_F (21.59).

We plot the Fermi velocity for several Fermi surfaces in Fig. 21.10. Quantization is neglected here. The Fermi velocity is shown for $v > \frac{1}{2}$. It is interesting that the Fermi velocity vanishes when the IR conformal dimension is $v_{k_F} = \frac{1}{2}$. Formally, it follows from the fact that $v_F \sim (2v - 1)$ [8]. The first Fermi surface is at the

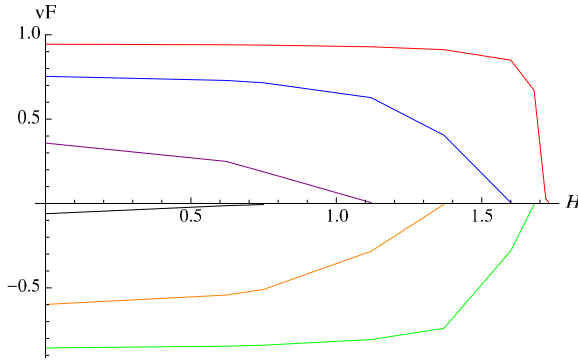


Fig. 21.10 Fermi velocity v_F vs. the magnetic field $h \rightarrow H$ (we set $g_F = 1$, $q = \frac{15}{\sqrt{3}}$) for the regime of Fermi liquids $v \geq \frac{1}{2}$. Fermi velocity vanishes at $v_{k_F} = \frac{1}{2}$ (x -axis). For the first Fermi surface, the *top curve*, Fermi velocity vanishes at $H_c \approx 1.70$. The region $H < H_c$ corresponds to the Fermi liquids and quasiparticle description. The *multiple lines* are for various Fermi surfaces in ascending order, with the first Fermi surface on the right. The Fermi velocity v_F has the same sign as the Fermi momentum k_F . As above, positive and negative v_F correspond to Fermi surfaces in the two components of the Green's function

far right. Positive and negative v_F correspond to the Fermi surfaces in the Green's functions G_1 and G_2 , respectively. The Fermi velocity v_F has the same sign as the Fermi momentum k_F . At small magnetic field values, the Fermi velocity is very weakly dependent on H and it is close to the speed of light; at large magnetic field values, the Fermi velocity rapidly decreases and vanishes (at $H_c = 1.70$ for the first Fermi surface). Geometrically, this means that with increasing magnetic field the zero mode wavefunction is supported near the black hole horizon Fig. 21.5, where the gravitational redshift reduces the local speed of light as compared to the boundary value. It was also observed in [8, 24] at small fermion charge values.

21.6 Hall and Longitudinal Conductivities

In this section, we calculate the contributions to Hall σ_{xy} and the longitudinal σ_{xx} conductivities directly in the boundary theory. This should be contrasted with the standard holographic approach, where calculations are performed in the (bulk) gravity theory and then translated to the boundary field theory using the AdS/CFT dictionary. Specifically, the conductivity tensor has been obtained in [11] by calculating the on-shell renormalized action for the gauge field on the gravity side and using the gauge/gravity duality $A_M \rightarrow j_\mu$ to extract the R charge current-current correlator at the boundary. Here, the Kubo formula involving the current-current correlator is used directly by utilizing the fermion Green's functions extracted from holography in [8]. Therefore, the conductivity is obtained for the charge carriers described by the fermionic operators of the boundary field theory.

The use of the conventional Kubo formula to extract the contribution to the transport due to fermions is validated in that it also follows from a direct AdS/CFT computation of the one-loop correction to the on-shell renormalized AdS action [17]. We study in particular stable quasiparticles with $\nu > \frac{1}{2}$ and at zero temperature. This regime effectively reduces to the clean limit where the imaginary part of the self-energy vanishes $\text{Im } \Sigma \rightarrow 0$. We use the gravity-“dressed” fermion propagator from (21.27) and to make the calculations complete, the “dressed” vertex is necessary, to satisfy the Ward identities. As was argued in [17], the boundary vertex which is obtained from the bulk calculations can be approximated by a constant in the low temperature limit. Also, according to [32, 33], the vertex only contains singularities of the product of the Green’s functions. Therefore, dressing the vertex will not change the dependence of the DC conductivity on the magnetic field [32, 33]. In addition, the zero magnetic field limit of the formulae for conductivity obtained from holography [17] and from direct boundary calculations [20] are identical.

21.6.1 Integer Quantum Hall Effect

Let us start from the “dressed” retarded and advanced fermion propagators [8]: G_R is given by (21.27) and $G_A = G_R^*$. To perform the Matsubara summation we use the spectral representation

$$G(i\omega_n, \mathbf{k}) = \int \frac{d\omega}{2\pi} \frac{A(\omega, \mathbf{k})}{\omega - i\omega_n}, \quad (21.68)$$

with the spectral function defined as $A(\omega, \mathbf{k}) = -\frac{1}{\pi} \text{Im } G_R(\omega, \mathbf{k}) = \frac{1}{2\pi i} (G_R(\omega, \mathbf{k}) - G_A(\omega, \mathbf{k}))$. Generalizing to a non-zero magnetic field and spinor case [30], the spectral function [34] is

$$A(\omega, \mathbf{k}) = \frac{1}{\pi} e^{-\frac{k^2}{|q\hbar|}} \sum_{l=0}^{\infty} (-1)^l (-h_1 v_F) \times \left(\frac{\Sigma_2(\omega, k_F) f(\mathbf{k}) \gamma^0}{(\omega + \varepsilon_F + \Sigma_1(\omega, k_F) - E_l)^2 + \Sigma_2(\omega, k_F)^2} + (E_l \rightarrow -E_l) \right), \quad (21.69)$$

where $\varepsilon_F = v_F k_F$ is the Fermi energy, $E_l = v_F \sqrt{2|q\hbar|l}$ is the energy of the Landau level, $f(\mathbf{k}) = P_- L_l(\frac{2k^2}{|q\hbar|}) - P_+ L_{l-1}(\frac{2k^2}{|q\hbar|})$ with spin projection operators $P_{\pm} = (1 \pm i\gamma^1 \gamma^2)/2$, we take $c = 1$, the generalized Laguerre polynomials are $L_n^\alpha(z)$ and by definition $L_n(z) = L_n^0(z)$, (we omit the vector part $\mathbf{k}\gamma$, it does not contribute to the DC conductivity), all γ ’s are the standard Dirac matrices, h_1 , v_F and k_F are real constants (we keep the same notations for the constants as in [8]). The self-energy $\Sigma \sim \omega^{2\nu k_F}$ contains the real and imaginary parts, $\Sigma = \Sigma_1 + i\Sigma_2$. The imaginary part comes from scattering processes of a fermion in the bulk, e.g. from

pair creation, and from the scattering into the black hole. It is exactly due to inelastic/dissipative processes that we are able to obtain finite values for the transport coefficients, otherwise they are formally infinite.

Using the Kubo formula, the DC electrical conductivity tensor is

$$\sigma_{ij}(\Omega) = \lim_{\Omega \rightarrow 0} \frac{\text{Im} \Pi_{ij}^R}{\Omega + i0^+}, \tag{21.70}$$

where $\Pi_{ij}(i\Omega_m \rightarrow \Omega + i0^+)$ is the retarded current-current correlation function; schematically the current density operator is $j^i(\tau, \mathbf{x}) = q v_F \sum_{\sigma} \bar{\psi}_{\sigma}(\tau, \mathbf{x}) \gamma^i \psi_{\sigma}(\tau, \mathbf{x})$. Neglecting the vertex correction, it is given by

$$\Pi_{ij}(i\Omega_m) = q^2 v_F^2 T \sum_{n=-\infty}^{\infty} \int \frac{d^2k}{(2\pi)^2} \text{tr}(\gamma^i G(i\omega_n, \mathbf{k}) \gamma^j G(i\omega_n + i\Omega_m, \mathbf{k})). \tag{21.71}$$

The sum over the Matsubara frequency is

$$T \sum_n \frac{1}{i\omega_n - \omega_1} \frac{1}{i\omega_n + i\Omega_m - \omega_2} = \frac{n(\omega_1) - n(\omega_2)}{i\Omega_m + \omega_1 - \omega_2}. \tag{21.72}$$

Taking $i\Omega_m \rightarrow \Omega + i0^+$, the polarization operator is now

$$\Pi_{ij}(\Omega) = \frac{d\omega_1}{2\pi} \frac{d\omega_2}{2\pi} \frac{n_{\text{FD}}(\omega_1) - n_{\text{FD}}(\omega_2)}{\Omega + \omega_1 - \omega_2} \int \frac{d^2k}{(2\pi)^2} \text{tr}(\gamma^i A(\omega_1, \mathbf{k}) \gamma^j A(\omega_2, \mathbf{k})), \tag{21.73}$$

where the spectral function $A(\omega, \mathbf{k})$ is given by (21.69) and $n_{\text{FD}}(\omega)$ is the Fermi-Dirac distribution function. Evaluating the traces, we have

$$\begin{aligned} \sigma_{ij} = & -\frac{4q^2 v_F^2 (h_1 v_F)^2 |qh|}{\pi \Omega} \\ & \times \text{Re} \sum_{l,k=0}^{\infty} (-1)^{l+k+1} \{ \delta_{ij} (\delta_{l,k-1} + \delta_{l-1,k}) + i \varepsilon_{ij} \text{sgn}(qh) (\delta_{l,k-1} - \delta_{l-1,k}) \} \\ & \times \int \frac{d\omega_1}{2\pi} \left(\tanh \frac{\omega_1}{2T} - \tanh \frac{\omega_2}{2T} \right) \left(\frac{\Sigma_2(\omega_1)}{(\tilde{\omega}_1 - E_l)^2 + \Sigma_2^2(\omega_1)} + (E_l \rightarrow -E_l) \right) \\ & \times \left(\frac{\Sigma_2(\omega_2)}{(\tilde{\omega}_2 - E_k)^2 + \Sigma_2^2(\omega_2)} + (E_k \rightarrow -E_k) \right), \end{aligned} \tag{21.74}$$

with $\omega_2 = \omega_1 + \Omega$. We have also introduced $\tilde{\omega}_{1,2} \equiv \omega_{1,2} + \varepsilon_F + \Sigma_1(\omega_{1,2})$ with ε_{ij} being the antisymmetric tensor ($\varepsilon_{12} = 1$), and $\Sigma_{1,2}(\omega) \equiv \Sigma_{1,2}(\omega, k_F)$. In the momentum integral, we use the orthogonality condition for the Laguerre polynomials $\int_0^{\infty} dx e^x L_l(x) L_k(x) = \delta_{lk}$.

From (21.74), the term symmetric/antisymmetric with respect to exchange $\omega_1 \leftrightarrow \omega_2$ contributes to the diagonal/off-diagonal component of the conductivity (note the

antisymmetric term $n_{\text{FD}}(\omega_1) - n_{\text{FD}}(\omega_2)$). The longitudinal and Hall DC conductivities ($\mathcal{J}\Omega \rightarrow 0$) are thus

$$\begin{aligned} \sigma_{xx} = & -\frac{2q^2(h_1 v_F)^2 |qh|}{\pi T} \int_{-\infty}^{\infty} \frac{d\omega}{2\pi} \frac{\Sigma_2^2(\omega)}{\cosh^2 \frac{\omega}{2T}} \\ & \times \sum_{l=0}^{\infty} \left(\frac{1}{(\tilde{\omega} - E_l)^2 + \Sigma_2^2(\omega)} + (E_l \rightarrow -E_l) \right) \\ & \times \left(\frac{1}{(\tilde{\omega} - E_{l+1})^2 + \Sigma_2^2(\omega)} + (E_{l+1} \rightarrow -E_{l+1}) \right), \end{aligned} \quad (21.75)$$

$$\sigma_{xy} = -\frac{q^2(h_1 v_F)^2 \text{sgn}(qh)}{\pi} \nu_h, \quad (21.76)$$

$$\nu_h = 2 \int_{-\infty}^{\infty} \frac{d\omega}{2\pi} \tanh \frac{\omega}{2T} \Sigma_2(\omega) \sum_{l=0}^{\infty} \alpha_l \left(\frac{1}{(\tilde{\omega} - E_l)^2 + \Sigma_2^2(\omega)} + (E_l \rightarrow -E_l) \right),$$

where $\tilde{\omega} = \omega + \varepsilon_F + \Sigma_1(\omega)$. The filling factor ν_h is proportional to the density of carriers: $|\nu_h| = \frac{\pi}{|qh|h_1 v_F} n$ (see derivation in [27]). The degeneracy factor of the Landau levels is α_l : $\alpha_0 = 1$ for the lowest Landau level and $\alpha_l = 2$ for $l = 1, 2, \dots$. Substituting the filling factor ν_h back to (21.76), the Hall conductivity can be written as

$$\sigma_{xy} = \frac{\rho}{h}, \quad (21.77)$$

where ρ is the charge density in the boundary theory, and both the charge q and the magnetic field h carry a sign (the prefactor $(-h_1 v_F)$ comes from the normalization choice in the fermion propagator (21.27), (21.69) as given in [8], which can be regarded as a factor contributing to the effective charge and is not important for further considerations). The Hall conductivity (21.77) has been obtained using the AdS/CFT duality for the Lorentz invariant 2 + 1-dimensional boundary field theories in [11]. We recover this formula because in our case the translational invariance is maintained in the x and y directions of the boundary theory.

Low frequencies give the main contribution in the integrand of (21.76). Since the self-energy satisfies $\Sigma_1(\omega) \sim \Sigma_2(\omega) \sim \omega^{2\nu}$ and we consider the regime $\nu > \frac{1}{2}$, we have $\Sigma_1 \sim \Sigma_2 \rightarrow 0$ at $\omega \sim 0$ (self-energy goes to zero faster than the ω term). Therefore, only the simple poles in the upper half-plane $\omega_0 = -\varepsilon_F \pm E_l + \Sigma_1 + i\Sigma_2$ contribute to the conductivity where $\Sigma_1 \sim \Sigma_2 \sim (-\varepsilon_F \pm E_l)^{2\nu}$ are small. The same logic of calculation has been used in [30]. We obtain for the longitudinal and Hall conductivities

$$\sigma_{xx} = \frac{2q^2(h_1 v_F)^2 \Sigma_2}{\pi T} \times \left(\frac{1}{1 + \cosh \frac{\varepsilon_F}{T}} + \sum_{l=1}^{\infty} 4l \frac{1 + \cosh \frac{\varepsilon_F}{T} \cosh \frac{E_l}{T}}{(\cosh \frac{\varepsilon_F}{T} + \cosh \frac{E_l}{T})^2} \right), \quad (21.78)$$

$$\sigma_{xy} = \frac{q^2(h_1 v_F)^2 \text{sgn}(qh)}{\pi} \times 2 \left(\tanh \frac{\varepsilon_F}{2T} + \sum_{l=1}^{\infty} \left(\tanh \frac{\varepsilon_F + E_l}{2T} + \tanh \frac{\varepsilon_F - E_l}{2T} \right) \right), \quad (21.79)$$

where the Fermi energy is $\varepsilon_F = v_F k_F$ and the energy of the Landau level is $E_l = v_F \sqrt{2|qh|l}$. Similar expressions were obtained in [30]. However, in our case the filling of the Landau levels is controlled by the magnetic field h through the field-dependent Fermi energy $v_F(h)k_F(h)$ instead of the chemical potential μ .

At $T = 0$, $\cosh \frac{\omega}{T} \rightarrow \frac{1}{2} e^{\frac{\omega}{T}}$ and $\tanh \frac{\omega}{2T} = 1 - 2n_{\text{FD}}(\omega) \rightarrow \text{sgn}\omega$. Therefore the longitudinal and Hall conductivities are

$$\sigma_{xx} = \frac{2q^2(h_1 v_F)^2 \Sigma_2}{\pi T} \sum_{l=1}^{\infty} l \delta_{\varepsilon_F, E_l} = \frac{2q^2(h_1 v_F)^2 \Sigma_2}{\pi T} \times n \delta_{\varepsilon_F, E_n}, \quad (21.80)$$

$$\begin{aligned} \sigma_{xy} &= \frac{q^2(h_1 v_F)^2 \text{sgn}(qh)}{\pi} 2 \left(1 + 2 \sum_{l=1}^{\infty} \theta(\varepsilon_F - E_l) \right) \\ &= \frac{q^2(h_1 v_F)^2 \text{sgn}(qh)}{\pi} \times 2(1 + 2n) \theta(\varepsilon_F - E_n) \theta(E_{n+1} - \varepsilon_F), \end{aligned} \quad (21.81)$$

where the Landau level index runs $n = 0, 1, \dots$. It can be estimated as $n = [\frac{k_F^2}{2|qh|}]$ when $v_F \neq 0$ ($[\]$ denotes the integer part), with the average spacing between the Landau levels given by the Landau energy $v_F \sqrt{2|qh|}$. Note that $\varepsilon_F \equiv \varepsilon_F(h)$. We can see that (21.81) expresses the integer quantum Hall effect (IQHE). At zero temperature, as we dial the magnetic field, the Hall conductivity jumps from one quantized level to another, forming plateaus given by the filling factor

$$\nu_h = \pm 2(1 + 2n) = \pm 4 \left(n + \frac{1}{2} \right), \quad (21.82)$$

with $n = 0, 1, \dots$ (Compare to the conventional Hall quantization $\nu_h = \pm 4n$, that appears in thick graphene.) Plateaus of the Hall conductivity at $T = 0$ follow from the stepwise behavior of the charge density ρ in (21.77):

$$\rho \sim 4 \left(n + \frac{1}{2} \right) \theta(\varepsilon_F - E_n) \theta(E_{n+1} - \varepsilon_F), \quad (21.83)$$

where n Landau levels are filled and contribute to ρ . The longitudinal conductivity vanishes except precisely at the transition point between the plateaus. In Fig. 21.11, we plot the longitudinal and Hall conductivities at $T = 0$, using only the terms after $\times \text{sign}$ in (21.79). In the Hall conductivity, plateau transition occurs when the Fermi level (in Fig. 21.11) of the first Fermi surface $\varepsilon_F = v_F(h)k_F(h)$ (Fig. 21.9) crosses the Landau level energy as we vary the magnetic field. By decreasing the magnetic field, the plateaus become shorter and increasingly more Landau levels contribute to the Hall conductivity. This happens because of two factors: the Fermi level moves

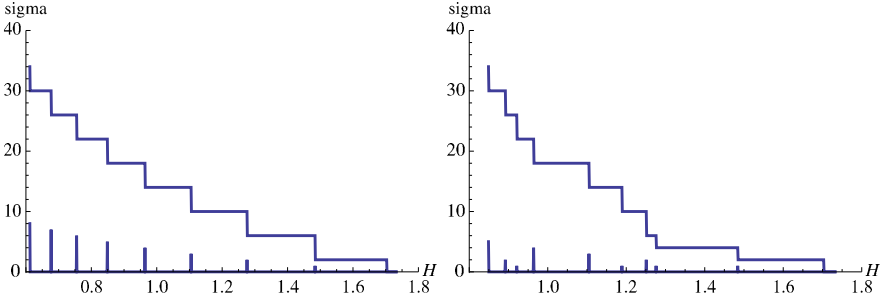


Fig. 21.11 Hall conductivity σ_{xy} and longitudinal conductivity σ_{xx} vs. the magnetic field $h \rightarrow H$ at $T = 0$ (we set $g_F = 1$, $q = \frac{15}{\sqrt{3}}$). *Left panel* is for IQHE. *Right panel* is for FQHE. At strong magnetic fields, the Hall conductivity plateau $\nu_h = 4$ appears together with plateaus $\nu_h = 2$ and $\nu_h = 6$ in FQHE (details are in [27]). Irregular pattern in the length of the plateaus for FQHE is observed in experiments on thin films of graphite at strong magnetic fields [28]

up and the spacing between the Landau levels becomes smaller. This picture does not depend on the Fermi velocity as long as it is nonzero.

21.6.2 Fractional Quantum Hall Effect

In [27], using the holographic description of fermions, we obtained the filling factor at strong magnetic fields

$$\nu_h = \pm 2j, \quad (21.84)$$

where j is the effective Landau level index. Equation (21.84) expresses the fractional quantum Hall effect (FQHE). In the quasiparticle picture, the effective index is integer $j = 0, 1, 2, \dots$, but generally it may be fractional. In particular, the filling factors $\nu = 2/m$ where $m = 1, 2, 3, \dots$ have been proposed by Halperin [35] for the case of bound electron pairs, i.e. $2e$ -charge bosons. Indeed, QED becomes effectively confining in ultraquantum limit at strong magnetic field, and the electron pairing is driven by the Landau level quantization and gives rise to $2e$ bosons. In our holographic description, quasiparticles are valid degrees of freedom only for $\nu > 1/2$, i.e. for weak magnetic field. At strong magnetic field, poles of the fermion propagator should be taken into account in calculation of conductivity. This will probably result in a fractional filling factor. Our pattern for FQHE Fig. 21.11 resembles the one obtained by Kopelevich in Fig. 3 [36] which has been explained using the fractional filling factor of Halperin [35].

The somewhat regular pattern behind the irregular behavior can be understood as a consequence of the appearance of a new energy scale: the average distance between the Fermi levels. For the case of Fig. 21.11, we estimate it to be $\langle \varepsilon_F^{(m)} - \varepsilon_F^{(m+1)} \rangle = 4.9$ with $m = 1, 2$. The authors of [30] explain the FQHE through the

opening of a gap in the quasiparticle spectrum, which acts as an order parameter related to the particle-hole pairing and is enhanced by the magnetic field (magnetic catalysis). Here, the energy gap arises due to the participation of multiple Fermi surfaces.

A pattern for the Hall conductivity that is strikingly similar to Fig. 21.11 arises in the AA and AB-stacked bilayer graphene, which has different transport properties from the monolayer graphene [37], compare with Figs. 2, 5 there. It is remarkable that the bilayer graphene also exhibits the insulating behavior in a certain parameter regime. This agrees with our findings of metal-insulating transition in our system.

21.7 Conclusions

We have studied strongly coupled electron systems in the magnetic field focussing on the Fermi level structure, using the AdS/CFT correspondence. These systems are dual to Dirac fermions placed in the background of the electrically and magnetically charged AdS-Reissner-Nordström black hole. At strong magnetic fields the dual system “lives” near the black hole horizon, which substantially modifies the Fermi level structure. As we dial the magnetic field higher, the system exhibits the non-Fermi liquid behavior and then crosses back to the conformal regime. In our analysis we have concentrated on the Fermi liquid regime and obtained the dependence of the Fermi momentum k_F and Fermi velocity v_F on the magnetic field. Remarkably, k_F exhibits the square root behavior, with v_F staying close to the speed of light in a wide range of magnetic fields, while it rapidly vanishes at a critical magnetic field which is relatively high. Such behavior indicates that the system may have a phase transition.

The magnetic system can be rescaled to a zero-field configuration which is thermodynamically equivalent to the original one. This simple result can actually be seen already at the level of field theory: the additional scale brought about by the magnetic field does not show up in thermodynamic quantities meaning, in particular, that the behavior in the vicinity of quantum critical points is expected to remain largely uninfluenced by the magnetic field, retaining its conformal invariance. In the light of current condensed matter knowledge, this is surprising and might in fact be a good opportunity to test the applicability of the probe limit in the real world: if this behavior is not seen, this suggests that one has to include the backreaction to metric to arrive at a realistic description.

In the field theory frame, we have calculated the DC conductivity using k_F and v_F values extracted from holography. The holographic calculation of conductivity that takes into account the fermions corresponds to the corrections of subleading order in $1/N$ in the field theory and is very involved [17]. As we are not interested in the vertex renormalization due to gravity (it does not change the magnetic field dependence of the conductivity), we have performed our calculations directly in the field theory with AdS gravity-dressed fermion propagators. Instead of controlling the occupancy of the Landau levels by changing the chemical potential (as is usual

in non-holographic setups), we have controlled the filling of the Landau levels by varying the Fermi energy level through the magnetic field. At zero temperature, we have reproduced the integer QHE of the Hall conductivity, which is observed in graphene at moderate magnetic fields. While the findings on equilibrium physics (Landau quantization, magnetic phase transitions and crossovers) are within expectations and indeed corroborate the meaningfulness of the AdS/CFT approach as compared to the well-known facts, the detection of the QHE is somewhat surprising as the spatial boundary effects are ignored in our setup. We plan to address this question in further work.

Interestingly, at large magnetic fields we obtain the correct formula for the filling factor characteristic for FQHE. Moreover our pattern for FQHE resembles the one obtained in [36] which has been explained using the fractional filling factor of Halperin [35]. In the quasiparticle picture, which we have used to calculate Hall conductivity, the filling factor is integer. In our holographic description, quasiparticles are valid degrees of freedom only at weak magnetic field. At strong magnetic field, the system exhibits non-Fermi liquid behavior. In this case, the poles of the fermion propagator should be taken into account to calculate the Hall conductivity. This can probably result in a fractional filling factor. We leave it for future work.

Notably, the AdS-Reissner-Nordström black hole background gives a vanishing Fermi velocity at high magnetic fields. It happens at the point when the IR conformal dimension of the corresponding field theory is $\nu = \frac{1}{2}$, which is the borderline between the Fermi and non-Fermi liquids. Vanishing Fermi velocity was also observed at high enough fermion charge [24]. As in [24], it is explained by the red shift on the gravity side, because at strong magnetic fields the fermion wavefunction is supported near the black hole horizon modifying substantially the Fermi velocity. In our model, vanishing Fermi velocity leads to zero occupancy of the Landau levels by stable quasiparticles that results in vanishing regular Fermi liquid contribution to the Hall conductivity and the longitudinal conductivity. The dominant contribution to both now comes from the non-Fermi liquid and conformal contributions. We associate such change in the behavior of conductivities with a metal-“strange metal” phase transition. Experiments on highly oriented pyrolytic graphite support the existence of a finite “offset” magnetic field h_c at $T = 0$ where the resistivity qualitatively changes its behavior [38–41]. At $T \neq 0$, it has been associated with the metal-semiconducting phase transition [38–41]. It is worthwhile to study the temperature dependence of the conductivity in order to understand this phase transition better.

Acknowledgements The work was supported in part by the Alliance program of the Helmholtz Association, contract HA216/EMMI “Extremes of Density and Temperature: Cosmic Matter in the Laboratory” and by ITP of Goethe University, Frankfurt (E. Gubankova), by a VIDI Innovative Research Incentive Grant (K. Schalm) from the Netherlands Organization for Scientific Research (NWO), by a Spinoza Award (J. Zaanen) from the Netherlands Organization for Scientific Research (NWO) and the Dutch Foundation for Fundamental Research of Matter (FOM). K. Schalm thanks the Galileo Galilei Institute for Theoretical Physics for the hospitality and the INFN for partial support during the completion of this work.

References

1. J. Zaanen, Quantum critical electron systems: the uncharted sign worlds. *Science* **319**, 1205 (2008)
2. P. de Forcrand, Simulating QCD at finite density. PoS **LAT2009**, 010 (2009). [arXiv:1005.0539](#) [hep-lat]
3. S.A. Hartnoll, J. Polchinski, E. Silverstein, D. Tong, Towards strange metallic holography. *J. High Energy Phys.* **1004**, 120 (2010). [arXiv:0912.1061](#) [hep-th]
4. P. Kovtun, D.T. Son, A.O. Starinets, Viscosity in strongly interacting quantum field theories from black hole physics. *Phys. Rev. Lett.* **94**, 111601 (2005). [arXiv:hep-th/0405231](#)
5. S.-S. Lee, A non-Fermi liquid from a charged black hole: a critical Fermi ball. *Phys. Rev. D* **79**, 086006 (2009). [arXiv:0809.3402](#) [hep-th]
6. M. Čubrović, J. Zaanen, K. Schalm, String theory, quantum phase transitions and the emergent Fermi-liquid. *Science* **325**, 439 (2009). [arXiv:0904.1993](#) [hep-th]
7. H. Liu, J. McGreevy, D. Vegh, Non-Fermi liquids from holography. *Phys. Rev. D* **83**, 065029 (2011). [arXiv:0903.2477](#) [hep-th]
8. T. Faulkner, H. Liu, J. McGreevy, D. Vegh, Emergent quantum criticality, Fermi surfaces, and AdS₂. *Phys. Rev. D* **83**, 125002 (2011). [arXiv:0907.2694](#) [hep-th]
9. S.A. Hartnoll, A. Tavanfar, Electron stars for holographic metallic criticality. *Phys. Rev. D* **83**, 046003 (2011). [arXiv:1008.2828](#) [hep-th]
10. S.A. Hartnoll, P.K. Kovtun, M. Mueller, S. Sachdev, Theory of the Nernst effect near quantum phase transitions in condensed matter, and in dyonic black holes. *Phys. Rev. B* **76**, 144502 (2007). [arXiv:0706.3215](#) [hep-th]
11. S.A. Hartnoll, P. Kovtun, Hall conductivity from dyonic black holes. *Phys. Rev. D* **76**, 066001 (2007). [arXiv:0704.1160](#) [hep-th]
12. P. Basu, J.Y. He, A. Mukherjee, H.-H. Shieh, Holographic non-Fermi liquid in a background magnetic field. [arxiv:0908.1436](#) [hep-th]
13. T. Albash, C.V. Johnson, Landau levels, magnetic fields and holographic Fermi liquids. *J. Phys. A, Math. Theor.* **43**, 345404 (2010). [arXiv:1001.3700](#) [hep-th]
14. T. Albash, C.V. Johnson, Holographic aspects of Fermi liquids in a background magnetic field. *J. Phys. A, Math. Theor.* **43**, 345405 (2010). [arXiv:0907.5406](#) [hep-th]
15. T. Albash, C.V. Johnson, A holographic superconductor in an external magnetic field. *J. High Energy Phys.* **0809**, 121 (2008). [arXiv:0804.3466](#) [hep-th]
16. N. Iqbal, H. Liu, M. Mezei, Q. Si, Quantum phase transitions in holographic models of magnetism and superconductors. [arXiv:1003.0010](#) [hep-th]
17. T. Faulkner, N. Iqbal, H. Liu, J. McGreevy, D. Vegh, From black holes to strange metals. [arXiv:1003.1728](#) [hep-th]
18. E. D'Hoker, P. Kraus, *J. High Energy Phys.* **1005**, 083 (2010). [arXiv:1003.1302](#) [hep-th]
19. A. Auerbach, Quantum magnetism approaches to strongly correlated electrons. [arxiv:cond-mat/9801294](#)
20. E. Gubankova, Particle-hole instability in the AdS₄ holography. [arXiv:1006.4789](#) [hep-th]
21. J.L. Davis, P. Kraus, A. Shah, Gravity dual of a quantum hall plateau transition. *J. High Energy Phys.* **0811**, 020 (2008). [arXiv:0809.1876](#) [hep-th]
22. E. Keski-Vakkuri, P. Kraus, Quantum Hall effect in AdS/CFT. *J. High Energy Phys.* **0809**, 130 (2008). [arXiv:0805.4643](#) [hep-th]
23. A.H. MacDonald, Introduction to the physics of the quantum Hall regime. [arXiv:cond-mat/9410047](#)
24. T. Hartman, S.A. Hartnoll, Cooper pairing near charged black holes. [arXiv:1003.1918](#) [hep-th]
25. F. Denef, S.A. Hartnoll, S. Sachdev, Quantum oscillations and black hole ringing. *Phys. Rev. D* **80**, 126016 (2009). [arXiv:0908.1788](#) [hep-th]
26. F. Denef, S.A. Hartnoll, S. Sachdev, Black hole determinants and quasinormal modes. *Class. Quant. Grav.* **27**, 125001 (2010). [arXiv:0908.2657](#) [hep-th]

27. E. Gubankova, J. Brill, M. Cubrovic, K. Schalm, P. Schijven, J. Zaanen, Holographic fermions in external magnetic fields. *Phys. Rev. D* **84**, 106003 (2011). [arXiv:1011.4051](#) [hep-th]
28. Y. Zhang, Z. Jiang, J.P. Small, M.S. Purewal, Y.-W. Tan, M. Fazlollahi, J.D. Chudow, J.A. Jaszczak, H.L. Stormer, P. Kim, Landau level splitting in graphene in high magnetic fields. *Phys. Rev. Lett.* **96**, 136806 (2006). [arXiv:cond-mat/0602649](#)
29. J.L. Noronha, I.A. Shovkovy, Color-flavor locked superconductor in a magnetic field. *Phys. Rev. D* **76**, 105030 (2007). [arXiv:0708.0307](#) [hep-ph]
30. V.P. Gusynin, S.G. Sharapov, Transport of Dirac quasiparticles in graphene: Hall and optical conductivities. *Phys. Rev. B* **73**, 245411 (2006). [arXiv:cond-mat/0512157](#)
31. E.V. Gorbar, V.A. Miransky, I.A. Shovkovy, Dynamics in the normal ground state of dense relativistic matter in a magnetic field. *Phys. Rev. D* **83**, 085003 (2011). [arXiv:1101.4954](#) [hep-th]
32. M.A.V. Basagoiti, Transport coefficients and ladder summation in hot gauge theories. *Phys. Rev. D* **66**, 045005 (2002). [arXiv:hep-ph/0204334](#)
33. J.M.M. Resco, M.A.V. Basagoiti, Color conductivity and ladder summation in hot QCD. *Phys. Rev. D* **63**, 056008 (2001). [arXiv:hep-ph/0009331](#)
34. N. Iqbal, H. Liu, Real-time response in AdS/CFT with application to spinors. *Fortschr. Phys.* **57**, 367 (2009). [arXiv:0903.2596](#) [hep-th]
35. B.I. Halperin, *Helv. Phys. Acta* **56**, 75 (1983)
36. Y. Kopelevich, B. Raquet, M. Goiran, W. Escoffier, R.R. da Silva, J.C. Medina Pantoja, I.A. Luk'yanchuk, A. Sinchenko, P. Monceau, Searching for the fractional quantum Hall effect in graphite. *Phys. Rev. Lett.* **103**, 116802 (2009)
37. Y.-F. Hsu, G.-Y. Guo, Anomalous integer quantum Hall effect in AA-stacked bilayer graphene. *Phys. Rev. B* **82**, 165404 (2010). [arXiv:1008.0748](#) [cond-mat]
38. Y. Kopelevich, V.V. Lemanov, S. Moehlecke, J.H.S. Torrez, Landau level quantization and possible superconducting instabilities in highly oriented pyrolytic graphite. *Fiz. Tverd. Tela* **41**, 2135 (1999) [*Phys. Solid State* **41**, 1959 (1999)]
39. H. Kempa, Y. Kopelevich, F. Mrowka, A. Setzer, J.H.S. Torrez, R. Hoehne, P. Esquinazi, *Solid State Commun.* **115**, 539 (2000)
40. M.S. Sercheli, Y. Kopelevich, R.R. da Silva, J.H.S. Torrez, C. Rettori, *Solid State Commun.* **121**, 579 (2002)
41. Y. Kopelevich, P. Esquinazi, J.H.S. Torres, R.R. da Silva, H. Kempa, F. Mrowka, R. Ocana, Metal-insulator-metal transitions, superconductivity and magnetism in graphite. *Stud. H-Temp. Supercond.* **45**, 59 (2003). [arXiv:cond-mat/0209442](#)

Dissipation-induced first-order decoherence phase transition in a noninteracting fermionic systemM. V. Medvedyeva,¹ M. T. Čubrović,² and S. Kehrein¹¹*Institute for Theoretical Physics, Georg-August-Universität Göttingen, Friedrich-Hund-Platz 1, D-37077 Göttingen, Germany*²*Institute for Theoretical Physics, Universität zu Köln, Zùlpicher Str. 77, D-50937 Köln, Germany*

(Received 21 October 2014; revised manuscript received 3 February 2015; published 13 May 2015)

We consider a quantum wire connected to the leads and subjected to dissipation along its length. The dissipation manifests as tunneling into (out of) the chain from (to) a memoryless environment. The evolution of the system is described by the Lindblad equation. Already infinitesimally small dissipation along the chain induces a quantum phase transition (QPT). This is a decoherence QPT: the reduced density matrix of a subsystem in the nonequilibrium steady state (far from the ends of the chain) can be represented as the tensor product of single-site density matrices. The QPT is identified from the jump of the current and the entropy per site as the dissipation becomes nonzero. We also explore the properties of the boundaries of the chain close to the transition point and observe that the boundaries behave as if they undergo a second-order phase transition as a function of the dissipation strength: the particle-particle correlation functions and the response to the electric field exhibit a power-law divergence. Disorder is known to localize one-dimensional systems, but the coupling to the memoryless environment pushes the system back into the delocalized state even in the presence of disorder. Interestingly, we observe a similar transition in the classical dissipative counterflow model: the current has a jump at the ends of the chain introducing an infinitely small dissipation.

DOI: [10.1103/PhysRevB.91.205416](https://doi.org/10.1103/PhysRevB.91.205416)

PACS number(s): 03.65.Yz, 72.10.-d, 72.15.Rn, 05.30.Fk

I. INTRODUCTION

Coupling to the environment can significantly change the properties of a quantum system. Intuitively, the presence of dissipation leads to a decrease of coherence in the system. It can induce various types of phase transitions [1–9].

The best known example of such a transition is exhibited by the spin-boson model: there is a critical value of the interaction between the two-level system and the bosonic environment, which localizes the system [10]. A more complicated example is the superconductor-metal transition in dissipative nanowires [6,7], which can be modeled as a dissipative XY -spin chain, with a coupling to the bosonic bath at every site of the chain. It was shown both analytically and numerically [6,8,9] that the system experiences a universal second-order phase transition at the critical value of the coupling to the environment.

These are examples in the presence of the bosonic bath. Realistically, especially in condensed matter systems, the bath can be also fermionic [11]. It is possible to describe it in a similar manner as the bosonic bath in the spin-boson model, i.e., using the Feynman-Vernon formalism. However, it is rather complicated to consider more than one or two sites in such a formulation. The problem is often simplified by studying a Lindblad-type equation [12,13]. This corresponds to a memoryless bath. Physically, this means that the quasiparticles in the bath are assumed to have a much smaller dynamical timescale compared to the excitations in the system. Even the memoryless dissipation induces a novel behavior in the quantum systems. For example, dissipation along the system can lead to the algebraic decoherence in strongly interacting systems [14].

Phase transitions have been observed in the presence of a particle or energy flow in various spin chains [15]. For example, the equilibrium phase diagram of the transverse field Ising model has two phases: ordered and disordered; while in the presence of particle flow a new phase appears, which carries a nonzero particle flux [16].

The density matrix of the nonequilibrium steady state (NESS) of a noninteracting fermionic system is associated with an effective Hamiltonian [3]. In this formalism, phase transitions can be observed directly from the spectrum of the effective Hamiltonian, which shows features absent in the closed system. For example, a topological phase transition has been found in a cold atomic system subjected to laser irradiation [3].

Equilibrium phase transitions are characterized by discontinuous derivatives of the free energy [17]: the order of the transition is equal to the order of the first discontinuous derivative. In a nonequilibrium situation the free energy is not a well-defined statistical quantity. The partition function, on the other hand, remains well defined also for a nonequilibrium system, as well as entropy, which is given by the logarithm of the number of microstates [18]. Starting from the partition function or entropy we can define the (nonequilibrium) susceptibilities even though the free energy is ill defined [17]. The susceptibility diverges at the transition point [19]. For the second-order quantum phase transition (QPT) the divergence is physical and detectable, while it is a δ -function-like divergence for a first-order transition. This means that in an infinite system undergoing a first-order phase transition, when the divergence equals the Dirac δ function, we can only observe the step (discontinuity) in susceptibility, while the (infinitely narrow) Dirac δ peak is not measurable.

A. Short overview

In this paper we study the fermionic chain connected to the memoryless bath at every site of the chain, hence we consider the Lindblad equation for noninteracting fermions [5,20–22]. The ends of the chain are connected to noninteracting memoryless leads [22,23]. The difference in chemical potential induces the particle flow in the system. We find a first-order QPT that separates the regimes of coherent and dissipative transport along the chain. The coherent state is characterized by the

constant current along the chain, while in the dissipative state the current induced by the coupling to the reservoirs decays exponentially inside the chain. QPT between the two happens already at an infinitesimally small coupling to the environment, i.e., the critical coupling value is zero. The transition can be understood microscopically from the fact that the density matrix is decomposed into the tensor product of one-site density matrices in the bulk. The phenomenological reason for the transition is breaking of the time-reversal symmetry by the dissipation along the chain. From the thermodynamic point of view, the transition is a consequence of the entropy-per-site jump. The bulk susceptibility also has a jump at the transition. These facts make us conclude that it is a first-order phase transition. We also detect the jump of the steady-state current at the ends of the chain for sufficiently long chains. We can observe this nonequilibrium QPT in the spectrum of the effective Hamiltonian of the NESS: the gap present for zero dissipation along the chain closes in the presence of dissipation. A nonequilibrium QPT in the system coupled to the Markovian bath has also been observed in the XY -spin chain [2,5] and in the XX -spin chain [1].

The phase transitions are normally considered in the thermodynamic limit and the effects of the boundaries (finite-size effects) are neglected (or, in numerical work, systematically eliminated, e.g., by finite-size scaling). When we discuss the transition between the coherent transport through the chain and decoherent state induced by dissipation, we cannot neglect the effects of the boundaries, because the particle current is due to the injection of particles at the ends of the chain. Therefore, we study the particle-particle correlation functions and the electrical susceptibility in the NESS at the ends of the chain and observe power-law divergences as a function of dissipation strength along the chain.

We also consider the workings of dissipation in the presence of disorder. We find that any memoryless dissipation extended along the chain destroys the localization by disorder. This result supports previous studies by the scattering matrix approach [24] and the Landauer-type approach with decoherence [25]. The phase transition to the dissipative state is universal and preserved in the presence of disorder.

II. MODEL AND FORMALISM

We are interested in the properties of the nonequilibrium steady state of a chain of noninteracting fermions linearly coupled to several noninteracting fermionic baths (reservoirs; we use the two terms as synonymous). The full Hamiltonian of such system is

$$H_{\text{full}} = H_{\text{sys}} + \sum_{i,\alpha} H_{i,\alpha,\text{coup}} + \sum_{i,\alpha} H_{i,\alpha,\text{bath}}, \quad (1)$$

where H_{sys} is the tight-binding Hamiltonian of the system:

$$H_{\text{sys}} = \sum_{\{ij\}} t_{ij}(a_i^\dagger a_j + \text{H.c.}) + \sum_i U_i a_i^\dagger a_i, \quad (2)$$

with $\{ij\}$ denoting the links between the sites, t_{ij} is the hopping amplitude between the sites i and j and U_i is an on-site potential. By $H_{i,\alpha,\text{bath}}$ we denote the Hamiltonian of the bath: the index i here stands for the site of the chain, while the index

α denotes different baths coupled to the same site:

$$H_{i,\alpha,\text{bath}} = \sum_k \epsilon_{i,\alpha,k} b_{i,\alpha,k}^\dagger b_{i,\alpha,k}. \quad (3)$$

The annihilation operators in the baths are denoted by symbol $b_{i,\alpha,k}$, while the annihilation operators in the chain are a_i . Finally $H_{i,\alpha,\text{coup}}$ is the coupling between the system and the bath, with the coupling strength $p_{i,\alpha,k}$:

$$H_{i,\alpha,\text{coup}} = \sum_k p_{i,\alpha,k} (b_{i,\alpha,k}^\dagger a_{i,\alpha} + \text{H.c.}). \quad (4)$$

In our model we have exactly two baths at every site which we can denote as “incoming” and “outgoing”, with $\alpha \in \{(i),(o)\}$. The baths are described by the spectral function:

$$J_{i,\alpha}(\omega) = \sum_k |p_{i,\alpha,k}|^2 \delta(\omega - \epsilon_{i,\alpha,k}). \quad (5)$$

For a noninteracting system it has been shown [11,26] that under the assumption of constant spectral density in the reservoirs

$$J_{i,\alpha}(\omega) = v_{i,\alpha}$$

and for the plus/minus infinite chemical potential in the reservoirs the time evolution of the system is described by the Lindblad equation:

$$\begin{aligned} i \frac{d\rho}{d\tau} &= \mathcal{L}\rho, \mathcal{L}\rho \\ &= [H, \rho] + i \sum_{j,i/o} \{2\ell_j^{(i/o)} \rho \ell_j^{\dagger(i/o)} - [\ell_j^{\dagger(i/o)} \ell_j^{(i/o)}, \rho]\}, \end{aligned} \quad (6)$$

where the operator \mathcal{L} is called the Liouvillian and ℓ_j are the Lindblad operators responsible for the coupling to the bath:

$$\ell_j^{(i)} = \sqrt{\Gamma_j^{(i)}} a_j^\dagger, \quad \ell_j^{(o)} = \sqrt{\Gamma_j^{(o)}} a_j, \quad (7)$$

$$\Gamma_j^{(i)} = \pi v_{j,+\infty} \sum_k |p_{i,+\infty,k}|^2, \quad \Gamma_j^{(o)} = \pi v_{j,-\infty} \sum_k |p_{i,-\infty,k}|^2, \quad (8)$$

with $v_{j,\pm\infty}$ being the density of states in reservoirs connected to the site j with plus/minus infinite chemical potential. The infinite chemical potential ensures Markovian dynamics in the bath [27]: in the reservoir at the chemical potential $+\infty$ there are always particles which can hop into the system and in the reservoir at the chemical potential $-\infty$ there is always room for new particles hopping out of the system, therefore such baths are memoryless. The finite bandwidth, finite chemical potential, and finite temperature of the reservoirs would make the evolution equation for the density matrix nonlocal in time [11,26].¹ Let us also note that the coefficients Γ are not necessarily small, they can have any value. The difference from the ordinary derivation [13] is that here both

¹In the above derivation we have not discussed temperature, as it does not matter in the case of infinite chemical potential. When the chemical potential in the reservoirs becomes finite, the temperature appears as an additional parameter.

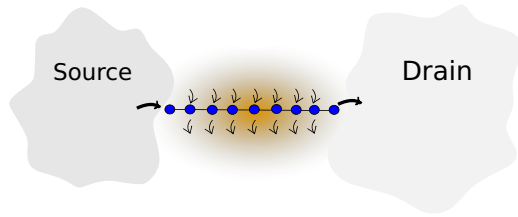


FIG. 1. (Color online) The setup of the problem: one-dimensional chain is connected to the source and the drain as in transport experiments. Every site of the chain is coupled to the environment, which models the dissipation from the leakage of the current due to imperfect insulation. The environment consists of two reservoirs at plus/minus infinite chemical potentials coupled at each site of the chain.

the system and the baths are noninteracting, therefore fewer assumptions are required to get the Lindblad form of the evolution equation.

Let us now apply the Lindblad formalism to our model. Our chain is L sites long and it is coupled to the source and the drain at infinite bias voltage at its ends:

$$\begin{aligned} \ell_1^{(i)} &= \sqrt{\Gamma^{(i)}} a_1^\dagger, & \ell_1^{(o)} &= 0, \\ \ell_L^{(i)} &= 0, & \ell_L^{(o)} &= \sqrt{\Gamma^{(i)}} a_L. \end{aligned}$$

There is also a dissipation along the chain into a finite temperature bath, which is represented by sources $\ell_\mu^{(i)} = \sqrt{d\Gamma_\mu^{(i)}} a_\mu^\dagger$ and drains $\ell_\mu^{(o)} = \sqrt{d\Gamma_\mu^{(o)}} a_\mu$, for $\mu = 2, \dots, L-1$. The $d\Gamma$ values are not infinitesimal: they are typically much smaller than $\Gamma^{(i,o)}$ but can take any value in principle; the notation $d\Gamma$ is just for convenience. Schematically, the dissipative wire setup we study is depicted in Fig. 1. From now on in the text and in the plots the Γ_μ values are measured in the units of the hopping t , which we assume to be constant along the chain (in other words we put $t_{ij} = t = 1$).

A. Solving the Lindblad equation

The solution of the Lindblad equations for noninteracting fermions is notably simplified in the superfermionic representation [21,22], which is based on the doubling of the degrees of freedom as in thermofield theory. Here instead of solving a differential equation for the evolution of the $2^L \times 2^L$ density matrix, the calculations are done with the $2L \times 2L$ matrices. The observables of the NESS are computed directly. What is more, the full-counting statistics of the transport through the ends of the chain can be obtained by introducing the counting field, which yields the generating function of the counting statistics [22,23]. We will present the results for the first cumulant of the generating function, i.e., the current, as well as for the ratio between the second and the first cumulant, which characterizes the noise in the system and is called the Fano factor.

We evaluate the current along the chain by averaging the local current operator over the NESS:

$$\hat{j}_k = -it(a_k^\dagger a_{k+1} - a_{k+1}^\dagger a_k). \quad (9)$$

At the ends of the chain the current and the Fano factor are given by the derivatives of the generating function.

The Liouvillian for noninteracting fermions in the superfermionic representation becomes quadratic after performing the particle-hole transformation [22], as the Liouvillian becomes diagonal in the basis $\{f, f^\ddagger, \tilde{f}, \tilde{f}^\ddagger\}$, see Appendix. The density matrix of the NESS is a vacuum for the operators f and \tilde{f} (see Appendix). As there exists a linear relation between the initial basis $\{a, a^\dagger, \tilde{a}, \tilde{a}^\dagger\}$ and the basis $\{f, f^\ddagger, \tilde{f}, \tilde{f}^\ddagger\}$, the density matrix of the NESS is quadratic:

$$\rho_{\text{NESS}} = \frac{\exp(\mathcal{H}_{mn} a^\dagger \tilde{a}^\dagger) |00\rangle_{a\tilde{a}}}{\langle I | \exp(\mathcal{H}_{mn} a^\dagger \tilde{a}^\dagger) |00\rangle_{a\tilde{a}}}, \quad \mathcal{H}_{jn} = \tilde{\kappa}_{ni}^{-1} \kappa_{ji}, \quad (10)$$

where the matrix κ is connected to the matrix of the eigenvectors P of the transformation which diagonalizes the particle-hole transformed Liouvillian [22] (see Appendix), namely $T = P^{-1}$, $\kappa_{kj} = T_{kj}$ and $\tilde{\kappa}_{kj} = T_{k+L,j}$ for $k, j = 1, \dots, L$. Notice that $i\mathcal{H}$ is a Hermitian matrix as ρ is Hermitian, and $\langle I |$ is the left vacuum, $|I\rangle = \sum_n |nn\rangle_{a\tilde{a}}$ [21], where by n we denote the state in the a basis. Therefore, $i\mathcal{H}$ can be considered as an effective Hamiltonian of the NESS.

III. DISSIPATION-INDUCED PHASE TRANSITION

In this section we first observe the dissipation-induced phase transition in the transport properties at the ends of the chain and in the bulk and then we characterize the transition in the thermodynamic limit. Afterwards we discuss some specific aspects of the transition at the ends of the chain by studying the response to electric field and the particle-particle correlation functions close to the ends and reveal its microscopic nature. Finally, we study the influence of the dissipation on the phenomenon of delocalization in disordered systems.

A. Observation of the transition

We model dissipation along the chain as tunneling to the metallic gate in the absence of good isolation of the one-dimensional chain from the environment. To implement this we couple a source and a sink to every site of the chain [21]. We also allow for disorder in the hybridization strengths $d\Gamma_\mu^{(i/o)}$ to account for different tunneling rates to the environment.

The fermionic chain coupled to the reservoirs only at its ends has a uniform current along its length due to particle conservation. Let us call the state of such a system coherent as the current at its ends depends on both couplings. On the other hand we call the state of the system decoherent when the current through a given end depends only on the coupling of the reservoir at this end.

We only expect to find a phase transition and the associated discontinuities in the thermodynamic limit, i.e., in an infinite system. For that reason we start by looking at a chain long enough that there is no dependence on its length, Fig. 2(b). We see a jump both in the current and in the Fano factor when the dissipation is switched on, Fig. 2(a). Reference [23] provides the large deviation calculation for the current distribution function of the chain coupled to the reservoirs only at its ends. The current distribution is discontinuous as a function of the couplings to the reservoirs and the author suggests that this is the reason of the phase transition also for the system dissipative along its length.

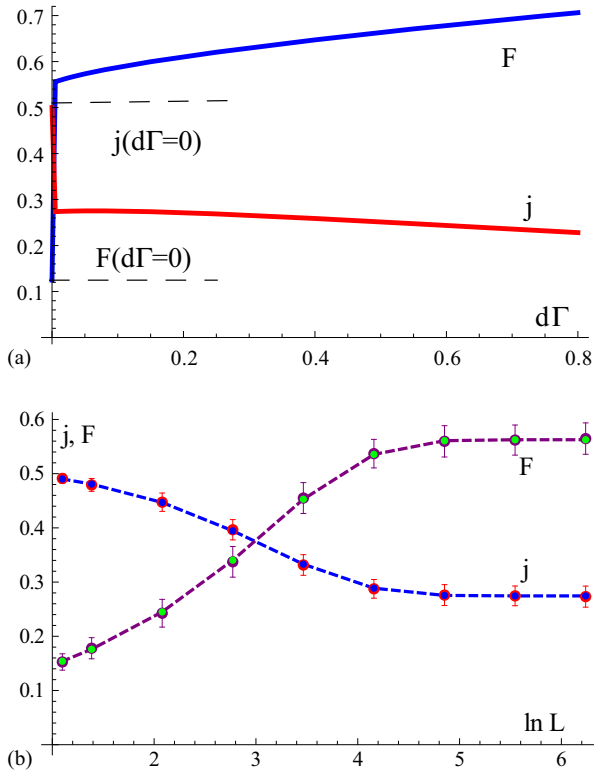


FIG. 2. (Color online) (a) The jump of the current, j , and the Fano factor, F , at infinitesimally small dissipation constant along the chain $d\Gamma = d\Gamma^{(i)} = d\Gamma^{(o)}$ ($\Gamma^{(i)} = \Gamma^{(o)} = 1$). (b) Dependence of the current j and the Fano factor F through the ends of the chain on the length L for random dissipation along the chain taken from the range $d\Gamma^{(i)}, d\Gamma^{(o)} \in (0, 0.04)$ (points with error bars) and for the constant dissipation with the strength $d\Gamma^{(i)} = d\Gamma^{(o)} = 0.02$ (points and the dashed lines). Here and everywhere else in the text and the plots the Γ_μ values are measured in the units of the hopping t .

In order to understand better the nature of the states on both sides of the transition, let us consider the current along the chain. We compute the expectation value of the local current operator (9) in the NESS for every link of the chain. For a nondissipative system it is constant along the chain due to the current conservation. For the dissipative case it decays exponentially inside the system, Fig. 3. One would certainly expect such behavior in the presence of the drains only. But in our setup we have both the source and the drain attached to every site of the chain. Therefore, we conclude that the exponential decrease of the current is connected to the coherence losses due to coupling to the memoryless environment, and not simply to the current leakage into the drains.

If we allow for a random distribution of the dissipation along the chain, the current averaged over disorder configurations decays with the same exponent as the current in the system with uniform dissipation, with the magnitude equal to the mean of the distribution of the disordered couplings, Fig. 3.

With increasing dissipation strength, the current through one end of the chain becomes only weakly dependent on the coupling at the other end of the chain because the coherence of the transport through the chain is lost upon adding the

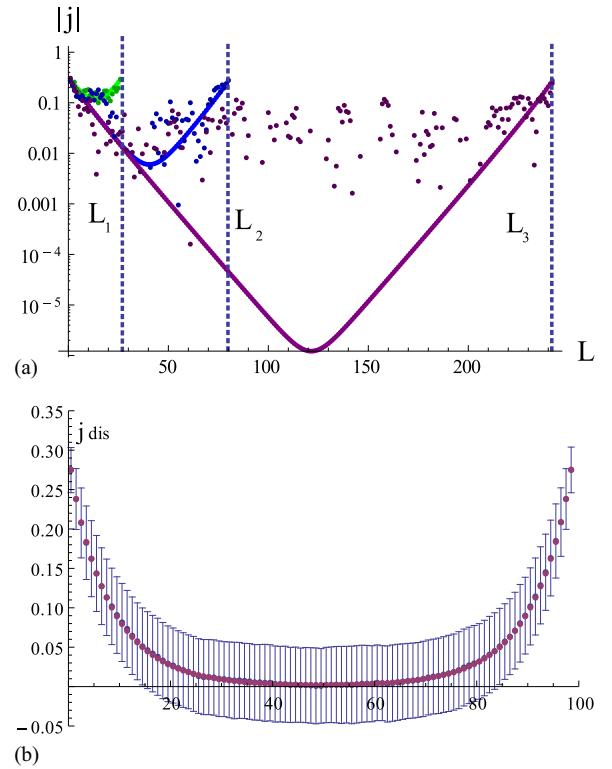


FIG. 3. (Color online) Exponential decay of the current along the chain. (a) Logarithmic scale, different lengths of the system. The currents in the system without randomness in dissipation are represented by the regular sets of points (forming solid lines). Darker, irregularly scattered points represent the current for one realization of the disorder in dissipation along the chain. (b) The current through a dissipative chain after averaging over different disorder realizations. The scale is linear (not logarithmic) to show the standard deviation of the (fluctuating, random) current. Notice that the negative values of the current are physical, because some realization of the (random) couplings $d\Gamma$ can give an overall current flowing in the opposite direction. The couplings at the ends of the chain are $\Gamma^{(i)} = \Gamma^{(o)} = 1$, $d\Gamma = 0.05$. For the average over disorder $d\Gamma_j^{(i)}, d\Gamma_j^{(o)} \in (0, 0.1)$, $j \in (2, L - 1)$.

dissipation along the chain, Fig. 4. Here we make a plot for the constant dissipation rate along the chain since the current averaged over disorder in coupling strengths is the same as in the case of the constant dissipation (see Fig. 3).

Both the presence of the jump in the transport characteristics at the ends of the chain and the coherence/decoherence transition in the current along the chain suggest that any nonzero dissipation along the chain induces the QPT. It is not a van der Waals-type transition, meaning there is no analog of the latent heat, that is, excitation of internal degrees of freedom, but the extra energy is instead exchanged with the bath.

1. Classical analogue

The Lindblad approximation for the driving at the ends of the chain and decoherence along the chain make our quantum model less quantum and more classical. This is exemplified by comparing our results with a classical model introduced

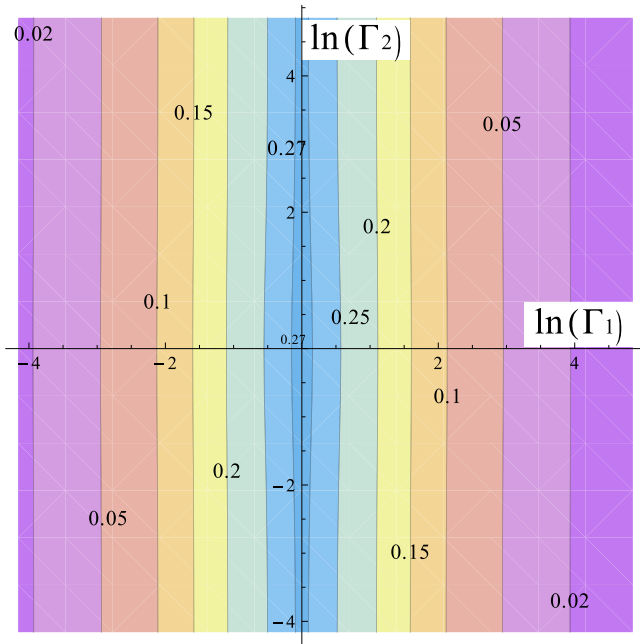


FIG. 4. (Color online) Logarithmic plot of the current flowing from the system into the reservoir at the beginning of the chain (denoted by 1) as a function of the hopping rates at the ends of the chain, in the presence of the constant dissipation along the chain, $d\Gamma^{(i)} = d\Gamma^{(o)} = 0.02$. Increasing the dissipation makes the current through one end independent of the coupling at the other end of the chain. In this plot we denote $\Gamma^{(i)} = \Gamma_1$, $\Gamma^{(o)} = \Gamma_2$.

by Roche, Derrida, and Doucot [28] for studying the classical version of the Landauer picture of a quantum conductor, where we also observe the exponential decay of the current inside the chain as well as the jump of the steady-state current at the ends of the chain upon introducing the dissipation along the chain.

We consider a counterflow model [28]: the system is modeled by an L -site chain, where each of the sites may contain two particles, one right-moving and one left-moving. It is analogous to the quantum scattering problem. Let us call the walls between the sites tunnel barriers. The time is discrete. At each time step the right-moving state on the left of the barrier and the left-moving state on the right of the barrier are transferred to the right-moving state on the right of the barrier and the left-moving state on the left of the barrier, respectively:

$$(0_{r,k-1}, 0_{l,k}) \rightarrow (0_{r,k}, 0_{l,k-1}), \quad (11)$$

$$(1_{r,k-1}, 1_{l,k}) \rightarrow (1_{r,k}, 1_{l,k-1}), \quad (12)$$

$$(0_{r,k-1}, 1_{l,k}) \rightarrow \begin{cases} (0_{r,k}, 1_{l,k-1}) \text{ with prob. } T, \\ (1_{r,k}, 0_{l,k-1}) \text{ with prob. } (1 - T) \end{cases} \quad (13)$$

$$(1_{r,k-1}, 0_{l,k}) \rightarrow \begin{cases} (1_{r,k}, 0_{l,k-1}) \text{ with prob. } T, \\ (0_{r,k}, 1_{l,k-1}) \text{ with prob. } (1 - T), \end{cases} \quad (14)$$

where on the left-hand/right-hand side of the arrow is the state before/after the time step respectively, 0 and 1 denote the state of the system (empty/full), the subscripts r/l stand for right-/left-moving and k stands for the cell number. The first and the last cell are updated at every time step to account for

the contact with the reservoirs:

$$(1_{r,1}, 0_{l,1}) \quad \text{with prob. } \rho_R, \quad (15)$$

$$(0_{r,1}, 0_{l,1}) \quad \text{with prob. } (1 - \rho_R), \quad (16)$$

$$(0_{r,L}, 1_{l,L}) \quad \text{with prob. } \rho_L, \quad (17)$$

$$(1_{r,L}, 1_{l,L}) \quad \text{with prob. } (1 - \rho_L). \quad (18)$$

The configuration space of this process grows exponentially with the the number of sites: it contains 2^L configurations. This makes it complicated to calculate the counting statistics using the transition matrix approach [28]. In general, the described model has a diffusive behavior: the current through the system decreases with increasing system size [28] (this happens because each transmission process is a stochastic process). In our model we obtain pure ballistic behavior by moving all particles in the middle of the chain (which are independent of the dynamics on the first and the last site) as a whole, which is just what ballistic propagation means.

While earlier work [28] considers only the flux of particles at the end of the chain, we introduce the dissipation in the middle of the chain as a classical analog of decoherence (from now on we call it decoherence to emphasize the lack of true quantum-mechanical coherence in the classical model) as a spontaneous appearance/disappearance of right/left moving particles in between two propagation steps. Therefore, our algorithm of time evolution of the dissipative chain is

(i) Initialize the time step:

(a) generate an arbitrary initial state in the first step;

(b) in the subsequent steps: update first the occupation on the first and the last site of the chain according to (15)–(18). Then update the occupation number in the middle, which changes due to decoherence: if both left- and right-moving states at the site k are empty, then with probability $d\Gamma^{(i)}/2$ one of them becomes occupied. If only the left- or right-moving state is empty, then this state becomes full with probability $d\Gamma^{(i)}$. The analogous update is done for hopping out of the chain with the rate $d\Gamma^{(o)}$.

(ii) Move the particles:

(a) the right/left movers on the site from 2 to $(L - 2)/3$ to $L - 1$ from are shifted in the ballistic way (the particle is moved by one site, if the site with the corresponding chirality on its way is empty);

(b) make a move of the states around the barriers according to rules (11)–(14);

(c) shift particles close to the ends if more ballistic motion is possible with respect to the configuration after (11)–(14) comparing to the initial configuration.

(iii) Repeat the steps (i) and (ii).

According to our numerical simulation the average over the time evolution of a single state equals to the average over different initial states evolved for a fixed time, which is long enough to approach the steady state, as we would expect in an ergodic system. We present the long-time averages over time of the evolution of a single state as it is less computationally consuming comparing to the other averaging procedure.

The current through the chain can be determined in two ways: as the difference between the right and left movers at each cell or as the number of the particle transmissions between

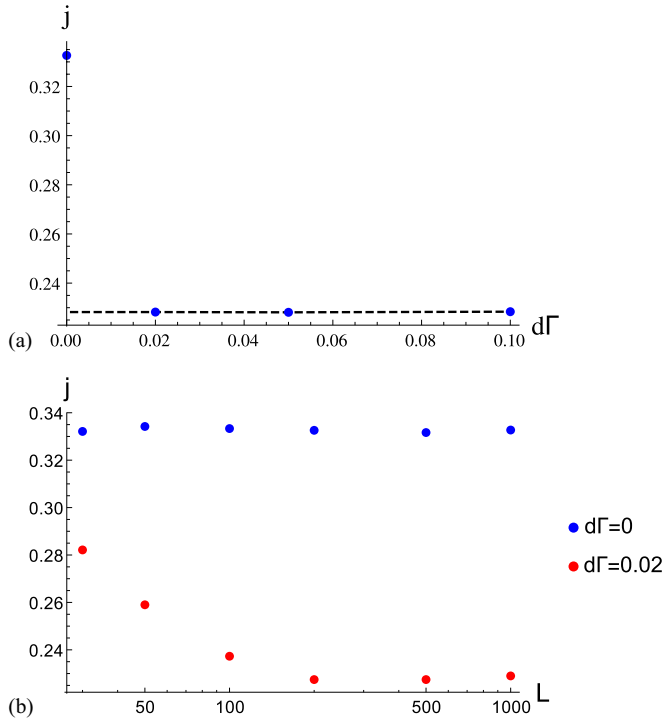


FIG. 5. (Color online) (a) The jump of the current at the end of the chain upon switching on the decoherence along the chain in the classical counterflow model. (b) Dependence of the current through the first site of the chain on the length of the chain. Compare to Fig. 3, where analogous behavior is observed for the quantum chain modeled by the Lindblad equation. $\Gamma_1^{(in)} = \Gamma_2^{(out)} = 0.5$

the neighboring cells. Qualitatively these approaches give the same answer for our decoherent problem.

To compare our numerical simulation with the Lindblad approach we fix $\rho_R = 1$ and $\rho_L = 0$ to model the leads at plus/minus infinite voltage. The time-averaged current decays exponentially from the ends of the chain toward the middle, Fig. 6. The saturation of the exponential decay in the middle happens due to finite time of averaging. The average current

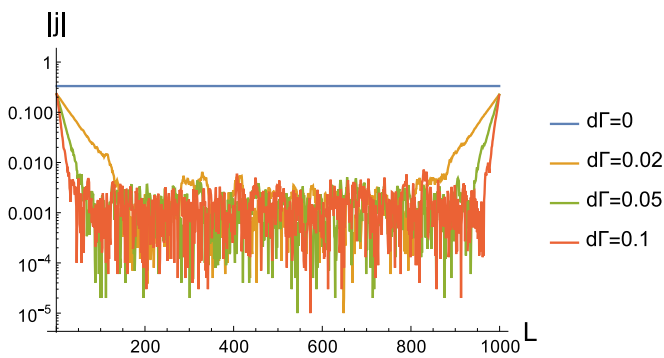


FIG. 6. (Color online) The dependence of the current on the site index for different decoherence rates $d\Gamma$ in logarithmic scale in the classical counterflow model: the exponential decay of the current from the ends toward the middle of the chain is clearly visible, suggesting a similar mechanism of decoherence as in the quantum chain in Fig. 4. $\Gamma_1^{(in)} = \Gamma_2^{(out)} = 0.5$, $t_{max} = 10^5$.

through the end of the chain jumps when decoherence is introduced in the system, Fig. 5. To observe the clear jump the number of time steps should be large enough that the system forgets about its initial configuration, at least about $L/d\Gamma$.

The behavior of the quantum chain is thus qualitatively reproduced by the classical stochastic model. It might therefore seem that the term quantum phase transition we have used for the transition in the quantum chain is a misnomer. This is not the case, since the classical counterflow model is stochastic and thus exhibits fluctuations around the expectation values, i.e., averaged values. The generating function of the counterflow model is thus analogous to the action of a quantum system, and the jump of the suitably defined classical current is formally analogous to the QPT observed earlier. A truly classical system (with no fluctuations) would not show such a phase transition.

B. First-order phase transition in the thermodynamic limit

Phase transitions are normally studied using the thermodynamic quantities and the response functions. In a nonequilibrium situation the partition function and the entropy are well-defined thermodynamic quantities. Here we concentrate on the entropy and the response to the electric field, and eventually explain the microscopic nature of the transition.

1. Entropy

The NESS is Gaussian, Eq. (10), as it can be represented as an exponent of a quadratic operator. Therefore, its effective Hamiltonian is a Hamiltonian of noninteracting fermions. In analogy with equilibrium statistical physics one can connect the entropy of the NESS to the eigenvalues μ_i of the effective Hamiltonian (10) [29]:

$$S = - \sum_i \left(\ln(1 + e^{-\epsilon_i}) + \frac{\epsilon_i}{1 + e^{\epsilon_i}} \right), \quad \mu_i = e^{-\epsilon_i}. \quad (19)$$

The entropy per unit length $S = S/L$ does not depend on the system length for sufficiently long systems and experiences a jump upon turning on the dissipation along the chain, Fig. 7. For a chain without dissipation the specific entropy always depends on the couplings to the reservoirs at the ends of the chain, while for a dissipative system it does not depend on the couplings to the leads in the thermodynamic limit (the contribution from the boundaries is of the order of $1/L$). The specific entropy tends to a value depending only on the ratio of the incoming and outgoing rates along the chain $\gamma = d\Gamma^{(i)}/d\Gamma^{(o)}$:

$$S = \ln(1 + \gamma) - \frac{\gamma}{1 + \gamma} \ln \gamma. \quad (20)$$

This corresponds to the entropy of the single site coupled to only two baths by the Lindblad operators $\sqrt{d\Gamma^{(i)}}a^\dagger$ and $\sqrt{d\Gamma^{(o)}}a$. Indeed, the reduced density matrix of a site in the middle of the chain is the same as for a single site coupled to two baths up to a factor exponentially small in L . The coupling to the rest of the chain is irrelevant. The current in the middle of the chain vanishes, but what is happening is even stronger: the correlation between two neighboring sites vanishes exponentially $\langle c_{i+1}^\dagger c_i \rangle_{\text{NESS}} = O[\exp(-\beta i)]$, where i is the number of the site in the middle of the chain and β is the

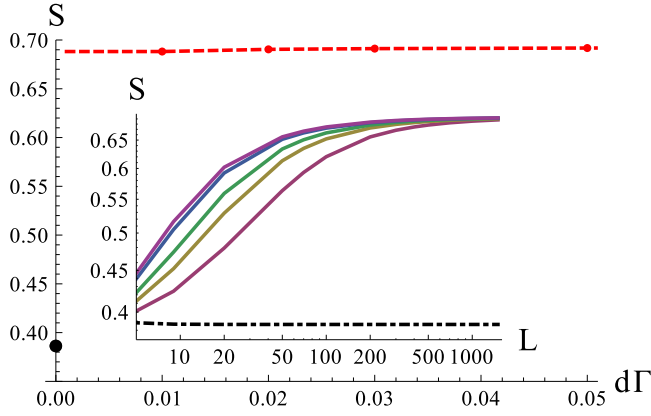


FIG. 7. (Color online) Entropy jump at the transition point as a function of the dissipation strength. The dashed line is in agreement with Eq. (20). Inset: dependence of the entropy on the chain length for different dissipation strengths $d\Gamma = 0.01, 0.02, 0.03, 0.04, 0.05, 0.06$ (from top to bottom solid curve respectively), the dash-dotted line corresponds to the entropy in the absence of the coupling to the environment, the point at $d\Gamma = 0$ at the main plot.

slope of the exponential decay. Therefore, we can write down the reduced density matrix of the middle part of the system neglecting the exponentially small correlations between the sites as a tensor product of the density matrix of one site connected to two baths.

2. Spatial decoupling in the density matrix

Such a spatial decoupling of a density matrix for a completely translationally invariant system (without current injection/removal at the ends) is evident. We can diagonalize the Liouvillian by the Fourier transform. Indeed, in terms of Ref. [22] the matrix M after the Fourier transform obtains the block structure:

$$\mathcal{L} = \sum_k (a_k^\dagger \tilde{a}_k) M_k \begin{pmatrix} a_k \\ \tilde{a}_k^\dagger \end{pmatrix} - i \sum_k (d\Gamma^{(i)} + d\Gamma^{(o)}), \quad (21)$$

$$M_k = \begin{pmatrix} -i\delta\Gamma + 2t \cos k & 2d\Gamma^{(o)} \\ -2d\Gamma^{(i)} & i\delta\Gamma + 2t \cos k \end{pmatrix} \quad (22)$$

with $\delta\Gamma = d\Gamma^{(i)} - d\Gamma^{(o)}$. Each of the matrices M_k can be diagonalized: $M_k = P_k^{-1} D_k P_k$, where D_k is a diagonal matrix and P_k is a matrix of eigenvectors. This transformation determines the basis where the Liouvillian is diagonal:

$$\begin{pmatrix} f_k \\ \tilde{f}_k^\dagger \end{pmatrix} = P \begin{pmatrix} a_k \\ \tilde{a}_k^\dagger \end{pmatrix}, \quad (f_k^\dagger \tilde{f}_k) = (a_k^\dagger \tilde{a}_k) P^{-1}, \quad (23)$$

$$\mathcal{L} = \sum_k (\lambda_k f_k^\dagger f_k - \lambda_k^* \tilde{f}_k^\dagger \tilde{f}_k). \quad (24)$$

Here we assumed that $D_k = \text{diag}(\lambda_k, \lambda_k^*)$ and $\text{Im}\lambda_k < 0$. This structure leads to cancellation of the constant term in the Liouvillian.

The steady state density matrix is determined as the vacuum of operators f_k and \tilde{f}_k . The transformation to the basis of the

a, a^\dagger occupation numbers gives the density matrix:

$$\rho = \sum_k \frac{\exp(\mathcal{H} a_k^\dagger \tilde{a}_k^\dagger) |00\rangle_{a_k \tilde{a}_k}}{a_k \tilde{a}_k \langle I | \exp(\mathcal{H} a_k^\dagger \tilde{a}_k^\dagger) |00\rangle_{a_k \tilde{a}_k}}, \quad (25)$$

$$\mathcal{H} = i \frac{d\Gamma^{(i)}}{d\Gamma^{(o)}}, \quad |I\rangle_{a_k \tilde{a}_k} = |00\rangle + |11\rangle. \quad (26)$$

The effective Hamiltonian \mathcal{H} is a constant, therefore the Fourier transform gives the density matrix which is a tensor product in position space:

$$\rho = \otimes_i \left(\frac{d\Gamma^{(o)}}{d\Gamma^{(o)} + d\Gamma^{(i)}} |00\rangle_{a_i \tilde{a}_i} + \frac{d\Gamma^{(i)}}{d\Gamma^{(o)} + d\Gamma^{(i)}} |11\rangle_{a_i \tilde{a}_i} \right). \quad (27)$$

We can thus conclude that the density matrix is local in space. For the case of disordered leakage along the chain one cannot perform the Fourier transform of the Liouvillian analytically but numerical calculation shows that the density matrix averaged over disorder is again represented by the tensor product of single-site density matrices. For a single realization of the disorder in the couplings along the chain the decomposition is not exact, as shown in Fig. 3(a) for the current through the chain for a single realization of the disorder.

3. Response to the electric field

The response functions are good indicators of the equilibrium phase transitions. Let us consider a response of the current to a constant electric field E applied along the chain. In the tight-binding model it is incorporated as a linearly growing on-site potential: $U_m = mEl_0$, where l_0 is the lattice constant. In most models of the transport one assumes that the current flow is due to an electric field applied along the system. Here we have a current through the chain due to the coupling to the reservoirs. The difference in on-site potential from site to site can be viewed as applying an additional field along the chain. For example, in a cold atom system one can imagine a lattice constructed with varying depths of the potential well. In the decoherent phase, the electric field changes the response function only locally: close to the ends we expect the susceptibility to be different from the middle of the system due to the presence of coherence because of the coupling to the reservoirs. The linear response of the current to the electric field applied along the chain vanishes, and only the quadratic part is left, Fig. 8, inset:

$$j_{\text{NESS}}(E, d\Gamma^{(i)}, d\Gamma^{(o)}; L) - j_{\text{NESS}}(0, d\Gamma^{(i)}, d\Gamma^{(o)}; L) = \sigma(d\Gamma^{(i)}, d\Gamma^{(o)}; L) E^2. \quad (28)$$

Here we also notice that there is a scaling with E : the dependence of the conductivity on length scales with E^2 for the same dissipation rates along the chain $d\Gamma^{(i)}, d\Gamma^{(o)}$. We attribute the quadratic dependence on E to the structure of the NESS. The Ohm's law is an outcome of the linear response theory, which implies that the current is a consequence of the electric field applied to the equilibrium system. In our case the situation is tremendously different—from the physical point of view, the current is already present in the system due to contact with the leads even before applying the electric field along the system. From the viewpoint of the response theory, the response is considered with respect to the nonequilibrium steady state. It

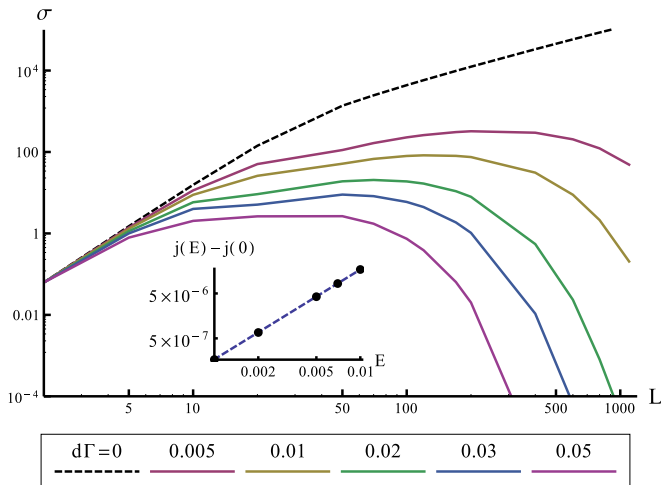


FIG. 8. (Color online) Main plot: the convergence of the nonlinear response to the electric field for long systems in the bulk of the chain. Solid lines correspond to different coupling strength $d\Gamma = 0.005, 0.01, 0.02, 0.03, 0.05$ (from top to bottom) and the dashed line is $d\Gamma = 0$. Inset: quadratic scaling of $j(E) - j(0)$ with the applied electric field (the scale in logarithmic).

is thus possible that the linear part of the response vanishes and only the nonlinear part is present.

The nonlinear response to the electric field vanishes in the bulk of the chain, Fig. 8. The response in the nondissipative system grows infinitely in the thermodynamic limit because of the translational invariance in the bulk. Indeed, when we make the hopping parameters disordered (i.e., make them vary along the chain), the infinite growth of σ is suppressed. Therefore, there is a discontinuity in the value of σ for infinitesimally small $d\Gamma$. It is consistent with the first-order phase transition.

C. Near-boundary effects

The symmetrized particle-particle correlation function:

$$C_i(k) = \langle a_{i+k}^\dagger a_i + a_i^\dagger a_{i+k} \rangle_{\text{NESS}} \quad (29)$$

provides further information about the transition. The correlations at the ends of the system are present and they decay exponentially: $C_i(k) \propto \exp(-k/\xi_i)$, $i \sim 1$ or $i \sim L$, where ξ is a correlation length, Fig. 11. We find the power-law divergence of the correlation length as the function of dissipation at zero dissipation rate along the chain. Inside infinitely long systems the correlations vanish: $\xi_i \rightarrow 0$, $i \sim L/2$, $L \rightarrow \infty$, as all coherence in the system is lost.

The nonlinear conductivity converges to a nonzero value at the boundaries of the chain, Fig. 9, unlike in the bulk of the chain, where it converges to zero. This happens due to some remaining coherence at the ends of the chain. Even more, there is a power-law scaling of the conductivity with dissipation strength, the parameter, which drives the phase transition, inset of Fig. 9.

To further corroborate the finding of the continuous QPT at the edges, let us now consider the spectrum of the effective Hamiltonian, \mathcal{H} . For the translationally invariant dissipative system from Sec. III B 2 the spectrum of the effective Hamiltonian is a δ function $\delta(\epsilon - \text{const} \times d\Gamma^{(i)}/d\Gamma^{(o)})$,

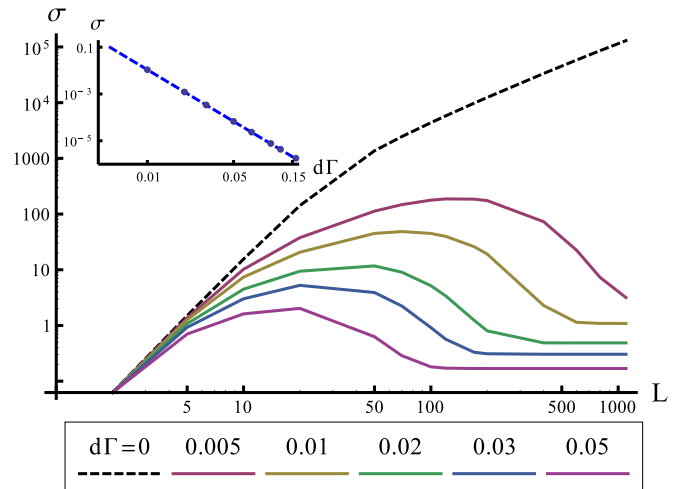


FIG. 9. (Color online) Main plot: the convergence of the nonlinear response to the electric field for long systems at the ends of the chain. Solid lines correspond to different coupling strength $d\Gamma = 0.005, 0.01, 0.02, 0.03, 0.05$ (from top to bottom) and the dashed line is $d\Gamma = 0$. Notice that the nonlinear conductivity at the ends points stays nonzero also in the thermodynamic limit. As in Fig. 8, the conductivity is infinite in the absence of dissipation. Inset: scaling of σ with disorder strength with power-law fit: $\sigma = \alpha d\Gamma^\beta$, $\beta = 3.161 \pm 0.001$.

where the constant comes from the freedom of choice of the effective Hamiltonian, which is connected to the freedom of choice of constants in front of the left and the right vacuum of the Liouvillian. When we take into account the whole chain with the end sites, the spectrum of the effective Hamiltonian is influenced by the presence of the ends of the chain: in the absence of the dissipation along the chain the lowest eigenvalue λ_{\min} of \mathcal{H} is 0, while in the presence of the dissipation λ_{\min} shifts to a nonzero value, Fig. 10. There is a power-law scaling of λ_{\min} with the strength of the dissipation, Fig. 10(b).

D. Disordered dissipative system

Let us consider a disordered system with random on-site potential U_i in the Hamiltonian (2). The values U_i are taken from the uniform distribution with the range $(0, dU)$.

It is known that in one spatial dimension disorder always localizes the conservative system [30]. This is the well-known Anderson localization: it happens because the electron waves always interfere so that the overall wave function is localized on the impurities. Such a system is an insulator as the overlap of the electron wave functions at different positions in the chain is exponentially small. This reasoning suggests the scaling hypothesis, which proposes that the conductivity in a disordered system should decrease exponentially with the system size, when the system is in the localized regime.

However, the presence of dissipation changes this: dissipation delocalizes the disordered system, as the dissipation breaks the interference, which is responsible for the localization. For averaging over disorder we used only 15 disorder configurations, as the uncertainties of the average are already small enough in that case (the error bars in the figure are of the size of the symbols in the plot). This happens because

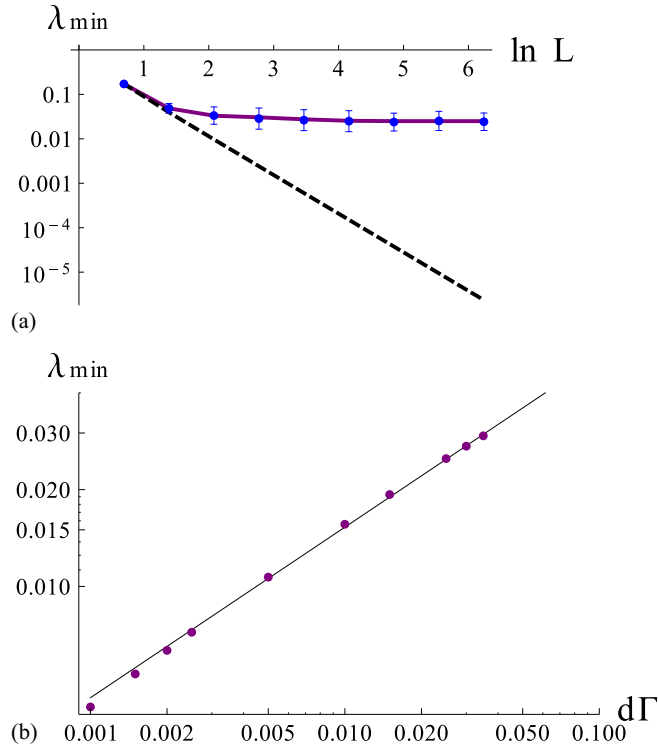


FIG. 10. (Color online) (a) The lowest eigenvalue λ_{\min} of the effective Hamiltonian (10) as a function of the system size for the system without (black dashed line) and with dissipation (blue points: averages over the disorder from the range $(0, d\Gamma)$, purple line: constant dissipation with $d\Gamma/2$, $d\Gamma = 0.025$). (b) The scaling of the lowest eigenvalue with disorder strength, $\lambda_{\min}(d\Gamma)$, and the power-law fit $\lambda_{\min} \propto d\Gamma^\beta$ with $\beta = 0.53 \pm 0.01$. The couplings to the source and the drain are $\Gamma^{(i)} = \Gamma^{(o)} = 1$.

the density matrix of an open quantum system contains the sectors with different particle numbers, hence the values of the current in the NESS can be considered as averaged not only

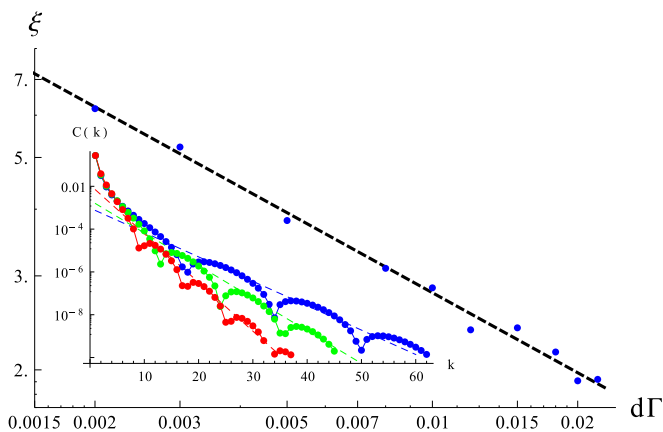


FIG. 11. (Color online) Dependence of the correlation length on the coupling to the environment for $\Gamma^{(i)} = \Gamma^{(o)} = 1$ (dots) and the power-law fit (dashed line). Inset: correlations at one end of the chain as a function of the position for different couplings strengths $d\Gamma = 0.005, 0.01, 0.02$ (from top to bottom: blue, green, red) and exponential fits, which determine the correlation length (dashed lines).

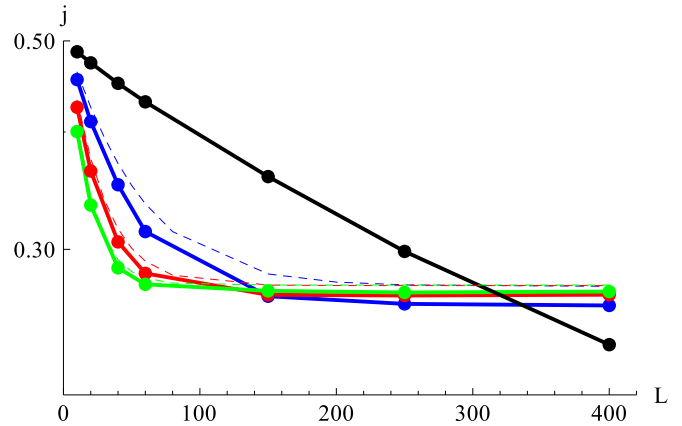


FIG. 12. (Color online) Dependence of the current through a disordered dissipative system on the length of the system for different values of the dissipation along the system, $d\Gamma = 0, 0.02, 0.03, 0.05$ (from top to bottom at small L : black, blue, red, green; solid lines: $dU = 0.3$, dashed lines: $dU = 0$; $\Gamma_1 = \Gamma_2 = 1$). The current through the system is independent of the system length for a sufficiently long system.

over disorder configurations, but also with respect to different particle numbers.

The general phenomenology of the clean system with dissipation is thus preserved also in the disordered system. The current again reaches a finite (though smaller) value in the thermodynamic limit, and the current at one end only weakly depends on the coupling at the other end. An example is seen in Fig. 12, where for simplicity we consider constant couplings to the environment along the chain and average only over the disorder realizations of the on-site potential.

IV. CONCLUSIONS AND DISCUSSION

We have considered the transport properties of a one-dimensional wire with leakage to the environment. In experimental systems, this leakage can happen due to misfabrication and the presence of the tunneling from the wire to a metallic region underneath the wire. We observe a first-order phase transition for infinitely long systems already at infinitesimal dissipation rate along the chain. From the microscopic point of view, this QPT means discontinuous behavior of the density matrix. On the macroscopic level it manifests itself in the jump in the current and the Fano factor. From the thermodynamic point of view we can say that the entropy jumps across the transition. The specific entropy in the dissipative phase is equal to the entropy of a single site coupled to the source and the drain.

Essentially, the phase transition is an anomaly: dissipation breaks the time-reversal invariance [31]. Upon taking the symmetry-breaking parameter (dissipation strength) to zero, we do not recover the result for unbroken symmetry. In the continuum limit it is analogous to the fact that, for example, viscosity effects in a fluid are nonperturbative and the flow undergoes a qualitative change for arbitrarily small nonzero dissipation: the scaling exponents of the correlation functions of the velocities jump at the transition between an ideal and viscous liquid [31]. To understand better the universality of

our finding, we have considered also the classical stochastic counterflow model, which describes a chain with two classes of asymmetric exclusion random walkers, left- and right-moving. In this case, dissipation is modeled by randomly creating or destroying the random walkers with certain probabilities at every (discrete) time step. This model, under suitable assumptions, again shows the same anomaly and the current jumps for arbitrarily small nonzero values of the dissipation. In the counterflow model, the role of quantum fluctuations is taken over by the stochastic fluctuations. In fluid dynamics, the velocity fluctuations make the system effectively quantum. The notion of QPT is thus justified, and the observation of anomaly—breaking of a classical symmetry at the quantum level, i.e., by the loop contributions to the action—becomes natural.

In a different context, the transport theory for dissipative systems has been developed in Refs. [24,32] in the language of the scattering matrices. Our Lindblad-based approach and the scattering approach are different in a few respects. First, let us consider a system without dissipation, coupled to two reservoirs at the ends. The scattering matrix theory describes the case when the wave coming from the reservoir into the system is coherent (just a plane wave), while the Lindblad approach describes the case of incoherent leads—the hopping in the chain happens stochastically. This is also reflected in the transport properties: while for coherent transport the conductivity is proportional to the number of open channels in the system, for the transport induced by incoherent hopping it is not [22]. Now let us move to the dissipative system. In the scattering matrix approach the dissipation is modeled through additional channels, which do not contribute to the transport (for the one-dimensional nondissipative problem the scattering matrix has the format 2×2 , for the incoming and the outgoing channel, while in the dissipative case the scattering matrix has a larger dimension, and only two channels describe the transport along the chain whereas the others describe the scattering in the side channels). The dissipation constructed in this way is coherent, while the Lindblad-like dissipation is incoherent.

It is interesting that the spin system coupled to the bosonic bath at every site experiences a second-order phase transition, and only at finite dissipation strength [6–9]. We do not know if the order of the transition is related to the presence or absence of memory or if it is determined by the statistics of the bath.

The phase transition in the quadratic fermionic systems was studied also in Refs. [2,5]. There, the XY chain coupled to the reservoirs at both ends was considered. The transition manifests itself in the change of behavior of the spin-spin correlation functions and the entanglement entropy, which does not depend on the system size on one side of the transition and grows linearly with the system length on the other side. The authors argue that the transition is of infinite order as all local observables are analytical across the transition. Subsequently the critical behavior has been observed also in the XX -spin chain [1] coupled to the environment at every site of the chain: the spin-spin correlation functions are short ranged in the nondissipative case, whereas they decay as a power law in the presence of the on-site decoherence. The transition we observe is significantly different from the previously studied cases since it is of the first order. This probably happens because the Refs. [2,5] consider the local dissipation (only at the ends

of the chain), while we are interested in the global dissipation. The difference with respect to the transition in Ref. [1] lies in the fact that the NESS is not Gaussian (Gaussianity allows usage of the Wick's theorem for the calculation of higher-order correlation functions in terms of two-point ones, while non-Gaussian states do not allow such expression): in our case the particle-particle correlation functions in the presence of dissipation decay exponentially, while for the XX chain with on-site dephasing there is a power-law decay of correlations.

The current in the steady dissipative state of the system decays exponentially inside the chain, because the coupling to the environment decreases the coherence of the quantum system. For the random dissipation along the chain, we find that the average current decreases inside the system with the same exponent as for the chain with the same dissipation at every site, which equals to the mean of the random coupling. One can try to measure the current along the dissipative chain with a scanning tunneling microscope (STM): if it decreases exponentially uniformly along the chain, then the dissipation model without disorder is a valid model, if the current inside the chain fluctuates, then the dissipation inside of the chain is random. The STM should be in the regime of a very low tunneling rate to the microscope tip, so that the tunneling to the tip does not destroy the dissipative state of the system itself.

We finish with an outlook. The state of the quantum system depends on the dimensionality, disorder, interaction, statistics, and symmetries. The dissipation adds one more axis to the phase diagram. It can lead to new types of behavior, already investigated in the spin-boson model [10], arrays of the dissipative Josephson junctions, and dissipative spin chains [6–9]. In the present paper we have investigated the behavior of the noninteracting fermionic system coupled to the Markovian bath and already have seen interesting quantum critical phenomena upon adding the dissipation along the chain. There are many unanswered questions: will this transition remain first order upon adding memory to the bath; what happens to it in the presence of interactions; do dimensionality and symmetries influence the behavior of the dissipative system, etc.

ACKNOWLEDGMENTS

This work was supported through CRC SFB 1073 (Project B03) of the Deutsche Forschungsgemeinschaft (DFG). We are grateful to Achim Rosch and Fabian Biebl for careful reading of the manuscript and helpful discussions.

APPENDIX: TRANSFORMATION OF THE LIOUVILLIAN TO THE DIAGONAL BASIS

The solution of the Lindblad equation (6) for noninteracting fermions is notably simplified in the super-fermionic representation [21,22]: operators acting from the right on the density matrix are introduced. They are denoted by a tilde. Then the Liouvillian can be written after the particle-hole

transformation $\tilde{a} = b^\dagger, \tilde{a}^\dagger = b$ in the quadratic form:

$$\mathcal{L} = (a^\dagger b^\dagger) \mathcal{M} \begin{pmatrix} a \\ b \end{pmatrix} - i \sum_{\mu} \Gamma_{\mu}^{(o)} - i \sum_{\mu} \Gamma_{\mu}^{(i)}, \quad (\text{A1})$$

where the matrix M can be represented as

$$\begin{aligned} \mathcal{M} = & H\delta_{aa} + H\delta_{bb} + i\Gamma_k^{(i)}\delta_{kk}(-\delta_{aa} + \delta_{bb}) \\ & + i\Gamma_k^{(o)}\delta_{kk}(\delta_{aa} - \delta_{bb}) - 2\Gamma_k^{(i)}\delta_{kk}\delta_{ba} + 2\Gamma_k^{(o)}\delta_{kk}\delta_{ab} \end{aligned} \quad (\text{A2})$$

with H being a tight-binding Hamiltonian of the system, δ_{xy} is the Kronecker symbol, for example δ_{aa} denotes the upper-left L by L part of the matrix \mathcal{M} , δ_{kk} stands for the diagonal of the matrix in the site space.

Due to this specific structure of \mathcal{M} the constant terms in the expression (A3) vanish after introducing a new set of the operators $\{f, f^\dagger, \tilde{f}, \tilde{f}^\dagger\}$ [22] and even more in this basis the Liouvillian becomes diagonal:

$$\mathcal{L}_f = \sum_i \lambda_i f_i^\dagger f_i - \sum_i \lambda_i^* \tilde{f}_i^\dagger \tilde{f}_i. \quad (\text{A3})$$

The operators $\{f^\dagger, \tilde{f}^\dagger\}$ are dual to the operators $\{f, \tilde{f}\}$, but not Hermitian conjugated, though the operators obey anticommutation relations. The operators $\{f, f^\dagger, \tilde{f}, \tilde{f}^\dagger\}$ are

linear combinations of the operators $\{a, a^\dagger, \tilde{a}, \tilde{a}^\dagger\}$:

$$\begin{aligned} a_m^\dagger &= \sum_{k_1} C_{mk_1}^{(1)} f_{k_1}^\dagger + C_{mk_1}^{(2)} \tilde{f}_{k_1}, \\ a_m &= \sum_{k_1} A_{mk_1}^{(1)} f_{k_1} + A_{mk_1}^{(2)} \tilde{f}_{k_1}^\dagger. \end{aligned}$$

The coefficient matrices C and A are connected to the matrix of the eigenvectors P of the matrix \mathcal{M} (see Ref. [22]):

$$P = \begin{pmatrix} A^{(1)} & A^{(2)} \\ A^{(3)} & A^{(4)} \end{pmatrix}, \quad (P^{-1})^T = \begin{pmatrix} C^{(1)} & C^{(2)} \\ C^{(3)} & C^{(4)} \end{pmatrix}. \quad (\text{A4})$$

In P the eigenvectors are ordered in the following way: first N of eigenvectors correspond to eigenvalues with a negative imaginary part, while the second half have a positive imaginary part and are complex conjugated to the first set. All matrices $A^{(i)}$ and $C^{(i)}$, $i = 1, \dots, 4$ have dimension $N \times N$.

In the f basis the Liouvillian operator is diagonal, therefore the stationary solution of the Lindblad equation (6) is the vacuum of the operators f :

$$f|\text{NESS}\rangle = 0, \quad \tilde{f}|\text{NESS}\rangle = 0.$$

It allows us to calculate the expectation values in the NESS: we transform the operator in the a basis to the f basis and take its expectation value with respect to the vacuum.

-
- [1] M. Žnidarič, *J. Stat. Mech.* (2010) L05002; *Phys. Rev. E* **83**, 011108 (2011).
- [2] T. Prosen and I. Pižorn, *Phys. Rev. Lett.* **101**, 105701 (2008).
- [3] C.-E. Bardyn, M. A. Baranov, C. V. Kraus, E. Rico, A. Imamoğlu, P. Zoller, and S. Diehl, *New J. Phys.* **15**, 085001 (2013); O. Viyuela, A. Rivas, and M. A. Martin-Delgado, *Phys. Rev. B* **86**, 155140 (2012).
- [4] H. T. Mebrahtu, I. V. Borzenets, D. E. Liu, H. Zheng, Y. V. Bomze, A. I. Smirnov, H. U. Baranger, and G. Finkelstein, *Nature (London)* **488**, 61 (2012).
- [5] T. Prosen and B. Žunkovič, *New J. Phys.* **12**, 025016 (2010); T. Prosen, *J. Stat. Mech.* (2010) P07020.
- [6] S. Sachdev, P. Werner, and M. Troyer, *Phys. Rev. Lett.* **92**, 237003 (2004).
- [7] P. Werner, Ph.D. thesis, ETH Zürich, 2005.
- [8] S. Pankov, S. Florens, A. Georges, G. Kotliar, and S. Sachdev, *Phys. Rev. B* **69**, 054426 (2004).
- [9] P. Werner, M. Troyer, and S. Sachdev, *J. Phys. Soc. Jpn. Suppl.* **74**, 67 (2005).
- [10] A. J. Leggett, S. Chakravarty, A. T. Dorsey, M. P. A. Fisher, A. Garg, and W. Zwerger, *Rev. Mod. Phys.* **59**, 1 (1987).
- [11] J. Jin, M. W.-Y. Tu, W.-M. Zhang, and Y. J. Yan, *New J. Phys.* **12**, 083013 (2010).
- [12] G. Lindblad, *Rep. Math. Phys.* **10**, 393 (1976).
- [13] H.-P. Breuer and F. Petruccione, *The Theory of Open Quantum Systems* (Oxford University Press, Oxford, 2007).
- [14] Z. Cai and T. Barthel, *Phys. Rev. Lett.* **111**, 150403 (2013).
- [15] Z. Racz, *Nonequilibrium Phase Transitions*, Lecture Notes, Les Houches, July 2002.
- [16] T. Antal, Z. Racz, and L. Sasvari, *Phys. Rev. Lett.* **78**, 167 (1997).
- [17] L. D. Landau and E. M. Lifshitz, *Statistical Physics*, 3rd ed. (Elsevier, Amsterdam, 1980).
- [18] M. Le Bellac, F. Mortessagne and G. G. Batrouni, *Equilibrium and Nonequilibrium Statistical Thermodynamics* (Cambridge University Press, Cambridge, 2004).
- [19] N. Goldenfeld, *Lectures on Phase Transitions and the Renormalization Group* (Perseus, New York, 1992).
- [20] S. Ajisaka, F. Barra, C. Mejia-Monasterio, and Toma Prosen, *Phys. Rev. B* **86**, 125111 (2012).
- [21] A. A. Dzhioev and D. S. Kosov, *J. Chem. Phys.* **134**, 044121 (2011); *J. Phys.: Condens. Matter* **24**, 225304 (2012).
- [22] M. V. Medvedyeva and S. Kehrein, arXiv:1310.4997.
- [23] M. Žnidarič, *Phys. Rev. Lett.* **112**, 040602 (2014).
- [24] K. Maschke and M. Schreiber, *Phys. Rev. B* **49**, 2295 (1994).
- [25] D. Roy and N. Kumar, *Phys. Rev. B* **77**, 064201 (2008).
- [26] M. W. Y. Tu and W.-M. Zhang, *Phys. Rev. B* **78**, 235311 (2008).
- [27] S. A. Gurvitz and Ya. S. Prager, *Phys. Rev. B* **53**, 15932 (1996); S. A. Gurvitz, *ibid.* **57**, 6602 (1998).
- [28] P.-E. Roche, B. Derrida, and B. Douçot, *Eur. Phys. J. B* **43**, 529 (2005).
- [29] I. Perschel and V. Eisler, *J. Phys. A: Math. Theor.* **42**, 504003 (2009).
- [30] F. Evers and A. D. Mirlin, *Rev. Mod. Phys.* **80**, 1355 (2008).
- [31] G. Falkovich, K. Gawędzki, and M. Vergassola, *Rev. Mod. Phys.* **73**, 913 (2001); G. Falkovich, *J. Phys. A: Math. Theor.* **42**, 123001 (2009).
- [32] K. Maschke and M. Schreiber, *Phys. Rev. B* **44**, 3835 (1991); G. Burmeister, K. Maschke, and M. Schreiber, *ibid.* **47**, 7095 (1993).

Quantum corrected phase diagram of holographic fermions

Mariya V. Medvedyeva,^a Elena Gubankova,^b Mihailo Čubrović,^c Koenraad Schalm^c
and Jan Zaanen^c

^a*Department of Physics, Georg-August-Universität Göttingen,
Friedrich-Hund-Platz 1, 37077 Göttingen, Germany*

^b*Institute for Theoretical Physics, J.W. Goethe-University,
D-60438 Frankfurt am Main, Germany*

^c*Instituut Lorentz, Delta-Institute for Theoretical Physics, Leiden University,
Niels Bohrweg 2, 2300 RA Leiden, Netherlands*

E-mail: mariya.medvedyeva@theorie.physik.uni-goettingen.de,
gubankova@th.physik.uni-frankfurt.de, mcubrovic@gmail.com,
kschalm@lorentz.leidenuniv.nl, jan@lorentz.leidenuniv.nl

ABSTRACT: We study the phases of strongly correlated electron systems in two spatial dimensions in the framework of AdS₄/CFT₃ correspondence. The AdS (gravity) model consists of a Dirac fermion coupled to electromagnetic field and gravity. To classify the ground states of strongly correlated electrons on the CFT side and to construct the full phase diagram of the system, we construct a quantum many-body model of bulk fermion dynamics, based on the WKB approximation to the Dirac equation. At low temperatures, we find a quantum corrected approximation to the electron star where the edge is resolved in terms of wave functions extended fully through AdS. At high temperatures, the system exhibits a *first* order thermal phase transition to a charged AdS-RN black hole in the bulk and the emergence of local quantum criticality on the CFT side. This change from the third order transition experienced by the semi-classical electron star restores the intuition that the transition between the critical AdS-RN liquid and the finite density Fermi system is of van der Waals liquid-gas type.

KEYWORDS: AdS-CFT Correspondence, Black Holes, Holography and condensed matter physics (AdS/CMT)

ARXIV EPRINT: [1302.5149](https://arxiv.org/abs/1302.5149)

Contents

1	Introduction	1
2	Holographic fermions in charged background	3
3	Equation of state of the WKB star	5
3.1	WKB hierarchy and semiclassical calculation of the density	5
3.1.1	WKB wave function	7
3.1.2	WKB density	8
3.2	Pressure and equation of state in the semiclassical approximation	9
3.2.1	Microscopic pressure	10
3.2.2	Thermodynamic pressure	12
4	Maxwell-Dirac-Einstein system	13
5	Phases of holographic fermions	16
5.1	Thermodynamics	17
5.2	Constructing the phase diagram: quantum corrections imply a first order thermal phase transition to AdS-RN	18
6	Discussion and conclusions	20

1 Introduction

The problem of fermionic quantum criticality has proven hard enough for condensed matter physics to keep seeking new angles of attack. The main problem we face is that the energy scales vary by orders of magnitude between different phases. The macroscopic, measurable quantities emerge as a result of complex collective phenomena and are difficult to relate to the microscopic parameters of the system. An illustrative example present the heavy fermion materials [3] which still behave as Fermi liquids but with vastly (sometimes hundredfold) renormalized effective masses. On the other hand, the strange metal phase of cuprate-based superconducting materials [4], while remarkably stable over a range of doping concentrations, shows distinctly non-Fermi liquid behavior. The condensed matter problems listed all converge toward a single main question in field-theoretical language. It is the classification of ground states of interacting fermions at finite density.

In this paper we attempt to understand these ground states in the framework of AdS/CFT, the duality between the strongly coupled field theories in d dimensions and a string configuration in $d + 1$ dimension. Holography (AdS/CFT correspondence) [1, 2] has become a well-established treatment of strongly correlated electrons by now, but it still has its perplexities and shortcomings. Since the existence of holographic duals to Fermi

surfaces has been shown in [8, 9], the next logical step is to achieve the understanding of the phase diagram: what are the stable phases of matter as predicted by holography, how do they transform into each other and, ultimately, can we make predictions on quantum critical behavior of real-world materials based on AdS/CFT.

The classification of ground states now translates into the following question: classify the stable asymptotically AdS geometries with charged fermionic matter in a black hole background. Most of the work done so far on AdS/CFT for strongly interacting fermions relies on bottom-up toy gravity models and does not employ a top-down string action. We stay with the same reasoning and so will work with Einstein gravity in $3 + 1$ dimensions. We note, however, that top-down constructions of holographic fermions exist [6, 11].

In this paper we construct a model dubbed “WKB star”, alluding to the fact that we treat the same large occupation number limit as the electron star [10] but go further from the ideal fluid limit of [10]. The main idea is to solve the fermionic equations of motion in the WKB limit *without* taking the fluid limit: the total density is the sum of the contributions of individual wave functions rather than an integral over them. The main approximation we introduce is thus just the quasiclassical treatment of fermions, inherent to WKB. The inverse occupation number serves as the control parameter of this approximation. In addition, we assume that the correction to the fluid limit is captured by the correction to the pressure. This assumption cannot be rigorously derived. We will discuss, however, the robustness of our findings with respect to this assumption. In addition to simply improving the mathematical treatment of the bulk many-body fermion system, we will show that some properties of the system change nonperturbatively in the fluid limit. In particular, the thermodynamic behavior of the system at finite temperature is changed compared to the electron star.

We will use a simple WKB formalism to approximate the many-body Fermi system in the AdS bulk. This adds quantum corrections to the Thomas-Fermi (fluid) approximation by taking into account finite level spacing. In other words, we do not take the limit of an infinite number of occupied levels but keep the occupation number finite. The occupation number itself acts as the control parameter of our approximation. The most notable feature, however, occurs in the transition from the semiclassical approximation at *infinite* occupation number to finite occupation number. We find that the finite density quantum many body phases with fermionic quasiparticles at high enough temperatures always exhibit a *first* order transition into the zero density AdS-RN phase. Intuitively, this can be interpreted as a universal van der Waals liquid-gas transition. On the other hand in the semiclassical fluid limit underlying the electron star, the transition was found to be continuous [12, 33]. With this re-emergence of the first order nature of the thermal phase transition at the quantum level our results confirm the intuition that a density driven phase transition is always first order as also indicated by the Dirac hair approximation [13]. We thus show with an explicit calculation that in the context of fermionic questions in AdS/CFT quantum “ $1/N$ ” corrections can be important and that the semiclassical fluid limit can be unreliable, at least at finite temperature. While the quantum corrections likely have important consequences also at $T = 0$, we have not explored the zero-temperature physics in this paper.

The outline of the paper is as follows. In the section 2 we describe the field content and geometry of our gravity setup, an Einstein-Maxwell-Dirac system in 3 + 1 dimension, and review the single-particle solution to the bulk Dirac equation. In section 3 we start from that solution and apply the WKB approximation to derive the Dirac wave function of a many-particle state in the bulk. Afterwards we calculate density and pressure of the bulk fermions — the semiclassical estimate and the quantum corrections, thus arriving at the equation of state. Section 4 contains the numerically self-consistent solution of the set of equations for fermions, gauge field and the metric. There we also describe our numerical procedure. Section 5 is the core, where we analyze thermodynamics and spectra of the field theory side and identify different phases as a function of the three parameters of the system: chemical potential μ , fermion charge e and conformal dimension Δ . Section 6 sums up the conclusions and offers some insight into possible broader consequences of our work and into future steps.

2 Holographic fermions in charged background

We wish to construct the gravity dual to a field theory at finite fermion density. We will specialize to 2+1-dimensional conformal systems of electron matter, dual to AdS₄ gravities. We consider a Dirac fermion of charge e and mass m in an electrically charged gravitational background with asymptotic AdS geometry. Adopting the AdS radius as the unit length, we can rescale the metric $g_{\mu\nu}$ and the gauge field A_μ :

$$g_{\mu\nu} \mapsto g_{\mu\nu} L^2, \quad A_\mu \mapsto LA_\mu. \tag{2.1}$$

In these units, the action of the system is:

$$S = \int d^4x \sqrt{-g} \left[\frac{1}{2\kappa^2} L^2 (R + 6) + \frac{L^2}{4} F^2 + L^3 \mathcal{L}_f \right] \tag{2.2}$$

where κ is the gravitational coupling and $F_{\mu\nu} = \partial_\mu A_\nu - \partial_\nu A_\mu$ is the field strength tensor. The fermionic Lagrangian is:

$$\mathcal{L}_f = \bar{\Psi} \left[e_A^\mu \Gamma^A \left(\partial_\mu + \frac{1}{4} \omega_\mu^{BC} \Gamma_{BC} - ieLA_\mu \right) - mL \right] \Psi \tag{2.3}$$

where $\bar{\Psi} = i\Psi^\dagger \Gamma^0$, e_A^μ is the vierbein and ω_μ^{AB} is the spin connection.

We shall be interested in asymptotically AdS solutions with an electric field. The U(1) gauge field is simply $A = \Phi dt$ and we parametrize our metric in four spacetime dimensions as:

$$ds^2 = \frac{f(z)e^{-h(z)}}{z^2} dt^2 - \frac{1}{z^2} (dx^2 + dy^2) - \frac{1}{f(z)z^2} dz^2 \tag{2.4}$$

The radial coordinate is defined for $z \geq 0$, where $z = 0$ is the location of AdS boundary. All coordinates are dimensionless, according to (2.1). This form of the metric is sufficiently general to model any configuration of static and isotropic charged matter. Development of a horizon at finite z is signified by the appearance of a zero of the function $f(z)$, $f(z_H) = 0$. From now on we will set $L = 1$.

We will now proceed to derive the equation of motion for the Dirac field. From (2.3), the equation reads:

$$e_A^\mu \Gamma^A \left(\partial_\mu + \frac{1}{4} \omega_\mu^{BC} \Gamma_{BC} - ieA_\mu \right) \Psi = m\Psi. \quad (2.5)$$

In the metric (2.4) we can always eliminate the spin connection [8] by transforming:

$$\Psi \mapsto (gg^{zz})^{-\frac{1}{4}} \Psi = \frac{e^{h(z)/4} z^{3/2}}{f(z)^{1/4}} \Psi \equiv a^{-1}(z) \Psi. \quad (2.6)$$

At this point it is convenient to adopt a specific representation of gamma matrices. We choose:

$$\Gamma^0 = \begin{pmatrix} 1 & 0 \\ 0 & -1 \end{pmatrix}, \quad \Gamma^{x,y,z} = \begin{pmatrix} 0 & \sigma_{1,2,3} \\ -\sigma_{1,2,3} & 0 \end{pmatrix}. \quad (2.7)$$

In this basis we define the radial projections Ψ_\pm as eigenvalues of the projection operator onto the time axis:

$$\Psi_\pm = \frac{1}{2} (1 \pm \Gamma^0) \Psi, \quad (2.8)$$

after which the Dirac equation in matrix form becomes:

$$\sqrt{f} \partial_z \begin{pmatrix} \Psi_+ \\ \Psi_- \end{pmatrix} = \hat{D} \begin{pmatrix} \Psi_+ \\ \Psi_- \end{pmatrix}. \quad (2.9)$$

Here the matrix \hat{D} is the differential operator along the transverse coordinates (x, y) and time, which we will specify shortly.

We will now set the stage for solution of the Dirac equation in the WKB approximation. We can separate the radial dynamics (along the z coordinate) from the motion in the $x - y$ plane. We can thus make the separation ansatz:

$$\begin{pmatrix} \Psi_+(t, z, x, y) \\ \Psi_-(t, z, x, y) \end{pmatrix} = \int \frac{d\omega}{2\pi} \begin{pmatrix} F(z)K_1(x, y) \\ -G(z)K_2(x, y) \end{pmatrix} e^{-i\omega t} \quad (2.10)$$

where the F, G are scalars and the modes $K_{1,2}$ are in-plane spinors. The Dirac equation then takes the form:

$$\begin{pmatrix} \partial_z F K_1 \\ -\partial_z G K_2 \end{pmatrix} = \begin{pmatrix} -\hat{\partial}/\sqrt{f(z)} & (\tilde{E}(\omega, z) + \tilde{M}(z)) \sigma_3 \\ (\tilde{E}(\omega, z) - \tilde{M}(z)) \sigma_3 & -\hat{\partial}/\sqrt{f(z)} \end{pmatrix} \begin{pmatrix} F K_1 \\ -G K_2 \end{pmatrix} \quad (2.11)$$

We recognize the matrix at the right hand side as \hat{D}/\sqrt{f} . The terms \tilde{E} and \tilde{M} have the meaning of local energy and mass terms, respectively:

$$\tilde{E}(z) = -\frac{e^{h(z)/2}}{f(z)} (\omega + e\Phi(z)), \quad \tilde{M}(z) = \frac{m}{z\sqrt{f(z)}}. \quad (2.12)$$

The in-plane operator $\hat{\partial}$ acts on each in-plane spinor as:

$$\hat{\partial} = \begin{pmatrix} 0 & i\vec{\partial} \\ -i\vec{\partial} & 0 \end{pmatrix} \quad (2.13)$$

with $\partial \equiv \partial_x + i\partial_y$. To maintain the separation of variables in (2.11), we require $\hat{\partial}K_i = \lambda_i K_i$, where $|\lambda_i|^2$ corresponds the momentum-squared of the in-plane motion of the particle. The physical requirement that this momentum be the same for both radial projections translates into the condition $|\lambda_2| = |\lambda_1|$. Consistency of the separation of variables then shows us that $K_2 = \sigma_3 K_1$ and thus $\lambda_1 = -\lambda_2 = k$. This solves the x, y -dependent part of the equation, in terms of $\rho \equiv \sqrt{x^2 + y^2}$ and $\phi = \arctan y/x$:

$$K_i(x, y) = \begin{pmatrix} J_{l-1/2}(\lambda_i \rho) e^{i(l-1/2)\phi} \\ J_{l+1/2}(\lambda_i \rho) e^{-i(l+1/2)\phi} \end{pmatrix}, \tag{2.14}$$

where J_a is the Bessel function of the first kind of order a (the second branch, with the modified Bessel function of the first kind Y_a , is ruled out as it diverges at $x = y = 0$). Now the reduced radial equation becomes:

$$\begin{pmatrix} \partial_z F \\ \partial_z G \end{pmatrix} = \begin{pmatrix} -\tilde{k} & \tilde{E} + \tilde{M} \\ \tilde{M} - \tilde{E} & \tilde{k} \end{pmatrix} \begin{pmatrix} F \\ G \end{pmatrix} \tag{2.15}$$

with $\tilde{k} = k/\sqrt{f}$ (let us note that eq. (2.15) is for the pair (F, G) , whereas the initial equation (2.11) is written for the bispinor $(FK_1, -GK_2)$). For the WKB calculation of the density, it is useful to remind that the wave function Ψ in eq. (2.10) has two quantum numbers corresponding to the motion in the (x, y) plane: they are simply the momentum projections k_x, k_y (or equivalently the momentum module λ and the angular momentum l). The radial eigenfunctions in z -direction provide a third quantum number n .

3 Equation of state of the WKB star

In this section we construct the model of the bulk fermions in an improved semiclassical approximation — the WKB star. We solve the Dirac equation in the WKB approximation, and the density is computed by summing a large number of energy levels. This is in the spirit of Thomas-Fermi approximation. However, we perform an exact summation of a *finite* number of WKB quantum-mechanical solutions for the wave functions rather than approximating the sum by an integral as implied in the semiclassical fluid limit. One of the drawbacks of the Thomas-Fermi fluid limit are sharp bounds (i.e., discontinuous first derivative) of density and pressure profiles along the radial direction (see e.g. [10, 12, 33]). As we have already argued, sharp bounds make it hard if not impossible to capture several phenomena. In this respect summing WKB wave functions goes beyond Thomas-Fermi; it includes quantum corrections as the number of occupied states is finite and all collective and individual profiles will be continuous without sharp edges. In further work one might start from our model and treat the quantum-mechanical (one loop) corrections in a more systematic way in order to bridge the gap between the electron star [10] and single-particle quantum mechanical calculation of Dirac hair [13].

3.1 WKB hierarchy and semiclassical calculation of the density

In the framework of quantum-many-body calculations, the first task is to construct the induced charge density $n(z)$. Physically, the origin of the induced charge in our model is

the pair production in the strong electromagnetic field of the black hole. To remind the reader, a (negatively) charged black hole in AdS space is unstable at low temperatures, and spontaneously discharges into the vacuum [24]. This means that there will be a non-zero net density of electrons $n(z)$. One can calculate $n(z)$ in a Hartree approximation as a density of non-interacting electrons, compute the collective effect on other fields by this density and iterate. Our novel approach is to use WKB methods to efficiently compute the many wave functions enumerated by the quantum numbers (λ, l, n) .

The algorithm for the WKB expansion of the wave function for Dirac equation is adopted from [31]. Even though every single step is elementary, altogether it seems to be less well known than its Schrödinger equivalent. We consider the Dirac equation in the form (2.9) and introduce the usual WKB phase expansion:

$$\Psi(z) = e^{\int_{z_0}^z dz y(z) \sqrt{f(z)}} \chi(z) \tag{3.1}$$

with the spinor part $\chi(z)$. The phase $y(z)$ can be expressed as the semiclassical expansion in \hbar ,¹

$$y(z) = y_{-1}(z) + y_0(z) + y_1(z) + \dots \tag{3.2}$$

The equations for the perturbative corrections now follow from (3.1)–(3.2):

$$\hat{D}\chi_0 = y_{-1}\chi_0, \tag{3.3}$$

$$\hat{D}\chi_1 = y_{-1}\chi_1 + y_0\chi_0 + \sqrt{f}\partial_z\chi_0, \tag{3.4}$$

...

$$\hat{D}\chi_n = y_{-1}\chi_n + \sqrt{f}\partial_z\chi_{n-1} + \sum_{i=0}^{n-1} y_{n-i-1}\chi_i. \tag{3.5}$$

Notice in particular that y_{-1}/χ_0 is an eigenvalue/eigenvector of \hat{D} . In our case the matrix \hat{D} has rank two, so there are two eigenvalues/eigenvectors for y_{-1}/χ_0 : y_{-1}^\pm and χ_0^\pm . To find the first order correction to the phase of the wave function y_0 , we multiply (3.4) from the left by the left eigenvalue $\tilde{\chi}_0^\pm$ of the matrix \hat{D} (\hat{D} is in general not symmetric, so the right and left eigenvalues are different):

$$y_0 = -\frac{(\partial_z\chi_0^\pm, \tilde{\chi}_0^\pm)}{(\tilde{\chi}_0^\pm, \chi_0^\pm)}. \tag{3.6}$$

so we can now construct the usual WKB solution of the form $\Psi_\pm = e^{i\theta_\pm}/\sqrt{q}$, where q is the WKB momentum and θ_\pm the phase. The term y_0 is just the first order correction to θ_\pm .

Finally, let us recall the applicability criterion of the WKB calculation. It is known that WKB approximation fails in the vicinity of turning points. The condition of applicability comes from comparing the leading and the next to leading term in the expansion (3.2):

$$\frac{y_0(z)}{y_{-1}(z)} \ll 1. \tag{3.7}$$

¹From the very beginning we put $\hbar = 1$. However, to elucidate the semiclassical nature of the expansion we give it here with explicit \hbar . Dirac equation becomes $\hbar\sqrt{f}\partial_z\hat{\Psi} = \hat{D}\hat{\Psi}$, where $\hat{\Psi} = (\Psi_+, \Psi_-)$, yielding the expansion $y(z) = \hbar^{-1}(y_{-1}(z) + \hbar y_0(z) + \hbar^2 y_1(z) + \dots)$.

In terms of $\tilde{E}(z)$ and $\tilde{M}(z)$ introduced in eq. (2.12) it gives at $k = 0$:

$$\frac{\tilde{M}(z)\partial_z\tilde{E}(z) - \tilde{E}(z)\partial_z\tilde{M}(z)}{\tilde{E}(z)(\tilde{E}(z) - \tilde{M}(z))} \ll 1. \quad (3.8)$$

3.1.1 WKB wave function

According to (3.3), the leading effective WKB momentum for the motion in z direction $q \equiv |y_{-1}^{\pm}|$ is:

$$q^2(z) = \tilde{E}^2(z) - \tilde{M}^2(z) - \tilde{k}^2(z). \quad (3.9)$$

The wave function in radial direction, $\Psi = (F, -G)$, is given by the superposition of two linear independent solutions

$$\Psi(z) = C_+\chi_+(z)e^{i\theta(z)} + C_-\chi_-(z)e^{-i\theta(z)}, \quad (3.10)$$

with the phase determined by

$$\theta(z) = \int^z (q(z') + \delta\theta(z')) dz' \quad (3.11)$$

$$\delta\theta(z) = \int^z \frac{\tilde{k}\partial_z\tilde{k} - q\partial_zq + (\tilde{E} - \tilde{M}) (\partial_z\tilde{E} + \partial_z\tilde{M})}{2\tilde{k}q} dz. \quad (3.12)$$

The constants C_+ and C_- are related by invoking the textbook boundary conditions [25] for the behavior of WKB wave function at the boundary of the classically allowed region ($q^2(z) > 0$) and the classically forbidden region ($q^2(z) < 0$). The wave function in the classically allowed region then reads:

$$\Psi(z) = \frac{C}{\sqrt{q(z)}} \begin{pmatrix} \sqrt{\tilde{E}(z) + \tilde{M}(z)} \sin(\theta(z) - \delta\theta(z)) \\ \sqrt{\tilde{E}(z) - \tilde{M}(z)} \sin\theta(z) \end{pmatrix}, \quad (3.13)$$

$$\delta\theta(z) = \text{ArcSin} \frac{q(z)}{\sqrt{\tilde{E}^2(z) - \tilde{M}^2(z)}}, \quad (3.14)$$

and C is the only remaining undetermined normalization constant. Integrating the probability density over all coordinates in the classically allowed region (z_1, z_2) gives the normalization condition:

$$C^2 \int_0^1 dz \frac{\sqrt{g_{3d}(z)}}{a(z)^2} \int dx \int dy C_{2d}^2 \Psi_{nk_xk_y}(z, x, y) \Psi_{n'k'_xk'_y}^\dagger(z, x, y) = 1. \quad (3.15)$$

The metric factor is $g_{3d}(z) = g(z)g^{tt}(z)$, and $a(z)$ is the conversion factor from (2.6). In the left-hand side of the equality we took into account the normalization of the continuous spectrum in the (x, y) plane. The integration in the perpendicular coordinates is trivial for the solution (2.14), as we can transform the integral into the integral over ρ, ϕ and the orthogonality relation for Bessel functions gives the definition of C_{2d}^2 :

$$C_{2d}^{-2} \int_0^\infty J(\lambda\rho)J(\lambda'\rho)\rho d\rho = \frac{\delta(\lambda - \lambda')}{\lambda} \quad (3.16)$$

and it allows us to express the normalization constant as:

$$C = \left(4\pi \int dz \frac{\sqrt{g^{tt}} \tilde{E}(z)}{\sqrt{g^{zz}} q(z)} \right)^{-1/2}, \quad (3.17)$$

where a factor of 2π comes from the integration over ϕ and an additional factor of 2 from the summation over the full four-component wave function, i.e. bispinor (each spinor gives $\tilde{E}(z)/q(z)$ after averaging over the fast oscillating phase θ). This completes the derivation of WKB wave function and allows us to compute the density.

3.1.2 WKB density

As in [31] we find the total density by summing single-particle wave functions in the classically allowed region. The WKB wave function is characterized by the quantum numbers (λ, l, n) with λ being the linear momentum in the $x - y$ plane, l — the orbital momentum in the $x - y$ plane and n — the energy level of the central motion in the potential well along z direction. The bulk density can be expressed as the sum over the cylindrical shells of the bulk Fermi surface. Each shell satisfies the Luttinger theorem in the transverse ($x - y$) direction and so the density carried by each shell $n_{xy}(z)$ can easily be found. We can then sum over all shells to arrive at the final answer which reads simply $\int dz n_z(z) n_{xy}(z)$. A similar qualitative logic for summing the Luttinger densities in the $x - y$ plane was used also in [14] although the model used in that paper is overall very different (see also the fully consistent treatment with regularization in [38]).

Let us start by noticing that the end points of the classically allowed region determine the limits of summation over n and λ : $q^2(\omega_n, \lambda) \geq 0$. Thus, the density in the WKB region is:

$$n(z) = \frac{2\pi}{a(z)^2} \int_0^{2\pi} d\phi \sum_{n: q^2(\omega_n, \lambda) \geq 0} \int_0^{\sqrt{f(z)(\tilde{E}^2(\omega, z) - \bar{M}^2(z))}} \lambda d\lambda \int_0^\infty d\rho \rho C_{2d}^2 |\Psi(z, x, y)|^2. \quad (3.18)$$

The limit of the sum over the level number n is determined by the requirement that WKB momentum be positive; in other words, we sum over occupied levels inside the potential well only. Remember that the bulk fields live at zero temperature, hence there is no Fermi-Dirac factor. The sum over the orbital quantum number l extends to infinity as the (x, y) plane is homogenous and the orbital number does not couple to the non-trivial dynamics along the radial direction. We can now invoke the (local) Bohr-Sommerfeld quantization rule:

$$\int dz q(z) = N_{\text{WKB}} \pi \quad (3.19)$$

to estimate the total number N_{WKB} of radial harmonics in the sum. The expression for N_{WKB} in combination with (3.17) then give:

$$C_n = \left(\frac{1}{4\pi^2} \frac{\partial \omega_n}{\partial n} \right)^{1/2}, \text{ for } q(z) \gg \delta\theta(z), z \approx 1. \quad (3.20)$$

Now we turn the summation over the quantum number n into the integration over energy and obtain for the *bulk* electron density (here we also performed the integration over ρ using

the explicit expression for the wave function (2.11) and the normalization condition (3.16) for the Bessel functions):

$$n(z) = \frac{4\pi}{a(z)^2} \int_0^{2\pi} d\phi \int_0^{\sqrt{f(z)(\tilde{E}^2(0,z) - \tilde{M}^2(z))}} d\lambda \lambda \int_0^{\mu_{loc}} d\omega \frac{\tilde{E}(\omega, z)}{4\pi^2 q(\omega, \lambda, z)}. \quad (3.21)$$

After performing first integral over ω and then over λ we get:²

$$n(z) = z^3 \frac{q_{\text{WKB}}^3 f^{3/2}(z)}{3\pi^2} \quad (3.22)$$

with q_{WKB} determined by

$$q_{\text{WKB}}^2 = \tilde{E}^2(0, z) - \tilde{M}^2(z). \quad (3.23)$$

Notice that this formula corresponds with common knowledge on the density of electron star [10]. However, even though the formal expression is the same, the self-consistent solution for the metric and gauge field is different because of the quantum correction we introduce to pressure. The difference is visualized in figure 1A where we preview our backreacted WKB star solutions and compare them to the semi-classical (electron star) limit. While the electron star density exhibits a discontinuity at the horizon, the WKB density smoothly falls off to zero. However, both models have a semiclassical “edge”: outside the region $z_1 < z < z_2$, the density is exactly zero. In reality, quantum tails change this picture. In [37] we show that (small) nonzero density extends all the way between the boundary and the horizon. However, it is not expected to change the finite temperature physics which is in the focus of this paper. We therefore do not take into account the quantum tails in further calculations, to avoid any distractions from the main message.

3.2 Pressure and equation of state in the semiclassical approximation

Following the logic behind the density calculation, we will now calculate the pressure p along the radial direction. It will actually prove easier to derive the expression for the (bulk) internal energy density first and then calculate the pressure. By definition, the energy density reads

$$\mathcal{E}(z) = \sum_{k_x, k_y} \int dx \int dy \int_0^{\mu_{loc}} d\omega \omega \Psi^\dagger(z) \Psi(z) = \sum_\lambda \int_0^{\mu_{loc}} d\omega \omega \frac{\tilde{E}(z)}{4\pi^2 q(z)} \quad (3.24)$$

where $\tilde{E}(z)$ is defined in (2.12), $\mu_{loc} = \mu e^{h(z)/2} / f(z)$ and the sum limits are the same as in (3.21). Performing the integration in a similar fashion as when computing $n(z)$ in (3.21)–(3.22), we obtain

$$\mathcal{E} = \frac{3}{4} e \Phi n + \frac{1}{2} f^2 \tilde{M}^2 \text{ArcSinh} \frac{\tilde{E}}{\tilde{M}}. \quad (3.25)$$

²The given result for n can be compared to the charge density in the electron star limit given in [17]. The metric functions used there are related to ours as $f \mapsto f e^{-h}/z^2$ and $g \mapsto 1/fz^2$, where our metric functions are on the right hand side. Likewise, our definition of q_{WKB} is related to k_F of [17] as $q_{\text{WKB}} = k_F / \sqrt{f}$. Now the *total* bulk charge is expressed in [17] as $Q = \int dz \tilde{n}_e(z)$ where $\tilde{n}_e(z) \sim n(z) e^{h/2}$. In our conventions $Q = \int dz \sqrt{-g} g^{zz} g^{tt} n = \int dz n(z) e^{h/2}$ thus giving the same result as in [17].

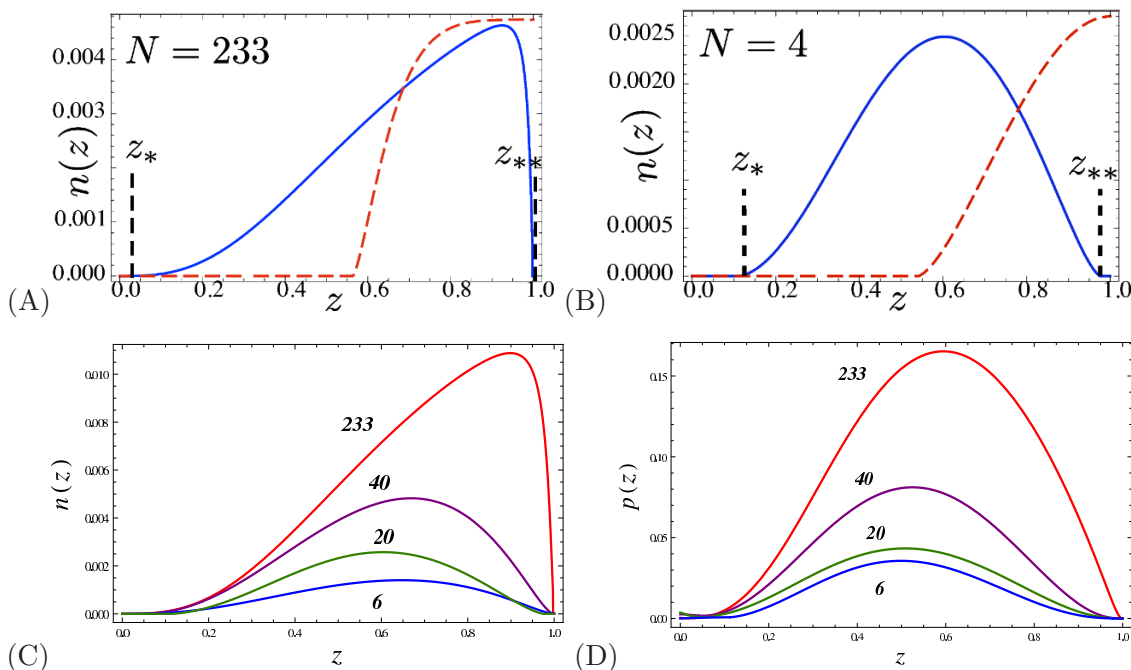


Figure 1. WKB bulk density $n(z)$ (eq. (3.22), blue lines) and electron star density (red dashed lines). Parameter values (A) $(\mu, e, m) = (1.7, 1, 0.1)$, (B) $(\mu, e, m) = (1.7, 10, 1)$. The classically allowed region lies between the turning points z_* and z_{**} , determined by the condition of vanishing WKB momentum ($q(z_*) = q(z_{**}) = 0$). The parameters for (A) are in the classical (electron star) regime, with $N_{\text{WKB}} \gg 1$ when WKB approximation is quite accurate. The plot (B) shows a case of small N_{WKB} where the WKB approximation becomes inadequate and further quantum corrections are likely to be important. (C) Bulk density for a range of values $(\mu, e, m) = (1.7, 1, 0.1)$ (red), $(\mu, e, m) = (1.7, 5, 0.1)$ (violet), $(\mu, e, m) = (1.7, 10, 1)$ (green) and $(\mu, e, m) = (1.7, 20, 1)$ (blue). For large specific charge of the fermion (and therefore a large number of WKB levels in the bulk) the solution is dominated by the classically allowed region and looks similar to the electron star limit. For smaller e/m values (and thus fewer WKB levels) the quantum correction in the near-boundary region becomes more important and the curves are visibly different from the fluid limit. (D) Thermodynamical pressure (eq. (3.34)), for the same parameter values as in (C).

Notice that the first term exactly corresponds to the electrostatic energy while the second is the one-loop term that encapsulates the quantum fluctuations. The above result is remarkably close to the Hartree vacuum polarization correction as it appears in various model energy functionals in literature.

3.2.1 Microscopic pressure

The easiest way to express the pressure is to make use of the first law of thermodynamics, which states

$$p(z) = \sqrt{g^{zz}} (e\Phi(z) - \mathcal{E}(z)). \quad (3.26)$$

There are two possible approaches to arrive at the pressure also directly from the equations of motion. We can express the radial pressure p from the microscopic fermionic

Lagrangian (2.3). By definition it reads

$$p = \sum_{n,\lambda} \left(\Psi_+^\dagger \sigma_3 \partial_z \Psi_- + \Psi_-^\dagger \sigma_3 \partial_z \Psi_+ \right) = \frac{1}{a^2} \left(\tilde{E}(F^2 + G^2) - \tilde{M}(F^2 - G^2) - 2\tilde{k}FG \right) \quad (3.27)$$

The equality follows directly from the Dirac equation, substituting the expressions for $\partial_z \Psi_\pm$ from (2.9). Now we can exploit the lowest order WKB solution (3.13) to get

$$p = \frac{2\pi}{a^2} \sum_{n,\lambda} C_n^2 \left(\frac{\tilde{E} - \tilde{M}}{q} - \tilde{k} \right), \quad (3.28)$$

which, after the momentum integration, gives:

$$p = 2\pi \sum_n C_n^2 e^{h/2} z^3 \sqrt{f} \left[(\tilde{E} - \tilde{M}) q_{\text{WKB}}^2(z) - \frac{2}{3} q_{\text{WKB}}^3(z) \right] \quad (3.29)$$

The explicit calculation is tedious but straightforward. Unlike the density case, the final sum is not readily performed to obtain a closed-form expression. Instead, we integrate numerically over the energy levels ω_n to obtain the function $p(z)$. However, even a quick look at (3.29) tells that it behaves as q_{WKB}^3 at leading order, for q_{WKB} large (the first and the third term will contribute as q_{WKB}^3). After the energy integration this term gains roughly a factor of μ , implying that $p \sim \mu n \sim \mu^4$, as we expect to recover in the fluid limit.

We have now calculated the radial pressure, i.e. the fermionic component of the stress tensor T_z^z . Due to local isotropy, it does not depend on the direction and position in the $x - y$ plane. The same happens in the fluid limit, as shown in [10]. The pressure in the perpendicular direction (in the $x - y$ plane) is analogously expressed as

$$p_\perp = - \sum_{n,\lambda} ik \left(\Psi_+^\dagger \sigma_1 \Psi_- + \Psi_-^\dagger \sigma_1 \Psi_+ \right) = \frac{2\pi}{a^2(z)} \sum_{n,\lambda} C_n^2 \frac{1}{q} \lambda \tilde{E} \quad (3.30)$$

The summation over λ , i.e. the value of the in-plane momentum can again be performed analytically, yielding:

$$p_\perp = 2\pi \sum_n C_n^2 e^{h/2} z^3 f q_{\text{WKB}}^2 \tilde{E}. \quad (3.31)$$

In fact, the above sum has a closed-form limit for $N_{\text{WKB}} \rightarrow \infty$:

$$p_\perp = f^2 e^{h/2} z^3 \frac{q_{\text{WKB}}^4}{12\pi^2}, \quad (3.32)$$

which obeys the relation $p_\perp \sqrt{g_{ii}} = n \sqrt{g_{00}}/3$, the covariant version of the relation $p = \mu n/4$. We will not make use of p_\perp as the ii component of the Einstein equations is not functionally independent of the 00 and zz components; the two metric functions f, h are determined from the two equations, and the third one can only serve as a consistency check.

3.2.2 Thermodynamic pressure

In a “near”-classical regime, at large occupation number, thermodynamics ought to work, so we can express the pressure from the energy density \mathcal{E} , as $p = -\partial E/\partial V$. This expression is still hard to calculate exactly. However, we can use the following trick to estimate p at the leading order. Consider a small change of the number density δn . It will introduce a small change of energy $\delta\mathcal{E}$, pressure δp and the volume of the bulk electron gas δV , the latter because the classically allowed region where $q_{\text{WKB}}^2 > 0$ will shift and grow (if $\delta n > 0$). Now since the metric is radially symmetric we can expand the volume $V = \int_{z_*}^{z_{**}} d^3x \frac{e^{-h(z)/2}}{z^4}$ around its initial value and find that the leading term in its variation behaves as $\delta V = V\delta\ell/(1-\ell) + \dots$, where $\ell \equiv z_{**} - z_*$ is the (dimensionless) length of the classically allowed interval along the z axis, i.e. the interval between the zeros of the WKB momentum $q_{\text{WKB}}(z) = \sqrt{\tilde{E}^2(z) - \tilde{M}^2(z)}$. This yields

$$\frac{\partial E}{\partial V} = \mathcal{E} + V \frac{\partial \mathcal{E}}{\partial V} = \mathcal{E} + V \frac{\delta \mathcal{E}(1-\ell)}{V\delta\ell} = \frac{\delta \mathcal{E}}{\delta \ell}. \tag{3.33}$$

Since all the processes we study are certainly adiabatic (looking at the whole system of gravity plus the matter fields), we can replace the variations by partial derivatives and write $p \sim \partial \mathcal{E}/\partial \ell$ as an approximation for the radial pressure. However, even this expression we are only able to evaluate in a very crude way. For $N_{\text{WKB}} \gg 1$, it is natural to assume (and confirmed by the numerics, see figure 1) that z_{**} is very close to the horizon, z_* is quite far from the horizon and $\ell \approx 1 - z_*$. For $z \sim z_*$, we assume that the electric potential does not deviate much from the linear law: $\Phi \sim \mu(1 - z)$, because z_* is not far from the boundary. This means that the metric function $h(z)$ can be well approximated by a linear function $h(z) \sim \text{const.}(1 - z)$. Solving the equation $q_{\text{WKB}}^2 = \tilde{E}^2(z_*) - \tilde{M}^2(z_*) = 0$, we get $\ell \sim 1 - \log \frac{e^2 \mu^2}{m^2}$, and (3.25) gives the thermodynamic pressure. However, we cannot get the numerical prefactor right in our approach, and this is important in order to satisfy the first law of thermodynamics, which in the fluid limit predicts $p = \mathcal{E}/4$. We therefore norm p_{thd} by hand by a constant factor C_{thd} . This gives:

$$p_{\text{thd}} = -C_{\text{thd}} \frac{\partial \mathcal{E}}{\partial \Phi} \frac{\partial \Phi}{\partial \mu} \frac{\partial \mu}{\partial \ell} \sim \frac{3}{4} e\mu(1 - z) \left(n + \frac{\tilde{M}^2 e^{-h}}{z \sqrt{\tilde{M}^2 + e^h \tilde{E}^2}} \right) \tag{3.34}$$

This is the relevant regime to compare with the electron star. We will call the estimate (3.34) thermodynamic pressure and denote it by p_{thd} to differentiate from the exact summation of WKB wave functions (3.29). These expression are also the equations of state of the system as they connect the pressure to the density. The thermodynamic pressure is more convenient for calculations. In spite of its approximate nature, (3.34) in particular yields a remarkably accurate result when compared with the quantum pressure at $N_{\text{WKB}} \gg 1$.

We can make the connection between the exact first law of thermodynamics (3.26) and the quick estimate (3.34) by showing them to be equal in the limit of small \tilde{E} , which is appropriate in the vicinity of the phase transition from WKB star to the RN black hole.

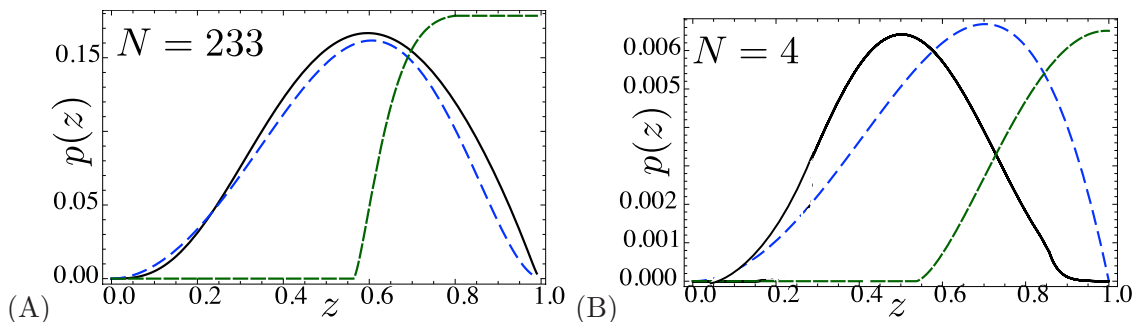


Figure 2. Comparison between full quantum pressure (dashed blue lines, eq. (3.29)) and thermodynamic pressure (solid black lines, eq. (3.34)) for two sets of parameters: $(\mu/T, e, m) = (1.7, 1, 0.1)$ (A) and $(\mu/T, e, m) = (1.7, 5, 1)$ (B). For comparison we plot also the fluid pressure $p = en\Phi/2$ (dashed green lines). Expectedly, for $N_{\text{WKB}} \gg 1$ (A) the thermodynamic approximation comes close to the exact summation while for N_{WKB} small the level spacing is large and the thermodynamic limit is no longer a good approximation to the sum of the contributions of individual levels. Notice that both ways of computing pressure yield similar results for large N_{WKB} but deviate at smaller N_{WKB} .

In this case expanding both equations in \tilde{E} , we find the same expression:

$$p \approx \frac{1}{4}e\Phi n + \frac{f}{z}\tilde{E}\tilde{M} + O(\tilde{E}^3). \quad (3.35)$$

Finally, it is illustrative to see how we reproduce the electron star pressure [10] in the limit of large density. For $n \rightarrow \infty$, the first term in \mathcal{E} and p_{thd} dominates and we obtain from (3.25) and (3.34)

$$p_{ES} = \frac{1}{4}e\Phi n \quad (3.36)$$

as expected for an ideal fluid, which corresponds to the electron star approach. The physical interpretation of this result (and of the pressure inside the classically allowed region in general) is that of a Fermi gas pressure which, as we know, survives also in the limit of classical thermodynamics. The comparison of p , p_{thd} and p_{ES} is summarized in figure 2, for high and low number of levels. While the thermodynamic approximation (3.34) is good when $N_{\text{WKB}} \gg 1$, for small N_{WKB} both the fluid limit and the thermodynamic limit eventually break down and the contributions of individual levels must be taken into account. Once again, the introduction of Airy corrections would extend the nonzero pressure to the whole AdS space, which is only expected to be relevant at $T = 0$ [37].

4 Maxwell-Dirac-Einstein system

We have now arrived at the point where we can look for a numerically self-consistent solution of the Einstein-Maxwell equations. The numerics uses an iterative procedure to converge toward the solution. Only in the IR region it is possible to use a scaling ansatz to estimate the scaling behavior of the metric and matter fields, akin to the procedure used in [20]. This is the first attempt at a numerically self-consistent solution including backreaction on the geometry with holographic fermions which goes beyond the fluid picture of [10].

Our calculation is similar to the one for relativistic ideal fluid (i.e. electron star) approximation. Because an ideal fluid is dissipation-less one can construct an action as put forward in [15] and used in [10, 12]. The Lagrangian of this charged fluid coupled to gravity and electromagnetism is

$$S = \int d^4x \left[\frac{1}{2\kappa^2} (R + 6) - \frac{1}{2q^2} (\partial_z \Phi)^2 + p \right]. \quad (4.1)$$

In other words, the contribution of fermions reduces to the pressure p . While we do not take the fluid limit in this paper, within the WKB star model we assume that in the first approximation the influence of the corrections to fluid limit ($N_{\text{WKB}} \rightarrow \infty$) is fully encapsulated by the correction to the classical (or fluid) pressure we found in (3.25)–(3.29). The emergent isotropy and its implied ideal nature of the fluid at large occupation number should ensure this.

To construct the backreacted geometry, we therefore “replace” the fermionic terms in the exact action (2.2) with our effective ideal fluid model in terms of the density and pressure of the bulk fermions. The total effective action is represented as $S = S_E + S_M + S_f$, the sum of Einstein, Maxwell and fluid part. The only nonzero component of the gauge field is Φ and the only non-vanishing derivatives are the radial derivatives ∂_z (the others average out to zero for symmetry reasons). The nonzero fermion pressure p is that considered in section 3.2 and there is a nonzero (local) charge density

$$j_e^0 = qn\sqrt{g^{00}} = qn \frac{ze^{h/2}}{\sqrt{f}}. \quad (4.2)$$

The fermion fluid term in the effective action thus becomes

$$S_f = - \int d^4x \sqrt{-g} (j_e^0 \Phi + p). \quad (4.3)$$

Due to the preserved spherical symmetry we may substitute these simplifications directly in the effective action to arrive at:

$$S_{\text{eff}} = \int d^4x \sqrt{-g} \left[\frac{1}{2\kappa^2} (R + 6) - \frac{z^4}{2} e^h \left(\frac{\partial \Phi}{\partial z} \right)^2 - j_e^0 \Phi + p \right]. \quad (4.4)$$

The only components of the stress tensor the fermion kinetic energy contributes to are the diagonal ones; the others vanish due to homogeneity and isotropy in time and in the $x - y$ plane. From (4.4) we get the equations for the energy-momentum tensor:

$$T_0^0 = -\frac{1}{2} z^4 e^h \left(\frac{\partial \Phi}{\partial z} \right)^2 + j_e^0 \Phi \quad (4.5)$$

$$T_z^z = -\frac{1}{2} z^4 e^h \left(\frac{\partial \Phi}{\partial z} \right)^2 + j_e^0 \Phi + mn + g_z^z p. \quad (4.6)$$

With the metric ansatz (2.4), we can now write down our equations of motion:

$$\frac{1}{\sqrt{-g}} \left(\partial_z e^{-h/2} \partial_z \Phi \right) = -j_e^0 \quad (4.7)$$

$$3f - z\partial_z f - 3 = T_0^0 \quad (4.8)$$

$$3f - z\partial_z f - 3zf\partial_z h - 3 = T_z^z \quad (4.9)$$

Notice that the ii component of the Einstein equations:

$$\frac{1}{2}(\partial_{zz}f - f\partial_{zz}h) + \frac{1}{4}(f\partial_z h^2 - 3\partial_z f\partial_z h) + \frac{f\partial_z h - 2\partial_z f}{z} + \frac{3f}{z^2} = T_i^i \quad (4.10)$$

with

$$T_i^i = -\frac{1}{2}z^4 e^h \left(\frac{\partial\Phi}{\partial z}\right)^2 + g_i^i p_\perp \quad (4.11)$$

is functionally dependent on the others and drops out. For that reason, (4.7)–(4.9) forms the complete system of Maxwell-Einstein equations. We do *not* need to know T_i^i or p_\perp nor to assume the isotropy (in the sense $T_i^i = T_z^z$).

In this article we shall only be interested in finite temperature solutions. The gravitational background is therefore a black hole with an horizon: a single zero in the warp function $f(z)$ at a finite value $z = z_H$.³ Physically the inescapability of the black hole horizon immediately suggests the following boundary conditions. The black hole horizon should have no hair so $\Phi(z_H) = 0$; $h(z)$ which characterizes the ratio of the UV and IR speed of light should be finite at the horizon: $h(z_H) = h_0$. Note that the effective WKB potential felt by the fermions blows up at the horizon and that the fermion wavefunctions therefore manifestly vanish at z_H . This same phenomenon is noted in the electron star at finite temperature which also has an “inner” edge outside the horizon [12, 33].

At AdS infinity the boundary conditions are standard in AdS/CFT: for the gauge field $\lim_{z \rightarrow 0} \Phi(z) = \mu$ fixes the chemical potential at the boundary ($z_0 \rightarrow 0$). We normalize $\lim_{z \rightarrow 0} f(z) = 1$, $\lim_{z \rightarrow 0} h(z) = 0$. Again the boundedness of the normalized WKB wavefunctions uniquely fixes the behavior of the fermions.

Finally, it remains to define the units used throughout the paper. The natural unit of energy and momentum is the chemical potential μ and we will express all quantities in units of μ . The two thermodynamic parameters are the chemical potential μ and T . As AdS/CFT is built on conformal field theories which have no intrinsic scale, the physics only depends on the ratio μ/T .

Let us conclude with an outline of the numerical algorithm, which is not completely trivial. The boundary conditions to be implemented are given at different points: some are given at the AdS boundary and some at the horizon. Since the system is nonlinear, it is necessary to either linearize the system or to shoot for the correct boundary conditions with the full nonlinear system. After experimenting with both, we have decided to iterate the full, non-simplified system of equations, integrating from the horizon and shooting for the conditions at the boundary. The iterative procedure consists of two steps: we start with the non-backreacted AdS-RN geometry and compute the density (semiclassical plus the quantum corrections) for the the electron charge equal to e/N (where e is the physical charge and N some positive integer), then we solve the system of Einstein-Maxwell equations (4.7)–(4.9), afterwards we increase the fermion charge to $2e/N$, calculate the

³At zero temperature, when the horizon vanishes due to fermionic backreaction (this includes also the case of Lifshitz geometry), the boundary condition for f guarantees also the smoothness of the solution on the horizon: $\partial_z f(z_H) = 0$. This condition ensures that we pick the correct branch of the solution as there are typically two families of functions $f(z)$ that satisfy the equations of motion and the condition $f(z) = 0$. One of them has a vanishing derivative whereas the other has finite derivative as $z \rightarrow 1$.

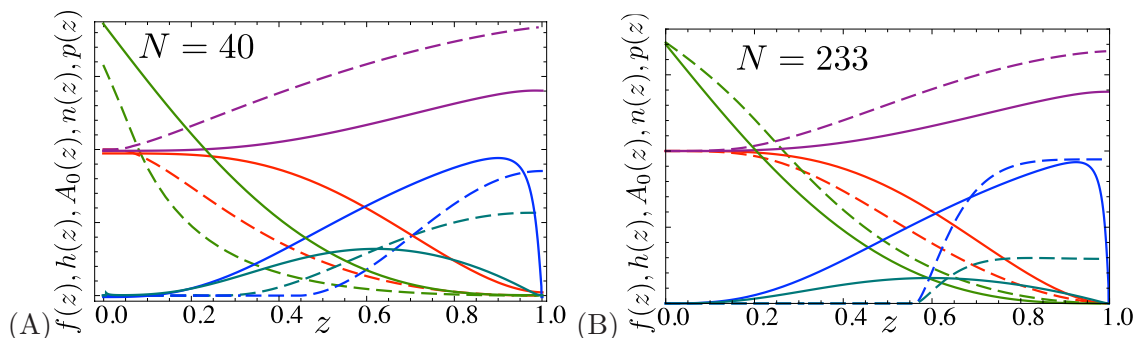


Figure 3. Profiles of the metric functions $f(z)$ (red) and $e^{-h(z)}$ (violet), the gauge field $\Phi(z)$ (green), density $n(z)$ (blue) and the pressure $p(z)$ (cyan) at zero temperature, for $(\mu/T, e, m) = (1.7, 1, 0.1)$ (A) and for $(\mu/T, e, m) = (1.7, 10, 0.1)$ (B). Solid lines are calculated from our model while dashed lines are the electron star solution for the same parameter values. For better visibility density and pressure are rescaled by a constant factor. Near the boundary we always have $h(z) \rightarrow 0$ and $\Phi(z) = \mu + O(z)$, in accordance with the universal AdS asymptotics of the solution but in the interior the solutions start to deviate. Most striking is the absence of sharp classical edges in density and pressure. The difference in pressure will turn out to be crucial in moving away from the fluid limit. Here we have not shown the solution with $N_{\text{WKB}} = 4$: this case deviates from the electron star ($N_{\text{WKB}} \rightarrow \infty$) so strongly that it does not make sense to compare it. Indeed, $4 \ll \infty$!

charge density in the background (f, h, Φ) taken from previous iteration and solve for this density the Einstein-Maxwell equations (4.7)–(4.9). We repeat this procedure for charge $3e/N, 4e/N$ etc. After N iterations we have arrived at the physical value of the charge e . Then we do more iterations with fixed charge e to ensure that the solution has converged, checking that the set of functions (f, h, Φ) does not change from iteration to iteration. In this way we achieve the self-consistent numerical solution of the Maxwell-Dirac-Einstein system of equations. The integration is always done from the horizon, shooting for the conditions for Φ and h at the boundary, since it is well known that integrating from the AdS boundary is a risky procedure as it is next to impossible to arrive at the correct branch of the solution at the horizon.

5 Phases of holographic fermions

We can now analyze the structure of both the bulk and the field theory side as a function of the parameters $T/\mu, e$ and m . We first shortly discuss the nature of the bulk solution for the geometry and gauge field and notice some qualitative properties. The typical way that the solutions to the WKB-Fermi-Einstein system (4.7)–(4.9) look is illustrated in figure 3. The near-horizon scaling of the metric and gauge field is of Lifshitz type, as expected in the light of earlier models [10, 34]. Notice that we are working at finite temperature and thus do *not* impose the IR boundary conditions for the metric functions which correspond to the Lifshitz geometry. Our finding of Lifshitz scaling is purely numerical, with the simple boundary conditions discussed above. In the figure, we plot also the electron star solution for comparison. One should be careful in comparing the two, however, as the electron star corresponds to the limit $e \rightarrow 0$ and thus cannot be compared directly (i.e., for the

same parameter values) to our WKB star. Our convention is to first define the electron star by choosing the *total* charge density Q and the parameter $\hat{m} = m/\epsilon\kappa$, where κ is the gravitational constant whose value is fixed by the normalization of the action (4.1). For the WKB star, we impose the same value of Q , while the value of m is found as $m = \hat{m}\epsilon\kappa$ (for WKB star we can control e as an independent parameter). Relative proximity of the solutions for large N seems to confirm that this is a physically meaningful way of comparing the models.

5.1 Thermodynamics

We can now use these full solutions to determine the macroscopic characteristics of the dual strongly coupled fermion system. Let us first derive the free energy of the boundary field theory. According to the dictionary, it is equal to the (Euclidean) on-shell action, which contains both bulk and boundary components:

$$F = S_{\text{bulk}}^{\text{on-shell}} + S_{\text{bnd}}^{\text{on-shell}}. \tag{5.1}$$

We have already discussed the bulk action in the previous section. We will again approximate the fermionic contribution (4.3) by its leading term, the pressure.

In computing the free energy using AdS/CFT a crucial part is often played by boundary terms in the action. It encapsulates the regularizing terms that eliminate $z \rightarrow 0$ divergences, enforces a Dirichlet boundary condition for the gauge field, but it also provides the kernel for the fermionic correlation functions [9, 36]

$$S_{\text{bnd}} = \oint_{\partial AdS} \sqrt{-h} \left(\frac{1}{2} n_\nu F^{\mu\nu} A^\mu + \bar{\Psi}_+ \Psi_- \right), \tag{5.2}$$

with h being the induced metric on the boundary ($h = \frac{1}{z^2}(-1/f(z=0), 1, 1)$) and Ψ_+ and Ψ_- are radial projections of the wave function as in eq. (2.8). By ∂AdS we have denoted the boundary of the AdS space. Let us now briefly show why these boundary fermion terms do not contribute to the free energy, but that the leading fermion contribution is the (one-loop) effective pressure. Essentially the point is that only normalizable modes of the field are occupied and hence they cannot contribute to the boundary action as they die off too fast. The Dirac field asymptotics at the boundary are given by [13]:

$$\Psi_+ = \frac{i\mu\gamma^0}{2m+1} B_- z^{5/2+m} + \dots, \quad \Psi_- = B_- z^{3/2+m} + \dots \tag{5.3}$$

At the same time the electromagnetic boundary term reduces to $\Phi\partial_z\Phi|_{z=0} = -\mu\rho$, where ρ is the total boundary (not only fermionic) charge density, read off from the subleading “response” of the bulk electrostatic potential $\lim_{z\rightarrow 0} \Phi(z) = \mu - \rho z + \dots$. The regularized boundary action now reads

$$S_{\text{bnd}} = \lim_{z_0\rightarrow 0} S(z_0) + \lim_{z_0\rightarrow 0} \int d^3x \left[\frac{3\mu}{2(2m+1)} \bar{B}_- i\gamma^0 B_- z_0^{1+2m} - \frac{1}{2} \mu\rho \right], \tag{5.4}$$

Since $m > -1/2$ is the fermionic unitarity bound in AdS/CFT, the first term always vanishes in the limit $z_0 \rightarrow 0$. The total on-shell action, i.e. the free energy is therefore

$$F = \int_{z_0}^{z_H} dz d^3x \sqrt{-g} \left[R + 6 + \frac{ze^{h/2} qm\Phi}{2\sqrt{f}} + p \right] - \frac{1}{2} \mu\rho \tag{5.5}$$

5.2 Constructing the phase diagram: quantum corrections imply a first order thermal phase transition to AdS-RN

The condensed matter context in which we are discussing AdS/CFT is that of an emergent finite density fermionic ground state out of an UV CFT. In the deep UV or at very high temperatures T/μ the chemical potential should be negligible and we should recover as the preferred groundstate the UV CFT at finite T/μ . The gravitational dual of this is the AdS-RN black hole. It describes a conformal critical phase with no Fermi surfaces. As we lower T/μ an instability should set in towards a state with a finite occupation number of fermions. In the probe analysis one indeed finds several normalizable wavefunctions signalling the existence of states with distinct occupation numbers. They are the bulk counterpart of the existence of non-Fermi-liquid Fermi surfaces [8, 9, 19, 21]. A crucial qualitative aspect is that due to their fermionic nature the wavefunctions of these normalizable modes can *never* “grow”. From a microscopic point of view it therefore appears that any fermion driven phase transition cannot be second order. In the fluid limit, however, the transition was found to be third order. There is no conflict because new analytic behavior can emerge in the fluid scaling limit where the *number of Fermi surfaces* is taken to infinity.⁴ It does mean that one has to be quite careful in the fluid limit as for fermions these corrections can change macroscopic quantities. For any finite number of Fermi surfaces we should discover a first order transition. We did indeed find this earlier in the Dirac hair approximation valid for $N_{\text{WKB}} = 1$ [13]. With the WKB construction put forward here, we will show that this is indeed so for any finite N_{WKB} .

Figure 4 shows the behavior of the free energy $F(T/\mu)$ of the WKB corrected star construction for different parameters e, m , corresponding to a different number of levels N_{WKB} (which roughly equals the number of Fermi surfaces. In the high temperature phase the preferred state with lowest $F(T/\mu)$ is that of the pure AdS-RN. Since there are no occupied fermionic states it is independent of the fermion charge and mass. In the low temperature phase the preferred phase is the WKB star. Where the phase transition occurs, one immediately sees the characteristic first order cusp in $F(T/\mu)$ whose non-analyticity indeed becomes clearer as N_{WKB} decreases. The panel (B) of the figure makes this clear by showing the vicinity of the phase transition.

The first order nature of the phase transition can in fact be understood analytically with this WKB construction. The argument is along similar lines as for the fluid limit of the electron star [12]. Assuming that the transition is dominated by the behavior of the fermions and that the contribution of the geometry change due to backreaction is small

⁴Note that there is a crucial subtlety in the fluid limit in AdS/CFT with a flat Minkowski-space boundary. Normally one needs a thermodynamic “fluid” limit to even be able to discuss the notion of a phase transition. In global AdS, or conventional Tolman-Oppenheimer-Volkov neutron stars, a bound on the number of radial modes, implies a countable number of states. However, this is not so in AdS/CFT with a flat Minkowski-space boundary. For each radial mode there is still a formal infinite number of modes distinguished by the transverse momentum. The phase transition discussed here is where one considers $N/V_{\text{transverse}} \rightarrow \infty$. It restores one’s intuition that the emergence of *each single Fermi surface* dual to each single radial mode is associated with a macroscopic phase transition. We thank Sean Hartnoll for emphasizing this.

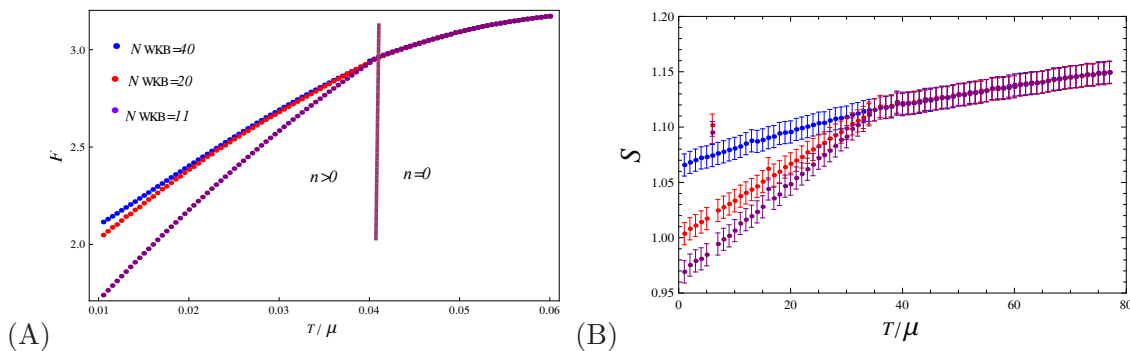


Figure 4. Free energy as a function of temperature $F(T)$. The abrupt change of the derivative signifies the first order transition between the finite density phase and the pure black hole (with zero bulk fermion density), in line with the analytical prediction of the first order transition from the second term in the bulk free energy in section 5.2. We show the calculations for three different values (μ, e, m) of the system parameters: $(1.7, 3, 0.1)$, $N_{\text{WKB}}(T=0) = 40$ in blue, $(1.7, 10, 0.1)$, $N_{\text{WKB}}(T=0) = 20$ in red and $(1.7, 10, 0.7)$, $N_{\text{WKB}}(T=0) = 11$ in violet. Notice how the slope of F in the low-temperature phase decreases as the number of levels increases: for $N_{\text{WKB}} \rightarrow \infty$ we reach the electron star limit when the transition becomes continuous. Panel (B) shows the vicinity of the critical temperature for three sets of parameter values, to make the cusp in $F(T)$ clearly visible. In the high temperature (RN) phase the curves $F(T)$ fall on top of each other as one expects for the RN black hole with $n = 0$. The behavior in the low-temperature phase (with non-zero density) is different for the three curves as the value of the charge affects the behavior of the bulk fermions. For presentation purposes, the curves have been rescaled to the same transition temperature; in general, however, $(T/\mu)_c$ is *not* universal and will differ for different corners of the parameter space.

near the critical temperature, the relevant part of the free energy of the system is given by

$$F_{\text{Fermi}} \approx \int_0^{z_H} p = \frac{e\mu}{2} \int_{z_*}^{z_{**}} (1-z)n + \frac{e\mu}{2} \int_{z_*}^{z_{**}} \frac{\tilde{M}^2 e^{-h}}{z \sqrt{\tilde{M}^2 + e^h \tilde{E}^2}} \equiv F_{\text{Fermi}}^{\text{fluid}} + \Delta F_{\text{Fermi}} \quad (5.6)$$

Starting from low temperatures and nonzero n , at the transition point the bulk density n vanishes. In the WKB construction that means that the turning points coincide: $z_* \rightarrow z_{**}$. The first, “fluid limit” term $F_{\text{Fermi}}^{\text{fluid}}$ in (5.6) is proportional to Φn and it is analyzed in detail in [12]. It yields the scaling $F_{\text{Fermi}}^{\text{fluid}} \sim (T - T_c)^3$. This indicates a third order transition at the semi-classical level. The new, second, quantum term will change this, however. The vanishing of the classically allowed region means $\tilde{E} \approx \tilde{M}$ in the whole (narrow) region $z_* < z < z_{**}$. One can thus expand $\tilde{E} = \tilde{M} + \delta z \times \delta \tilde{E} / \delta z + \dots$ and analyze the leading terms in δz . It is easy to see that its expansion starts from a constant. Since for vanishing δz the density can be assumed constant throughout the WKB star, we estimate the integral in ΔF_{Fermi} as

$$\Delta F_{\text{Fermi}} \approx \frac{\Phi \tilde{M}^2 e^{-h}}{\sqrt{\tilde{M}^2 + e^h \tilde{E}^2}} \delta z = (\text{const.} + O(\delta z)) \delta z, \quad (5.7)$$

where $\delta z = z_{**} - z_*$. Therefore, the second term scales as $\Delta F_{\text{Fermi}} \sim \delta z$. Now, for a vanishing bulk charged fluid/emerging charged black hole, the principle of detailed balance predicts that the charge of the former equals the charge of the latter: $n\delta z = n_{\text{BH}}\delta z_H$,

where the charge densities of the bulk and the black hole are n and n_{BH} , respectively, and δz_H is the change in the position of the black hole horizon. Since the densities can be assumed constant for vanishing δz and δz_H , we find $\delta z \sim \delta z_H \sim T - T_c$. We can now write $F_{\text{Fermi}} = F_{\text{Fermi}}^{\text{fluid}} + \Delta F_{\text{Fermi}}$. We know that $F_{\text{Fermi}}^{\text{fluid}} \sim (T - T_c)^3$ [12], but we have now shown that

$$\Delta F_{\text{Fermi}} \sim T - T_c. \tag{5.8}$$

At the quantum level the *transition is always of first order*. The quantum correction is subleading at general T values, but becomes leading as the phase transition point is approached. Finally, we remark that, if one considers the bulk free (or internal) energy $\int dz \mathcal{E}$ given in eq. (3.24) using the similar scaling reasoning, one arrives at the same conclusion: $F \sim T - T_c$. This confirms the intuition that the bulk and boundary thermodynamics are equivalent at leading order, i.e. the difference $F_{\text{bulk}} - F$ does not contain first-order terms in $T - T_c$ and thus does not change the order of the transition. Now the exact free energy differs from our WKB star calculation, as we have assumed that the correction to the fluid limit is fully captured by the correction to pressure. However, an additional term in F *cannot decrease the order of the transition*: it can introduce new singularities (of some order α , scaling as $(T - T_c)^\alpha$) but cannot cancel out the term.

The numerics just confirms this analytic prediction of a first order phase transition. The field theory interpretation of the discontinuous nature of the transition to a phase with Fermi surfaces is simple: fermions do not break any symmetry but the discharge of the black hole does signify that the ground state is reconstructed due to the formation of a rigid Fermi surface. The only way to reconstruct the ground state without breaking any symmetries is precisely the first order transition of the density van der Waals liquid-gas type. This is the macroscopic counterpart to the probe analysis where the Grassman nature of fermions Pauli blocks the growing of mode functions. A van der Waals liquid-gas first order type transition is indeed seen in [13] for the first order transition from $N_{\text{WKB}} = 1$ Dirac hair state to AdS-RN. The confusing point was that electron star/AdS-RN transition valid in the strict $N_{\text{WKB}} \rightarrow \infty$ fluid limit was found to be third order [12, 33]. Here we show that this change in the nature of the phase transition is an artifact of this $N_{\text{WKB}} \rightarrow \infty$ limit. Instead the expected first order behavior is recovered for any finite value of N_{WKB} .

6 Discussion and conclusions

In this paper we have constructed the WKB star as an improved semiclassical model of holographic fermions in AdS₄ space, aimed at understanding the phase diagram of strongly coupled Fermi and non-Fermi liquids. The model combines a WKB approximation with a Hartree summation to approximate a finite N_{WKB} charged fermion state in AdS coupled to both gravity and electromagnetism. The dominant effect is a quantum correction to the pressure and energy density ("vacuum polarization") of the conventional $N_{\text{WKB}} \rightarrow \infty$ classical model — the electron star. This finite N_{WKB} approach has allowed us to address the intermediate fermion charges which cannot be modeled satisfyingly with any of the previously used models.

By studying the free energy of the system we can now construct the full phase diagram of the system. Most importantly, we find a *universal first order phase transition from a finite density to a zero density (Reissner-Nordström, quantum critical) phase*. The discontinuity of the density comes from the quantum term in the internal energy. This term is always present but its relative contribution to the free energy decreases with the inverse of the number of radial modes N_{WKB} . The extreme limit $N_{\text{WKB}} \rightarrow \infty$ reproduces the unexpected third order continuous phase transition found in [12, 33]. Nevertheless, in any real system with finite fermion charge the discontinuity will be present, which fits into the general expectation that the thermal phase transition of a fermionic system should be of the van der Waals (liquid-gas, Ising) type.

So far three distinct approaches aiming at capturing the stable phases of holographic fermionic matter have appeared: the electron star [10], Dirac hair [13] and the confined Fermi liquid model [14]. The electron star is essentially a charged fermion rewriting of the well-known Oppenheimer-Volkov equations for a neutron star in AdS background. The bulk is thus modeled as a semiclassical fluid. It is a controlled approximation in the certain limit of the parameter values. The mystery is its field theory dual: it is a hierarchically ordered (infinite) multiplet of fermionic liquids with stable quasiparticles [17]. On the other end of the spectrum is Dirac hair, which reduces the bulk fermion matter to a single radial harmonic. The Dirac hair approach is based on the truncation of the full non-local equations of motion. As a consequence the field theory dual is a single Fermi liquid, however its gravitational consistency properties are not yet fully understood. In [18] we have shown that Dirac hair and electron star can be regarded as the extreme points of a continuum of models, dialing from deep quantum - a single radial mode - to a classical regime - a very large occupation number - in the bulk. They correspond to two extreme phases in the field theory phase diagram: a multiplet of a very large number of Fermi liquids and a single Fermi liquid. The third approach [14] performs a Hartree summation of the exact quantum mechanical wave functions to capture the fermion density. While the paper [14] applies the Hartree method to a specific model (confined Fermi liquid, where the confinement is introduced through modifying the bulk geometry), the main idea can be used in any background. This approach is more general than the single-particle approach of [13] and it naturally extends the single harmonic Dirac hair state with a single Fermi surface to a state with multiple Fermi surfaces. Our main motivation is to construct a complementary model that extends from the other end — the semi-classical fluid — down to a state with a countable but large number of Fermi surfaces. We aim for a system which is general enough to encompass the middle ground between extreme quantum and extreme classical regimes in the original deconfined setup. In the recent model of “quantum electron star” [16] the same goal is set but the method used is different and is based on the deconfined limit of [14].

In constructing the WKB star, we were also guided by the strengths and weaknesses of these existing models. On the one hand, the Dirac hair is a fully quantum-mechanical model which shows its strength in particular near the boundary (the ultraviolet of the field theory) but becomes worse in the interior, i.e. close to the horizon (the infrared of the field theory) where density is high and the resulting state of matter cannot be well

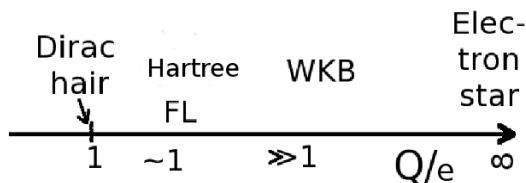


Figure 5. Applicability of various approximations as a function of the ratio of the fermion charge and the total charge of the system, Q/e : Dirac hair, confined Fermi liquid, our present WKB-model, electron star. Dirac hair and electron star are the simplest and most flexible approximations but limited to the extreme ends of the Q/e axis. Compare also to figure 10 in [18].

described by a single wave function. On the other hand, the electron star yields a very robust description of high-density matter in the interior but its sharp boundary at some radius r_c is clearly incompatible with a fully quantum description. It is thus obvious that the physically interesting model lies somewhere in-between the two approaches.

How to relate the electron star [10], Dirac hair [13] and the (confined) Hartree Fermi liquid [14] to our new phase diagram? All models use the same microscopic action for a Dirac fermion with charge e and mass m , but the system is approximated in different ways. The electron star is the fluid limit of the equations of motion, yielding the Oppenheimer-Volkov equations in the bulk. As explained in [18], this approximation is valid in the limit of infinite occupation number $N_{\text{WKB}} \rightarrow \infty$, $e \rightarrow 0$ with the total charge density fixed $Q = N_{\text{WKB}}e$. In addition, the mass $m \rightarrow 0$ while $\hat{m} = m/\sqrt{N_{\text{WKB}}}e$ is fixed. The Dirac hair departs from the opposite limit, treating the bulk fermion as a single collective excitation with $N_{\text{WKB}} = 1$. To obtain a macroscopic charge density one essentially has to take $e \gg 1$. Finally, the confined Fermi liquid of [14] and its deconfined version [16] improve on the Dirac Hair by using a standard Hartree summation of the non-interacting bulk Fermi gas. It works for all $N_{\text{WKB}} \sim \mathcal{O}(1)$ and this significantly increases the region of applicability but at the cost of substantial practical complications, in particular if one wishes to take into account the backreaction on the metric [16]. Our model takes a similar summation approach but simplifies the wave function calculation drastically by using the WKB approximation. This inherently assumes semiclassical dynamics and large number of energy levels $N_{\text{WKB}} \gg 1$ in the bulk. The WKB star is thus independent of [13] but draws heavily on the electron star and the dialing concept of [18]. Since we do *not* make the assumption of zero energy spacing $N_{\text{WKB}} \rightarrow \infty$ necessary for the fluid approximation, our model thus works well in the intermediate regime where N_{WKB} is finite but large compared to unity. This message is illustrated in figure 5, emphasizing the singular nature of both the electron star and the Dirac hair.

One obvious downside of the WKB star is that the WKB approximation breaks down when N_{WKB} , the occupation number, is low. In particular, it means that the accuracy of our method is lowest close to the phase transition to the RN phase. However, for reasons outlined in the section 5.2, we can argue that the order of the phase transition cannot change, i.e. the first-order singularity in the free energy will not be canceled out by the corrections to WKB. Our treatment is an improvement over the strict $N_{\text{WKB}} \rightarrow \infty$ limit of

the electron star model used in [12, 33] to analyze the phase transition, however it remains a task for further work to approach the transition point with a more accurate method which is not limited to large occupation numbers. The recent paper [38] constructs a solution with finite fermion density in AdS₄ without using WKB: this turns out to be much more involved, but allows one to move away from the large N_{WKB} regime.

The natural next step departing from this WKB treatment is to employ a fully quantum-mechanical density functional method. It is, in fact, not a significant complication compared to the approach of this paper: the recipe for computing the density n will be replaced by a somewhat more complicated functional of the gauge field and the metric, which needs to be computed iteratively. We anticipate that this will not alter the qualitative picture, although the numbers might change significantly. The main conclusion of our paper is that the singular fluid limit of bulk fermions when coupled to AdS gravity can lead to macroscopically anomalous results. Finite N_{WKB} corrections are crucial to get the correct answer.

Acknowledgments

This research was supported in part by a Spinoza Award (J. Zaanen) from the Netherlands Organization for Scientific Research (NWO) and the Dutch Foundation for Fundamental Research on Matter (FOM). We are grateful to H. Liu, S.S. Gubser and A. Karch for valuable discussions.

References

- [1] S.A. Hartnoll, *Lectures on holographic methods for condensed matter physics*, *Class. Quant. Grav.* **26** (2009) 224002 [[arXiv:0903.3246](#)] [[INSPIRE](#)].
- [2] J. McGreevy, *Holographic duality with a view toward many-body physics*, *Adv. High Energy Phys.* **2010** (2010) 723105 [[arXiv:0909.0518](#)] [[INSPIRE](#)].
- [3] H.V. Löhneysen, A. Rosch, M. Vojta and P. Wölfle, *Fermi-liquid instabilities at magnetic quantum phase transitions*, *Rev. Mod. Phys.* **79** (2007) 1015 [[cond-mat/0606317](#)].
- [4] M. Gurvitch and A.T. Fiory, *Resistivity of La_{1.825}Sr_{0.175}CuO₄ and YBa₂Cu₃O₇ to 1100 K: Absence of saturation and its implications*, *Phys. Rev. Lett.* **59** (1987) 1337.
- [5] A. Donos, J.P. Gauntlett, N. Kim and O. Varela, *Wrapped M5-branes, consistent truncations and AdS/CMT*, *JHEP* **12** (2010) 003 [[arXiv:1009.3805](#)] [[INSPIRE](#)].
- [6] O. DeWolfe, S.S. Gubser and C. Rosen, *Fermi surfaces in maximal gauged supergravity*, *Phys. Rev. Lett.* **108** (2012) 251601 [[arXiv:1112.3036](#)] [[INSPIRE](#)].
- [7] A. Donos, J.P. Gauntlett and C. Pantelidou, *Magnetic and electric AdS solutions in string- and M-theory*, *Class. Quant. Grav.* **29** (2012) 194006 [[arXiv:1112.4195](#)] [[INSPIRE](#)].
- [8] H. Liu, J. McGreevy and D. Vegh, *Non-Fermi liquids from holography*, *Phys. Rev. D* **83** (2011) 065029 [[arXiv:0903.2477](#)] [[INSPIRE](#)].
- [9] M. Čubrović, J. Zaanen and K. Schalm, *String Theory, Quantum Phase Transitions and the Emergent Fermi-Liquid*, *Science* **325** (2009) 439 [[arXiv:0904.1993](#)] [[INSPIRE](#)].

- [10] S.A. Hartnoll and A. Tavanfar, *Electron stars for holographic metallic criticality*, *Phys. Rev. D* **83** (2011) 046003 [[arXiv:1008.2828](#)] [[INSPIRE](#)].
- [11] J.P. Gauntlett, J. Sonner and D. Waldram, *Universal fermionic spectral functions from string theory*, *Phys. Rev. Lett.* **107** (2011) 241601 [[arXiv:1106.4694](#)] [[INSPIRE](#)].
- [12] S.A. Hartnoll and P. Petrov, *Electron star birth: a continuous phase transition at nonzero density*, *Phys. Rev. Lett.* **106** (2011) 121601 [[arXiv:1011.6469](#)] [[INSPIRE](#)].
- [13] M. Čubrović, J. Zaanen and K. Schalm, *Constructing the AdS Dual of a Fermi Liquid: AdS Black Holes with Dirac Hair*, *JHEP* **10** (2011) 017 [[arXiv:1012.5681](#)] [[INSPIRE](#)].
- [14] S. Sachdev, *A model of a Fermi liquid using gauge-gravity duality*, *Phys. Rev. D* **84** (2011) 066009 [[arXiv:1107.5321](#)] [[INSPIRE](#)].
- [15] R.C. Tolman, *Static solutions of Einstein's field equations for spheres of fluid*, *Phys. Rev. D* **55** (1939) 364.
- [16] A. Allais, J. McGreevy and S.J. Suh, *A quantum electron star*, *Phys. Rev. Lett.* **108** (2012) 231602 [[arXiv:1202.5308](#)] [[INSPIRE](#)].
- [17] S.A. Hartnoll, D.M. Hofman and D. Vegh, *Stellar spectroscopy: Fermions and holographic Lifshitz criticality*, *JHEP* **08** (2011) 096 [[arXiv:1105.3197](#)] [[INSPIRE](#)].
- [18] M. Cubrovic, Y. Liu, K. Schalm, Y.-W. Sun and J. Zaanen, *Spectral probes of the holographic Fermi groundstate: dialing between the electron star and AdS Dirac hair*, *Phys. Rev. D* **84** (2011) 086002 [[arXiv:1106.1798](#)] [[INSPIRE](#)].
- [19] N. Iqbal, H. Liu and M. Mezei, *Semi-local quantum liquids*, *JHEP* **04** (2012) 086 [[arXiv:1105.4621](#)] [[INSPIRE](#)].
- [20] S.A. Hartnoll, J. Polchinski, E. Silverstein and D. Tong, *Towards strange metallic holography*, *JHEP* **04** (2010) 120 [[arXiv:0912.1061](#)] [[INSPIRE](#)].
- [21] T. Faulkner, H. Liu, J. McGreevy and D. Vegh, *Emergent quantum criticality, Fermi surfaces and AdS₂*, *Phys. Rev. D* **83** (2011) 125002 [[arXiv:0907.2694](#)] [[INSPIRE](#)].
- [22] E. Gubankova et al., *Holographic fermions in external magnetic fields*, *Phys. Rev. D* **84** (2011) 106003 [[arXiv:1011.4051](#)] [[INSPIRE](#)].
- [23] D.F. Mross, J. McGreevy, H. Liu and T. Senthil, *A controlled expansion for certain non-Fermi liquid metals*, *Phys. Rev. B* **82** (2010) 045121 [[arXiv:1003.0894](#)] [[INSPIRE](#)].
- [24] G. Horowitz, A. Lawrence and E. Silverstein, *Insightful D-branes*, *JHEP* **07** (2009) 057 [[arXiv:0904.3922](#)] [[INSPIRE](#)].
- [25] L.D. Landau and E.M. Lifshitz, *Quantum Mechanics. Nonrelativistic theory*, Nauka, Moskva Russia (1989).
- [26] T. Faulkner, N. Iqbal, H. Liu, J. McGreevy and D. Vegh, *Strange metal transport realized by gauge/gravity duality*, *Science* **329** (2010) 1043 [[INSPIRE](#)].
- [27] T. Hartman and S.A. Hartnoll, *Cooper pairing near charged black holes*, *JHEP* **06** (2010) 005 [[arXiv:1003.1918](#)] [[INSPIRE](#)].
- [28] N. Iqbal and H. Liu, *Real-time response in AdS/CFT with application to spinors*, *Fortsch. Phys.* **57** (2009) 367 [[arXiv:0903.2596](#)] [[INSPIRE](#)].
- [29] L.D. Landau and E.M. Lifshitz, *Statistical Physics 2*, Nauka, Moskva Russia (1978).

- [30] N. Iqbal, H. Liu, M. Mezei and Q. Si, *Quantum phase transitions in holographic models of magnetism and superconductors*, *Phys. Rev. D* **82** (2010) 045002 [[arXiv:1003.0010](#)] [[INSPIRE](#)].
- [31] D. Voskresensky and A. Senatorov, *Rearrangement of the vacuum in strong electric and gravitational fields*, *Sov. J. Nucl. Phys.* **36** (1982) 208 [[INSPIRE](#)].
- [32] J.H. She and J. Zaanen, *BCS Superconductivity in Quantum Critical Metals*, *Phys. Rev. B* **80** (2009) 184518.
- [33] V.G.M. Puletti, S. Nowling, L. Thorlacius and T. Zingg, *Holographic metals at finite temperature*, *JHEP* **01** (2011) 117 [[arXiv:1011.6261](#)] [[INSPIRE](#)].
- [34] T. Faulkner and J. Polchinski, *Semi-holographic Fermi liquids*, *JHEP* **06** (2011) 012 [[arXiv:1001.5049](#)] [[INSPIRE](#)].
- [35] L. Huijse and S. Sachdev, *Fermi surfaces and gauge-gravity duality*, *Phys. Rev. D* **84** (2011) 026001 [[arXiv:1104.5022](#)] [[INSPIRE](#)].
- [36] N. Iqbal, H. Liu and M. Mezei, *Lectures on holographic non-Fermi liquids and quantum phase transitions*, [arXiv:1110.3814](#) [[INSPIRE](#)].
- [37] M. Čubrović, *Holography, Fermi surfaces and criticality*, Ph.D. Thesis, Leiden University, Leiden Netherlands (2013).
- [38] A. Allais and J. McGreevy, *How to construct a gravitating quantum electron star*, *Phys. Rev. D* **88** (2013) 066006 [[arXiv:1306.6075](#)] [[INSPIRE](#)].

Spectral probes of the holographic Fermi ground state: Dialing between the electron star and AdS Dirac hair

Mihailo Čubrović,^{*} Yan Liu,[†] Koenraad Schalm,[‡] Ya-Wen Sun,[§] and Jan Zaanen^{||}

Institute Lorentz for Theoretical Physics, Leiden University, P.O. Box 9506, Leiden 2300RA, The Netherlands

(Received 19 July 2011; published 6 October 2011)

We argue that the electron star and the anti-de Sitter (AdS) Dirac hair solution are two limits of the free charged Fermi gas in AdS. Spectral functions of holographic duals to probe fermions in the background of electron stars have a free parameter that quantifies the number of constituent fermions that make up the charge and energy density characterizing the electron star solution. The strict electron star limit takes this number to be infinite. The Dirac hair solution is the limit where this number is unity. This is evident in the behavior of the distribution of holographically dual Fermi surfaces. As we decrease the number of constituents in a fixed electron star background the number of Fermi surfaces also decreases. An improved holographic Fermi ground state should be a configuration that shares the qualitative properties of both limits.

DOI: [10.1103/PhysRevD.84.086002](https://doi.org/10.1103/PhysRevD.84.086002)

PACS numbers: 11.25.Tq, 04.40.Nr, 71.10.Hf

I. INTRODUCTION

The insight provided by the application of the anti-de Sitter/conformal field theory (AdS/CFT) correspondence to finite density Fermi systems has given brand-new perspectives on the theoretical robustness of non-Fermi liquids [1–3]; on an understanding of the non-perturbative stability of the regular Fermi liquid equivalent to order parameter universality for bosons [4,5]; and most importantly on the notion of fermionic criticality, Fermi systems with no scale. In essence strongly coupled conformally invariant Fermi systems are one answer to the grand theoretical question of fermionic condensed matter: *Are there finite density Fermi systems that do not refer at any stage to an underlying perturbative Fermi gas?*

It is natural to ask to what extent AdS/CFT can provide a more complete answer to this question. Assuming, almost tautologically, that the underlying system is strongly coupled and there is in addition some notion of a large N limit, the Fermi system is dual to classical general relativity with a negative cosmological constant coupled to charged fermions and electromagnetism. As AdS/CFT maps quantum numbers to quantum numbers, finite density configurations of the strongly coupled large N system correspond to solutions of this Einstein-Maxwell-Dirac theory with finite charge density. Since the AdS fermions are the only object carrying charge, and the gravity system is weakly coupled, one is immediately inclined to infer that the generic solution is a weakly coupled charged Fermi gas coupled to AdS gravity: in other words an AdS electron

star [6,7], the charged equivalent of a neutron star in asymptotically anti-de Sitter space [8,9].

Nothing can seem more straightforward. Given the total charge density Q of interest, one constructs the free fermionic wave functions in this system, and fills them one by one in increasing energy until the total charge equals Q . For macroscopic values of Q these fermions themselves will backreact on the geometry. One can compute this backreaction; it changes the potential for the free fermions at subleading order. Correcting the wave functions at this subleading order, one converges on the true solution order by order in the gravitational strength $\kappa^2 E_{\text{full system}}^2$. Here $E_{\text{full system}}$ is the energy carried by the Fermi system and κ^2 is the gravitational coupling constant $\kappa^2 = 8\pi G_{\text{Newton}}$ in the AdS gravity system. Perturbation theory in κ is dual to the $1/N$ expansion in the associated condensed matter system.

The starting point of the backreaction computation is to follow Tolman-Oppenheimer-Volkov (TOV) and use a Thomas-Fermi (TF) approximation for the lowest order one-loop contribution [6–9]. The Thomas-Fermi approximation applies when the number of constituent fermions making up the Fermi gas is infinite. For neutral fermions this equates to the statement that the energy-spacing between the levels is negligible compared to the chemical potential associated with Q , $\Delta E/\mu \rightarrow 0$. For charged fermions the Thomas-Fermi limit is more direct: it is the limit $q/Q \rightarrow 0$, where q is the charge of each constituent fermion.¹

This has been the guiding principle behind the approaches [6–11] and the recent papers [12,13], with the natural assumption that all corrections beyond Thomas-Fermi are small quantitative changes rather than qualitative

^{*}cubrovic@lorentz.leidenuniv.nl

[†]liu@lorentz.leidenuniv.nl

[‡]kschalm@lorentz.leidenuniv.nl

[§]sun@lorentz.leidenuniv.nl

^{||}jan@lorentz.leidenuniv.nl

¹For a fermion in an harmonic oscillator potential $E_n = \hbar(n - 1/2)\omega$, thus $\Delta E/E_{\text{total}} = 1/\sum_1^N (n - 1/2) = 2/N^2$.

ones. On closer inspection, however, this completely natural TF-electron star poses a number of puzzles. The most prominent perhaps arises from the AdS/CFT correspondence finding that every normalizable fermionic wave function in the gravitational bulk corresponds to a fermionic quasiparticle excitation in the dual condensed matter system. In particular occupying a particular wave function is dual to having a particular Fermi-liquid state [4]. In the Thomas-Fermi limit the gravity dual thus describes an infinity of Fermi liquids, whereas the generic condensed matter expectation would have been that a single (few) liquid(s) would be the generic ground state away from the strongly coupled fermionic quantum critical point at zero charge density. This zoo of Fermi surfaces is already present in the grand canonical approaches at fixed μ (extremal AdS-Reissner-Nordström [AdS-RN] black holes) [3] and a natural explanation would be that this is a large N effect. This idea, that the gravity theory is dual to a condensed matter system with N species of fermions, and increasing the charge density “populates” more and more of the distinct species of Fermi liquids, is very surprising from the condensed matter perspective. Away from criticality one would expect the generic ground state to be a single Fermi liquid or some broken state due to pairing. To pose the puzzle sharply, once one has a fermionic quasiparticle one should be able to adiabatically continue it to a free Fermi gas, which would imply that the free limit of the strongly coupled fermionic CFT is not a single but a system of order N fermions with an ordered distribution of Fermi momenta. A possible explanation of the multitude of Fermi surfaces that is consistent with a single Fermi surface at weak coupling is that AdS/CFT describes so-called “deconfined and/or fractionalized Fermi liquids” where the number of Fermi surfaces is directly tied to the coupling strength [12–16]. It would argue that fermionic quantum criticality goes hand in hand with fractionalization for which there is currently scant experimental evidence.

The second puzzle is more technical. Since quantum numbers in the gravity system equal the quantum numbers in the dual condensed matter system, one is inclined to infer that each subsequent AdS fermion wave function has incrementally higher energy than the previous one. Yet analyticity of the Dirac equation implies that all normalizable wave functions must have strictly vanishing energy [17]. It poses the question how the order in which the fermions populate the Fermi gas is determined.

The third puzzle is that in the Thomas-Fermi limit the Fermi gas is gravitationally strictly confined to a bounded region; famously, the TOV-neutron star has an edge. In AdS/CFT, however, all information about the dual condensed matter system is read off at asymptotic AdS infinity. Qualitatively, one can think of AdS/CFT as an “experiment” analogous to probing a spatially confined Fermi gas with a tunneling microscope held to the exterior

of the trap. Extracting the information of the dual condensed matter system is probing the AdS Dirac system confined by a gravitoelectric trap instead of a magneto-optical trap for cold atoms. Although the Thomas-Fermi limit should reliably capture the charge and energy densities in the system, its abrupt nonanalytic change at the edge (in a trapped system) and effective absence of a density far away from the center are well known to cause qualitative deficiencies in the description of the system. Specifically Friedel oscillations—quantum interference in the outside tails of the charged fermion density, controlled by the ratio q/Q and measured by a tunneling microscope—are absent. Analogously, there could be qualitative features in the AdS asymptotics of both the gravitoelectric background and the Dirac wave functions in that adjusted background that are missed by the TF approximation. The AdS asymptotics in turn *specify* the physics of the dual condensed matter system and since our main interest is to use AdS/CFT to understand quantum critical fermion systems where q/Q is finite, the possibility of a qualitative change inherent in the Thomas-Fermi limit should be considered.

There is another candidate AdS description of the dual of a strongly coupled finite density Fermi system: the AdS black hole with Dirac hair [4,5]. One arrives at this solution when one starts one’s reasoning from the dual condensed matter system, rather than the Dirac fields in AdS gravity. Insisting that the system collapses to a generic single species Fermi-liquid ground state, the dual gravity description is that of an AdS Einstein-Dirac-Maxwell system with a single nonzero normalizable Dirac wave function. To have a macroscopic backreaction the charge of this single Dirac field must be macroscopic. The intuitive way to view this solution is as the other simplest approximation to free Fermi gas coupled to gravity. What we mean is that the full gravitoelectric response is in all cases controlled by the total charge Q of the solution: as charge is conserved it is proportional to the constituent charge q times the number of fermions $n_{F_{\text{AdS}}}$ and the two simple limits correspond to $n_F \rightarrow \infty$, $q \rightarrow 0$ with $Q = qn_F$ fixed or $n_F \rightarrow 1$, $q \rightarrow Q$. The former is the Thomas-Fermi electron star, the latter is the AdS Dirac hair solution. In the context of AdS/CFT there is a significant difference between the two solutions in that the Dirac hair solution clearly does not give rise to the puzzles 1, 2 and 3: there is by construction no zoo of Fermi surfaces and therefore no ordering. Moreover since the wave function is demanded to be normalizable, it manifestly encodes the properties of the system at the AdS boundary. On the other hand the AdS Dirac hair solution does pose the puzzle that under normal conditions the total charge Q is much larger than the constituent charge q both from the gravity/string theory point of view and the condensed matter perspective. Generically one would expect a Fermi gas electron star rather than Dirac hair.

In this paper we shall provide evidence for this point of view that the AdS electron star and the AdS Dirac hair solution are two limits of the same underlying system. Specifically we shall show that (1) the electron star solution indeed has the constituent charge as a free parameter which is formally sent to zero to obtain the Thomas-Fermi approximation. (2) The number of normalizable wave functions in the electron star depend on the value of the constituent charge q . We show this by computing the electron star spectral functions. They depend in similar way on q as the first AdS/CFT Fermi system studies in an AdS-RN background. In the formal limit where $q \rightarrow Q$, only one normalizable mode remains and the spectral function wave function resembles the Dirac hair solution, underlining their underlying equivalence. Since both approximations have qualitative differences as a description of the AdS dual to strongly coupled fermionic systems, we argue that an improved approximation that has characteristics of both is called for.

The results here are complimentary to and share an analysis of electron star spectral functions with the two recent papers [12,13] that appeared in the course of this work (see also [18] for fermion spectral functions in general Lifshitz backgrounds). Our motivation to probe the system away from the direct electron star limit differs: we have therefore been more precise in defining this limit and in the analysis of the Dirac equation in the electron star background.

II. EINSTEIN-MAXWELL THEORY COUPLED TO CHARGED FERMIONS

The Lagrangian that describes both the electron star and Dirac hair approximation is Einstein-Maxwell theory coupled to charged matter

$$S = \int d^4x \sqrt{-g} \left[\frac{1}{2\kappa^2} \left(R + \frac{6}{L^2} \right) - \frac{1}{4q^2} F^2 + \mathcal{L}_{\text{matter}}(e_\mu^A, A_\mu) \right], \quad (2.1)$$

where L is the AdS radius, q is the electric charge, and κ is the gravitational coupling constant. It is useful to scale the electromagnetic interaction to be of the same order as the gravitational interaction and measure all lengths in terms of the AdS radius L ,

$$g_{\mu\nu} \rightarrow L^2 g_{\mu\nu}, \quad A_\mu \rightarrow \frac{qL}{\kappa} A_\mu. \quad (2.2)$$

The system then becomes

$$S = \int d^4x \sqrt{-g} \left[\frac{L^2}{2\kappa^2} \left(R + 6 - \frac{1}{2} F^2 \right) + L^4 \mathcal{L}_{\text{matter}} \left(L e_\mu^A, \frac{qL}{\kappa} A_\mu \right) \right]. \quad (2.3)$$

Note that in the rescaled variables the effective charge of charged matter now depends on the ratio of the electromagnetic to gravitational coupling constant, $q_{\text{eff}} = qL/\kappa$. For the case of interest, charged fermions, the Lagrangian in these variables is

$$L^4 \mathcal{L}_{\text{fermions}} \left(L e_\mu^A, \frac{qL}{\kappa} A_\mu \right) = -\frac{L^2}{\kappa^2} \bar{\Psi} \left[e_A^\mu \Gamma^A \left(\partial_\mu + \frac{1}{4} \omega_\mu^{BC} \Gamma_{BC} - i \frac{qL}{\kappa} A_\mu \right) - m L \right] \Psi, \quad (2.4)$$

where $\bar{\Psi}$ is defined as $\bar{\Psi} = i\Psi^\dagger \Gamma^0$. Compared to the conventional normalization the Dirac field has been made dimensionless $\Psi = \kappa\sqrt{L}\psi_{\text{conventional}}$. With this normalization all terms in the action have a factor L^2/κ^2 and it will therefore scale out of the equations of motion

$$R_{\mu\nu} - \frac{1}{2} g_{\mu\nu} R - 3g_{\mu\nu} = \left(F_{\mu\rho} F_\nu{}^\rho - \frac{1}{4} g_{\mu\nu} F_{\rho\sigma} F^{\rho\sigma} + T_{\mu\nu}^{\text{fermions}} \right), \\ D_\mu F^{\mu\nu} = -q_{\text{eff}} J_{\text{fermions}}^\nu \quad (2.5)$$

with

$$T_{\mu\nu}^{\text{fermions}} = \frac{1}{2} \bar{\Psi} e_{A(\mu} \Gamma^A \left[\partial_{\nu)} + \frac{1}{4} \omega_{\nu)}^{BC} \Gamma_{BC} - i \frac{qL}{\kappa} A_{\nu)} \right] \Psi - \frac{\kappa^2 L^2}{2} g_{\mu\nu} \mathcal{L}_{\text{fermions}}, \quad (2.6)$$

$$J_{\text{fermions}}^\nu = i \bar{\Psi} e_A^\nu \Gamma^A \Psi, \quad (2.7)$$

where the symmetrization is defined as $B_{(\mu} C_{\nu)} = B_\mu C_\nu + B_\nu C_\mu$ and the Dirac equation

$$\left[e_A^\mu \Gamma^A \left(\partial_\mu + \frac{1}{4} \omega_\mu^{BC} \Gamma_{BC} - i \frac{qL}{\kappa} A_\mu \right) - m L \right] \Psi = 0. \quad (2.8)$$

The stress-tensor and current are to be evaluated in the specific state of the system. For a single excited wave function, obeying (2.8), this gives the AdS Dirac hair solution constructed in [4]. (More specifically, the Dirac hair solution consists of a radially isotropic set of wave functions with identical momentum size $|\vec{k}| = \sqrt{k_x^2 + k_y^2}$, such that the Pauli principle plays no role.) For multiple occupied fermion states, even without backreaction due to gravity, adding the contributions of each separate solution to (2.8) rapidly becomes very involved. In such a many-body system, the collective effect of the multiple occupied fermion states is better captured in a ‘‘fluid’’ approximation

$$T_{\mu\nu}^{\text{fluid}} = (\rho + p) u_\mu u_\nu + p g_{\mu\nu}, \quad N_\mu^{\text{fluid}} = n u_\mu \quad (2.9)$$

with

$$\rho = \langle u^\mu T_{\mu\nu} u^\nu \rangle_{\text{matter only}}, \quad n = -\langle u_\mu J^\mu \rangle_{\text{matter only}}. \quad (2.10)$$

In the center-of-mass rest frame of the multiple fermion system [$u_\mu = (e_{t_0}, 0, 0, 0)$], the expressions for the stress-tensor and charge density are given by the one-loop equal-time expectation values (as opposed to time-ordered correlation functions)

$$\rho = \left\langle \bar{\Psi}(t) e_0^t \Gamma^0 \left(\partial_t + \frac{1}{4} \omega_t^{AB} \Gamma_{AB} - i q_{\text{eff}} A_t \right) \Psi(t) \right\rangle. \quad (2.11)$$

By the optical theorem the expectation value is equal to twice the imaginary part of the Feynman propagator²

$$\begin{aligned} \rho(r) &= \lim_{\beta \rightarrow \infty} 2 \int \frac{d^3 k d\omega}{(2\pi)^4} [\omega(r) - \mu_{\text{loc}}(r)] \text{Im Tr} i \Gamma^0 G_F^\beta(\omega, k) \\ &= \lim_{\beta \rightarrow \infty} \int \frac{d k d\omega}{4\pi^3} [k^2(\omega - \mu)] \left[\frac{1}{2} - \frac{1}{2} \tanh\left(\frac{\beta}{2}(\omega - \mu)\right) \right] \text{Tr}(i \Gamma^0)^2 \frac{\kappa^2}{L^2} \pi \delta((\omega - \mu) - \sqrt{k^2 + (mL)^2}) \\ &= \lim_{\beta \rightarrow \infty} \frac{\kappa^2}{\pi^2 L^2} \int d\omega f_{FD}(\beta(\omega - \mu)) [(\omega - \mu)^2 - (mL)^2] [\omega - \mu] \frac{(\omega - \mu) \theta(\omega - \mu - mL)}{\sqrt{(\omega - \mu)^2 - (mL)^2}} \\ &= \frac{1}{\pi^2} \frac{\kappa^2}{L^2} \int_{mL}^{\mu_{\text{loc}}} dE E^2 \sqrt{E^2 - (mL)^2}. \end{aligned} \quad (2.13)$$

The normalization κ^2/L^2 follows from the unconventional normalization of the Dirac field in Eq. (2.4).⁴ Similarly

$$\begin{aligned} n &= \frac{1}{\pi^2} \frac{\kappa^2}{L^2} \int_{mL}^{\mu_{\text{loc}}} dE E \sqrt{E^2 - (mL)^2} \\ &= \frac{1}{3\pi^2} \frac{\kappa^2}{L^2} (\mu_{\text{loc}}^3 - (mL)^3)^{3/2}. \end{aligned} \quad (2.14)$$

The adiabatic approximation is valid for highly localized wave functions, i.e. the expression must be dominated by high momenta (especially in the radial direction). The exact expression on the other hand will not have a

²From unitarity for the S matrix $S^\dagger S = 1$ one obtains the optical theorem $T^\dagger T = 2 \text{Im} T$ for the transition matrix T defined as $S \equiv 1 + iT$.

³That is, one can redefine spinors $\chi(r) = f(r)\Psi(r)$ such that the connection term is no longer present in the equation of motion.

⁴One can see this readily by converting the dimensionless definition of ρ , Eq. (2.11), to the standard dimension. Using capitals for dimensionless quantities and lower-case for dimensional ones,

$$\begin{aligned} \rho &\sim \langle \Psi \partial_T \Psi \rangle \sim \kappa^2 L^2 \langle \psi \partial_t \psi \rangle \\ &\sim \kappa^2 L^2 \int_m^\mu d\epsilon \epsilon^2 \sqrt{\epsilon^2 - m^2} \\ &\sim \frac{\kappa^2}{L^2} \int_{mL}^{\mu L} dE E^2 \sqrt{E^2 - (mL)^2} \end{aligned}$$

with $\mu L = \mu_{\text{loc}}$ above.

$$\rho = \lim_{t \rightarrow t'} 2 \text{Im Tr} \left[e_0^t \Gamma^0 \left(\partial_t + \frac{1}{4} \omega_t^{AB} \Gamma_{AB} - i q_{\text{eff}} A_t \right) G_F^{\text{AdS}}(t', t) \right]. \quad (2.12)$$

In all situations of interest, all background fields will only have dependence on the radial AdS direction; in that case the spin connection can be absorbed in the normalization of the spinor wave function.³ In an adiabatic approximation for the radial dependence of e_{t_0} and A_t —where $\mu_{\text{loc}}(r) = q_{\text{eff}} e_0^t(r) A_t(r)$ and $\omega(r) = -i e_0^t(r) \partial_t$;—this yields the known expression for a many-body fermion system at finite chemical potential,

continuum of solutions to the harmonic condition $-\Gamma^0 \omega + \Gamma^i k_i + \Gamma^z k_z - \Gamma^0 \mu_{\text{loc}} - imL = 0$. Normalizable solutions to the AdS Dirac equations only occur at discrete momenta—one can think of the gravitational background as a potential well. The adiabatic approximation is therefore equivalent to the Thomas-Fermi approximation for a Fermi gas in a box.

To get an estimate for the parameter range where the adiabatic approximation holds, consider the adiabatic bound $\partial_r \mu_{\text{loc}}(r) \ll \mu_{\text{loc}}(r)^2$. Using the field equation for $A_0 = \mu_{\text{loc}}/q_{\text{eff}}$,

$$\partial_r^2 \mu_{\text{loc}} \sim q_{\text{eff}}^2 n, \quad (2.15)$$

this bound is equivalent to requiring

$$\begin{aligned} \partial_r^2 \mu_{\text{loc}} \ll \partial_r \mu_{\text{loc}}^2 &\Rightarrow \left(\frac{qL}{\kappa}\right)^2 n \ll 2\mu_{\text{loc}} \partial_r \mu_{\text{loc}} \\ &\Rightarrow \left(\frac{qL}{\kappa}\right)^2 n \ll \mu_{\text{loc}}^3, \end{aligned} \quad (2.16)$$

where in the last line we used the original bound again. If the chemical potential scale is considerably higher than the mass of the fermion, we may use (2.14) to approximate $n \sim \frac{\kappa^2}{L^2} \mu_{\text{loc}}^3$. Thus the adiabatic bound is equivalent to

$$q = \frac{q_{\text{eff}} \kappa}{L} \ll 1, \quad (2.17)$$

the statement that the constituent charge of the fermions is infinitesimal. Note that in the rescaled action (2.3) and (2.4), L/κ plays the role of $1/\hbar$, and Eq. (2.17) is thus equivalent to the semiclassical limit $\hbar \rightarrow 0$ with q_{eff} fixed. Since AdS/CFT relates $L/\kappa \sim N_c$ this acquires the meaning in the context of holography that there is a large N_c scaling limit [12,13] of the CFT with fermionic operators where the renormalization group (RG) flow is ‘‘adiabatic.’’ Returning to the gravitational description the additional assumption that the chemical potential is much larger than the mass is equivalent to

$$\begin{aligned} \frac{Q_{\text{phys}}^{\text{total}}}{V_{\text{spatial AdS}}} &= \frac{LQ_{\text{eff}}^{\text{total}}}{\kappa V_{\text{spatial AdS}}} \\ &\equiv \frac{L}{\kappa V_{\text{spatial AdS}}} \int dr \sqrt{-g_{\text{induced}}}(q_{\text{eff}} n) \\ &\simeq \frac{1}{V_{\text{spatial AdS}}} \int dr \sqrt{-g} \frac{q_{\text{eff}} \kappa}{L} \mu_{\text{loc}}^3(r) \gg q(mL)^3. \end{aligned} \quad (2.18)$$

This implies that the total charge density in AdS is much larger than that of a single charged particle (as long as $mL \sim 1$). The adiabatic limit is therefore equivalent to a thermodynamic limit where the Fermi gas consists of an infinite number of constituents, $n \rightarrow \infty$, $q \rightarrow 0$ such that the total charge $Q \sim nq$ remains finite.

The adiabatic limit of a many-body fermion system coupled to gravity are the Tolman-Oppenheimer-Volkov equations. Solving this in asymptotically AdS gives us the charged neutron or electron star constructed in [7]. Knowing the quantitative form of the adiabatic limit, it is now easy to distinguish the electron star solution from the ‘‘single wave function’’ Dirac hair solution. The latter is trivially the single particle limit $n \rightarrow 1$, $q \rightarrow Q$ with the total charge Q finite. The electron star and Dirac hair black hole are opposing limit-solutions of the same system. We shall now make this connection more visible by identifying a formal dialing parameter that interpolates between the two solutions.

To do so we shall need the full adiabatic Tolman-Oppenheimer-Volkov equations for the AdS electron star [7]. Since the fluid is homogeneous and isotropic, the background metric and electrostatic potential will respect these symmetries and will be of the form [recall that we are already using ‘‘dimensionless’’ lengths, Eq. (2.2)]

$$\begin{aligned} ds^2 &= -f(r)dt^2 + g(r)dr^2 + r^2(dx^2 + dy^2), \\ A &= h(r)dt, \end{aligned} \quad (2.19)$$

where $f(r)$, $g(r)$, $h(r)$ are functions of r ; the horizon is located at $r = 0$ and the boundary is at $r = \infty$. Combining this ansatz with a rescaling $mL = q_{\text{eff}} \hat{m}$ the bosonic background equations of motion become [7]

$$\begin{aligned} \frac{1}{r} \left(\frac{f'}{f} + \frac{g'}{g} \right) - \frac{gh\sigma}{\sqrt{f}} &= 0, \\ \rho &= \frac{q_{\text{eff}}^4 \kappa^2}{\pi^2 L^2} \int_{\hat{m}}^{h/\sqrt{f}} d\epsilon \epsilon^2 \sqrt{\epsilon^2 - \hat{m}^2}, \\ \frac{f'}{rf} + \frac{h^2}{2f} - g(3+p) + \frac{1}{r^2} &= 0, \\ \sigma &= \frac{q_{\text{eff}}^4 \kappa^2}{\pi^2 L^2} \int_{\hat{m}}^{h/\sqrt{f}} d\epsilon \epsilon \sqrt{\epsilon^2 - \hat{m}^2}, \\ h'' + \frac{2}{r} h' - \frac{g\sigma}{\sqrt{f}} \left(\frac{rhh'}{2} + f \right) &= 0, \quad -p = \rho - \frac{h}{\sqrt{f}} \sigma, \end{aligned} \quad (2.20)$$

where we have used that $\mu_{\text{loc}} = q_{\text{eff}} h/\sqrt{f}$ and $\sigma = nq_{\text{eff}}$ is the rescaled local charge density. What one immediately notes is that the Tolman-Oppenheimer-Volkov equations of motion for the background only depend on the parameters $\hat{\beta} \equiv \frac{q_{\text{eff}}^4 \kappa^2}{\pi^2 L^2}$ and \hat{m} , whereas the original Lagrangian and the fermion equation of motion also depend on $q_{\text{eff}} = (\frac{\pi^2 L^2 \hat{\beta}}{\kappa^2})^{1/4}$. It is therefore natural to guess that the parameter $q_{\text{eff}} = qL/\kappa$ will be the interpolating parameter away from the adiabatic electron star limit toward the Dirac hair black hole (BH).

Indeed in these natural electron star variables the adiabatic bound (2.17) translates into

$$\hat{\beta} \ll \frac{L^2}{\kappa^2} = \frac{q_{\text{eff}}^2}{q^2}. \quad (2.21)$$

Thus we see that for a given electron star background with $\hat{\beta}$ fixed decreasing κ/L improves the adiabatic fluid approximation whereas increasing κ/L makes the adiabatic approximation poorer and poorer. ‘‘Dialing κ/L up/down’’ therefore *interpolates* between the electron star and the Dirac hair BH. Counterintuitively improving adiabaticity by decreasing κ/L corresponds to increasing q_{eff} for fixed q , but this is just a consequence of recasting the system in natural electron star variables. A better way to view improving adiabaticity is to decrease the microscopic charge q but while keeping q_{eff} fixed; this shows that a better way to think of q_{eff} is as the total charge rather than the effective constituent charge.

The parameter $\kappa/L = q/q_{\text{eff}}$ parametrizes the gravitational coupling strength in units of the AdS curvature, and one might worry that ‘‘dialing κ/L up’’ pushes one outside the regime of classical gravity. This is not the case. One can easily have $\hat{\beta} \gg 1$ and tune κ/L toward or away from the adiabatic limit within the regime of classical gravity. From Eq. (2.17) we see that the edge of validity of the adiabatic regime $\hat{\beta} \simeq L^2/\kappa^2$ is simply equivalent to a microscopic charge $q = 1$ which clearly has a classical gravity description. It is not hard to see that the statement above is the equivalent of changing the level splitting in the Fermi gas, while keeping the overall energy/charge fixed. In a Fermi

gas microscopically both the overall energy and the level splitting depends on \hbar . Naively increasing \hbar increases both, but one can move away from the adiabatic limit either by decreasing the overall charge density, keeping \hbar fixed, or by keeping the charge density fixed and raising \hbar . Using again the analogy between κ/L and \hbar , the electron star situation is qualitatively the same, where one should think of $\hat{\beta} \sim q^4 L^2 / \kappa^2$ parametrizing the microscopic charge. One can either insist on keeping κ/L fixed and *increase* the microscopic charge $\hat{\beta}$ to increase the level splitting or one can keep $\hat{\beta}$ fixed and increase κ/L . In the electron star, however, the background geometry changes with $\hat{\beta}$ in addition to the level splitting, and it is therefore more straightforward to keep $\hat{\beta}$ and the geometry fixed, while dialing κ/L .

We will now give evidence for our claim that the electron star and Dirac hair solution are two opposing limits. To do so, we need to identify an observable that goes either beyond the adiabatic background approximation or beyond the single particle approximation. Since the generic intermediate state is still a many-body fermion system, the more natural starting point is the electron star background and to perturb away from there. Realizing then that the fermion equation of motion already depends directly on the dialing parameter q_{eff} the obvious observables are the single fermion spectral functions in the electron star background. Since one must specify a value for q_{eff} to compute these, they directly probe the microscopic charge of the fermion and are thus always beyond the strict electron star limit $q \rightarrow 0$. In the next two sections we will compute these and show that they indeed reflect the interpretation of q_{eff} as the interpolating parameter between the electron star and Dirac hair BH.

III. FERMION SPECTRAL FUNCTIONS IN THE ELECTRON STAR BACKGROUND

To compute the fermion spectral functions in the electron star background we shall choose a specific representative of the family of electron stars parametrized by $\hat{\beta}$ and \hat{m} . Rather than using $\hat{\beta}$ and \hat{m} the metric of an electron star is more conveniently characterized by its Lifshitz-scaling behavior near the interior horizon $r \rightarrow 0$. From the field equations (2.20) the limiting interior behavior of $f(r)$, $g(r)$, $h(r)$ is

$$f(r) = r^{2z} + \dots, \quad g(r) = \frac{g_\infty}{r^2} + \dots, \quad h(r) = h_\infty r^z + \dots \quad (3.1)$$

The scaling behavior is determined by the dynamical critical exponent z , which is a function of $\hat{\beta}$, \hat{m} [7] and it is conventionally used to classify the metric instead of $\hat{\beta}$. The full electron star metric is then generated from this horizon scaling behavior by integrating up an irrelevant RG-flow [19,20]

$$\begin{aligned} f &= r^{2z}(1 + f_1 r^{-\alpha} + \dots), \\ g &= \frac{g_\infty}{r^2}(1 + g_1 r^{-\alpha} + \dots), \\ h &= h_\infty r^z(1 + h_1 r^{-\alpha} + \dots) \end{aligned} \quad (3.2)$$

with

$$\alpha = \frac{2+z}{2} - \frac{\sqrt{9z^3 - 21z^2 + 40z - 28 - \hat{m}^2 z(4-3z)^2}}{2\sqrt{(1-\hat{m}^2)z-1}}. \quad (3.3)$$

Scaling $f_1 \rightarrow b f_1$ is equal to a coordinate transformation $r \rightarrow b^{1/\alpha} r$ and $t \rightarrow b^{z/\alpha} t$, and the sign of f_1 is fixed to be negative in order to be able to match onto an asymptotically AdS₄ solution. Thus $f_1 = -1$ and g_1 and h_1 are then uniquely determined by the equations of motion.

Famously, integrating the equations of motion up the RG-flow outward toward the boundary fails at a finite distance r_s . This is the edge of the electron star. Beyond the edge of the electron star, there is no fluid present and the spacetime is that of an AdS₄-RN black hole with the metric

$$f = c^2 r^2 - \frac{\hat{M}}{r} + \frac{\hat{Q}^2}{2r^2}, \quad g = \frac{c^2}{f}, \quad h = \hat{\mu} - \frac{\hat{Q}}{r}. \quad (3.4)$$

Demanding the full metric is smooth at the radius of electron star r_s determines the constants c , \hat{M} , and \hat{Q} . The dual field theory is defined on the plane $ds^2 = -c^2 dt^2 + dx^2 + dy^2$.

The specific electron star background we shall choose without loss of generality is the one with $z = 2$, $\hat{m} = 0.36$ (Fig. 1),⁵ smoothly matched at $r_s \simeq 4.25252$ onto an AdS-RN black hole.

The CFT fermion spectral functions now follow from solving the Dirac equation in this background [1,2]

$$\left[e_A^\mu \Gamma^A \left(\partial_\mu + \frac{1}{4} \omega_{\mu AB} \Gamma^{AB} - i q_{\text{eff}} A_\mu \right) - m_{\text{eff}} \right] \Psi = 0, \quad (3.5)$$

where q_{eff} and m_{eff} in terms of the parameters of the electron star equal

$$\begin{aligned} q_{\text{eff}} &= \left(\frac{\pi^2 L^2 \hat{\beta}}{\kappa^2} \right)^{1/4}, \\ m_{\text{eff}} &= q_{\text{eff}} \hat{m} = \hat{m} \left(\frac{\pi^2 L^2 \hat{\beta}}{\kappa^2} \right)^{1/4}. \end{aligned} \quad (3.6)$$

In other words, we choose the same mass and charge for the probe fermion and the constituent fermions of the electron star.⁶ For a given electron star background, i.e. a

⁵This background has $c \simeq 1.021$, $\hat{M} \simeq 3.601$, $\hat{Q} \simeq 2.534$, $\hat{\mu} \simeq 2.132$, $\hat{\beta} \simeq 19.951$, $g_\infty \simeq 1.887$, $h_\infty = 1/\sqrt{2}$, $\alpha \simeq -1.626$, $f_1 = -1$, $g_1 \simeq -0.4457$, $h_1 \simeq -0.6445$.

⁶One could of course choose a different probe mass and charge, corresponding to an extra charged fermion in the system. However, even though the electron star only cares about the equation of state, this would probably not be a self-consistent story as this extra fermion should also backreact.

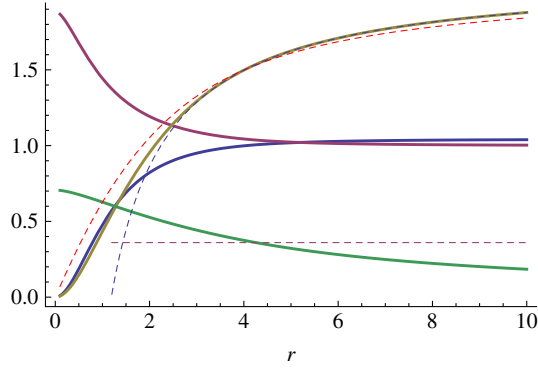


FIG. 1 (color online). Electron star metric for $z = 2$, $\hat{m} = 0.36$, $c \approx 1.021$, $\hat{M} \approx 3.601$, $\hat{Q} \approx 2.534$, $\hat{\mu} \approx 2.132$ compared to pure AdS. Shown are $f(r)/r^2$ (blue), $r^2 g(r)$ (red), and $h(r)$ (orange). The asymptotic AdS-RN value of $h(r)$ is the dashed blue line. For future use we have also given $\mu_{\text{loc}} = h/\sqrt{f}$ (green) and $\mu_{q_{\text{eff}}} = \sqrt{g^{ii} h}/\sqrt{f}$ (red dashed). At the edge of the star $r_s \approx 4.253$ (the intersection of the purple dashed line setting the value of m_{eff} with μ_{loc}) one sees the convergence to pure AdS in the constant asymptotes of $f(r)/r^2$ and $r^2 g(r)$.

fixed $\hat{\beta}$, \hat{m} the fermion spectral function will therefore depend on the ratio L/κ . For $L/\kappa \gg \hat{\beta}^{1/2}$ the poles in these spectral functions characterize the occupied states in a many-body gravitational Fermi system that is well approximated by the electron star. As L/κ is lowered for fixed $\hat{\beta}$ the electron star background becomes a poorer and poorer approximation to the true state and we should see this reflected in both the number of poles in the spectral function and their location.

Projecting the Dirac equation onto two-component Γ^z eigenspinors

$$\Psi_{\pm} = (-g^{rr})^{-(1/4)} e^{-i\omega t + ik_x x^i} \begin{pmatrix} y_{\pm} \\ z_{\pm} \end{pmatrix} \quad (3.7)$$

and using isotropy to set $k_y = 0$, one can choose a basis of Dirac matrices where one obtains two decoupled sets of two simple coupled equations [1]

$$\sqrt{g_{ii} g^{rr}} (\partial_r \mp m_{\text{eff}} \sqrt{g_{rr}}) y_{\pm} = \mp i(k_x - u) z_{\pm}, \quad (3.8)$$

$$\sqrt{g_{ii} g^{rr}} (\partial_r \pm m_{\text{eff}} \sqrt{g_{rr}}) z_{\pm} = \pm i(k_x + u) y_{\pm}, \quad (3.9)$$

where $u = \sqrt{\frac{g_{ii}}{-g_{tt}}} (\omega + q_{\text{eff}} h)$. In this basis of Dirac matrices the CFT Green's function $G = \langle \bar{\mathcal{O}}_{\psi_+} i\gamma^0 \mathcal{O}_{\psi_+} \rangle$ equals

$$G = \lim_{\epsilon \rightarrow 0} \epsilon^{-2mL} \begin{pmatrix} \xi_+ & 0 \\ 0 & \xi_- \end{pmatrix} \Big|_{r=(1/\epsilon)}, \quad \text{where } \xi_+ = \frac{iy_-}{z_+}, \quad (3.10)$$

$$\xi_- = -\frac{iz_-}{y_+}.$$

Rather than solving the coupled equations (3.8) it is convenient to solve for ξ_{\pm} directly [1],

$$\sqrt{\frac{g_{ii}}{g_{rr}}} \partial_r \xi_{\pm} = -2m_{\text{eff}} \sqrt{g_{ii}} \xi_{\pm} \mp (k_x \mp u) \pm (k_x \pm u) \xi_{\pm}^2. \quad (3.11)$$

For the spectral function $A = \text{Im Tr} G_R$ we are interested in the retarded Green's function. This is obtained by imposing infalling boundary conditions near the horizon $r = 0$. Since the electron star is a “zero-temperature” solution this requires a more careful analysis than for a generic horizon. To ensure that the numerical integration we shall perform to obtain the full spectral function has the right infalling boundary conditions, we first solve Eq. (3.11) to first subleading order around $r = 0$. There are two distinct branches. When $\omega \neq 0$ and $k_x r/\omega$, r^2/ω is small, the infalling boundary condition near the horizon $r = 0$ is (for $z = 2$)

$$\xi_+(r) = i - i \frac{k_x r}{\omega} + i \frac{(k_x^2 - 2im_{\text{eff}}\omega)r^2}{2\omega^2} - i \frac{f_1 k_x r^{1-\alpha}}{2\omega} + \dots$$

$$\xi_-(r) = i + i \frac{k_x r}{\omega} + i \frac{(k_x^2 - 2im_{\text{eff}}\omega)r^2}{2\omega^2} + i \frac{f_1 k_x r^{1-\alpha}}{2\omega} + \dots \quad (3.12)$$

When $\omega = 0$, i.e. $k_x r/\omega$ is large, and $r/k_x \rightarrow 0$,

$$\xi_+(r) = -1 + \frac{(q_{\text{eff}} h_{\infty} + m_{\text{eff}})r}{k_x} + \left(\frac{\omega}{k_x r} - \frac{\omega}{2\sqrt{g_{\infty} k_x^2}} \right) + \dots$$

$$\xi_-(r) = 1 + \frac{(q_{\text{eff}} h_{\infty} - m_{\text{eff}})r}{k_x} + \left(\frac{\omega}{k_x r} - \frac{\omega}{2\sqrt{g_{\infty} k_x^2}} \right) + \dots, \quad (3.13)$$

the boundary conditions (3.13) become real. As (3.11) are real equations, the spectral function vanishes in this case. This is essentially the statement that all poles in the Green's function occur at $\omega = 0$ [17]. The fact that the electron star $\omega = 0$ boundary conditions (3.11) are real ensures that there is no “oscillatory region” for k less than some critical value $k < k_o$ in the spectral function as is the case for pure AdS-RN [1,3,21,22]. We discuss this in detail in the Appendix.

Numerical results and discussion

We can now solve for the spectral functions numerically. In Fig. 2 we plot the momentum distribution function (MDF) (the spectral function as a function of k) for fixed $\omega = 10^{-5}$, $z = 2$, $\hat{m} = 0.36$ while changing the value of κ . Before we comment on the dependence on $q_{\text{eff}} \sim \kappa^{-1/2}$ which studies the deviation away from the adiabatic limit of a given electron star background (i.e. fixed dimensionless charge and fixed dimensionless energy density), there are several striking features that are immediately apparent:

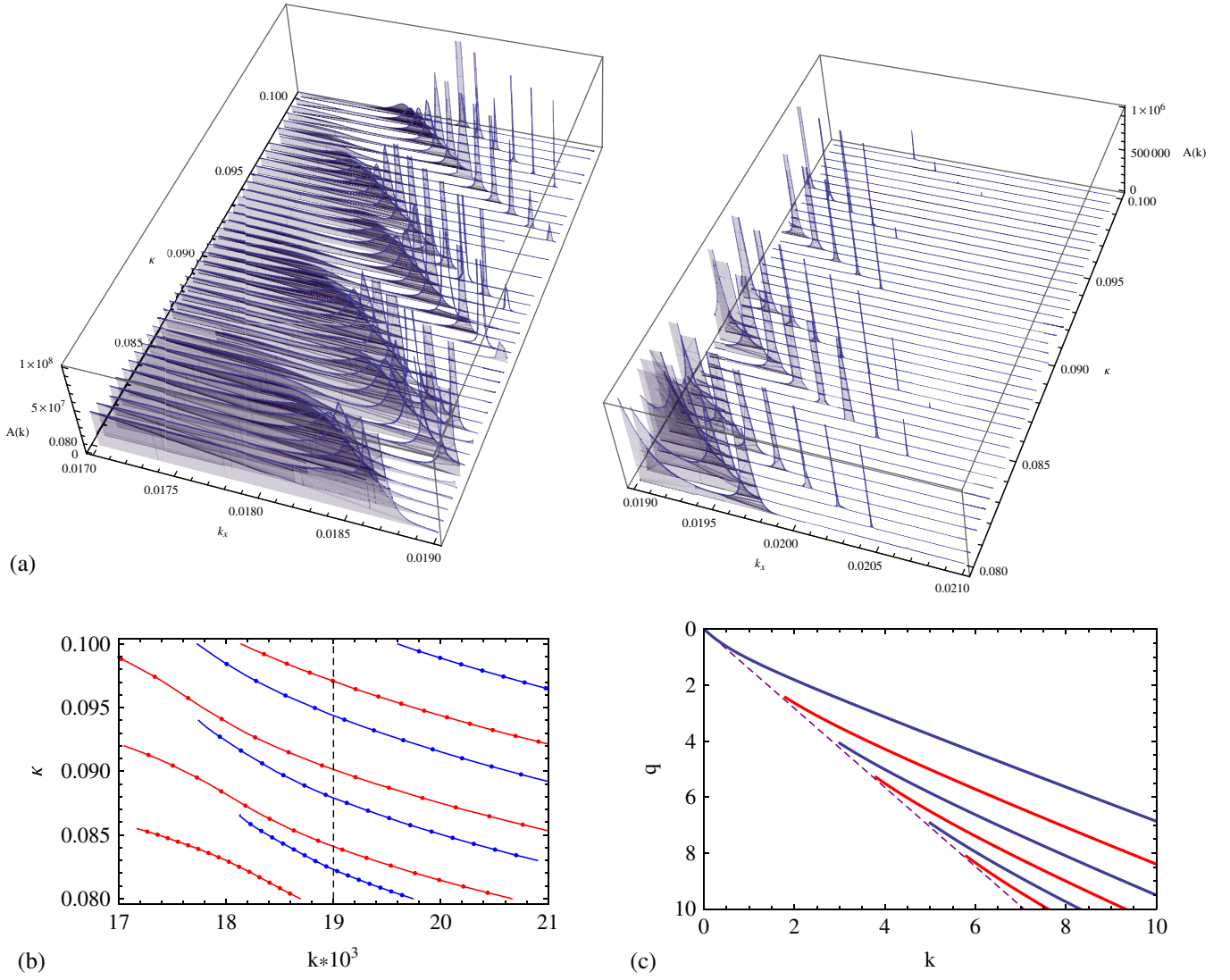


FIG. 2 (color online). (a) Electron star MDF spectral functions as a function of κ for $z = 2$, $\hat{m} = 0.36$, $\omega = 10^{-5}$. Because the peak height and weights decrease exponentially, we present the adjacent ranges $k \in [0.017, 0.019]$ and $k \in [0.019, 0.021]$ in two different plots with different vertical scale. (b, c) Locations of peaks of spectral functions as a function of κ : comparison between the electron star (b) for $z = 2$, $\hat{m} = 0.36$, $\omega = 10^{-5}$ [the dashed gray line denotes the artificial separation in the three-dimensional representations in (a)] and AdS-RN (c) for $m = 0$ as a function of q in units where $\mu = \sqrt{3}$. These two Fermi-surface “spectra” are qualitatively similar.

(i) As expected, there is a multitude of Fermi surfaces. They have very narrow width and their spectral weight decreases rapidly for each higher Fermi momentum k_F (Fig. 3). This agrees with the exponential width $\Gamma \sim \exp(-(\frac{k_F}{\omega})^{1/(\zeta-1)})$ predicted by [23] for gravitational backgrounds that are Lifshitz in the deep interior, which is the case for the electron star. This prediction is confirmed in [12,13,18] and the latter two papers also show that the weight decreases in a corresponding exponential fashion. This exponential reduction of both the width and the weight as k_F increases explains why we only see a finite number of peaks, though we expect a very large number. In the next section we will be able to

count the number of peaks, even though we cannot resolve them all numerically.

(ii) The generic value of k_F of the peaks with visible spectral weight is *much* smaller than the effective chemical potential μ in the boundary field theory. This is quite different from the AdS-RN case where the Fermi momentum and chemical potential are of the same order. A numerical study cannot answer this, but the recent paper [13] explains this.⁷

(iii) Consistent with the boundary value analysis, there is no evidence of an oscillatory region.

⁷In view of the verification of the Luttinger count for electron star spectra in [12,13], this had to be so.

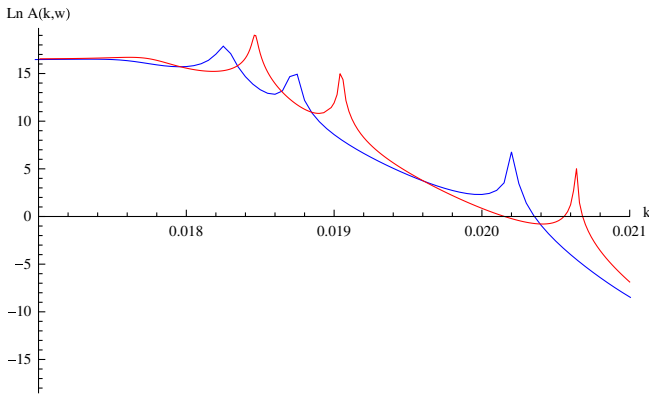


FIG. 3 (color online). Electron star MDF spectral functions with multiple peaks as a function of k for $\omega = 10^{-5}$, $z = 2$, $\hat{m} = 0.36$. The blue curve is for $\kappa = 0.091$; the red curve is for $\kappa = 0.090$. Note that the vertical axis is logarithmic. Visible is the rapidly decreasing spectral weight and increasingly narrower width for each successive peak as k_F increases.

The most relevant property of the spectral functions for our question is that as κ is increased the peak location k_F decreases orderly and peaks *disappear* at various threshold values of k . This is the support for our argument that changing κ changes the number of microscopic constituents in the electron star. Comparing the behavior of the various Fermi momenta k_F in the electron star with the results in the extremal AdS-RN black hole, they are qualitatively identical when one equates $\kappa^{-1/2} \sim q_{\text{eff}}$ with the charge of the probe fermion. We may therefore infer from our detailed understanding of the behavior of k_F for AdS-RN that also for the electron star as k_F is lowered peaks truly disappear from the spectrum until by extrapolation ultimately one remains: this is the AdS Dirac hair solution [4].

We can only make this inference qualitatively as the rapid decrease in spectral weight of each successive peak prevents an exact counting of Fermi surfaces in the numerical results for the electron star spectral functions. One aspect that we can already see is that as κ decreases all present peaks shift to higher k , while new peaks emerge from the left for smaller kappa. This suggests a fermionic version of the UV/IR correspondence, where the peak with *lowest* k_F corresponds to the last occupied level, i.e. highest “energy” in the AdS electron star. We will now address both of these points in more detail.

IV. FERMI SURFACE ORDERING: k_F FROM A SCHRÖDINGER FORMULATION

Our analysis of the behavior of boundary spectral functions as a function of κ relies on the numerically quite evident peaks. Strictly speaking, however, we have not shown that there is a true singularity in the Green’s function at $\omega = 0$, $k = k_F$. We will do so by showing that the

AdS Dirac equation, when recast as a Schrödinger problem, has quasinormalizable solutions at $\omega = 0$ for various k . As is well known, in AdS/CFT each such solution corresponds to a true pole in the boundary Green’s function. Using a WKB approximation for this Schrödinger problem we will in addition be able to estimate the number of poles for a fixed κ and thereby provide a quantitative value for the deviation from the adiabatic background.

We wish to emphasize that the analysis here is general and captures the behavior of spectral functions in all spherically symmetric and static backgrounds alike, whether AdS-RN, Dirac hair, or electron star.

The $\omega = 0$ Dirac equation (3.5) for one set of components (3.8) and (3.9) with the replacement $iy_- \rightarrow y_-$, equals

$$\begin{aligned} \sqrt{g_{ii}g^{rr}}\partial_r y_- + m_{\text{eff}}\sqrt{g_{ii}}y_- &= -(k - \hat{\mu}_{q_{\text{eff}}})z_+, \\ \sqrt{g_{ii}g^{rr}}\partial_r z_+ - m_{\text{eff}}\sqrt{g_{ii}}z_+ &= -(k + \hat{\mu}_{q_{\text{eff}}})y_-, \end{aligned} \quad (4.1)$$

where $\hat{\mu}_{q_{\text{eff}}} = \sqrt{\frac{g_{ii}}{-g_{tt}}}q_{\text{eff}}A_t$ and we will drop the subscript x on k_x . In our conventions z_+ (and y_+) is the fundamental component dual to the source of the fermionic operator in the CFT [1,2]. Rewriting the coupled first-order Dirac equations as a single second-order equation for z_+ ,

$$\begin{aligned} \partial_r^2 z_+ + \mathcal{P}\partial_r z_+ + \mathcal{Q}z_+ &= 0, \\ \mathcal{P} &= \frac{\partial_r(g_{ii}g^{rr})}{2g_{ii}g^{rr}} - \frac{\partial_r \hat{\mu}_{q_{\text{eff}}}}{k + \hat{\mu}_{q_{\text{eff}}}}, \\ \mathcal{Q} &= -\frac{m_{\text{eff}}\partial_r \sqrt{g_{ii}}}{\sqrt{g_{ii}g^{rr}}} + \frac{m_{\text{eff}}\sqrt{g_{rr}}\partial_r \hat{\mu}_{q_{\text{eff}}}}{k + \hat{\mu}_{q_{\text{eff}}}} - m_{\text{eff}}^2 g_{rr} \\ &\quad - \frac{k^2 - \hat{\mu}_{q_{\text{eff}}}^2}{g_{ii}g^{rr}}, \end{aligned} \quad (4.2)$$

the first thing one notes is that both \mathcal{P} and \mathcal{Q} diverge at some $r = r_*$, where $\hat{\mu}_{q_{\text{eff}}} + k = 0$. Since $\hat{\mu}_{q_{\text{eff}}}$ is (chosen to be) a positive semidefinite function which increases from $\hat{\mu}_{q_{\text{eff}}} = 0$ at the horizon, this implies that for negative k (with $-k < \hat{\mu}_{q_{\text{eff}}}|_{\infty}$) the wave function is qualitatively different from the wave function with positive k which experiences no singularity. The analysis is straightforward if we transform the first derivative away and recast it in the form of a Schrödinger equation by redefining the radial coordinate,

$$\frac{ds}{dr} = \exp\left(-\int^r dr' \mathcal{P}\right) \Rightarrow s = c_0 \int_{r_{\infty}}^r dr' \frac{|k + \hat{\mu}_{q_{\text{eff}}}|}{\sqrt{g_{ii}g^{rr}}}, \quad (4.3)$$

where c_0 is an integration constant whose natural scale is of order $c_0 \sim q_{\text{eff}}^{-1}$. This is a simpler version of the generalized k -dependent tortoise coordinate introduced in [3]. In the new coordinates the equation (4.2) is of the standard form,

$$\partial_s^2 z_+ - V(s)z_+ = 0 \quad (4.4)$$

with potential

$$V(s) = -\frac{g_{ii}g^{rr}}{c_0^2|k + \hat{\mu}_{q_{\text{eff}}}|^2} \mathcal{Q}. \quad (4.5)$$

The above potential (4.5) can also be written as

$$V(s) = \frac{1}{c_0^2(k + \hat{\mu}_{q_{\text{eff}}})^2} \left[(k^2 + m_{\text{eff}}^2 g_{ii} - \hat{\mu}_{q_{\text{eff}}}^2) + m_{\text{eff}} g_{ii} \sqrt{g^{rr}} \partial_r \ln \frac{\sqrt{g_{ii}}}{k + \hat{\mu}_{q_{\text{eff}}}} \right]. \quad (4.6)$$

We note again the potential singularity for negative k , but before we discuss this we first need the boundary conditions. The universal boundary behavior is at spatial infinity and follows from the asymptotic AdS geometry. In the adapted coordinates $r \rightarrow \infty$ corresponds to $s \rightarrow 0$ as follows from $ds/dr \simeq c_0(k + \hat{\mu}_{q_{\text{eff}}}|_\infty)/r^2$. The potential therefore equals

$$V(s) \simeq \frac{1}{s^2} (m_{\text{eff}} + m_{\text{eff}}^2) + \dots \quad (4.7)$$

and the asymptotic behavior of the two independent solutions equals $z_+ = a_1 s^{-m_{\text{eff}}} + b_1 s^{1+m_{\text{eff}}} + \dots$. The second solution is normalizable and we thus demand $a_1 = 0$.

In the interior, the near-horizon geometry generically is Lifshitz

$$ds^2 = -r^{2z} dt^2 + \frac{1}{r^2} dr^2 + r^2(dx^2 + dy^2) + \dots, \quad (4.8)$$

$$A = h_\infty r^z dt + \dots,$$

with finite dynamical critical exponent z —AdS-RN, which can be viewed as a special case, where $z \rightarrow \infty$, will be given separately. In adapted coordinates the interior $r \rightarrow 0$ corresponds to $s \rightarrow -\infty$ and it is easy to show that in this limit potential behaves as

$$V(s) \simeq \frac{1}{c_0^2} + \frac{1}{s^2} (m_{\text{eff}} \sqrt{g_\infty} + m_{\text{eff}}^2 g_\infty - h_\infty^2 q_{\text{eff}}^2 g_\infty) + \dots \quad (4.9)$$

Near the horizon the two independent solutions for the wave function z_+ therefore behave as

$$z_+ \rightarrow a_0 e^{-s/c_0} + b_0 e^{s/c_0}. \quad (4.10)$$

The decaying solution $a_0 = 0$ is the normalizable solution we seek.

Let us now address the possible singular behavior for $k < 0$. To understand what happens, let us first analyze the potential qualitatively for positive k . Since the potential is positive semidefinite at the horizon and the boundary, the Schrödinger system (4.4) only has a zero-energy normalizable solution if $V(s)$ has a range $s_1 < s < s_2$, where it is negative. This can only occur at locations where $k^2 <$

$\hat{\mu}_{q_{\text{eff}}}^2 - m_{\text{eff}}^2 g_{ii} - m_{\text{eff}} g_{ii} \sqrt{g^{rr}} \partial_r \ln \frac{\sqrt{g_{ii}}}{k + \hat{\mu}_{q_{\text{eff}}}}$. Defining a “re-normalized” position dependent mass $m_{\text{ren}}^2 = m_{\text{eff}}^2 g_{ii} + m_{\text{eff}} g_{ii} \sqrt{g^{rr}} \partial_r \ln \frac{\sqrt{g_{ii}}}{k + \hat{\mu}_{q_{\text{eff}}}}$ this is the intuitive statement that the momenta must be smaller than the local chemical potential $k^2 < \hat{\mu}_{q_{\text{eff}}}^2 - m_{\text{ren}}^2$. For positive k the saturation of this bound $k^2 = \hat{\mu}_{q_{\text{eff}}}^2 - m_{\text{ren}}^2$ has at most two solutions, which are regular zeroes of the potential. This follows from the fact that $\hat{\mu}_{q_{\text{eff}}}^2$ decreases from the boundary toward the interior. If the magnitude $|k|$ is too large the inequality cannot be satisfied, the potential is strictly positive, and no solution exists. For negative k , however, the potential has in addition a triple pole at $k^2 = \hat{\mu}_{q_{\text{eff}}}^2$; two poles arise from the prefactor and the third from the $m_{\text{eff}} \partial_r \ln(k + \hat{\mu}_{q_{\text{eff}}})$ term. This pole always occurs closer to the horizon than the zeroes and the potential therefore qualitatively looks like that in Fig. 4. (Since $\hat{\mu}_{q_{\text{eff}}}$ decreases as we move inward from the boundary, starting with $\hat{\mu}_{q_{\text{eff}}}^2 > \hat{\mu}_{q_{\text{eff}}}^2 - \mu^2 > k^2$, one first saturates the inequality that gives the zero in the potential as one moves inward.) Such a potential cannot support a zero-energy bound state, i.e. Eq. (4.4) has no solution for negative k . In the case $m_{\text{eff}} = 0$ a double zero changes the triple pole to a single pole and the argument still holds. This does not mean that there are no $k < 0$ poles

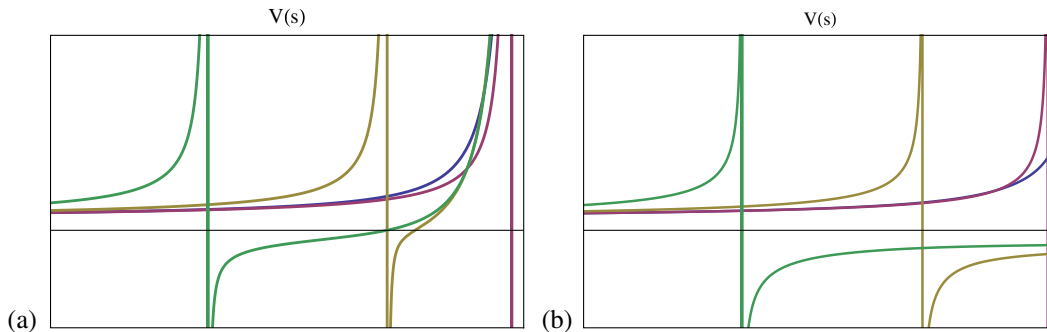


FIG. 4 (color online). The behavior of the Schrödinger potential $V(s)$ for z_+ when k is negative. Such a potential has no zero-energy bound state. The potential is rescaled to fit on a finite range. As $|k|$ is lowered below k_{max} for which the potential is strictly positive, a triple pole appears which moves toward the horizon on the left (a). The blue, red, orange, and green curves are decreasing in $|k|$). The pole hits the horizon for $k = 0$ and disappears. (b) shows the special case $m_{\text{eff}} = 0$ where two zeroes collide with two of the triple poles to form a single pole.

in the CFT spectral function. They arise from the other physical polarization y_+ of the bulk fermion Ψ . From the second set of decoupled first-order equations for the other components of the Dirac equation (after replacing $iz_- \rightarrow z_-$)

$$\begin{aligned}\sqrt{g_{ii}g^{rr}}\partial_r y_+ - m_{\text{eff}}\sqrt{g_{ii}}y_+ &= -(k - \hat{\mu}_{q_{\text{eff}}})z_-, \\ \sqrt{g_{ii}g^{rr}}\partial_r z_- + m_{\text{eff}}\sqrt{g_{ii}}z_- &= -(k + \hat{\mu}_{q_{\text{eff}}})y_+, \end{aligned} \quad (4.11)$$

and the associated second-order differential equation of motion for y_+ ,

$$\begin{aligned}\partial_r^2 y_+ + \mathcal{P}\partial_r y_+ + \mathcal{Q} &= 0, \\ \mathcal{P} &= \frac{\partial_r(g_{ii}g^{rr})}{2g_{ii}g^{rr}} - \frac{\partial_r \hat{\mu}_{q_{\text{eff}}}}{-k + \hat{\mu}_{q_{\text{eff}}}}, \\ \mathcal{Q} &= -\frac{m_{\text{eff}}\partial_r \sqrt{g_{ii}}}{\sqrt{g_{ii}g^{rr}}} + \frac{m_{\text{eff}}\sqrt{g_{rr}}\partial_r \hat{\mu}_{q_{\text{eff}}}}{-k + \hat{\mu}_{q_{\text{eff}}}} - m_{\text{eff}}^2 g_{rr} \\ &\quad - \frac{k^2 - \hat{\mu}_{q_{\text{eff}}}^2}{g_{ii}g^{rr}}, \end{aligned} \quad (4.12)$$

one sees that the Schrödinger equation for y_+ is the $k \rightarrow -k$ image of the equation (4.4) for z_+ and thus y_+ will only have zero-energy solutions for $k < 0$. For simplicity we will only analyze the z_+ case. Note that this semipositive definite momentum structure of the poles is a feature of any AdS-to-Lifshitz metric different from AdS-RN, where one can have negative k solutions [3].

The exact solution of (4.4) with the above boundary conditions corresponding to poles in the CFT spectral function is difficult to find. By construction the system is however equivalent to a Schrödinger problem of finding a zero-energy solution z_+ in the potential (4.5) and can be solved in the WKB approximation (see e.g. [3,24]). The WKB approximation holds when $|\partial_s V| \ll |V|^{3/2}$. Notice that this is more general than the background adiabaticity limit $m_{\text{eff}} \gg 1$, $q_{\text{eff}} \gg 1$ with $\hat{\beta}$, \hat{m} fixed. Combining background adiabaticity with a scaling limit $k \gg 1$, $m_{\text{eff}} \gg 1$, $q_{\text{eff}} \gg 1$ with $c_0 k$ fixed and k parametrically larger than $\hat{\mu}_{q_{\text{eff}}}$, one recovers the WKB potential solved in [12,13]. As our aim is to study the deviation away from the background adiabatic limit we will be more general and study the WKB limit of the potential itself, without direct constraints on q_{eff} , m_{eff} . And rather than testing the inequality $|\partial_s V| \ll |V|^{3/2}$ directly, we will rely on the rule of thumb that the WKB limit is justified when the number of nodes in the wave function is large. We will therefore estimate the number n of bound states and use $n \gg 1$ as an empirical justification of our approach.⁸ With this criterion we will be able to study the normalizable solutions

⁸A large number of bound states n implies $|\partial_s V| \ll |V|^{3/2}$ if the potential has a single minimum but as is well known there are systems, e.g. the harmonic oscillator, where the WKB approximation holds for small n as well.

to the Dirac equation/pole structure of the CFT spectral functions as a function of κ/L .

The potential is bounded both in the AdS boundary and at the horizon, and decreases toward intermediate values of r . We therefore have a standard WKB solution consisting of three regions:

- (i) In the regions where $V > 0$, the solution decays exponentially,

$$z_+ = c_{1,2} V^{-1/4} \exp\left(\pm \int_{r_{1,2}}^r dr' [c_0 \sqrt{g^{ii}g_{rr}}(k + \hat{\mu}_{q_{\text{eff}}})\sqrt{V}]\right). \quad (4.13)$$

Here r_1, r_2 are the turning points where $V(r_1) = 0 = V(r_2)$.

- (ii) In the region $r_1 < r < r_2$, i.e. $V < 0$, the solution is

$$z_+ = c_3 (-V)^{-1/4} \text{Re}\left[\exp\left(i \int_{r_1}^r dr' [c_0 \sqrt{g^{ii}g_{rr}}(k + \hat{\mu}_{q_{\text{eff}}})\sqrt{-V}] - i\pi/4\right)\right], \quad (4.14)$$

with the constant phase $-i\pi/4$ originating in the connection formula at the turning point r_1 .

Finding a WKB solution shows us that the peaks seen numerically are true poles in the spectral function. But it also allows us to estimate the number of peaks that the numerical approach could not resolve. The WKB quantization condition

$$\int_{r_1}^{r_2} dr' [c_0 \sqrt{g^{ii}g_{rr}}(k + \hat{\mu}_{q_{\text{eff}}})\sqrt{-V}] = \pi(n + 1/2) \quad (4.15)$$

counts the number of bound states with negative semi-definite energy. Note that n does not depend on the integral constant as there is also a factor $1/c_0$ in $\sqrt{-V}$. Since V depends on k , we will see that as we increase k this number decreases. The natural interpretation in the context of a bulk many-body Fermi system is that this establishes the ordering of the filling of all the $\omega = 0$ momentum shells in the electron star. For a fixed k one counts the modes that have been previously occupied and, consistent with our earlier deduction, the lowest/highest k_F corresponds to the last/first occupied state. Though counterintuitive from a field theory perspective where normally $E \sim k_F$, this UV/IR correspondence is very natural from the AdS bulk, if one thinks of the electron star as a trapped electron gas. The last occupied state should then be the outermost state from the center, but this state has the lowest effective chemical potential and hence lowest k_F .

Let us now show this explicitly by analyzing the potential and the bound states in the electron star and the AdS-RN case can be found in the Appendix.

The potential (4.6) for the electron star is given in Fig. 5 and the number of bound states as a function of k in Fig. 6. As stated the number of states decreases with increasing k , consistent with the analogy of the pole distribution of the

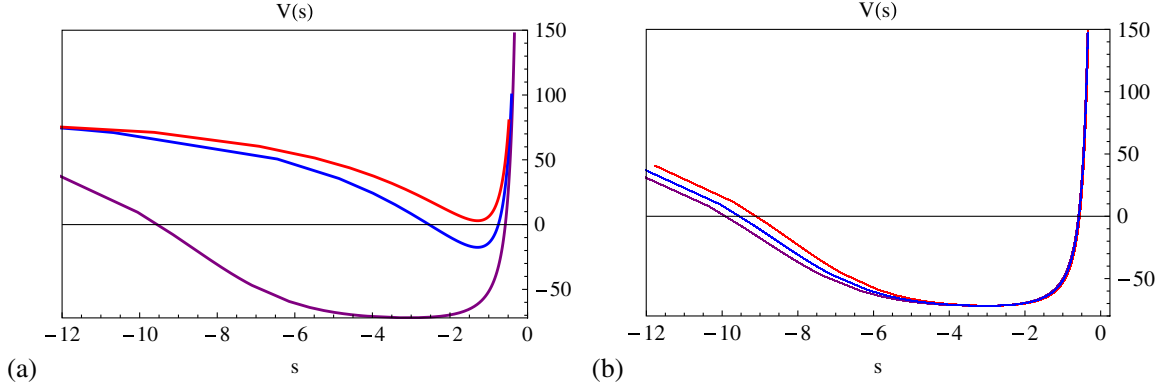


FIG. 5 (color online). The Schrödinger potential $V(s)$ for the fermion component z_+ of in the electron star (ES) background $\hat{m} = 0.36$, $z = 2$, $c_0 = 0.1$. (a) shows the dependence on the momentum $k = 0.0185$ (purple), $k = 5$ (blue), $k = 10$ (red) for $\kappa = 0.092$. (b) shows the dependence on $\kappa = 0.086$ (purple), $\kappa = 0.092$ (blue), $\kappa = 0.1$ (red) for $k = 0.0185$. Recall that $s = 0$ is the AdS boundary and $s = -\infty$ is the near-horizon region.

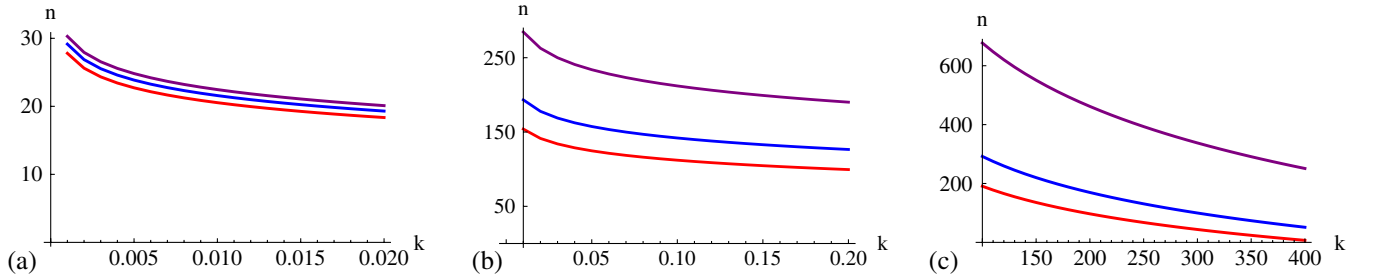


FIG. 6 (color online). The WKB estimate of the number of bound states n as a function of the momentum k for $\kappa = 0.086$ (purple), 0.092 (blue), 0.1 (red) (a); for $\kappa = 0.001$ (purple), 0.002 (blue), 0.003 (red) (b); and for $\kappa = 10^{-5}$ (purple), 3×10^{-5} (blue), 5×10^{-5} (red) (c). Note the parametric increase in number of states as the adiabaticity of the background improves for smaller κ . These three panels are for the electron star background with $\hat{m} = 0.36$, $z = 2$. Since $n \gg 1$ in all cases, WKB gives a valid estimate.

spectral functions compared with AdS-RN. Moreover, we clearly see the significant increase in the number of states as we decrease κ/L thereby improving the adiabaticity of the background. This vividly illustrates that the adiabatic limit corresponds to a large number of constituents. As all numbers of states are far larger than 1, the use of the WKB is justified. From the trend that dialing κ/L up there will be fewer Fermi surfaces one can conjecture that the Dirac hair has only one Fermi surface and it was shown in [5] that this is indeed the case.

V. CONCLUSION AND DISCUSSION

These electron star spectral function results directly answer two of the three questions raised in the introduction.

- (i) They show explicitly how the fermion wave functions in their own gravitating potential well are ordered despite the fact that they all have strictly vanishing energy: In a fermionic version of the UV-IR correspondence they are ordered *inversely* in k , with the “lowest”/first occupied state having the highest k and the “highest”/last occupied state having the lowest k . With the qualitative AdS/CFT

understanding that scale corresponds to distance away from the interior, one can intuitively picture this as literally filling geometrical shells of the electron star, with the outermost/highest/last shell at large radius corresponding to the wave function with lowest local chemical potential and hence lowest k .

- (ii) The decrease of the number of bound states—the number of occupied wave functions in the electron star—as we decrease $q_{\text{eff}} = \hat{\beta}^{1/4} \sqrt{\frac{\pi L}{\kappa}}$ for a fixed electron star background extrapolates naturally to a limit where the number of bound states is unity. This extrapolation pushes the solution beyond its adiabatic regime of validity. In principle we know what the correct description in this limit is: it is the AdS Dirac hair solution constructed in [4]. The dependence of the number of bound states on κ/L therefore illustrates that the electron star and Dirac hair solutions are two limiting cases of the gravitationally backreacted Fermi gas.

With this knowledge we can schematically classify the ground state solutions of AdS Einstein-Maxwell gravity

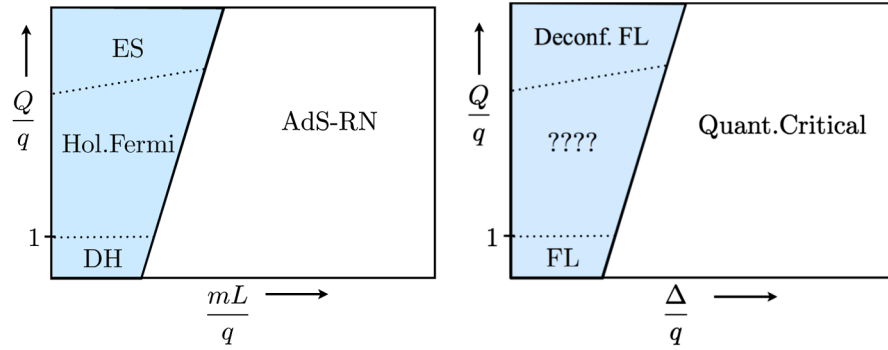


FIG. 7 (color online). Schematic diagram of the different ground state solutions of strongly coupled fermions implied by holography for fixed charge density Q . Here q is the constituent charge of the fermions and $mL \sim \Delta$ the mass/conformal scaling dimension of the fermionic operator. One has the gravitational electron star (ES)/Dirac hair (DH) solution for large/small Q/q and small mL/q dual a deconfined Fermi liquid/regular Fermi liquid in the CFT. For $mL/q \sim \Delta/q$ large the ground state remains the fermionic quantum critical state dual to AdS-RN.

minimally coupled to charged fermions at finite charge density.⁹ For large mass mL in units of the constituent charge q , the only solution is a charged AdS-Reissner-Nördstrom black hole. For a low enough mass-to-charge ratio, the black hole becomes unstable and develops hair. If in addition the total charge density Q is of the order of the microscopic charge q this hairy solution is the Dirac hair configuration constructed in [4], whereas in the limit of large total charge density Q one can make an adiabatic Thomas-Fermi approximation and arrive *à la* Tolman-Oppenheimer-Volkov at an electron star (Fig. 7).

Translating this solution space through the AdS/CFT correspondence one reads off that in the dual strongly coupled field theory, one remains in the critical state if the ratio of the scaling dimension to the charge Δ/q is too large. For a small enough value of this ratio, the critical state is unstable and forms a novel scaleful ground state. The generic condensed matter expectation of a unique Fermi liquid is realized if the total charge density is of the same order as the constituent charge. Following [12–16] the state for $Q \gg q$ is some deconfined Fermi liquid.

The gravity description of either limit has some deficiencies, most notably the lack of an electron star wave function at infinity and the unnatural restriction to $Q = q$ for the Dirac hair solution. A generic solution for $Q \geq q$ with wave function tails extending to infinity as the Dirac hair would be a more precise holographic dual to the strongly interacting large N Fermi system. Any CFT information can then be cleanly read off at the AdS boundary. A naive construction could be to superpose Dirac hair onto the electron star; in principle one can achieve this

solution by a next-order Hartree-Fock or local density approximation computation.

This best-of-both-worlds generic solution ought to be the true holographic dual of the strongly interacting Fermi ground state. If one is able to answer convincingly how this system circumvents the wisdom that the ground state of an interacting many-body system of fermions is a generic single quasiparticle Landau Fermi liquid, then one would truly have found a finite density Fermi system that does not refer at any stage to an underlying perturbative Fermi gas.

ACKNOWLEDGMENTS

We thank S. Hartnoll, A. Karch, H. Liu, T. K. Ng, and B. Overbosch for discussions and correspondence. K. S. is very grateful to the Hong Kong Institute for Advanced Studies for the hospitality during the completion of this work. This research was supported in part by a VIDI Innovative Research Incentive Grant (K. Schalm) from the Netherlands Organisation for Scientific Research (NWO), a Spinoza Grant (J. Zaanen) from the Netherlands Organisation for Scientific Research (NWO) and the Dutch Foundation for Fundamental Research on Matter (FOM).

APPENDIX: SCHRÖDINGER ANALYSIS IN THE REISSNER-NORDSTRÖM CASE

For AdS-RN the Schrödinger analysis requires a separate discussion of the near-horizon boundary conditions, which we present here for completeness and comparison. The reason is that for AdS-RN there is a special scale k_o below which the boundary condition turns complex (Eq. (26) in [1]). This scale k_o is related to the surprising existence of an oscillatory region in the spectral function. For $k > k_o$ the boundary conditions are real as they are for the electron star for all k . AdS-RN boundary conditions are therefore qualitatively different from electron star spectral functions, but only for $k < k_o$. This difference is not

⁹One should always keep in mind that the setup under study here is phenomenological in nature; a full string theory embedding might introduce other fields which could prevent the electron star or Dirac hair from being the true ground state of the system.

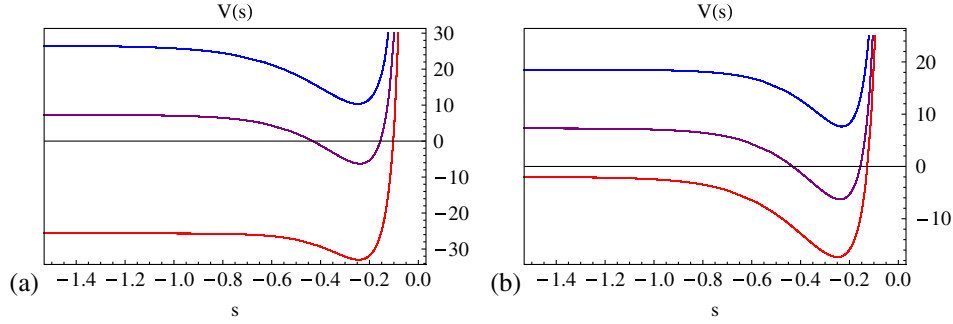


FIG. 8 (color online). The Schrödinger potential $V(s)$ for the fermion component z_+ in the AdS-RN background $r_+ = 1$, $\mu = \sqrt{3}$, $g_F = 1$, $mL = 0.4$, $c_0 = 0.1$. (a) shows the dependence on the momentum $k = 1$ (red), $k = 2$ (purple), $k = 3$ (blue) for charge $q = 2.5$. (b) shows the dependence on the charge q —analogous to κ in the ES background. Shown are the values $q = 2$ (blue), $q = 2.5$ (purple), $q = 3$ (red) for the momentum $k = 2$. In both panels, the red potentials correspond to the oscillatory region $\nu_k^2 < 0$, the purple potentials show the generic shape that can support an $\omega = 0$ bound state, and the blue potentials are strictly positive and no zero-energy bound state is present. Recall that $s = 0$ is the AdS boundary and $s = -\infty$ is the near-horizon region.

relevant to the analogy between electron star spectral functions and the distinct poles in the AdS-RN spectral function in Fig. 2 as the latter only occur for $k > k_o$. Part of this analysis is originally worked out in [3].

The AdS-RN black hole with metric

$$ds^2 = L^2 \left(-f(r)dt^2 + \frac{dr^2}{f(r)} + r^2(dx^2 + dy^2) \right), \quad (\text{A1})$$

$$f(r) = r^2 \left(1 + \frac{3}{r^4} - \frac{4}{r^3} \right), \quad (\text{A2})$$

$$A = \mu \left(1 - \frac{1}{r} \right) dt, \quad (\text{A3})$$

has near-horizon geometry $\text{AdS}_2 \times \mathbb{R}^2$

$$ds^2 = -6(r-1)^2 dt^2 + \frac{dr^2}{6(r-1)^2} + (dx^2 + dy^2), \quad (\text{A4})$$

$$A = \sqrt{3}(r-1) dt. \quad (\text{A5})$$

A coordinate redefinition of r in Eq. (4.8) to $r = (r_{\text{AdS}_2} - 1)^{1/z}$ shows that this corresponds to a dynamical critical exponent $z = \infty$ and is outside the validity of the previous analysis.

Before we proceed, recall that the existence of $\text{AdS}_2 \times \mathbb{R}^2$ near-horizon region allows for a semianalytic determination of the fermion spectral functions with the self-energy $\Sigma \sim \omega^{2\nu_{k_F}}$ controlled by the IR conformal dimension $\delta_k = 1/2 + \nu_k$ with

$$\nu_k = \frac{1}{\sqrt{6}} \sqrt{m^2 + k^2 - \frac{q^2}{2}}. \quad (\text{A6})$$

When ν_k is imaginary, which for $q^2 > 2m^2$ always happens for small k , the spectral function exhibits oscillatory behavior, but generically has finite weight at $\omega = 0$. When ν_k is real, there are poles in the spectral functions at a finite

number of different Fermi momenta k_F . The associated quasiparticles can characterize a non-Fermi liquid ($\nu_{k_F} < 1/2$), a marginal Fermi liquid ($\nu_{k_F} = 1/2$), or irregular Fermi liquid ($\nu_{k_F} > 1/2$) with linear dispersion but width $\Gamma \neq \omega^2$ [3].

The analytic form of the near-horizon metric allows us to solve exactly for the near-horizon potential V in terms of $s = \frac{c_0}{\sqrt{6}}(k + q/\sqrt{2}) \ln(r-1) + \dots$. As noted in [3] one remarkably obtains that the near-horizon potential for $s \rightarrow -\infty$ is proportional to the self-energy exponent,

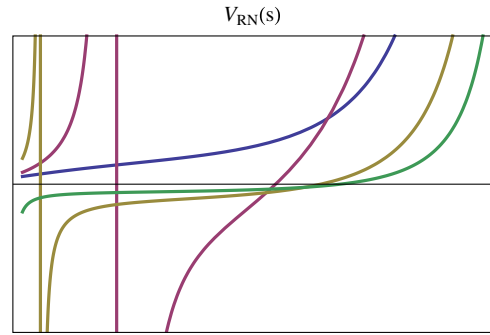


FIG. 9 (color online). The qualitative behavior for negative k of the Schrödinger potential $V(s)$ for the fermion component z_+ of the AdS-RN background $r_+ = 1$, $\mu = \sqrt{3}$, $g_F = 1$, $mL = 0.1$. The radial coordinate has been rescaled to a finite domain such that the full potential can be represented in the figure; on the right is the AdS boundary and left is the near-horizon region and the range is slightly extended beyond the true horizon, which is exactly at the short vertical line-segments on the right. Potentials are given for $q = 12/\sqrt{3}$, with different values of k . For $k = -15$ (blue), the potential is strictly positive. For $k = -10$ (purple) and $k = -7$ (orange), both of their potentials have triple poles and the pole can be seen to move toward the horizon on the left as k decreases. For $k = -4$ (green), the potential has no pole and reaches a finite negative value at the horizon. The pole disappears for $|k| < q/\sqrt{2}$ leaving a regular bounded potential which can support zero-energy bound states.

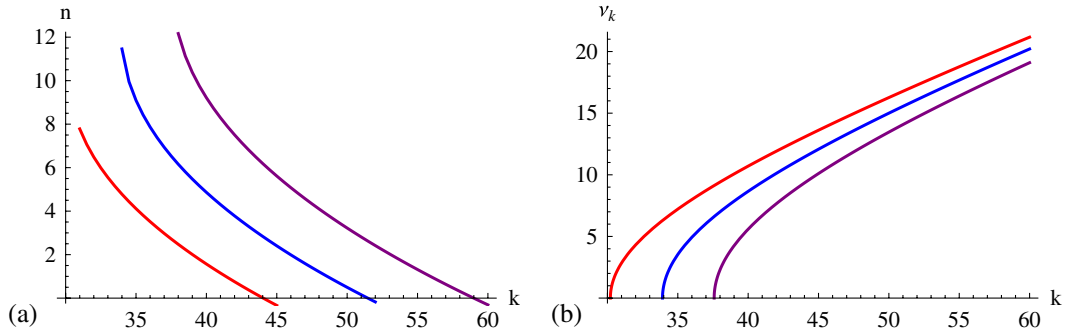


FIG. 10 (color online). (a) The WKB estimate of the number of bound states n in the AdS-RN Schrödinger potential for z_+ with $mL = 10$. The WKB approximation only applies to large values of the charge $q = 45$ (red), $q = 50$ (blue), $q = 55$ (purple). (b) gives the associated values of the IR conformal dimension $\nu_k = \frac{1}{\sqrt{6}}\sqrt{m^2 + k^2 - \frac{q^2}{2}}$. Both panels are for the extremal AdS-RN background with $\mu = \sqrt{3}$, $r_+ = 1$, $g_F = 1$.

$$V(s) \simeq \frac{6}{c_0^2(k + q/\sqrt{2})^2} \nu_k^2 + \dots \quad (\text{A7})$$

One immediately recognizes the oscillatory region $\nu_k^2 < 0$ of the spectral function as an $\omega = 0$ Schrödinger potential which is “free” at the horizon $s = -\infty$ (Fig. 8) and no bound state can form. Comparing with our previous results, we see that this oscillatory region is a distinct property of AdS-RN. For any Lifshitz near-horizon metric the potential is always positive-definite near the horizon and all $\omega = 0$ solutions will be bounded (see also [12,13]). As we increase k , ν_k^2 becomes positive, then the AdS-RN potential is also positive at the horizon and bound zero-energy states can form. Increasing k further, one reaches a maximal k_{\max} , above which the potential is always positive and no zero-energy bound state exists anymore.

Because the near-horizon boundary conditions for AdS-RN differ from the general analysis, the possible singularity in the potential for $k < 0$ also requires a separate study. This is clearly intimately tied to the existence of an oscillatory regime in the spectral function, as the previous analysis does apply for $\nu_k^2 > 0$. The clearest way to understand what happens for $\nu_k^2 < 0$ is to analyze the potential

explicitly. Again if $|k| > k_{\max}$ the potential is strictly positive-definite, and no zero-energy bound state exists. As we decrease the magnitude of $k < 0$, a triple pole will form near the boundary when $k = -\hat{\mu}_{q_{\text{eff}}}(s)$, soon followed by a zero at $k = -\sqrt{\hat{\mu}_{q_{\text{eff}}}(s)^2 - m_{\text{ren}}(s)^2}$ (see Fig. 4). As we approach the horizon, in the general case where $\lim_{r \rightarrow 0} \hat{\mu}_{q_{\text{eff}}} = h_{\infty} q_{\text{eff}} r + \dots$, this pole at $r_* = -k/(h_{\infty} q_{\text{eff}})$ hits the horizon and disappears precisely when $k = 0$. In AdS-RN, however, where $\lim_{r \rightarrow 1} \hat{\mu}_{q_{\text{eff}}} = \frac{q}{\sqrt{2}} + \frac{\sqrt{2}q}{3}(r-1) + \dots$, the pole at $r_*^{RN} - 1 = \frac{3}{\sqrt{2}q}(k + \frac{q}{\sqrt{2}})$ hits the horizon and disappears at $k = -\frac{q}{\sqrt{2}}$. For negative values of k whose magnitude is less than $|k| < \frac{q}{\sqrt{2}}$, the potential is regular and bounded and can and does have zero-energy solutions. Figure 9 shows this disappearance of the pole for the AdS-RN potential.

Counting solutions through WKB is also more complicated for AdS-RN. For $\mathcal{O}(1)$ values of q there are only few Fermi surfaces and the WKB approximation does not apply. For large q it does, however. For completeness we show the results in Fig. 10.

-
- [1] H. Liu, J. McGreevy, and D. Vegh, *Phys. Rev. D* **83**, 065029 (2011).
[2] M. Cubrovic, J. Zaanen, and K. Schalm, *Science* **325**, 439 (2009).
[3] T. Faulkner, H. Liu, J. McGreevy, and D. Vegh, *Phys. Rev. D* **83**, 125002 (2011).
[4] M. Cubrovic, J. Zaanen, and K. Schalm, [arXiv:1012.5681](https://arxiv.org/abs/1012.5681).
[5] M. Cubrovic, J. Zaanen, and K. Schalm (work in progress).
[6] S. A. Hartnoll, J. Polchinski, E. Silverstein, and D. Tong, *J. High Energy Phys.* **04** (2010) 120.
[7] S. A. Hartnoll and A. Tavanfar, *Phys. Rev. D* **83**, 046003 (2011).
[8] J. de Boer, K. Papadodimas, and E. Verlinde, *J. High Energy Phys.* **10** (2010) 020.
[9] X. Arsiwalla, J. de Boer, K. Papadodimas, and E. Verlinde, *J. High Energy Phys.* **01** (2011) 144.
[10] V. G. M. Puletti, S. Nowling, L. Thorlacius, and T. Zingg, *J. High Energy Phys.* **01** (2011) 117.
[11] S. A. Hartnoll and P. Petrov, *Phys. Rev. Lett.* **106**, 121601 (2011).
[12] S. A. Hartnoll, D. M. Hofman, and D. Vegh, [arXiv:1105.3197](https://arxiv.org/abs/1105.3197).
[13] N. Iqbal, H. Liu, and M. Mezei, [arXiv:1105.4621](https://arxiv.org/abs/1105.4621).
[14] S. A. Hartnoll, D. M. Hofman, and A. Tavanfar, *Europhys. Lett.* **95**, 31002 (2011).

- [15] S. Sachdev, *Phys. Rev. Lett.* **105**, 151602 (2010).
- [16] L. Huijse and S. Sachdev, *Phys. Rev. D* **84**, 026001 (2011).
- [17] H. Liu and T. Faulkner (private communication).
- [18] N. Iizuka, N. Kundu, P. Narayan, and S.P. Trivedi, [arXiv:1105.1162](https://arxiv.org/abs/1105.1162).
- [19] S.S. Gubser and A. Nellore, *Phys. Rev. D* **80**, 105007 (2009).
- [20] K. Goldstein, S. Kachru, S. Prakash, and S.P. Trivedi, *J. High Energy Phys.* **08** (2010) 078.
- [21] D. Guarrera and J. McGreevy, [arXiv:1102.3908](https://arxiv.org/abs/1102.3908).
- [22] T. Faulkner, N. Iqbal, H. Liu, J. McGreevy, and D. Vegh, [arXiv:1101.0597](https://arxiv.org/abs/1101.0597).
- [23] T. Faulkner and J. Polchinski, *J. High Energy Phys.* **06** (2011) 012.
- [24] G.T. Horowitz and M.M. Roberts, *J. High Energy Phys.* **11** (2009) 015.

RECEIVED: March 28, 2011

REVISED: August 29, 2011

ACCEPTED: September 4, 2011

PUBLISHED: October 6, 2011

Constructing the AdS dual of a Fermi liquid: AdS black holes with Dirac hair

Mihailo Čubrović, Jan Zaanen and Koenraad Schalm

*Institute Lorentz for Theoretical Physics, Leiden University,
P.O. Box 9506, Leiden 2300RA, The Netherlands*

E-mail: cubrovic@lorentz.leidenuniv.nl, jan@lorentz.leidenuniv.nl,
kschalm@lorentz.leidenuniv.nl

ABSTRACT: We provide evidence that the holographic dual to a strongly coupled charged Fermi liquid has a non-zero fermion density in the bulk. We show that the pole-strength of the stable quasiparticle characterizing the Fermi surface is encoded in the AdS probability density of a single normalizable fermion wavefunction in AdS. Recalling Migdal's theorem which relates the pole strength to the Fermi-Dirac characteristic discontinuity in the number density at ω_F , we conclude that the AdS dual of a Fermi liquid is described by occupied on-shell fermionic modes in AdS. Encoding the occupied levels in the total spatially averaged probability density of the fermion field directly, we show that an AdS Reissner-Nordström black hole in a theory with charged fermions has a critical temperature, at which the system undergoes a first-order transition to a black hole with a non-vanishing profile for the bulk fermion field. Thermodynamics and spectral analysis support that the solution with non-zero AdS fermion-profile is the preferred ground state at low temperatures.

KEYWORDS: Black Holes in String Theory, AdS-CFT Correspondence, Holography and condensed matter physics (AdS/CMT)

Contents

1	Introduction	1
2	From Green’s function to AdS/CFT rules for a Fermi liquid	4
2.1	The AdS dual of a stable Fermi liquid: applying Migdal’s relation holographically	8
2.1.1	Boundary conditions and normalizability	11
3	An AdS black hole with Dirac hair	12
3.1	Thermodynamics	16
3.2	At the horizon: entropy collapse to a Lifshitz solution	17
3.3	A BH with Dirac hair	18
3.3.1	Finite fermion density solutions in AdS-RN	19
3.3.2	Finite fermion density in AdSS	22
3.4	Confirmation from fermion spectral functions	23
4	Discussion and conclusion	24

1 Introduction

Fermionic quantum criticality is thought to be an essential ingredient in the full theory of high T_c superconductivity [1, 2]. The cleanest experimental examples of quantum criticality occur in heavy-fermion systems rather than high T_c cuprates, but the experimental measurements in heavy fermions raise equally confounding theoretical puzzles [3]. Most tellingly, the resistivity scales linearly with the temperature from the onset of superconductivity up to the crystal melting temperature [4] and this linear scaling is in conflict with single correlation length scaling at criticality [5]. The failure of standard perturbative theoretical methods to describe such behavior is thought to indicate that the underlying quantum critical system is strongly coupled [6, 7].

The combination of strong coupling and scale-invariant critical dynamics makes these systems an ideal arena for the application of the AdS/CFT correspondence: the well-established relation between strongly coupled conformal field theories (CFT) and gravitational theories in anti-de Sitter (AdS) spacetimes. An AdS/CFT computation of single-fermion spectral functions — which are directly experimentally accessible via Angle-Resolved Photoemission Spectroscopy [8–10] — bears out this promise of addressing fermionic quantum criticality [11–15] (see also [16, 17]). The AdS/CFT single fermion spectral function exhibits distinct sharp quasiparticle peaks, associated with the formation of a Fermi surface, emerging from a scale-free state. The fermion liquid which this

Fermi surface captures is generically singular: it has either a non-linear dispersion or non-quadratic pole strength [11, 13]. The precise details depend on the parameters of the AdS model.

From the AdS gravity perspective, peaks with linear dispersion correspond to the existence of a stable charged fermionic quasinormal mode in the spectrum of a charged AdS black hole. The existence of a stable charged bosonic quasinormal mode is known to signal the onset of an instability towards a new ground state with a pervading Bose condensate extending from the charged black hole horizon to the boundary of AdS. The dual CFT description of this charged condensate is spontaneous symmetry breaking as in a superfluid and a conventional superconductor [18–21]. For fermionic systems empirically the equivalent robust $T = 0$ ground state is the Landau Fermi Liquid — the quantum ground state of a system with a finite number of fermions. The existence of a stable fermionic quasinormal mode suggests that an AdS dual of a finite fermion density state exists.

Here we shall make a step towards the set of AdS/CFT rules for CFTs with a finite fermion density. The essential ingredient will be Migdal’s theorem, which relates the characteristic jump in fermion occupation number at the energy ω_F of the highest occupied state to the pole strength of the quasiparticle. The latter we know from the spectral function analysis and its AdS formulation is therefore known. Using this, we can show that the fermion number discontinuity is encoded in the *probability density* of the normalizable wavefunction of the dual AdS fermion field.

This shows that the AdS dual of a Fermi liquid is given by a system with occupied fermionic states in the bulk. The Fermi liquid is clearly not a scale invariant state, but any such states will have energy, momentum/pressure and charge and will change the interior geometry from AdS to something else. Which particular (set of) state(s) is the right one, it does not yet tell us, as this conclusion relies only on the asymptotic behavior of fermion fields near the AdS boundary. Here we shall take the simplest such state: a single fermion.¹ Constructing first a set of equations in terms of the spatially averaged density, we find the associated backreacted asymptotically AdS solution. This approximate solution is already good enough to solve several problems of principle:

- A charged AdS black hole in the presence of charged fermionic modes has a critical temperature below which fermionic Dirac “hair” forms. For our effective single fermion solution, the derivative of the free energy has the characteristic discontinuity of a first order transition. In AdS/CFT this has to be the case: In contrast to bosonic quasinormal modes, a fermionic quasinormal mode can never cause a linear instability indicative of a continuous phase transition. In the language of spectral functions, the pole of the retarded Green’s function can never cross to the upper-half plane [13].² The absence of a perturbative instability between this conjectured Dirac “black hole hair” solution and the “bald” charged AdS black hole can be explained if the transition is a first order gas-liquid transition. The existence of first order transition follows from a thermodynamic analysis of the free energy rather than a spectral analysis of small fluctuations.

¹These solutions are therefore the AdS extensions of [22–25].

²Ref. [41] argues that the instability can be second order.

- This solution with finite fermion profile is the preferred ground state at low temperatures compared to the bare charged AdS black hole. The latter is therefore a false vacuum in a theory with charged fermions. Confusing a false vacuum with the true ground state can lead to anomalous results. Indeed the finite temperature behavior of fermion spectral functions in AdS Reissner-Nordström, exhibited in the combination of the results of [11, 13] and [12], shows strange behavior. The former [11, 13] found sharp quasiparticle peaks at a frequency $\omega_F = 0$ in natural AdS units, whereas the latter [12] found sharp quasiparticle peaks at finite Fermi energy $\omega_F \neq 0$. As we will show, both peaks in fact describe the same physics: the $\omega_F \neq 0$ peak is a finite temperature manifestation of (one of the) $\omega = 0$ peaks in [13]. Its shift in location at finite temperature is explained by the existence of the nearby true finite fermion density ground state, separated by a potential barrier from the AdS Reissner-Nordström solution.
- The solution we construct here only considers the backreaction on the electrostatic potential. We show, however, that the gravitational energy density diverges at the horizon. This ought to be, as one expects the infrared geometry to change due to fermion profile. The charged AdS-black hole solution corresponds to a CFT system in a state with large ground state entropy. This is the area of the extremal black-hole horizon at $T = 0$. Systems with large ground-state entropy are notoriously unstable to collapse to a low-entropy state, usually by spontaneous symmetry breaking. In a fermionic system it should be the collapse to the Fermi liquid. The final state will generically be a geometry that asymptotes to Lifshitz type, i.e. the background breaks Lorentz-invariance and has a double-pole horizon with vanishing area, as expounded in [26]. Indeed the gravitational energy density diverges at the horizon in a similar way as other systems that are known to gravitationally backreact to a Lifshitz solution. The fully backreacted geometry includes important separate physical aspects — it is relevant to the stability and scaling properties of the Fermi liquid — and will be considered in a companion article.

The Dirac hair solution thus captures the physics one expects of the dual of a Fermi liquid. We have based its construction on a derived set of AdS/CFT rules to describe systems at finite fermion density. Qualitatively the result is as expected: one also needs occupied fermionic states in the bulk. Next to our effective single fermion approximation, another simple candidate is the backreacted AdS-Fermi-gas [26]/electron star [27] which appeared during the course of this work.³ The difference between the two approaches are the assumptions used to reduce the interacting Fermi system to a tractable solution. Ideally, one should carefully track all the fermion wavefunctions as in the recent article [38]. As explained in [31] the Fermi-gas and the single Dirac field are the two “local” approximations to the generic non-local multiple fermion system in the bulk, in very different regimes of applicability. The electron-star/Fermi-gas is considered in the Thomas-Fermi limit where the microscopic charge of the constituent fermions is sent to zero keeping the overall charge

³See also [28, 29]. An alternative approach to back-reacting fermions is [30].

fixed, whereas the single Dirac field clearly is the ‘limit’ where the microscopic charge equals the total charge in the system. This is directly evident in the spectral functions of both systems. The results presented here show that each pole in the CFT spectral function corresponds to a unique occupied Fermi state in the bulk; the electron star spectra show a parametrically large number of poles [31–33], whereas the Dirac hair state has a single quasiparticle pole by construction. The AdS-Dirac-hair black hole derived here therefore has the benefit of a direct connection with a unique Fermi liquid state in the CFT. This is in fact the starting point of our derivation.

In the broader context, the existence of both the Dirac hair and backreacted Fermi gas solution is not a surprise. It is a manifestation of *universal* physics in the presence of charged AdS black holes. The results here, and those of [11, 13, 26, 27], together with the by now extensive literature on holographic superconductors, i.e. Bose condensates, show that at sufficiently low temperature in units of the black-hole charge, the electric field stretching to AdS-infinity causes a spontaneous discharge of the bulk vacuum outside of the horizon into the charged fields of the theory — whatever their nature. The positively charged excitations are repelled by the black hole, but cannot escape to infinity in AdS and they form a charge cloud hovering over the horizon. The negatively charged excitations fall into the black-hole and neutralize the charge, until one is left with an uncharged black hole with a condensate at finite T or a pure asymptotically AdS-condensate solution at $T = 0$. As [26, 27] and we show, the statistics of the charged particle do not matter for this condensate formation, except in the way it forms: bosons superradiate and fermions nucleate. The dual CFT perspective of this process is “entropy collapse”. The final state therefore has negligible ground state entropy and is stable. The study of charged black holes in AdS/CFT is therefore a novel way to understand the stability of charged interacting matter which holds much promise.

2 From Green’s function to AdS/CFT rules for a Fermi liquid

We wish to show how a solution with finite fermion number — a Fermi liquid — is encoded in AdS. The exact connection and derivation will require a review of what we have learned of Dirac field dynamics in AdS/CFT through Green’s functions analysis. The defining signature of a Fermi liquid is a quasi-particle pole in the (retarded) fermion propagator,

$$G_R = \frac{Z}{\omega - \mu_R - v_F(k - k_F)} + \text{regular} \tag{2.1}$$

Phenomenologically a non-zero residue at the pole, Z , also known as the pole strength, is the indicator of a Fermi liquid state. Migdal famously related the pole strength to the occupation number discontinuity at the pole $\omega = 0$.

$$Z = \lim_{\epsilon \rightarrow 0} [n_F(\omega - \epsilon) - n_F(\omega + \epsilon)] \tag{2.2}$$

where

$$n_F(\omega) = \int d^2k f_{FD} \left(\frac{\omega}{T} \right) \text{Im}G_R(\omega, k).$$

with f_{FD} the Fermi-Dirac distribution function. Vice versa, a Fermi liquid with a Fermi-Dirac jump in occupation number at the Fermi energy $\omega_F = 0$ has a low-lying quasiparticle excitation. Using our knowledge of fermionic spectral functions in AdS/CFT we shall first relate the pole-strength Z to known AdS quantities. Then using Migdal's relation, the dual of a Fermi liquid is characterized by an asymptotically AdS solution with non-zero value for these very objects.

The Green's functions derived in AdS/CFT are those of charged fermionic operators with scaling dimension Δ , dual to an AdS Dirac field with mass $m = \Delta - \frac{d}{2}$. We shall focus on $d = 2 + 1$ dimensional CFTs. In its gravitational description this Dirac field is minimally coupled to $3 + 1$ dimensional gravity and electromagnetism with action

$$S = \int d^4x \sqrt{-g} \left[\frac{1}{2\kappa^2} \left(R + \frac{6}{L^2} \right) - \frac{1}{4} F_{MN}^2 - \bar{\Psi} (\not{D} + m) \Psi \right]. \quad (2.3)$$

For zero background fermions, $\Psi = 0$, a spherically symmetric solution is a charged AdS₄ black-hole background

$$\begin{aligned} ds^2 &= \frac{L^2 \alpha^2}{z^2} (-f(z) dt^2 + dx^2 + dy^2) + \frac{L^2}{z^2} \frac{dz^2}{f(z)}, \\ f(z) &= (1-z)(1+z+z^2-q^2z^3), \\ A_0^{(bg)} &= 2q\alpha(z-1). \end{aligned} \quad (2.4)$$

Here $A_0^{(bg)}$ is the time-component of the U(1)-vector-potential, L is the AdS radius and the temperature and chemical potential of the black hole equal

$$T = \frac{\alpha}{4\pi} (3 - q^2), \quad \mu_0 = -2q\alpha, \quad (2.5)$$

where q is the black hole charge.

To compute the Green's functions we need to solve the Dirac equation in the background of this charged black hole:

$$e_A^M \Gamma^A (D_M + ieg A_M) \Psi + m \Psi = 0, \quad (2.6)$$

where the vielbein e_A^M , covariant derivative D_M and connection A_M correspond to the fixed charged AdS black-hole metric and electrostatic potential (2.4) Denoting $A_0 = \Phi$ and taking the standard AdS-fermion projection onto $\Psi_{\pm} = \frac{1}{2}(1 \pm \Gamma^Z)\Psi$, the Dirac equation reduces to

$$(\partial_z + \mathcal{A}_{\pm}) \Psi_{\pm} = \mp \mathcal{T} \Psi_{\mp} \quad (2.7)$$

with

$$\begin{aligned} \mathcal{A}_{\pm} &= -\frac{1}{2z} \left(3 - \frac{zf'}{2f} \right) \pm \frac{mL}{z\sqrt{f}}, \\ \mathcal{T} &= \frac{i(-\omega + g\Phi)}{\alpha f} \gamma^0 + \frac{i}{\alpha\sqrt{f}} k_i \gamma^i. \end{aligned} \quad (2.8)$$

Here γ^μ are the 2+1-dimensional Dirac matrices, obtained after decomposing the 3+1 dimensional Γ^μ -matrices.

Explicitly the Green's function is extracted from the behavior of the solution to the Dirac equation at the AdS-boundary. The boundary behavior of the bulk fermions is

$$\begin{aligned}\Psi_+(\omega, k; z) &= A_+ z^{\frac{3}{2}-m} + B_+ z^{\frac{5}{2}+m} + \dots, \\ \Psi_-(\omega, k; z) &= A_- z^{\frac{5}{2}-m} + B_- z^{\frac{3}{2}+m} + \dots,\end{aligned}\tag{2.9}$$

where $A_\pm(\omega, k)$, $B_\pm(\omega, k)$ are not all independent but related by the Dirac equation at the boundary

$$A_- = -\frac{i\mu}{(2m-1)}\gamma^0 A_+, \quad B_+ = -\frac{i\mu}{(2m+1)}\gamma^0 B_-.\tag{2.10}$$

The CFT Green's function then equals [11, 12, 34]

$$G_R = \lim_{z \rightarrow 0} z^{-2m} \frac{\Psi_-(z)}{\Psi_+(z)} - \text{singular} = \frac{B_-}{A_+}.\tag{2.11}$$

In other words B_- is the CFT response to the (infinitesimal) source A_+ . Since in the Green's function the fermion is a fluctuation, the functions $\Psi_\pm(z)$ are now probe solutions to the Dirac equation in a fixed gravitational and electrostatic background (for ease of presentation we are considering $\Psi_\pm(z)$ as numbers instead of two-component vectors). The boundary conditions at the horizon/AdS interior determine which Green's function one considers, e.g. infalling horizon boundary conditions yield the retarded Green's function. For non-zero chemical potential this fermionic Green's function can have a pole signalling the presence of a Fermi surface. This pole occurs precisely for a (quasi-)normalizable mode, i.e. a specific energy ω_F and momentum k_F where the external source $A_+(\omega, k)$ vanishes (for infalling boundary conditions at the horizon).

Knowing that the energy of the quasinormal mode is always $\omega_F = 0$ [11] and following [13], we expand G_R around $\omega = 0$ as:

$$G_R(\omega) = \frac{B_+^{(0)} + \omega B^{(1)+} + \dots}{A_+^{(0)} + \omega A_+^{(1)} + \dots}.\tag{2.12}$$

A crucial point is that in this expansion we are assuming that the pole will correspond to a stable quasiparticle, i.e. there are no fractional powers of ω less than unity in the expansion around $\omega_F = 0$ [13]. Fermions in AdS/CFT are of course famous for allowing more general pole-structures corresponding to Fermi-surfaces without stable quasiparticles [13], but those Green's functions are not of the type (2.1) and we shall therefore not consider them here. The specific Fermi momentum k_F associated with the Fermi surface is the momentum value for which the first ω -independent term in the denominator vanishes $A_+^{(0)}(k_F) = 0$ — for this value of $k = k_F$ the presence of a pole in the Green's functions at $\omega = 0$ is manifest. Writing $A_+^{(0)} = a_+(k - k_F) + \dots$ and comparing with the standard quasi-particle propagator,

$$G_R = \frac{Z}{\omega - \mu_R - v_F(k - k_F)} + \text{regular}\tag{2.13}$$

we read off that the pole-strength equals

$$Z = B_-^{(0)}(k_F)/A_+^{(1)}(k_F).$$

We thus see that a non-zero pole-strength is ensured by a non-zero value of $B_-(\omega = 0, k = k_F)$ — the “response” *without* corresponding source as $A^{(0)}(k_F) \equiv 0$. Quantitatively the pole-strength also depends on the value of $A_+^{(1)}(k_F) \equiv \partial_\omega A_+(k_F)|_{\omega=0}$, which is always finite. This is not a truly independent parameter, however. The size of the pole-strength has only a relative meaning w.r.t. to the integrated spectral density. This normalization of the pole strength is a global parameter rather than an AdS boundary issue. We now show this by proving that $A_+^{(1)}(k_F)$ is inversely proportional to $B_-^{(0)}(k_F)$ and hence Z is completely set by $B_-^{(0)}(k_F)$, i.e. $Z \sim |B_-^{(0)}(k_F)|^2$. Consider a transform $\widetilde{W}(\Psi_{+,A}, \Psi_{+,B})$ of the Wronskian $W(\Psi_{+,A}, \Psi_{+,B}) = \Psi_{+,A} \partial_z \Psi_{+,B} - (\partial_z \Psi_{+,A}) \Psi_{+,B}$ for two solutions to the second order equivalent of the Dirac equation for the field Ψ_+

$$(\partial_z^2 + P(z)\partial_z + Q_+(z)) \Psi_+ = 0 \tag{2.14}$$

that is conserved (detailed expressions for $P(z)$ and $Q_+(z)$ are given in eq. (2.21)):

$$\widetilde{W}(\Psi_{+,A}(z), \Psi_{+,B}(z), z; z_0) = \exp\left(\int_{z_0}^z P(z)\right) W(\Psi_{+,A}(z), \Psi_{+,B}(z)), \quad \partial_z \widetilde{W} = 0. \tag{2.15}$$

Here z_0 is the infinitesimal distance away from the boundary at $z = 0$ which is equivalent to the UV-cut-off in the CFT. Setting $k = k_F$ and choosing for $\Psi_{+,A} = A_+ z^{3/2-m} \sum_{n=0}^\infty a_n z^n$ and $\Psi_{+,B} = B_+ z^{5/2+m} \sum_{n=0}^\infty b_n z^n$ the real solutions which asymptote to solutions with $B_+(\omega, k_F) = 0$ and $A_+(\omega, k_F) = 0$ respectively, but for a value of ω infinitesimally away from $\omega_F = 0$, we can evaluate \widetilde{W} at the boundary to find,⁴

$$\widetilde{W} = z_0^3(1 + 2m)A_+B_+ = \mu z_0^3 A_+ B_- \tag{2.16}$$

The last step follows from the constraint (2.10) where the reduction from two-component spinors to functions means that γ^0 is replaced by one of its eigenvalues $\pm i$. Taking the derivative of \widetilde{W} at $\omega = 0$ for $k = k_F$ and expanding $A_+(\omega, k_F)$ and $B_-(\omega, k_F)$ as in (2.12), we can solve for $A_+^{(1)}(k_F)$ in terms of $B_-^{(0)}(k_F)$ and arrive at the expression for the pole strength Z in terms of $|B_-^{(0)}(k_F)|^2$:

$$Z = \frac{\mu z_0^3}{\partial_\omega \widetilde{W}|_{\omega=0, k=k_F}} |B_-^{(0)}(k_F)|^2. \tag{2.17}$$

Because $\partial_\omega \widetilde{W}$, as \widetilde{W} , is a number that is independent of z , this expression emphasizes that it is truly the nonvanishing subleading term $B_-^{(0)}(\omega_F, k_F)$ which sets the pole strength, up to a normalization $\partial_\omega \widetilde{W}$ which is set by the fully integrated spectral density. This integration is always UV-cut-off dependent and the explicit z_0 dependence should therefore

⁴ $P(z) = -3/z + \dots$ near $z = 0$

not surprise us.⁵ We should note that, unlike perturbative Fermi liquid theory, Z is a dimensionful quantity of mass dimension $2m + 1 = 2\Delta - 2$, which illustrates more directly its scaling dependence on the UV-energy scale z_0 . At the same time Z is real, as it can be shown that both $\partial_\omega \widetilde{W}|_{\omega=0, k=k_F} = \mu z_0^3 A_+^{(1)} B_-^{(0)}$ and $B_-^{(0)}$ are real [13].

2.1 The AdS dual of a stable Fermi liquid: applying Migdal’s relation holographically

We have thus seen that a solution with nonzero $B_-(\omega_F, k_F)$ whose corresponding external source vanishes (by definition of ω_F, k_F), is related to the presence of a quasiparticle pole in the CFT. Through Migdal’s theorem its pole strength is related to the presence of a discontinuity of the occupation number, and this discontinuity is normally taken as the characteristic signature of the presence of a Fermi Liquid. Qualitatively we can already infer that an AdS gravity solution with non-vanishing $B_-(\omega_F, k_F)$ corresponds to a Fermi Liquid in the CFT. We thus seek solutions to the Dirac equation with vanishing external source A_+ but non-vanishing response B_- coupled to electromagnetism (and gravity). The construction of the AdS black hole solution with a finite single fermion wavefunction is thus analogous to the construction of a holographic superconductor [19] with the role of the scalar field now taken by a Dirac field of mass m .

This route is complicated, however, by the spinor representation of the Dirac fields, and the related fermion doubling in AdS. Moreover, relativistically the fermion Green’s function is a matrix and the pole strength Z appears in the time-component of the vector projection $\text{Tr} \gamma^i G$. As we take this and the equivalent jump in occupation number to be the signifying characteristic of a Fermi liquid state in the CFT, it would be much more direct if we can derive an AdS radial evolution equation for the vector-projected Green’s function and hence the occupation number discontinuity directly. From the AdS perspective is also more convenient to work with bilinears such as Green’s functions, since the Dirac fields always couple pairwise to bosonic fields.

To do so, we start again with the two decoupled second order equations equivalent to the Dirac equation (2.7)

$$(\partial_z^2 + P(z)\partial_z + Q_\pm(z)) \Psi_\pm = 0 \tag{2.20}$$

⁵Using that \widetilde{W} is conserved, one can e.g. compute it at the horizon. There each solution $\Psi_{+,A}(\omega, k_F; z)$, $\Psi_{+,B}(\omega, k_F; z)$ is a linear combination of the infalling and outgoing solution

$$\begin{aligned} \Psi_{+,A}(z) &= \bar{\alpha} (1-z)^{-1/4+i\omega/4\pi T} + \alpha (1-z)^{-1/4-i\omega/4\pi T} + \dots \\ \Psi_{+,B}(z) &= \bar{\beta} (1-z)^{-1/4+i\omega/4\pi T} + \beta (1-z)^{-1/4-i\omega/4\pi T} + \dots \end{aligned} \tag{2.18}$$

yielding a value of $\partial_\omega \widetilde{W}$ equal to $(P(z) = 1/2(1-z) + \dots \text{ near } z = 1)$

$$\partial_\omega \widetilde{W} = \frac{i}{2\pi T} \mathcal{N}(z_0) (\bar{\alpha}\beta - \bar{\beta}\alpha) \tag{2.19}$$

with $\mathcal{N}(z_0) = \exp \int_{z_0}^z dz \left[P(z) - \frac{1}{2(1-z)} \right]$.

with

$$\begin{aligned}
 P(z) &= (\mathcal{A}_- + \mathcal{A}_+) - [\partial_z, \mathcal{T}] \frac{\mathcal{T}}{T^2}, \\
 Q_{\pm}(z) &= \mathcal{A}_- \mathcal{A}_+ + (\partial_z \mathcal{A}_{\pm}) - [\partial_z, \mathcal{T}] \frac{\mathcal{T}}{T^2} \mathcal{A}_{\pm} + T^2.
 \end{aligned}
 \tag{2.21}$$

Note that both $P(z)$ and $Q_{\pm}(z)$ are matrices in spinor space. The general solution to this second order equation — with the behavior at the horizon/interior appropriate for the Green’s function one desires — is a matrix valued function $(M_{\pm}(z))^{\alpha}_{\beta}$ and the field $\Psi_{\pm}(z)$ equals $\Psi_{\pm}(z) = M_{\pm}(z)\Psi_{\pm}^{(\text{hor})}$. Due to the first order nature of the Dirac equation the horizon values $\Psi_{\pm}^{(\text{hor})}$ are not independent but related by a z -independent matrix $S\Psi_+^{(\text{hor})} = \Psi_-^{(\text{hor})}$, which can be deduced from the near-horizon behavior of (2.10); specifically $S = \gamma^0$. One then obtains the Green’s function from the on-shell boundary action (see e.g. [12, 35])

$$S_{\text{bnd}} = \oint_{z=z_0} d^d x \bar{\Psi}_+ \Psi_- \tag{2.22}$$

as follows: Given a boundary source ζ_+ for $\Psi_+(z)$, i.e. $\Psi_+(z_0) \equiv \zeta_+$, one concludes that $\Psi_+^{(\text{hor})} = M_+^{-1}(z_0)\zeta_+$ and thus $\Psi_+(z) = M_+(z)M_+^{-1}(z_0)\zeta_+$, $\Psi_-(z) = M_-(z)SM_+^{-1}(z_0)\zeta_+$. Substituting these solutions into the action gives

$$S_{\text{bnd}} = \oint_{z=z_0} d^d x \bar{\zeta}_+ M_-(z_0) S M_+^{-1}(z_0) \zeta_+ \tag{2.23}$$

The Green’s function is obtained by differentiating w.r.t. $\bar{\zeta}_+$ and ζ_+ and discarding the conformal factor z_0^{2m} with m the AdS mass of the Dirac field (one has to be careful for $mL > 1/2$ with analytic terms [35])

$$G = \lim_{z_0 \rightarrow 0} z_0^{-2m} M_-(z_0) S M_+^{-1}(z_0). \tag{2.24}$$

Since $M_{\pm}(z)$ are determined by evolution equations in z , it is clear that the Green’s function itself is also determined by an evolution equation in z , i.e. there is some function $G(z)$ which reduces in the limit $z \rightarrow 0$ to $z_0^{2m}G$. One obvious candidate is the function

$$G^{(\text{obv})}(z) = M_-(z) S M_+^{-1}(z). \tag{2.25}$$

Using the original Dirac equations one can see that this function obeys the non-linear evolution equation

$$\partial_z G^{(\text{obv})}(z) = -\mathcal{A}_- G^{(\text{obv})}(z) - \mathcal{T} M_+ S M_+^{-1} + \mathcal{A}_+ G^{(\text{obv})}(z) + G^{(\text{obv})}(z) \mathcal{T} G^{(\text{obv})}(z). \tag{2.26}$$

This is the approach used in [11], where a specific choice of momenta is chosen such that M_+ commutes with S . For a generic choice of momenta, consistency requires that one also considers the evolution equation for $M_+(z)S M_+^{-1}(z)$.

There is, however, another candidate for the extension $G(z)$ which is based on the underlying boundary action. Rather than extending the kernel $M_-(z_0)M_+^{-1}(z_0)$ of the boundary action we extend the constituents of the action itself, based on the individual

fermion wavefunctions $\Psi_{\pm}(z) = M_{\pm}(z)S^{\frac{1}{2}\mp\frac{1}{2}}M_{\pm}^{-1}(z_0)$. We define an extension of the matrix $G(z)$ including an expansion in the complete set $\Gamma^I = \{\mathbb{1}, \gamma^i, \gamma^{ij}, \dots, \gamma^{i_1, i_d}\}$ (with $\gamma^4 = i\gamma^0$)

$$G^I(z) = \bar{M}_+^{-1}(z_0)\bar{M}_+(z)\Gamma^I M_-(z)SM_+^{-1}(z_0), \quad G^I(z_0) = \Gamma^I G(z_0) \quad (2.27)$$

where $\bar{M} = i\gamma^0 M^\dagger i\gamma^0$. Using again the original Dirac equations, this function obeys the evolution equation

$$\partial_z G^I(z) = -(\bar{\mathcal{A}}_+ + \mathcal{A}_-)G^I(z) - \bar{M}_{+,0}^{-1}\bar{M}_-(z)\bar{\mathcal{T}}\Gamma^I M_-(z)SM_{+,0}^{-1} + \bar{M}_{+,0}^{-1}\bar{M}_+(z)\Gamma^I \mathcal{T}M_+(z)SM_{+,0}^{-1} \quad (2.28)$$

Recall that $\mathcal{T}\gamma^{i_1 \dots i_p} = \mathcal{T}^{[i_1 \gamma \dots i_p]} + \mathcal{T}_j \gamma^{j i_1 \dots i_p}$. It is then straightforward to see that for consistency, we also need to consider the evolution equations of

$$\mathcal{J}_+^I = \bar{M}_{+,0}^{-1}\bar{M}_+(z)\Gamma^I M_+(z)SM_{+,0}^{-1}, \quad \mathcal{J}_-^I = \bar{M}_{+,0}^{-1}\bar{M}_-(z)\Gamma^I M_-(z)SM_{+,0}^{-1}$$

and

$$\bar{G}^I = \bar{M}_{+,0}^{-1}\bar{M}_-(z)\Gamma^I M_+(z)SM_{+,0}^{-1}.$$

They are

$$\begin{aligned} \partial_z \mathcal{J}_+^{i_1 \dots i_p}(z) &= -2\text{Re}(\mathcal{A}_+) \mathcal{J}_+^{i_1 \dots i_p} - \bar{\mathcal{T}}^{[i_1 \bar{G}^{i_2 \dots i_p]}(z) \\ &\quad - \bar{\mathcal{T}}_j \bar{G}^{j i_1 \dots i_p}(z) - G^{[i_1 \dots i_{p-1}}(z) \mathcal{T}^{i_p]} - G^{i_1 \dots i_p j}(z) \mathcal{T}_j \\ \partial_z \mathcal{J}_-^{i_1 \dots i_p}(z) &= -2\text{Re}(\mathcal{A}_-) \mathcal{J}_-^{i_1 \dots i_p} + \bar{\mathcal{T}}^{[i_1 G^{i_2 \dots i_p]}(z) \\ &\quad + \bar{\mathcal{T}}_j G^{j i_1 \dots i_p}(z) + \bar{G}^{[i_1 \dots i_{p-1}}(z) \mathcal{T}^{i_p]} + \bar{G}^{i_1 \dots i_p j}(z) \mathcal{T}_j \\ \partial_z \bar{G}^{i_1 \dots i_p}(z) &= -(\bar{\mathcal{A}}_- + \mathcal{A}_+) \bar{G}^{i_1 \dots i_p} - \bar{\mathcal{T}}^{[i_1 \mathcal{J}_+^{i_2 \dots i_p]}(z) \\ &\quad - \bar{\mathcal{T}}_j \mathcal{J}_+^{j i_1 \dots i_p}(z) - \mathcal{J}_-^{[i_1 \dots i_{p-1}}(z) \mathcal{T}^{i_p]} + \mathcal{J}_-^{i_1 \dots i_p j}(z) \mathcal{T}_j \end{aligned} \quad (2.29)$$

The significant advantage of these functions G^I , \bar{G}^I , \mathcal{J}_\pm^I is that the evolution equations are now linear. This approach may seem overly complicated. However, if the vector \mathcal{T}^i happens to only have a single component nonzero, then the system reduces drastically to the four fields \mathcal{J}_\pm^i , $G^\mathbb{1}$, $\bar{G}^\mathbb{1}$. We shall see below that a similar drastic reduction occurs, when we consider only spatially and temporally averaged functions $J^I = \int dt d^2x \mathcal{J}_\pm^I$.

Now the two extra currents \mathcal{J}_\pm^I have a clear meaning in the CFT. The current $G^I(z)$ reduces by construction to Γ^I times the Green's function $G^\mathbb{1}(z_0)$ on the boundary, and clearly $\bar{G}^I(z)$ is its hermitian conjugate. The current \mathcal{J}_+^I reduces at the boundary to $\mathcal{J}_+^I = \Gamma^I M_{+,0} SM_{+,0}^{-1}$. Thus \mathcal{J}_+^I sets the normalization of the linear system (2.29). The interesting current is the current \mathcal{J}_-^I . Using that $\bar{S} = S^{-1}$, it can be seen to reduce on the boundary to the combination $\bar{\mathcal{J}}_+^\mathbb{1} \bar{G}^\mathbb{1} \Gamma^I G^\mathbb{1}$. Thus, $(\bar{\mathcal{J}}_+^\mathbb{1})^{-1} \mathcal{J}_-^\mathbb{1}$ is the norm squared of the Green's function, i.e. the probability density of the off-shell process.

For an off-shell process or a correlation function the norm-squared has no real functional meaning. However, we are specifically interested in solutions in the absence of an external source, i.e. the *on-shell* correlation functions. In that case the analysis is quite different. The on-shell condition is equivalent to choosing momenta to saturate the pole in the Green's function, i.e. it is precisely choosing dual AdS solutions whose leading external source A_\pm

vanishes. Then M_+ and M_- are no longer independent, but $M_{+,0} = \delta B_+ / \delta \Psi_+^{(\text{hor})} = -\frac{i\mu\gamma^0}{2m+1} M_{-,0} S$. As a consequence all boundary values of $\mathcal{J}_-^I(z_0), G^I(z_0), \bar{G}^I(z_0)$ become proportional; specifically using $S = \gamma^0$ one has that

$$\mathcal{J}_-^0(z_0)|_{\text{on-shell}} = \frac{(2m+1)}{\mu} \gamma^0 G^{\mathbb{I}}(z_0)|_{\text{on-shell}} \quad (2.30)$$

is the ‘‘on-shell’’ Green’s function. Now, the meaning of the on-shell correlation function is most evident in thermal backgrounds. It equals the density of states $\rho(\omega(k)) = -\frac{1}{\pi} \text{Im} G_R$ times the Fermi-Dirac distribution [36]

$$\text{Tr} i \gamma^0 G_F^I(\omega_{\text{bare}}(k), k)|_{\text{on-shell}} = 2\pi f_{FD} \left(\frac{\omega_{\text{bare}}(k) - \mu}{T} \right) \rho(\omega_{\text{bare}}(k)) \quad (2.31)$$

For a Fermi liquid with the defining off-shell Green’s function (2.1) $\omega_{\text{bare}}(k_F) - \mu \equiv \omega = 0$ and $\rho(\omega_{\text{bare}}(k)) = Z_{z_0} \delta^2(k - k_F) \delta(\omega) + \dots$. Thus we see that the boundary value of $\mathcal{J}_-^{(0)}(z_0)|_{\text{on-shell}} = Z f_{FD}(0) \delta^3(0)$ indeed captures the pole strength directly times a product of distributions. This product of distributions can be absorbed in setting the normalization. An indication that this is correct is that the determining equations for $G^I, \bar{G}^I, \mathcal{J}_\pm^I$ remain unchanged if we multiply $G^I, \bar{G}^I, \mathcal{J}_\pm^I$ on both sides with $M_{+,0}$. If $M_{+,0}$ is unitary it is just a similarity transformation. However, from the definition of the Green’s function, one can see that this transformation precisely removes the pole. This ensures that we obtain finite values for $G^I, \bar{G}^I, \mathcal{J}_\pm^I$ at the specific pole-values ω_F, k_F where the distributions would naively blow up.

2.1.1 Boundary conditions and normalizability

We have shown that a normalizable solution to \mathcal{J}_-^0 from the equations (2.29) correctly captures the pole strength directly. However, ‘normalizable’ is still defined in terms of an absence of a source for the fundamental Dirac field Ψ_\pm rather than the composite fields \mathcal{J}_\pm^I and G^I . One would prefer to determine normalizability directly from the boundary behavior of the composite fields. This can be done. Under the assumption that the electrostatic potential Φ is regular, i.e.

$$\Phi = \mu - \rho z + \dots \quad (2.32)$$

the ‘‘connection’’ \mathcal{T}^I is subleading to the connection \mathcal{A} near $z = 0$. Thus the equations of motion near $z = 0$ do not mix the various \mathcal{J}_\pm^I, G^I and the composite fields behave as

$$\begin{aligned} \mathcal{J}_+^I &= j_{3-2m}^I z^{3-2m} + j_{4+}^I z^4 + j_{5+2m}^I z^{5+2m} + \dots, \\ \mathcal{J}_-^I &= j_{5-2m}^I z^{5-2m} + j_{4-}^I z^4 + j_{3+2m}^I z^{3+2m} + \dots, \\ G^I &= I_{4-2m}^I z^{4-2m} + I_3^I z^3 + I_{4+2m}^I z^{4+2m} + I_5^I z^5 + \dots, \end{aligned} \quad (2.33)$$

with the identification

$$\begin{aligned} j_{3-2m}^I &= \bar{A}_+ \Gamma^I A_+, & j_{4+}^I &= \bar{A}_+ \Gamma^I B_+ + \bar{B}_+ \Gamma^I A_+, & j_{5+2m}^I &= \bar{B}_+ \Gamma^I B_+, \\ j_{3+2m}^I &= \bar{A}_- \Gamma^I A_-, & j_{4-}^I &= \bar{A}_- \Gamma^I B_- + \bar{B}_- \Gamma^I A_-, & j_{5-2m}^I &= \bar{B}_- \Gamma^I B_-, \\ I_{4-2m}^I &= \bar{A}_+ \Gamma^I A_-, & I_3^I &= \bar{A}_+ \Gamma^I B_-, & I_{4+2m}^I &= \bar{B}_+ \Gamma^I B_-, & I_5^I &= \bar{B}_+ \Gamma^I A_-. \end{aligned} \quad (2.34)$$

A ‘normalizable’ solution in \mathcal{J}_-^I and thus \mathcal{J}_-^0 is therefore defined by the vanishing of *both* the leading *and* the subleading term.

3 An AdS black hole with Dirac hair

Having determined a set of AdS evolution equations and boundary conditions that compute the pole strength Z directly through the currents $\mathcal{J}_-^{(0)}(z)$ and $G^I(z)$, we can now try to construct the AdS dual of a system with finite fermion density, including backreaction. As we remarked in the beginning of section 2.1, the demand that the solutions be normalizable means that the construction of the AdS black hole solution with a finite single fermion wavefunction is analogous to the construction of a holographic superconductor [19] with the role of the scalar field now taken by the Dirac field. The starting point therefore is the charged AdS₄ black-hole background (2.4) and we should show that at low temperatures this AdS Reissner-Nordström black hole is unstable towards a solution with a finite Dirac profile. We shall do so in a simplified “large charge” limit where we ignore the gravitational dynamics, but as is well known from holographic superconductor studies (see e.g. [19–21]) this limit already captures much of the essential physics. In a companion article [37] we will construct the full backreacted ground state including the gravitational dynamics.

In this large charge non-gravitational limit the equations of motion for the action (2.3) reduce to those of U(1)-electrodynamics coupled to a fermion with charge g in the background of this black hole:

$$\begin{aligned} D_M F^{MN} &= ig e_A^N \bar{\Psi} \Gamma^A \Psi, \\ 0 &= e_A^M \Gamma^A (D_M + ieg A_M) \Psi + m \Psi. \end{aligned} \tag{3.1}$$

Thus the vielbein e_A^M and covariant derivative D_M remain those of the fixed charged AdS black hole metric (2.4), but the vector-potential now contains a background piece $A_0^{(bg)}$ plus a first-order piece $A_M = A_M^{(bg)} + A_M^{(1)}$, which captures the effect of the charge carried by the fermions.

Following our argument set out in previous section that it is more convenient to work with the currents $\mathcal{J}_\pm^I(z), G^I(z)$ instead of trying to solve the Dirac equation directly, we shall first rewrite this coupled non-trivial set of equations of motion in terms of the currents while at the same time using symmetries to reduce the complexity. Although a system at finite fermion density need not be homogeneous, the Fermi liquid ground state is. It therefore natural to make the ansatz that the final AdS solution is static and preserves translation and rotation along the boundary. As the Dirac field transforms non-trivially under rotations and boosts, we cannot make this ansatz in the strictest sense. However, in some average sense which we will make precise, the solution should be static and translationally invariant. Then translational and rotational invariance allow us to set $A_i = 0$, $A_z = 0$, whose equations of motions will turn into constraints for the remaining degrees of freedom. Again denoting $A_0 = \Phi$, the equations reduce to the following after the projection

onto $\Psi_{\pm} = \frac{1}{2}(1 \pm \Gamma^Z)\Psi$.

$$\begin{aligned} \partial_z^2 \Phi &= \frac{-gL^3 \alpha}{z^3 \sqrt{f}} (\bar{\Psi}_+ i\gamma^0 \Psi_+ + \bar{\Psi}_- i\gamma^0 \Psi_-), \\ (\partial_z + \mathcal{A}_{\pm}) \Psi_{\pm} &= \mp \mathcal{T} \Psi_{\mp} \end{aligned} \quad (3.2)$$

with

$$\begin{aligned} \mathcal{A}_{\pm} &= -\frac{1}{2z} \left(3 - \frac{zf'}{2f} \right) \pm \frac{mL}{z\sqrt{f}}, \\ \mathcal{T} &= \frac{i(-\omega + g\Phi)}{\alpha f} \gamma^0 + \frac{i}{\alpha\sqrt{f}} k_i \gamma^i. \end{aligned} \quad (3.3)$$

as before.

The difficult part is to “impose” staticity and rotational invariance for the non-invariant spinor. This can be done by rephrasing the dynamics in terms of fermion current bilinears, rather than the fermions themselves. We shall first do so rather heuristically, and then show that the equations obtained this way are in fact the flow equations for the Green’s functions and composites $\mathcal{J}^I(z)$, $G^I(z)$ constructed in the previous section. In terms of the local vector currents⁶

$$J_{+}^{\mu}(x, z) = \bar{\Psi}_{+}(x, z) i\gamma^{\mu} \Psi_{+}(x, z), \quad J_{-}^{\mu}(x, z) = \bar{\Psi}_{-}(x, z) i\gamma^{\mu} \Psi_{-}(x, z), \quad (3.4)$$

or equivalently

$$J_{+}^{\mu}(p, z) = \int d^3 k \bar{\Psi}_{+}(-k, z) i\gamma^{\mu} \Psi_{+}(p+k, z), \quad J_{-}^{\mu}(p, z) = \int d^3 k \bar{\Psi}_{-}(-k, z) i\gamma^{\mu} \Psi_{-}(p+k, z). \quad (3.5)$$

rotational invariance means that spatial components J_{\pm}^i should vanish on the solution — this solves the constraint from the A_i equation of motion, and the equations can be rewritten in terms of J_{\pm}^0 only. Staticity and rotational invariance in addition demand that the bilinear momentum p_{μ} vanish. In other words, we are only considering temporally and spatially averaged densities: $J_{\pm}^{\mu}(z) = \int dt d^2 x \bar{\Psi}(t, x, z) i\gamma^{\mu} \Psi(t, x, z)$. Analogous to the bilinear flow equations for the Green’s function, we can act with the Dirac operator on the currents to obtain an effective equation of motion, and this averaging over the relative frequencies ω and momenta k_i will set all terms with explicit k_i -dependence to zero.⁷

⁶In our conventions $\bar{\Psi} = \Psi^{\dagger} i\gamma^0$.

⁷To see this consider

$$(\partial + 2\mathcal{A}_{\pm}) \Psi_{\pm}^{\dagger}(-k) \Psi_{\pm}(k) = \mp \frac{\Phi}{f} (\Psi_{-}^{\dagger} i\gamma^0 \Psi_{+} + \Psi_{+}^{\dagger} i\gamma^0 \Psi_{-}) + \frac{ik_i}{\sqrt{f}} (\Psi_{-}^{\dagger} \gamma^i \Psi_{+} - \Psi_{+}^{\dagger} \gamma^i \Psi_{-}). \quad (3.6)$$

The term proportional to Φ is relevant for the solution. The dynamics of the term proportional to k_i is

$$(\partial + \mathcal{A}_{+} + \mathcal{A}_{-}) (\Psi_{-}^{\dagger} \gamma^i \Psi_{+} - \Psi_{+}^{\dagger} \gamma^i \Psi_{-}) = -2i \frac{k^i}{\sqrt{f}} (\Psi_{+}^{\dagger} \gamma^0 \Psi_{+} + \Psi_{-}^{\dagger} \gamma^0 \Psi_{-}). \quad (3.7)$$

The integral of the r.h.s. over k^i vanishes by the assumption of translational and rotational invariance. Therefore the l.h.s. of (3.7) and thus the second term in eq. (3.6) does so as well.

Restricting to such averaged currents and absorbing a factor of g/α in Φ and a factor of $g\sqrt{L^3}$ in Ψ_{\pm} , we obtain effective equations of motion for the bilinears directly

$$\begin{aligned} (\partial_z + 2\mathcal{A}_{\pm}) J_{\pm}^0 &= \mp \frac{\Phi}{f} I, \\ (\partial_z + \mathcal{A}_+ + \mathcal{A}_-) I &= \frac{2\Phi}{f} (J_+^0 - J_-^0), \\ \partial_z^2 \Phi &= -\frac{1}{z^3 \sqrt{f}} (J_+^0 + J_-^0), \end{aligned} \tag{3.8}$$

with $I = \bar{\Psi}_- \Psi_+ + \bar{\Psi}_+ \Psi_-$, and all fields are real. The remaining constraint from the A_z equation of motion decouples. It demands $\text{Im}(\bar{\Psi}_+ \Psi_-) = \frac{i}{2}(\bar{\Psi}_- \Psi_+ - \bar{\Psi}_+ \Psi_-) = 0$. What the equations (3.8) tell us is that for nonzero J_{\pm}^0 there is a charged electrostatic source for the vector potential Φ in the bulk.

Momentarily we will motivate the effective equations (3.8) at a more fundamental level. Before that there are several remarks to be made

- These equations contain more information than just current conservation $\partial_{\mu} J^{\mu} = 0$. In an isotropic and static background current conservation is trivially true as $\partial_{\mu} J^{\mu} = \partial_0 J^0 = -i \int d\omega e^{-i\omega t} \omega J^0(\omega) = 0$ as $J^0(\omega \neq 0) = 0$.
- We have scaled out the electromagnetic coupling. $\text{AdS}_4/\text{CFT}_3$ duals for which the underlying string theory is known generically have $g = \kappa/L$ with κ the gravitational coupling constant as defined in (2.3). Thus, using standard $\text{AdS}_4/\text{CFT}_3$ scaling, a finite charge in the new units translates to a macroscopic original charge of order $L/\kappa \propto N^{1/3}$. This large charge demands that backreaction of the fermions in terms of its bilinear is taken into account as a source for Φ .
- The equations are local. From the fundamental point of view, that one considers finite density in the bulk, this is strange to say the least. Generic multi-fermion configurations are non-local, see e.g. [38]. These equations can therefore never capture the full bulk fermion dynamics. Our starting point has been a single fermion perspective, where the Pauli blocking induced non-locality is absent. In that context local equations are fine. We have also explicitly averaged over all directions parallel to the boundary and, as we have shown in the previous section (see also footnote 7), it is this averaging that tremendously simplifies the equations. The most curious part may be that this unaveraged set of equations — and therefore also eqs (3.8) — are all local in the radial direction z . From the AdS perspective a many-fermion system should be non-local democratically and thus also exhibit non-locality in z , yet from the CFT perspective where z -dynamics encode RG-flow, it is eminently natural. We leave the resolution of this paradox to future work.

The justification of using (3.8) to construct the AdS dual of a regular Fermi liquid is the connection between local fermion bilinears and the CFT Green's function. The complicated flow equations (2.29) reduce precisely to the first two equations in (3.8) upon performing the spacetime averaging and the trace, i.e. $J_{\pm}^0 = \int d^3k \text{Tr} \mathcal{J}_{\pm}^0$ and $I = \int d^3k \text{Tr} (G^{\mathbb{1}} + \bar{G}^{\mathbb{1}})$.

Combined with the demand that we only consider normalizable solutions and the proof that \mathcal{J}_\pm^0 is proportional to the pole-strength, the radial evolution equations (3.8) are the (complicated) AdS recasting of the RG-flow for the pole-strength. This novel interpretation ought to dispel some of the a priori worries about our unconventional treatment of the fermions through their semi-classical bilinears. There is also support from the gravity side, however. Recall that for conventional many-body systems and fermions in particular one first populates a certain set of states and then tries to compute the macroscopic properties of the collective. In a certain sense the equations (3.8) formulate the same program but in opposite order: one computes the generic wavefunction charge density with and by imposing the right boundary conditions, i.e. normalizability, one selects only the correct set of states. This follows directly from the equivalence between normalizable AdS modes and quasiparticle poles that are characterized by well defined distinct momenta k_F (for $\omega = \omega_F \equiv 0$). The demand that any non-trivial Dirac hair black hole is constructed from normalizable solutions of the composite operators (i.e. their leading and subleading asymptotes vanish⁸) thus means that one imposes a superselection rule on the spatial averaging in the definition of J_\pm^I :

$$\begin{aligned} J_\pm^0(z)|_{\text{normalizable}} &\equiv \int d^3k \bar{\Psi}_\pm(-k) i\gamma^0 \Psi_\pm(k)|_{\text{normalizable}} \\ &= \int d^3k \delta^2(|k| - |k_F|) |B_\pm^{(0)}(k)|^2 z^{4+2m\pm 1} + \dots \end{aligned} \quad (3.9)$$

We see that the constraint of normalizability from the bulk point of the view, implies that one selects precisely the on-shell bulk fermion modes as the building blocks of the density J_\pm^0 .

In turn this means that the true system that eqs. (3.8) describe is somewhat obscured by the spatial averaging. Clearly even a single fermion wavefunction is in truth the full set of two-dimensional wavefunctions whose momentum k^i has length k_F . However, the averaging could just as well be counting more, as long as there is another set of normalizable states once the isotropic momentum surface $|k| = |k_F|$ is filled. Pushing this thought to the extreme, one could even speculate that the system (3.8) gives the correct quantum-mechanical description of the many-body Fermi system: the system which gravitational reasoning suggests is the true ground state of the charged AdS black hole in the presence of fermions.

To remind us of the ambiguity introduced by spatial averaging, we shall give the boundary coefficient of normalizable solution for $J_-^0 = \int d^3k \mathcal{J}_-^0$ a separate name. The quantity $\mathcal{J}_-^0(z_0)$ is proportional to the pole strength, which via Migdal's relation quantifies the characteristic occupation number discontinuity at $\omega_F \equiv 0$. We shall therefore call the coefficient $\int d^3k |B_-|^2|_{\text{normalizable}} = \Delta n_F$.

⁸One can verify that the discussion in section 2.1.1 holds also for fully backreacted solutions. The derivation there builds on the assumption that the boundary behavior of the electrostatic potential is regular. It is straightforward to check in (3.8) that indeed precisely for normalizable solutions, i.e. in the absence of explicit fermion-sources, when both the leading and subleading terms in J_\pm^0 and I vanish, the boundary behavior the scalar potential remains regular, as required.

3.1 Thermodynamics

At a very qualitative level the identification $J_-^0|_{norm}(z) \equiv \Delta n_F z^{3+2m} + \dots$ can be argued to follow from thermodynamics as well. From the free energy for an AdS dual solution to a Fermi liquid, one finds that the charge density directly due to the fermions is

$$\rho_{\text{total}} = -2 \frac{\partial}{\partial \mu} F = \frac{-3}{2m+1} \frac{\Delta n_F}{z_0^{-1-2m}} + \rho + \dots, \quad (3.10)$$

with z_0^{-1} the UV-cutoff as before. The cut-off dependence is a consequence of the fact that the system is interacting, and one cannot truly separate out the fermions as free particles. Were one to substitute the naive free fermion scaling dimension $\Delta = m + 3/2 = 1$, the cutoff dependence would vanish and the identification would be exact.

We can thus state that in the interacting system there is a contribution to the charge density from a finite number of fermions proportional to

$$\rho_F = \frac{-3}{2\Delta - 2} \frac{\Delta n_F}{z_0^{2-2\Delta}} + \dots, \quad (3.11)$$

although this contribution formally vanishes in the limit where we send the UV-cutoff z_0^{-1} to infinity.

To derive eq. (3.10), recall that the free energy is equal to minus the on-shell action of the AdS dual theory. Since we disregard the gravitational backreaction, the Einstein term in the AdS theory will not contain any relevant information and we consider the Maxwell and Dirac term only. We write the action as,

$$S = \int_{z_0}^1 \sqrt{-g} \left[\frac{1}{2} A_N D_M F^{MN} - \bar{\Psi} \not{D} \Psi - m \bar{\Psi} \Psi \right] + \oint_{z=z_0} \sqrt{-h} \left(\bar{\Psi}_+ \Psi_- + \frac{1}{2} A_\mu n_\alpha F^{\alpha\mu} \right), \quad (3.12)$$

where we have included an explicit fermionic boundary term that follows from the AdS/CFT dictionary [12] and n_α is a normal vector to the boundary. The boundary action is not manifestly real, but its on-shell value which contributes to the free energy is real. Recall that the imaginary part of $\bar{\Psi}_+ \Psi_-$ decouples from eqs. (3.8). The boundary Dirac term in (3.12) is therefore equal to $I = 2\text{Re}(\bar{\Psi}_+ \Psi_-)$.

To write the free energy in terms of the quantities μ , ρ and Δn_F , note that the on-shell bulk Dirac action vanishes. Importantly the bulk Maxwell action does contribute to the free energy. Its contribution is

$$\begin{aligned} F_{\text{bulk}} &= \lim_{z_0 \rightarrow 0} \int_{z_0}^1 dz d^3x \left[\frac{1}{2} \Phi \partial_{zz} \Phi \right]_{\text{on-shell}} \\ &= - \lim_{z_0 \rightarrow 0} \int_{z_0}^1 dz d^3x \left[\frac{1}{2z^3 \sqrt{f}} \Phi (J_+^0 + J_-^0) \right]_{\text{on-shell}}, \end{aligned} \quad (3.13)$$

where we have used the equation of motion (3.8). This contribution should be expected, since the free energy should be dominated by infrared, i.e. near horizon physics. Due to the logarithmic singularity in the electrostatic potential (eq. (3.17)) this bulk contribution diverges, but this divergence should be compensated by gravitational backreaction. At the same time the singularity is so mild, however, that the free energy, the integral of the Maxwell term, remains finite in the absence of the Einstein contribution.

Formally, i.e. in the limit $z_0 \rightarrow 0$, the full free energy arises from this bulk contribution (3.13). The relation (3.10) between the charge density and Δn_F follows only from the regularized free energy, and is therefore only a qualitative guideline. Empirically, as we will show, it is however, a very good one (see figure 1 in the next section). Splitting the regularized bulk integral in two

$$F_{\text{bulk}} = \int_{z^*}^1 dz d^3x \left[\frac{1}{2z^3 \sqrt{f}} \Phi(J_+^0 + J_-^0) \right]_{\text{on-shell}} + \lim_{z_0 \rightarrow 0} \int_{z_0}^{z^*} dz d^3x \left[\frac{1}{2z^3 \sqrt{f}} \Phi(J_+^0 + J_-^0) \right]_{\text{on-shell}}, \quad (3.14)$$

we substitute the normalizable boundary behavior of $\Psi_+ = B_+ z^{5/2+m} + \dots$, $\Psi_- = B_- z^{3/2+m} + \dots$ and $\Phi = \mu - \rho z + \dots$, and obtain for the regularized free energy

$$F = F_{\text{horizon}}(z_*) + \lim_{z_0 \rightarrow 0} \int_{z_0}^{z^*} d^3x dz \left[\frac{-1}{2z^3} \mu |B_-|^2 z^{3+2m} + \dots \right] + \oint \frac{d^3x}{z_0^3} \left[-\bar{B}_+ B_- z_0^{4+2m} + \frac{1}{2} \mu \rho z_0^3 \right]. \quad (3.15)$$

Using that $B_+ = -i\mu\gamma^0 B_- / (2m+1)$ (eq. (2.10)), the second bulk term and boundary contribution are proportional, and the free energy schematically equals

$$F = F^{\text{horizon}} + \lim_{z_0 \rightarrow 0} \int d^3x \left[\frac{3\mu}{2(2m+1)} \bar{B}_- i\gamma^0 B_- z_0^{1+2m} - \frac{1}{2} \mu \rho \right]. \quad (3.16)$$

With the UV-regulator z_0^{-1} finite, this yields the charge density in eq. (3.10) after one recalls that $\bar{B}_- = B_-^\dagger i\gamma^0$.

With the derived rule that the AdS dual to a Fermi liquid has a nonzero normalizable component in the current J_-^0 , we will now construct an AdS solution that has this property: an AdS black hole with Dirac hair. Ignoring backreaction, these are solutions to the density equations (3.8). In its simplest form the interpretation is that of the backreaction due to a single fermion wavefunction, but as explained the spatial averaging of the density combined with the selection rule of normalizability could be capturing a more general solution.

3.2 At the horizon: entropy collapse to a Lifshitz solution

Before we can proceed with the construction of non-trivial Dirac hair solutions to eqs. (3.8), we must consider the boundary conditions at the horizon necessary to solve the system. Insisting that the right-hand-side of the dynamical equations (3.8) is subleading at the horizon, the near-horizon behavior of J_\pm^0 , I , Φ is:

$$\begin{aligned} J_\pm^0 &= J_{\text{hor},\pm} (1-z)^{-1/2} + \dots, \\ I &= I_{\text{hor}} (1-z)^{-1/2} + \dots, \\ \Phi &= \Phi_{\text{hor}}^{(1)} (1-z) \ln(1-z) + (\Phi_{\text{hor}}^{(2)} - \Phi_{\text{hor}}^{(1)}) (1-z) + \dots \end{aligned} \quad (3.17)$$

If we insist that Φ is regular at the horizon $z = 1$, i.e. $\Phi_{\text{hor}}^{(1)} = 0$, so that the electric field is finite, the leading term in J_\pm^0 must vanish as well, i.e. $J_{\text{hor},\pm} = 0$, and the system reduces to a free Maxwell field in the presence of an AdS black hole and there is no fermion density profile in the bulk. Thus in order to achieve a nonzero fermion profile in the bulk, we must have an explicit source for the electric-field on the horizon. Strictly speaking, this

invalidates our neglect of backreaction as the electric field and its energy density at the location of the source will be infinite. As we argued above, this backreaction is in fact expected to resolve the finite ground-state entropy problem associated with the presence of a horizon. The backreaction should remove the horizon completely, and the background should resemble the horizonless metrics found in [26, 27, 39]; the same horizon logarithmic behavior in the electrostatic potential was noted there. Nevertheless, as the divergence in the electric field only increases logarithmically as we approach the horizon, and our results shall hinge on the properties of the equations at the opposite end near the boundary, we shall continue to ignore it here. We shall take the sensibility of our result after the fact, as proof that the logarithmic divergence at the horizon is indeed mild enough to be ignored.

The identification of the boundary value of J_-^0 with the Fermi liquid characteristic occupation number jump Δn_F rested on the insistence that the currents are built out of AdS Dirac fields. This deconstruction also determines a relation between the horizon boundary conditions of the composite fields J_\pm^0 , I . If $\Psi_\pm(z) = C_\pm(1-z)^{-1/4} + \dots$ then $J_{\text{hor},\pm} = C_\pm^2$ and $I_{\text{hor}} = C_+C_-$. As the solution $\Phi_{\text{hor}}^{(1)}$ is independent of the solution $\Phi_{\text{hor}}^{(2)}$ which is regular at the horizon, we match the latter to the vector-potential of the charged AdS black hole: $\Phi_{\text{hor}}^{(2)} = -2gq \equiv g\mu_0/\alpha$. Recalling that $\Phi_{\text{hor}}^{(1)} = -(J_{\text{hor},+} + J_{\text{hor},-})$, we see that the three-parameter family of solutions at the horizon in terms of C_\pm , $\Phi_{\text{hor}}^{(2)}$ corresponds to the three-parameter space of boundary values A_+ , B_- and μ encoding a fermion-source, the fermion-response/expectation value and the chemical potential.

We can now search whether within this three-parameter family a finite normalizable fermion density solution with vanishing source $A_+ = 0$ exists for a given temperature T of the black hole.

3.3 A BH with Dirac hair

The equations are readily solved numerically with a shooting method from the horizon. We consider both an uncharged AdS-Schwarzschild solution and the charged AdS Reissner-Nordström solution. Studies of bosonic condensates in AdS/CFT without backreaction have mostly been done in the AdS-Schwarzschild (AdSS) background ([19, 20] and references therein). An exception is [40], which also considers the charged RN black hole. As is explained in [40], they correspond to two different limits of the exact solution: the AdSS case requires that $\Delta n_F \gtrsim \mu$ that is, the total charge of the matter fields should be dominant compared to the charge of the black hole. On the other hand, the RN limit is appropriate if $\Delta n_F \ll \mu$. It ignores the effect of the energy density of the charged matter sector on the charged black hole geometry. The AdS Schwarzschild background is only reliable near T_c , as at low temperatures the finite charged fermion density is comparable to μ . The RN case is under better control for low temperatures, because near $T = 0$ the chemical potential can be tuned to stay larger than fermion density.

We shall therefore focus primarily on the solution in the background of an AdS RN black hole, i.e. the system with a heat bath with chemical potential μ — non-linearly determined by the value of $\Phi_{\text{hor}}^{(2)} = \mu_0$ at the horizon — which for low T/μ should show the characteristic Δn_F of a Fermi liquid. The limit in which we may confidently ignore backreaction is $\Phi_{\text{hor}}^{(1)} \ll \mu_0$ for $T \lesssim \mu_0$ — for AdSS the appropriate limit is $\Phi_{\text{hor}}^{(1)} \ll T$ for $\mu_0 \ll T$.

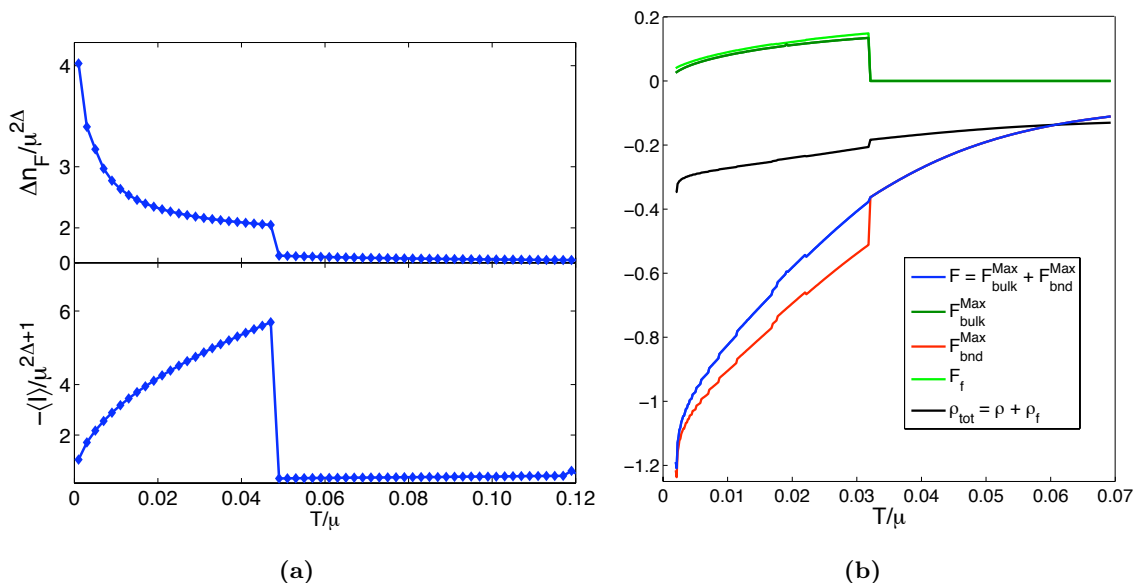


Figure 1. (a) Temperature dependence of the Fermi liquid occupation number discontinuity Δn_F and operator I for a fermionic field of mass $m = -1/4$ dual to an operator of dimension $\Delta = 5/4$. We see a large density for T/μ small and discontinuously drop to zero at $T \approx 0.05\mu$. At this same temperature, the proxy free energy contribution per particle (the negative of I) vanishes. (b) The free energy $F = F^{\text{fermion}} + F^{\text{Maxwell}}$ (eq. (3.12)) as a function of T/μ ignoring the contribution from the gravitational sector. The blue curve shows the total free energy $F = F^{\text{Maxwell}}$, which is the sum of a bulk and a boundary term. The explicit fermion contribution F_{fermion} vanishes, but the effect of a non-zero fermion density is directly encoded in a non-zero $F_{\text{bulk}}^{\text{Maxwell}}$. The figure also shows this bulk $F_{\text{bulk}}^{\text{Maxwell}}$ and the boundary contribution $F_{\text{bnd}}^{\text{Maxwell}}$ separately and how they sum to a continuous F_{total} . Although formally the explicit fermion contribution $F_f \sim I$ in equation (3.16) vanishes, the bulk Maxwell contribution is captured remarkably well by its value when the cut-off is kept finite. The light-green curve in the figure shows F_f for a finite $z_0 \sim 10^{-6}$. For completeness we also show the total charge density, eq. (3.10). The dimension of the fermionic operator used in this figure is $\Delta = 1.1$.

3.3.1 Finite fermion density solutions in AdS-RN

Figure 1 shows the behavior of the occupation number discontinuity $n_F \equiv |B_-|^2$ and the fermion free-energy contribution I as a function of temperature in a search for normalizable solutions to eqs.(3.8) with the aforementioned boundary conditions. We clearly see a first order transition to a finite fermion density, as expected. The underlying Dirac field dynamics can be recognized in that the normalizable solution for $J_-^0(z)$ which has no leading component near the boundary by construction, also has its subleading component vanishing (figure 2).⁹

⁹Although the Dirac hair solution has charged matter in the bulk, there is no Higgs effect for the bulk gauge field, and thus there is no direct spontaneous symmetry breaking in the boundary. Indeed one would not expect it for the Fermi liquid ground state. There will be indirect effect on the conductivity similar to [27]. We thank Andy O’Bannon for his persistent inquiries to this point.

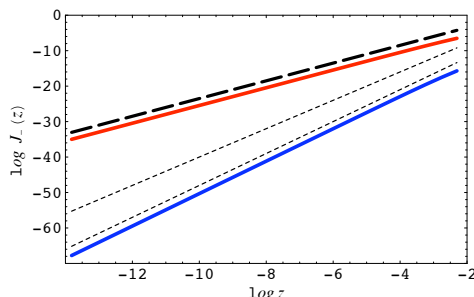


Figure 2. The boundary behaviour of $J_-(0)$ in for a generic solution (blue) to eqs. (3.8) and a normalizable Dirac-hair solution (red) for $m = -1/4$ in the background of an AdS-RN black hole with $\mu/T = 128.8$. The dotted lines show the scaling $z^{11/2}$ and z^4 of the leading and subleading terms in an expansion of $J_-(z)$ near $z = 0$; the dashed line shows the scaling $z^{5/2}$ of the sub-subleading expansion whose coefficient is $|B_-(\omega_F, k_F)|^2$. That the Dirac hair solution (red) scales as the subsubleading solution indicates that the current J_-^0 faithfully captures the density of the underlying normalizable Dirac field.

Analyzing the transition in more detail in figure 3, we find:

1. The dimensionless number discontinuity $\Delta n_F/\mu^{2\Delta}$ scales as $T^{-\delta}$ in a certain temperature range $T_F < T < T_c$, with $\delta > 0$ depending on g and Δ , and T_F typically very small. At $T = T_c > T_F$ it drops to zero discontinuously, characteristic of a first order phase transition.
2. At low temperatures, $0 < T < T_F$, the power-law growth comes to a halt and ends with a plateau where $\Delta n_F/\mu^{2\Delta} \sim \text{const.}$ (figure 3a). It is natural to interpret this temperature as the Fermi temperature of the boundary Fermi liquid.
3. The fermion free energy contribution $I/\mu^{2\Delta+1}$ scales as $T^{1/\nu}$ with $\nu > 1$ for $0 < T < T_c$, and drops to zero discontinuously at T_c . As I empirically equals minus the free energy per particle, it is natural that $I(T = 0) = 0$, and this in turn supports the identification of $\Delta n_F(T = 0)$ as the step in number density at the Fermi energy.

One expects that the exponents δ, ν are controlled by the conformal dimension Δ .¹⁰ The dependence of the exponent δ on the conformal dimension is shown in figure 3a. While a correlation clearly exists, the data are not conclusive enough to determine the relation $\delta = \delta(\Delta)$. The clean power law $T^{-\delta}$ scaling regime is actually somewhat puzzling. These values of the temperature, $T_F < T < T_c$, correspond to a crossover between the true Fermi liquid regime for $T < T_F$ and the conformal phase for $T > T_c$, hence there is no clear ground for a universal scaling relation for δ , which seems to be corroborated by the data (figure 3b). At the same time, the scaling exponent ν appears to obey $\nu = 2$ with great precision (figure 3b, inset) independent of Δ and g .

A final consideration, needed to verify the existence of a finite fermion density AdS solution dual to a Fermi liquid, is to show that the ignored backreaction stays small. In particular, the divergence of the electric field at the horizon should not affect the result.

¹⁰The charge g of the underlying conformal fermionic operator scales out of the solution.

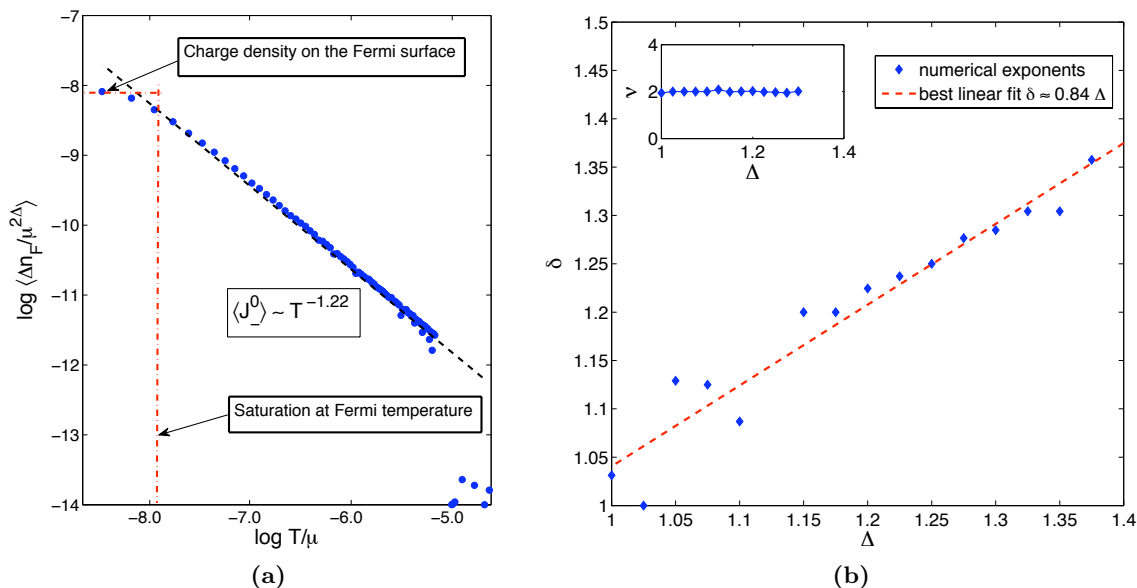


Figure 3. (a) Approximate power-law scaling of the Fermi liquid characteristic occupation number discontinuity $\Delta n_F / \mu^{2\Delta} \sim T^{-\delta}$ as a function of T/μ for $\Delta = 5/4$. This figure clearly shows the saturation of the density at very low T/μ . The saturation effect is naturally interpreted as the influence of the characteristic Fermi energy. (b) The scaling exponent δ for different values of the conformal dimension Δ . There is a clear correlation, but the precise relation cannot be determined numerically. The scaling exponent of the current $I/\mu^{2\Delta+1} \sim T^{-1/\nu}$ obeys $\nu = 2$ with great accuracy, on the other hand (Inset).

The total bulk electric field $E_z = -\partial_z \Phi$ is shown in figure 4a, normalized by its value at $z = 1/2$. The logarithmic singularity at the horizon is clearly visible. At the same time, the contribution to the total electric field from the charged fermions is negligible even very close to the horizon.¹¹ This suggests that our results are robust with respect to the details of the IR divergence of the electric field.

The diverging backreaction at the horizon is in fact the gravity interpretation of the first order transition at T_c : an arbitrarily small non-zero density leads to an abrupt change in the on shell bulk action. As the latter is the free energy in the CFT, it must reflect the discontinuity of a first order transition. A full account of the singular behavior at the horizon requires self-consistent treatment including the Einstein equations. At this level, we can conclude that the divergent energy density at the horizon implies that the near-horizon physics becomes substantially different from the AdS_2 limit of the RN metric. It is natural to guess that the RN horizon disappears completely, corresponding to a ground state with zero entropy, as hypothesized in [26]. This matches the expectation that the finite fermi-density solution in the bulk describes the Fermi-liquid. The underlying assumption in the above reasoning is that the total charge is conserved.

¹¹It is of the order 10^{-4} , starting from $z = 0.9999$. We have run our numerics using values between $1 - 10^{-6}$ and $1 - 10^{-2}$ and found no detectable difference in quantities at the boundary.

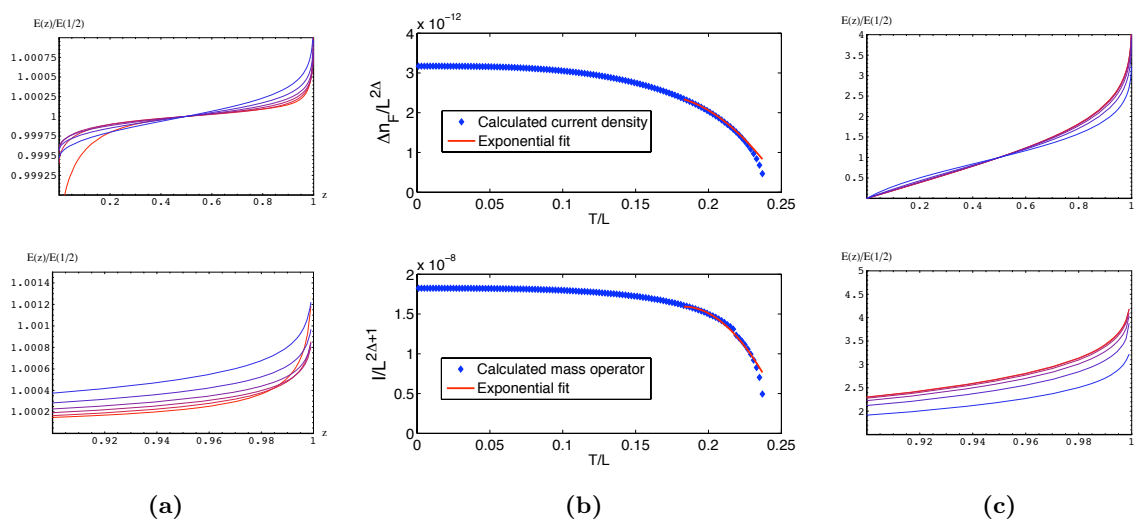


Figure 4. (a) The radial electric field $-E_z = \partial\Phi/\partial z$, normalized to the midpoint value $E_z(z)/E_z(1/2)$ for whole interior of the finite fermion density AdS-RN solution (upper) and near the horizon (lower). One clearly sees the soft, log-singularity at the horizon. The colors correspond to increasing temperatures from $T = 0.04\mu$ (lighter) to $T = 0.18\mu$ (darker), all with $\Delta = 1.1$. (b) The occupation number jump Δn_F and free energy contribution I as a function of temperature in AdS-Schwarzschild. We see the jump Δn_F saturate at low temperatures and fall off at high T . An exponential fit to the data (red curve) shows that in the critical region the fall-off is stronger than exponential, indicating that the transition is first order. The conformal dimension of the fermionic operator is $\Delta = 1.1$. (c) The radial electric field $-E_z = \partial\Phi/\partial z$, normalized to the midpoint value ($E_z(z)/E_z(1/2)$) for the finite fermion density AdS-Schwarzschild background. The divergence of the electric field E_z is again only noticeable near the horizon and can be neglected in most of the bulk region.

3.3.2 Finite fermion density in AdSS

For completeness, we will describe the finite fermion-density solutions in the AdS Schwarzschild geometry as well. In these solutions the charge density is set by the density of fermions alone. They are therefore not reliable at very low temperatures $T \ll T_c$ when gravitational backreaction becomes important. The purpose of this section is to show the existence of finite density solutions does not depend on the presence of a charged black hole set by the horizon value $\Phi_{\text{hor}}^{(2)} = \mu_0$, but that the transition to a finite fermion density can be driven by the charged fermions themselves.

Figure 4b shows the nearly instantaneous development of a non-vanishing expectation value for the occupation number discontinuity Δn_F and I in the AdS Schwarzschild background. The rise is not as sharp as in the RN background. It is, however, steeper than exponential, and we may conclude that the system undergoes a discontinuous first order transition to a AdS Dirac hair solution. The constant limit reached by the fermion density as $T \rightarrow 0$ has no meaning as we cannot trust the solution far away from T_c .

The backreaction due to the electric field divergence at the horizon can be neglected, for the same reason as before (figure 4c).

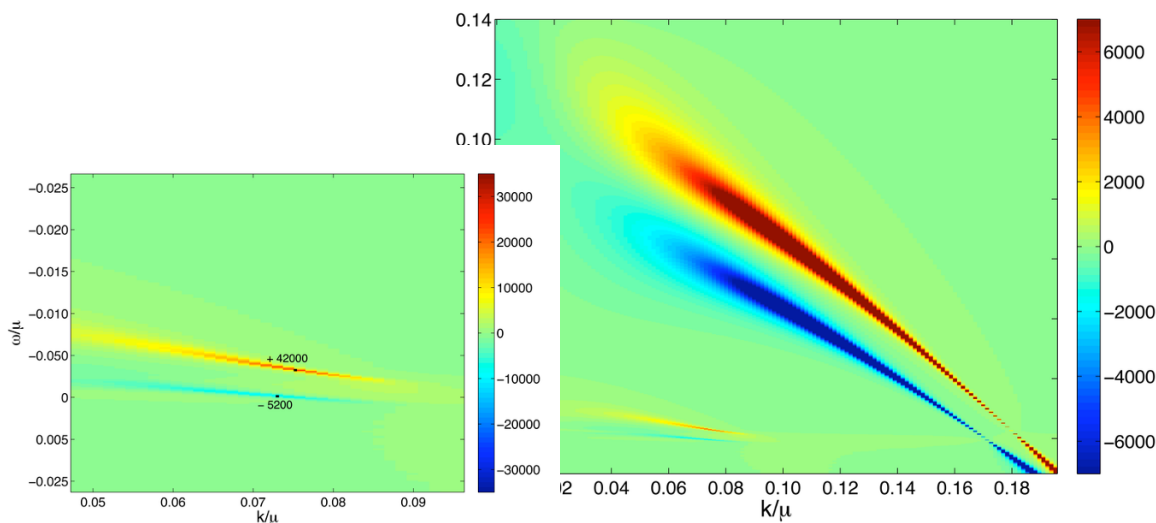


Figure 5. The single-fermion spectral function in the probe limit of pure AdS Reissner-Nordström (red/yellow) *minus* the spectrum in the finite density system (blue). The conformal dimension is $\Delta = 5/4$, the probe charge $g = 2$, and $\mu/T = 135$. We can see two quasiparticle poles near $\omega = 0$, a non-FL pole with $k_F^{\text{probe}} \simeq 0.11\mu$ and $k_F^{\Delta n_F} \simeq 0.08\mu$ respectively and a FL-pole with $k_F^{\text{probe}} \simeq 0.18\mu$ and $k_F^{\Delta n_F} \simeq 0.17\mu$. The dispersion of both poles is visibly similar between the probe and the finite density background. At the same time, the non-FL pole has about 8 times less weight in the finite density background, whereas the FL-pole has gained about 6.5 times more weight.

3.4 Confirmation from fermion spectral functions

If, as we surmised, the finite fermion density phase is the true Fermi-liquid-like ground state, the change in the fermion spectral functions should be minimal as the characteristic quasiparticle peaks are already present in the probe limit, i.e. pure AdS Reissner-Nordström [11, 12]. Figure 5 shows that quasiparticle poles near $\omega = 0$ with similar analytic properties can be identified in both the probe pure AdS-RN case and the AdS-RN Dirac-hair solution. The explanation for this similarity is that the electrostatic potential Φ almost completely determines the spectrum, and the change in Φ due to the presence of a finite fermion density is quite small. Still, one expects that the finite fermion density system is a more favorable state. This indeed follows from a detailed comparison between the spectral functions $A(\omega; k)$ in the probe limit and the fermion-liquid phase (figure 5). We see that:

1. All quasiparticle poles present in the probe limit are also present in the Dirac hair phase, at a slightly shifted value of k_F . This shift is a consequence of the change in the bulk electrostatic potential Φ due to the presence of the charged matter. For a Fermi-liquid-like quasiparticle corresponding to the second pole in the operator with $\Delta = 5/4$ and $g = 2$ we find $k_F^{\text{probe}} - k_F^{\Delta n_F} = 0.07\mu$. The non-Fermi-liquid pole, i.e. the first pole for the same conformal operator, has $k_F^{\text{probe}} - k_F^{\Delta n_F} = 0.03\mu$.
2. The dispersion exponents ν defined through $(\omega - E_F)^2 \sim (k - k_F)^{2/\nu}$, also maintain roughly the same values as both solutions. This is visually evident in the near similar

slopes of the ridges in figure 5. In the AdS Reissner-Nordström background, the dispersion coefficients are known analytically as a function of the Fermi momentum: $\nu_{k_F} = \sqrt{2\frac{k_F^2}{\mu^2} - \frac{1}{3} + \frac{1}{6}(\Delta - 3/2)^2}$ [13]. The Fermi-liquid-like quasiparticle corresponding to the second pole in the operator with $\Delta = 5/4$ and $g = 2$ has $\nu_{k_F}^{\text{probe}} = 1.02$ vs. $\nu^{\Delta n_F} = 1.01$. The non-Fermi-liquid pole corresponding to the first pole for the same conformal operator, has $\nu_{k_F}^{\text{probe}} \approx 0.10$, and $\nu^{\Delta n_F} = 0.12$.

3. The most distinct property of the finite density phase is the redistributed spectral weight of the poles. The non-Fermi liquid pole reaches its maximum height about 10^4 , an order of magnitude less than in the probe limit, whereas the second, Fermi liquid-like pole, increases by an order of magnitude. This suggests that the finite density state corresponds to the Fermi-liquid like state, rather than a non-Fermi liquid.
4. As we mentioned in the introduction, part of the reason to suspect the existence of an AdS-RN Dirac-hair solution is that a detailed study of spectral functions in AdS-RN reveals that the quasiparticle peak is anomalously sensitive to changes in T . This anomalous temperature dependence disappears in the finite density solution. Specifically in pure AdS-RN the position ω_{max} where the peak height is maximum, denoted E_F in [12], does not agree with the value ω_{pole} , where the pole touches the real axis in the complex ω -plane, for any finite value of T , and is exponentially sensitive to changes in T (figure 6). In the AdS-RN Dirac hair solution the location ω_{max} and the location ω_{pole} do become the same. Figure 6b shows that the maximum of the quasiparticle peak always sits at $\omega \simeq 0$ in finite density Dirac hair solution, while it only reaches this as $T \rightarrow 0$ in the probe AdS-RN case.

4 Discussion and conclusion

Empirically we know that the Fermi liquid phase of real matter systems is remarkably robust and generic. This is corroborated by analyzing effective field theory around the Fermi surface, but as it assumes the ground state it cannot explain its genericity. If the Fermi liquid ground state is so robust, this must also be a feature of the recent holographic approaches to strongly interacting fermionic systems. Our results here indicate that this is so. We have used Migdal’s relation to construct AdS/CFT rules for the holographic dual of a Fermi liquid: the characteristic occupation number discontinuity Δn_F is encoded in the normalizable subsubleading component of the spatially averaged fermion density $J_-^0(z) \equiv \int d^3k \Psi(\omega = 0, -k, z) i\gamma^0 \Psi(\omega = 0, k, z)$ near the AdS boundary. This density has its own set of evolution equations, based on the underlying Dirac field, and insisting on normalizability automatically selects the on-shell wavefunctions of the underlying Dirac-field.

The simplest AdS solution that has a non-vanishing expectation value for the occupation number discontinuity Δn_F is that of a single fermion wavefunction. Using the density approach — which through the averaging appears to describe a class of solutions rather than one specific solution — we have constructed the limit of this solution where gravitational backreaction is ignored. At low black hole temperatures this solution with fermionic

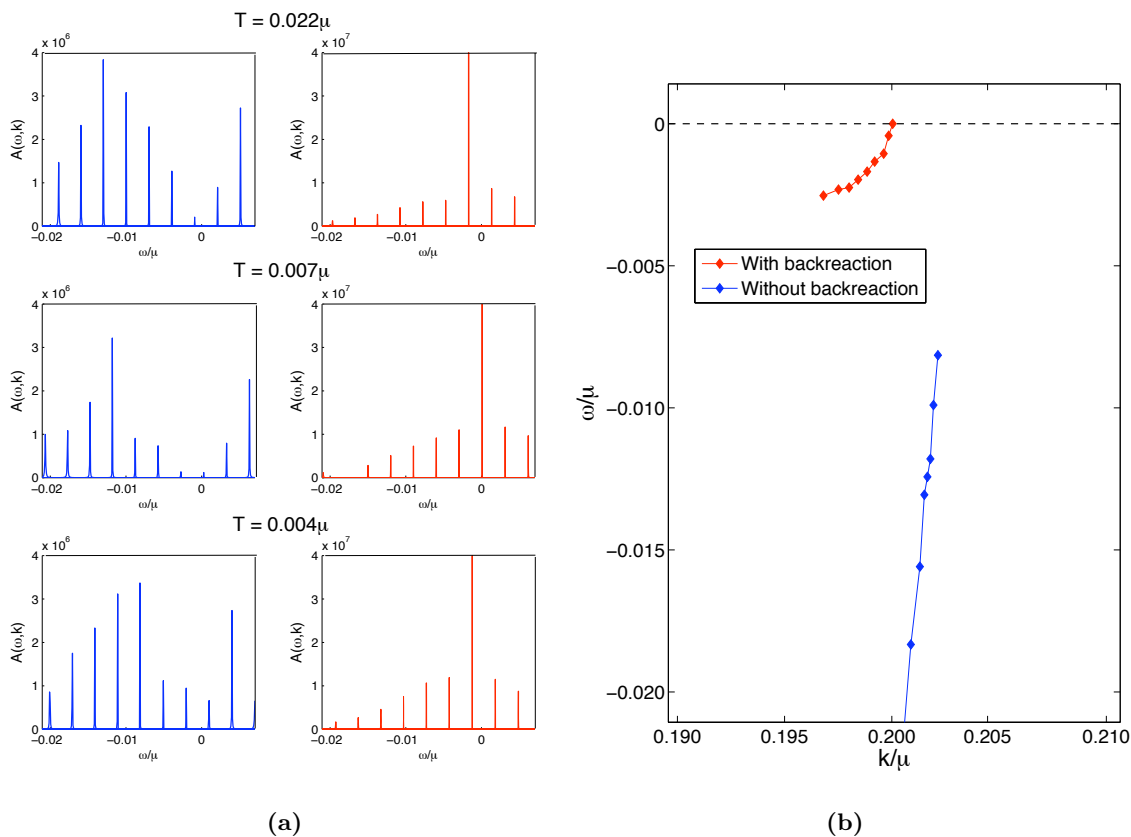


Figure 6. (a) Single fermion spectral functions near $\omega = 0$ in pure AdS Reissner-Nordström (blue) and in the finite fermion density background (red). In the former the position of the maximum approaches $\omega = 0$ as T is lowered whereas in the latter the position of the maximum close to $T = 0$ for all values of T . (b) Position of the maximum of the quasiparticle peak in k - ω plane, for different temperatures and $\Delta = 5/4$. The probe limit around a AdS-RN black hole (blue) carries a strong temperature dependence of the ω_{\max} value, with $\omega_{\max, T \neq 0} \neq 0$. In the finite fermion density background, the position of the maximum (red) is nearly independent of temperature and stays at $\omega = 0$.

“Dirac hair” is the preferred ground state. Through an analysis of the free energy, we argue that this gravitational solution with a non-zero fermion profile precisely corresponds to a system with a finite density of fermions. A spectral analysis still reveals a zoo of Fermi-surfaces in this ground state, but there are indications that in the full gravitationally backreacted solution only a Landau Fermi-liquid type Fermi surface survives. This follows in part from the relation between the spectral density and the Fermi momentum of a particular Landau liquid-like Fermi surface; it also agrees with the prediction from Luttinger’s theorem. Furthermore, the spectral analysis in the finite density state shows no anomalous temperature dependence present in the pure charged black-hole single spectral functions. This also indicates that the finite density state is the true ground state.

The discovery of this state reveals a new essential component in the study of strongly coupled fermionic systems through gravitational duals, where one should take into account

the expectation values of fermion bilinears. Technically the construction of the full gravitationally backreacted solution is a first point that is needed to complete our finding. A complete approach to this problem will have to take into account the many-body physics in the bulk. Within the approach presented in this paper, it means the inclusion of additional fermion wavefunctions, filling the bulk Fermi surface. The realization, however, that expectation values of fermion bilinears can be captured in holographic duals and naturally encode phase separations in strongly coupled fermion systems should find a large set of applications in the near future.

Acknowledgments

We thank F. Benini, J. de Boer, E. Gubankova, S. Hartnoll, C. Herzog, E. Kiritsis, H. Liu, M. Medvedyeva, J. McGreevy, A. O'Bannon, G. Policastro, and J. Sonner for extensive discussions. We are very grateful to the KITP Santa Barbara for its generous hospitality and the organizers and participants of the AdS/CMT Workshop (July 2009). KS thanks the Galileo Galilei Institute for Theoretical Physics for the hospitality and the INFN for partial support during the completion of this work. This research was supported in part by a VIDI Innovative Research Incentive Grant (K. Schalm) from the Netherlands Organization for Scientific Research (NWO), a Spinoza Award (J. Zaanen) from the Netherlands Organisation for Scientific Research (NWO) and the Dutch Foundation for Fundamental Research on Matter (FOM).

Open Access. This article is distributed under the terms of the Creative Commons Attribution Noncommercial License which permits any noncommercial use, distribution, and reproduction in any medium, provided the original author(s) and source are credited.

References

- [1] C.M. Varma, Z. Nussinov and W. van Saarloos, *Singular Fermi Liquids*, *Phys. Rept.* **361** (2002) 267 [[cond-mat/0103393](#)].
- [2] J.H. She and J. Zaanen, *BCS Superconductivity in Quantum Critical Metals*, *Phys. Rev.* **B80** (2009) 184518 [[arXiv:0905.1225](#)].
- [3] H. v. Löhneysen, A. Rosch, M. Vojta and P. Wölfle, *Fermi-liquid instabilities at magnetic quantum phase transitions*, *Rev. Mod. Phys.* **79** (2007) 1015 [[cond-mat/0606317](#)].
- [4] M. Gurvitch and A.T. Fiory, *Resistivity of La_{1.825}Sr_{0.175}CuO₄ and YBa₂Cu₃O₇ to 1100 K: Absence of saturation and its implications*, *Phys. Rev. Lett.* **59** (1987) 1337.
- [5] P. Phillips and C. Chamon, *Breakdown of One-Parameter Scaling in Quantum Critical Scenarios for the High-Temperature Copper-oxide Superconductors*, *Phys. Rev. Lett.* **95** (2005) 107002 [[cond-mat/0412179](#)].
- [6] J. Zaanen, *Quantum critical electron systems: the uncharted sign worlds*, *Science* **319** (2008) 1205.
- [7] J.M. Luttinger, *Fermi Surface and Some Simple Equilibrium Properties of a System of Interacting Fermions*, *Phys. Rev.* **119** (1960) 1153 [[SPIRES](#)].

- [8] J.C. Campuzano, M.R. Norman and M. Randeria, *Photoemission in the High- T_c Superconductors*, in *Handbook of Physics: Physics of Conventional and Unconventional Superconductors*, K.H. Benneman and J.B. Ketterson eds., Springer Verlag, (2004) [[cond-mat/0209476](#)].
- [9] A. Damascelli, Z. Hussain and Z.-X. Shen, *Angle-resolved photoemission studies of the cuprate superconductors*, *Rev. Mod. Phys.* **75** (2003) 473 [[cond-mat/0208504](#)] [[SPIRES](#)].
- [10] X.-J. Zhou, T. Cuk, T. Devereaux, N. Nagaosa and Z.-X. Shen, *Angle-Resolved Photoemission Spectroscopy on Electronic Structure and Electron-Phonon Coupling in Cuprate Superconductors* in *Handbook of High-Temperature Superconductivity: Theory and Experiment*, J.R. Schrieffer, Springer Verlag, (2007) [[cond-mat/0604284](#)].
- [11] H. Liu, J. McGreevy and D. Vegh, *Non-Fermi liquids from holography*, *Phys. Rev. D* **83** (2011) 065029 [[arXiv:0903.2477](#)] [[SPIRES](#)].
- [12] M. Cubrovic, J. Zaanen and K. Schalm, *String Theory, Quantum Phase Transitions and the Emergent Fermi-Liquid*, *Science* **325** (2009) 439 [[arXiv:0904.1993](#)] [[SPIRES](#)].
- [13] T. Faulkner, H. Liu, J. McGreevy and D. Vegh, *Emergent quantum criticality, Fermi surfaces and AdS $_2$* , *Phys. Rev. D* **83** (2011) 125002 [[arXiv:0907.2694](#)] [[SPIRES](#)].
- [14] T. Faulkner, N. Iqbal, H. Liu, J. McGreevy and D. Vegh, *From black holes to strange metals*, [arXiv:1003.1728](#) [[SPIRES](#)].
- [15] T. Faulkner, N. Iqbal, H. Liu, J. McGreevy and D. Vegh, *Strange metal transport realized by gauge/gravity duality*, *Science* **329** (2010) 1043 [[SPIRES](#)].
- [16] S.-S. Lee, *A Non-Fermi Liquid from a Charged Black Hole: A Critical Fermi Ball*, *Phys. Rev. D* **79** (2009) 086006 [[arXiv:0809.3402](#)] [[SPIRES](#)].
- [17] S.-J. Rey, *String theory on thin semiconductors: Holographic realization of Fermi points and surfaces*, *Prog. Theor. Phys. Suppl.* **177** (2009) 128 [[arXiv:0911.5295](#)] [[SPIRES](#)].
- [18] S.S. Gubser, *Breaking an Abelian gauge symmetry near a black hole horizon*, *Phys. Rev. D* **78** (2008) 065034 [[arXiv:0801.2977](#)] [[SPIRES](#)].
- [19] S.A. Hartnoll, C.P. Herzog and G.T. Horowitz, *Building a Holographic Superconductor*, *Phys. Rev. Lett.* **101** (2008) 031601 [[arXiv:0803.3295](#)] [[SPIRES](#)].
- [20] S.A. Hartnoll, C.P. Herzog and G.T. Horowitz, *Holographic Superconductors*, *JHEP* **12** (2008) 015 [[arXiv:0810.1563](#)] [[SPIRES](#)].
- [21] S.A. Hartnoll, *Lectures on holographic methods for condensed matter physics*, *Class. Quant. Grav.* **26** (2009) 224002 [[arXiv:0903.3246](#)] [[SPIRES](#)].
- [22] F. Finster, J. Smoller and S.-T. Yau, *Non-Existence of Black Hole Solutions to Static, Spherically Symmetric Einstein-Dirac Systems — a Critical Discussion*, [gr-qc/0211043](#) [[SPIRES](#)].
- [23] F. Finster, J. Smoller and S.-T. Yau, *Absence of stationary, spherically symmetric black hole solutions for Einstein-Dirac-Yang-Mills equations with angular momentum*, *Adv. Theor. Math. Phys.* **4** (2002) 1231 [[gr-qc/0005028](#)] [[SPIRES](#)].
- [24] F. Finster, J. Smoller and S.-T. Yau, *The interaction of Dirac particles with non-Abelian gauge fields and gravity: Bound states*, *Nucl. Phys. B* **584** (2000) 387 [[gr-qc/0001067](#)] [[SPIRES](#)].

- [25] F. Finster, J. Smoller and S.-T. Yau, *Non-existence of black hole solutions for a spherically symmetric, static Einstein-Dirac-Maxwell system*, *Commun. Math. Phys.* **205** (1999) 249 [[SPIRES](#)].
- [26] S.A. Hartnoll, J. Polchinski, E. Silverstein and D. Tong, *Towards strange metallic holography*, *JHEP* **04** (2010) 120 [[arXiv:0912.1061](#)] [[SPIRES](#)].
- [27] S.A. Hartnoll and A. Tavanfar, *Electron stars for holographic metallic criticality*, *Phys. Rev. D* **83** (2011) 046003 [[arXiv:1008.2828](#)] [[SPIRES](#)].
- [28] J. de Boer, K. Papadodimas and E. Verlinde, *Holographic Neutron Stars*, *JHEP* **10** (2010) 020 [[arXiv:0907.2695](#)] [[SPIRES](#)].
- [29] X. Arsiwalla, J. de Boer, K. Papadodimas and E. Verlinde, *Degenerate Stars and Gravitational Collapse in AdS/CFT*, *JHEP* **01** (2011) 144 [[arXiv:1010.5784](#)] [[SPIRES](#)].
- [30] L.-Y. Hung, D.P. Jatkar and A. Sinha, *Non-relativistic metrics from back-reacting fermions*, *Class. Quant. Grav.* **28** (2011) 015013 [[arXiv:1006.3762](#)] [[SPIRES](#)].
- [31] M. Cubrovic, Y. Liu, K. Schalm, Y.-W. Sun and J. Zaanen, *Spectral probes of the holographic Fermi groundstate: dialing between the electron star and AdS Dirac hair*, [arXiv:1106.1798](#) [[SPIRES](#)].
- [32] S.A. Hartnoll, D.M. Hofman and D. Vegh, *Stellar spectroscopy: Fermions and holographic Lifshitz criticality*, *JHEP* **08** (2011) 096 [[arXiv:1105.3197](#)] [[SPIRES](#)].
- [33] N. Iqbal, H. Liu and M. Mezei, *Semi-local quantum liquids*, [arXiv:1105.4621](#) [[SPIRES](#)].
- [34] N. Iqbal and H. Liu, *Real-time response in AdS/CFT with application to spinors*, *Fortsch. Phys.* **57** (2009) 367 [[arXiv:0903.2596](#)] [[SPIRES](#)].
- [35] R. Contino and A. Pomarol, *Holography for fermions*, *JHEP* **11** (2004) 058 [[hep-th/0406257](#)] [[SPIRES](#)].
- [36] E.M. Lifshitz and L.P. Pitaevskii, *Statistical physics. Part 2*, Pergamon Press, Oxford U.K. (1980).
- [37] M. Čubrović, J. Zaanen and K. Schalm, *Stability of the Fermi Liquid from holography*, to appear.
- [38] S. Sachdev, *A model of a Fermi liquid using gauge-gravity duality*, [arXiv:1107.5321](#) [[SPIRES](#)].
- [39] K. Goldstein, S. Kachru, S. Prakash and S.P. Trivedi, *Holography of Charged Dilaton Black Holes*, *JHEP* **08** (2010) 078 [[arXiv:0911.3586](#)] [[SPIRES](#)].
- [40] T. Albash and C.V. Johnson, *A Holographic Superconductor in an External Magnetic Field*, *JHEP* **09** (2008) 121 [[arXiv:0804.3466](#)] [[SPIRES](#)].
- [41] R.-G. Cai, Z.-Y. Nie, B. Wang and H.-Q. Zhang, *Quasinormal Modes of Charged Fermions and Phase Transition of Black Holes*, [arXiv:1005.1233](#) [[SPIRES](#)].

Holographic fermions in external magnetic fieldsE. Gubankova,^{1,*} J. Brill,² M. Čubrović,² K. Schalm,² P. Schijven,^{2,†} and J. Zaanen²¹*Institute for Theoretical Physics, J. W. Goethe-University, D-60438 Frankfurt am Main, Germany*²*Institute Lorentz for Theoretical Physics, Leiden University, P.O. Box 9506, Leiden 2300RA, The Netherlands*

(Received 19 November 2010; published 2 November 2011)

We study the Fermi-level structure of 2 + 1-dimensional strongly interacting electron systems in external magnetic field using the gauge/gravity duality correspondence. The gravity dual of a finite density fermion system is a Dirac field in the background of the dyonic AdS-Reissner-Nordström black hole. In the probe limit, the magnetic system can be reduced to the nonmagnetic one, with Landau-quantized momenta and rescaled thermodynamical variables. We find that at strong enough magnetic fields, the Fermi surface vanishes and the quasiparticle is lost either through a crossover to conformal regime or through a phase transition to an unstable Fermi surface. In the latter case, the vanishing Fermi velocity at the critical magnetic field triggers the non-Fermi-liquid regime with unstable quasiparticles and a change in transport properties of the system. We associate it with a metal–“strange-metal” phase transition. Next, we compute the DC Hall and longitudinal conductivities using the gravity-dressed fermion propagators. For dual fermions with a large charge, many different Fermi surfaces contribute and the Hall conductivity is quantized as expected for integer quantum Hall effect (QHE). At strong magnetic fields, as additional Fermi surfaces open up, new plateaus typical for the fractional QHE appear. The somewhat irregular pattern in the length of fractional QHE plateaus resembles the outcomes of experiments on thin graphite in a strong magnetic field. Finally, motivated by the absence of the sign problem in holography, we suggest a lattice approach to the AdS calculations of finite density systems.

DOI: 10.1103/PhysRevD.84.106003

PACS numbers: 11.25.Tq, 71.27.+a

I. INTRODUCTION

The study of strongly interacting fermionic systems at finite density and temperature is a challenging task in condensed matter and high energy physics. Analytical methods are limited or not available for strongly coupled systems, and numerical simulation of fermions at finite density breaks down because of the sign problem [1]. There has been an increased activity in describing finite density fermionic matter by a gravity dual using the holographic AdS/CFT correspondence [2]. The gravitational solution which is dual to the finite chemical potential system is the electrically charged AdS-Reissner-Nordström black hole, which provides a background where only the metric and Maxwell fields are nontrivial and all matter fields vanish. In the classical gravity limit, the decoupling of the Einstein-Maxwell sector holds and leads to universal results, which is an appealing feature of applied holography. Indeed, the celebrated result for the ratio of the shear viscosity over the entropy density [3] is identical for many strongly interacting theories and has been considered a robust prediction of the AdS/CFT correspondence.

However, an extremal black hole alone is not enough to describe finite density systems as it does not source the matter fields. In holography, at leading order, the Fermi

surfaces are not evident in the gravitational geometry, but can only be detected by external probes; either probe D-branes [2] or probe bulk fermions [4–7]. Here, we shall consider the latter option, where the free Dirac field in the bulk carries a finite charge density [8]. We ignore electromagnetic and gravitational backreaction of the charged fermions on the bulk space-time geometry (probe approximation). At large temperatures, $T \gg \mu$, this approach provides a reliable hydrodynamic description of transport at a quantum criticality (in the vicinity of superfluid-insulator transition) [9]. At small temperatures, $T \ll \mu$, in some cases, sharp Fermi surfaces emerge with either conventional Fermi-liquid scaling [5] or of a non-Fermi-liquid type [6] with scaling properties that differ significantly from those predicted by the Landau Fermi-liquid theory. The nontrivial scaling behavior of these non-Fermi liquids has been studied semianalytically in [7] and is of great interest as high- T_c superconductors and metals near the critical point are believed to represent non-Fermi liquids.

What we shall study is the effects of magnetic field on the holographic fermions. A magnetic field is a probe of finite density matter at low temperatures, where the Landau-level physics reveals the Fermi-level structure. The gravity dual system is described by an AdS dyonic black hole with electric and magnetic charges Q and H , respectively, corresponding to a 2 + 1-dimensional field theory at finite chemical potential in an external magnetic field [10]. Probe fermions in the background of the dyonic black hole have been considered in [11,12]; and probe

*Also at ITEP, Moscow, Russia

†Present address: Albert-Ludwigs-Universität Freiburg D-79104 Freiburg, Germany

bosons in the same background have been studied in [13]. Quantum magnetism is considered in [14].

The Landau quantization of momenta due to the magnetic field found there shows again that the AdS/CFT correspondence has a powerful capacity to unveil that certain quantum properties known from quantum gases have a much more ubiquitous status than could be anticipated theoretically. A first highlight is the demonstration [15] that the Fermi surface of the Fermi gas extends way beyond the realms of its perturbative extension in the form of the Fermi liquid. In AdS/CFT, it appears to be gravitationally encoded in the matching along the scaling direction between the “UV” Dirac waves falling in from the “UV” boundary and the true IR excitations living near the black hole horizon. This IR physics can insist on the disappearance of the quasiparticle but, if so, this “critical Fermi liquid” is still organized “around” a Fermi surface. The Landau quantization, the organization of quantum gaseous matter in quantized energy bands (Landau levels) in a system of two space dimensions pierced by a magnetic field oriented in the orthogonal spatial direction, is a second such quantum gas property. Following Ref. [11], we shall describe here that despite the strong interactions in the system, the holographic computation reveals the same strict Landau-level quantization. Arguably, it is the mean-field nature imposed by large N limit inherent in AdS/CFT that explains this. The system is effectively noninteracting to first order in $1/N$. The Landau quantization is not manifest from the geometry, but, as we show, this statement is straightforwardly encoded in the symmetry correspondences associated with the conformal compactification of AdS on its flat boundary (i.e., in the UV conformal field theory [CFT]).

An interesting novel feature in strongly coupled systems arises from the fact that the background geometry is only sensitive to the total energy density $Q^2 + H^2$ contained in the electric and magnetic fields sourced by the dyonic black hole. Dialing up the magnetic field is effectively similar to a process where the dyonic black hole loses its electric charge. At the same time, the fermionic probe with charge q is essentially only sensitive to the Coulomb interaction gqQ . As shown in [11], one can therefore map a magnetic to a nonmagnetic system with rescaled parameters (chemical potential, fermion charge) and same symmetries and equations of motion, as long as the Reissner-Nordström geometry is kept.

Translated to more experiment-compatible language, the above magnetic-electric mapping means that the spectral functions at nonzero magnetic field h are identical to the spectral function at $h = 0$ for a reduced value of the coupling constant (fermion charge) q , provided the probe fermion is in a Landau-level eigenstate. A striking consequence is that the spectrum shows conformal invariance for arbitrarily high magnetic fields, as long as the system is at negligible to zero density. Specifically, a detailed analysis

of the fermion spectral functions reveals that at strong magnetic fields, the Fermi-level structure changes qualitatively. There exists a critical magnetic field at which the Fermi velocity vanishes. Ignoring the Landau-level quantization, we show that this corresponds to an effective tuning of the system from a regular Fermi-liquid phase with linear dispersion and stable quasiparticles to a non-Fermi liquid with fractional power-law dispersion and unstable excitations. This phenomenon can be interpreted as a transition from metallic phase to a “strange metal” at the critical magnetic field and corresponds to the change of the infrared conformal dimension from $\nu > 1/2$ to $\nu < 1/2$, while the Fermi momentum stays nonzero and the Fermi surface survives. Increasing the magnetic field further, this transition is followed by a strange-metal–conformal crossover and eventually, for very strong fields, the system always has near-conformal behavior where $k_F = 0$ and the Fermi surface disappears.

For some Fermi surfaces, this surprising metal–strange-metal transition is not physically relevant, as the system prefers to directly enter the conformal phase. Whether a fine tuned system exists that does show a quantum critical phase transition from a Fermi liquid to a non-Fermi liquid is determined by a Diophantine equation for the Landau-quantized Fermi momentum as a function of the magnetic field. Perhaps these are connected to the magnetically driven phase transition found in AdS₅/CFT₄ [16]. We leave this subject for future work.

Overall, the findings of Landau quantization and “discharge” of the Fermi surface are in line with the expectations: both phenomena have been found in a vast array of systems [17] and are almost tautologically tied to the notion of a Fermi surface in a magnetic field. Thus, we regard them also as a sanity check of the whole bottom-up approach of fermionic AdS/CFT [4–6,15], giving further credit to the holographic Fermi surfaces as having to do with the real world.

Next, we use the information of magnetic effects the Fermi surfaces extracted from holography to calculate the quantum Hall and longitudinal conductivities. Generally speaking, it is difficult to calculate conductivity holographically beyond the Einstein-Maxwell sector, and extract the contribution of holographic fermions. In the semiclassical approximation, one-loop corrections in the bulk setup involving charged fermions have been calculated [15]. In another approach, the backreaction of charged fermions on the gravity-Maxwell sector has been taken into account and incorporated in calculations of the electric conductivity [8]. We calculate the one-loop contribution on the CFT side, which is equivalent to the holographic one-loop calculations as long as vertex corrections do not modify physical dependencies of interest [15,18]. As we dial the magnetic field, the Hall plateau transition happens when the Fermi surface moves through a Landau level. One can think of a difference between the Fermi energy and the

energy of the Landau level as a gap, which vanishes at the transition point and the 2 + 1-dimensional theory becomes scale invariant. In the holographic D3–D7 brane model of the quantum Hall effect, plateau transition occurs as D-branes move through one another [19]. In the same model, a dissipation process has been observed as D-branes fall through the horizon of the black hole geometry that is associated with the quantum Hall insulator transition. In the holographic fermion liquid setting, dissipation is present through interaction of fermions with the horizon of the black hole. We have also used the analysis of the conductivities to learn more about the metal–strange-metal phase transition, as well as the crossover back to the conformal regime at high magnetic fields.

We conclude with the remark that the findings summarized above are, in fact, somewhat puzzling when contrasted to the conventional picture of quantum Hall physics. It is usually stated that the quantum Hall effect requires three key ingredients: Landau quantization, quenched disorder,¹ and (spatial) boundaries, i.e., a finite-sized sample [20]. The first brings about the quantization of conductivity, the second prevents the states from spilling between the Landau levels, ensuring the existence of a gap, and the last one, in fact, allows the charge transport to happen (as it is the boundary states that actually conduct). In our model, only the first condition is satisfied. The second is put by hand by assuming that the gap is automatically preserved, i.e., that there is no mixing between the Landau levels. There is, however, no physical explanation as to how the boundary states are implicitly taken into account by AdS/CFT.

The paper is organized as follows. We outline the holographic setting of the dyonic black hole geometry and bulk fermions in Sec. II. In Sec. III, we prove the conservation of conformal symmetry in the presence of the magnetic fields. Section IV is devoted to the holographic fermion liquid, where we obtain the Landau-level quantization, followed by a detailed study of the Fermi surface properties at zero temperature in Sec. V. We calculate the DC conductivities in Sec. VI, and compare the results with available data in graphene. In Sec. VII, we show that the fermion sign problem is absent in the holographic setting, therefore allowing lattice simulations of finite density matter in principle.

II. HOLOGRAPHIC FERMIONS IN A DYONIC BLACK HOLE

We first describe the holographic setup with the dyonic black hole and the dynamics of Dirac fermions in this

¹Quenched disorder means that the dynamics of the impurities is “frozen”, i.e. they can be regarded as having infinite mass. When coupled to the Fermi liquid, they ensure that below some scale, the system behaves as if consisting of noninteracting quasiparticles only.

background. In this paper, we exclusively work in the probe limit, i.e., in the limit of large fermion charge q .

A. Dyonic black hole

We consider the gravity dual of 3-dimensional conformal field theory with global $U(1)$ symmetry. At finite charge density and in the presence of a magnetic field, the system can be described by a dyonic black hole in 4-dimensional anti-de Sitter space-time, AdS_4 , with the current J_μ in the CFT mapped to a $U(1)$ gauge field A_M in AdS. We use μ, ν, ρ, \dots , for the space-time indices in the CFT and M, N, \dots , for the global space-time indices in AdS.

The action for a vector field A_M coupled to AdS_4 gravity can be written as

$$S_g = \frac{1}{2\kappa^2} \int d^4x \sqrt{-g} \left(\mathcal{R} + \frac{6}{R^2} - \frac{R^2}{g_F^2} F_{MN} F^{MN} \right), \quad (1)$$

where g_F^2 is an effective dimensionless gauge coupling and R is the curvature radius of AdS_4 . The equations of motion following from Eq. (1) are solved by the geometry corresponding to a dyonic black hole, having both electric and magnetic charge:

$$\begin{aligned} ds^2 &= g_{MN} dx^M dx^N \\ &= \frac{r^2}{R^2} (-f dt^2 + dx^2 + dy^2) + \frac{R^2}{r^2} \frac{dr^2}{f}. \end{aligned} \quad (2)$$

The redshift factor f and the vector field A_M reflect the fact that the system is at a finite charge density and in an external magnetic field:

$$\begin{aligned} f &= 1 + \frac{Q^2 + H^2}{r^4} - \frac{M}{r^3}, \\ A_t &= \mu \left(1 - \frac{r_0}{r} \right), \\ A_y &= hx, \\ A_x &= A_r = 0, \end{aligned} \quad (3)$$

where Q and H are the electric and magnetic charge of the black hole, respectively. Here, we chose the Landau gauge; the black hole chemical potential μ and the magnetic field h are given by

$$\mu = \frac{g_F Q}{R^2 r_0}, \quad h = \frac{g_F H}{R^4}, \quad (4)$$

with r_0 as the horizon radius determined by the largest positive root of the redshift factor $f(r_0) = 0$:

$$M = r_0^3 + \frac{Q^2 + H^2}{r_0}. \quad (5)$$

The boundary of the AdS is reached for $r \rightarrow \infty$. The geometry described by Eqs. (2) and (3) describes the boundary theory at finite density, i.e., a system in a charged

medium at the chemical potential $\mu = \mu_{\text{bh}}$ and in transverse magnetic field $h = h_{\text{bh}}$, with charge, energy, and entropy densities given, respectively, by

$$\rho = 2 \frac{Q}{\kappa^2 R^2 g_F}, \quad \epsilon = \frac{M}{\kappa^2 R^4}, \quad s = \frac{2\pi}{\kappa^2} \frac{r_0^2}{R^2}. \quad (6)$$

The temperature of the system is identified with the Hawking temperature of the black hole, $T_H \sim |f'(r_0)|/4\pi$,

$$T = \frac{3r_0}{4\pi R^2} \left(1 - \frac{Q^2 + H^2}{3r_0^4}\right). \quad (7)$$

Since Q and H have dimensions of $[L]^2$, it is convenient to parametrize them as

$$Q^2 = 3r_*^4, \quad Q^2 + H^2 = 3r_{**}^4. \quad (8)$$

In terms of r_0 , r_* , and r_{**} , the above expressions become

$$f = 1 + \frac{3r_{**}^4}{r^4} - \frac{r_0^3 + 3r_{**}^4/r_0}{r^3}, \quad (9)$$

with

$$\mu = \sqrt{3} g_F \frac{r_*^2}{R^2 r_0}, \quad h = \sqrt{3} g_F \frac{\sqrt{r_{**}^4 - r_*^4}}{R^4}. \quad (10)$$

The expressions for the charge, energy, and entropy densities, as well as for the temperature, are simplified as

$$\begin{aligned} \rho &= \frac{2\sqrt{3}}{\kappa^2 g_F} \frac{r_*^2}{R^2}, & \epsilon &= \frac{1}{\kappa^2} \frac{r_0^3 + 3r_{**}^4/r_0}{R^4}, \\ s &= \frac{2\pi}{\kappa^2} \frac{r_0^2}{R^2}, & T &= \frac{3}{4\pi} \frac{r_0}{R^2} \left(1 - \frac{r_{**}^4}{r_0^4}\right). \end{aligned} \quad (11)$$

In the zero temperature limit, i.e., for an extremal black hole, we have

$$T = 0 \rightarrow r_0 = r_{**}, \quad (12)$$

which in the original variables reads $Q^2 + H^2 = 3r_0^4$. In the zero temperature limit (12), the redshift factor f as given by Eq. (9) develops a double zero at the horizon:

$$f = 6 \frac{(r - r_{**})^2}{r_{**}^2} + \mathcal{O}((r - r_{**})^3). \quad (13)$$

As a result, near the horizon, the AdS_4 metric reduces to $\text{AdS}_2 \times \mathbb{R}^2$ with the curvature radius of AdS_2 given by

$$R_2 = \frac{1}{\sqrt{6}} R. \quad (14)$$

This is a very important property of the metric, which considerably simplifies the calculations, in particular, in the magnetic field.

In order to scale away the AdS_4 radius R and the horizon radius r_0 , we introduce dimensionless variables

$$\begin{aligned} r &\rightarrow r_0 r, & r_* &\rightarrow r_0 r_*, & r_{**} &\rightarrow r_0 r_{**}, \\ M &\rightarrow r_0^3 M, & Q &\rightarrow r_0^2 Q, & H &\rightarrow r_0^2 H, \end{aligned} \quad (15)$$

and

$$\begin{aligned} (t, \vec{x}) &\rightarrow \frac{R^2}{r_0} (t, \vec{x}), & A_M &\rightarrow \frac{r_0}{R^2} A_M, & \omega &\rightarrow \frac{r_0}{R^2} \omega, \\ \mu &\rightarrow \frac{r_0}{R^2} \mu, & h &\rightarrow \frac{r_0^2}{R^4} h, & T &\rightarrow \frac{r_0}{R^2} T, & ds^2 &\rightarrow R^2 ds^2. \end{aligned} \quad (16)$$

Note that the scaling factors in the above equation that describes the quantities of the boundary field theory involve the curvature radius of AdS_4 , not AdS_2 .

In the new variables, we have

$$\begin{aligned} T &= \frac{3}{4\pi} (1 - r_{**}^4) = \frac{3}{4\pi} \left(1 - \frac{Q^2 + H^2}{3}\right), \\ f &= 1 + \frac{3r_{**}^4}{r^4} - \frac{1 + 3r_{**}^4}{r^3}, & A_t &= \mu \left(1 - \frac{1}{r}\right), \\ \mu &= \sqrt{3} g_F r_*^2 = g_F Q, & h &= g_F H, \end{aligned} \quad (17)$$

and the metric is given by

$$ds^2 = r^2 (-f dt^2 + dx^2 + dy^2) + \frac{1}{r^2} \frac{dr^2}{f}, \quad (18)$$

with the horizon at $r = 1$ and the conformal boundary at $r \rightarrow \infty$.

At $T = 0$, r_{**} becomes unity, and the redshift factor develops the double zero near the horizon,

$$f = \frac{(r - 1)^2 (r^2 + 2r + 3)}{r^4}. \quad (19)$$

As mentioned before, due to this fact, the metric near the horizon reduces to $\text{AdS}_2 \times \mathbb{R}^2$, where the analytical calculations are possible for small frequencies [7]. However, in the chiral limit $m = 0$, analytical calculations are also possible in the bulk AdS_4 [21], which we utilize in this paper.

B. Holographic fermions

To include the bulk fermions, we consider a spinor field ψ in the AdS_4 of charge q and mass m , which is dual to an operator \mathcal{O} in the boundary CFT_3 of charge q and dimension

$$\Delta = \frac{3}{2} + mR, \quad (20)$$

with $mR \geq -\frac{1}{2}$ and in dimensionless units corresponding to $\Delta = \frac{3}{2} + m$. In the black hole geometry, Eq. (2), the quadratic action for ψ reads as

$$S_\psi = i \int d^4x \sqrt{-g} (\bar{\psi} \Gamma^M \mathcal{D}_M \psi - m \bar{\psi} \psi), \quad (21)$$

where $\bar{\psi} = \psi^\dagger \Gamma^t$, and

$$\mathcal{D}_M = \partial_M + \frac{1}{4} \omega_{abM} \Gamma^{ab} - iqA_M, \quad (22)$$

where ω_{abM} is the spin connection, and $\Gamma^{ab} = \frac{1}{2}[\Gamma^a, \Gamma^b]$. Here, M and a, b denote the bulk space-time and tangent space indices, respectively, while μ, ν are indices along the boundary directions, i.e., $M = (r, \mu)$. Gamma matrix basis (Minkowski signature) is given by Eq. (A12) as in [7].

We will be interested in spectra and response functions of the boundary fermions in the presence of magnetic field. This requires solving the Dirac equation in the bulk [5,6]:

$$(\Gamma^M \mathcal{D}_M - m)\psi = 0. \quad (23)$$

From the solution of the Dirac equation at small ω , an analytic expression for the retarded fermion Green's function of the boundary CFT at zero magnetic field has been obtained in [7]. Near the Fermi surface, it reads as [7]:

$$G_R(\Omega, k) = \frac{(-h_1 v_F)}{\omega - v_F k_\perp - \Sigma(\omega, T)}, \quad (24)$$

where $k_\perp = k - k_F$ is the perpendicular distance from the Fermi surface in momentum space, h_1 and v_F are real constants calculated below, and the self-energy $\Sigma = \Sigma_1 + i\Sigma_2$ is given by [7]

$$\begin{aligned} \Sigma(\omega, T)/v_F &= T^{2\nu} g\left(\frac{\omega}{T}\right) \\ &= (2\pi T)^{2\nu} h_2 e^{i\theta - i\pi\nu} \frac{\Gamma(\frac{1}{2} + \nu - \frac{i\omega}{2\pi T} + \frac{i\mu_q}{6})}{\Gamma(\frac{1}{2} - \nu - \frac{i\omega}{2\pi T} + \frac{i\mu_q}{6})}, \end{aligned} \quad (25)$$

where ν is the zero temperature conformal dimension at the Fermi momentum, $\nu \equiv \nu_{k_F}$, given by Eq. (58), $\mu_q \equiv \mu q$, h_2 is a positive constant, and the phase θ is such that the poles of the Green's function are located in the lower half of the complex frequency plane. These poles correspond to quasinormal modes of the Dirac equation (23), and they can be found numerically solving $F(\omega_*) = 0$ [22], with

$$F(\omega) = \frac{k_\perp}{\Gamma(\frac{1}{2} + \nu - \frac{i\omega}{2\pi T} + \frac{i\mu_q}{6})} - \frac{h_2 e^{i\theta - i\pi\nu} (2\pi T)^{2\nu}}{\Gamma(\frac{1}{2} - \nu - \frac{i\omega}{2\pi T} + \frac{i\mu_q}{6})}. \quad (26)$$

The solution gives the full motion of the quasinormal poles $\omega_*^{(n)}(k_\perp)$ in the complex ω plane as a function of k_\perp . It has been found in [7,22], that, if the charge of the fermion is large enough compared to its mass, the pole closest to the real ω axis bounces off the axis at $k_\perp = 0$ (and $\omega = 0$). Such behavior is identified with the existence of the Fermi momentum k_F , indicative of an underlying strongly coupled Fermi surface.

At $T = 0$, the self-energy becomes $T^{2\nu} g(\omega/T) \rightarrow c_k \omega^{2\nu}$, and the Green's function obtained from the solution to the Dirac equation reads [7]

$$G_R(\Omega, k) = \frac{(-h_1 v_F)}{\omega - v_F k_\perp - h_2 v_F e^{i\theta - i\pi\nu} \omega^{2\nu}}, \quad (27)$$

where $k_\perp = \sqrt{k^2} - k_F$. The last term is determined by the IR AdS₂ physics near the horizon. Other terms are determined by the UV physics of the AdS₄ bulk.

The solutions to (23) have been studied in detail in [5–7]. Here, we simply summarize the novel aspects due to the background magnetic field (formal details can be found in the Appendix A).

- (i) The background magnetic field h introduces a discretization of the momentum (see Appendix A for details):

$$k \rightarrow k_{\text{eff}} = \sqrt{2|qh|l}, \quad \text{with } l \in N, \quad (28)$$

with Landau-level index l [12,22]. These discrete values of k are the analogue of the well-known Landau levels that occur in magnetic systems.

- (ii) There exists a (noninvertible) mapping on the level of Green's functions, from the magnetic system to the nonmagnetic one by sending

$$(H, Q, q) \mapsto \left(0, \sqrt{Q^2 + H^2}, q\sqrt{1 - \frac{H^2}{Q^2 + H^2}}\right). \quad (29)$$

The Green's functions in a magnetic system are thus equivalent to those in the absence of magnetic fields. To better appreciate that, we reformulate Eq. (29) in terms of the boundary quantities:

$$(h, \mu_q, T) \mapsto \left(0, \mu_q, T\left(1 - \frac{h^2}{12\mu^2}\right)\right), \quad (30)$$

where we used dimensionless variables defined in Eqs. (15) and (17). The magnetic field thus effectively decreases the coupling constant q and increases the chemical potential $\mu = g_F Q$, such that the combination $\mu_q \equiv \mu q$ is preserved [11]. This is an important point, as the equations of motion actually only depend on this combination and not on μ and q separately [11]. In other words, Eq. (30) implies that the additional scale brought about by the magnetic field can be understood as changing μ and T independently in the effective nonmagnetic system instead of only tuning the ratio μ/T . This point is important when considering the thermodynamics.

- (iii) The discrete momentum $k_{\text{eff}} = \sqrt{2|qh|l}$ must be held fixed in the transformation (29). The bulk-boundary relation is particularly simple in this case, as the Landau levels can readily be seen in

the bulk solution, only to remain identical in the boundary theory.

- (iv) Similar to the nonmagnetic system [11], the IR physics is controlled by the near-horizon $\text{AdS}_2 \times \mathbb{R}^2$ geometry, which indicates the existence of an IR CFT, characterized by operators \mathcal{O}_l , $l \in N$ with operator dimensions $\delta = 1/2 + \nu_l$:

$$\nu_l = \frac{1}{6} \sqrt{6 \left(m^2 + \frac{2|qh|l}{r_{**}^2} \right) - \frac{\mu_q^2}{r_{**}^4}}, \quad (31)$$

in dimensionless notation, and $\mu_q \equiv \mu q$. At $T = 0$, when $r_{**} = 1$, it becomes

$$\nu_l = \frac{1}{6} \sqrt{6(m^2 + 2|qh|l) - \mu_q^2}. \quad (32)$$

The Green's function for these operators \mathcal{O}_l is found to be $\mathcal{G}_l^R(\omega) \sim \omega^{2\nu_l}$, and the exponents ν_l determine the dispersion properties of the quasiparticle excitations. For $\nu > 1/2$, the system has a stable quasiparticle and a linear dispersion, whereas, for $\nu \leq 1/2$, one has a non-Fermi liquid with power-law dispersion and an unstable quasiparticle.

III. MAGNETIC FIELDS AND CONFORMAL INVARIANCE

Despite the fact that a magnetic field introduces a scale, in the absence of a chemical potential, all spectral functions are essentially still determined by conformal symmetry. To show this, we need to establish certain properties of the near-horizon geometry of a Reissner-Nordström black hole. This leads to the AdS_2 perspective that was developed in [7]. The result relies on the conformal algebra and its relation to the magnetic group, from the viewpoint of the infrared CFT that was studied in [7]. Later on, we will see that the insensitivity to the magnetic field also carries over to AdS_4 and the UV CFT in some respects. To simplify the derivations, we consider the case $T = 0$.

A. The near-horizon limit and Dirac equation in AdS_2

It was established in [7] that an electrically charged extremal AdS -Reissner-Nordström black hole has an AdS_2 throat in the inner bulk region. This conclusion carries over to the magnetic case with some minor differences. We will now give a quick derivation of the AdS_2 formalism for a dyonic black hole, referring the reader to [7] for more details (that remain largely unchanged in the magnetic field).

Near the horizon $r = r_{**}$ of the black hole described by the metric (2), the redshift factor $f(r)$ develops a double zero:

$$f(r) = 6 \frac{(r - r_{**})^2}{r_{**}^2} + \mathcal{O}((r - r_{**})^3). \quad (33)$$

Now consider the scaling limit

$$r - r_{**} = \lambda \frac{R_2^2}{\zeta}, \quad t = \lambda^{-1} \tau, \quad (34)$$

$$\lambda \rightarrow 0 \quad \text{with} \quad \tau, \zeta \text{ finite.}$$

In this limit, the metric (2) and the gauge field reduce to

$$ds^2 = \frac{R_2^2}{\zeta^2} (-d\tau^2 + d\zeta^2) + \frac{r_{**}^2}{R_2^2} (dx^2 + dy^2) \quad (35)$$

$$A_\tau = \frac{\mu R_2^2 r_0}{r_{**}^2} \frac{1}{\zeta}, \quad A_x = Hx,$$

where $R_2 = \frac{R}{\sqrt{6}}$. The geometry described by this metric is indeed $\text{AdS}_2 \times \mathbb{R}^2$. Physically, the scaling limit given in Eq. (34) with finite τ corresponds to the long time limit of the original time coordinate t , which translates to the low frequency limit of the boundary theory:

$$\frac{\omega}{\mu} \rightarrow 0, \quad (36)$$

where ω is the frequency conjugate to t . (One can think of λ as being the frequency ω). Near the AdS_4 horizon, we expect the AdS_2 region of an extremal dyonic black hole to have a CFT_1 dual. We refer to [7] for an account of this $\text{AdS}_2/\text{CFT}_1$ duality. The horizon of AdS_2 region is at $\zeta \rightarrow \infty$ (the coefficient in front of $d\tau$ vanishes at the horizon in Eq. (35)), and the infrared CFT (IR CFT) lives at the AdS_2 boundary at $\zeta = 0$. The scaling picture given by Eqs. (34) and (35) suggests that in the low frequency limit, the 2-dimensional boundary theory is described by this IR CFT (which is a CFT_1). The Green's function for the operator \mathcal{O} in the boundary theory is obtained through a small frequency expansion and a matching procedure between the two different regions (inner and outer) along the radial direction and can be expressed through the Green's function of the IR CFT [7].

The explicit form for the Dirac equation (A28) in the magnetic field is of little interest for the analytical results that follow; for completeness, we give it in the Appendix A. Of primary interest is its limit in the IR region with metric given by Eq. (35):

$$\left(-\frac{1}{\sqrt{g_{\zeta\zeta}}} \sigma^3 \partial_\zeta - m + \frac{1}{\sqrt{-g_{\tau\tau}}} \sigma^1 \left(\omega + \frac{\mu_q R_2^2 r_0}{r_{**}^2 \zeta} \right) - \frac{1}{\sqrt{g_{ii}} i \sigma^2 \lambda_l} \right) F^{(l)} = 0, \quad (37)$$

where the effective momentum of the l -th Landau level is $\lambda_l = \sqrt{2|qh|l}$, $\mu_q \equiv \mu q$, and we omit the index of the spinor field. To obtain Eq. (37), it is convenient to pick the gamma matrix basis as $\Gamma^{\hat{\zeta}} = -\sigma_3$, $\Gamma^{\hat{\tau}} = i\sigma_1$, and $\Gamma^{\hat{i}} = -\sigma_2$. We can write explicitly:

$$\begin{pmatrix} \frac{\zeta}{R_2} \partial_\zeta + m & -\frac{\zeta}{R_2} \left(\omega + \frac{\mu_q R_2^2 r_0}{r_{**}^2 \zeta} \right) + \frac{R}{r_{**}} \lambda_l \\ \frac{\zeta}{R_2} \left(\omega + \frac{\mu_q R_2^2 r_0}{r_{**}^2 \zeta} \right) + \frac{R}{r_{**}} \lambda_l & \frac{\zeta}{R_2} \partial_\zeta - m \end{pmatrix} \begin{pmatrix} y \\ z \end{pmatrix} = 0. \quad (38)$$

Note that the AdS₂ radius R_2 enters for the (τ, ζ) directions. At the AdS₂ boundary, $\zeta \rightarrow 0$, the Dirac equation to the leading order is given by

$$\zeta \partial_\zeta F^{(l)} = -UF^{(l)},$$

$$U = R_2 \begin{pmatrix} m & -\frac{\mu_q R_2 r_0}{r_{**}^2} + \frac{R}{r_{**}} \lambda_l \\ \frac{\mu_q R_2 r_0}{r_{**}^2} + \frac{R}{r_{**}} \lambda_l & -m \end{pmatrix}. \quad (39)$$

The solution to this equation is given by the scaling function $F^{(l)} = Ae_+ \zeta^{-\nu_l} + Be_- \zeta^{\nu_l}$, where e_\pm are the real eigenvectors of U and the exponent is

$$\nu_l = \frac{1}{6} \sqrt{6 \left(m^2 + \frac{R^2}{r_{**}^2} 2|qh|l \right) R^2 - \frac{\mu_q^2 R^4 r_0^2}{r_{**}^4}}. \quad (40)$$

The conformal dimension of the operator \mathcal{O} in the IR CFT is $\delta_l = \frac{1}{2} + \nu_l$. Comparing Eq. (40) to the expression for the scaling exponent in [7], we conclude that the scaling properties and the AdS₂ construction are unmodified by the magnetic field, except that the scaling exponents are now fixed by the Landau quantization. This ‘‘quantization rule’’ was already exploited in [22] to study de Haas-Alphen oscillations.

IV. SPECTRAL FUNCTIONS

In this section, we will explore some of the properties of the spectral function, in both plane wave and Landau-level basis. We first consider some characteristic cases in the plane wave basis and make connection with the angle-resolved photoemission spectroscopy (ARPES) measurements.

A. Relating to the ARPES measurements

In reality, ARPES measurements cannot be performed in magnetic fields so the holographic approach, allowing a direct insight into the propagator structure and the spectral function, is especially helpful. This follows from the observation that the spectral functions as measured in ARPES are always expressed in the plane wave basis of the photon. Thus, in a magnetic field, when the momentum is not a good quantum number anymore, it becomes impossible to perform the photoemission spectroscopy.

In order to compute the spectral function, we have to choose a particular fermionic plane wave as a probe. Since the separation of variables is valid throughout the bulk, the basis transformation can be performed at every constant

r -slice. This means that only the x and y coordinates have to be taken into account (the plane wave probe lives only at the CFT side of the duality). We take a plane wave propagating in the $+x$ direction with spin up along the r -axis. In its rest frame, such a particle can be described by

$$\Psi_{\text{probe}} = e^{i\omega t - ip_x x} \begin{pmatrix} \xi \\ \xi \end{pmatrix}, \quad \xi = \begin{pmatrix} 1 \\ 0 \end{pmatrix}. \quad (41)$$

Near the boundary (at $r_b \rightarrow \infty$), we can rescale our solutions of the Dirac equation making use of Eqs. (A23), (A24), and (B1):

$$F_l = \begin{pmatrix} \zeta_l^{(1)}(\tilde{x}) \\ \xi_+^{(l)}(r_b) \zeta_l^{(1)}(\tilde{x}) \\ \zeta_l^{(2)}(\tilde{x}) \\ -\xi_+^{(l)}(r_b) \zeta_l^{(2)}(\tilde{x}) \end{pmatrix}, \quad \tilde{F}_l = \begin{pmatrix} \zeta_l^{(1)}(\tilde{x}) \\ \xi_-^{(l)}(r_b) \zeta_l^{(1)}(\tilde{x}) \\ -\zeta_l^{(2)}(\tilde{x}) \\ \xi_-^{(l)}(r_b) \zeta_l^{(2)}(\tilde{x}) \end{pmatrix}, \quad (42)$$

with rescaled \tilde{x} defined after Eq. (A20). This representation is useful since we calculate the components $\xi_\pm(r_b)$ related to the retarded Green’s function in our numerics (we keep the notation of [7]).

Let \mathcal{O}_l and $\tilde{\mathcal{O}}_l$ be the CFT operators dual to F_l and \tilde{F}_l , respectively, and c_k^\dagger, c_k be the creation and annihilation operators for the plane wave state Ψ_{probe} . Since the states F and \tilde{F} form a complete set in the bulk, we can write

$$\begin{aligned} c_p^\dagger(\omega) &= \sum_l (U_l^*, \tilde{U}_l^*) \begin{pmatrix} \mathcal{O}_l^\dagger(\omega) \\ \tilde{\mathcal{O}}_l^\dagger(\omega) \end{pmatrix} \\ &= \sum_l (U_l^* \mathcal{O}_l^\dagger(\omega) + \tilde{U}_l^* \tilde{\mathcal{O}}_l^\dagger(\omega)), \end{aligned} \quad (43)$$

where the overlap coefficients $U_l(\omega)$ are given by the inner product between Ψ_{probe} and F :

$$\begin{aligned} U_l(p_x) &= \int dx F_l^\dagger i\Gamma^0 \Psi_{\text{probe}} \\ &= - \int dx e^{-ip_x x} \xi_+(r_b) (\zeta_l^{(1)\dagger}(\tilde{x}) - \zeta_l^{(2)\dagger}(\tilde{x})), \end{aligned} \quad (44)$$

with $\bar{F} = F^\dagger i\Gamma^0$ and a similar expression for \tilde{U}_l involving $\xi_-(r_b)$. The constants U_l can be calculated analytically using the numerical value of $\xi_\pm(r_b)$ and by noting that the Hermite functions are eigenfunctions of the Fourier transform. We are interested in the retarded Green’s function, defined as

$$\begin{aligned} G_{\mathcal{O}_l}^R(\omega, p) &= -i \int d^x t e^{i\omega t - ip \cdot x} \theta(t) G_{\mathcal{O}_l}^R(t, x) \\ G_{\mathcal{O}_l}^R(t, x) &= \langle 0 | [\mathcal{O}_l(t, x), \bar{\mathcal{O}}_l(0, 0)] | 0 \rangle \\ G^R &= \begin{pmatrix} G_{\mathcal{O}} & 0 \\ 0 & \tilde{G}_{\mathcal{O}} \end{pmatrix}, \end{aligned} \quad (45)$$

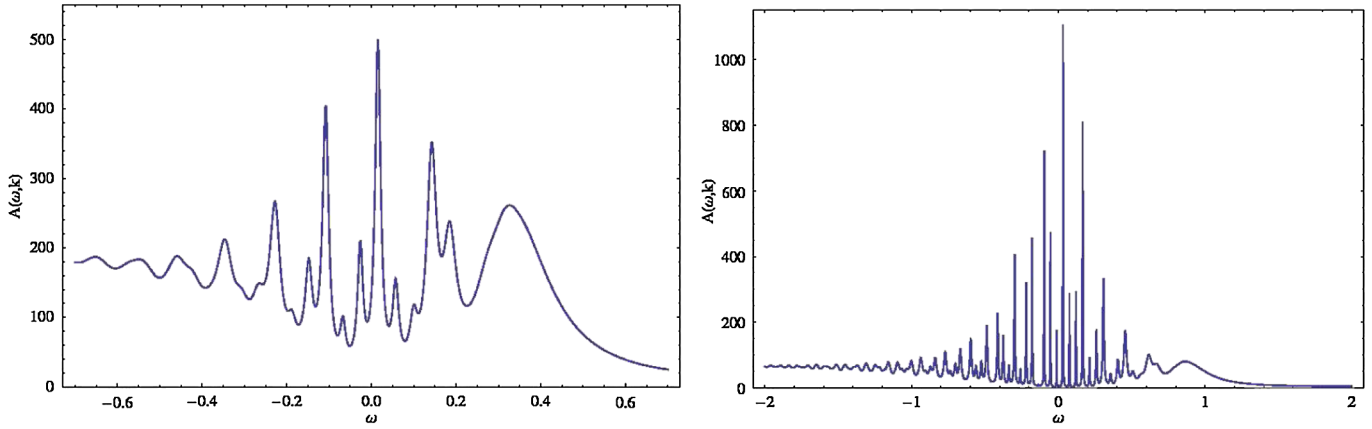


FIG. 1 (color online). Two examples of spectral functions in the plane wave basis for $\mu/T = 50$ and $h/T = 1$. The conformal dimension is $\Delta = 5/4$ (left) and $\Delta = 3/2$ (right). Frequency is in the units of effective temperature T_{eff} . The plane wave momentum is chosen to be $k = 1$. Despite the convolution of many Landau levels, the presence of the discrete levels is obvious.

where $\tilde{G}_{\mathcal{O}}$ is the retarded Green's function for the operator \mathcal{O} .

Exploiting the orthogonality of the spinors created by \mathcal{O} and \mathcal{O}^\dagger and using Eq. (43), the Green's function in the plane wave basis can be written as

$$\begin{aligned} G_{c_p}^R(\omega, p_x) &= \sum_l \text{tr} \left(\tilde{U} \right) (U^*, \tilde{U}^*) G^R \\ &= (|U_l(p_x)|^2 G_{\mathcal{O}_l}^R(\omega, l) + |\tilde{U}_l(p_x)|^2 \tilde{G}_{\mathcal{O}_l}^R(\omega, l)). \end{aligned} \quad (46)$$

In practice, we cannot perform the sum in Eq. (46) all the way to infinity, so we have to introduce a cutoff Landau-level l_{cut} . In most cases, we are able to make l_{cut} large enough that the behavior of the spectral function is clear.

Using the above formalism, we have produced spectral functions for two different conformal dimensions and fixed chemical potential and magnetic field (Fig. 1). Using the plane wave basis allows us to directly detect the Landau levels. The unit used for plotting the spectra (here and later on in the paper) is the effective temperature T_{eff} [5]:

$$T_{\text{eff}} = \frac{T}{2} \left(1 + \sqrt{1 + \frac{3\mu^2}{(4\pi T)^2}} \right). \quad (47)$$

This unit interpolates between μ at $T/\mu = 0$ and T at $T/\mu \rightarrow \infty$ and is convenient for the reason that the relevant quantities (e.g., Fermi momentum) are of order unity for any value of μ and h .

B. Magnetic crossover and disappearance of the quasiparticles

Theoretically, it is more convenient to consider the spectral functions in the Landau-level basis. For definiteness, let us pick a fixed conformal dimension $\Delta = \frac{5}{4}$ which corresponds to $m = -\frac{1}{4}$. In the limit of weak magnetic

fields, $h/T \rightarrow 0$, we should reproduce the results that were found in [5].

In Fig. 2(a), we indeed see that the spectral function, corresponding to a low value of μ/T , behaves as expected for a nearly conformal system. The spectral function is approximately symmetric about $\omega = 0$, it vanishes for $|\omega| < k$, up to a small residual tail due to finite temperature, and for $|\omega| \gg k$, it scales as ω^{2m} .

In Fig. 2(b), which corresponds to a high value of μ/T , we see the emergence of a sharp quasiparticle peak. This peak becomes the sharpest when the Landau-level l corresponding to an effective momentum $k_{\text{eff}} = \sqrt{2|qh|l}$ coincides with the Fermi momentum k_F . The peaks also broaden out when k_{eff} moves away from k_F . A more complete view of the Landau quantization in the quasiparticle regime is given in Fig. 3, where we plot the dispersion relation (ω - k map). Both the sharp peaks and the Landau levels can be visually identified.

Collectively, the spectra in Fig. 2 show that conformality is only broken by the chemical potential μ and not by the magnetic field. Naively, the magnetic field introduces a new scale in the system. However, this scale is absent from the spectral functions, visually validating the discussion in the previous section that the scale h can be removed by a rescaling of the temperature and chemical potential.

One thus concludes that there is some value h'_c of the magnetic field, depending on μ/T , such that the spectral function loses its quasiparticle peaks and displays near-conformal behavior for $h > h'_c$. The nature of the transition and the underlying mechanism depends on the parameters (μ_q, T, Δ). One mechanism, obvious from the rescaling in Eq. (29), is the reduction of the effective coupling q as h increases. This will make the influence of the scalar potential A_0 negligible and push the system back toward conformality. Generically, the spectral function shows no sharp change but is more indicative of a crossover.

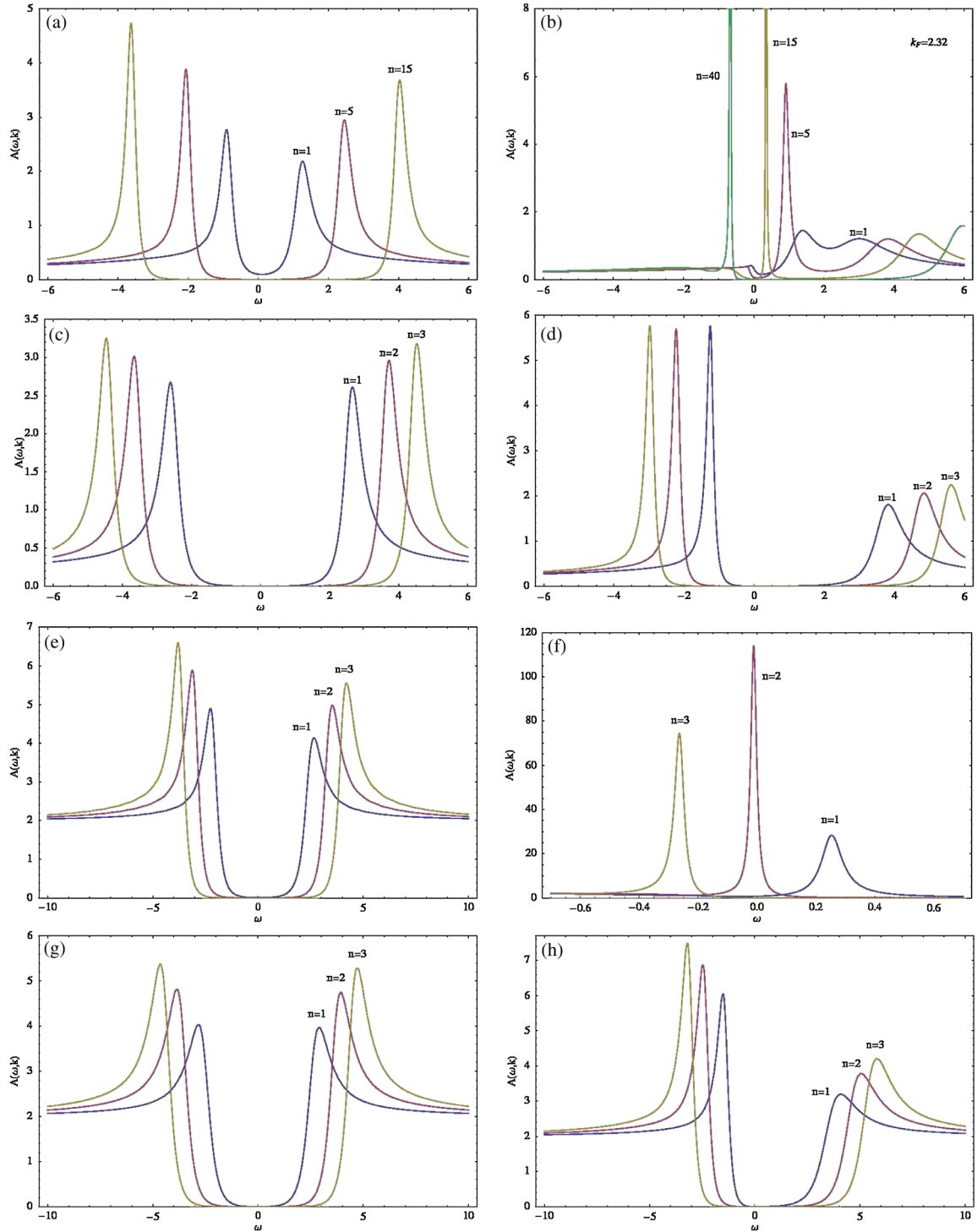


FIG. 2 (color online). Some typical examples of spectral functions $A(\omega, k_{\text{eff}})$ vs ω in the Landau basis, $k_{\text{eff}} = \sqrt{2|q\hbar|n}$. The top four correspond to a conformal dimension $\Delta = \frac{5}{4}$ ($m = -\frac{1}{4}$), and the bottom four to $\Delta = \frac{3}{2}$ ($m = 0$). In each plot, we show different Landau levels, labeled by index n , as a function of μ/T and h/T . The ratios take values $(\mu/T, h/T) = (1, 1), (50, 1), (1, 50), (50, 50)$ from left to right. The conformal case can be identified when μ/T is small, regardless of h/T (plots in the left panel). Nearly conformal behavior is seen when both μ/T and h/T are large. This confirms our analytic result that the behavior of the system is primarily governed by μ . Departure from the conformality and sharp quasiparticle peaks are seen when μ/T is large and h/T is small in parts (b) and (f). Multiple quasiparticle peaks arise whenever $k_{\text{eff}} = k_F$. This suggests the existence of a critical magnetic field, beyond which the quasiparticle description becomes invalid and the system exhibits a conformal-like behavior. As before, the frequency ω is in units of T_{eff} .

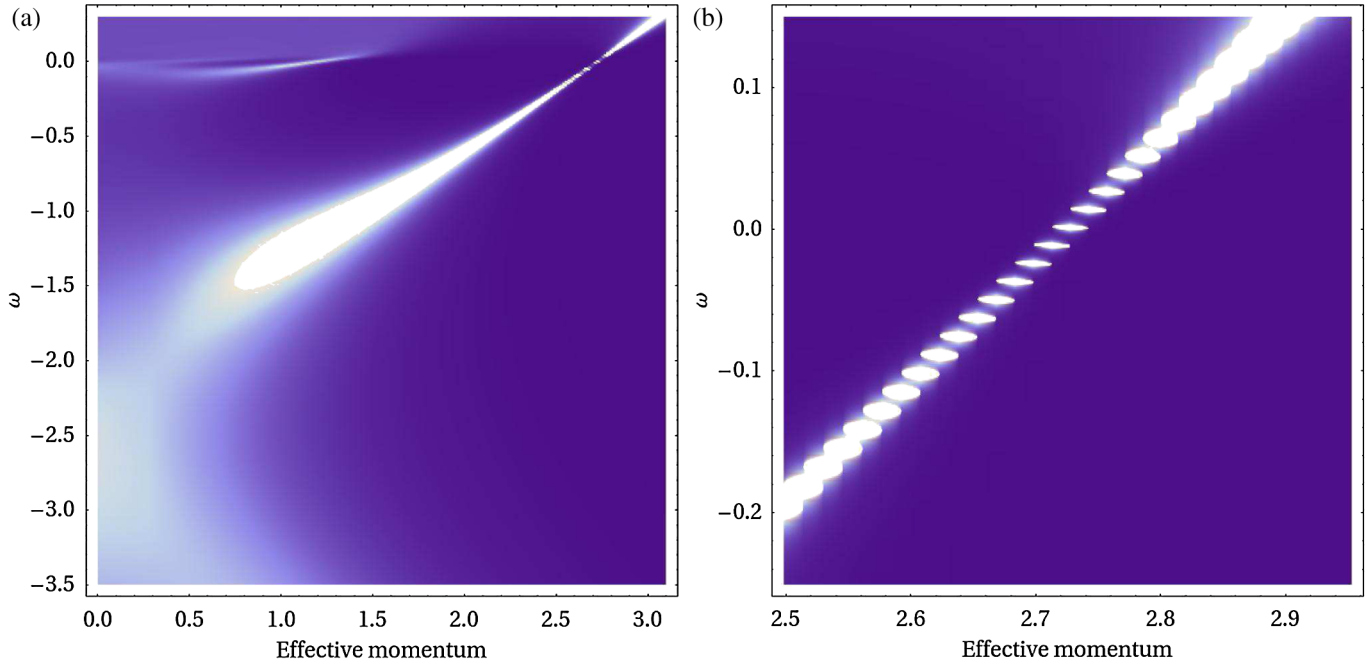


FIG. 3 (color online). Dispersion relation ω vs k_{eff} for $\mu/T = 50$, $h/T = 1$, and $\Delta = \frac{5}{4}$ ($m = -\frac{1}{4}$). The spectral function $A(\omega, k_{\text{eff}})$ is displayed as a density plot. (a) On a large energy and momentum scale, we clearly see that the peaks disperse almost linearly ($\omega \approx v_F k$), indicating that we are in the stable quasiparticle regime. (b) A zoom-in near the location of the Fermi surface shows clear Landau quantization.

A more interesting phenomenon is the disappearance of coherent quasiparticles at high effective chemical potentials. For the special case $m = 0$, we can go beyond numerics and study this transition analytically, combining the exact $T = 0$ solution found in [21] and the mapping (30). In the next section, we will show that the transition is controlled by the change in the dispersion of the quasiparticle and corresponds to a sharp phase transition. Increasing the magnetic field leads to a decrease in phenomenological control parameter ν_{k_F} . This can give rise to a transition to a non-Fermi liquid when $\nu_{k_F} \leq 1/2$, and,

finally, to the conformal regime at $h = h'_c$ when $\nu_{k_F} = 0$ and the Fermi surface vanishes.

C. Density of states

As argued at the beginning of this section, the spectral function can look quite different depending on the particular basis chosen. Though the spectral function is an attractive quantity to consider due to connection with ARPES experiments, we will also direct our attention to basis-independent and manifestly gauge invariant quantities. One of them is the density of states, defined by

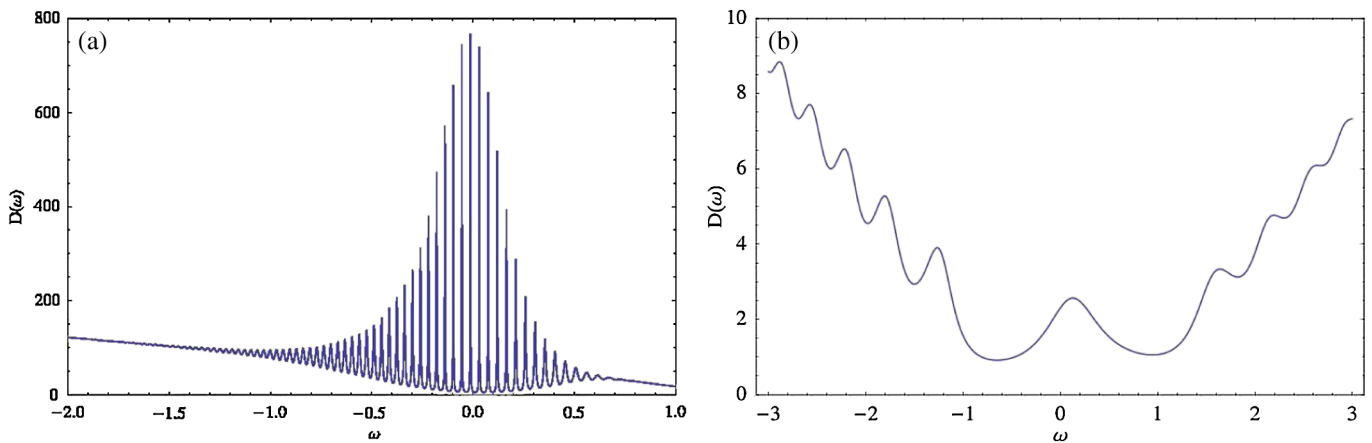


FIG. 4 (color online). Density of states $D(\omega)$ for $m = -\frac{1}{4}$ and (a) $\mu/T = 50$, $h/T = 1$, and (b) $\mu/T = 1$, $h/T = 1$. Sharp quasiparticle peaks from the splitting of the Fermi surface are clearly visible in (a). The case (b) shows square-root level spacing characteristic of a (nearly) Lorentz invariant spectrum, such as that of graphene.

$$D(\omega) = \sum_l A(\omega, l), \quad (48)$$

where the usual integral over the momentum is replaced by a sum since only discrete values of the momentum are allowed.

In Fig. 4, we plot the density of states for two systems. We clearly see the Landau splitting of the Fermi surface. A peculiar feature of these plots is that the density of states seems to grow for negative values of ω . This, however, is an artifact of our calculation. Each individual spectrum in the sum Eq. (48) has a finite tail that scales as ω^{2m} for large ω , so each term has a finite contribution for large values of ω . When the full sum is performed, this fact implies that $\lim_{\omega \rightarrow \infty} D(\omega) \rightarrow \infty$. The relevant information on the density of states can be obtained by regularizing the sum, which, in practice, is done by summing over a finite number of terms only and then considering the peaks that lie on top of the resulting finite-sized envelope. The physical point in Fig. 4(a) is the linear spacing of Landau levels, corresponding to a nonrelativistic system at finite density. This is to be contrasted with Fig. 4(b), where the level spacing behaves as $\propto \sqrt{h}$, appropriate for a Lorentz invariant system and realized in graphene [23].

V. FERMI LEVEL STRUCTURE AT ZERO TEMPERATURE

In this section, we solve the Dirac equation in the magnetic field for the special case $m = 0$ ($\Delta = \frac{3}{2}$). Although there are no additional symmetries in this case, it is possible to get an analytic solution. Using this solution, we obtain Fermi-level parameters such as k_F and v_F and consider the process of filling the Landau levels as the magnetic field is varied.

A. Dirac equation with $m = 0$

In the case $m = 0$, it is convenient to solve the Dirac equation including the spin connection (Eq. (A2)) rather than scaling it out:

$$\left(-\frac{\sqrt{g_{ii}}}{\sqrt{g_{rr}}} \sigma^1 \partial_r - \frac{\sqrt{g_{ii}}}{\sqrt{-g_{tt}}} \sigma^3 (\omega + qA_t) + \frac{\sqrt{g_{ii}}}{\sqrt{-g_{tt}}} \sigma^1 \frac{1}{2} \omega_{\hat{r}\hat{t}} - \sigma^1 \frac{1}{2} \omega_{\hat{x}\hat{r}x} - \sigma^1 \frac{1}{2} \omega_{\hat{y}\hat{r}y} - \lambda_l \right) \otimes 1 \begin{pmatrix} \psi_1 \\ \psi_2 \end{pmatrix} = 0, \quad (49)$$

where $\lambda_l = \sqrt{2|qh|l}$ are the energies of the Landau levels $l = 0, 1, \dots$, $g_{ii} \equiv g_{xx} = g_{yy}$, $A_t(r)$ is given by Eq. (3), and the gamma matrices are defined in Eq. (A12). In the basis of Eq. (A12), the two components ψ_1 and ψ_2 decouple. Therefore, in what follows, we solve for the first component only (we omit index 1). Substituting the spin connection, we have [18]:

$$\left(-\frac{r^2 \sqrt{f}}{R^2} \sigma^1 \partial_r - \frac{1}{\sqrt{f}} \sigma^3 (\omega + qA_t) - \sigma^1 \frac{r\sqrt{f}}{2R^2} \left(3 + \frac{rf'}{2f} \right) - \lambda_l \right) \psi = 0, \quad (50)$$

with $\psi = (y_1, y_2)$. It is convenient to change to the basis

$$\begin{pmatrix} \tilde{y}_1 \\ \tilde{y}_2 \end{pmatrix} = \begin{pmatrix} 1 & -i \\ -i & 1 \end{pmatrix} \begin{pmatrix} y_1 \\ y_2 \end{pmatrix}, \quad (51)$$

which diagonalizes the system into a second order differential equation for each component. We introduce the dimensionless variables as in Eqs. (15)–(17) and make a change of the dimensionless radial variable:

$$r = \frac{1}{1-z}, \quad (52)$$

with the horizon now being at $z = 0$ and the conformal boundary at $z = 1$. Performing these transformations in Eq. (50), the second order differential equations for \tilde{y}_1 reads

$$\left(f \partial_z^2 + \left(\frac{3f}{1-z} + f' \right) \partial_z + \frac{15f}{4(1-z)^2} + \frac{3f'}{2(1-z)} + \frac{f''}{4} + \frac{1}{f} \left((\omega + q\mu z) \pm \frac{if'}{4} \right)^2 - iq\mu - \lambda_l^2 \right) \tilde{y}_1 = 0. \quad (53)$$

The second component \tilde{y}_2 obeys the same equation with $\mu \mapsto -\mu$.

At $T = 0$,

$$f = 3z^2(z - z_0)(z - \bar{z}_0), \quad z_0 = \frac{1}{3}(4 + i\sqrt{2}). \quad (54)$$

The solution of this fermion system at zero magnetic field and zero temperature $T = 0$ has been found in [21]. To solve Eq. (53), we use the mapping to a zero magnetic field system, Eq. (29). The combination $\mu_q \equiv \mu q$ at nonzero h maps to $\mu_{q,\text{eff}} \equiv \mu_{\text{eff}} q_{\text{eff}}$ at zero h as follows:

$$\begin{aligned} \mu_q &\mapsto q \sqrt{1 - \frac{H^2}{Q^2 + H^2}} \cdot g_F \sqrt{Q^2 + H^2} \\ &= \sqrt{3} q g_F \sqrt{1 - \frac{H^2}{3}} = \mu_{q,\text{eff}}, \end{aligned} \quad (55)$$

where at $T = 0$, we used $Q^2 + H^2 = 3$. We solve Eq. (53) for zero modes, i. e., $\omega = 0$, and at the Fermi surface $\lambda = k$ and implement Eq. (55).

Near the horizon ($z = 0$, $f = 6z^2$), we have

$$6z^2 \tilde{y}''_{1;2} + 12z \tilde{y}'_{1;2} + \left(\frac{3}{2} + \frac{(\mu_{q,\text{eff}})^2}{6} - k_F^2 \right) \tilde{y}_{1;2} = 0, \quad (56)$$

which gives the following behavior:

$$\tilde{y}_{1;2} \sim z^{-(1/2)\pm\nu_k}, \quad (57)$$

with the scaling exponent ν following from Eq. (32):

$$\nu = \frac{1}{6}\sqrt{6k^2 - (\mu_{q,\text{eff}})^2}, \quad (58)$$

at the momentum k . Using MAPLE, we find the zero-mode solution of Eq. (53) with a regular behavior $z^{-(1/2)+\nu}$ at the horizon [18,21]:

$$\begin{aligned} \tilde{y}_1^{(0)} = & N_1(z-1)^{3/2}z^{-(1/2)+\nu}(z-\bar{z}_0)^{-(1/2)-\nu} \\ & \times \left(\frac{z-z_0}{z-\bar{z}_0} \right)^{1/4(-1-\sqrt{2}\mu_{q,\text{eff}}/z_0)} {}_2F_1\left(\frac{1}{2} + \nu - \frac{\sqrt{2}}{3}\mu_{q,\text{eff}}, \nu \right. \\ & \left. + i\frac{\mu_{q,\text{eff}}}{6}, 1 + 2\nu, \frac{2i\sqrt{2}z}{3z_0(z-\bar{z}_0)}\right), \end{aligned} \quad (59)$$

and

$$\begin{aligned} \tilde{y}_2^{(0)} = & N_2(z-1)^{3/2}z^{-(1/2)+\nu}(z-\bar{z}_0)^{-(1/2)-\nu} \\ & \times \left(\frac{z-z_0}{z-\bar{z}_0} \right)^{1/4(-1+\sqrt{2}\mu_{q,\text{eff}}/z_0)} {}_2F_1\left(\frac{1}{2} + \nu + \frac{\sqrt{2}}{3}\mu_{q,\text{eff}}, \nu \right. \\ & \left. - i\frac{\mu_{q,\text{eff}}}{6}, 1 + 2\nu, \frac{2i\sqrt{2}z}{3z_0(z-\bar{z}_0)}\right), \end{aligned} \quad (60)$$

where ${}_2F_1$ is the hypergeometric function and N_1, N_2 are normalization factors. Since normalization factors are constants, we find their relative weight by substituting solutions given in Eq. (59) back into the first order differential equations at $z \sim 0$,

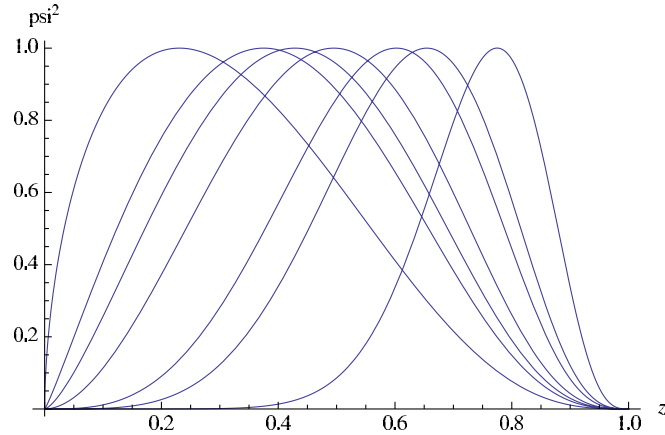


FIG. 5 (color online). Density of the zero-mode $\psi^{0\dagger}\psi^0$ vs the radial coordinate z (the horizon is at $z = 0$, and the boundary is at $z = 1$) for different values of the magnetic field h for the first (with the largest root for k_F) Fermi surface. We set $g_F = 1$ ($h \rightarrow H$) and $q = \frac{15}{\sqrt{3}}$ ($\mu_{q,\text{eff}} \rightarrow 15\sqrt{1 - \frac{H^2}{3}}$). From right to left, the values of the magnetic field are $H = \{0, 1.4, 1.5, 1.6, 1.63, 1.65, 1.68\}$. The amplitudes of the curves are normalized to unity. At weak magnetic fields, the wave function is supported away from the horizon, while, at strong fields, it is supported near the horizon.

$$\frac{N_1}{N_2} = -\frac{6i\nu + \mu_{q,\text{eff}}}{\sqrt{6}k} \left(\frac{z_0}{\bar{z}_0} \right)^{\mu_{q,\text{eff}}/\sqrt{2}z_0}. \quad (61)$$

The same relations are obtained when calculations are done for any z . The second solution $\tilde{\eta}_{1;2}^{(0)}$, with behavior $z^{-(1/2)-\nu}$ at the horizon, is obtained by replacing $\nu \rightarrow -\nu$ in Eq. (59).

To get insight into the zero-mode solution (59), we plot the radial profile for the density function $\psi^{(0)\dagger}\psi^{(0)}$ for different magnetic fields in Fig. 5. The momentum chosen is the Fermi momentum of the first Fermi surface (see the next section). The curves are normalized to have the same maxima. Magnetic field is increased from right to left. At small magnetic field, the zero modes are supported away from the horizon, while at large magnetic field, the zero modes are supported near the horizon. This means that at large magnetic field, the influence of the black hole to the Fermi level structure becomes more important.

B. Magnetic effects on the Fermi momentum and Fermi velocity at $T = 0$

In the presence of a magnetic field, there is only a true pole in the Green's function whenever the Landau level crosses the Fermi energy [22]

$$2l|qh| = k_F^2. \quad (62)$$

As shown in Fig. 2, whenever Eq. (62) is satisfied, the spectral function $A(\omega)$ has a (sharp) peak. This is not surprising, since quasiparticles can be easily excited from the Fermi surface. From Eq. (62), the spectral function $A(\omega)$ and the density of states on the Fermi surface $D(\omega)$ are periodic in $\frac{1}{h}$ with the period

$$\Delta\left(\frac{1}{h}\right) = \frac{2\pi q}{A_F}, \quad (63)$$

where $A_F = \pi k_F^2$ is the area of the Fermi surface [22]. This is a manifestation of the de Haas-van Alphen quantum oscillations. At $T = 0$, the electronic properties of metals depend on the density of states on the Fermi surface. Therefore, an oscillatory behavior as a function of magnetic field should appear in any quantity that depends on the density of states on the Fermi energy. Magnetic susceptibility [22] and magnetization together with the superconducting gap [24] have been shown to exhibit quantum oscillations. Every Landau level contributes an oscillating term, and the period of the l -th level oscillation is determined by the value of the magnetic field h that satisfies Eq. (62) for the given value of k_F . Quantum oscillations (and the quantum Hall effect, which we consider later in the paper) are examples of phenomena in which Landau-level physics reveals the presence of the Fermi surface. The superconducting gap found in the quark matter in magnetic fields [24] is another evidence for the existence of the (highly degenerate) Fermi surface and the corresponding Fermi momentum.

Generally, a Fermi surface controls the occupation of energy levels in the system: The energy levels below the Fermi surface are filled, and those above are empty (or nonexistent). Here, however, the association to the Fermi momentum can be obscured by the fact that the fermions form highly degenerate Landau levels. Thus, in two dimensions, in the presence of the magnetic field, the corresponding effective Fermi surface is given by a single point in the phase space that is determined by n_F , the Landau index of the highest occupied level, i.e., the highest Landau level below the chemical potential.² Increasing the magnetic field, Landau levels “move up” in the phase space, leaving only the lower levels occupied, so that the effective Fermi momentum scales roughly (excluding interactions) as a square root of the magnetic field, $k_F \sim \sqrt{n_F} \sim k_F^{\max} \sqrt{1 - h/h_{\max}}$. High magnetic fields drive the effective density of the charge carriers down, approaching the limit when the Fermi momentum coincides with the lowest Landau level.

Many phenomena observed in the paper can thus be qualitatively explained by Landau quantization. As discussed before, the notion of the Fermi momentum is lost at very high magnetic fields. In what follows, the quantitative Fermi-level structure at zero temperature, described by k_F and v_F values, is obtained as a function of the magnetic field using the solution of the Dirac equation given by Eqs. (59) and (60). As in [11], we neglect first the discrete nature of the Fermi momentum and velocity in order to obtain general understanding. Upon taking the quantization into account, the smooth curves become combinations of step functions following the same trend as the smooth curves (without quantization). While usually the grand canonical ensemble is used, where the fixed chemical potential controls the occupation of the Landau levels [25], in our setup, the Fermi momentum is allowed to change as the magnetic field is varied, while we keep track of the IR conformal dimension ν .

The Fermi momentum is defined by the matching between IR and UV physics [7]. Therefore, it is enough to know the solution at $\omega = 0$, where the matching is performed. To obtain the Fermi momentum, we require that the zero-mode solution is regular at the horizon ($\psi^{(0)} \sim z^{-(1/2)+\nu}$) and normalizable at the boundary. At the boundary $z \sim 1$, the wave function behaves as

$$a(1-z)^{3/2-m} \begin{pmatrix} 1 \\ 0 \end{pmatrix} + b(1-z)^{3/2+m} \begin{pmatrix} 0 \\ 1 \end{pmatrix}. \quad (64)$$

To require it to be normalizable is to set the first term $a = 0$; the wave function at $z \sim 1$ is then

$$\psi^{(0)} \sim (1-z)^{3/2+m} \begin{pmatrix} 0 \\ 1 \end{pmatrix}. \quad (65)$$

²We would like to thank Igor Shovkovy for clarifying the issue with the Fermi momentum in the presence of the magnetic field.

Equation (65) leads to the condition $\lim_{z \rightarrow 1} (z-1)^{-3/2} \times (\tilde{y}_2^{(0)} + i\tilde{y}_1^{(0)}) = 0$, which, together with Eq. (59), gives the following equation for the Fermi momentum as function of the magnetic field [18,21]:

$$\begin{aligned} & \frac{2F_1(1 + \nu + \frac{i\mu_{q,\text{eff}}}{6}, \frac{1}{2} + \nu - \frac{\sqrt{2}\mu_{q,\text{eff}}}{3}, 1 + 2\nu, \frac{2}{3}(1 - i\sqrt{2}))}{2F_1(\nu + \frac{i\mu_{q,\text{eff}}}{6}, \frac{1}{2} + \nu - \frac{\sqrt{2}\mu_{q,\text{eff}}}{3}, 1 + 2\nu, \frac{2}{3}(1 - i\sqrt{2}))} \\ &= \frac{6\nu - i\mu_{q,\text{eff}}}{k_F(-2i + \sqrt{2})}, \end{aligned} \quad (66)$$

with $\nu \equiv \nu_{k_F}$ given by Eq. (58). Using MATHEMATICA to evaluate the hypergeometric functions, we numerically solve the equation for the Fermi surface, which gives effective momentum as if it were continuous, i.e., when quantization is neglected. The solutions of Eq. (66) are given in Fig. 6. There are multiple Fermi surfaces for a given magnetic field h . Here, and in all other plots, we choose $g_F = 1$. Therefore, $h \rightarrow H$ and $q = \frac{15}{\sqrt{3}}$. In Fig. 6, positive and negative k_F correspond to the Fermi surfaces in the Green's functions G_1 and G_2 . The relation between two components is $G_2(\omega, k) = G_1(\omega, -k)$ [6]. Therefore, Fig. 6 is not symmetric with respect to the x-axis. Effective momenta terminate at the dashed line $\nu_{k_F} = 0$. Taking into account Landau quantization of $k_F \rightarrow \sqrt{2|qh|l}$ with $l = 1, 2, \dots$, the plot consists of stepwise functions tracing the existing curves (we depict only positive k_F). Indeed, Landau

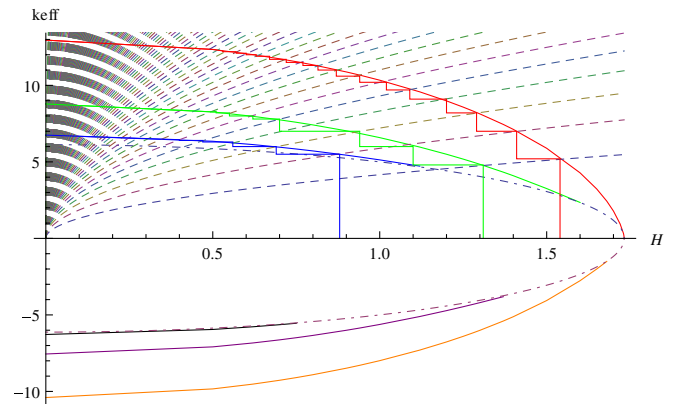


FIG. 6 (color online). Effective momentum k_{eff} vs the magnetic field $h \rightarrow H$ (we set $g_F = 1$, $q = \frac{15}{\sqrt{3}}$). As we increase the magnetic field, the Fermi surface shrinks. Smooth solid curves represent the situation as if momentum is a continuous parameter (for convenience), stepwise solid functions are the real Fermi momenta, which are discretized due to the Landau-level quantization: $k_F \rightarrow \sqrt{2|qh|l}$, with $l = 1, 2, \dots$, where $\sqrt{2|qh|l}$ are Landau levels given by dotted lines (only positive discrete k_F are shown). At a given h , there are multiple Fermi surfaces. From right to left are the first, second, etc., Fermi surfaces. The dashed-dotted line is $\nu_{k_F} = 0$, where k_F is terminated. Positive and negative k_{eff} correspond to Fermi surfaces in two components of the Green's function.

quantization can be also seen from the dispersion relation at Fig. 3, where only discrete values of effective momentum are allowed, and the Fermi surface has been chopped up as a result of quantization, Fig. 3(b).

Our findings agree with the results for the (largest) Fermi momentum in a 3-dimensional magnetic system considered in [26] (compare the stepwise dependence $k_F(h)$ with Fig. (5) in [26]).

In Fig. 7, the Landau-level index l is obtained from $k_F(h) = \sqrt{2|qh|l}$, where $k_F(h)$ is a numerical solution of Eq. (66). Only those Landau levels which are below the Fermi surface are filled. In Fig. 6, as we decrease magnetic field, first nothing happens until the next Landau level crosses the Fermi surface, which corresponds to a jump up to the next step. Therefore, at strong magnetic fields,

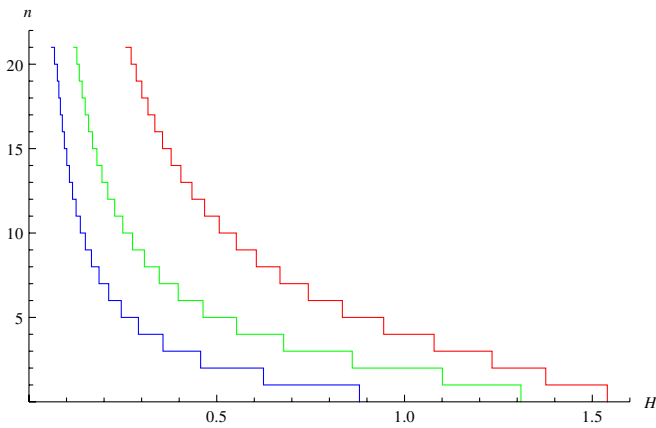


FIG. 7 (color online). Landau-level numbers n , corresponding to the quantized Fermi momenta vs the magnetic field $h \rightarrow H$ for the three Fermi surfaces with positive k_F . We set $g_F = 1$, $q = \frac{15}{\sqrt{3}}$. From right to left are the first, second, and third Fermi surfaces.

fewer states contribute to transport properties, and the lowest Landau level becomes more important (see the next section). At weak magnetic fields, the sum over many Landau levels has to be taken, ending with the continuous limit as $h \rightarrow 0$, when quantization can be ignored.

In Fig. 8, we show the IR conformal dimension as a function of the magnetic field. We have used the numerical solution for k_F . Fermi-liquid regime takes place at magnetic fields $h < h_c$, while non-Fermi liquids exist in a narrow band at $h_c < h < h'_c$, and at h'_c the system becomes near-conformal.

In this figure, we observe the pathway of the possible phase transition exhibited by the Fermi surface (ignoring Landau quantization): It can vanish at the line $\nu_{k_F} = 0$, undergoing a crossover to the conformal regime, or cross the line $\nu_{k_F} = 1/2$ and go through a non-Fermi-liquid regime, and, subsequently, cross to the conformal phase. Note that the primary Fermi surface with the highest k_F and ν_{k_F} seems to directly cross over to conformality, while the other Fermi surfaces first exhibit a strange-metal phase transition. Therefore, all the Fermi momenta with $\nu_{k_F} > 0$ contribute to the transport coefficients of the theory. In particular, at high magnetic fields, only the first (largest) Fermi momentum $k_F^{(1)}$ is nonzero and the lowest Landau level $n = 0$ becomes increasingly important. The lowest Landau level contributes to the transport with half-degeneracy factor, as compared to the higher Landau levels.

In Fig. 9, we plot the Fermi momentum k_F as a function of the magnetic field for the first Fermi surface (the largest root of Eq. (66)). Quantization is neglected here. At the left panel, the relatively small region between the dashed lines corresponds to non-Fermi liquids $0 < \nu < \frac{1}{2}$. At large magnetic field, the physics of the Fermi surface is captured

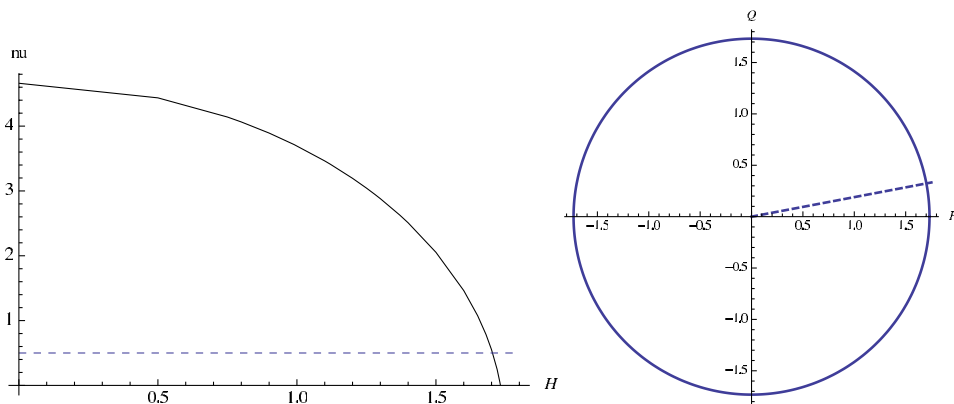


FIG. 8 (color online). Left panel: the IR conformal dimension $\nu \equiv \nu_{k_F}$ calculated at the Fermi momentum vs the magnetic field $h \rightarrow H$ (we set $g_F = 1$, $q = \frac{15}{\sqrt{3}}$). Calculations are done for the first Fermi surface. The dashed line is for $\nu = \frac{1}{2}$ (at $H_c = 1.7$), which is the border between the Fermi liquids $\nu > \frac{1}{2}$ and non-Fermi liquids $\nu < \frac{1}{2}$. Right panel: the phase diagram in terms of the chemical potential and the magnetic field $\mu^2 + h^2 = 3$ (in dimensionless variables $h = g_F H$, $\mu = g_F Q$; we set $g_F = 1$). Fermi liquids are above the dashed line ($H < H_c$), and non-Fermi liquids are below the dashed line ($H > H_c$).

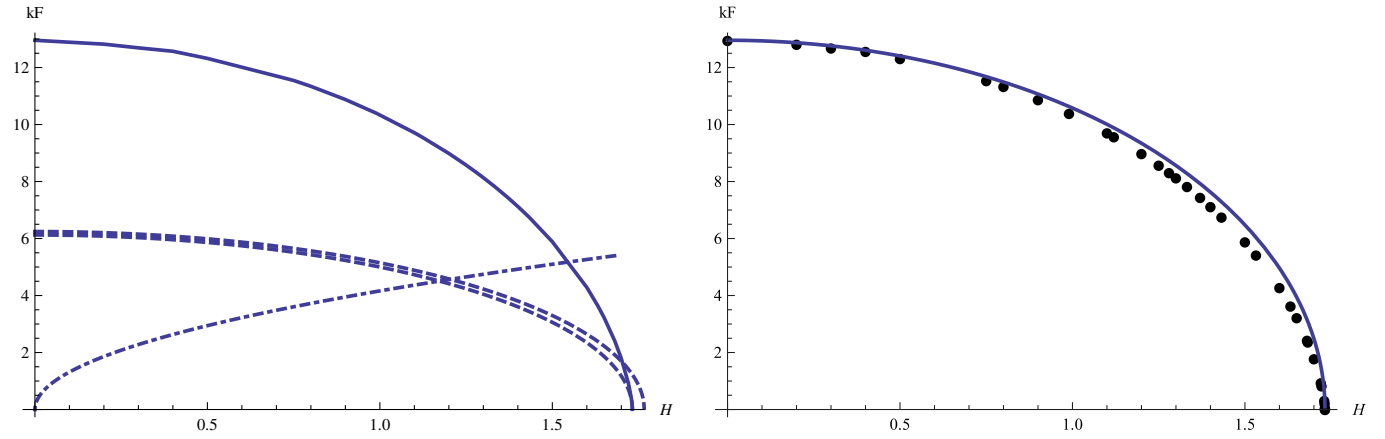


FIG. 9 (color online). Fermi momentum k_F vs the magnetic field $h \rightarrow H$ (we set $g_F = 1$, $q = \frac{15}{\sqrt{3}}$) for the first Fermi surface. Left panel: The inner (closer to x -axis) dashed line is $\nu_{k_F} = 0$, and the outer dashed line is $\nu_{k_F} = \frac{1}{2}$. The region between these lines corresponds to non-Fermi liquids $0 < \nu_{k_F} < \frac{1}{2}$. The dashed-dotted line is for the first Landau level $k_1 = \sqrt{2qH}$. The first Fermi surface hits the border line between Fermi and non-Fermi liquids $\nu = \frac{1}{2}$ at $H_c \approx 1.7$, and it vanishes at $H_{\max} = \sqrt{3} = 1.73$. Right panel: Circles are the data points for the Fermi momentum calculated analytically, and the solid line is a fit function $k_F^{\max} \sqrt{1 - \frac{H^2}{3}}$ with $k_F^{\max} = 12.96$.

by the near-horizon region (see also Fig. 5), which is $\text{AdS}_2 \times \mathbb{R}^2$. At the maximum magnetic field, $H_{\max} = \sqrt{3} \approx 1.73$, when the black hole becomes entirely magnetically charged, the Fermi momentum vanishes when it crosses the line $\nu_{k_F} = 0$. This only happens for the first Fermi surface. For the higher Fermi surfaces, the Fermi momenta terminate at the line $\nu_{k_F} = 0$ (Fig. 6). Note the Fermi momentum for the first Fermi surface can be almost fully described by a function $k_F = k_F^{\max} \sqrt{1 - \frac{H^2}{3}}$. It is tempting to view the behavior $k_F \sim \sqrt{H_{\max} - H}$ as a phase transition in the system, although it strictly follows from the linear scaling for $H = 0$ by using the mapping (29). (Note that also $\mu = g_F Q = g_F \sqrt{3 - H^2}$.) Taking into account the discretization of k_F , the plot will consist of an array of step functions tracing the existing curve. Our findings agree with the results for the Fermi momentum in a 3-dimensional magnetic system considered in [26], compare to Fig. 5 there.

The Fermi velocity given in Eq. (27) is defined by the UV physics. Therefore, solutions at nonzero ω are required. The Fermi velocity is extracted from matching two solutions in the inner and outer regions at the horizon. The Fermi velocity as a function of the magnetic field for $\nu > \frac{1}{2}$ is [18,21]

$$v_F = \frac{1}{h_1} \left(\int_0^1 dz \sqrt{g/g_{tt}} \psi^{(0)\dagger} \psi^{(0)} \right)^{-1} \lim_{z \rightarrow 1} \frac{|\tilde{y}_1^{(0)} + i\tilde{y}_2^{(0)}|^2}{(1-z)^3},$$

$$h_1 = \lim_{z \rightarrow 1} \frac{\tilde{y}_1^{(0)} + i\tilde{y}_2^{(0)}}{\partial_k (\tilde{y}_2^{(0)} + i\tilde{y}_1^{(0)})}, \quad (67)$$

where the zero-mode wave function is taken at k_F (Eq. (59)).

We plot the Fermi velocity for several Fermi surfaces in Fig. 10 and for the first Fermi surface in Fig. 11. Quantization is neglected here. The Fermi velocity is shown for $\nu > \frac{1}{2}$. It is interesting that the Fermi velocity vanishes when the IR conformal dimension is $\nu_{k_F} = \frac{1}{2}$. Formally, it follows from the fact that $v_F \sim (2\nu - 1)$ [7]. The first Fermi surface is at the far right. Positive and negative v_F correspond to the Fermi surfaces in the Green's functions G_1 and G_2 , respectively. The Fermi velocity v_F has the same sign as the Fermi momentum k_F . At small magnetic field values, the Fermi velocity is

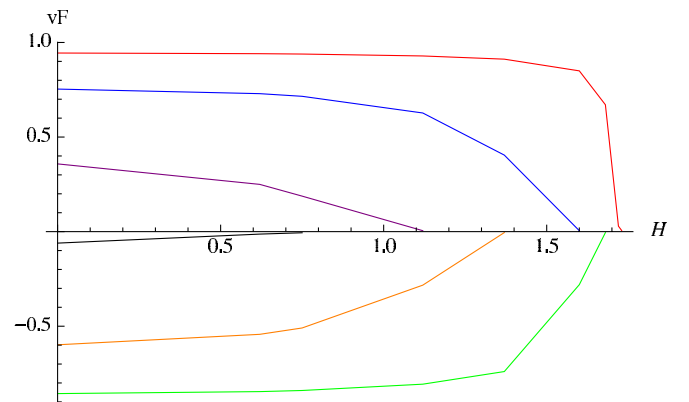


FIG. 10 (color online). Fermi velocity v_F vs the magnetic field $h \rightarrow H$ (we set $g_F = 1$, $q = \frac{15}{\sqrt{3}}$) for the regime of Fermi liquids $\nu \geq \frac{1}{2}$. Fermi velocity vanishes at $\nu_{k_F} = \frac{1}{2}$ (x -axis). The multiple lines are for various Fermi surfaces in ascending order, with the first Fermi surface on the right. The Fermi velocity v_F has the same sign as the Fermi momentum k_F . As above, positive and negative v_F correspond to Fermi surfaces in the two components of the Green's function.

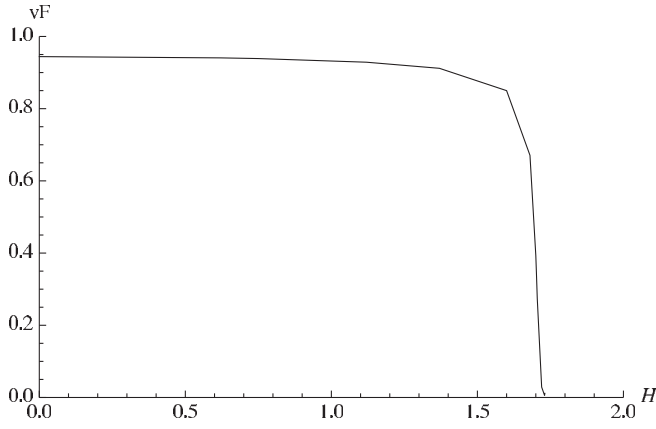


FIG. 11. Fermi velocity v_F vs the magnetic field $h \rightarrow H$ (we set $g_F = 1$, $q = \frac{15}{\sqrt{3}}$) for the first Fermi surface. Fermi velocity vanishes at $\nu_{k_F} = \frac{1}{2}$ at $H_c \approx 1.7$. The region $H < H_c$ corresponds to the Fermi liquids and quasiparticle description.

very weakly dependent on H , and it is close to the speed of light. At large magnetic field values, the Fermi velocity rapidly decreases and vanishes (at $H_c = 1.70$ for the first Fermi surface (Fig. 11)). Geometrically, this means that, with increasing magnetic field, the zero-mode wave function is supported near the black hole horizon (Fig. 5), where the gravitational redshift reduces the local speed of light, as compared to the boundary value. It was also observed in [7,21] at small fermion charge values.

VI. HALL AND LONGITUDINAL CONDUCTIVITIES

In this section, we calculate the contributions to Hall σ_{xy} and the longitudinal σ_{xx} conductivities directly in the boundary theory. This should be contrasted with the standard holographic approach, where calculations are performed in the (bulk) gravity theory and then translated to the boundary field theory using the AdS/CFT dictionary. Specifically, the conductivity tensor has been obtained in [10] by calculating the on-shell renormalized action for the gauge field on the gravity side and using the gauge/gravity duality $A_M \rightarrow j_\mu$ to extract the R charge current-current correlator at the boundary. Here, the Kubo formula involving the current-current correlator is used directly by utilizing the fermion Green's functions extracted from holography in [7]. Therefore, the conductivity is obtained for the charge carriers described by the fermionic operators of the boundary field theory.

The use of the conventional Kubo formula to extract the contribution to the transport due to fermions is validated in that it also follows from a direct AdS/CFT computation of the one-loop correction to the on-shell renormalized AdS action [15]. We study, in particular, stable quasiparticles with $\nu > \frac{1}{2}$ and at zero temperature. This regime effectively reduces to the clean limit where the imaginary part of the

self-energy vanishes $\text{Im}\Sigma \rightarrow 0$. We use the gravity-“dressed” fermion propagator from Eq. (27), and, to make the calculations complete, we need to use the dressed vertex to satisfy the Ward identities. As was argued in [15], the boundary vertex, which is obtained from the bulk calculations, can be approximated by a constant in the low-temperature limit. Also, according to [27], the vertex only contains singularities of the product of the Green's functions. Therefore, dressing the vertex will not change the dependence of the DC conductivity on the magnetic field [27]. In addition, the zero magnetic field limit of the formulae for conductivity obtained from holography [15] and from direct boundary calculations [18] are identical.

A. Integer quantum Hall effect

Let us start from the dressed retarded and advanced fermion propagators [7]: G_R is given by Eq. (27) and $G_A = G_R^*$. To perform the Matsubara summation, we use the spectral representation

$$G(i\omega_n, \vec{k}) = \int \frac{d\omega}{2\pi} \frac{A(\omega, \vec{k})}{\omega - i\omega_n}, \quad (68)$$

with the spectral function defined as $A(\omega, \vec{k}) = -\frac{1}{\pi} \text{Im}G_R(\omega, \vec{k}) = \frac{1}{2\pi i}(G_R(\omega, \vec{k}) - G_A(\omega, \vec{k}))$. Generalizing to a nonzero magnetic field and spinor case [25], the spectral function [28] is

$$A(\omega, \vec{k}) = \frac{1}{\pi} e^{-k^2/|qh|} \sum_{l=0}^{\infty} (-1)^l (-h_1 v_F) \times \left(\frac{\Sigma_2(\omega, k_F) f(\vec{k}) \gamma^0}{(\omega + \varepsilon_F + \Sigma_1(\omega, k_F) - E_l)^2 + \Sigma_2(\omega, k_F)^2} + (E_l \rightarrow -E_l) \right), \quad (69)$$

where $\varepsilon_F = v_F k_F$ is the Fermi energy, $E_l = v_F \sqrt{2|qh|} l$ is the energy of the Landau level, $f(\vec{k}) = P_- L_l(\frac{2k^2}{|qh|}) - P_+ L_{l-1}(\frac{2k^2}{|qh|})$ with spin projection operators $P_\pm = (1 \pm i\gamma^1 \gamma^2)/2$, we take $c = 1$, the generalized Laguerre polynomials are $L_n^\alpha(z)$ and by definition $L_n(z) = L_n^0(z)$, (we omit the vector part $\vec{k} \vec{\gamma}$ as it does not contribute to the DC conductivity), all γ 's are the standard Dirac matrices, and h_1 , v_F , and k_F are real constants (we keep the same notations for the constants as in [7]). The self-energy $\Sigma \sim \omega^{2\nu_{k_F}}$ contains the real and imaginary parts, $\Sigma = \Sigma_1 + i\Sigma_2$. The imaginary part comes from scattering processes of a fermion in the bulk, e.g., from pair creation, and from the scattering into the black hole. It is exactly due to inelastic/dissipative processes that we are able to obtain finite values for the transport coefficients; otherwise they are formally infinite.

Using the Kubo formula, the DC electrical conductivity tensor is

$$\sigma_{ij}(\Omega) = \lim_{\Omega \rightarrow 0} \frac{\text{Im}\Pi_{ij}^R}{\Omega + i0^+}, \quad (70)$$

where $\Pi_{ij}(i\Omega_m \rightarrow \Omega + i0^+)$ is the retarded current-current correlation function; schematically the current density operator is $j^i(\tau, \vec{x}) = qv_F \sum_{\sigma} \bar{\psi}_{\sigma}(\tau, \vec{x}) \gamma^i \psi_{\sigma}(\tau, \vec{x})$. Neglecting the vertex correction, it is given by

$$\begin{aligned} \Pi_{ij}(i\Omega_m) &= q^2 v_F^2 T \sum_{n=-\infty}^{\infty} \int \frac{d^2k}{(2\pi)^2} \text{tr}(\gamma^i G(i\omega_n, \vec{k}) \\ &\quad \times \gamma^j G(i\omega_n + i\Omega_m, \vec{k})). \end{aligned} \quad (71)$$

The sum over the Matsubara frequency is

$$\begin{aligned} \sigma_{ij} &= -\frac{4q^2 v_F^2 (h_1 v_F)^2 |qh|}{\pi\Omega} \text{Re} \sum_{l,k=0}^{\infty} (-1)^{l+k+1} \{ \delta_{ij} (\delta_{l,k-1} + \delta_{l-1,k}) + i\epsilon_{ij} \text{sgn}(qh) (\delta_{l,k-1} - \delta_{l-1,k}) \} \\ &\quad \times \int \frac{d\omega_1}{2\pi} \left(\tanh \frac{\omega_1}{2T} - \tanh \frac{\omega_2}{2T} \right) \left(\frac{\Sigma_2(\omega_1)}{(\tilde{\omega}_1 - E_l)^2 + \Sigma_2^2(\omega_1)} + (E_l \rightarrow -E_l) \right) \left(\frac{\Sigma_2(\omega_2)}{(\tilde{\omega}_2 - E_k)^2 + \Sigma_2^2(\omega_2)} + (E_k \rightarrow -E_k) \right), \end{aligned} \quad (74)$$

with $\omega_2 = \omega_1 + \Omega$. We have also introduced $\tilde{\omega}_{1,2} \equiv \omega_{1,2} + \varepsilon_F + \Sigma_1(\omega_{1,2})$, with ϵ_{ij} being the antisymmetric tensor ($\epsilon_{12} = 1$), and $\Sigma_{1,2}(\omega) \equiv \Sigma_{1,2}(\omega, k_F)$. In the momentum integral, we use the orthogonality condition for the Laguerre polynomials $\int_0^{\infty} dx e^{-x} L_l(x) L_k(x) = \delta_{lk}$.

$$\begin{aligned} \sigma_{xx} &= -\frac{2q^2 (h_1 v_F)^2 |qh|}{\pi T} \int_{-\infty}^{\infty} \frac{d\omega}{2\pi} \frac{\Sigma_2^2(\omega)}{\cosh^2 \frac{\omega}{2T}} \sum_{l=0}^{\infty} \left(\frac{1}{(\tilde{\omega} - E_l)^2 + \Sigma_2^2(\omega)} + (E_l \rightarrow -E_l) \right) \\ &\quad \times \left(\frac{1}{(\tilde{\omega} - E_{l+1})^2 + \Sigma_2^2(\omega)} + (E_{l+1} \rightarrow -E_{l+1}) \right), \end{aligned} \quad (75)$$

$$\sigma_{xy} = -\frac{q^2 (h_1 v_F)^2 \text{sgn}(qh)}{\pi} \nu_h, \quad \nu_h = 2 \int_{-\infty}^{\infty} \frac{d\omega}{2\pi} \tanh \frac{\omega}{2T} \Sigma_2(\omega) \sum_{l=0}^{\infty} \alpha_l \left(\frac{1}{(\tilde{\omega} - E_l)^2 + \Sigma_2^2(\omega)} + (E_l \rightarrow -E_l) \right), \quad (76)$$

where $\tilde{\omega} = \omega + \varepsilon_F + \Sigma_1(\omega)$. The filling factor ν_h is proportional to the density of carriers: $|\nu_h| = \frac{\pi}{|qh| h_1 v_F} n$ (we derive this relation below in Eq. (89)). The degeneracy factor of the Landau levels is α_l : $\alpha_0 = 1$ for the lowest Landau level, and $\alpha_l = 2$ for $l = 1, 2, \dots$. Substituting the filling factor ν_h back to Eq. (76), the Hall conductivity can be written as

$$\sigma_{xy} = \frac{\rho}{h}, \quad (77)$$

where ρ is the charge density in the boundary theory, and both the charge q and the magnetic field h carry a sign (the prefactor $(-h_1 v_F)$ comes from the normalization choice in the fermion propagator, Eqs.(27) and (69), as it was defined

$$T \sum_n \frac{1}{i\omega_n - \omega_1} \frac{1}{i\omega_n + i\Omega_m - \omega_2} = \frac{n(\omega_1) - n(\omega_2)}{i\Omega_m + \omega_1 - \omega_2}. \quad (72)$$

Taking $i\Omega_m \rightarrow \Omega + i0^+$, the polarization operator is now

$$\begin{aligned} \Pi_{ij}(\Omega) &= \frac{d\omega_1}{2\pi} \frac{d\omega_2}{2\pi} \frac{n_{\text{FD}}(\omega_1) - n_{\text{FD}}(\omega_2)}{\Omega + \omega_1 - \omega_2} \\ &\quad \times \int \frac{d^2k}{(2\pi)^2} \text{tr}(\gamma^i A(\omega_1, \vec{k}) \gamma^j A(\omega_2, \vec{k})), \end{aligned} \quad (73)$$

where the spectral function $A(\omega, \vec{k})$ is given by Eq. (69), and $n_{\text{FD}}(\omega)$ is the Fermi-Dirac distribution function. Evaluating the traces, we have

From Eq. (74), the term symmetric/antisymmetric with respect to exchange $\omega_1 \leftrightarrow \omega_2$ contributes to the diagonal/off-diagonal component of the conductivity (note the antisymmetric term $n_{\text{FD}}(\omega_1) - n_{\text{FD}}(\omega_2)$). The longitudinal and Hall DC conductivities ($\Omega \rightarrow 0$) are thus

in [7], which can be regarded as a factor contributing to the effective charge and is not important for further considerations). The Hall conductivity given by Eq. (77) has been obtained using the AdS/CFT duality for the Lorentz invariant 2 + 1-dimensional boundary field theories in [10]. We recover this formula because, in our case, the translational invariance is maintained in the x and y directions of the boundary theory.

Low frequencies give the main contribution in the integrand of Eq. (76). Since the self-energy satisfies $\Sigma_1(\omega) \sim \Sigma_2(\omega) \sim \omega^{2\nu}$ and we consider the regime $\nu > \frac{1}{2}$, we have $\Sigma_1 \sim \Sigma_2 \rightarrow 0$ at $\omega \sim 0$ (self-energy goes to zero faster than the ω term). Therefore, only the simple poles in the upper half-plane $\omega_0 = -\varepsilon_F \pm E_l + \Sigma_1 + i\Sigma_2$ contribute

to the conductivity where $\Sigma_1 \sim \Sigma_2 \sim (-\varepsilon_F \pm E_l)^{2\nu}$ are small. The same logic of calculation has been used in [25]. We obtain for the longitudinal and Hall conductivities

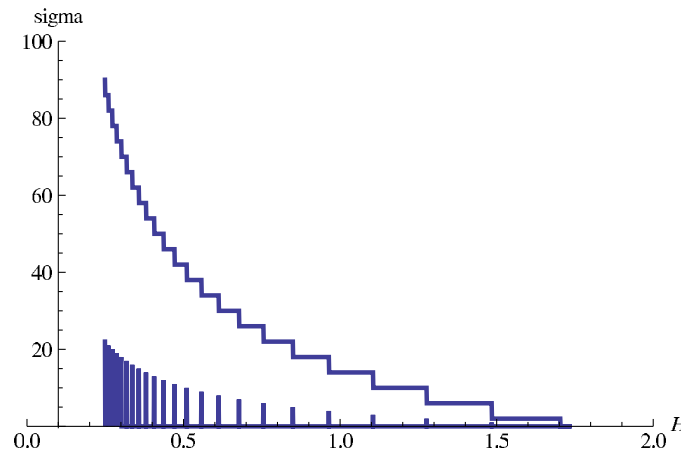
$$\sigma_{xx} = \frac{2q^2(h_1 v_F)^2 \Sigma_2}{\pi T} \times \left(\frac{1}{1 + \cosh \frac{\varepsilon_F}{T}} + \sum_{l=1}^{\infty} 4l \frac{1 + \cosh \frac{\varepsilon_F}{T} \cosh \frac{E_l}{T}}{(\cosh \frac{\varepsilon_F}{T} + \cosh \frac{E_l}{T})^2} \right) \quad (78)$$

$$\sigma_{xy} = \frac{q^2(h_1 v_F)^2 \text{sgn}(qh)}{\pi} \times 2 \left(\tanh \frac{\varepsilon_F}{2T} + \sum_{l=1}^{\infty} \left(\tanh \frac{\varepsilon_F + E_l}{2T} + \tanh \frac{\varepsilon_F - E_l}{2T} \right) \right), \quad (79)$$

where the Fermi energy is $\varepsilon_F = v_F k_F$, and the energy of the Landau level is $E_l = v_F \sqrt{2|qh|}l$. Similar expressions were obtained in [25]. However, in our case, the filling of the Landau levels is controlled by the magnetic field h through the field-dependent Fermi energy $v_F(h)k_F(h)$ instead of the chemical potential μ .

At $T = 0$, $\cosh \frac{\omega}{T} \rightarrow \frac{1}{2} e^{\omega/T}$ and $\tanh \frac{\omega}{2T} = 1 - 2n_{\text{FD}}(\omega) \rightarrow \text{sgn} \omega$. Therefore, the longitudinal and Hall conductivities are

$$\sigma_{xx} = \frac{2q^2(h_1 v_F)^2 \Sigma_2}{\pi T} \sum_{l=1}^{\infty} l \delta_{\varepsilon_F, E_l} = \frac{2q^2(h_1 v_F)^2 \Sigma_2}{\pi T} \times n \delta_{\varepsilon_F, E_n}, \quad (80)$$



$$\sigma_{xy} = \frac{q^2(h_1 v_F)^2 \text{sgn}(qh)}{\pi} 2 \left(1 + 2 \sum_{l=1}^{\infty} \theta(\varepsilon_F - E_l) \right) = \frac{q^2(h_1 v_F)^2 \text{sgn}(qh)}{\pi} \times 2(1 + 2n) \theta(\varepsilon_F - E_n) \theta(E_{n+1} - \varepsilon_F), \quad (81)$$

where the Landau-level index runs $n = 0, 1, \dots$. It can be estimated as $n = \lfloor \frac{k_F^2}{2|qh|} \rfloor$ when $v_F \neq 0$ ($\lfloor \cdot \rfloor$ denotes the integer part), with the average spacing between the Landau levels given by the Landau energy $v_F \sqrt{2|qh|}$. Note that $\varepsilon_F \equiv \varepsilon_F(h)$. We can see that Eq. (81) expresses the integer quantum Hall effect (IQHE). At zero temperature, as we dial the magnetic field, the Hall conductivity jumps from one quantized level to another, forming plateaus given by the filling factor

$$\nu_h = \pm 2(1 + 2n) = \pm 4 \left(n + \frac{1}{2} \right), \quad (82)$$

with $n = 0, 1, \dots$. (Compare to the conventional Hall quantization $\nu_h = \pm 4n$ that appears in thick graphene). Plateaus of the Hall conductivity at $T = 0$ follow from the stepwise behavior of the charge density ρ in Eq. (77):

$$\rho \sim 4 \left(n + \frac{1}{2} \right) \theta(\varepsilon_F - E_n) \theta(E_{n+1} - \varepsilon_F), \quad (83)$$

where n Landau levels are filled and contribute to ρ . The longitudinal conductivity vanishes, except precisely at the transition point between the plateaus. In Fig. 12, we plot the longitudinal and Hall conductivities at $T = 0$, using only the terms after the \times sign in Eq. (79). In the Hall conductivity, plateau transition occurs when the Fermi level (in Fig. 12) of the first Fermi surface $\varepsilon_F = v_F(h)k_F(h)$ (Figs. 9 and 11) crosses the Landau-level energy as we vary the magnetic field. By decreasing the

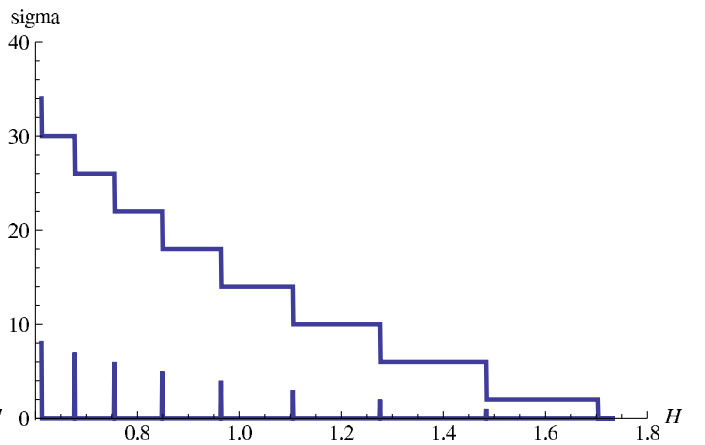


FIG. 12 (color online). Hall conductivity σ_{xy} and longitudinal conductivity σ_{xx} vs the magnetic field $h \rightarrow H$ at $T = 0$ (we set $g_F = 1$, $q = \frac{15}{\sqrt{3}}$). Contribution from the first Fermi surface is taken. By decreasing the magnetic field, the Fermi surface crosses the Landau levels, producing the Hall conductivity plateaus characteristic for IQHE. Longitudinal conductivity has picks at the beginning of each plateau. The right panel is a zoom-in for large h of the left one.

magnetic field, the plateaus become shorter, and increasingly more Landau levels contribute to the Hall conductivity. This happens because of two factors: the Fermi level moves up, and the spacing between the Landau levels becomes smaller. This picture does not depend on the Fermi velocity as long as it is nonzero.

In the boundary field theory, we express the charge density of the carriers (the difference between the densities of “electrons” and “holes”) through the Fermi energy ε_F (as it is done in [25]):

$$n = \text{tr}(\gamma^0 \tilde{G}(\tau, \mathbf{0})), \quad \tau \rightarrow 0, \quad (84)$$

where $\tilde{G}(\tau, \vec{x})$ is the translation-invariant part of the Green’s function $G(\tau, \vec{x})$ from Eq. (68). Using the spectral function representation given by Eq. (69), the charge density reads

$$n = T \sum_{n=-\infty}^{\infty} \int \frac{d^2 k}{(2\pi)^2} \int_{-\infty}^{\infty} \frac{d\omega}{2\pi} \frac{\text{tr}(\gamma^0 A(\omega, \vec{k}))}{\omega - i\omega_n}. \quad (85)$$

We express the Matsubara sum in terms of the contour integral over real frequencies:

$$T \sum_{n=-\infty}^{\infty} F(i\omega_n) \rightarrow -\frac{i}{4\pi} \int_C dz \tanh \frac{z}{2T} F(z), \quad (86)$$

where C runs anticlockwise and encircles the poles of \tanh along the upper- and lower-half imaginary axis. We have for the charge density

$$n = \frac{1}{2} \int \frac{d^2 k}{(2\pi)^2} \int_{-\infty}^{\infty} \frac{d\omega}{2\pi} \tanh \frac{\omega}{2T} \text{tr}(\gamma^0 A(\omega, \vec{k})). \quad (87)$$

Substituting the spectral function (69) and integrating over momenta, we obtain

$$n = -\frac{2|qh|h_1 v_F}{\pi} \int_{-\infty}^{\infty} \frac{d\omega}{2\pi} \tanh \frac{\omega}{2T} \Sigma_2(\omega) \times \sum_{l=0}^{\infty} \alpha_l \left(\frac{1}{(\tilde{\omega} - E_l)^2 + \Sigma_2^2(\omega)} + (E_l \rightarrow -E_l) \right), \quad (88)$$

where the degeneracy factor is $\alpha_0 = 1$ for the lowest Landau level, and $\alpha_l = 2$ for the higher Landau levels $l \geq 1$, $\tilde{\omega} = \omega + \varepsilon_F + \Sigma_1(\omega)$. Integrating over frequencies and taking into account that Σ_2 is effectively very small near the Fermi surface, we obtain

$$n = \frac{|qh|h_1 v_F}{\pi} \times 2 \left(\tanh \frac{\varepsilon_F}{2T} + \sum_{l=1}^{\infty} \left(\tanh \frac{\varepsilon_F + E_l}{2T} + \tanh \frac{\varepsilon_F - E_l}{2T} \right) \right). \quad (89)$$

Comparing this to Eq. (79), we obtain the relation $|v_h| = \frac{\pi}{|qh|h_1 v_F} n$. When the Fermi energy vanishes ($\varepsilon_F = 0$), the spectral function (69) is even in ω . From Eq. (88), the carrier density of stable quasiparticles vanishes when $\varepsilon_F = 0$. At the end of this section, we discuss a situation

with no stable charge carriers and physical consequences of it.

Equations (79)–(89) are obtained assuming that the states are localized around the Landau levels. In quantum Hall effect (QHE) models, impurities are added to prevent the states from “spilling” between the Landau levels and to provide the necessary occupation number of the levels. In our holographic calculations, however, the complex self-energy arises not from the impurities but from various scattering processes into the black hole. Here, the limit $\text{Im}\Sigma \rightarrow 0$ has been considered, which corresponds to a simplified field theory model [25] (the cited reference also considers the case with impurities). This approximation suffices to obtain the integer QHE [25] and for our initial studies of the fractional QHE. We leave the implementation of a physical model with impurities for future work.

B. Fractional quantum Hall effect

In a holographic setting, using the AdS geometry is equivalent to a calculation in a box. Therefore, for large enough fermion charge q , there are multiple Fermi surfaces, as shown in Figs. 6 and 10. Labeling the Fermi surfaces with $\nu > \frac{1}{2}$ by $m = 1, 2, \dots$, we represent, as in [21], the spectral function $A(\omega, \vec{k})$ as a sum over the spectral functions of individual Fermi surfaces given by Eq. (69). Ignoring the mixing term, the DC conductivity becomes a direct sum over the individual conductivities. By decreasing the magnetic field, new Fermi surfaces gradually appear, as can be seen in Figs. 6 and 7. Therefore, the conductivity tensor is

$$\sigma_{ij} = \sum_m \sigma_{ij}^{(m)} \theta(h_{\max}^{(m)} - h), \quad (90)$$

where $\sigma_{ij}^{(m)}$ involves the Fermi momentum $k_F^{(m)}$ and velocity $v_F^{(m)}$, respectively. At the maximum magnetic field $h_{\max}^{(m)}$, a new $k_F^{(m)}$ opens up; $h_{\max}^{(m)}$ is found numerically.

Including one, two, three, and four Fermi surfaces, we obtain the following quantization rule for the filling factor in the Hall conductivity:

$$\begin{aligned} \text{1FS: } \nu_h &= 2(1 + 2n), \\ \text{plateaus} &\rightarrow 2, 6, 10, \dots, \\ \text{2FS's: } \nu_h &= 4(1 + n + k), \\ \text{plateaus} &\rightarrow 4, 8, 12, \dots, \\ \text{3FS's: } \nu_h &= 2(3 + 2(n + k + p)), \\ \text{plateaus} &\rightarrow 6, 10, 14, \dots, \\ \text{4FS's: } \nu_h &= 4(2 + n + k + p + r), \\ \text{plateaus} &\rightarrow 8, 12, 16, \dots, \end{aligned} \quad (91)$$

with $n, k, p, r = 0, 1, \dots$. An odd number of Fermi surfaces produces the plateaus present in the IQHE, while an

even number of Fermi surfaces produces the additional plateaus appearing in the fractional quantum Hall effect (FQHE). For a large enough fermion charge q , many Fermi surfaces contribute, and the primary effect of the change in H is the opening of a new Fermi surface, rather than the occupation of the next plateau. Thus, at large q we expect a filling fraction pattern at large h to become

$$\nu_h = \pm 2j, \quad (92)$$

where $j = 1, 2, \dots$, is the effective Landau-level index counting the number of contributing Landau levels. This is indeed observed in the FQHE at strong magnetic fields. The quantization rule (91) persists as long as new Fermi surfaces open up with decreasing h . However, the first two plateaus present in the FQHE $\nu_h = 0, \pm 1$ are absent in Eq. (92). In order to get the Hall plateau $\nu_h = \pm 1$, the mixing term between two Fermi surfaces should probably be taken into account (incoherent superposition), whereas the conductivity (90) includes the diagonal terms only. We discuss the issue with $\nu_h = 0$ further.

In Fig. 13, we plot the Hall and longitudinal conductivities at $T = 0$ with three Fermi surfaces contributing (Eq. (90)), where the individual conductivities $\sigma^{(m)}$ are given by Eq. (79). We fit the Fermi momenta by

$$k_F^{(m)} = k_{F_{\max}}^{(m)} \sqrt{1 - \frac{h^2}{3}} + \delta^{(m)}, \quad (93)$$

with $k_{F_{\max}}^{(1)} = 12.96$, $\delta^{(1)} = 0.$, $k_{F_{\max}}^{(2)} = 10.29$, $\delta^{(2)} = 1.5$, $k_{F_{\max}}^{(3)} = 9.75$, $\delta^{(3)} = 3$, and use Eq. (93) together with the numerical solutions for $\nu_F^{(m)}$ in Fig. 13. In Fig. 13, at strong magnetic fields, the Hall conductivity

plateau $\nu_h = 4$ originates from two Fermi surfaces together with the plateaus $\nu_h = 2$ and $\nu_h = 6$, when one and three Fermi surfaces contribute, respectively. As we decrease the magnetic field further, three Fermi surfaces produce plateaus characteristic for IQHE, Eq. (82). The longitudinal conductivity shows a Dirac delta-like peak at the beginning of each plateau. Since a finite contribution to the conductivity arises as one of the three Fermi surfaces crosses the next Landau level, the pattern is less regular (i.e., the plateaus have changing length) than in the case when only one Fermi surface contributes. In Fig. 13, we compare the Hall conductivities with one and three Fermi surfaces participating. The irregular behavior of the Hall conductivity is explained naturally from the picture with multiple Fermi surfaces. Qualitatively similar regularity of the plateaus' length is seen in experiments on thin films of graphite at strong magnetic fields [23]. The actual physics behind this, however, might be quite different, as in this system, multiple sheets of the Fermi surface arise due to the (hexagonal) lattice on the UV scale, which is an effect beyond the scope of our current model.

The somewhat regular pattern behind the irregular behavior can be understood as a consequence of the appearance of a new energy scale: the average distance between the Fermi levels. For the case of Fig. 13, we estimate it to be $\langle \varepsilon_F^{(m)} - \varepsilon_F^{(m+1)} \rangle = 4.9$. The authors of [25] explain the FQHE through the opening of a gap in the quasiparticle spectrum, which acts as an order parameter related to the particle-hole pairing and is enhanced by the magnetic field (magnetic catalysis). Here, the energy gap arises due to the participation of multiple Fermi surfaces.

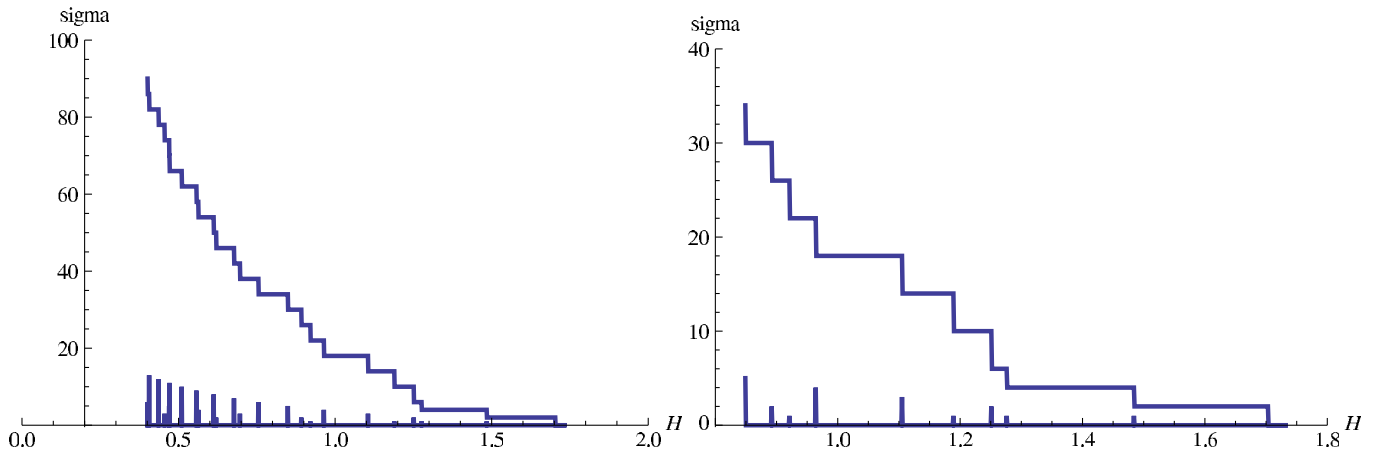


FIG. 13 (color online). Hall conductivity σ_{xy} and longitudinal conductivity σ_{xx} vs the magnetic field $h \rightarrow H$ at $T = 0$ (we set $g_F = 1$, $q = \frac{15}{\sqrt{3}}$). Contribution from the first three Fermi surfaces are taken. At strong magnetic fields, the Hall conductivity plateau $\nu_h = 4$ appears from two Fermi surfaces together with plateaus $\nu_h = 2$ and $\nu_h = 6$ when one and three Fermi surfaces contribute, respectively. This quantization rule is characteristic for the FQHE. At intermediate and weak magnetic fields, the Hall conductivity plateaus are produced as one of the three Fermi surfaces crosses the Landau levels, resulting in the quantization rule of the IQHE. An irregular pattern in the length of the plateaus is observed in the experiment on thin films of graphite at strong magnetic fields [23]. The right panel is a zoom-in for large h of the left one.

A pattern for the Hall conductivity that is strikingly similar to Fig. 13 arises in the bilayer graphene (compare with Figs. 2 and 5 in Ref. [29]), which has different transport properties from the monolayer graphene [29]. It is remarkable that the bilayer graphene also exhibits the insulating behavior in a certain parameter regime. This agrees with our findings of metal-insulating transition in our system.

C. Metal–strange-metal phase transition

The previous discussion of conductivities and QHE is valid provided that the Fermi velocity is nonzero. However, we have shown that v_F vanishes at relatively strong magnetic fields (for the first Fermi surface, it happens at h_c as in Fig. 8 and 11). In the AdS/CFT setting, the Fermi velocity vanishes when the IR anomalous dimension is $\nu = \frac{1}{2}$, signaling the onset of a nontrivial power-law dispersion in Green's function $G^{-1}(\omega) \sim \omega - v_f k_\perp + \omega^{2\nu}$ (the pole in the self-energy $\Sigma \rightarrow G_R^{IR} \sim \omega^{2\nu}$ and the pole in the prefactor of the linear term $\sim \omega$ [7]). Vanishing of v_F was observed in [21] at large enough fermion charge. Note that if v_F is zero for some interval of the magnetic field, it leads to the Hall plateau with the filling factor $\nu_h = 0$ present in FQHE.

The vanishing of the Fermi velocity of the stable quasiparticle leads to zero carrier density at leading order:

$$v_F = 0 \rightarrow n = 0. \quad (94)$$

This means that all contribution to conductivity comes from the other terms, containing the contribution from the non-Fermi-liquid excitations and the conformal regime. This qualitatively changes the transport properties of the system, as can be seen in Fig. 14.

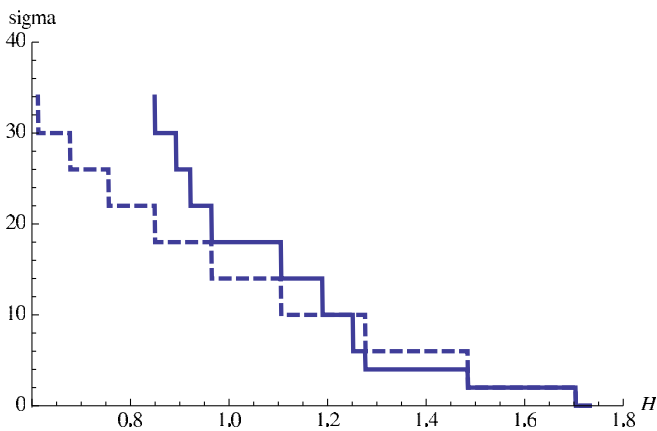


FIG. 14 (color online). Comparison of the Hall conductivities σ_{xy} vs the magnetic field $h \rightarrow H$ from one Fermi surface (dashed line) and from three Fermi surfaces (solid line). We set $g_F = 1$ and $q = \frac{15}{\sqrt{3}}$. At strong magnetic fields, a new plateau $\nu_h = 4$ appears in the multiple-Fermi-surface picture, yielding a pattern characteristic of FQHE.

The finite offset magnetic field has been observed in experiments on highly oriented pyrolytic graphite in magnetic fields [30]. In particular, analyzing the basal-plane resistivity gave an approximate scaling relation between the critical temperature of the metal-semiconducting transition and the magnetic field has been found $T_c \sim \sqrt{h - h_c}$. It suggests that at $T = 0$, there is a threshold magnetic field h_c above which the resistivity qualitatively changes. Interestingly, the existence of such a threshold magnetic field follows from the AdS/CFT calculations (h_c when $\nu = \frac{1}{2}$).

A phase transition is usually governed by an order parameter which exhibits a critical behavior. In our case, there is no such order parameter. However, it is interesting to note that the Fermi momentum, according to Eq. (93), behaves as $k_F \sim \sqrt{h_{\max} - h}$, which is in line with the postulated critical behavior in the system, while the Fermi surface itself behaves as order parameter.

To obtain a complete picture of the metal–strange-metal phase transition, one needs to perform calculations in the non-Fermi-liquid regime, taking into account the unstable quasiparticle pole. It is also necessary to study the temperature dependence of the DC conductivities $\sigma_{xy}(T)$ and $\sigma_{xx}(T)$. We leave it for future study.

VII. ABSENCE OF THE SIGN PROBLEM IN HOLOGRAPHY

In this section, we show that the fermion determinant in the gravity dual theory does not have a sign problem and hence can be simulated by a lattice Monte-Carlo algorithm. Until recently, most of the work on AdS/CFT and applied holography focused on the classical gravity (leading $1/N$ in field theory) limit. However, many thermodynamic and electric properties depend on matter fields (e.g., the electrical conductivity depends on whether or not the theory has a Fermi surface). In classical gravity, the Einstein-Maxwell sector decouples, and matter fields run in loops representing quantum oscillations. In order to include matter fields in the bulk, one needs to calculate loop corrections, which corresponds to going beyond the leading order in $1/N$. A study of one-loop bulk physics was done in [31] and recently in [22]. It shows that analytical calculations of quantum corrections in the bulk are quite involved. The study of quantum oscillations in the gravity dual will likely improve our understanding of finite density systems in general.

As is well known, a finite density field theory in most cases cannot be simulated on the lattice because of the infamous sign problem [1]. In the field theory action, chemical potential is introduced via the term $\bar{\psi} \mu \gamma^0 \psi$, which is Hermitian and therefore gives a complex determinant. At the same time, in the bulk action, finite density is introduced through the electrically charge black hole, and does not involve even matter fields. This is the reason why the applied holography gives universal predictions.

In the leading order, the minimal gravitational dual at finite density and temperature is the electrically charged AdS-Reissner-Nordström black hole, where only the metric and Maxwell fields are present. Therefore, the Einstein-Maxwell sector gives results which do not depend, for example, on the charge and mass of matter fields in the gravitational bulk space-time, i.e., are universal for a class of field theories with different charge and scaling dimensions of the operators. The fact that the chemical potential enters via the electric field in the covariant derivative leads to the real and positive definite fermion determinant, which is suitable for lattice simulations. We show it formally below.

In a semiclassical approach to gravity, the action includes the Einstein-Maxwell sector S_g with fields collectively denoted as g, A in Eq. (1), and the matter sector with the fermion fields S_ψ , Eq. (21). The latter is given as (Euclidean signature):

$$S_\psi = \int d^4x_E \sqrt{-g_E} \bar{\psi} (D + m) \psi, \quad (95)$$

where $D \equiv \Gamma_E^M \mathcal{D}_M$ and the covariant derivative is $\mathcal{D}_M = \partial_M + \frac{1}{4} \omega_{abM} \Gamma^{ab} - iqA_M$. We can always scale away the spin connection by redefining the spinor field as in Eq. (A6). Finite density is described by the electrically charged black hole with charge Q that generates the imaginary time component of the vector potential A_{t_E} (Eq. (17)). Radial profile of the vector potential $A_{t_E} = \mu(1 - \frac{1}{r})$ (in dimensionless units) ensures a finite chemical potential at the field theory boundary $A_{t_E} \rightarrow \mu$ at $r \rightarrow \infty$, where $\mu = g_F Q$ (in dimensionless units). Integrating out the fermion fields, the gravitational partition function can be written schematically as

$$Z = \sum_{g_*, A_*} \det(D(g_*, A_*) + m) e^{-S_g[g_*, A_*]}, \quad (96)$$

where S_g is the Euclidean gravitational action at the saddle points g_*, A_* . The determinant describes fluctuations about the saddle point solution g_*, A_* and corresponds to $1/N$ correction to the large N limit of a dual gauge theory. Because the Euclidean gamma matrices are Hermitian by convention (the signature of the metric fixes the Hermiticity), we have $\Gamma_E^{0\dagger} = \Gamma_E^0$ and $\Gamma_E^{i\dagger} = \Gamma_E^i$ with $i = 1, 2, 3$, so the covariant derivative is anti-Hermitian. Now it remains to be shown that the determinant of this anti-Hermitian differential operator is real and positive definite [32].

Using the anticommutation relations $\{\Gamma_E^5, \Gamma_E^{0,i}\} = 0$, we have

$$\Gamma_E^5 D \Gamma_E^5 = -D = D^\dagger, \quad (97)$$

where $D \equiv D(g, A)$. Therefore, the determinant

$$\det D = \det(\Gamma_E^5 D \Gamma_E^5) = \det D^\dagger = (\det D)^* \quad (98)$$

is real. To show the positive definiteness, we remind the reader that the eigenmodes of an anti-Hermitian derivative operator come in pairs. If (λ, ψ) is an eigenmode of D ,

$$D\psi = \lambda\psi, \quad (99)$$

then, from Eq. (99):

$$D(\Gamma_E^5 \psi) = (-\lambda)(\Gamma_E^5 \psi), \quad (100)$$

so $(-\lambda, \Gamma_E^5 \psi)$ is also an eigenmode of D . Because of anti-Hermiticity, from Eq. (97),

$$D(\Gamma_E^5 \psi) = \lambda^*(\Gamma_E^5 \psi). \quad (101)$$

This eigenvalue is completely imaginary (or zero), $-\lambda = \lambda^*$. The determinant is a product of all the paired eigenvalues,

$$\det(D + m) \rightarrow \prod_i (\lambda_i + m)(-\lambda_i + m) = \prod_i (|\lambda_i + m|^2), \quad (102)$$

which is positive definite (or zero).

In field theory, the eigenmodes of the operator $D + \mu\gamma_E^4 + m$ still come in pairs (λ, ψ) and $(-\lambda, \gamma_E^5 \psi)$. However, since $\mu\gamma_E^4$ is Hermitian, λ is no longer purely imaginary, and, therefore, $\det(D + \mu\gamma_E^4 + m)$ is not necessarily positive. The sign problem occurs when \det is negative for some gauge configurations, or, in other words, it is generically present when considering interacting matter at finite density.

VIII. CONCLUSIONS

We have studied strongly coupled electron systems in the magnetic field, focusing on the Fermi-level structure, using the AdS/CFT correspondence. These systems are dual to Dirac fermions placed in the background of the electrically and magnetically charged AdS-Reissner-Nordström black hole. At strong magnetic fields, the dual system “lives” near the black hole horizon, which substantially modifies the Fermi-level structure. As we dial the magnetic field higher, the system exhibits the non-Fermi-liquid behavior and then crosses back to the conformal regime. In our analysis, we have concentrated on the the Fermi-liquid regime and obtained the dependence of the Fermi momentum k_F and Fermi velocity v_F on the magnetic field. Remarkably, k_F exhibits the square root behavior, with v_F staying close to the speed of light in a wide range of magnetic fields, while it rapidly vanishes at a critical magnetic field, which is relatively high. Such behavior indicates that the system may have a phase transition.

The magnetic system can be rescaled to a zero-field configuration, which is thermodynamically equivalent to the original one. This simple result can actually be seen already at the level of field theory: The additional scale

brought about by the magnetic field does not show up in thermodynamic quantities, meaning, in particular, that the behavior in the vicinity of quantum critical points is expected to remain largely uninfluenced by the magnetic field, retaining its conformal invariance. In light of current condensed matter knowledge, this is surprising and might in fact be a good opportunity to test the applicability of the probe limit in the real world. If this behavior is not seen, this suggests that one has to include the backreaction to the metric to arrive at a realistic description.

In the field theory frame, we have calculated the DC conductivity using k_F and v_F values extracted from holography. The holographic calculation of conductivity that takes into account the fermions corresponds to the corrections of subleading order in $1/N$ in the field theory and is very involved [15]. As we are not interested in the vertex renormalization due to gravity (it does not change the magnetic field dependence of the conductivity), we have performed our calculations directly in the field theory with AdS-gravity-dressed fermion propagators. Instead of controlling the occupancy of the Landau levels by changing the chemical potential (as is usual in nonholographic setups), we have controlled the filling of the Landau levels by varying the Fermi energy level through the magnetic field. At zero temperature, we have reproduced the integer QHE of the Hall conductivity, which is observed in graphene at moderate magnetic fields. Our findings on equilibrium physics (Landau quantization, magnetic phase transitions, and crossovers) are within expectations and indeed corroborate the meaningfulness of the AdS/CFT approach in line with the well-known facts. However, the detection of the QHE is somewhat surprising, as the spatial boundary effects are ignored in our setup. We plan to address this question in future work.

Interestingly, the AdS geometry produces several Fermi surfaces. Theories where the gravity duals have larger fermion charge q possess more Fermi surfaces. We find that, in a multi-Fermi surface picture, the Hall conductivity is quantized in a way reminiscent of fractional QHE. By reducing the magnetic field, new Fermi surfaces open up and the quantization of Hall conductivity alternates between two different patterns, corresponding to odd and even numbers of Fermi surfaces. It turns out that an odd number of the Fermi surfaces results in IQHE plateaus, while an even number of surfaces gives new plateaus characteristic for the FQHE. In a multi-Fermi surface picture, the quantum Hall plateaus show a less regular pattern that agrees with experiments on thin graphite in strong magnetic field [23]. In our model, it happens due to the fact that, as one of several Fermi surfaces crosses the Landau level, the Hall conductivity jumps to a new plateau. This process is not synchronized between different Fermi surfaces. We associate the average distance between the Fermi levels with the energy gap usually arising in the FQHE.

Notably, the AdS-Reissner-Nordström black hole background gives a vanishing Fermi velocity at high magnetic fields. It happens at the point when the IR conformal dimension of the corresponding field theory is $\nu = \frac{1}{2}$, which is the border line between the Fermi and non-Fermi liquids. Vanishing Fermi velocity was also observed at high enough fermion charge [21]. As in [21], it is explained by the red shift on the gravity side because at strong magnetic fields, the fermion wave function is supported near the black hole horizon, modifying substantially the Fermi velocity. In our model, vanishing Fermi velocity leads to zero occupancy of the Landau levels by stable quasiparticles that results in vanishing regular Fermi-liquid contribution to the Hall conductivity and the longitudinal conductivity. The dominant contribution to both now comes from the non-Fermi liquid and conformal contributions. We associate such change in the behavior of conductivities with a metal–strange-metal phase transition. Experiments on highly oriented pyrolytic graphite support the existence of a finite “offset” magnetic field h_c at $T = 0$, where the resistivity qualitatively changes its behavior [30]. At $T \neq 0$, it has been associated with the metal-semiconducting phase transition [30]. It is worthwhile to study the temperature dependence of the conductivity in order to understand this phase transition better.

Finally, we suggest as a possibly interesting extension of the current AdS/CFT methodology to compute the gravity dual of the finite density matter in Monte-Carlo lattice simulations. This is possible since the sign problem does not arise in the holographic setting of a finite density system. Unlike the conventional field theory setup, finite density in holography is introduced through an electrically charged black hole, and does not involve matter fields (this is also the reason why holography gives universal results: It does not depend on the expectation values of matter fields at the leading order). In the gravity geometry, Dirac fermions are coupled minimally to the electric field via the covariant derivative. We have shown that the covariant derivative is anti-Hermitian in the Euclidean signature, leading to the real and positive definite fermion determinant. This makes it possible to simulate finite density systems on the lattice in the AdS-gravity geometry, using the curved space-time lattice formulation [33]. The simplest holographic setup which describes a finite charge density system includes a local $U(1)$ gauge symmetry. Finite density systems with global $U(1)$ symmetry can not be simulated numerically in field theory due to the problem with the Gauss law in the lattice formulation. Another important advantage of performing the Monte-Carlo simulation is that it includes the quantum fluctuations for the gauge and gravitational field. So far, most calculations have been done in the probe limit, with the frozen background for the metric and gauge fields. Analytic calculations which include backreaction are usually involved and are done in the next-to-leading order,

e.g., [8]. Holographic lattice calculations allow us to consider dynamical gauge and gravity fields with matter, which mimics complicated strong interactions in finite density systems and opens a way toward studying novel state of matter and instability mechanisms.

ACKNOWLEDGMENTS

We thank Tom Faulkner, Michael Fromm, Tom Hartman, Sean Hartnoll, Nabil Iqbal, Hong Liu, Mark Mezei, Hiranmaya Mishra, Volodya Miransky, Yusuke Nishida, Owe Philipsen, Igor Shovkovy, Tian Zhang, Darius Sadri, Chang Yu Hou, Andrej Mesaroš, and Vladimir Juričić for helpful input and discussions. The work was supported in part by the Alliance program of the Helmholtz Association, Contract No. HA216/EMMI “Extreme Density and Temperature: Cosmic Matter in the Laboratory” and by ITP of Goethe University, Frankfurt (E. Gubankova); by a VIDI Innovative Research Incentive Grant (K. Schalm) from the Netherlands Organization for Scientific Research (NWO); by a Spinoza Award (J. Zaanen) from the Netherlands Organization for Scientific Research (NWO); and the Dutch Foundation for Fundamental Research of Matter (FOM). K. Schalm thanks the Galileo Galilei Institute for Theoretical Physics for the hospitality and the INFN for partial support during the completion of this work.

APPENDIX A: DIRAC EQUATION IN MAGNETIC FIELD

Here, we solve analytically the part of the Dirac equation which depends on magnetic field and space-time coordinates of the boundary theory. The free spinor action in the geometry given by Eq. (2) and in the presence of a magnetic field (3) is given by Eq. (21).

Using the translational invariance,

$$\psi(t, x, y, r) = \int d\omega dk e^{-i\omega t + ik y} \psi(\omega, k, x, r), \quad (\text{A1})$$

with $k \equiv k_y$, the Dirac equation (Eq. (23)) can be written as

$$\begin{aligned} & \left(\frac{1}{\sqrt{-g_{tt}}} \Gamma^{\hat{t}} \left(-i\omega + \frac{1}{2} \omega_{\hat{t}\hat{t}} \Gamma^{\hat{t}\hat{t}} - iqA_t(r) \right) + \frac{1}{\sqrt{g_{rr}}} \Gamma^{\hat{r}} \partial_r \right. \\ & + \frac{1}{\sqrt{g_{ii}}} \Gamma^{\hat{x}} \left(\partial_x + \frac{1}{2} \omega_{\hat{x}\hat{x}} \Gamma^{\hat{x}\hat{x}} \right) + \frac{1}{\sqrt{g_{ii}}} \Gamma^{\hat{y}} \left(ik + \frac{1}{2} \omega_{\hat{y}\hat{y}} \Gamma^{\hat{y}\hat{y}} \right. \\ & \left. \left. - iqA_y(x) \right) - m \right) \psi(\omega, k, x, r) = 0, \quad (\text{A2}) \end{aligned}$$

where $g_{ii} \equiv g_{xx} = g_{yy}$, and $A_t(r) = \mu(1 - r_0/r)$, $A_y(x) = hx$. From the torsion-free condition, $\omega_b^a \wedge e^b = -de^a$, we find the spin connection [34] for the metric (2),

$$\omega_{\hat{t}\hat{r}} = -\frac{\partial_r(\sqrt{-g_{tt}})}{\sqrt{g_{rr}}} dt, \quad \omega_{\hat{r}\hat{x}} = \frac{\partial_r(\sqrt{g_{ii}})}{\sqrt{g_{rr}}} dx^i, \quad (\text{A3})$$

where $i = x, y$. Note that

$$-\Gamma^{\hat{t}} \Gamma^{\hat{r}} = \Gamma^{\hat{x}} \Gamma^{\hat{x}} = \Gamma^{\hat{y}} \Gamma^{\hat{y}} = \Gamma^{\hat{r}}, \quad (\text{A4})$$

and

$$\begin{aligned} \frac{1}{4} e_a^M \Gamma^{\hat{a}} \omega_{\hat{b}\hat{c}M} \Gamma^{\hat{b}\hat{c}} &= \frac{1}{4} \frac{1}{\sqrt{-g_{tt}}} \frac{\partial_r(\sqrt{-g_{tt}})}{\sqrt{g_{rr}}} \Gamma^{\hat{r}} \\ &+ \frac{2}{4} \frac{1}{\sqrt{g_{ii}}} \frac{\partial_r \sqrt{g_{ii}}}{\sqrt{g_{rr}}} \Gamma^{\hat{r}} \\ &= \frac{1}{\sqrt{g_{rr}}} \Gamma^{\hat{r}} \partial_r \ln \left(-\frac{g}{g_{rr}} \right)^{1/4}, \quad (\text{A5}) \end{aligned}$$

where g is the determinant of the metric. Therefore, we can rescale the spinor field:

$$\psi = \left(-\frac{g}{g_{rr}} \right)^{-1/4} \Phi \quad (\text{A6})$$

and remove the spin connection completely. The new covariant derivative does not contain the spin connection, so $\mathcal{D}'_M = \partial_M - iqA_M$.

In new field variables, the Dirac equation is given by

$$\begin{aligned} & \left(\frac{\sqrt{g_{ii}}}{\sqrt{g_{rr}}} \Gamma^{\hat{r}} \partial_r - \frac{\sqrt{g_{ii}}}{\sqrt{-g_{tt}}} \Gamma^{\hat{t}} i \left(\omega + \mu_q \left(1 - \frac{r_0}{r} \right) \right) - \sqrt{g_{ii}} m \right. \\ & \left. + \Gamma^{\hat{x}} \partial_x + \Gamma^{\hat{y}} i(k - qhx) \right) \Phi(\omega, k, x, r) = 0, \quad (\text{A7}) \end{aligned}$$

with $\mu_q \equiv \mu q$. We separate the x - and r -dependent parts:

$$\begin{aligned} P(r) &= \frac{\sqrt{g_{ii}}}{\sqrt{g_{rr}}} \Gamma^{\hat{r}} \partial_r - \frac{\sqrt{g_{ii}}}{\sqrt{-g_{tt}}} \Gamma^{\hat{t}} i \left(\omega + \mu_q \left(1 - \frac{r_0}{r} \right) \right) - \sqrt{g_{ii}} m, \\ Q(x) &= \Gamma^{\hat{x}} \partial_x + \Gamma^{\hat{y}} i(k - qhx), \quad (\text{A8}) \end{aligned}$$

and the Dirac equation is

$$(P(r) + Q(x))\Phi = 0. \quad (\text{A9})$$

Even though $[P(r), Q(x)] \neq 0$, one can find a transformation matrix U such that $[UP(r), UQ(x)] = 0$ and then look for common eigenvectors of $UP(r)$ and $UQ(x)$ as they are commuting Hermitian operators, i.e., the Dirac equation reads

$$UP(r)\Phi_l = -UQ(x)\Phi_l = \lambda_l \Phi_l, \quad (\text{A10})$$

where l labels the Landau levels. We use l for the Landau index, so as not to confuse it with the Matsubara frequency index n . Transformation matrix U should satisfy the conditions

$$\begin{aligned} \{U, \Gamma^{\hat{t}}\} &= 0, & \{U, \Gamma^{\hat{r}}\} &= 0, \\ [U, \Gamma^{\hat{x}}] &= 0, & [U, \Gamma^{\hat{y}}] &= 0, \end{aligned} \quad (\text{A11})$$

which do not fix U completely. It is convenient to use the following basis [7]:

$$\begin{aligned}\Gamma^{\hat{r}} &= \begin{pmatrix} -\sigma^3 & 0 \\ 0 & -\sigma^3 \end{pmatrix}, & \Gamma^{\hat{t}} &= \begin{pmatrix} i\sigma^1 & 0 \\ 0 & i\sigma^1 \end{pmatrix}, \\ \Gamma^{\hat{x}} &= \begin{pmatrix} -\sigma^2 & 0 \\ 0 & \sigma^2 \end{pmatrix}, & \Gamma^{\hat{y}} &= \begin{pmatrix} 0 & \sigma^2 \\ \sigma^2 & 0 \end{pmatrix}, \\ \Gamma^{\hat{s}} &= \begin{pmatrix} 0 & i\sigma^2 \\ -i\sigma^2 & 0 \end{pmatrix}.\end{aligned}\quad (\text{A12})$$

Note that the following relation holds

$$\Gamma^{\hat{s}} = \Gamma^{\hat{0}}\Gamma^{\hat{1}}\Gamma^{\hat{2}}\Gamma^{\hat{3}} \quad (\text{A13})$$

as expected, with $0 \rightarrow t$, $1 \rightarrow x$, $2 \rightarrow y$, and $3 \rightarrow r$. In the representation of Eq. (A12), we can choose

$$U = \begin{pmatrix} -i\sigma^2 & 0 \\ 0 & -i\sigma^2 \end{pmatrix}. \quad (\text{A14})$$

We split the 4-component spinors into two 2-component spinors (we do not write zero entries) $F = (F_1, F_2)^T$, where the index $\alpha = 1, 2$ is the Dirac index of the boundary theory, using projectors

$$\begin{aligned}\Pi_\alpha &= \frac{1}{2}(1 - (-1)^\alpha \Gamma^{\hat{r}}\Gamma^{\hat{t}}), \\ \alpha &= 1, 2, \quad \Pi_1 + \Pi_2 = 1,\end{aligned}\quad (\text{A15})$$

which commute with the Dirac operator of Eq. (37), and $F_\alpha = \Pi_\alpha \Phi$, $\alpha = 1, 2$, decouple from each other. Gamma matrices in Eq. (A12) were chosen in such a way that this decoupling is possible.

Writing the Dirac equation (A10) for $F = (F_1, F_2)^T$, we have

$$\begin{aligned}\left(-\frac{\sqrt{g_{ii}}}{\sqrt{g_{rr}}}\sigma^1\partial_r + \sqrt{g_{ii}}i\sigma^2m\right. \\ \left.- \frac{\sqrt{g_{ii}}}{\sqrt{-g_{tt}}}\sigma^3(\omega + \mu_q(1 - r_0/r)) - \lambda_l\right) \otimes 1 \begin{pmatrix} F_1 \\ F_2 \end{pmatrix} = 0 \\ 1 \otimes \begin{pmatrix} i\partial_x + \lambda_l & (k - qhx) \\ (k - qhx) & -i\partial_x + \lambda_l \end{pmatrix} \begin{pmatrix} F_1 \\ F_2 \end{pmatrix} = 0,\end{aligned}\quad (\text{A16})$$

where in $X \otimes Y$, X acts inside F_1 or F_2 , and Y acts between F_1 and F_2 . In Eq. (A16), the 1 in the first equation shows that there is no mixing of F_1 and F_2 by the operator $UP(r)$, and the 1 in the second equation shows that there is no mixing inside F_1 or F_2 by the operator $UQ(x)$. Therefore, the solution can be represented as

$$\begin{pmatrix} F_1 \\ F_2 \end{pmatrix} = \begin{pmatrix} f_l^{(1)}(r)g_l^{(1)}(x) \\ f_l^{(2)}(r)g_l^{(1)}(x) \\ f_l^{(1)}(r)g_l^{(2)}(x) \\ f_l^{(2)}(r)g_l^{(2)}(x) \end{pmatrix}. \quad (\text{A17})$$

We do not write explicitly the dependence on ω and k . It is convenient to make a unitary transformation:

$$\begin{pmatrix} \zeta^{(1)} \\ \zeta^{(2)} \end{pmatrix} = M \begin{pmatrix} g^{(1)} \\ g^{(2)} \end{pmatrix}, \quad M = \begin{pmatrix} 1 & -i \\ -i & 1 \end{pmatrix}. \quad (\text{A18})$$

Dirac equations for each component are written as:

$$\begin{aligned}\left(\frac{\sqrt{g_{ii}}}{\sqrt{g_{rr}}}\partial_r + \sqrt{g_{ii}}m\right)f_l^{(1)}(r) \\ + \left(-\frac{\sqrt{g_{ii}}}{\sqrt{-g_{tt}}}(\omega + \mu_q(1 - r_0/r)) + \lambda_l\right)f_l^{(2)}(r) = 0, \\ \left(\frac{\sqrt{g_{ii}}}{\sqrt{g_{rr}}}\partial_r - \sqrt{g_{ii}}m\right)f_l^{(2)}(r) \\ + \left(\frac{\sqrt{g_{ii}}}{\sqrt{-g_{tt}}}(\omega + \mu_q(1 - r_0/r)) + \lambda_l\right)f_l^{(1)}(r) = 0,\end{aligned}\quad (\text{A19})$$

$$(\partial_{\tilde{x}} - \tilde{x})\zeta^{(1)} + \tilde{\lambda}_l\zeta^{(2)} = 0, \quad (\partial_{\tilde{x}} + \tilde{x})\zeta^{(2)} - \tilde{\lambda}_l\zeta^{(1)} = 0. \quad (\text{A20})$$

In Eq. (A20), for the x -dependent part, we have rescaled $\tilde{x} = \sqrt{|qh|}(x - \frac{k}{qh})$ with $k \equiv k_y$ and $\lambda_l = \sqrt{|qh|}\tilde{\lambda}_l$. The second order ordinary differential equations

$$-\partial_{\tilde{x}}^2\zeta^{(\rho)} + \tilde{x}^2\zeta^{(\rho)} - \tilde{\lambda}_l^2\zeta^{(\rho)} - (-1)^\rho\zeta^{(\rho)} = 0, \quad (\text{A21})$$

with $\rho = 1, 2$, are solved by substitution $\zeta^{(\rho)} = e^{-\tilde{x}^2/2}\tilde{\zeta}^{(\rho)}$. This is exactly the Schrödinger equation for a harmonic oscillator, so the eigenfunctions are Hermite polynomials, and we obtain the following solutions, indexed by an integer $l \in \mathbb{Z}$ that is related to the eigenvalue λ_l by $\lambda_l = \sqrt{2|qh|}l$:

$$\zeta_l^{(1)}(\tilde{x}) = N_{l-1}e^{-\tilde{x}^2/2}H_{l-1}(\tilde{x}) \quad \zeta_l^{(2)}(\tilde{x}) = N_l e^{-\tilde{x}^2/2}H_l(\tilde{x}). \quad (\text{A22})$$

The normalization constant N_l is proportional to $1/\sqrt{2^l l!}$. Substituting the solutions from Eq. (A22) into the first order eigenvalue equation with x -dependence gives the following solutions:

$$F_l = \begin{pmatrix} f_l^{(1)}(r)\zeta_l^{(1)}(\tilde{x}) \\ f_l^{(2)}(r)\zeta_l^{(1)}(\tilde{x}) \\ f_l^{(1)}(r)\zeta_l^{(2)}(\tilde{x}) \\ -f_l^{(2)}(r)\zeta_l^{(2)}(\tilde{x}) \end{pmatrix}, \quad \lambda_l = \sqrt{2|qh|}l, \quad (\text{A23})$$

and

$$\tilde{F}_l = \begin{pmatrix} \tilde{f}_l^{(1)}(r)\zeta_l^{(1)}(\tilde{x}) \\ \tilde{f}_l^{(2)}(r)\zeta_l^{(1)}(\tilde{x}) \\ -\tilde{f}_l^{(1)}(r)\zeta_l^{(2)}(\tilde{x}) \\ \tilde{f}_l^{(2)}(r)\zeta_l^{(2)}(\tilde{x}) \end{pmatrix}, \quad \lambda_l = -\sqrt{2|qh|l}. \quad (\text{A24})$$

Solving the first order x -dependent equation, we get the same eigenvalue, but slightly different eigenfunctions, for different signs of qh . In particular, e.g., for F , the pairs $f^{(1)}(\zeta^{(1)}, \zeta^{(2)})^T$ and $f^{(2)}(\zeta^{(1)}, -\zeta^{(2)})^T$ correspond to $qh > 0$ and $qh < 0$, respectively. A different sign of qh stands for the positive and negative Landau-level index l .

Finally, the general solution to the Dirac equation is given by a linear combination of Eqs. (A23) and (A24):

$$F_{\text{sol}} = \sum_l (a_l F_l + b_l \tilde{F}_l). \quad (\text{A25})$$

Using the eigenvalues determined by Eqs. (A23) and (A24) in the equation for the radial part (A19), we get

$$\left(-\frac{1}{\sqrt{g_{rr}}} \sigma^3 \partial_r - m + \frac{1}{\sqrt{-g_{tt}}} \sigma^1 (\omega + \mu_q (1 - r_0/r)) - \frac{1}{\sqrt{g_{tt}}} i \sigma^2 \sqrt{2|qh|l} \right) \otimes 1 \begin{pmatrix} F_1 \\ F_2 \end{pmatrix} = 0, \quad (\text{A26})$$

with $l = 0, 1, \dots$; and the same for \tilde{F} replacing $\sqrt{2|qh|l} \rightarrow -\sqrt{2|qh|l}$. It coincides with eq. (A14) in [7] (Dirac equation at zero magnetic field) with the momentum replaced by the Landau-level eigenvalue [22]

$$k \rightarrow \pm \sqrt{2|qh|l}. \quad (\text{A27})$$

Equation (A27) also gives a prescription on how to treat the limit of zero magnetic field $h \rightarrow 0$. The limit is to be taken keeping, e.g., $2|qh|(l+1) \equiv k_F^2$ fixed as $h \rightarrow 0$. In a compact form, the Dirac equation in a magnetic field (A7) is given by

$$\left(\frac{1}{\sqrt{g_{rr}}} \Gamma^{\hat{r}} \partial_r - \frac{1}{\sqrt{-g_{tt}}} \Gamma^{\hat{t}} i (\omega + qA_t) - m - \frac{1}{\sqrt{g_{tt}}} U^{-1} \sqrt{2|qh|l} \right) F(r) = 0, \quad (\text{A28})$$

with $F = (F_1, F_2)^T$, $l = 0, 1, \dots$, for \tilde{F} replace $\sqrt{2|qh|l} \rightarrow -\sqrt{2|qh|l}$, and U^{-1} is the matrix inverse to the matrix given by Eq. (A14):

$$U^{-1} = \begin{pmatrix} i\sigma^2 & 0 \\ 0 & i\sigma^2 \end{pmatrix}, \quad (\text{A29})$$

which we use in the main text.

APPENDIX B: SPECTRAL FUNCTION

In what follows, we use the dimensionless variables (15)–(17). Following the analysis of [7], the flow of the Green's function is determined by

$$G_R(\omega, l) = \lim_{\epsilon \rightarrow 0} \epsilon^{-2m} \begin{pmatrix} \xi_+^{(l)} & 0 \\ 0 & \xi_-^{(l)} \end{pmatrix} \Big|_{r=1/\epsilon}, \quad (\text{B1})$$

where $\xi_+^{(l)}(r) = \frac{f^{(2)}}{f^{(1)}}$ and $\xi_-^{(l)}(r) = \frac{\tilde{f}^{(2)}}{\tilde{f}^{(1)}}$ from the solutions (A23) and (A24). In obtaining this relation, we absorbed the coefficients appearing in Eq. (A25) into the definitions of the radial functions. The functions $\xi_{\pm}^{(l)}$ satisfy the following differential equation [7]:

$$\sqrt{\frac{g_{tt}}{g_{rr}}} \partial_r \xi_{\pm}^{(l)} = -2m \sqrt{g_{tt}} \xi_{\pm}^{(l)} + (u(r) \pm \lambda_l)^2 (\xi_{\pm}^{(l)})^2 + (u(r) \mp \lambda_l), \quad (\text{B2})$$

with $u(r)$ given by

$$u(r) = \sqrt{\frac{g_{tt}}{-g_{rr}}} (\omega + qA_t(r)). \quad (\text{B3})$$

Writing explicitly in the metric given by Eq. (18), we have

$$r^2 \sqrt{f} \partial_r \xi_{\pm}^{(l)} = -2mr \xi_{\pm}^{(l)} + (u(r) \pm \lambda_l) (\xi_{\pm}^{(l)})^2 + (u(r) \mp \lambda_l), \quad (\text{B4})$$

where $u(r)$ is given by

$$u(r) = \frac{1}{\sqrt{f}} \left(\omega + \mu_q \left(1 - \frac{1}{r} \right) \right), \quad (\text{B5})$$

with $f = \frac{(r-1)^2(r^2+2r+3)}{r^4}$ at $T = 0$. Near the horizon ($r = 1$), the flow equation reduces to

$$r^2 \partial_r \xi_{\pm}^{(l)} = \frac{1}{f} (\xi_{\pm}^{(l)} + 1)^2, \quad (\text{B6})$$

which, due to the double zero in f , has a regular solution only if $\xi_{\pm}(r=1) = \pm i$. Writing the radial equation in terms of ξ and choosing the infalling boundary conditions fixes $\xi_{\pm}^{(l)}(r=1) = i$.

The key quantity that we extract from the Green's function is the fermionic spectral function

$$A(\omega, l_x, k_y) = \text{Tr}(\text{Im} G_R(\omega, l_x, k_y)), \quad (\text{B7})$$

which we analyze in the main text of the paper.

- [1] J. Zaanen, *Science* **319**, 1205 (2008); P. de Forcrand, Proc. Sci., LAT2009 (2009) 010 [arXiv:1005.0539]; M. P. Lombardo, K. Splittorff, and J.J.M. Verbaarschot, *ibid.* LAT2009 (2009) 171 [arXiv:0912.3109].
- [2] S. A. Hartnoll, J. Polchinski, E. Silverstein, and D. Tong, *J. High Energy Phys.* **04** (2010) 120; S. A. Hartnoll, C. P. Herzog, and G. T. Horowitz, *ibid.* **12** (2008) 015.
- [3] P. Kovtun, D. T. Son, and A. O. Starinets, *Phys. Rev. Lett.* **94**, 111601 (2005).
- [4] S. -S. Lee, *Phys. Rev. D* **79**, 086006 (2009).
- [5] M. Čubrović, J. Zaanen, and K. Schalm, *Science* **325**, 439 (2009).
- [6] H. Liu, J. McGreevy, and D. Vegh, *Phys. Rev. D* **83**, 065029 (2011).
- [7] T. Faulkner, H. Liu, J. McGreevy, and D. Vegh, *Phys. Rev. D* **83**, 125002 (2011); T. Faulkner, N. Iqbal, H. Liu, J. McGreevy, and D. Vegh, arXiv:1101.0597.
- [8] S. A. Hartnoll and A. Tavanfar, *Phys. Rev. D* **83**, 046003 (2011).
- [9] S. A. Hartnoll, P. K. Kovtun, M. Mueller, and S. Sachdev, *Phys. Rev. B* **76**, 144502 (2007).
- [10] S. A. Hartnoll and P. Kovtun, *Phys. Rev. D* **76**, 066001 (2007).
- [11] P. Basu, J. Y. He, A. Mukherjee, and H.-H. Shieh, *Phys. Rev. D* **82**, 044036 (2010).
- [12] T. Albash and C. V. Johnson, *J. Phys. A* **43**, 345404 (2010); **43**, 345405 (2010).
- [13] T. Albash and C. V. Johnson, *J. High Energy Phys.* **09** (2008) 121; arXiv:0906.0519.
- [14] N. Iqbal, H. Liu, M. Mezei, and Q. Si, *Phys. Rev. D* **82**, 045002 (2010).
- [15] T. Faulkner, N. Iqbal, H. Liu, J. McGreevy, and D. Vegh, arXiv:1003.1728.
- [16] E. D'Hoker and P. Kraus, *J. High Energy Phys.* **05** (2010) 083. E. D'Hoker and P. Kraus, *Classical Quantum Gravity* **27**, 215022 (2010).
- [17] A. Auerbach, “*Quantum Magnetism Approaches to Strongly Correlated Electrons*,” Chia Laguna Summer School 1997 (unpublished).
- [18] E. Gubankova, in Workshop on P- and CP-Odd Effects in Hot and Dense Matter, Brookhaven National Laboratory, 2010 (unpublished).
- [19] J. L. Davis, P. Kraus, and A. Shah, *J. High Energy Phys.* **11** (2008) 020; E. K. -Vakkuri and P. Kraus, *ibid.* **09** (2008) 130.
- [20] A. H. MacDonald, arXiv:cond-mat/9410047.
- [21] T. Hartman and S. A. Hartnoll, *J. High Energy Phys.* **06** (2010) 005.
- [22] F. Denef, S. A. Hartnoll, and S. Sachdev, *Phys. Rev. D* **80**, 126016 (2009); F. Denef, S. A. Hartnoll, and S. Sachdev, *Classical Quantum Gravity* **27**, 125001 (2010).
- [23] Y. Zhang, Z. Jiang, J. P. Small, M. S. Purewal, Y.-W. Tan, M. Fazlollahi, J. D. Chudow, J. A. Jaszczak, H. L. Stormer, and P. Kim, *Phys. Rev. Lett.* **96**, 136806 (2006).
- [24] J. L. Noronha and I. A. Shovkovy, in International Symposium on Exotic States of Nuclear Matter, Catania, Italy, 2007 (unpublished); J. L. Noronha and I. A. Shovkovy, *Phys. Rev. D* **76**, 105030 (2007).
- [25] E. V. Gorbar, V. P. Gusynin, V. A. Miransky, and I. A. Shovkovy, *Phys. Rev. B* **66**, 045108 (2002); V. P. Gusynin and S. G. Sharapov, *ibid.* **73**, 245411 (2006); V. P. Gusynin, V. A. Miransky, S. G. Sharapov, and I. A. Shovkovy, *ibid.* **74**, 195429 (2006); V. P. Gusynin and S. G. Sharapov, *Phys. Rev. Lett.* **95**, 146801 (2005).
- [26] E. V. Gorbar, V. A. Miransky, and I. A. Shovkovy, *Phys. Rev. D* **83**, 085003 (2011).
- [27] M. A. V. Basagoiti, *Phys. Rev. D* **66**, 045005 (2002); J. M. M. Resco and M. A. V. Basagoiti, *ibid.* **63**, 056008 (2001).
- [28] N. Iqbal and H. Liu, *Fortschr. Phys.* **57**, 367 (2009).
- [29] Y.-F. Hsu and G.-Y. Guo, *Phys. Rev. B* **82**, 165404 (2010).
- [30] Y. Kopelevich, V. V. Lemanov, S. Moehlecke, and J. H. S. Torrez, *Fiz. Tverd. Tela (Leningrad)* **41**, 2135 (1999); [*Sov. Phys. Solid State* **41**, 1959 (1999)]; H. Kempa, Y. Kopelevich, F. Mrowka, A. Setzer, J. H. S. Torrez, R. Hoehne, and P. Esquinazi, *Solid State Commun.* **115**, 539 (2000); M. S. Sercheli, Y. Kopelevich, R. R. da Silva, J. H. S. Torrez, and C. Rettori, *ibid.* **121**, 579 (2002); Y. Kopelevich, P. Esquinazi, J. H. S. Torres, R. R. da Silva, H. Kempa, F. Mrowka, and R. Ocana, *Stud. High Temp. Supercond.* **45**, 59 (2003).
- [31] S. S. Gubser and I. Mitra, *Phys. Rev. D* **67**, 064018 (2003); S. S. Gubser and I. R. Klebanov, *Nucl. Phys.* **B656**, 23 (2003); T. Hartman and L. Rastelli, *J. High Energy Phys.* **01** (2008) 019.
- [32] Tian Zhang (unpublished).
- [33] S. Catterall, *J. High Energy Phys.* **07** (2010) 066; **01** (2009) 040; S. Catterall, D. Ferrante, and A. Nicholson, arXiv:0912.5525; P. H. Damgaard and S. Matsuura, *J. High Energy Phys.* **07** (2007) 051.
- [34] S. M. Carroll, *Spacetime and Geometry: An Introduction to General Relativity* (Benjamin Cummings, San Francisco, 2003).

Fractional kinetic model for chaotic transport in nonintegrable Hamiltonian systems

Mihailo Čubrović*

Institute of Physics, P. O. B. 57, 11001 Belgrade, Serbia and Montenegro and Department of Astronomy-Petnica Science Center, P. O. B. 6, 14104 Valjevo, Serbia and Montenegro

(Received 14 April 2005; published 31 August 2005)

We propose a kinetic model of transport in nonintegrable Hamiltonian systems, based on a fractional kinetic equation with spatially dependent diffusion coefficient. The diffusion coefficient is estimated from the remainder of the optimal normal form for the given region of the phase space. After partitioning the phase space into building blocks, a separate equation can be constructed for each block. Solving the kinetic equations approximately and estimating the diffusion time scales, we convolve the solutions to get the description of the macroscopic behavior. We show that, in the limit of infinitely many blocks, one can expect an approximate scaling relation between the Lyapunov time and the diffusion (or escape) time, which is either an exponential or a power law. We check our results numerically on over a dozen Hamiltonians and find a good agreement.

DOI: [10.1103/PhysRevE.72.025204](https://doi.org/10.1103/PhysRevE.72.025204)

PACS number(s): 05.45.-a, 05.60.Cd, 05.20.Dd

Statistical treatment of chaotic transport is one of the most difficult problems in nonintegrable Hamiltonian dynamics. Despite its importance for many practical problems in various fields, e.g., plasma physics [1,2] and dynamical astronomy [3], we still lack a general and consistent kinetic theory of transport. The main reason is the complicated nature of the phase space of the typical nonintegrable Hamiltonian system, since it usually contains a “topological zoo” of regular and chaotic structures mixed on an arbitrarily small scale. The most promising way for overcoming these difficulties is, in our opinion, the so-called fractional kinetics of the phase space [4]. Fractional kinetics has become a broad topic of research not only in Hamiltonian dynamics but also in very different areas such as solid-state physics [5] and physics of complex systems [6]. The basic advantage of the fractional kinetic equation (FKE) for describing chaotic transport is that its fractional nature allows one to include the self-similarity of phase space and time, which arises from the first principles, i.e., from the dynamical equations. Especially important is the phenomenon of the so-called stickiness [3] or dynamical trapping [7], which leads to long intervals of quasiregular motion.

The particular issue that has largely motivated this research is the phenomenon of approximate scaling of diffusion time scales with the Lyapunov exponents or perturbation strength. A number of papers have been published on this topic, e.g., [8]; we are also inspired by the building block method of [9].

The basic idea of our model is to consider a FKE in the action space with a nonhomogenous diffusion coefficient and to combine, i.e., convolve the results to obtain the expected macroscopic behavior. We use the following form of the FKE:

$$\frac{\partial^\beta P(I,t)}{\partial t^\beta} = \frac{\partial^\alpha [D(I)P(I,t)]}{\partial |I|^\alpha} + \delta(I)t^{-\beta}/\Gamma(1-\beta), \quad (1)$$

where $0 < \beta < 1$ and $0 < \alpha < 2$. Its derivation from the Hamiltonian equations and discussion of assumptions involved can be found, e.g., in [4]. Although, strictly speaking, one should consider a vector of actions, we shall assume that diffusion along one action coordinate is independent of the others and consider I as a scalar; alternatively, one could interpret that as considering only one action variable, whereas the diffusion along the others is many orders of magnitude smaller. Both cases have been described in various systems [2,4].

We estimate the diffusion coefficient \mathcal{D} as the remainder of the normal form for the dynamics in the vicinity of a stable domain, e.g., invariant torus. Splitting the Hamiltonian $H(I, \phi)$ into an action-only integrable part $H_0(I) = \omega I$ and the nonintegrable remainder $H_1(I, \phi)$, one can obtain the estimate for the remainder of the form $O(f(I))$, i.e., as a function of the action. Treating the influence of the nonintegrable remainder on the dynamics as the microscopic transport mechanism, we take $f(I)$ from the above estimate for the diffusion coefficient. Two optimal normal forms are known as Nekhoroshev and Birkhoff normal forms. Their remainders [10] give the diffusion coefficients \mathcal{D}_N and \mathcal{D}_B :

$$\mathcal{D}_N = \mathcal{D}_0 \exp[-1/|I|^\theta], \quad (2a)$$

$$\mathcal{D}_B = \mathcal{D}_0 |I|^\theta, \quad (2b)$$

where \mathcal{D}_0 denotes the constant part, which is, in general, dependent on the properties of the Hamiltonian. For both cases, there is a constraint $\theta > 2$. The two cases roughly correspond to local nonoverlapping or overlapping of the resonances.

The last step before solving the FKE is the estimation of the fractional exponents α and β . These are intimately related to the self-similarity of the structures involved, and can be determined from the exponents of the renormalization group of kinetics of the particular system. This has to be

*Electronic address: cygnus@eunet.yu

done numerically for all but the simplest systems [4]. In our computations, we have employed a “building block” approach similar to that of [9], partitioning the phase space into several regions, each described with its own FKE, with the diffusion coefficient (2a) or (2b). However, instead of considering only ballistic flights and Markovian diffusion, as in [9], we propose the adoption of a set of (α, β) pairs. The values of the exponents can then be determined by sampling the flights (longer than a certain threshold T_0), and then fitting the distribution of their lengths and durations as $\ell^{-(1+\alpha)}$ and $t^{-(1+\beta)}$, respectively.

It is hardly surprising that we were unable to find the exact solutions for the FKE (1), with the diffusion coefficients (2a) and (2b), in their most general form. However, the long-term behavior can be found by expanding the space derivative on the right-hand side of (1) according to the generalizations of the Leibniz’s rule and chain rule for the fractional operator $d^\alpha/d|\ell|^\alpha$; see, e.g., [11] for mathematical details. For the case (2a), we obtain the solution, up to the normalization factor,

$$P(I, t) = E_\beta(-y_0^{4/\alpha} - y^{4/\alpha}) \mathcal{I}_1 \left(\frac{2e^{-y}}{\mathcal{D}_0^{3/2}} \sqrt{\frac{y_0}{t^\beta y}} \right), \quad (3)$$

where \mathcal{I} denotes the modified Bessel function of the first kind, $y(I, t) = |I|/[(\theta-2)\sqrt{\mathcal{D}_0 I^\theta t^\beta}]$, and $y_0 = y(I_0, t)$, with I_0 denoting the value of the action at $t=0$. The Mittag-Leffler function is denoted by E_β . For the Birkhoff case, one obtains

$$P(I, t) = \frac{y}{\sqrt{I}} E_\beta(-y_0^{4/\alpha} - y^{4/\alpha}) \mathcal{I}_p(2y_0 y), \quad (4)$$

with $p = (\theta-1)/(\theta-2)$. We note that, for $I, t \gg 1$, both y and y_0 tend to zero. The asymptotic expansions of the Mittag-Leffler and the Bessel function can then be used to show that the solutions $P(I, t)$ fall off in the infinity sufficiently sharply to be valid probability distributions. They are the main exact result of our analysis. We shall use them here to apply the more advanced building block model and to obtain the approximate scaling relations between the diffusion and Lyapunov time scales.

Convolution over all the solutions $(\star_{i=1}^N)$ can be performed in the usual way, with some entrance probabilities (actually, statistical weights of each block) p_i ,

$$P_{res}(I, t) = \star_{i=1}^N p_i P_i(I, t), \quad (5)$$

which give the resulting probability distribution $P_{res}(I, t)$. We propose this way for examining the behavior of particular systems. In the limit of infinitely many blocks [20], however, one can derive a generic relation between the short-time and long-time diffusion scales.

We next proceed to estimate the typical diffusion time scales. These can be related to the “escape times” one often encounters in simulations, e.g., [8]. Strictly speaking, the escape time can only be defined in open systems, as the time to cross the Lyapunov curve (see [13] for a definition). Otherwise, escape time is usually a more or less qualitative term meant to describe, generally, the time needed to enter a large connected chaotic region (“stochastic see”) or to experience

a qualitative change of dynamical behavior. In what follows, we shall consider the escape time as the time scale needed to reach a fixed I ; without loss of generality, we may assume $I=1$.

For fixed I , the solution (3) has a maximum about $2\sqrt{y_0}/(t^\beta y) \approx \mathcal{D}_0^{3/2}$. Solving this for time t , we obtain the estimate of the time to reach $I=1$,

$$T_{I=1} \approx \left(\frac{16(I/I_0)^{\theta-2}}{\mathcal{D}_0} \right)^{1/\beta}. \quad (6)$$

Similarly, (4) reaches its peak at $2yy_0 \approx 1$, which gives the following $T_{I=1}$:

$$T_{I=1} \approx \left(\frac{(I/I_0)^{1-\theta/2}}{(\theta-2)\mathcal{D}_0} \right)^{1/\beta}. \quad (7)$$

On the other hand, the short (microscopic) time scale of (1) is about $\mathcal{D}(I)/(\omega e^{\beta/\alpha})$, which may be interpreted as the average time between two “collisions;” in our case, this corresponds to a time needed to cross a single resonance, bearing in mind that resonance interactions and overlaps are the main physical mechanisms of transport. Moreover, this time scale is often considered to be a valid estimate of the Lyapunov time T_{Lyap} [1,3].

Let us now notice that the solutions (3) and (4), with their exit time scales (6) and (7), can be written in the form of Fox’s H functions [6]. By convolving these functions, one gets, after a straightforward but tedious calculation, a Fox’s function again, which may have two asymptotic behaviors. They scale with the short-time scale of (3) and (4) either as an exponential law or as a power law. The asymptotic behavior depends on the weights p_i and on the sum of transport exponents $2\beta_i/\alpha_i$ for each building block. Accepting this reasoning and inserting the above estimate for T_{Lyap} into (6) and (7), we obtain the approximate scalings for escape time T_{esc} ,

$$T_{esc} \propto \exp(T_{Lyap}^\kappa), \quad (8a)$$

$$T_{esc} \propto T_{Lyap}^\nu. \quad (8b)$$

Let us hold onto this result for a moment. The scaling of this type has been conjectured long ago (e.g., [14]), and it is implicitly suggested also by the classic work of Chirikov concerning the regimes of resonance nonoverlapping and overlapping [15] (the first one being known also as the Nekhoroshev regime). More recently, transition between the Nekhoroshev and Chirikov regime has been explored by Froeschle and others [16]. However, we show here that the scaling (8a) and (8b) arises from both basic regimes of chaotic dynamics, and that its type is determined also by the fractional exponents α and β of different building blocks. Physically, this means that the sticky (and thus non-Markovian) nature of self-similar structures in the phase space can “mimic” the effects of the resonance nonoverlapping. This is logical, since both phenomena effectively put a barrier into the transport channels. The scalings can be expected to be universal for a given system but are clearly nonuniversal for different systems, since they depend on the properties of the Hamiltonian. It should also be noted that, for N -dimensional ($N > 2$) systems, one should take into ac-

TABLE I. Hamiltonians of the form $H_{Int} + \epsilon H_{Pert}$ explored in the simulations. For each Hamiltonian, we give the integrable part H_{Int} , the perturbation part H_{Pert} , the range of the values of ϵ in the simulations, the exponents of the scalings κ and ν , and the range of the values of ϵ for the transition regime. Variables (I_i, ϕ_i) denote the action-angle variables, whereas (x, y, z) are the physical space coordinates. HO2 and HO3 denote the harmonic oscillator in two and three dimensions, respectively. HH2 and HH3 refer to the integrable Henon-Heiles Hamiltonian [13] in two and three dimensions: $(\dot{x}^2 + \dot{y}^2 + x^2 + y^2 - 2/3y^3)/2$ and $(\dot{x}^2 + \dot{y}^2 + \dot{z}^2 + x^2 + y^2 + z^2 - 2/3z^3)/2$, respectively. Hamiltonian H_8 is the egg-crate system taken from [4], H_9 is the sixth-order Toda lattice, i.e., the integrable Henon-Heiles system perturbed with its sixth-order expansion [1], and H_{14} is taken from [16]. See the text for further comments.

H	H_{Int}	H_{Pert}	ϵ	κ	ν	ϵ_{trans}
H_1	HO2	ϵxy	1.00–4.00	0.65 ± 0.07	0.87 ± 0.05	1.50–1.60
H_2	HO2	$\epsilon x^2 y$	0.87–3.50	0.45 ± 0.05	1.98 ± 0.06	1.28–1.32
H_3	HO2	$-\epsilon x^2 y^2$	1.50–6.00	1.09 ± 0.03	1.70 ± 0.04	3.32–3.70
H_4	HH2	ϵxy	0.00–3.50	0.77 ± 0.08	0.53 ± 0.03	0.15–0.20
H_5	HH2	$\epsilon x^2 y$	1.00–4.00	0.15 ± 0.03	1.25 ± 0.06	1.12–1.16
H_6	HH2	$-\epsilon x^2 y$	1.00–4.00	0.71 ± 0.05	0.88 ± 0.04	1.55–1.66
H_7	HH2	$-\epsilon / \sqrt{x^2 + y^2}$	0.00–3.50	0.33 ± 0.05	0.57 ± 0.03	1.60–1.70
H_8	$(\dot{x}^2 + \dot{y}^2)/2 + \cos x + \cos y$	$\epsilon \cos x \cos y$	0.00–2.00	0.22 ± 0.04	1.12 ± 0.08	0.34–0.37
H_9	HH2	sixth-order Toda lattice expansion	0.00–4.00	0.58 ± 0.03	1.44 ± 0.04	0.55–0.60
H_{10}	$I_1^2/2 + 2\pi I_2$	$\epsilon(\cos \phi_1 + \cos(\phi_1 - \phi_2))$	0.00–3.00	1.21 ± 0.04	1.82 ± 0.07	1.20–1.32
H_{11}	$I_1^2/2 + 2\pi I_2 + \cos \phi_1$	$\epsilon(\cos(\phi_1 - \phi_2) + \cos(\phi_1 + \phi_2))$	0.00–3.00	0.45 ± 0.05	1.75 ± 0.07	0.85–0.90
H_{12}	HO3	$\epsilon x^2 y z$	0.00–2.00	0.22 ± 0.03	0.57 ± 0.03	0.33–0.45
H_{13}	HH3	$\epsilon x z^2$	0.80–4.00	0.41 ± 0.04	1.03 ± 0.08	1.20–1.31
H_{14}	$(I_1^2 + I_2^2)/2 + I_3$	$\epsilon / (\cos \phi_1 + \cos \phi_2 + \cos \phi_3 + 4)$	0.000–0.100	0.19 ± 0.03	1.00 ± 0.04	0.055–0.060

count the Arnold diffusion. However, this should be negligible as long as the number of the degrees of freedom is sufficiently low, especially if we take into account a recent result which proves its superexponentially slow nature for a certain class of systems [17].

We have performed thorough numerical tests of our results, by integrating ensembles of particles initially placed in a cell of the phase space of the given Hamiltonian. We have inspected the behavior of the perturbed (quasi-integrable) Hamiltonian systems, i.e., of the form $H = H_{Int} + \epsilon H_{Pert}$, since the constant part of the diffusion coefficient \mathcal{D}_0 can then easily be estimated as ϵ^2 . We have observed the time evolution of the “distribution function,” i.e., concentration of the particles in the phase space, the escape times, and the scaling exponents [by fitting to (8a) and (8b)]. We have also calculated the finite time Lyapunov exponent (FTLE, see [18] for a definition), as the numerical estimate for $1/T_{Lyap}$. The escape time was measured as the time of crossing the Lyapunov curves, for open systems, or as the time of the beginning of the first long interval of normal diffusion, for the closed systems [21]. Details on the simulations and on the approximate scalings of the form (8a) and (8b) found numerically are summed up in Table I.

Figure 1 gives the comparison between the analytically and numerically obtained distribution functions, for each of the cases (3) and (4). Overall agreement can be seen, although it is not perfect. Typical results for the $T_{esc}(T_{Lyap})$ relation are shown in Fig. 2. Agreement with the predicted approximate scalings is good. The regimes are rather clearly separated and the transient regime is short, although it does exist. This behavior could be described as a phase transition between two regimes of chaotic transport, an idea which is not new for dynamical systems.

We are unable to explain the abrupt transition from one scaling regime into another, which occurs in most of our simulations, and resembles a phase transition. This kind of behavior could be better described by a discrete model. An obvious choice is a multiply branched tree (as proposed in [19]) or a network, with the transition probabilities derived from our results for the distribution functions. This would actually be a formalization of the building block model, which already (implicitly) includes a network of blocks.

In conclusion, we have proposed a method for obtaining (and solving) the kinetic equations of chaotic diffusion. The

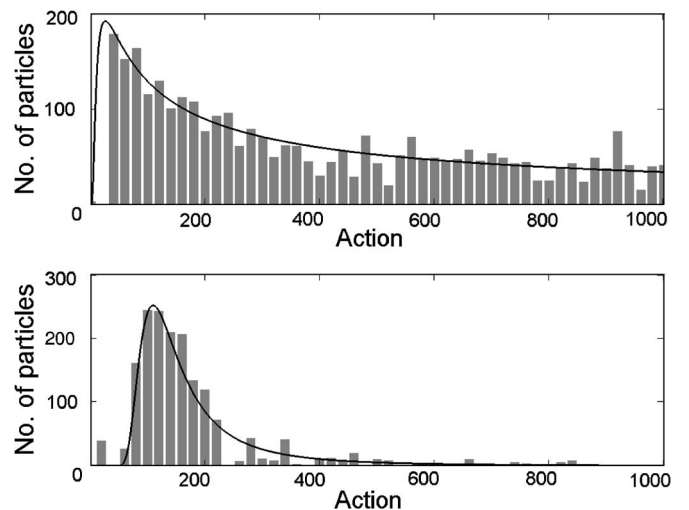


FIG. 1. Analytical (solid line) and numerical (histogram) distribution functions $P(I_1, t)$ for the Hamiltonian H_{14} . Action is in relative units. (a) Nonoverlapping resonances for $\epsilon=0.030$. (b) Overlapping resonances for $\epsilon=0.060$.

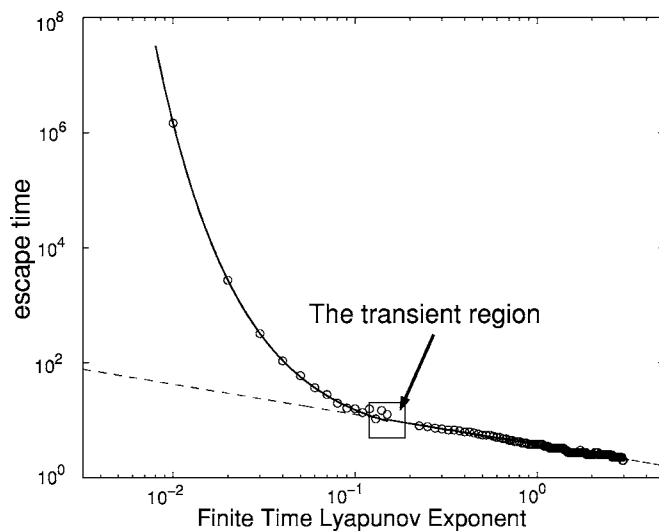


FIG. 2. An example of the scaling relations between finite time Lyapunov exponent and escape time. The solid lines denote the least-squares fit to the scaling relations (8). Scales are logarithmic on both axes, thus the power-law fit is a straight line. The dashed reference line for the power law is also shown, as well as the transient region. Time is in relative units from the simulation. The Hamiltonian is H_4 .

method is based upon using the normal forms of dynamics as the basic blocks of kinetics. In general case, some parameters of the model, including the fractional exponents of FKE, have to be computed from the simulations, as the current state of Hamiltonian theory does not allow us to estimate them from the dynamical equations, as noted also in [4]. We have also demonstrated a generic approximate scaling of the macroscopic diffusion time, often regarded to in simulations as escape time, with the Lyapunov (microscopic) time scale. We especially underline that both the power law and the exponential form of scaling can arise from both possible forms of the diffusion coefficient, and that the scaling behavior arises from combining the two, i.e., as a kind of collective behavior.

I am grateful to researchers from the Group for Nonlinear Optics, Institute of Physics, Belgrade, for discussions and support during the preparation of this paper and for the processor time for the simulations. I am also indebted to Robert S. MacKay, Harry Varvoglis, and George M. Zaslavsky for helpful comments, and for some of the references. Work at the Institute of Physics is supported by the Ministry of Science and Environment Protection, under Project No. OI 1475.

-
- [1] A. J. Lichtenberg and M. A. Lieberman, *Regular and Stochastic Motion* (Springer-Verlag, New York, 1983).
- [2] J. D. Meiss, *Rev. Mod. Phys.* **64**, 795 (1992).
- [3] G. Contopoulos, *Order and Chaos in Dynamical Astronomy* (Springer, Berlin, 2002).
- [4] G. M. Zaslavsky, *Phys. Rep.* **371**, 461 (2002).
- [5] J. Klafter, M. F. Shlesinger, and G. Zumofen, *Phys. Today* **49**, 33 (1996).
- [6] R. Metzler and J. Klafter, *Phys. Rep.* **339**, 1 (2000).
- [7] G. M. Zaslavsky, *Physica D* **168-169**, 292 (2002).
- [8] I. I. Shevchenko, *Phys. Lett. A* **241**, 53 (1998); J. Aguirre, J. C. Vallejo, and M. A. F. Sanjuan, *Phys. Rev. E* **64**, 066208 (2001); J. Aguirre and M. A. F. Sanjuan, *ibid.* **67**, 056201 (2003).
- [9] S. Denisov, J. Klafter, and M. Urbakh, *Phys. Rev. E* **66**, 046217 (2002).
- [10] A. Morbidelli and M. Vergassola, *J. Stat. Phys.* **89**, 549 (1997).
- [11] I. Podlubny, *Fractional Differential Equations* (Academic, New York, 1998); A. I. Saichev and G. M. Zaslavsky, *Chaos* **7**, 753 (1997).
- [12] G. M. Zaslavsky, *Physica A* **288**, 431 (2000).
- [13] H. E. Kandrup, C. Siopis, G. Contopoulos, and R. Dvorak, *Chaos* **9**, 524 (1999).
- [14] A. Morbidelli and C. Froeschle, *Celest. Mech. Dyn. Astron.* **63**, 227 (1996).
- [15] B. V. Chirikov, *Phys. Rep.* **52**, 265 (1979).
- [16] C. Froeschle, M. Guzzo, and E. Lega, *Science* **289**, 2108 (2000); M. Guzzo, E. Lega, and C. Froeschle, *Physica D* **163**, 1 (2002).
- [17] A. Morbidelli and A. Giorgilli, *J. Stat. Phys.* **78**, 1607 (1997).
- [18] N. Voglis and G. Contopoulos, *J. Phys. A* **27**, 4899 (1994).
- [19] J. D. Meiss and E. Ott, *Physica D* **20**, 387 (1986).
- [20] This should be realistic for most systems, since each block, in a typical case, actually has a multifractal structure [12], which is analogous to consisting of many “sub-blocks,” each one having different fractional exponents.
- [21] The length of this interval has to be determined empirically. It should warrant that the particle has entered the large connected stochastic sea, so that the probability that the particle is trapped again is very low.

Semistiff polymer model of unfolded proteins and its application to NMR residual dipolar couplings

M. Čubrović^{1,2}, O.I. Obolensky^{1,a}, and A.V. Solov'yov^{1,b}

¹ Frankfurt Institute for Advanced Studies, Ruth-Moufang-Str. 1, 60438 Frankfurt am Main, Germany

² Institute of Physics, P.O. Box 57, 11001 Belgrade, Serbia

Received 14 March 2008 / Received in final form 15 September 2008 / Published online 15 October 2008
© EDP Sciences, Società Italiana di Fisica, Springer-Verlag 2008

Abstract. We present a new statistical model of unfolded proteins in which the stiffness of polypeptide backbone is taken into account. We construct and solve a mean field equation which has the form of a diffusion equation and derive the distribution function for conformations of unfolded polypeptides. Accounting for the stiffness of the protein backbone results in a more accurate description of general properties of a polypeptide chain, such as its gyration radius. We then use the distribution function of a semistiff protein within a previously developed theoretical framework [J. Biomol. NMR **39**, 1 (2007)] to determine the nuclear magnetic resonance (NMR) residual dipolar couplings (RDCs) in unfolded proteins. The calculated RDC profiles (dependence of the RDC value on the residue number) exhibit a more prominent bell-like shape and a better agreement with experimental data as compared to the previous results obtained with the random flights chain model.

PACS. 87.10.-e General theory and mathematical aspects – 82.56.Pp NMR of biomolecules – 82.56.Dj High resolution NMR

1 Introduction and motivation

High-resolution, liquid-state nuclear magnetic resonance (NMR) spectroscopy has proven to be an invaluable tool in investigation of the structure and dynamics of biomacromolecules, including folded and, recently, unfolded proteins. One of the NMR observables from which one can infer structural and dynamical information is the so-called residual dipolar couplings (RDCs) [1]. These couplings are direct dipole-dipole interactions between the spins of two nuclei, e.g., ¹⁵N and a ¹H nuclei, detected in NMR experiments by a shift in the resonant frequency of nuclear spin flip transitions. They can be measured independently for each amino acid residue in a polypeptide chain.

Analysis of RDC profiles (dependence of the RDC value on the residue number) has been shown to be very informative in structure validation and refinement of folded proteins [1]. However, for unfolded proteins reliable interpretation of RDC measurements remains elusive even though a significant amount of experimental data has been accumulated (see [2] for a survey). Theoretically, one can predict the RDC profiles by performing numeri-

cal sampling of the conformational space of the unfolded polypeptide. For example, in [3,4] ensembles of unfolded conformations were constructed from amino acid-specific distributions of Ramachandran angles ϕ/ψ taken from the loop regions of high-resolution X-ray structures in the protein data base. This method allows one to predict the RDC profiles with a reasonable accuracy, but it lacks the ability to explain on a basic level the obtained results, serving, therefore, as a black box with a limited use for interpretation of experimental data.

In [2] it was shown that the basic trends in RDC profiles and the underlying physical and mathematical principles leading to these trends can be revealed by statistical analysis not based on numerical sampling of conformational space (see also similar, although less mathematically rigorous, work [5]). Two general features of RDC profiles were predicted for unfolded polypeptide chains. The first one is that shorter chains have larger (in absolute value) RDCs under same experimental conditions. The second feature predicted in [2,5] is that the RDCs are larger for the amino acid residues in the middle of the chain, leading to the bell-like shape of RDC profiles. Despite the simplicity of the model (random flights chain) used in [2,5] to mimic the unfolded polypeptides, both these trends seem to be present in the experiments carried out under conditions prohibiting formation of native-like structures [2].

^a Present address: National Center for Biotechnology Information, NLM/NIH, 8600 Rockville Pike, Bethesda, MD 20894, USA

^b e-mail: solovyov@fias.uni-frankfurt.de

Our goal in this paper is to improve the quality of the model which is used for simulating the unfolded polypeptide chain. We formulate here a new statistical model of unfolded proteins in which the stiffness of polypeptide backbone is taken into account. We demonstrate that accounting for the stiffness of the protein backbone results in a more accurate description of general properties of a polypeptide chain, such as its gyration radius.

Stiff polymer model is a well-known concept in polymer physics, much used since the pioneering paper of Sato et al. [6]. The idea is to introduce an energy cost for bending of the polymer, thus favoring the extended conformations. The most versatile formalism for doing so is the so-called wormlike chain model, in which the bending energy density is proportional to the square of the curvature of the polymer contour. It has been developed to its full strength only recently [7], with the introduction of new theoretical tools to account for various generalizations and boundary conditions. The starting point in the papers cited above is the mean-field description which has the form of a diffusion equation in tangent space. However, this approximation becomes less and less satisfactory for polymers with low stiffness [8]. We show in this paper (followed by a more technical discussion in [9]) that a better continuum limit for the case of low stiffness is obtained in the real space, which turns out to have, again, the form of the diffusion equation. Also, the question of how the wormlike chain model arises from discrete stiff chains has, to the best of our knowledge, not been addressed so far. In the following section we will start from a discrete model and pass to a continuum limit, which will turn out to be exactly the low-stiffness (the usual term in polymer physics is semiflexible or semistiff) limit of the wormlike chain model.

The developed semistiff polymer model is applied to the calculation of RDCs within the theoretical framework of [2]. The calculated RDC profiles exhibit a more prominent bell-like shape and a better agreement with experimental data as compared to the previous results obtained with the random flights chain model.

In the concluding section, we will also discuss possible further steps in interpreting the RDC measurements, as well as the importance of our results from a more general perspective.

2 Theory

2.1 Introduction to the problem

We first give a general and informal consideration of the problem, before describing in more detail the interaction potential in our system and the procedure to calculate the necessary quantities. The ultimate goal is finding the relation between the dipolar couplings and the physical parameters of the unfolded polypeptide, and extracting the information on the shape and other properties of the polypeptide from the RDC measurements. Unfolded polypeptides are in many aspects similar to simple linear polymers, having no well-defined secondary structure.

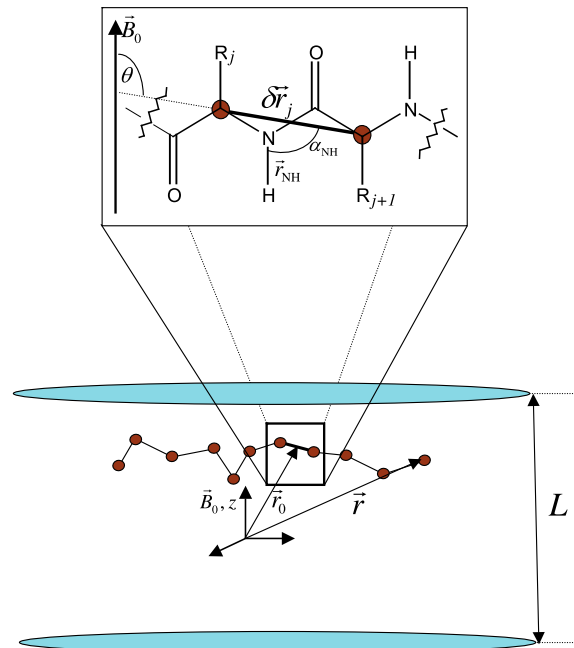


Fig. 1. Schematic picture of a polymer chain in a restricting medium modelled with a set of parallel barriers. The barrier-to-barrier distance is L . External magnetic field vector is $B_0\mathbf{e}_z$. The vectors \mathbf{r} and \mathbf{r}_0 are the position vectors of points in the chain, defined in the fourth section. Inset: structure of a single monomer unit. The angles α_{NH} and Θ are defined for each segment. The residues (side chains) are denoted by R_j and R_{j+1} , while the radius vector of the j th segment is $\delta\mathbf{r}_j$.

For clarity we will pose the problem for a discrete chain first, although the calculations will be performed in the continuum limit. The quantity to be calculated is the dipole-dipole coupling between two nuclei. We will deal with the $^{15}\text{N}-^1\text{H}$ couplings in this paper. The energy (actually, the frequency) of the coupling is given by [2]:

$$D_{\text{NH}} = \frac{\mu_0 \hbar \gamma_{\text{N}} \gamma_{\text{H}}}{4\pi^2 r_{\text{NH}}^3} P_2(\alpha_{\text{NH}}) \langle P_2(\cos \Theta) \rangle, \quad (1)$$

where μ_0 is the magnetic permeability constant, γ_{N} and γ_{H} are gyromagnetic ratios for the nitrogen and the hydrogen nucleus and r_{NH} is the internuclear distance (assumed to be fixed). The function P_2 stands for the Legendre polynomial of the second order. The angles α_{NH} and Θ characterize the orientation of a chain segment with respect to the external field. These are in turn determined by the conformation of the chain, therefore connecting the measured couplings to the structure of the polypeptide. The average (denoted by angular brackets) is to be carried out over all possible conformations of the chain, i.e. over the state space of the chain.

The meaning of the angles α_{NH} and Θ is best seen from Figure 1. The former is the angle between the vector \mathbf{r}_{NH} , i.e. the internuclear vector, and the axis of the j th segment, denoted in Figure 1 by $\delta\mathbf{r}_j$. On the other hand, Θ stands for the angle between $\delta\mathbf{r}_j$ and the z -axis, which is the direction of the external magnetic field.

The origin of non-zero RDCs lies in the restricting medium (bicelles or polyacrylamide gels, usually) in which the denaturated protein is solvated in experiments. Actual shape and geometry of the confining barriers may vary but the overall effect will be similar and will result in an effective confinement of the polymer. In the simplest approximation, one may regard the restricting barriers to be parallel to each other, at some distance L , as given in the Figure 1. The influence of the confinement is crucial even if the distance L is large compared to the length of the polypeptide (as is the case for typical experimental conditions). Confinement only induces a mild “deformation” of the average shape of the polypeptide coil. It is this deformation, however, which gives rise to non-zero expectation value of the term $P_2(\cos\Theta)$. The calculation of this value will be in focus of the rest of the paper.

2.2 Stiffness of polypeptide chain

The discrete chain is represented as an array of N segments, each denoted by index $j = 1 \dots N$. The information on structure of the chain is contained in the distribution function $P(N, \mathbf{r}, \mathbf{r}_0)$ which gives probability to find the chain in a conformation with the end points at \mathbf{r}_0 and \mathbf{r} . The usual approach of polymer physics would be to write the action (or, equivalently, path integral) for the chain based on some empirical potential [10]. As we will, for the most part, work in the mean-field approximation, we will refrain from this approach and write directly the equation for the distribution function. The statistical weight of each conformation is determined by its Boltzmann weight, supposing that the system is sufficiently close to equilibrium. To specify these weights completely, one needs to employ an empirical potential for segment-to-segment interactions.

Empirical potentials for polypeptides, generally, may include the following terms: bond extensibility, bond angle stiffness, rotation about the so-called Ramachandran dihedral angles (see, e.g., [11]) and non-bonded interactions, including, possibly, Coulombic interactions, hydrogen bonds, excluded volume interactions, etc. We will deal with the non-bonded interactions in a separate publication [12]; it can be shown that these do not contribute significantly to the problem of interpreting the NMR spectroscopic data that we are primarily concerned with in this paper. Bond extensibility is, in general, negligible in polypeptides and better results are usually obtained in the framework of fixed bond lengths [13]. So, all of our segments are assumed to have the same length a .

The stiffness is an all-present effect in polymer physics and is usually characterized either by the persistence length L_p [10] or in terms of the bond angle θ and its discrepancies from some optimal value θ_0 [14]. The connection between the two descriptions is given by $L_p = ak_\theta\beta$; as usual, $\beta = (kT)^{-1}$. In our model, for typical values of k_θ and β , L_p is a few segments long. However, L_p is not very practical for nonzero θ_0 . Geometrically, it is equal to the segment length of an effective freely jointed chain

with the same macroscopic properties as the stiff chain. This geometric analogy is lost for $\theta_0 > 0$.

For most polymers, the optimal angle is $\theta_0 = 0$; in our case, the structure of polypeptide backbone $-\text{N}-\text{C}-\text{C}-\text{N}-$ results in a non zero value of θ_0 [11], which is actually the tetrahedral angle characterizing the bond geometry of the carbon atom. The radius-vector of the j th segment relative to the end of the previous segment will be denoted by $\delta\mathbf{r}_j$. The bond stiffness is obviously a nearest-neighbor interaction, involving pairs of subsequent segments. Dihedral angles are for *unfolded* polypeptides usually considered in a purely local approximation, thus leading to no site-to-site interaction. Therefore, the potential of our system is of the form:

$$V = \sum_{j=1}^{N-1} V_\theta(\theta_j) + \sum_{j=1}^N V_{\phi\psi}(\phi_j, \psi_j). \quad (2)$$

Still, even in this approximation, distribution of dihedral angles shows nontrivial behavior if the polypeptide is not a homopolymer, i.e. if various segments have different energy minima. One final remark is that we assume various degrees of freedom to be decoupled; it is also a common approximation, and a necessary one for the problem to be tractable.

The Ramachandran part of the potential, $V_{\phi\psi}$, cannot be treated in the mean-field approximation for the reason mentioned in the previous paragraph: the energy landscape is strongly site-specific and therefore evades a description in the framework of mean-field theory. On the other hand, the decoupling of the degrees of freedom suggests that the effects of stiffness can be considered independently. In this paper, we will explore exactly the influence of stiffness, leaving the theory for Ramachandran angles for further work.

Hence, we are only interested for the potential V_θ . An often-employed potential in both analytical and numerical work, with slight differences from author to author, described in [14], is the following one:

$$V_\theta(\theta_j) = -k_\theta \cos(\theta - \theta_0) + O\left((\theta - \theta_0)^3\right). \quad (3)$$

The correction to the cosine term in (3) can be any function which is “small” compared to the leading term in the cosine, i.e. containing only third and higher order terms in the angular displacement $\theta_j - \theta_0$. It will turn out later that these corrections are, in our method, of secondary importance anyway, so the exact form of this correction is not relevant. In other words, the exact form of the anharmonic terms is not relevant; a different form would produce different higher-order terms for the diffusion coefficient but these are (by definition) beyond the scope of any model based on diffusion equation.

In the following subsection, we will give our mean-field model for a semistiff (semiflexible) chain. For some purposes the mean-field treatment can provide sufficiently accurate estimates and it is also of interest for other problems, not connected to protein physics.

2.3 Diffusion equation formalism for semistiff polymers

For the rest of this paper, we will take the continuum limit. The index of a segment in the chain (chemical coordinate s) is now a variable taking values from the interval $(0, N)$, where N is the total segment number. This framework is, of course, only suitable for the chains which are not too short.

The formalism we employ here is best suited for small stiffness; typical values of k_θ in (3) are of the order of 10ϵ , with $\epsilon = 10^{-23}$ J (0.624×10^{-4} eV), which is small compared to systems like double-stranded DNA.

One can start from the statistical weight of the j th segment having a bond angle θ_j expressed in terms of its radius-vector $\delta\mathbf{r}_j$:

$$p_0(\delta\mathbf{r}_j) = \frac{\beta k_\theta}{4\pi a^2 \sinh \beta k_\theta} \delta(\delta r_j - a) \exp(\beta k_\theta \cos \theta_j). \quad (4)$$

The above equation is nothing but the Boltzmann weight with appropriate normalization. Since the experiments with unfolded proteins are usually performed at room temperature, we take $T = 300$ K for all calculations throughout the paper. In other words, the chain is modelled as a random walk with one-step memory (which is implicitly included in (4) via the bond angle depending on the previous segment). It is a variation on the persistent random walk problem, well-known and often encountered in theory of stochastic processes [15]. The usual formalism of master equations leads to the conclusion that the continuum limit of this process is a diffusion equation; we show that in more detail in a separate publication [9].

For a three-dimensional model, diffusion coefficient becomes the diffusion tensor $\hat{\mathcal{D}}$ represented with a three-by-three matrix, the component \mathcal{D}_{ij} being, by definition:

$$\mathcal{D}_{ij} = \frac{1}{2} \int d\delta\mathbf{r} p_0(\delta\mathbf{r}) \delta r_i \delta r_j. \quad (5)$$

A straightforward calculation then shows that the off-diagonal components vanish; furthermore, the two ‘‘transversal’’ components (perpendicular to the tangent vector at the given point) are equal and will be denoted by \mathcal{D}_\perp ; the ‘‘longitudinal’’ one is denoted by \mathcal{D}_\parallel . They are obtained to be:

$$\mathcal{D}_\perp = \frac{a^2}{\sinh \beta k_\theta} \left(\frac{\cosh \beta k_\theta}{\beta k_\theta} - \frac{\sinh \beta k_\theta}{\beta^2 k_\theta^2} \right) \quad (6)$$

$$\mathcal{D}_\parallel = \frac{a^2 \cos^2 \theta_0}{\sinh \beta k_\theta} \left(\frac{\sinh \beta k_\theta}{\beta^2 k_\theta^2} + \frac{\sinh \beta k_\theta}{2} - \frac{\cosh \beta k_\theta}{\beta k_\theta} \right). \quad (7)$$

The above result was derived by rotating the diffusion tensor in the local tangent coordinate system. The higher order terms can be included to modify the cosine potential, by means of perturbative corrections (so-called higher-order correlation terms) to the diffusion coefficient. The full formalism for computation of these corrections can be found in [16]. For example, the harmonic potential for the

bond angle, also often employed [14] in various models, can be modelled in this way. Let us right away define also the coefficient $\mu \equiv 2\mathcal{D}_\perp/\mathcal{D}_\parallel$, as we will use it throughout the paper.

The non-isotropic diffusion tensor gives rise to the following diffusion equation:

$$\frac{\partial P}{\partial N} = \mathcal{D}_\parallel \frac{\partial^2 P}{\partial r^2} + \frac{2\mathcal{D}_\parallel}{r} \frac{\partial P}{\partial r} + \frac{\mathcal{D}_\perp}{r^2} \Delta_{S^2} P, \quad (8)$$

where Δ_{S^2} is the angular part of the Laplacian in spherical coordinates, i.e., the two-dimensional Laplace-Beltrami operator.

We first look for a fundamental solution (in terminology of the theory of partial differential equations), i.e. for a solution in the whole space, vanishing at the infinity and starting at \mathbf{r}_0 , leading to the initial-boundary condition $P(0, \mathbf{r}, \mathbf{r}_0) = \delta(\mathbf{r} - \mathbf{r}_0)/4\pi$. Then one can use well-developed tools for solving diffusion equations. The easiest way is to rewrite (8) as the Schrödinger equation in imaginary time for a particle in a spherical potential given by $U(r) = \ell(\ell+1)(\mu/2-1)/r^2$. It is easy to see that $U(r)$ defined in this way is a well only for $\mu < 2$, i.e. for $\mathcal{D}_\perp < \mathcal{D}_\parallel$, otherwise, it is repulsive. The physical interpretation of this fact is that the diffusion with large \mathcal{D}_\perp corresponds to the states with high angular momenta (notice the position of \mathcal{D}_\perp in (8)). But since arbitrarily high angular momenta are only possible for unbounded states, this means the the imaginary time description of the diffusion corresponds to a particle in a repulsive potential. Conversely, when \mathcal{D}_\parallel dominates over \mathcal{D}_\perp , the primary contribution to the energy comes from the radial part of the Laplace operator; hence, angular momentum cannot be arbitrarily high, which is consistent with a bounded state in a potential well.

However, one can use the same eigenbasis for both of the above cases; only the coefficients of the expansion will be different. The eigenfunctions of the radial part of the equation read as:

$$u_1(\ell, \mathcal{E}, r) = \frac{C_1(\ell, \mathcal{E})}{\sqrt{r}} J_\kappa \left(-\sqrt{\frac{\mathcal{E}}{\mathcal{D}_\parallel}} r \right) \quad (9)$$

$$u_2(\ell, \mathcal{E}, r) = \frac{C_2(\ell, \mathcal{E})}{\sqrt{r}} Y_\kappa \left(-\sqrt{\frac{\mathcal{E}}{\mathcal{D}_\parallel}} r \right), \quad (10)$$

with $\kappa = [1/4 + \mu\ell(\ell+1)/2]^{1/2}$, and correspond to the states of definite energy \mathcal{E} and angular momentum ℓ of the particle. The Bessel functions of the first (second) kind are denoted by J_α and Y_α . Right away we see that $C_2 = 0$ for all \mathcal{E} and ℓ , as the Bessel functions of the second kind diverge at short distances. Hence, only the (9) states contribute to the solution.

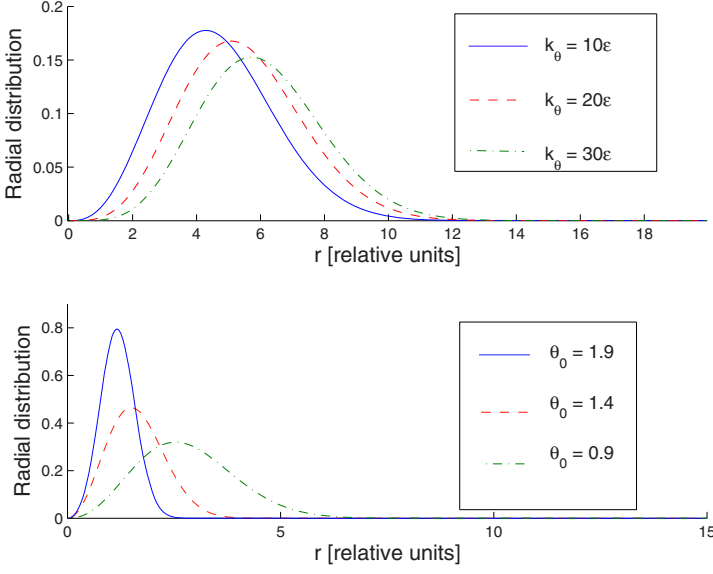


Fig. 2. (Color online) Top – radial distribution functions $P(N, r)$ for various values of stiffness, with $\theta_0 = 1.9$. Bottom – radial distribution functions $P(N, r)$ for various values of θ_0 , with $k_\theta = 50\epsilon$. The length of the chain $N = 50$.

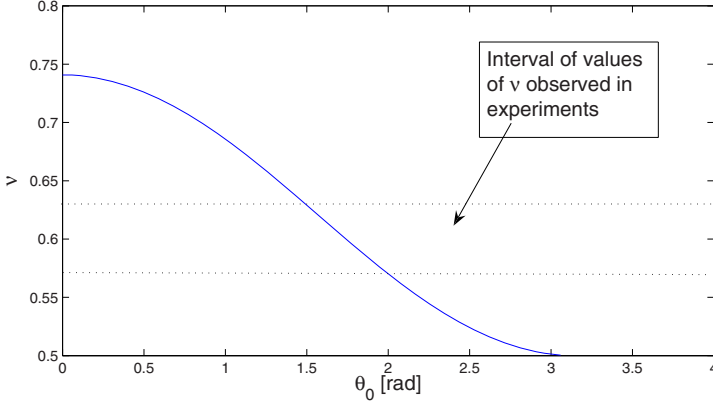


Fig. 3. Dependence of the scaling exponent ν for the gyration radius on θ_0 . We have set $k_\theta = 20\epsilon$. The dashed lines denote the interval of the gyration radii measured experimentally in unfolded polypeptides (about 0.6). The exponent ν is defined through the scaling relation $\langle R_g^2 \rangle \propto N^{2\nu}$.

The solution that satisfies our boundary conditions is then obtained by standard methods and reads as:

$$P_\ell(N, \mathbf{r}, \mathbf{r}_0) = C_n(\kappa, N) \left(\frac{r}{r_0} \right)^{2\kappa+1/2} \frac{1}{\mathcal{D}_\parallel N} \times \exp \left(-\frac{r^2 + r_0^2}{4\mathcal{D}_\parallel N} \right) \mathcal{I}_\kappa \left(\frac{|\mathbf{r} \cdot \mathbf{r}_0|}{2\mathcal{D}_\parallel N} \right), \quad (11)$$

where \mathcal{I} stands for the modified Bessel function of the first kind. The normalization constant $C_n(N)$ is equal to:

$$C_n(\kappa, N) = 3\pi 2^{2+\kappa} \kappa (\mathcal{D}_\parallel N)^{1+\kappa/2} \Gamma(1+\kappa) \Gamma(3\kappa/2) \times {}_1F_1 \left(1 + 3\kappa/2, 1 + \kappa, \frac{r_0^2}{4\mathcal{D}_\parallel N} \right), \quad (12)$$

with ${}_1F_1(a, b, x)$ denoting the confluent hypergeometric function of its arguments (see [17] for a definition). We obtain the above result by expanding (11) into power series, integrating and resumming. Dependence of the normalization constant on N and κ is explicitly written, as this dependence will play a role

in later sections. The large- N asymptotic form of $C_n(\kappa, N)$ reads as:

$$C_n(\kappa, N) \approx 3\pi 2^{2+\kappa} \kappa (\mathcal{D}_\parallel N)^{1+\kappa/2} \times \Gamma \left(\frac{3\kappa}{2} \right) \left(1 + \frac{3\kappa + 2}{2\kappa + 2} \frac{r_0^2}{4\mathcal{D}_\parallel N} \right). \quad (13)$$

We will need this asymptotic form later on. Notice that the normalization constant is dependent on N , as one would expect. The solution explicitly depends on ℓ . It is actually the sum of all partial waves (characterized by the value of ℓ) that provide a solution of finite norm (i.e. no scattering to infinity, which would correspond to the “blowup” of the chain) and finite localization radius (i.e. no “falling to the center”, which would correspond to the collapse of the chain).

To understand better the general properties of the model, it is helpful to analyze the behavior of the solution (11) depending on the parameters k_θ and θ_0 . We will first discuss the radial distribution function $P(N, r)$, defined as $\int \int d\phi d\theta \sin \theta r^2 P(N, \mathbf{r}, \mathbf{r}_0)$. The results for selected values are given in Figure 2. It is seen that in the whole physically sensible range of parameters, the stiffness

k_θ , once it moves away from zero, only mildly flattens the distribution function. On the other hand, the bending angle does influence it significantly. An informal explanation is that letting k_θ grow, provided it is neither too close to zero nor too large, results in less bending of the chain but (as k_θ is not very large) the chain still does bend relatively often and still has the shape of a slightly flattened sphere; therefore, various parts of the chain still propagate in almost uncorrelated directions and it is not very important how long (on average) they are. On the other hand, large preferential angle θ_0 brings a systematic effect, which accumulates and substantially changes the shape of the chain.

It is also instructive to look at the behavior of the gyration radius (expectation value of the squared distance from the center of mass of the polymer), given in Figure 3. As one could expect, it grows significantly with θ approaching zero, as in that case, the most extended configurations are preferred. This case agrees with the equations for the gyration radius cited in [10]. On the other hand, for values of θ_0 close to π , the chain, on a macroscopic scale, behaves almost as a Gaussian freely jointed chain, hence ν approaches its Gaussian value 0.5. The gyration radius for the continuum limit in the case of non-zero θ_0 has, to the best of our knowledge, not been addressed so far. The plot in Figure 3 shows the range of the preferential bond angle values that correspond to the experimental result, $\nu \approx 0.6$ [3]. This range roughly corresponds to the value of θ_0 suggested by the geometry of bonds in polypeptides: $\theta_0 \approx 1.8$ radians [14]; in our calculations, we use $\theta_0 = 1.83$ radians. Hence, our model is able to reproduce the observed scaling exponent of the gyration radii and allows us to conclude that the proximity of its value to the scaling exponent ν_{saw} of the self-avoiding random walk ($\nu_{saw} \approx 0.59$) is pure coincidence. The distribution of bond angles (which are dominant degrees of freedom in terms of typical energies and time scales) alone accounts for the gyration radius scaling, whereas the self-avoidance (together with other non-bonded interactions) only produces small corrections (for more details see [12]).

3 The calculation of RDC values

3.1 Basic considerations

Having described our model of unfolded polypeptides, we now turn to the calculation of RDC values. The general theory is given in [2] and the basic idea is also mentioned in the introduction section of this paper. Here we discuss the more formal aspects of the procedure and state the results.

We will consider the simplest model, in which the restricting medium is modelled as a set of parallel planar absorbing barriers at the distance L from each other, as shown in Figure 1 [2]. This effectively means that all the paths which intersect the barrier are removed from consideration. The exact solution with these boundary conditions is difficult to find; therefore, we resort to the method

of images, common in problems such as diffusion and electrostatics [19]. Staying at the first order approximation, the solution reads as [2]:

$$f(N, \mathbf{r}, \mathbf{r}_0) = P(N, \mathbf{r}, \mathbf{r}_0) - P(N, \mathbf{r}', \mathbf{r}_0) - P(N, \mathbf{r}'', \mathbf{r}_0), \quad (14)$$

with \mathbf{r}' and \mathbf{r}'' being the points symmetric to \mathbf{r} with respect to the barriers, and $f(N, \mathbf{r}, \mathbf{r}_0)$ denoting the probability density function for the appropriate boundary conditions (whereas P stands for the fundamental solution in the whole space).

As can be seen from the defining expression, the RDC of the j th segment is determined by the value of the angle Θ of the $C_j^\alpha - C_{j+1}^\alpha$ segment with respect to the direction of the magnetic field. Therefore, we wish to find the distribution function for this angle, denoted $f(\Theta)$. As elucidated in more detail in [2], $f(\Theta)$ equals the joint cumulative distribution for a chain of length j starting at $\mathbf{r}_j - \delta\mathbf{r}_j/2$ and reaching some position \mathbf{r}_{01} , and a chain of length $N - j$ starting at $\mathbf{r}_j + \delta\mathbf{r}_j/2$ and ending at some position \mathbf{r}_{02} . Cumulative distribution, by definition, enumerates the states with prescribed position of one end of the chain ($\mathbf{r} \pm \delta\mathbf{r}_j/2$), independently of the coordinate of the other end (\mathbf{r}_{01} or \mathbf{r}_{02}). Therefore, for $C(N, \mathbf{r})$ we have, in general:

$$C(N, \mathbf{r}) = \int d\mathbf{r}_0 f(N, \mathbf{r}, \mathbf{r}_0). \quad (15)$$

At this point, one should notice that the dependence of the cumulative distributions on x and y vanishes due to symmetry. We may therefore denote them by $C(N, z)$. Integrating over the initial positions of the chains, \mathbf{r}_{01} and \mathbf{r}_{02} , we arrive at the following equation for $f(\Theta)$:

$$f(\Theta) \propto \int_{-L/2}^{L/2} dz C\left(j, z - \frac{a \cos \Theta}{2}\right) \times C\left(N - j, z + \frac{a \cos \Theta}{2}\right), \quad (16)$$

where the proportionality constant is easy to determine from the previous equations, keeping track of all constant factors from the beginning. We have exploited the fact that the segment lengths are all equal ($|\delta\mathbf{r}_j| = a$), as well as the definition of the angle Θ .

3.2 Angular averaging: elementary method

The final step is performing the necessary integrations, i.e., calculating the average over $f(\Theta)$. Conceptually the simplest way of doing this is expanding (16) in a power series and integrating it term by term. This is the most feasible way for obtaining quick, low-accuracy estimates. We first sketch this method.

One starts by expanding the cumulative distribution functions in powers of $a \cos \Theta$. The odd terms obviously vanish. The even terms are then integrated by parts bearing in mind the fact that the distribution $f(N, \mathbf{r}, \mathbf{r}_0)$ vanishes at the boundaries due to confinement. The averaging

in equation (1) is then readily performed. The result up to the fourth order in a has the form:

$$D_{\text{NH}} = KP_2(\alpha_{\text{NH}}) \times \left[B - \frac{3}{8} \frac{C_n(\kappa, N_1)C_n(\kappa, N - N_1 - 1)}{C_n(\kappa, N)} a^2 - \frac{1}{384} \frac{C_n(\kappa - 1, N_1)C_n(\kappa - 1, N)}{C_n(\kappa, N)} a^2 + \frac{1}{64} \frac{C_n(\kappa - 1, N_1)C_n(\kappa - 1, N - N_1 - 1)}{C_n(\kappa - 1, N)} a^4 \right]. \quad (17)$$

The constant K is defined in (1) and reads as:

$$K = \frac{\mu_0 \hbar \gamma_{\text{N}} \gamma_{\text{H}}}{4\pi^2 r_{\text{NH}}^3}. \quad (18)$$

The constant term B in (17) is small (about two orders of magnitude smaller than the a -dependent terms) and we ignore it in our calculations. When calculating D_{NH} , we have used the asymptotic form for the normalization constant, as given in (13). Bearing in mind the limited accuracy of our formalism (simple toy-model potential, mean-field approach, etc.), one may safely ignore also the quartic term, as well as the second quadratic term (due to its large denominator). We have found for the examples below that this approximation leads to insignificant changes of the computed RDC curves.

3.3 Angular averaging: advanced method

A more elaborate but substantially more general scheme, allowing in principle calculations of arbitrarily high accuracy, is based upon the formalism of quantum theory of angular momentum. We again start from (16), which is the exact result (not approximate, like the series expansion subsequently performed in the previous subsection). The idea is to refrain from using the closed-form solution (11) and use the series expansion of $P(N, \mathbf{r}, \mathbf{r}_0)$ over the radial eigenfunctions (9) and spherical harmonics. The former is more convenient and more informative for most purposes but the latter allows us to use numerous identities of the angular momentum theory to obtain simpler expressions for the average of $P_2(\cos \Theta)$.

The starting point is the solution in the whole space:

$$P(N, \mathbf{r}, \mathbf{r}_0) = \sum_{\ell=0}^{\infty} A_{\ell} R_{\ell}(N, |\mathbf{r} - \mathbf{r}_0|) P_{\ell}(\cos \theta), \quad (19)$$

where A_{ℓ} are the appropriate coefficients determined by the eigenfunctions (9), R_{ℓ} are radial functions, obtained by integrating the eigenfunctions over the “energy” variable \mathcal{E} , and θ is the azimuthal angle. Reflections in the planes $z = \pm L/2$, which give the image solutions, are then readily obtained in the form $\hat{\mathcal{R}}_{\pi, \mathbf{e}_z} \hat{P}_{\pm \frac{L}{2}, \mathbf{e}_z} P(N, \mathbf{r}, \mathbf{r}_0)$, which is easy to prove from elementary considerations. The operators denote the rotation for a given angle about the given

axis, spatial inversion and spatial translation for a given vector, in that order. The rotation for π about the z -axis and the spatial inversion act upon the angular part simply by multiplying it with $(-1)^{\ell}$. Only the translation has a nontrivial action. A lengthy calculation, making use of the Wigner functions and identities with Clebsch-Gordan coefficients as given in [20], results in:

$$P_{\ell}(\theta', \phi) = K_{\ell} \sum_{\lambda=0}^{\infty} (-1)^{\lambda+\ell} f_r(\lambda, \ell, r) \times \sum_{\Lambda=|\ell-\lambda}^{\ell+\lambda} \frac{(2\ell+1)(2\lambda+1)}{2\Lambda+1} |\langle \Lambda 0 | \ell 0 \lambda 0 \rangle|^2. \quad (20)$$

For the left image, where we have introduced the notation:

$$K_{\ell} = \sum_{j=0}^{\ell} \left(-\frac{L}{2} \right)^{\ell-j} \sqrt{2(\ell-j)-1} \frac{(\ell+j)!}{(\ell-j)!} \times \left[\frac{(2\ell)!(2j)!}{(2\ell+2j)!} \right]^{1/2}, \quad (21)$$

$$f_r(\lambda, \ell, r) = \frac{(2rL)^{\ell}}{(4r^2 + L^2)^{\lambda+\ell/2}} F \times \left(\frac{2\lambda+\ell}{4}, \frac{2\lambda+\ell+2}{4}; \lambda + \frac{3}{2}, \frac{16r^2 L^2}{(4r^2 + L^2)^2} \right), \quad (22)$$

and the angular brackets stand for the Clebsch-Gordan coefficients, whereas F is the confluent hypergeometric function, and the angle in the new coordinate system is denoted by θ' . The other image looks the same, except that the functions (22) now contain $-L$ in place of L . Finding the cumulative distribution is straightforward, inserting the expressions for $P(N, \mathbf{r}, \mathbf{r}_0)$ and its two images in (15) and integrating. Notice that the initial position is contained only in the radial functions R_{ℓ} , which can be integrated analytically as their integrals reduce to the familiar Bessel integrals.

The last step is multiplying the two cumulative distribution functions as in (16) and integrating over z . At this step the symmetry of the problem nullifies all the terms containing the product of an even and an odd functions of z , and the triangle rule for addition of angular momenta further reduces the number of non-zero terms. We are thus left with a *finite* sum which, to the second order, gives the result for $P_2(\cos \Theta)$ that coincides with (17). The fourth order term differs from the corresponding term in (17), however, as in this approach, due to the orthogonality of the Legendre polynomials, we capture the *exact* value of the coefficient in front of the fourth (or any other desired) order term in the expansion. In the elementary method, the expansion is in powers of a and in number of images. The latter expansion is an uncontrollable approximation, since the $2n$ th image can contribute a term of the order $2n - 2$ in a . The advanced method captures the whole contribution of given order in a .

At the present level of accuracy of our model, this increase in accuracy is not crucial. However, the generality of the formalism applied in this subsection might prove to be necessary if the subtler effects as the Ramachandran rotations or long-range interactions are included. Also, the described method allows an equally straightforward calculation of the expectation value of $P_\ell(\cos\Theta)$ for any ℓ . This case will appear if other observables in addition to direct dipole-dipole couplings are measured. We therefore propose this approach for any further work on this problem.

4 Examples

The purpose of this section is to test our predictions on experimental data and judge the accuracy and usefulness of our theory. Therefore, we do not analyze in detail any of the systems and contend ourselves just to compare our curves with the experimental ones.

In all the cases that we consider, we take the stiffness k_θ equal to 20ϵ and preferential bond angle $\theta_0 = 1.83$ (in radians). These values have been recommended in [14] and also according to other authors the peptide bond is expected to be well described by these values. The interplanar distance is taken fixed to $L = 100a$, where a is the length of a single segment. In both experiments that we analyze [21,22], this length is cited to be about 40 nm while the segment length is 0.38 nm. So, our value for the interplanar distance roughly corresponds to the experimental one; exact equality is not essential since the experimental setup is difficult to control concerning the interplanar distance [22] and the actual distribution of interplanar values is probably rather fat-tailed. In our theory, the segment length does not enter the final expressions and therefore can take any arbitrary value.

The first case we consider is the urea-denaturated apomyoglobin, an experiment reported in [21], and analyzed also in the previous study by two of the authors [2]. The result is seen in Figure 4. The same paper also reports on measurements of acid denaturated apomyoglobin, which cannot be well described with our model, probably because the native-like topology is still present in this case, as the authors themselves state [21].

Another example is ubiquitin, one of the proteins which are intrinsically disordered also in their native state. The measurements are taken from [22].

The second case, in Figure 5, shows somewhat better agreement with experiment than the first one (χ^2 about 30 percent better). In part, this is probably due to the difference between the two proteins. Ubiquitin is known to be a strongly disordered protein [22] and behaves essentially as a perfect statistical coil, so various local deviations from the mean value of RDCs tend to average out. On the other hand, apomyoglobin probably retains some native-like structure even in the unfolded state; this is particularly probable for the regions formed by several subsequent segments which are completely above or below the average RDC value, that are visible in the measurements given in Figure 4. These are probably regions with strong close-neighbor interactions, that behave like

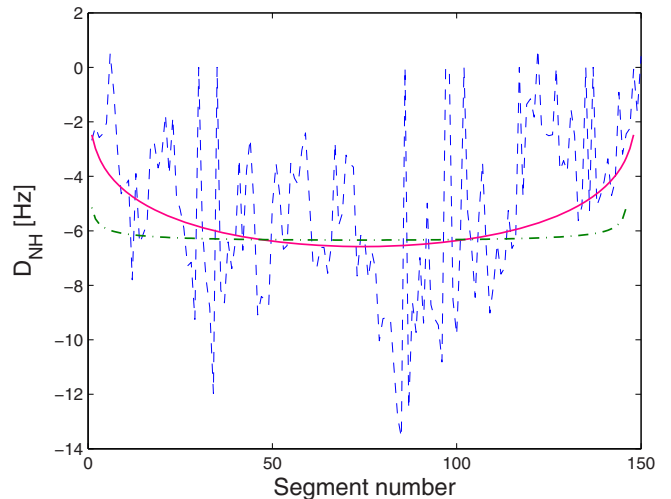


Fig. 4. (Color online) Comparison of experimental (blue dashed line) and theoretical (red full line) RDCs for unfolded apomyoglobin. The prediction of the random flight theory [2] is also shown (green dash-dotted line). General bell shape is observed but it is obvious that local conformational properties induce large deviations from the mean field curve, predicted by our model.

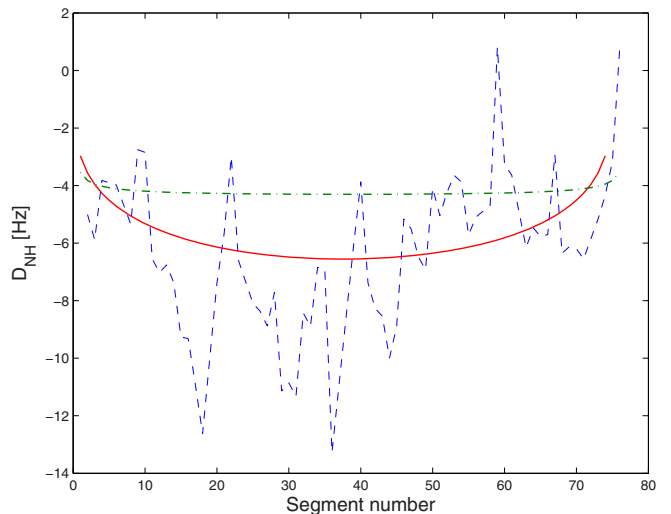


Fig. 5. (Color online) Comparison of experimental (blue dashed line) and theoretical (red full line) RDCs for unfolded ubiquitin. The random flight theory prediction [2] is also shown (green dash-dotted line). One again sees the local variations superimposed on the global bell-shaped curve.

partially folded secondary structures and therefore choose one of the conformations, some of them with significantly higher probability than the others. Finally, we point out that both examples demonstrate that the current model provides a more realistic description of the polypeptide than the non-interacting random flight model.

5 Discussion and conclusion

We have presented a theoretical method for reproducing the spatial structure of unfolded polypeptides, in particular the NMR spectroscopic measurements of NH dipolar couplings. Our approach requires the use of the empirical potentials and model parameters; therefore, it is not an *ab initio* approach. Nevertheless, all the parameters entering the calculation are either measured (or controlled) in the experiment itself (temperature, interplanar distance) or more or less standard and well-known values (optimal bond angle, bond stiffness). Bond stiffness is the “most empirical” of them but it also seems to vary very little in various numerical models [14,18]. The results seem encouraging and reveal general properties of disordered proteins.

First, it seems that the assumption of the effective decoupling of the degrees of freedom is justified by the RDC curves. The global shape of the chain, which is determined primarily by the statistical nature of polypeptide chain conformations in unfolded state and is well described within the semistiff polymer model, gives rise to the bell shape of the curves, also detected in experiments. On the other hand, the specificities of the segments lead to the local deviations of the RDC values from the smooth bell-shaped distribution. We plan to extend our model in further work, applying the linear response theory in order to reproduce these local structures.

The method will be subject to a number of improvements in the future. Besides applying the linear response formalism to improve the results, we also plan to assess in more detail the influence of long range interactions and intrachain contacts. Also, it is possible to use the results of the numerical work to identify the optimal Ramachandran angles for unfolded polypeptides. This will allow us to account for even richer secondary structure than that produced by a restricted database search, as the problem of weighting would be eliminated, with the energy values of different (ϕ, ψ) points being read off numerically obtained potential energy surfaces.

We are grateful to NoE EXCELL for the support of this research, as well as to Alexander Yakubovich for helpful discussions. M. Č. also acknowledges his gratitude to FIAS and Meso-Bio-Nano group for financial support and warm hospitality during the work on this project. Work at the Institute of Physics is supported by the Ministry of Science Project OI141031.

References

1. M. Blackledge, *Prog. Nucl. Magn. Reson. Spectrosc.* **46**, 23 (2005)
2. O.I. Obolensky, K. Schlepckow, H. Schwalbe, A.V. Solov'yov, *J. Biomol. NMR* **39**, 1 (2007)
3. A.K. Jha, A. Colubri, K.F. Freed, T.R. Sosnick, *Proc. Natl. Acad. Sci.* **102**, 13099 (2005)
4. P. Bernado et al., *Proc. Natl. Acad. Sci.* **102**, 17002 (2005)
5. M. Louhivuori et al., *J. Am. Chem. Soc.* **125**, 15647 (2003)
6. N. Sato, K. Takahashi, Y. Yunoki, *J. Phys. Soc. Jpn* **22**, 219 (1967)
7. B. Hamprecht, H. Kleinert, *Phys. Rev. E* **71**, 031803 (2005); H. Kleinert, A. Chervyakov, *J. Phys. A: Math. Gen.* **39**, 8231 (2006)
8. H. Kleinert, *Path integrals in quantum mechanics, statistics, polymer physics and financial markets* (Berlin, 2003)
9. M. Čubrović, O.I. Obolensky, A.V. Solov'yov, submitted
10. K. Kroy, E. Frey, *Phys. Rev. Lett.* **77**, 2581 (1996); H. Changbong, D. Thirumalai, *J. Chem. Phys.* **124**, 104905 (2006)
11. A.B. Rubin, *Biophysics* (Nauka, Moscow, 2004) (in Russian)
12. M. Čubrović, O. Obolensky, A.V. Solov'yov, in preparation
13. R.K. Murarka, A. Liwo, H.A. Scheraga, *J. Chem. Phys.* **127**, 155103 (2007)
14. D.K. Klimov, D. Thirumalai, *Phys. Rev. Lett.* **79**, 317 (1997); T. Veitshans, D.K. Klimov, D. Thirumalai, *Fold. Des.* **7**, 11 (1997)
15. B.D. Hughes, *Random Walks and Random Environments* (Clarendon Press, Oxford, 1995)
16. G.M. Zaslavsky, *Phys. Rep.* **371**, 461 (2002); W. Ebeling, I. Sokolov, *Statistical Thermodynamics and Stochastic Theory of Nonequilibrium systems* (World Scientific, 2002)
17. A.D. Polianin, *Handbook of linear partial differential equations* (CRC Press, 2002)
18. I.A. Solov'yov, A.V. Yakubovich, A.V. Solov'yov, W. Greiner, *Eur. Phys. J. D* **46**, 227 (2007); A.V. Yakubovich, I.A. Solov'yov, A.V. Solov'yov, W. Greiner, *Eur. Phys. J. D* **46**, 215 (2007)
19. E.M. Lifshitz, L.D. Landau, L.P. Pitaevskii, *Electrodynamics of continuous media* (World Scientific, 1989)
20. D.A. Varshalovich, A.N. Moskalev, V.K. Khersonskii, *Quantum theory of angular momentum* (World Scientific, 1988)
21. W. Fieber, S. Kristjansdottir, F.M. Poulsen, *J. Mol. Biol.* **339**, 1191 (2004)
22. S. Meier, S. Grzesiek, M. Blackledge, *J. Am. Chem. Soc.* **129**, 9799 (2007)
23. H.M. Berman et al., *Nucl. Acids Res.* **28**, 235 (2003)

Chapter 21

Holographic Description of Strongly Correlated Electrons in External Magnetic Fields

E. Gubankova, J. Brill, M. Čubrović, K. Schalm, P. Schijven, and J. Zaanen

21.1 Introduction

The study of strongly interacting fermionic systems at finite density and temperature is a challenging task in condensed matter and high energy physics. Analytical methods are limited or not available for strongly coupled systems, and numerical simulation of fermions at finite density breaks down because of the sign problem [1, 2]. There has been an increased activity in describing finite density fermionic matter by a gravity dual using the holographic AdS/CFT correspondence [3]. The gravitational solution dual to the finite chemical potential system is the electrically charged AdS-Reissner-Nordström (RN) black hole, which provides a background where only the metric and Maxwell fields are nontrivial and all matter fields vanish.

E. Gubankova (✉)
ITP, J. W. Goethe-University, D-60438 Frankfurt am Main, Germany
e-mail: gubankova@th.physik.uni-frankfurt.de

E. Gubankova
ITEP, Moscow, Russia

J. Brill · M. Čubrović · K. Schalm · P. Schijven · J. Zaanen
Instituut Lorentz, Leiden University, Niels Bohrweg 2, 2300 RA Leiden, The Netherlands

J. Brill
e-mail: jellebrill@gmail.com

M. Čubrović
e-mail: cubrovic@lorentz.leidenuniv.nl

K. Schalm
e-mail: kschalm@lorentz.leidenuniv.nl

P. Schijven
e-mail: aphexedpiet@gmail.com

J. Zaanen
e-mail: jan@lorentz.leidenuniv.nl

In the classical gravity limit, the decoupling of the Einstein-Maxwell sector holds and leads to universal results, which is an appealing feature of applied holography. Indeed, the celebrated result for the ratio of the shear viscosity over the entropy density [4] is identical for many strongly interacting theories and has been considered a robust prediction of the AdS/CFT correspondence.

However, an extremal black hole alone is not enough to describe finite density systems as it does not source the matter fields. In holography, at leading order, the Fermi surfaces are not evident in the gravitational geometry, but can only be detected by external probes; either probe D-branes [3] or probe bulk fermions [5–8]. Here we shall consider the latter option, where the free Dirac field in the bulk carries a finite charge density [9]. We ignore electromagnetic and gravitational backreaction of the charged fermions on the bulk spacetime geometry (probe approximation). At large temperatures, $T \gg \mu$, this approach provides a reliable hydrodynamic description of transport at a quantum criticality (in the vicinity of superfluid-insulator transition) [10]. At small temperatures, $T \ll \mu$, in some cases sharp Fermi surfaces emerge with either conventional Fermi-liquid scaling [6] or of a non-Fermi liquid type [7] with scaling properties that differ significantly from those predicted by the Landau Fermi liquid theory. The non-trivial scaling behavior of these non-Fermi liquids has been studied semi-analytically in [8] and is of great interest as high- T_c superconductors and metals near the critical point are believed to represent non-Fermi liquids.

What we shall study is the effects of magnetic field on the holographic fermions. A magnetic field is a probe of finite density matter at low temperatures, where the Landau level physics reveals the Fermi level structure. The gravity dual system is described by a AdS dyonic black hole with electric and magnetic charges Q and H , respectively, corresponding to a $2 + 1$ -dimensional field theory at finite chemical potential in an external magnetic field [11]. Probe fermions in the background of the dyonic black hole have been considered in [12–14]; and probe bosons in the same background have been studied in [15]. Quantum magnetism is considered in [16].

The Landau quantization of momenta due to the magnetic field found there, shows again that the AdS/CFT correspondence has a powerful capacity to unveil that certain quantum properties known from quantum gases have a much more ubiquitous status than could be anticipated theoretically. A first highlight is the demonstration [17] that the Fermi surface of the Fermi gas extends way beyond the realms of its perturbative extension in the form of the Fermi-liquid. In AdS/CFT it appears to be gravitationally encoded in the matching along the scaling direction between the ‘bare’ Dirac waves falling in from the ‘UV’ boundary, and the true IR excitations living near the black hole horizon. This IR physics can insist on the disappearance of the quasiparticle but, if so, this ‘critical Fermi-liquid’ is still organized ‘around’ a Fermi surface. The Landau quantization, the organization of quantum gaseous matter in quantized energy bands (Landau levels) in a system of two space dimensions pierced by a magnetic field oriented in the orthogonal spatial direction, is a second such quantum gas property. We shall describe here following [12], that despite the strong interactions in the system, the holographic computation reveals the same strict Landau-level quantization. Arguably, it is the mean-field nature imposed by

large N limit inherent in AdS/CFT that explains this. The system is effectively non-interacting to first order in $1/N$. The Landau quantization is not manifest from the geometry, but as we show this statement is straightforwardly encoded in the symmetry correspondences associated with the conformal compactification of AdS on its flat boundary (i.e., in the UV CFT).

An interesting novel feature in strongly coupled systems arises from the fact that the background geometry is only sensitive to the total energy density $Q^2 + H^2$ contained in the electric and magnetic fields sourced by the dyonic black hole. Dialing up the magnetic field is effectively similar to a process where the dyonic black hole loses its electric charge. At the same time, the fermionic probe with charge q is essentially only sensitive to the Coulomb interaction gqQ . As shown in [12], one can therefore map a magnetic to a non-magnetic system with rescaled parameters (chemical potential, fermion charge) and same symmetries and equations of motion, as long as the Reissner-Nordström geometry is kept.

Translated to more experiment-compatible language, the above magnetic-electric mapping means that the spectral functions at nonzero magnetic field h are identical to the spectral function at $h = 0$ for a reduced value of the coupling constant (fermion charge) q , provided the probe fermion is in a Landau level eigenstate. A striking consequence is that the spectrum shows conformal invariance for arbitrarily high magnetic fields, as long as the system is at negligible to zero density. Specifically, a detailed analysis of the fermion spectral functions reveals that at strong magnetic fields the Fermi level structure changes qualitatively. There exists a critical magnetic field at which the Fermi velocity vanishes. Ignoring the Landau level quantization, we show that this corresponds to an effective tuning of the system from a regular Fermi liquid phase with linear dispersion and stable quasiparticles to a non-Fermi liquid with fractional power law dispersion and unstable excitations. This phenomenon can be interpreted as a transition from metallic phase to a “strange metal” at the critical magnetic field and corresponds to the change of the infrared conformal dimension from $\nu > 1/2$ to $\nu < 1/2$ while the Fermi momentum stays nonzero and the Fermi surface survives. Increasing the magnetic field further, this transition is followed by a “strange-metal”-conformal crossover and eventually, for very strong fields, the system always has near-conformal behavior where $k_F = 0$ and the Fermi surface disappears.

For some Fermi surfaces, this surprising metal-“strange metal” transition is not physically relevant as the system prefers to directly enter the conformal phase. Whether a fine tuned system exists that does show a quantum critical phase transition from a FL to a non-FL is determined by a Diophantine equation for the Landau quantized Fermi momentum as a function of the magnetic field. Perhaps these are connected to the magnetically driven phase transition found in AdS₅/CFT₄ [18]. We leave this subject for further work.

Overall, the findings of Landau quantization and “discharge” of the Fermi surface are in line with the expectations: both phenomena have been found in a vast array of systems [19] and are almost tautologically tied to the notion of a Fermi surface in a magnetic field. Thus we regard them also as a sanity check of the whole bottom-up approach of fermionic AdS/CFT [5–7, 17], giving further credit to the holographic Fermi surfaces as having to do with the real world.

Next we use the information of magnetic effects the Fermi surfaces extracted from holography to calculate the quantum Hall and longitudinal conductivities. Generally speaking, it is difficult to calculate conductivity holographically beyond the Einstein-Maxwell sector, and extract the contribution of holographic fermions. In the semiclassical approximation, one-loop corrections in the bulk setup involving charged fermions have been calculated [17]. In another approach, the backreaction of charged fermions on the gravity-Maxwell sector has been taken into account and incorporated in calculations of the electric conductivity [9]. We calculate the one-loop contribution on the CFT side, which is equivalent to the holographic one-loop calculations as long as vertex corrections do not modify physical dependencies of interest [17, 20]. As we dial the magnetic field, the Hall plateau transition happens when the Fermi surface moves through a Landau level. One can think of a difference between the Fermi energy and the energy of the Landau level as a gap, which vanishes at the transition point and the $2 + 1$ -dimensional theory becomes scale invariant. In the holographic D3–D7 brane model of the quantum Hall effect, plateau transition occurs as D-branes move through one another [21, 22]. In the same model, a dissipation process has been observed as D-branes fall through the horizon of the black hole geometry, that is associated with the quantum Hall insulator transition. In the holographic fermion liquid setting, dissipation is present through interaction of fermions with the horizon of the black hole. We have also used the analysis of the conductivities to learn more about the metal-strange metal phase transition as well as the crossover back to the conformal regime at high magnetic fields.

We conclude with the remark that the findings summarized above are in fact somewhat puzzling when contrasted to the conventional picture of quantum Hall physics. It is usually stated that the quantum Hall effect requires three key ingredients: Landau quantization, quenched disorder¹ and (spatial) boundaries, i.e., a finite-sized sample [23]. The first brings about the quantization of conductivity, the second prevents the states from spilling between the Landau levels ensuring the existence of a gap and the last one in fact allows the charge transport to happen (as it is the boundary states that actually conduct). In our model, only the first condition is satisfied. The second is put by hand by assuming that the gap is automatically preserved, i.e. that there is no mixing between the Landau levels. There is, however, no physical explanation as to how the boundary states are implicitly taken into account by AdS/CFT.

We outline the holographic setting of the dyonic black hole geometry and bulk fermions in Sect. 21.2. In Sect. 21.3 we prove the conservation of conformal symmetry in the presence of the magnetic fields. Section 21.4 is devoted to the holographic fermion liquid, where we obtain the Landau level quantization, followed by a detailed study of the Fermi surface properties at zero temperature in Sect. 21.5. We calculate the DC conductivities in Sect. 21.6, and compare the results with available data in graphene.

¹Quenched disorder means that the dynamics of the impurities is “frozen”, i.e. they can be regarded as having infinite mass. When coupled to the Fermi liquid, they ensure that below some scale the system behaves as if consisting of non-interacting quasiparticles only.

21.2 Holographic Fermions in a Dyonic Black Hole

We first describe the holographic setup with the dyonic black hole, and the dynamics of Dirac fermions in this background. In this paper, we exclusively work in the probe limit, i.e., in the limit of large fermion charge q .

21.2.1 Dyonic Black Hole

We consider the gravity dual of 3-dimensional conformal field theory (CFT) with global $U(1)$ symmetry. At finite charge density and in the presence of magnetic field, the system can be described by a dyonic black hole in 4-dimensional anti-de Sitter space-time, AdS_4 , with the current J_μ in the CFT mapped to a $U(1)$ gauge field A_M in AdS . We use μ, ν, ρ, \dots for the spacetime indices in the CFT and M, N, \dots for the global spacetime indices in AdS .

The action for a vector field A_M coupled to AdS_4 gravity can be written as

$$S_g = \frac{1}{2\kappa^2} \int d^4x \sqrt{-g} \left(\mathcal{R} + \frac{6}{R^2} - \frac{R^2}{g_F^2} F_{MN} F^{MN} \right), \quad (21.1)$$

where g_F^2 is an effective dimensionless gauge coupling and R is the curvature radius of AdS_4 . The equations of motion following from (21.1) are solved by the geometry corresponding to a dyonic black hole, having both electric and magnetic charge:

$$ds^2 = g_{MN} dx^M dx^N = \frac{r^2}{R^2} (-f dt^2 + dx^2 + dy^2) + \frac{R^2}{r^2} \frac{dr^2}{f}. \quad (21.2)$$

The redshift factor f and the vector field A_M reflect the fact that the system is at a finite charge density and in an external magnetic field:

$$f = 1 + \frac{Q^2 + H^2}{r^4} - \frac{M}{r^3}, \quad (21.3)$$

$$A_t = \mu \left(1 - \frac{r_0}{r} \right), \quad A_y = hx, \quad A_x = A_r = 0,$$

where Q and H are the electric and magnetic charge of the black hole, respectively. Here we chose the Landau gauge; the black hole chemical potential μ and the magnetic field h are given by

$$\mu = \frac{g_F Q}{R^2 r_0}, \quad h = \frac{g_F H}{R^4}, \quad (21.4)$$

with r_0 is the horizon radius determined by the largest positive root of the redshift factor $f(r_0) = 0$:

$$M = r_0^3 + \frac{Q^2 + H^2}{r_0}. \quad (21.5)$$

The boundary of the *AdS* is reached for $r \rightarrow \infty$. The geometry described by (21.2)–(21.3) describes the boundary theory at finite density, i.e., a system in a charged medium at the chemical potential $\mu = \mu_{\text{bh}}$ and in transverse magnetic field $h = h_{\text{bh}}$, with charge, energy, and entropy densities given, respectively, by

$$\rho = 2 \frac{Q}{\kappa^2 R^2 g_F}, \quad \varepsilon = \frac{M}{\kappa^2 R^4}, \quad s = \frac{2\pi}{\kappa^2} \frac{r_0^2}{R^2}. \quad (21.6)$$

The temperature of the system is identified with the Hawking temperature of the black hole, $T_H \sim |f'(r_0)|/4\pi$,

$$T = \frac{3r_0}{4\pi R^2} \left(1 - \frac{Q^2 + H^2}{3r_0^4} \right). \quad (21.7)$$

Since Q and H have dimensions of $[L]^2$, it is convenient to parametrize them as

$$Q^2 = 3r_*^4, \quad Q^2 + H^2 = 3r_{**}^4. \quad (21.8)$$

In terms of r_0 , r_* and r_{**} the above expressions become

$$f = 1 + \frac{3r_{**}^4}{r^4} - \frac{r_0^3 + 3r_{**}^4/r_0}{r^3}, \quad (21.9)$$

with

$$\mu = \sqrt{3} g_F \frac{r_*^2}{R^2 r_0}, \quad h = \sqrt{3} g_F \frac{\sqrt{r_{**}^4 - r_*^4}}{R^4}. \quad (21.10)$$

The expressions for the charge, energy and entropy densities, as well as for the temperature are simplified as

$$\rho = \frac{2\sqrt{3}}{\kappa^2 g_F} \frac{r_*^2}{R^2}, \quad \varepsilon = \frac{1}{\kappa^2} \frac{r_0^3 + 3r_{**}^4/r_0}{R^4}, \quad s = \frac{2\pi}{\kappa^2} \frac{r_0^2}{R^2}, \quad (21.11)$$

$$T = \frac{3}{4\pi} \frac{r_0}{R^2} \left(1 - \frac{r_{**}^4}{r_0^4} \right).$$

In the zero temperature limit, i.e., for an extremal black hole, we have

$$T = 0 \quad \rightarrow \quad r_0 = r_{**}, \quad (21.12)$$

which in the original variables reads $Q^2 + H^2 = 3r_0^4$. In the zero temperature limit (21.12), the redshift factor f as given by (21.9) develops a double zero at the horizon:

$$f = 6 \frac{(r - r_{**})^2}{r_{**}^2} + \mathcal{O}((r - r_{**})^3). \quad (21.13)$$

As a result, near the horizon the AdS_4 metric reduces to $AdS_2 \times \mathbb{R}^2$ with the curvature radius of AdS_2 given by

$$R_2 = \frac{1}{\sqrt{6}}R. \quad (21.14)$$

This is a very important property of the metric, which considerably simplifies the calculations, in particular in the magnetic field.

In order to scale away the AdS_4 radius R and the horizon radius r_0 , we introduce dimensionless variables

$$\begin{aligned} r &\rightarrow r_0 r, & r_* &\rightarrow r_0 r_*, & r_{**} &\rightarrow r_0 r_{**}, \\ M &\rightarrow r_0^3 M, & Q &\rightarrow r_0^2 Q, & H &\rightarrow r_0^2 H, \end{aligned} \quad (21.15)$$

and

$$\begin{aligned} (t, \mathbf{x}) &\rightarrow \frac{R^2}{r_0}(t, \mathbf{x}), & A_M &\rightarrow \frac{r_0}{R^2}A_M, & \omega &\rightarrow \frac{r_0}{R^2}\omega, \\ \mu &\rightarrow \frac{r_0}{R^2}\mu, & h &\rightarrow \frac{r_0^2}{R^4}h, & T &\rightarrow \frac{r_0}{R^2}T, \\ ds^2 &\rightarrow R^2 ds^2. \end{aligned} \quad (21.16)$$

Note that the scaling factors in the above equation that describes the quantities of the boundary field theory involve the curvature radius of AdS_4 , not AdS_2 .

In the new variables we have

$$\begin{aligned} T &= \frac{3}{4\pi}(1 - r_{**}^4) = \frac{3}{4\pi}\left(1 - \frac{Q^2 + H^2}{3}\right), & f &= 1 + \frac{3r_{**}^4}{r^4} - \frac{1 + 3r_{**}^4}{r^3}, \\ A_t &= \mu\left(1 - \frac{1}{r}\right), & \mu &= \sqrt{3}g_F r_*^2 = g_F Q, & h &= g_F H, \end{aligned} \quad (21.17)$$

and the metric is given by

$$ds^2 = r^2(-f dt^2 + dx^2 + dy^2) + \frac{1}{r^2} \frac{dr^2}{f}, \quad (21.18)$$

with the horizon at $r = 1$, and the conformal boundary at $r \rightarrow \infty$.

At $T = 0$, r_{**} becomes unity, and the redshift factor develops the double zero near the horizon,

$$f = \frac{(r-1)^2(r^2 + 2r + 3)}{r^4}. \quad (21.19)$$

As mentioned before, due to this fact the metric near the horizon reduces to $AdS_2 \times \mathbb{R}^2$ where the analytical calculations are possible for small frequencies [8]. However, in the chiral limit $m = 0$, analytical calculations are also possible in the bulk AdS_4 [24], which we utilize in this paper.

21.2.2 Holographic Fermions

To include the bulk fermions, we consider a spinor field ψ in the AdS_4 of charge q and mass m , which is dual to an operator \mathcal{O} in the boundary CFT_3 of charge q and dimension

$$\Delta = \frac{3}{2} + mR, \tag{21.20}$$

with $mR \geq -\frac{1}{2}$ and in dimensionless units corresponds to $\Delta = \frac{3}{2} + m$. In the black hole geometry, (21.2), the quadratic action for ψ reads as

$$S_\psi = i \int d^4x \sqrt{-g} (\bar{\psi} \Gamma^M \mathcal{D}_M \psi - m \bar{\psi} \psi), \tag{21.21}$$

where $\bar{\psi} = \psi^\dagger \Gamma^t$, and

$$\mathcal{D}_M = \partial_M + \frac{1}{4} \omega_{abM} \Gamma^{ab} - iq A_M, \tag{21.22}$$

where ω_{abM} is the spin connection, and $\Gamma^{ab} = \frac{1}{2} [\Gamma^a, \Gamma^b]$. Here, M and a, b denote the bulk space-time and tangent space indices respectively, while μ, ν are indices along the boundary directions, i.e. $M = (r, \mu)$. Gamma matrix basis (Minkowski signature) is given in [8].

We will be interested in spectra and response functions of the boundary fermions in the presence of magnetic field. This requires solving the Dirac equation in the bulk [6, 7]:

$$(\Gamma^M \mathcal{D}_M - m)\psi = 0. \tag{21.23}$$

From the solution of the Dirac equation at small ω , an analytic expression for the retarded fermion Green’s function of the boundary CFT at zero magnetic field has been obtained in [8]. Near the Fermi surface it reads as [8]:

$$G_R(\Omega, k) = \frac{(-h_1 v_F)}{\omega - v_F k_\perp - \Sigma(\omega, T)}, \tag{21.24}$$

where $k_\perp = k - k_F$ is the perpendicular distance from the Fermi surface in momentum space, h_1 and v_F are real constants calculated below, and the self-energy $\Sigma = \Sigma_1 + i \Sigma_2$ is given by [8]

$$\Sigma(\omega, T)/v_F = T^{2\nu} g \left(\frac{\omega}{T} \right) = (2\pi T)^{2\nu} h_2 e^{i\theta - i\pi\nu} \frac{\Gamma(\frac{1}{2} + \nu - \frac{i\omega}{2\pi T} + \frac{i\mu_q}{6})}{\Gamma(\frac{1}{2} - \nu - \frac{i\omega}{2\pi T} + \frac{i\mu_q}{6})}, \tag{21.25}$$

where ν is the zero temperature conformal dimension at the Fermi momentum, $\nu \equiv \nu_{k_F}$, given by (21.58), $\mu_q \equiv \mu q$, h_2 is a positive constant and the phase θ is such that the poles of the Green’s function are located in the lower half of the complex frequency plane. These poles correspond to quasinormal modes of the Dirac

equation (21.23) and they can be found numerically solving $F(\omega_*) = 0$ [25, 26], with

$$F(\omega) = \frac{k_{\perp}}{\Gamma(\frac{1}{2} + \nu - \frac{i\omega}{2\pi T} + \frac{i\mu_q}{6})} - \frac{h_2 e^{i\theta - i\pi\nu} (2\pi T)^{2\nu}}{\Gamma(\frac{1}{2} - \nu - \frac{i\omega}{2\pi T} + \frac{i\mu_q}{6})}, \quad (21.26)$$

The solution gives the full motion of the quasinormal poles $\omega_*^{(n)}(k_{\perp})$ in the complex ω plane as a function of k_{\perp} . It has been found in [8, 25, 26], that, if the charge of the fermion is large enough compared to its mass, the pole closest to the real ω axis bounces off the axis at $k_{\perp} = 0$ (and $\omega = 0$). Such behavior is identified with the existence of the Fermi momentum k_F indicative of an underlying strongly coupled Fermi surface.

At $T = 0$, the self-energy becomes $T^{2\nu} g(\omega/T) \rightarrow c_k \omega^{2\nu}$, and the Green's function obtained from the solution to the Dirac equation reads [8]

$$G_R(\Omega, k) = \frac{(-\hbar_1 v_F)}{\omega - v_F k_{\perp} - h_2 v_F e^{i\theta - i\pi\nu} \omega^{2\nu}}, \quad (21.27)$$

where $k_{\perp} = \sqrt{k^2} - k_F$. The last term is determined by the IR AdS_2 physics near the horizon. Other terms are determined by the UV physics of the AdS_4 bulk.

The solutions to (21.23) have been studied in detail in [6–8]. Here we simply summarize the novel aspects due to the background magnetic field [27]

- The background magnetic field h introduces a discretization of the momentum:

$$k \rightarrow k_{\text{eff}} = \sqrt{2|qh|l}, \quad \text{with } l \in N, \quad (21.28)$$

with Landau level index l [13, 14, 25, 26]. These discrete values of k are the analogue of the well-known Landau levels that occur in magnetic systems.

- There exists a (non-invertible) mapping on the level of Green's functions, from the magnetic system to the non-magnetic one by sending

$$(H, Q, q) \mapsto \left(0, \sqrt{Q^2 + H^2}, q \sqrt{1 - \frac{H^2}{Q^2 + H^2}} \right). \quad (21.29)$$

The Green's functions in a magnetic system are thus equivalent to those in the absence of magnetic fields. To better appreciate that, we reformulate (21.29) in terms of the boundary quantities:

$$(h, \mu_q, T) \mapsto \left(0, \mu_q, T \left(1 - \frac{h^2}{12\mu^2} \right) \right), \quad (21.30)$$

where we used dimensionless variables defined in (21.15), (21.17). The magnetic field thus effectively decreases the coupling constant q and increases the chemical potential $\mu = g_F Q$ such that the combination $\mu_q \equiv \mu q$ is preserved [12]. This is an important point as the equations of motion actually only depend on this combination and not on μ and q separately [12]. In other words, (21.30) implies that the additional scale brought about by the magnetic field can be understood as

changing μ and T independently in the effective non-magnetic system instead of only tuning the ratio μ/T . This point is important when considering the thermodynamics.

- The discrete momentum $k_{\text{eff}} = \sqrt{2|qh|l}$ must be held fixed in the transformation (21.29). The bulk-boundary relation is particularly simple in this case, as the Landau levels can readily be seen in the bulk solution, only to remain identical in the boundary theory.
- Similar to the non-magnetic system [12], the IR physics is controlled by the near horizon $AdS_2 \times \mathbb{R}^2$ geometry, which indicates the existence of an IR CFT, characterized by operators \mathcal{O}_l , $l \in N$ with operator dimensions $\delta = 1/2 + \nu_l$:

$$\nu_l = \frac{1}{6} \sqrt{6 \left(m^2 + \frac{2|qh|l}{r_{**}^2} \right) - \frac{\mu_q^2}{r_{**}^4}}, \quad (21.31)$$

in dimensionless notation, and $\mu_q \equiv \mu q$. At $T = 0$, when $r_{**} = 1$, it becomes

$$\nu_l = \frac{1}{6} \sqrt{6(m^2 + 2|qh|l) - \mu_q^2}. \quad (21.32)$$

The Green's function for these operators \mathcal{O}_l is found to be $\mathcal{G}_l^R(\omega) \sim \omega^{2\nu_l}$ and the exponents ν_l determines the dispersion properties of the quasiparticle excitations. For $\nu > 1/2$ the system has a stable quasiparticle and a linear dispersion, whereas for $\nu \leq 1/2$ one has a non-Fermi liquid with power-law dispersion and an unstable quasiparticle.

21.3 Magnetic Fields and Conformal Invariance

Despite the fact that a magnetic field introduces a scale, in the absence of a chemical potential, all spectral functions are essentially still determined by conformal symmetry. To show this, we need to establish certain properties of the near-horizon geometry of a Reissner-Nordström black hole. This leads to the AdS_2 perspective that was developed in [8]. The result relies on the conformal algebra and its relation to the magnetic group, from the viewpoint of the infrared CFT that was studied in [8]. Later on we will see that the insensitivity to the magnetic field also carries over to AdS_4 and the UV CFT in some respects. To simplify the derivations, we consider the case $T = 0$.

21.3.1 The Near-Horizon Limit and Dirac Equation in AdS_2

It was established in [8] that an electrically charged extremal AdS -Reissner-Nordström black hole has an AdS_2 throat in the inner bulk region. This conclusion carries over to the magnetic case with some minor differences. We will now give a quick derivation of the AdS_2 formalism for a dyonic black hole, referring the reader to [8] for more details (that remain largely unchanged in the magnetic field).

Near the horizon $r = r_{**}$ of the black hole described by the metric (21.2), the redshift factor $f(r)$ develops a double zero:

$$f(r) = 6 \frac{(r - r_{**})^2}{r_{**}^2} + \mathcal{O}((r - r_{**})^3). \quad (21.33)$$

Now consider the scaling limit

$$r - r_{**} = \lambda \frac{R_2^2}{\zeta}, \quad t = \lambda^{-1} \tau, \quad \lambda \rightarrow 0 \text{ with } \tau, \zeta \text{ finite.} \quad (21.34)$$

In this limit, the metric (21.2) and the gauge field reduce to

$$ds^2 = \frac{R_2^2}{\zeta^2} (-d\tau^2 + d\zeta^2) + \frac{r_{**}^2}{R^2} (dx^2 + dy^2), \quad (21.35)$$

$$A_\tau = \frac{\mu R_2^2 r_0}{r_{**}^2} \frac{1}{\zeta}, \quad A_x = Hx$$

where $R_2 = \frac{R}{\sqrt{6}}$. The geometry described by this metric is indeed $AdS_2 \times R^2$. Physically, the scaling limit given in (21.34) with finite τ corresponds to the long time limit of the original time coordinate t , which translates to the low frequency limit of the boundary theory:

$$\frac{\omega}{\mu} \rightarrow 0, \quad (21.36)$$

where ω is the frequency conjugate to t . (One can think of λ as being the frequency ω .) Near the AdS_4 horizon, we expect the AdS_2 region of an extremal dyonic black hole to have a CFT_1 dual. We refer to [8] for an account of this AdS_2/CFT_1 duality. The horizon of AdS_2 region is at $\zeta \rightarrow \infty$ (coefficient in front of $d\tau$ vanishes at the horizon in (21.35)) and the infrared CFT (IR CFT) lives at the AdS_2 boundary at $\zeta = 0$. The scaling picture given by (21.34)–(21.35) suggests that in the low frequency limit, the 2-dimensional boundary theory is described by this IR CFT (which is a CFT_1). The Green's function for the operator \mathcal{O} in the boundary theory is obtained through a small frequency expansion and a matching procedure between the two different regions (inner and outer) along the radial direction, and can be expressed through the Green's function of the IR CFT [8].

The explicit form for the Dirac equation in the magnetic field is of little interest for the analytical results that follow. It can be found in [27]. Of primary interest is its limit in the IR region with metric given by (21.35):

$$\left(-\frac{1}{\sqrt{g_{\zeta\zeta}}} \sigma^3 \partial_\zeta - m + \frac{1}{\sqrt{-g_{\tau\tau}}} \sigma^1 \left(\omega + \frac{\mu_q R_2^2 r_0}{r_{**}^2 \zeta} \right) - \frac{1}{\sqrt{g_{ii} l \sigma^2 \lambda_l}} \right) F^{(l)} = 0, \quad (21.37)$$

where the effective momentum of the l th Landau level is $\lambda_l = \sqrt{2|q\hbar|l}$, $\mu_q \equiv \mu q$ and we omit the index of the spinor field. To obtain (21.37), it is convenient to

pick the gamma matrix basis as $\Gamma^{\hat{\zeta}} = -\sigma_3$, $\Gamma^{\hat{\tau}} = i\sigma_1$ and $\Gamma^{\hat{t}} = -\sigma_2$. We can write explicitly:

$$\begin{pmatrix} \frac{\zeta}{R_2} \partial_{\zeta} + m & -\frac{\zeta}{R_2} \left(\omega + \frac{\mu_q R_2^2 r_0}{r_{**}^2 \zeta} \right) + \frac{R}{r_{**}} \lambda_l \\ \frac{\zeta}{R_2} \left(\omega + \frac{\mu_q R_2^2 r_0}{r_{**}^2 \zeta} \right) + \frac{R}{r_{**}} \lambda_l & \frac{\zeta}{R_2} \partial_{\zeta} - m \end{pmatrix} \begin{pmatrix} y \\ z \end{pmatrix} = 0. \quad (21.38)$$

Note that the AdS_2 radius R_2 enters for the (τ, ζ) directions. At the AdS_2 boundary, $\zeta \rightarrow 0$, the Dirac equation to the leading order is given by

$$\zeta \partial_{\zeta} F^{(l)} = -U F^{(l)}, \quad U = R_2 \begin{pmatrix} m & -\frac{\mu_q R_2 r_0}{r_{**}^2} + \frac{R}{r_{**}} \lambda_l \\ \frac{\mu_q R_2 r_0}{r_{**}^2} + \frac{R}{r_{**}} \lambda_l & -m \end{pmatrix}. \quad (21.39)$$

The solution to this equation is given by the scaling function $F^{(l)} = A e_+ \zeta^{-\nu_l} + B e_- \zeta^{\nu_l}$ where e_{\pm} are the real eigenvectors of U and the exponent is

$$\nu_l = \frac{1}{6} \sqrt{6 \left(m^2 + \frac{R^2}{r_{**}^2} 2|qh|l \right) R^2 - \frac{\mu_q^2 R^4 r_0^2}{r_{**}^4}}. \quad (21.40)$$

The conformal dimension of the operator \mathcal{O} in the IR CFT is $\delta_l = \frac{1}{2} + \nu_l$. Comparing (21.40) to the expression for the scaling exponent in [8], we conclude that the scaling properties and the AdS_2 construction are unmodified by the magnetic field, except that the scaling exponents are now fixed by the Landau quantization. This ‘‘quantization rule’’ was already exploited in [25, 26] to study de Haas-van Alphen oscillations.

21.4 Spectral Functions

In this section we will explore some of the properties of the spectral function, in both plane wave and Landau level basis. We first consider some characteristic cases in the plane wave basis and make connection with the ARPES measurements.

21.4.1 Relating to the ARPES Measurements

In reality, ARPES measurements cannot be performed in magnetic fields so the holographic approach, allowing a direct insight into the propagator structure and the spectral function, is especially helpful. This follows from the observation that the spectral functions as measured in ARPES are always expressed in the plane wave basis of the photon, thus in a magnetic field, when the momentum is not a good quantum number anymore, it becomes impossible to perform the photoemission spectroscopy.

In order to compute the spectral function, we have to choose a particular fermionic plane wave as a probe. Since the separation of variables is valid through-

out the bulk, the basis transformation can be performed at every constant r -slice. This means that only the x and y coordinates have to be taken into account (the plane wave probe lives only at the CFT side of the duality). We take a plane wave propagating in the $+x$ direction with spin up along the r -axis. In its rest frame such a particle can be described by

$$\Psi_{\text{probe}} = e^{i\omega t - ip_x x} \begin{pmatrix} \xi \\ \xi \end{pmatrix}, \quad \xi = \begin{pmatrix} 1 \\ 0 \end{pmatrix}. \quad (21.41)$$

Near the boundary (at $r_b \rightarrow \infty$) we can rescale our solutions of the Dirac equation, details can be found in [27]:

$$F_l = \begin{pmatrix} \zeta_l^{(1)}(\tilde{x}) \\ \xi_+^{(l)}(r_b) \zeta_l^{(1)}(\tilde{x}) \\ \zeta_l^{(2)}(\tilde{x}) \\ -\xi_+^{(l)}(r_b) \zeta_l^{(2)}(\tilde{x}) \end{pmatrix}, \quad \tilde{F}_l = \begin{pmatrix} \zeta_l^{(1)}(\tilde{x}) \\ \xi_-^{(l)}(r_b) \zeta_l^{(1)}(\tilde{x}) \\ -\zeta_l^{(2)}(\tilde{x}) \\ \xi_-^{(l)}(r_b) \zeta_l^{(2)}(\tilde{x}) \end{pmatrix}, \quad (21.42)$$

with rescaled \tilde{x} defined in [27]. This representation is useful since we calculate the components $\xi_{\pm}(r_b)$ related to the retarded Green's function in our numerics (we keep the notation of [8]).

Let \mathcal{O}_l and $\tilde{\mathcal{O}}_l$ be the CFT operators dual to respectively F_l and \tilde{F}_l , and c_k^\dagger, c_k be the creation and annihilation operators for the plane wave state Ψ_{probe} . Since the states F and \tilde{F} form a complete set in the bulk, we can write

$$c_p^\dagger(\omega) = \sum_l (U_l^*, \tilde{U}_l^*) \begin{pmatrix} \mathcal{O}_l^\dagger(\omega) \\ \tilde{\mathcal{O}}_l^\dagger(\omega) \end{pmatrix} = \sum_l (U_l^* \mathcal{O}_l^\dagger(\omega) + \tilde{U}_l^* \tilde{\mathcal{O}}_l^\dagger(\omega)) \quad (21.43)$$

where the overlap coefficients $U_l(\omega)$ are given by the inner product between Ψ_{probe} and F :

$$U_l(p_x) = \int dx F_l^\dagger i \Gamma^0 \Psi_{\text{probe}} = - \int dx e^{-ip_x x} \xi_+(r_b) (\zeta_l^{(1)\dagger}(\tilde{x}) - \zeta_l^{(2)\dagger}(\tilde{x})), \quad (21.44)$$

with $\bar{F} = F^\dagger i \Gamma^0$, and similar expression for \tilde{U}_l involving $\xi_-(r_b)$. The constants U_l can be calculated analytically using the numerical value of $\xi_{\pm}(r_b)$, and by noting that the Hermite functions are eigenfunctions of the Fourier transform. We are interested in the retarded Green's function, defined as

$$\begin{aligned} G_{\mathcal{O}_l}^R(\omega, p) &= -i \int d^x dt e^{i\omega t - ip \cdot x} \theta(t) G_{\mathcal{O}_l}^R(t, x) \\ G_{\mathcal{O}_l}^R(t, x) &= \langle 0 | [\mathcal{O}_l(t, x), \tilde{\mathcal{O}}_l(0, 0)] | 0 \rangle \\ G^R &= \begin{pmatrix} G_\theta & 0 \\ 0 & \tilde{G}_\theta \end{pmatrix}, \end{aligned} \quad (21.45)$$

where \tilde{G}_θ is the retarded Green's function for the operator $\tilde{\mathcal{O}}$.

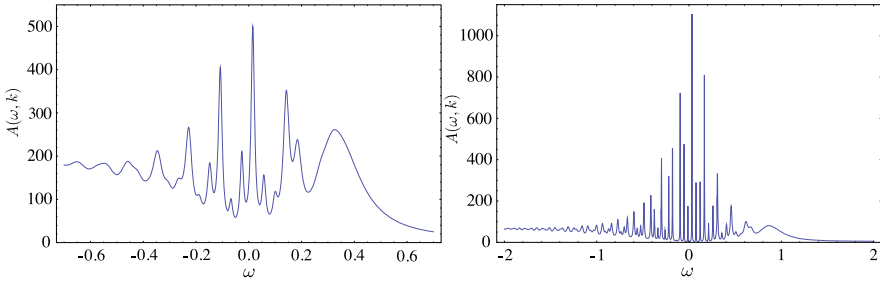


Fig. 21.1 Two examples of spectral functions in the plane wave basis for $\mu/T = 50$ and $h/T = 1$. The conformal dimension is $\Delta = 5/4$ (left) and $\Delta = 3/2$ (right). Frequency is in the units of effective temperature T_{eff} . The plane wave momentum is chosen to be $k = 1$. Despite the convolution of many Landau levels, the presence of the discrete levels is obvious

Exploiting the orthogonality of the spinors created by \mathcal{O} and \mathcal{O}^\dagger and using (21.43), the Green’s function in the plane wave basis can be written as

$$G_{c_p}^R(\omega, p_x) = \sum_l \text{tr} \left(\begin{matrix} U \\ \tilde{U} \end{matrix} \right) (U^*, \tilde{U}^*) G^R = (|U_l(p_x)|^2 G_{\mathcal{O}_l}^R(\omega, l) + |\tilde{U}_l(p_x)|^2 \tilde{G}_{\mathcal{O}_l}^R(\omega, l)). \tag{21.46}$$

In practice, we cannot perform the sum in (21.46) all the way to infinity, so we have to introduce a cutoff Landau level l_{cut} . In most cases we are able to make l_{cut} large enough that the behavior of the spectral function is clear.

Using the above formalism, we have produced spectral functions for two different conformal dimensions and fixed chemical potential and magnetic field (Fig. 21.1). Using the plane wave basis allows us to directly detect the Landau levels. The unit used for plotting the spectra (here and later on in the paper) is the effective temperature T_{eff} [6]:

$$T_{\text{eff}} = \frac{T}{2} \left(1 + \sqrt{1 + \frac{3\mu^2}{(4\pi T)^2}} \right). \tag{21.47}$$

This unit interpolates between μ at $T/\mu = 0$ and T and is of order $T/\mu \rightarrow \infty$, and is convenient for the reason that the relevant quantities (e.g., Fermi momentum) are of order unity for any value of μ and h .

21.4.2 Magnetic Crossover and Disappearance of the Quasiparticles

Theoretically, it is more convenient to consider the spectral functions in the Landau level basis. For definiteness let us pick a fixed conformal dimension $\Delta = \frac{5}{4}$ which corresponds to $m = -\frac{1}{4}$. In the limit of weak magnetic fields, $h/T \rightarrow 0$, we should reproduce the results that were found in [6].

In Fig. 21.2(A) we indeed see that the spectral function, corresponding to a low value of μ/T , behaves as expected for a nearly conformal system. The spectral function is approximately symmetric about $\omega = 0$, it vanishes for $|\omega| < k$, up to a small residual tail due to finite temperature, and for $|\omega| \gg k$ it scales as ω^{2m} .

In Fig. 21.2(B), which corresponds to a high value of μ/T , we see the emergence of a sharp quasiparticle peak. This peak becomes the sharpest when the Landau level l corresponding to an effective momentum $k_{\text{eff}} = \sqrt{2|qh|l}$ coincides with the Fermi momentum k_F . The peaks also broaden out when k_{eff} moves away from k_F . A more complete view of the Landau quantization in the quasiparticle regime is given in Fig. 21.3, where we plot the dispersion relation (ω - k map). Both the sharp peaks and the Landau levels can be visually identified.

Collectively, the spectra in Fig. 21.2 show that conformality is only broken by the chemical potential μ and not by the magnetic field. Naively, the magnetic field introduces a new scale in the system. However, this scale is absent from the spectral functions, visually validating the discussion in the previous section that the scale h can be removed by a rescaling of the temperature and chemical potential.

One thus concludes that there is some value h'_c of the magnetic field, depending on μ/T , such that the spectral function loses its quasiparticle peaks and displays near-conformal behavior for $h > h'_c$. The nature of the transition and the underlying mechanism depends on the parameters (μ_q, T, Δ) . One mechanism, obvious from the rescaling in (21.29), is the reduction of the effective coupling q as h increases. This will make the influence of the scalar potential A_0 negligible and push the system back toward conformality. Generically, the spectral function shows no sharp change but is more indicative of a crossover.

A more interesting phenomenon is the disappearance of coherent quasiparticles at high effective chemical potentials. For the special case $m = 0$, we can go beyond numerics and study this transition analytically, combining the exact $T = 0$ solution found in [24] and the mapping (21.30). In the next section, we will show that the transition is controlled by the change in the dispersion of the quasiparticle and corresponds to a sharp phase transition. Increasing the magnetic field leads to a decrease in phenomenological control parameter ν_{k_F} . This can give rise to a transition to a non-Fermi liquid when $\nu_{k_F} \leq 1/2$, and finally to the conformal regime at $h = h'_c$ when $\nu_{k_F} = 0$ and the Fermi surface vanishes.

21.4.3 Density of States

As argued at the beginning of this section, the spectral function can look quite different depending on the particular basis chosen. Though the spectral function is an attractive quantity to consider due to connection with ARPES experiments, we will also direct our attention to basis-independent and manifestly gauge invariant quantities. One of them is the density of states (DOS), defined by

$$D(\omega) = \sum_l A(\omega, l), \quad (21.48)$$

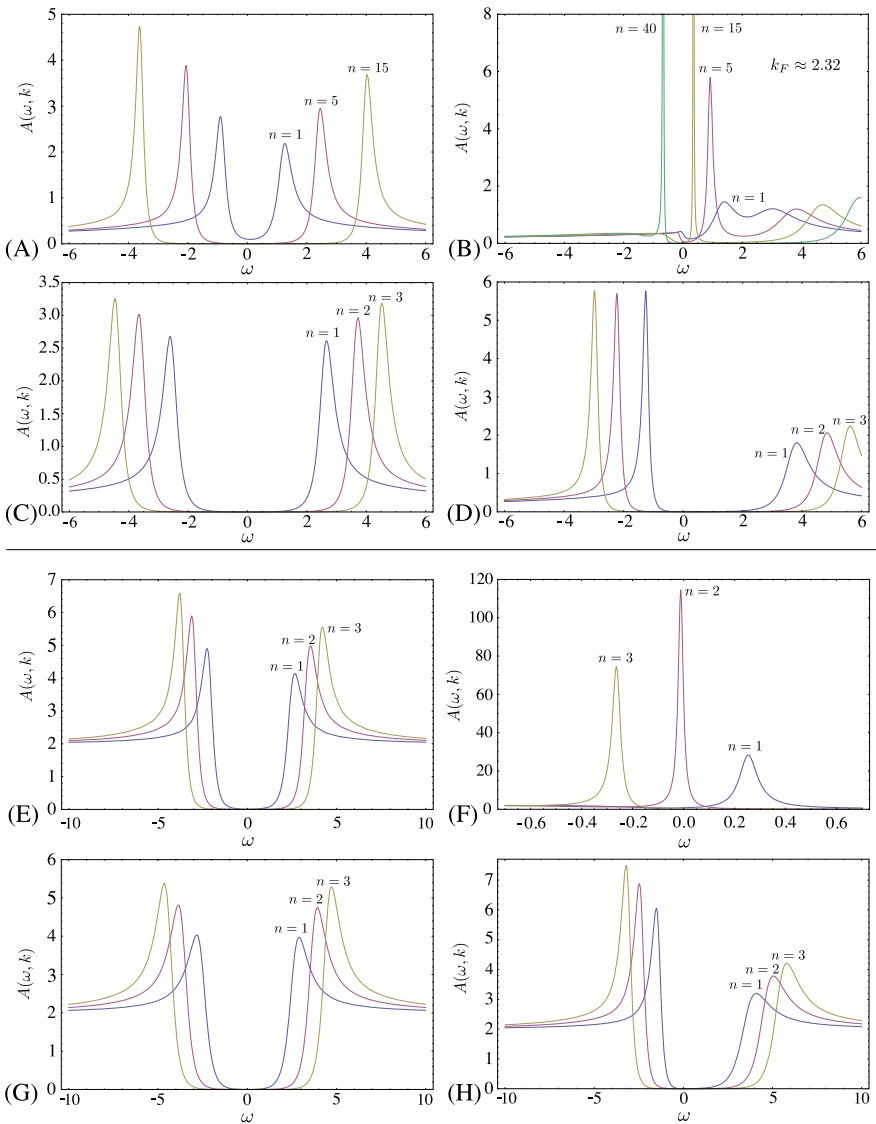


Fig. 21.2 Some typical examples of spectral functions $A(\omega, k_{\text{eff}})$ vs. ω in the Landau basis, $k_{\text{eff}} = \sqrt{2|q\hbar|n}$. The top four correspond to a conformal dimension $\Delta = \frac{5}{4}$ ($m = -\frac{1}{4}$) and the bottom four to $\Delta = \frac{3}{2}$ ($m = 0$). In each plot we show different Landau levels, labelled by index n , as a function of μ/T and h/T . The ratios take values $(\mu/T, h/T) = (1, 1), (50, 1), (1, 50), (50, 50)$ from left to right. Conformal case can be identified when μ/T is small regardless of h/T (plots in the left panel). Nearly conformal behavior is seen when both μ/T and h/T are large. This confirms our analytic result that the behavior of the system is primarily governed by μ . Departure from the conformality and sharp quasiparticle peaks are seen when μ/T is large and h/T is small in 21.2(B) and 21.2(F). Multiple quasiparticle peaks arise whenever $k_{\text{eff}} = k_F$. This suggests the existence of a critical magnetic field, beyond which the quasiparticle description becomes invalid and the system exhibits a conformal-like behavior. As before, the frequency ω is in units of T_{eff}

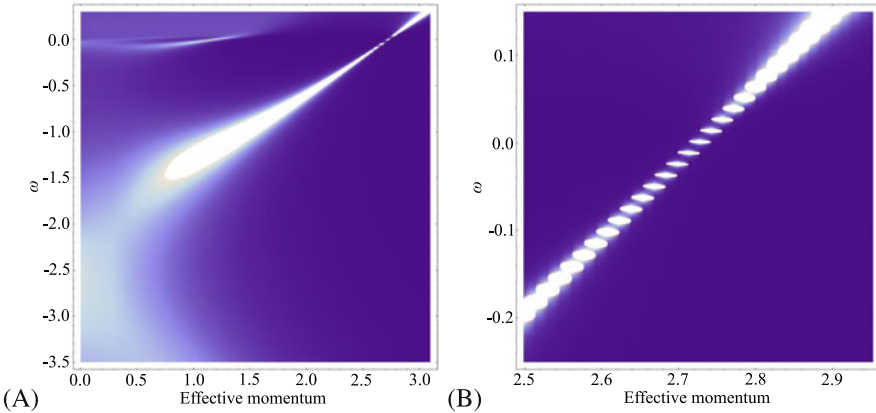


Fig. 21.3 Dispersion relation ω vs. k_{eff} for $\mu/T = 50$, $h/T = 1$ and $\Delta = \frac{5}{4}$ ($m = -\frac{1}{4}$). The spectral function $A(\omega, k_{\text{eff}})$ is displayed as a density plot. **(A)** On a large energy and momentum scale, we clearly see that the peaks disperse almost linearly ($\omega \approx v_F k$), indicating that we are in the stable quasiparticle regime. **(B)** A zoom-in near the location of the Fermi surface shows clear Landau quantization

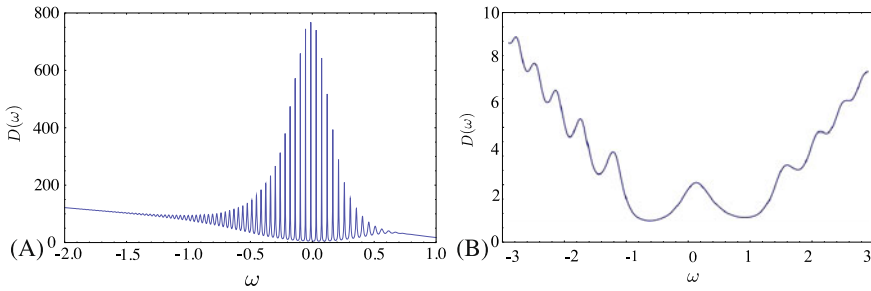


Fig. 21.4 Density of states $D(\omega)$ for $m = -\frac{1}{4}$ and **(A)** $\mu/T = 50$, $h/T = 1$, and **(B)** $\mu/T = 1$, $h/T = 1$. Sharp quasiparticle peaks from the splitting of the Fermi surface are clearly visible in **(A)**. The case **(B)** shows square-root level spacing characteristic of a (nearly) Lorentz invariant spectrum such as that of graphene

where the usual integral over the momentum is replaced by a sum since only discrete values of the momentum are allowed.

In Fig. 21.4, we plot the density of states for two systems. We clearly see the Landau splitting of the Fermi surface. A peculiar feature of these plots is that the DOS seems to grow for negative values of ω . This, however, is an artefact of our calculation. Each individual spectrum in the sum (21.48) has a finite tail that scales as ω^{2m} for large ω , so each term has a finite contribution for large values of ω . When the full sum is performed, this fact implies that $\lim_{\omega \rightarrow \infty} D(\omega) \rightarrow \infty$. The relevant information on the density of states can be obtained by regularizing the sum, which in practice is done by summing over a finite number of terms only, and then considering the peaks that lie on top of the resulting finite-sized envelope. The

physical point in Fig. 21.4(A) is the linear spacing of Landau levels, corresponding to a non-relativistic system at finite density. This is to be contrasted with Fig. 21.4B where the level spacing behaves as $\propto \sqrt{\hbar}$, appropriate for a Lorentz invariant system and realized in graphene [28].

21.5 Fermi Level Structure at Zero Temperature

In this section, we solve the Dirac equation in the magnetic field for the special case $m = 0$ ($\Delta = \frac{3}{2}$). Although there are no additional symmetries in this case, it is possible to get an analytic solution. Using this solution, we obtain Fermi level parameters such as k_F and v_F and consider the process of filling the Landau levels as the magnetic field is varied.

21.5.1 Dirac Equation with $m = 0$

In the case $m = 0$, it is convenient to solve the Dirac equation including the spin connection (see details in [27]) rather than scaling it out:

$$\left(-\frac{\sqrt{g_{ii}}}{\sqrt{g_{rr}}}\sigma^1\partial_r - \frac{\sqrt{g_{ii}}}{\sqrt{-g_{tt}}}\sigma^3(\omega + qA_t) + \frac{\sqrt{g_{ii}}}{\sqrt{-g_{tt}}}\sigma^1\frac{1}{2}\omega_{\hat{r}\hat{t}} - \sigma^1\frac{1}{2}\omega_{\hat{x}\hat{r}x} - \sigma^1\frac{1}{2}\omega_{\hat{y}\hat{r}y} - \lambda_l \right) \otimes 1 \begin{pmatrix} \psi_1 \\ \psi_2 \end{pmatrix} = 0, \quad (21.49)$$

where $\lambda_l = \sqrt{2|qh|l}$ are the energies of the Landau levels $l = 0, 1, \dots$, $g_{ii} \equiv g_{xx} = g_{yy}$, $A_t(r)$ is given by (21.3), and the gamma matrices are defined in [27]. In this basis the two components ψ_1 and ψ_2 decouple. Therefore, in what follows we solve for the first component only (we omit index 1). Substituting the spin connection, we have [20]:

$$\left(-\frac{r^2\sqrt{f}}{R^2}\sigma^1\partial_r - \frac{1}{\sqrt{f}}\sigma^3(\omega + qA_t) - \sigma^1\frac{r\sqrt{f}}{2R^2}\left(3 + \frac{rf'}{2f}\right) - \lambda_l \right) \psi = 0, \quad (21.50)$$

with $\psi = (y_1, y_2)$. It is convenient to change to the basis

$$\begin{pmatrix} \tilde{y}_1 \\ \tilde{y}_2 \end{pmatrix} = \begin{pmatrix} 1 & -i \\ -i & 1 \end{pmatrix} \begin{pmatrix} y_1 \\ y_2 \end{pmatrix}, \quad (21.51)$$

which diagonalizes the system into a second order differential equation for each component. We introduce the dimensionless variables as in (21.15)–(21.17), and make a change of the dimensionless radial variable:

$$r = \frac{1}{1-z}, \quad (21.52)$$

with the horizon now being at $z = 0$, and the conformal boundary at $z = 1$. Performing these transformations in (21.50), the second order differential equations for \tilde{y}_1 reads

$$\left(f \partial_z^2 + \left(\frac{3f}{1-z} + f' \right) \partial_z + \frac{15f}{4(1-z)^2} + \frac{3f'}{2(1-z)} + \frac{f''}{4} + \frac{1}{f} \left((\omega + q\mu z) \pm \frac{if'}{4} \right)^2 - iq\mu - \lambda_l^2 \right) \tilde{y}_1 = 0. \quad (21.53)$$

The second component \tilde{y}_2 obeys the same equation with $\mu \mapsto -\mu$.

At $T = 0$,

$$f = 3z^2(z - z_0)(z - \bar{z}_0), \quad z_0 = \frac{1}{3}(4 + i\sqrt{2}). \quad (21.54)$$

The solution of this fermion system at zero magnetic field and zero temperature $T = 0$ has been found in [24]. To solve (21.53), we use the mapping to a zero magnetic field system (21.29). The combination $\mu_q \equiv \mu q$ at non-zero h maps to $\mu_{q,\text{eff}} \equiv \mu_{\text{eff}} q_{\text{eff}}$ at zero h as follows:

$$\mu_q \mapsto q \sqrt{1 - \frac{H^2}{Q^2 + H^2}} \cdot g_F \sqrt{Q^2 + H^2} = \sqrt{3} q g_F \sqrt{1 - \frac{H^2}{3}} = \mu_{q,\text{eff}} \quad (21.55)$$

where at $T = 0$ we used $Q^2 + H^2 = 3$. We solve (21.53) for zero modes, i.e. $\omega = 0$, and at the Fermi surface $\lambda = k$, and implement (21.55).

Near the horizon ($z = 0$, $f = 6z^2$), we have

$$6z^2 \tilde{y}_{1;2}'' + 12z \tilde{y}_{1;2}' + \left(\frac{3}{2} + \frac{(\mu_{q,\text{eff}})^2}{6} - k_F^2 \right) \tilde{y}_{1;2} = 0, \quad (21.56)$$

which gives the following behavior:

$$\tilde{y}_{1;2} \sim z^{-\frac{1}{2} \pm \nu k}, \quad (21.57)$$

with the scaling exponent ν following from (21.32):

$$\nu = \frac{1}{6} \sqrt{6k^2 - (\mu_{q,\text{eff}})^2}, \quad (21.58)$$

at the momentum k . Using Maple, we find the zero mode solution of (21.53) with a regular behavior $z^{-\frac{1}{2} + \nu}$ at the horizon [20, 24]:

$$\begin{aligned} \tilde{y}_1^{(0)} &= N_1 (z - 1)^{\frac{3}{2}} z^{-\frac{1}{2} + \nu} (z - \bar{z}_0)^{-\frac{1}{2} - \nu} \left(\frac{z - z_0}{z - \bar{z}_0} \right)^{\frac{1}{4}(-1 - \sqrt{2}\mu_{q,\text{eff}}/z_0)} \\ &\times {}_2F_1 \left(\frac{1}{2} + \nu - \frac{\sqrt{2}}{3} \mu_{q,\text{eff}}, \nu + i \frac{\mu_{q,\text{eff}}}{6}, 1 + 2\nu, \frac{2i\sqrt{2}z}{3z_0(z - \bar{z}_0)} \right), \end{aligned} \quad (21.59)$$

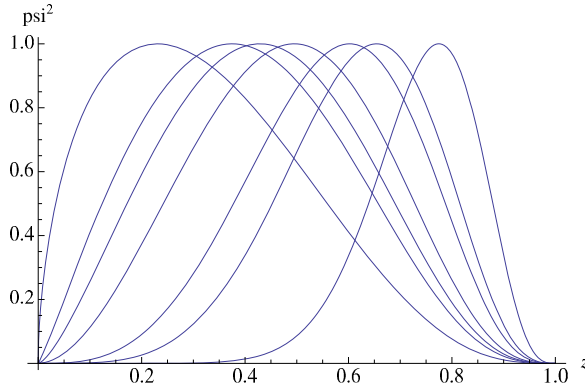


Fig. 21.5 Density of the zero mode $\psi^{0\dagger}\psi^0$ vs. the radial coordinate z (the horizon is at $z = 0$ and the boundary is at $z = 1$) for different values of the magnetic field h for the first (with the largest root for k_F) Fermi surface. We set $g_F = 1$ ($h \rightarrow H$) and $q = \frac{15}{\sqrt{3}}$ ($\mu_{q,\text{eff}} \rightarrow 15\sqrt{1 - \frac{H^2}{3}}$). From right to left the values of the magnetic field are $H = \{0, 1.40, 1.50, 1.60, 1.63, 1.65, 1.68\}$. The amplitudes of the curves are normalized to unity. At weak magnetic fields, the wave function is supported away from the horizon while at strong fields it is supported near the horizon

and

$$\tilde{y}_2^{(0)} = N_2(z - 1)^{\frac{3}{2}}z^{-\frac{1}{2}+\nu}(z - \bar{z}_0)^{-\frac{1}{2}-\nu}\left(\frac{z - z_0}{z - \bar{z}_0}\right)^{\frac{1}{4}(-1+\sqrt{2}\mu_{q,\text{eff}}/z_0)} \times {}_2F_1\left(\frac{1}{2} + \nu + \frac{\sqrt{2}}{3}\mu_{q,\text{eff}}, \nu - i\frac{\mu_{q,\text{eff}}}{6}, 1 + 2\nu, \frac{2i\sqrt{2}z}{3z_0(z - \bar{z}_0)}\right), \quad (21.60)$$

where ${}_2F_1$ is the hypergeometric function and N_1, N_2 are normalization factors. Since normalization factors are constants, we find their relative weight by substituting solutions given in (21.59) back into the first order differential equations at $z \sim 0$,

$$\frac{N_1}{N_2} = -\frac{6i\nu + \mu_{q,\text{eff}}}{\sqrt{6}k}\left(\frac{z_0}{\bar{z}_0}\right)^{\mu_{q,\text{eff}}/\sqrt{2}z_0}. \quad (21.61)$$

The same relations are obtained when calculations are done for any z . The second solution $\tilde{\eta}_{1;2}^{(0)}$, with behavior $z^{-\frac{1}{2}-\nu}$ at the horizon, is obtained by replacing $\nu \rightarrow -\nu$ in (21.59).

To get insight into the zero-mode solution (21.59), we plot the radial profile for the density function $\psi^{(0)\dagger}\psi^{(0)}$ for different magnetic fields in Fig. 21.5. The momentum chosen is the Fermi momentum of the first Fermi surface (see the next section). The curves are normalized to have the same maxima. Magnetic field is increased from right to left. At small magnetic field, the zero modes are supported away from the horizon, while at large magnetic field, the zero modes are supported near the horizon. This means that at large magnetic field the influence of the black hole to the Fermi level structure becomes more important.

21.5.2 Magnetic Effects on the Fermi Momentum and Fermi Velocity

In the presence of a magnetic field there is only a true pole in the Green's function whenever the Landau level crosses the Fermi energy [25, 26]

$$2l|qh| = k_F^2. \quad (21.62)$$

As shown in Fig. 21.2, whenever the equation (21.62) is satisfied the spectral function $A(\omega)$ has a (sharp) peak. This is not surprising since quasiparticles can be easily excited from the Fermi surface. From (21.62), the spectral function $A(\omega)$ and the density of states on the Fermi surface $D(\omega)$ are periodic in $\frac{1}{h}$ with the period

$$\Delta\left(\frac{1}{h}\right) = \frac{2\pi q}{A_F}, \quad (21.63)$$

where $A_F = \pi k_F^2$ is the area of the Fermi surface [25, 26]. This is a manifestation of the de Haas-van Alphen quantum oscillations. At $T = 0$, the electronic properties of metals depend on the density of states on the Fermi surface. Therefore, an oscillatory behavior as a function of magnetic field should appear in any quantity that depends on the density of states on the Fermi energy. Magnetic susceptibility [25, 26] and magnetization together with the superconducting gap [29] have been shown to exhibit quantum oscillations. Every Landau level contributes an oscillating term and the period of the l th level oscillation is determined by the value of the magnetic field h that satisfies (21.62) for the given value of k_F . Quantum oscillations (and the quantum Hall effect which we consider later in the paper) are examples of phenomena in which Landau level physics reveals the presence of the Fermi surface. The superconducting gap found in the quark matter in magnetic fields [29] is another evidence for the existence of the (highly degenerate) Fermi surface and the corresponding Fermi momentum.

Generally, a Fermi surface controls the occupation of energy levels in the system: the energy levels below the Fermi surface are filled and those above are empty (or non-existent). Here, however, the association to the Fermi momentum can be obscured by the fact that the fermions form highly degenerate Landau levels. Thus, in two dimensions, in the presence of the magnetic field the corresponding effective Fermi surface is given by a single point in the phase space, that is determined by n_F , the Landau index of the highest occupied level, i.e., the highest Landau level below the chemical potential.² Increasing the magnetic field, Landau levels 'move up' in the phase space leaving only the lower levels occupied, so that the effective Fermi momentum scales roughly (excluding interactions) as a square root of the magnetic field, $k_F \sim \sqrt{n_F} \sim k_F^{\max} \sqrt{1 - h/h_{\max}}$. High magnetic fields drive the effective density of the charge carriers down, approaching the limit when the Fermi momentum coincides with the lowest Landau level.

²We would like to thank Igor Shovkovy for clarifying the issue with the Fermi momentum in the presence of the magnetic field.

Many phenomena observed in the paper can thus be qualitatively explained by Landau quantization. As discussed before, the notion of the Fermi momentum is lost at very high magnetic fields. In what follows, the quantitative Fermi level structure at zero temperature, described by k_F and v_F values, is obtained as a function of the magnetic field using the solution of the Dirac equation given by (21.59), (21.60). As in [12], we neglect first the discrete nature of the Fermi momentum and velocity in order to obtain general understanding. Upon taking the quantization into account, the smooth curves become combinations of step functions following the same trend as the smooth curves (without quantization). While usually the grand canonical ensemble is used, where the fixed chemical potential controls the occupation of the Landau levels [30], in our setup, the Fermi momentum is allowed to change as the magnetic field is varied, while we keep track of the IR conformal dimension ν .

The Fermi momentum is defined by the matching between IR and UV physics [8], therefore it is enough to know the solution at $\omega = 0$, where the matching is performed. To obtain the Fermi momentum, we require that the zero mode solution is regular at the horizon ($\psi^{(0)} \sim z^{-\frac{1}{2}+\nu}$) and normalizable at the boundary. At the boundary $z \sim 1$, the wave function behaves as

$$a(1-z)^{\frac{3}{2}-m} \begin{pmatrix} 1 \\ 0 \end{pmatrix} + b(1-z)^{\frac{3}{2}+m} \begin{pmatrix} 0 \\ 1 \end{pmatrix}. \tag{21.64}$$

To require it to be normalizable is to set the first term $a = 0$; the wave function at $z \sim 1$ is then

$$\psi^{(0)} \sim (1-z)^{\frac{3}{2}+m} \begin{pmatrix} 0 \\ 1 \end{pmatrix}. \tag{21.65}$$

Equation (21.65) leads to the condition $\lim_{z \rightarrow 1} (z-1)^{-3/2} (\tilde{y}_2^{(0)} + i\tilde{y}_1^{(0)}) = 0$, which, together with (21.59), gives the following equation for the Fermi momentum as function of the magnetic field [20, 24]

$$\frac{{}_2F_1(1+\nu + \frac{i\mu_{q,\text{eff}}}{6}, \frac{1}{2} + \nu - \frac{\sqrt{2}\mu_{q,\text{eff}}}{3}, 1+2\nu, \frac{2}{3}(1-i\sqrt{2}))}{{}_2F_1(\nu + \frac{i\mu_{q,\text{eff}}}{6}, \frac{1}{2} + \nu - \frac{\sqrt{2}\mu_{q,\text{eff}}}{3}, 1+2\nu, \frac{2}{3}(1-i\sqrt{2}))} = \frac{6\nu - i\mu_{q,\text{eff}}}{k_F(-2i + \sqrt{2})}, \tag{21.66}$$

with $\nu \equiv \nu_{k_F}$ given by (21.58). Using Mathematica to evaluate the hypergeometric functions, we numerically solve the equation for the Fermi surface, which gives effective momentum as if it were continuous, i.e. when quantization is neglected. The solutions of (21.66) are given in Fig. 21.6. There are multiple Fermi surfaces for a given magnetic field h . Here and in all other plots we choose $g_F = 1$, therefore $h \rightarrow H$, and $q = \frac{15}{\sqrt{3}}$. In Fig. 21.6, positive and negative k_F correspond to the Fermi surfaces in the Green's functions G_1 and G_2 . The relation between two components is $G_2(\omega, k) = G_1(\omega, -k)$ [7], therefore Fig. 21.6 is not symmetric with respect to the x-axis. Effective momenta terminate at the dashed line $\nu_{k_F} = 0$. Taking into account Landau quantization of $k_F \rightarrow \sqrt{2|qh|l}$ with $l = 1, 2, \dots$, the plot consists of stepwise functions tracing the existing curves (we depict only positive k_F). Indeed

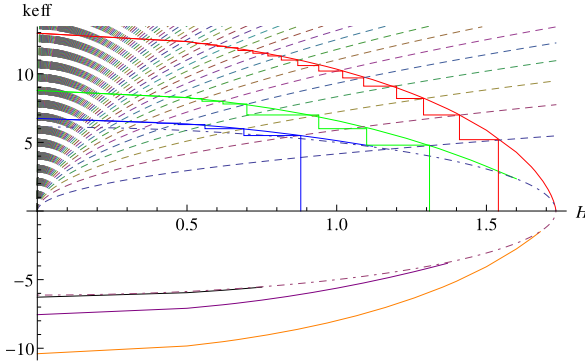
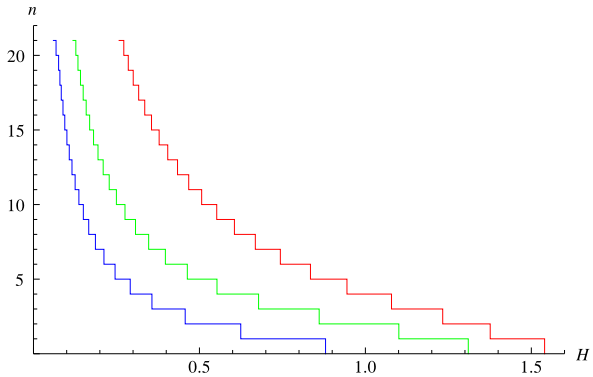


Fig. 21.6 Effective momentum k_{eff} vs. the magnetic field $h \rightarrow H$ (we set $g_F = 1$, $q = \frac{15}{\sqrt{3}}$). As we increase magnetic field the Fermi surface shrinks. *Smooth solid curves* represent situation as if momentum is a continuous parameter (for convenience), *stepwise solid functions* are the real Fermi momenta which are discretized due to the Landau level quantization: $k_F \rightarrow \sqrt{2|qh|l}$ with $l = 1, 2, \dots$ where $\sqrt{2|qh|l}$ are Landau levels given by *dotted lines* (only positive discrete k_F are shown). At a given h there are multiple Fermi surfaces. From right to left are the first, second etc. Fermi surfaces. The *dashed-dotted line* is $v_{k_F} = 0$ where k_F is terminated. Positive and negative k_{eff} correspond to Fermi surfaces in two components of the Green's function

Fig. 21.7 Landau level numbers n corresponding to the quantized Fermi momenta vs. the magnetic field $h \rightarrow H$ for the three Fermi surfaces with positive k_F . We set $g_F = 1$, $q = \frac{15}{\sqrt{3}}$. From right to left are the first, second and third Fermi surfaces



Landau quantization can be also seen from the dispersion relation at Fig. 21.3, where only discrete values of effective momentum are allowed and the Fermi surface has been chopped up as a result of it Fig. 21.3(B).

Our findings agree with the results for the (largest) Fermi momentum in a three-dimensional magnetic system considered in [31], compare the stepwise dependence $k_F(h)$ with Fig. 21.5 in [31].

In Fig. 21.7, the Landau level index l is obtained from $k_F(h) = \sqrt{2|qh|l}$ where $k_F(h)$ is a numerical solution of (21.66). Only those Landau levels which are below the Fermi surface are filled. In Fig. 21.6, as we decrease magnetic field first nothing happens until the next Landau level crosses the Fermi surface which corresponds to a jump up to the next step. Therefore, at strong magnetic fields, fewer states contribute

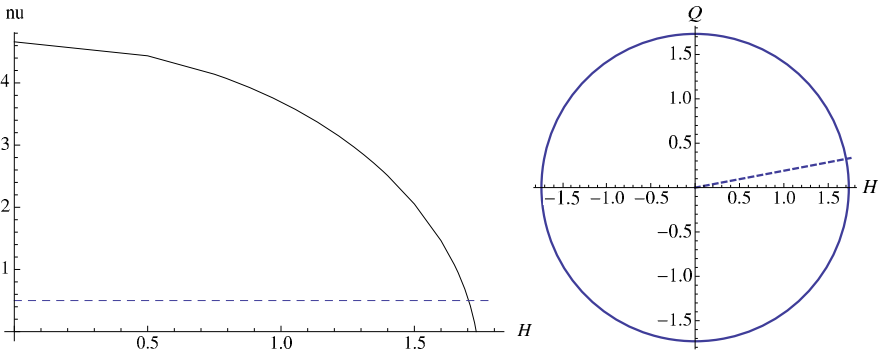


Fig. 21.8 *Left panel.* The IR conformal dimension $\nu \equiv \nu_{k_F}$ calculated at the Fermi momentum vs. the magnetic field $h \rightarrow H$ (we set $g_F=1, q = \frac{15}{\sqrt{3}}$). Calculations are done for the first Fermi surface. *Dashed line* is for $\nu = \frac{1}{2}$ (at $H_c = 1.70$), which is the border between the Fermi liquids $\nu > \frac{1}{2}$ and non-Fermi liquids $\nu < \frac{1}{2}$. *Right panel.* Phase diagram in terms of the chemical potential and the magnetic field $\mu^2 + h^2 = 3$ (in dimensionless variables $h = g_F H, \mu = g_F Q$; we set $g_F = 1$). Fermi liquids are above the *dashed line* ($H < H_c$) and non-Fermi liquids are below the *dashed line* ($H > H_c$)

to transport properties and the lowest Landau level becomes more important (see the next section). At weak magnetic fields, the sum over many Landau levels has to be taken, ending with the continuous limit as $h \rightarrow 0$, when quantization can be ignored.

In Fig. 21.8, we show the IR conformal dimension as a function of the magnetic field. We have used the numerical solution for k_F . Fermi liquid regime takes place at magnetic fields $h < h_c$, while non-Fermi liquids exist in a narrow band at $h_c < h < h'_c$, and at h'_c the system becomes near-conformal.

In this figure we observe the pathway of the possible phase transition exhibited by the Fermi surface (ignoring Landau quantization): it can vanish at the line $\nu_{k_F} = 0$, undergoing a crossover to the conformal regime, or cross the line $\nu_{k_F} = 1/2$ and go through a non-Fermi liquid regime, and subsequently cross to the conformal phase. Note that the primary Fermi surface with the highest k_F and ν_{k_F} seems to directly cross over to conformality, while the other Fermi surfaces first exhibit a “strange metal” phase transition. Therefore, all the Fermi momenta with $\nu_{k_F} > 0$ contribute to the transport coefficients of the theory. In particular, at high magnetic fields when for the first (largest) Fermi surface $k_F^{(1)}$ is nonzero but small, the lowest Landau level $n = 0$ becomes increasingly important contributing to the transport with half degeneracy factor as compared to the higher Landau levels.

In Fig. 21.9, we plot the Fermi momentum k_F as a function of the magnetic field for the first Fermi surface (the largest root of (21.66)). Quantization is neglected here. At the left panel, the relatively small region between the dashed lines corresponds to non-Fermi liquids $0 < \nu < \frac{1}{2}$. At large magnetic field, the physics of the Fermi surface is captured by the near horizon region (see also Fig. 21.5) which is $AdS_2 \times R^2$. At the maximum magnetic field, $H_{\max} = \sqrt{3} \approx 1.73$, when the black hole becomes pure magnetically charged, the Fermi momentum vanishes when it

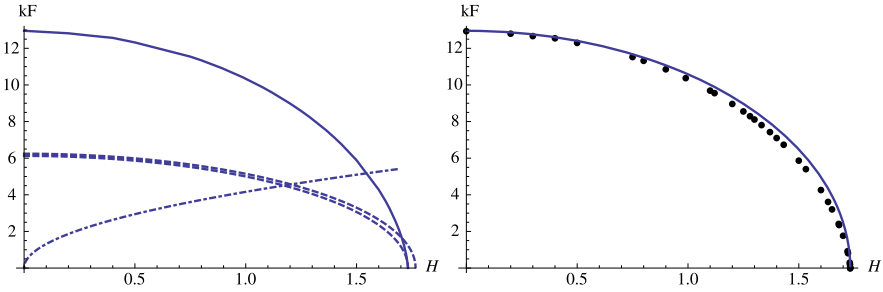


Fig. 21.9 Fermi momentum k_F vs. the magnetic field $h \rightarrow H$ (we set $g_F = 1, q = \frac{15}{\sqrt{3}}$) for the first Fermi surface. *Left panel.* The *inner* (closer to x-axis) *dashed line* is $v_{k_F} = 0$ and the *outer dashed line* is $v_{k_F} = \frac{1}{2}$, the region between these lines corresponds to non-Fermi liquids $0 < v_{k_F} < \frac{1}{2}$. The *dashed-dotted line* is for the first Landau level $k_1 = \sqrt{2qH}$. The first Fermi surface hits the *border-line* between a Fermi and non-Fermi liquids $v = \frac{1}{2}$ at $H_c \approx 1.70$, and it vanishes at $H_{\max} = \sqrt{3} = 1.73$. *Right panel.* *Circles* are the data points for the Fermi momentum calculated analytically, *solid line* is a fit function $k_F^{\max} \sqrt{1 - \frac{H^2}{3}}$ with $k_F^{\max} = 12.96$

crosses the line $v_{k_F} = 0$. This only happens for the first Fermi surface. For the higher Fermi surfaces the Fermi momenta terminate at the line $v_{k_F} = 0$, Fig. 21.6. Note the Fermi momentum for the first Fermi surface can be almost fully described by a function $k_F = k_F^{\max} \sqrt{1 - \frac{H^2}{3}}$. It is tempting to view the behavior $k_F \sim \sqrt{H_{\max} - H}$ as a phase transition in the system although it strictly follows from the linear scaling for $H = 0$ by using the mapping (21.29). (Note that also $\mu = g_F Q = g_F \sqrt{3 - H^2}$.) Taking into account the discretization of k_F , the plot will consist of an array of step functions tracing the existing curve. Our findings agree with the results for the Fermi momentum in a three dimensional magnetic system considered in [31], compare with Fig. 21.5 there.

The Fermi velocity given in (21.27) is defined by the UV physics; therefore solutions at non-zero ω are required. The Fermi velocity is extracted from matching two solutions in the inner and outer regions at the horizon. The Fermi velocity as function of the magnetic field for $v > \frac{1}{2}$ is [20, 24]

$$v_F = \frac{1}{h_1} \left(\int_0^1 dz \sqrt{g/g_{tt}} \psi^{(0)\dagger} \psi^{(0)} \right)^{-1} \lim_{z \rightarrow 1} \frac{|\tilde{y}_1^{(0)} + i\tilde{y}_2^{(0)}|^2}{(1-z)^3}, \quad (21.67)$$

$$h_1 = \lim_{z \rightarrow 1} \frac{\tilde{y}_1^{(0)} + i\tilde{y}_2^{(0)}}{\partial_k (y_2^{(0)} + i\tilde{y}_1^{(0)})},$$

where the zero mode wavefunction is taken at k_F (21.59).

We plot the Fermi velocity for several Fermi surfaces in Fig. 21.10. Quantization is neglected here. The Fermi velocity is shown for $v > \frac{1}{2}$. It is interesting that the Fermi velocity vanishes when the IR conformal dimension is $v_{k_F} = \frac{1}{2}$. Formally, it follows from the fact that $v_F \sim (2v - 1)$ [8]. The first Fermi surface is at the

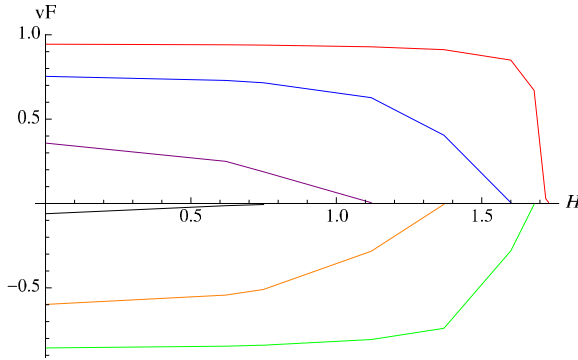


Fig. 21.10 Fermi velocity v_F vs. the magnetic field $h \rightarrow H$ (we set $g_F = 1$, $q = \frac{15}{\sqrt{3}}$) for the regime of Fermi liquids $v \geq \frac{1}{2}$. Fermi velocity vanishes at $v_{k_F} = \frac{1}{2}$ (x -axis). For the first Fermi surface, the *top curve*, Fermi velocity vanishes at $H_c \approx 1.70$. The region $H < H_c$ corresponds to the Fermi liquids and quasiparticle description. The *multiple lines* are for various Fermi surfaces in ascending order, with the first Fermi surface on the right. The Fermi velocity v_F has the same sign as the Fermi momentum k_F . As above, positive and negative v_F correspond to Fermi surfaces in the two components of the Green's function

far right. Positive and negative v_F correspond to the Fermi surfaces in the Green's functions G_1 and G_2 , respectively. The Fermi velocity v_F has the same sign as the Fermi momentum k_F . At small magnetic field values, the Fermi velocity is very weakly dependent on H and it is close to the speed of light; at large magnetic field values, the Fermi velocity rapidly decreases and vanishes (at $H_c = 1.70$ for the first Fermi surface). Geometrically, this means that with increasing magnetic field the zero mode wavefunction is supported near the black hole horizon Fig. 21.5, where the gravitational redshift reduces the local speed of light as compared to the boundary value. It was also observed in [8, 24] at small fermion charge values.

21.6 Hall and Longitudinal Conductivities

In this section, we calculate the contributions to Hall σ_{xy} and the longitudinal σ_{xx} conductivities directly in the boundary theory. This should be contrasted with the standard holographic approach, where calculations are performed in the (bulk) gravity theory and then translated to the boundary field theory using the AdS/CFT dictionary. Specifically, the conductivity tensor has been obtained in [11] by calculating the on-shell renormalized action for the gauge field on the gravity side and using the gauge/gravity duality $A_M \rightarrow j_\mu$ to extract the R charge current-current correlator at the boundary. Here, the Kubo formula involving the current-current correlator is used directly by utilizing the fermion Green's functions extracted from holography in [8]. Therefore, the conductivity is obtained for the charge carriers described by the fermionic operators of the boundary field theory.

The use of the conventional Kubo formula to extract the contribution to the transport due to fermions is validated in that it also follows from a direct AdS/CFT computation of the one-loop correction to the on-shell renormalized AdS action [17]. We study in particular stable quasiparticles with $\nu > \frac{1}{2}$ and at zero temperature. This regime effectively reduces to the clean limit where the imaginary part of the self-energy vanishes $\text{Im } \Sigma \rightarrow 0$. We use the gravity-“dressed” fermion propagator from (21.27) and to make the calculations complete, the “dressed” vertex is necessary, to satisfy the Ward identities. As was argued in [17], the boundary vertex which is obtained from the bulk calculations can be approximated by a constant in the low temperature limit. Also, according to [32, 33], the vertex only contains singularities of the product of the Green’s functions. Therefore, dressing the vertex will not change the dependence of the DC conductivity on the magnetic field [32, 33]. In addition, the zero magnetic field limit of the formulae for conductivity obtained from holography [17] and from direct boundary calculations [20] are identical.

21.6.1 Integer Quantum Hall Effect

Let us start from the “dressed” retarded and advanced fermion propagators [8]: G_R is given by (21.27) and $G_A = G_R^*$. To perform the Matsubara summation we use the spectral representation

$$G(i\omega_n, \mathbf{k}) = \int \frac{d\omega}{2\pi} \frac{A(\omega, \mathbf{k})}{\omega - i\omega_n}, \quad (21.68)$$

with the spectral function defined as $A(\omega, \mathbf{k}) = -\frac{1}{\pi} \text{Im } G_R(\omega, \mathbf{k}) = \frac{1}{2\pi i} (G_R(\omega, \mathbf{k}) - G_A(\omega, \mathbf{k}))$. Generalizing to a non-zero magnetic field and spinor case [30], the spectral function [34] is

$$A(\omega, \mathbf{k}) = \frac{1}{\pi} e^{-\frac{k^2}{|q\hbar|}} \sum_{l=0}^{\infty} (-1)^l (-h_1 v_F) \times \left(\frac{\Sigma_2(\omega, k_F) f(\mathbf{k}) \gamma^0}{(\omega + \varepsilon_F + \Sigma_1(\omega, k_F) - E_l)^2 + \Sigma_2(\omega, k_F)^2} + (E_l \rightarrow -E_l) \right), \quad (21.69)$$

where $\varepsilon_F = v_F k_F$ is the Fermi energy, $E_l = v_F \sqrt{2|q\hbar|l}$ is the energy of the Landau level, $f(\mathbf{k}) = P_- L_l(\frac{2k^2}{|q\hbar|}) - P_+ L_{l-1}(\frac{2k^2}{|q\hbar|})$ with spin projection operators $P_{\pm} = (1 \pm i\gamma^1 \gamma^2)/2$, we take $c = 1$, the generalized Laguerre polynomials are $L_n^\alpha(z)$ and by definition $L_n(z) = L_n^0(z)$, (we omit the vector part $\mathbf{k}\gamma$, it does not contribute to the DC conductivity), all γ ’s are the standard Dirac matrices, h_1 , v_F and k_F are real constants (we keep the same notations for the constants as in [8]). The self-energy $\Sigma \sim \omega^{2\nu k_F}$ contains the real and imaginary parts, $\Sigma = \Sigma_1 + i\Sigma_2$. The imaginary part comes from scattering processes of a fermion in the bulk, e.g. from

pair creation, and from the scattering into the black hole. It is exactly due to inelastic/dissipative processes that we are able to obtain finite values for the transport coefficients, otherwise they are formally infinite.

Using the Kubo formula, the DC electrical conductivity tensor is

$$\sigma_{ij}(\Omega) = \lim_{\Omega \rightarrow 0} \frac{\text{Im} \Pi_{ij}^R}{\Omega + i0^+}, \tag{21.70}$$

where $\Pi_{ij}(i\Omega_m \rightarrow \Omega + i0^+)$ is the retarded current-current correlation function; schematically the current density operator is $j^i(\tau, \mathbf{x}) = q v_F \sum_{\sigma} \bar{\psi}_{\sigma}(\tau, \mathbf{x}) \gamma^i \psi_{\sigma}(\tau, \mathbf{x})$. Neglecting the vertex correction, it is given by

$$\Pi_{ij}(i\Omega_m) = q^2 v_F^2 T \sum_{n=-\infty}^{\infty} \int \frac{d^2k}{(2\pi)^2} \text{tr}(\gamma^i G(i\omega_n, \mathbf{k}) \gamma^j G(i\omega_n + i\Omega_m, \mathbf{k})). \tag{21.71}$$

The sum over the Matsubara frequency is

$$T \sum_n \frac{1}{i\omega_n - \omega_1} \frac{1}{i\omega_n + i\Omega_m - \omega_2} = \frac{n(\omega_1) - n(\omega_2)}{i\Omega_m + \omega_1 - \omega_2}. \tag{21.72}$$

Taking $i\Omega_m \rightarrow \Omega + i0^+$, the polarization operator is now

$$\Pi_{ij}(\Omega) = \frac{d\omega_1}{2\pi} \frac{d\omega_2}{2\pi} \frac{n_{\text{FD}}(\omega_1) - n_{\text{FD}}(\omega_2)}{\Omega + \omega_1 - \omega_2} \int \frac{d^2k}{(2\pi)^2} \text{tr}(\gamma^i A(\omega_1, \mathbf{k}) \gamma^j A(\omega_2, \mathbf{k})), \tag{21.73}$$

where the spectral function $A(\omega, \mathbf{k})$ is given by (21.69) and $n_{\text{FD}}(\omega)$ is the Fermi-Dirac distribution function. Evaluating the traces, we have

$$\begin{aligned} \sigma_{ij} = & -\frac{4q^2 v_F^2 (h_1 v_F)^2 |qh|}{\pi \Omega} \\ & \times \text{Re} \sum_{l,k=0}^{\infty} (-1)^{l+k+1} \{ \delta_{ij} (\delta_{l,k-1} + \delta_{l-1,k}) + i \varepsilon_{ij} \text{sgn}(qh) (\delta_{l,k-1} - \delta_{l-1,k}) \} \\ & \times \int \frac{d\omega_1}{2\pi} \left(\tanh \frac{\omega_1}{2T} - \tanh \frac{\omega_2}{2T} \right) \left(\frac{\Sigma_2(\omega_1)}{(\tilde{\omega}_1 - E_l)^2 + \Sigma_2^2(\omega_1)} + (E_l \rightarrow -E_l) \right) \\ & \times \left(\frac{\Sigma_2(\omega_2)}{(\tilde{\omega}_2 - E_k)^2 + \Sigma_2^2(\omega_2)} + (E_k \rightarrow -E_k) \right), \end{aligned} \tag{21.74}$$

with $\omega_2 = \omega_1 + \Omega$. We have also introduced $\tilde{\omega}_{1,2} \equiv \omega_{1,2} + \varepsilon_F + \Sigma_1(\omega_{1,2})$ with ε_{ij} being the antisymmetric tensor ($\varepsilon_{12} = 1$), and $\Sigma_{1,2}(\omega) \equiv \Sigma_{1,2}(\omega, k_F)$. In the momentum integral, we use the orthogonality condition for the Laguerre polynomials $\int_0^{\infty} dx e^x L_l(x) L_k(x) = \delta_{lk}$.

From (21.74), the term symmetric/antisymmetric with respect to exchange $\omega_1 \leftrightarrow \omega_2$ contributes to the diagonal/off-diagonal component of the conductivity (note the

antisymmetric term $n_{\text{FD}}(\omega_1) - n_{\text{FD}}(\omega_2)$). The longitudinal and Hall DC conductivities ($\mathcal{J}\Omega \rightarrow 0$) are thus

$$\begin{aligned} \sigma_{xx} = & -\frac{2q^2(h_1 v_F)^2 |qh|}{\pi T} \int_{-\infty}^{\infty} \frac{d\omega}{2\pi} \frac{\Sigma_2^2(\omega)}{\cosh^2 \frac{\omega}{2T}} \\ & \times \sum_{l=0}^{\infty} \left(\frac{1}{(\tilde{\omega} - E_l)^2 + \Sigma_2^2(\omega)} + (E_l \rightarrow -E_l) \right) \\ & \times \left(\frac{1}{(\tilde{\omega} - E_{l+1})^2 + \Sigma_2^2(\omega)} + (E_{l+1} \rightarrow -E_{l+1}) \right), \end{aligned} \quad (21.75)$$

$$\sigma_{xy} = -\frac{q^2(h_1 v_F)^2 \text{sgn}(qh)}{\pi} \nu_h, \quad (21.76)$$

$$\nu_h = 2 \int_{-\infty}^{\infty} \frac{d\omega}{2\pi} \tanh \frac{\omega}{2T} \Sigma_2(\omega) \sum_{l=0}^{\infty} \alpha_l \left(\frac{1}{(\tilde{\omega} - E_l)^2 + \Sigma_2^2(\omega)} + (E_l \rightarrow -E_l) \right),$$

where $\tilde{\omega} = \omega + \varepsilon_F + \Sigma_1(\omega)$. The filling factor ν_h is proportional to the density of carriers: $|\nu_h| = \frac{\pi}{|qh|h_1 v_F} n$ (see derivation in [27]). The degeneracy factor of the Landau levels is α_l : $\alpha_0 = 1$ for the lowest Landau level and $\alpha_l = 2$ for $l = 1, 2, \dots$. Substituting the filling factor ν_h back to (21.76), the Hall conductivity can be written as

$$\sigma_{xy} = \frac{\rho}{h}, \quad (21.77)$$

where ρ is the charge density in the boundary theory, and both the charge q and the magnetic field h carry a sign (the prefactor $(-h_1 v_F)$ comes from the normalization choice in the fermion propagator (21.27), (21.69) as given in [8], which can be regarded as a factor contributing to the effective charge and is not important for further considerations). The Hall conductivity (21.77) has been obtained using the AdS/CFT duality for the Lorentz invariant 2 + 1-dimensional boundary field theories in [11]. We recover this formula because in our case the translational invariance is maintained in the x and y directions of the boundary theory.

Low frequencies give the main contribution in the integrand of (21.76). Since the self-energy satisfies $\Sigma_1(\omega) \sim \Sigma_2(\omega) \sim \omega^{2\nu}$ and we consider the regime $\nu > \frac{1}{2}$, we have $\Sigma_1 \sim \Sigma_2 \rightarrow 0$ at $\omega \sim 0$ (self-energy goes to zero faster than the ω term). Therefore, only the simple poles in the upper half-plane $\omega_0 = -\varepsilon_F \pm E_l + \Sigma_1 + i\Sigma_2$ contribute to the conductivity where $\Sigma_1 \sim \Sigma_2 \sim (-\varepsilon_F \pm E_l)^{2\nu}$ are small. The same logic of calculation has been used in [30]. We obtain for the longitudinal and Hall conductivities

$$\sigma_{xx} = \frac{2q^2(h_1 v_F)^2 \Sigma_2}{\pi T} \times \left(\frac{1}{1 + \cosh \frac{\varepsilon_F}{T}} + \sum_{l=1}^{\infty} 4l \frac{1 + \cosh \frac{\varepsilon_F}{T} \cosh \frac{E_l}{T}}{(\cosh \frac{\varepsilon_F}{T} + \cosh \frac{E_l}{T})^2} \right), \quad (21.78)$$

$$\sigma_{xy} = \frac{q^2(h_1 v_F)^2 \text{sgn}(qh)}{\pi} \times 2 \left(\tanh \frac{\varepsilon_F}{2T} + \sum_{l=1}^{\infty} \left(\tanh \frac{\varepsilon_F + E_l}{2T} + \tanh \frac{\varepsilon_F - E_l}{2T} \right) \right), \quad (21.79)$$

where the Fermi energy is $\varepsilon_F = v_F k_F$ and the energy of the Landau level is $E_l = v_F \sqrt{2|qh|l}$. Similar expressions were obtained in [30]. However, in our case the filling of the Landau levels is controlled by the magnetic field h through the field-dependent Fermi energy $v_F(h)k_F(h)$ instead of the chemical potential μ .

At $T = 0$, $\cosh \frac{\omega}{T} \rightarrow \frac{1}{2} e^{\frac{\omega}{T}}$ and $\tanh \frac{\omega}{2T} = 1 - 2n_{\text{FD}}(\omega) \rightarrow \text{sgn}\omega$. Therefore the longitudinal and Hall conductivities are

$$\sigma_{xx} = \frac{2q^2(h_1 v_F)^2 \Sigma_2}{\pi T} \sum_{l=1}^{\infty} l \delta_{\varepsilon_F, E_l} = \frac{2q^2(h_1 v_F)^2 \Sigma_2}{\pi T} \times n \delta_{\varepsilon_F, E_n}, \quad (21.80)$$

$$\begin{aligned} \sigma_{xy} &= \frac{q^2(h_1 v_F)^2 \text{sgn}(qh)}{\pi} 2 \left(1 + 2 \sum_{l=1}^{\infty} \theta(\varepsilon_F - E_l) \right) \\ &= \frac{q^2(h_1 v_F)^2 \text{sgn}(qh)}{\pi} \times 2(1 + 2n)\theta(\varepsilon_F - E_n)\theta(E_{n+1} - \varepsilon_F), \end{aligned} \quad (21.81)$$

where the Landau level index runs $n = 0, 1, \dots$. It can be estimated as $n = [\frac{k_F^2}{2|qh|}]$ when $v_F \neq 0$ ($[\]$ denotes the integer part), with the average spacing between the Landau levels given by the Landau energy $v_F \sqrt{2|qh|}$. Note that $\varepsilon_F \equiv \varepsilon_F(h)$. We can see that (21.81) expresses the integer quantum Hall effect (IQHE). At zero temperature, as we dial the magnetic field, the Hall conductivity jumps from one quantized level to another, forming plateaus given by the filling factor

$$\nu_h = \pm 2(1 + 2n) = \pm 4 \left(n + \frac{1}{2} \right), \quad (21.82)$$

with $n = 0, 1, \dots$ (Compare to the conventional Hall quantization $\nu_h = \pm 4n$, that appears in thick graphene.) Plateaus of the Hall conductivity at $T = 0$ follow from the stepwise behavior of the charge density ρ in (21.77):

$$\rho \sim 4 \left(n + \frac{1}{2} \right) \theta(\varepsilon_F - E_n)\theta(E_{n+1} - \varepsilon_F), \quad (21.83)$$

where n Landau levels are filled and contribute to ρ . The longitudinal conductivity vanishes except precisely at the transition point between the plateaus. In Fig. 21.11, we plot the longitudinal and Hall conductivities at $T = 0$, using only the terms after $\times \text{sign}$ in (21.79). In the Hall conductivity, plateau transition occurs when the Fermi level (in Fig. 21.11) of the first Fermi surface $\varepsilon_F = v_F(h)k_F(h)$ (Fig. 21.9) crosses the Landau level energy as we vary the magnetic field. By decreasing the magnetic field, the plateaus become shorter and increasingly more Landau levels contribute to the Hall conductivity. This happens because of two factors: the Fermi level moves

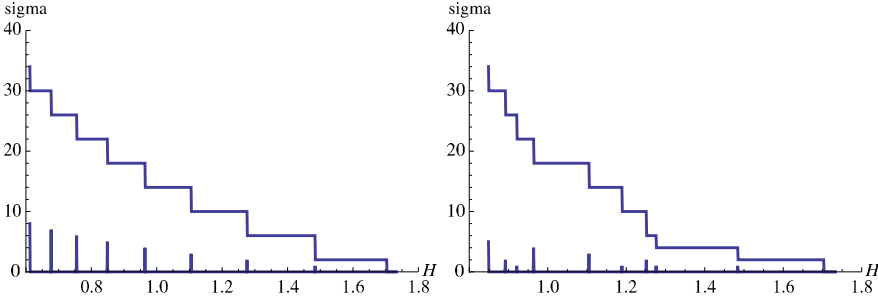


Fig. 21.11 Hall conductivity σ_{xy} and longitudinal conductivity σ_{xx} vs. the magnetic field $h \rightarrow H$ at $T = 0$ (we set $g_F = 1, q = \frac{15}{\sqrt{3}}$). *Left panel* is for IQHE. *Right panel* is for FQHE. At strong magnetic fields, the Hall conductivity plateau $\nu_h = 4$ appears together with plateaus $\nu_h = 2$ and $\nu_h = 6$ in FQHE (details are in [27]). Irregular pattern in the length of the plateaus for FQHE is observed in experiments on thin films of graphite at strong magnetic fields [28]

up and the spacing between the Landau levels becomes smaller. This picture does not depend on the Fermi velocity as long as it is nonzero.

21.6.2 Fractional Quantum Hall Effect

In [27], using the holographic description of fermions, we obtained the filling factor at strong magnetic fields

$$\nu_h = \pm 2j, \tag{21.84}$$

where j is the effective Landau level index. Equation (21.84) expresses the fractional quantum Hall effect (FQHE). In the quasiparticle picture, the effective index is integer $j = 0, 1, 2, \dots$, but generally it may be fractional. In particular, the filling factors $\nu = 2/m$ where $m = 1, 2, 3, \dots$ have been proposed by Halperin [35] for the case of bound electron pairs, i.e. $2e$ -charge bosons. Indeed, QED becomes effectively confining in ultraquantum limit at strong magnetic field, and the electron pairing is driven by the Landau level quantization and gives rise to $2e$ bosons. In our holographic description, quasiparticles are valid degrees of freedom only for $\nu > 1/2$, i.e. for weak magnetic field. At strong magnetic field, poles of the fermion propagator should be taken into account in calculation of conductivity. This will probably result in a fractional filling factor. Our pattern for FQHE Fig. 21.11 resembles the one obtained by Kopelevich in Fig. 3 [36] which has been explained using the fractional filling factor of Halperin [35].

The somewhat regular pattern behind the irregular behavior can be understood as a consequence of the appearance of a new energy scale: the average distance between the Fermi levels. For the case of Fig. 21.11, we estimate it to be $\langle \varepsilon_F^{(m)} - \varepsilon_F^{(m+1)} \rangle = 4.9$ with $m = 1, 2$. The authors of [30] explain the FQHE through the

opening of a gap in the quasiparticle spectrum, which acts as an order parameter related to the particle-hole pairing and is enhanced by the magnetic field (magnetic catalysis). Here, the energy gap arises due to the participation of multiple Fermi surfaces.

A pattern for the Hall conductivity that is strikingly similar to Fig. 21.11 arises in the AA and AB-stacked bilayer graphene, which has different transport properties from the monolayer graphene [37], compare with Figs. 2, 5 there. It is remarkable that the bilayer graphene also exhibits the insulating behavior in a certain parameter regime. This agrees with our findings of metal-insulating transition in our system.

21.7 Conclusions

We have studied strongly coupled electron systems in the magnetic field focussing on the Fermi level structure, using the AdS/CFT correspondence. These systems are dual to Dirac fermions placed in the background of the electrically and magnetically charged AdS-Reissner-Nordström black hole. At strong magnetic fields the dual system “lives” near the black hole horizon, which substantially modifies the Fermi level structure. As we dial the magnetic field higher, the system exhibits the non-Fermi liquid behavior and then crosses back to the conformal regime. In our analysis we have concentrated on the Fermi liquid regime and obtained the dependence of the Fermi momentum k_F and Fermi velocity v_F on the magnetic field. Remarkably, k_F exhibits the square root behavior, with v_F staying close to the speed of light in a wide range of magnetic fields, while it rapidly vanishes at a critical magnetic field which is relatively high. Such behavior indicates that the system may have a phase transition.

The magnetic system can be rescaled to a zero-field configuration which is thermodynamically equivalent to the original one. This simple result can actually be seen already at the level of field theory: the additional scale brought about by the magnetic field does not show up in thermodynamic quantities meaning, in particular, that the behavior in the vicinity of quantum critical points is expected to remain largely uninfluenced by the magnetic field, retaining its conformal invariance. In the light of current condensed matter knowledge, this is surprising and might in fact be a good opportunity to test the applicability of the probe limit in the real world: if this behavior is not seen, this suggests that one has to include the backreaction to metric to arrive at a realistic description.

In the field theory frame, we have calculated the DC conductivity using k_F and v_F values extracted from holography. The holographic calculation of conductivity that takes into account the fermions corresponds to the corrections of subleading order in $1/N$ in the field theory and is very involved [17]. As we are not interested in the vertex renormalization due to gravity (it does not change the magnetic field dependence of the conductivity), we have performed our calculations directly in the field theory with AdS gravity-dressed fermion propagators. Instead of controlling the occupancy of the Landau levels by changing the chemical potential (as is usual

in non-holographic setups), we have controlled the filling of the Landau levels by varying the Fermi energy level through the magnetic field. At zero temperature, we have reproduced the integer QHE of the Hall conductivity, which is observed in graphene at moderate magnetic fields. While the findings on equilibrium physics (Landau quantization, magnetic phase transitions and crossovers) are within expectations and indeed corroborate the meaningfulness of the AdS/CFT approach as compared to the well-known facts, the detection of the QHE is somewhat surprising as the spatial boundary effects are ignored in our setup. We plan to address this question in further work.

Interestingly, at large magnetic fields we obtain the correct formula for the filling factor characteristic for FQHE. Moreover our pattern for FQHE resembles the one obtained in [36] which has been explained using the fractional filling factor of Halperin [35]. In the quasiparticle picture, which we have used to calculate Hall conductivity, the filling factor is integer. In our holographic description, quasiparticles are valid degrees of freedom only at weak magnetic field. At strong magnetic field, the system exhibits non-Fermi liquid behavior. In this case, the poles of the fermion propagator should be taken into account to calculate the Hall conductivity. This can probably result in a fractional filling factor. We leave it for future work.

Notably, the AdS-Reissner-Nordström black hole background gives a vanishing Fermi velocity at high magnetic fields. It happens at the point when the IR conformal dimension of the corresponding field theory is $\nu = \frac{1}{2}$, which is the borderline between the Fermi and non-Fermi liquids. Vanishing Fermi velocity was also observed at high enough fermion charge [24]. As in [24], it is explained by the red shift on the gravity side, because at strong magnetic fields the fermion wavefunction is supported near the black hole horizon modifying substantially the Fermi velocity. In our model, vanishing Fermi velocity leads to zero occupancy of the Landau levels by stable quasiparticles that results in vanishing regular Fermi liquid contribution to the Hall conductivity and the longitudinal conductivity. The dominant contribution to both now comes from the non-Fermi liquid and conformal contributions. We associate such change in the behavior of conductivities with a metal-“strange metal” phase transition. Experiments on highly oriented pyrolytic graphite support the existence of a finite “offset” magnetic field h_c at $T = 0$ where the resistivity qualitatively changes its behavior [38–41]. At $T \neq 0$, it has been associated with the metal-semiconducting phase transition [38–41]. It is worthwhile to study the temperature dependence of the conductivity in order to understand this phase transition better.

Acknowledgements The work was supported in part by the Alliance program of the Helmholtz Association, contract HA216/EMMI “Extremes of Density and Temperature: Cosmic Matter in the Laboratory” and by ITP of Goethe University, Frankfurt (E. Gubankova), by a VIDI Innovative Research Incentive Grant (K. Schalm) from the Netherlands Organization for Scientific Research (NWO), by a Spinoza Award (J. Zaanen) from the Netherlands Organization for Scientific Research (NWO) and the Dutch Foundation for Fundamental Research of Matter (FOM). K. Schalm thanks the Galileo Galilei Institute for Theoretical Physics for the hospitality and the INFN for partial support during the completion of this work.

References

1. J. Zaanen, Quantum critical electron systems: the uncharted sign worlds. *Science* **319**, 1205 (2008)
2. P. de Forcrand, Simulating QCD at finite density. PoS **LAT2009**, 010 (2009). [arXiv:1005.0539](#) [hep-lat]
3. S.A. Hartnoll, J. Polchinski, E. Silverstein, D. Tong, Towards strange metallic holography. *J. High Energy Phys.* **1004**, 120 (2010). [arXiv:0912.1061](#) [hep-th]
4. P. Kovtun, D.T. Son, A.O. Starinets, Viscosity in strongly interacting quantum field theories from black hole physics. *Phys. Rev. Lett.* **94**, 111601 (2005). [arXiv:hep-th/0405231](#)
5. S.-S. Lee, A non-Fermi liquid from a charged black hole: a critical Fermi ball. *Phys. Rev. D* **79**, 086006 (2009). [arXiv:0809.3402](#) [hep-th]
6. M. Čubrović, J. Zaanen, K. Schalm, String theory, quantum phase transitions and the emergent Fermi-liquid. *Science* **325**, 439 (2009). [arXiv:0904.1993](#) [hep-th]
7. H. Liu, J. McGreevy, D. Vegh, Non-Fermi liquids from holography. *Phys. Rev. D* **83**, 065029 (2011). [arXiv:0903.2477](#) [hep-th]
8. T. Faulkner, H. Liu, J. McGreevy, D. Vegh, Emergent quantum criticality, Fermi surfaces, and AdS₂. *Phys. Rev. D* **83**, 125002 (2011). [arXiv:0907.2694](#) [hep-th]
9. S.A. Hartnoll, A. Tavanfar, Electron stars for holographic metallic criticality. *Phys. Rev. D* **83**, 046003 (2011). [arXiv:1008.2828](#) [hep-th]
10. S.A. Hartnoll, P.K. Kovtun, M. Mueller, S. Sachdev, Theory of the Nernst effect near quantum phase transitions in condensed matter, and in dyonic black holes. *Phys. Rev. B* **76**, 144502 (2007). [arXiv:0706.3215](#) [hep-th]
11. S.A. Hartnoll, P. Kovtun, Hall conductivity from dyonic black holes. *Phys. Rev. D* **76**, 066001 (2007). [arXiv:0704.1160](#) [hep-th]
12. P. Basu, J.Y. He, A. Mukherjee, H.-H. Shieh, Holographic non-Fermi liquid in a background magnetic field. [arxiv:0908.1436](#) [hep-th]
13. T. Albash, C.V. Johnson, Landau levels, magnetic fields and holographic Fermi liquids. *J. Phys. A, Math. Theor.* **43**, 345404 (2010). [arXiv:1001.3700](#) [hep-th]
14. T. Albash, C.V. Johnson, Holographic aspects of Fermi liquids in a background magnetic field. *J. Phys. A, Math. Theor.* **43**, 345405 (2010). [arXiv:0907.5406](#) [hep-th]
15. T. Albash, C.V. Johnson, A holographic superconductor in an external magnetic field. *J. High Energy Phys.* **0809**, 121 (2008). [arXiv:0804.3466](#) [hep-th]
16. N. Iqbal, H. Liu, M. Mezei, Q. Si, Quantum phase transitions in holographic models of magnetism and superconductors. [arXiv:1003.0010](#) [hep-th]
17. T. Faulkner, N. Iqbal, H. Liu, J. McGreevy, D. Vegh, From black holes to strange metals. [arXiv:1003.1728](#) [hep-th]
18. E. D'Hoker, P. Kraus, *J. High Energy Phys.* **1005**, 083 (2010). [arXiv:1003.1302](#) [hep-th]
19. A. Auerbach, Quantum magnetism approaches to strongly correlated electrons. [arxiv:cond-mat/9801294](#)
20. E. Gubankova, Particle-hole instability in the AdS₄ holography. [arXiv:1006.4789](#) [hep-th]
21. J.L. Davis, P. Kraus, A. Shah, Gravity dual of a quantum hall plateau transition. *J. High Energy Phys.* **0811**, 020 (2008). [arXiv:0809.1876](#) [hep-th]
22. E. Keski-Vakkuri, P. Kraus, Quantum Hall effect in AdS/CFT. *J. High Energy Phys.* **0809**, 130 (2008). [arXiv:0805.4643](#) [hep-th]
23. A.H. MacDonald, Introduction to the physics of the quantum Hall regime. [arXiv:cond-mat/9410047](#)
24. T. Hartman, S.A. Hartnoll, Cooper pairing near charged black holes. [arXiv:1003.1918](#) [hep-th]
25. F. Denef, S.A. Hartnoll, S. Sachdev, Quantum oscillations and black hole ringing. *Phys. Rev. D* **80**, 126016 (2009). [arXiv:0908.1788](#) [hep-th]
26. F. Denef, S.A. Hartnoll, S. Sachdev, Black hole determinants and quasinormal modes. *Class. Quant. Grav.* **27**, 125001 (2010). [arXiv:0908.2657](#) [hep-th]

27. E. Gubankova, J. Brill, M. Cubrovic, K. Schalm, P. Schijven, J. Zaanen, Holographic fermions in external magnetic fields. *Phys. Rev. D* **84**, 106003 (2011). [arXiv:1011.4051](#) [hep-th]
28. Y. Zhang, Z. Jiang, J.P. Small, M.S. Purewal, Y.-W. Tan, M. Fazlollahi, J.D. Chudow, J.A. Jaszczak, H.L. Stormer, P. Kim, Landau level splitting in graphene in high magnetic fields. *Phys. Rev. Lett.* **96**, 136806 (2006). [arXiv:cond-mat/0602649](#)
29. J.L. Noronha, I.A. Shovkovy, Color-flavor locked superconductor in a magnetic field. *Phys. Rev. D* **76**, 105030 (2007). [arXiv:0708.0307](#) [hep-ph]
30. V.P. Gusynin, S.G. Sharapov, Transport of Dirac quasiparticles in graphene: Hall and optical conductivities. *Phys. Rev. B* **73**, 245411 (2006). [arXiv:cond-mat/0512157](#)
31. E.V. Gorbar, V.A. Miransky, I.A. Shovkovy, Dynamics in the normal ground state of dense relativistic matter in a magnetic field. *Phys. Rev. D* **83**, 085003 (2011). [arXiv:1101.4954](#) [hep-th]
32. M.A.V. Basagoiti, Transport coefficients and ladder summation in hot gauge theories. *Phys. Rev. D* **66**, 045005 (2002). [arXiv:hep-ph/0204334](#)
33. J.M.M. Resco, M.A.V. Basagoiti, Color conductivity and ladder summation in hot QCD. *Phys. Rev. D* **63**, 056008 (2001). [arXiv:hep-ph/0009331](#)
34. N. Iqbal, H. Liu, Real-time response in AdS/CFT with application to spinors. *Fortschr. Phys.* **57**, 367 (2009). [arXiv:0903.2596](#) [hep-th]
35. B.I. Halperin, *Helv. Phys. Acta* **56**, 75 (1983)
36. Y. Kopelevich, B. Raquet, M. Goiran, W. Escoffier, R.R. da Silva, J.C. Medina Pantoja, I.A. Luk'yanchuk, A. Sinchenko, P. Monceau, Searching for the fractional quantum Hall effect in graphite. *Phys. Rev. Lett.* **103**, 116802 (2009)
37. Y.-F. Hsu, G.-Y. Guo, Anomalous integer quantum Hall effect in AA-stacked bilayer graphene. *Phys. Rev. B* **82**, 165404 (2010). [arXiv:1008.0748](#) [cond-mat]
38. Y. Kopelevich, V.V. Lemanov, S. Moehlecke, J.H.S. Torrez, Landau level quantization and possible superconducting instabilities in highly oriented pyrolytic graphite. *Fiz. Tverd. Tela* **41**, 2135 (1999) [*Phys. Solid State* **41**, 1959 (1999)]
39. H. Kempa, Y. Kopelevich, F. Mrowka, A. Setzer, J.H.S. Torrez, R. Hoehne, P. Esquinazi, *Solid State Commun.* **115**, 539 (2000)
40. M.S. Sercheli, Y. Kopelevich, R.R. da Silva, J.H.S. Torrez, C. Rettori, *Solid State Commun.* **121**, 579 (2002)
41. Y. Kopelevich, P. Esquinazi, J.H.S. Torres, R.R. da Silva, H. Kempa, F. Mrowka, R. Ocana, Metal-insulator-metal transitions, superconductivity and magnetism in graphite. *Stud. H-Temp. Supercond.* **45**, 59 (2003). [arXiv:cond-mat/0209442](#)



Vortex dynamics of counterpropagating laser beams in photorefractive materials

Mihailo Čubrović¹ · Milan Petrović^{2,3}

Received: 13 October 2017 / Accepted: 12 October 2018
© Springer Science+Business Media, LLC, part of Springer Nature 2018

Abstract

We study vortex patterns of counterpropagating laser beams in a photorefractive crystal, with or without the background photonic lattice. The vortices are effectively planar and have two “flavors” because there are two opposite directions of beam propagation. In a certain parameter range, the vortices form stable equilibrium configurations which we study using the methods of statistical field theory and generalize the Berezinsky–Kosterlitz–Thouless transition of the XY model to the “two-flavor” case. In the nonequilibrium regime, the patterns exhibit an Andronov–Hopf bifurcation which may lead to oscillations (limit cycle), chaos or decay to zero intensity due to radiation losses. We show how to identify various pathways toward instability from intensity patterns, i.e. from experiment.

Keywords Vortex · BKT transition · Photorefractive optics · Statistical field theory

1 Introduction

Nonlinear optical systems are a rich arena for studies of various fundamental physical phenomena. The strong response of the nonlinear optical medium to the propagation of light makes it a typical strongly correlated system, with many phenomena similar to those in other strongly interacting systems in areas such as condensed matter. Their complex dynamics offers an opportunity to study spatiotemporal chaos and optical turbulence

This article is part of the Topical Collection on Focus on Optics and Bio-photonics, Photonica 2017.

Guest Edited by Jelena Radovanovic, Aleksandar Krmpot, Marina Lekic, Trevor Benson, Mauro Pereira, Marian Marciniak.

✉ Mihailo Čubrović
mcubrovic@gmail.com

Milan Petrović
petrovic@ipb.ac.rs

¹ Scientific Computing Laboratory, Institute of Physics, University of Belgrade, Pregrevica 118, Belgrade 11080, Serbia

² Institute of Physics, P. O. B. 57, Belgrade 11001, Serbia

³ Texas A&M University at Qatar, Doha P.O.Box 23874, Qatar

(Cross and Hohenberg 1993; Rabinovich et al. 2000). On the other hand, they often also exhibit stable, equilibrium configurations in a certain parameter range, which are naturally studied by statistical physics methods. Vortices and other topological configurations (Alexander et al. 2007; Anderson 2007; Fetter 2009), long-range order (Anderson 2007), quenched disorder and glassy behavior (Antenucci et al. 2015a, b; Ghofraniha 2015; Perret et al. 2012) are universal in a broad range of systems such as cold atoms (Bagnato et al. 2015; Malomed et al. 2016) and magnetic systems, and the relative simplicity of experiments in optics makes it an excellent testing ground for strongly coupled models.

In this paper we study a specific and experimentally realizable nonlinear optical system: laser beams counterpropagating (CP) through a photorefractive (PR) crystal. This means we have an elongated PR crystal (with one longitudinal and two transverse dimensions) and two laser beams shone onto each end. We thus effectively have two fields, one forward-propagating and one backward-propagating. The optical response of the crystal depends nonlinearly on the *total* intensity of both beams, which means the beams effectively interact with each other. This system has been thoroughly investigated for phenomena such as dynamical solitons (Denz et al. 2003; Petrović et al. 2011, 2005; Jović et al. 2008), vortex stability on the photonic lattice (Alexander et al. 2007; Terhalle et al. 2008; Čubrović and Petrović 2017) and topological invariants (Rechtsman et al. 2013).

We first recast the system in Lagrangian and then in Hamiltonian form so it can be studied as a field theory, which depends parametrically on the time t . Then we consider the time dynamics of the system and show that in a broad parameter range the patterns relax to a static configuration which can be studied within *equilibrium* field theory. By renormalization group (RG) analysis, we obtain the phase diagram of static vortex configurations. The phase diagram is obviously closely related to the famous Berezinsky–Kosterlitz–Thouless (BKT) vortex unbinding transition in the XY model (Berezinsky 1971; Kosterlitz and Thouless 1973) except that having two components of the field produces additional phases and phase transitions, due to forward–backward beam interaction. The analytical insight we obtain also allows us to avoid overextensive numerics – analytical construction of the phase diagram tells us which patterns can in principle be expected in different corners of the parameter space.

Next we focus on the nonequilibrium regime, classify the fixed points and study possible routes of instability. We emphasize the pictorial and “rule-of-thumb” criteria to recognize various instabilities, in order to facilitate experimental checks. At the end we will discuss the perspective of studying dynamical criticality, i.e. instabilities which consist in moving from one vortex phase to another in real time, a phenomenon which is intimately connected to the difficult questions of quench dynamics and thermalization in many-body systems.

2 Counterpropagating beams in photorefractive medium: equations of motion

Consider a photorefractive crystal of length L irradiated by two paraxial head-on laser beams which propagate from the opposite faces of the crystal in the z -direction. Photorefractive crystals induce self-focusing of the beams—the vacuum (linear) wave equation is modified by the addition of a friction-like term, so the diffusion of the light intensity (the broadening of the beam) is balanced out by the self-focusing of the beam. The physical ground for this is the redistribution of the charges in the crystal due to the Kerr effect.

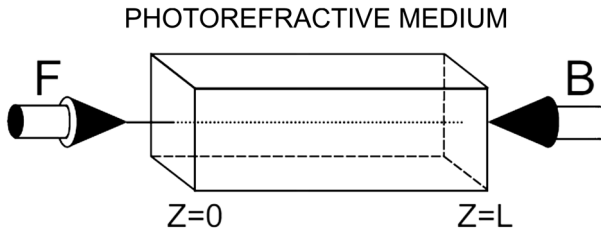


Fig. 1 Experimental setup for the study of the CP beams in the PR crystal. The crystal has the shape of a parallelepiped, and the beams propagate along the longitudinal, z -axis: the forward (F)-beam from $z = 0$ to $z = L$, and the backward (B)-beam the other way round. The intensity patterns can be observed at the transverse faces of the crystal, at $z = 0$ and $z = L$

The nonlinearity is contained in the change of the refraction index which is determined by the induced charge density. A sketch of the system is given in Fig. 1. Before entering the crystal, the laser beams can be given any desirable pattern of both intensity and phase. In particular, one can create vortices (winding of the phase) making use of the phase masks (Denz et al. 2003).

Assuming the electromagnetic field of the form $\mathbf{E} = e^{i\omega t + i\mathbf{q}\mathbf{r}} (F e^{ikz} + B e^{-ikz})$, we can write equations for the so-called envelopes F and B of the forward- and backward-propagating beams along the z -axis (the frequency, transverse and longitudinal momentum are denoted respectively by ω, \mathbf{q}, k). The wave equations for F and B are now:

$$\pm i \partial_z \Psi_{\pm}(z;x, y;t) + \Delta \Psi_{\pm}(z;x, y;t) = \Gamma E(z;x, y;t) \Psi_{\pm}(z;x, y;t), \tag{1}$$

where the plus and minus signs on the left-hand side stand for the forward- and backward-propagating component of the beam amplitude doublet $\Psi \equiv (\Psi_+, \Psi_-) \equiv (F, B)$, and Γ is the dimensionless PR coupling constant. From now on we will use $\alpha \in \{+, -\}$ to denote the two beams (F and B) and call it a flavor index, in analogy with field theory. The vorticity (winding number of the phase) will be called vortex charge as usual. The charge field E on the right-hand side of the equation is the electric field sourced by the charges in the crystal (i.e., it does not include the external electric field of the beams). Its evolution is well represented by a relaxation-type equation (notice that the derivative $\partial_t E$ is strictly negative) (Petrović et al. 2011):

$$\frac{\tau}{1 + I(z;x, y;t)} \partial_t E(z;x, y;t) + E(z;x, y;t) = - \frac{I(z;x, y;t)}{1 + I(z;x, y;t)}. \tag{2}$$

Here, $I \equiv I_p + I_x$ is the total light intensity at a given point, $I_p \equiv |F|^2 + |B|^2$ is the beam intensity and I_x the intensity of the fixed background. The meaning of I_x is that the crystal is all the time irradiated by some constant light source, independent of the counter-propagating beams with envelopes F, B . The relaxation time is τ . The form of the non-linearity accounts for the saturation of the crystal; notice that a simple quartic non-linear Schrödinger equation would not account for the saturation.¹ In the numerical calculations,

¹ One might also worry that a realistic crystal is anisotropic, while our equation is isotropic. Nevertheless, comparison to experiment (Neshev et al. 2004; Fleischer et al. 2004; Dreischuh et al. 2002) shows that this model is able to describe actual measurements rather well. Also, the effects of anisotropy can be suppressed in experiment by illuminating the crystal by *uniform* light for very long times before starting the experiment (Cohen et al. 2002).

we solve Eqs. (1), (2) with no further assumptions, using a slightly modified version of the beam propagation method (Sandfuchs et al. 2001). For analytical results we will need to transform them further assuming a vortex pattern. The Eq. (2) is completely phenomenological, but it excellently represents the experimental results (Denz et al. 2003). We will first consider the equilibrium regime, and then the nonequilibrium dynamics.

For slow time evolution (in absence of pulses), we can Laplace-transform the Eq. (2) in time ($E(t) \mapsto E(u) = \int_0^\infty dt e^{-ut} E(t)$) to get the algebraic relation

$$E(z;x, y;u) = -\frac{\Psi^\dagger \Psi + I_x - \tau E_0}{1 + \tau u + I_x + \Psi^\dagger \Psi} = -1 + \frac{1 + \tau u + \tau E_0}{1 + \tau u + I_x + \Psi^\dagger \Psi}. \quad (3)$$

The original system (1) can now be described by the Lagrangian:

$$\mathcal{L} = i\Psi^\dagger \sigma_3 \partial_z \Psi - |\nabla \Psi|^2 + \Gamma \Psi^\dagger \Psi - \Gamma(1 + \tau E_0 + \tau u) \log(1 + \tau u + I_x + \Psi^\dagger \Psi), \quad (4)$$

where σ_3 is the Pauli matrix $\sigma_3 = \text{diag}(1, -1)$. This has the form $\mathcal{L} = i\Psi^\dagger \sigma_3 \partial_z \Psi - |\nabla \Psi|^2 - V_{\text{eff}}(\Psi^\dagger, \Psi)$, i.e. the Lagrangian of a non-relativistic field theory (a two-component nonlinear Schrödinger field equation) in $2 + 1$ dimensions (x, y, z), where the role of time is played by the longitudinal distance z , and the physical time t (or u upon the Laplace transform) is a parameter.

3 Stable vortex configurations and the phase diagram

Following the same steps as for the textbook XY model we can arrive at an effective Hamiltonian for stable vortex configurations. For details we refer the reader to Čubrović and Petrović (2017). Assuming the vortex solution of the form

$$\Psi_{0\pm}(\mathbf{r}) = \psi_{0\pm}(r) e^{i\delta\theta_\pm(\phi) + i\theta_{0\pm}(\phi)}, \quad (5)$$

where $\theta_\pm(\phi)$ is the singular part of the phase and $\theta_{0\pm}(\phi)$ the regular part, we want to integrate out both the amplitude fluctuations and the regular part of the phase and arrive at a description of the systems solely in terms of vortex charges. This is done by expanding the Lagrangian (4) to quadratic order in both amplitude and phase fluctuations and integrating them out. Then the usual Legendre transform yields the vortex Hamiltonian:

$$\mathcal{H}_{\text{vort}} = \sum_{i < j} (g Q_{i\alpha} Q_{j\alpha} + g' Q_{i\alpha} \times Q_{j\beta}) \log r_{ij} + \sum_i (g_0 Q_{i\alpha} Q_{i\alpha} + g_1 Q_{i\alpha} \times Q_{i\beta}). \quad (6)$$

We denote the flavor \pm by Greek indices, and the summation convention is understood.² Furthermore, we denote $Q_\alpha \times Q_\beta \equiv Q_{i+} Q_{j-} + Q_{i-} Q_{j+}$. The first term is the expected Coulomb interaction of vortices from the XY model (Berezinsky 1971; Kosterlitz and Thouless 1973); notice that only like-flavored charges interact through this term (because the kinetic term $|\nabla \Psi|^2$ is homogenous quadratic). The second term is the forward–backward interaction, also with Coulomb-like (logarithmic) radial dependence. This interaction is generated by the coupling of amplitude fluctuations $\delta\psi_\alpha(r)$ to the phase fluctuations. In a system without amplitude fluctuations, i.e. classical spin system, this term would not be generated. The third and fourth term constitute the energy of the vortex core. The self-interaction

² There is no difference between upper and lower indices as both flavors always enter the sum with positive sign.

constants g_0, g_1 are of course dependent on the vortex core size and behave roughly as $g \log a/\epsilon, g' \log a/\epsilon$, where ϵ is the UV cutoff. The final results will not depend on ϵ , as expected, since g_0, g_1 can be absorbed in the fugacity y (see the next subsection). Expressions for the coupling constants in terms of original parameters are given in Čubrović and Petrović (2017); they can be used to relate the theoretical phase diagram to experiment.

To describe the phase diagram, we will perform the renormalization group (RG) analysis. Here we follow closely the calculation for conventional vortex systems. We consider the fluctuation of the partition function δZ upon the formation of a virtual vortex pair at positions $\mathbf{r}_1, \mathbf{r}_2$ ³ with charges $q_\alpha, -q_\alpha$, (with $\mathbf{r}_1 + \mathbf{r}_2 = 2\mathbf{r}$ and $\mathbf{r}_1 - \mathbf{r}_2 = \mathbf{r}_{12}$), in the background of a vortex pair at positions $\mathbf{R}_1, \mathbf{R}_2$ (with $\mathbf{R}_1 + \mathbf{R}_2 = 2\mathbf{R}$ and $\mathbf{R}_1 - \mathbf{R}_2 = \mathbf{R}_{12}$) with charges $Q_{1\alpha}, Q_{2\alpha}$. It is also convenient to replace the core self-interaction constants $g_{0,1}$ with the fugacity parameter defined as $y \equiv \exp[-\beta(g_0 + g_1) \log \epsilon]$. We also introduce the notation $\beta \equiv L$ in analogy with the inverse temperature β in standard statistical mechanics but of course the physical meaning of β in our system is very different: we have no thermodynamic temperature or thermal noise, and the third law of thermodynamics is not satisfied for the “temperature” $1/\beta$. We merely use the β -notation for reasons of formal similarity, not as a complete physical analogy.

This is a straightforward but lengthy calculation and we state just the resulting flow equations:

$$\frac{\partial g}{\partial \ell} = -16\pi(g^2 + g'^2)y^4, \quad \frac{\partial g'}{\partial \ell} = -2\pi g g' y^4, \quad \frac{\partial y}{\partial \ell} = 2\pi(1 - g - g')y. \tag{7}$$

Notice that if one puts $g' = 0$, they look very much like the textbook XY model RG flow, except that the fugacity enters as y^4 instead of y^2 (simply because every vortex contributes two charges). We can find fixed points analytically and then numerically integrate the flow equations to find exact phase borders. The fugacity y can flow to zero (meaning that the vortex creation is suppressed and the vortices tend to bind) or to infinity, meaning that vortices can exist at finite density. At $y = 0$ there is a fixed line $g + g' = 1$. This line is attracting for the half-plane $g + g' > 1$; otherwise, it is repelling. There are three more attraction regions when $g + g' < 1$. First, there is the point $y \rightarrow \infty, g = g' = 0$ which has no analogue in single-component vortex systems. Then, there are two regions when $g \rightarrow \infty$ and $g' \rightarrow \pm\infty$ (and again $y \rightarrow \infty$). Of course, the large g, g' regime is strongly interacting and the perturbation theory eventually breaks down. What happens when g, g' flow toward very large values is that the intensity at the vortex core becomes very large, so the lowest-order, quadratic Hamiltonian needs to be supplemented by higher-order terms in intensity fluctuations. To integrate them out, one needs to perform a diagrammatic expansion which leads to quartic- and higher-order terms in vortex charges Q_α in the effective vortex Hamiltonian [Eq. (6)], ultimately correcting the flow at large g, g' to flow toward finite values g_*, g'_* and g_{**}, g'_{**} .

The RG flows in the $g - g'$ plane are given in Fig. 2. The situation is now the following:

1. The attraction region of the fixed line is the vortex insulator phase (INS): the creation rate of the vortices is suppressed to zero. There is no vortex charge conservation.

³ The boldface vectors are the coordinate vectors in the plane.

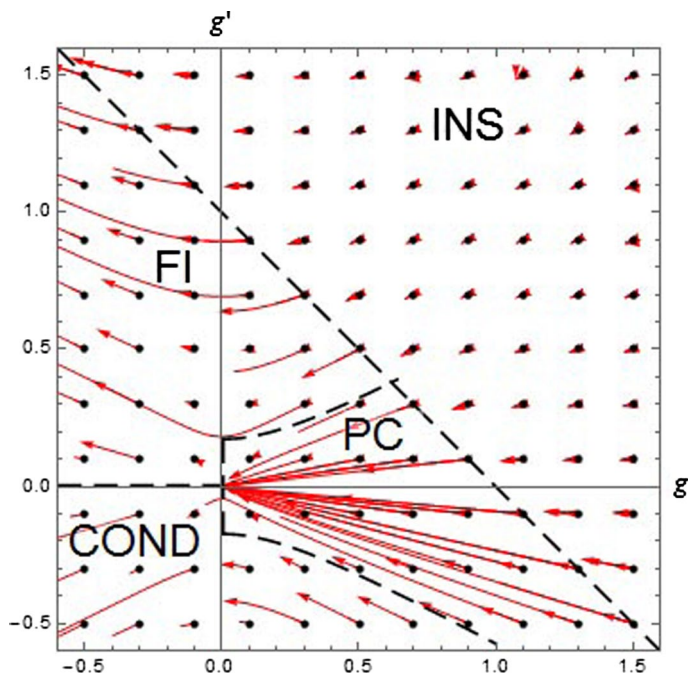


Fig. 2 Phase diagram for the clean system in the g – g' plane, at the mean-field level with RG flows. We show the flows for a grid of initial points, denoted by black dots; red lines are the flows. Four phases exist, whose boundaries are delineated by black dashed lines: conductor (COND), insulator (INS), frustrated insulator (FI) and perfect conductor (PC). The straight line $g + g' = 1$ is obtained analytically whereas the other phase boundaries can only be found by numerical integration of the flow Eq. (7). The flows going to infinity are the artifacts of the perturbative RG; they correspond to finite values which are beyond the scope of our analytical approach. Notice how the flows in the $g + g' > 1$ phase all terminate at different values

2. The zero-coupling fixed point attracts the trajectories in the vortex perfect conductor phase (PC): only the fugacity controls the vortices and arbitrary charge configurations can form. Each vortex charge, Q_+ and Q_- , is separately conserved.
3. In the attraction region of the fixed point with $g_* < 0$ and $g'_* > 0$ (formally they flow to $-\infty$ and $+\infty$, respectively), same-sign F - and B -charges attract each other and those with the opposite sign which repel each other. This is the frustrated insulator (FI): it conserves only the combination $Q_+ + Q_-$, and only vortices with charge $(Q_+, -Q_+)$ are stable.
4. The fixed point with $g_{**}, g'_{**} < 0$ (formally both flow to $-\infty$) corresponds to the conductor phase (COND). This phase preserves one of the charges, Q_+ or Q_- , i.e. either $(Q_+, 0)$ - or $(0, Q_-)$ -vortices proliferate.

In the half-plane $g + g' > 1$ every point evolves toward a different, finite point (g, g') in the same half-plane. In the other half-plane we see the regions of points moving toward the origin or toward one of the two directions at infinity. In the future we plan to apply this formalism also to multi-component vortices in Bose–Einstein condensates (Ma et al. 2016) and in particular in type-1.5 superconductors (Silae and Babev 2012), where even more complex phenomena, including frustration, are observed as a consequence of multi-component interaction.

An interesting line of research consists in adding disorder to the above system. We consider this problem in Čubrović and Petrović (2017) and find that the system can be approximated by a random-coupling *and* random-field two-component XY-like model, related to the Cardy–Ostlund model (1982). The replica formalism (Castellana and Parisi 2015) then predicts a glassy phase with slow dynamics, strong correlations and no long-range order. This is however a separate story and we will leave it out here. Interested readers can consult (Čubrović and Petrović 2017) and look at related work in Antenucci et al. (2015a, b).

4 Time-dependent regime

Here our goal is twofolds. First, we have to show that at least for some boundary conditions and parameter values there is a stable fixed point of the time evolution, so that the system reaches a time-independent, equilibrium pattern. The reason is that the whole formalism of the previous chapter is only valid for such configurations, as it departs from equilibrium statistical mechanics. Second, we want to check other, non-static behaviors as they are interesting in their own right and experimentally relevant (but one should not expect them to be described by an equilibrium phase diagram like Fig. 2).

Time dynamics can be studied in a straightforward way, making use of the relaxation Eq. (2) to write down the first-order evolution equations for Ψ_{\pm} :

$$\frac{\partial \Psi_{\alpha}^{\pm}}{\partial t} = -\frac{\Gamma}{\tau} \frac{((1+I)E+I)}{\alpha k - q^2 - \Gamma E} \Psi_{\alpha}^{\pm}, \quad \frac{\partial E}{\partial t} = -\frac{1}{\tau} ((1+I)E+I). \tag{8}$$

This system has three equilibrium points. One is the trivial equilibrium with zero intensity (“0” point):

$$(\Psi_{+}^{\pm}, \Psi_{-}^{\pm}, E) = \left(0, 0, -\frac{I_x}{1+I_x}\right),$$

and the remaining two are related by a discrete symmetry $\Psi_{\pm} \mapsto \Psi_{\mp}$ (“±” points). The “+” point is

$$(\Psi_{+}^{\pm}, \Psi_{-}^{\pm}, E) = \left(\sqrt{\frac{E(1+I_x)+I_x}{1+E}} e^{i\phi_{+}}, 0, E\right),$$

and the “-” point has instead $\Psi_{+} = 0$ and $\Psi_{-} = \sqrt{(E(1+I_x)+I_x)/(1+E)} \exp(i\phi_{-})$. Notice that the phase ϕ_{\pm} remains free to vary so the “±” solutions support vortices. We first ask what is the stability criterion for a nontrivial solution, i.e. one of the “±” points, as this is the main criterion for the applicability of the equilibrium statistical mechanics methods in the previous section. Introducing the amplitudes of the fluctuations from equilibrium as $X_{1,3} = \Re \delta \Psi_{\pm}, X_{2,4} = \Im \delta \Psi_{\pm}, X_5 = \delta E$, we can do a first-order stability analysis as the system is non-degenerate. Rescaling $X_1 \mapsto (1+E_0)^{-3/4} (I_x + E_0(1+I_x))^{1/2}$ and $t \mapsto t((1+E_0)/(I_x + E_0(1+I_x)))^{1/4}$, the equation of motion for the “±” point reads

$$\partial_t \begin{pmatrix} X_1 \\ X_5 \end{pmatrix} = \begin{pmatrix} -\frac{a_{\pm}}{\Gamma E_0 + k + q^2} & -1 \\ 1 & -\frac{a_{\pm}}{\Gamma E_0 + k + q^2} \end{pmatrix} \begin{pmatrix} X_1 \\ X_5 \end{pmatrix} + O(X_1^2 + X_5^2; X_2, X_3, X_4), \tag{9}$$

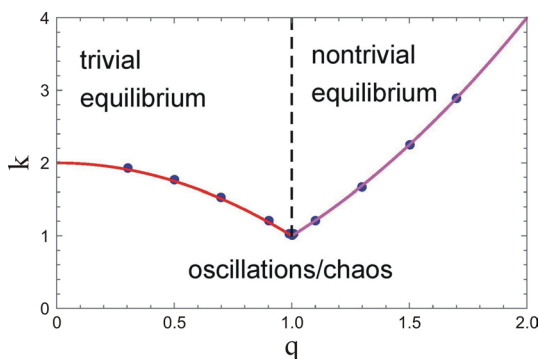


Fig. 3 Stability diagram in the q - k plane. The onset of instability for $k < k_c(q)$ is found numerically for a range of q values. The solid lines are the analytical prediction for the stability of the “0” point ($k_c = q^2$, magenta) and of the “+” point ($k_c = \Gamma E_0 - q^2 \approx \Gamma - q^2$, red). The black dashed line at $q = q_c \approx 1$ separates the stability regions of the two points. The domain of applicability of our main results is the top right corner (nontrivial equilibrium), above $k > k_{\min} \sim 1/L$ and for not too large q values. Parameter values: $\Gamma = 2, I_x = 0$

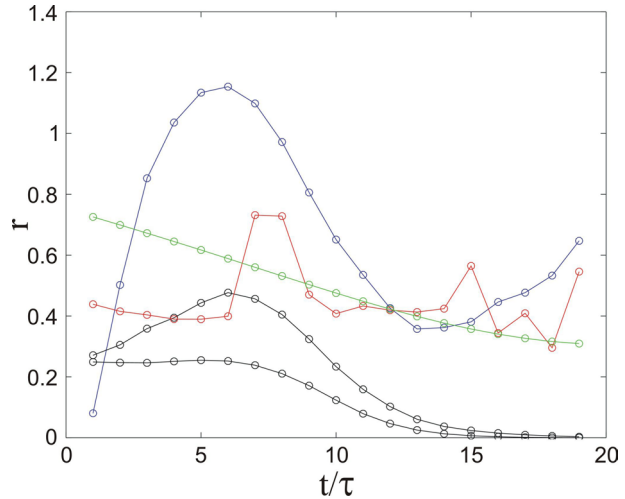
with a_{\pm} being some (known) *positive* functions of Γ, E_0, I_x (independent of k, q). This is precisely the normal form for the Andronov–Hopf bifurcation (Arnol’d et al. 1994), and the bifurcation point lies at $k = -\Gamma E_0 - q^2$. To remind, the bifurcation happens when the off-diagonal element in the linear term changes sign: the fixed point is stable when $a_{\pm}/(\Gamma E_0 + k + q^2)$ is positive. The sign of the nonlinear term determines the supercritical/subcritical nature of the bifurcation.⁴

Now the textbook analysis of the Andronov–Hopf bifurcation tells us that stable “+” equilibrium exists for $k > -\Gamma E_0 - q^2$ where E_0 is best found numerically. Exactly the same condition holds for the “-” point. For $k < -\Gamma E_0 + q^2$, dynamics depends on the sign of the nonlinear term in Eq. (9). For the positive sign we expect periodically changing patterns and for the negative sign (subcritical bifurcation), various possibilities arise: the system may wander chaotically between the “+” and the “-” points, or it may end up in the attraction region of the “0” point and fall onto the trivial solution with zero intensity. Naively, the attraction regions of the two fixed points (“±” and “0”) are separated by the condition $-\Gamma E_0 - q^2 = q^2$, i.e. $q_c = \sqrt{-\Gamma E_0(\Gamma, \tau)/2}$, where we have emphasized that E_0 is in general non-universal. The actual boundary may be more complex however, as our analysis is based on finite-order expansion around the fixed points, which is not valid far away from them.

The numerical stability diagram is given in Fig. 3. The stability limit turns out to be $k > \Gamma - q^2$, i.e. $E_0 \approx -1$. The curves separating the attraction regions of the three equilibrium points follow exactly the quadratic scaling in q as predicted by the analytical stability analysis. The equilibrium region lies in the top right corner of the diagram (nontrivial equilibrium), above $k \approx 1/L$. This is where the patterns evolve towards static

⁴ Negative sign means the fixed point is stable everywhere before the bifurcation and is replaced by a stable limit cycle after the bifurcation (supercritical). Positive sign means the fixed point coexists with the stable limit cycle before the bifurcation and the (X_1, X_5) plane is divided among their attraction regions; after the bifurcation there is no stable solution at all (subcritical). However, one should not take the stability in the whole (X_1, X_5) plane in the supercritical case too seriously. We have expand the equations of motion in the vicinity of the fixed points and the expansion ceases to be valid far away from the origin.

Fig. 4 Time evolution of the relaxation rate r for the various situations from Figs. 5 and 6, illustrating the relaxation to non-trivial (non-zero intensity) equilibrium, i.e. “ \pm ” fixed points (Fig. 5a, c, black), limit cycle (6a, blue), chaos (6b, red) and the relaxation to trivial (zero intensity) equilibrium, i.e. “0” fixed point (6c, green). In the main text we mainly study the cases like the black curves, where time-independent stable configurations are seen. The circles are data points from numerics and the lines are just to guide the eye



long-time configurations. The top left corner describes “boring” situations, when all light ultimately radiates away from the crystal and intensity drops to zero. The bottom region contains nontrivial dynamics: depending on parameters, it may contain a limit cycle (corresponding to oscillating patterns) or aperiodic wandering among an alphabet of unstable patterns (chaos).

Formally, both k and q can be any real numbers. In practice, however, k is discrete and its minimal value is of the order $1 / L$. The spatial momentum q lies between the inverse of the transverse length of the crystal (which is typically an order of magnitude smaller than L , i.e. minimal q can be assumed equal to zero) and some typical small-scale cutoff which in our case is the vortex core size.

Now we test our conclusions numerically. A convenient quantity to differentiate between different stability regimes is the relaxation rate

$$r \equiv \frac{1}{X} \frac{dX}{dt} = \frac{\sum_{x,y} |X(t_{j+1};x,y) - X(t_j;x,y)|^2}{\sum_{x,y} |X(t_j;x,y)|^2}, \tag{10}$$

which is expected to reach zero for a generic relaxation process, where in the vicinity of an asymptotically stable fixed point $X \sim X_{\text{eq}} + xe^{-rt}$ will be generically nonzero for a limit cycle or chaos, and will asymptote to a constant for the “0” point, where $X_{\text{eq}} = 0$ so we get $(1/X)dX/dt \sim r$.

Figure 4 summarizes these possibilities in terms of the relaxation rate r , whereas Figs. 5 and 6 show how the patterns evolve in some representative cases. The black curves in Fig. 4 show the situation which is in the focus of this work – the approach toward static equilibrium. This corresponds to the phases from Fig. 2. In Fig. 5 we see how the equilibrium configurations are reached (for three phases). In each case we start with a regular lattice of circular vortices. In the PC phase (Fig. 5a) the vortices expand somewhat but in principle retain the original configuration (and charges). The other two phases (Fig. 5b, c) have nontrivial transient dynamics and undergo the lattice inversion, but eventually (for times about $t \approx 20 - 25\tau$) they stabilize and form a static inverse lattice (with charges $(3, -3)$ in the FI case and with zero charge in the INS case).

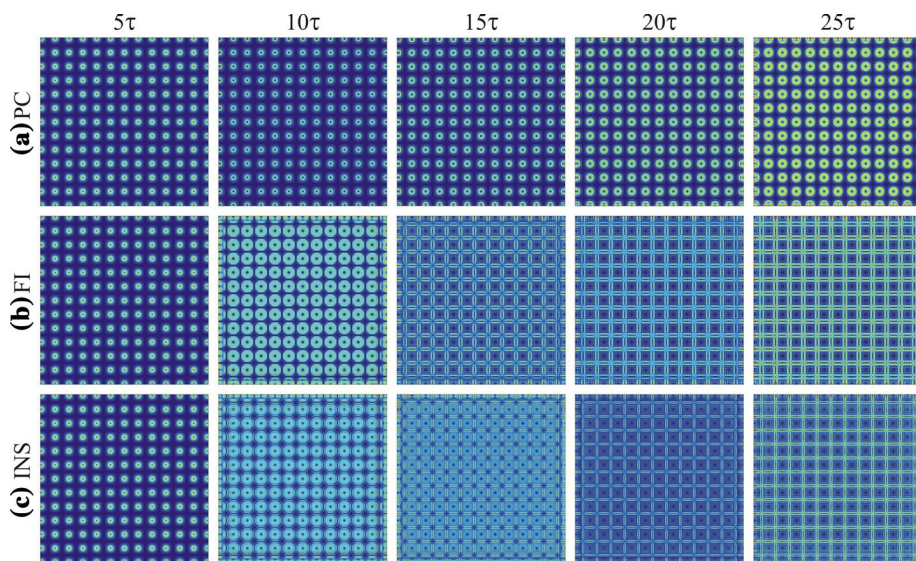


Fig. 5 Time evolution of patterns at five different times: **a** perfect conductor phase, **b** frustrated insulator phase and **c** insulator phase. In all cases the approach to equilibrium is obvious, and we expect that for long times a thermodynamic description is justified

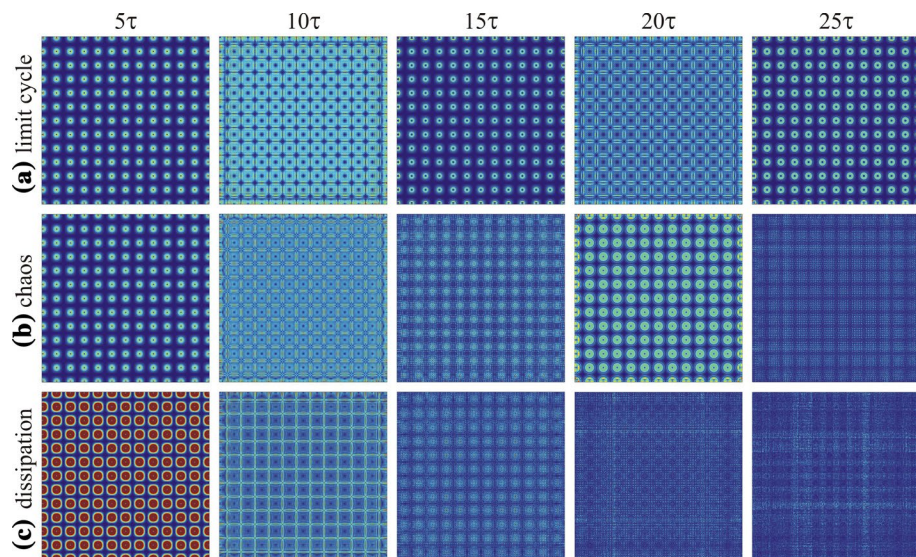


Fig. 6 Time evolution of non-equilibrium patterns. In **a** the limit cycle leads to permanent oscillatory behavior, in **b** wandering along the unstable manifold between the equilibrium points gives rise to chaos and in **c** dissipation wins and dynamics dies out. The parameters are the same as in the previous figure, except that the length L is increased thrice

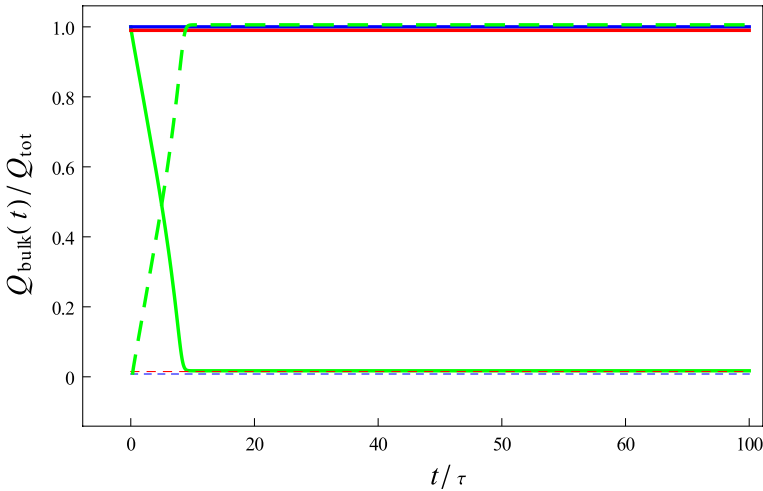


Fig. 7 Same systems as in Fig. 6 but now for the time dependence of the F -vortex charge in the bulk (full lines) and the vortex current flow through their boundary (dashed lines). While the limit cycle (blue) and chaos (red) keep all vortex charge in the bulk, dissipation toward the trivial equilibrium (green) has a systematic vortex flow toward the edges. This is a finite-size effect which would not happen in an infinite field (but it does happen in real-world PR crystals which are, of course, finite)

The other curves in Fig. 4 describe dynamics which does not result in a nontrivial static pattern. The blue curve shows a limit cycle leading to periodic oscillations of the pattern, with half-period about 10τ . The corresponding patterns are seen in Fig. 6a, where we see how the vortex lattice keeps coming back to the original configuration at times $\approx 5\tau, 10\tau, 15\tau$. The red curve corresponds to the chaotic regime with aperiodic dynamics and no relaxation, as in Fig. 6b. Here the pattern keeps changing, wandering among the original lattice (for $t = 5\tau, 20\tau$), the inverse lattice (for $t = 10\tau$) and more or less incoherent patterns (for $t = 15\tau, 25\tau$). Finally, the green curve in Fig. 4 reaches a constant value of r . This corresponds to the pattern which radiates away in Fig. 6c, with total intensity being almost zero for $t > 20\tau$. Here one might wonder what happens to the vortex charge when the initially regular vortex lattice ends up as an incoherent, low-intensity configuration which obviously does not support vortices. The explanation is that the vortex charge flows outward, eventually reaching the edges of the crystal. The finite-size effects then invalidate the vortex charge conservation, as the usual proof that the winding number of the phase is a topological invariant crucially depends on considering the winding at infinity. Vortex charge thus dissipates at the edges. This is demonstrated in Fig. 7, which presents the same systems as in Fig. 6a–c but shows the ratio of the total bulk vortex charge $Q_{\text{bulk}}(t)$ to the total initial vortex charge Q_{tot} . Total initial charge is calculated by definition, as the integrated vorticity of the F -beam, $Q_{\text{tot}} = \int dx \int dy |\omega_F|$, with

$$\omega_F = (\cos \theta_F \partial_x \theta_F, \sin \theta_F \partial_y \theta_F), \tag{11}$$

and all the quantities are taken at $t = 0$. The integral $\int dx \int dy |\omega_F|$ equals precisely the total F -vortex charge summed over all vortices. The bulk charge is computed by subtracting the integrated vorticity flow along the boundary:

$$Q_{\text{bulk}}(t) = Q_{\text{tot}} - \int_0^t dt' \oint d\mathbf{l} \cdot \omega_F(t). \tag{12}$$

Figure 7 shows that the sum of the bulk charge and the vortex current through the boundary is preserved in all cases, including when chaos or dissipation makes the pattern incoherent. In the last case, however, all the vortex charge flows toward the boundaries – this is a finite-size effect which would be absent in infinite field but is observable in realistic PR-crystals which are of finite dimensions. In practice, the matters are even more complicated as the boundary surface carries also new physics (surface polarization etc.), so the starting equations of motion would have to be modified. We believe, however, that the basic picture of vortex charge dissipating at the boundary still remains, because the mapping from the internal $U(1)$ phase onto the loop in the coordinate plane is explicitly broken by the boundary (whatever its detailed physics might be), and the vortex charge nonconservation at the boundary follows from this breaking.

The next task is to consider in more detail the decay of an ordered phase, either to chaos or to a limit cycle (radiating away all intensity is likely a trivial process, fully described by the approximately constant decay rate). We plan to address this problem in further work, and to relate the results to the question of quench dynamics in vortex systems.

Acknowledgements Work at the Institute of Physics is funded by Ministry of Education, Science and Technological Development, under Grants Nos. OI171033 and OI171017. M.P. is also supported by the NPRP 8-028-1-001 project of the Qatar National Research Fund (a member of the Qatar Foundation).

References

- Alexander, T.J., Desyatnikov, A.S., Kivshar, Y.S.: Multivortex solitons in triangular photonic lattices. *Opt. Lett.* **32**, 1293–1295 (2007)
- Anderson, P.W.: Two new vortex liquids. *Nat. Phys.* **3**, 160–162 (2007)
- Antenucci, F., Conti, C., Crisanti, A., Leuzzi, L.: General phase diagram of multimodal ordered and disordered lasers in closed and open cavities. *Phys. Rev. Lett.* **114**, 043901 (2015a)
- Antenucci, F., Crisanti, A., Leuzzi, L.: Complex spherical $2 + 4$ spin glass: a model for nonlinear optics in random media. *Phys. Rev. A* **91**, 053816 (2015b)
- Arnol'd, V.I., Afraimovich, V.S., Il'yashenko, Y.S., Shil'nikov, L.P.: *Bifurcation Theory and Catastrophe Theory*. Springer, Berlin (1994)
- Bagnato, V.S., Frantzeskakis, D.J., Kevrekidis, P.G., Malomed, B.A., Mihalache, D.: Bose–Einstein condensation: twenty years after. *Rom. Rep. Phys.* **67**, 5–50 (2015)
- Berezinsky, V.L.: Destruction of long range order in one-dimensional and two-dimensional systems having a continuous symmetry group. I. Classical systems. *Sov. Phys. JETP* **32**, 493–500 (1971)
- Cardy, J.L., Ostlund, S.: Random symmetry-breaking fields and the XY model. *Phys. Rev. B* **25**, 6899–6909 (1982)
- Castellana, M., Parisi, G.: Non-perturbative effects in spin glasses. *Nat. Sci. Rep.* **5**, 8697 (2015). [arXiv:1503.02103](https://arxiv.org/abs/1503.02103) [cond-mat.dis-nn]
- Cohen, O., Lan, S., Harmon, T., Giordmaine, J.A., Segev, M.: Spatial vector solitons consisting of counter-propagating fields. *Opt. Lett.* **27**, 2013–2015 (2002)
- Cross, M., Hohenberg, P.: Pattern formation outside of equilibrium. *Rev. Mod. Phys.* **65**, 851–1112 (1993)
- Čubrović, M., Petrović, M.: Quantum criticality in photorefractive optics: vortices in laser beams and anti-ferromagnets. *Phys. Rev. A* **96**, 053824 (2017). [arXiv:1701.03451](https://arxiv.org/abs/1701.03451) [physics.optics]
- Denz, C., Schwab, M., Weinau, C.: *Transverse Pattern Formation in Photorefractive Optics*. Springer, Berlin (2003)
- Dreisruh, E., Chervonkov, S., Neshev, D., Paulus, G.G., Walther, H.: Generation of lattice structures of optical vortices. *J. Opt. Soc. Am. B* **19**, 550–556 (2002)
- Fetter, A.L.: Rotating trapped Bose–Einstein condensates. *Rev. Mod. Phys.* **81**, 647–691 (2009)
- Fleischer, J.W., Bartal, G., Cohen, O., Manela, O., Segev, M., Hudock, J., Christodoulides, D.N.: Observation of vortex-ring “discrete” solitons in 2D photonic lattices. *Phys. Rev. Lett.* **92**, 123904 (2004)
- Ghofraniha, N.: Experimental evidence of replica symmetry breaking in random lasers. *Nat. Commun.* **6**, 6058 (2015). arxiv.org/abs/1407.5428 [cond-mat.dis-nn]

- Jović, D.M., Petrović, M.S., Belić, M.R.: Counterpropagating pattern dynamics: from narrow to broad beams. *Opt. Commun.* **281**, 2291–2300 (2008)
- Kosterlitz, J., Thouless, D.: The Kosterlitz–Thouless phase in a hierarchical model. *J. Phys. C* **6**, 1181–1203 (1973)
- Ma, X., Driben, R., Malomed, B., Meoer, T., Schumacher, S.: Two-dimensional symbiotic solitons and vortices in binary condensates with attractive cross-species interaction. *Nat. Sci. Rep.* **6**, 34847 (2016). [arXiv:1606.08579](https://arxiv.org/abs/1606.08579) [physics.optics]
- Malomed, B., Torner, L., Wise, F., Mihalache, D.: On multidimensional solitons and their legacy in contemporary atomic, molecular and optical physics. *J. Phys. B: At. Mol. Opt. Phys.* **49**, 170502 (2016)
- Neshev, D.N., Alexander, T.J., Ostrovskaya, E.A., Kivshar, Y.S.: Observation of discrete vortex solitons in optically induced photonic lattices. *Phys. Rev. Lett* **92**, 123903 (2004)
- Perret, A., Ristivojevic, Z., Le Doussal, P., Schehr, G., Wiese, K.: Super-rough glassy phase of the random field XY model in two dimensions. *Phys. Rev. Lett.* **109**, 157205 (2012). [arXiv:1204.5685](https://arxiv.org/abs/1204.5685) [cond-mat.dis-nn]
- Petrović, M.S., Belić, M.R., Denz, C., Kivshar, YuS: Counterpropagating optical beams and solitons. *Lasers Photonics Rev.* **5**, 214–233 (2011). [arXiv:0910.4700](https://arxiv.org/abs/0910.4700) [physics.optics]
- Petrović, M., Jović, D., Belić, M., Schröder, J., Jander, P., Denz, C.: Two dimensional counterpropagating spatial solitons in photorefractive crystals. *Phys. Rev. Lett* **95**, 053901 (2005)
- Rabinovich, M.I., Ezersky, A.B., Weidman, P.D.: *The Dynamics of Patterns*. World Scientific, Singapore (2000)
- Rechtsman, M.C., Zeuner, J.M., Plotnik, Y., Lumer, Y., Podolsky, D., Dreisow, F., Nolte, S., Segev, M., Szameit, A.: Photonic Floquet topological insulators. *Nature* **496**, 196–200 (2013). [arXiv:1212.3146](https://arxiv.org/abs/1212.3146) [physics]
- Sandfuchs, O., Kaiser, F., Belić, M.R.: Self-organization and Fourier selection of optical patterns in a nonlinear photorefractive feedback system. *Phys. Rev. A* **64**, 063809 (2001)
- Silae, M., Babev, E.: Microscopic derivation of two-component Ginzburg–Landau model and conditions of its applicability in two-band systems. *Phys. Rev. B* **85**, 134514 (2012). [arXiv:1110.1593](https://arxiv.org/abs/1110.1593) [cond-mat.supr-con]
- Terhalle, B., Richter, T., Desyatnikov, A.S., Neshev, D.N., Krolikowski, W., Kaiser, F., Denz, C., Kivshar, Y.S.: Observation of multivortex solitons in photonic lattices. *Phys. Rev. Lett* **101**, 013903 (2008)

P r o c e e d i n g s

of the

10th MATHEMATICAL PHYSICS MEETING: School and Conference on Modern Mathematical Physics

September 9–14, 2019, Belgrade, Serbia

Editors

B. Dragovich, I. Salom and M. Vojinović

Institute of Physics

Belgrade, 2020

SERBIA

Autor: Grupa autora

Naslov: 10th MATHEMATICAL PHYSICS MEETING: SCHOOL AND CONFERENCE ON MODERN MATHEMATICAL PHYSICS (Deseti naučni skup iz matematičke fizike: škola i konferencija iz savremene matematičke fizike)

Izdavač: Institut za fiziku, Beograd, Srbija

Izdanje: Prvo izdanje
(SFIN year XXXIII Series A: Conferences, No. A1 (2020))

Štampa: Zemunplast, Beograd

Tiraž: 150

ISBN: 978-86-82441-51-9

1. Dragović Branko
Matematička fizika-Zbornici

**CIP – Каталогизација у публикацији
Народна библиотека Србије, Београд**

51-7:53(082)

MATHEMATICAL Physics Meeting: School and Conference on Modern Mathematical Physics (10 ; 2019 ; Beograd)

Proceedings of the 10th Mathematical Physics Meeting: School and Conference on Modern Mathematical Physics, September 9-14, 2019, Belgrade, Serbia / [organizers Institute of Physics, Belgrade ... [et al.]] ; editors B. [Branko] Dragovich, I. [Igor] Salom and M. [Marko] Vojinović. - 1. izd. - Belgrade : Institute of Physics, 2020 (Beograd : Zemunplast). - XII, 383 str. : ilustr. ; 28 cm. - (SFIN ; year 33. Ser. A, Conferences, ISSN 0354-9291 ; n^o A1, (2020))

Nasl. u kolofonu: Deseti naučni skup iz matematičke fizike: škola i konferencija iz savremene matematičke fizike. - Tiraž 150. - Str. VII: Preface / editors. - Napomene i bibliografske reference uz radove. - Bibliografija uz svaki rad.

ISBN 978-86-82441-51-9

1. Dragović, Branko, 1945- [urednik] [аутор додатног текста]
а) Математичка физика -- Зборници

COBISS.SR-ID 13561865

CONTENTS

Review and Research Works

D. Benisty, E. Guendelman, E. Nissimov and S. Pacheva Non-Riemannian volume elements dynamically generate inflation	1
F. Bulnes Baryogenesis until dark matter: H-particles proliferation	15
M. Burić and D. Latas Singularity resolution in fuzzy de Sitter cosmology	27
D. J. Cirilo-Lombardo Dynamical symmetries, coherent states and nonlinear realizations: the $SO(2,4)$ case	37
M. Čubrović Fermions, hairy blackholes and hairy wormholes in anti-de Sitter spaces	59
Lj. Davidović, I. Ivanišević and B. Sazdović Courant and Roytenberg bracket and their relation via T-duality	87
Lj. Davidović and B. Sazdović T-duality between effective string theories	97
M. Dimitrijević Ćirić Nonassociative differential geometry and gravity	111
S. Giaccari and L. Modesto Causality in nonlocal gravity	121
J. Leech, M. Šuvakov and V. Dmitrašinović Hyperspherical three-body variables applied to Sakumichi and Suganuma's lattice QCD data	137
N. Manojlović, I. Salom and N. Cirilo António XYZ Gaudin model with boundary terms	143

S. Marjanović and V. Dmitrašinović Numerical study of classical motions of two equal-mass opposite-charge ions in a Paul trap	161
A. Miković Piecewise flat metrics and quantum gravity	167
D. Minić From quantum foundations of quantum field theory, string theory and quantum gravity to dark matter and dark energy	183
M. Mintchev and P. Sorba Entropy production in systems with spontaneously broken time-reversal	219
B. Nikolić and D. Obrić From 3D torus with H-flux to torus with R-flux and back	233
T. Radenković and M. Vojinović Construction and examples of higher gauge theories	251
I. Salom, N. Manojlović and N. Cirilo António The spin 1 XXZ Gaudin model with boundary	277
D. Simić Velocity memory effect for gravitational waves with torsion	287
O. C. Stoica Chiral asymmetry in the weak interaction via Clifford algebras	297
M. Stojanović, M. Milošević, G. Đorđević and D. Dimitrijević Holographic inflation with tachyon field as an attractor solution	311
F. Sugino Highly entangled quantum spin chains	319
M. Szczańchor Two type of contraction of conformal algebra and the gravity limit	331

M. Szydłowski, A. Krawiec and P. Tambor Can information criteria fix the problem of degeneration in cosmology?	339
V. Vanchurin A quantum-classical duality and emergent space-time	347
O. Vaneeva Transformation properties of nonlinear evolution equations in 1+1 dimensions	367
Talks not included in the Proceedings	377
List of participants	381

Fermions, hairy blackholes and hairy wormholes in anti-de Sitter spaces*

Mihailo Čubrović[†]

Center for the Study of Complex Systems,
Institute of Physics Belgrade, Serbia

ABSTRACT

We discuss the existence, properties and construction (analytical and numerical) of hairy black holes with fermionic matter in asymptotically anti-de-Sitter space. The negative cosmological constant makes hairy black holes stable, and the nucleation mechanism can make the formation of hair at the horizon energetically and entropically preferable to conventional black holes. The difficulties intrinsic to fermions at finite density – the Pauli principle and exchange interactions – require some drastic approximations in calculating the stress-energy tensor and geometry. We will consider several methods on the market – Hartree-Fock, WKB, and fluid-mechanical methods, and consider the dual field theories of these constructions. Then we will apply the same methods to the construction of wormholes; fermions are a natural candidate for wormhole source matter as they have a Dirac sea of negative energies, and negative energy-momentum density is the condition for wormhole formation. The field theory interpretation of wormholes is still open but has to do with strongly entangled systems. The paper combines a pedagogical introduction to the basic methods and results (obtained in the last 10+ years) with an account of fresh research results, mainly on the wormhole applications and non-planar black holes.

1. Introduction

AdS black holes are a favorite topic, not only in relation to holography but also in general: AdS space behaves like a potential box, the cosmological constant provides an effective repulsive force at large distances and the existence of a boundary at spatial infinity makes bound states possible. All of

*The author acknowledges funding provided by the Institute of Physics Belgrade through the grant by the Ministry of Education, Science and Technological Development. The author acknowledges the use of the Sci-Hub service. The results described here would never have been possible without the teaching, help and collaboration from Jan Zanen, Koenraad Schalm, Yan Liu, Ya-Wen Sun, Elena Gubankova, Mariya Medvedyeva, Vladan Djukić and Nicolas Chagnet.

[†] e-mail address: mcubrovic@gmail.com

this brings about the famous result that hairy black holes are indisputably possible, and well-studied. In full (global) AdS space, one may have small black holes, which barely see the boundary and radiate like in asymptotically flat space, and large black holes, which reach an equilibrium state with the Hawking radiation at given temperature and remain stable forever (eternal AdS black holes). We will focus on the latter, as they can be treated as (semi)classical stationary systems. Clearly, just like the Hawking radiation, matter and gauge fields can likewise equilibrate between the black hole horizon and AdS boundary, possibly forming hair – by definition, it means nonzero density of some field (and possibly nonzero expectation values of other operators, like charge density, spin, etc) at the horizon itself. This in turn means that the geometry changes as opposed to the no-hair case: the hair itself enters the stress-energy tensor, and the outcome is a hairy black hole geometry, where a horizon still exists but with a different metric. At zero temperature, hair tends to remove extremal black holes in favor of zero-area horizons, with zero Bekenstein-Hawking entropy. We will soon discuss several explicit examples of this phenomenon.

The above story acquires an additional dimension thanks primarily to the AdS/CFT correspondence (gauge/gravity duality) [1, 2, 3] – the fact that the bulk gravity physics is equivalent to a quantum field theory in flat space in one dimension less, whose operators act as boundary sources of the AdS (bulk) fields. The actions in AdS (with field Φ) and in CFT (with field \mathcal{O} , which acts as a boundary source to Φ) are equal:

$$\begin{aligned}
 S_{\text{AdS}} &= S_{\text{CFT}} \\
 S_{\text{AdS}} &= \int \mathcal{D}\Phi \exp \left(- \int_{\text{AdS}} d^{D+1}x \sqrt{-g} \mathcal{L}_{\text{AdS}}(\Phi, \partial_\mu \Phi) + \oint_{\partial} d^D x \sqrt{-h} \mathcal{O} \Phi \right) \\
 S_{\text{CFT}} &= \int \mathcal{D}\mathcal{O} \exp \left(- \int d^D x \mathcal{L}_{\text{CFT}}(\mathcal{O}) \right), \tag{1}
 \end{aligned}$$

where we have denoted by ∂ the boundary of the AdS space, $g_{\mu\nu}$ is the AdS metric and $h_{\mu\nu}$ is the induced metric at the boundary. From now on, integrals over the bulk of AdS will be denoted just by \int , understanding that the integral is over the whole space. At this place we do not intend to explain AdS/CFT and its applications in any detail; suffice to say that one can obtain thermodynamic potentials and correlation functions in field theory, which has found important applications in condensed matter theory, quantum chromodynamics and conformal field theory. Interested readers can consult [4, 5, 6] for reviews. In this work we deal with the gravity side of the correspondence – the formation of a hairy black hole with fermionic matter, which corresponds to a finite electron density phase in field theory. We assume the familiarity with the basic notions of AdS space and quantum field theory in curved spacetime, for example at the level of [7] and [8], respectively.

Mathematically, the topic of this review is the solution of the coupled Einstein-Maxwell-Dirac system with the total action $S_{\text{AdS}} = S_{\text{bulk}} + S_{\partial}$.

The bulk action reads:

$$\begin{aligned}
 S_{\text{bulk}} &= S_{\text{E}} + S_{\text{M}} + S_{\text{Dir}} \\
 S_{\text{E}} &= \int d^4x \sqrt{-g} (R + 6) \\
 S_{\text{M}} &= - \int d^4x \sqrt{-g} \frac{\hat{F}^2}{4} \\
 S_{\text{Dir}} &= - \int d^4x \sqrt{-g} \left(\frac{1}{2} \bar{\Psi} D_\mu e_a^\mu \Gamma^a \Psi + \frac{1}{2} \bar{\Psi} e_a^\mu \Gamma^a \Psi + m \bar{\Psi} \Psi \right). \quad (2)
 \end{aligned}$$

Here, $\hat{F}_{\mu\nu} = \partial_\mu A_\nu - \partial_\nu A_\mu$ is the electromagnetic (EM) field strength tensor, and the cosmological constant in AdS₄ is $6/L^2$, where the AdS radius $L = 1$ is set to unity, as we will mainly work on the Poincare patch of AdS space, so all other dimensionful quantities can be expressed in terms of L . The Dirac bispinor Ψ has mass m and charge q , and the covariant derivative

$$D_\mu = e_\mu^a D_a = \partial_\mu - \frac{i}{8} [\Gamma^a, \Gamma^b] \omega_{ab}^\mu - iq A_\mu \quad (3)$$

depends on the spin connection ω_{ab}^μ and the gauge field A_μ , and the gamma matrices satisfy the usual relations $[\Gamma^a, \Gamma^b] = 2\eta^{ab}$, with the Minkowski metric η . We will be using the mostly plus convention. Obviously, $\Psi = 0$ is a solution, and in this case we get a Schwarzschild black hole if the EM field is also zero, or a charged Reissner-Nordstrom (RN) black hole for nonzero field strength. The question is, are there other solutions, with nonzero profile Ψ ? Such solutions describe hairy black holes at finite temperature: the horizon is typically still there, but the geometry is changed. At zero temperature, the black hole might disappear. Since AdS space has a boundary, there is also a boundary contribution to the action, as in (1), depending on extrinsic curvature K , boundary cosmological constant λ and the boundary values of the fields:

$$S_\partial = \oint_\partial d^3x \sqrt{-h} \left[K - \lambda - \frac{1}{2} n_\mu A_\nu \hat{F}^{\mu\nu} - \frac{1}{2} \bar{\Psi} \Psi \right]. \quad (4)$$

The classical equations of motion do not depend on the boundary action. However, S_∂ is still important (1) to make sure there is a good action principle, i.e., that the on-shell solutions are indeed minima of the action¹ (2) to regularize any UV divergences (3) to get correct thermodynamics. The last point will be particularly important: one way to see that the hairy black hole and not the bald black hole is the true vacuum will be the fact that the action on the hairy solution is lower.

Solving the system (2) is a problem in quantum field theory at finite density. We work with classical general relativity (GR) and classical EM

¹Remember that the (bulk) Euler-Lagrange equations are only a necessary condition for the minimum of the action.

field, but *fermions are never classical*; this is the first important lesson. The Pauli principle always introduces nonlocal correlations which show as the exchange interaction. Another way of saying this is that the pressure of a fermionic gas or fluid always includes the quantum contribution which is absent in both classical and bosonic gas; that is the reason that organized matter such as stars, planets, chairs and notebooks has rigidity and does not collapse onto itself. Therefore, even though we do gravity at $\hbar = 0$, the fermions even at leading order need to be tackled quantum-mechanically. This means calculating the *fermionic determinant*:

$$Z_{\text{Dir}} = \int \mathcal{D}\bar{\Psi}\mathcal{D}\Psi e^{-S_{\text{Dir}}} = [\det(D_\mu e_a^\mu \Gamma^a + e_a^\mu \Gamma^a D_\mu + m)]^{1/2}. \quad (5)$$

We have put the equality sign under quotation marks because the determinant is actually the product of the eigenenergies of all the modes (an infinity of them), which is not only badly divergent (that could be regulated) but is also impossible to calculate because of the *fermion sign problem*, the fact that the fermionic modes enter the path integral with a sign that can be plus or minus. This makes the measure in the path integral (5) non-probabilistic and makes it impossible to expand around a classical solution in a controlled way. Fortunately, the AdS metric turns out to simplify the problem enough that it can be tackled in a way which is tractable and, while of course not exact, can be systematically improved in a perturbative way. This is in fact the motivation behind AdS/CFT modelling of strongly correlated electron systems: the fermion sign problem is fatal for strongly coupled field theories in flat space, but in GR with AdS boundary conditions it transforms into a difficult but doable task.

Is the journey worthwhile? In line with the broad scope of the Belgrade Mathematical Physics Meetings, we have anticipated a broad readership of this paper and thus we have decided to give a very general and perhaps rather dry introduction to the topic of fermionic hairy black holes. This necessarily means that we will not touch upon the many interesting applications: AdS/CFT and its applications to quantum chromodynamics and condensed matter physics, the black hole information problem, the critical phenomena in gravitational collapse and the black hole solutions in string theory. We do discuss one special topic that we currently find very interesting: hairy wormholes generated by fermion matter, where many of the methods used for hairy black holes can be successfully applied. The main task of the paper is to provide a tutorial on the basic methodology and calculation techniques, bringing the reader to the point that he can understand and repeat the calculations from the literature and start doing his own. The existing literature is rather heterogenous and there is no single text to recommend. We will give the references we deem particularly useful throughout the paper, without the pretention of being exhaustive; the choice of references is certainly dictated also by our prejudices and tastes.

Plan of the paper. In Section 2 we first explain the instabilities of AdS space and AdS black holes to a nonzero density profile of fermions, and in-

roduce the basic concepts that will keep appearing throughout the paper: effective potential and the bound states of the fermionic wavefunctions. In Section 3 we first treat the problem in the consistent one-loop (Hartree-Fock) approximation, calculating the determinant (5) by definition, from the individual wavefunctions for different states. We find this job surprisingly difficult – it is still an active research area. But we are able to give a qualitative picture of the outcome and sketch the phase diagram, depending on the chemical potential μ and fermion mass and charge m, q . As we move toward the high-fermion-density corner of the phase diagram, the things simplify. The simplest and "most classical" limit of the problem is the limit of large density. It is a rule of thumb that for fermions, the role of interactions diminishes as the density grows. At high density, WKB approximation works very well. At highest densities, we find semiclassical fluid with an equation of state that takes into account the fermionic pressure, similar in spirit to the Oppenheimer-Volkov equations for neutron stars. In section 4 we apply these methods to a different topic – hairy wormholes instead of black holes. This problem has recently gained notoriety and might carry some important messages for the black hole information problem. The final section sums up the conclusions.

2. Planar AdS black holes and fermion nucleation

In this and the next section we will focus on large planar black holes on the Poincare patch of AdS space. Large black holes can reach equilibrium with the AdS boundary so they do not emit Hawking radiation and can exist eternally. The Poincare patch of AdS₄ space is a coordinate chart with a single boundary on one end and interior on the other end. It does not cover the whole AdS space but is simpler to work with than global AdS and is good enough to describe the instability at the horizon. The metric of pure AdS space without a black hole is given by

$$ds^2 = r^2 (-dt^2 + d\vec{x}^2) + \frac{dr^2}{r^2} = \frac{1}{z^2} (-dt^2 + d\vec{x}^2 + dz^2) \quad (6)$$

where $r = 1/z$ is the radial coordinate, t is time and $\vec{x} = (x, y)$ are the transverse coordinates. The AdS boundary is at $r = \infty$ ($z = 0$), and the interior is at $r = 0$ ($z = \infty$). From now on we will mainly use the z coordinate; we will always specify explicitly if a different radial coordinate is used. In AdS/CFT, the radial coordinate corresponds to the energy scale in field theory: the near-boundary region encodes for the physics at high energies, in the ultraviolet (UV), and the deep interior, with z large, is the infrared (IR). Even though we do not consider the CFT dual here, we will still adopt the UV/IR terminology.

In the presence of a point electric charge e we get a Reissner-Nordstrom (RN) black hole with the horizon at $z_h = 1$, with charge e , mass M and

temperature T :

$$ds^2 = \frac{1}{z^2} \left(-f(z)dt^2 + d\vec{x}^2 + \frac{dz^2}{f(z)} \right), \quad f(z) = 1 - Mz^3 + e^2z^4$$

$$M = z_h^3 + e^2, \quad A = \frac{ez_h}{2\sqrt{\pi}}(1 - z/z_h)dt, \quad T = \frac{3z_h}{4\pi} \left(1 - \frac{e^2}{3z_h^4} \right) \quad (7)$$

For $e = 0$ we get the Schwarzschild AdS black hole, and for $e = \sqrt{3}z_h^2$ the black hole becomes extremal, with temperature $T = 0$. To see this, remember that the black hole temperature is given by $f(z \rightarrow z_H) = 4\pi T(z - z_H) + \dots$, so plugging in f from above we indeed get the correct expression for T . Importantly, the near-horizon region of a black hole is an AdS space [7]. This IR AdS space (near $z = z_h$) has a priori nothing to do with the AdS asymptotics in the UV (near $z = 0$); it is there also for black holes in flat or dS space. At $T = 0$, rescaling $z - e/\sqrt{3} \mapsto 1/6\epsilon\xi$ and expanding in ϵ to lowest order gives the metric

$$ds^2 = \frac{1}{6}(-dt^2 + d\xi^2) + \frac{e^2}{3}d\vec{x}^2, \quad A_t = \frac{1}{\sqrt{6}\xi}. \quad (8)$$

This is $\text{AdS}_2 \times R^2$ geometry, a direct product of AdS with a plane. At finite temperature, a similar rescaling can be worked out, yielding again an AdS_2 throat. Since the throat describes the near-horizon region, instabilities of the black hole can be figured out from possible instabilities of this IR AdS space. Once again, this is *not* the whole AdS_4 , which is always stable far from the horizon, in the UV (otherwise our whole classical gravity approach crumbles down), it is just a region near the horizon, in IR.

In order to write the equations of motion, we have to choose a basis for the gamma matrices and the form of the Dirac bispinor (remember that only two out of four components are really independent degrees of freedom). A convenient representation is

$$\Gamma^0 = \sigma^1 \otimes i\sigma_2, \quad \Gamma^1 = \sigma^1 \otimes \sigma_1, \quad \Gamma^2 = \sigma^1 \otimes \sigma^3, \quad \Gamma^z = \sigma^3 \otimes \hat{1}. \quad (9)$$

so that the Dirac equation in a spherically symmetric metric defined as $\text{diag}(g_{tt}, g_{ii}, g_{ii}, g_{zz})$ gives two equivalent decoupled pairs of equations. Taking the Dirac bispinor in the form $\Psi = (\psi_1, \chi_1, i\chi_2, i\psi_2)^T$, the equations for $\psi_{1,2}$ read [9, 10]:²

$$\partial_z \psi_{1,2} \pm \hat{m} \psi_{1,2} - (\mp \hat{E} + \hat{k}) \psi_{2,1} = 0 \quad (10)$$

$$\hat{m} \equiv m\sqrt{g_{zz}}, \quad \hat{\mu} \equiv \sqrt{\frac{g_{zz}}{-g_{tt}}} A_t, \quad \hat{E} \equiv q\hat{\mu} + E\sqrt{\frac{g_{zz}}{-g_{tt}}}, \quad \hat{k} \equiv \sqrt{\frac{g_{zz}}{g_{ii}}} k. \quad (11)$$

²Since only two components of the Dirac bispinor are independent, the system for $\chi_{1,2}$ yields no new information.

We have Fourier-transformed the derivatives over time and transverse spatial dimensions as $\partial_t = -i\omega$, $\partial_x = ik_x$, $\partial_y = ik_y$, and we have exploited the spherical symmetry to set $k_x = k$, $k_y = 0$. The quantities \hat{E} , \hat{k} , $\hat{\mu}$ can be informally interpreted as "local" values of the energy, momentum and chemical potential, respectively. The "local" values equal E , k , μ at the AdS boundary, grow monotonously toward the horizon and diverge there, a consequence of the infinite redshift seen by a faraway observer. An important idea is to consider the Schrödinger form of the Dirac equation instead, differentiating (10) once with respect to z , decoupling the equations for $\psi_{1,2}$, and eliminating the first derivatives $\psi'_{1,2}$ by introducing the tortoise coordinate s instead of z . The resulting picture is that of a zero-energy Schrödinger equation, of the form $\partial_s^2 \psi_{1,2} - V_{\text{eff}}(s)\psi_{1,2} = 0$, in an effective potential $V_{\text{eff}}(s)$.³ Near the horizon, the potential is constant at leading order [11]:

$$V_{\text{eff}}(s \rightarrow -\infty) = \frac{m^2 + 12k^2/\mu^2 - 2q^2}{(q/\sqrt{2} + k)^2} + \dots \quad (12)$$

It is true that the Schrödinger form is only a consequence of the Dirac equation, not equivalent to it: extra conditions must be imposed on the Schrödinger solution to make it satisfy the Dirac equation. But the effective potential is great for qualitative insights and it contains the basic idea of the black hole instability in a very transparent way. The near-horizon potential can contain bound states if it is negative, hence the instability criterion for a fermionic mode with momentum k is that the numerator of (12) is negative. Fermions fill up the potential well starting from $k = 0$ up to some maximum k for which (12) reaches zero. Therefore, the instability first sets in when V_{eff} is negative for $k \rightarrow 0$, so we get our first rule-of-thumb prediction: the black hole will be surrounded by a gas of fermions and become hairy when

$$m < q\sqrt{2}. \quad (13)$$

But this is just one end of the potential well; what happens at the other end? Plugging in the pure AdS metric (6) into (12) we get

$$V_{\text{AdS}}(s \rightarrow 0) = \frac{m^2 + m + k^2}{(k + \mu)^2} \frac{1}{s^2} + \dots, \quad (14)$$

which is always non-negative, and grows to infinity. This is good – there is never an instability in the far UV, and the fermionic hair can never come arbitrarily close to the AdS boundary. It also means that bound states in the interior will indeed exist whenever (13) is negative. The physical picture is the following: in the presence of EM and gravitational field of the black hole, fermions are pair-created. These pairs are virtual, and

³This is a simple exercise that we will do many times; the reader should be able to do the necessary (straightforward) calculations leading to the expression for $s(z)$ and $V_{\text{eff}}(s)$.

they only have a finite probability of becoming long-living if the external potential energy is large enough. In that case, bound states form, and there is a solution of (2) with nonzero fermion density. In the literature, this is sometimes called fermion nucleation. For scalars, similar logic leads to the Breitenlohner-Freedman bound, which puts a constraint on the scalar mass for the stability of the UV (with fermions, as we have seen, UV is always stable), and in IR it similarly gives a criterion for forming hair [5]. We also see from (14) and Fig. 1 that the potential well becomes shallower as k grows, so the bound states only exist up to some maximum $k = k_F$ which is really the Fermi momentum of the bulk Fermi sea.

From (12,14) we can understand the behavior of the effective potential. In Fig. 1, we give the function $V(s)$ in the whole space, from $z = 0$ ($s = 0$), to $z = z_h$ ($s = -\infty$). The fermionic modes fill the potential well until they reach the energy $E = 0$. From (12), higher modes correspond to higher momentum k . The fermionic density is thus given by a sum over these bound states. The easiest case is in fact an extremely deep well: the energy levels are so dense and so numerous that they can be approximated by a continuum; this is called electron star limit. But the most interesting regime is the one with only a few wavefunctions, which really describes the transition to a hairy solution. This is a much harder nut to crack.

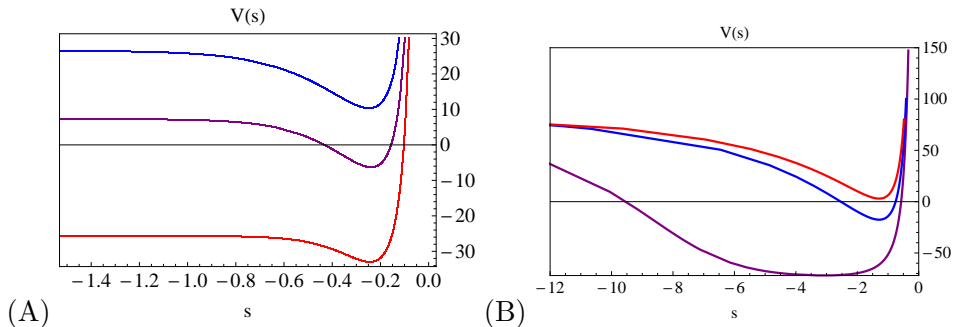


Figure 1: Effective potential V_{eff} , as a function of the tortoise coordinate $s \equiv \int_0^z dz g_{zz}(z)$, in the RN metric (A), and in the Lifshitz metric (B), for $q = 1$, $m = 0.4$, $\mu = 1$, and three momentum values increasing from violet to blue to red: $k = 1, 2, 3$ (A) and $k = 0, 5, 10$ (B). In both cases, the negative potential well becomes shallower and shallower and eventually disappears as k grows, so we fill the bulk Fermi sea up from $k = 0$ to some maximal $k = k_F$. In the black hole background, the potential is flat for $s \rightarrow -\infty$, which corresponds to the AdS_2 near-horizon region and signifies an instability as the bound states extend all the way to the horizon ($s = -\infty$). In the backreacted Lifshitz metric the potential grows for $s \rightarrow -\infty$, suggesting that deep IR is stable: the true vacuum is the Lifshitz geometry, not RN. Taken over from [14].

3. Fermionic hair

Now that we have convinced ourselves that hairy solutions, with finite fermion density, have to exist, we need to solve the full system of Einstein, Maxwell and Dirac equations to find them. Clearly, a more general ansatz for the metric than (7) is needed now, and we will write it as

$$ds^2 = -\frac{F(z)G(z)}{z^2}dt^2 + \frac{1}{z^2}d\vec{x}^2 + \frac{1}{F(z)z^2}dz^2, \quad (15)$$

leading to Einstein-Maxwell equations

$$1 - F + zF'/3 - T_{tt}^{\text{tot}}FG/3z^2 = 0 \quad (16)$$

$$G' + z(T_{tt}^{\text{tot}}/F^2 + T_{zz}^{\text{tot}}G) = 0 \quad (17)$$

$$A_t'' - G'/2GA_t' + qn\sqrt{G}/\sqrt{F}z^3 = 0, \quad (18)$$

where $T_{\mu\nu}^{\text{tot}}$ is the total stress-energy tensor, both from the electric field (which is easy to find) and from the fermions (which is our big problem). A typical situation in hairy problems is that formulating the physically meaningful boundary conditions is not so easy. Notice the Einstein equations are first-order, so we need one boundary condition for each function (F and G), whereas the Maxwell equation is second-order and requires two boundary conditions. Let us now summarize what boundary behavior we expect on physical grounds.

1. The AdS asymptotics for the metric and gauge field require $F(z \rightarrow 0), G(z \rightarrow 0) = 1, A_t(z \rightarrow 0) = \mu$. So far it's all simple.
2. The main puzzle for the IR geometry is – does the horizon disappear or not? At $T = 0$ we do not expect that the degenerate RN horizon can survive. So we do not expect zeros in F, G but we do expect their derivatives to vanish in order to have a smooth solution (finite derivatives at $z \rightarrow \infty$ would likely give divergent curvature). Thus at $T = 0$ we need $F'(z \rightarrow \infty) = G'(z \rightarrow \infty) = 0$ or, in other words, $F(z \rightarrow \infty) = \text{const.} + O(1/z)$ and likewise for G . At finite temperature, general GR arguments suggest there is a horizon at some $z = z_h$ satisfying $F'(z \rightarrow z_h) = 4\pi T$.
3. The IR behavior of the gauge field is related to the question: *is all the charge carried by the fermions, or the charge is shared between the fermions and the horizon?* The Gauss-Ostrogradsky theorem for the AdS space, with a UV boundary and either a horizon or a smooth far-away IR takes the form [12]:

$$\oint_{\partial} d^3x \sqrt{-h}|_{z \rightarrow 0} \star \hat{F} = \int d^4x \sqrt{-g} qn + \oint_{\text{IR}} d^3x \sqrt{-h_{\text{IR}}}|_{z=z_{\text{IR}}} \star \hat{F} \quad (19)$$

Here, $\star \hat{F}$ is the coordinate-invariant flux of the 2-form \hat{F} , and h_{IR} is the induced metric on the surface normal to the radial direction at

$z_{\text{IR}} = z_h$ or $z_{\text{IR}} = \infty$, depending on whether there is a horizon or not. In principle, the IR charge might be shared between the horizon and the fermions. However, we will find that in the semiclassical calculation there are no solutions where the charge is shared – any backreaction will always expell all the charge from the IR.

4. The boundary conditions for the Dirac equation present no problems and are pretty standard in AdS space [13]. In the UV, out of the two branches, we want the subleading one, with the motivation to preserve the AdS asymptotics, i.e., to perturb the space as little as possible in the UV. In particular, the near-boundary expansion of (11) gives

$$\begin{aligned}\psi_1(z \rightarrow 0) &= \frac{E + \mu q - k}{2m - 1} A_2 z^{5/2-m} + B_1 z^{3/2+m} + \dots \\ \psi_2(z \rightarrow 0) &= A_2 z^{3/2-m} + \frac{E + \mu q + k}{2m + 1} B_1 z^{5/2+m} + \dots, \quad (20)\end{aligned}$$

so we pick $A_2 = 0$, as the leading contribution for $z \rightarrow 0$ comes from the $z^{3/2}$ term. In the IR, the metric determines the boundary conditions: if there is a horizon, we need $\Psi(z = z_h) \rightarrow 0$ for stability, if not, then to avoid infinite energy density at large z we require $\partial_z \Psi(z \rightarrow \infty) = 0$, for otherwise a nonconstant density profile would give rise to a diverging curvature. The attentive reader should be alarmed: this means two boundary conditions for each component (one in UV and one in IR), but the equations are only first-order. The resolution is that for given momenta, the energy is not arbitrary but fixed by the dispersion relation $E(k)$; thus solving the Dirac equation in an effective potential well introduces energy quantization, as one would expect.

What remains is to find the fermionic stress tensor. Since spinors couple to the spin connection e_a^μ and not directly to the metric, the stress tensor is expressed as

$$T_{\mu\nu} = \left\langle \frac{1}{4} e_{\mu\alpha} \bar{\Psi} \Gamma^a D_\nu \Psi + (\mu \leftrightarrow \nu) \right\rangle, \quad (21)$$

and the expectation value $\langle \dots \rangle$ reminds us that the fermions are never classical. At zero temperature, the state is pure and can be represented as the sum of (appropriately normalized) radial modes with energies E_ℓ , where ℓ is the radial quantum number, and the energies E_ℓ are all ≤ 0 . At finite temperature, the state is mixed and gets a contribution from both positive and negative energies E_ℓ , with thermal weights $w_\ell = \exp(-\beta E_\ell)/Z$, the partition sum being $Z = \sum_\ell \exp(-\beta E_\ell)$. With this in mind, we can write out (21) as

$$T_{tt} = e_{t0} \sum_{\ell=1}^N w_\ell \int_0^{k_F} \frac{k dk}{(2\pi)^2} \left(\psi_{1;\ell}^\dagger \psi_{1;\ell} + \psi_{2;\ell}^\dagger \psi_{2;\ell} \right) (E_\ell + q A_t)$$

$$\begin{aligned}
 T_{ii} &= e_{i1} \sum_{\ell=1}^N w_{\ell} \int_0^{k_F} \frac{k dk}{(2\pi)^2} \left(\psi_{1;\ell}^{\dagger} \psi_{1;\ell} - \psi_{2;\ell}^{\dagger} \psi_{2;\ell} \right) k \\
 T_{zz} &= e_{z3} \sum_{\ell=1}^N w_{\ell} \int_0^{k_F} \frac{k dk}{(2\pi)^2} \left(\psi_{1;\ell}^{\dagger} \partial_z \psi_{2;\ell} - \psi_{2;\ell}^{\dagger} \partial_z \psi_{1;\ell} \right). \quad (22)
 \end{aligned}$$

For brevity, we write $\psi_{1,2;\ell} \equiv \psi_{1,2}(E_{\ell}, k; z)$. We will consider in detail just the $T = 0$ case, when the weights w_{ℓ} effectively just pick the ground state and cut off all the others, but we will later discuss the results (without details of the calculations) also at finite T . The spectrum is discrete and gapped in the radial direction, so the integral $\int dE/2\pi$ becomes a sum, however in the transverse directions the system remains gapless, filling the whole (spherical) Fermi sea in the k -momentum space, as long as the dispersion relation $E(k) = E_{\ell} \leq 0$ is satisfied for some ℓ . The highest such k , for which $E_{\ell} = 0$, is the Fermi momentum k_F , and the possible momenta are $0 \leq k \leq k_F$. It is this continuous quantum number k that makes our life difficult. Here, indeed, our easy path comes to an end, because a self-consistent calculation of the wavefunctions certainly cannot be done in a closed form. Here we must resort to approximations. The number of occupied levels N is a good guide on the kind of approximation one needs to make. One can rephrase it as the ratio Q/q , where Q is the total fermion charge $\int d^4x \sqrt{-g} q \Psi^{\dagger} \Psi$. The thermodynamic limit, where the number of particles goes to infinity and the charge of an individual fermion to zero so that $N \rightarrow \infty, q \rightarrow 0, Q = Nq = \text{const.}$, is at one extreme. We expect that the problem approaches the classical regime in this case, and it will turn out to be true. The opposite limit is $Q/q = 1$, with just a single excitation, the hairy black hole at birth. We expect this to be likewise a simple limit, however it will turn out not to be quite true. In-between we dial between the quantum mechanics of $N = 1$ and the classical field theory of $N \rightarrow \infty$ [14].

Phase diagram. Before doing that, we can sum up our qualitative knowledge on a phase diagram (Fig. 2). From (12-14), bound states form for small enough m values (panel (A)); if (13) is valid beyond the probe approximation, the borderline is $m = q\sqrt{2}$. Left of this line there is a hairy solution, to the right of it the AdS₂ near-horizon region (and the whole RN black hole) remain. The hairy solutions are best described in different ways depending on the number of filled levels ($N = Q/q$); this is the topic of the rest of this section. One can also plot the situation at finite temperature (panel (B)). The phases remain the same; more precisely, the extremal black hole becomes a finite-temperature black hole, and the hairy solutions also smoothly develop a hairy horizon (thermal horizon with nonzero fermion density $n(z_h)$). What changes is the order of the phase transition: at $T = 0$ it is continuous, and at finite temperature it is discontinuous.

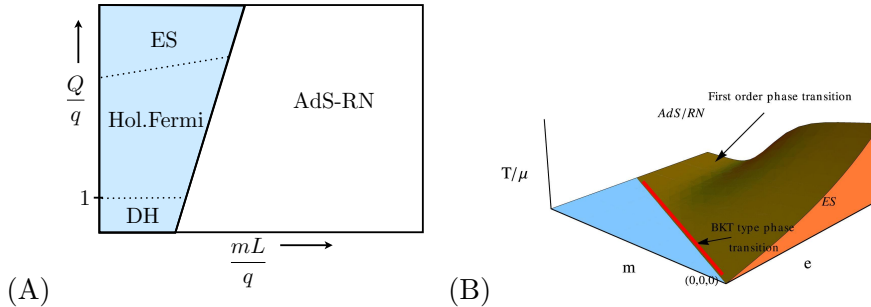


Figure 2: (A) Phase diagram as a function of the total-to-fermion-charge ratio Q/q (y -axis), and the fermion mass (in units of AdS radius L) over charge ratio mL/q (x -axis). For large masses, the effective potential is positive and the ground state is the bald RN black hole, with quantum critical dual field theory. For smaller masses, hair develops, which corresponds to a Fermi liquid in dual field theory. For $Q \sim q$ (few wavefunctions), the single-wavefunction Dirac hair approximation works; for $Q/q \rightarrow \infty$ we approach the semiclassical fluid (electron star) limit; between them there is a smooth crossover with unclear properties, both in AdS and in the holographic dual. Notice different notational conventions for the total charge from the main text (e vs. Q). Taken over from [15]. (B) Adding nonzero temperature as the third axis, we obtain also the thermal phase transitions between the black hole and the hairy solution, which are generically first order, smoothing out to an infinite order (BKT) transition at $T = 0$ – the red line in (B) is the bold black line between the RN and hairy (blue) region in (A).

3.1. Quantum hairy black holes

A controlled approximation is to solve the problem perturbatively, at one-loop order in fermionic fields. This is nothing but the textbook Hartree-Fock (HF) method, but in curved space. Dynamical spacetime makes a big difference: it introduces an additional strongly nonlinear component of the system, making the solution landscape larger and less predictable, and the UV and IR divergences can appear also in the Einstein equations and need explicit regulators. In fact, this is still an open problem – nobody has yet classified the solutions of the Einstein-Maxwell-Dirac system even in the Hartree-Fock approximation, and we do not know what surprises might lurk in this corner of the phase diagram. The HF electrodynamics contains two diagrams, a vacuum bubble that renormalizes the chemical potential

as $\hat{\mu}(z) \mapsto \hat{\mu}(z) + \delta\hat{\mu}(z)$ (the Hartree term):

$$\delta\hat{\mu}(z) \equiv q \sum_{\ell=1}^N \int \frac{kdk}{2\pi} \left(\psi_1^\dagger(E_\ell, k; z) \psi_1(E_\ell, k; z) + \psi_2^\dagger(E_\ell, k; z) \psi_2(E_\ell, k; z) \right) \quad (23)$$

and the exchange interaction (the Fock term). The explicit z -dependence of the Hartree correction is a gory reminder that the problem is solved in inhomogenous background. This is also the reason why already the Hartree correction is nontrivial: unlike the textbook situation where the shift $\delta\mu$ merely changes the numbers, here it is a radial function $\delta\mu(z)$ and its influence is also qualitative. So far, nobody even tried to do the whole HF calculation, and even just the Hartree term is not easy. We are plagued (1) by the UV divergences introduced by the modes close to $k = k_F$ which, as we have seen, peak most sharply near the boundary and can shatter the AdS space into pieces if not properly renormalized (2) by the IR divergences introduced by the modes with k close to zero, which extend far into large z values and can make the system unstable to forming a naked singularity.

Hard-wall Fermi liquid. The only case which is under good control is the hard-wall model of [12]: the UV divergences are resolved simply by not backreacting on the metric, i.e. solving just the Maxwell-Dirac system in fixed AdS metric (6) even without a black hole, and the IR divergences disappear by cutting off the space at some arbitrary z_0 , so that we simply eliminate the IR region. The approximations are rather drastic, but they allow a complete solution. In pure AdS space, the solutions $\psi_{1,2}$ can be found analytically in terms of Bessel functions, the states form discrete and gapped bands, and we only have to solve the Maxwell equation (18). The outcome is given in Fig. 3. Hard wall acts as an infinite potential barrier, so the wavefunctions should die on it, and the condition $\psi_{1,2}(z_0) = 0$ determines the dispersion relation. The wall should not be charged, so in (19) the second term on the right-hand side equals zero, meaning that $A'_t(z_0) = 0$. The picture is that of a Fermi liquid, nicely filling the Fermi sea at momenta $k \leq k_F$ and having long-living quasiparticles. This model is an important starting point for more complicated setups, and has the advantage of being intuitive, but by itself is too simplistic. Indeed, we want to talk about hairy black holes, and here we don't even have one, as it is hidden behind the hard wall!

An attempt to study a simple setup but with a black hole was made in [16]. In this approach, we are limited to a single energy level, $\ell = 1$. This is justified only when the hair is just starting to form, right at the transition point. There is again no backreaction on metric, but the (fixed) metric is now taken to be the RN black hole. This is actually a big jump in difficulty: the wavefunctions oscillate near the horizon at any nonzero energy (Fig. 4(A)), so they can satisfy the IR boundary condition at any energy and momentum (we can always pick the phase so that $\psi'(z_h) = 0$), and the spectrum is continuous as there is no wall to create a gap. This

is what forces us to consider the single-mode case: with the gapped hard-wall model we could add a *finite* number of modes, but now there is a *continuum* of them, N going to infinity even for arbitrarily small Q/q . The only way out is to *assume* there one mode only and solve the resulting Dirac-Maxwell system. This setup is convenient for understanding the transition itself, which turns out to be discontinuous (first-order) at finite temperature (Fig. 4(B)), and likely infinite-order (Berezinskii-Kosterlitz-Thouless, BKT) at zero temperature, as we shall soon see.

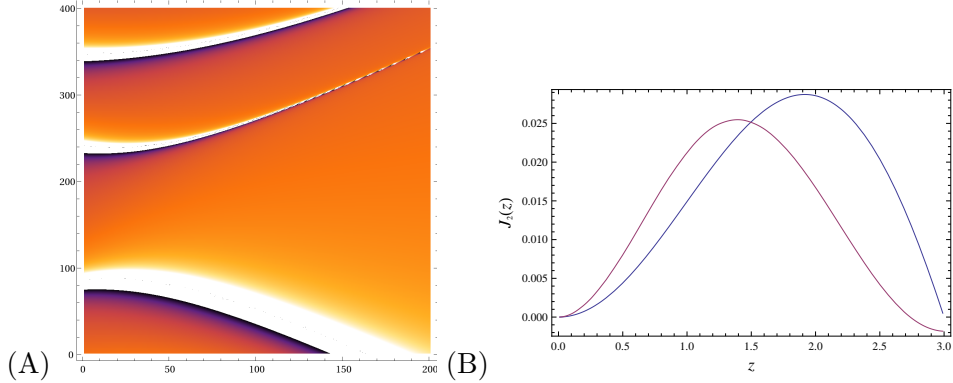


Figure 3: (A) Dispersion relation $E_\ell(k)$ for the first two electron bands $\ell = 1, 2$ in hard-wall AdS space, for $\mu = 1, m = 1, q = 2$. The first band from bottom is the hole band, not an an electron band – its contribution can be absorbed in the redefinition of the parameters and it does not contribute to hair. The colormap shows the resolvent of the Dirac operator, $(D_z \Gamma^z + \vec{D} \cdot \vec{\Gamma} - m - E)^{-1}$, thus the bright white regions show the places where the resolvent diverges and a discrete bound state is formed. The horizontal axis is the momentum and the vertical axis the energy, both in computational units. (B) Wavefunctions $\psi_{1,2}$ (here for $\ell = 1$ and $k = 1$) are smooth everywhere - what happen exactly at the horizon we do not know in this model, as the space is cut off at $z = 3$.

Quantum electron star. The single-mode approach has taught us a lesson: already at the level of the gauge field only, the changes from the finite fermion density are drastic, and the resulting stress tensor is large at the horizon, so a change of the black hole metric is certainly expected. However, when we try to solve the Einstein equations, things become almost intractable. Both UV and IR divergences appear: the former because the currents diverge in continuous space, and the latter because the discrete bands fuse into a continuum in IR. The latter issue is most easily regularized by a hard wall, but a hard wall does not make much sense if we want to backreact on geometry. The regularization of the UV divergences is systematically discussed in [17, 18] and the bottom line is that there is a logarithmic short-distance divergence which can be regularized by point

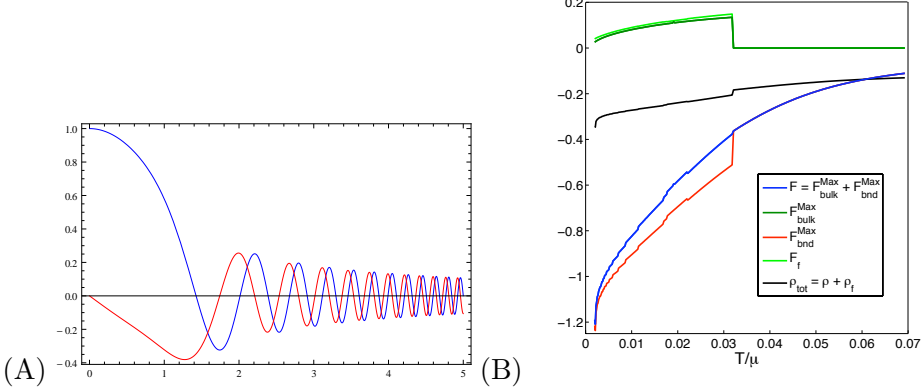


Figure 4: (A) Wavefunctions $\psi_{1,2}$ in RN background, for $\ell = 1$ and $k = 1$, always oscillate and approach an essential singularity at the horizon, which indicates an instability: the metric changes and the degenerate horizon disappears. (B) The bulk action (or free energy F , from AdS/CFT correspondence) of the Maxwell (electric field), in blue, consists of the bulk and boundary contribution (dark green and red), the former practically identical to the contribution from fermions. All these are computed from the action (2-4). While the *total* free energy is continuous, it has a cusp, made manifest by the slight jump in density (black), a sign of first-order hair-forming transition.

splitting; in this procedure the cosmological constant becomes renormalized. This is not a drastic change: it will just change the numbers but not qualitative behavior. The IR problem is still unsolved. The approach of [18] is to put the system in global AdS space⁴ whose radial slices are spheres, not planes, so the AdS radius provides a regulator. A perhaps more physical approach, motivated by consistent truncations from string theory, is to introduce a non-minimally coupled scalar, i.e., a dilaton that introduces a soft wall and suppresses the IR degrees of freedom in a continuous way, without an abrupt cutoff at some z_0 , so the total bulk action is now

$$\begin{aligned}
 S_{\text{bulk}} = & \int d^4x \sqrt{-g} \left[R - V(\Phi) - \frac{1}{2} (\partial\Phi)^2 - \frac{Z(\Phi)}{4} \hat{F}^2 \right] - \\
 & - \int d^4x \sqrt{-g} \bar{\Psi} \left(\frac{1}{2} D_a \Gamma^a e^\Phi + \frac{1}{2} e^\Phi D_a \Gamma^a + m \right) \Psi, \quad (24)
 \end{aligned}$$

where the dilaton potential reproduces the AdS cosmological constant near the boundary, i.e., $\Phi(z \rightarrow 0) = 0$ and $V(\Phi \rightarrow 0) = 6$, $Z(\Phi \rightarrow 0) = 1$. It is not clear if one can ever remove the IR regulator. That is precisely the

⁴Dual field theory then lives on a sphere instead of a plane.

reason that we regard the dilaton regulator as more physical, since string theory constructions as a rule contain non-minimally coupled scalars, and the action (24) can be obtained by consistent truncation; whereas global AdS is essentially an ad hoc solution, though a very interesting one, with possible applications in AdS/condensed matter duality, where systems that live on surfaces (such as a sphere) appear naturally.

While this is still very much a work in progress,⁵ preliminary results suggest that the RN-to-hairy-black-hole transition at zero temperature is an infinite-order (BKT) transition, where all derivatives of S remain smooth (Fig. 5). This is the point where the potential just starts deviating very slightly from the flat IR behavior in Fig. 1(A). At the end of this section we will try to understand this (still conjectural) numerical finding analytically.

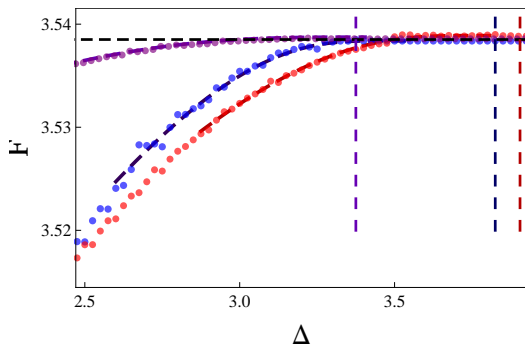


Figure 5: The bulk action (here denoted as free energy F , from AdS/CFT correspondence) as a function of the fermion mass (here denoted as $\Delta = 3/2 + m$) is very well fit by the BKT function $\exp(-c/\sqrt{\Delta_c - \Delta})$. The parameter c is determined by the chemical potential (we plot for three values $mu = 1.0, 1.5, 2.0$ in violet, blue, green). To the right of the transition point the action is independent of m as there is no hair, fermion density is zero, and so nothing depends on the fermion parameters. To the left of the transition point, the fermions form hair of nonzero density. Nobody knows yet how the near-horizon metric changes.

3.2. WKB star and electron star

WKB approach. We have followed the logical chain of reasoning from the point where the hair starts growing, having $Q/q \sim 1$ and deforming the black hole just a slight bit, towards larger and larger hair, eventually reaching the regime $Q/q \gg 1$. But this last regime is the easiest to approach, as the fermions become as close to classical as they can possibly be. A good starting point is the controlled expansion in \hbar , where we solve the

⁵With N. Chagnet, V. Djukić and K. Schalm.

Dirac equation in the eikonal approximation or, in other words, the WKB approach [15]. We express the wavefunction as

$$\psi_{1,2} = e^{i\theta_{\pm}}/\sqrt{p}, \quad p \equiv \sqrt{\hat{E}^2 - \hat{m}^2 - \hat{k}^2}, \quad (25)$$

where p has the role of the canonical momentum. The wavefunction is nonzero between the turning points z_{\pm} , determined by the equation $p(z_{\pm}) = 0$. The explicit form of the phase θ_{\pm} as well as higher-order corrections to the phase can be found in [15], but the reader should in fact have no difficulty in deriving them, following the usual WKB procedure (though for the Dirac equation instead of the Schrödinger equation). Now the density and pressure are found by inserting the solution (25) into (22). The procedure can be iterated to obtain self-consistent solutions, but now we solve the whole system including the Einstein equations. It is instructive to plot the total on-shell action (2) as a function of temperature (remember that finite temperature is imposed through the corresponding boundary condition for the metric function F).⁶ Fig. 6 plots the dependence $\mathcal{F}(T)$ in the vicinity of the transition value T_c : the derivative $\partial\mathcal{F}/\partial T$ undergoes a jump which is nothing but the entropy $\mathcal{S} \equiv \partial\mathcal{F}/\partial T$. We thus find a *first-order phase transition* at the point when Fermi hair starts forming. Of course, don't forget that the WKB approach is in fact *not* to be trusted very near the transition point: at the transition N changes from 0 to 1, which is far from the regime $N \ll 1$. But the qualitative insight that at finite temperature the system undergoes a non-symmetry-breaking transition is likely robust and we expect to prove it also within the more rigorous fully quantum-mechanical approach of the previous subsection. It is a hairy version of the celebrated Hawking-Page transition [19], and confirms the intuition that the high-temperature phase is always a black hole; but now, the low-temperature phase is not simply a gas, but a dense fluid in AdS.

Plotting the density and pressure in Fig. 7(A), one finds that for high values of N they tend to a constant value in deep interior. This motivates the fluid ansatz taken in the electron star limit, now to be considered.

Electron star. Electron star is a charged, AdS version of the neutron stars, described as perfect fluid by the Oppenheimer-Volkov equations. The idea is to *assume* that the fermionic matter is a perfect fluid, and then express the energy density ρ , pressure p and charge density n in terms of *integrals* over energy and momenta (i.e., assume that the bound states are infinitely close, and the gaps between them vanish). The fluid approximation thus becomes exact in the limit of $N \rightarrow \infty$, as we expect from a semiclassical approximation. Anticipating the current and stress tensor of the form

$$T_{\mu\nu} = (\rho + p)u_{\mu}u_{\nu} + pg_{\mu\nu}, \quad N_{\mu} = nu_{\mu}, \quad (26)$$

⁶In AdS/CFT, the bulk on-shell action \mathcal{S} precisely equals the free energy \mathcal{F} of the CFT side. But even without considering the details of the CFT, we can still make use of this interpretation to detect a phase transition in the system.

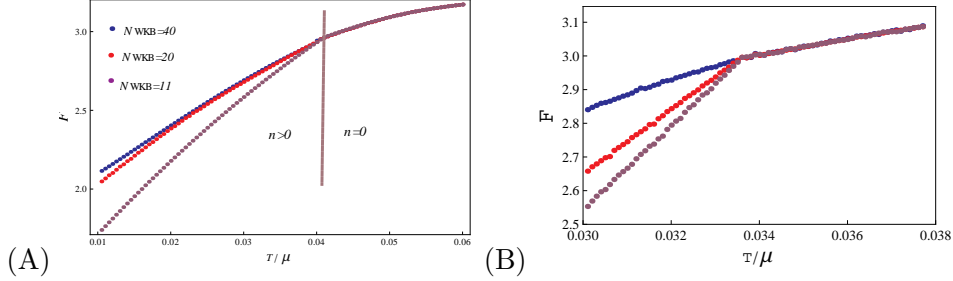


Figure 6: (A) The on-shell action or free energy as a function of temperature, in the presence of fermions. For low temperatures, the fermion density is finite and the derivative $\partial\mathcal{F}/\partial T$ jumps at $T = T_c$, a sign of first-order transition with the development of the hair. This is in line with the Dirac hair result in the previous figure, and indeed for the lowest number of levels N_{WKB} the transition is the sharpest. In (B) we zoom in into the transition region.

we can write the density starting from (22) and making use the optical theorem to relate it to the imaginary part of the Feynmann propagator G_F . This spells out as

$$\begin{aligned}
 \rho &= \int_0^{\hat{E}^2 - k^2} \frac{dE}{2\pi} \int_0^{k_F} \frac{d^3k}{(2\pi)^3} \hat{E} \Im \text{Tr} \Gamma^0 G_F(E, k) \\
 &= \int_0^{\hat{E}^2 - k^2} dE \int \frac{k^2 dk}{4\pi^3} \frac{1}{2} \left(1 - \tanh \left(\frac{\beta}{2} \hat{E} \right) \right) \text{Tr} (i\Gamma^0)^2 \delta \left(\hat{E} - \sqrt{k^2 + m^2} \right) \\
 &= \frac{1}{\pi^2} \int_m^{\hat{\mu}} dE E^2 \sqrt{E^2 - m^2}. \tag{27}
 \end{aligned}$$

We similarly find the number density n , whereas the pressure need not be computed explicitly: since we work with an isotropic free Fermi fluid, its equation of state has to be $p = \rho - qn\hat{\mu}$. It is here that the approximate nature of the electron star with respect to the WKB star becomes obvious (Fig. 7): in WKB star there is an extra term in the pressure, coming from the nodes of the WKB wavefunction. One can check that the integral in (27) indeed approaches a constant as we go into deep interior. On the other hand, at some z_* when $\hat{\mu}(z_*) = m$ the density falls to zero: the star is a classical object and has a sharp border. So for $0 < z < z_*$ we continue the metric to the RN metric (the metric outside a charged isotropic object).

Since we can express n, ρ, p explicitly, we get a nice system of local ordinary differential equations in F, G, A_t , with all quantum expectation values pulled under the rug. This completes the circle, and brings another universal message: *due to Pauli principle, fermionic operators are never local, except in two extreme cases: when only one state is occupied (so the format of the Slater determinant is 1×1 , i.e., it contains a single state), or*

when infinitely many states are occupied, so the Slater determinant turns into a classical, continuous probability density. In Fig. 7 we can see how the WKB solution captures the quantum "tails" near the turning points, which the electron star does not have. It is also instructive to compare this solution to the Oppenheimer-Volkov equations in flat space: in the latter case, $\hat{m} \sim 1/\sqrt{F}$ is always larger than $\hat{\mu} \sim 1/F\sqrt{G}$, unlike in AdS where $\hat{m} \sim 1/z\sqrt{F}$ and for $z > z_*$ it becomes smaller than the local chemical potential, so the integral in (27) has a nonzero range. This is because AdS acts like a potential box that can hold the charged fermions together against electrostatic repulsion. In flat space that does not happen, and we have only neutron stars, not electron stars.

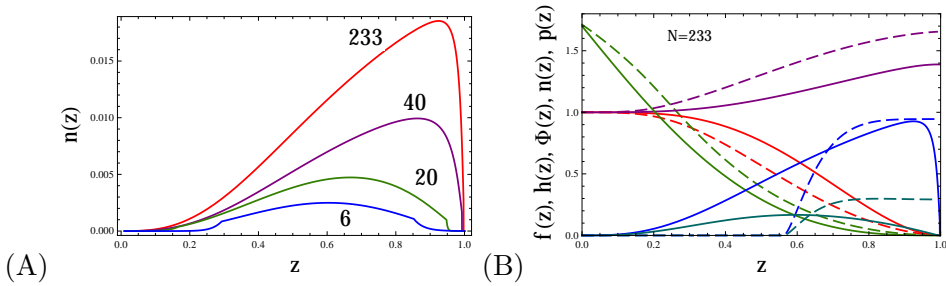


Figure 7: (A) Density of the finite temperature WKB star at various fillings N_{WKB} ; besides the classically allowed region, there are also exponentially decaying tails in the classically forbidden region, where $V_{\text{eff}} > 0$. (B) In the electron star (fluid limit), there are no such tails and the star has a sharp border. Taken over from [15]. (B) Comparison of the WKB solution (full lines) and the electron star solution (dashed lines) at the same chemical potential, fermion charge and mass. We plot the metric functions f, h (F, G in the main text) in red and violet, the gauge field Φ (A_t in the main text) in green, and density and pressure n, p in blue and dark green. The metric solutions do not differ much, despite the long quantum WKB tails, absent in the electron star.

3.3. Lifshitz metric, BKT transition and the missing pieces

In the framework of the electron star model, the Einstein-Maxwell equations can be solved analytically, thanks to the fact that, in deep IR, $n, \rho, p = \text{const.}$ and we can employ a scaling ansatz for the metric. The idea is to match the IR expansion around the scaling solution to the UV expansion around pure AdS. With ansatz of the form $g_{tt} \propto -1/z^\alpha$, $g_{ii} \propto 1/z^\beta$ and $g_{zz} = 1/z^2$ (one metric component we can fix at will as it amounts to picking the gauge for the metric), equations of motion give the IR solution

$$ds^2 = -\frac{1}{z^{2\zeta}} dt^2 + \frac{1}{z^2} d\vec{x}^2 + \frac{1}{z^\zeta} dz^2$$

$$A_t = \frac{1}{z\zeta}, \quad \mathcal{L} = \frac{2}{z^2\zeta} + 6 - \partial_z A_t^2 - n A_t^2 - p_\perp, \quad (28)$$

where in the expression for the total Lagrangian density in the second line, we have inserted in the action (2) the solutions for the metric and the gauge field, as well as the constant (z -independent) solution obtained for ρ in (27) and similarly for n, p . Three important conclusions can be drawn: (1) the IR metric is scale-invariant, with anisotropic scaling of time and space, so that the scaling transformation has the form $t \mapsto \lambda t$, $\vec{x} \mapsto \vec{x}\lambda^{1/\zeta}$ (2) the on-shell Lagrangian density effectively describes a *massive vector field*, with mass squared equal to fermion density n (3) the fermionic contribution to the action equals the pressure. The second point agrees with the known result that Lifshitz black holes are generated by Proca fields [21], and what happens is the Abelian-Higgs mechanism: fermion density acquires a finite expectation value which in turn breaks the $U(1)$ symmetry, giving the photon a mass. The third point is expected within a fluid model, since the action of an ideal Lorentz-invariant (semi)classical fluid equals its pressure [7]. In the fluid limit we can also understand the first-order transition at finite temperature, because it is just a van der Waals-type liquid-gas transition.

We have seen that the thermal transition from RN to a Lifshitz black hole is of first order, and that the $T = 0$ transition is apparently a BKT (infinite order) transition. The latter is not quite clear yet because, as we have emphasized, nobody has yet managed to peek into the deep IR, it remains hidden behind the hard wall. But if we tentatively accept the numerical evidence for the infinite-order transition, can we understand it theoretically? The key lies in understanding how the AdS_2 throat disappears. The conformality-breaking mechanism of [22, 23] gives an idea, though the details are still missing. The crucial moment is that the near-horizon geometry is AdS_2 . Right at the horizon ($s \rightarrow -\infty$) the potential is approximately constant. In the UV of the AdS_2 throat, which is around some finite value s_0 , the potential behaves as $-c/(s - s_0)^2$. This inverse-square potential is known to describe conformal quantum mechanics when $c > -1/4$. For $c = -1/4$ the conformal invariance breaks. discrete states appear and the effective potential is not consistent unless regularized as

$$V_{\text{eff}} = \frac{c}{(s - s_0)^2} - v\delta(s - s_0), \quad (29)$$

and the solution of the effective Schrödinger equation is

$$\psi(r) = c_+(s - s_0)^{\alpha_+} + c_-(s - s_0)^{\alpha_-}, \quad \alpha_\pm = \frac{1}{2} \pm \sqrt{c + \frac{1}{4}}, \quad (30)$$

and the ratio c_+/c_- is given in terms of Bessel functions $J_{1/2}$ and $J_{-1/2}$:

$$\frac{c_+}{c_-} = -\epsilon^{\alpha_- - \alpha_+} \frac{\gamma + \alpha_-}{\gamma + \alpha_+}, \quad \gamma = \sqrt{v} \frac{J_{1/2}(\sqrt{v})}{J_{-1/2}(\sqrt{v})} \quad (31)$$

The solution (30) diverges at $s = s_0$ unless we introduce a cutoff at some distance ϵ from s_0 . Imposing the renormalization condition that c_+/c_- remains independent of ϵ , we get the β -function of the renormalization group as (ℓ being the RG scale):

$$\beta \equiv \frac{d\gamma}{d\ell} = (c + 1/4) - (\gamma + 1/2)^2. \quad (32)$$

And we're done: the fixed points of the above flow equation are easily found to be $-\alpha_{\mp}$. For $\gamma = -\alpha_{\mp}$ we get the solution for ψ from (30) with $c_{\pm} = 0$ respectively. The free energy scaling is obtained as $S_{\text{on-shell}} = \mathcal{F} \propto \int d\ell/\beta$, which gives just the form found in Fig. 5. However, the presence of both a hard-wall cutoff in z and the soft-wall dilaton, completely unaccounted for in the above analysis, clearly suggest more work is needed for everything to click together.

4. Wormholes with fermion hair

The lengthy review we have given so far is meant to be self-contained and helpful for those interested in understanding and contributing to the problem of black hole instabilities with fermionic matter. As we have seen, it contains some puzzling questions and is of more than technical interest (after all, the whole field has been active mostly for the last fifteen years or so). But we also want to point out that with the methodological powerhouse of the HF, WKB and fluid methods, one can tackle new problems. A recent issue where fermions at finite density seem very relevant is the search for traversable wormholes.

The motivation for this story lies mainly in the celebrated black hole information paradox: as far as we know, the Hawking radiation is thermalized, meaning that the information content of the matter falling into the black hole is lost. A possible way out or, at least, a way to better understand the issue, is to consider the maximally extended Carter-Penrose diagram of a black hole, which contains two horizons and two spacetimes. If transport between the two were possible, one could imagine that the information is not lost because the matter falling into one horizon is entangled with the matter on the opposite side. This is the idea of the ER=EPR conjecture [24]. In order to build a traversable wormhole, one needs negative that the stress-energy tensor averaged over a geodesic be negative, thus violating the so-called averaged negative energy condition (ANEC) [25, 26]. This will never happen with conventional classical matter. One needs either exotic fields or quantum corrections. Recently however, a few traversable wormholes have been realized with only standard-model matter. The most "conservative" is the setup of [27] which creates negative energy by considering a particle-hole symmetric spectrum of massless fermions in a magnetic monopole field: because of the negative Landau levels, the net energy is negative. The starting point is thus a pair of magnetically charged RN black holes with magnetic charges H and $-H$, with the hope that the

negative energy Landau levels will push the averaged stress tensor to large enough absolute values to open up a wormhole. In this way, [27] constructs a quasi-stationary (long-living) wormhole in *asymptotically flat* space. In AdS, negative energy density can easily be constructed by coupling the two boundaries nonlocally: in this way temporary wormholes, opening up for the finite duration of the perturbation, can be constructed [28], and even eternal wormholes are possible but at the cost of much more exotic boundary CFTs and their couplings [29, 30, 31]. Here we are interested in making a wormhole in a more "down-to-earth" manner, by growing negative-energy fermion levels as in [27]. The task is to make such wormholes more stable, and to see if they survive at higher fermion density rather than just a single wavefunction as in [27]. Here the previously developed methods can help us.

Magnetic electron star. The crucial consequence of the magnetic field is the Landau quantization. The motion along the x -coordinate is quantized into discrete levels, whereas the motion along y is not quantized and introduces degeneracy. The quantization along x -axis makes our life somewhat easier – even without any IR cutoff the ground state wavefunction now has a discrete quantum number, the Landau level m_j . The magnetic field breaks the spherical symmetry of the wavefunctions down to cylindrical, so it is convenient to introduce the polar angles θ, ϕ :

$$ds^2 = -A(z)dt^2 + B(z)dz^2 + C(z) \left(d\theta^2 + \sin^2 \theta d\phi^2 \right) \quad (33)$$

and to pick a different gamma matrix basis: $\Gamma^0 = \iota\sigma_1 \otimes \hat{1}$, $\Gamma^1 = \sigma_2 \otimes \hat{1}$, $\Gamma^2 = \sigma_3 \otimes \sigma_1$, $\Gamma^3 = \sigma_3 \otimes \sigma_2$. Separating the variables and representing the wavefunction as

$$\Psi = \sum_{m_j=-j}^j (\psi_+(m_j; z), \psi_-(m_j; z)) \otimes (\eta_1(m_j; \theta), \eta_3(m_j; \theta)) e^{im_j\phi}, \quad (34)$$

where j is the total number of Landau levels $j = (H - 1)/2$, we get the fully spin-polarized solution ($\eta_2 = 0$) for zero fermion mass:

$$\psi_{\pm}(m_j; z) = \exp \left(\pm \iota E(m_j) \int_0^z dz' \sqrt{\frac{B(z')}{A(z')}} \right), \quad (35)$$

$$\eta_1(m_j; \theta) = \frac{e^{\iota H \sin \theta / 2}}{\sqrt{\sin \theta}} \left(\tan \frac{\theta}{2} \right)^{m_j}.$$

For nonzero mass, we can perform a Foldy-Wouthuysen transform starting from the above solution. Unlike the massless case considered in [27], the resulting stress-energy tensor will not be traceless, but that is precisely what will give us extra stability. The reason this is consistent is the Landau quantization: the levels for different m_j are gapped from each other and

each Landau level can be treated as a single-particle solution which does not mix with other Landau levels. This results in the stress tensor

$$\langle T_{zz} \rangle = \frac{E_n}{(1+z^2)^2} (\sin 2\alpha - \cos 2\alpha), \quad \tan \alpha = -m/E(m_j). \quad (36)$$

Fig. 8(A) shows the radial pressure T_{rr} as a function of energy, the outcome being that *positive* stress energy tensor is produced for $0 > E > -m$. In order to avoid this positive contribution, the Landau level spacing has to be large enough, i.e., larger than the mass gap (at zero mass this condition is trivially satisfied, as it simply means that any finite $E(m_j = 1)$ will do; this is the case studied in [27]). The simplest gapping mechanism we can think of is the chemical potential, i.e. an electrostatic field in addition to the magnetostatic one. The black hole thus has to become dyonic, with magnetic charge H and electric charge e . Assuming we have ensured the negativity of (36), we can write it in the form $T_{zz} = -\tau/(1+z^2)^2$, with τ a positive constant. Its magnitude roughly determines the size of the wormhole opening.

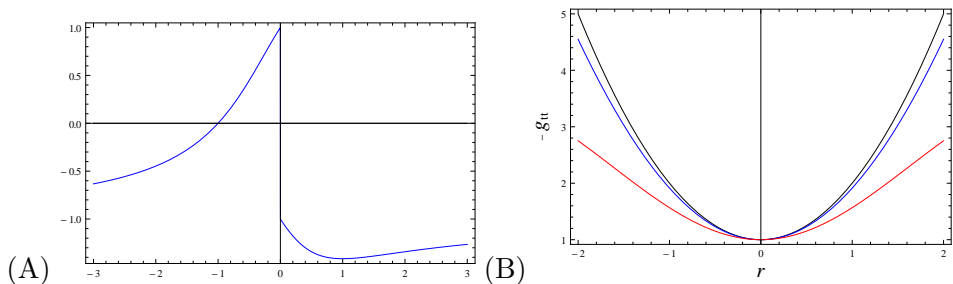


Figure 8: (A) Radial component of the stress-energy tensor $\langle T_{rr} \rangle$ as a function of the (discrete) fermion energy E . Positive contribution only comes when $> E(m_j) > -m$. In order to avoid this range of energies we need a nonzero chemical potential (i.e., electric field, resulting in a dyonic black hole) to stabilize the wormhole with massive fermionic hair. (B) The solution for the metric component g_{tt} in the intermediate region, as a function of the radial coordinate r , for $\tau = 0, 0.05, 0.10$ (black, blue, red). Wormhole solutions (blue, red) are quantitatively very close to the unperturbed black hole (black) but qualitatively different as there is no zero anymore.

Wormhole solution and matching. Having computed the stress-energy tensor (36), we can solve the Einstein equations. The strategy is again matching the expansions, but now we have three regions: the far region which is asymptotically AdS or even flat (we have mentioned that in the presence of magnetic field discrete bound states can form even in absence of AdS boundary), the intermediate region is a slightly perturbed near-horizon AdS₂ region of our magnetic RN geometry, and the inner region, the wormhole throat that opens up, turns out to be a *global* AdS₂ at leading order,

so it has a spherical boundary continuing onto the intermediate regions. The inner, near-global-AdS₂ metric in the form (33) at leading order reads

$$\begin{aligned} A(z) &= R_0^2 \left[1 + z^2 - 8\pi\tau \left(z^2 + (3z + z^3) \arctan z - \log(1 + z^2) \right) \right] \\ B(z) &= R_0^4/A(z), \quad C(z) = R_0^2 [1 + 8\pi\tau (1 + z \arctan z)]. \end{aligned} \quad (37)$$

This solution is to be matched to the intermediate-region solution. Now large z corresponds to the wormhole mouth, i.e., the matching is to be done at large z , where small z is the "center" of the wormhole throat. The solution to match onto is the RN black hole metric:

$$\begin{aligned} ds^2 &= -l^2 f(r) dt^2 + \frac{dr^2}{f(r)} + r^2 (d\theta^2 + \sin^2 \theta d\phi^2) \\ l &= \frac{R_0}{2\pi^2\tau}, \quad R = \frac{r - \sqrt{\pi}\sqrt{e^2 + H^2}}{2\pi^2\tau}. \end{aligned} \quad (38)$$

The solution thus exists for any choice of e and H . But for large e (in other words, for a large chemical potential), the density of the hair will increase significantly and we should repeat the WKB star or electron star approach. In AdS this is a simple matter, proving the stability of the configuration even at high densities. The interesting question is, can it work also in asymptotically flat space? In absence of magnetic field, the answer is certainly no – without an AdS boundary, there is nothing to equilibrate the electrostatic repulsion of electrons. But in the presence of magnetic field, one might obtain a stable charged hairy wormhole if the change in the near-horizon geometry is sufficient to effectively decrease the electrostatic energy density. This is the logical immediate task for future work.

We finish this short review of our work in progress on hairy wormholes with a somewhat more ambitious task. The dyonic wormhole model considered here is obviously quite simplistic and artificial. A much more realistic model is to start from a pair of Kerr black holes and see if these can open up a wormhole in a manner analogous to the scenario we have considered. In this case the magnetic field would be generated self-consistently by the (rotating) fermionic hair, removing the need for the magnetic monopole charge. Such an object would come much closer to realistic astrophysical matter.

5. Instead of a conclusion

We have given a crack and practical review of the insights and technologies needed to describe and understand hairy black holes in anti-de Sitter space. The phase diagram in the presence of nonzero fermion density is quite rich, and it involves two deep and universal phenomena. First, the finite-temperature hairy black holes develop through a discontinuous phase

transition akin to the Hawking-Page transition (indeed, it is precisely the Hawking-Page transition but at finite density). The standard lore that at high enough temperatures black holes will always form is confirmed. Notice this is true at any fermion mass and charge, and thus at any occupation number, from a single wavefunction to the fluid limit, so the finding is definitely robust. Second, at zero temperature the transition is driven by the fermionic charge and/or chemical potential, i.e., electric charge of the black hole. In this case the black hole vanishes infinitely slowly, in a BKT transition that can be understood as the breaking of the one-dimensional conformal symmetry of the wavefunctions in the effective inverse-square potential well. This is solely the consequence of the near-horizon physics, independent of the AdS boundary. Similar conformality-breaking infinite-order transitions are known in various backgrounds in string theory. Maybe one could relate the case described here to some consistent top-down model.

As mentioned in the Introduction, we have deliberately left out extensions and applications of the formalism described, for reasons of space and also generality of discussion. The field of applications closest to our experience is the AdS/CFT correspondence. Electrically charged black holes are dual to field theories at finite $U(1)$ density. The transition from a bald black hole to a hairy black hole is thus a transition between two phases at equal chemical potential. How do they differ then? We know that a black hole is dual to the Coulomb (deconfined) phase of some non-Abelian finite-temperature gauge theory [1, 4]; in the simplest setup coming from type IIB string theory, it is the $\mathcal{N} = 4$ supersymmetric $SU(N)$ theory. Coulomb phase means that the $U(1)$ charge is carried by $SU(N)$ -gauge-charged operators, in our case fermions ("mesinos") and thus not visible to low-energy probes, since at low energies all operators are likely $SU(N)$ -gauge-neutral. The hairy phase describes a dual field theory where the charge is carried by gauge-neutral operators ("baryons") and thus visible to probes such as a photon. This viewpoint was tried and confirmed in [11, 12, 15, 23]. It has realizations in condensed matter systems such as strange metals and heavy fermion materials. In this case, the gauge fields are emergent and arise from the spin-charge separation, and the transition between a black hole and a hairy geometry is a transition between a non-Fermi liquid, where most of the charge is carried by complicated excitations that are not directly seen in the spectrum, and a Fermi liquid where the fundamental degrees of freedom are just renormalized electrons. In QCD, this picture describes the phase diagram at intermediate energy scales and finite densities, where a black hole describes quark-gluon plasma, and a hairy solution describes either the color condensate or conventional barionic matter depending on the details of the model. One can learn a lot on AdS/condensed matter and AdS/QCD from [5, 6].

Finally, the search for wormhole solutions and how fermionic hair might stabilize them is likely to become very important in the future, in connection to the quantum information theory and the firewall, ER=EPR and other approaches to the black hole information problem. One can use much

of the formalism developed for hairy black holes, but the interpretation is still challenging. It is also unclear how realistic the wormhole proposal is if we work with only conventional, standard model matter, i.e. is it just an important proof of concept or a realistic model?

References

- [1] J. Maldacena, *The large N limit of superconformal field theories and super-gravity*, Adv. Math. Theor. Phys. **2**, 231 (1998). [arXiv:hep-th/971120]
- [2] S. S. Gubser, I. R. Klebanov and A. M. Polyakov, *Gauge theory correlators from non-critical string theory*, Phys. Lett. B **428**, 105 (1998). [arXiv:hep-th/9802109]
- [3] E. Witten, *Anti de Sitter space and holography*, Adv. Math. Theor. Phys. **2**, 253 (1998). [arXiv:hep-th/9802150]
- [4] O. Aharony, S. S. Gubser, J. Maldacena, H. Ooguri and Y. Oz, *Large N field theories, string theory and gravity*, Phys. Rep. **323**, 183 (2000). [arXiv:hep-th/9905111]
- [5] J. Zaanen, Y.-W. Sun, Y. Liu and K. Schalm, *Holographic duality in condensed matter physics*, Cambridge University Press, 2015.
- [6] M. Ammon and J. Erdmenger, *Gauge/gravity duality: foundations and applications*, Cambridge University Press, 2015.
- [7] S. W. Hawking and G. F. R. Ellis, *The large-scale structure of space-time*, Cambridge University Press, 2010.
- [8] N. D. Birrel and P. C. W. Davies, *Quantum fields in curved space*, Cambridge University Press, 1982.
- [9] H. Liu, J. McGreevy, D. Vegh, "Non-Fermi liquids from holography", Phys. Rev. D **83**, 065029 (2011). [arXiv:0903.2477[hep-th]]
- [10] M. Čubrović, J. Zaanen and K. Schalm, "String Theory, Quantum Phase Transitions and the Emergent Fermi-Liquid", Science **325**, 439 (2009). [arXiv:0904.1993[hep-th]]
- [11] T. Faulkner, H. Liu, J. McGreevy and D. Vegh, *Emergent quantum criticality, Fermi surfaces, and AdS₂*, Phys. Rev. D **83**, 125002 (2011). [arXiv:0907.2694 [hep-th]].
- [12] S. Sachdev, *A model of a Fermi liquid using gauge-gravity duality*, Phys. Rev. D **84**, 066009 (2011). [arXiv:1107.5321 [hep-th]]
- [13] W. Mück and K. S. Viswanathan, *Conformal field theory correlators from classical field theory on anti-de Sitter space: Vector and spinor fields*, Phys. Rev. **D58**, 106006 (1998). [arXiv:hep-th/9805145]
- [14] M. Čubrović, Y. Liu, K. Schalm, Y.-W. Sun and J. Zaanen, *Spectral probes of the holographic Fermi groundstate: Dialing between the electron star and AdS Dirac hair*, Phys. Rev. **D84**, 086002 (2011). [arXiv:1106.1798 [hep-th]]
- [15] M. Medvedyeva, E. Gubankova, M. Cubrovic, K. Schalm, J. Zaanen, *Quantum corrected phase diagram of holographic fermions*, JHEP **2013**, 025 (2013). [arXiv:1302.5149[hep-th]].
- [16] M. Čubrović, J. Zaanen, K. Schalm, *Constructing the AdS dual of a Fermi liquid: AdS Black holes with Dirac hair*, JHEP **2011**, 17 (2011). [arXiv:1012.5681[hep-th]]
- [17] A. Allais, J. McGreevy and X. Josephine Suh, *Quantum electron star*, Phys. Rev. Lett **108**, 231602 (2012). [arXiv:1202.5308[hep-th]]
- [18] A. Allais and J. McGreevy, *How to construct a gravitating quantum electron star*, Phys. Rev. **D88**, 066006 (2013). [arXiv:1306.6075[hep-th]]

- [19] S. Hawking and D. Page, *Thermodynamics of black holes in anti de Sitter space*, Comm. Math. Phys. **87**, 577 (1977).
- [20] S. A. Hartnoll, A. Tavanfar, *Electron stars for holographic metallic criticality*, Phys. Rev. D **83**, 046003 (2011). [arXiv:1008.2828[hep-th]]
- [21] K. Balasubramanian and J. McGreevy, *An analytic Lifshitz black hole*, Phys. Rev. D **80**, 104039 (2009). [arXiv:0909.0263[hep-th]]
- [22] D. B. Kaplan, J.-W. Lee, D. T. Son, M. A. Stephanov, *Conformality Lost*, Phys. Rev. D **80**, 125005 (2009). [arXiv:0905.4752[hep-th]].
- [23] M. Čubrović, *Confinement/deconfinement transition from symmetry breaking in gauge/gravity duality*, JHEP **2016**, 102 (2016). [arXiv:1605.07849[hep-th]]
- [24] J. Maldacena and L. Susskind, *Cool horizons for entangled black holes*, Fortschr. Phys. **61** 781 (2013). [arXiv:1306.0533[hep-th]]
- [25] M. S. Morris and K. Thorne, *Wormholes in spacetime and their use for interstellar travel: A tool for teaching general relativity* Am. J. Phys **56**, 395 (1988).
- [26] D. Hochberg and M. Visser, *Null energy condition in dynamic wormholes*, Phys. Rev. Lett **81**, 746 (1998).
- [27] J. Maldacena, A. Milekhin and F. Popov, *Traversable wormholes in four dimensions*, (2018). [arXiv:1807.04726[hep-th]]
- [28] P. Gao, D. L. Jafferis and A. C. Wall, *Traversable wormholes via a double trace deformation*, JHEP **12**, (2017) 151. [arXiv:1608.05687[hep-th]]
- [29] Z. Fu, B. Grado-White and D. Marolf, *A perturbative perspective on self-supporting wormholes*, Class. Quant. Grav. **36**, (2019) 045006. [arXiv:1807.07917[hep-th]]
- [30] D. Marolf and S. McBride, *Simple perturbatively traversable wormholes from bulk fermions*, (2019). [arXiv:1908.03998[hep-th]]
- [31] J. Maldacena and X.-L. Qi, *Eternal traversable wormhole*, (2018). [arXiv:1804.00491[hep-th]]

Replica wormholes in the IB matrix model

Mihailo Čubrović

Institute of Physics Belgrade, Serbia

cubrovic@ipb.ac.rs



Averaging, gravity and all that

- Exciting story of the black hole information problem and the Page curve (2019-present)
- In a nutshell: black hole evaporation reproduces the Page curve if the semiclassical partition function includes nontrivial spacetime topologies – wormholes
- Wormholes lead to the factorization problem in AdS/CFT:

$$Z = \text{[Diagram of a sphere with a blue shaded region]}$$

$$Z^2 = \text{[Diagram of two spheres with blue shaded regions]} + \text{[Diagram of a cylinder with blue shaded regions]}$$

Averaging, gravity and all that

- Exciting story of the black hole information problem and the Page curve (2019-present)
- In a nutshell: black hole evaporation reproduces the Page curve if the semiclassical partition function includes nontrivial spacetime topologies – wormholes
- Wormholes lead to the factorization problem in AdS/CFT:

$$\langle Z \rangle = \text{[Diagram of a sphere with a blue shaded interior]} \quad \langle Z^2 \rangle = \text{[Diagram of two spheres with a blue shaded interior]} + \text{[Diagram of a cylinder with a blue shaded interior]}$$

- Is gravity an ensemble average?
- Is the ensemble fundamental (=disorder) or emergent (chaotic dynamics)?

Averaging and IIB matrix model

- The matrix formulation of type IIB string theory – Ishibashi-Kawai-Kitazawa-Tsuchiya (IKKT) model
- Perfect testing ground for our puzzle:
 - rich dynamics (full nonperturbative string theory?)
 - 0-dimensional – no derivatives \Rightarrow simpler path integral structure than dynamical models
 - toy models for string theory vacua and black hole solutions
- Inspired by the 0-dimensional (time-frozen) SYK model (Saad, Shenker, Stanford & Yan [2103.16754])
- Wormholes and half-wormholes found in 0-dimensional SYK but hinge crucially on the Majorana-only structure of the model

Outline

- Setup: semiclassical D-brane solutions in the IKKT model
- Replicas in the partition functions – wormholes vs. half-wormholes vs. fraction-holes
- Fraction-holes re-establish factorization and always dominate the ensemble in our examples

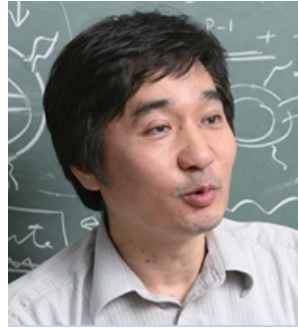
Outline

- Setup: semiclassical D-brane solutions in the IKKT model
- Replicas in the partition functions – wormholes vs. half-wormholes vs. fraction-holes
- Fraction-holes re-establish factorization and always dominate the ensemble in our examples

IKKT model



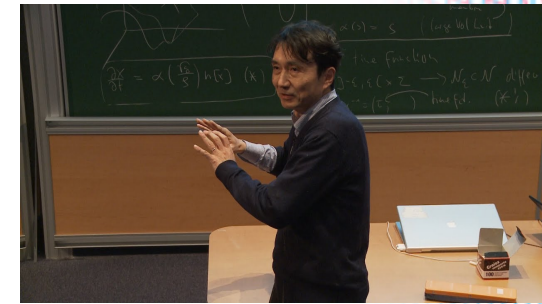
N. Ishibashi



H. Kawai



Y. Kitazawa



A. Tsuchiya

- Discretization of the Schild action for type IIB string theory in 0 dimensions:

$$S = \frac{1}{4} [X^\mu, X^\nu]^2 + \frac{1}{2} \bar{\Psi}_\alpha \Gamma_\mu [X^\mu, \Psi_\alpha] + \beta$$

$$\mu = 1 \dots 10, \quad \alpha = 1 \dots 16$$

X^μ – bosonic coordinates $\rightarrow N \times N$ Hermitian matrices

Ψ_α – Majorana-Weyl spinors $\rightarrow N \times N$ Hermitian matrices

IKKT model for D-branes

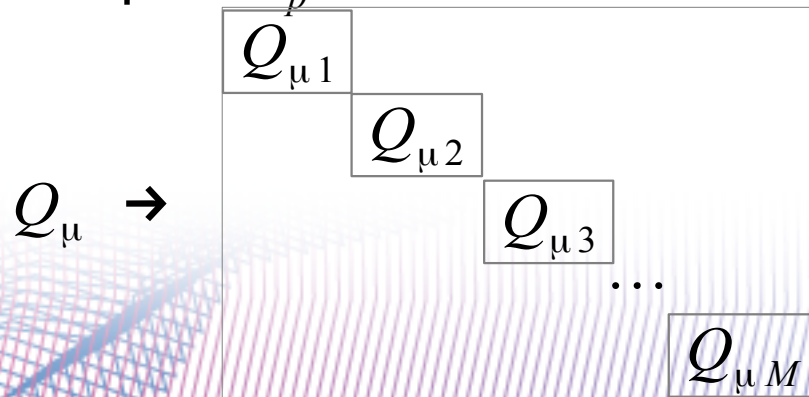
- Discretization of the Schild action for type IIB string theory:

$$S = \frac{1}{4} [X^\mu, X^\nu]^2 + \frac{1}{2} \bar{\Psi}_\alpha \Gamma_\mu [X^\mu, \Psi_\alpha] + \beta \quad \mu=1\dots 10, \quad \alpha=1\dots 16$$

- Non-perturbative formulation of string theory?
- Remember: IIB string theory has D_p brane excitations with p odd: $p=-1$ – D-instantons, $p=1$ – strings, etc.
- Single D_p brane solution of the matrix model (IKKT 1997, Aoki, Iso, Kawai, Kitazawa, Tada & Tsuchiya 1999):

$$X^\mu = (Q_1, P_1, Q_2, P_2, \dots, Q_{(p+1)/2}, P_{(p+1)/2}, 0, \dots, 0), \quad [Q^\mu, P^\nu] = i \frac{\omega^{\mu\nu}}{N}$$

- Multiple D_p branes: block-diagonal matrices



stack of M D_p branes

Quenching of the IKKT model

- Divide the fields into slow (quenched, semi-classical) and fast degrees of freedom:

$$X^\mu = A^\mu + a^\mu \quad Z = \int DX^\mu \exp(-iS[X^\mu]) \rightarrow \int Da^\mu \exp(-iS[A^\mu, a^\mu])$$

- Partition function summed over fast variables only; A_μ play the role of semiclassical background fields
- Inspired also by the derivation of the IKKT model from discretized 10d Yang-Mills (Eguchi&Kawai 1982, Parisi 1982, Gross&Kitazawa 1982)
- Averaged quantities:
$$\langle Z \rangle = \int DA^\mu \int Da^\mu \exp(-iS[A^\mu, a^\mu])$$
- What is the relation of $\langle Z \rangle$ to Z ? If $\langle Z \rangle \sim Z$ then Z is "self-averaging".

Outline

- Setup: semiclassical D-brane solutions in the IKKT model
- Replicas in the partition functions – wormholes vs. half-wormholes vs. fraction-holes
- Fraction-holes re-establish factorization and always dominate the ensemble in our examples

The question

- IKKT model with quenching
- Background fields: solutions for D_p branes and stacks of wrapped D_p branes
- Expanding the action for small fluctuations a_μ :
$$S = S[A_{Dp}^\mu, a^\mu] = S_0[A_{Dp}] + a^\mu K_{\mu\nu}[A_{Dp}]a^\nu + \dots$$
- **The central question:** are the partition functions and correlation functions self-averaging? Do they factorize?

$$\langle Z^n \rangle \stackrel{?}{\approx} \langle Z \rangle^n + \text{small corrections}$$

Setup

- Single D_1 brane (string):

$$A_1 = Q, A_2 = P, A_3 = \dots = A_{10} = 0, \quad [Q, P] = \frac{i}{2\pi L}$$

- Assume $A_{1,2}$ are random Hermitian matrices with eigenvalue distribution $\wp(\lambda_i^{1,2})$, $i = 1 \dots N$

$$S = a^\mu \left(\hat{P}_\alpha \hat{P}^\alpha \delta_{\mu\nu} + 2 \hat{F}_{\mu\nu} \right) a^\nu, \quad \hat{P}^\alpha = [P^\alpha, \cdot], \quad \hat{F}^{\mu\nu} = [[P^\mu, P^\nu], \cdot]$$

- Partition function diverges without a cutoff on λ_i^μ
- Often in the literature: \wp is uniform in the interval $[-L, L]$
- (Hyper)Gaussian distribution \wp more amenable to analytical work and also arises in a controlled way in some setups

$$\wp(\lambda_i^\mu) = \exp\left[-(\lambda_i^\mu - \lambda_0)^{2m} / 2 L^2\right] \text{ with } m=1, \lambda_0=0$$

- Compute Z, Z^2, Z^4 vs. $\langle Z \rangle, \langle Z^2 \rangle, \langle Z^4 \rangle$

Collective field formalism

- Partition function:

$$\langle Z \rangle = \int Da_\alpha \int D\lambda_i \exp\left[-a_\mu P^2(\lambda_i) a_\mu\right] \wp(\lambda_i)$$

- Can solve exactly for Gaussian eigenvalue distribution ($m=1$)

$$\langle Z \rangle = \int Da_\mu \int D\lambda_i \prod_{i<j} (\lambda_i - \lambda_j)^2 \exp\left[-a_\mu^{ij} (\lambda_i^2 + \lambda_j^2) a_\mu^{kl} - \delta_{ik} \delta_{jl} \frac{\lambda_i^2}{2L^2}\right]$$

$$W = \frac{1}{2} \log \det \left(\frac{I}{2} L^2 + 2 a_\mu^+ a_\mu - 2 I \text{Tr} a_\mu^+ a_\mu + \text{higher order} \right)$$

- But we want a general formalism for $\langle Z^2 \rangle, \langle Z^4 \rangle$ and more complicated backgrounds
- The trick: collective fields – used for SYK and similar models (Sachdev et al 2017, Saad-Shenker-Stanford-Yao 2021)

Collective field formalism

- The trick: collective fields – used for SYK and similar models (Sachdev et al 2017, Saad-Shenker-Stanford-Yao 2021)

$$\langle Z \rangle = \int D a_\mu \int D \lambda_i \int D g \exp \left[-a_\mu P^2 a_\mu - \frac{4}{L^{2N-2}} (\text{Tr } g - \text{Tr } a_\mu a_\mu) \delta(g - a_\mu a_\mu) \right] \wp(\lambda_i)$$

$$\langle Z \rangle = \int D a_\mu \int D \lambda_i \int D g \int D s \exp \left[-a_\mu P^2 a_\mu - \frac{4}{L^{2N-2}} (\text{Tr } g - \text{Tr } a_\mu a_\mu) - i s (g - a_\mu a_\mu) \right] \wp(\lambda_i)$$

$$\langle Z \rangle = \int D g \int D s \exp \left[-\frac{1}{2} \log \det s - i s g - \frac{4}{L^{2N-2}} \text{Tr } g \right]$$

- Solution: $s = 2iT I$, $g = \frac{L^{2N-2}}{4} I$
- For $\langle Z \rangle$ this is not a very useful result, it merely estimates the strength of the fluctuation
- Higher-order corrections likely just small perturbations
- But the formalism works also for $\langle Z^n \rangle$

Two-replica system

- Two replicas – left (L) and right (R) system
- Now collective fields have the replica index $A \in \{L, R\}$:

$$\langle Z^2 \rangle = \int D a_A^\mu \int D \lambda_i \int D g_{AB} \int D s_{AB} e^{-W} \wp(\lambda_i)$$

$$W = a_A P^2 a_A + V(g_{AB}) - V(a_A a_B) + i s_{AB} (g_{AB} - a_A a_B)$$

- Integrating out the fluctuations and averaging:

$$\langle Z^2 \rangle = \int d a_A^\mu \int D g_{AB} \int D s_{AB} \exp \left[-i s_{AB} g_{AB} + i s_{AB} a_A a_B - V(g_{AB}) \right]$$

- Fourth-order potential:

$$V_4 = \frac{2}{L^{2N-2}} \text{Tr}(g_{LL} + g_{RR}) + \frac{4}{L^{2N-4}} \text{Tr}(g_{LL} + g_{RR})^2 - \frac{4}{L^{2N-4}} \text{Tr}(g_{LL}^2 + g_{LL} g_{RR} + g_{RR} g_{LL} + g_{RR}^2)$$

Two-replica system

- Two replicas – left (L) and right (R) system
- Now collective fields have the replica index $A \in \{L, R\}$:

$$\langle Z^2 \rangle = \int D a_A^\mu \int D \lambda_i \int D g_{AB} \int D s_{AB} e^{-W} \wp(\lambda_i)$$

$$W = a_A P^2 a_A + V(g_{AB}) - V(a_A a_B) + i s_{AB} (g_{AB} - a_A a_B)$$

- Integrating out the fluctuations and averaging:

$$\langle Z^2 \rangle = \int d a_A^\mu \int D g_{AB} \int D s_{AB} \exp \left[-i s_{AB} g_{AB} + i s_{AB} a_A a_B - V(g_{AB}) \right]$$

- Fourth-order potential:

$$V_4 = \frac{2}{L^{2N-2}} \text{Tr}(g_{LL} + g_{RR}) + \frac{4}{L^{2N-4}} \text{Tr}(g_{LL} + g_{RR})^2 - \frac{4}{L^{2N-4}} \text{Tr}(g_{LL}^2 + g_{LL} g_{RR} + g_{RR} g_{LL} + g_{RR}^2)$$

- Disordered and non-disordered component:

$$\langle Z^2 \rangle = \int d s_{AB} \Phi(s_{AB}, a_A a_B) \chi(s_{AB}, g_{AB})$$

Four-replica system

- Replicas L, R, L', R'
- Only Φ contributes further replicas: $\langle Z^4 \rangle \propto \langle \Phi^2(s_{AB}, a_A a_B) \rangle$
- Four-field combinations appear: $G_{AAB'B'} \equiv a_A a_A a_{B'} a_{B'}$, $S_{AAB'B'}$
- Effective action:

$$W_4 = \frac{1}{2} \log \det s_{AB} + \frac{1}{2} \log \det s_{A'B'} + \frac{1}{2} \log \det S_{AAB'B'} - i S_{AAB'B'} G_{AAB'B'} + \frac{8}{L^{2N-4}} \text{Tr } g_{AA} \text{Tr } g_{BB} - \frac{4}{L^{2N-4}} \text{Tr } G_{AAB'B'}$$

- Solutions

- trivial solution: $\langle Z^4 \rangle \sim \langle Z \rangle^4 \sim Z^4$
- wormhole: $\langle Z^4 \rangle \sim Z^4 \neq \langle Z \rangle^4$
- half-wormhole: $\langle Z^4 \rangle \sim \langle Z \rangle^4 \neq Z^4$
- wormhole + half wormhole: $\langle Z^4 \rangle \sim \langle Z \rangle^4 \sim Z^4$

Trivial solution

Trivial solution: $s = g = S = G = 0$

L
●

R
●

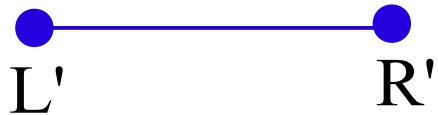
●
L'

●
R'

Wormhole

$$\text{Wormhole: } s = 2iL^{N-2} \hat{I} \otimes \hat{E}, \quad g = \frac{1}{4} L^{N-2} \hat{I} \otimes \hat{E}$$
$$S = G = 0$$

$\hat{I}_{N \times N}$ - internal unit matrix; $\hat{E}_{2 \times 2}$ - replica space unit matrix

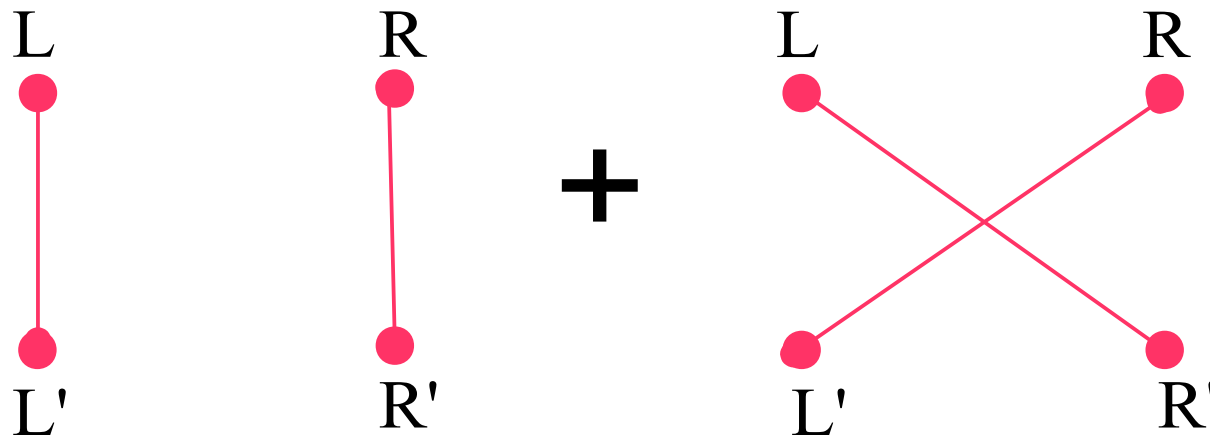


Half-wormhole

Half-wormhole: $s=g=0$

$$S_{LLL'L'} = S_{LLR'R'} = S_{RRL'L'} = S_{RRR'R'} = 4iL^{2N-4} \hat{I}$$

$$G_{LLL'L'} = G_{LLR'R'} = G_{RRL'L'} = G_{RRR'R'} = -\frac{1}{8} L^{2N-4} \hat{I}$$



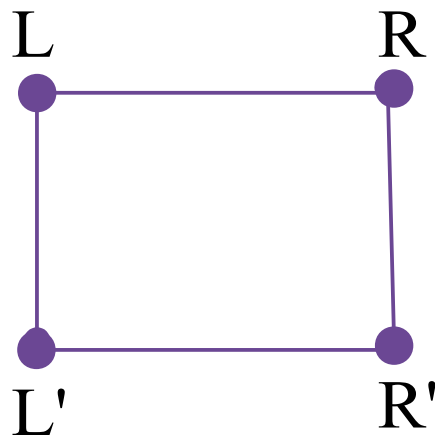
Wormhole + half-wormhole

Wormhole + half wormhole:

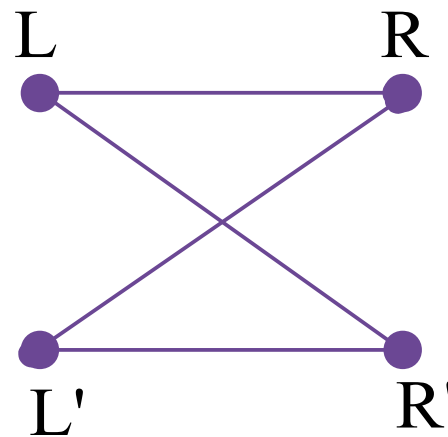
$$s = 2iL^{N-2} \hat{I} \otimes \hat{E}, \quad g = \frac{1}{4} L^{N-2} \hat{I} \otimes \hat{E}$$

$$S_{LLL'L'} = S_{LLR'R'} = S_{RRL'L'} = S_{RRR'R'} = 4iL^{2N-4} \hat{I}, \quad G = -\frac{1}{8} L^{2N-4} \hat{I}$$

$$G_{LLL'L'} = G_{LLR'R'} = G_{RRL'L'} = G_{RRR'R'} = -\frac{1}{8} L^{2N-4} \hat{I}$$

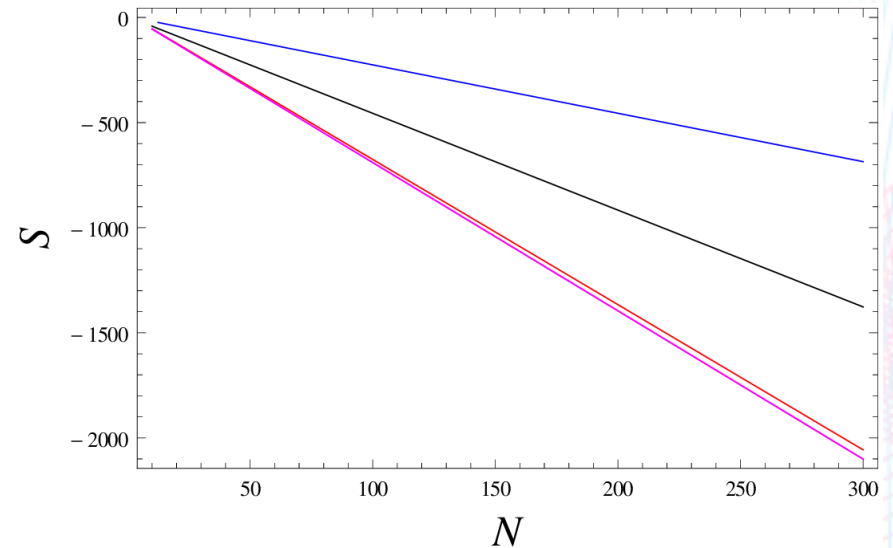
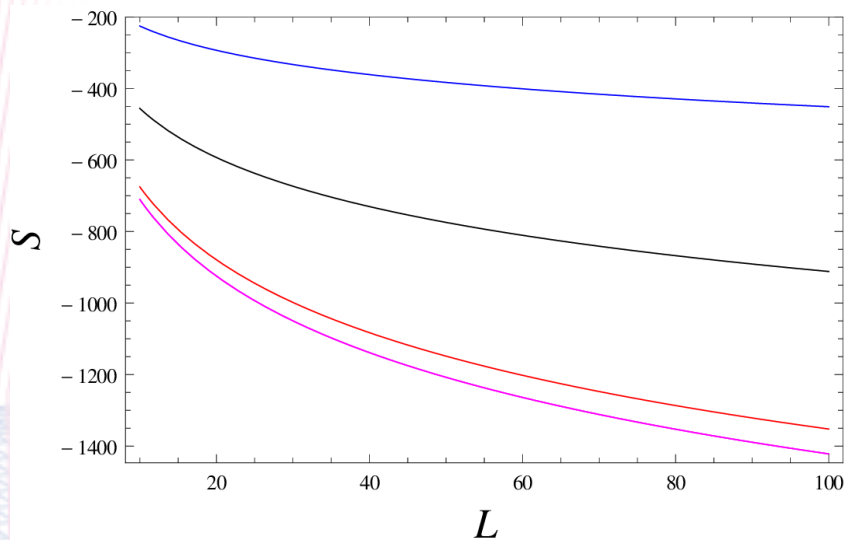


+



False vacua and the true vacuum

- Trivial solution: $s = g = S = G = 0$
- Wormhole: $s, g \neq 0, S = G = 0$
- Half-wormhole: $s = g = 0, S, G \neq 0$
- Wormhole + half wormhole: $s, g, S, G \neq 0$



- Black – trivial; Blue – wormhole; Red – half-hole; Violet – whole + half-whole – **lowest free energy**

Outline

- Setup: semiclassical D-brane solutions in the IKKT model
- Replicas in the partition functions – wormholes vs. half-wormholes vs. fraction-holes
- Fraction-holes re-establish factorization and always dominate the ensemble in our examples

Dp brane stacks and "black holes"

- The celebrated 5D extremal black hole in IIB string theory: Q_1 D1 branes wrapped on S^1 and Q_5 D5 branes wrapped on T^5
- Here: rough toy model inspired by D1-D5 brane black holes
- D1/D5 branes: block-diagonal matrices

$$\mu=1\dots 5: A^\mu = B^\mu + C^\mu$$

$$B^1 = \text{diag} \left(B_{\bar{1}}^1, B_{\bar{2}}^1 \dots B_{\bar{Q}_1}^1 \right), \quad C^\mu = \text{diag} \left(C_{\bar{1}}^\mu, C_{\bar{2}}^\mu \dots C_{\bar{Q}_5}^\mu \right)$$

$$\mu=6\dots 10: A^\mu = 0$$

- Compactification radii $R_{1,5} \Rightarrow$ entries of B^μ, C^μ discretized:

$$A_{ij}^\mu, B_{ij}^\mu \in \frac{2\pi\mathbb{Z}}{R_{1,5}}$$

- Supersymmetry \Rightarrow need to include fermions

Dp brane stacks and "black holes"

- Additional collective fields from fermions:

$$\mathcal{Y}_{AB} \equiv \bar{\Psi}_A \Psi_B, \quad A, B \in \{L, L', R, R'\}$$

- Complicated saddle point equations:

$$W_{\text{D1D5}} = \frac{1}{2} \log \det s_{AB} + \frac{1}{2} \log \det s_{A'B'} + \frac{1}{2} \log \det S_{AAB'B'} - \log \det \sigma_{AB} + V_b + V_f$$

$$V_b = -i S_{AAB'B'} G_{AAB'B'} + \frac{8}{L^{2N-4}} \text{Tr } g_{AA} \text{Tr } g_{BB} - \frac{4}{L^{2N-4}} \text{Tr } G_{AAB'B'}$$

$$V_f = \frac{L^2}{4} \mathcal{Y}_{AB'} - \mathcal{Y}_{AA} s_{AA}^{-1} \mathcal{Y}_{AA} + \log \left(\Sigma_{LR} \Sigma_{L'R'} - \Sigma_{LL'} \Sigma_{RR'} + \Sigma_{LR'} \Sigma_{RL'} \right)$$

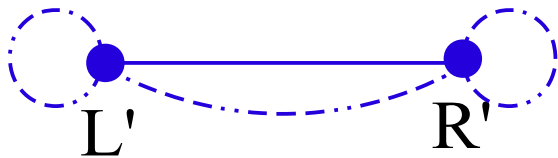
- Two gross simplifications:

- assume $R_{1,5} \rightarrow \infty$ i.e., disregard the compactification

- assume maximally symmetric structure of $g_{AA}, \mathcal{Y}_{AB}, G_{AA, B'B'}$

Wormhole

Wormhole: $s = 2iL^{N-2} \hat{I} \otimes \hat{E}$, $g = \frac{1}{4} L^{N-2} \hat{I} \otimes \hat{E}$
 $\Sigma = iL^{-2} \hat{I} \otimes \begin{pmatrix} 11 \\ 11 \end{pmatrix}$, $\gamma = \frac{1}{4} L^{-2} \hat{I} \otimes \begin{pmatrix} 11 \\ 11 \end{pmatrix}$
 $S = G = 0$



$$\langle Z^2 \rangle \approx \text{wormhole}$$



$$\langle Z^2 \rangle - \langle Z \rangle^2 \sim O(1)$$

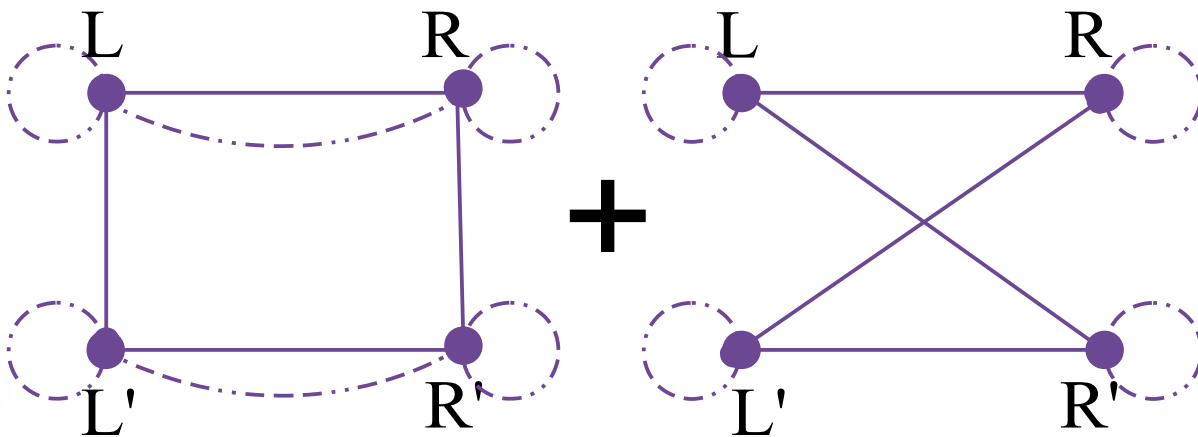
Wormhole + fraction-holes

Wormhole: $s = 2iL^{N-2} \hat{I} \otimes \hat{E}$, $g = \frac{1}{4} L^{N-2} \hat{I} \otimes \hat{E}$

Half-hole: $S_{LLL'L'} = S_{LLR'R'} = S_{RRL'L'} = S_{RRR'R'} = 4iL^{2N-4} \hat{I}$, $G = -\frac{1}{8} L^{2N-4} \hat{I}$

$$G_{LLL'L'} = G_{LLR'R'} = G_{RRL'L'} = G_{RRR'R'} = -\frac{1}{8} L^{2N-4} \hat{I}$$

$$\Sigma = iL^{-2} \hat{I} \otimes \sigma_1, \quad \gamma = \frac{1}{8} L^{-2} \hat{I} \otimes \begin{pmatrix} 1 & 1 \\ 1 & 1 \end{pmatrix}$$



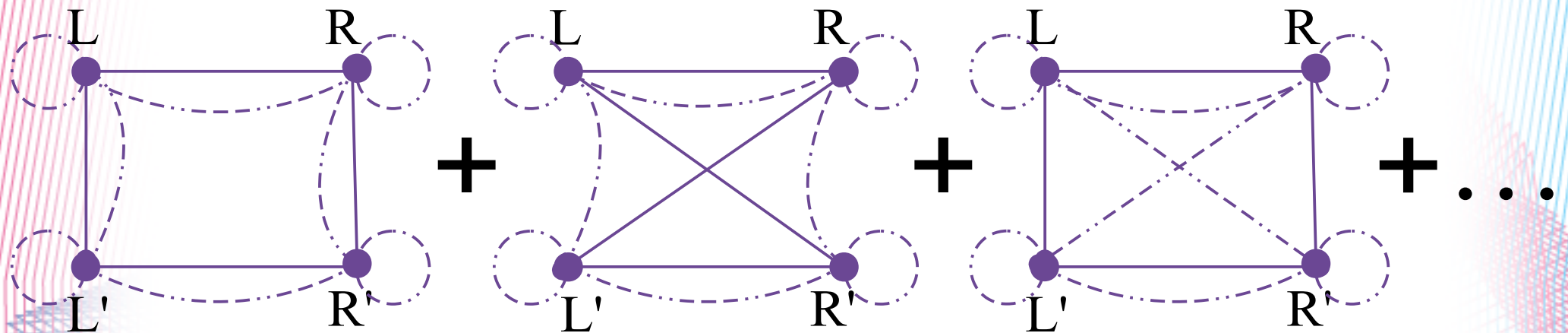
Wormhole + fraction-holes

Wormhole: $s = 2iL^{N-2} \hat{I} \otimes \hat{E}$, $g = \frac{1}{4} L^{N-2} \hat{I} \otimes \hat{E}$

Quarter-hole: $\Sigma = iL^{N-4} \hat{I} \otimes \sigma_1$, $\gamma = \frac{1}{8} L^{N-4} \hat{I} \otimes \begin{pmatrix} 1 & 1 \\ 1 & 1 \end{pmatrix}$

$$\gamma'_{ABCD} \equiv \bar{\Psi}_A \Psi_B \bar{\Psi}_C \Psi_D$$

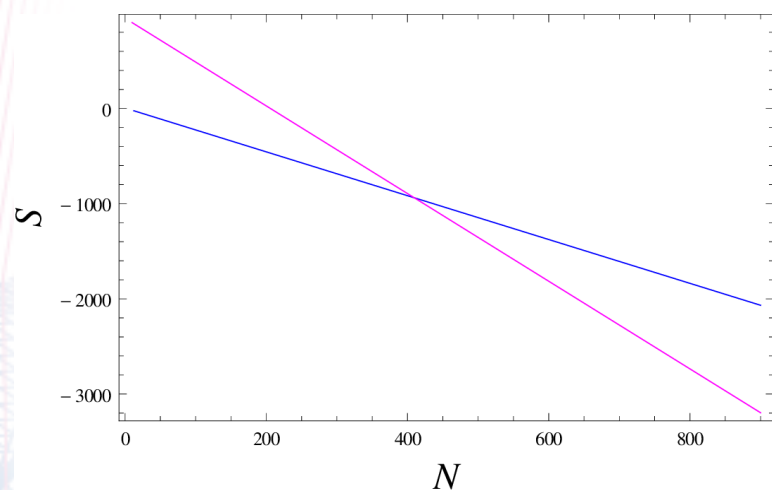
$$\Sigma' = 4iL^{2N-6} \hat{I} \otimes \sigma_1 \otimes \sigma_1, \gamma = \frac{1}{32} L^{2N-6} \hat{I} \otimes (1)_{4 \times 4}$$



Wormhole + fraction-holes

$$\langle Z^4 \rangle \approx \text{wormhole} + \text{1/2-hole} + \text{1/4-hole} + \dots \sim \langle Z \rangle^4$$

$$\langle Z^4 \rangle_{\text{WH}} \sim Z_{\text{WH}}^4 \qquad \sim \langle Z \rangle^4 - \langle Z^4 \rangle_{\text{WH}}$$



- Blue – wormhole
- Violet – whole + fraction-wholes
- No trivial solution nor fraction-only solution
- The optimal solution has both self-averaging and factorization

Morale of the story

- The wormhole/replicas/factorization puzzle can be stated in a precise way in the IIB matrix model
- Similar to the SYK/2D gravity models, there are both wormhole and half-wormhole solutions but...
- ... here we have an infinite series of fraction-holes for D_p brane backgrounds
- The true vacuum is always the wormhole + fraction-holes solution \Rightarrow ***the true vacuum always has both factorization and self-averaging***
- Many questions: Interpretation? Relation to the wormhole saddle which reproduces the Page curve?

Activities | Google Chrome | Tue 01:26 | en | 4G

Secure | https://ibstrings2021.math.tecnico.ulisboa.pt/programme

Iberian Strings 2021

January 19-22

Online meeting organized by Instituto Superior Técnico, Lisboa, Portugal

Programme

Move the mouse over the schedule to see start and end times and complete clipped titles.

	Tue, 19 Jan 2021	Wed, 20 Jan 2021	Thu, 21 Jan 2021	Fri, 22 Jan 2021
9-11	Malcom Perry Soft Charges, Soft Hair and Black Hole Entropy	Johanna Edmenger Information geometry and QFT	Jerome Gauffret Geometric Entanglement for AdS/CFT and Black Hole Entropy	Lárus Thorlacius Entanglement islands
	David Mateos Strong coupling dynamics and entanglement in de Sitter space	Marin Saeeta A Holographic Complexity Correspondence	Anayeli Ramirez Li 4 BPS, AdS ₂ , CFT ₂	Roberto Emparan Quantum BTZ black hole
	Coffee break	Coffee break	Coffee break	Coffee break
11-13	Matteo Baggioli How small hydrodynamics can go	Mihailo Cubrovic Lyapunov spectra in traversable wormholes and their holographic duals	Salvatore Basile String-Whimpy theory, string theory and WKB analysis	Narjia Tomasevic Multi-mouth traversable wormholes
	Pablo Cano New higher-curvature variations of J _T	Kevin Nguyen Slow scrambling in extremal BTZ and microstate geometries	Gabriel Larios Galusa-Rena spectra and consistent truncations	Tomas Andrade Existence of black cosmic censorship in black hole collisions
	Miguel Sanchez-Garrido Bubble Mergers from Holography	Johannes Lahrahn A Non-Relativistic Limit of NS-NS Gravity	Matthias Cencar Kalauza-Klein fermion mass matrices from exceptional Field Theory and $V = 1$ Lenses	Matteo Rosello Arithmetic of decay walls through continued fractions: a new exact dS ₂ counting solution in $V = 4$ CHL models
	Yogi Bea New insights from Real-time Dynamics	Edward Massad New insights on the quality of M theory background	Matteo Henkel Gravitational Entropy and IR UV connections in Gaiotto Exchange	Pablo Emanuel León Torres Massive supermembranes in non-compact dimensions
13-15	Lunch	Lunch	Lunch	Lunch

Activities | Google Chrome | Tue 01:25 | en | 4G

Secure | https://ibstrings2021.math.tecnico.ulisboa.pt/abstracts?abstract=6065#abstract=6065

Description | Registration | Programme | Abstracts | Participants | Contacts | Search

Mihailo Cubrovic

University of Belgrade

Lyapunov spectra in traversable wormholes and their holographic duals

2021/01/20, 11:00 – 11:30

We study the decay of out-of-time-ordered correlators (OTOC) in an AdS traversable wormhole and its gravity dual, two coupled Sachdev-Ye-Kitaev models ("left" and "right" subsystem). The gravity calculation of OTOC involves perturbative equations more involved than for a black hole, as the perturbation has complex kinematics and can bounce back and forth through the wormhole many times. The outcome is a phase diagram with three regions. One is black hole like with uniform exponential growth and the Lyapunov exponent $\lambda = 2\pi T$ ("the chaos bound"). The intermediate phase has OTOCs with a spectrum of different exponents for different operator modes, all below the maximal chaos bound. The third phase has exponentially small Lyapunov exponents, behaving as $\exp(-1/T)$, in accordance with a recent field-theory calculation in the literature. The Lyapunov spectrum carries more information than just the maximum exponent: it can be related e.g. to teleportation fidelity from left to right subsystem.

Frank Elsenhauer

Max Planck Institute for extraterrestrial Physics

The Discovery of the Massive Black Hole in the Center of the Galaxy. Outreach colloquium on the occasion of the Nobel Prize in Physics 2020

2021/01/20, 17:30 – 18:30

Outreach colloquium on the discovery of a supermassive compact object at the centre of our galaxy.

Black Holes are among the most mysterious objects in the Universe. They are so massive and compact that nothing - not even light - can escape their gravity. The 2020 Nobel Prize in Physics was awarded to Roger Penrose for showing that these exotic objects are a direct consequence of Einstein's general theory of relativity, and to Reinhard Genzel and Andrea Ghez for the discovery of such a monster in the center of our Galaxy. Our presentation will portray the 40 year journey from the first indications to the overwhelming observational evidence for an extremely heavy and compact object in the Galactic Center, for which a supermassive black hole is the only known explanation. Using the world's largest telescopes and most advanced optics technology, astronomers can now follow the stars orbiting the central object, precisely measure its mass, and detect the stunning effects of general relativity. In our talk we will present both the spectacular observations and the technology behind.

Zachary Elgood

Universidad Autónoma de Madrid

The first law of heterotic stringy black hole mechanics at zeroth order in α'

2021/01/22, 16:30 – 17:00

We re-derive the first law of black hole mechanics in the context of the Heterotic Superstring effective action compactified on a torus to leading order in α' , using Wald's formalism, covariant Lie derivatives and momentum maps. The Kalb-Ramond field strength of this theory has Abelian Chern-Simons terms which induce Nicolai-Townsend transformations of the Kalb-Ramond field. We show how to deal with all these gauge symmetries deriving the first law in terms of manifestly gauge-invariant quantities. In the presence of Chern-Simons terms, several definitions of the conserved charges exist, but the formalism picks up only one of them to play a role in the first law. The derivation of a first law is a necessary step towards the derivation of a manifestly gauge-invariant entropy formula which is still lacking in the literature. In its turn, this entropy formula is needed to compare unambiguously macroscopic and microscopic black hole entropies.

Activities | Google Chrome | Tue 13:52 | en | 4G

www2.yukawa.kyoto-u.ac.jp/~gtf/web/2021/

Leonard Susskind (Stanford)
Does the Holographic Principle Apply to de Sitter space, and if so, How?

Topics Covered

There have been annual workshops in Kyoto on string theory and quantum field theory for a long time, which are definitely the largest in this field in Japan. This year marks the 25th anniversary. [The contents of the past conferences are archived here.](#) This year we invite a few speakers from abroad and all the talks will be in English. We plan to have a few parallel sessions for short talks if we receive a large amount of applicants.

Registration

The registration has been closed. The registration information can be changed [here](#).

There is no registration fee.

The workshop will be held purely online, due to the worsening COVID situation in Kyoto.

The deadline of the registration for giving talks is **Thursday, July 1st**.
The deadline of the registration requesting financial support is also **Thursday, July 1st**.
The deadline of the registration for participation is **Monday, August 9th**.

The workshop consists of oral sessions and poster sessions. At the registration, a short oral talk or a presentation at virtual poster sessions can be chosen. We plan to have a few parallel sessions for short talks if we receive a large amount of applicants. We will try to accommodate your preference, but we may need to limit the number of talks. The abstract submitted at the registration will be announced at the web site later.

Slides in oral sessions and files in poster sessions will be uploaded at this web site and submitted to the [online Japanese Journal 素粒子論研究](#) (translated as "Research in high-energy physics"). We will not separately publish proceedings for this workshop. Please contact the organizers if you do not want to disclose your slides or poster files. All the talks will be broadcast online.

The organizers

Masashi Hamanaka (Nagoya University)
Koji Hashimoto (Kyoto University)
Yasuaki Hikida (Kyoto University)
Masazumi Honda (Kyoto University)
Kazuo Hosomichi (National Defense Academy)
Hiroschi Kunimoto (Kyoto University)
Kazunobu Maruyoshi (Seikei University, chair)
Takeshi Morita (Shizuoka University)
Keita Ni (Kyoto University)
Toshifumi Noumi (Kobe University)
Tadakatsu Sakai (Nagoya University/KMI)
Makoto Sakamoto (Kobe University)
Shigeki Sugimoto (Kyoto University)
Yuji Tachikawa (IPMU)
Tadashi Takayanagi (Kyoto University)
Satoshi Yanaguchi (Osaka University)
Kentaroh Yoshida (Kyoto University)

If you have any questions not covered in this webpage, please send an email to maruyoshi@st.seikei.ac.jp.